JOINT EUROPEAN TORUS JET

JET JOINT UNDERTAKING

PROGRESS REPORT 1987

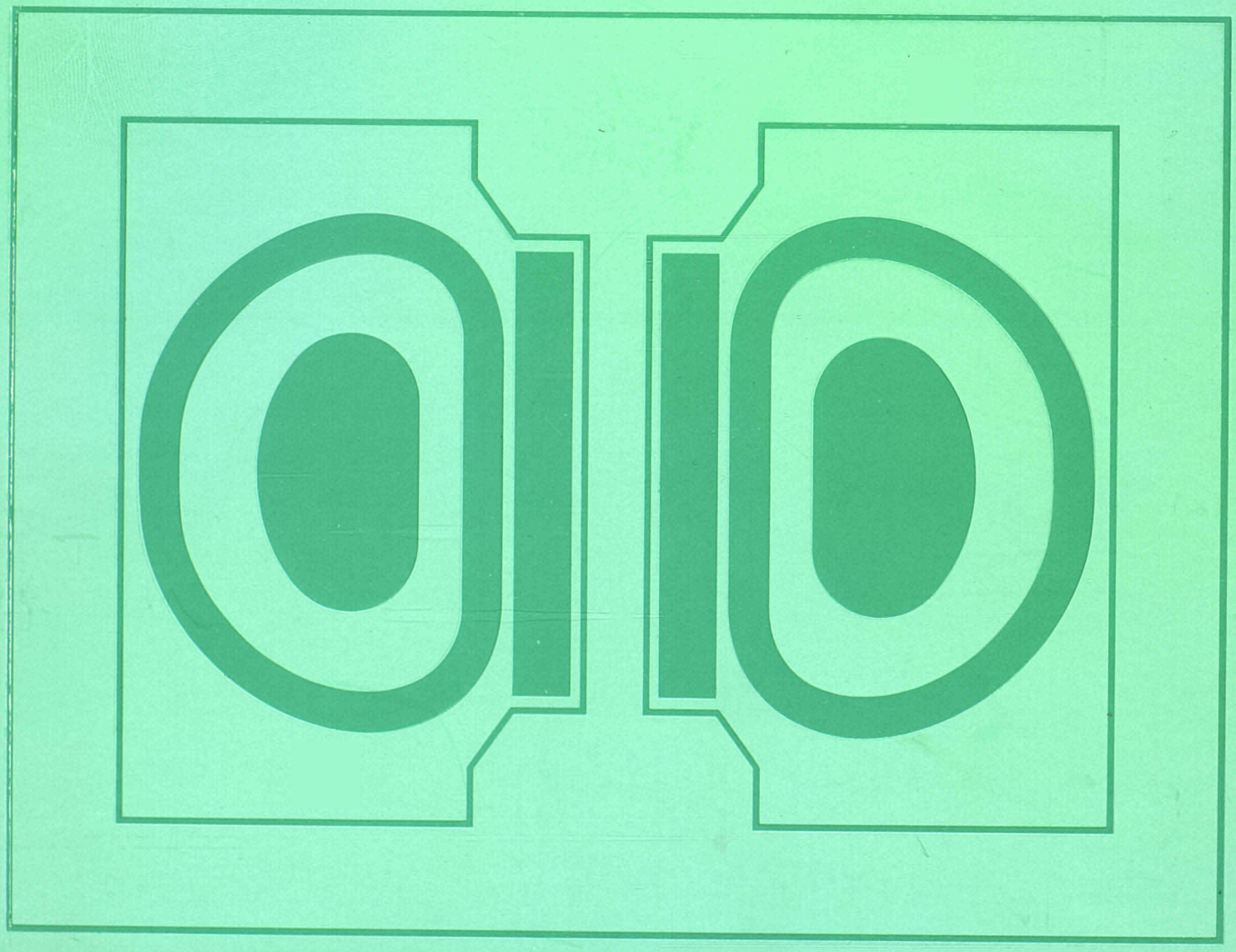

EUR 11597 EN
EUR-JET-PR5

JET JOINT UNDERTAKING

PROGRESS REPORT 1987

MARCH 1988

This document is intended for information only
and should not be used as a technical reference.

. (EUR-JET-PR5) March 1988.
Editorial work on this report was carried out by B. E. Keen
The preparation for publication was undertaken by
the Documentation Service Unit, Culham Laboratory. UK.

Printed in England

Contents

Foreword

JET Progress Reports were introduced at the start of the Operations Phase in 1983 to provide a more detailed account of JET's scientific and technical progress than that contained in the JET Annual Reports. The early Progress Reports in 1983 and 1984 provided good reference documents of developments and results during the early operation period, before JET advances were published in the conventional literature. These described the main activities and advances made on JET during the relevant periods, and concentrated on the scientific and technical involvement of the relevant JET Departments.

Subsequently, from 1985, JET results received world-wide dissemination at International Conferences and meetings and in various scientific journals, at an earlier stage. There was then less need for such a detailed record of all JET events, as the machine operated almost in a routine manner. Therefore, it was decided in 1985 to change the format of the Progress Report, so that it provide an overview summary of the scientific and technical advances during the year, and was supplemented by appendices of detailed contributions (in preprint form) of the more important JET articles published during the year. The change in format was introduced to reflect that change in circumstances. This is the fifth JET Progress Report which covers the fourth full year of JET's operation and follows that revised scheme.

The document is still aimed not only at specialists and experts engaged in nuclear fusion and plasma physics, but also at a more general scientific community. To assist in meeting these general aims, the Report contains a brief summary of the background to the Project, describes the basic objectives of JET and the principal design aspects of the machine. In addition, the Project Team structure is included as it is within this structure that the activities and responsibilities for machine operation are carried out and the scientific programme is executed.

From the technical viewpoint, 1987 proved another successful year for JET. At the beginning of 1987, JET was midway through the second of four experimental phases. This second phase is devoted to Additional Heating studies to observe the effects on plasma temperatures and confinement properties of large powers of ion cyclotron resonance heating (ICRH) and of neutral beam heating, singly and in combination.

The machine entered a planned shutdown for the first half of 1987, whilst it underwent extensive modifications and enhancements. Inside the vacuum vessel, new water cooled belt limiters were installed which replaced the eight uncooled discrete limiters; further carbon protection tiles were added to permit higher additional powers to the plasma; and uncooled carbon dump plates were fitted near magnetic X-points to permit high additional powers in the magnetic limiter configuration.

Outside the vessel, new supports were added to withstand vertical instabilities and radial disruptions at higher plasma currents and elongations; and the poloidal field coil system was modified to provide potential for higher current operation with longer flat-tops in both the material limiter ($\sim$7MA) and the magnetic limiter (X-point) ($\sim$4MA) configurations. On peripheral systems, eight water-cooled RF antennae were installed to permit higher power RF plasma heating ($\sim$24MW); a second neutral beam (NB) box was installed to permit 20MW total NB heating power; and a multi-pellet injector was installed capable of fuelling the plasma with solid D pellets of diameters 2.7mm, 4mm and 6mm at speeds up to 1.3kms^{-1}.

The machine started operation again on schedule at the end of June 1987. The first priority was then to recommission the machine in its new configuration and to commission the new equipment with plasma under operating conditions and to optimize its performance. The first experiments demonstrated the success of the modifications and the enhancements introduced during the shutdown. The plasma start-up conditions were greatly improved and permitted a reestablishment of plasma current of 5MA but with a longer 10s flat-top. Subsequently, a 6MA plasma current with a flat-top of 2s was reached.

These successes were most encouraging but operation of the machine above original design rated values was carried out with great care. A number of technical restrictions were imposed to operate the machine within conservative limits. The forces acting on the vessel during disruptions or vertical instabilities could pose risks to the mechanical integrity of the vessel and were limited by restricting operation at large plasma currents to smaller plasma elongations. The power deposited by the plasma on the water cooled RF antennae or the inboard wall was also limited to avoid damage to antennae or wall protections. These technical limitations were being addressed and tests or design modifications were being planned to allow further progress in 1988 and 1989.

On the scientific side, the general objective of Phase IIB (mid 1987-mid 1988) of Additional Heating Studies is to explore the most promising regimes for energy confinement (currents moving towards 7MA in the material limiter mode, and towards 4MA in the magnetic limiter mode) and for high fusion yield (high T_e and T_i regimes including also significant non-thermal fusion yield) at increased ICRF power (20MW) and neutral beam heating power (20MW at 80kV). The ultimate objective is to achieve full performance with the simultaneous operation of all systems. 1987 operation was a period of consolidation of this regime to ensure that the new systems were operating efficiently and to optimize their performance. During the six-month period of operation, the total number of tokamak pulses was 2889 (compared with the record number of 4902 in the 11 months of operation in 1986). In spite of the

complexity of operation with the introduction of new systems, there was a clear shift to the use of higher plasma currents compared with operations in previous years.

In spite of the exploratory nature of some of the experiments during 1987, significant results were achieved. With the upgraded ion cyclotron resonance frequency (ICRF) heating system of eight antennae, up to 16MW of power was coupled into the plasma. In such experiments during a relatively quiescient sawtooth-free ('monster' sawtooth) regime, bulk plasma ion heating was achieved (using He^3 minority ions) yielding ion temperatures on axis of 8keV in ^4He plasmas and 7keV in deuterium plasmas. In both cases, the plasma electron temperatures were up to 10keV. With a plasma current of 3.5MA, and RF power input of 16MW, a plasma stored energy of 6MJ and a D-D fusion rate of $1.4x10^{15}s^{-1}$ was achieved.

Following the successful first year of neutral injection experiments in 1986, 1987 proved to be a more difficult and somewhat disappointing year. During the major shutdown, a considerable amount of work involving planned improvements and modifications to both Octant No.8 and No.4 injection systems were successfully completed. Subsequently, three separate major hardware failures occurred during commissioning and re-commissioning of the Octant No.8 system. These faults were not associated with actual beam operation. Nevertheless, significant results were obtained during 1987. In combined NB and RF heating, a record total power of 22MW was deposited in the plasma and values of central electron temperature of 10keV with central ion temperature of 8.5keV were obtained in the material limiter configuration. In addition, during the sawtooth-free ('monster sawtooth') period of a material limiter discharge, comparable temperatures were obtained with ~15MW of combined RF and NB heating.

Only limited magnetic limiter (X-Point) experiments were carried out during 1987, mainly due to technical problems associated with the neutral beam system. Even so, stable discharges were established with a single null magnetic separatrix configuration at 3.5MA plasma current for several seconds. When neutral beam power was available and exceeded a certain threshold power, transition to the higher plasma confinement (H-mode) regime was re-established. Experiments showed a strong dependence of threshold power on toroidal field and a weak dependence on plasma current.

The use of small pellets of solid deuterium is one of the possible methods of fuelling a fusion reactor. Initial experiments have been carried out with a multi-pellet injector which JET and the US Department of Energy have jointly installed and are jointly operating under the umbrella of the Bilateral Agreement on Fusion Research. Using 2.7 and 4mm deuterium pellets, peaked density profiles with central densities well over $10^{20}m^{-3}$ have been achieved in ohmic discharges with decay times in the several seconds range. Such plasmas are planned as clean high density targets for auxiliary heating. Density build-up with a string of 10 pellets, as early as 1.5s into the plasma current ramp-up, have produced an early relatively clean high-density plasma that appears remarkably tolerant of pellet disturbances. Although, it is early to draw any definite conclusions on the role of multi-pellet injection in JET, promising and interesting features have been observed. High peak and average densities and the clean plasma produced are encouraging results.

A record value of the fusion product $< n_i(0)\tau_E T_i(0) >$ of $2x10^{20}m^{-3}.s.keV$ was achieved in 1986 with 10MW of neutral beam heating during X-point operation in the H-mode. During 1987, with limited magnetic limiter operation in the H-mode, this same maximum fusion product of $2x10^{20}m^{-3}.s.keV$ was repeated. In this case, this was achieved with only ~6MW of neutral beam input into a 3MA X-point plasma, following optmization of the various plasma parameters. However, a significant improvement was made in the fusion product with RF heating alone. A value of $1.2x10^{20}m^{-3}.s.keV$ ($n_i(0)=3.8x10^{19}$, $T_i(0)=8keV$, and $\tau_E=0.4s$) was reached using He^3 minority heating ($P_{RF}=16MW$) in a 3.5MA deuterium plasma.

The scientific results so far achieved on JET are most encouraging. In terms of plasma parameters - density, temperature and confinement - JET has already reached the stage where each of these parameters is within a factor of two or three of those needed for a fusion reactor. Considerable effort has been devoted towards the design, procurement and commissioning of equipment for installation during the 1988 shutdown and at later stages. This task is of utmost importance as the preparations will determine the future performance of JET.

New additions proposed for JET aim to build up a high density and high temperature plasma in the central region, where α-particles could be observed, while maintaining a sufficiently high energy confinement time. This is planned by: tailoring the current profile using lower hybrid current drive and neutral beam injection to eliminate or reduce sawteeth oscillations and obtain improved temperatures; increasing the central density by high velocity pellet injection; reducing edge density by edge pumping; achieving high central temperatures by on-axis ICRF heating and high energy neutral beam heating. In addition, the confinement will be improved by increasing the plasma current up to 7MA in limiter discharges and over 4MA in X-point magnetic limiter configurations. Since operations at these plasma currents constitute a considerable extension of the original design parameters, a study has been undertaken to reassess the machine and its power supplies.

The most encouraging results obtained so far are a tribute to the dedication and skill of all who work on the Project. They also reflect the co-operation and assistance received from Associated Laboratories and from the Commission of the European Communities. They support the confidence and guidance given to the management of the Project by the JET Council, JET Executive Committee and JET Scientific Council. I am sure that with such dedication from all sides, the Project will face with confidence the many problems and challenges that are likely to be encountered in the future.

Dr. P.H. Rebut
Director
March 1988

Introduction, Background and Report Summary

Introduction

The JET Progress Reports are aimed both at specialists engaged in plasma physics and nuclear fusion research and at the more general scientific community. This is in contrast to the JET Annual Reports, which are intended to provide overview descriptions of the scientific, technical and administrative status of the JET programme, which is understandable to the average member of the public. To meet the general aims of the Progress Report, it contains a brief summary of the background to the Project, it describes the basic objectives of JET and the principal design aspects of the machine. In addition, the Project Team structure is detailed, as it is within this framework that the activities and responsibilities for machine organization are carried out and the scientific programme is executed.

As for the 1985 and 1986 JET Progress Reports, the main part of the 1987 Report provides overview summaries of scientific and technical advances made during the year, supplemented by appendices of detailed contributions (in preprint form) of the most important JET technical articles produced during this year. The final part of the Report briefly sets out developments underway to further improve JET's performance and plans for future experiments through to its foreseen completion in 1992.

Background

Objectives of JET

The Joint European Torus (JET) is the largest single project of the nuclear fusion research programme of the European Atomic Energy Community (EURATOM). The project was designed with the essential objective of obtaining and studying plasma in conditions and with dimensions approaching those needed in a fusion reactor.

The studies are aimed at:

(a) investigating plasma processes and scaling laws, as plasma dimensions and parameters approach those necessary for a fusion reactor;
(b) examining and controlling plasma-wall interactions and impurity influxes in near-reactor conditions;
(c) demonstrating effective heating techniques, capable of approaching reactor temperatures in JET, in the presence of the prevailing loss processes (particularly, RF and Neutral Beam Heating processes);
(d) studying alpha-particle production, confinement and subsequent plasma interaction and heating produced as a result of fusion between deuterium and tritium.

Two of the key technological issues in the subsequent development of a fusion reactor are faced for the first time in JET. These are the use of tritium and the application of remote maintenance and repair techniques. The physics basis of the post-JET programme will be greatly strengthened if other fusion experiments currently in progress are successful. The way should then be clear to concentrate on the engineering and technical problems involved in progressing from an advanced experimental device like JET to a prototype power reactor.

Basic JET Design

To meet these overall aims, the basic JET apparatus was designed as a large tokamak device with overall dimensions of about 15m in diameter and 12m in height. A diagram of the apparatus is shown in Fig.1 and its principal parameters are given in Table I. At the heart of the machine, there is a toroidal vacuum vessel of major radius 2.96m having a D-shaped cross-section 2.5m wide by 4.2m high. During operation of the machine, a small quantity of gas (hydrogen, deuterium or tritium) is introduced into the vacuum chamber and is heated by passing a large current through the gas. Originally, the machine was designed to carry 4.8MA, but has already been modified to achieve 7MA. This current is produced by transformer action using the massive eight-limbed magnetic circuit, which dominates the apparatus (see Fig.1). A set of coils around the centre limb of the magnetic circuit forms the primary winding of the transformer with the plasma acting as the single turn secondary. Additional heating of the plasma is provided by propagating and dissipating high power radio frequency waves in the plasma and by injection beams of energetic neutral atoms into the torus.

The plasma is confined away from the walls of the vacuum vessel by a complex system of magnetic fields, in which the main component, the toroidal field, is provided by 32 D-shaped coils surrounding the vacuum vessel. This field, coupled with that produced by the current flowing through the plasma, forms the basic magnetic field for the tokamak confinement system, which provides a full design field at the plasma centre of 3.45T. The poloidal coils, position around the outside of the vacuum vessel, shape and position the plasma in operation.

Initial experiments have been undertaken using hydrogen and deuterium plasmas, but in the later stages of the operation, it is planned to operate with deuterium-tritium plasmas, so that fusion reactions can occur to produce significant α-particle heating in the plasma.

In order to reach conditions close to those relevant to a fusion reactor, a plasma density of $\sim 10^{20} m^{-3}$ at a temperature of 10keV would be needed. Even with a current of up to 7MA in JET, this would be inadequate

TABLE I
Principal Parameters

Parameter	*Value*
Plasma minor radius (horizontally), a	1.25m
Plasma minor radius (vertically), b	2.10m
Plasma major radius, R_0	2.96m
Plasma aspect ratio, R_0/a	2.37
Plasma elongation ratio, e=b/a	1.68
Flat top pulse length	10s
Toroidal magnetic field (plasma centre)	3.45T
Plasma current, D shaped plasma	4.8MA
Volt-seconds available	34Vs
Toroidal field peak power	380MW
Poloidal field peak power	300MW
Additional heating power (into torus)	~50MW
Weight of vacuum vessel	108t
Weight of toroidal field coils	364t
Weight of iron core	2800t

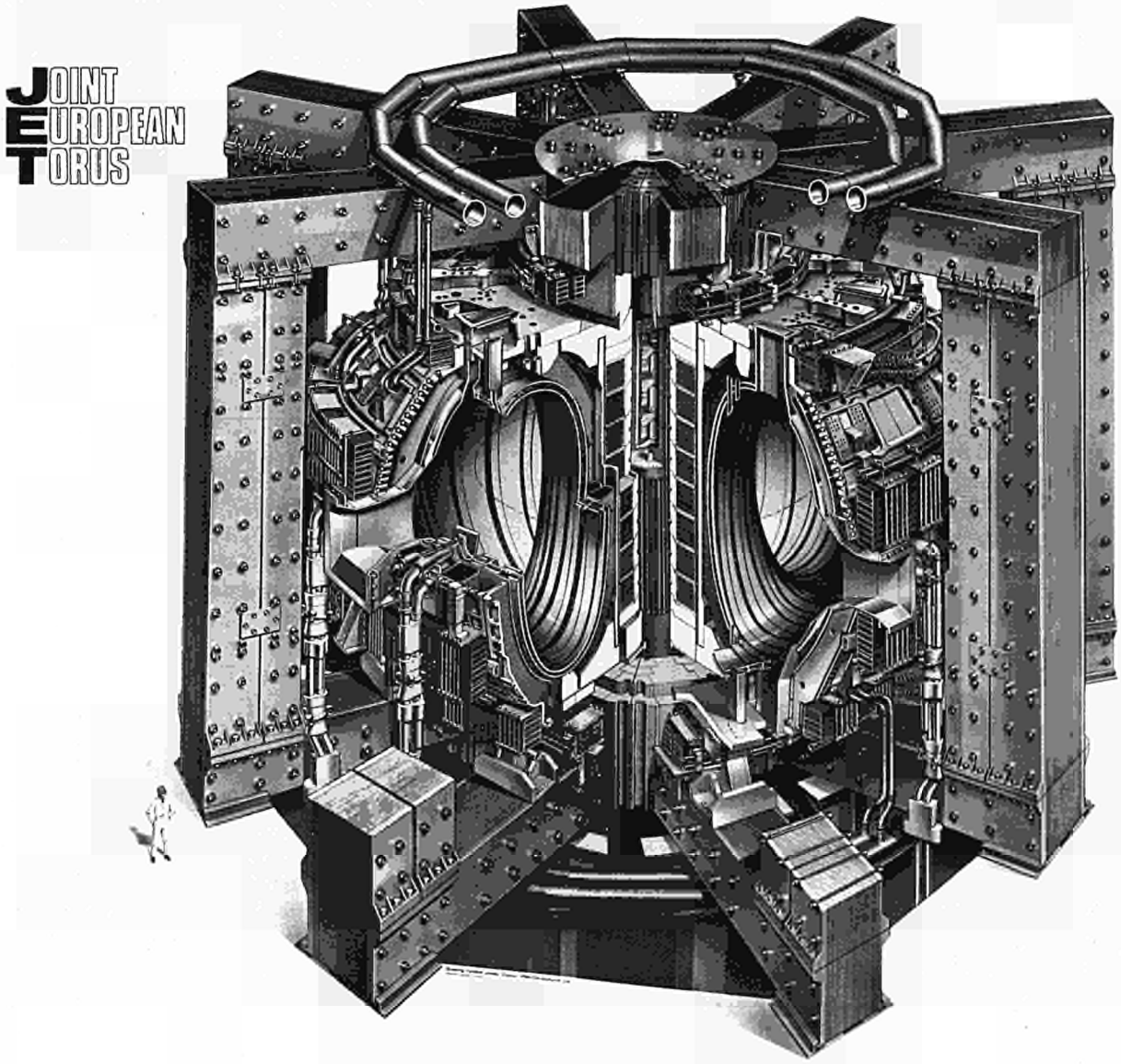

Fig.1: Diagram of the JET Tokamak

to provide the temperature required using ohmic heating alone. Consequently, additional heating is required and two main systems are being used at JET, as follows:

- Injection into the plasma of highly energetic neutral atoms (Neutral Injection Heating)
- Coupling of high power electromagnetic radiation to the plasma (Radio Frequency (RF) heating).

The total power into the torus will increase in discrete steps up to ~50MW.

Project Team Structure

The Project structure adopted, for management purposes, is divided into four Departments (see Table II):

- Machine and Development Department
- Experimental Department
- Heating and Theory Department
- Administration Department

In addition, some scientific and technical duties are carried out within the Directorate and in the Coordinating Staff Unit.

The main duties of the Administration Department have been described in previous JET Annual Reports. This Report concentrates on progress made in the scientific and technical areas during 1987. To aid this description, the functions of these Departments are described below.

Machine and Development Department

The Machine and Development Department is responsible for the performance capacity of the machine as well as equipment for the active phase, together with enhancements directly related to it (excluding heating) and the integration of any new elements on to the machine. In addition, the Department is responsible for machine services. The Department contains three Divisions:

(a) Magnet and Power Supplies Division, which is responsible for the design, installation, operation, maintenance and modification of all power supply equipment needed by the Project. In addition, the Department is responsible for maintenance and operation of the coil systems, structural components and machine instrumentation;

(b) First Wall Division, which is responsible for the vital area of plasma wall interactions. Its main tasks include the provision and maintenance inside the vacuum vessel of conditions leading to high quality plasma discharges. The Division develops, designs, procures and installs first wall systems and components, such as limiters, wall protections and internal pumping devices. The area of responsibility encompasses the vacuum vessel as a whole, together with its associated systems, such as pumping, bake-out and gas introduction;

TABLE II

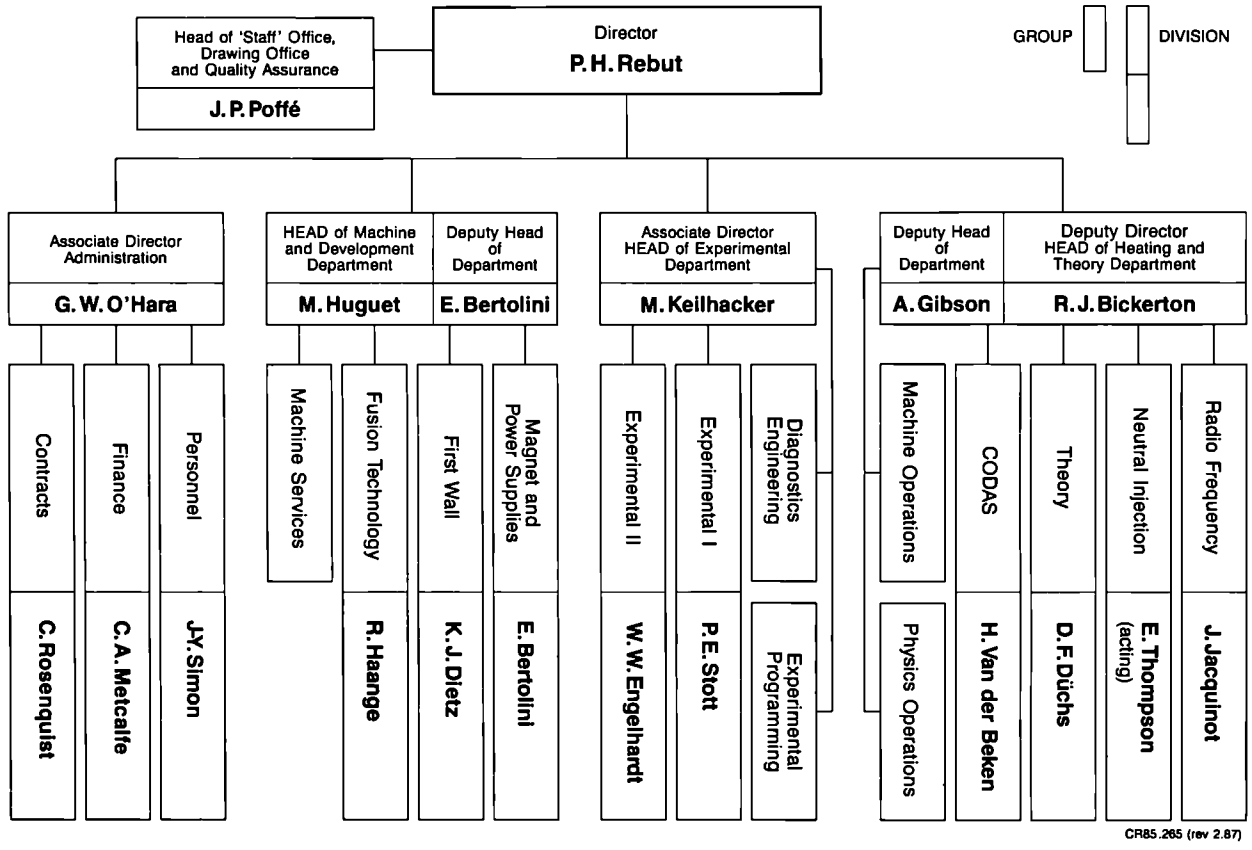

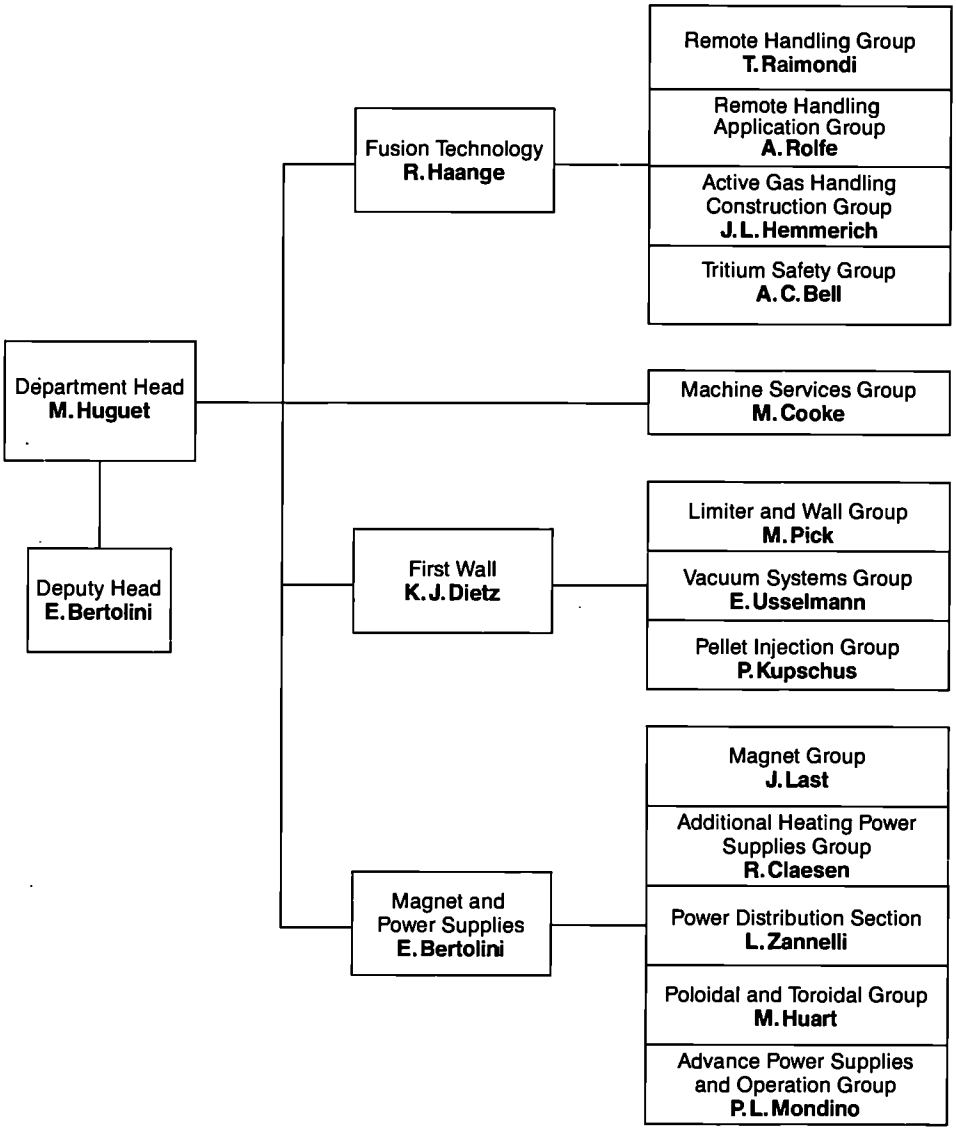

Fig.2: Machine and Development Department, Group Structure (December 1987)

(c) Fusion Technology Division, which is responsible for the design and development of remote handling methods and tools to cope with the requirements of the JET device, and for maintenance, inspection and repairs. Tasks also include the design and construction of facilities for handling of tritium.

The Structure of the Machine and Development Department to Group Leader level is shown in Fig.2 and the list of staff within the Department is shown in Fig.3.

Experimental Department

The main functions of the Department relate to the measurement and validation of plasma parameters. The main tasks are:

- to conceive and define a set of coherent measurements;
- to be responsible for the construction of necessary diagnostics;
- to be responsible for the operation of the diagnostics and the quality of measurements and the definition of the plasma parameters;
- to play a major role in the interpretation of data.

The Department contains two Groups (on Diagnostics Engineering and Data Processing and Analysis Group) and two Divisions:

(a) Experimental Division 1 (ED1), which is responsible for specification, procurement and operation of approximately half the JET diagnostic systems. ED1 undertakes electrical measurements, electron temperature measurements, surface and limiter physics and neutron diagnostics;

(b) Experimental Division 2 (ED2), which is responsible for specification, procurement and operation of the other half of the JET diagnostic systems. ED2 undertakes all spectroscopic diagnostics, bolometry, interferometry, the soft X-ray array and neutral particle analysis.

MACHINE AND DEVELOPMENT DEPARTMENT

Head of Department: M. Huguet
Deputy Head of Department: E. Bertolini

D Carre	L Nickesson	M Walravens
Mrs H Marriott	L Sonnerup	

MAGNET AND POWER SUPPLIES DIVISION
Head: E Bertolini

Mrs C Allen	D Halliwell	A Santagiustina
P Bertoldi	M Huart	S Shaw
T Bonicelli	A Keymer	A Skinstad
I Borch	J R Last	S Turley
O Buc	V Marchese	J van Veen
D Cacaut	G Marcon	N Walker
J Carwardine	L Mears	Mrs L T Wall
C Christodoulopoulos	A Moissonnier	C R Wilson
R Claesen	P Mondino	G C Wilson
Mrs A Cranstone	G Murphy	M E Young
E Daly	Mrs J Nolan	L Zannelli
H T Fielding	P Noll	J Zwart
J Goff	C Raymond	

FUSION TECHNOLOGY DIVISION
Head: R Haange

A C Bell	J L Hemmerich	P Presle
S J Booth	Mrs M E Jones	T Raimondi
P Brown	L P D F Jones	J Removille
C Caldwell-Nichols	A Konstantellos	J J Riley
R Cusack	E Küssel	A Tesini
L Galbiati	A Nowak	M Tschudin
A Galetsas	Miss S Perrissin-Fabert	M Wykes
J Gowman		

FIRST WALL DIVISION
Head: K Dietz

W P Bailey	L Grobusch	J Orchard
L Baylor	G Hammet	M Pick
B Bignaux	D Holland	L Rossi
H Buttgereit	Mrs I Hyde	R L Shaw
G Celentano	G Israel	K Sonnenberg
P Colestock	H Jensen	R Thomas
Mrs D Cranmer	T Jernigan	E Usselmann
W Daser	P Kupschus	M Walravens
E Deksnis	P McCarthy	T Winkel
C Froger	S Milora	M Zarnstorff
M Gadeberg		

Fig.3: Project Team Staff in Machine and Development Department (December 1987)

The structure of the Experimental Department to Group Leader level is shown in Fig.4 and the list of staff in the Department is shown in Fig.5.

Heating and Theory Department

Heating and Theory Department is responsible for heating the plasma, the theory of tokamak physics, the organisation of experimental data, and the day to day operation of the machine. The main functions of the Department are:

- following the theory of tokamak physics;
- heating the plasma and analysis of its effects;
- centralising the interpretation of experimental results and investigating their coherence;
- organising data acquisition and computers;
- preparing and co-ordinating operation of the machine across the different Departments.

The Department is composed of three groups (Machine Operations Group, Physics Operation Group and Data Management Group) and four Divisions:

(a) Control and Data Acquisition System Division (CODAS), which is responsible for the implementation, upgrading and operation of computer-based control and data acquisition systems for JET;

(b) Neutral Beam Heating Division, which is responsible for the construction, installation, commissioning and operation of the neutral injection system, including development towards full power operation of the device. The Division also participates in studies of the physics of neutral beam heating;

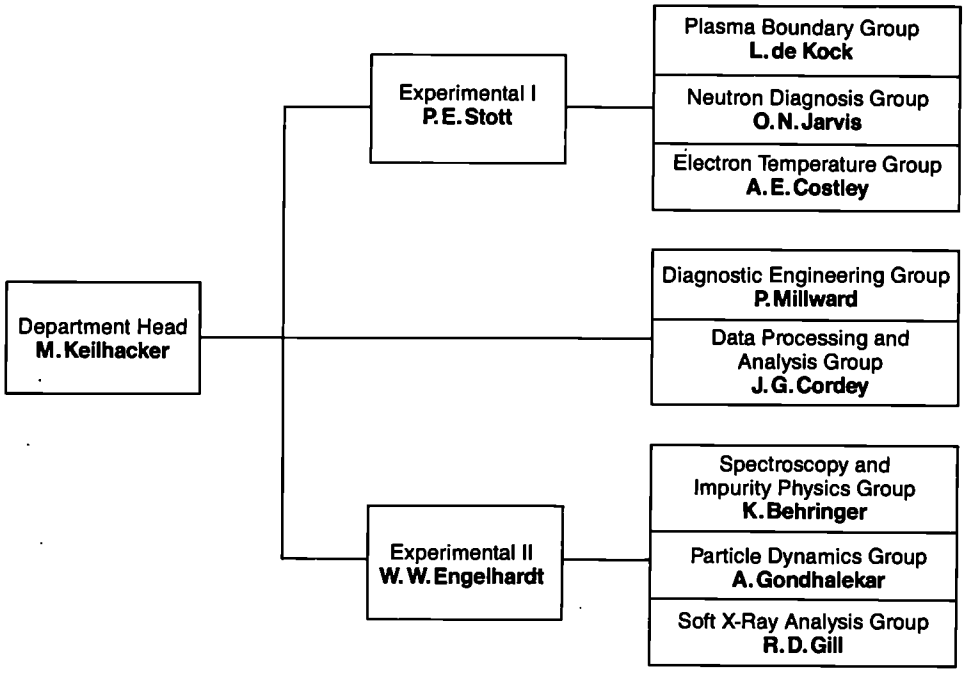

Fig.4: Experimental Department, Group Structure (December 1987)

EXPERIMENTAL DEPARTMENT

Head of Department: M. Keilhacker

M Barnes
C H Best
J Christiansen
J G Cordey
C J Hancock
J Hoekzema
Miss J Kedward
P Millward
M Newman
R Oord
Miss A Reichenau
J Reid
P J Roberts
F Sieweke
Miss K Slavin
Mrs P Stubberfield
A R Talbot
A Tiscornia
E van der Goot
M L Watkins
C H Wilson
D Wilson

EXPERIMENTAL DIVISION I

Head: P Stott

Miss N Avery
D Bartlett
B W Brown
D Campbell
J Coad
A Costley
L de Kock
J Fessey
C Gowers
P J Harbour
M Hone
I Hurdle
O Jarvis
J Källne
G Neill
C Nicholson
P Neilsen
R Prentice
P Roach
G Sadler
A Stevens
Miss D Strange
D Summers
P van Belle
J Vince

EXPERIMENTAL DIVISION II

Head: W Engelhardt

K Behringer
G Braithwaite
J L Bonnerue
A D Cheetham
S Corti
Miss G Denne
A Edwards
Mrs A Flowers
R Gill
A Gondhalekar
J Holm
Mrs S Humphreys
E Källne
L Lamb
G Magyar
J L Martin
P Morgan
J O'Rourke
A Ravestein
J Ryan
B K Scheidt
Mrs M Paddon
M Stamp
M von Hellerman
B Viaccoz

Fig.5: Project Team Staff in the Experimental Department (December 1987)

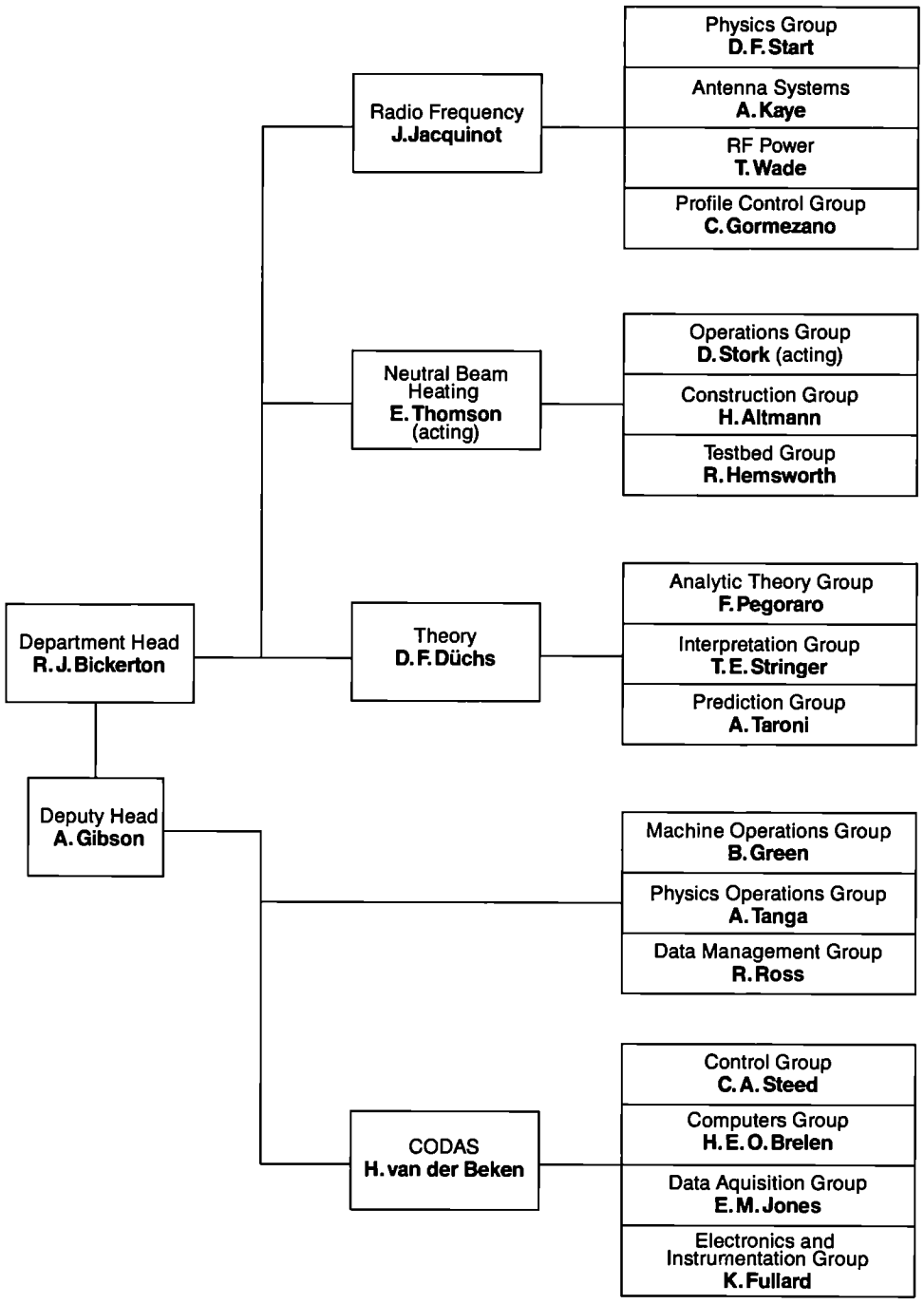

Fig.6: Heating and Theory Department, Group Structure (December 1987)

(c) Radio Frequency Heating Division, which is responsible for the design, construction, commissioning and operating the RF heating system during the different stages of its development to full power. The Division also participates in studies of the physics of RF heating;

(d) Theory Division, which is responsible for prediction by computer simulation of JET performance, interpretation of JET data and the application of analytic plasma theory to gain an understanding of JET physics.

The structure of the Heating and Theory Department to Group Leader level is shown in Fig.6, and the list of staff in the Department is shown in Fig.7.

In addition, all Divisions are involved in:

- execution of the experimental programme;
- interpretation of results in collaboration with other appropriate Divisions and Departments;
- making proposals for future experiments.

Directorate

Within the Directorate are two scientific and technical groups, Scientific Assistants to the Director and Technical Assistant to the Director (including

HEATING AND THEORY DEPARTMENT

Head of Department: R. J. Bickerton
Deputy Head of Department: A. Gibson

K Adams	M Hughes	Mrs M E Rowe
P Chuilon	P Lomas	P Rutter
A Conway	C Lowry	W Smith
D Cook	M Macrae	Miss A Strange
S Cooper	M Malacarne	A Tanga
T Dale	Mrs M Pacco-Düchs	P Thomas
B Green	D Pratt	R Thomson
N Green	R Rigley	B Tubbing
R Hausherr	J Roberts	M Walker
C Hookham	R T Ross	J Wesson

THEORY DIVISION
Head: D F Düchs

M Brusati	Mrs S Hutchinson	R Simonini
W Core	B Keegan	P Smeulders
Mrs S Costar	E Lazzaro	E Springmann
A Galway	Miss M Nave	T E Stringer
N A Gottardi	F Pegoraro	A Taroni
T Hellsten	C Sack	

NEUTRAL BEAM HEATING DIVISION
Acting Head: E Thompson

H Altmann	A Goede	D Martin
A Browne	R Hemsworth	P Massmann
C D Challis	F Hurd	C Mayaux
D Cooper	D Hurford	W Obert
J F Davies	J Jensen	S Papastergiou
G Deschamps	A Jones	D Raisbeck
A Dines	T T C Jones	Mrs S Sinclair
D Ewers	D Kausch	D Stork
H Falter	F Long	R Tivey
Mrs S Gerring	J Lundqvist	

RADIO FREQUENCY HEATING DIVISION
Head: J Jacquinot

V Bhatnagar	A Franklin	P Murray
S C Booth	B Glossop	M Pain
G Bosia	C Gormezano	J Plancoulaine
M Brandon	E Hanley	M Schmid
H Brinkschulte	R Horn	Miss V Shaw
M Bures	G Jessop	G Sibley
G Cottrell	A Kaye	D Start
T Dobbing	M Lennholm	T Wade
D T Edwards	Miss J Maymond	C Walker

CONTROL AND DATA ACQUISITION SYSTEMS DIVISION
Head: H van der Beken

Mrs A M Bellido	J J Davis	D Nassi
Mrs L Brookes	S E Dorling	C G Pollard
M Botman	R F Herzog	G Rhoden
H Brelen	E M Jones	C A Steed
W Brewerton	G J Kelly	B A Wallender
T Budd	N G Kidd	I D Young
P Card	J G Krom	

Fig.7: Project Team Staff in the Heating and Theory Department (December 1987)

Publications Office), whose main tasks are as follows:

- Scientific Assistants to the Director, who assist and advise the Director on scientific aspects of JET operation and future development;
- Technical Assistant to the Director, who assists and advises the Director on organizational and technical matters related to JET operation and also acts as JET Publications Officer.

Coordinating Staff Unit

The Coordinating Staff Unit is responsible for the provision of engineering services to the whole project

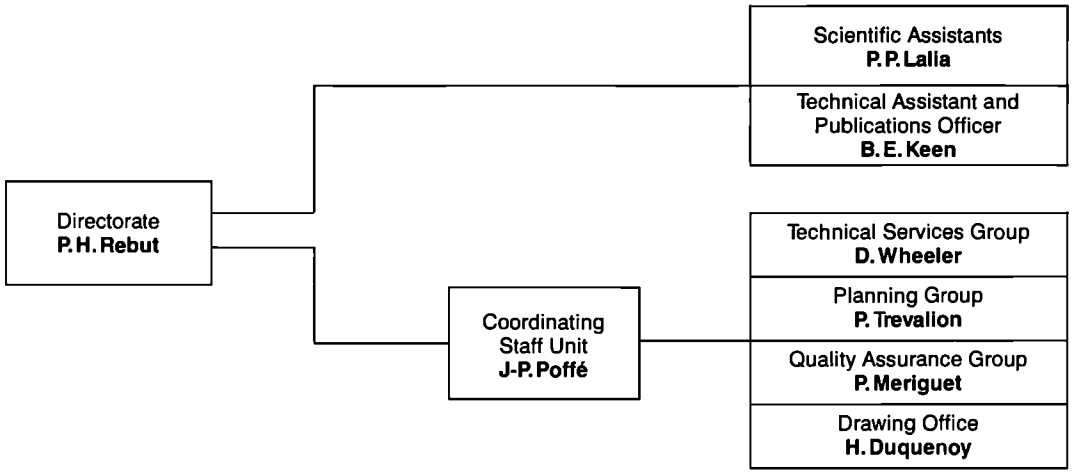

Fig.8: Directorate and Coordinating Staff Unit, Group Structure (December 1987)

DIRECTORATE AND COORDINATING STAFF UNIT

Director: Dr P H Rebut

DIRECTORATE

Mrs S-J Ashwood
M Drew
Mrs M Hicks
M Hugon
B E Keen
P P Lallia
J McMahon
P Mendonca
T O'Hanlon
Mrs C Simmons
Ms M Straub
Mrs J Talbot
Mrs H S Tyndel

COORDINATING STAFF UNIT

Head: J-P Poffé

Ms L Ashby
P Barker
G Dalle-Carbonare
Mrs D Dalziel
N Davies
H Duquenoy
G Edgar
L French
M Guillet
Mrs E Harries
R Howes
Mrs N McCullough
S McLaughlin
P Meriguet
H Panissie
P Trevalion
C Woodward

and for the implementation of specific coordinating tasks at the Project level.
It comprises four groups:

- the Technical Services Group;
- the Planning Group;
- the Drawing Office
- the Quality Assurance Group

The structure of the Directorate and Coordinating Staff Unit to Group Leader level is shown in Fig.8 and the list of staff in these areas is shown in Fig.9.

Report Summary

Section 1 of this Report provides a brief introduction and background information relevant to the Report. Sections 2 and 3 sets out an overview of progress on JET during 1987 and with a survey of scientific and technical achievements during 1987 sets these advances in their general context. This summary is specifically cross-referenced to reports and articles prepared and presented by JET staff during 1987. The more important of these articles which are of general interest, are reproduced as appendices to this Report.

Section 4 is devoted to future plans and certain developments which might enable improvements/ modifications of the machine to further improve its overall performance. These improvements might overcome certain limitations encountered generally on Tokamaks, particularly concerned with density limits, with plasma MHD behaviour, with impurities and with

plasma transport. Some attention has been devoted to methods of surmounting these limitations and these are detailed in this section.

The Appendices contain a list of work topics carried out under Task Agreements with various Association Laboratories, and selected articles prepared by JET authors are reproduced in detail, providing some details of the activities and achievements made on JET during 1987. In addition, a full list is included of all Articles, Reports and Conference papers published in 1987 by JET authors.

Technical Achievements During 1987

Torus Systems

New elements which had been procured during 1986 were installed and commissioned mostly during the first half of 1987. Such components were the interface for the multiple pellet injector; the in-vessel components such as the belt limiter and carbon fibre wall protection; and auxiliary equipment like the baking plant. In addition, extensive maintenance work was carried out on vacuum equipment, e.g. pumps and instrumentation.

The second half of the year was dedicated to gaining operational experience with the new equipment and implementing necessary minor modifications. In addition, preparations for the 1989 shutdown were started, especially on procurement contracts for major new in-vessel components which had to be placed for such items as saddle coils, separatrix dump plates and related wall protection tiles. Development work for the prototype high-speed pellet injector also had to be brought to a state where selection could be made and technical solutions to the remaining problems could be identified.

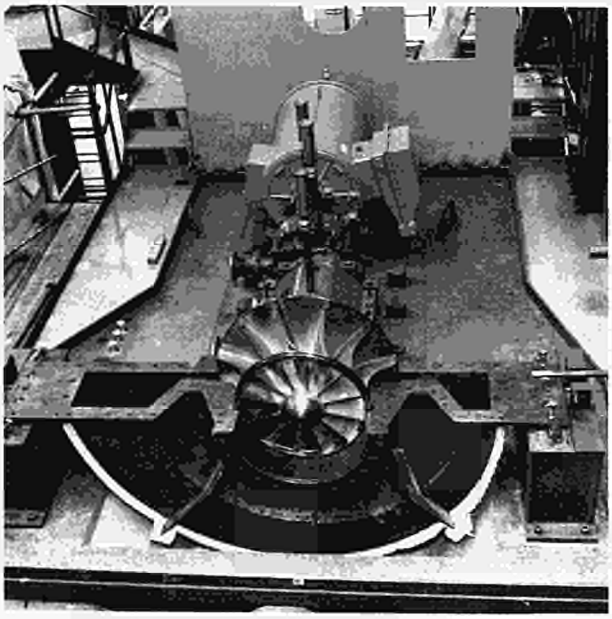

Fig.10 The blower for the gas baking system.

Vacuum Systems

The pumping system underwent a major maintenance during the 1987 shutdown, in which pumps, gauges and valves were checked and serviceable parts were exchanged (e.g. the bearings for the main turbo pumps). As a consequence, extensive recommissioning work was required at the end of the shutdown.

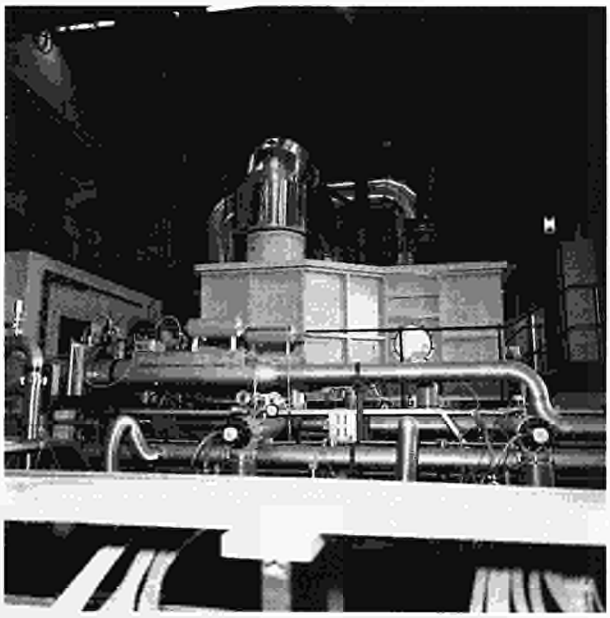

Fig.11 The gas baking system blower enclosed in a gas tight housing.

The gas baking system was completely rebuilt to be compatible with JET's active phase of operation. The blower (Fig.10) was enclosed in a gas tight housing (Fig.11) in order to prevent heating gas (which might be active at a later stage) from leaking through the shaft seal to the outside environment. The enclosure necessitated a new water cooled driving motor (310 kW) and accordingly required a new control system (Fig.12).

A further major activity during the shutdown was the provision of services for leak testing of new in-vessel components before and after installation into the vessel for such items as belt-limiters, RF antennae, electrical feedthroughs, windows, etc.

In addition, other activities started which are required for a simplified safe and reliable operation of auxiliary

Fig.12 Control system for gas baking system.

systems during the tritium phase. On the gas introduction system, an all metal gas inlet valve with a piezo-electric drive was developed and installed on the torus. It allows throughputs of up to 800mbℓs^{-1} (for deuterium) and can be used simultaneously for gas puffing at the start of a discharge and dosing during a discharge. In contrast to the existing dosing valves, it is vacuum tight in the closed position. This valve is undergoing tests and, if proven reliable, it could replace the existing fast gas inlet and dosing valves. the number of valves in the gas introduction system could then be reduced from 24 to 12.

A leak test telescope is under construction, based on a standard quadrupole mass analyser which will be placed under vacuum in front of the component to be leak tested. Spatial resolution is achieved by a differentially pumped tube (telescope) in front of the measuring head. Phase sensitive detection of pressure differentials should allow the detection leak rates as small as 10^{-6}mbℓs^{-1} from a distance of 50cm. The special Omegatron based leak detector which was developed during 1986 was used on JET and it is now possible to detect leaks of 10^{-9}mbℓs^{-1} even in the presence of deuterium with the vessel at ambient temperature.

The radiation resistance of absolute manometers and residual gas analysers is not yet sufficient for operation during the tritium phase, and development has started to remedy this situation. A proof of principle experiment for a residual gas analyser was set-up which eliminates radiation sensitive electronics close to the measuring head. An operational prototype is now being planned.

A collecting system for exhaust gases from the torus was set-up in order to investigate the particular balance between gas inlet and gas outlet and to study the gas composition of the gases pumped out. In particular, data resulting from these measurements are required for the tritium system. Preliminary results indicate that during plasma operation only ~25% of the deuterium injected into JET is released even after waiting for times of up to eight hours. Such an effect could be explained by co-deposition of graphite and hydrogen inside the vessel during a discharge and may have serious implications for the tritium inventory. Further investigations of how to surmount this problem are underway.

In-vessel Components

During the shutdown, more than 50% of the internal surface was covered with graphite tiles. This includes 15m^2 of carbon tiles installed in the new toroidal limiter, the 40 poloidal belts of graphite tiles covering the U-joints and bellows, as well as a 2m high ring (~20m^2) of carbon tiles at the inner wall of the torus. A ring of tiles in the equatorial plane of the torus consists of carbon fibre reinforced graphite (CFC). Fig.13 is an internal view of the vacuum vessel showing belt limiter, octant joint and bellows protection, inner wall protection and RF-antennae [1].

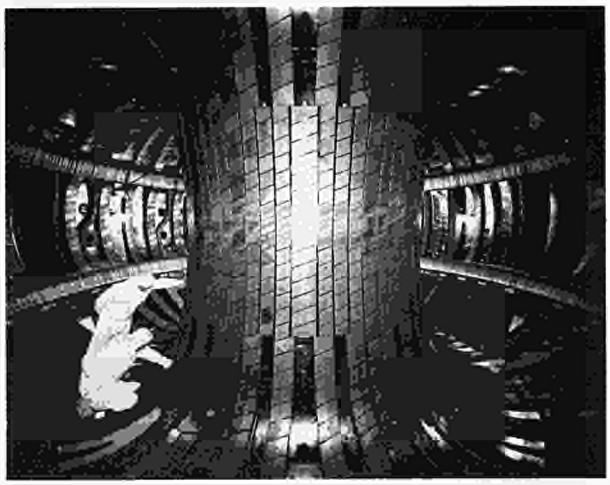

Fig.13 Internal view of the vacuum vessel at the end of the 1987 shutdown.

Operational experience with the new components show that its power bearing qualities are good. However, small modifications to the surface shape of the inner wall will have to be introduced to increase the power handling capabilities up to 40MW for 10s. The regions close to the octant joints especially will require some shimming. Severe power loading conditions (up to 500MJm^{-2} during disruptions) did not result in failure of the CFC tiles, although severe erosion (up to 2mm per event) was observed. Fine grain graphite fractured under such power loadings, and was observed during earlier JET operation periods[2].

The belt limiter was installed and positioned as accurately as possible with a maximum deviation of ±1mm from a perfect circle. Evenly distributed power loading was observed in a toroidal direction by proper adjustment of the plasma position, between the upper and lower belt. As a consequence, the belt limiter can now handle power loadings in excess of 40MW for 10s.

During the next major shutdown which is planned to

start at the end of 1988, the inside of the vacuum vessel will undergo its last major modifications; saddle coils, divertor dump plates and modified wall protection will be introduced. Eight saddle coils will be installed, four located at the top and four at the bottom of the vessel, each with an area of $\sim 6\,m^2$ covering one and a half octants each. The coils have three windings and will be driven at voltages of up to 5 kV, currents up to 5 kA and frequencies from DC to 10,000 Hz. They will be used to stabilize the $m=2$, $n=1$ instability mode by counteracting mode locking. The coils are bakeable to $\sim 500°C$ and will be protected from the plasma by fine grain graphite. The coils are now under manufacture and will be available for installation during the 1988 shutdown.

Divertor dump plates will be installed at the top and the bottom of the machine for use during high current X-point operations. The surface in contact with the plasma will be $\sim 26\,m^2$. These consist of a water-cooled support structure (Nicrofer 7612) covered with 24 mm thick tiles of CFC graphite. The tiles are pressure contacted to a backplate and inertia cooling is employed. Prototype dump plates have been manufactured and their series production is now underway.

The existing wall protection has had to be modified in order to blend in with the saddle coils and the dump plates. To prevent runaway damage and to allow for higher power loadings during normal operation, more CFC graphite will be used and protruding edges will be removed.

For the last few years, preparation has been made to use beryllium as an alternative to graphite in the event that major difficulties are experienced with graphite subjected to high power loads in discharges of long duration. Problems might be encountered with impurity production, dilution, density limits, density control and tritium inventory. High power long pulse operation in JET has not yet started and, therefore, it is too early to arrive at firm conclusions. Beryllium could be used as soon as it is deemed necessary as the beryllium tiles for the belt limiter are now available. The graphite belt limiter tiles would be exchanged for beryllium and all other areas of the vessel directly in contact with plasma would be covered by a beryllium layer $\sim 10\,\mu m$ thick. Four evaporators capable of evaporating 1 kg beryllium each are available for that purpose. For a few tens of discharges, after each deposition, the vessel would be available with a surface consisting mainly of beryllium. Evaporator tests have been carried out with nickel being evaporated instead of using beryllium. Tests will be repeated with beryllium as soon as it is decided to introduce this material into the torus.

Pellet Injection

In a collaboration agreement between the U.S. Department of Energy (USDoE) and JET, a multi-pellet injector was installed, commissioned, and operated. It consists of the pellet launcher, auxiliary equipment (called the Pellet Interface) and the respective controls. The pellet launcher was provided by DoE and built by Oak Ridge National Laboratory (ORNL), U.S.A., and delivers pellets with sizes of 2.7, 4 and 6 mm from three different barrels at repetition frequencies of several per second each. It was delivered in April and is scheduled to operate on JET until the end of 1989[3]. It was installed on the Pellet Interface, the major part of which is the pellet injector box (PIB) and its large cryopump system of the type used in the JET neutral beam injectors. Cryopump, conventional vacuum system and the liquid helium distribution to the launcher were already assembled and commissioned and so were the pellet diagnostics (pellet in-flight photography, mass and speed measurement) and the associated controls[4]. Despite the careful clarification of the specification details to assure a good match between the launcher and the Pellet Interface, considerable effort was needed to merge the two systems into one unit, especially with the dual-control system.

The entire injector (Fig.14) is now being operated from JET's main Control Room and, during the operational phase in the second half of 1987, has delivered multiple pellets of all three sizes to the plasma.

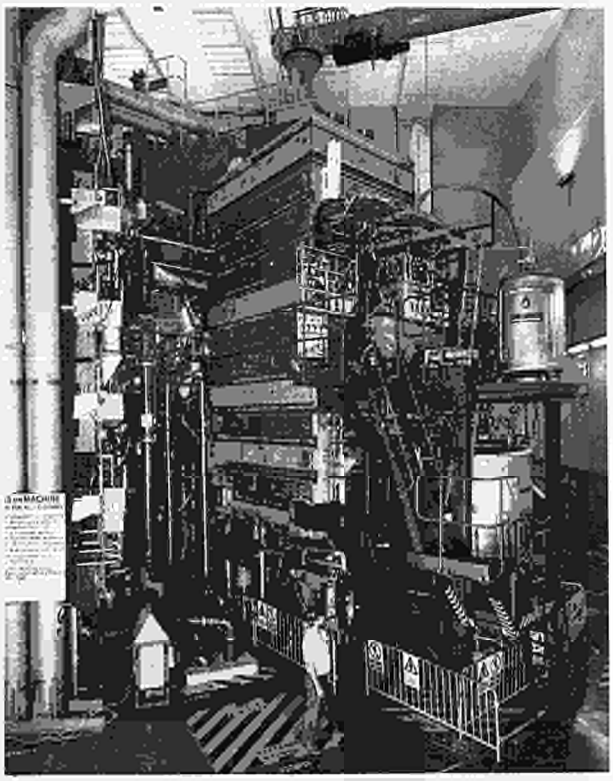

Fig.14 View of the multi-pellet injector installed on JET.

The Agreement on Pellet Injection Collaboration with the U.S. Department of Energy, within the framework of the EURATOM–USDoE Bilateral Agreement on Fusion Research, was signed in 1987. The collaboration is now well underway; the launcher was brought to JET and on average four scientists will participate in the joint pellet programme up to the end of 1989. The strength

of the U.S. team, though fluctuating in numbers, has been maintained over most of 1987. The pellet injector was operated jointly and successfully and the participation of U.S. scientists and engineers has proved fruitful.

In parallel with the operation of the pellet injector, development towards a prototype high-speed launcher has proceeded. It is planned to install a launcher at JET at the end of 1988 (in addition to the ORNL launcher), which will be able to deliver 6mm pellets at a rate of one per discharge and at speeds exceeding $4\,km\,s^{-1}$. During 1987, the basic problems have been identified and possible solutions have been tested [5]. For the prototype, a two-stage gun will be employed with the pellet encapsulated in a cartridge during the acceleration phase. Maximum speeds of $3800\,m\,s^{-1}$ have been achieved so far using this technique. This limitation resulted from the driving system, which will be modified to increase the speed.

Containment of Forces Acting on the Vacuum Vessel

In the course of the reassessment of the behaviour of all machine components in preparation for operation at plasma currents up to 7MA, considerable effort was devoted to better estimating the forces acting on the vacuum vessel and the strength of the vessel itself. The events which generate large forces in the vacuum vessel are radial plasma disruptions and vertical instabilities which produce respectively larger radial and vertical forces on the vessel.

The forces arising in the case of a radial disruption are caused by induced currents in the toroidal and poloidal directions and these currents interact, respectively, with the poloidal and toroidal field to give rise to resultant centripetal forces. The induced toroidal currents have been analysed with the help of the NET Team, Garching, F.R.G., using the computer code Proteus. Induced poloidal currents are due to the paramagnetic behaviour of the plasma and have been analysed analytically. For the stress analysis of the vacuum vessel, a large and complete finite element model has been established.

The result of the calculations showed that during a disruption starting at a current of 7MA, the total resultant centripetal force acting on the vessel would be close to 3000 tonnes (i.e. about five times the force due to atmospheric pressure alone). Moreover, the distribution of the forces would result in large radial displacements of the inboard wall of the vessel and of the vertical ports at the upper and lower parts of the vessel. These displacements and the associated level of stress in certain critical areas (in particular, at the base of the vertical ports) could have in the long term endangered the structural integrity of the vessel itself and also perhaps of some of the in-vessel water cooled components, such as the X-point dump plates. Therefore, it was decided to strengthen the vessel against such forces. At the end of 1987 a design featuring reinforcing closed rings welded inside the vessel at the inboard wall was in preparation.

Considerable effort was also devoted to better understanding phenomena associated with the generation of vertical forces during vertical instabilities. A model was developed by the University of Napoli, Italy, where the forces were no longer explained by poloidal currents driven by a MHD effect, but instead by a local pressure effect due to the deformation of the plasma when it hit the vessel wall.

Tests where vertical instabilities were triggered intentionally were also conducted to better characterize the forces and the associated vessel displacements. The vertical force depends in a complex way on the plasma current, the configuration of the vertical and shaping field and also the toroidal field through the q value. The tests have allowed the formulation of more accurate scaling laws, in order to extrapolate the intensity of the expected vertical force at large plasma currents. According to these scaling laws the maximum vertical force to be expected at 7MA would be in the range 800–1000 tonnes.

The vacuum vessel supports, which were installed during the 1987 shutdown, did not initially behave as expected. This was in part due to the fact that the design had been based on the vessel movements measured during JET Pulse No.1947, when a vertical instability was first observed. Vertical instabilities in 1987 were generally not as fast as in Pulse No.1947 and as a result the inertial brakes would not properly lock. This difficulty was circumvented by decreasing the stiffness of the springs which controlled the position of the inertial brakes.

Another problem was that of friction. The free displacement of the brakes during slow thermal expansion or contraction of the vessel would not take place due to friction in the bearings. Therefore, some of the brakes would lock while the vacuum vessel was being heated up from room temperature to 300°C, or cooled down. This was a serious problem since restraining the natural expansion or contraction of the vessel was unduly stressing some critical welds at the base of the vertical ports.

New bearings based on a low friction PTFE based material were manufactured and when installed these improved the situation but did not fully cure the problem. At the end of 1987, it seemed that residual friction was still present and was due to overheating and clearances were over-tight in the spherical bearings connecting the brakes to the ports. Modifications are planned to eliminate this problem. It was also decided to fit the inertial brakes with active locking devices which would guarantee that all brakes would lock during plasma operation. This new feature is planned for installation in 1988.

From the vertical instability tests conducted in 1987, it became apparent that the forces acting during a vertical instability are not truly vertical but also contain

radial components which provide a moment and twist to the vessel about the equatorial plane. Although the vessel supports contain the vertical components adequately, the twisting moment cannot be resisted and result in large radial displacements of the vertical ports. These displacements do not seem to pose a serious problem as far as the vacuum vessel is concerned but affect systems attached to the ports. For this reason, it was planned to reduce the amplitude of these displacements by hydraulic dampers.

References

[1] M. Pick, G. Celentano, E. Deksnis, K.J. Dietz, R. Shaw, K. Sonnenberg, M. Walravens, 'Experience with Graphite in JET.' Proc. of 12th Symp. Fus. Eng., Monterey, U.S.A., October 1987;

[2] K.J. Dietz, 'Experience with Limiter and Wall Materials in JET.' J. Nucl. Mat. **154–156** (1987);

[3] S. Milora, S. Combs, C. Fonst, F. Gethers, 'A Three-Barrel Repeating Pneumatic Pellet Injector for Plasma Fuelling of the Joint European Torus', Proc. of 12th Symp. Fus. Eng. Monterey, U.S.A., October 1987;

[4] P. Kupschus, W. Bailey, M. Gadeberg L. Hedley, P. Twynam, T. Szabo, D. Evans, 'The JET Multi-Pellet Injector Launcher Machine Interface', Proc. of 12th Symp. Fus. Eng., Monterey, U.S.A., October 1987:

[5] K. Sonnenberg, P. Kupschus, W. Bailey, J. Helm, P. Krehl, G. Claudet, F. Disdier, J. Lafferranderie, 'High-Speed Pellet Development', Proc. of 12th Symp. Fus. Eng., Monterey, U.S.A., October 1987.

Power Supplies and Magnet Systems

The JET electromagnetic system is made up of the toroidal and poloidal coils, the purpose of which is to establish, maintain and control the tokamak magnetic configuration (see Fig.15). It includes the toroidal coils, the poloidal coil P1, acting as primary winding of the tokamak transformer and the coils P2, P3 and P4 to control plasma radial position, vertical position and shape. In order to perform these functions, the coils must be energized by suitable DC power supplies, whose voltages and currents are controlled in real-time by the plasma position and current control system (PPCC). Additional DC power supplies energize the neutral beam and radio frequency plasma additional heating systems. The total installed DC power rquired by JET is well in excess of 1500MVA with a peak above 1000MW and a energy content per pulse up to 10,000MJ. More than half of the power and of the energy is taken directly from the Grid at 400kV and the rest is provided by two vertical shaft flywheel generators. Consequently, a major feature of the JET power supply scheme is the 400kV–33kV distribution system. Auxiliary power is supplied by the 20MVA, 11kV–3.3kV–415V distribution system.

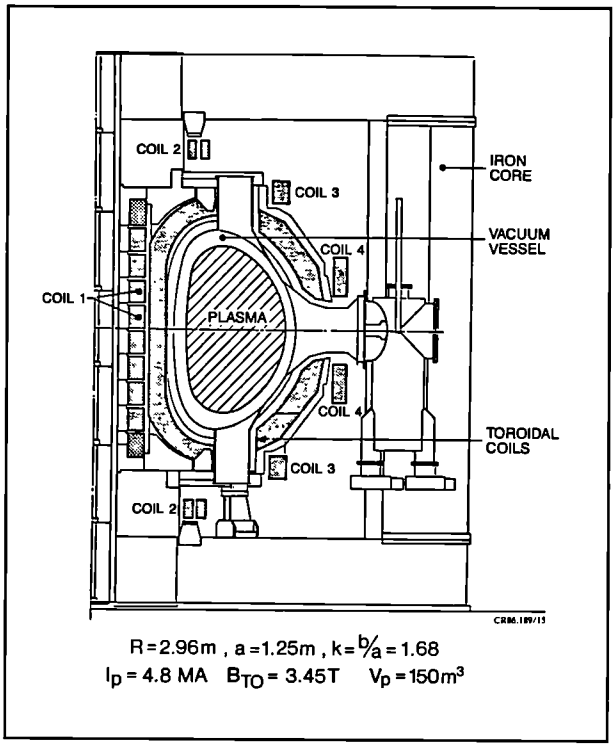

Fig.15 Cross-section of JET showing toroidal and poloidal coils.

The development programme to bring JET, first to its full design performance and subsequently well above, calls for continuous modification and upgrading of the electromagnetic system. The key objective of 1987 was to extend the JET operating regime to above 5MA in material limiter configurations and to above 3MA in magnetic limiter ('X-Point') configurations. The JET electromagnetic system has been upgraded to allow plasma currents up to 7MA with material limiter and up to 4MA with magnetic limiter, while detailed studies have been carried out to investigate the feasibility of setting up X-Point configurations approaching 7MA.

Magnet System

During the 1986–87 shutdown, major modifications have been carried out on the magnet systems, as follows:

(a) two subcoils were added to the poloidal coil P1 increasing the total to ten, with the objective of reducing stray fields at breakdown, and thus improving plasma start-up conditions. This involved dismantling the whole upper part of the machine (Fig.16);

(b) an additional busbar was connected to the six central subcoils (see Fig.15) to allow separate control of the current in these coils relative to the end coils. This enabled an increase in available flux swing by increasing the maximum current in the central coils from 40kA to 60kA and an improved flexibility in control of plasma shape. This was made possible by taking advantage of the centering force of the toroidal coils which counteract the outward force of P1, when energized.

During this work a design problem was discovered.

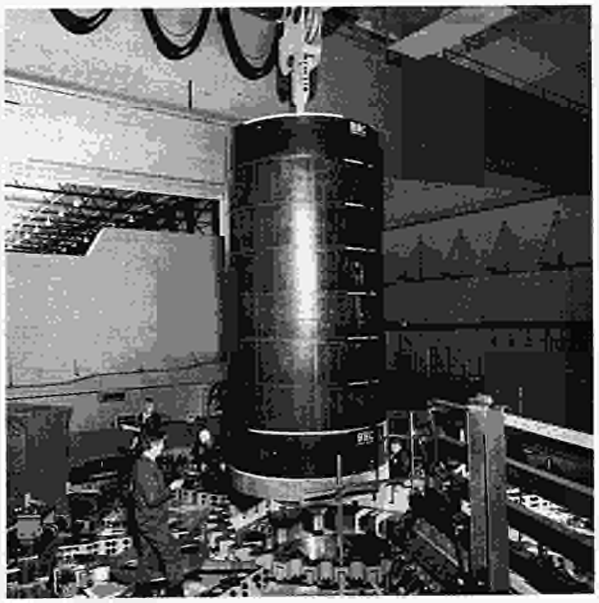

Fig.16 The disassembly of the top of the JET Machine to make a ten subcoil stack within the P1 coil.

When the P1 coil was removed and the stack disassembled, some slight damage was observed on the subcoils. Keys which located and prevented relative rotation of the subcoils were fractured due to the torsional action of the toroidal field coils. To prevent re-occurrence of this effect the subcoil interface was modified: the number of interlocking keys was increased from 1 to 12 per subcoil and spring assemblies were fitted so that the coils returned to their starting point after each pulse (Fig.17). New equipment to monitor rotational displacement was also installed. Modifications were also made to the coil busbar system to match power supply requirements and to the coil protection system to allow asymmetric single X-point operation.

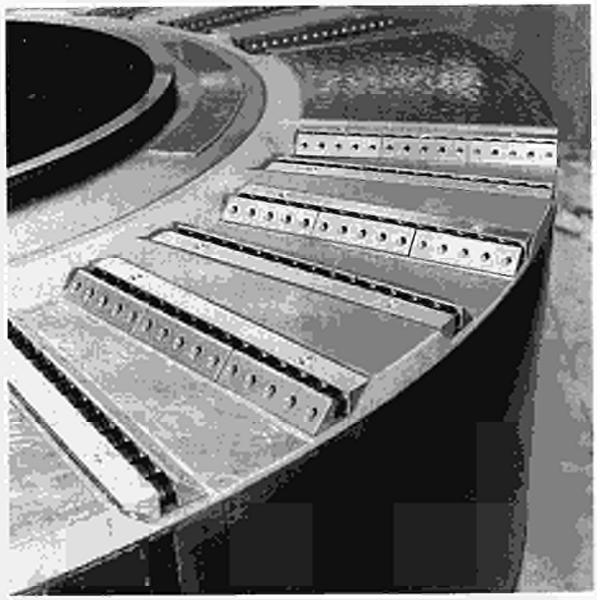

Fig.17 Assembly of the new spring keys between the P1 subcoils to improve electromechanical behaviour during operation.

Magnet Power Supplies

Implementation of enhancements to the poloidal power supplies has been a major activity. A modulation circuit has been integrated into the existing poloidal circuit, leading to the new circuit shown in Fig.18. Besides previous key functions of establishing and controlling plasma current, the circuit now makes provision for the following additions:

(a) stray fields at breakdown are further reduced (below the level obtained with the installation of ten P1 subcoils), by supplying from the PFX circuit the six central subcoils with a slightly lower current (a few kA) than the premagnetization current (nominal value 40 kA), flowing in the end subcoils;

(b) the rate of increase of the plasma current is controlled during the early phase of the pulse, by the additional switching network. This is complemented by upgrading the voltage capability of the vertical field amplifiers (PVFA) with the addition of booster amplifiers;

(c) the flux swing is enhanced (up to 40 Wb) by supplying the central six P1 subcoils with a 60 kA current from PFX (while the end subcoils carry 40 kA);

(d) X-point configurations above the 1986 plasma current levels are actively established using PFX by maintaining currents up to 40 kA in the central P1 subcoils above the value in the end subcoils.

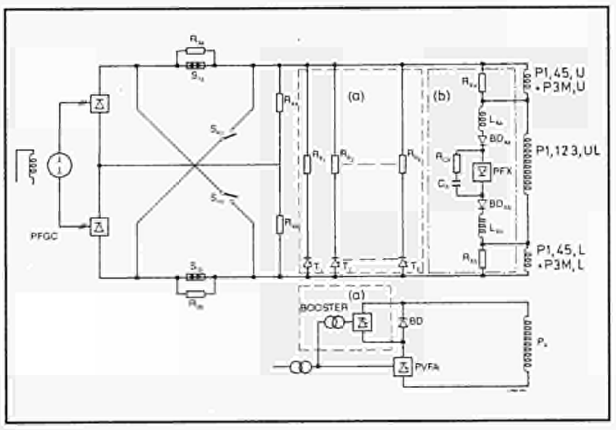

Fig.18 The new poloidal circuit, showing (a) the additional switching network, (b) the PFX unit, and (c) the booster amplifiers.

Item (a) has not yet been implemented, but the remaining features are now available, except that the 10 kV PVFA booster (to be delivered during early 1988) is currently replaced by a temporary 2.8 kV booster.

The possibility of using this modified circuit for operation at X-point plasma currents well above 4 MA has been abandoned, as it would require a new P2 coil to provide the flux requirements (3 times higher) and the upper support structure of the toroidal coils would need strengthening against the substantially increased twisting force. Although a preliminary study has shown that such a scheme would be feasible, the time and effort involved would make such a modification impractical

within the planned life of the Project. However, a new scheme has been proposed in which a 7MA X-point configuration could be achieved by driving the upper and lower P4 coils out of balance by about 500 ampere-turns. Thus, additional windings would not be required. This scheme would also have the advantage of transferring the additional shear stresses on the toroidal coils towards less stressed regions and so make additional structural supports unnecessary. The selected scheme shown in Fig.19, basically relies on modifications of the PVFA control scheme only. This makes the new domain of operation available by mid-1988, provided the stress analysis on the coils proves acceptable (as suggested by preliminary calculations).

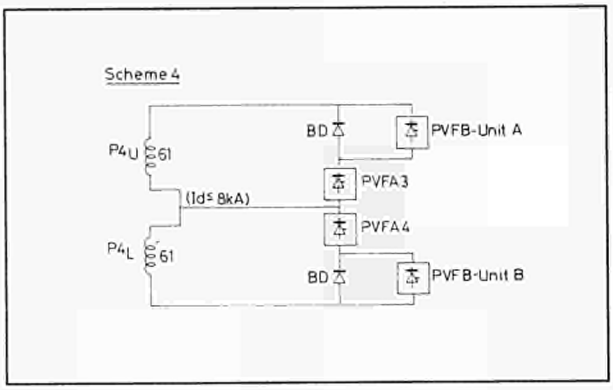

Fig.19 The scheme proposed for establishing X-point configurations up to 7MA.

Designs for power supply schemes (1–5kA, 1–2kV, 0–10kHz) to energize eight saddle coils have also been evaluated with the help of two study contracts with major manufacturers . These will be used to feedback stabilize the $m=2$ and $n=1$ oscillation modes (thus preventing ensuing radial disruptions).

Plasma Control

The Plasma Position and Current Control (PPCC) system has been enhanced by replacing the analogue plasma current controller by a new digital subsystem which includes the feedback control of the difference current between the central and the end sections of the P1 coil. Two signals are generated by this system: one for the excitation of the poloidal flywheel generator convertor, used for feedback control of the premagnetization current and the plasma current; and the other signal is used for voltage control of the PFX amplifier, employed for feedback control of the P1 coil difference current. The new system also includes facilities for automatic current limitation in the central and end sections of the P1 coil. The system has performed successfully during JET operation.

Detailed design has started of a dual system for the stabilization of the vertical plasma position. The present stabilization system provides an automatic feedback loop gain correction for the case when one of the two series connected radial field amplifiers trips due to an internal fault. The additional objective of the dual system is also to harden the circuit against single faults in the measurement and control section. For this purpose, vertical position changes are measured at two opposite octants to control independently the voltage of the two amplifiers: a 1kHz AC test signal is continuously injected at the input of each magnetic signal amplifier and the corresponding AC component in the two control signals is compared with that of a dummy channel to discover any abnormal signal transmission. In the event of a fault in one measurement branch, the control signal of the healthy branch is routed to both radial field amplifiers.

Moreover, experimental tests have shown that

Fig.20 Outdoor AC-DC high voltage power supplies for neutral beams and ICRH. The bays for the LHCD power supplies are also shown.

magnetic signal integrators can be omitted if proportional feedback control is added to the existing integral feedback control of the average radial field amplifier current, without sacrifice in stabilization performance. This result allows a substantial simplification of the stabilization system.

Additional Heating Power Supplies

There are three systems of additional heating power supplies (Fig.20): the neutral beam and the ion cyclotron radio frequency systems already in operation, and the lower hybrid radio frequency system at present under procurement.

There are three subsystems of the neutral beam power supplies already installed. These are the Testbed, Octant No.8 and Octant No.4 systems, of which the Testbed, with two 80kV, 60A beam lines operates routinely. Only six beam lines are operational in the Octant No.8 system due to both beam line and power supply problems. A fire in the protection system enclosure No.5 caused vaporization of mercury from the power supply ignitrons of one crowbar, thus making the enclosure equipment unusable. Extensive design modifications/additions have been introduced into the protection circuits and all crowbar insulators have now been replaced by non-flammable materials.

The Octant No.4 system has been completed and commissioning with PINI's has started, including all modifications already implemented in the Octant No.8 system. At present, four beam lines are under commissioning with PINI's and the whole system is scheduled for operation at the end of January 1988. A set of new power supplies (525V, 270A with current rates up to $300 A s^{-1}$) have been designed and are under procurement. These will energize coils for active control of stray magnetic fields inside the two PINI boxes, when operating at plasma currents up to 7MA.

The full system of eight ICRH (Ion Cyclotron Radiofrequency Heating) Generators is operating routinely. However, during 1987, the system has been gradually upgraded by replacing all 1.5MW tetrodes with 2.0MW tetrodes in the RF generators. A new set of power supplies has been designed to supply the drivers, while the existing power supplies (originally designed to include the drivers) will eventually supply only the output stage of the generators. Since the new driver power supplies are still under manufacture and not all the 2.0MW tetrodes are available, only three generators were operated at the new power level, using the ICRH testbed power supply to supply the three drivers as a temporary measure. The design of the new set of LHCD (Lower Hybrid Current Drive) power supplies has been completed, together with the tendering procedures, leading to the placing of two major orders, one for the main power supply and the other for the crowbars due to protect the klystrons. There will be five of these power supplies, one for the Testbed and four for the actual system. Each supply will feed four klystrons, delivering a voltage to be regulated between −40 and −70kV at a current of 100A. Delivery will start at the end of 1988. However, the Testbed will have a temporary supply much earlier, making use (with minor modifications) of one of the neutral beam power supplies.

Power Distribution

With the 400kV system already developed to its full capacity, effort on power distribution has been fully devoted to a major extension of the AC auxiliary power system, to cope with requirements for diagnostics, electromagnetic system, additional heating, CODAS, buildings and machine services. At the end of the shutdown (June 1987), over 100km of new cables of forty different types are installed. Activity was split into 13 major areas involving up to eighty workers.

Even after resuming operations, design and installation work continued. Major jobs included electrical services for the new building J20 and the toroidal magnet cooling water chillers. In addition, routine maintenance of the 400kV–33kV and 11kV–3.3kV–415V distribution systems was carried out and a long list of small jobs was completed entailing handling of about 6,000 documents.

JET Operation

The Division is heavily involved in operation, with four (out of seven) Engineers-in-Charge, five Power Supply Operation Engineers (the same professional staff serving also as Session Leaders during Machine commissioning), twelve Power Supply Operators, eight Additional Heating Power Supply Operators and four stand-by electricians and fitters. Moreover, the Division also provides an Electrical Engineer on-call service throughout the year, with six people involved in these duties. These operational duties are additional to the continuing key role of the Divisional staff in the implementation of the Project Development Plan, which still requires the placing and managing of a large number of major contracts each one preceded by the appropriate design work.

Of the new systems made operational during 1987, each have met the design performance, as follows:

(a) The P1 coil stack, with 10 subcoils, have allowed stray fields to be reduced by more than a factor of two, which, in conjunction with the additional switching network and the temporary PVFA booster, has made 22kV, 40kA premagnetization breakdown possible, thus allowing good plasma start-up in the required scenarios;

(b) the PFX scheme, with the four busbar connection to the P1 coils, has allowed an increase in the flux swing, so that plasma currents of 5MA for 10s and of 6MA for 2s could be sustained. X-point configurations up to 3.5MA plasma currents for more than 8s have been established. It has also permitted greater flexibility in plasma shape control.

Future Activities

Effort has been devoted to future schemes within the forward JET Programme, as follows:

(i) Magnet System

(a) implementation of the scheme for the extension of X-point operation up to 7MA (see Fig.19), which implies a new PVFA and Booster layout (to allow for independent control of the upper and lower P4 coil current), a new control device, additional machine protections, additions to DMSS (Direct Magnet Safety System), new features in the PPCC and an extensive system analysis in both operational and fault conditions;

(b) extension of the current capability of the vertical field amplifiers (PVFA), the shaping amplifers (PSFA) and PFX, if necessary, to 40kA, 15s;

(c) upgrading PFX in voltage by using existing power supply (PVFA2) as a booster;

(d) digitization of the plasma position control and implementation of the dual control system for PRFA (Poloidal Radial Field Amplifiers), to make available two fully independent systems for controlling vertical instabilities. It is also proposed to implement an automatic reduction of destabilizing shaping currents in the event of reaching stabilization limits;

(e) completion of tests on the toroidal prototype coil to assess ultimate shear stress capabilities of electrical insulation and bonding material;

(f) completion of engineering analysis, aided by computer codes, for the stresses on both toroidal and poloidal coils in the new operating scenarios;

(g) detailed design, tender specifications and contract procedures for the power supplies for the feedback control of the $m = 2$ and $n = 1$ modes, when a decision to proceed is taken;

(h) tender technical specification and contract procedures for the active and reactive power compensation systems to shield the Grid from excessive demand expected by the implementation of all JET new features;

(i) specification and procurement of inductors and resistances required for the active stray field compensation circuit (see Fig.18);

(j) improvement in reliability of power supplies by better maintenance procedures and design modifications;

(ii) Additional Heating

(k) on the NB systems, completion of modifications required in the power supplies to improve reliability and availability; installation and commissioning of the power supplies for stray field compensation in the PINI box; procurement of all the necessary components for 160kV operation;

(l) installation and commissioning of the power supplies for the upgrade of ICRH drivers;

(m) supervision of contracts for LHCD power supplies and installation of the first unit before the end of 1988;

(n) modification of a pair of neutral beam power supplies to be used, on alternative weeks, for neutral beams or for the LHCD testbed;

(o) routine maintenance;

(iii) Power Distribution

(p) procurement installation and commissioning of new cubicles and cabling for pellet injection, remote handling, LHCD, J20 and J25 buildings, lighting in J2, J4 and J1H;

(q) full implementation of the earthing of all metallic structures in the Torus Hall;

(r) routine maintenance of the 400kV–33kV and 11kV–3.3kV–415V distribution systems;

(iv) JET Operation

(s) commissioning on JET of all new equipment due to come into operation, as itemized above;

(t) serving as Session Leaders, Engineers-in-Charge, Power Supply Operation Engineers and other operational duties as mentioned previously.

Neutral Beam Heating System

Following the very successful first year of neutral injection experiments during 1986, 1987 proved to be more difficult and a somewhat disappointing period in terms of injection into the tokamak. During the major 1987 shutdown period, a considerable amount of work involving planned improvements and modifications to both the Octant No.8 and No.4 injection systems were successfully completed. Subsequently, three separate major hardware failures occurred during the commissioning (and re-commissioning) of the Octant No.8 injection system. These faults which are described below were not associated with actual beam operation and they occurred at times during which no voltage was applied to the beam sources, and hence no power was being extracted.

Work in the N.B. Testbed has continued both in support of the injection systems installed on the tokamak and, in conjunction with further development of high heat transfer elements. Considerable upgrading of the cryogenic plant was successfully completed to allow routine simultaneous operation of three large cryopumps plus additional liquid helium supplies (i.e. for the Octant No.8 and No.4 N.B. systems and for the pellet injection system).

Neutral Beam Operations

Neutral Beam injection into the tokamak was severely curtailed during 1987, due to a series of faults, none of which was directly related to actual operation of the beam system.

Shortly after restarting the Octant No.8 N.B. system in mid-1987 after shutdown, a water leak developed spontaneously in one of the second-stage neutralizers. Following replacement of this component and recovery from the water leak, a second neutralizer failed. Neither failure was associated with beam operation and was due to delamination between layers of electrodeposited copper. All of these components will be replaced by new

neutralizers manufactured using technologies other than electrodeposition.

A third and different fault occurred during subsequent re-commissioning of the system. One of the ignitron crowbars suffered a catastrophic failure prior to a beam pulse. The resulting fire (confined to one protection system) resulted in only six power systems out of the full complement of eight being available. Considerable down-time was necessary during which all the power systems were modified to include additional protection circuitry and to replace combustible materials in the crowbar unit by ceramic components. The six beams of the Octant No.8 system were eventually brought into synchronous operation with the tokamak in December 1987.

Conditioning of the tokamak beam entrance duct was accomplished in approximately six beam pulses into the tokamak as evidenced by direct measurements of the neutral gas pressure in the duct (see Fig.21). The first beam pulse clearly desorbs a large quantity of gas from the walls of the duct, but subsequent pulses show the gas release is almost one order of magnitude less.

Immediately following duct conditioning, the first long pulse injection experiments resulted in re-establishing H-mode confinement in single-null X-point discharges. The injected power is presently being increased from 6MW D° at 70kV extraction to 7.5MW at 80kV from the six sources available. Operation of all eight sources is expected by mid-1988 following the repair of the damaged power supply.

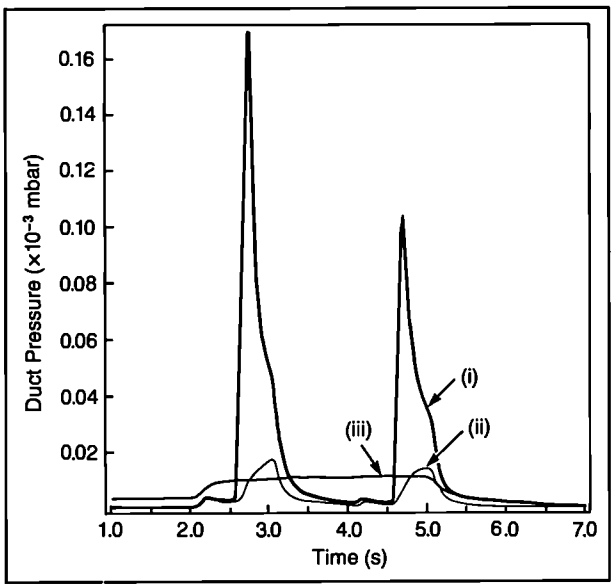

Fig.21 Measured pressure in beam duct for three different cases: (i) two of the first beam pulses (~ 1MW for 0.5s) through the duct liners (ii) the subsequent repeated pulse and (iii) the asymptotic behaviour for a 6MW, 3s beam pulse.

Octant No.4 N.B. system has been brought into operation and is in the final stages of commissioning. All eight plasma sources have been successfully operated and beam extraction obtained from four sources. Commissioning of the systems up to full power is paced by the availability of the power systems. Injection into the tokamaks is scheduled for early 1988.

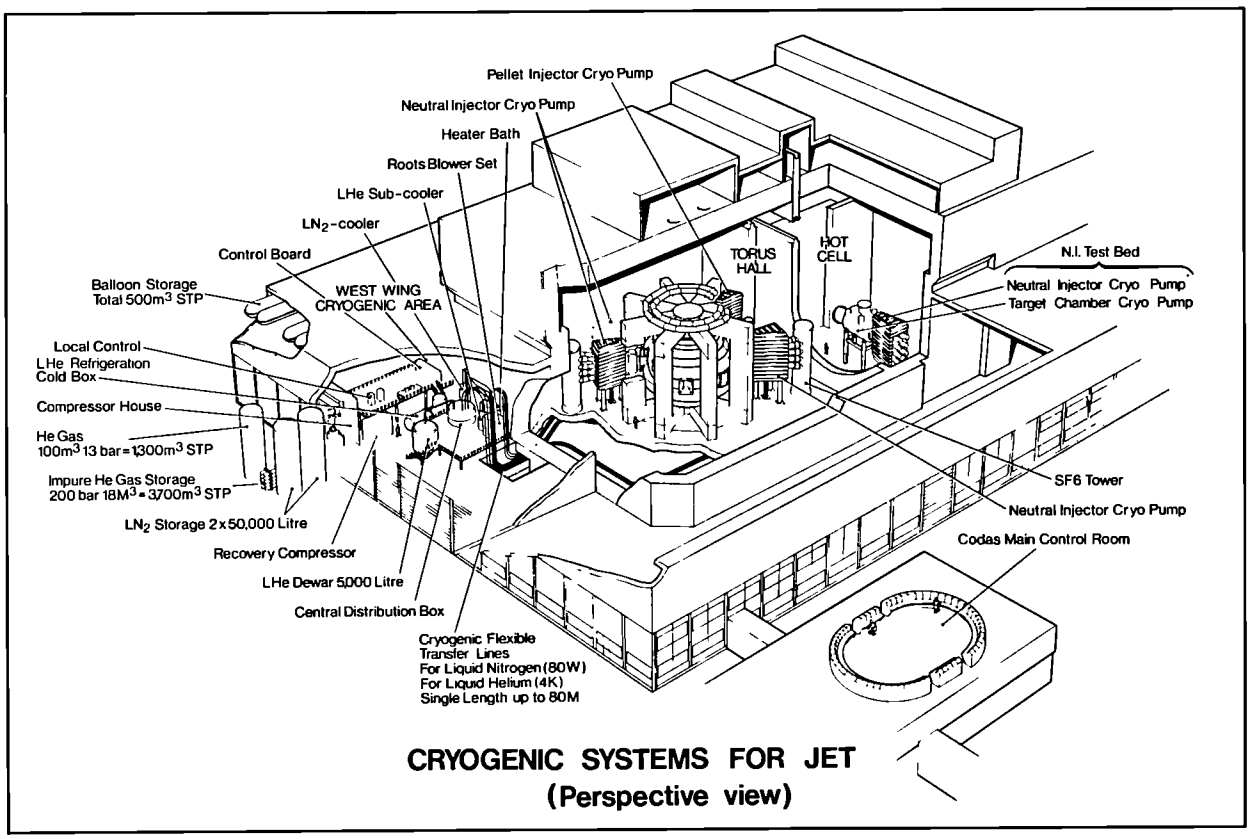

Fig.22 Schematic of cryosystem after upgrading;

Cryo-Systems

The main activities have been the refurbishing and upgrading of the liquid helium (LHe) cryoplant and of the liquid nitrogen (LN_2) supply system, the installation, test and commissioning of the cryopump system for the multi-pellet injector, the installation and commissioning of the LHe supply system for the pellet launcher and, since the beginning of the operation phase of JET, the routine simultaneous operation of three cyropump systems (two neutral injector, one pellet injector) together with the transfer of bulk LHe ($\sim 1000\ell$/day) to the pellet launchers (see Fig.22).

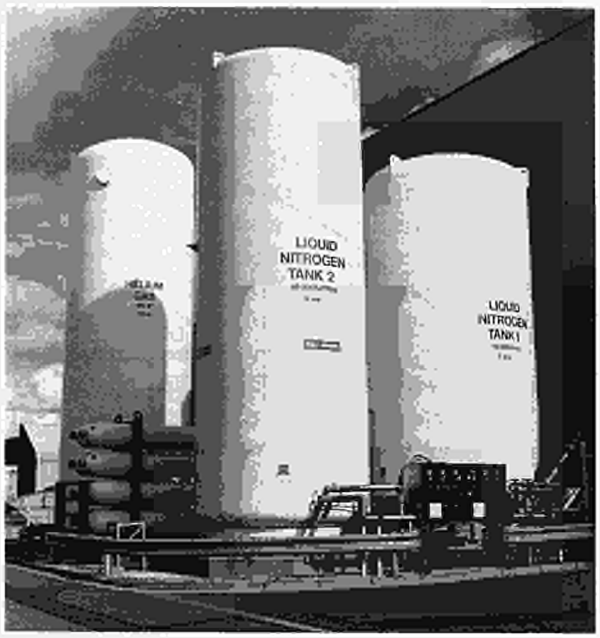

Fig.23 Upgraded Cryosystem showing LN_2 tank, LHe buffer tank, and high pressure storage cylinder;

In particular, the main developments have been, as follows:

(i) Liquid Nitrogen (LN_2) and Liquid Helium (LHe) Supply System

(a) the LN_2 system storage capacity was upgraded by 60,000 litres to a new total of 110,000 litres (see Fig.23), and integrated into the existing system with a new control system and software:

(b) the LHe refrigerator capacity was upgraded from approximately 500W to a new total in excess of 800W at 4.2K to cope with the additional requirement of the pellet injector system. The upgrade of the power was achieved by installation of new enlarged turbines, new heat exchangers, an upgraded cold ejector and by modifying the process control;

(c) the storage capacity for gaseous helium was upgraded by installing a new He buffer tank ($100m^3$, 15bar) high pressure storage cylinders with a new total capacity of $200m^3$ at 250bar and low pressure recovery balloons with a new total of $400m^3$ storage capacity. The installation of an upgraded purifier and He recovery compressor was postponed until 1988;

(ii) *Cryopump Systems*

(d) a new cryopump system for the pellet injection system ($8x10^6\ell s^{-1}$ pumping speed) has been installed, tested and commissioned. The good performance of the NB cryopump systems allowed identical system to be used without modifications to the pump structure;

(iii) *Cryo-supply*

(e) the cryo-supply for the pellet injection cryopump system and that for the pellet injection launcher has been installed, tested and successfully commissioned (a total system of six 80m long cryolines and related control valves);

(iv) *Control and Instrumentation*

(f) the control and instrumentation of the cryopump systems has been redesigned to give direct communication between the cryoplant and the cryogenic loads. New signal condition cubicles with controllers were designed, installed and integrated into the local computer control system. The installation of a new computer supervisory system on top of the local microprocessor allows easy communication, data analysis and alarm handling. Considerable effort was made to 'clean' the software, improve its reliability and to adjust it to the needs of reliable operation from the main control room via CODAS;

(v) *Operation*

(g) the routine, reliable and simultaneous operation of three cryopmps with different requirements (NI:D_2 operation with LHe at 1.2bar, PI:H_2 operation at 1.0bar and daily regeneration) from the main control room together with a considerable liquid helium bulk supply (up to 1000ℓ/day) to the pellet launcher can be regarded as a major achievement.

Neutral Beam Testbed

During the year, three major activities have been carried out on the NB Testbed, as follows.

(i) *Further Analysis of the Second Quadrant Test*

The central support column together with the beam deflection magnets, the magnet liners, the various ion dumps and the beamline calorimeter of the second JET injector were installed in the Testbed in 1986.

Beams at both 80kV and 160kV were fired through the system from each of the alternative positions of one quadrant of this system and the performance of each of the components measured. A preliminary analysis was given in the 1986 Progress Report, but the detailed evaluation took place during the first quarter of 1987. The detailed analysis confirmed the broad conclusions of the preliminary analysis, and the most significant results are summarised below.

(a) neutralisation of the 140kV deuterium beams was

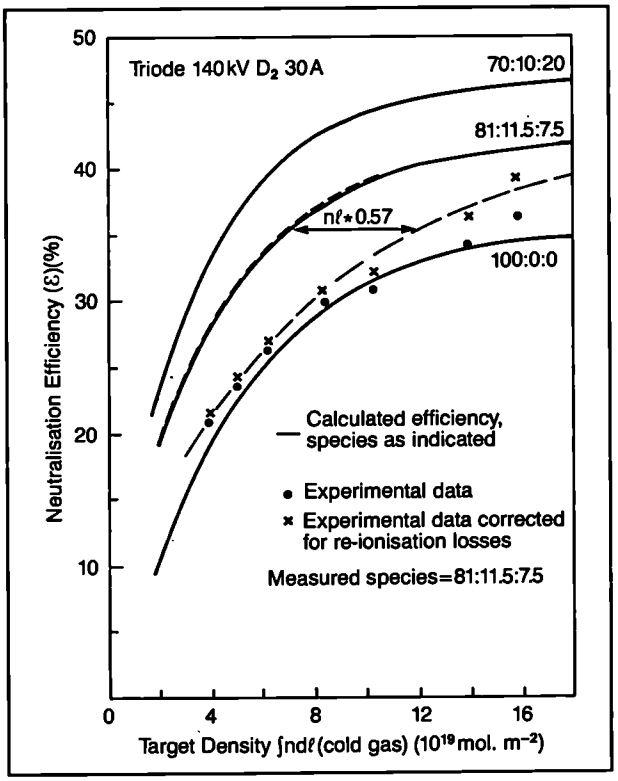

Fig.24 Neutralisation efficiency of the 140kV deuterium beam, measured during the second quadrant test;

significantly below the expected value if the gas in the neutraliser is assumed to be at room temperature (see Fig.24). The effect is believed to be due to heating of the neutraliser gas by the beam [1]. These results are consistent with data for hydrogen beams previously reported [2]. Using this data, the power to JET from one injector operating in D_2 with eight sources at 140kV, 30A can be predicted and is shown in Fig.25;

(b) the deflection ion beam profiles on the Full Energy Ion Dump (FEID) were measured with deuterium beams with energies up to 160kV (37A) and with hydrogen beams with energies of up to 70kV (46A). From systematic scans in neutraliser gas target density, horizontal and vertical beam alignment and beam perveance, it was determined that over the full range of operating JET conditions, the deflected deuteron, or proton, beams were well contained within the extent of the FEID. The power density on the front surface FEID hypervapotrons was within the safe operating limits of the FEID (<1.1 kW.cm^{-2}). The loading on the side of the hypervapotron elements making up the FEID was $<10\%$ of the front loading everywhere, with the peak in the side loading occurring away from the peak in the front loading (as expected). This does not affect the safety of the system. Additionally it was concluded that the system would not be acceptable for operation at higher beam parameters (e.g. 80kV, 60A hydrogen beams or 160kV, 30A deuterium beams);

(c) the detailed deflected beam profiles measured during the test allowed a detailed comparison between these and predicted profiles using measured or theoretical magnetic fields and particle tracing. Such a comparison would then enable some confidence (or otherwise) to be attached to the prediction for alternative beam systems (e.g. 160kV tritium beams).

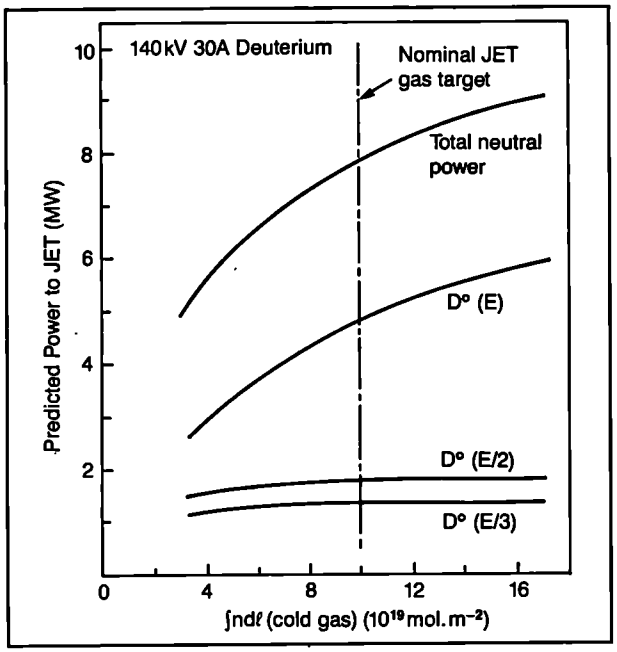

Fig.25 Predicted power to JET from one injector with eight sources operating at 140kV in deuterium.

(ii) *Hypervapotron Tests*

(a) Curved Vapotron Test. Two main hypervapotron tests were carried out during 1987. The Full Energy Ion Dumps (FEID's) have been shown by the two quadrant tests as the weakest component of the JET injectors. Therefore, it was proposed to increase the safety margin associated with these components by increasing the surface area of the FEID's. To achieve this, the angle of the vee formed by the opposing hypervapotron elements was to be reduced. However, this would have resulted in an unacceptably deep dump if the dump width at the entrance was maintained. To overcome this, the angle in a region where the expected power density would be sufficiently low was increased by having a curved vapotron.

A test set-up consisting of two vees of the proposed design suitable for insertion into the NI Testbed was manufactured. The basic test consisted of adjusting the beam parameters to obtain the desired power density using short (<150ms) pulses fired onto the (short pulse) vertical inertial calorimeter array.

The main results were:

with a power density on the vapotron surface of

$\sim 1 kW.cm^{-2}$, the thermocouples indicated temperatures of $>350°C$, compared with the expected value of $\sim 290°C$, and the temperature did not reach a steady value, but continued to rise throughout the pulse;
- the temperature in the vapotron was dependent on water flow rate, decreasing with flow at flows above the nominal $24m^3.hr^{-1}$. This was not expected;
- excessive ($>440°C$) and increasing, temperatures were recorded when the power density was increased to $\sim 1.3 kW.cm^{-2}$.

These data were tentatively interpreted as due to a 'total power' effect, possible due to excessive vapour build up in the water channel. The total power incident on one of the elements was significantly higher than had been put onto a hypervapotron element during pervious power density limit tests [3]. During the previous tests, the total power was $\sim 200kW$ and the power density limit was $\sim 1.5 kW.cm^{-2}$. In this test, the total power was $\sim 325kW$ when the peak power density was $1 kW.cm^{-2}$. Overall, it was clear that a Full Energy Ion Dump based on this design would not give an improvement in system safety.

(b) Total Power Vapotron Test. This test was designed to investigate whether a limit existed on the total power that could be incident upon a hypervapotron element, independent of the known power density limit. For this purpose, a JET standard 900mm long hypervapotron element was suspended in the beam, with the beam incident on the surface at $\sim 15°$ to the surface. The element intercepted $\sim 500kW$ when the peak power density was $\sim 1 kW cm^{-2}$. The experiment was similar to that test with the curved vapotron element, except that the water flow and pressure were varied systematically.

The main results were:
- downstream thermocouples showed a higher temperature than upstream thermocouples for the same power density;
- the measured temperature decreased as the flow was increased;
- temperature was proportional to 1/PV (P = water pressure, V = water velocity).

In previous measurements [3] with total power restricted to $<200kW$, the local temperature was independent of total power, and proportional to the local power density. These new results clearly showed that the total power falling on the element affected its performance. If the effect was due to the proportion of voidage in the coolant channel, then the temperature should be a function of both the water flow and 1/PV. Both were found to be the case. The conclusion was that there was a total power effect, which probably arose from the proportion of voidage in the coolant channel. The present elements were capable of handling $\sim 550kW$ with a peak power density of $\sim 930 W.cm^{-2}$, for a water flow of $\sim 13 m^3 hr^{-1}$ at a pressure of ~ 6 bar.

(iii)*PINI Conditioning*

All JET PINI's are subjected to complete conditioning before they are deemed suitable for installation on the injectors. This process begins with 'pre-testing' for vacuum leaks, of high voltage hold-off tests and testing of the filament transformer. The tetrode PINI's are then conditioned with beams up to 80kV. The PINI's are characterised, in which their perveance is measured at various extraction voltages, the arc efficiency is measured over the full operating range, the extracted species are measured at set extraction voltages, the power loading on various components (grids, etc.) are determined, and the alignment of the extracted beam is carefully measured. For the first set of PINI's, this work was carried out under contract by UKAEA, Culham Laboratory. For the later PINI's and for all the 160kV PINI's, this work will be carried out on the Testbed at JET. This year a total of seven 80kV tetrode PINI's have been fully conditioned and characterised. The final test in this conditioning process is 100 consecutive 5s pulses at 80kV and perveance matched current (typically $\sim 60A$). To pass this test, the source must achieve $>90\%$ beam on time for $>90\%$ of the pulses. So far all the sources have exceeded these values.

Engineering and Development Work

During operation, stray magnetic fields from the plasma and poloidal coil system affect the neutral injection system. To minimise these, part of the beamline is fitted with a magnetic shield of 5cm thick soft iron. The shielding design was based on a 3D computer computation which predicted stray fields of $<10^{-4}T$ around the beam sources. However, the measured fields exceeded this value. Thus, the stray field deflects ionised beams on passing through the neutraliser. The remedy requires off-set beam steering, depending on the stray field strength.

In practice, beam resteering is required for $I_p > 3MA$. Extrapolation from $I_p = 5MA$ up to $I_p = 7MA$, shows that unacceptably high stray fields would leak through the magnetic shielding. Consequently, installation of an active magnetic shield was planned. The basic system consists of both horizontal and vertical axis coils fitted inside the existing shielding and passing around the outer perimeter of the system. Electro-magnetic coils carrying up to 270A over 60 turns were fitted with both horizontal and vertical axes to the inside of the existing soft-iron magnetic shielding. Magnetic probes at the back of the NIB monitor the stray magnetic field from the tokamak and control the current in these coils in a feedback loop. The system is designed to cancel stray fields up to $1.5 \times 10^{-3}T$ near the beam sources and neutraliser positions.

Following two incidents with the duct liner through deflected re-ionised particles, the ducts of both Octants

No.4 and No.8 systems were fitted with inertially-cooled copper liners. Both rotary high-vacuum valves were similarly lined with copper panels in preparation for 7MA plasma current operation. The design of a complete remotely handleable middle port adaptor and duct liner was started with a view to commencing manufacture in mid-1988.

Development work for the tritium beamline continued with tests on individual beam stopping elements. The present elements have a maximum power collecting ability of about 500kW and a development programme with the Testbed Group aims at improving this performance.

A re-design of the second stage neutralisers took place with a view to replacing the present electro-deposited copper components. Two failures during 1987 indicate that their reliability is not-acceptable.

References

[1] J.R. Pamela, Gas Heating Effects in Neutralisers of Neutral Beam Injection Lines, Rev. Sci. Inst., **57**, (6), 1986, pp1066–1068;

[2] R.S. Hemsworth et al, Neutralisation Measurements for the JET Injector, Proc. 13th Conf. on Contr. Fus. and Plasma Heating, Schliersee, F.G.R., 1986, pp297–300;

[3] H.D. Falter et al, LBL Hypervapotron Tests, Internal Report, March 1983.

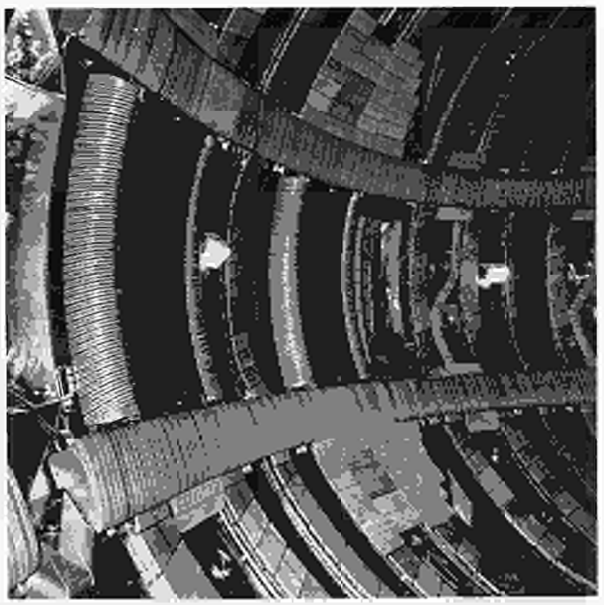

Fig.26: Photograph of two of the eight water-cooled antennae (one is only partially shown) installed between the two belt limiters. Marks in the centre of the graphite side protections were produced by the plasma heat load.

Radio Frequency Heating System

The activities on the RF Heating Systems during 1987 have been dominated by the installation, commissioning and operation of the full performance ICRF system and by the design, procurement and testing of components for the Lower Hybrid Current Drive system which is described in a later section of this report.

Installation of Second Generation Antennae

During the shutdown between December 1986 and April 1987, eight ICRF antennae were installed between the two toroidal belt limiters (Fig.26). These antennae were constructed with a newly designed central conductor (Fig.27), which allowed both monopole and toroidal dipole configurations to be achieved by changing the relative phase between the two striplines. From operation of previous antennae, the monopole mode was known to give good coupling and the toroidal dipole was chosen for its low perturbation of the plasma edge and corresponding reduced impurity release. The resonant frequency of the new antennae was designed for 37MHz (compared with 30MHz for the A_o antennae), in order to improve the coupling at the high frequency end of the operating range. The antennae screens are water-cooled

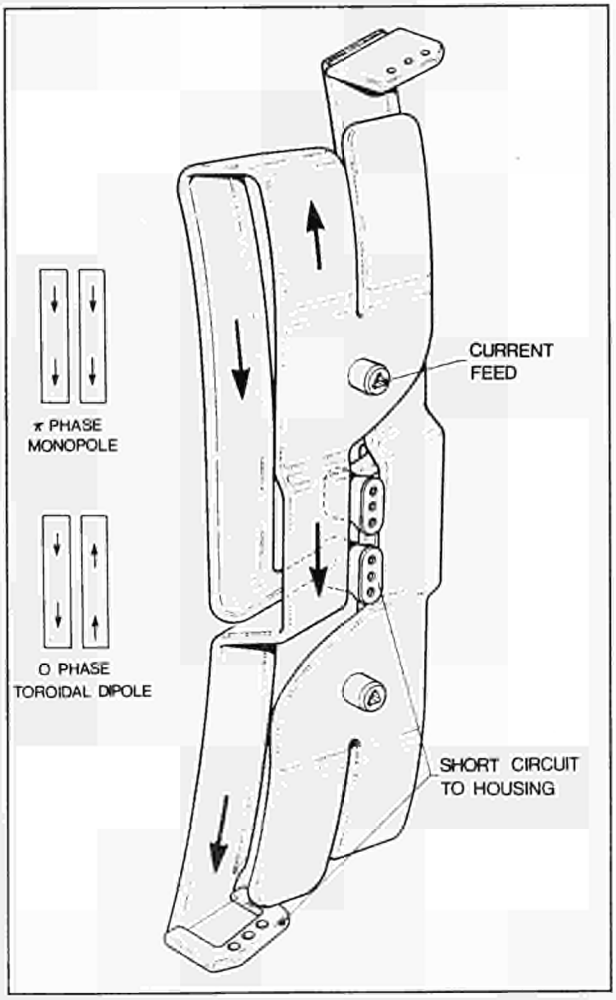

Fig.27: Geometry of the new antenna central conductor which operates either in monopole or in dipole phasing, while keeping antenna resonating around 42MHz.

which allows operation with maximum power for up to 20s. Protection from the plasma is afforded by columns of graphite tiles along the vertical sides of the antennae and each tile is located between nickel fins for good radiative heat transfer to the water-cooled manifold. The screens were coated with a 1μ layer of carbon prior to installation to minimise the sputtering of nickel impurity within the plasma. Installation was carried out with the help of the remote handling boom to demonstrate the feasibility of this kind of operation.

Generator and Transmission Line

The eight units of the ICRF generator plant and transmission lines were all available for plasma operation in August 1987 (Fig.28). At that time, the generators consisted of seven 3MW units (using Eimac tetrode tubes) and two 4MW units (using Thomson tubes). Progressive replacement of the Eimac by Thomson tetrodes has taken place during each minor shutdown and three units had been converted by the end of 1987. Completion is expected by the end of 1988. The electrical lengths of the transmission lines have been made precisely equal by means of trombone-type phase-shifters adjustable remotely and this will allow the system to be operated as a matched phased array for current drive and MHD stabilisation studies. Other hardware installations included: a closed circuit airflow to cool the vacuum transmission lines; generator interlocks for use with the vacuum transmission lines; and the antenna water cooling system. A separate line and switching system to supply RF power to the Testbed is also operational.

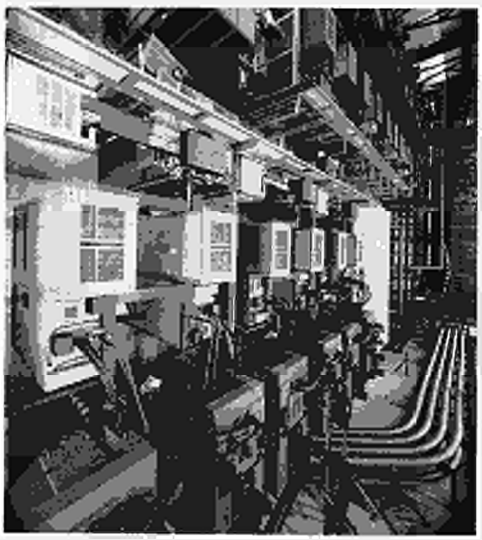

Fig.28: Top view of the recently completed ICRF power plant presently rated at 24 MW (generator output). Part of the coaxial transmission lines can be seen.

The software controlling the plant has been substantially enlarged to accommodate the AGH generators and facilitate their operation. A major timesaving improvement is the capability to store the settings for pulses with good antenna matching and, when required, to recall these settings and write them directly into the plant. The software associated with ICRF power modulation now allows both square and sinusoidal voltage waveform to be applied to all generators with easily adjustable frequency and depth of modulation.

Plasma Operation

Initial coupling studies showed coupling resistances of typically 2Ω and 5Ω in the dipole and monopole configurations, respectively, as expected from previous experience and calculations. At low power, eigenmodes are strongly excited by the monopole due to the preponderance of radiated power at low values of parallel wave number, $k_{\parallel}$. At high power, the single pass absorption increases and tends to damp out the eigenmode structure. However, the presence of these structures and associated sensitivity of coupling to plasma density (which rises with increasing RF power) imposes some restrictions on the rate at which the power can be turned on. Typically the power can be ramped up in 0.5s without undue perturbation from the eigenmodes.

Operating the eight antennae at a single frequency using the generators in an 'master/slave' configuration has improved reliability. In particular, it has removed generator trips due to the fluctuations in reflected power caused by beats which arise when nearby antennae are operated at close, but not identical, frequencies. Several selected frequencies in the 25MHz – 47MHz band have been commissioned for this 'homodyne' type of operation. To date, 16 MW of coupled power has been achieved with both monopole and dipole phasings. This value of net coupled power is slightly in excess of the original design parameter ($\sim$15MW). In the near future, the change of output tetrodes as well as the installation of additional DC power supplies should increase the power capability to 20 MW. A new phase control system will allow the antennae to be used as a phased array and the software controlling the plant will be enhanced to automatically tune the system for optimum coupling.

Remote Handling

Further progress has been made in specifying, acquiring and commissioning major items of remote handling equipment. This equipment comprises special tools to suit the features and to provide access to JET components; end-effectors to lift and attach large components; large, high-precision transporters to carry the equipment to all parts of the JET machine; and control systems for all this equipment:

During 1987, further efforts were devoted to analysis of tasks inside and outside the vessel to provide the basis for specifications of equipment and to supply material for data bases which will be used to direct operations.

The introduction of tritium into the machine, which will require that all work on the JET machine is performed by remote control from outside the Torus Hall, is now proposed for mid-1991. Until this time, increasing background radiation, the generation of slightly activated dust and the use of beryllium will necessitate special equipment and methods for gaining access and carrying out hands-on work safely inside the torus.

In 1987, the Tritium Group in Fusion Technology Division has been restructured. The Active Gas Handling Construction Group was formed to complete the design, and to procure, install, commission and operate the Active Gas Handling System (AGHS). The Tritium Safety Group was set up to deal with the safety assessments, obtaining of statutory approvals, radiological protection instrumentation, and procurement and accounting of tritium.

Transporters

The Articulated Boom was used in its fully extended configuration during the 1987 shutdown to install 32 belt limiter segments, eight housings and eight screens of the RF antennae. The boom was controlled from a portable handbox either by rate or position control of single joints, or by resolved motion of the end effectors to the vacuum vessel or final positioning of components. Some experiments were carried out with the 'teach-repeat' mode. Difficulties were encountered because the available software only permitted resolved motion in the last three joints and movement of the other joints only two at a time. Additional software was specified and prepared to overcome these limitations. It is now being commissioned.

It was possible to adjust the position of a 350kg antenna cantilevered at 10m distance from the first joint to within a few millimetres by inching at extremely low speeds. Oscillations were however generated during the trajectories at higher speeds due to the elasticity of the joints. New control algorithms have been computer simulated obtaining considerable improvement in the trajectory control, particularly needed during entrance into the port of the vessel. These will be incorporated into the boom control and tested in early 1988. Numerous improvements suggested by the shutdown experiments were made to the family of end effectors designed to handle limiters and antennae. These are mounted on the boom or on the turret truck used to convey components to the boom.

A new boom extension and relevant controls have been procured and are being commissioned. It will be used initially on a turret truck for trials on mock-ups of ex-vessel operations and, later, on the crane-mounted telescopic transporter (TARM). Trials of in-vessel operations will be done using the articulated boom and the spare octant. The extensive wiring and installation of control cubicles for these mock-up areas is nearing completion, as is the wiring between Torus Hall, cubicles and Remote Handling Control Room.

The TARM for ex-vessel maintenance has been ordered after international tender and is due for completion in early 1989. It is composed of a 17m telescopic mast which will be suspended from the crane and a telescopic arm with an articulated end section. It will have a control system for up to 30° of freedom including the TV camera supports. Rotary actuators with improved stiffness for the boom or TARM articulations have been developed and a prototype manufactured.

An evaluation of modifications needed for operating the main crane in active conditions is in progress and a seal assembly to prevent tritium diffusion through the cable passage in the shielding beams has been developed and tested.

The low-level transporter was used to install eight turbomolecular-pumps under visual control of an operator. The additional equipment needed to convert it into a fully remote-controlled unit was specified and a call for tender was issued.

Servomanipulators

The first of the two MASCOT IV units was delivered in mid 1987, after debugging and final tuning of its control system. The second unit has been completed ready for delivery in its basic configuration. The supply will be completed by the software for advanced functions, i.e. teach-and-repeat, tool weight suppression and constraints of the trajectory on planes or lines. The teach-and-repeat function has been tested, the others will be ready in early 1988. The automatic connector for changeover between manipulator and end effectors has been commissioned. Gaitering has been designed and procured.

In-Vessel Inspection System

After feasibility tests and detailed design, the high-temperature probes were ordered and manufacture is nearing completion. The prototype was tested at 350°C in a rig set-up. As with the previous model, space restrictions called for painstaking rearrangement of wiring and connectors to eliminate noise and faults. The device is equipped with sensors to detect cooling water leaks.

A recent improvement is the provision of continuous lighting using four vacuum tight assemblies of silica light-guides illuminated by small powerful purpose-designed projectors sited above the penetrations. Fig.29 shows the arrangement of a high-temperature in-vessel lighting system.

Special Tools

The range of over twenty types of special tool developed during 1986 was used extensively in the 1987 shutdown for installation of the new water cooled belt-limiters and antennae. Over two hundred vacuum seal welds were performed with automatic remote handling compatible

weld tools and no leaks were experienced during subsequent operation. Work is continuing on the development of the tools for use in the D-T phase and the design of some new tools for use in the 1988 major shutdown has started.

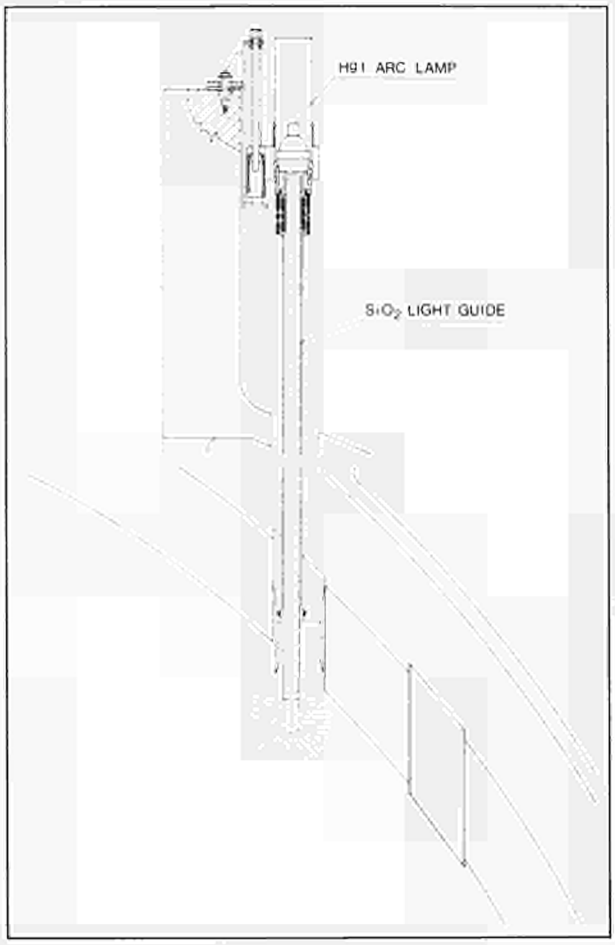

Fig.29 Arrangement of a high temperature in-vessel lighting system.

Remote Handling Integrated Control System

Work on the Remote Handling Control Room has started with the installation of all power, lighting, ventilation and cabling systems. The prototype Remote Handling Workstation has been tested in respect of the Articulated Boom and the welding power pack (Protig) control. Two new production units are being manufactured for use in the Control Room during 1988 in connection with the mock-up programme.

Work on the Graphics Workstation by personnel from KfK Karlsruhe, F.R.G., under a contract of assignment has resulted in the generation of a real-time 3-D computer generated display of the articulated boom and its end-effectors inside the torus (see Fig.30). This system has been successfully commissioned and connected to the articulated boom. This phase of the work is now being completed by the generation of full system documentation and work on the generation of a similar system for ex-vessel remote handling work is now being defined.

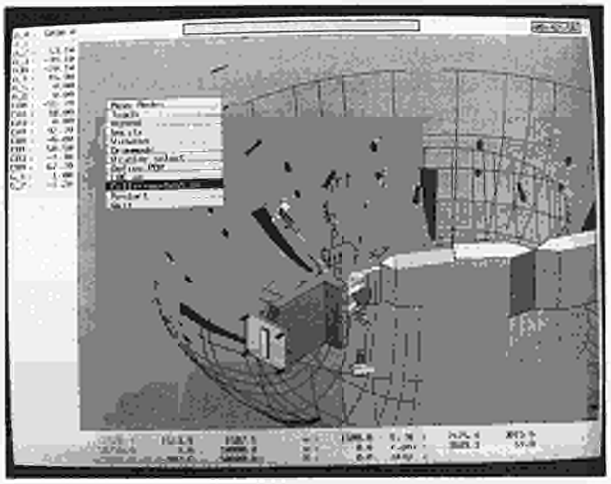

Fig.30 A real-time 3-D computer generated display of the articulated boom and its end effectors inside the torus.

The overall communication structure of the Remote Handling Integrated Control System has been greatly simplified by the introduction of an Ethernet link. This will be used for non time-critical applications such as data transfer from transporters to the Graphics Workstation and the control of fixed cameras.

The Protig has been successfully enhanced to facilitate fully remote control of welding from the Remote Handling Workstation via a dedicated serial link. JET now has a system capable of welding with the tool up to 100m from the Protig and with the Protig and gas supplies fully remote from the control room.

The first phase of the Closed Circuit TV system comprising seventy video input by forty monitor output and forty audio input by ten speaker output crossbars have been installed and commissioned. This allows video and audio selection for display on any of the Workstation and Control Room monitors. The second phase comprising an array of cameras with integral lights, microphones and pan-tilt heads to be fixed on the Torus Hall walls and other Remote Handling operational areas will be installed in 1988.

Active Handling

Work on the specification, design and procurement of active handling equipment for use on JET after installation of beryllium has been proceeding. The Torus Access Cabin, procured in 1986, was successfully used during the 1987 major shutdown. A strategy for maintaining the torus ex-vessel equipment in the presence of beryllium has been derived and a design of PVC isolator suitable for handling some standard JET components has been developed and tested. A rationalised isolator design for all torus interfaces is now being pursued.

The requirements for Active Handling facilities in the D-T phase are being identified based on the known remote handling tasks, decontamination requirements and potential waste arisings. The potential wastes and

how to handle and transport them has been derived from both internal studies and from a study contract undertaken for JET by UKAEA Harwell Laboratory. The requirements and techniques for decontamination have been derived from internal studies and the results of a test programme on the effect that tritiated workpieces have on Remote Handling tools during cutting and welding operations. This has been undertaken by JET personnel using facilities at TSTA, USDoE, Los Alamos, U.S.A.

Control and Data Acquisition System (CODAS)

The Control and Data Acquisition System (CODAS) Division is responsible for the design, procurement, implementation, upgrade and operation of the computer-based control and data acquisition system of JET. This system, based on a network of NORSK DATA minicomputers, allows centralised control and monitoring. The various components of JET have been logically grouped in subsystems like Vacuum, Toroidal Field, Poloidal Field, etc. Each subsystem is controlled and monitored by one computer and the various computer actions are co-ordinated by supervisory software running on the machine console computer. This supervisory function includes the countdown sequences for each plasma discharge.

The allocation and configuration of all CODAS computers is given in Table III, and Tables IV and V provide

TABLE III
CODAS Computer Configuration at the end of 1987

Subsystem	*Usage*	*Model*	*Memory (MByte)*	*Disks (MByte)*
AH*	NI Additional Heating (Oct 8)	ND110	2.0	1×75 1×450
AN*	Analysis and Storage	ND560	4.0	1×75 2×450
AS	Assembly Database	Compact	0.75	1×45
CB	Message Switcher B	ND110	2.0	1×70 1×450
CP	Cable Database	ND530	5.0	1×75 1×450
DA*	On-line Diagnostic	ND520	3.0	2×75
DB*	On-line Diagnostic	ND520	3.0	1×75 1×450
DC*	On-line Diagnostic	ND520	5.0	2×75
DD*	On-line Diagnostic	ND520	3.0	2×75
DE*	On-line Diagnostic	ND520	3.0	2×75
DF*	On-line Diagnostic	ND520	3.0	2×75
DG*	On-line Diagnostic	ND520	3.0	2×75
DH	Diagnostic Conditioning	ND550	5.0	1×75 1×450
EC*	Experiment Console	ND570	5.0	1×75 1×450
EL	Electronic	ND110	1.0	1×75
GS*	General Services	ND110	1.5	2×75
CC	CODAS Commissioning	ND110	1.5	2×70
LH	Lower Hybrid	ND110	2.0	1×75
MC*	Machine Console	ND110	1.5	1×75
PF*	Poloidal Field	ND110	3.0	1×75 1×288
PL*	Pellet Launcher	ND110	1.5	1×75
PM*	Pulse Management	ND550	5.0	1×75 1×450
RB*	Radio Frequency Test Bed	ND110	1.25	2×75
RF*	Radio Frequency	ND100	2.0	1×75
RH	Remote Handling	ND110	1.5	1×75
SA*	Message Switching & JPF Collection	ND110	2.0	1×70 1×450
SB	Standby System/Backup	ND110	2.0	2×75 1×288 1×70
SD	Built-in, Pool, Computer dB	Compact	1.25	2×45
SS*	Safety and Access	ND110	2.0	2×70
TB*	NI Test Bed	ND110	1.5	1×75 1×450
TF*	Toroidal Field	ND110	1.5	1×75
TR	Tritium	ND110	1.5	1×75
TS	Test	ND530	3.0	2×75
VC*	Vacuum	ND110	2.0	1×75
YB	Integration	ND530	3.0	1×75 1×450
YC*	NI Additional Heating (Oct 4)	ND110	2.0	1×75 1×450
YD	Sc Dpt Development	ND570	5.0	1×75 1×450
YE	CODAS Development	ND520	5.0	1×75 1×450

* indicates on-line computers used for operation and testbed

other quantitative data. Further detailed information can be found in previous publications[1-4].

The main developments during 1987 and the orientation for 1988 are summarised below.

TABLE IV
Quantative Information on CODAS Installation

Item	End 1986	End 1987
CODAS interface cubicle	128	138
CAMAC crates	198	223
CAMAC modules	2982	3364
Eurocard modules (signal conditioning)	6254	6927
Computer terminal (including PCs and IBM terminals for 1987)	238	333
CAMAC serial loop (fibre optic)	21	24
On-line computers	20	24
Off line and comissioning computers	15	14
Size of JPF	9MB	15MB
Number of diagnostics on-line with CODAS	26	27
Number of diagnostics under commissioning with CODAS	8	6

TABLE V
Review of CODAS Electronics Stock Holding
(installed, pre-procurement and spares)

	End 87	End 86
1. CAMAC system modules	873	760
2. CAMAC digital I/O modules	814	738
3. Timing system (CAMAC & Eurocard)	1,202	1,073
4. CAMAC analogue I/O modules	1,086	1,073
5. CAMAC display modules	360	322
6. CAMAC auxiliary controllers	127	110
7. CAMAC powered crates	262	227
8. U-port adaptor	184	155
9. CISS modules	856	753
10. CCTV	544	470
11. Cubicle frames	345	280
12. Console devices (not CAMAC)	504	387
13. Power supplies modules	1,614	1,570
14. Intercom, Public address, Computer terminal Network	578	552
15. Pool instruments	934	889
16. Analogue I/O in Eurocard	2,485	2,006
17. Digital I/O in Eurocard	4,718	4,584
18. Eurocard sub-racks	860	751
Increase	1,655	10%

New Systems

The Pellet Launcher (PL) computer has been included in the operational system. As the launcher was developed and tested in the USA (ORNL-JET collaboration), its integration required special development such as sequencer, NORD-microVAX link and NORD-Allen Bradley links, all supported by the CODAS standard CAMAC-based front-end microprocessor. Studies and design for the new pellet testbed and high-speed pellet interface are underway.

The global design of the tritium control system and its interface with CODAS has been agreed and the detailed design is underway. The operation of a prototype scheme is planned for June 1988. As part of the design, it was decided to include ETHERNET as part of the CODAS standard protocol. It will also be used in other areas such as the Remote Handling system.

Detailed design of part of the interface to the Lower Hybrid Current Drive (LHCD) system has been completed and its first operation on the testbed is planned in 1988. Large parts of the special software developed for the operation of the Radio Frequency system will be transported to the LHCD system.

Expansion and Enhancement of Existing Systems

The basic computer system architecture has been modified as indicated in Fig.31. This change has the following advantages:

(a) As the JET Pulse Files (JPF) are collected now on the message switching computer, the concatenation process can take full advantage of parallel transmission

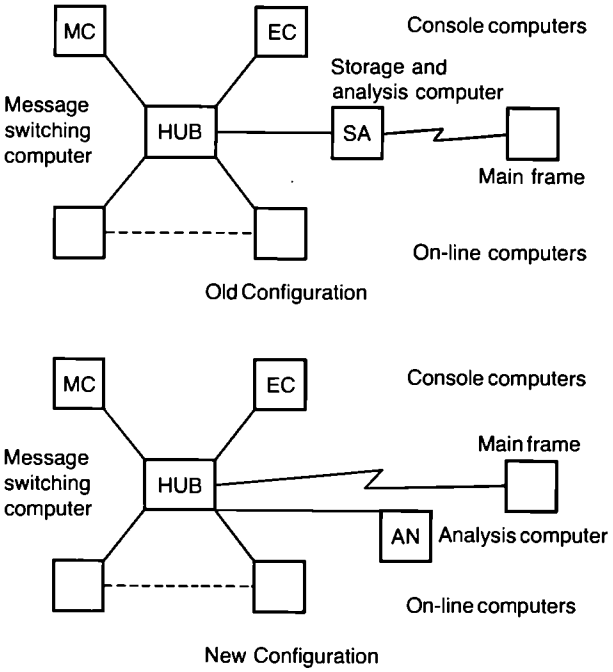

Fig.31. Basic Computer Systems Architecture

avoiding the bottleneck of the HUB-SA link;

(b) As the Analysis Computer (AN) is now loosely coupled to the operation, there are fewer restrictions on users.

This change alone has brought an improvement on the data collection throughput from 14kByte/s to 47kByte/s.

The configuration of the data link between the JET Mainframe computer located at the UKAEA Harwell

Laboratory and the JET site has been reviewed and a robust three leg system using three 2MBd British Telecom lines has been selected. This system uses the Hyperchannel implementation to support:

- the channel attached IBM peripherals installed on the JET site;
- the dedicated JPF transfer protocol;
- the generalised file transfer system between JET and Harwell.

The tests of the new CODAS-Hyperchannel interface were successful and a transfer speed, in test mode, of 187kByte/s was achieved. The final version of the software is expected in early 1988 and a transfer speed of about 150kByte/s is expected in normal operation. These improvements will allow JET to cope with the increase of the JPF size, which has now reached 15MByte/pulse, without slowing down the JET pulse repetition rate.

The implementation of the new magnetic configuration and the standard usage of single null X-point configuration has required significant changes to the digital plasma current control and to the Direct Magnet Safety System for the poloidal field system. The change to digital control of the plasma radial position and shape is planned for 1988.

The RF control system has been expanded to eight antennae operation. Software development was implemented to ease routine operation and more automated operation, like matching, will be implemented in 1988. Distributed power modulation has been designed and tested and an expansion to excite a travelling wave mode of propagation for control of MHD activities will be implemented in early 1988.

The allocation of tasks between the General Service (GS) and Safety and Access (SS) computers has been reviewed. After analysis of operation requirements, it has been decided to implement a special well secured enclosure in Building J2 to house:

- the Tritium computer;
- the Remote Handling computer;
- the Access Control computer (which also supports the Radiological Dosimetry Service).

These computers support services do not follow the normal pattern of JET operation and this installation will allow provision of high reliability services.

The high level software (called Level 1) to support JET operation in an efficient manner has been widely reviewed at the JET level. This led to changes in parts of the original concept. As a consequence, there will be some delays in its implementation but it will be a tool better adapted to the safe operation of JET. Some parts, such as preparation of the Pulse Schedule, are already available. More components will be commissioned during 1988 and it is expected to have a full system available when operation resumes after the 1988 shutdown. The software structure is open and will allow the inclusion of more algorithms at a later date. These algorithms are mostly of two classes: those which allow automatic 'translation' from plasma physics parameters into machine setting parameters; and those which allow the validation of physics or machine setting parameters.

At a more routine level, other tasks have absorbed considerable CODAS manpower effort:

(a) new building installations imposed extensive modification to the CODAS Terminal Network. An upgrade was required of the terminal multiplexer allowing installation of a satellite station in the new J20 building and detailed design of new signal routing;

(b) as more experience was gained and, to ease operation, many modifications were required in hardware (390 in 1987) and software (375 in 1987);

(c) the Central Interlock and Safety System had to be modified to provide services adapted to new requirements;

(d) Ten new cubicles were built, installed and commissioned;

(e) Sixteen new diagnostics were brought into commissioning or operation.

As delivery of computers and peripherals started in 1980, and as full support of the operation should be guaranteed until the end of 1992, a full review of configuration has been initiated. This review has two main goals:

(a) to provide sufficient computer power to cope with the increase of requested services;

(b) to renew obsolete and worn out equipment which would not provide sufficient reliability for efficient operation of JET.

General Remarks

The development and requirements of JET operation has led to a large development of front end microprocessor applications. At present, there are twenty-eight applications running in 87 CAMAC based front end microprocessors. At least nine new applications are currently planned for 1988. This provides confirmation of the actual trend in process control development.

The load created by the support of JET operation and the effort required in its healthy extension is competing strongly with the necessary effort to bring CODAS to a high level of reliability. This is compounded by the large turnover of staff experienced recently and increasing difficulties in recruiting team members or even well qualified contract staff. This has been most acutely felt in the field of Electronics and Instrumentation. During 1987, the Division lost ten team members and was able to recruit only five.

References

[1] Computer Control and Data Acquisition at JET H. van der Beken, IEEE Transactions on Nuclear Science, August 1987, Fifth Conference on Real-Time Computer Applications in Nuclear, Particle and Plasma Physics, San Francisco, U.S.A. (1987);

[2] 'CODAS: The JET Control and Data Acquisition System', H. van der Beken, C.H. Best, K. Fullard, R.F. Herzog,

E.M. Jones, C.A. Steed, Fusion Technology Journal, 11, No 1, 1987.

[3] 'Front-end Embedded Microprocessors in the JET Computer Based Control System past, present, and Future', C.A. Steed, H. van der Beken, M.L. Browne, K. Fullard, K. Reed, M. Tilley, V. Schmidt, 12th Symposium on Fusion Engineering (SOFE), Monterey, U.S.A., October 1987;

[4] 'The Joint European Torus Personnel Dosimetry Service', T. Budd, D.M. Baker, IAEA Seminar on Application of Computer Technology to Radiation Protection, IAEA-SR-136, Bled, Yugoslavia, June 1987

JET Data Management

A separate JET Data Management Group is responsible for the provision of a Mainframe service for scientific and engineering computing. This includes the provision of appropriate, software and hardware systems. The Group is also responsible for the management of JET data, and the organisation and control of routine data processing.

A major achievement in 1987 was the establishment of a JET Mainframe Data Processing Centre. The Centre is based on an IBM 3090/200E, dual processor mainframe with a vector facility. There are some 70 GBytes of disc storage and a further 240 GBytes of IBM Mass Storage. The complex is housed in a new building at UKAEA Harwell Laboratory and operated for JET, under contract by a team from that Laboratory. The JET mainframe is also connected to the Harwell Laboratory CRAY 2 Computer.

The transfer of the complete JET workload, including the transfer of about 60 GBytes of data, from the Harwell IBM 3084Q to the JET mainframe was achieved very efficiently with no interuption to normal service. The transfer was completed during June/July within a month of the delivery of the hardware and no user changes were imposed. The whole project from approval to production operation was accomplished within 6 months. The improvement in the computing service was dramatic. A good interactive response is now provided for scientific and technical users and for users of the JET Drawing Office CAD systems. Prompt execution of the intershot analysis is provided together with rapid turn-around of the batch work-load.

A Data Management Help Disk provides contact between users and operators and systems programmers and ensures the smooth running of the system. There have also been significant improvements in the communications network between the JET site and the Computer Centre which are reported more fully in the CODAS section of this report.

In terms of stored JET Data, some 60 GBytes of raw JPF are currently stored using the cached Mass Store system. In addition, about 12 GBytes of processed data are available on-line under the PPF system. High level Data Base and Statistical Analysis and display systems especially using SAS products, have been developed and improved for use with analysis of selected JET data.

Diagnostic Systems

The status of JET's diagnostic systems at the end of 1987 is summarised in Table VI and their general layout in the machine is shown in Fig.32. The staged introduction of the diagnostic systems onto JET has proceeded from the start of JET operation in June 1983 and is now nearing completion. The present status is that, of 44 systems in total, 33 are in routine operation, 6 are being installed/commissioned and 5 have still to be constructed. Operational experience has been good and many of the systems are now operating automatically with minimal manual supervision. The resulting measurements are of a high quality in terms of accuracy and reliability, and provide essential information on plasma behaviour in JET. Further details on specific diagnostic systems are given below.

Magnetic Measurements

The magnetic measurement system described in previous reports has continued to work routinely and reliably. Front end processing has been adapted for the planned plasma currents up to 7MA. The software controlling the connection of different optical trigger signals to different sets of ADC's has been completed. A centralised network for the distribution of optical triggers to and from other diagnostic and machine systems became fully operational. Special B_θ pick-up coils were installed in the vessel near the X-point region to allow much better resolution in this area. The signals have been successfully incorporated into the interpretation codes. In addition, B_θ pick-up coils with a frequency response up to 0.5MHz have been installed in the vessel to allow a more detailed study of MHD fluctuations.

Plasma Boundary Probes

The plasma boundary probes are mainly single Langmuir probes. Their number has been substantially increased so that plasma parameters can be measured in nearly all important areas. There are two pairs in the RF antenna protection tiles in sections 1D and 5D; twenty in the belt limiter in order to monitor the symmetry of the plasma loading; and eight probes in the X-point target plates. In addition, Langmuir probes have been deployed successfully on the Fast Transfer System (KY2) and in the vertical probe drive (KY3). Excellent technical performance was obtained with a probe constructed almost entirely from high quality graphite (and a small alumina insulator).

An extensive experimental data set of boundary measurements has been compiled showing the scaling with the main plasma parameters. A fast-moving Langmuir probe has been delivered to JET to allow a scan of the profile within 200ms. This probe is designed to cross the plasma boundary and reach about 5cm inside the main plasma.

TABLE VI
Status of the JET Diagnostics Systems, December 1987

System	Diagnostic	Purpose	Association	Status (Dec. '87)	Compatibility with tritium	Level of automation
KB1	Bolometer Array	Time and space resolved total radiated power	IPP Garching	Operational	Yes	Semi-automatic
KC1	Magnetic Diagnostics	Plasma current, loop volts, plasma position, shape of flux surfaces, diamagnetic loop, fast MHD	JET	Operational	Yes	Fully automatic
KE1	Single Point Thomson Scattering	T_e and n_e at one point several times	Risø	Operational	Yes	Fully automatic
KE3	Lidar Thomson Scattering	T_e and n_e profiles	JET and Stuttgart University	Operational	Yes	Fully automatic
KG1	Multichannel Far Infrared Interferometer	$\int n_e ds$ on 6 vertical chords and 2 horizontal chords	CEA Fontenay-aux-Roses	Operational	Yes	Semi-automatic
KG2	Single Channel Microwave Interferometer	$\int n_e ds$ on 1 vertical chord	JET and FOM Rijnhuizen	Operational	Yes	Fully automatic
KG3	Microwave Reflectometer	n_e profiles and fluctuations	JET	(1) Prototype system operational (2) Multichannel system in commissioning.	Yes	(1) Not automatic (2) Will be fully automatic
KG4	Polarimeter	$\int n_e B_p ds$ on 6 vertical chords	CEA Fontenay-aux Roses	Operational	Yes	Semi-automatic
KH1	Hard X-ray Monitors	Runaway electrons and disruptions	JET	Operational	Yes	Fully automatic
KH2	X-ray Pulse Height Spectrometer	Plasma purity monitor and T_e on axis	JET	Operational	Yes	Semi-automatic
KJ1	Soft X-ray Diode Arrays	MHD instabilities and location of rational surfaces	IPP Garching	Operational	No	Semi-automatic
KK1	Electron Cyclotron Emission Spatial Scan	T_e (r,t) with scan time of a few milliseconds	NPL, UKAEA Culham and JET	Operational	Yes	Fully automatic
KK2	Electron Cyclotron Emission Fast System	T_e (r,t) on microsecond time scale	FOM, Rijnhuizen	Operational	Yes	Fully automatic
KK3	Electron Cyclotron Emmission Heterodyne	T_e(r,t) with high spatial resolution	JET	Operational	Yes	Not yet implemented
KL1	Limiter surface temperature	Monitor of hot spots on limiter, walls and RF antennae	JET and KFA Jülich	Operational	No	Fully automatic
KL3	Infrared belt limiter viewing	Temperature of belt limiters	JET	Commissioning	No	Will be fully automatic
KM1	2.4MeV Neutron Spectrometer	Neutron spectra in D-D discharges, ion temperatures and energy distributions	UKAEA Harwell	Commissioning	Not applicable	Semi-automatic
KM3	2.4MeV Time-of-Flight Neutron Spectrometer		NEBESD, Studsvik	Operational	Not applicable	Fully automatic
KM4	2.4MeV Spherical Ionisation Chamber		KFA Jülich	Commissioning	Yes	Will be fully automatic
KM2	14MeV Neutron Spectrometer	Neutron spectra in D-T discharges, ion temperatures and energy distributions	UKAEA Harwell	Under Construction	Yes	Not yet installed
KM5	14MeV Time-of-Flight Neutron Spectrometer		SERC, Gothenberg		Yes	Not yet installed
KM7	Time-resolved neutron yield monitor	Triton burning studies	JET and UKAEA Harwell	Operational	Not applicable	Fully automatic
KN1	Time Resolved Neutron Yield Monitor	Time resolved neutron flux	UKAEA Harwell	Operational	Yes	Fully automatic
KN2	Neutron Activation	Absolute fluxes of neutrons	UKAEA Harwell	Operational	Yes	Semi-automatic
KN3	Neutron Yield Profile Measuring System	Space and time resolved profile of neutron flux	UKAEA Harwell	Operational	Yes	Fully automatic
KN4	Delayed Neutron Activation	Absolute fluxes of neutrons	Mol	Commissioning	Yes	Fully automatic
KP2	Fusion Product Detectors	Charged particles produced by fusion reactions	JET	Operational	No	Semi-automatic
KR1	Neutral Particle Analyser Array	Ion distribution function, T_i(r)	ENEA Frascati	Operational	Yes, after modification	Semi-automatic
KR2	Active Phase NPA	Ion distribution function, T_i(r)	ENEA Frascati	Under study	Yes	Fully automatic
KS1	Active Phase Spectroscopy	Impurity behaviour in active conditions	IPP Garching	Operational early '88	Yes	Not yet implemented
KS2	Spatial Scan X-ray Crystal Spectroscopy	Space and time resolved impurity density profiles	IPP Garching	Operational	No	Not yet implemented
KS3	H-alpha and Visible Light Monitors	Ionisation rate, Z_{eff}, Impurity fluxes	JET	Operational	Yes	Semi-automatic
KS4	Charge Exchange Recombination Spectroscopy (using heating beam)	Fully ionized light impurity concentration, $T_i(r)$, rotation velocities	JET	Operational	Yes	No
KT3	Active phase CX spectroscopy		JET	Under construction	Yes	Not yet implemented
KT1	VUV Spectroscopy Spatial Scan	Time and space resolved impurity densities	CEA Fontenay-aux-Roses	Operational	No	Semi-automatic
KT2	VUV Broadband Spectroscopy	Impurity survey	UKAEA Culham	Operational	No	Fully automatic
KT4	Grazing Incidence Spectoscopy	Impurity survey	UKAEA Culham	Operational	No	Semi-automatic
KX1	High Resolution X-ray Crystal Spectroscopy	Ion temperature by line broadening	ENEA Frascati	Operational	Yes	Fully automatic
KY1	Surface Analysis Station	Plasma wall and limiter interactions including release of hydrogen isotope recycling	IPP Garching	Operational	Yes	Automated, but not usually operated unattended
KY2	Surface Probe Fast Transfer System		UKAEA Culham	Operational	Yes	
KY3	Plasma Boundary Probes	Vertical probe drives for electrical and surface collecting probes	JET, UKAEA Culham and IPP Garching	Operational	No Under study	
KY4	Fixed Langmuir Probes (X-point and belt limiter)	Edge parameters	JET	Operational	Yes	Semi-automatic
KZ1	Pellet Injector Diagnostic	Particle transport, fuelling	IPP Garching	Operational	Yes	Not automatic
KZ3	Laser Injected Trace Elements	Particle transport, T_i	JET	Under construction	Yes, after mocification	Not yet implemented

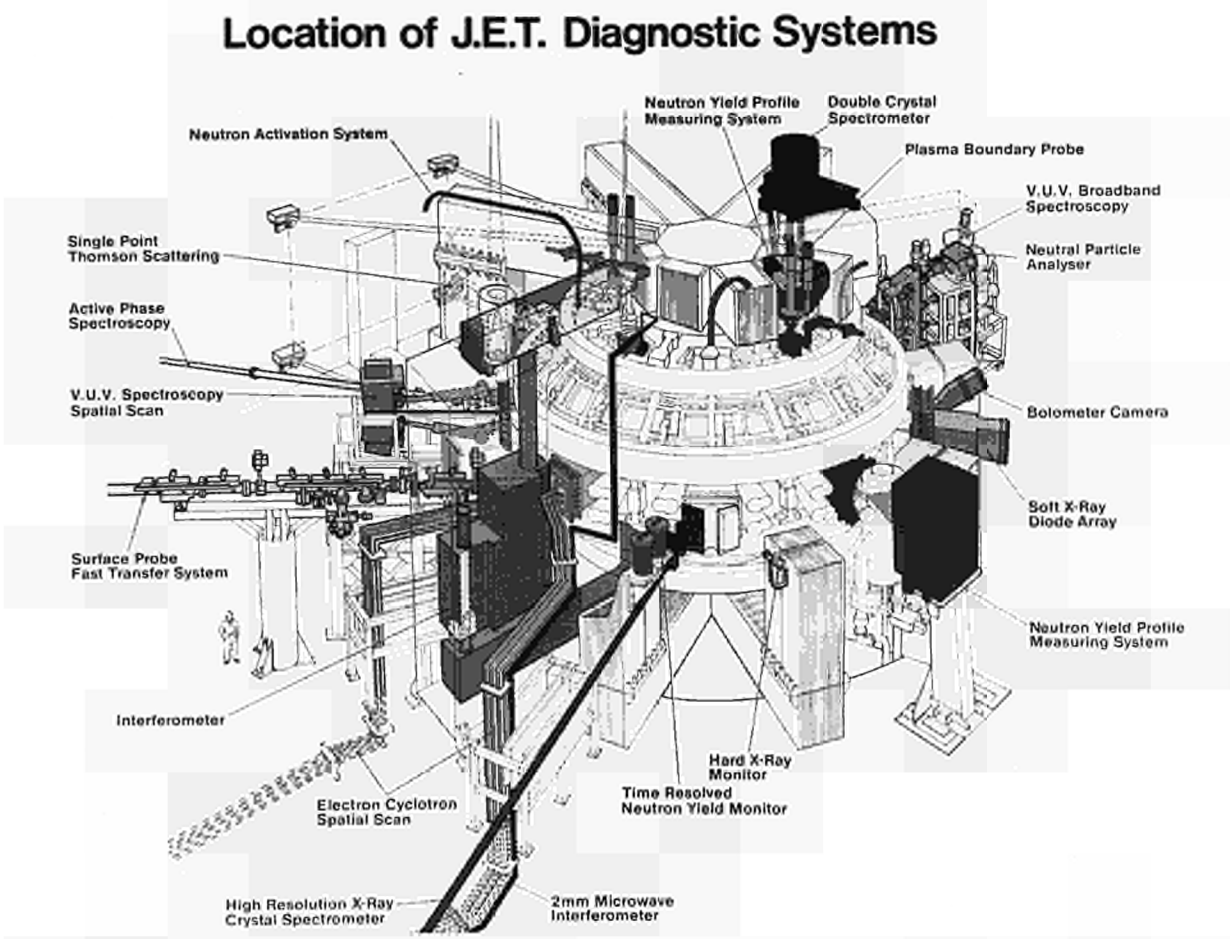

Fig.32: General layout of Diagnostics in the Machine.

Plasma Wall Interactions

The study of surfaces exposed to plasma has continued with its main aim to identify the detailed processes for hydrogen retention and re-emission (important for density control and wall pumping) and for impurity production (erosion/redeposition of carbon and nickel).

Samples of limiters, protection tiles and small, well-prepared long-term samples have been retrieved from the vessel at each vessel opening. Surface analysis has been performed in the in-house facility (KY1) with ion-beam and Auger techniques, as well as analysis in external laboratories. In particular, erosion/deposition on a discrete limiter used up to the end of 1986 has been completed and results indicate agreement with a description based on physical sputtering under the measured plasma conditions.

Time resolved measurements have become routinely available this year using the Fast Transfer System (KY2). Transfer under vacuum is possible to an integral surface analysis system (KY1) that also provides sputter ion-guns for cleaning the surface. On-line analyses have been performed on exposed samples within a twelve hour period. The system has been described more extensively in previous reports.

Limiter Diagnostics

The automated monitoring TV system based on CCD cameras equipped with filters near $\lambda = 900\,\mathrm{nm}$ has continued to give valuable operational information on the loading of belt limiters, RF antennae and X-point tiles. A new system based on a cooled infra-red array working at $\lambda \approx 3-5\,\mu\mathrm{m}$, that has already been successfully tested on the machine, has been delivered to JET and is awaiting installation.

Electron Cyclotron Emission (ECE) System

The Michelson and Fabry-Perot interferometers and the grating polychromator have been operated routinely during the year, and the electron temperature data provided has been used in the overall assessment of JET plasmas and in a wide variety of plasma physics studies. In addition, the heterodyne radiometer, which provides measurements of the time dependence of the electron temperature at eight locations in the plasma with very good spatial and temporal resolutions (typically $\gtrsim 2\,\mathrm{cm}$ and $\gtrsim 10\,\mu\mathrm{s}$) has been used in specific studies. In particular, it has been used to measure the temperature in the edge region ($3.8\,\mathrm{m} < R < 4.1\,\mathrm{m}$), and in studies of density limit disruptions.

The systematic comparisons of temperatures measured by ECE with those obtained with the Single Point Thomson Scattering System have continued, and preliminary comparisons have been made with temperature profiles measured with the new LIDAR

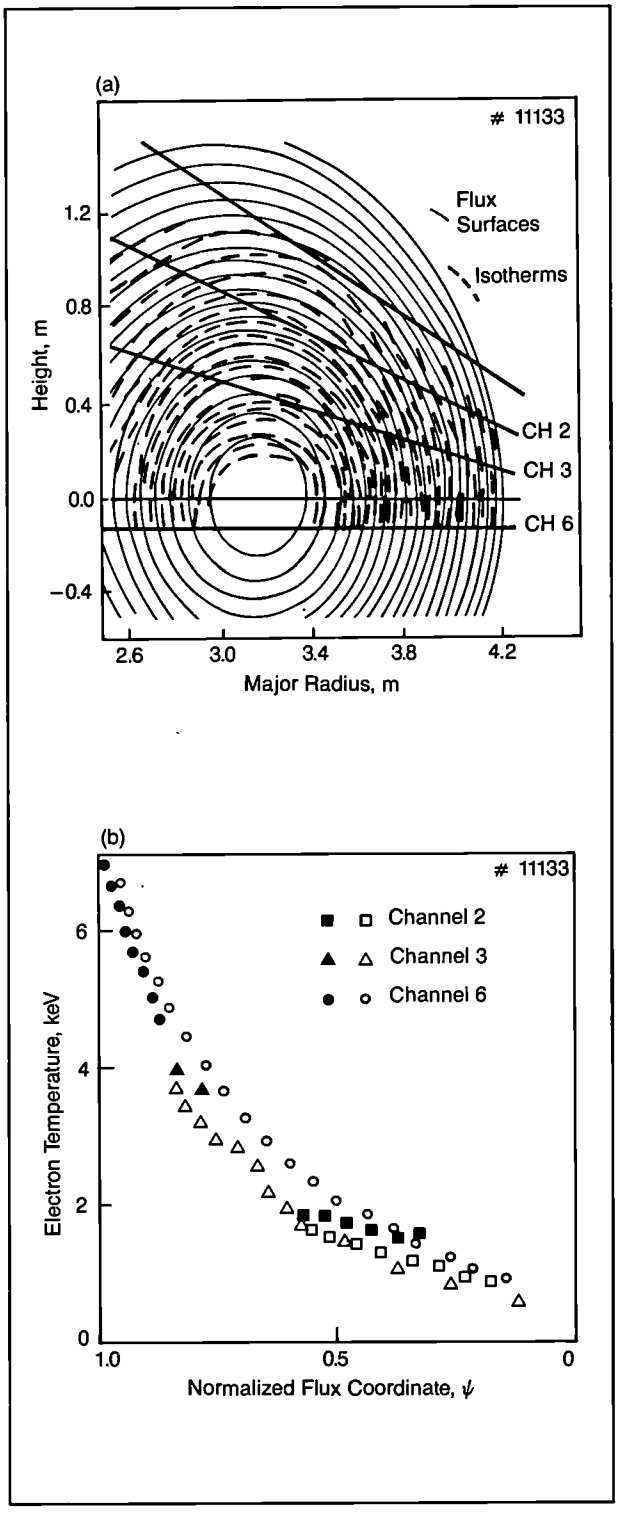

Fig.33 (a) Lines of constant magnetic flux in the poloidal cross-section derived from the magnetics diagnostics (solid lines) compared with the lines of constant temperature derived from measurements along the three ECE viewing channels, A, B, C (dotted lines); b) the electron temperature plotted against a normalized flux co-ordinate ψ (which varies from 0 at the plasma edge to 1 at the plasma centre) for each of the three viewing directions. The discharge has 5.6MW of ICRH applied. The measurements show that the temperature is constant on a flux surface.

diagnostic. In general, agreement has been obtained to within the estimated uncertainties (typically ± 10%). Routine measurements of the system response have been made using large-area thermal sources, including measurements with the calibration source mounted inside the vacuum vessel, and these have shown that the system is stable over long periods (≳18 months), to within a few percent.

Measurements made with the Michelson interferometers along three different viewing chords have been combined to derive the contours of constant temperature (isothermals) in the poloidal cross-section. These have been compared with the contours of constant magnetic flux obtained from magnetic diagnostics. The comparisons have been made for a wide variety of plasma conditions (ohmic, X-point, and additional heating) and agreement, within experimental uncertainties has almost always been obtained (see, Fig.33). There is one notable exception (i.e. single-null H-mode discharges) and this is currently under investigation.

Two upgrades to hardware have been initiated. A system for processing the scanning Michelson interferometer data in real-time has been designed and is being constructed by a manufacturer, under contract to JET. This system will provide the electron temperature profile and derivatives from it (e.g. $\int T_e(R)dR$) and this information will be used to provide a safety interlock for the JET multi-pellet injector, and more generally in the operation of JET. In addition, the number of channels of the heterodyne radiometer is being increased to 44, so this instrument will be able to provide useful data for most plasma conditions of interest in the JET programme. Both upgrades will become available during 1988.

Microwave Transmission Interferometry and Reflectometry

The microwave transmission interferometer has continued routine use for measurements of the line-of-sight electron density and for plasma control purposes. Minor improvements to the system have been made and have improved even further its high reliability (≳98%).

Considerable progress has been made with the multichannel reflectometer diagnostic. This system will probe the plasma with radiation propagating in the ordinary mode ($\boldsymbol{E}_{\parallel}\boldsymbol{B}$) at twelve frequencies in the range 18–80GHz, and so density layers in the range $0.4–8\times10^{19}\mathrm{m}^{-3}$ will be investigated. It will have two modes of operation: narrow band swept and fixed frequency. In the former mode, it should determine the radial positions of the different density layers (i.e. the density profile) at repetition rates up to 5kHz. In the latter mode, the magnitude and direction of any rapid movements of the density layers will be determined.

During 1987, the construction of the antenna, transmission waveguide, and combiner and separator systems, was completed and these subsystems were

installed on JET. The construction of the sophisticated source, detection and control electronics equipment, being carried out by the FOM Instituut voor Plasmafysica, The Netherlands, was also completed and the equipment for two channels was installed at JET. Preliminary observations were made with these channels during the last week of plasma operation.

Experiments have also investigated the possibilities of reflectometry on JET with waves propagating in the less commonly used extraordinary mode ($E_{\perp}B$). Both the lower and upper cut-off layers have been used successfully, and local density changes such as those due to sawteeth measured. The position of the cut-off layers depends on the magnetic field $B(R)$ as well as on $n_e(R)$. By combining data from the O-mode and E-mode reflectometers, it should be possible to obtain information on the local magnetic field and this possibility is being explored. An upgraded E-mode instrument is planned for 1988. This is aimed particularly at measurements and radial correlations of density fluctuations.

Thomson Scattering

The Single-Point Laser Thomson scattering system has been operated routinely during the year. The data provided by the system have been used in the assessment of overall performance of JET plasmas, and in the validation of the electron temperatures measured by Electron Cyclotron Emission (ECE) Systems.

Considerable progress has been made with the LIDAR Thomson Scattering system. In this new diagnostic, the backscattered light spectrum generated by a short ruby laser pulse (300ps duration), as it traverses the equatorial plasma diameter, is recorded as a function of time by a fast (700MHz bandwidth) detection and digitizing system. Analysis of the scattered spectrum yields the electron temperature and density in the usual way. However, by the time-of-flight or LIDAR method, the position of the laser pulse within the plasma is also known at any instant. Thus, by additionally analysing the time dependence of the spectrum, both T_e and n_e are spatially resolved as a function of the radial position. An additional merit is that the background plasma light signal is very low due to the short integration time for each spatial point.

First results on electron temperature profiles in JET were obtained in Autumn 1986 with single pulse laser operation. During the 1987 shutdown, the system was completed and now comprises six spectral channels covering the wavelength range 400–800nm. The calibration needed for the density evaluation was also performed. The required measurement of the vignetting of the collection optics along the line-of-sight was carried out by Raman scattering from air in the vacuum vessel at atmospheric pressure. To determine absolute density profiles, the line integral of the density as measured by this diagnostic is normalized to the corresponding line intergral measured by the FIR interferometer in a series of reference discharges.

The spatial resolution of the diagnostic is about 12cm. The dynamic range of the electron temperature measurements, defined by an increase of the statistical errors by a factor ×2, is determined by the spectral channel distribution. For the present system, it is approximately 0.3–20keV. At $T_e = 6$keV and $n_e = 3\times10^{19}\text{m}^{-3}$, the statistical errors of the electron temperature are ±6% whereas those of the density are ±4%. Possible systematic errors are more difficult to assess, but application of the χ^2 Goodness-of-Fit Test to a large number of measurements indicates that the systematic errors are within the limits of statistical errors. At present, measurements are taken with a repetition rate of 0.5Hz over the whole duration of the JET discharges.

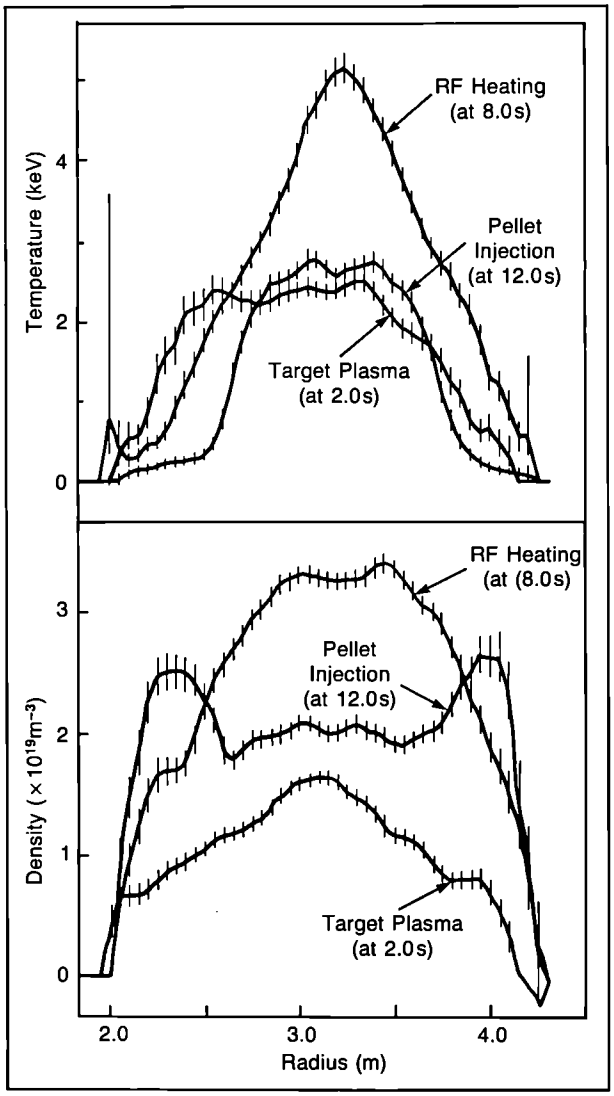

Fig.34 Plot showing the evolution of electron temperature (T_e) and density (n_e) of a discharge with additional heating and pellet injection. 5MW of ICRH was applied between 7 and 11s leading to the high temperature profiles and the increased density observed at 8.0s. A single pellet was injected at 12s, the temperature and density profiles at 12s are taken a few milliseconds after the pellet injection. The shoulders on the density profile indicate the pellet deposition.

Fig.34 shows an example of the evolution of the T_e and n_e profiles during a discharge with RF heating and pellet injection.

The system has operated routinely since July 1987. The temperature and density profiles obtained have been compared with the ECE and FIR interferometer results for a number of shots. Good agreement has been found when comparing the density profiles, in particular, and hollow density profiles indicated by the interferometer have been confirmed by the LIDAR measurements. Comparisons with ECE temperature profiles show an agreement to within about 10%.

Neutron Flux Measurements

The neutron emission strength is an important indicator of plasma quality and must be measured as accurately and reliably as possible. The Neutron Yield Monitor, a set of ^{235}U fission chambers, is the primary source of information on neutron strengths. To avoid unsuspected systematic errors, it is desirable to calibrate this diagnostic in two or more independent ways. Three calibration techniques have now been employed: (i) using a neutron source placed inside the JET vacuum chamber during a machine opening; (ii) using the Neutron Activation system to position samples close to the vacuum vessel for irradiation during a discharge and, afterwards, to remove them to a remote counting station for analysis; and (iii) by studying the induced radioactivity in the material of the vacuum vessel itself. The three techniques provide calibrations which agree within their individual estimated accuracies of ±15%.

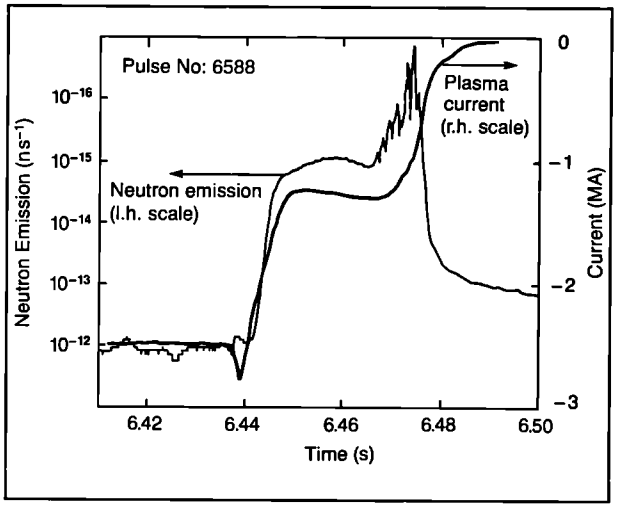

Fig.35: The plot shows the plasma current on Pulse No.: 6588 falling from −2.8MA to 0.2MA in a time interval of 50ms. There is a distinct hesitation midway down the plasma current collapse. The plot also shows the stength of the neutron production (solid line) on a logarithmic scale covering six decades with peak emission corresponding to a strength of nearly $10^{17}ns^{-1}$. The duration of the neutron pulse coincides with the hesitation in the plasma current decay. The obvious implications is that a runaway electron current of 1.5MA has been generated. Total neutron emission = $5x10^{13}$ neutrons.

The fission chambers have also been used in an extensive study of the photoneutron emission which accompanies most major plasma disruptions. Fig.35 shows the behaviour of the plasma current and neutron emission strength for a typical disruption at 2.8MA. Photoneutron production requires the presence of runaway electrons with energies well in excess of 8MeV. The strong correlation between the hesitation in the fall of the plasma current and the period of steady neutron emission shows that the plasma current is substantially carried by runaway electrons at this time. The total number of photoneutrons produced in a disruption is plotted in Fig.36 as a function of plasma current. The observed neutron yield scales as Y(neutrons/disruption) $=7\times10^{12}I_p^{2.6}$, where I_p is in MA. It is estimated that the fraction of the poloidal magnetic field energy ($\approx 4I_p^2$MJ) converted to runaway electron production is approximately $2\times10^{-2}I_p^{0.6}$, corresponding to 4MJ for a 5MA disruption.

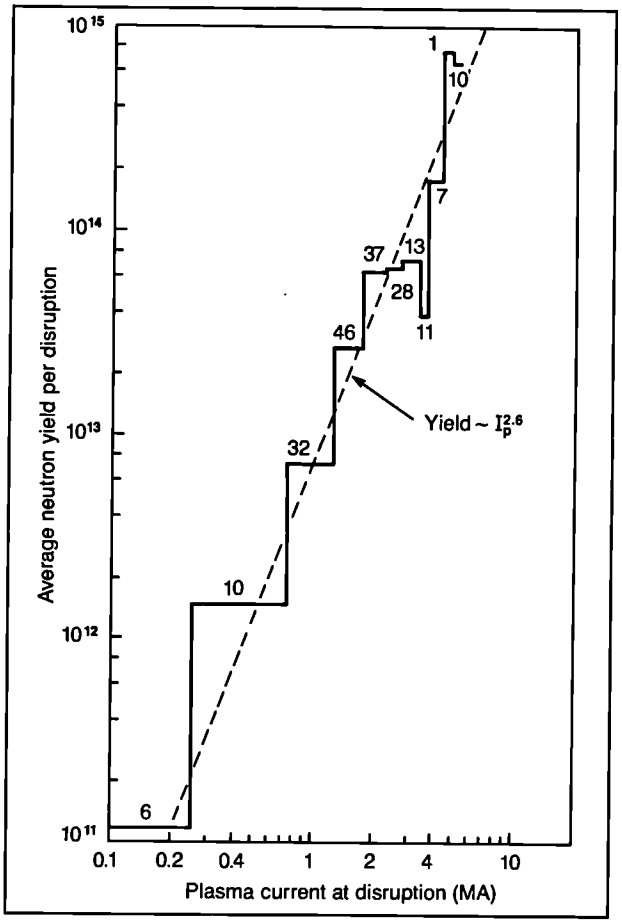

Fig.36: A histogram showing the average number of photoneutrons produced per disruption as a function of plasma current at the instant of the disuption. For each plasma current interval (0.5MA), the number of disruptions in the class is indicated. The dependence of the neutron yield (Y) on plasma current (I_p, in MA) isapproximately $Y=7x10^{12}\ I_p{}^{2\ 6}$.

Neutron Emission Profiles

To understand the strength of the total neutron emission from a fusion plasma, it is essential either to have reliable

information on ion temperature profiles or to make direct measurements of the radial profile of the neutron emission. Of course, once the neutron emission profile is known, ion temperature profiles can be deduced.

The Neutron Profile Monitor provides a total of nineteen lines-of-sight across the plasma, from which contours of neutron emission intensity can be deduced. This diagnostic was first installed in late 1986. After an initial evaluation of its performance, substantial improvements were made during the 1987 shutdown and the diagnostic is now acquiring reliable data on a routine basis. Fig.37 shows measurements of neutron emission observed along a well-collimated line-of-sight passing horizontally through the centre of the plasma taken for a 5MA, 3.4T discharge during ICRF heating with 10MW of power coupled to the plasma. The central neutron emission intensity changes by in excess of a factor ×3 during the sawtooth period.

Neutron Spectroscopy

Three neutron spectrometers are currently being operated: ^{3}He ionization chamber spectrometers located in the Torus Hall and in the Roof Laboratory and a time-of-flight spectrometer also in the Roof Laboratory. These spectrometers should be regarded as parts of a single spectrometer facility. The ionization chambers offer high efficiency and good energy resolution but are severly limited in count-rate capability. The time-of-flight spectrometer has a wide dynamic range but is not very efficient and gives good results only at the highest neutron rates so far experienced at JET. Taken together, they provide coverage for a neutron intensity range of some three orders of magnitude.

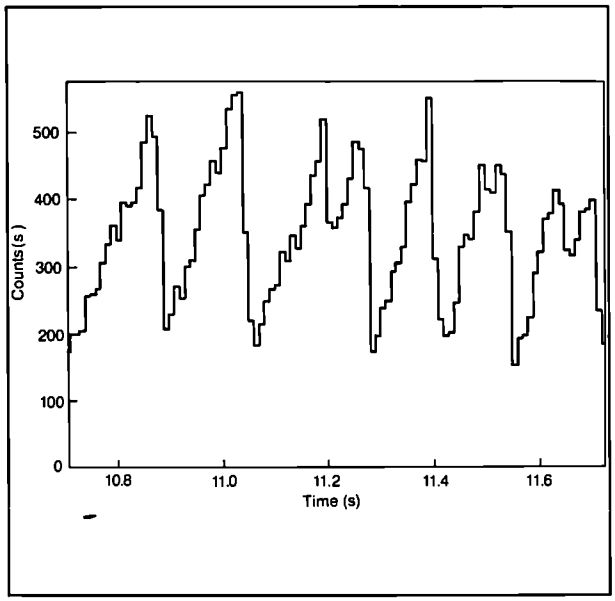

Fig.37: Count rate recorded with a central channel of the neutron profile monitors during a period of ICRF heating for Pulse No.12957. The strong modulation of the neutron emission from the centre of the plasma is clearly shown.

The reason for providing two orthogonal lines-of-sight is that the neutron energy spectrum from D^0 beam-plasma interactions depends on viewing direction so that comparison between different directions should assist interpretation of the results. Preliminary work shows that the neutron spectra obtained for D^0 beam-heating conditions are reproduced quite well by computed spectra using data from standard JET diagnostics (Fig.38). This implies a fair measure of self-consistency between all involved data and calculations based on the classical slowing down of the injected particles.

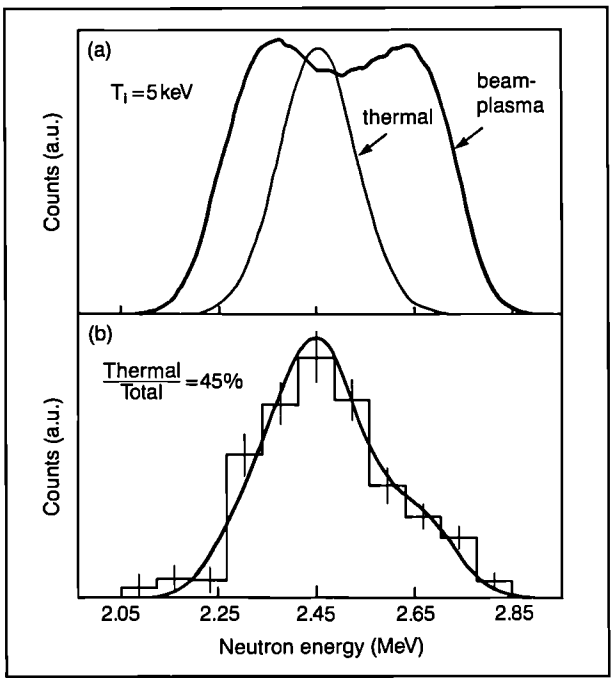

Fig.38: (upper) - Computed neutron energy spectrum for 80 keV beam injected deuterons interacting with a 5 keV deuterium plasma. The thermal contribution is also shown.
(lower) - Computed spectrum (beam – plasma and thermal contribution in 55:45 proportion) compared with spectrum measured along a radial line-of-sight.

Neutron energy spectra can indicate the presence of neutrons emitted from unexpected sources. Some recent high power (17MW) ICRF heated discharges have been observed in which deuterons have been accelerated to energies of over 1 MeV. The neutrons emitted in reactions between these high energy deuterons and thermal deuterons exhibit a considerable kinematic broadening about the nominal 2.45MeV emission energy. On occasions, more neutrons can be produced from this mechanism than from thermal reactions.

Triton Burn-up Studies

The confinement and slowing down of the 1 MeV tritons emitted from the D+D → T+p reaction have been studied by observing the 14MeV neutrons from T+D → n+^{4}He reactions induced by the fast tritons. Two approaches have been pursued. The first involves the use of the neutron activation system to determine the ratio of 14MeV to 2.5MeV neutrons emitted during a discharge, as this is directly related to the triton burn-up probability. The second approach was to record the

instantaneous emission strength of the 14 MeV neutrons during a brief period of D^0 neutral beam heating, see Fig.39. It is found that the burn-up fraction obtained from a classical calculation is about 20% higher than the experimentally determined values. Further, it is found that the time-dependence can only be reproduced if the slowing-down rate is increased by 20%. Both findings are consistent with errors in the normalizations for Z_{eff} or T_e data that lie within the experimental uncertainties. It appears that our assumption of classical behaviour for the tritons is acceptable, within the present uncertainties.

Gamma Ray Studies

Gamma-rays are emitted as a weak branch of all the light particle fusion reactions. This circumstance is particularly useful as it provides a means of monitoring the ^{3}He-D reaction. The 16 MeV gamma-rays emitted from this reaction when ^{3}He is the minority ion species heated by the ICRF have been used to demonstrate the generation of about 10 kW of fusion power.

Apart from the fusion reaction gamma-radiation, it has also proved possible to detect radiation from nuclear reactions between energetic particles (protons, deuterons, ^{3}He ions) with carbon impurity ions in

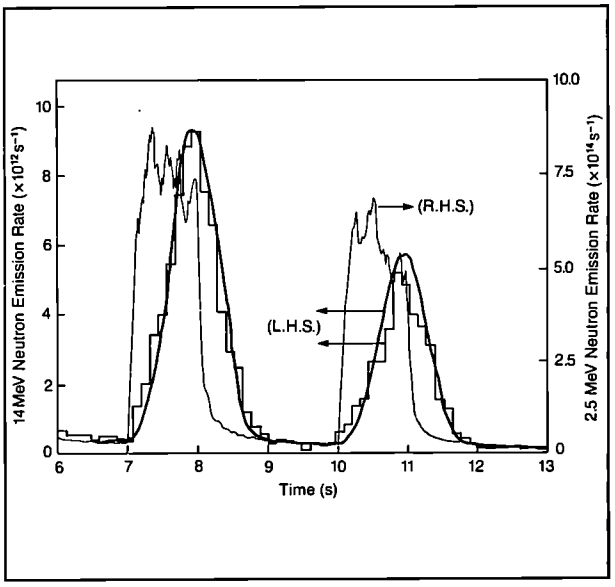

Fig.39: The 2.5 MeV neutron emission (dotted line, r.h. scale) and 14 MeV neutron emission (dashed, l.h. scale) recorded for Pulse No.10894 when the neutral beam injectors were fired twice. The theoretical curve (thin line, l.h. scale) reproduces the 14 MeV neutron emission for the case when the classical stopping power formula for tritons is multipled by a factor x1.2.

discharges with significant high-energy tails due to ICRF heating. The exothermic reactions $^{12}C(D,p)^{13}C$ and $^{12}C(^3He,p)^{14}N$ are particularly strong. Gamma-radiation energy spectra have been recorded with a large NaI crystal scintallator; individual lines can mostly be associated with the decay of excited states in ^{14}N. The 7 MeV gamma-ray line has indicated that accelerated ^{3}He ions attain energies in excess of 2 MeV in some discharges.

Interferometry and Polarimetry

The multi-chord far-infrared (195 μm) interferometer continues to be essential apparatus for measurements of density needed for real-time control of JET operation, and for interpretation of plasma behaviour. The interferometer system has been upgraded in two respects. Following installation of new components in the torus, only six vertical and two lateral chords remain. Components in the optical train for the two lateral chords are susceptible to vibration and displacement. To compensate for these in the plasma density measurement at 195 μm, a simultaneous measurement at a shorter wavelength, (119 μm from a CO_2-laser pumped alcohol vapour laser) is made in the two lateral chords.

The six vertical chords have been equipped to simultaneously measure the Faraday rotation of the plane of polarization and the phase shift of the 195 μm beam. The radial electron density and poloidal magnetic field profiles are evaluated and the radial distribution of the toroidal plasma current-density, j(r), is deduced. j(r) is a crucial quantity in the assessment of MHD behaviour of a tokamak. Fig.40 shows the evolution of

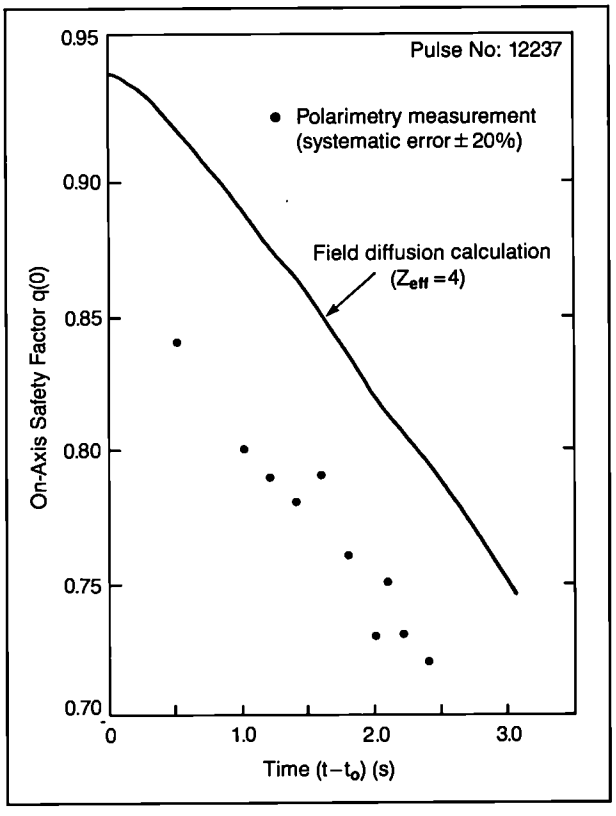

Fig.40: The evolution of the safety factor on axis, q(0), during a period of sawtooth stabilization (monster sawtooth phase). (t_o marks the beginning of the stabilizatin phase).

the safety factor on axis, q(0), during a period of sawtooth stabilization induced by application of ICRF power in JET (the so-called monster sawtooth phase). Although the absolute value of q(0) may be in error, by ± 20%, the relative change in q(0) during the period of sawtooth stabilization has been accurately measured.

Within the tolerance of the absolute error, the measurement is supported by model field-diffusion calculations.

Single-Shot Pellet Injector

The single-shot pellet injector system has been extensively modified so that it now shares the space it previously occupied with the multi-pellet injector. The modification entailed (i) removal of the buffer volumes, fast valves and pumps needed to prevent the propellant gas entering the torus and replacement of these with one cryo-pump box which is shared with the multi-pellet injector; (ii) reorientation of the cryostat due to space considerations; (iii) installation of new single-piece barrels for the 3.6mm and 4.6mm pellets; (iv) improved pellet diagnostic station to monitor the size and quality of the pellets. The modified injector has been operated successfully with improved pellet quality. This facility, with pellets of hydrogen or deuterium or mixtures of the two (also doped with neon, when needed) will be used to elucidate particle transport, aspects of recycling and fuelling, and relationship between particle and thermal transport by simultaneous measurements of particle and thermal diffusivities.

Neutral Particle Analysis

The array of neutral particle analyzers has operated continuously in all plasma conditions and provided valuable data on ion temperature profiles, ion velocity distributions and the physics of ICRF heating.

To continue this role into the neutron intensive environment of the near future and later into tritium operation, an upgrading of the analyzers is necessary. A study of a new detection system combining energy selection using an electrostatic field, and mass selection employing a time-of-flight (TOF) technique has been performed for JET under contract by Euratom-ENEA Association, Frascati, Italy. In Fig.41, a schematic of the electrostatic energy analysis is shown.

A new analyzer using this detection system is under construction using 15 TOF detectors. This will allow, with the help of a suitable neutron shield, simultaneous measurement of H, D and T particles at 15 different energies. The new analyzer is planned for installation during the 1988 shutdown.

Soft X-Ray Diode Arrays

The diode array system built by EURATOM-IPP Association, Garching, F.R.G., consists of two X-ray imaging cameras which view the plasma from orthogonal directions. The diagnostic is used to investigate MHD plasma properties and to measure the radiation profiles with coarse energy resolution using different absorption filters. In 1987, an additional set of five toroidal arrays was installed which allows the determination of toroidal MHD mode numbers.

Further studies have been undertaken of the sawtooth instability and these have shown that the so-called

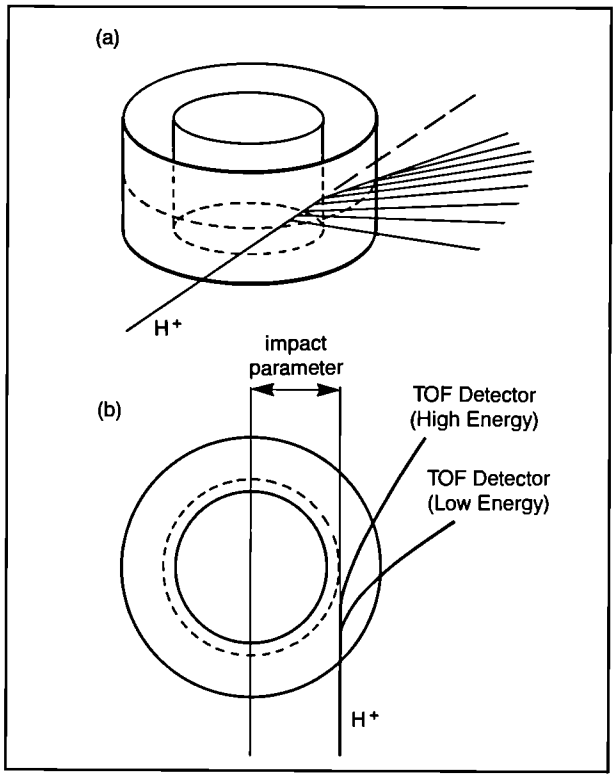

Fig.41: Cylindrical electrostatic plates for energy selection.

monster sawtooth crash has a similar structure to normal sawteeth (i.e. the central plasma is rapidly displaced off-axis and then collapses to give a much flattened profile). This result has produced difficulties in our understanding of the JET sawtooth collapses as interchange modes. The toroidal cameras have confirmed the m=n=1 nature of the sawtooth collapse and have been routinely used for n-number determination.

The vertical X-ray camera has continued to provide detailed measurements on pellet ablation and penetration following injection with the multipellet system. This new system also produces the long lived snake oscillation which is a small region of the plasma on the q=1 surface with very much enhanced electron density. Very high peak densities have been observed and further observations have been made on their creation and subsequent long lifetime, including their persistence through the sawtooth crash and the injection of subsequent pellets into the plasma.

Detailed studies of density-limit disruptions have continued and much progress has been made in understanding the complicated sequence of minor disruptions preceding the final catastrophic loss of plasma. The role of the m=2 oscillation has been clarified and the structure of minor disruptions with and without an m=1 mode have been studied in detail. Observations on the major disruption have shown the rapid escape of plasma and a large increase in X-radiation. The latter has been adequately explained by an impurity influx model.

Radiation profiles during multipellet injection experiments have been observed to have surprisingly peaked profiles. However, calculations of the X-ray emission, taking account of the known density and temperature profiles, have shown reasonable agreement with experiment. Similar calculations have shown good agreement with the very broad profiles seen in X-point and H-mode operation.

The radiation shield for the horizontal camera is being constructed and will be installed in 1988. It is then planned to make a detailed assessment of the lifetime of this diagnostic during the D-D and D-T phases of operation.

Soft X-Ray Pulse Height Analysis

The three detector pulse height analysis (PHA) system has been reconfigured during 1987 to allow operation into the JET active phase. The detectors are now installed in the Diagnostic Hall where they view the plasma through a small aperture in the Torus Hall wall which acts as an efficient neutron shield.

The diagnostic routinely measures impurity concentrations and electron temperatures and a radiation code is used which successfully models both the spectra from this diagnostic and the profiles observed by the diode array system. The diagnostic is also able to measure non-thermal tails in the electron distribution function.

High Resolution X-Ray Spectroscopy

A high resolution curved crystal spectrometer (radius of curvature 24m) was operated continuously during 1987. The instrument measures characteristic X-ray spectra in the wavelength region around 0.2nm which covers H- and He-like ionisation stages of metal impurities such as Cr and Ni. During 1987, the instrument was equipped with a new diffracting crystal (Ge 440) to increase the sensitivity. H- and He-like Ni spectra were recorded with an energy resolution of 20,000 which is sufficient to measure accurately the widths of Doppler-broadened line profiles over a wide temperature range. Nickel ion temperatures have been measured routinely during the various operational scenarios, in the range 1.5-14keV. The time resolution achieveable is dependent on the signal to noise level at the detector and varies from 20ms to several seconds. During RF and NB heating, typical integration times were a few hundred ms, and with RF alone a time resolution of 20ms was frequently achieved. In addition to measuring the central impurity ion temperature, the X-ray spectra provides information on plasma rotation from line shifts. Toroidal velocities of $0.5\text{-}3\text{x}10^3 ms^{-1}$ have been recorded during NB and of $5-8\text{x}10^2 ms^{-1}$ during RF heating. The intensity of the measured X-ray line measures the absolute concentration of nickel in the plasma. During 1987, nickel concentrations of typically $0.1-1\text{x}10^{15}\text{m}^{-3}$ were measured for various operating schemes on JET.

Wide Band X-Ray Spectroscopy

Two Double Crystal Monochromators, built by EURATOM-IPP Association, Garching, FRG, were installed on JET during 1987. Both instruments are capable of measuring spectrally resolved soft X-ray emission from the plasma in the wavelength range 0.1-2.1nm, covering radiation from highly ionized light impurities (such as O) as well as from metal impurities (such as Ni and Cr). To cover the entire spectral range, three to four pairs of crystals with different lattice constants are necessary.

The spatial scan double crystal monochromator provides spectrally resolved ($E/\Delta E \sim 500$) radial profiles of the plasma at a maximum rate of nine profiles per second. The instrument is directly attached to a main vertical port on top of the JET torus allowing a sufficiently wide horizontal aperture for a continuous spatial scan. During early 1987, an absolute calibration of the instrument was carried out, and a new vacuum interface to the new vessel support was constructed and installed. The diagnostic reached its full operational capacity at the end of 1987 when it obtained first radial profiles of highly ionized nickel. Fig.42 shows Abel inverted radial profiles of H- and He-like nickel.

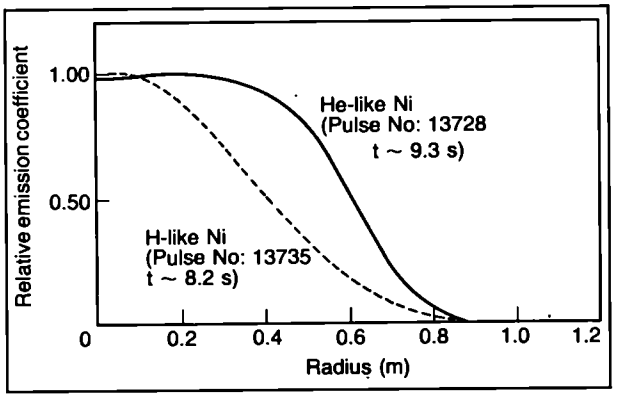

Fig.42: Radial profiles of H-like (1s-2p Lyα2) and He-like (1s-2p, W) emission from nickel measured with the spatial scan double crystal monochromator ($T_e = 10keV$).

The active phase double crystal monochromator provides medium ($E/\Delta E \sim 500$) and high resolution ($E/\Delta E \sim 5000$) spectral surveys for one horizontal line-of-sight through the plasma centre. A full wavelength scan for the entire range of a crystal pair can be performed in 0.5s. The instrument is planned for active phase operation on JET as one of the main impurity survey diagnostics and, consequently, has been installed in a concrete shielding outside the biological wall of the Torus Hall. The high vacuum beamline connecting the monochromator with the torus was completed and commissioned in late 1987. Both medium and high resolution collimators have been successfully aligned. The active phase double crystal monochromator is expected to be fully operational in early-1988.

Summary of Machine Operation

During the 1987 operation period (weeks 30 – 52), there were essentially three periods of operation:

(a) During weeks 30 to 33, much time was spent in commissioning systems modified during the major shutdown. Nevertheless, it was possible to recommission the machine in its modified state and the significant advantages of the modified P1 coil (ten subcoils instead of eight) and the additional switching network in the OH circuit were rapidly demonstrated. Further, the eight RF antennae and multi-pellet injector were successfully operated. However, there were some teething troubles with the new vessel restraints and two water leaks in neutralisers of the Octant No.8 neutral beam injector delayed commissioning of this system;

(b) During weeks 34 to 42, some in-vessel work was carried out but a certain amount of interference to operation was caused by imperfect operation of the vessel restraints, in spite of remedial work. The belt limiters and RF antennae screens and other in-vessel components were cooled, and successful plasma operation achieved. The poloidal field circuit was successfully reconfigured to provide additional radial position control required for higher plasma energies resulting from increased heating power. Both Ohmic and RF heating operation performances were extended, but neutral beam heating was further delayed by power supply problems. The modified cryogenic system was successfully operated with its three major loads; the pellet injector and two neutral beam injectors;

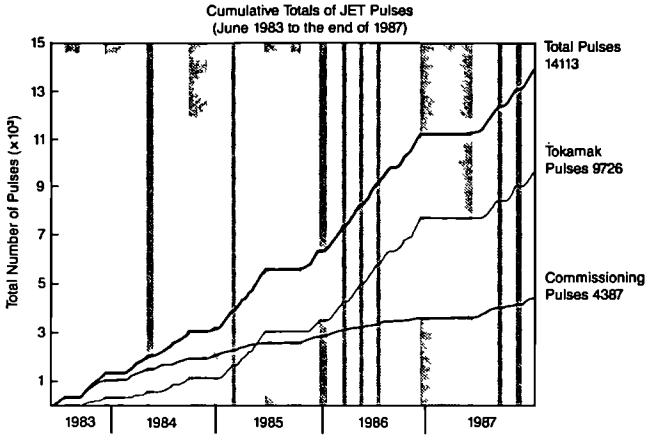

Fig.44: Cumulative total of JET Pulses.

(c) During weeks 43 to 52, about half of the time was spent in commissioning the PFX amplifier and its controls. The large degree of operational flexibility introduced by PFX and its ability to provide different current distributions in the main primary coil P1 were quickly demonstrated. Further advances were made in the performances of Ohmic heating (6MA full aperture plasma, 3.5MA single X-point plasma), and RF heating. The neutral beam injector at Octant No.8 was finally brought into operation, and half of the tokamak plasma programme was devoted to combined neutral beam and RF heating.

In all, there were 133.5 days of operation in 1987, during the June-December period. About 50% of these days were devoted to experimental operation, with 20% for each of Ohmic and RF heating, and about 10% for combined neutral beam and RF heating. The allocation of time to the different activities and the number of days involved in the various tokamak operational

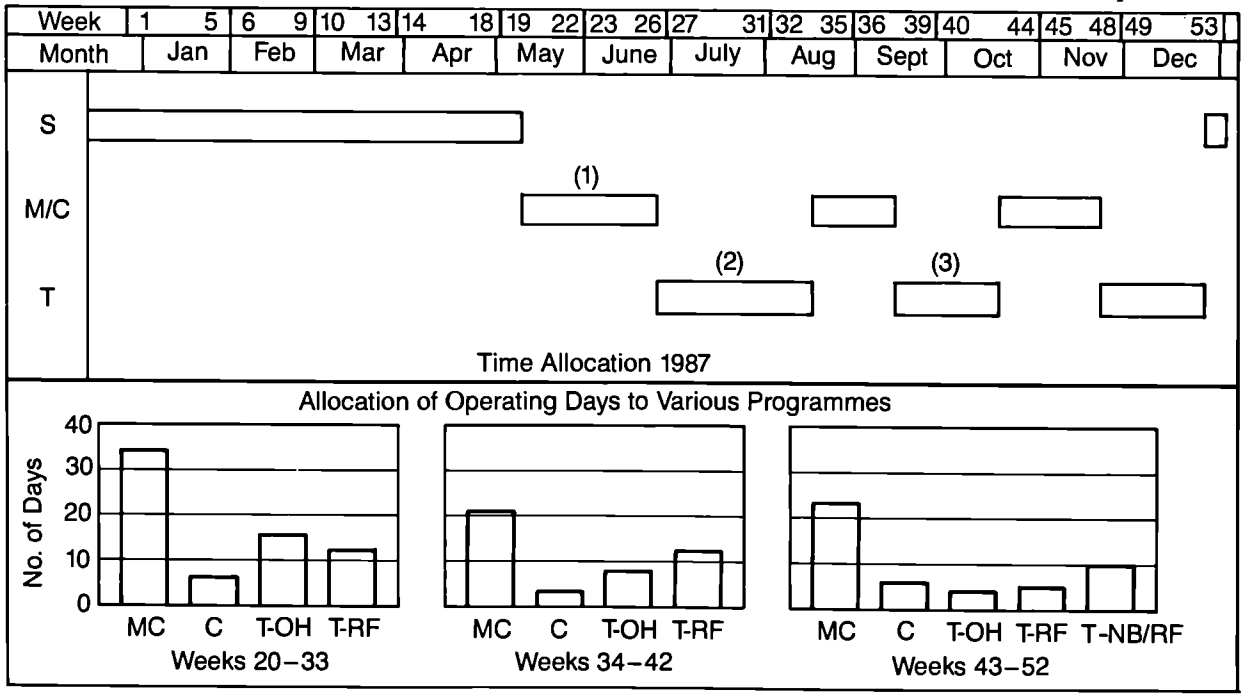

Fig.43: Allocation of time to different activities of the operating programme for 1987 (S=Shutdown; M/C=Machine Commissioning; and T=Tokamak Operation).

programmes is shown in Fig.43.

Operation became more complex than before with the introduction of new and modified systems. The organisation of operational time remained largely the same as that in 1986 except that, in an attempt to recover lost time, commissioning was carried out in double-shift-day operation.

The total number of pulses was 2889 in 1987 (compared with 4902 in 1986 and 3132 for 1985) bringing the total number of pulses to 14113 (see Fig.44). Even though many of the pulses were of the commissioning type, the relative number of tokamak pulses continued to increase.

Summary of JET Technical Achievements

During the first half of 1987 the machine was shutdown undergoing major modifications to upgrade the performance in accordance with the JET Development Plan.

A major and unexpected task which had to be undertaken was the repair of the central poloidal field coil stack which was found to be damaged upon dismantling in December 1986. A new design featuring interlocking keys between subcoils and spring assemblies embedded on the key system was developed and implemented in an extremely short time, allowing the repaired coil stack to be re-installed in the machine by May 1987. The poloidal field coil stack was increased from eight to ten subcoils, as planned.

At the same time, the first wall of the JET vacuum vessel was being completely transformed. Additional wall protection tiles were fitted on all bellows protection plates and octant joints providing a total of forty graphite protection belts in the poloidal direction. A new type of carbon fibre reinforced graphite tiles were also installed at the inboard wall in the vicinity of the equatorial plane where most damage due to plasma disruptions had been found to occur.

The eight discrete graphite limiters were removed and replaced by two toroidal belts of the belt limiter. This assembly, which included the installation of the cooling water pipework inside the vessel, required for the first time the use of specially developed remote handling tools for cutting and welding. The belt limiter was assembled within remarkable small dimensional tolerances, thus allowing a uniform distribution of the power deposited by the plasma.

The three uncooled RF antennae (A_0) were replaced by eight cooled RF antennae (A_1), each featuring a water-cooled screen for long duration pulses. With the introduction of the belt limiters and cooled antennae, JET had water cooled components directly facing the plasma for the first time. It is remarkable that the commissioning and operation of this internal water cooling system did not raise any insurmountable problems.

On the mechanical side, the vacuum vessel was fitted with new inertial supports designed to resist the large vertical forces occurring during vertical instabilities. When first installed, these supports did not perform initially as expected due to excessive friction in some bearings. This was rectified in October 1987, and from then, the supports behaved as expected.

1987 was a very busy year for power supplies with the development and towards the end of the year the full implementation of the new ohmic heating circuit for operation at 7 MA in the limiter mode and 4 MA in the X-point mode. The new systems which were successfully introduced into operation were: the switching network to control the rate of rise of the plasma current; the PFX power supply to control the current in the six centre subcoils of the ohmic heating coil stack; and the temporary booster amplifier for the poloidal vertical field circuit. The tight planning and quality control for both installation and commissioning allowed all these units (together with the associated safety interlock and control systems) to be brought successfully into operation on schedule.

A major study of the operating conditions of the machine and power supplies for plasma currents up to 7 MA in the limiter mode and 4 MA in the X-point mode was undertaken in 1987. This study was to determine the safe limits of operation for the major components of the machine and identify the necessary changes to overcome difficulties. By the end of 1987, analysis of the JET coils was complete. The prototype toroidal field coil was undergoing tests to check its fatigue strength against transverse forces at the collar tooth. The analysis of the vacuum vessel was well underway and uncovered some potentially serious structural problems due to disruptions at high currents. Some design changes were being discussed to overcome these difficulties.

JET plasma operation restarted in June 1987. Experiments demonstrated the success of the modifications and enhancements introduced during the shutdown. The plasma start-up conditions were greatly improved as a result of the reduction of stray fields and of the increased voltage capability of the plasma radial position control systems. These improved conditions permitted the use of a larger premagnetisation current (up to 40 kA) and obtaining plasma currents of 5 MA with 10 s flat-top. Subsequently, the use of PFX allowed a 6 MA plasma current with a flat-top of 2 s to be reached.

These successes were most encouraging but the operation of the machine above design rated values was carried out with very great care. A number of technical restrictions were imposed to operate the machine within conservative limits. The forces acting on the vessel during disruptions or vertical instabilities could endanger the mechanical integrity of the vessel and had to be limited by restricting operation at large plasma currents or large plasma elongations. The power deposited by the plasma on the water cooled RF antennae or the inboard wall had

to be limited to avoid damage to antennae or wall protections. The transverse forces acting on the toroidal field coils had to be limited to prevent damage in the critical area of the collar tooth. All these technical limitations were being addressed and tests or design modifications were being planned by the end of 1987 in order to allow further progress in 1988 and 1989.

Development work on remote handling systems continued successfully. The articulated boom was once again used extensively during the shutdown, together with special purpose cutting and welding tools for the installation of the belt limiter and antennae inside the vacuum vessel. A major contract was placed for the procurement of the telescopic arm which will be suspended from the JET main crane and allow remote handling operations on the outside of the machine.

The work on tritium handling was reorganised and two new groups created: one for the design and construction of the tritium plant, and the other for the safety studies and licensing of the tritium plant and tritium operation. By the end of the year, the plant design was well advanced and a major contract had been placed for the isotope separation system by cryodistillation.

Scientific Achievements During 1987

Global Power Balance and Plasma Characteristics

The main emphasis of the 1987 additional heating experiments has been exploitation of the new ICRF heating system. Technical problems with the neutral beam (NB) system seriously reduced the number of NB experiments performed. In addition, H-mode discharges obtained using NB are described in a following section on Separatrix Experiments and H-Mode Phenomena. In this section, use has been made of 1986 NB data to compare the hot-ion and hot-electron regimes. Although the experimental conditions were slightly different, the similarity of the best 1986 and the 1987 ICRF heating results show that the comparison is valid.

Most of the 1987 ICRF heating experiments were performed using the hydrogen minority scheme. The background hydrogen released by the vacuum vessel walls was frequently used, so the minority concentration is now known accurately. Neutral particle analyser (NPA) measurements indicate that the hydrogen concentration is typically 5% of that of the majority species. Where the minority gas has been injected, the main plasma parameters were not significantly affected by the amount used. Both deuterium and helium were used as the majority species with similar results.

Monster sawteeth normally occur in ICRH discharges with $I_p(MA)/B_T(T) < 1.2$ and heating powers above a few MW. Their characteristics are described in the following section on Sawtooth Oscillations. The main effect that they have on the power balance is to promote the thermal decoupling of the electrons and the ions in the plasma core. In addition, since the temperature profiles are not periodically flattened by sawteeth, the total energy content can be up to 20% higher.

The following sections make use of various determinations of the total plasma energy content. The most direct of these is that obtained with the diamagnetic loop (W_{dia}). Alternative values for the energy content are obtained from analysis of the equilibrium poloidal fields (W_{mhd}) and measurements of the profiles of temperature and density (W_{kin}).

Fast Ion Energy

Some of the initial 1987 ICRH data was obtained from a power scan at $I_p = 2MA$ and $B_t = 2.2T$. W_e(the electron energy content), W_{kin} and W_{dia} for this scan are plotted against total power in Fig.45. At low powers W_{kin} and W_{dia} agree reasonably well. As the power increases, a difference opens up amounting to 30% of W_{kin} at 10MW total power. This difference is due to the energy (W_f) contained by the minority particles which contributes to W_{dia} but not to W_{kin}.

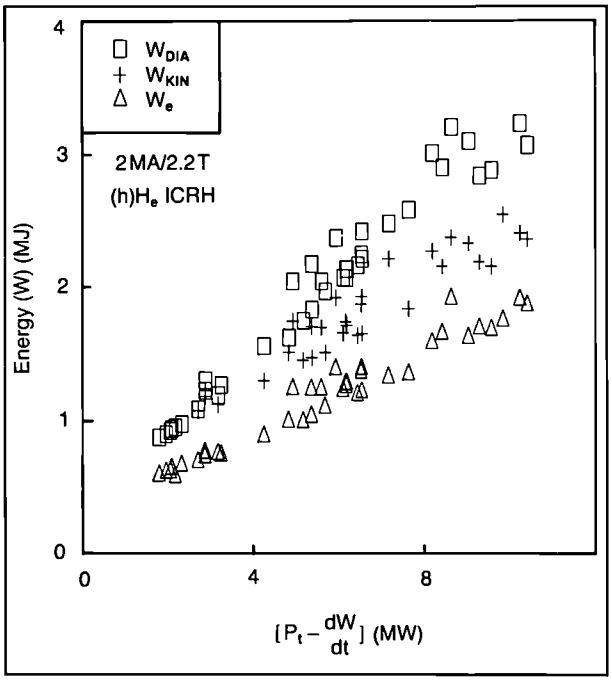

Fig.45: The electron, kinetic and diamagnetic energy contents against total heating power for a $I_p = 2MA$, $B_t = 2T$ hydrogen minority ICRH power scan.

The RF power is primarily coupled to the motion of the minority particles perpendicular to the magnetic field to which the diamagnetic loop is sensitive. In fact, since the diamagnetic loop signal is weighted by a factor of 1.5 to account for the parallel energy in an isotropic distribution, the energy difference shown in Fig.45 is an overestimate of the fast ion content. W_f can be measured using the relationship:

$$W_f = 2/3\ (W_{dia} - W_{kin})$$

A simple approximation is obtained for the fast ion energy content when RF power per minority particle is high enough that electron friction dominates. This is given by

$$W_{f,th} = P_{RF}\tau_s/2$$

where P_{RF} is the ICRF heating power and τ_s is the classical slowing-down time.

W_f is compared with $W_{f,th}$ in Fig.46. The central electron temperature and density have been used for the slowing-down time. Although W_f scales correctly, it is a factor 5 less than the calculated value. The discrepancy can be slightly reduced by taking account of the efficiency for launching fast waves and the reduction in τ_s is due to the finite resonance volume. However, the values for the efficiency and the resonance volume, which are obtained from the analysis of ICRF modulation experiments, are not sufficient to account for the factor of 5.

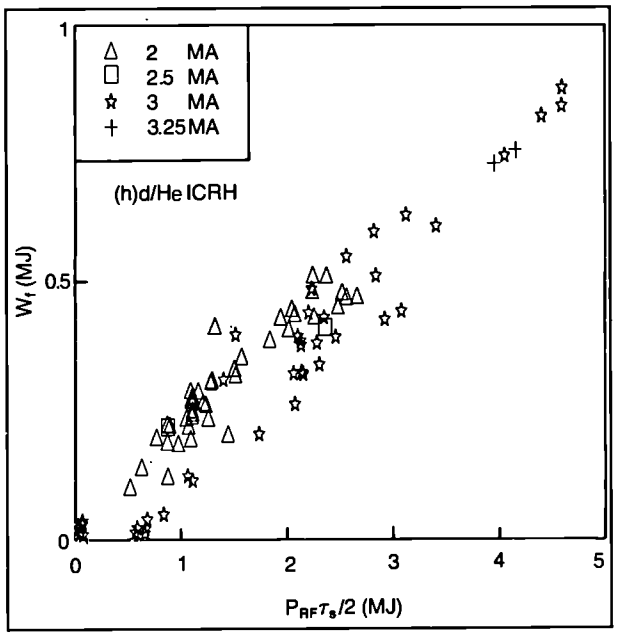

Fig.46: The fast ion energy content obtained from W_{dia} and W_{kin} compared with the theoretical value based on the central classical slowing-down time.

That minority ions are accelerated to very high energies by the RF fields, as predicted by theory, is very clearly demonstrated by the detection of gamma-rays from their excitation of the nuclei of plasma impurities. Also, the response of W_{dia} and W_{mhd} to RF modulation is in the 2:1 ratio expected for perpendicular motion. In view of these correctly predicted features of the experimental data, the quantitative discrepancy shown in Fig.46 is somewhat puzzling. Further experiments and analysis will be undertaken to clarify this issue.

The Safety Factor Dependence of Energy Confinement

Part of the JET programme is based on increasing the plasma performance by operating at high plasma current. Therefore, it is of interest to investigate the extent of the confinement deterioration caused by the widening of the sawtooth region at low values of safety factor, q. Following the power scan at $I_p = 2$MA and $B_t = 2.2$T, another scan at $I_p = 4$MA and $B_t = 2.3$T was performed. Hydrogen minority ICRF in deuterium data was selected for comparison of these scans.

Fig.47 shows W_{dia} plotted against total heating power for both conditions. Although the 4MA data starts with a higher energy content, the 2MA plasmas showed a better response to the ICRF heating. A good measure of the effectiveness of additional heating is given by the incremental confinement time ($\tau_{inc} = \delta W/\delta t$). τ_{inc} was 285ms at 2MA and 195ms at 4MA.

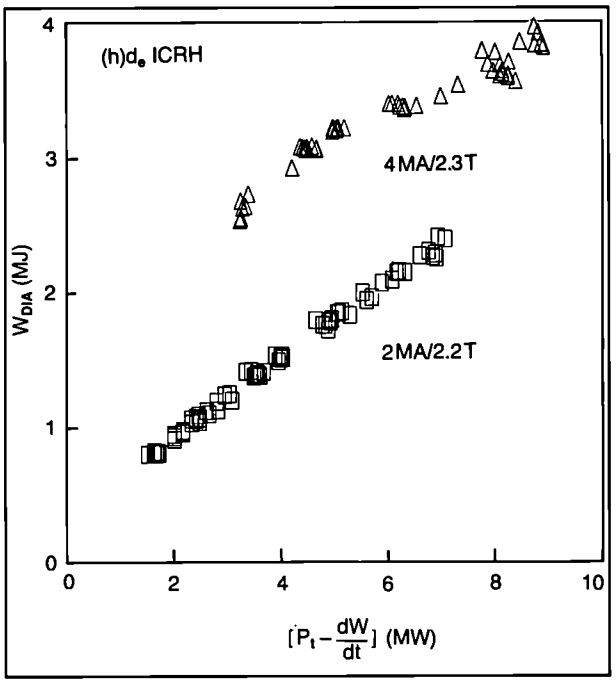

Fig.47: The diamagnetic energy content against the total heating power for $I_p = 2MA$, $B_t = 2.2T$ and $I_p = 4MA$, $B_t = 2.3T$ hydrogen minority in deuterium ICRH power scans.

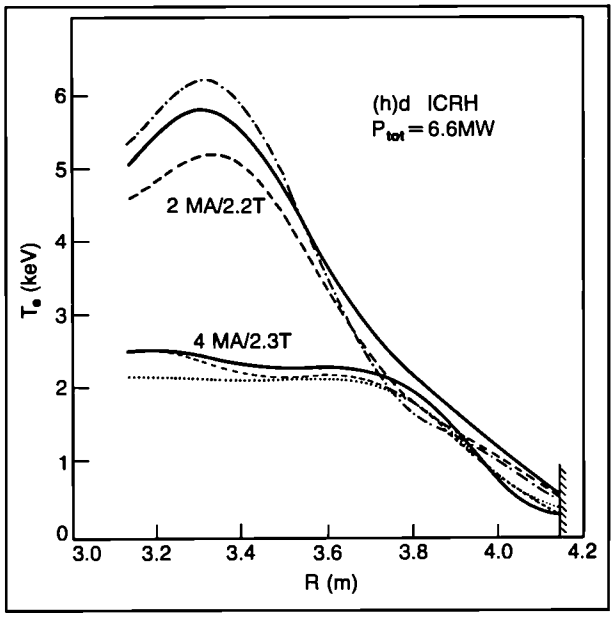

Fig.48: The electron temperature profiles for two discharges from the scans with total heating powers of 6.6MW. At 2MA the volume average electron density was $1.8x10^{19}m^{-3}$ and at 4MA it was $3.7x10^{19}m^{-3}$.

The 2MA plasmas had highly peaked temperature profiles characteristic of monster sawteeth. The 4MA plasmas had strong, normal sawteeth and flattened temperature profiles. Fig.48 shows the electron temperature profiles from two discharges with 6.6MW total heating power. The density at 4MA was nearly twice that at 2MA and it is this which is responsible for the low central temperature at 4MA because of the approximate inverse temperature dependence on density.

The better heating performance of the 2MA data could be ascribed to the effect of sawteeth. However, the plot of W_{kin} against power shown in Fig.49 indicates that this is not the whole story. The solid lines in this figure show the predictions of Goldston L-mode scaling. The curves for W_{kin} show that the kinetic incremental confinement times (τ_{inc}) of the two scans are comparable at $\approx$ 180ms. The improvement of the 2MA data over L-mode scaling is mainly due to the profile peaking during monster sawteeth.

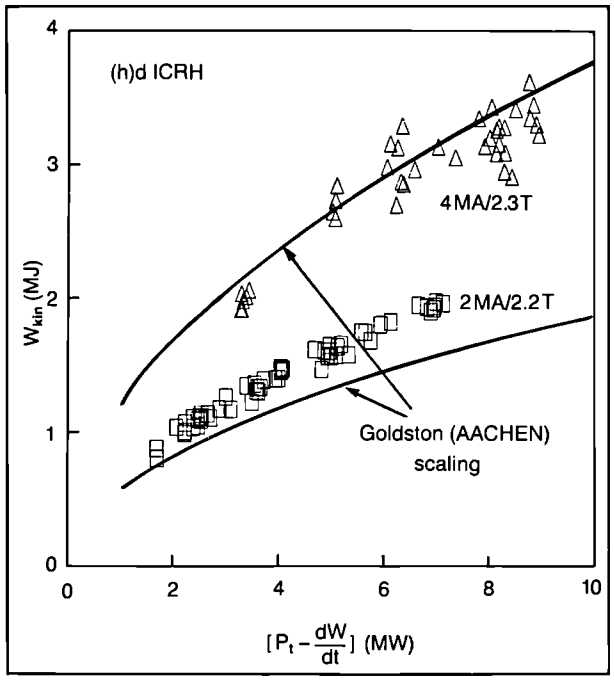

Fig.49: The kinetic energy content versus total heating power for the 2 and 4MA power scans. The solid lines show the predictions of Goldston L-mode scaling ($W_L = 3.7x10^{-5} R^{1.7} {}^5b^{0.5} a^{-0.87} I_p P_t^{0.5}$).

The improvement of τ_{inc} in the 2MA diamagnetic data is due to the fast ion component. The 4MA plasmas had twice the density and a lower central temperature which results in a factor of 5 smaller slowing-down time. Therefore, the 4MA plasmas would be expected to have had a much smaller W_f.

The fast minority ions could produce a substantial fusion yield in certain operating conditions (e.g. tritium minority ICRF in deuterium) and so make moderate q scenarios more attractive. That the 2MA discharges can have such a large proportion of their energy content tied up in fast ions without deleterious effects on the thermal energy confinement is an interesting result which is most encouraging for the prospects of α-particle heating in future ignition devices.

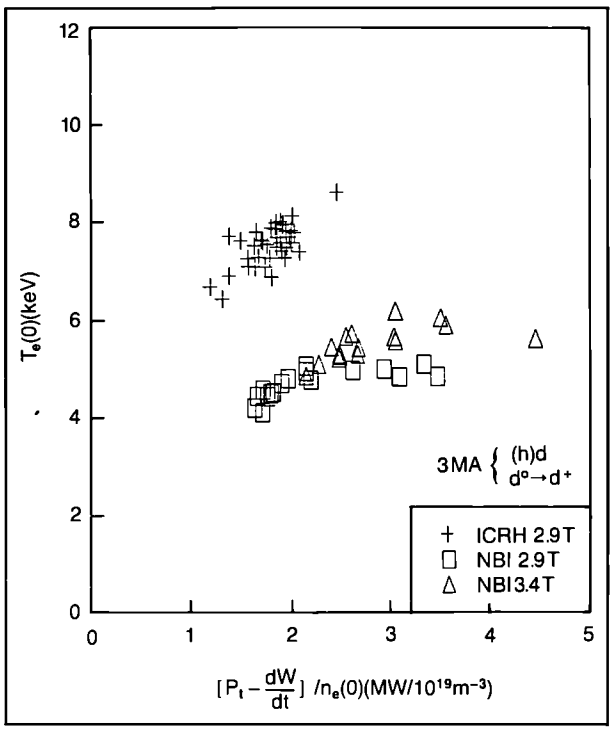

Fig.50: The central electron temperature obtained from ECE diagnostics against heating power over central electron density for 3MA ICRF and NB heated discharges.

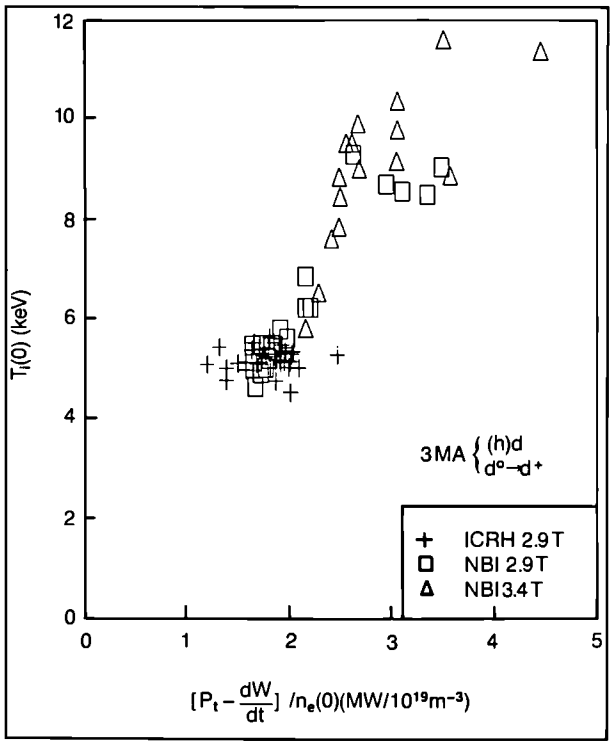

Fig.51: The central ion temperature determined from the Doppler broadening of Ni^{25+} against heating power over central density for 3MA ICRF and NB heated discharges.

Energy Confinement in the Hot Electron Regime

An important feature of ICRF heating is that the minority ions are accelerated to high energies so that the power transfer is primarily to the electrons. In contrast, NB heating tends to heat the plasma ions once the electron temperature is raised above a level which is proportional to the beam energy. At high electron temperatures and low densities, the ions and electrons decouple so that hot ion or hot electron discharges can be made depending on the species to which the heating scheme transfers power.

Hot ion plasmas were produced in JET with NB heating in 1986. Central ion temperatures up to 12keV were obtained with the electrons at 6keV. ICRH hot electron plasmas have been produced in similar operating conditions in 1987. Figs.50 and 51 compare the central temperatures obtained in 3MA NB and ICRF heated discharges. [It should be noted that the electron temperatures shown in Fig.50 were obtained with the ECE diagnostic which is now known to have a magnetic field dependent correction. The highest temperature in Fig.50 is an overestimate by approximately 15%. Eventually, this will be corrected by cross calibration with the LIDAR Thomson Scattering data]. The scatter in ion temperature of the NBH discharges is due to sawteeth. In both cases, the temperature of the species which is not heated remains roughly constant with power per particle. Remarkably, the overall plasma energy confinement is the same in both conditions, as shown in Fig.52 that the losses through the electron and ion channels are comparable and should provide fairly strong constraints on theories describing tokamak confinement.

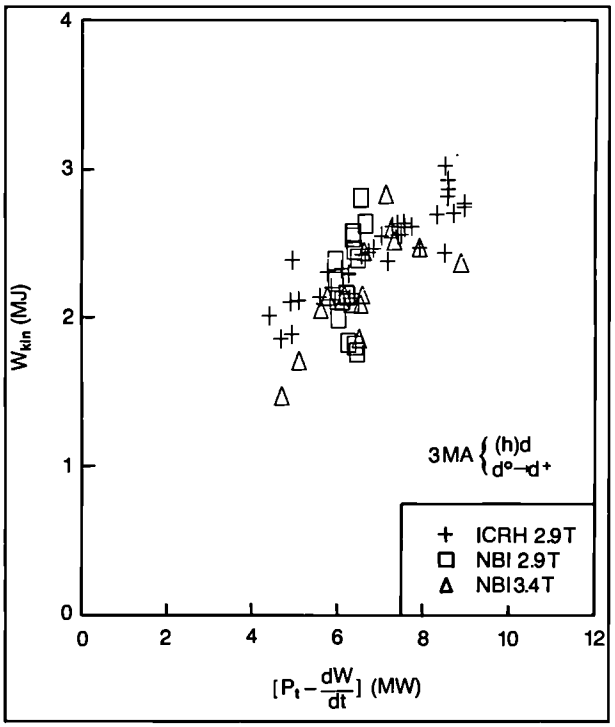

Fig.52: The kinetic energy content of 3MA ICRF and NB heated plasmas against total heating power.

Hot electron plasmas with monster sawteeth have been produced with plasma currents from 1.3 to 4MA. Figs.53 and 54 show the central 2-3.5MA temperature and W_{kin}dependences on plasma current for a series of discharges with fixed q and input power. The linear increase of plasma thermal insulation with magnetic field strength is clearly demonstrated in circumstances where sawteeth do not play a role.

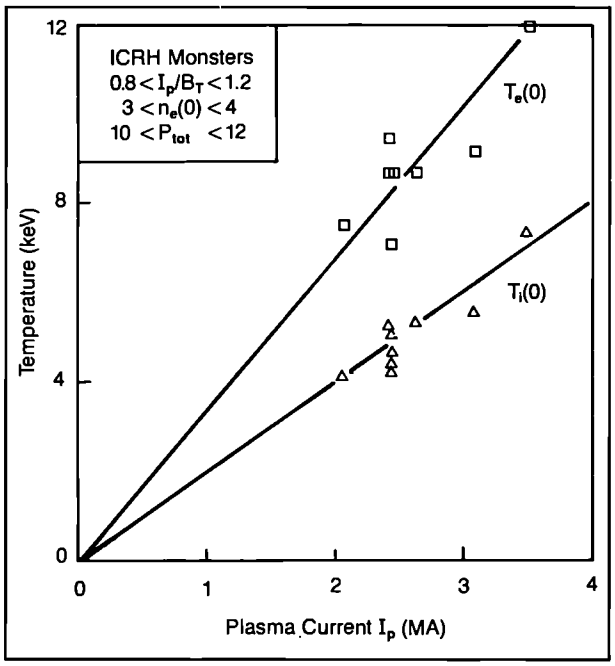

Fig.53: The central electron and ion temperatures versus plasma current for monster sawtooth discharges with the total heating power 10–12MW and $I_p/B_T \approx 1$.

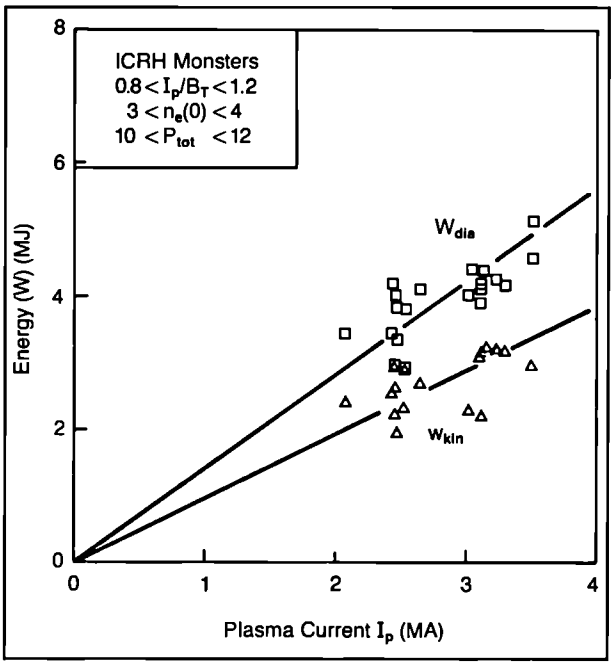

Fig.54: The kinetic and diamagnetic energy contents versus plasma current for monster sawtooth discharges with total heating power 10–12MW and $I_p/B_T \approx 1$.

On- and Off-axis Heating

Preliminary experiments have been performed to investigate the effect of high power off-axis heating. The purpose was to check whether the shape of the electron temperature profile could be modified to a significant degree and to determine whether there was a transport threshold in either temperature or pressure gradient.

By moving the ICRH resonance position in a I_p=2MA and B_t=2.5T plasma the shape of the temperature profile could be altered as shown in Fig.55. Central heating produced monster sawteeth with their peaked profiles. Moving the resonance to 45% of the minor radius reduced the core temperature gradient but outside the resonance the profiles were the same. The position of the sawtooth inversion radius for the off-axis case is shown. The sawtooth region is sufficiently small that it cannot explain the change in profiles shapes.

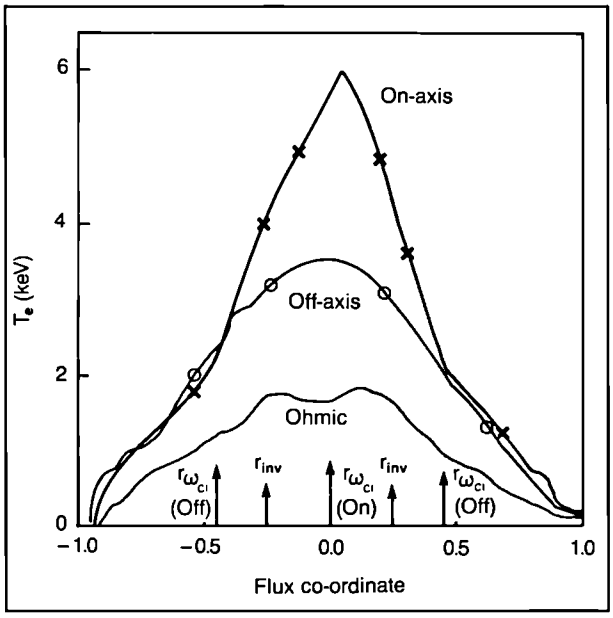

Fig.55: The electron temperature profiles obtained with Ohmic heating, on- an off- axis ICRH in I_p=2MA, B_t=2.5T plasmas. The arrows indicate the ICRH resonance positions and the inversion radius for the off-axis case.

Mixtures of on- and off-axis heating were additive in their effect on both the electron temperature profile and the plasma energy content. In Fig.56, W_{kin} is compared with a model in which different incremental confinement times are used to represent the effect of on- and off-axis heating. The description of the data by this model is satisfactory. These results show the importance that the plasma heat source is placed at the plasma centre to ensure maximum heating.

It has not been possible to reduce the core temperature gradient below the Ohmic heating value with off-axis heating. This was due in part to the fact that the available power did not reduce the Ohmic heating sufficiently. Also, there was a certain amount of direct coupling of the RF power to the electrons by Landau damping. Therefore, no direct signs of a transport threshold have as yet been observed.

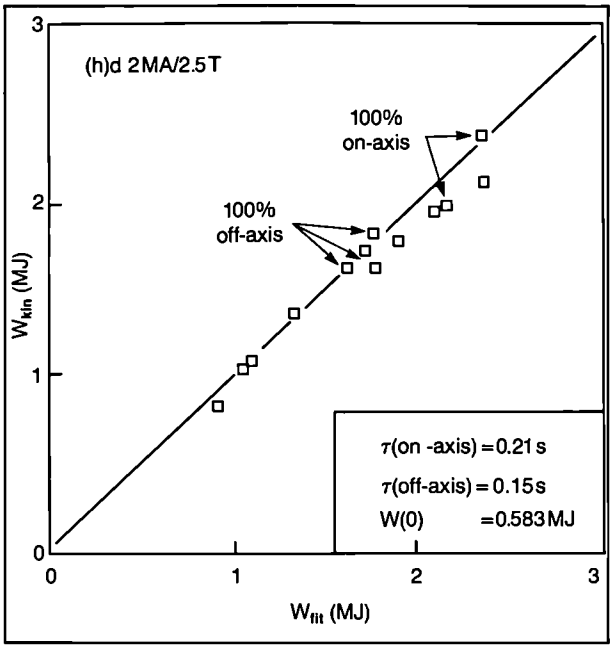

Fig.56: The kinetic energy content compared with a model in which different incremental confinement times (τ_{inc}) are used to represent the effects of on- and off- axis heating.

Heat Transport

Work on local heat transport has been carried out along two main lines of analysis:

- by *interpretative* transport codes, aimed at deriving scaling of local transport coefficients from measured density and temperature profiles;
- by *predictive* transport codes, aimed at computing plasma profiles close to the experimental values using local transport models.

Various degrees of sophistication in computation have been used ranging from time-dependent codes (solving the full set of transport equations coupled to equilibrium codes) to steady-state codes (solving only one temperature equation coupled with the magnetic field diffusion equation).

A wide range of discharges has been analysed. In some cases, results have been available from ad hoc experiments (in particular, a few ICRH off-axis heating experiments). Experimental results, both from the 1987 campaign and previous years of operation (mainly 1986), have been studied.

The interpretative approach has shown that the local heat transport can be assumed to be diffusive. The heat diffusion coefficient, χ, without any attempt at distinguishing electron and ion energy fluxes, appears to be an inverse function of the plasma current: ($\chi \propto 1/I$). In addition, estimates of χ at three different radii (ρ/a = ½, ⅓, ¾) show that χ is an increasing function of ρ/a.

More controversial is the existence of an 'inward heat-pinch' in the heat flux. Such a term would lead to an offset linear scaling law of the incremental confinement

time fitting experimental data, but its introduction is mainly justified by the analysis of available data on heat pulse propagation. However, the uncertainties related to all analyses that have been performed so far do not allow a firm conclusion on the existence or scaling of the 'inward heat pinch'. This term must be considered as a 'working hypothesis' or as an approximation of more sophisticated models such as the one based on the existence of a 'critical T_e gradient'. Available data on heat fluxes can also be well interpreted with a diffusion coefficient χ that depends non-linearly on the local temperature (or pressure) gradient.

Interpretative analysis at a more sophisticated level, on a reduced number of discharges, has shown that in trying to distinguish between electron and ion heat fluxes, a much larger ion heat flux must be assumed (more than ten times) than that predicted by neoclassical theories. In addition, the relevant scaling of χ_i seems to be different from neoclassical values in cases where the ion temperature profile has been available for analysis (from the NPA diagnostic). There are more and more indications that in JET discharges, including H-modes, $\chi_i \gtrsim \chi_e$ must be assumed.

Experimental results of JET electron temperature profiles show a remarkable degree of 'profile resilience' (Fig.57). In interpretative code analysis, this shows up in the fact that $\nabla T_e/T_e$ appears to depend on global quantities (such as the safety factor at the boundary) rather than on local quantities. The scattering in data of $\nabla T_e/T_e$ is however large and no firm conclusion can be derived.

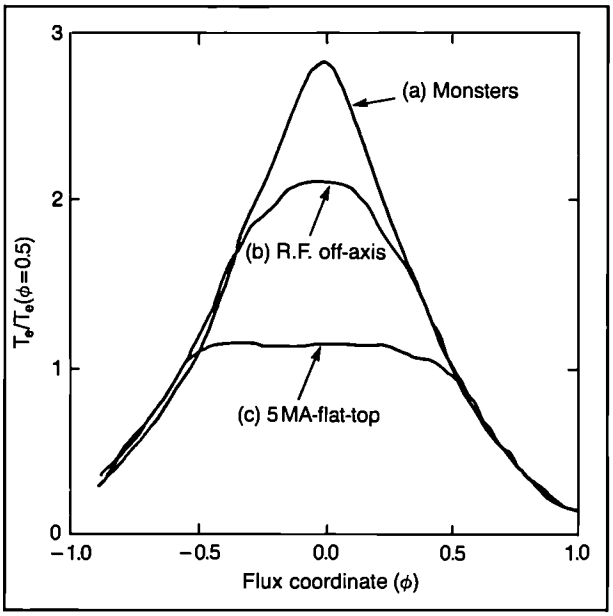

Fig.57 Average normalised electron temperature profiles for different plasma conditions versus flux coordinate for (a) 'Monsters' (averaged over 49 profiles), (b) ICRH off-axis heating (averaged over 4 discharges) and (c) 5MA discharges (averaged over 13 discharges). These normalised profiles, obtained with the LIDAR diagnostic, show a remarkable degree of 'profile resilience' in the region not perturbed by sawtooth activity.

One possible explanation of 'profile resilience' and its relationship with confinement degradation with power is related to the 'critical T_e gradient' model, derived from the assumption of partial ergodicity of magnetic field lines in the intermediate plasma region (Fig.58). Another promising model is related to resistive MHD modes and implies degradation and 'profile resilience', since χ is linearly dependent on the pressure gradient.

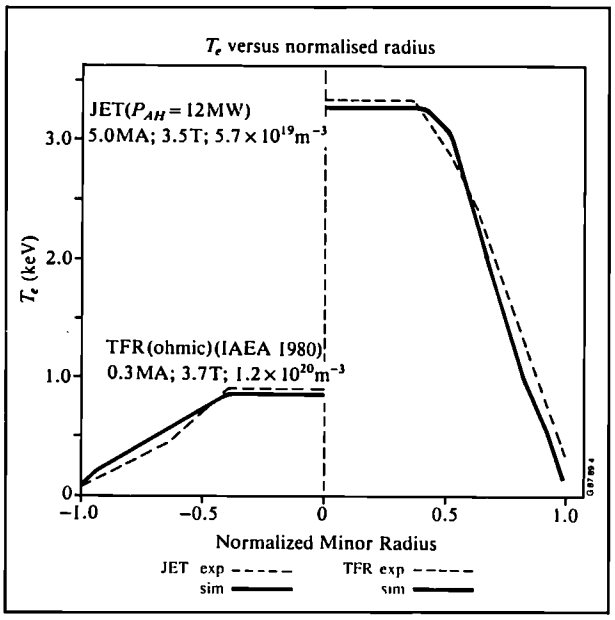

Fig.58 Examples of simulation of experimental T_e profiles using the 'critical gradient' heat flux model.

Preliminary results show that the two models are difficult to distinguish in steady state situations at the present level of input power. Much more data must be analysed. In particular, in non-steady state situations and with plasmas of different sizes, the merits and possible limitations of the two models must be assessed.

Predictive computations have shown that, in JET, none of the transport models derived from the theory of electrostatic microinstabilities is really satisfactory. All these models require ad hoc modifications to reproduce the observed temperature profiles as well as global scaling of energy confinement times.

The predictive approach, which first pointed out the requirement of a strongly anomalous ion heat flux in JET, has confirmed that in a wide range of situations (ohmic, ICRF, NBI, 'monsters', and H-modes), the assumption $\chi_i \gtrsim \chi_e$ at present allows the best simulation of JET results.

Local transport data banks containing carefully validated results from diagnostics producing the relevant profiles are being set up at JET. Similarly, data banks are being created with results of the principal codes used for analysis. These banks will allow proper comparisons of experimental and computed results, aiming to simplify the difficult task of finding and assessing local transport models.

Impurities and Radiation Studies

During the 1987 shut-down, further analysis of the 1986 impurity data was carried out. Studies of impurity behaviour in helium discharges and comparison with deuterium results allowed conclusions on impurity production processes. Changes in impurity transport during 1986 H-mode plasmas were investigated and radiation profiles explained. In particular, plasma conditions after the shut-down were compared with those before. For this purpose, and for better demonstration of previously observed impurity trends with plasma current or density, a spectroscopic database was established during 1987. It contains absolutely calibrated intensities of selected spectral lines together with other plasma information. Details are given in the following.

Spectroscopy Database

Impurity concentrations in JET plasmas are obtained by detailed analysis of several VUV line intensities of each important impurity species using a transport code [1]. Cross checks are carried out with Z_{eff} obtained from visible bremsstrahlung and total radiation measured by bolometers. Evaluation of impurity concentrations has been attempted on a simpler basis, for routine application to a large number of pulses. Calibrated intensities of many impurity lines have been derived from spectra from the VUV survey spectrometer and stored with respective plasma parameters from the transport database. Although there are some limitations, this procedure can establish basic impurity behaviour during an experimental campaign and provide relevant background information for individual results.

For metal impurities (Ni, Cr, Fe), spectral lines from the plasma interior (Ni XXV, Ni XXVI, Cr XXII, Fe XXIV) allow a relatively easy assessment of impurity content. Since these ions are close to corona ionisation equilibrium, the intensity scales approximately as $[n_e(0)^2]$ for a given concentration. It decreases with $T_e(0)$ as respective shells move out to lower density and become narrower at higher temperature. Thus, an estimate of the nickel concentration of the plasma may be obtained from the relation:

$$c_{Ni} \approx 4\times10^{-20}\, I(\text{Ni XXV})\, [T_e(0)/n_e(0)]^2 \qquad (1)$$

(I is in photons/s cm^2, T_e in keV, and n_e in 10^{19}m^{-3}).

Light impurity concentrations (C, O) are much more difficult to calculate from the available peripheral line intensities (C IV, O VI). The position and width of these shells are determined by the edge profiles of T_e and n_e and the respective local transport coefficients. For a very rough estimate of oxygen concentration, the following formula can be used:

$$c_O = b\times I(\text{O VI}).\langle T_e\rangle^{\alpha}/\langle n_e\rangle^{\beta} \qquad (2)$$

where $\langle T_e\rangle$ and $\langle n_e\rangle$ are the volume averaged electron temperature and electron density. A similar equation for carbon could be used, based on C IV. The parameters b, α and β are only approximately known, at present, for standard limiter discharges. Fig.59 shows the ratio of Z_{eff}, calculated from the impurity mixture given by the standard analysis, to Z_{eff} from bremsstrahlung plotted versus $\langle n_e\rangle$. Considering the simple analysis, the result is quite satisfactory after adjustment of the constants b for oxygen and carbon for agreement with detailed spectroscopic results and results from charge-exchange recombination spectroscopy (CXRS). The coefficients α and β have been chosen in such a way that there were no noticeable trends of Z_{eff} (impurities)/Z_{eff} (brems) with average temperature or density. Thus, the constants in Eq.2 are slightly different from the ones predicted by the transport code for constant T_e and n_e profiles. The scatter of datapoints in Fig.59 is mainly due to uncertainties in carbon concentration, and high values are pronounced in the lower density range.

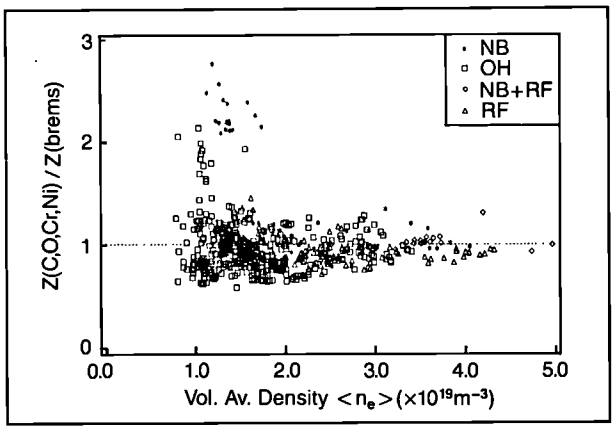

Fig.59 Z_{eff} calculated from the impurity mixture (standard analysis) divided by Z_{eff}(brems) as a function of density.

Due to limitations in the interpretation of edge radiation, light impurity concentrations during inner wall and H-mode discharges have as yet been based on charge-exchange recombination spectroscopy (KS4). However, this method requires the presence of the heating neutral beams. More recently, the grazing incidence spectrometer (KT4) has provided more reliable assessment of light impurity behaviour, from the H^- and He-like stages of oxygen and carbon, further inside the plasma. Eventually, both the KS4 results and calibrated KT4 intensities will be included in the spectroscopic database allowing a comprehensive study of JET light impurities.

General Impurity Behaviour 1986/1987 —Limiter Discharges in Deuterium

The basic behaviour of the important JET impurities C, O, Cr and Ni (on a logarithmic scale) is shown in Fig.60 for ohmic limiter discharges in deuterium. In addition, $[Z_{eff}-1]$ (from visible bremsstrahlung) and a measure of the total impurity content are shown.

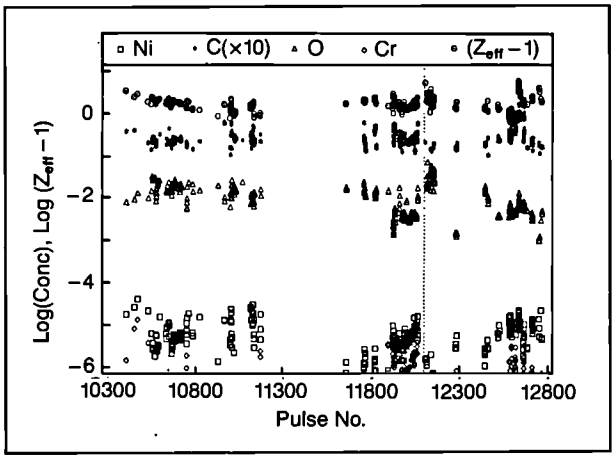

Fig.60 Impurity concentrations (standard analysis) and [$Z_{eff}-1$] versus Pulse No. for late 1986 and early 1987 operation periods. A leak in the gas introduction system is indicated by the dashed vertical line. (The carbon results have been multiplied ×10 to avoid interference with the oxygen data).

Late in 1986 (Pulse Nos. <11300), Z_{eff} was in the range 2–3 which, from Fig.60, was essentially a consequence of $c_O \approx 1\,\% \; n_e$ and $c_C \approx 3\,\% \; n_e$. The nickel concentrations were small but with considerable scatter due to different currents, densities and RF operation histories. However, early in the operation period Cr and Ni concentrations were comparable or even $c_{Cr} > c_{Ni}$, while later on Cr had almost disappeared. This behaviour is probably due to wearing of the chromium coating on the 2D RF antenna.

For 1987 operation, the first ~100 plasma pulses are not included in Fig.60 due to low plasma current or helium operation. Subsequent light impurity concentrations were similar to those in late 1986, which meant that vessel conditioning after shut-down was quickly achieved. As observed before, metal impurities were very low at the start but developed to their normal levels in the course of operation. A leak in the gas introduction system at Pulse No. ~12100 clearly manifests itself in Fig.60 by higher oxygen concentrations. Subsequent helium discharges (before and after Pulse No. ~12300) reduced oxygen to below 1 % n_e. Generally, oxygen and metal impurities appeared to be anti-correlated, while the relation of oxygen and carbon was difficult to establish. However, carbon results are the most uncertain in this standard analysis.

Fig.61 provides an overview of nickel concentrations in deuterium ohmic limiter plasmas in 1986. Even within the scatter, it is clear that nickel concentrations fall with density at a given current and increase with current at a given density. This behaviour has been observed previously before [1] and is easily understood in terms of an edge temperature sensitive sputtering yield. The highest values in ohmic plasmas were in the 10^{-4} range, suggesting that nickel was insignificant for both Z_{eff} and radiation. During inner wall pulses, a similar situation existed with metal levels. As previously reported, ICRF heating led to higher metal concentrations in all types of discharges [2–5].

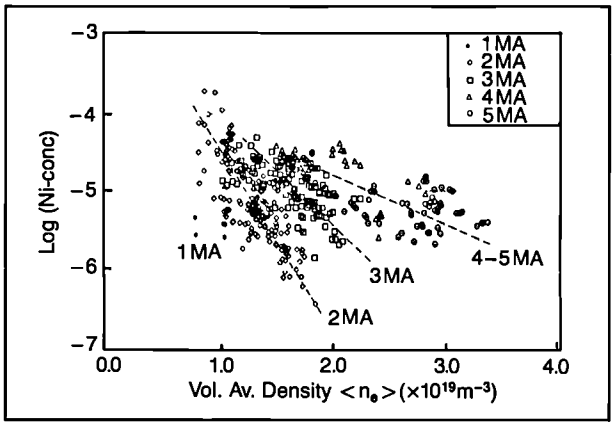

Fig.61 Nickel concentrations as a function of current and density.

The increase of nickel and chromium densities during ICRF heating, normalized to RF power, is shown in Figs.62a and b, for hydrogen minority heating in deuterium plasmas for $I_p = 2.0$ and 2.5 MA in early 1986 operation (Pulse Nos. 7000–9000). Within considerable scatter, 1MW ICRH power resulted in about 10^{15} more nickel ions/m^3 and somewhat less increase in chromium. The larger scatter in the Cr data must originate from varying power fractions coupled by the Octant No. 2D antenna. Included in both diagrams are five points of a special study in the quadrupole antenna configuration,

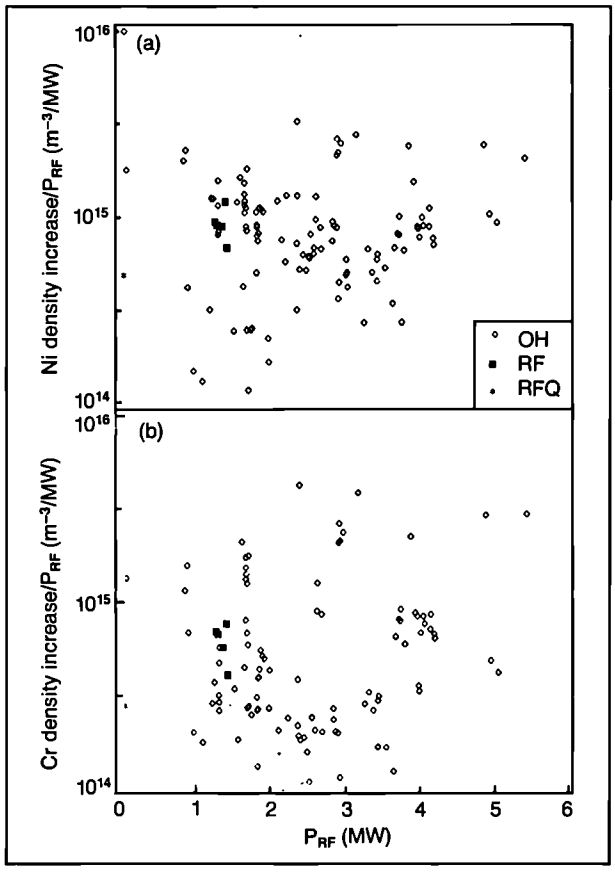

Fig.62 Normalized increase in (a) nickel and (b) chromium during 2 MA H-minority RF heating. The filled squares refer to quadrupole operation.

while the other data refer to dipole mode. There is no significant difference between dipole and quadrupole operation, although some reduction in chromium (but not in nickel) was detected when comparing the quadrupole results with previous reference dipole discharges.

Fig.63 shows an overview of carbon impurity behaviour. Carbon concentrations from standard analysis follow a precisely similar pattern as nickel, except the variation is much smaller. Thus, the prevailing opinion is confirmed that carbon must be produced by physical sputtering rather than chemical effects [3]. Most concentrations in Fig.63 lie in the 2–5% range. All additional heating methods lead to an increase in carbon at a given density, while the usual falling trend with $\langle n_e \rangle$ is maintained. Higher power input (i.e. higher edge temperatures) leading to higher carbon production is certainly another indication of physical rather than chemical sputtering.

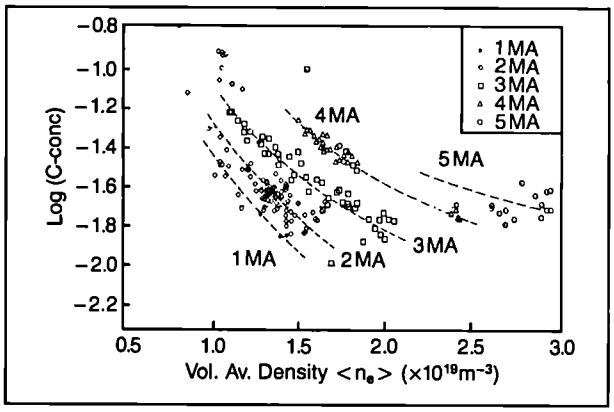

Fig.63 Carbon concentrations as a function of current and density.

No systematic trends of oxygen levels with either density or current have been observed. The ohmic results were between 0.5 and 1.5%n_e. Neutral beam or combined heating led to relatively high oxygen concentrations. All trends are in good agreement with previous observations [1,5]. However, the dependence of carbon concentrations on current and density has never been shown so clearly before, proving unambiguously the sensitivity of the respective production yield to edge temperature.

Limiter Discharges in Helium

(i) Helium and Impurity Fluxes

To calculate helium particle confinement, the total helium influx, ϕ_{He}, (i.e. mainly the limiter flux in limiter discharges) was derived from the intensity of the HeI $2p^1P^0-3d^1D$ transition at 667.8nm in the visible spectrum. Unlike H_α, the interpretation of this line (i.e. the number of ionisation events/photon) requires knowledge of the edge temperature. Helium fluxes and confinement times have been calculated for several ^{3}He discharges using edge temperatures from probe measurements. In these cases ($I_p = 3$MA, $\bar{n}_e \approx 3\times10^{19}$m^{-3}), ϕ_{He} in He discharges was almost twice the corresponding ϕ_D value in deuterium discharges with the same $\bar{n}_e$ (i.e. about 10^{22} particles/s). The respective electron particle confinement times were in the 100–200ms range. The density scaling of τ_p (He) has been derived from a comparison of 3MA pulses, $\bar{n}_e \approx 3\times10^{19}$m^{-3}, and 1MA pulses, $\bar{n}_e \approx 1.3\times10^{19}$m^{-3}, assuming that τ_p does not depend on plasma current. During the density plateaus, ϕ_{He} scaled approximately as $\bar{n}_e^2$.

The number of ionisation events/photon, required for deriving the carbon flux from CII $3s^2S-3p^2P^0$, 657.8nm, depends on temperature in a similar way to HeI, which means that the production yield of carbon by helium can be measured easily from the two line intensities without knowledge of the electron temperature. The flux ratio ϕ_C/ϕ_{He} has been measured as a function of time in several helium pulses. The yield usually starts above 10% at the beginning when the electron density is low and drops to ~5% as the density increases. During RF heating, the carbon production appears slightly enhanced, which could be due to the additional deuterium influx. A production yield of 5–10% is a reasonable result for 3 MA and the respective densities, but may be slightly on the low side. However, even in this simple case, realistic error bars are probably ±50% due to combined uncertainties in atomic data.

Fig.64 shows part of the visible limiter spectra for two similar discharges (Pulse No.10353, in D, and Pulse No.10324 in ^{3}He). The influxes of deuterium, carbon and oxygen can be derived from D_γ and CII and OII ion lines for this wavelength range. In the ^{3}He discharge, D_γ is about a factor ×10 lower than in D, demonstrating that the deuterium fraction in the helium plasma is small. The CII line intensity is virtually the same in both spectra. Since the edge temperature in He is higher than in D, the resulting carbon flux is somewhat higher in the He case. Using the previous result $\phi_C/\phi_{He} \approx 10\%$, the conclusion is that carbon production by deuterium must be similar (i.e. about 10%, in agreement with previous statements) [3]. The oxygen influx in Pulse No.10353 is about 4% of ϕ_D, which means that oxygen is responsible for about half the carbon flux.

An interesting feature of Fig.64 is the simultaneous disappearance of deuterium and oxygen lines in the helium discharge. This means that oxygen impurity levels are much lower in helium than in deuterium. Furthermore, it is clear that, in contrast to carbon, oxygen is produced by chemical effects involving hydrogen.

(ii) Impurities in Helium Plasmas

The main impurities in He plasmas have been investigated using the spectroscopy database. As in deuterium, nickel concentrations decrease with density, but absolute values are substantially higher. This result is not surprising since sputtering coefficients are higher

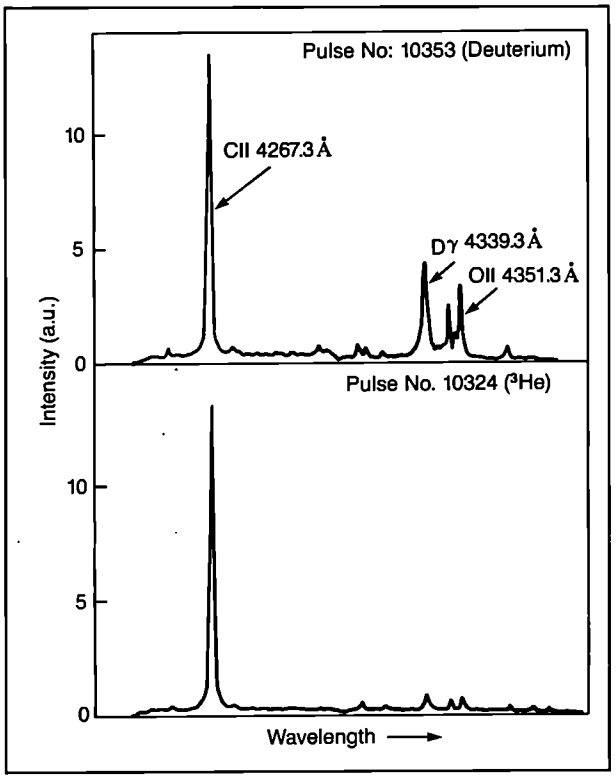

Fig.64 Part of the limiter spectra recorded during similar D and ^{3}He discharges showing D_γ, OII and CII lines as an indication of the respective influxes.

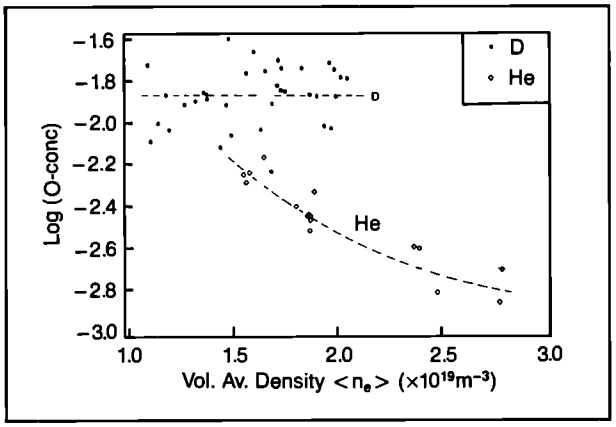

Fig.65 Oxygen concentrations in D and He discharges (I_p=3MA).

for He at all temperatures and, in addition, the helium edge temperatures are higher than those of D discharges at the same density $\bar{n}_e$. Similar behaviour might be expected for carbon due to the reduction of oxygen, the carbon concentration in helium plasmas seems to be comparable to that in deuterium pulses.

Oxygen concentrations from the standard analysis are plotted versus $\langle n_e \rangle$ in Fig.65. Values for deuterium are about 1–2%n_e and show no trend with density. In contrast, the helium data are about 0.5%n_e at low densities and fall rapidly with increasing $\langle n_e \rangle$. Further investigations show that the residual deuterium flux follows the same trend. Indeed, there is a close correlation of ϕ_D and c_0. Thus, oxygen would be completely absent in He discharges, if there was no residual deuterium flux. The lower values of c_o are the reason for higher edge temperatures in He plasmas and for a higher density limit.

Impurity Transport during H-mode Plasmas

The main impurity results for the JET H-mode plasmas have already been reported [6, 7]. Z_{eff} was essentially determined by the light oxygen and carbon impurities, from CXRS measurements. However, total radiation profiles of the bulk plasma showed broad edge shells extending far into the plasma interior, dissimilar to the usual light impurity radiation, even taking into account some change in ionisation balance due to the presence of the beam neutrals. There was no way to explain radiation by metal impurities, unless the metal concentration was underestimated by orders of magnitude. This is most unlikely, since all spectroscopic (VUV and X-ray) and soft X-ray measurements yield consistently low results. Therefore, the bolometer profiles must indicate a substantial change in particle transport.

From different ionisation stages of nickel, particularly Nixxvii, radiating in the plasma centre, and from Nixxv, at $r/a \approx 0.75$, as well as from the soft X-ray profiles, it was concluded that impurity accumulation at the plasma centre did not occur in JET H-mode discharges. However, a change in particle transport at the plasma edge was evident from the different behaviour of Nixxv and Nixviii, radiating close to the boundary at $r/a \approx 0.92$. Fig.66 shows the nickel concentration as a function of time in Pulse No.10755, obtained from these two stages on the basis of the usual transport model. The results are consistent, within errors, up to the H-mode start at about 12 s. During the H-mode, nickel levels from the plasma edge are clearly lower by almost an order of magnitude, although they have considerable error bars due to the sensitivity to the plasma edge parameters. Since the source term for nickel is certainly zero in this part of the plasma, this profile change indicates a higher inward drift velociy v_D or, more precisely, a higher ratio of v_D/D. A similar profile change was observed for the electron density. Analysis of the Nixxvi line radiation gives roughly the same result as Nixxv, while Nixxvii (normalized to the ohmic period of the pulse) results in lower values again, as shown in Fig.66. This latter fact, as well as the hollowness of the bolometer profiles, suggest hollow impurity density distributions in the plasma centre, probably a consequence of the non-stationary nature of the H-mode discharges. There is also evidence that the electron density profiles are slightly hollow. Towards the end of the H-mode, particles are first lost from the plasma edge, as demonstrated by the decrease of the Nixviii results. The plasma interior follows with some time delay.

A tentative transport model was used to explain the

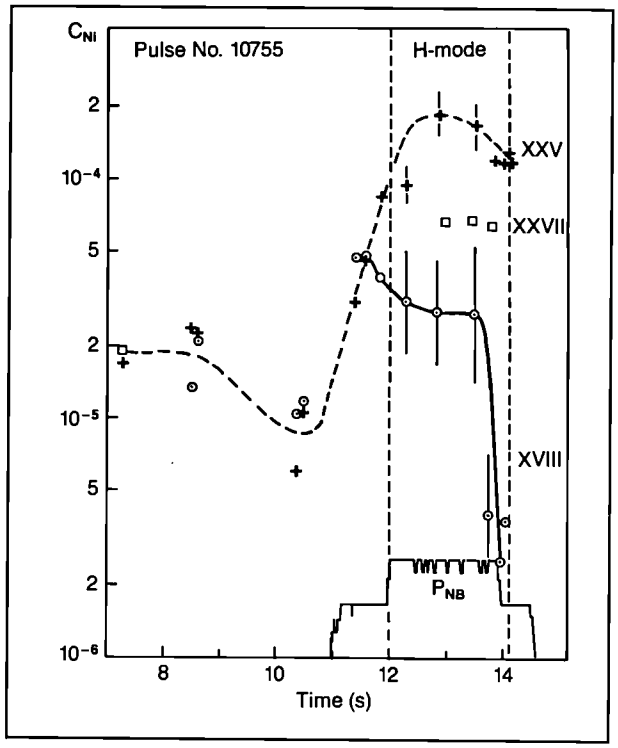

Fig.66 Nickel concentrations from different nickel ionisation stages as a function of time in Pulse No.10755. The discrepancy during H-mode demonstrates the change in particle transport.

measured bolometer profiles, the behaviour of the different nickel ionisation stages and the improvement of particle confinement. It is assumed that v_D has a high negative value in the outer plasma region (between 0.95 and 1.2 m) with a peak value of about 25 ms^{-1}. Inside this region, $v_D = 0$. To explain the observed hollowness of the radiation profile at the experimental ramp rate $[(1/P_{rad}) \cdot (dP_{rad}/dt)] \approx 1\,s^{-1}$, the diffusion coefficient in the plasma interior must be smaller than usual (i.e. about 0.2 $m^2 s^{-1}$). It was then assumed that it increased in a parabolic manner up to an edge value of 1.5 $m^2 s^{-1}$ similar to previous bulk plasma results.

From experimental data, the increase of total radiation during the H-mode is due mainly to oxygen, particularly, line radiation from O VIII. C VI line radiation also contributes a significant amount to total radiation losses during H-mode plasmas. The modification of transport explains the increase in O VIII and C VI radiation from the plasma interior, as observed. Furthermore, the calculated radial profile of the oxygen radiation agrees well with the bolometer measurements.

When applying the modified transport model to interpretation of nickel line radiation, the conclusion is that the result from Ni XXVII, not surprisingly, represents the concentration of nickel on axis. To obtain the central value from Ni XXV and Ni XVIII, the former results must be multiplied by 0.4 and 1.8, respectively. After this correction, the individual measurements of Fig.66 are in good agreement. From code calculations, impurity particle confinement improved by about a factor five during the H-mode.

The impurity density profile, resulting from the transport modification transport and the non-stationary situation, is shown in Fig.67, together with the electron density profile (from the FIR interferometer). There are clearly similarities in the two distributions suggesting similar transport for deuterium and impurities. The impurity profiles are expected to be more hollow than $n_e(r)$, since impurities enter the plasma from the edge, while the bulk plasma is, to a large extent, fuelled by heating beams.

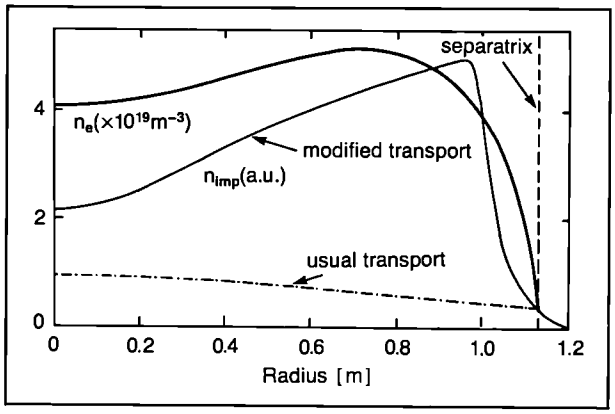

Fig.67 Impurity ion density profiles from the simulation and measured electron density profile for Pulse No.10818, at 13.0s.

First Results during Monster Sawteeth and after Pellet Injection

During monster sawteeth, a slight peaking in the centre of both electron and nickel densities was observed, but much less than neoclassically expected accumulation. In a few cases after pellet injection, strongly peaked electron density profiles were recorded lasting for about 1 s. Under these circumstances, the nickel profiles at to changed, developing narrow centrally peaked distributions. The peaking factor and the time development could be explained by neoclassical inward drift, provided the anomalous diffusion coefficient was substantially reduced. These apparent changes of particle transport are still under investigation.

References

[1] Impurity and Radiation Studies during the JET Ohmic Heating Phase, K H Behringer, P G Carolan, B Denne, G Decker, W W Engelhardt, M J Forrest, et al., Nucl. Fusion 26(1986)751

[2] Metal Sources and General Impurity Behaviour in JET Plasmas during ICRH, K H Behringer, B Denne, M J Forrest, N C Hawkes, H Kaye, P D Morgan, et al., Proc.of the 13th European Conf.on Contr.Fusion and Plasma Heating, I 176, Schliersee 1986

[3] Spectroscopic Studies of Plasma-Wall-Interaction and Impurity Behaviour in Tokamaks, K H Behringer, JET-P(86)35 and J.Nucl.Mater. 145-147(1987)145 (Princeton 1986)

[4] Impurity Influx Behaviour in JET, M F Stamp, K H Behringer, M J Forrest, P D Morgan, H P Summers, JET-P(86)35 and J.Nucl.Mater.145-147(1987)236

[5] Impurity Production Mechanisms and Behaviour during Additional Heating in JET, K H Behringer, A Boileau,

F Bombarda, B Denne, W W Engelhardt, M J Forrest, et al., Proc. of the 11th Int.Conf.on Plasma Phys. and Contr.Nucl. Fusion Research, paper IAEA-CN-47/A-IV-1, Kyoto 1986

[6] Impurity Behaviour in X-Point Plasmas on JET, B Denne, K H Behringer, A Boileau, G Fussmann, M v Hellermann, L Horton, et al., Proc.of the 14th European Conf.on Contr.Fusion and Plasma Heating, Madrid 1987

[7] Magnetic Separatrix Experiments in JET, A Tanga, K H Behringer, R J Bickerton, M Brusati, B Denne, A Gibson, et al., Nucl.Fusion 27(1987)1877

Plasma Boundary Phenomena

The physics of the scrape-off-layer (SOL) plasma, outside the last closed magnetic flux surface, is important in understanding the release and transport of impurities, the recycling of plasma at the walls and the energy confinement properties of the core plasma. The studies of the plasma boundary can be roughly divided into the following areas:

(a) recycling of the hydrogen isotopes in the plasma boundary and in the material surfaces surrounding the plasma;

(b) the plasma boundary conditions and the scaling of the edge parameters with plasma global parameters such as average plasma density and total input power;

(c) the mechanisms of the production of impurities and measurements of impurity fluxes. Impurity transport also determines the erosion and redeposition of impurities on the limiters and the wall.

Recycling and Gas Inventory

During 1987, measurements of the time dependence of plasma density continued to show net pumping effects during a discharge, similar to that observed in 1986. This pumping effect lasts for many discharges and it has been shown to occur at all surfaces in contact with the plasma including the belt limiter, the inner bumper limiter and the X-point protection tiles. There is no significant change in the pumping rate when the wall temperature (300°C) is larger than the limiter temperature (200°C). Wall pumping can be described by a model assuming dynamic retention by diffusion of hydrogen in the bulk carbon. However, the temperature dependence cannot be explained easily unless the surface temperaures are different from the measured bulk temperatures. Another mechanism which may be responsible is the codeposition of carbon and hydrogen isotopes on some surfaces, resulting in the permanent burial of the hydrogen. However, it has not yet been possible to explain the pumping quantitatively in terms of this process nor does it explain the observed temperature dependence.

The release rate of gas after a discharge has also been studied in some detail. The rate of release decays to a small value after about 30 minutes (see Fig.68). The integration of the total amount of gas released has been measured over a series of discharges. In normal ohmic discharges, a large fraction (70–90%) of the gas

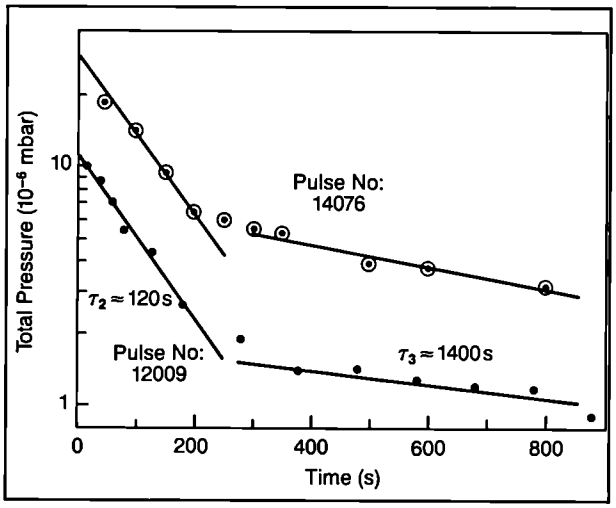

Fig.68 Decay of total pressure after the end of a discharge.

introduced is trapped permanently in the vessel. After disruptive discharges, a larger fraction (although frequently less than 100%) of the gas is released. Long-term accumulation of hydrogen in walls and limiters has been measured by means of surface analysis indicating that H-C-codeposition might play an important role in the long term retention of hydrogen.

Recycling behaviour in helium discharges has also been studied. No wall pumping is observed in helium discharges. It has also been shown that the helium tokamak discharges are effective in releasing hydrogen isotopes previously trapped in the wall. Helium glow discharges remove hydrogen but do not appear to be as effective as tokamak discharges. The release of hydrogen is understood in terms of energy transfer to the lattice atoms by incident helium ions. The helium implanted in the surface is known to have a high diffusion coefficient in carbon and is thus released rather than trapped itself.

During 1986, a significant number of D(d,p)T nuclear reactions occurred during deuterium neutral beam injection leading to the production of tritium. A detailed survey of the tritium trapped in the walls has been carried out by burning carbon samples and using scintillation counters to detect the tritium decay from the resultant tritiated water. Typical surface concentrations are $\sim 10^{11}$ atoms cm^{-2}, which is readily detectable. A poloidal distribution of the tritium in Octant No.5 is shown in Fig.69. There is an apparent asymmetry with a higher flux going to the top of the torus than to the bottom. The tritium has been measured to have a most probable depth of 3–6μm but to have a tail penetrating many millimetres into the solid. However, more than 98% is contained within the first 20μm.

Plasma Boundary Parameters

An array of twenty integral Langmuir probes was incorporated in the belt limiters when installed in the vacuum vessel, in early 1987. These have allowed routine

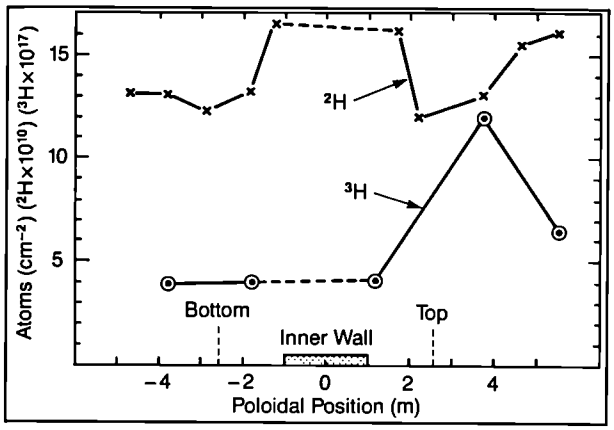

Fig.69 Poloidal tritium distribution.

measurements of the toroidal and up/down symmetry of the plasma. Remarkably good toroidal symmetry has been observed under most operating conditions, indicating that very high positional accuracy of the belt limiter has been achieved. Initial up/down asymmetries were easily compensated by varying the vertical position of the plasma. Results of measurement of the plasma ion flux to probes at different positions are shown in Fig.70. Measurements of the radial gradient of this flux indicate that the limiter is within a few millimetres of a common flux surface. The oscillations in the ion flux observed show evidence of phase coherence between fluctuations in octants diametrically opposite each other. Measurements with probes in equivalent positions on two ICRH antennae show that the antennae in Octant No.1 is 6–8 mm closer to the plasma than that in Octant No.5. An example of profiles of flux, temperature and density from the two pairs of antennae is shown in Fig.71. The effect of the positional difference is clearly seen.

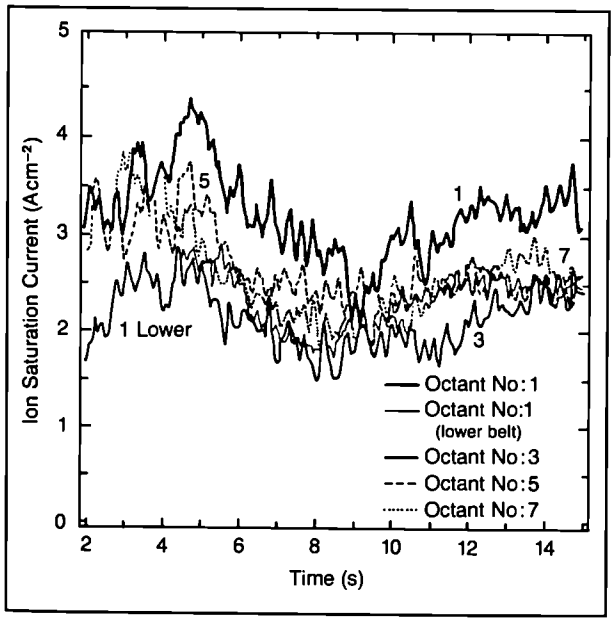

Fig.70 Saturation current (I_{sat}) versus time for different probes.

There is much less consistency in the probe measurements from shot-to-shot with the new belt limiter configuration than during operation with discrete limiters, reported in the 1986 Progress Report. Both edge density and temperature do not follow the scaling with global parameters observed previously. However, the order of magnitude of the edge temperature, ~10–50 eV and density $1-3\times10^{18}\,m^{-3}$ is similar to the earlier values. The variability is probably due to the changing contact on upper and lower belt limiters and the variable effect of the RF antenna as the elongation and ellipticity of the plasma change.

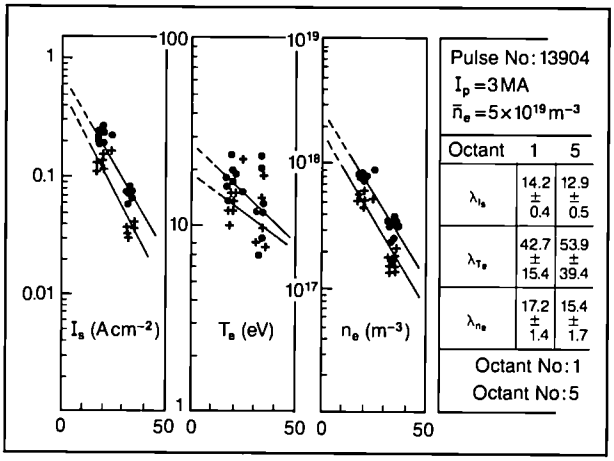

Fig.71 Electron Temperature (T_e) profiles from antenna probes.

Edge Modelling

The measured edge conditions in JET, electron temperature and density in the scrape-off-layer (SOL), reported in 1986, have been successfully related to the central plasma parameters for ohmic JET discharges using analytic models. A simple diffusion model, derived originally by Engelhardt et al [1], can be shown to give the relation [2]:

$$n_e(a)=\frac{\bar{\sigma}\bar{v}_{iz}\lambda_n\bar{n}_e^{\,2}}{6\bar{v}_n}$$

between the edge density $n_e(a)$ and the average plasma density $\bar{n}_e$, where $\bar{v}_n$ is the average penetration velocity of the recycling hydrogen, $\bar{\sigma}\bar{v}_{iz}$ is the average electron impact ionization rate over the mean-free path of the neutral hydrogen and λ_n is the SOL width. Results are shown in Fig.72 employing the approximations $\bar{v}_n = 3\times10^4\,m\,s^{-1}$, $\bar{\sigma}\bar{v}_{iz}=3\times10^{14}\,m^3s^{-1}$, and $\lambda_n=30$ mm. A simple analytic model of energy balance reproduces the measured edge temperature, as a function of n_e and I_p, to within a factor of about three. Monte Carlo neutral code modelling[3] is currently directed at providing better estimates of $\bar{v}_n$ and $\bar{\sigma}\bar{v}_{iz}$ with a view to explaining the I_p-dependence of $n_e(a)$ (see Fig.72).

Values of the cross-field diffusion coefficient at the plasma edge, $D_\perp$, have been obtained from measurements of λ_n for different ohmic discharge conditions.

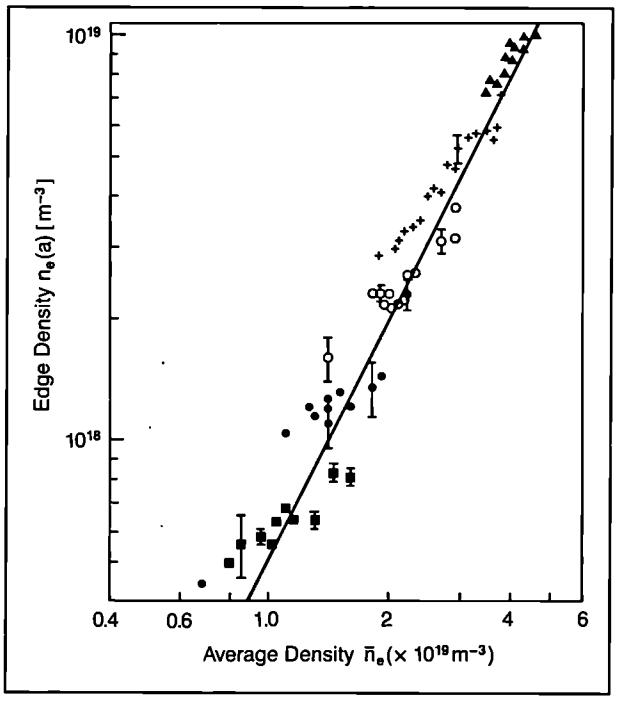

Fig.72 Scaling of edge density with model.

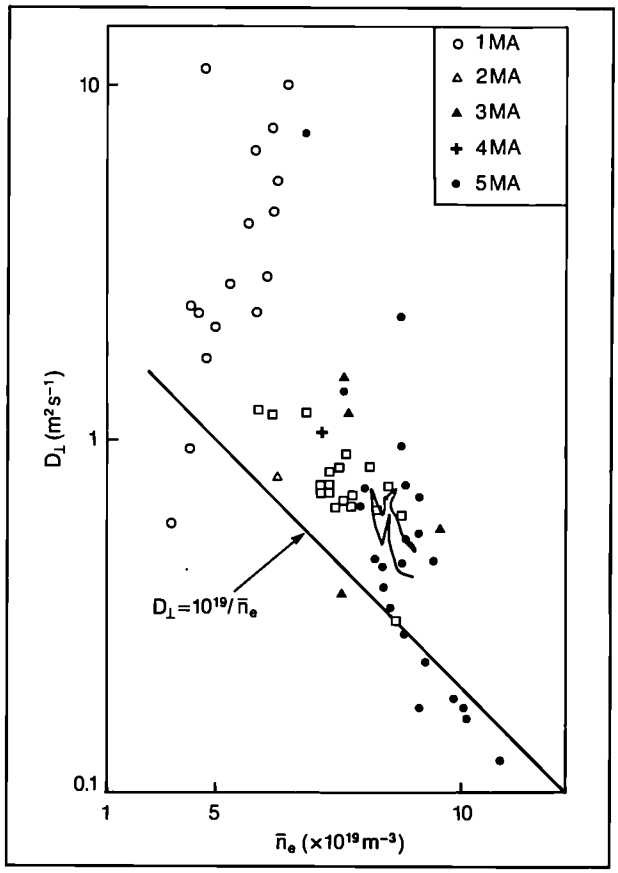

Fig.73 Perpendicular diffusion ($D_\perp$) versus average density ($\bar{n}_e$).

In relating λ_n to $D_\perp$, account was taken of two specific aspects of the JET configuration: (a) the poloidally-varying cross-section of plasma flux tubes in the scrape-off layer and (b) the discrete/continuous different limiter configurations. Results shown in Fig.73 are similar to values measured in the central JET plasma and approximate to $D_\perp = 10^{19}/\bar{n}_e$, the INTOR-ALCATOR value.

A two-dimensional impurity neutral/ion transport code, LIM ('Limiter Impurity'), has been developed to study the behaviour of impurities in limiter-controlled discharges. One type of output is the shape of the different ionization clouds near the limiter, which by comparison with spectroscopic measurements provide information on the transport-controlling conditions near the limiter. The primary output of the code is the calculation of the effectiveness of impurities released from the limiter in reaching the plasma centre, a process which is strongly influenced by transport conditions in the immediate vicinity of the limiter.

Edge Impurity Measurements

Radial influxes of impurities are measured spectroscopically. Time resolved parallel impurity fluxes have been measured using collector surfaces rotating behind a window, which are introduced into the boundary horizontally 385mm above the outer mid-plane using the Fast Transfer System (FTS). Detailed comparisons of parallel fluxes of carbon and metals with the plasma flux measured using Langmuir probes have been made for a pair of 3.5MA discharges (with low levels of ICRH heating) (Pulse Nos:13840 and 13841). The amounts of impurities collected were large during start-up and as the boundary approached the probes during the flat-top, consistent with Langmuir probe data, before decreasing during the rampdown. The carbon and nickel ion fluxes collected during the flat-top were $\sim 3.3\times10^{16}$ and $\sim 1\times10^{14}$atoms $cm^{-2}s^{-1}$ at a distance of 30mm from the LCFS: the value of the plasma ion flux in this region is in the range $12–3\times10^{16}$ ions cm^{-2s-1}, assuming singly charged ions. Collector probes have also been used to monitor impurity levels in the boundary during RF and NB heated discharges, and demonstrate that the nickel level varies with ICRH power. Collector probes are now being analysed routinely at JET in the Surface Analysis Station to which they are transferred directly, under vacuum, from the FTS.

Measurements of erosion of limiter tiles exposed during the 1986 campaign have been made. Typically, 0.1mm of carbon has been removed from the surface nearest the plasma with a similar amount being deposited radially further out. This simultaneous erosion and redeposition has been modelled by sputtering due to the plasma flux, followed by ionisation of the impurities and subsequent diffusion radially into and out of the plasma. A detailed model agrees well quantitatively with the measured erosion/deposition profile. The redeposition layer has been studied using

sectioning techniques and microscopy and has been shown to consist of layers of carbon, nickel and deuterium (Fig.74). This process thus explains the 'clean up' of metal from the limiter during normal ohmic discharges as well as explaining, at least qualitatively, the pumping of the plasma described above.

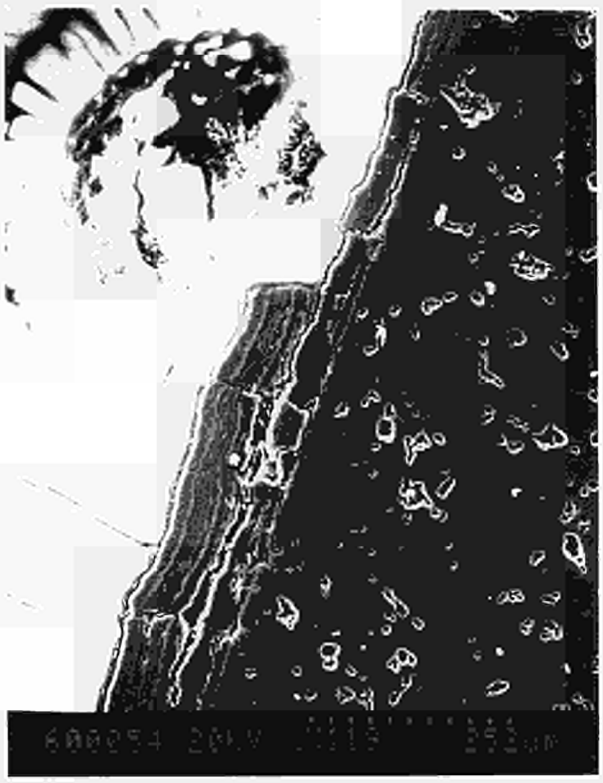

Fig.74 The redeposition layer.

References

[1] W. Engelhardt et al, J. Nucl. Mater. **111** & **112** (1982) 337;

[2] P.C. Stangeby, J. Nucl. Mater. **145** & **146** (1987) 106;

[3] R. Simonini (1987), JET (NIMBUS Code), Private Communication.

Disruptions

The programme of work on the understanding and control of disruptions has concentrated on five areas; (i) measurement and analysis of the localised flattening of the electron temperature at disruptions; (ii) the locking of the MHD precursor instability; (iii) the fast energy loss mechanisms; (iv) the fast current decay which follows the energy loss; and (v) analysis and design of a magnetic feedback system to control disruptions. A substancial diagnostic capability has also led to theoretical advances as described below.

Temperature Flattening

Part of the energy loss in disruptions is believed to be due to transport of energy across the magnetic island formed by an m = 2 tearing mode. Detailed investigations using a high-resolution heterodyne radiometer have allowed measurement of this behaviour. Fig.75 shows temperature profiles in the vicinity of the q = 2 surface for a soft disruption. The unflattened profile is that through the X-point, as located by the magnetic signal, and the flattened profile is that through the O-point shortly after the disruption. The form of these profiles indicates a non-symetric magnetic island as predicted by theory when toroidal effects are included.

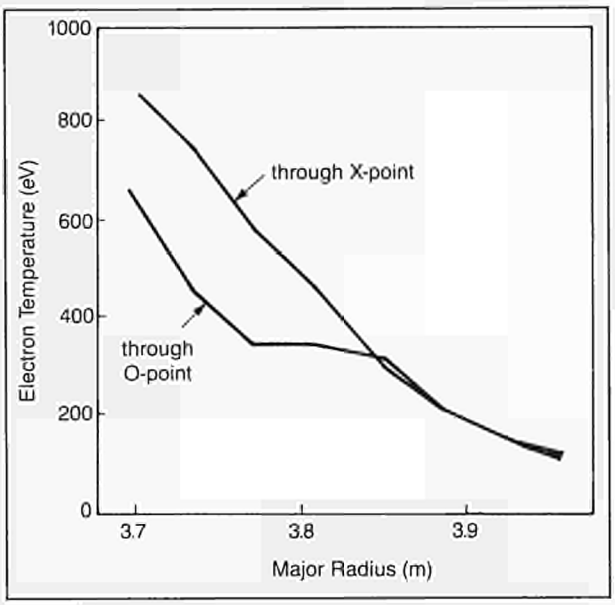

Fig.75 Temperature measured by the electron cyclotron emission (ECE) diagnostic during the soft disruption phase. The profiles show the effect of an m=2 magnetic island.

Mode Locking

Fig.76(a) shows the time behaviour of the signal of one of the magnetic coils located at the vacuum vessel and gives (dB_θ/dt), the time derivative of the poloidal magnetic field. This signal measures the n = 1 perturbation of the magnetic field due to MHD instabilities in the plasma. Under normal conditions, this signal is oscillatory because the MHD instability and its associated magnetic islands rotate around the torus. The amplitude of the magnetic perturbation increases as the disruption is approached, but its frequency reduces and is finally brought to zero rather rapidly. This process is called mode-locking.

The proposed theoretical interpretation of this behaviour is that the oscillatory radial magnetic field of the instability induces surface currents in external conductors and the interaction of this current with the radial field produces a $\mathbf{j} \times \mathbf{B}$ force in the conductor. There is a reaction in the plasma where a similar $\mathbf{j} \times \mathbf{B}$ force appears and this reaction causes a change in velocity of the plasma in such a way as to slow the motion of the magnetic perturbation.

Calculations illustrating this process have been carried out assuming that the predominant interaction is with

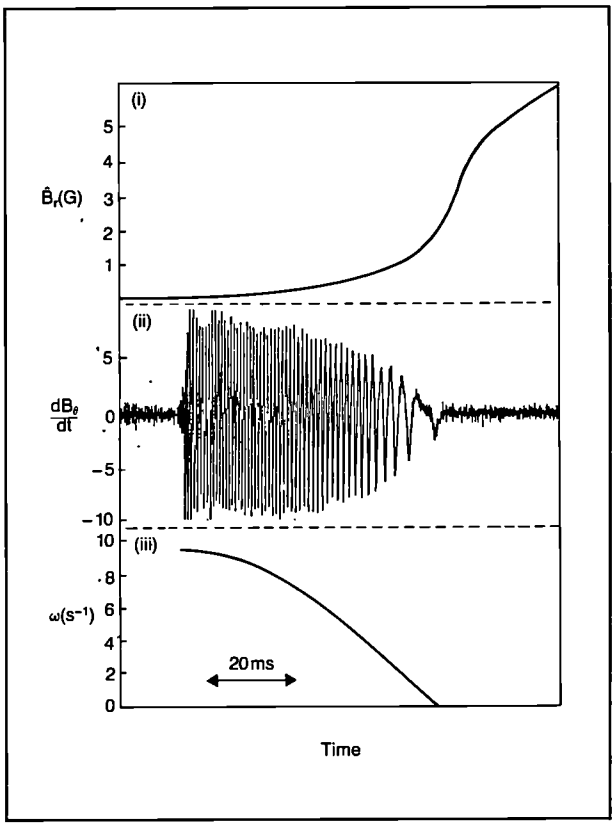

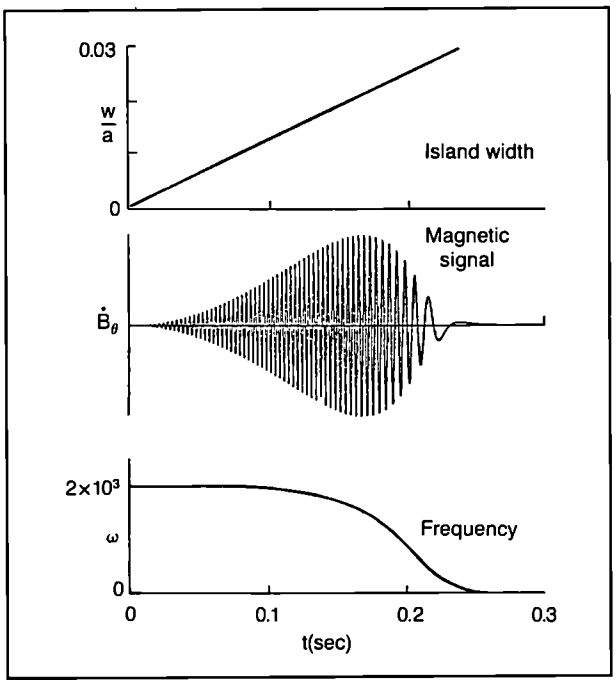

Fig.76 (a) Magnetic measurements as a function of time during mode locking; i) the magnitude of the perturbed radial magnetic field whose growth corresponds to the island growth; ii) the time derivative of the poloidal magnetic field; and iii) the frequency of B_θ as derived from the B_θ trace. (b) Simulation of mode-locking behaviour in which the island width of a growing tearing mode is calculated and the frequency of the associated magnetic perturbation is brought to zero through interaction with the vacuum vessel.

the vacuum vessel. Fig.76(b) shows the growth of an m = 2 magnetic island arising from an unstable current profile. After some time, the interaction with the vessel appears and the island is brought to rest. Comparison of timescales with the experiment indicates that it is the toroidal momentum which is changed and that the mass involved is intermediate between that of the magnetic island and that of the whole plasma.

The effects of the currents induced in the vacuum vessel only have a significant stabilising effect on the instability, if the resonant surface is close to the plasma surface. For m = 2, this implies the safety factor, q, above and rather close to 2.

Fast Energy Loss

Fig.77(a) shows the behaviour of the central electron temperature measured using the E.C.E. diagnostic during the energy quench of a density limit disruption. The temperature falls in two stages, the first accounting for about two-thirds of the complete drop. However, with regard to the resistance of the plasma the second phase is more significant. The fall to a very low temperature would account for the increased resistance which gives rise to the rapid current quench of $\sim 100\,MAs^{-1}$. There is evidence that the increase in resistance is due to cooling caused by the influx of carbon. Fig.77(b) shows the sudden increase in soft X-radiation which occurs at the time of the energy quench and analysis of this measurement indicates an influx of low-Z impurities. In an experiment designed specifically to study this event, the intensity of the 3p-2s line of CIII was monitored together with the visible bremsstrahlung. The results from two of the fifteen channels are shown in Fig.77(c). The increase in intensity of the carbon line was by a factor of $\sim 10^3$, and together with the increase in the bremsstrahlung implies a substantial influx of carbon and a confirmation of the low temperature indicated by the ECE measurement.

Fast Current Decay

The current decays following density limit disruptions show a number of interesting features and also have implications for the energy loss process itself. Fig.78 shows a typical fast current decay with a maximum $(dI/dt) \sim 200\,MAs^{-1}$. If the decay is interpreted as being due to the resistivity caused by Coulomb collisions, it is consistent with a low electron temperature ($\sim 10\,eV$). The enormously increased power input to the plasma, now gigawatts rather than megawatts, appears to be balanced by impurity line radiation. Although the time resolution of the bolometry does not allow a precise investigation, the integrated power is similar to the measured ohmic energy input.

The hesitation in the decay shown in Fig.78 is due to the runaway component of the current. The current was probably generated by the increase in the electric field

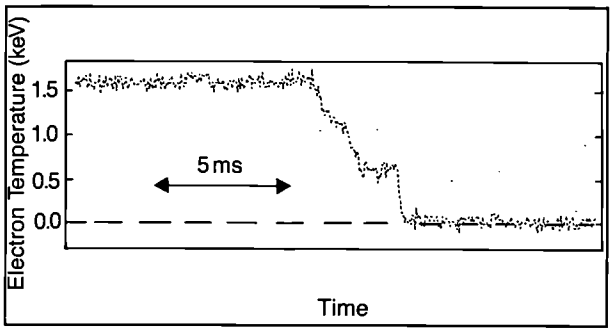

Fig.77 (a) Rapid-collapse of the electron temperature at the time of a hard disruption. The collapse occurs in two places and finally reduces the electron temperature to a very low value;

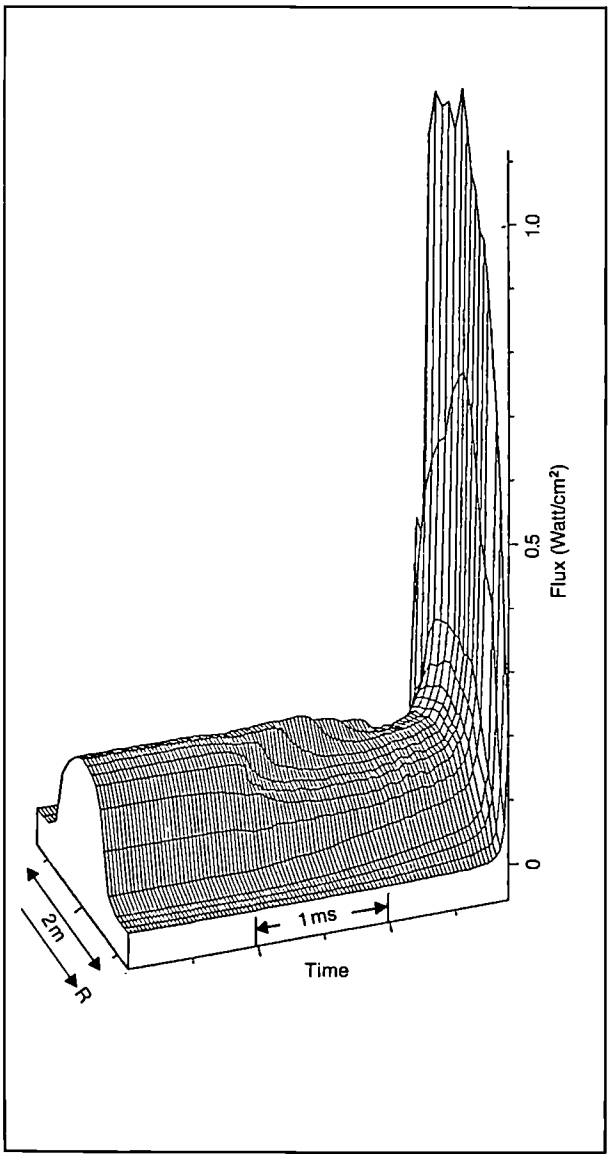

Fig.77 (b) Soft X-Ray emission measured across the major radius at the time of the disruption. The initial fall associated with the temperature fall is followed by a rapid and large increase in emission;

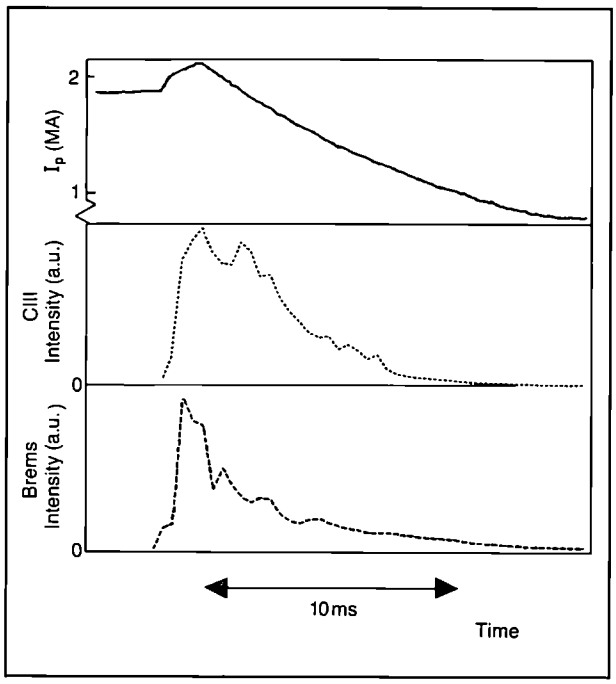

Fig.77 (c) Shows the large increase in CIII radiation and bremsstrahlung at the time of disruption.

by a factor $\sim 10^3$ associated with the collapse of the electron temperature.

Physics of Feedback Control

Theoretical analysis and computer codes have been used to understand the physics of the feedback control of disruptions. The proposed scheme will apply a magnetic field with a helical component designed to stabilise the m=2, n=1 tearing mode. Interest has centered on the identification of a fast inertial instability. This instability is driven by the out-of-phase field of the applied feedback and results in a phase instability. The precise growth rate of the instability depends upon the freedom of the plasma to undergo poloidal acceleration and on the mass of plasma involved. The feedback control

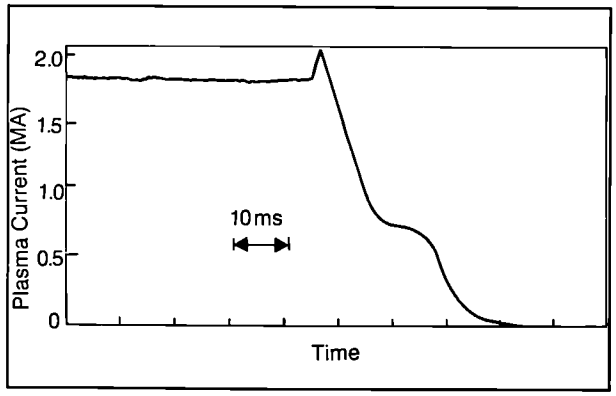

Fig.78 Plasma current during a disruption.

system must respond to the growth of this instability in addition to that of the m=2 tearing mode. A typical growth time for the phase instability might be ~1 ms.

Sawtooth Oscillations

Sawtooth oscillations have for many years been reorganized as one of the fundamental instabilities of tokamak plasmas. Analysis of sawtooth activity in JET plasmas in recent years has led to considerable revision of understanding of sawteeth and the development of a new theoretical model for the instability [1]. In addition, recent investigations of sawtooth behaviour during experiments with powerful additional heating have revealed a new plasma regime in which sawteeth are stabilized and quiescent plasmas are achieved for periods of nearly 3 s. The stabilization mechanism in these experiments is not understood, however, and these results have raised new questions about the theory of the sawtooth instability.

Detailed studies of the sawtooth collapse have confirmed previously reported observations on the timescale (~100μs) [2] and topology of the collapse, which occurs as an m=n=1 helical distortion of the plasma core followed by a poloidal redistribution of the flux surfaces [3]. In addition, there is a rapid flow of energy across the sawtooth inversion radius, (shown in Fig.79), which leads to the flattening of the temperature profile on a timescale ~100μs. This sequence of events occurs for all sawtooth collapses in JET, irrespective of the presence or absence of precursor activity. During the sawtooth collapse, a substantial magnetic perturbation is observed at the plasma edge (i.e. the 'gong' mode) [4]. This perturbation has a dominant toroidal motion number n=1, which, as illustrated in Fig.80, has a time evolution which is in remarkable agreement with that exhibited by the motion of the centroid of the soft X-ray emission profile [5]. This confirms not only that the instability has a dominantly n=1 nature, but that the soft X-rays provide an accurate monitor of the central magnetic surfaces during the growth of the instability.

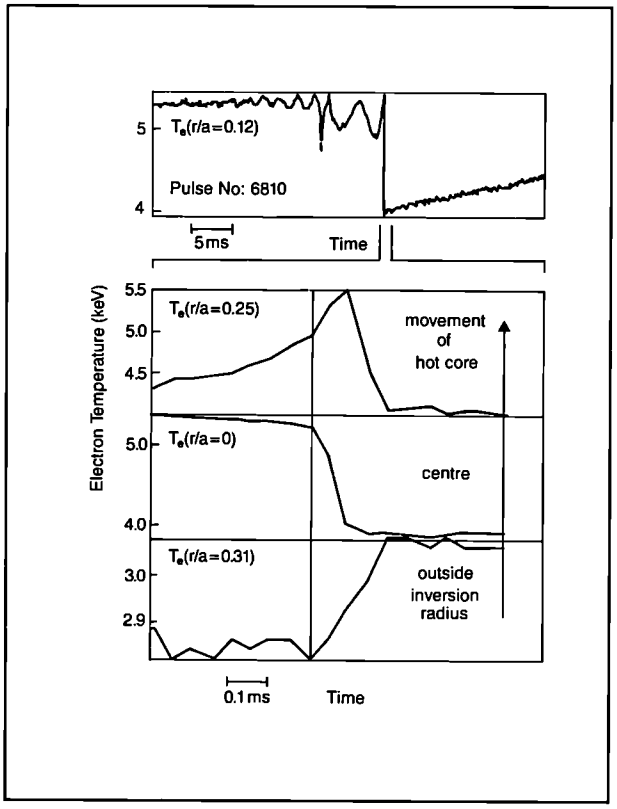

Fig.79: Change in electron temperature at three radii during a sawooth collapse, showing the rapid transport of energy across the sawtooth inversion radius.

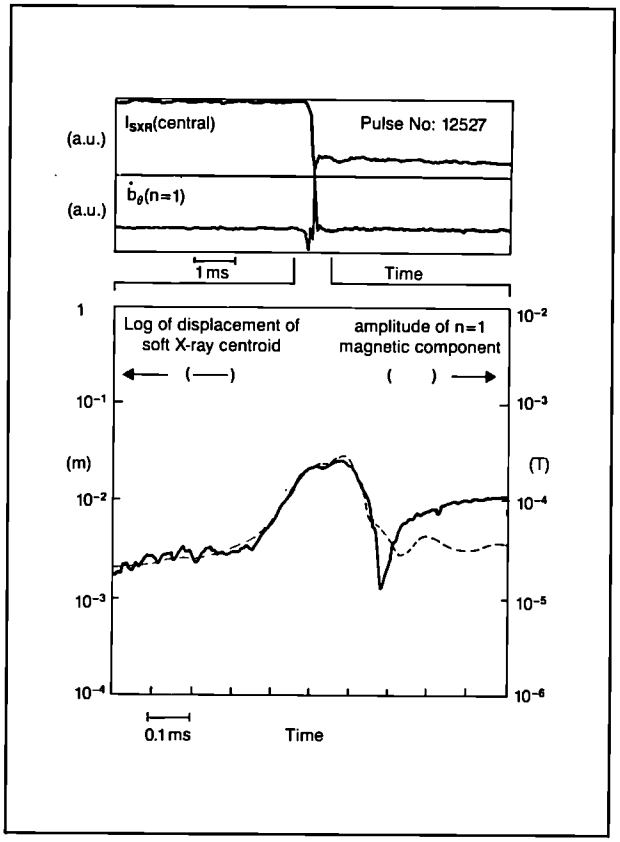

Fig.80: Comparison of the growth of the displacement of the centroid of the soft X-ray emission profile and the n=1 component of the edge magnetic perturbation during a sawtooth collapse.

Considerable efforts have been devoted to developing a theoretical understanding of the sawtooth instability [6]. However, there has been a growing realization that, in spite of significant agreement between certain observations and predictions of the quasi-interchange model, several aspects of the JET results defy explanation in terms of existing theories. In particular, it is found that the rate of growth of the instability growth rate is much too rapid. In addition, the mechanism for the rapid redistribution of energy which accompanies the collapse is not understood, although a number of explanations involving higher order ideal modes or small-scale turbulence have been proposed. Most

significantly, the observation, that sawteeth may be spontaneously stabilized with the central safety factor, q(0), well below unity, raises a fundamental question about present understanding of the sawtooth instability.

One of the most remarkable results obtained in JET recently has been the observation that during high power additional heating experiments, particularly with ICRH, sawteeth may be spontaneously suppressed [7]. The phenomenon (called a 'monster' sawtooth) illustrated in Fig.81, has been observed at plasma currents up to 5MA in discharges with ICRH heating and with combined ICRH and NB heating. This regime has

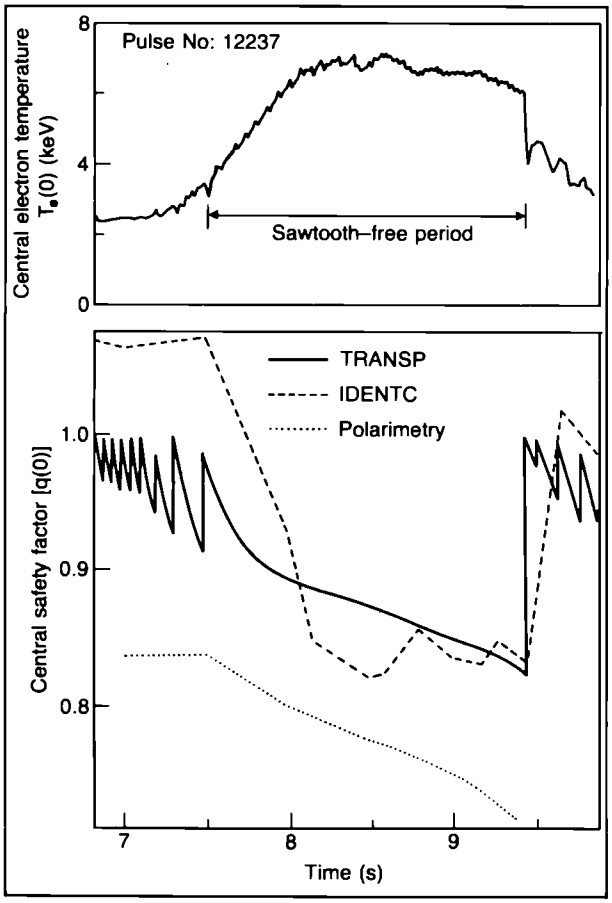

Fig.81: (a) Behaviour of central electron temperature during the longest sawtooth-free period obtained to date($\tau_s = 2.83$ s); (b) Comparison of electron temperature profiles measured by LIDAR Thomson Scattering during the ohmic and sawtooth-free regimes.

proved beneficial since the long quiescent period (up to 2.8s, or ~7 energy replacement times) has enabled plasma transport properties to be assessed in plasmas free from the disturbance of sawteeth, and has also permitted the benefits of sawtooth stabilization in the near-ignition regime to be analysed. While a small improvement in confinement is obtained (τ_E may increase by up to 20%), it appears that the major advantage of sawtooth stabilization will be an increase in the fusion power product due to the peaked temperature profiles which occur. Fig.81(b) compares electron temperature profiles, measured by the LIDAR-Thomson Scattering diagnostic, during the ohmic and sawtooth-free regimes. The predicted increase in the thermonuclear fusion power may be further enhanced by the reactions of non-thermal particles accelerated by RF fields.

This regime has been observed under a wide range of plasma conditions in JET: $2.1 < B_t < 3.4$T, $1.5 < I_p < 5.0$MA, $3.4 < q_\psi < 8.4$, and $n_e < 4 \times 10^{19} m^{-3}$. Furthermore, sawtooth-free periods have been observed in both H and He^3 ICRH minority heating schemes and in both monopole and dipole antenna configurations, although there is a substantial variation in the power threshold. The regime is also attained during combined heating experiments, and there is preliminary evidence that it may be accessed by NBI heating alone.

Sawtooth stabilization has been observed in other tokamaks as a result of current profile modification due to lower hybrid current drive. However, the JET results indicate that another stabilization mechanism may be responsible for the sawtooth suppression observed.

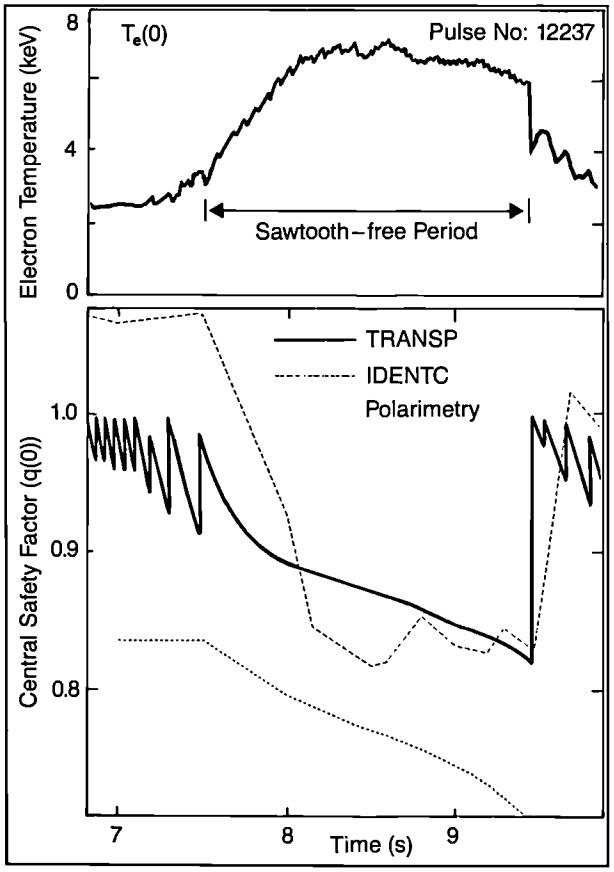

Fig.82: Comparison of the evolution of q(0) during a sawtooth-free period as determined by FIR polarimetry, resistive diffusion calculations (TRANSP) and magnetic equilibrium calculations (IDENTC). In each case, systematic uncertainties are ~ ±20%.

Analysis of the evolution of the q-profile during sawtooth-free periods indicates that q(0) decreases continuously during the quiescent period, attaining a value of ~0.8 before the crash, which terminates this period. As shown in Fig.82, this is confirmed by far-infrared polarimetry, by resistive diffusion calculations (using TRANSP) and by magnetic equilibrium calculations (using IDENTC).

These observations have cast fundamental doubts on existing theories of the sawtooth instability. Further questions are raised by the nature of the collapse terminating the stable period (see Fig.83), which exhibits the same behaviour as the collapse of normal sawteeth. It is essentially an m=n=1 instability, which has a similar collapse time (~100μs), but a larger centroid displacement (factor ~3) and a correspondingly larger inversion radius (~50%). The similarity between the behaviour shown in Fig.83 and that predicted by the ideal instability model of the collapse, which assumes that $1-q(0)<10^{-2}$, has not been explained. However, perhaps the most fundamental issue raised, is that of the stability of m=1 modes under these conditions (i.e. how does the plasma cross the ideal instability boundary at q(0)~1, and why does the resistive mode appear to be stable despite the fact that q(0)<1?) The present hypothesis is that the stabilization involves the energetic ion population which is accelerated by the RF fields, but the details of the mechanism are unclear.

A second MHD phenomenon believed to be related to the existence of a non-thermal ion component is the so-called 'fishbone' instability. This was first observed in the PDX tokamak, and was ascribed to the existence of fast, beam-injected, trapped particles (i.e. particles with high perpendicular energies). The instability normally takes the form of bursts of MHD activity, with m=n=1 in the plasma centre, and has previously been

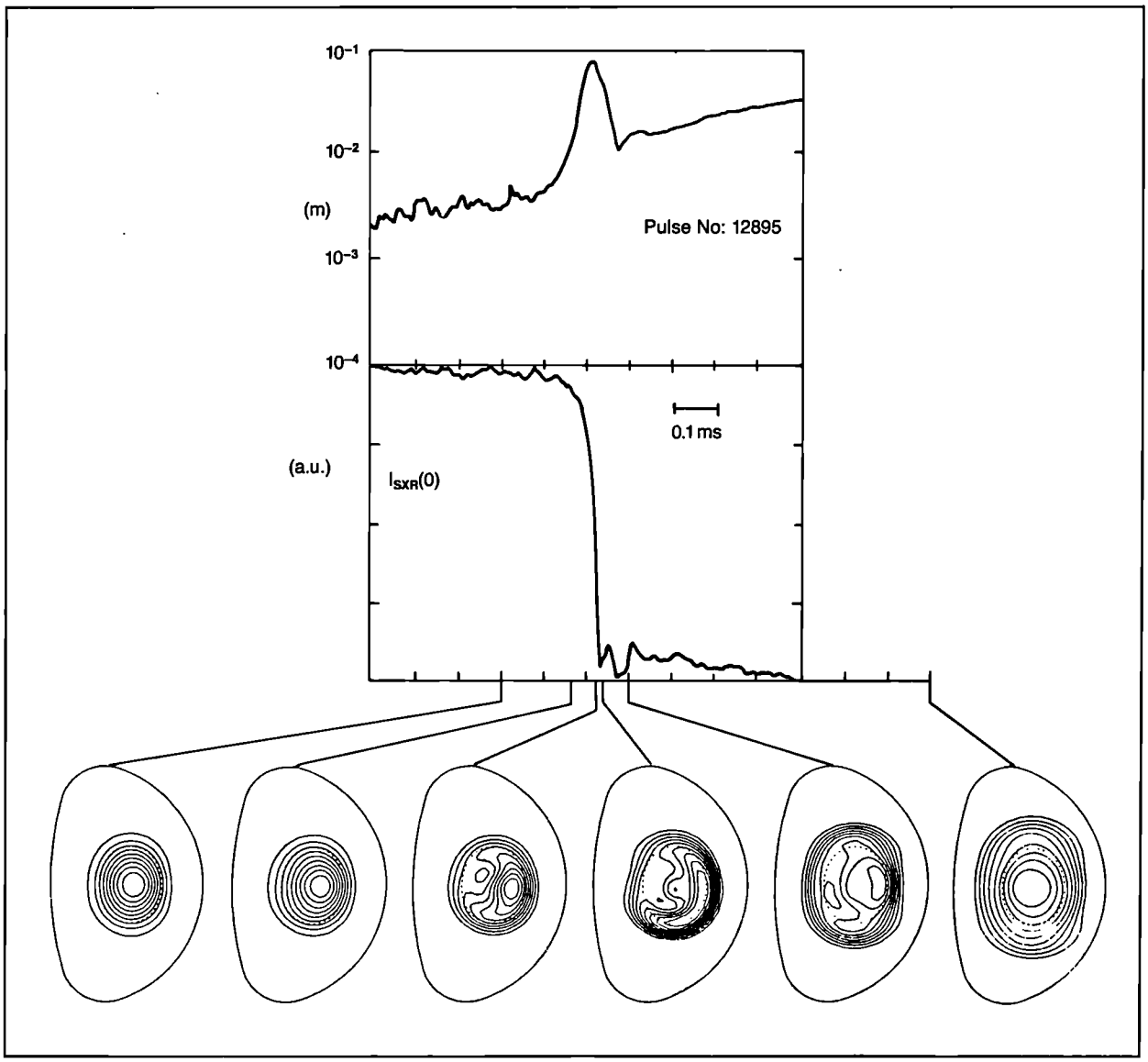

Fig.83: Contours of soft X-ray emissivity during the collapse terminating a sawtooth-free period.

observed in JET beam-heated discharges. Recently, however, such bursts have been observed for the first time in ICRF-heated discharges, as shown in Fig.84, and are interpreted as further evidence of a substantial high-energy trapped ion population. In contrast to observations on other devices, these instabilities do not appear at present to be associated with a loss of fast particles or degradation in confinement.

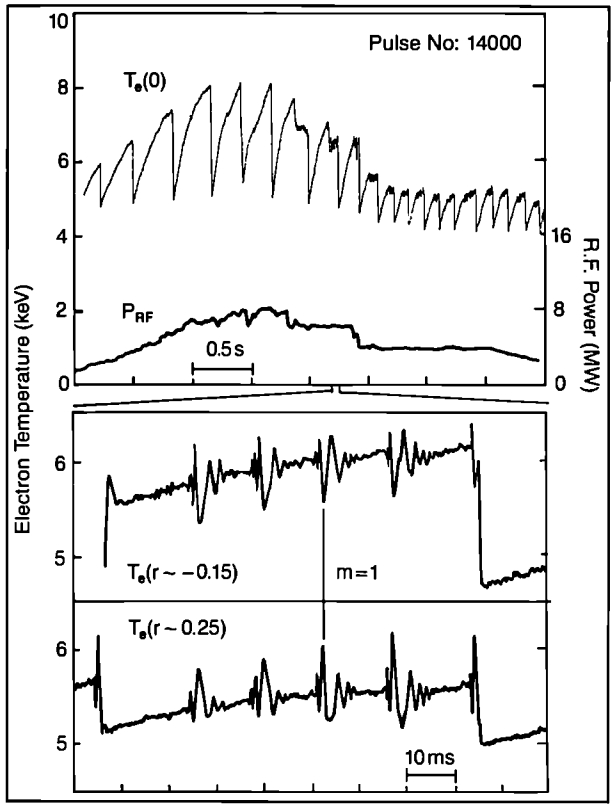

Fig.84: Bursts of MHD activity (m = n = 1) in the central electron temperature during ion cyclotron resonance heating. These are similar to 'fishbone' instabilities which are observed on other tokamaks during neutral beam injection.

References

[1] J.A. Wesson, Plasma Physics and Controlled Fusion 28(1A) (1986) 243;
[2] D.J. Campbell et al., Nucl. Fusion, 26 (1986) 1085;
[3] A.W. Edwards et al., Phys. Rev. Lett 57 (1986) 210:
[4] P.A. Duperrex et al., Proc. 12th EPS Conf., Budapest (1985) 1 126;
[5] D.J. Campbell et al., Bull. Am. Phys. Soc. 32 (1987) 1838;
[6] J.A. Wesson et al., Proc. 11th Int. Conf. on Plasma Phys. and Contr. Nucl. Fusion Research, Kyoto (1987) 2 3;
[7] D.J. Campbell et al., Report JET-P(87)20.

Separatrix Experiments and H-Mode Phenomena

The main objectives of measurements with a magnetic separatrix (or X-Point) configuration are: (i) to compare the global confinement chaacteristics of separatrix and limiter discharges; and (ii) to study the conditions for the creation of a high density, highly radiative, cool plasma region near the X-point capable of screening and isolating the bulk plasma. In these configurations, the plasma is detached from both the limiter and the inner wall and recycling occurs in an open divertor region near the X-point. Further experiments have been carried out with plasma currents up to 3.5MA in the single null (SN) configuration (see Fig.85).

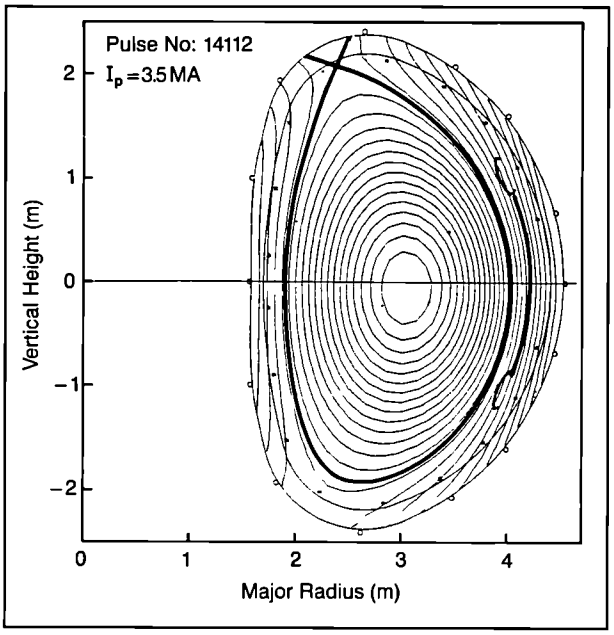

Fig.85: Magnetic flux surfaces for single-null X-point at I_p=3.5MA (Pulse No:14112).

During the last months of the 1986 experimental campaign, neutral beam heating of single-null X-point discharges had been successful in achieving H-mode plasmas with energy confinement times a factor of two larger than those of comparable limiter discharges. However, due to the 1987 shutdown (until June 1987) and various technical problems associated with the neutral beam injection systems, it took until December 1987 before H-mode plasmas were again obtained. Nevertheless, as soon as the neutral beam power exceeded the threshold values for H-mode transition in X-point discharges, the H-mode results of 1986 were reproduced. In addition, with only a few days of operation and with only NB power up to 6MW, a number of new results were obtained.

A wider scan of toroidal magnetic field confirmed the previous tentative observation of a very strong dependence of the threshold power. The maximum plasma current for H-mode operation was increased from 3MA in 1986 to 3.5MA in 1987 with a concomitant increase in the energy confinement time. Most importantly, variations in the radial distance between the separatrix and belt limiters resulted in changes in the frequency and period of short L-phases that interrupted H-mode periods and allowed the density and plasma radiation to be kept at quasi-stationary levels.

Fig.86 shows the variation with toroidal magnetic field of power required for the occurrence of an H-transition.

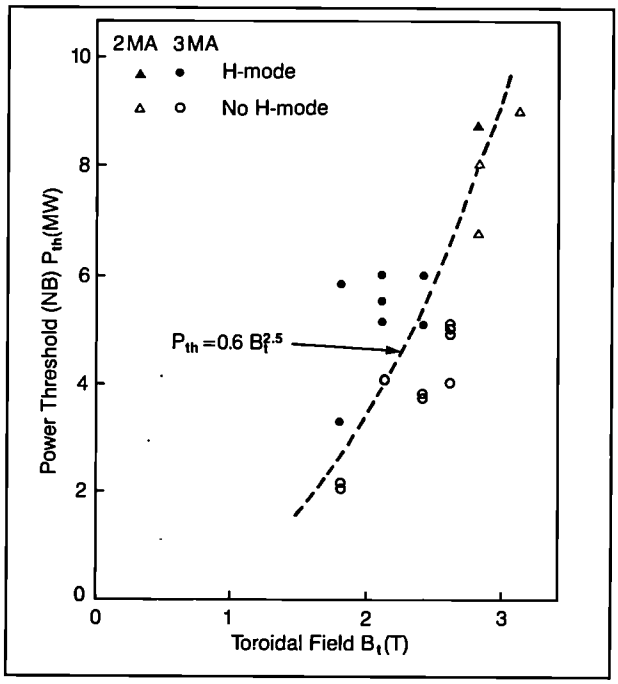

Fig.86: The variation of NB power rquired for the occurrence of an H-mode transition with toroidal magnetic field. The dotted line is the relationship $P_{th}(MW)=0.6[B\ (T)]^{2.5}$.

Within particular uncertainties, (such as the steps in which the NB power can be varied (~ 1MW)), the results indicate a scaling of threshold power of $P \sim 0.6B^{2.5}$ (and only a weak dependence on plasma current). Such a result, if extrapolated to higher fields and other machines, could lead to the need for excessively large powers to achieve H-mode plasmas in high-field tokamaks (such as CIT).

So far, only a very preliminary analysis of the 1987 H-mode shots has been carried out. One result is that the global energy confinement time, τ_E, appears to have little or only a very weak dependence on toroidal magnetic field (in the range 1.8 to 2.4T) (in accordance with similar observations on ASDEX, DIII-D and JFT-2M).

For the small number of H-mode pulses obtained in 1987, τ_E is plotted versus (P_t-dW/dt) in Fig.87, where it is compared with 1986 H-mode data. Only data with $(dW/dt) \leq 0.2\ P_t$ is shown. The general trend that τ_E for 1987 plasmas is somewhat smaller than for 1986 plasmas is partly due to the newly installed belt limiters reducing the maximum cross-section of single-null X-point plasmas by about 10%. Whether there is a confinement degradation with increasing heating power is not clear without more detailed analysis of the existing data (comprising the effects of power deposition and radiation profiles) and an extension of H-mode results to higher power levels (up to 15-20MW with NB and 20MW of ICRF heating which should be available early in 1988).

Fig.88 shows typical profiles of plasma density and electron temperature before and during an H-mode phase, measured with the newly installed LIDAR Thomson scattering system. The most pronounced changes between the L- and H-mode phases are seen in the density profiles. After the H-transition, the plasma density profile is flat or even slightly hollow with two distinct shoulders at the edge. Typical density gradients at the edge are about $2x10^{20}m^{-4}$. These shoulders disappear when ELMs (edge localised modes) are present.

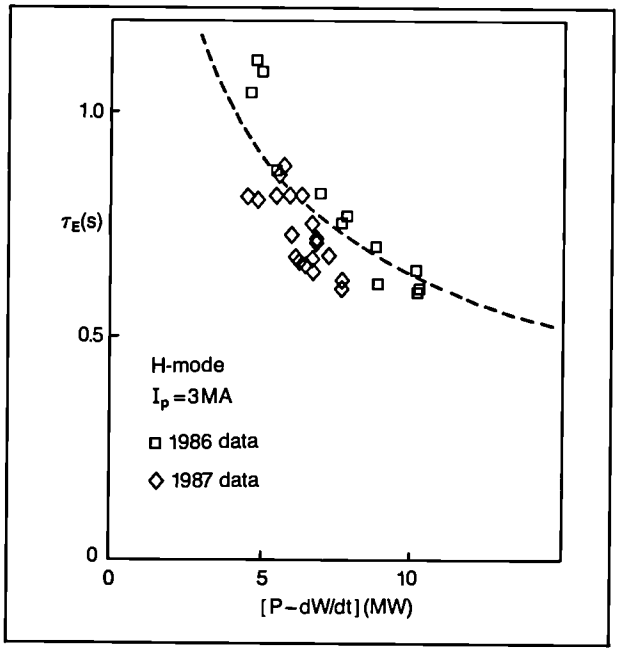

Fig.87: The energy confinement time, τ_E, versus $[P_t - dW/dt]$ for 1986 and 1987 H-mode data at I_p = 3 MA. (The dotted curve is ×2 Goldston scaling).

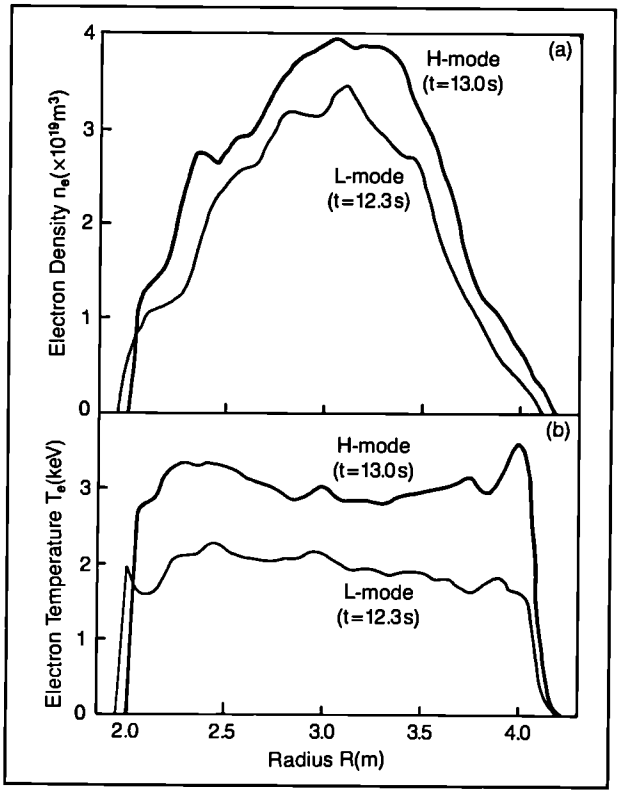

Fig.88: Typical profiles of (a) plasma density and (b) electron temperature before and during an H-mode.

In the electron temperature profile, there is a general increase at the onset of the H-mode but no dramatic change in shape. The electron temperature profile stays roughly similar throughout the H-phase while the plasma density increases by up to a factor x3. The ion temperature profile measured by CXRS and by NPA is Gaussian and similar to the electron temperature profile.

Fig.89 shows how variations in the radial distance between the separatrix and the belt limiters affect not only the duration of the first H-mode period but also of the subsequent L-phases that alternate with H-mode phases. For a certain optimum distance between separatrix and limiters, the frequency of these L- and H-mode periods allows the plasma density and radiation to be kept at a quasi-stationary level without a large adverse effect on the average energy confinement time. In the examples shown, the total length of L- and H-mode periods is limited by the length of the available neutral beam pulses. If the latter would be increased, the length of the L-H-mode train should be limited finally by accumulation of impurities in the plasma centre for which there is already some indication in present experiments.

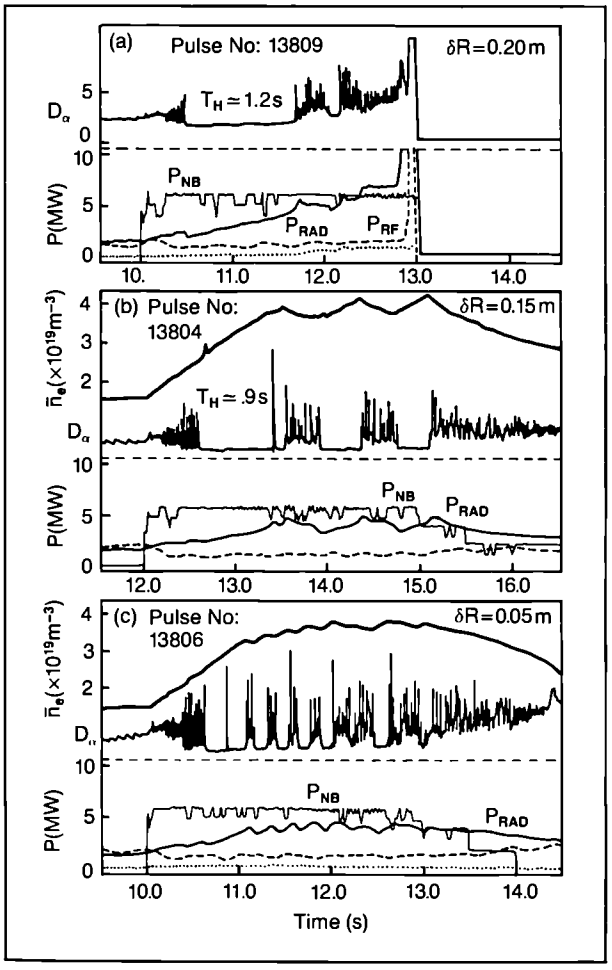

Fig.89:The effect of the variation in the radial distance (δR) between the separatrix and belt limiter: (a) δR = 0.20m; (b) δR = 0.15m; and (c) δR = 0.05m.

Radio Frequency Heating

During the year, major enhancements in the RF heating system have taken place and, since July, eight ICRF antennae have been operating at selected frequencies within the range 23–57MHz. Most units have a generator power capability of up to 3MW although progressive upgrading to 4MW is proceeding. At present, four units have this extended performance. The antennae screens are water-cooled which allows RF pulses up to 20s long. Each antennae comprises two elements which can be phased to give either monopole (in-phase) or toroidal dipole (π-phasing) modes of operation. There has been no need for antennae conditioning and the system works particularly well with the same frequency on each unit (homodyne operation). The RF plant settings for optimum coupling can be stored by CODAS and down-loaded when required. This facility enables switching from monopole to dipole modes of operation at high power on consecutive pulses. This procedure has identified the dipole mode as releasing least impurities during operation. The maximum power coupled into the plasma so far is 16MW for 2s in both monopole and dipole modes which have typical coupling resistances (R_c) of 5Ω and 2.5Ω, respectively.

The coupling resistance R_c in monopole mode shows strong oscillations as the toroidal field B_T is ramped linearly in time as shown in Fig.90. From the relative separation of the resistance peaks ($\Delta B_T/B_T \sim 3\%$), it is clear that these oscillations are due to the existence of radial eigenmodes between the antenna and the Alfven wave cut-off close to the (central) ion-ion hybrid

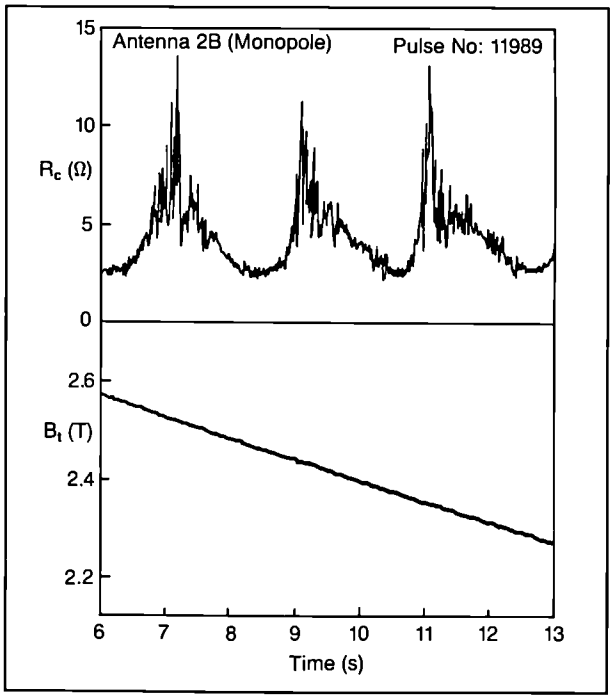

Fig.90 Radial eigenmode structure observed in the variation of coupling resistance with magnetic field.

resonance. Similar oscillations occur during density ramps, as expected, and a slab model has correctly reproduced the sawtooth-like shape of the oscillations. Scaling measurements revealed a lack of density dependence for R_c with monopole phasing, whereas the dipole coupling shows a linear increase with density. This behaviour has been reproduced by theoretical calculations and can be understood in terms of the widely different parallel wavenumber ($k_{\|}$) spectra of these antennae phasings and the $k_{\|}$ dependence of the depth of the evanescent layer at the plasma edge.

Plasma heating studies have been carried out using both hydrogen and ^{3}He minority ions, usually with the minority cyclotron resonance on-axis for optimum efficiency. Hydrogen minority heating in ^{3}He plasmas has produced central electron temperatures $T_e(0)$ up to 9.5 keV as shown in Fig.91.

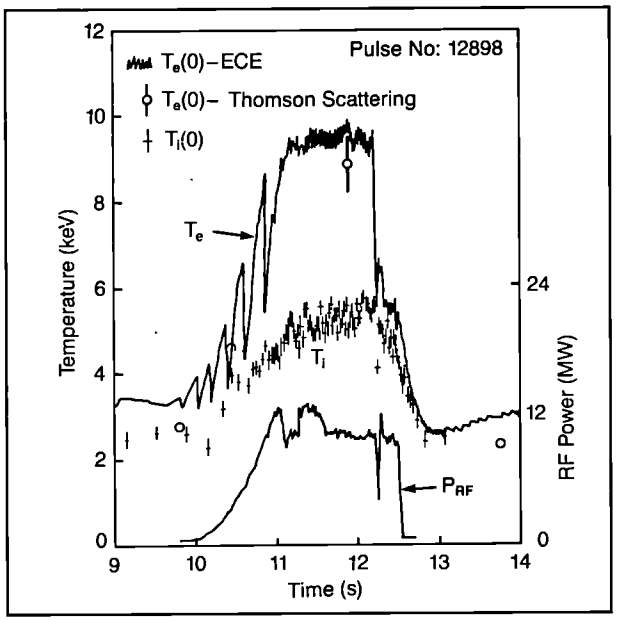

Fig.91 Central electron and ion temperature during ICRF heating (^{3}He(H), I_p=2.45 MA, B_t=2.4 T, K=1.5, q_ψ=5.3, $\bar{n}_e$=2.0×10^{19} m^{-3}, T_e=3 keV).

As the RF power is ramped up, the plasma exhibits the usual giant sawteeth but then switches to a sawtooth-free period (or so-called 'monster' sawtooth) during which $T_e(0)$ is constant. The electron temperature profile is extremely peaked, as shown by the average value of only 3 keV. The central ion temperature continues to rise throughout the stable period due to equipartion. Bulk plasma ion heating has been achieved with ^{3}He minority ions yielding ion temperatures on axis of 8 keV in ^{4}He plasmas and 7 keV in deuterium plasmas. The energy confinement degrades with additional heating but the asympotic (or incremental) confinement time increases with the plasma current I_p, provided the safety factor q is kept constant. This is shown in Fig.92 where the plasma energy content, as given by the diamagnetic loop, is plotted against total input power for I_p=2 MA and I_p=2.5 MA with $I_p/B_T \approx 1$ MA/T. However, this favourable scaling is less marked for currents above 3 MA.

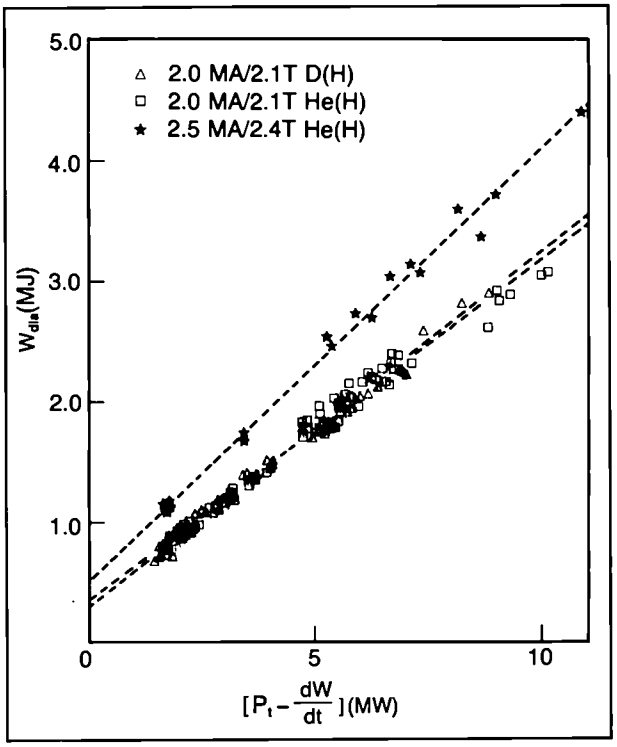

Fig.92 Energy content versus total power. The incremental confinement time is 0.29 s for 2.0 MA discharges and 0.36 s for 2.5 MA plasmas.

At 3.5 MA, an RF power input of 16 MW has produced a plasma stored energy of 6 MJ and a D-D fusion rate of 1.4×10^{15} s^{-1}. In these discharges, a significant fraction of the stored energy comes from the minority ions (Fig.93) which are expected to produce high fusion yield in (D)T heating schemes.

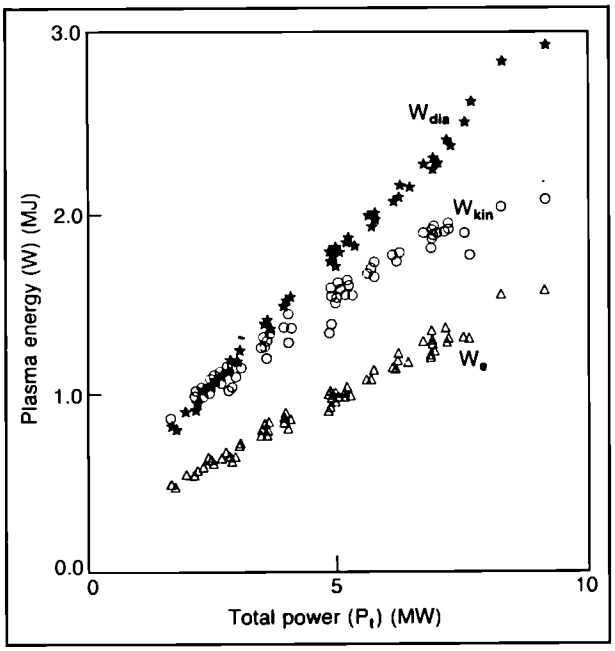

Fig.93 Diamagnetic and kinetic measurements of the plasma energy content (W), as a function of total power input (P_t). The difference between the measurements is due to the fast minority ion component.

ICRF power modulation experiments at 5Hz have been carried out during 'monster' sawteeth to study central power deposition profiles and thermal transport inside the $q = 1$ surface. Diamagnetic and equilibrium measurements of the modulated global energy content showed that at least 85% of the coupled RF power was utilized for plasma heating. Almost all the modulated component resided in perpendicular energy, in agreement with Fokker-Planck calculations of the minority ion distribution function. The modulated electron temperature response $\tilde{T}_e(r)$ was studied using a 12 channel ECE polychromater. Fourier analysis was used to obtain the 5 Hz component which was found to have an amplitude of approximately 100 eV in the plasma centre where the steady temperature was 6.5 keV. The radial profile of $\tilde{T}_e$ is shown in Fig.94(a) and was close to Gaussian with a width of 30cm. The phase of $\tilde{T}_e$ (Fig.94(b)) lagged the RF power by about 100° on the magnetic axis and increased monotonically to 140° at the $q = 1$ surface. The amplitude and phase profiles have been interpreted using a heat diffusion model which assumes a Gaussian power deposition profile and takes account of both direct and collisional electron heating. The data were well reproduced using a power profile width of 20cm (in agreement with full wave calculations), a thermal diffusivity in the range

$$2\,m^2s^{-1} < \chi_e < 4\,m^2s^{-1}$$

and a direct heating fraction of ~0.08.

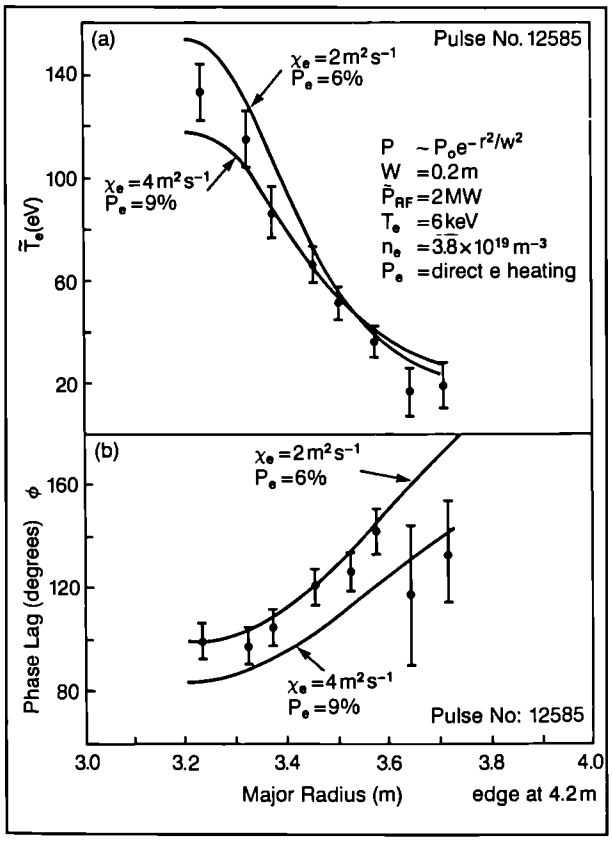

Fig.94 Radial profiles of (a) the amplitude and (b) phase of the modulated electron temperature in response to modulated RF power.

The operating conditions under which monster sawteeth are produced have been continuously developed and, notably, now include both hydrogen and ^{3}He minority heating schemes with both monopole and dipole antennae configurations. Operation with the plasma current and toroidal field B_t in the ratio $I_p/B_t \sim 1$ MA/T also appears to be optimum. Polarimetric measurements show that the safety factor on-axis decreases monotonically during the sawtooth-free period and this is in good agreement with magnetic field diffusion calculations provided the resistivity is neoclassical. With short duration RF pulses, the crash of the monster sawtooth occurs some tens of milliseconds after the RF is switched off, with the time delay decreasing as the RF pulse is lengthened as shown in Fig.95. This result could be due to the destabilizing effect of $q(0)$ decreasing monotonically during the pulse, in competition with a stabilizing influence of the fast minority ions which decays after the ICRF is switched off. Preliminary experiments have shown that the sawtooth free period can be extended up to 2.8 s by ramping the plasma current (although the reason for this is unclear).

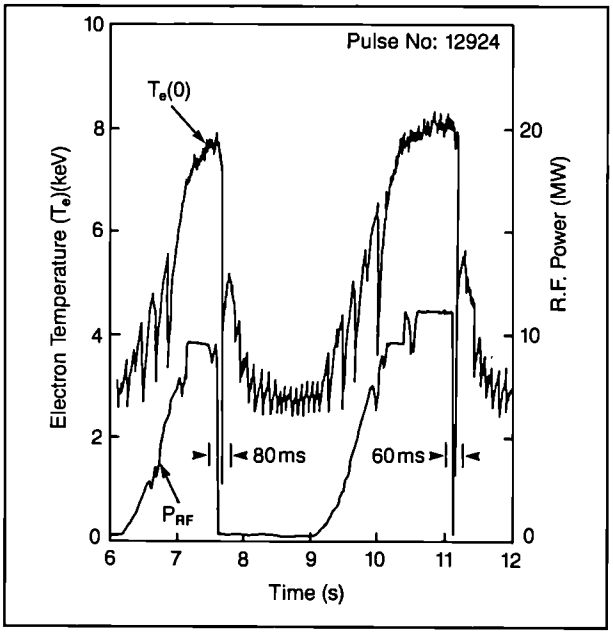

Fig.95 Monster sawteeth during short RF pulses. The crash occurs some tens of milliseconds after the RF switch-off. ($I_p = 2.45MA$, $B_t = 2.4T$, $\bar{n}_e = 2 \times 10^{19} m^{-3}$. When RF power is switched-off before the crash of the 'monster', the crash occurs within a fraction of the fast ion slowing-down time).

Neutral Beam Heating

Due to hardware difficulties described earlier in the technical section of this report, there is a paucity of new data. Nevertheless, significant experiment results were obtained during 1987. In particular, H-mode confinement was re-established and the power threshold for the L-H-mode transition established for a limited range of toroidal field. Combined NB and RF heating with a total power of 22MW resulted in values of

$T_e(0) = 10\,\text{keV}$ with $T_i(0) = 8.5\,\text{keV}$. During the sawtooth-free ('monster sawtooth') period of a limiter discharge, comparable temperatures were also obtained with ~15 MW of additional heating.

Further analysis of the 1986 data has led to significant progress in two areas, as follows.

Non-Inductive Current Drive during Neutral Beam Heating

In previous beam driven current experiments in JET, substantial non-inductive toroidal currents (up to 0.6 MA) were driven in low-density plasmas. The currents were deduced from the plasma loop voltage and the plasma resistivity as calculated from the ECE temperature profile and Z_{eff} as measured from visible bremsstrahlung. The calculated effect of changes in plasma resistivity only on the plasma loop voltage due to beam heating is shown in Fig.96(a). The predicted beam driven current including trapped-particle effects is able to account for some of the change in the measured loop voltage, as shown in Fig.96(b). A recalculated predicted neo-classical 'bootstrap' current [1], using the Lao-Hirschmann flux surface geometry and following a moment approach [2], is of the same magnitude as the remaining non-inductive current, as shown in Fig.96(c).

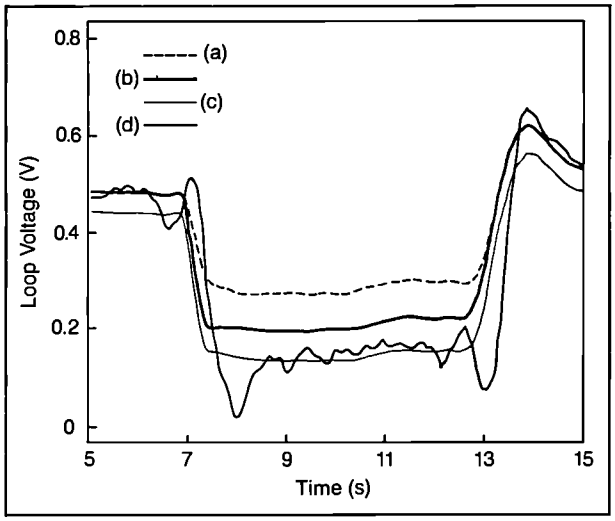

Fig.96 Measured plasma loop voltage V_{loop} during beam injection into a low current (1 MA) discharge, compared with theoretical predictions for certain effects: (a) predictions from conductivity change only; (b) conductivity change plus beam driven current; (c) conductivity change plus beam driven current plus bootstrap current; (d) measured value.

Comparison of the inferred non-inductive current with the predicted beam driven current for many JET pulses (Fig.97), including counter-injection pulses where the sense of the beam driven current is reversed, shows the predicted beam driven current is too small by typically 200 kA. Fig.98 shows that if the predicted bootstrap current is included the data is moved onto the $x = y$ line, showing that good agreement between the experimentally inferred and predicted non-inductive current only exists if both the beam driven current and bootstrap current are considered. Bootstrap current predictions for high-density JET plasmas not considered here are about 0.75 MA and may become significant as JET approaches full performance.

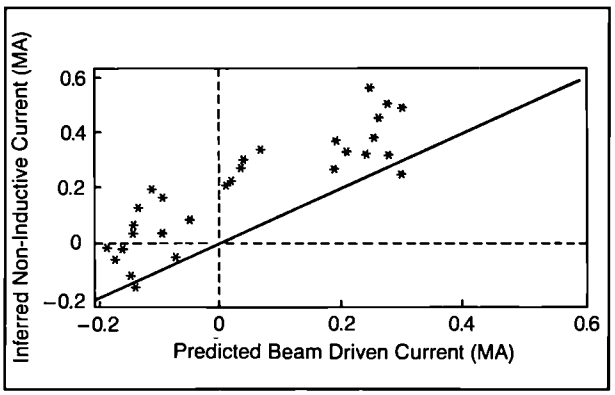

Fig.97 Total non-inductive current inferred from the measured loop voltage and calculated resistivity during beam heating versus predicted beam-driven current.

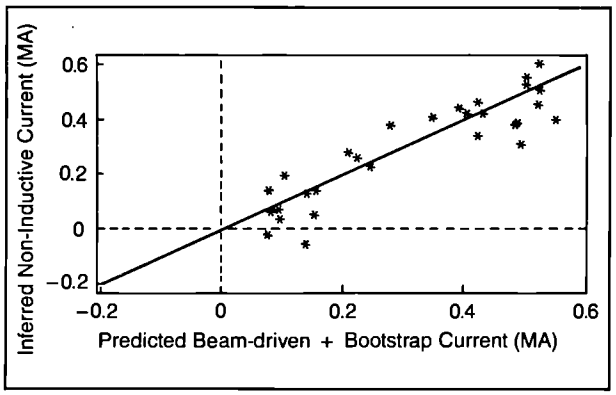

Fig.98 Total non-inductive current inferred from the measured loop voltage and calculated resistivity during beam heating versus predicted beam-driven and bootstrap current.

Fuelling Characteristics of NB Heated Plasmas

Further analysis of the density behaviour of NB heated plasmas has been carried out, based on 1986 data. The analysis is based on the two-reservoir model for hydrogenic recycling previously reported [3]. The principal result, obtained by fitting the model predictions to NB [4] and otherwise induced density transients (e.g. plasma movements [5]), is the existence of a dynamic retention time, $\tau_s \sim 1$ s for hydrogen in the graphite surfaces at which recycling takes place. This result applies over a wide range of plasma conditions in JET. Consequently, the main fuelling characteristic during NB is an asymptotic beam fuelling efficiency $\epsilon < 1$. A simultaneous analysis of the H_α limiter light evolution and the density rise during NBI implies a prompt reflection coefficient $r > 0.4$ [4]. The density rise at the onset of the H-mode (Fig.99) may be readily interpreted in terms of a shift in the equilibrium between the plasma and graphite reservoirs produced by an instantaneous increase in τ_p [4]; the evolution of the density fits the model accurately in this case (Fig.100).

For inner-wall limited NB heated plasmas following helium discharge conditioning, the density achieved a steady-state value in the presence of continuous beam

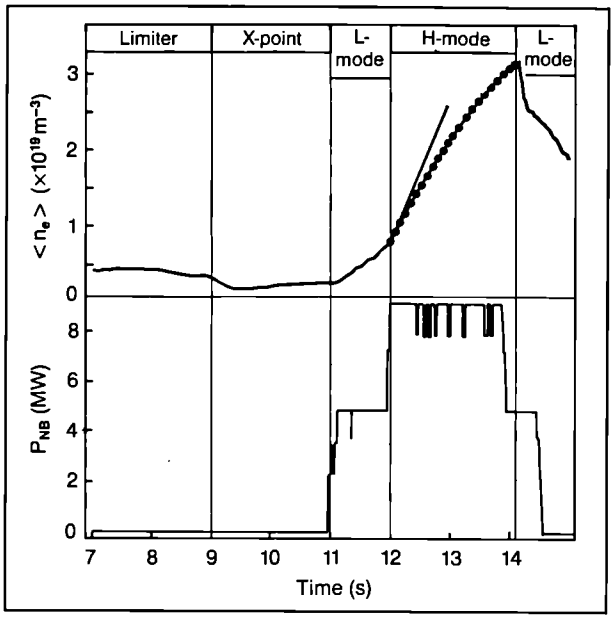

Fig.99 Evolution of volume averaged electron density $\langle n_e \rangle$ during Pulse No:10755. During the H-mode phase, the discrete points represent the best-fit of the two-reservoir model to the measured density (solid line). The injected power (P_{NB}) is also shown. At the NB onset of the H-mode, the rate of increase of plasma electron content (N_p) exceeds the NB fuelling rate by a factor ~2.3.

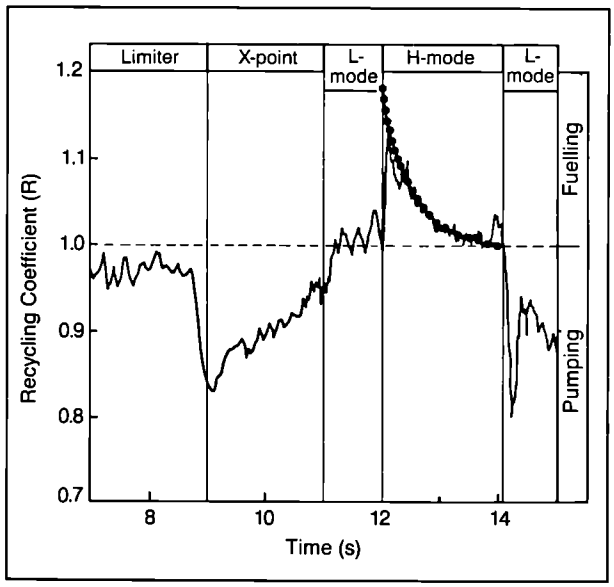

Fig.100 Evolution of global recycling coefficient (R) during Pulse No.10755, determined from H_α intensity measured at the vessel walls, limiters, and X-point and inner-wall protection tiles. During the H-mode phase, the value of R predicted by the fit of the two-reservoir model is indicated by the discrete points.

fuelling. This implies the existence of a particle sink, assumed to be due to trapping of hydrogenic atoms at strongly binding trap sites in the graphite left vacant following ion-induced desorption during helium conditioning. Equilibrium is achieved when the beam fuelling rate balances the fraction of the plasma particle efflux which is trapped in the inner wall graphite tiles. As the vacant trap sites are refilled, the trapping probability falls until the behaviour reverts to normal, i.e., $\epsilon > 0$. In practice, deconditioning took place within ~6 inner-wall discharges with NB pulses of 5MW for 4s ($\phi_b \sim 10^{21} s^{-1}$). Assuming the build up of trapped hydrogen is approximately exponential with total fluence, the density behaviour of successive NB discharges can be qualitatively modelled[4]. In conclusion, two types of limiter pumping are identified; a non-saturable pumping effect which is a consequence of finite τ_s, and stronger, but saturable pumping following helium conditioning. It is required to maximise the ratio of core to edge fuelling rates for peaked density profiles necessary in optimising thermonuclear Q, and both types of pumping control could be exploited. The non-saturable pumping effect may assume a great importance in full performance JET plasmas since reduced particle confinement time, τ_p (<100ms) and hence low ϵ (<0.2) is predicted, allowing greater core fuelling by NB and pellets for a given rate of increase of density, n_e.

References

[1] R.J. Bickerton, J.W. Connor and J.B. Taylor, Nature (Physical Science) **229**, 110 (1971).

[2] .B. Kim, J.D. Callen and H. Hamnén, 'Neo-classical current and transport in auxiliary heated Tokamaks' (JET Internal Report, to be published).

[3] JET Progress Report EUR 11113EN (EUR-JET-PR4) (1986);

[4] T.T.C. Jones et al., 'Neutral Beam and Edge Fuelling Effects in JET Discharges', 14th European Conference on Controlled Fusion and Plasma Physics (Madrid, Spain, 1987), Europhysics Conference Abstracts, Vol.11D, Part I, p17 (1987);

[5] J. Ehrenberg et al., 'The Effects of Wall and Limiter Material Properties on Hydrogen Recycling in JET', 14th European Conference on Controlled Fusion and Plasma Physics (Madrid, Spain, 1987), Europhysics Conference Abstracts, Vol.11D, Part II, p706 (1987).

Particle Transport and Fuelling

Many options for optimization of plasma and heating performance in JET, for maximizing Q (the ratio of total fusion power production to the total heating power input) rely on control of plasma density and its spatial profile. The requirement is to maximize $n_i(0)$, the peak density of the hydrogen isotope ions, while keeping $<n_e>$, the volume averaged electron density constant. This is achieved by maximizing the profile peakedness, $n_i(0)/<n_i>$, and plasma purity, $n_i(0)/n_e(0)$, while fuelling the core by pellet injection (PI) and central neutral beam (NB) injection and simultaneously reducing the competing edge fuelling due to recycling by deploying pump-limiters and also, if possible, pumping by conditioned walls. The different elements that determine the density profile (i.e.the particle transport) and ingredients of the fuel input (i.e. PI, NB; recycling and pumping) have been analysed in detail. In addition, their scaling to reference plasma conditions at full performance in JET, has been carried out. The

requirements for density profile peakedness, and the fuelling and pumping capabilities may then be matched and optimization of JET performance assessed.

One controlling element in the evolution of the density profile is the fuel source strength and its spatial profile. PI and NB are envisaged as the core fuelling sources, with strength $\phi_{NB} \sim 10^{21} s^{-1}$ and $\phi_{PI} \sim 1-3 \times 10^{21} s^{-1}$. The edge fuelling source, due to recycling, is about an order of magnitude larger, and thus the dominant source. The scope for controlling it is small, vigorous wall/limiter conditioning procedures and deployment of pump-limiters will enable the recycling coefficient, R, to be varied in the range $0.9 \leq R \leq 1$ in the reference plasma [1]. Therefore, extensive measurements have therefore been carried out of the influx of H/D from the limiter and wall, and its scaling with the different plasma and heating parameters to assess the strength of the recycling fuel source for the reference plasma. The total rate of influx, ϕ_R, of H/D due to recycling in ohmically heated plasmas, is described by the expression

$$\phi_R(10^{22}\ s^{-1}) \approx <n_e(10^{19}\ m^{-3})>^2 / I_p(MA) \quad (1)$$

The influx is deduced from absolute measurements of H_α/D_α emission. These measurements are supported by Langmuir probe measurements of the particle outflux. Analysis of ϕ_R during ICRF heating leads to the inference that in steady state at constant $<n>$, ϕ_R is only weakly dependent on the applied ICRF power (P_{RF}), whereas at constant P_{RF} a density dependence similar to that with ohmic heating (OH) alone is found. However, application of ICRF power causes fuelling due to desorption of gas which is weakly bound on the surrounding surfaces. Thus, the density increases with applied ICRF power, and therefore ϕ_R also increases as in Eq.F1. Similarly for NB heating, ϕ_R is only weakly dependent on P_{NB} in the steady state at constant $<n>$. Since NB is also a strong fuelling source, $<n>$ increases with $P_{NB}$and, therefore, ϕ_R also increases, as in Eq. 1. A critical remaining question is whether ϕ_R depends on profile peakedness, $n(0)/<n>$, at constant $<n>$,ϕ_R decreases when $n(0)/<n>$ increases [2], the dependence shown in Eq. 1 is appropriate when the profile shape is approximately constant.

The conventional characterisation of influx into a tokamak plasma due to recycling makes use of the equation

$$\phi_R = R(N_p/\tau_p)$$

Where N_p is the total number of plasma particles of a particular species, R is the recycling coefficient and τ_p the particle confinement time. Eq. 1 describes observations in steady state with $R \sim 1$. However, transiently R can significantly deviate from unity, as with pellet fueling [2]. A more physical description of ϕ_R, capable of modelling both transient and steady state behaviour of R, is one in which the following considerations are included:

(a) Only a fraction γ of the particle flux incident on the surfaces surrounding the plasma is promptly reflected;

(b) The non-reflected flux penetrates the surface and the particles are retained in the material for a characteristic time, τ_s, controlled by material properties;

(c) In the absence of external fuelling, the plasma and the surrounding surfaces constitute a closed system of two coupled reservoirs in which the total number of H/D atoms, N_o, is conserved. Particles added to the system are shared between the two reservoirs according to their respective containment times.

These considerations give

$$\phi_R = \frac{\gamma N_p}{\tau_p} + \frac{(N_o - N_p)}{\tau_s}$$

This forms a two reservoir model of particle dynamics between the plasma and the surfaces surrounding it [3]. For a given external fuelling source rate ϕ_{ex}, the evolution of N_p, and hence R and ϕ_R, is described by

$$dN_p/dt = -(1-\gamma)\frac{N_p}{\tau_p} + \frac{(N_o + \int \phi_{ex}\, dt - N_p)}{\tau_s} + \phi_{ex}$$

This equation has been extensively tested for NB [3], PI fuelling, and transient inner-wall pumping [4], by comparing the forms predicted for $N_p(t)$ and $\phi_R(t)$ against experimental observations. In particular, the model predicts that in the steady state, the density increase for NB and PI is characterized by an asymptomatic fuelling efficiency $\epsilon \lesssim 1$, a necessary consequence of finite τ_s, values as low as $\epsilon \approx 0.2$ have been observed in JET [3]. $\epsilon = \tau_p/[\tau_p + \tau_s(1-\gamma)]$ is the asymptotic ratio of the total increase in the plasma particle content and the total number of particles injected into the plasma. ϵ represents how particles added to the system are shared between the two reservoirs.

The second important element controlling the density profile is the particle transport. Extensive measurements and analysis of electron density transport have been made. The measured radial electron flux greatly exceeds the corresponding neo-classical flux for the plasma condition in JET. The anomalous electron flux is described by a model consisting of diffusive and convective terms:

$$\Gamma_e = -D.\nabla n_e + n_e.V$$

$n_e(r)$, $\Gamma_e(r)$, D(r), V(r) are the electron density, radial electron flux, diffusion coefficient and velocity, respectively. The evolution of the electron density profile is then described by the continuity equation:

$$\frac{dn_e}{dt} + \nabla \Gamma_e = S_e$$

where $S_e(r)$ is the electron source. In JET, the coefficients D(r) and V(r) have been determined in a number of different ways in steady-state and transient situations, covering a wide range in plasma parameters $B\phi$, T_e, $\bar{n}_e$ for Ohmic, ICRF and NBI heating [1]. The diffusion coefficient exhibits a dependence of the form $<D> \propto f(T_e)/I_p$, where $f(T_e)$ is a weak function of $T_e$and $<D>$ the volume averaged value of D. No dependence of $<D>$ on heating method or power level has been identified. There is no evidence in JET that $<D>$ and

V depend on $n_e(r)$ or $S_e(r)$. Similarly, the convective flux, $\Gamma_p = n_e V$ (often referred to as the particle pinch) is found to be independent of the plasma parameters, heating mode, $n_e(r)$ and $S_e(r)$. The magnitiudes deduced for the transport coefficients are $D(r) = D_o(1+2r^2/a^2)$, with $0.3 \leq D_o(m^2 s^{-1}) \leq 0.5$ and $V(r) = -V_o(r/a)^\alpha$, with $0.4 \leq V_o(m.s^{-1}) \leq 1$ and $\alpha \sim 2$. It is conjectured that all charged particle species follow this kind of transport, with the same coefficients. This conjecture is partially supported by measurements of impurity transport in JET [5].

A model has been developed in which the fuelling, recycling and particle transport elements are synthesized in order to determine the density profiles that might obtain in the reference plasma, and to assess the implications for optimization of JET performance [1]. The total source is made up of S_c, a core source (NB and PI) and S_E, an edge source due to recycling flux. The relative strength of the two sources control the density profile. Two models for the core source are considered: (i) S_c is deposited inside the core region $r/a \leq 0.25$ with a parabolic profile; (ii) $\frac{1}{3}S_c$ is deposited inside the core region with a parabolic profile, and the remaining $\frac{2}{3}S_c$ forms a uniform pedestal outside. Model (ii) corresponds to NB fuelling profile, while NB + PI would correspond to an intermediate profile between models (i) and (ii). The profile of S_E is determined by neutral transport into the plasma and subsequent ionization of these neutrals, as discussed previously [6]. The total particle source, $S(r) = S_c + S_E$, is parameterized interms of the ratio S_E/S_c. The resulting density profile is parameterized in terms of the peak to volume-averaged density ratio, $n(0)/\langle n \rangle$. Fig.101 shows the dependence of $n(0)/\langle n \rangle$ on S_E/S_c, at constant $\langle n \rangle$, for the models of S_c for a reference plasma with $B_t = 3.4T$, $I_p = 7MA$, $\langle n \rangle = 4\times10^{19} m^{-3}$, $V = 130 m^{-3}$, limited by outer-limiter or inner-wall, $P_{RF} \sim 20MW$, $P_{NB} \sim 20MW$ ($\phi_{NB} \sim 10^{21} s^{-1}$), multiple pellet injection fuelling ($\phi_{PI} \sim 1-3\times10^{21} s^{-1}$) and pump-limiter and conditioned inne- wall for recycling control. In Fig.101, the particle confinement time, τ_p, increases when the core source becomes more dominant, which corresponds to observation in pellet fuelled plasmas [2].

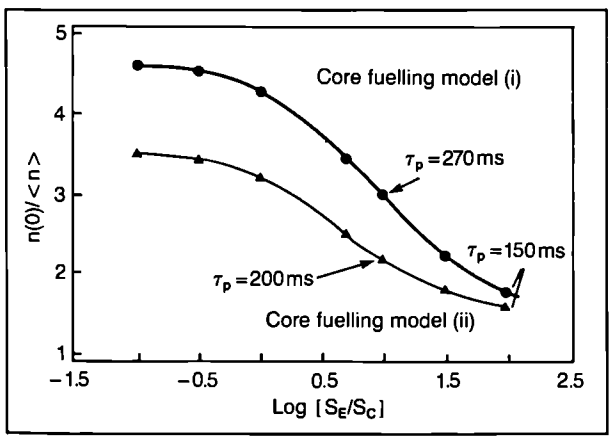

Fig.101 The dependence of $n(0)/\langle n \rangle$ on S_E/S_c at constant $\langle n \rangle$ for two different models of S_c.

Table VII summerizes the relevant plasma and fuelling parameters, and the $n(0)/\langle n \rangle$ values that are achievable. Two options are considered for core fuelling, one using central NB, and the second one employing pellet fuelling in addition, where the pellets are assumed to penetrate into the plasma core. Column (i) is for fuelling by central NB alone. In column (ii), pellet fuelling is added, where the pellet size is matched to give a steady state (i.e. $(dN_p/dt) = 0$, requiring $R \approx 0.9$). In column (iii), a larger pellet is considered. To demand $(dN_p/dt) = 0$ would require pumping corresponding to $R = 0.73$, which is unlikely to be available. However, given that $R = 0.9$ and $\epsilon = 0.2$, this gives asymptotically $(dN_p/dt) = 3\times10^{20} s^{-1}$, or 6% s, which may be acceptable. Thus, transiently, significantly more pellet fuelling could be applied, giving more peaked profiles as shown in Table VII(iii).

In conclusion, high values of profile peakedness, $n(0)/\langle n \rangle \sim 3$ appears feasible in the steady state at $\langle n \rangle = 4\times10^{19} m^{-3}$ with edge pumping to give $R \sim 0.9$, as shown in Table VII(ii).

TABLE VII

$\langle n \rangle (m^{-3})$	4×10^{19}		
$V(m^3)$	130		$N_p = 5.2\times10^{21}$
P(MW)	20(NB)+20(ICRF)		
$\phi_{NB}(s^{-1})$	1.1×10^{21}		
Options	(i)	(ii)	(iii)
$\phi_{PI}(s^{-1})$	0	1.2×10^{21} (3mm×1Hz)	3×10^{21} (4mm×1Hz)
$\phi_R(s^{-1})$	3.5×10^{22}	2.1×10^{22}	1.5×10^{22}
$\tau_p(s)$	0.15	0.25	0.35
S_E/S_c	35	9	3.7
$n(0)/\langle n \rangle$	1.7	2.7	3.25
$\frac{\phi pump}{\phi_R} = (1-R)$	0.03	0.11	0.27
R	0.97	0.89	0.73

References

[1] A. Gondhalekar, et al., Bull.Am.Phys.Soc.32(1987)1839 and JET Report, JET-IR(87)18
[2] A. Gondhalekar, et al., 11th Int.Conf.on Plasma Phys.and Contr.Nucl.Fusion Research, Kyoto,1986.
[3] T.T.C. Jones, et al., Bull.Am.Phys.Soc. 31(1986)1590, and 14th Euro.Conf.on Contr.Fusion and Plasma Phys., Madrid 1987,Europhys.Conf.Abstracts, Vol.11D, Part I, p.17.
[4] J. Ehrenberg, et al., 14th Euro.Conf.on Contr.Fusion and Plasma Phys., Madrid 1987, Europhys. Conf.Abstracts, Vol.11D, Part II,p.706.
[5] K. Behringer, et al., 11th Int.Conf.on Plasma Phys. and Contr.Nucl.Fusion Research, Kyoto 1986.
[6] A. Gondhalekar, et al., Bull.Am.Phys.Soc.30(1985)1525, and JET Report, JET-P(85)31.

Pellet Injection

The JET Multi-Pellet Injector was brought into operation in late summer and systematic investigations with pellet injection started in late 1987 under the Collaborative Agreement with the USDoE. The main aims were to increase the central plasma density in a more controlled way and to improve the purity of the plasma. The possibility of increased energy confinement following pellet injection as claimed in some experiments will be investigated when peaked density profiles ($n_e(0)/n_e > 2.5$) is achieved. A large number of experimental pulses have been undertaken with on average more than three deuterium pellets per discharge. So far, mainly 2.7 and 6mm pellets have been used with nominally 9×10^{20} and 3×10^{21} deuterons, respectively, leading to average density increases of 8×10^{18} and $2.5\times10^{19}m^{-3}$ for a $120m^3$ volume plasma. Pellet speeds were about $1300ms^{-1}$. Detailed evaluation of these shots is underway but will take some time due to the existence of particular problems with some diagnostics to cope with the rapid changes induced by pellet events. Therefore, it is a tedious and time-consuming procedure to reconstruct the time evolution of radial profiles from raw signals, needed for more detailed and subtle evaluation.

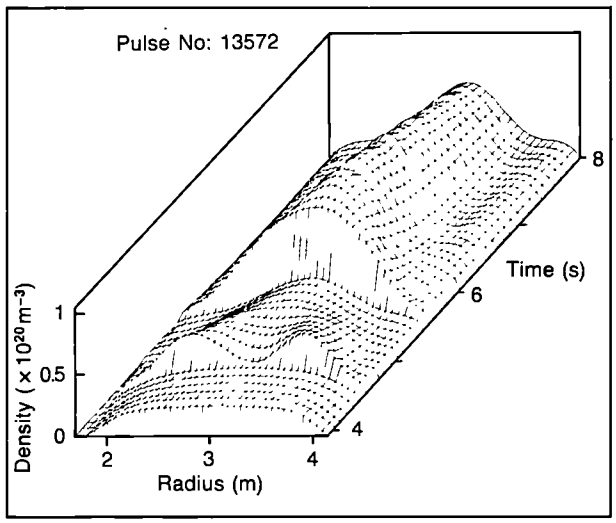

Fig.102: Time evolution of density verus radius for a 3MA plasma (Pulse No:13572) showing effects of pellet injection at t=4.5s and 8.5s;

Initial experiments have fallen into three main categories. Particular examples are the following:

- Attempts to create peaked density profiles with high central density as a target for further auxiliary heating were carried out. Fig.102 shows the time evolution of the electron density versus the major radius of a 2.5MA and 3T discharge (Pulse No.13572) without auxiliary heating. One 4mm pellet was injected into the current flat-top at 4.5s and a combination of 2.7 and 4mm pellets followed successively and created a very peaked profile with an on-axis density of more than $1.2\times10^{20}m^{-3}$ (average density of $4\times10^{19}m^{-3}$) decaying over 2s to $8\times10^{19}m^{-3}$ still with a peaking factor of 3 (measured by the LIDAR diagnostic). The on-axis electron temperature (about twice the volume average) dropped with the first pellet from 3 to 2keV and with the combination to 1keV but recovered in about 2s leading at 7.5s to a central electron pressure peak of 0.25bar; tentative estimates give Z_{eff} values of about 2 during this time (lower still for the pellet event itself) and an energy confinement time of about 0.6s;
- Heating such profiles with auxiliary heating (primarily RF) was attempted. These efforts have not yet been successful due mainly to a very fast deterioration of the peaked density profile (<100msec), leading to a flat density profiles (but among the highest in average densities). An example is shown in Fig.103 (Pulse No.13544). Fig.103(a) shows the volume average density build-up with three 4mm pellets. Figs.103(b) and (c) show how a 16MW RF pulse drives the plasma stored energy up to 6MJ (electron temperature 8keV on-axis and 2.8keV on average). The high D-D reaction rate of $1.5\times10^{15}s^{-1}$ (all thermal deuterons) suggests a relatively clean plasma. The central electron pressure is estimated at about 0.6bar. The heating attempts were further complicated by the occurrence of MHD locked modes usually associated with m=2 mode induced by injection of pellets too close together. In turn, this deteriorated the peakedness of profiles.Considerable efforts will be devoted to avoiding these locked

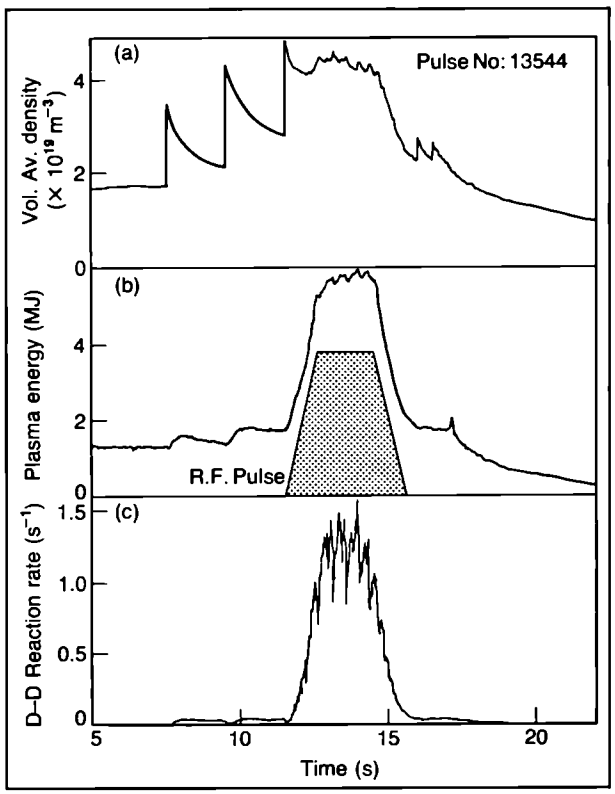

Fig.103: Effect of addition of pellets: (a) average density build-up with three 4mm pellets; (b) and (c) addition of 16MW RF powers builds up plasma stored energy;

modes in future experiments;

- Attempts were made to build up a dense peaked clean plasma from the beginning of the discharge. An example is shown in Fig.104. The volume averaged density versus time in the ramp-up of a 3MA discharge shows a staircase like build-up, with a fuelling efficiency of about 70%. The first event at 1.5s consists of a 4mm pellet (to maintain the temperature at 1.5keV and allow the penetration of the smaller pellets) combined with a 2.7mm pellet and followed by a string of 10×2.7mm pellets. This latter string was too high in repetition frequency so that the plasma disrupted at the tenth pellet in a radiative collapse having exceeded the disruptive density limit by a factor of ×2. Nevertheless, the density built up in a peaked profile at 3.5s (see insert in Fig.104). Apart from the energy balance criteria the plasma was stable and quiescent and this method looks encouraging for future work.

It is too early to draw final conclusions on the role of multi-pellet injection for reaching the final JET objectives but promising and interesting features have been observed. The high peak and average densities and the clean high-deuteron plasmas are encouraging results.

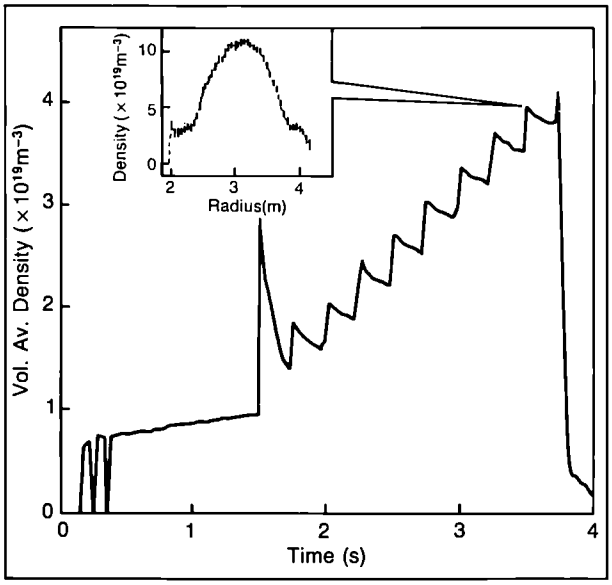

Fig.104: Volume averaged density versus time in the ramp-up of a 3MA discharge. The first pellets are at t=1.5s (one 4mm plus one 2.7mm) followed by a string of ten ×2.7m pellets. The insert shows the density profile at t=3.5s.

Theory

Theoretical work at JET concentrates on the prediction of JET performance by computer simulation, the interpretation of JET data and the application of analytic plasma theory to gain an understanding of plasma behaviour in JET.

Interpretation plays a key role in the assessment of plasma performance and hence in optimisation studies and programme planning. Prediction work continuously checks the measured behaviour against the different computational models and provides a basis for long term programme planning. A major role of analytic theory is to compare the observed behaviour against that expected from existing analysis and to modify the latter when there is divergence. However, traditional analytic theory is carried out only by a small number of staff who continuously review published plasma theory, assess its relevance to JET and, where necessary, adapt it accordingly. Experience over the past years has clearly shown the need to develop our own theoretical work, both in-house and through external contracts. Valuable assistance in this area has been provided by a number of Visiting Scientists, extended visits of Associated Staff, Fellowship and Article-14 contracts.

The central task is to construct a quantitative theoretical model of tokamak plasmas which (i) can describe measurements on JET with sufficient accuracy; (ii) can predict future plasma performance in JET and other tokamaks; and (iii) can be used to analyse and understand complex nonlinear mechanisms in the plasma. This model should ultimately reflect all important plasma physics effect in a concise and quantitative manner, (i.e. be a true representation of JET's plasma physics experience).

At present, several major plasma features can be described only by empirical prescriptions. Efforts must be made to replace these by analytically derived (i.e. theoretically understood) formulations, especially when the model is required to make reliable predictions outside the measured plasma parameter range.

The model should be validated continuously by comparison with measured data. This task demands on the one hand the identification of sensitive parameters from theory and, on the other hand, building-up the appropriate data banks from measurements. The quantities measured directly on JET often require complex mathematical and computational reduction procedures, and intricate error assessment before being suitable for comparison. The production of such banks of evaluated measured data is strongly coupled with data interpretation and with checks on the consistency of measurements, for which the above-mentioned full plasma model is a useful tool.

The activities of the Division can be subdivided under the headings:

— Data Banks and Connected Software;
— Code Development for Code Library;
— Data Interpretation;
— Tokamak Plasma Model Development;
— Predictive Computations;
— Analytic Plasma Theory.

Some of the activities and achievements in these areas are highlighted in the following paragraphs.

The JET SURVEY DATA bank, which gives the complete history of the JET plasma, has been continued and now contains more than 7,700 plasma pulses characterised by about 200,000 time traces. This bank

is updated daily. It has been complemented by the JOTTER Journal which stores detailed engineering information (control waveforms, settings, etc.), and contains data from mid-1986 onwards. Both banks are effectively accessed and updated through the NOMAD2 data base management system.

Mainly for the purpose of detailed comparison with theoretical predictions, a data bank ('NOMAD-bank') with carefully validated time traces and spatial profiles has been created for a small number of selected discharges. It mainly contains the magnetic configuration, profiles of density and temperatures, two-dimensional (2D) radiation losses and thermal fluxes.

Some of the recent code development has been aimed at making existing codes more user-friendly, or facilitating their use in special applications (e.g. X-point plasmas or MHD stability calculations). The INVERSX magnetic equilibrium code, which evaluates the magnetic field produced by a specified set of coil and plasma currents, including the magnetic circuit, has played a vital role in setting up X-point configurations, and in designing new high current operations. The reliability of the plasma current profiles, derived from external magnetic coil and loop signals, has been improved by including other diagnostic information, such as the diamagnetic signal. Earlier predictions by this code that the safety factor on-axis is significantly below unity have recently been confirmed by polarimetry measurements.

Analysis has continued of local energy transport, which derives the electron and ion energy fluxes as a function of radius and time. The new operating regimes increase the scope for scaling studies, but so far there is no theory which satisfactorily explains the anomalous transport. Analysis of density and temperature profiles shows that the pressure profile in X-point plasmas is sometimes hollow.

Numerical modelling studies have included the energy transport across a partially ergodised magnetic field, and the heat and particle fluxes in the plasma scrape-off layer. The latter model includes the JET belt limiters, and has been used to study the performance of proposed pumped limiters. A simplified model for the RF power deposition has been developed. Unlike the ray tracing or global wave codes, this is fast enough to be included in predictive or interpretive transport codes.

The transport code model which best reproduces the JET temperature profiles is based on the observation of profile consistency for the electrons. This model imposes a Gaussian shape on the electron temperature profile, with magnitude chosen to give agreement with an empirical energy confinement law. The ion thermal diffusivity is found to be comparable to that of the electrons, and to scale quite differently from neoclassical values. The model reproduces both the steady state and time evolution in JET, and has been used to predict the performance of 'Next-Step' devices.

A wide range of problems of relevance to JET have been studied analytically. These include the locking of the $m \leq 2$ tearing mode, due to its interaction with a resistive wall, and the related problem of its feedback stabilisation by a time dependent helical current at the plasma boundary. It has been shown that the stability of the monster sawteeth observed in JET may be due to the energetic trapped ions produced by the RF heating. These ions are 'rigid' with respect to an $m=1$ perturbation, and this can stabilise the mode. Problems relevant to ion cyclotron heating include the nonlinear generation of Ion Bernstein waves, mode conversion, and enhanced diffusion of energetic ions by the RF field. Particle loss from the helical high density filament sometimes seen in JET after pellet injection (the so-called 'snake'), has been analysed. The effect of energetic ions, produced by additional heating, on neoclassical currents and transport, has also been studied.

Summary of JET Scientific Progress and Perspective

During the major shutdown in the first half of 1987, new systems were added to the machine, as follows:

- assembly and installation of the water-cooled ICRF antennae;
- installation of eight water-cooled ICRF antennae;
- installation of uncooled dump plates near the X-points;
- modification of the central poloidal field coil with 10 sub-coils and other modifications of the sub-coils to increase the potential of the machine for increased current and pulse duration;
- assembly of new vessel supports to withstand vertical instabilities and radial disruptions at higher plasma currents and elongations;
- connection of the second Neutral Injector Beam Line;
- installation of the joint US-JET Multi-Pellet Injector (ORNL Launcher).

During the second half of 1987, experiments were pursued to determine the effects of these new additions, and some have already been reported in detail at various International Conferences (see Appendix III).

Plasma operation started again in mid-June and operation in excess of 4MA was quickly re-established. There was steady progress towards higher current operation with longer flat-tops and the additional heating power was also progressively increased throughout the period. Over the same period, improved diagnostics were brought into operation; in particular, the LIDAR system to measure electron temperature and density profiles; the polarimeter to allow deduction of the radial profile of the safety factor, q; and the spatial scan crystal spectrometer to measure the spatial distribution of impurities.

The main parameters achieved in JET by the end of 1987 are summarised in Table VIII. The most significant improvements were:

- the plasma current was increased to 6MA (with a 2s

TABLE VIII
Summary of Main JET Parameters (at late 1987)
(Not necessarily in the same plasma pulse)

Toroidal Field	B_T(T)	≤	3.4
Plasma Current	I_p(MA)	≤	5.0 6.0
Duration of max. I_p	t_p(s)	≤	(for 10s)(for 2s)
Plasma major radius	R_o(m)	≤	3.0
Horizontal minor radius	a(m)	≤	3.0
Vertical minor radius	b(m)	≤	2.0
Elongation	b/a	≤	1.70
Safety factor at Plasma boundary	q_{cyl}	≤	1.5
	q_ψ	≤	2.1
Vol. average electron density	$\bar{n}_e$ ($10^{19}m^{-3}$)	≤	6.0
Central electron temperature	T_e(keV)	≤	10.0
Central ion temperature	T_i(keV)	≤	12.0
Global energy conf. time	τ_E(s)	≤	1.2
Fusion performance parameter	$(n_i T_i \tau_E)$ ($10^{19}m^{-3}$.keV.s)	≤	20.0
Input ICRF power	P_{RF}(MW)	≤	18.0
Input NBI power	P_{NB}(MW)	≤	9.0
Total input power	P_t(MW)	≤	22.0
Stored plasma energy	W_p(MJ)	≤	6.5

flat-top) and at 5MA, a flat-top time of 10s was achieved. With the new system, it is expected that, after further planned installations, 6MA plasma currents for 6-7s and 7MA for 3-4s can be achieved:

- the X-point single-null magnetic configuration has already been obtained with a plasma current of 3.5MA for 8s, and the H-mode of confinement has been achieved with $\tau_E = 0.75$s for additional NB powers of 6MW. A 4MA X-point configuration is expected shortly;
- ICRF heating powers up to 18MW have been supplied to the plasma from the eight RF antennae. In this situation, electron temperatures (T_e) of 10keV were reached;
- the first NB box was brought back into operation after some modifications and 7MW NB power has been injected into the plasma. The second NB box is now connected to the machine and is in its final commissioning. It should be ready for operation in February 1988 (providing total NB power of ~20MW deuterons);
- sawteeth oscillations of the central electron and ion temperatures have been observed with both RF and combined (RF & NB) heating. Methods are under investigation to stabilize these oscillations at their peak temperature values and to improve the confinement time τ_E. With on-axis RF heating under particular circumstances, stabilization of the sawteeth has been observed for periods up to 2.8s (monster sawteeth). In this case, with 16MW RF power and 6MW NB (total input ~22MW), electron temperatures of 10keV and ion temperatures of 8.5keV were obtained with an energy of 6.5MJ in the plasma.

Additional Heating Studies

ICRF Heating

With the upgraded ion cyclotron resonance frequency (ICRF) heating system of eight antennae (source power 8×3MW) up to 16MW of power (for 2s) has been coupled into the plasma using both the monopole and dipole modes of antenna operation. The facility which enable switching from monopole to dipole mode of operation on successive pulses identified the dipole mode as releasing fewer metal impurities (from the screen) into the plasma during operation.

ICRF heating studies have been carried out using both hydrogen and ^{3}He minority ions, usually with the minority ion cyclotron resonance on-axis for optimum efficiency. The energy given to the minority ions is then redistributed through collisions to the plasma ions and electrons, thus raising the ion and electron temperatures in the plasma.

In such experiments during a relatively quiescent sawtooth-free ('monster' sawtooth) regime, bulk plasma ion heating has been achieved (using He^3 minority ions) yielding ion temperatures on axis of 8keV in ^{4}He plasmas and 7keV in deuterium plasma.

However, the plasma electron temperatures were up to 10keV. The energy confinement degrades with additional heating. In a plasma with plasma current of 3.5MW, an RF power input of 16MW has produced a plasma stored energy of 6MJ and a D-D fusion rate of $1.4\times10^{15}s-^{1}$. In these discharges, a significant fraction of the stored energy comes from the minority ions which are expected to produced high fusion yield in (D)T heating schemes.

By modulating the ICRF, power experiments have been carried out to study central power deposition profiles. These confirmed that the wave power is mostly deposited in a narrow central region of the plasma extending radially about 0.6m where the applied wave frequency closely matched the magnetic field region of the resonant ion species.

Measurements of the modulated global energy content showed that at least 85% of the coupled RF power was utilized for plasma heating. Almost all the modulated component resided in perpendicular energy, in agreement with calculations.

NB Heating

Following the successful first year of neutral injection experiments in 1986, 1987 proved to be a more difficult and somewhat disappointing year in terms of injection into the tokamak. Following the major shutdown, during which a considerable amount of work involving planned improvements and modifications to both Octant No.8 and No.4 injection systems was successfully completed, three separate major hardware failures occurred during the commissioning and subsequent re-commissioning of the Octant No.8 system. These faults were not associated with actual beam operation and occurred at times during which the applied power to the beam sources was zero.

Monster Sawtooth Oscillations

Sawtooth oscillations occur in almost all JET discharges. With central deposition of additional power, especially ICRF, sawteeth may develop large amplitudes (up to doubling the central electron temperature) and long periods (up to 0.6s). It has been observed that ultra-long sawteeth (called 'monsters') can occur, with durations exceeding 2s. During this time period, the central electron temperature can reach values up to 10keV; usually, the ion temperature also rises and thermonuclear reactivity is improved. A strong reduction of MHD activity with low m, n numbers is observed and there is no apparent impurity accumulation.

Detailed JET studies of the sawtooth collapse have confirmed previously observations on the timescale ($\sim100\mu s$) and topology of the collapse, which occur as an m=n=1 helical distortion of the plasma core followed by a poloidal redistribution of the flux surfaces. In addition, there is a rapid flow of energy across the sawtooth inversion radius, leading to a flattening of the temperature profile (on a timescale $\sim100\mu s$). This sequence of events occurs for all sawtooth collapses in JET irrespective of the presence or absence of precursor activity. Considerable effort has been devoted to developing a theoretical understanding of the sawtooth instability.

During high power additional heating experiments, particularly with ICRH, sawteeth may be spontaneously suppressed. This phenomenon (called 'monster' sawtooth) has been observed at plasma currents up to 5MA in discharges with ICRH heating and with combined ICRH and NB heating. The long quiescent periods (up to 2.8s) has enabled the assessment of plasma transport properties in plasmas free from sawteeth, and has also permitted an analysis of the benefits of sawtooth stabilization in the near-ignition regime. While a small improvement in confinement is obtained (τ_E may increase by up to 20%), the major advantage is an increase in the fusion product due to the peaked temperature profiles which occur. This regime has been observed under a wide range of plasma conditions in JET: $2.1<B_t<3.4T$, $1.5<I_p<5.0MA$, $3.4<q_\psi<8.4$, and $n_e<4\times10^{19}m^{-3}$, in both H and ^{3}He ICRF minority. The regime is also attained during combined (RF and NB) heating experiments, and there is some evidence that it may be accessed by NB heating alone.

Monster sawteeth durations up to 2.8s have been achieved, and H minority heating has produced central electron temperatures up to about 10keV. Bulk plasma ion heating has been achieved with ^{3}He minority ions yielding ion temperatures on axis of 8keV in ^{4}He plasmas and 7keV in deuterium plasmas. The energy confinement degrades with additional heating but the asympotic (or incremental) confinement time increases with plasma current provided the safety factor q is kept constant. With 16MW of RF power a plasma stored energy of 6MJ and a D-D fusion rate of $1.4\times10^{15}s^{-1}$ has been produced. In these discharges a significant fraction of the stored energy comes from the minority ions which are expected to produce high fusion yield in (D)T heating schemes.

Disruption Studies and Density Limits

A tokamak disruption is a dramatic event in which plasma confinement is suddenly destroyed and this is followed by a complete loss of current in a short period of time. These instabilities pose a major threat in tokamak research in that the limit the range of density and current in which stable operation can be achieved, and their occurrence leads to large mechanical stresses and intense heat loads on the vessel.

A diagram of stable operating parameters can be constructed of normalized current ($1/q\propto I_p/B_t$, where q is the safety factor, I_p is plasma current and B_t the toroidal field) versus the normalized density $\bar{n}R/B_t$ (where $\bar{n}$ is average density and R the major radius) as shown in Fig.105. In ohmic plasmas, the density limit is $\bar{n}_c(OH)(m^{-3})=1.2\times10^{20}B_T(T)/qR(m)$. This limit depends on plasma purity. In RF heated discharges, it is only slightly increased, possibly because the effect of

the extra power is cancelled by an increase in impurities. In neutral beam heated plasmas, the limit is substantially increased, as shown in Fig.105, to $\bar{n}_e(\mathrm{NB})(\mathrm{m}^{-3}) = 2.0\times10^{20}\, B_T(\mathrm{T})/qR(\mathrm{m})$. Switching off neutral beams at high density causes to disrupt, which indicates that the power input plays an important role in the disruption mechanism. Experiments with pellets have also exceeded the OH density limit.

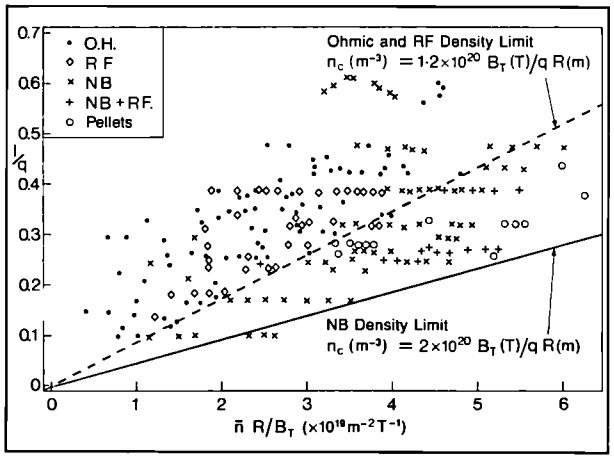

Fig.105: Normalized current $[1/q = 2\pi RI_P/AB_t\ ]$ *versus normalized density* $[\,= \bar{n}R/B_t]$.

Density limit disruptions are always preceded by an increase in the impurity radiation at the plasma edge. This causes a contraction of the electron temperature profile, which is followed by the growth of MHD activity and the plasma becomes disruptively unstable. Observations and theoretical considerations both show that the central plasma density can be increased by deep fuelling, possibly by high-speed pellet or NB injection.

Pellet Injection

JET and the US Department of Energy have jointly installed and are jointly operating a multi-pellet injector under the umbrella of the Bilateral Agreement on Fusion Research. The pellet launcher (built by Oak Ridge National Laboratory (ORNL), U.S.A., can deliver multiple pellets of solid hydrogen fuel from three different barrels in parallel in the sizes 2.7, 4 and 6mm diameter, (length approximately equal to diameter) at a maximum frequency of several per second with nominal speeds of up to $1500\mathrm{ms}^{-1}$. Pellet injection into plasmas was started in the second half of 1987, but is still in its early phase of investigation and only a few features have so far been studied.

Using the 2.7 and 4mm deuterium pellets, peaked density profiles from multi-pellet injection with central densities well over $10^{20}\mathrm{m}^{-3}$ have been achieved in ohmic discharges with decay times in the several seconds range. Some of these plasmas showed no sawtoothing for several seconds after injection. Such plasmas are planned as high density, low Z_{eff} targets for auxiliary heating. However, attempts to heat these plasmas with central deposition of ICRH have been troubled by the frequent occurrence of locked modes and the consequential rapid pump-out of density. This leads to broad density profiles with maximum density still in the highest range so far. With 15MW of RF, a D-D reaction rate of $1.5\times10^{14}\mathrm{s}^{-1}$ with an ion temperature of around 6keV has been produced. Density build-up with a string of 10 pellets, as early as 1.5s into the plasma current ramp up, have produced an early relatively clean high-density plasma that seemed remarkably tolerant of pellet disturbances.

Energy Confinement

The total energy confinement time of JET in all plasma configurations is defined as:

$$\tau_E = W_K/(P_t\text{-}dW/dt)$$

where W_K is the kinetic energy and P_t is the total input power to the plasma without subtracting radiation losses. The values of τ_E reported are quasi-stationary.

In the material limiter configuration the energy confinement time on JET falls with increasing heating power as seen in a number of other experiments. This degradation in confinement time is independent of the type of additional heating, whether NB, RF or combined. The rate of increase in kinetic energy with power input $\Delta W_K/\Delta P_t$, appears to reach a limit of between 0.1 and 0.3MJ/MW at high powers. This indicates that there is a lower limit to the global energy confinement time, τ_E, in JET of between 0.1 and 0.3s. Although a weak dependence on plasma density has been found for the energy confinement time, there is a favourable scaling with plasma current. The way in which the energy confinement time falls with increasing heating power is shown in Fig.106.

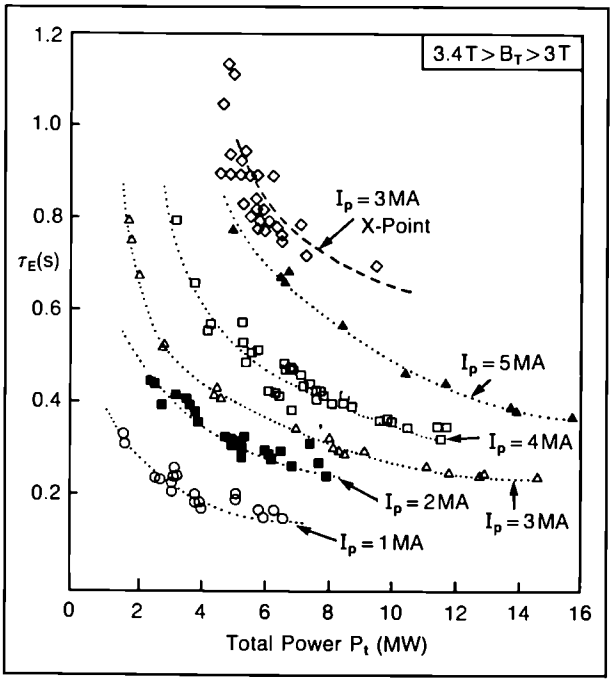

Fig.106: Energy confinement time (τ_E) *as a function of additional heating power for various plasma currents.*

The global energy confinement time results can be fitted by a simple power law relationship. However, measured radial propagation of heat pulses following sawtooth crashes, strongly supports a linear offset relationship between plasma kinetic energy and power input of the form:

$$W_K(P_t) = (0) + \tau_{inc} P_t$$

The best fit in the case of JET limiter or inner wall discharges gives: $W(0) = 0.225 n^{0.6} I^{0.5} B^{0.4}$ and the incremental confinement time, $\tau_{inc} = 0.050I$. The units are W(MJ), n($\times 10^{-19} m^{-3}$), I(MA), B(T), τ_{inc}(s).

Magnetic Separatrix Operations

Stable discharges with magnetic separatrix (or X-point) configurations have been maintained in JET for several seconds, at plasma currents up to 3.5MA (in the single-null configuration). The main objectives have been to compare the global confinement characteristics of separatrix and limiter discharges and to study the conditions for the creation of a high density, highly radiative, cool plasma region near the X-point capable of screening and isolating the bulk plasma. In these configurations, the plasma is detached from both the limiter and the inner wall and recycling occurs in an open divertor region near the X-point.

Due to technical problems, only limited neutral beam (NB) heating experiments were performed before late 1987 and then only up to 6MW power was available during X-point discharges. However, as soon as the neutral beam power exceeded the threshold values for H-mode transition in X-point discharges, the H-mode results of 1986 were reproduced. A wider scan of toroidal magnetic field confirmed a very strong dependence of the threshold power, P_{th}, and indicated a scaling of $P_{th} \sim 0.6 B_T^{2.5}$ (and only a weak dependence on plasma current). Confinement times up to $\tau_E = 0.75$s were obtained with NB input power of 6MW.

A preliminary analysis of the 1987 H-mode energy confinement times, τ_E, show only a weak dependence on toroidal magnetic field (in the range 1.8 to 2.4T). 1987 confinement times are slightly smaller than 1986 plasmas, which is partly due to the new belt limiters reducing the cross-section of single-null X-point plasmas by about 10%. It is not clear whether confinement times degrade with increasing heating power without more detailed analysis of existing data and with an extension of H-mode results to higher power levels (up to 15-20MW with NB and 20MW of ICRF heating which should be available early in 1988).

Pronounced changes between the L- and H-mode phases have been seen in the density profiles Following the H-transition, the plasma density profile is flat or even slightly hollow. However, the electron temperature profile shows a general increase in temperature at the H-mode onset but no dramatic change in shape. The temperature profile stays roughly similar throughout the H-phase whereas the plasma density increases by up to a factor of $\times 3$. The radial distance between the separatrix and the belt limiters affected not only the duration of the first H-mode period but also of the subsequent L-phases alternating with H-mode phases. The total duration of L-and H-mode periods has been limited by the length of the neutral beam pulses. When this is increased, the length of the L/H-mode train should be limited finally by accumulation of impurities in the plasma centre.

Attempts to produce the H-mode with RF Heating alone were not successful during limited experiments. Further attempts will be carried out in 1988.

Plasma Boundary Phenomena

Analysis of measurements in the plasma boundary have shown that the edge density and temperature scale consistently with the plasma average density and the total input power. The edge density increases as the square of the line average density, while the edge temperature decreases with the square of increasing density but increases with the input power. During ICRH the boundary layer broadens and the temperature in the boundary generally increases, while during NBI the increase in density more than compensates for the increased input power and the edge temperature generally decreases.

When the belt limiters were installed, the edge temperature and density were much less consistent for given discharge conditions than with the previous discrete limiter configuration. However, probes at various toroidal locations showed good toroidal symmetry. Up/down symmetry was readily obtained using the feedback control of the vertical position.

Recycling of the plasma at the walls has been studied under a variety of conditions. It has been shown that pumping occurs at all surfaces including the belt limiter, inner bumper limiter and X-point protection tiles. There was no significant change in the pumping rate when the wall temperature was changed from 150°C to 300°C. Measurements of outgassing after a normal discharge indicate that a large fraction (70-90%) of the gas introduced remains trapped in the vessel indefinitely. The only explanation for this at present is that there is co-deposition of carbon and hydrogen isotopes on some surfaces, leading to permanent trapping. This has not yet been verified quantitatively.

Impurities and Effective Charge of the Plasma

The main impurities in JET plasmas are carbon, oxygen and nickel, with some chlorine observed occasionally. The nickel concentration $c_{Ni} (= n_{Ni}/n_e)$depends significantly on the previous history of ICRF heating and is usually $< 10^{-5}$ in ohmic heating campaigns. During ICRF heating, nickel is released from the antenna screens and subsequently deposited on limiters and protection tiles. After high power ICRH pulses, $c_{Ni} \approx 10^{-3}$ was measured during the ohmic plasma phases and several 10^{-3} during ICRH. Oxygen concentrations,

$c_o(=n_o/n_e)$ have been 0.5-1 % in deuterium plasmas. In helium plasmas, c_o was about a factor ×10 lower due to smaller oxygen influxes from walls and limiters. This lower oxygen production by helium is a clear indication of a chemical production mechanism. Carbon appears to be produced by physical sputtering and was several % in both D and He discharges with a tendency to increase during additional heating.

Impurity transport in JET has been studied from accidental metal injections and from the radial impurity ion profiles. Confinement times and profiles could usually be described by an anomalous diffusion coefficient $D \approx 1 m^2/s$ and by an inward drift ($\propto r$) with velocity $v_D(a) = 2 ms^{-1}$. Under certain plasma conditions impurity accumulation was expected, following experience of other experiments, sawtooth-free plasmas, H-mode plasmas and discharges with peaked electron density profiles after pellet injection. During long, sawtooth-free periods ('monster sawteeth'), subsequent changes of the total ion profiles of nickel have shown no sign of nickel accumulation.

The global impurity content is monitored routinely throughout each pulse by measuring the radial profile effective ion charge, Z_{eff}, of the plasma. During the ohmic phase, $Z_{eff}(r)$ is peaked on axis with $Z_{eff}(0)/Z_{eff}(a) < 2$ and $Z_{eff}(0)/Z_{eff} < 1.3$. Whilst the precise value of Z_{eff} is sensitive to previous machine operation, in general, Z_{eff} decreases with increasing density and increases with current. During the application of high ICRF powers (>5MW), there is a gradual rise in Z_{eff}. The $Z_{eff}(r)$ profile becomes flatter due to increased impurity production at the plasma edge, resulting from the power loading of the RF antennae. The injection of D neutral beams or pellets reduces Z_{eff}. In NB heating cases, the relative shape of $Z_{eff}(r)$ is essentially unchanged as, even though the beam can increase the D source on axis by over two orders of magnitude, recycling at the plasma edge dominates the global particle balance. However, in pellet injection penetration to the axis is achieved, and the $Z_{eff}(r)$ profile becomes flatter with prompt reductions of $Z_{eff}(0)$ by factors of $\lesssim 3$, due to the abrupt dilution of the impurities in the core. Values of Z_{eff} of ~2 are common for discharges in a well-conditioned vacuum vessel. The dominant impurity is carbon, with oxygen being the second most important, usually at a concentration of 2 to 3 times less. This implies that at the plasma centre the ratio n_D/n_e is $\lesssim 0.5$. However, following pellet injection, for which values of $Z_{eff}(0)$ of $\lesssim 1.3$ have been achieved, the ratio n_D/n_e is $\gtrsim 0.9$.

Progress Towards Breakeven

A record value of the fusion product $< n_i(0)\tau_E T_i(0) >$ of $2 \times 10^{20} m^{-3}$.s.keV was achieved in 1986 with 10MW of neutral beam heating during X-point operation in the H-mode. In addition, for limiter discharges, the values of the fusion products obtained for ohmic heating, RF, NB and combinations of these methods were similar. This was a result of the degradation in confinement time offsetting gains made in the values of the other parameters.

During 1987, with limited magnetic limiter operation in the H-mode, this same maximum fusion parameter of $2 \times 10^{20} m^{-3}$.s.keV was repeated. In this case, this was

TABLE IX
Maximum values of $\langle n_i(0)\tau_E T_i(0) \rangle$

Experimental Programme	Peak Density	Energy Confinement	Ion Temperature	Fusion Product	Q_{DT} Equivalent	Plasma Current
	$n_i(0)$ ($\times 10^{19} m^{-3}$)	τ_E (s)	$T_i(0)$ (keV)	$\langle n_i(0)\tau_E T_i(0) \rangle$ ($\times 10^{19} m^{-3}$.s.keV)	Q_{DT}	I_p (MA)
Ohmic (4.6MW)	4.0	1.0	3.1	12	0.010	5
ICRF (16MW)	3.8	0.4	8.0	12	0.025	3
Pellet + ICRF	4.0	0.27	7.5	8	0.20*	3
NBI (6MW)						
High n:	4.4	0.4	4.0	7	0.10*	3
Low n:	1.5	0.4	10.0	6	0.20*	3
Combined NBI + RF (15MW)	4.0	0.35	7.5	10	0.20*	3
X-point						
(NBI-10MW)	5.0	0.65	6.0	20.0	0.15*	3
(NB-6MW)	4.0	0.90	5.5	20.0	0.15*	

* Beam-Plasma reactions are dominant

achieved with only ~6MW of neutral beam input into a 3MA X-point plasma, following optimization of the various plasma parameters. However, a significant improvement was made in the fusion product with RF heating alone. A value of $1.2\times10^{20}m^{-3}$.s.keV ($n_i(0)=3.8\times10^{19}$, $T_i(0)=8$keV, and $\tau_E=0.4$s) was reached using H^3 minority heating ($P_{RF}=16$MW) in a 3.5MA deuterium plasma. The maximum values of the fusion product and the corresponding values of plasma temperature, density and energy confinement time are given in Table IX for different operating scenarios.

In the RF heated plasm with the highest fusion product, nearly 16MW of power produced a plasma stored energy in excess of 6MJ and a D–D fusion rate of $1.4\times10^{15}s^{-1}$. In this discharge, a significant fraction of the stored energy resulted from the minority ions which are expected to produc high fusion yield in (D)T heating schemes. However, the maximum neutron yield obtained so far is that of $3\times10^{15}s^{-1}$ produced previously with neutral beam heating. This resulted mainly from D-D reactions occurring between the deuterium particles in the heating beams and the plasma. The best ratio of fusion power to input power obtained was $Q_{DD}=3.5\text{x}10^{-4}$ which is equivalent to $Q_{DT}\sim0.2$, if tritium were introduced into the machine under these conditions. This would correspond to a fusion power production of above 1MW. This enhanced reaction rate is due to interactions between the plasma and neutral heating beams.

Developments and Future Plans

In 1978, the original aims of JET were set out in the JET Design Proposal, EUR-JET-R5, which described the objectives as follows:

'The essential objective of JET is to obtain and study a plasma in conditions and dimensions approaching those needed in a thermo-nuclear reactor. These studies will be aimed at defining the parameters, the size and the working conditions of a Tokamak reactor. The realisation of this objective involves four main areas of work:

(1) the scaling of plasma behaviour as parameters approach the reactor range;
(2) the plasma-wall interaction in these conditions;
(3) the study of plasma heating; and
(4) the study of alpha-particle production, confinement and consequent plasma heating.

The problems of plasma-wall interaction and of heating the plasma must in any case be solved in order to approach the conditions of interest.

An important part of the experimental programme will be to use JET to extend to a reactor-like plasma, results obtained and innovations made in smaller apparatus as a part of the general Tokamak programme. These would include: various additional heating methods, first wall materials, the control of the plasma profiles, and plasma formation.'

Ten years later, the objectives of JET are unchanged and the same four areas of work remain the focus of the Project's activities. The study of energy confinement and its degradation with additional heating is covered by areas (1) and (3). The study of different low-Z (i.e. low atomic number) materials, edge effects, exhaust and fuelling is covered by area (2). The study of α-particles, area (4) must clearly wait until areas (2) and (3) have been successfully addressed, as α-particles will need to be produced in sufficient quantities for their effect on the plasma to be observed.

The JET aims clearly state that JET is an experimental device and that, to achieve its objectives, the latest developments in Tokamak physics must be allowed to influence its programme. The proposed programme includes some new additions and enhancements to overcome confinement degradation and to push the parameters of the JET plasma even closer to those needed in a thermonuclear reactor. This is in complete agreement with the original objectives laid down for JET.

While present achievements show that the first three objectives of JET are being actively addressed and substantial progress is being made, the strategy for JET can be summarised as a strategy 'to optimise the fusion product $\langle n_i(0)\tau_E\ T_i(0)\rangle$'. For the energy confinement time, τ_E, this involves maintaining, with full additional heating, the values that have already been reached with ohmic heating alone. This means overcoming confinement degradation. For the density and ion temperature, it means increasing their central values $n_i(0)$ and $T_i(0)$ to such an extent that D-T operation would produce α-particles in sufficient quantity to be able to analyse their effects on the plasma.

The further additions to JET aim to build up a high density and high temperature plasma in the centre of the discharge, where α-particles could be observed, while maintaining an acceptably high global energy confinement time. The mechanisms involved are:

(a) to decouple the temperature profile from the current density profile through the use of lower hybrid current drive and neutral beam injection to ensure that, at higher central temperatures, the current density in the centre does not reach the critical value that causes sawteeth oscillations;

(b) to reduce the edge density by edge pumping, since it is observed that the temperature at the $q=1$ surface is higher when the edge density is lower. Other advantages of lowering the density in the outer region are the inhibition of disruptions and a higher efficiency from the lower hybrid current drive system;

(c) to increase the density of deuterium and tritium ions in the central region to $1-2\times10^{20}\,m^{-3}$ by high velocity pellet injection;

(d) to achieve high central temperatures (12–15 keV) by the combination of 'on-axis' ion cyclotron resonance frequency (ICRF) heating, neutral beam injection at 140 keV and current profile control, which is aimed at maintaining the conditions of giant sawteeth for longer periods;

(e) to improve the confinement by operating at higher discharge currents (~7 MA) with low-Z material limiters or with the discharge decoupled from the limiter in the magnetic separatrix (X-point) configuration at currents

exceeding 4MA.

The following sections describe various developments which are underway on JET to implement these enhancements.

Future High Current Operation

Assessment of the machine capability to operate above design performance has been underway during 1987 (the so called 7MA Study). The objectives of this study are to verify the stresses on the tokamak and its major subsystems when operating with plasma current at 7MA, 10s flat-top in material limiter configuration and at 4MA, 10s flat-top in the magnetic limiter (separatrix or X-point) configuration, in both normal and fault conditions (of which, the vertical instabilities and radial disruptions are the most severe).

Major activities in this area have been the following:

a) for the toroidal field coils, the main problem is the out of plane forces due to increased poloidal fields, especially in the collar tooth region. This has been studied using new detailed finite-element models and finally by mechanical tests on a prototype toroidal coil. This coil has completed 20,000 cycles at full design transverse load and will be tested at progressively higher forces until its ultimate strength is established;

b) for the poloidal field coils, the main problem is the central magnetizing coil (P1), which must run at increased current. Here again, progressively more complex finite-element models are being developed. A problem of thermal stress has been identified and a modified cooling system will be installed in 1988;

c) several tests have been performed during 1987 to investigate the forces on the vessel arising from vertical instabilities and to estimate the expected forces at high plasma current. In these tests, stabilization of the vertical position was disabled during the plasma current flat-top. A vertical force of about 700 tonnes for a vertical instability of a 7MA plasma with elongation 1.6 is estimated from tests performed at 3.4MA. These investigations are supported by simulations and analyses which are being carried out in cooperation with the University of Naples, Italy and the NET Team, Garching, F.R.G., (using their PROTEUS equilibrium code).

During the 1987 shutdown, the poloidal field system was modified to increase the available flux for operation of the plasma current up to 7MA. Plasma currents of 6MA have already been achieved and 7MA should be obtained soon. Modifications were made to allow differential current in the driving transformer coils. This permits shaping of the plasma by the combined multipolar fields of the shaping circuit and stray fields from the primary coils. Single-null X-point configurations at plasma currents up to 3.5MA have been obtained and 4MA (Fig.107) should be possible, shortly.

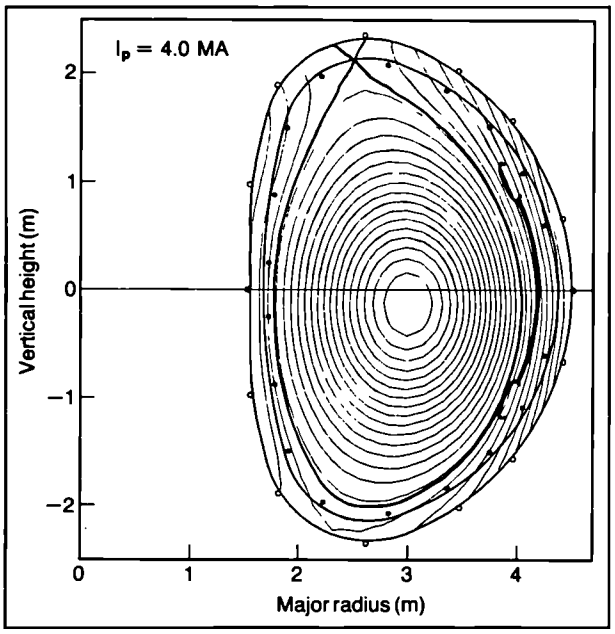

Fig.107: Calculated X-Point Single-Null Configuration at $I_p = 4MA$.

Recently, it has been proposed that it should be possible to further increase the plasma current in the X-Point Configuration by using a particular coil configuration in which the shaping coils produce a non-zero radial field which can be balanced by differential current in the main vertical field coils. The result of an equilibrium calculation which shows plasma equilibrium with a plasma current of 7MA in Fig.108.

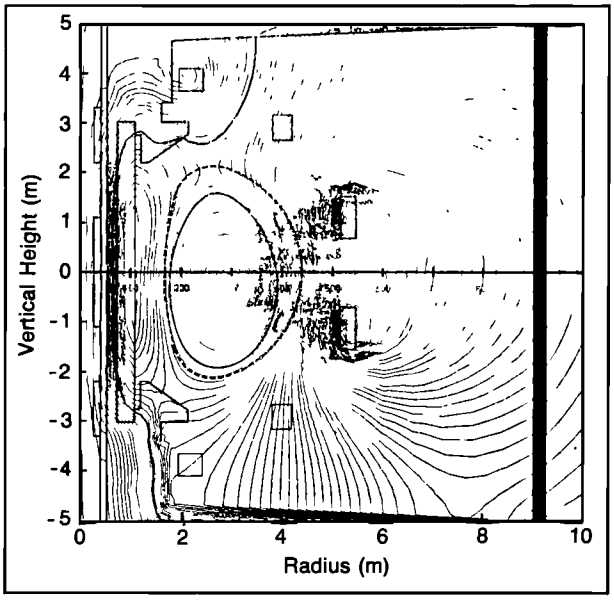

Fig.108: Predicted magnetic flux plot for single-null configuration at $I_p = 7MA$.

Engineering of this configuration still requires analysis of shear stresses caused on the toroidal field coils and forces on the vacuum vessel in the event of accidental loss of control of the vertical position of the plasma. These analyses are presently under investigation.

Stabilization of Disruptions

In JET, as in all other tokamaks, the range of stable operation in current and density is limited by disruptions. While these limits will permit the stable operation of JET at currents up to 7 MA, considerable care is needed to programme the current and density decay at the end of the discharge, particularly after the additional heating is turned off, in order to avoid disruptions occurring at high currents. At these high currents, disruptions could present a serious risk to the machine. The problems of disruptions have been known for many years, and considerable effort has been devoted to understanding and avoiding them.

In JET, it is proposed to stabilize disruptions by magnetic feedback. This will utilise the fact that the disruption is usually preceded by a slowly growing $m=2$ instability resulting in the development of a magnetic island at the $q=2$ rational magnetic surface. This will be detected by diagnostic pick-up coils, and will be used as input to a feedback circuit. This circuit will drive currents in large saddle coils mounted inside the vacuum vessel to produce magnetic field perturbation, that will cancel the perturbations due to the growing instability.

The physics of disruptions is complex and it is not a straightforward matter to determine the consequences of stabilizing one element, namely the $m=2$ mode. Furthermore, the feedback procedure is itself rather complicated and the physics involved needs careful consideration. Inevitably, certain questions remain unanswered, and probably some of these can be answered only by experiment. Meanwhile, the detailed system design is proceeding on a time-scale consistent with the installation of the in-vessel components during the 1988 shutdown.

Many factors constrain the size of the saddle coils and their locations inside the vacuum vessel. In particular,

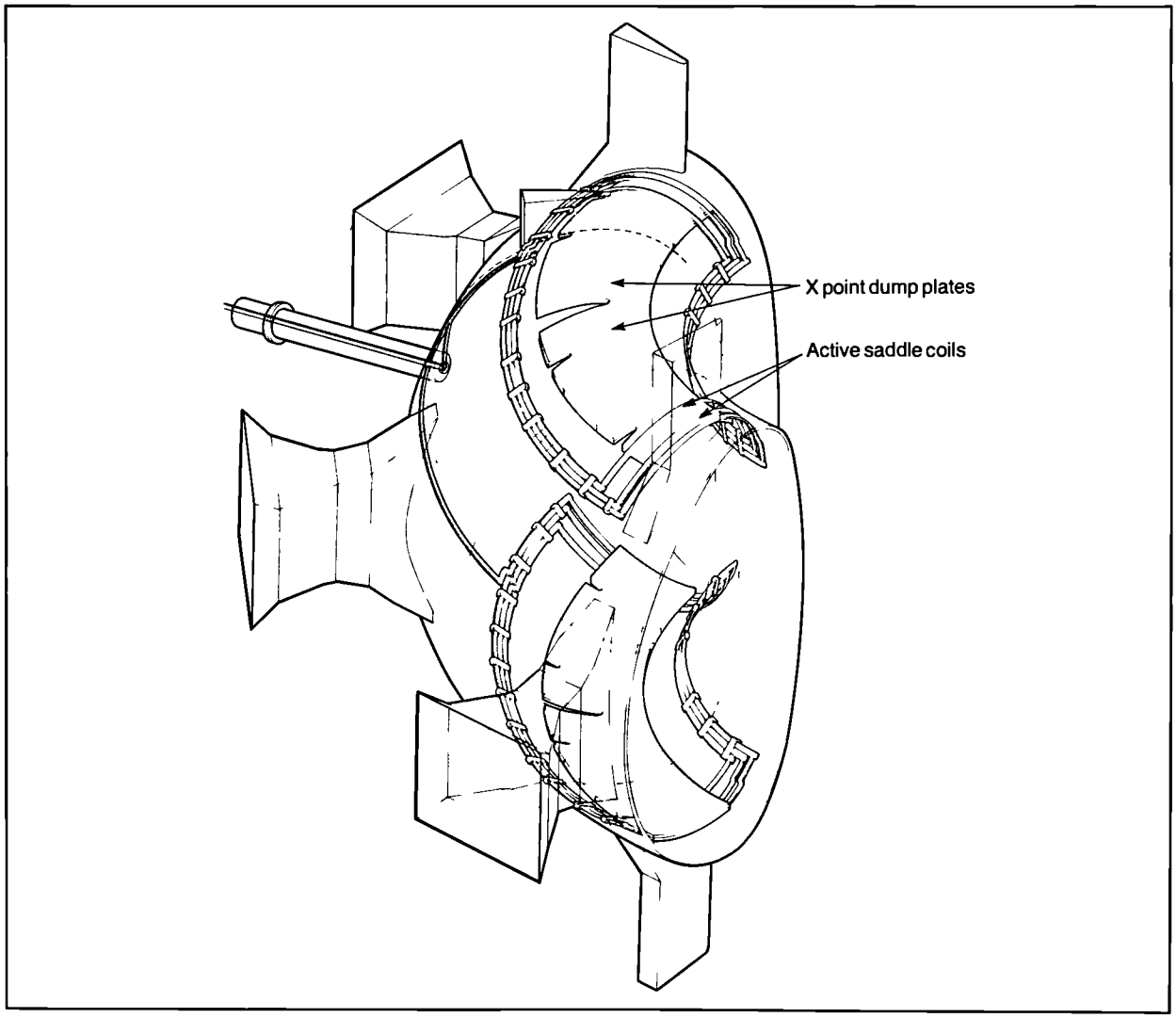

Fig.109 Location and extent of active Saddle Coils within the torus

the coils have been located so that they do not restrict the planned operation of JET with diverted or limiter discharges. The coils have also been located to minimize their impact on JET diagnostics. Within these constraints the coil size and locations have been optimized to couple applied power most efficiently into the $m = 2, n = 1$ mode. This is important because power coupled into other modes might drive them unstable. Several different coil systems were considered and assessed using a computer code which calculates the various Fourier components of the vacuum field.

The feedback coils will be installed inside the JET vacuum vessel as shown schematically in Fig.109. These will be arranged as saddle coils, four above the horizontal centre line and four below. Each coil will span two octants and will be approximately 2m long in the toroidal direction. Each coil will consist of three turns, each with a cross-section of 20×70mm, fabricated of Inconel 600. The coils will be insulated from the vacuum vessel walls by alumina balls and supported from the rigid sectors of the vacuum vessel by a series of clamping devices. The coils will be prefabricated in several parts which will be assembled inside the vacuum vessel during the 1988 shutdown. The coils will be connected by busbars to insulating feedthroughs in existing ports of the vacuum vessel. The detailed mechanical design of the coils has been completed and tenders are presently being sought for the contract to construct them.

The design of the feedback amplifier has received less priority due to the high work load on Magnet and Power Supply Division in connection with other machine improvements which are being implemented at this time. However, the main requirements have been established and various schemes to meet them are being considered. The power supply is being designed as a modular system, so that low power experiments can start with the procurement of part of the power supply.

Current Drive and Profile Control

Some control of the plasma current can be obtained in JET using the additional heating methods already used, such as:

(a) neutral beam current drive, and/or ion cyclotron resonance frequency current drive;

(b) by making proper use of certain physical properties of plasma discharges such as the bootstrap current.

However, the main tool to control the current profile in JET will be the Lower Hybrid Current Drive (LHCD) system (as described in the 1986 JET Progress Report). The main motiviation of the LHCD system remains the stabilisation of sawtooth oscillations in order:

(a) to benefit from a higher reactivity of the plasma core by sustaining peaked profiles in plasma density and temperature;

(b) to avoid the deleterious effects associated with the crash of giant sawteeth (e.g. persistent locked MHD modes and impurity influx due to large excursions of the limiter surface).

In addition, an objective is to determine the LHCD current necessary for non-inductive operation of large Tokamaks.

Recent ICRF heating results on JET at high power demonstrated both the benefits of the stable period and the deleterious effects following the crash of very large sawteeth. The incremental energy confinement time is remarkably high ($\tau_{inc} \sim 280$ to 400ms) for the conditions in which the improved regime is observed. However, the parameter space of the monster sawtooth regime is limited to a narrow range of I_p / B_t. Although further experimentation will probably improve the parameter space, it appears now increasingly necessary to use LHCD to control the current profile and to extend the domain of the monster sawtooth regime to the three basic scenarios for which JET expects to reach the highest fusion parameter, ($n_i \tau_E T_i$) (low density beam-target, H-mode, 7MA limiter).

The data base of the physics and efficiency of LHCD is rapidly expanding. Regimes of improved confinement have clearly been associated with sawtooth stabilisation and current drive, which broadens the current profile. In this way, ASDEX, JT60 and PLT have obtained high central electron temperatures and improved confinement.

The efficiency of current drive has improved as expected due to a better definition of the radiated spectrum (PLT) and to a favourable scaling with the electron temperature (JT60, T7). A plasma current of 2MA has been sustained for 1.5s in JT60 with 3MW of LHCD and without inductive contribution (at $n_e \sim 0.5 \times 10^{19} m^{-3}$). The JET system will benefit from a further improved spectrum and from even higher electron temperature. It is now likely that operation close to the Fisch and Karney limit will be approached (2MA driven current for 10MW power at a density of $5 \times 10^{19} m^{-3}$) assuming a directivity of 70%. This will give some safety margin in keeping $q(0) > 1$ in order to achieve (in combination with NBI and ICRF) sawtooth stabilisation in the three high fusion parameter scenarios.

JET has placed new Task Agreements and Article 14 contracts with CEA (Cadarache, France), UKAEA (Culham, U.K.) and Instituto Superior Technico (Lisbon, Portugal). They cover the physics of LHCD and extensive testing of components using the existing CEA source at 3.7GHz. Another contract is under discussion with IPP Garching, F.R.G., on the anti-multipactor coating.

The theoretical effort on the LHCD physics at JET has mainly been devoted to the following points:

(a) estimate of the amount of current needed to control the current profile in JET;

(b) establishment of codes to predict the LH current localisation as a function of the plasma and of the wave

parameters;

(c) optimisation of the wave spectrum by taking into account the specific geometry of the launcher environment.

The amount of RF current drive needed to sustain a highly peaked discharge in JET, with a high central electron temperature, has been estimated to be 80% of the total current by assuming a neoclassical resistivity scaling law. This amount decreases to 50% by taking into account the bootstrap current and to 35% by assuming Spitzer resistivity and bootstrap current. Transient effects may also reduce that value during a 10s flat top 7MA current discharge in JET.

Detailed calculations of the wave propagation and damping using a version of Bonoli's code adapted to the JET geometry have clearly shown off-axis current drive.

The LHCD programme at JET aims at eventually installing a prototype launcher (LOP) during the 1988 shutdown, with a nominal power of 2MW and a full size launcher (L1), during the 1990 shutdown. LOP will test most of the design features of L1, such as the L1 requirements linked with tritium containment and remote handling capability. The aims of LOP are to gain construction and installation experience as well as obtaining operational experience on the various controls of the launcher: power, phase and position which are of great importance for the success of the experiment.

The RF power will be coupled through a single large horizontal JET port (Octant No.3) by a multijunction-type phased waveguide array. A sketch of the proposed launcher is shown in Fig.110. The choice of a multi-junction grill allows a good match to the klystron over a wide range of plasma conditions and thus provides flexibility in the acceptable position of the grill relative to the plasma surface. Its interest is to reduce the number of 384 waveguides down to 48 multi-junctions.

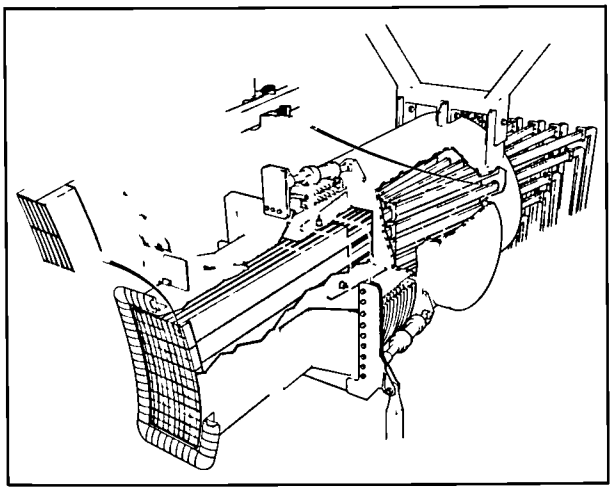

Fig.110 The Proposed Launcher

The salient features of the design are the following:

(a) feedback control of the phasing between multi-junctions in order to achieve the narrow wave spectrum required from physics considerations. Moreover this wave spectrum should be varied between 1.3 and 2.3 by proper phasing adjustment within a JET pulse;

(b) active control of the launcher radial position during a JET pulse in order to operate the system in matched conditions, i.e. to couple the maximum allowable power during significant variations of the scrape-off plasma density;

(c) operation during the tritium phase of JET which requires the built-in safety systems preventing tritium leakage outside the torus, remote handling capabilities and emphasis on the reliability of the system.

The main features of the Lower Hybrid Current Drive system are given in Table X.

The conceptual design of the various subsystems is also complete and comprises:

- the launcher (384 waveguides in 48 units);
- the generator (24 klystrons delivering 12MW at f=3.7GHz);
- the transmission line (40m long);
- the control command logic and data acquisition.

Eighteen major contributions representing about 80% of total system have been selected and the first stage of the contracts have been released.

High power tests of the first klystrons have already been performed. HF power up to 680kW for 10s have been obtained on a well-matched load. The testbed area which includes two klystrons with their corresponding ancillaries and control command is being installed and will be ready in early 1988.

High power tests of some components of the waveguide transmission line have been performed. Low power testing of the main microwave components, (power splitter, phase shifters, etc.) have been completed. A first prototype of the multi-junction has passed initial testing at high power at CEA Cadarache, France.

The LHCD programme is well on course to achieve two critical milestones:

(a) completion of the 2MW prototype generator and launcher for mid 1988. This launcher will be installed on JET if the high power testing is successful allowing performance of preliminary plasma experiments;

(b) completion of the 12MW system for the 1990 shutdown. The power can be upgraded at the same time to 17MW, depending upon further testing of klystrons.

Density Control

During the active phase of JET, density control will rely on two systems; (i) high speed pellet injection for density increase; and (ii) edge pumping by pump limiters for plasma exhaust. These systems were selected as experience showed that by injecting gas into the torus only modest densities could be achieved with rather flat density profiles and relatively high Z_{eff} values. However, pellet injection can yield peaked profiles at high densities and with low Z_{eff} values. These profiles are favoured to obtain scientific break-even, but in order to achieve these

TABLE X

Lower Hybrid System for JET

Frequency	3.7GHz
Power (generator)	12MW
No. of klystrons	24
No. of waveguides	384
No. of waveguides horizontal	32
No. of waveguides vertical	12
Waveguide dimension	72×9mm
Power density	4kW/cm
Maximum reflected power	
without circulators	2%
with circulators	8%
Waveguide material	Copper coated Stainless Steel
Maximum temperature	500°C
Stroke	300mm
Total weight of the launcher	~8t
Pressure (during a pulse)	10^4m bar
Pumping speed	10^5 1 s^{-1}
Phase control	10°
Length of the transmission line	~40m
Estimated inertion losses	~1dB
Central $N_{\|\|}$ value	1.8
Range of $N_{\|\|}$	1.3–2.3
Estimated driven current at $\bar{n}_e = 2\times10^{19}m^{-3}$	3–5MA
Estimated driven current at $\bar{n}_e = 5\times10^{19}m^{-3}$	1–2MA

conditions pellets have to reach the centre of the discharge. With the low pellet speeds available at present (~1.4kms^{-1}), deep penetration occurs only at low plasma temperatures, and speeds in excess of 5 km s^{-1} will be required, in the future.

In order to maintain peaked density profiles during a sequence of injected pellets, edge pumping of about 10^{22} particles per second will be required. It is not yet clear whether the wall pumping, which is the present main pumping mechanism can be used in the future, because most of the pumped particles are retained in the vessel walls. As an alternative, pump limiters are being developed.

High Speed Pellet Injector Development

Development work on high speed pellets has been undertaken and has been brought to a state that a system for the prototype pellet injector can be specified.

Successful experiments have been carried out in which a pellet cryostat, from Centre d'Études Nucleaires Grenoble (CENG), France, was coupled to a two-stage gun (3cm inner cylinder diameter; 1m piston stroke) at Ernst Mach Institut Freiburg (EMI), F.R.G. It was found that deuterium pellets could survive peak accelerations of $\lesssim 5\times10^6 ms^{-2}$, and velocities up to 2.7kms^{-1} were reached. It is unlikely that much higher velocities could be achieved even with a fully optimized system, as the pellet suffers from heavy erosion which destabilizes the pellet and does not allow the use of much longer barrels. However, it has been shown that by supporting the deuterium pellet by a sabot (casing for a projectile), higher peak accelerations are possible and the destabilizing effect of the pellet erosion can be avoided. As a result, much higher velocities up to 3.8kms^{-1} have been reached. First experiments have also been performed which demonstrate that the sabot can be prevented from injection into the plasma together with the solid deuterium. Employing a split sabot and by using an internal pressure build-up, the two halves of the sabot can be radially separated from the deuterium pellet outside the barrel. Subsequently, they can be dumped into a conical target with a central hole through which the deuterium can enter the plasma. Different methods are envisaged to generate pressure inside the sabot.

The development work for optimizing the deuterium

ice formation at CENG has now resulted in a well defined parameter field for the cryocondensation of deuterium pellets. Work has also started on building a cryostat which allows the deuterium pellet to be inserted into a sabot after its formation.

From the above results, a suitable extrapolation has been made to define the prototype gun, which will be a two stage gas driven piston device capable of delivering up to 6mm diameter pellets, with velocities of 4–5 km s^{-1} at a rate of one per tokamak discharge. The gun will be tested during the first half of 1988 and later coupled to the low speed multi-pellet injector on the torus.

Pump Limiter

Initially, it was envisaged that a prototype pump limiter would operate at JET as early as 1989. When this proposal was made, large uncertainties existed with respect to the parameters of the plasma boundary in the belt limiter configuration. Therefore, it was proposed that initially a prototype pump limiter would be installed with reduced performance. Operation during 1989 would then allow scrutiny of design parameters and incorporation of necessary changes into the final actively cooled pump limiters. These were scheduled for installation in 1990. Since the initial proposal, which dates from the end of 1985, a number of new developments at JET (e.g. X-point and inner wall operation) have taken place, which necessitated a reassessment of the concept.

As a result, the pump limiter, which initially was designed only for operation with the belt limiter had to be made compatible with other operational modes. This was achieved by redesigning the pump limiter head for higher power densities which allowed operation of the pump limiter in various configurations:

- with the belt limiter;
- with an inner wall discharge under load-sharing conditions;
- with an X-point discharge;
- as a stand-alone limiter for a limited time.

The various scenarios and the estimated particle removal rates are shown in Table XI

TABLE XI

Scenario	Particle removal in % of the total outflux
Belt Limiter	0.5-2
Inner Wall	1-4
Separatrix	1-4
Stand Alone*	5-10

* a few seconds only

The redesign of the pump limiter takes advantage of the high heat conductivity of compression annealed pyrolitic graphite used for the leading edge. The material can be mounted on a cooled support structure, to remove the heat between pulses. The cooling during a discharge would be inertial cooling. Complicated, expensive, and failure prone structures (e.g. swirl tubes), would no longer be employed.

This new approach provides the advantages that, the revised pump limiter is capable of working with a number of scenarios; active cooling is no longer needed; and critical design parameters can be measured in advance.

During 1987, negotiations between JET and the U.S. Department of Energy (USDoE) were carried out to implement an agreement on collaboration on the pump limiter. This includes component tests in the U.S. and the joint operation of density control experiments.

Tritium Handling

The JET time schedule requires that the Active Gas Handling System is ready for final commissioning by mid-1990 and is able to commence D-T operation in mid-1991. To achieve this schedule, components will have to be installed by early 1990. The multi-column cyrogenic distillation for isotope separation was identified as the time critical item and a design and procurement contract was placed by the end of 1987.

The design of the cryogenic forevacuum system and the main part of the impurity processing system was finalised and tender action is scheduled for early 1988. Prototype tests were conducted on components of the cryogenic forevacuum system in the test rig at JET. Mixtures of hydrogen and helium were successfully pumped without carryover of hydrogen into the helium cryosorption section. First tests of nitrogen impurity retention in a deuterium-nitrogen mixture indicate retention of more than 99% of nitrogen in the impurity retention section of the cryotransfer pump. Further tests on prototype components will be conducted in early 1988 with improved analytic equipment to establish whether the impurity retention section can reduce the impurity content to the required very low level.

A consultancy contract has been negotiated with CEA, France for assistance in the design and commissioning of the gas chromatogrphic isotope separation system. Flow diagrams and a layout mechanical design were prepared during 1987.

The designs and proposals for components of the Active Gas Handling System were presented and discussed in a Tritium Experts Meeting held at JET in December 1987. The meeting was attended by European scientific tritium experts.

The basic principles of the documentation necessary to justify the safety of operation of the Active Gas Handling System have been agreed with the UKAEA Safety and Reliability Directorate (SRD). There are four stages, the first of which, the Preliminary Safety Analysis Report (PSAR) has been issued in draft form and,

following comments from SRD, and the results of a HAZOP (Hazard and Operability) study, it was being revised at the end for 1987. It reviews the potential hazards, sets down the safety criteria and carries out a preliminary safety analysis which makes an initial assessment of the accident sequences resulting from a number of initiating events such as loss of electrical power. The preliminary assessment shows that the design safety criteria should be capable of being met. The next stage is to carry out a more thorough analysis on each subsystem of the plant once the design details are available. Good progress has been made on the first subsystem, the impurity processing system. The analysis for the cryodistillation system is being carried out by the supplier.

A procedure has been set up for assessment of the compatibility of torus systems with tritium operation. Assessments have been made for a number of diagnostics and progress has been made on assessment of other torus systems.

Close contact has been maintained between JET, UKAEA Culham Laboratory, SRD and HM Inspectorate of Pollution (HMIP) to ensure that the external organisations have an opportunity to comment on JET's proposals before they are finalised.

SRD have formally stated that they have no major misgivings on the Preliminary Safety Analysis Report. This has cleared the way for the preparation of the second stage reports. The preliminary part of the second stage report for the cryodistillation system has been endorsed by SRD, subject to a commitment to further safety analysis by JET and the supplier. A submission to HMIP to justify the height of the exhaust stack on the Active Gas Handling System building has been accepted.

Future Plans

The future JET programme has been divided into phases governed by the availability of new equipment and fitting within the accepted lifetime of the Project (up to the end of 1992, but yet to be formally approved by the Council of Ministers) (see Fig.111). One major shutdown about every eighteen months is planned to allow all the necessary modifications to be made for the following operational period. It is envisaged that the tritium phase will last for fifteen months. During this period, a few

JET PROGRAMME

1983	1984	1985	1986	1987	1988	1989	1990	1991	1992
PHASE I		PHASE IIA		PHASE IIB		PHASE IIIA		PHASE IIIB	PHASE IV
Ohmic Heating Studies		Additional Heating Studies				Full Power Optimisation Studies			Tritium Phase

Ohmic Systems	5MA	Vessel restraints and improved volt-seconds for 7MA operation			
Separatrix		Additional P1 Coils	Cooled separatrix dump plates		
Limiters	Eight carbon mid-plane limiters	Carbon belt limiters	Beryllium belt limiters		
Pellets	Single pellet injector	ORNL multiple pellet injector ($1.5 km\,s^{-1}$)	Prototype high speed pellet injector ($>3 km\,s^{-1}$)	[Multiple high speed pellet injector]*	
Pump limiters				Adjustable pump limiter	
NBI	First NBI line (80kV)	Second NBI line (2×80kV)	One line modified to 140kV	Second line modified to 140kV	
ICRH	Three A_0 antennae	Eight A_1 antennae			
LHCD			Prototype system	Full system	
Disruption control			Saddle coils		
Tritium and Remote handling				Tritium plant and main RH modifications	Final modifications

**To proceed if successful development takes place outside JET*

CR86.2 (rev.24/2/88) - Ro1540, H1.P CR86.2

Fig.111: The JET Programme.

thousand discharges are foreseen to study α-particle production, confinement and heating of the plasma.

It is a crowded programme, where many activities are pursued in parallel, and where four new systems or pieces of equipment (viz. the use of beryllium, lower hybrid current drive, feedback control of disruptions and handling of tritium) represent completely new physics issues for JET. It assumes no major breakdowns, no sizeable delays in the delivery of equipment and provision of adequate staffing and funding levels. The programme still allows flexibility to respond to new information and results from JET or from other tokamaks but provides only limited opportunity to pursue any arising physics issues.

On the JET programme, Phase I, the Ohmic Heating Phase, was completed in September 1984, and Phase IIA was completed in December 1986. The present Phase IIB (Additional Heating Studies) is midway through its programme, and future phases are as follows.

Phase IIB (mid-1987 - mid-1988)

The general objective of this phase is to explore the most promising regimes for energy confinement (currents up to 7 MA in the limiter mode, 4 MA in the X-point mode) and for high fusion yield (high T_e and T_i regimes including also significant non-thermal fusion yield) at increased ICRF power (20MW) and neutral beam heating power (20MW at 80kV). The ultimate objective is to achieve full performance with the simultaneous operation of all systems.

Phase IIIA (mid-1988 - end of 1989)

During the shutdown at the beginning of this phase, the following items should be installed:

-Prototype single shot high-speed pellet injector:
-Conversion of one neutral injector to 140keV;
-Beryllium belt limiter;
-Final modifications to the electro-magnetic system for X-point operation and cooled separatrix dump plates;
-Testbed for lower hybrid current drive and prototype module;
-Disruption control system, using internal saddle coils.

The main aims of this phase will be to consolidate the operation of JET at full performance with long pulses (> 10s) at full additional heating power (20MW ICRH, 10MW NB at 80kV, 7.5MW NB at 140kV). The effect on confinement of the current and density profiles using pellet injection and current drive by ICRH, NBI and LHCD in quasi stationary states will be established. The use of beryllium as a low-Z wall and limiter material represents an option in the programme. The potential benefit expected from this use is a reduction of the impurity level by gettering oxygen, allowing good confinement over an extended range of parameters.

Phase IIIB (early 1990 - mid 1991)

After the shutdown at the beginning of this phase the following systems should be operational:

-Final lower hybrid current drive system for profile control;
-Adjustable pump limiter;
-Both neutral injectors at 140keV;
-All remote handling systems required for the active phase;
-Multiple pellet injector system (if successful development takes place outside JET);
-Diagnostic systems required for active phase.

The commissioning of the tritium plant should also take place during this phase.

The main aims of this phase will be to reach maximum performance with deuterium plasmas and to establish operating regimes to be used in the tritium phase (limiter, X-point, non-thermal, or any other modes of operation which have proved successful). These regimes will also be modified and enhanced by the plasma control systems (acting on current profile, density profile, impurities and disruptions) at their full capacity.

During this phase, the machine will be upgraded to the status compatible with full radioactive operation (i.e. remote handling systems tested, tritium compatibility of systems completed, shielding requirements implemented, tritium plant commissioned, neutral beam and pellet injectors upgraded for tritium beam and pellet injection).

Phase IV (D-T Phase (mid 1991 - end of 1992)

Deuterium-Tritium (D-T) operation should begin when the conditions achieved in deuterium alone suggest that significant α-particle heating would be achieved in D-T.

The main aims of this phase is to operate JET with D-T plasmas. In the light of present knowledge, all of the currently planned new equipment will be needed to bring the performance to a level justifying the introduction of tritium in the torus. The phase will develop along two main directions:

(a) Establishment of Tritium Operation
The characteristics of D-T plasmas will be studied, including their confinement properties and impurity content. An important element will be the control of the composition of the core plasma using tritium neutral beam injection and/or pellets. New scenarios will be explored leading to the optimisation of ICRH and NBI for D-T plasmas;

(b) High Fusion Yields and the Detection of α-Particle Heating
The study and optimisation of intensely heated D-T plasmas will be required both for the maximisation of the fusion yield and for the database for future devices. It is anticipated that current and density profile controls will have important roles.

The main questions to be studied should be:

- Are the α-particles confined?
- Do the α-particles behave as expected (slowing down classically and giving most of their energy to

the electrons?)

– What kind of confinement degradation does the α-particle heating cause?

The answer to this last question will directly influence the size of a reactor.

The production rate and spatial distribution of the initial source should be given by the measured neutron yield and source distribution. Direct loss of energetic α-particles should be measured with detectors at the wall of the torus. The heating effect should be detectable through the changes in plasma temperature and density. For this purpose, the α-particle power needs to be at least 20% of the total power input from other sources (i.e. Q_{DT} of about unity). The preferential localisation of the α-particle heating in the plasma core should make such experiments easier.

Appendix I

JET Task Agreements 1987

Title	*Associations (JET Responsible Officer)*	*Duration of Agreement*	*Present Status*
RF HEATING DIVISION			
ICRF CURRENT DRIVE EFFECTS– ● Localized currents driven by asymmetric heating of minorityions ● Potential of fast wave current drive in non-Maxwellian plasmas ● Aspects of combined ICRF and neutral beam heating and current drive	EUR-UKAEA CULHAM LABORATORY (CUL/TA6/1) (J. Jaquinot)	Novenber 1984-December 1987	● Work nearly completed
LOWER HYBRID CURRENT DRIVE ON JET– ● Exchange of knowledge ● Design and construction ofspecial item ● High power tests	EUR-CEA CADARACHE (CEA/TA4) (J. Jaquinot)	January 1987-December 1988	● Work continuing ● Large number of high power tests of JET items at Cadarache
PHYSICS OF LOWER HYBRID CURRENT DRIVE ON JET ● set-up predictive and interpretive codes ● participation in the LHCD programme at JET	UNIVERSIDAD TECHNICA DI LISBOA (UTL/TA1) (J. Jaquinot)	October 1987-October 1990	● Work continuing
PREPARATION OF THE LOWER HYBRID CURRENT DRIVE SYSTEM FOR JET ● position control of the launcher ● wave damping by energetic ions ● preparation of profile control experiments	EUR/UKAEA CULHAM LABORATORY (CUL/TA7) (C. Gormanzo)	Junel987-December 1988	● Work continuing
EXPERIMENTAL DIVISION I			
PHYSICS OF SHAPED CROSS-SECTIONS	CULHAM, UK (CUL/TA4) (P. E. Stott)	March 1983-December 1987	● Work continuing
EDGE PLASMAS & PLASMA SURFACE INTERACTIONS	CULHAM, UK (CUL/TA2) (P. E. Stott)	June 1983-June 1989	● Work proceeding
PLASMA WALL INTERACTIONS	GARCHING, FRG (IPP/TA2) (P. E. Stott)	January 1984-June 1989	● Work proceeding
MHD ACTIVITY, DISRUPTION AND RF WAVEFIELDS, EDGE PLASMAS UNDER INTENSE RF FIELDS	LAUSANNE, SWITZERLAND (CRPP/TA1) (P. E. Stott)	March 1984-December 1987	● Work proceeding
NEUTRON PRODUCTION, RELATED PHYSICS AND ASSOCIATED DIAGNOSTICS	SWEDEN (SERC/TA1) (P. E. Stott)	January 1984-December 1990	● Work proceeding
PLASMA SURFACE INTERACTIONS	SWEDEN (NFR/TA2) (P. E. Stott)	July 1987-July 1990	● Work proceeding

Title	*Associations (JET Responsible Officer)*	*Duration of Agreement*	*Present Status*
NEUTRON PRODUCTION RELATED PHYSICS	HARWELL, UK (HAR/TA1) (P.E. Stott)	August 1985-April 1988	● Work Proceeding
NEUTRON PRODUCTION RELATED PHYSICS AND ASSOCIATED	FRASCATI, ITALY (ENEA/TA3) (P.E. Stott)	January 1986-January 1989	● Work proceeding
ECE MEASUREMENTS	FOM, NETHERLANDS (FOM/TA1) (P.E. Stott)	March 1985-March 1988	● Work proceeding
PHYSICS OF TURBULENT AND CONVECTIVE TRANSPORT, MHD AND RELATED DIAGNOSTICS	FOM, NETHERLANDS (FOM/TA2) (P.E. Stott)	November 1987-October 1990	● Work starting
EXPERIMENTAL DIVISION II			
BULK IMPURITY PHYSICS AND IMPURITY RELATED DIAGNOSTICS	EUR-IPP FRG (W.W. Engelhardt)	Started February 1983	● Work proceeding
IMPURITY ANALYSIS	EUR-UKAEA CULHAM LABORATORY (CUL/TA1) (W.W. Engelhardt)	Started February 1983	● Work proceeding
SPECTROSCOPIC MEASUREMENTS: INTERPRETATION AND IMPURITY ANALYSIS	EUR-CEA FAR (W.W. Engelhardt)	Started July 1984	● Work proceeding
PHYSICS OF ION AND ELECTRON ENERGY TRANSPORT AND RELATED DIAGNOSTICS	EUR-ENEA CREF (W.W. Engelhardt)	Started October 1983	● Work proceeding
THEORY DIVISION			
TESTING THEORETICAL TRANSPORT MODELS AGAINST JET DATA	EUR-UKAEA CULHAM LABORATORY (CUL/TA5) (T.E. Stringer)	Started December 1986	● Work proceeding

Appendix II

Articles, Reports and Conference Papers Published in 1987

1. First measurements of neutron emission profiles on JET.
   Adams J.M., Jarvis O.N., Kallne J., Sadler G., Syme D.B., Swinhoe M.T., Watkins N., van Belle P., Verschuur K.
   Controlled Fusion and Plasma Physics: 14th European Conference, Madrid, 22-26 June 1987. Contributed papers, part 3. European Physical Society, 1987.
   pp.1224-1227.
   (Also as Report JET-P(87)23, pp.37-40.)
2. Ion velocity distributions in the presence of combined neutral-beam and ICRF-heating; a semianalytical analysis.
   Anderson D., Eriksson L.G., Lisak M., Core W., Hamnen H., Hellsten T.
   Fusion Theory Meeting, Wepion, Belgium, 16-18 June 1986.
   Abstracts. p.36.
3. Overview of the JET ICRF power plant operation and development.
   Anderson R.J., Plancoulaine J., Schmid M.
   Fusion Technology 1986, Procs. 14th Symposium, Avignon, 8-12 September 1986.
   Vol.1.Oxford, Pergamon for the Commission of the European Communities, 1986.
   pp.339-345.
4. Cold, warm and hot plasma models for the heating with low-frequency waves.
   Appert K., Hellsten T., Vaclavik J., Villard L.
   Fusion Theory Meeting, Wepion, Belgium, 16-18 June 1986.
   Abstracts. p.9.
5. The Joint European Torus personnel dosimetry service.
   Baker D.M., Budd T.
   Joint European Torus JET. 1987.
   7p. Report JET-P(87)25
   Presented at an IAEA Seminar on The application of Computer Technology to Radiation Protection, IAEA-SR-136, held in Bled, 22-26 June 1987.
6. Design and calibration of the JET neutral particle analyzer.
   Bartiromo R., Bracco G., Brusati M., Grosso G., Mantovani S., Tilia B., Zanza V.
   Review of Scientific Instruments
   Vol.58 no.5 May 1987
7. Disruption studies in JET.
   Bartlett D., Campbell D., Costley A., Duperrex P.A., Edwards A., Gill R., Gottardi N. Granetz R., Haynes P., Hender T., Hugon M., Jackel H., Lazzaro E., Lopes Cardozo N., Oyevaar T., Salmon N., Schuller F., Smeulders P., Snipes J., Stott P., Tonetti G., Ward D., Weller A., Wesson J.,
   American Physical Society. Bulletin.
   vol.32 no.9 October 1987 (Program of the 29th Ann. Mtg. Div. Plasma Phys., San Diego, 2-6 November 1987. Abstracts.)
   p.1838, 5V 10.
8. Measurement and analysis of two-dimensional electron temperature profiles in JET using ECE.
   Bartlett D.V., Campbell D.J., Costley A.E., Kissel S.E., Nowak S., Brusati M., Lazzaro E.,
   Controlled Fusion and Plasma Physics: 14th European Conference, Madrid, 22-26 June 1987. Contributed papers, part 3. European Physical Society, 1987.pp.1252-1255.
   (Also as Report JET-P(87)23, pp.53-56.)
9. Studies of tritium burn-up in JET deuterium discharges.
   Batistoni P., Martone M., Pillon M., Rapisarda M., Argyle J., Huxtable G., Syme D.B., Bittoni E., Verschuur K., Gorini G., Jarvis O.N., Kallne J., Sadler G.,
   Controlled Fusion and Plasma Physics: 14th European Conference, Madrid, 22-26 June 1987. Contributed papers, part European Physical Society, 1987.
   pp.
   (Also as Report JET-P(87)23, pp.41-44.)
10. Description of the impurity transport code 'STRAHL'.
    Behringer K
    Joint European Torus, JET. 1987. 20p.
    Report JET-R(87)08
11. Impurity production mechanisms and behaviour during additional heating in JET.

Behringer K.H., Boileau A., Bombarda F., Denne G.B., Engelhardt W., Forrest M.J., Fussmann G., Giannella R., Gottardi N.A., von Hellermann M., Horton L., Jackel H., Jupen C., Kallne E., Lawson K.D., Magyar G., McCracken G.M., Morgan P.D., Muller E.R., Peacock N.J., Ramette J., Saoutic B., Stamp M.F., Summers H.P., Tallents G., Weller A.,
Plasma Physics and Controlled Nuclear Fusion Research, 11th Int. Conf., Kyoto, 13-20 November 1986.
Volume 1. Vienna, IAEA. 1987.
pp.197-206.

12. Impurity transport during the JET H-mode.
Fusion Technology 1986, Procs. 14th Symposium, Avignon, 8–12 September 1986.
Vol.1. Oxford, Pergamon for the Commission of the European Communities, 1986.
pp.263–271. 21.
Edge density, edge temperature characterisation of separatrix discharges in JET.
Bhatnagar V.P., Odajima K., Ellis J.J., Jacquinot J., Start D.F.H.
American Physical Society. Bulletin.
vol.32 no.9 October 1987 (Program of the 29th Ann. Mtg. Div. Plasma Phys., San Diego, 2–6 November 1987. Abstracts.)
p.1837, 5V 5.

13. Space resolved measurement of impurity radiation on the JET tokamak.
Behringer K.H., Denne B., Magyar G., Breton C., de Michelis C., Ramette J., Saoutic B.
JET papers presented to Workshop on High Temperature Plasma Diagnostics, Varenna, Italy, September 1986.
Joint European Torus, JET. 1986.
pp.145–153. Report
JET–P(86)45

14. Spectroscopic studies of plasma–wall interaction and impurity behaviour in tokamaks.
Behringer K.H.
Journal of Nuclear Materials
vol.145–147 February (II) 1987 (Procs. 7th Int. Conf. on Plasma–Surface Interactions in Controlled Fusion Devices, Princeton, 5–9 May 1986)
pp.145–153. 15.

15. Status of visible spectroscopy on JET.
Behringer K.H., Engelhardt W.W., Horton L., Morgan P.D., Stamp M.F., Summers H.P., von Hellerman M., Forrest M.J., Peacock N.J.
Joint European Torus JET. 1987.
27p.
Report JET–P(87)27
Paper presented at the XIII Symp. on the Physics of Ionised Gases, Sibenik, Yugoslavia, 1–5 September 1986.

16. Contamination of the JET limiters with metals during the different operational phases.
Behrisch R., Ehrenberg J., Bergsaker H., Coad J.P., de Kock L., Emmoth B., Kukral H., Martinelli A.P., McCracken G.M., Partridge W.
Journal of Nuclear Materials
vol.145–147 February (II) 1987 (Procs. 7th Int. Conf. on Plasma–Surface Interactions in Controlled Fusion Devices, Princeton, 5–9 May 1986)
pp.731–735 17.

17. Hydrogen and deuterium retention in wall samples of JET.
Behrisch R., Ehrenberg J., Wielunski M., Martinelli A.P., Bergsaker H., Emmoth B., de Kock L., Coad J.P.
Journal of Nuclear Materials
vol.145–147 February (II) 1987 (Procs. 7th Int. Conf. on Plasma–Surface Interactions in Controlled Fusion Devices, Princeton, 5–9 May 1986)
pp.723–726.

18. Hydrogen isotope retention in the JET limiters.
Bergsaker H., Behrisch R., Coad J.P., Ehrenberg J., Emmoth B., Martinelli A.P., Erents S.K., McCracken G.M., Partridge J.W.
Journal of Nuclear Materials
vol.145–147 February (II) 1987 (Procs. 7th Int. Conf. on Plasma–Surface Interactions in Controlled Fusion Devices, Princeton, 5–9 May 1986)
pp.727–730.

19. Preliminary measurements of impurity fluxes using time resolved collector probes in JET.
Bergsaker H., Coad J.P., de Kock L., Emmoth B., Hancock J., Stevens A., Vince J.
Controlled Fusion and Plasma Physics:
14th European Conference, Madrid, 22–26 June 1987. Contributed papers, part 2.
European Physical Society, 1987.
pp.732–735.
(Also as Report JET–P(87)23, pp.13–16.)

20. The JET magnet power supplies and plasma control systems
Bertolini E., Mondino P.L., Noll P.
Fusion Technology
vol.11 No.1 January 1987 (Special issue on design, construction, and first operational experience on the Joint European Torus (JET))
pp.71-119

21. The development of the JET electromagnetic system.
Bertolini E., Last J.R., Mondino P.L., Noll P., Santagiustina A.

Fusion Technology 1986,Procs. 14th Symposium, Avignon, 8-12th September 1986. vol.1. Oxford, Pergamon for the Commission of the European Communities, 1986. pp.263-271

22. Enquiry on Nuclear Fusion for Peaceful Uses, by the 12th Committee of Industry of the Italian Parliament
Bertolini E.
Joint European Torus (JET)
Report JET-R(87)13

23. Experiments with diverse ICRH scenarios on JET.
Bhatnagar V.P., Ellis J.J., Jacquinot J., Start D.F.H.
Controlled Fusion and Plasma Physics: 14th European Conference, Madrid, 22–26 June 1987.
Contributed papers, part 3. European Physical Society, 1987. pp.805–808.
(Also as Report JET–P(87)23, pp.85–88.)

24. Comparison between experiment and theory.
Bickerton R.J., Taroni A., Watkins M.L., Wesson J.
Royal Society. Philosophical Transactions. Series A
vol.322 no.1563 29 June 1987 (The JET Project and the prospects for controlled nuclear fusion: Discussion held 12–13 March 1986) pp.173–188.
(Also as Report JET–P(86)28)

25. Operational limits and confinement in JET.
Bickerton R.J., presenter, and The JET Team: Adams J.M., Altmann H., Anderson R.J., Bailey W., Bartlett D.V., Behringer K., Bertoldi P., Bertolini E., Best C.H., Bhatnagar V., Boileau A., Bonicelli T., Booth S.J., Boschi A., Bosia G., Botman M., Bracco G., Brelen H., Brinkschulte H., Browne M.L., Brusati M., Budd T., Bures M., Buttgereit H., Cacaut D., Caldwell–Nichols C., Callen J.D., Campbell D.J., Carwardine J., Celentano G., Challis C.D., Cheetham A., Christiansen J.P., Christodoulopoulos C., Chuilon P., Claesen R., Coad J.P., Cohen S.A., Conroy S., Cooke M., Cordey J.G., Core W., Corti S., Costley A.E., Cottrell G.A., Cox M., Cripwell P., Cross D., David C., de Kock L., de Matteis A., Deksnis E., Deng J., Denne G.B., Deschamps G., Dietz K.J., Dobbing J., Dorling S.E., Düchs D.F., Duesing G., Duperrex P.A., Duquenoy H., Edwards A.W., Ehrenberg J., Engelhardt W., Erents S.K., Eriksson B.T., Falter H., Forrest M.J., Froger C., Fullard K., Gadeberg M., Galetsas A., Gibson A., Gill R.D., Goede A., Gondhalekar A., Gorini G., Gormezano C., Gottardi N.A., Gowers C.W., Granetz R., Green B.J., Griph F.S., Haange R., Hamnen J.H., Hancock C.J., Harbour P.J., Haynes P., Hellsten T., Hemmerich J.L., Hemsworth R., Hendriks F., Herzog R.F., Hirsch K., Hoekzema J., Horton L., How J., Huart M., Hubbard A., Hugon M., Huguet M., Ingram B., Jackel H., Jacquinot J., Jankowicz Z., Jarvis O.N., Joffrin E., Jones E.M., Jones P., Jones T.T.C., Kallne E., Kallne J., Kaye A., Keen B.E., Keilhacker M., Knowlton S., Konstantellos A., Kovanen M., Kupschus P., Lallia P., Last J.R., Lauro–Taroni L., Lazzaro E., Lobel R.C., Lomas P.J., Lopes–Cardozo N., Lorenz–Gottardi M., Lowry C., Magyar G., Maisonnier D., Malacarne M., Marchese V., Massmann P., McCracken G.M., Mead M.J., Meriguet P., Mills S.F., Millward P., Moissonnier A., Mondino P.L., Moreau D., Morgan P.D., Morsi H., Murphy G., Nave M.F., Nickesson L., Nielsen P., Noll P., Nowak S., Obert W., O'Brien D., Odajima K., O'Rourke J., Oyevaar T., Pacco M.G., Paillere J., Pain M., Papastergiou S., Pasini D., Paume M., Peacock N.J., Pick M., Plancoulaine J., Poffe J–P., Prentice R., Raimondi T., Ramette J., Raymond C., Rebut P–H., Removille J., Riediker W., Rimini F., Robinson D.C., Rolfe A., Ross R.T., Rupprecht G., Rushton R., Sack H.C., Sadler G., Saffert J., Salmon N., Salzmann H., Santagiustina A., Schmid M., Schuller F.C., Selin K., Shaw R., Shibonuma K., Sillen R., Simonini R., Smeulders P., Snipes J.A., Sonnenberg K., Sonnerup L., Stamp M.F., Stangeby P., Start D.F.H., Steed C.A., Stork D., Stott P.E., Stringer T.E., Summers D.R., Summers H.P., Tagle A.J., Tamnen H., Tanga A., Taroni A., Tesini A., Thomas P.R., Thompson E., Thomsen K., Tibone F., Trevalion P., Tschudin M., Tubbing B.J., Usselmann E., Van der Beken H., Van Montfoort J.E., von Hellermann M., Wade T., Walker C., Wallander B.A., Walravens M., Walter K., Ward D., Watkins M.L., Watson M., Wesson J.A., Westerhoff E., Wilks J., Winkel T., Woodward C., Wykes M., Young D., Zannelli L., Zwart J.W.
Plasma Physics and Controlled Fusion vol.29 no.10A October 1987 (Controlled Fusion and Plasma Physics, 14th Euro. Phys. Soc., Plasma Physics Division Conf., 22–26 June 1987, Madrid. Invited papers.) pp.1219–1233.
(Also available as JET–P(87)37)

26. The deduction of low–Z ion temperature and

densities in the JET tokamak using charge exchange recombination spectroscopy.
Boileau A., von Hellerman M., Horton L.D., Spence J., Summers H.P.,
Joint European Torus JET. September 1987.
67p.
Report JET–P(87)44
(Submitted to Nuclear Fusion)

27. Power and phase control in the JET lower hybrid current drive system.
Bosia G., David C., Gormezano C., Jacquinot J., Knowlton S., Moreau D., Pain M., Wade T.J.,
JET papers presented at the 7th APS Topical Conf. on Applications of Radio Frequency Power to Plasmas, Kissimmee, Florida, 4–6 May 1987.
Joint European Torus, JET. 1987.
pp.13–16.
Report JET–P(87)40

28. Ion energy transport in JET discharges.
Bracco G., Brusati M., Corti S., Rimini F., Taroni A., Romanelli F., Sack C., Tibone F., Zanza V.,
Controlled fusion and plasma physics. 14th Euro. Conf., Madrid, 22–26 June 1987. Contributed papers. Part 1. European Physical Society, 1987.
p.173–176.
(Also as Report JET–P(87)23, pp.153–156.)

29. Heat shock resistance of graphite determined with a CO_2 laser.
Brinkschulte H., Deksnis E., Bransden A.S.
Joint European Torus, JET. 1987.
9p.
Report JET–P(87)43

30. Heat transport in JET.
Brusati M., Galway A., Hamnen H., Rimini F., Stringer T.E.
Controlled fusion and plasma physics. 14th Euro. Conf., Madrid, 22–26 June 1987. Contributed papers. Part 1. European Physical Society, 1987.
pp.177–180.
(Also as Report JET–P(87)23, pp.181–184.)

31. Computerised radiation protection in the working environment at JET.
Budd T., Caldwell–Nichols C.J., Green B., Marshall M.
Joint European Torus JET. 1987.
9p.
Report JET–P(87)24
Presented at IAEA Seminar on the Application of Computer Technology to Radiation Protection Bled, 22–26 June 1987.

32. Behaviour of particle influxes and edge recycling during ICRF heating on JET.
Bures M., Bhatnagar V.P., Evrard M.P., Gondhalekar A., Jacquinot J., Jones T.T.C., Morgan P.D., Start D.F.H.,
Controlled Fusion and Plasma Physics: 14th European Conference, Madrid, 22–26 June 1987. Contributed papers, part 2 European Physical Society, 1987.
pp.722–725.
(Also as Report JET–P(87)23, pp.77–80.)

33. The modification of the plasma edge and impurity production by antenna phasing during ICRF heating on JET.
Bures M., Jacquinot J., Kaye A., Brinkschulte H., Lawson K.D., Tagle J.A.,
Joint European Torus JET. March 1987.
16p.
Report JET–P(87)18

34. Radiative Gaunt factors.
Burgess A., Summers H.P.,
Royal Astronomical Society. Monthly Notices vol.226 no.2 15 May 1987
pp.257–272.

35. Heating effectiveness for auxiliary heating in JET.
Callen J.D., Christiansen J.P., Cordey J.G., Thomas P.R.,Thomsen K.
American Physical Society. Bulletin. vol.32 no.9 October 1987 (Program of the 29th Ann. Mtg. Div. Plasma Phys., San Diego, 2–6 November 1987. Abstracts.)
p.1837, 5V 2.

36. Modelling of temperature profiles and transport scaling in auxiliary heated tokamaks.
Callen J.D., Christiansen J.P., Cordey J.G., Thomas P.R., Thomsen K.,
Nuclear Fusion vol.27 no.11 November 1987
pp.1857–1875.
(Also as Report JET–P(87)10)

37. Modelling of temperature profile responses to heating profiles in JET.
Callen J.D., Christiansen J.D., Cordey J.G.,
Controlled fusion and plasma physics. 14th Euro. Conf., Madrid, 22–26 June 1987. Contributed papers. Part 1.
European Physical Society. 1987.
pp.261–264.
(Also as Report JET–P(87)23, pp.117–120.)

38. Current and temperature profile evolution in JET.
Campbell D.J., Christiansen J.P., Cordey J.G., Lazzaro E., Nave M.F.F., Schueller F.C., Thomas P.R.
Joint European Torus JET. 1987.
13p.
Report JET–P(87)46
Submitted to Nuclear Fusion.

39. Sawteeth and disruptions in JET.
Campbell D.J., Duperrex P.A., Edwards A.W., Gill R.D., Gowers C.W., Granetz R.,

Hugon M., Lomas P.J., Lopes-Cardozo N., Malacarne M., Nave M.F., Robinson D.C., Schuller F.C., Smeulders P., Snipes J.A., Stott P.E., Tonetti G., Tubbing B.J., Weller A., Wesson J.A.,
Plasma Physics and Controlled Nuclear Fusion Research, 11th Int. Conf., Kyoto, 13-20 November 1986. Volume 1. Vienna, IAEA. 1987.
pp.433-445.

40. Studies of the sawtooth instability in JET.
Campbell D.J., Edwards A.W., Gill .D., Granetz R.S., Lopes Cardozo N., van Milligan B., Tammen R., Tubbing B.J.D., Weller A., Wesson J.A.,
American Physical Society. Bulletin. vol.32 no.9 October 1987 (Program of the 29th Ann. Mtg. Div. Plasma Phys., San Diego, 2-6 November 1987. Abstracts.)
p.1838, 5V 11.

41. Transient stabilization of sawteeth by additional heating in JET.
Campbell D.J., Bartlett D.V., Bhatnagar V.P., Mures M., Cottrell G.A., Duperrex P.A., Challis C.D., Cordey J.G., Edwards A.W., Gormezano C., Gowers C.W., Granetz R.S., Hamnen H., Hellsten T., Jacquinot J., Lazzaro E., Lomas P.J., Lopes Cardozo N., Mantica P., Snipes J.A., Start D.F.H., Stork D., Stott P.E., Thomas P.R., Thompson E., Thomsen K., Tonetti G., Wesson J.A.,
Controlled fusion and plasma physics. 14th Euro. Conf., Madrid, 22-26 June 1987. Contributed papers. Part 1. European Physical Society, 1987.
pp.21-24.
(Also as Report JET-P(87)23, pp.61-64.)

42. The JET belt limiter.
Celentano G., Deksnis E., Shaw R., Sonnenberg K., Booth J.,
Fusion Technology 1986, Procs. 14th Symposium, Avignon, 8-12 September 1986. Vol.1. Oxford, Pergamon for the Commission of the European Communities, 1986.
pp.581-587.

43. Neutral beam current drive studies at JET.
Challis C., Cordey J.G., Hamnen H., Campbell D., Christiansen J., Cox M., Lazzaro E., Muir D., Stork D., Stubberfield P., Thompson E.,
Controlled Fusion and Plasma Physics: 14th European Conference, Madrid, 22-26 June 1987.
Contributed papers, part 3 European Physical Society, 1987.
pp.1026-1029.
(Also as Report JET-P(87)23, pp.97-100.)

44. Profile effects associated with pellet fueling of JET.
Cheetham A.D., Gondhalekar A., Campbell D.J., Gottardi N., Granetz R., Morgan P.D., O'Rourke J.
Controlled fusion and plasma physics. 14th Euro. Conf., Madrid, 22-26 June 1987. Contributed papers. Part 1.
European Physical Society, 1987.
pp.205-208.
(Also as Report JET-P(87)23, pp.169-172.)

45. Results of pellet injection experiments in JET.
Cheetham A.D., Gondalekar A., Buchl K., Bures M., Campbell D., Edwards A., Granetz R., Gottardi N., Hendricks F., Morgan P.D., O'Rourke J., Schuller F., Watkins M., Weller A.,
JET papers presented to Workshop on High Temperature Plasma Diagnostics, Varenna,Italy, September 1986.
Joint European Torus, JET. 1986.
pp.38-43.
Report JET-P(86)45

46. Determination of plasma equilibrium in JET.
Christiansen J.P., Callen J.D., Granetz R.
American Physical Society. Bulletin.
vol.32 no.9 October 1987 (Program of the 29th Ann. Mtg. Div. Plasma Phys., San Diego, 2-6 November 1987. Abstracts.)
p.1768, 3E 8.

47. Heat flux analysis of auxiliary heating data from JET.
Christiansen J.P., Cordey J.G., Callen J.D., Muir D.G.
Controlled Fusion and Plasma Physics: 14th European Conference, Madrid, 22-26 June 1987. Contributed papers, part 1
European Physical Society, 1987.
pp.273-276.
(Also as Report JET-P(87)23, pp.113-116.)

48. Integrated analysis of data from JET.
Christiansen J.P.
Journal of Computational Physics
vol.73 no.1 November 1987 (Keith V. Roberts Memorial Issue)
pp.85-106.

49. Analysis of Local Heat Flux in JET
Christiansen J.P., Callen J.D., Cordey J.G., Thomsen K.
Joint European Torus JET
Report JET-P(87)48

50. The JET neutral injection 160kV transmission lines, the associated snubbers and the SF6 tower for the termination of the transmission lines housing of the snubbers and voltage breaks.
Claesen R., Baur U., Bertolini E., Celentano G., Mondino P.L., Rebut P-H.

Fusion Technology 1986, Procs. 14th Symposium, Avignon, 8–12 September 1986. Vol.1. Oxford, Pergamon for the Commission of the European Communities, 1986. pp.941–947.

51. Neutral beam injection and radio-frequency power supplies.
Claesen R., Mondino P.L.
Fusion Technology
vol.11 No.1 January 1987 (Special issue on design, Construction, and first operational experience on the Joint European Torus (JET))
pp.141-162.

52. Carbon erosion and deposition at the JET limiters.
Coad J.P., Behrisch R., Roth J., de Kock L., Ehrenberg J., Israel G., Goodall D.H.J., Wang W., Wielunski M.
Controlled Fusion and Plasma Physics: 14th European Conference, Madrid, 22–26 June 1987. Contributed papers, part 2
European Physical Society, 1987.
pp.744–747.
(Also as Report JET–P(87)23, pp.9–12.)

53. Depth profiling experiments on JET wall samples.
Coad J.P., Davies B.J., Edge G.J., von Seggern J., McCracken G.M.
Journal of Nuclear Materials
vol.145–147 February (II) 1987 (Procs. 7th Int. Conf. on Plasma–Surface Interactions in Controlled Fusion Devices, Princeton, 5–9 May 1986)
pp.736–740.

54. Glow discharge carbonisation in JET.
Coad J.P., Behringer K.H., Dietz K.J.
Journal of Nuclear Materials
vol.145–147 February (II) 1987 (Procs. 7th Int. Conf. on Plasma–Surface Interactions in Controlled Fusion Devices, Princeton, 5–9 May 1986)
pp.747–750.

55. Edge dynamics in pellet–fuelled inner–wall JET discharges.
Cohen S.A., Ehrenberg J., Bartlett D.V., Campbell D.J., Cheetham A.D., de Kock L., Gondhalekar A., Gottardi N., Granetz R., Houlberg W., Jaeckel H., Lazzaro E., Morgan P., O'Rourke J., Pick M., Stamp M.F., Summers D.D.R., van der Goot E., Watkins M., Weller A.
Controlled Fusion and Plasma Physics: 14th European Conference, Madrid, 22–26 June 1987. Contributed papers, part 2
European Physical Society, 1987.
pp.694–697.
(Also as Report JET–P(87)23, pp.17–20)

56. Particle balance and wall pumping in tokamaks.
Cohen S.A., Ehrenberg J., Jones T.T.C., Gondhalekar A., Bures M., Coad P., de Kock L., Harbour P., Morgan P.D., O'Rourke J., Tagle J.A.
Watkins M., Erents S.K.
Plasma Physics and Controlled Fusion
vol.29 no.10A October 1987 (Controlled Fusion and Plasma Physics, 14th Euro. Phys.Soc., Plasma Physics Division Conf., 22–26June 1987, Madrid. Invited papers.)
pp.1205–1217.
(Also as ReportJET–P(87)39)

57. Energy confinement in JET ohmically heated plasmas: June 1983 – December 1985.
Cordey J.G.
Joint European Torus JET. February 1987.
23p.
ReportJET–R(87)02

58. Energy confinement in JET with ohmic heating and strong auxiliary heating.
Cordey J.G., Bartlett D.V., Bhatnagar V., Bickerton R.J., Bures M., Callen J.D., Campbell D.J., Challis C.D., Christiansen J.P., Corti S., Costley A.E., Cottrell G.A., Duesing G., Fessey J., Gadeberg M., Gibson A., Gondhalekar A., Gottardi N.A., Gowers C.W., von Hellermann M., Hendriks F., Horton L., Jackel H., Jacquinot J., Jarvis O.N., Jones T.T.C., Kallne E., Kallne J., Keilhacker M., Kissel S., de Kock L., Lallia P., Lazzaro E., Lomas P.J., Lopes–Cardozo N., Morgan P.D., Nielsen P., O'Rourke J., Prentice R., Ross R.T., Sadler G., Schuller F.C., Stabler A., Smeulders P., Stamp M.F., Stork D., Stott P.E., Summers D.R., Tanga A., Thomas P.R., Thompson E., Thomsen K., Tonetti G., Tubbing B.J., Watkins M.L.
Plasma Physics and Controlled Nuclear Fusion Research, 11th Int. Conf., Kyoto, 13–20 November 1986. Volume 1. Vienna, IAEA. 1987.
pp.99–110.
(Also as ReportJET–P(86)44)

59. Heat flux studies in JET.
Cordey J.G., Christiansen J.P., Callen J.D., Muir D., Keilhacker M., Watkins M.
American Physical Society. Bulletin.
vol.32 no.9 October 1987 (Program of the 29th Ann. Mtg. Div. Plasma Phys., San Diego, 2–6 November 1987. Abstracts.)
p.1836, 5V 1.

60. Heat flux analysis of auxiliary heating data from JET.
Cordey J.G., Callen J.D., Christiansen J.P., Muir D.G.

Controlled fusion and plasma physics. 14th Euro. Conf., Madrid, 22–26 June 1987. Contributed papers. Part 1. European Physical Society. 1987.
pp.273–276.
(Also as Report JET–P(87)23, pp.113–116.)

61. Latest results from JET.
Cordey J.G.
American Physical Society. Bulletin.
vol.32no.9October 1987 (Program of the 29th Ann. Mtg. Div. Plasma Phys., San Diego, 2–6 November 1987. Abstracts.)
p.1711, 1I 2.

62. Prospects for alpha particle heating in JET in the hot ion regime.
Cordey J.G., Keilhacker M., Watkins M.L.
Physica Scripta
vol.T161987(The Role of Alpha Particles in Magnetically Confined Fusion Plasmas, Aspenasgarden, Goteborg, Sweden, 24–27 June 1986)
pp.127–132.
(Also as ReportJET–P(86)38)

63. Beam–plasma fusion yield in rotating tokamak plasmas.
Core W.G.F., van Belle P., Sadler G.
Controlled fusion and plasma physics. 14th Euro. Conf., Madrid, 22–26 June 1987. Contributed papers. Part 1. European Physical Society, 1987.
pp.49–52.
(Also as ReportJET–P(87)23, pp.157–160.)

64. A model of the JET Iron Core
Core W.G.F., Christiansen J.P.
Joint European Torus JET
Report JET-R(87)11

65. Measurement and simulation of slowing down spectra of fast ions during neutral beam injection in JET.
Corti S., Bracco G., Core W., Giannelli A., Zanza V.
Controlled Fusion and Plasma Physics: 14th European Conference, Madrid, 22–26 June 1987. Contributed papers, part 3
European Physical Society, 1987.
pp.1030–1033.
(Also as ReportJET–P(87)23, pp.145–148.)

66. Diagnosis of fusion plasmas using reflectometry.
Costley A.E.
JET papers presented to Workshop on High Temperature Plasma Diagnostics, Varenna, Italy, September 1986. Joint European Torus, JET. 1986.
pp.121–138.
ReportJET–P(86)45

67. Recent developments and applications of electron cyclotron emission.
Costley A.E.
JET papers presented to Workshop on High Temperature Plasma Diagnostics, Varenna, Italy, September 1986.
Joint European Torus, JET. 1986.
pp.101–120.
ReportJET–P(86)45

68. ICRF acceleration of beam ions in JET.
Cottrell G., Bhatnagar V.P., Cordey J.G., Core W.G., Corti S., Hamnen H., Hellsten T., Jacquinot J., Sand F., Start D.F.H., Watkins M.
JET papers presented at the 7th APS Topical Conf. on Applications of Radio Frequency Power to Plasmas, Kissimmee, Florida, 4–6 May 1987.
Joint European Torus, JET. 1987.
pp.9–12.
ReportJET–P(87)40

69. Superthermal radiation from fusion products in JET.
Cottrell G.A., Dendy R.O.
Physical Review Letters
vol.60 no.14 January 1988
pp.33–36.
(Also as ReportJET–P(87)45)

70. Aspects of combined ICRF and neutral beam heating and current drive.
Cox M., Start D.F.H.
Joint European Torus JET. July 1987.
14p.
ReportJET–P(87)34
Submitted for publication in Procs. Int. Conf. on Plasma Physics, Kiev, April 1987.

71. JET scrape–off layer data scaling for ohmic and combined heating discharges (ICRH + NBI).
de Kock L., Tagle J.A., Erents S.K., McCracken G.
American Physical Society. Bulletin.
vol.32 no.9 October 1987 (Program of the 29th Ann. Mtg. Div. Plasma Phys., San Diego, 2–6 November 1987. Abstracts.)
p.1837, 5V 4.

72. JET: Recent results and edge phenomena.
de Kock L., presenter, and Behringer K., Behrisch R., Bergsaker H., Bickerton R.J., Borgesen P., Boschi A., Braun E., Brinkschulte H., Bures M., Campbell D.J., Christiansen J., Cordey J.G., Coad J.P., Denne B., Dietz K.J., Duesing G., Emmoth B., Engelhardt W., Gondhalekar A., Gregoli S., Harbour P., Hemmerich J., Israel G., Jacquinot J., Koizlik K., Lallia P., Lazzaro E.E., Linke J., Lowry C., Lomas P., Moller W., Morgan P., Schuller F.C., Sonnenberg K., Stamp M., Stangeby P., Stott P., Summers D., Tagle J.A., Tanga A.,

Thomas P.R., Thompson E., Thomsen K., Valisa M., Von Seggern J., Watkins M.L., Erents S.K., Forrest M., Goodall D., McCracken G., Partridge J.
Journal of Nuclear Materials
vol.145–147 February (II) 1987 (Procs. 7th Int. Conf. on Plasma–Surface Interactions in Controlled Fusion Devices, Princeton, 5–9 May 1986)
pp.26–40.

73. Preparation for D–T phase operation in JET.
Dean J.R., Raimondi T., Riediker W., Rolfe A.
Fusion Technology 1986, Procs. 14th Symposium, Avignon, 8–12 September 1986. Vol.1. Oxford, Pergamon for the Commission of the European Communities, 1986.
pp.201–213.

74. JET remote maintenance during active operation
Dean J.R., Raimondi T.
Fusion Technology, vol.1 No.1 January 1987 (Special issue on design, construction, and the first operational experience on the Joint European Torus (JET))
pp.253-281

75. Impurity behaviour in X–point plasmas on JET.
Denne B., Behringer K., Boileau A., Fussmann G., von Hellermann M., Horton L., Ramette J., Saoutic B., Stamp M.F., Tallents G.
Controlled fusion and plasma physics. 14th Euro. Conf., Madrid, 22–26 June 1987. Contributed papers. Part 1. European Physical Society, 1987.
pp.109–112.
(Also as ReportJET–P(87)23, pp.149–152.)

76. Spectral lines of highly–ionized atoms for the diagnostics of fusion plasmas.
Denne B., Hinnov E.
Physica Scripta
vol.35 no.6 June 1987
pp.811–818.

77. Design aspects of in vessel components.
Dietz K.J.
Plasmamaterial interaction/high heat flux data needs for the next step ignition and steady state devices. Procs. Japan–US Workshop P–92, Nagoya University, 26–30 January 1987. Nagoya University, Institute of Plasma Physics. May 1987.
pp.498–500.

78. Experience with graphite in JET.
Dietz K.J.
Plasmamaterial interaction/high heat flux data needs for the next step ignition and steady state devices. Procs. Japan–US Workshop P–92, Nagoya University, 26–30 January 1987. Nagoya University, Institute of Plasma Physics. May 1987.
pp.111–131.

79. Anomalous transport in JET plasmas.
Duchs D.F., Stringer T.E., Taroni A., Brusati M., Gottardi N.A., Hellsten T., Tibone F.
Plasma Physics and Controlled Nuclear Fusion Research, 11th Int. Conf., Kyoto, 13–20 November 1986. Volume 1.
Vienna, IAEA. 1987.
pp.325–335.
(Also as ReportJET–P(86)44)

80. Creation of electric fields in tokamak plasmas.
Duchs D.F.
Zeitschrift fur Naturforschung A
vol.42no.10October 1987
pp.1193–1198.
(Also as Report JET–P(87)38)

81. Quantitative modelling of JET plasmas by computational methods.
Duchs D.F.
Royal Society. Philosophical Transactions. Series A
vol.322 no.1563 29 June 1987 (The JET Project and the prospects for controlled nuclear fusion: Discussion held 12–13 March 1986)
pp.133–145.

82. Neutral beam injection system
Duesing G., Altmann H., Falter H., Goede A., Haange R., Hemsworth R.S., Kupschus P., Stork D., Thompson E.
Fusion Technology, vol.11 No.1 January 1987 (Special issue on design, construction, and first operational experience on the Joint European Torus (JET))
pp.163-202

83. First neutral–beam heating experiments in JET.
Duesing G., Lomas P., Stabler A., Thomas P., Thompson E.
Royal Society. Philosophical Transactions. Series A
vol.322 no.1563 29 June 1987 (The JET Project and the prospects for controlled nuclear fusion: Discussion held 12–13 March 1986)
pp.109–123.

84. The vacuum systems of the nuclear fusion facility JET.
Duesing G.
Vacuum
vol.37 no.3/4 1987 (Vacuum 86: Vacuum Science, Technology & Applications, University of Strathclyde, Glasgow, 25–27 March 1986).
pp.309–315.

85. Fluctuations and confinement in JET.
Duperrex P.A., Malacarne M., Cripwell P., Edwards A.W., Gill R.D., Granetz R.S.,

Hubbard A., Simonet F., Snipes J., Weller A., Matthews G.
Controlled fusion and plasma physics. 14th Euro. Conf., Madrid, 22–26 June 1987. Contributed papers. Part 1. European Physical Society, 1987.
pp.93–96.
(Also as Report JET–P(87)23, pp.69–72.)

86. The effects of wall and limiter material properties on hydrogen recycling in JET.
Ehrenberg J., Cohen S.A., de Kock L., Harbour P.J., Morgan P.D., Stamp M.F., Summers D.D.R.
Controlled Fusion and Plasma Physics: 14th European Conference, Madrid, 22–26 June 1987. Contributed papers, part 2 European Physical Society, 1987.
pp.706–709.
(Also as Report JET–P(87)23, pp.93–96.)

87. Modelling of isotope exchange experiments in JET.
Ehrenberg J.
Journal of Nuclear Materials vol.145–147 February (II) 1987 (Procs. 7th Int. Conf. on Plasma–Surface Interactions in Controlled Fusion Devices, Princeton, 5–9 May 1986)
pp.551–555.

88. Recycling of impurities at the JET limiters.
Ehrenberg J., Stott P.E., Behrisch R., de Kock L., McCracken G.M.
Journal of Nuclear Materials vol.145–147 February (II) 1987 (Procs. 7th Int. Conf. on Plasma–Surface Interactions in Controlled Fusion Devices, Princeton, 5–9 May 1986)
pp.621–625.

89. The redistribution of metals on the JET vessel wall.
Ehrenberg J., Behrisch R., Coad J.P., de Kock L., Martinelli A.P., Goodall D.H.J., McCracken G.M.
Journal of Nuclear Materials vol.145–147 February (II) 1987 (Procs. 7th Int. Conf. on Plasma–Surface Interactions in Controlled Fusion Devices, Princeton, 5–9 May 1986)
pp.741–746.

90. First measurements with a neutron time–of–flight spectrometer on the JET–tokamak.
Elevant T., Olsson M., Grosshoeg G., Lorenzen J., Sadler G., van Belle P.
American Physical Society. Bulletin.
vol.32 no.9 October 1987 (Program of the 29th Ann. Mtg. Div. Plasma Phys., San Diego, 2–6 November 1987. Abstracts.)
p.1870, 6W 4.

91. Stochastic stability of a plasma torus.
Elsasser K., Duchs D., Sack Ch.
Physics Letters. Series A
vol.120 no.2 2 February 1987
pp.57–63.

92. Indirect studies of erosion and deposition on graphite probes in the limiter shadow in tokamaks.
Emmoth B., Bergsaker H., Nagata S., Wienhold P., Coad J.P.
Controlled fusion and plasma physics. 14th Euro. Conf., Madrid, 22–26 June 1987. Contributed papers. Part 2. European Physical Society, 1987.
pp.728–731.

93. Wall effects and impurities in JET.
Engelhardt W.
Royal Society. Philosophical Transactions. Series A
vol.322 no.1563 29 June 1987 (The JET Project and the prospects for controlled nuclear fusion: Discussion held 12–13 March 1986)
pp.79–94.

94. The Dependence of Tokamak Edge Conditions on Global Plasma Parameters in JET
Erents S.K., Tagle J.A., McCracken G.M., Strangeby P.C., de Kock L.
Joint European Torus JET
Report JET-R(87)53

95. Density and temperature changes in the JET edge plasma due to neutral beam injection.
Erents S.K., Tagle J.A., McCracken G.M.
Controlled Fusion and Plasma Physics: 14th European Conference, Madrid, 22–26 June 1987. Contributed papers, part 2 European Physical Society, 1987.
pp.740–743.
(Also as ReportJET–P(87)23, pp.25–28.)

96. Plasma electron density measurements from the JET 2 mm wave interferometer.
Fessey J.A., Gowers C.W., Hugenholtz C.A.J., Slavin K.
Journal of Physics E. Scientific Instruments vol.20 no.2 February 1987
pp.169–174.

97. Comments on ICRH Current Drive in JET
Fried B., Hellsten T., Moreau D.
Joint European Torus JET
Report JET-P(87)47

98. Computer-to-process interface in JET's control and diagnostic systems.
Fullard K., Dorling S.E., van Montfoort J.E.
Fusion Technology 1986, Procs. 14th Symposium, Avignon, 8-12 September 1986. Vol.2. Oxford, Pergamon for the Commission of the European Communities, 1986.
pp.1467-1472.

99. Effects on Doppler Profiles in Beam-heated Plasmas
Fussman G.
Joint European Torus JET
Report JET-P(87)62

100. Neutral particle emission during ICRF heating experiment in JET.
Giannella R., Barbato E., Corti S., Zanza V., Bracco G., Gambier D. J.
Joint European Torus JET. June 1987.
28p.
ReportJET-P(87)30
Submitted to Nuclear Fusion.

101. High Resolution X-ray Spectroscopy at JET
Gianella R.
Joint European Torus JET
Report JET-P(87)53

102. Resistively heated plasma in JET: characteristics and implications.
Gibson A.
Royal Society. Philosophical Transactions. Series A
vol.322 no.1563 29 June 1987 (The JET Project and the prospects for controlled nuclear fusion: Discussion held 12-13 March 1986)
pp.67-78.

103. Summary on tokamak experiments.
Gibson A.
Plasma physics and controlled nuclear fusion research, 11th Int. Conf., Kyoto, 13-20 November 1986.
Vienna, IAEA, 1987.
Vol.3, pp.479-495.
(Also as ReportJET-P(87)01)

104. Plasma Physics and Controlled Nuclear Fusion Research (Summaries of the 11th IAEA Int. Conf., Kyoto, 13-20 November 1986).
Gibson A., Hancox R., and others
Nuclear Fusion
vol.27 no.3 March 1987
pp.481-516.

105. Performance of the first JET neutral beam injector.
Goede A. P. H., Challis C., Jones T. T. C., Stabler A., Stork D., Thompson E.
Fusion Technology 1986, Procs. 14th Symposium, Avignon, 8-12 September 1986.
Vol.2. Oxford, Pergamon for the Commission of The European Communities, 1986.
pp.1139-1144.

106. Engineering, Manufacture and Test of the Bending Magnets of the JET Neutral Beam Injector
Goede A. P. H., Neilsen B. R., Shone F., Sønderskov T., Thompson E.
Joint European Torus JET
Report JET-P(87)60

107. Physics Design of the Deflection Magnets of the JET Neutral Beam Injector
Goede A. P. H., Neilson B. R., Thompson E.
Joint European Torus JET
Report JET-P(87)63

108. Control of density profile and particle exhaust in JET.
Gondhalekar A., Cheetham A., Cohen S. A., Houlberg W., Jones T. T. C., Morgan P. D., O'Rourke J., Sonnenberg K., Watkins M.
American Physical Society. Bulletin.
vol.32 no.9 October 1987 (Program of the 29th Ann. Mtg. Div. Plasma Phys., San Diego, 2-6 November 1987. Abstracts.)
p.1838, 5V 9.

109. Pellet fuelling of JET plasma during ohmic, ICRF and NBI heating.
Gondhalekar A., Bures M., Campbell D., Cheetham A., Cohen S. A., Cordey J. G., Corti S., Edwards A. W., Ehrenberg J., Gill R. D., Granetz R., Hendriks F., Houlberg W., Jackel H., Jones T. T. C., Keilhacker M., Magyar G., Mantica P., Mertens V., Morgan P. D., Nielsen P., O'Rourke J., Sadler G., Schuller F. C., Stamp M. F., Tanga A., Thomas P. R., Watkins M. L., Weller A.
Plasma physics and controlled nuclear fusion research, 11th Int. Conf., Kyoto, 13-20 November 1986.
Vienna, IAEA, 1987.
Vol.3, pp.457-466.
(Also as ReportJET-P(86)44)

110. The tritium safety programme at JET.
Gordon C W
Joint European Torus JET. November 1986.
11p.
ReportJET-P(86)41
Presented at IAEA Technical Committee Meeting on Fusion Reactor Safety, Culham Laboratory, 3 November 1986.

111. Calculation of the classical triton burn-up in JET deuterium plasmas.
Gorini G., Batistoni P., Bittoni E., Kallne J., Podda S., Taroni A.
Joint European Torus JET. July 1987.
18p.
ReportJET-P(87)35
Submitted to Nuclear Fusion

112. Practical ways of profile control. Summary of the Session. 5th Euro. Tokamak Programme Workshop, Toledo, Spain, 17-19 December 1986.
Gormezano C.
Joint European Torus, JET. February 1987.
12p.
ReportJET-P(87)09

113. First T_e profile results from the JET Lidar-Thomson scattering system.
Gowers C., Brown B., Gadd A., Gadeberg M., Hirsch K., Murmann H., Nielsen P., Salzmann H., Schrodter C.
Controlled Fusion and Plasma Physics: 14th European Conference, Madrid, 22-26 June

1987. Contributed papers, part 3 European Physical Society, 1987.
pp.1236-1239.
(Also as ReportJET-P(87)23, pp.57-60.)
114. The JET Lidar Thomson scattering system.
Gowers C., Gadeberg M., Hirsch K., Nielsen P., Salzmann H., Schrodter C., Brown B., Costley A.E., Edwards B., Rand D.
JET papers presented to Workshop on High Temperature Plasma Diagnostics, Varenna, Italy, September 1986.
Joint European Torus, JET. 1986.
pp.29-37.
ReportJET-P(86)45
115. Study of MHD phenomena in JET with small-signal X-ray imaging.
Granetz R.S., Edwards A.W., Gill R.D., Weller A.
Controlled Fusion and Plasma Physics: 14th European Conference, Madrid, 22-26 June 1987. Contributed papers, part 3
European Physical Society, 1987.
pp.1256-1259.
(Also as ReportJET-P(87)23, pp.141-144.)
116. X-Ray Tomography on JET
Granetz R., Smeulders P.
Joint European Torus JET
Report JET-P(87)49
117. X-ray tomography and new physics results from JET.
Granetz R.S., Edwards A.W., Gill R.D., Weller A., Wesson J.
JET papers presented to Workshop on High Temperature Plasma Diagnostics, Varenna, Italy, September 1986.
Joint European Torus, JET. 1986.
pp.58-63.
ReportJET-P(86)45
118. Operating Experience with JET 1983-1986
Green B.J., Chuilon P., Noble B., Saunders R., Webberley D.
Joint European Torus JET
Report JET-R(87)09
119. Results of the Joint European Torus
Green B.J.
Joint European Torus JET
Report JET-R(87)06
120. Analysis of theoretical problems for ICRF heating in tokamaks.
Hellsten T., Appert K., Vaclavik J., Villard L.
Joint European Torus JET. 1987.
45p.
Report JET-R(87)09
121. Power deposition for ion cyclotron heating in large tokamaks.
Hellsten T., Villard L.
Joint European Torus, JET. June 1987.
22p.
ReportJET-P(87)29
Submitted for publication in Nuclear Fusion
122. Simplified model for ICRH power deposition in large tokamaks.
Hellsten T., Villard L.
Controlled Fusion and Plasma Physics: 14th European Conference, Madrid, 22-26 June 1987. Contributed papers, part 3
European Physical Society, 1987.
pp.1000-1003.
(Also as Report JET-P(87)23, pp.161-164.)
123. Primary vacuum pumps for the fusion reactor fuel cycle.
Hemmerich J.L.
Joint European Torus JET. 1987.
29p.
Report JET-P(87)03
124. The JET pulse termination network.
How J.A., Browne M.L., Cooper S.R., Green B.J., Lomas P.J., Noll P., Schuller F.C., Steed C.A., Tilley M., van der Beken H.
Fusion Technology 1986, Procs. 14th Symposium, Avignon, 8-12 September 1986.
Vol.2. Oxford, Pergamon for the Commission of the European Communities, 1986.
pp.1421-1426.
125. Operation of the magnet power supplies. Reliability and improvements.
Huart M., Moissonnier A., Eriksson T., Raymond C.
Fusion Technology 1986, Procs. 14th Symposium, Avignon, 8-12 September 1986.
Vol.1. Oxford, Pergamon for the Commission of the European Communities, 1986.
pp.883-890.
126. Electron density measurements on JET using a microwave reflectometer.
Hubbard A.,Costley A.E., Fessey J.A., Prentice R., Ward D.
JET papers presented to Workshop on High Temperature Plasma Diagnostics, Varenna, Italy, September 1986.
Joint European Torus, JET. 1986. pp.22-28.
ReportJET-P(86)45
127. A simple fixed-frequency reflectometer for plasma density profile measurements on JET.
Hubbard A.E., Costley A.E., Gower C.W.
Journal of Physics E. Scientific Instruments vol.20no.4April 1987
pp.423-427.
128. Alpha particle diagnostics. Progress report December 1985-June 1986.
Hughes T.P.
Joint European Torus JET. 1986.
27p.
Report JET-R(86)10
129. Calculations of Thomson scattering functions for alpha-particle diagnostics in JET plasmas.

Hughes T.P., Smith S.R.P.
Joint European Torus, JET. September 1987.
13p.
ReportJET-P(87)46
Submitted for publication in Nuclear Fusion

130. Heat transport in partially stochastic tokamak magnetic fields.
Hugon M., Brusati M., Lallia P.P., Rebut P-H.
Joint European Torus JET. April 1987.
9p.
ReportJET-P(87)13
Presented at the 7th Int. Conf. on Plasma Physics, Kiev, April 1987.

131. The JET Machine: Design, construction, and operation of the major systems
Huguet M., Dietz K., Hemmerich J.L., Last J.R.
Fusion Technology
vol.11 No.1 January 1987 (Special issue on design, construction, and first operational experience on the Joint European Torus (JET))
pp.43-70

132. Design, manufacture and assembly of the JET machine.
Huguet M.
Royal Society. Philosophical Transactions. Series A
vol.322 no.1563 29 June 1987 (The JET Project and the prospects for controlled nuclear fusion: Discussion held 12-13 March 1986)
pp.31-46.

133. Technical aspects of the new JET development plan.
Huguet M.
Fusion Technology 1986, Procs. 14th Symposium, Avignon, 8-12 September 1986.
Vol.1. Oxford, Pergamon for the Commission of the European Communities, 1986.
pp.253-262.

134. Feasibility of Alpha particle diagnostic by collective microwave scatering in tokamak fusion experiments
Hutchinson I.
Joint European Torus JET
Report JET-R(87)07

135. Additional heating experiments on JET with ion-cyclotron waves.
Jacquinot J., Bhatnagar V., Brinkschulte H., Bures M., Corti S., Cottrell G.A., Evrand M., Gambier D., Kaye A., Lallia P.P., Sand F., Schueller C., Tanga A., Thomsen K., Wade T.
Royal Society. Philosophical Transactions. Series A
vol.322 no.1563 29 June 1987 (The JET Project and the prospects for controlled nuclear fusion: Discussion held 12-13 March 1986)
pp.95-107.

136. High power ICRF heating in JET.
Jacquinot J.
American Physical Society. Bulletin.
vol.32 no.9 October 1987 (Program of the 29th Ann. Mtg. Div. Plasma Phys., San Diego, 2-6 November 1987. Abstracts.)
p.1713, 11 6.

137. Plans for current profile control in JET.
Jacquinot J., Gormezano C., Rebut P-H., Bosia G., Anderson R.J., Brinkschulte H., Cordey J.G., David C., Dobbing J.A., Kaye A.S., Moreau D., Wade T.J.
Fusion Technology 1986, Procs. 14th Symposium, Avignon, 8-12 September 1986.
Vol.1. Oxford, Pergamon for the Commission of the European Communities, 1986.
pp.287-298.

138. Results of RF heating on JET and future prospects.
Jacquinot J., Bosia G., Bures M., Cottrell G.A., Gormezano C., Hellsten T., Kaye A.S., Moreau D., Sand F., Start D.F.H., Thomas P.R., Thomsen K., Wade T., and others
Joint European Torus JET. May 1987.
10p.
ReportJET-P(87)21
Paper presented at the 7th APS Topical Conf. on Application of RF Power to Plasmas, Kissimmee, Florida, 4-6 May 1987.

139. Power balance in the bulk plasma and in the scrape-off layer during H and L mode divertor discharges in JET.
Jaeckel H.J., Harbour P.J., Gottardi N., Deksnis E.B., Morgan P.D., Summers D.D.R., Tagle J.A.
Controlled Fusion and Plasma Physics: 14th European Conference, Madrid, 22-26 June 1987. Contributed papers, part 2 European Physical Society, 1987.
pp.718-721.
(Also as ReportJET-P(87)23, pp.21-24.)

140. Determination of the deuterium plasma density ratio n(sub d)/n(sub e) through neutron measurements.
Jarvis O.N., Gorini G., Kallne J., Merlo V., Sadler G., van Belle P.
Nuclear Fusion
vol.27 no.11 November 1987
pp.1755-1763.
(Also as ReportJET-P(87)08)

141. Effect of the magnetic field on fusion reaction rates.
Jarvis O.N.
Plasma Physics and Controlled Fusion
vol.29 no.7 July 1987
p.949.

142. Ion temperature measurements using neutron spectrometry.

Jarvis O.N., Corti S., Hone M., Gorini G., Kallne J., Merlo V., Morgan P.D., Sadler G., van Belle P.
Controlled Fusion and Plasma Physics: 14th European Conference, Madrid, 22-26 June 1987. Contributed papers, part 3 European Physical Society, 1987.
pp.1220-1223.
(Also as Report JET-P(87)23, pp33-36.)

143. Meeting report: Summary of the Workshop on Alpha-Particle Diagnostics, Abingdon, UK, 9-10 December 1986.
Jarvis O.N., Costley A.E.
Fusion Technology
vol.12 no.1 July 1987
pp.169-171.

144. Photoneutron Production Accompanying Plasma Disruptions
Jarvis O.N., Sadler G., Thompson J.L.
Joint European Torus JET
Report JET-P(87)50

145. Time resolved measurement of triton burn-up in beam heated deuterium plasmas.
Jarvis O.N., Conroy S., Sadler G., Huxtable G.
American Physical Society. Bulletin.
vol.32no.9October 1987 (Program of the 29th Ann. Mtg. Div. Plasma Phys., San Diego, 2-6 November 1987. Abstracts.)
p.1838, 5V 13.

146. Fusion Product Measurements in JET
Jarvis O.N.
Joint European Torus JET
Report JET-R(87)15

147. Large transporters for teleoperation on JET.
Jones P.D.F., Raimondi T.
Joint European Torus, JET. 1987.
7p.
ReportJET-P(87)41

148. Neutral beam and edge fuelling effects in JET discharges.
Jones T.T.C., Thompson E., Gondhalekar A., Lomas P.J., Morgan P.D., O'Rourke J., Stork D.
Controlled fusion and plasma physics. 14th Euro. Conf., Madrid, 22-26 June 1987. Contributed papers. Part 1.
European Physical Society, 1987.
pp.17-20.
(Also as ReportJET-P(87)23, pp.101-104.)

149. X-ray spectroscopy in fusion research.
Kallne E., Kallne J.
Physica Scripta vol.T171987 (Procs. 8th Int. Conf. on Vacuum Ultraviolet Radiation Physics, Lund, Sweden, 4-8 August 1986)
pp.152-165.

150. Measurement of the burn-up of fast ^{3}He and ^{3}H ions in deuterium plasmas.
Kallne J., Gorini G., Jarvis O.N., Martin G., Merlo V., Sadler G., van Belle P.
Physica Scripta vol.T161987(The Role of Alpha Particles in Magnetically Confined Fusion Plasmas, Aspenasgarden, Goteborg, Sweden, 24-27 June 1986)
pp.160-170.
(Also as Report JET-P(86)34)

151. Radio-frequency heating system
Kaye A., Jaquinot J., Lallia P., Wade T.
Fusion Technology.Vol.11 No.1 January 1987 (Special issue on design, construction, and the first operational experience on the Joint European Torus (JET))
pp.203-234

152. Dr. Hans-Otto Wüster, 1927-1985: An appreciation and dedication.
Keen B.E.
Fusion Technology, Vol.11 No.1 January 1987 (Special issue on design, construction, and first operational experience on the Joint European Torus (JET))
pp.9-10

153. Preface: Special issue on the Joint European Torus.
Keen B.E.
Fusion Technology, Vol.11 No.1 January 1987 (Special issue on design, construction, and first operational experience of the Joint European Torus (JET))

154. Meeting to mark the retirement of Prof. D. Palumbo (JET Joint Undertaking, Abingdon, UK, 18 June 1986)
Keen B.E.
Plasma Physics and Controlled Fusion
vol.29no.10BOctober 1987 (Symposium Procs: Meeting to mark the retirement of Prof. Donato Palumbo, JET Joint Undertaking, Abingdon, UK, 18 June 1986).
pp.1415-1417.

155. H-mode confinement in JET.
Keilhacker M., Cordey J.G., Muir D.G., Watkins M.L., Bishop C.M.
Controlled fusion and plasma physics. 14th Euro. Conf., Madrid, 22-26 June 1987. Contributed papers. Part 3.
European Physics Society. 1987.
pp.1339-1342.
(Also as Report JET-P(87)23, pp.73-76.)

156. H-mode confinement in tokamaks.
Keilhacker M.
Plasma Physics and Controlled Fusion
vol.29 no.10A October 1987 (Controlled Fusion and Plasma Physics, 14th Euro. Phys. Soc., Plasma Physics Division Conf., 22-26 June 1987, Madrid. Invited papers.)
pp.1401-1413.
(Also as Report JET-P(87)36)

157. Moment approach to flows, currents and transport in auxiliary heated tokamaks.
Kim Y.B., Callen J.D., Hamnen H.
Controlled Fusion and Plasma Physics. 14th Euro. Conf., Madrid, 22-26 June 1987. Contributed papers. Part 3.
European Physical Society, 1987.
pp.1200-1203.
(Also as Report JET-P(87)23, pp.173-176.)

158. Moment approach to neoclassical flows, currents and transport in auxiliary heated tokamaks.
Kim Y.B., Callen J.D., Hamnen H.
American Physical Society. Bulletin.
vol.32 no.9 October 1987 (Program of the 29th Ann. Mtg. Div. Plasma Phys., San Diego, 2-6 November 1987. Abstracts.)
p.1919, 8T 16.

159. Plasma current profile control in JET by lower hybrid current drive.
Knowlton S., Gormezano C., Moreau D., Anderson R.J., Bhatnagar V.P., Bosia G., Brinkschulte H., David C., Dobbing J.A., Jacquinot J., Kaye A.S., Pain M., Start D.F.H.
Controlled Fusion and Plasma Physics: 14th European Conference, Madrid, 22-26 June 1987. Contributed papers, part 3
European Physical Society, 1987.
pp.827-830.
(Also as Report JET-P(87)23, pp.89-92.)

160. Experimental test of 6 mm diameter D_2 pellets produced by in situ condensation.
Lafferranderie J., Claudet G., Disdier F., Kupschus P., Sonnenberg K.
Commissariat a l'Energie Atomique.
September 1986.
8p.
Report CEA-CONF-8744
Paper presented at 14th Symp. on fusion technology (SOFT-14), Avignon, 8-12 September 1986.

161. Full power in the European tokamak.
Lallia P.P., Hugon M.
La Recherche. In French
vol.18no.189June 1987
pp.840-843.

162. Overview on 1986 JET results by the JET Team.
Lallia P.P.
Joint European Torus JET. February 1987.
12p.
ReportJET-P(87)06
Paper presented at 5th Euro. Tokamak Programme Workshop, Toledo, 17-19 December 1986.
To be published in Plasma Physics and Controlled Fusion.

163. Tritium compatibility measurements of turbomolecular pump oil in a miniaturised viscosimeter.
Lasser R., Klatt K-H., Triefenbach D., Hemmerich J.L.
Journal of Nuclear Materials
vol.148no.2April 1987
pp.145-147.

164. The JET magnets: operational experience and plans for upgrade.
Last J.R., Cacaut D., Zwart J.W.
Fusion Technology 1986, Procs. 14th Symposium, Avignon, 8-12 September 1986. Vol.2. Oxford, Pergamon for the Commission of the European Communities, 1986.
pp.1643-1648.

165. Determination of equilibrium global parameters from external magnetic measurements in JET discharges with auxiliary heating.
Lazzaro E., Mantica P.
Joint European Torus JET. 1987.
10p.
Report JET-P(87)42

166. Experimental Identification of Tokamak Equilibrium using Magnetic and Diamagnetic Signals
Lazzaro E., Mantica P.
Joint Europea Torus JET
Report JET-P(87)58

167. Feedback control of amplitude and frequency of disruptive modes.
Lazzaro E., Nave M.F.F.
Controlled Fusion and Plasma Physics: 14th European Conference, Madrid, 22-26 June 1987. Contributed papers, part 3
European Physical Society, 1987.
pp.1059-1062.
(Also as Report JET-P(87)23, pp.185-188.)

168. Feedback control of rotating resistive modes.
Lazzaro E., Nave M.F.F.
Joint European Torus JET. 1987.
15p.
Report JET-P(87)54

169. High current operation in JET.
Lomas P., Green B.J., How J., Malacarne M., Noll P., Schueller F.C., Snipes J., Tanga A., Thomas P.
American Physical Society. Bulletin.
vol.32no.9October 1987 (Program of the 29th Ann. Mtg. Div. Plasma Phys., San Diego, 2-6 November 1987. Abstracts.)
p.1837, 5V 3.

170. Heat pulse propagation: diffusive models checked against full transport calculations.
Lopes Cardozo N., Tubbing B., Tibone F.,Taroni A.
Joint European Torus JET. June 1987.
17p.

Submitted to Nuclear Fusion.

171. Heat pulse propagation in relation to the energy confinement in JET.
Lopes Cardozo N. J.,
Tubbing B. J. D.,Campbell D. J., Cheetham A., Gondhalekar A.
Controlled fusion and plasma physics. 14th Euro. Conf., Madrid, 22-26 June 1987. Contributed papers. Part 1.
European Physical Society. 1987.
pp.281-284.
(Also as Report JET-P(87)28, pp.65-68.)

172. The limiter as a passive diagnostic.
Lowry C. G.
JET papers presented to Workshop on High Temperature Plasma Diagnostics, Varenna, Italy, September 1986.
Joint European Torus, JET. 1986.
pp.1-6.
Report JET-P(86)45

173. Operating the JET multichannel FIR interferometer.
Magyar G., O'Rourke J.
JET papers presented to Workshop on High Temperature Plasma Diagnostics, Varenna, Italy, September 1986.
Joint European Torus, JET. 1986.
pp.139-144.
Report JET-P(86)45

174. Fluctuations during JET discharges with H-mode.
Malacarne M., Cripwell P., Duperrex P. A., Edwards A. W., Gill R. D., Granetz R. S., Simonet F., Snipes J., Weller A.
Plasma Physics and Controlled Fusion
vol.29 no.12 December 1987
pp.1675-1686.
(Also as Report JET-P(87)22)

175. Turbulent fluctuations and confinement in JET.
Malacarne M., Duperrex P. A.
Nuclear Fusion
vol.27 no.12 December 1987
pp.2113-2130.
(Also as Report JET-P(87)26)

176. JET and Industry
Maple J. H. C.
Joint European Torus JET
Report JET-R(87)05

177. 15 MeV proton emission from JET plasmas exhibiting sawtooth behaviour: results and interpretation.
Martin G., Jarvis O. N., Kallne J., Merlo V., Sadler G., van Belle P.
Physica Scripta
vol.T16 1987(The Role of Alpha Particles in Magnetically Confined Fusion Plasmas, Aspenasgarden, Goteborg, Sweden, 24-27 June 1986)
pp.171-175.
(Also as Report JET-P(86)26)

178. Carbon protection tiles for JET.
Massmann P., Deksnis E., Falter H. D., Hemsworth R. S., Shaw R., Stabler A.
Fusion Technology 1986, Procs. 14th Symposium, Avignon, 8-12 September 1986. Vol.1. Oxford, Pergamon for the Commission of the European Communities, 1986.
pp.545-551.

179. Engineering aspects of JET diagnostic systems
Millward P., Ainsworth A., Caldwell-Nichols C. J., Lobel R., Hancock C. J.
Fusion Technology, Vol.11 No.1 January 1987 (special issue on design, construction, and first operational experience on the Joint European Torus (JET))
pp.235-252

180. A Practical Experience of using Special Remote Handling Tools on JET
Mills S. F., Schreibmaier J., Tesini A., Wykes M.
Joint European Torus JET
Report JET-R(87)16

181. Design, commissioning and early operation of the power supply and protection system for the extraction grid of the JET neutral injuectors at 160kV.
Mondino P. L., Claesen R., Dobbing J. A., Baigger P. A.
Fusion Technology 1986, Procs. 14th Symposium,Avignon, 8-12 September 1986. Vol.1. Oxford, Pergamon for the Commission of the European Communities, 1986.
pp.933-939.

182. The development of the JET poloidal field power supplies to reach the nominal flux swing capability.
Mondino P. L., Bonicelli T., Huart M., Santaguistina A.
Fusion Technology 1986, Procs. 14th Symposium, Avignon, 8-12 September 1986. Vol.1. Oxford, Pergamon for the Commission of the European Communities, 1986.
pp.859-866.

183. Optimization of slow wave multijunction antennae for current drive.
Moreau D., David C., Gormzano C., Knowlton S., Anderson R. J., Bosia G., Brinkschulte H., Dobbing J. A., Jacquinot J., Kaye A. S., Pain M.
JET papers presented at the 7th APS Topical Conf. on Applications of Radio Frequency Power to Plasmas, Kissimmee, Florida, 4-6 May 1987.
Joint European Torus, JET. 1987.
pp.5-8.

Report JET-P(87)40

184. Potentiality of fast wave current drive in non-Maxwellian plasmas.
Moreau D., Start D.F.H., O'Brien M.R., Cox M.
Controlled fusion and plasma physics. 14th Euro. Conf., Madrid, 22-26 June 1987. Contributed papers. Part 3. European Physical Society, 1987.
pp.1007-1010.

185. Visible radiation studies on JET using a multi-chord poloidal array.
Morgan P.D., O'Rourke J.J.
Controlled Fusion and Plasma Physics: 14th European Conference, Madrid, 22-26 June 1987. Contributed papers, part 3
European Physical Society, 1987.
pp.1240-1243.
(Also as Report JET-P(87)23, pp.129-132.)

186. Mode locking in tokamaks.
Nave M.F.F., Wesson J.A.
Controlled Fusion and Plasma Physics: 14th European Conference, Madrid, 22-26 June 1987. Contributed papers, part 3
European Physical Society, 1987.
pp.1103-1106.
(Also as Report JET-P(87)23, pp.177-180.)

187. Stability of the ideal m = 1 mode in a tokamak.
Nave M.F.F., Wesson J.A.
Fusion Theory Meeting, Wepion, Belgium, 16-18 June 1986. Abstracts. p.22.
(Also as Report JET-P(87)31)

188. JET electron temperature and density profile evolution from the LIDAR Thomson scattering system during auxiliary heating and pellet injection.
Nielsen P., Gadd A., Gowers C., Hirsch K., Salzmann H.
American Physical Society. Bulletin. vol.32 no.9 October 1987 (Program of the 29th Ann. Mtg. Div. Plasma Phys., San Diego, 2-6 November 1987. Abstracts.)
p.1839, 5V 14.

189. Operation and performance of the large scale JET cryopump system.
Obert W., Haange R., Jones A., Kussel E., Mayaux C., Roberts R.
Fusion Technology 1986, Procs. 14th Symposium, Avignon, 8-12 September 1986. Vol.1. Oxford, Pergamon for the Commission of the European Communities, 1986.
pp.479-486.

190. Modelling of pellet injection experiments with Onsager-symmetric transport relations.
O'Rourke J.
Nuclear Fusion
vol.27 no.12 December 1987
pp.2075-2083.

191. The JET X-ray pulse height analysis system.
Pasini D., Gill R.D., Holm J., van der Goot E., Weller A.
Joint European Torus JET. July 1987.
18p.
Report JET-P(87)32
Submitted to Review of Scientific Instruments

192. The X-ray pulse height analysis system at JET.
Pasini D., Gill R.D., Holm J., MacFadyen A., van der Goot E., Weller A., Denne B., Gowers C.W., Morgan P.D., Tallents G.J.
JET papers presented to Workshop on High Temperature Plasma Diagnostics, Varenna, Italy, September 1986.
Joint European Torus, JET. 1986.
pp.44-49.
Report JET-P(86)45

193. The JET Project and Prospects for Controlled Nuclear Fusion
Editors: Pease R.S., Bickerton R.J., Keen B.E.
Publishers: The Royal Society (1987)

194. High frequency magnetic measurements in JET plasmas during auxiliary heating.
Pochelon A., de Kock L.C., Duperrex P.A., Keller R.
American Physical Society. Bulletin.
vol.32 no.9 October 1987 (Program of the 29th Ann. Mtg. Div. Plasma Phys., San Diego, 2-6 November 1987. Abstracts.)
p.1838, 5V 12.

195. The JET multichannel reflectometer.
Prentice R., Costley A.E., Fessey J.A., Hubbard A.E.
JET papers presented to Workshop on High Temperature Plasma Diagnostics, Varenna, Italy, September 1986.
Joint European Torus, JET. 1986.
pp.7-15.
Report JET-P(86)45

196. The design and manufacture of television systems for inspection and maintenance in the JET torus.
Quartly J., Galbiati L.
ANS Transactions vol.55 November 1987 (1987 Winter Meeting, Los Angeles, California, 15-19 November 1987)
pp.666-668.

197. Design and operation of the remote maintenance system in JET.
Raimondi T.
Joint European Torus JET. 1987.
8p.
Report JET-P(87)02
To be published in Procs. of ANS Remote Systems and Robotics in Hostile Environments, Pasco, USA, 29 March - 2 April 1987.

198. The JET in-vessel inspection system.

Raimondi T., Cusack R., Galbiati L.
Fusion Technology 1986, Procs. 14th Symposium, Avignon, 8-12 September 1986. Vol.2. Oxford, Pergamon for the Commission of the European Communities, 1986. pp.1833-1838.

199. JET XUV spectroscopy: first results.
Ramette J., Behringer K., Denne B., Griffin W., Hawkes N.C., Magyar G., Mattioli M., Peacock N.J., Saoutic B., Schwob J.L.
Controlled Fusion and Plasma Physics: 14th European Conference, Madrid, 22-26 June 1987. Contributed papers, part 3 European Physical Society, 1987. pp.1244-1247.
(Also as Report JET-P(87)23, pp.133-136.)

200. Electron heat transport in tokamaks.
Rebut P.H., Watkins M.L., Lallia P.P.
Controlled fusion and plasma physics. 14th Euro. Conf., Madrid, 22-26 June 1987. Contributed papers. Part 1. European Physical Society, 1987. pp.172-172C.
(Also as Report JET-P(87)23, pp.125-128.)

201. The history and future of the JET fusion programme.
Rebut P-H.
Plasma Physics and Controlled Fusion vol.29 no.10B October 1987 (Symposium Procs: Meeting to mark the retirement of Prof. Donato Palumbo, JET Joint Undertaking, Abingdon, UK, 18 June 1986). pp.1419-1424.

202. Magnetic islands and chaos induced by heat flow.
Rebut P-H., Brusati M., Hugon M., Lallia P.
Plasma Physics and Controlled Nuclear Fusion Research, 11th Int. Conf., Kyoto, 13-20 November 1986. Vol.2. Vienna, IAEA. 1987. pp.187-196.
(Also as Report JET-P(86)44)

203. The JET experiment: Evolution, present status and prospects
Rebut P-H., Keen B.E.
Fusion Technology, Vol.11 No.1 January 1987 (Special issue on design, construction, and first experience on the Joint European Torus (JET)) pp.13-42

204. JET: evolution, status and prospects.
Rebut P-H., Lallia P.
Royal Society. Philosophical Transactions. Series A vol.322 no.156329 June 1987 (The JET Project and the prospects for controlled nuclear fusion: Discussion held 12-13 March 1986) pp.17-30.

205. JET latest results and implications for a reactor.
Rebut P-H., Lallia P.P.
Joint European Torus JET. April 1987. 24p.
Report JET-P(87)15
Paper presented to 7th Int. Conf. on Plasma Physics, Kiev, 6-10 April 1987.

206. Erosion of long-term wall samples in JET.
Roth J., Ehrenberg J., Wittmaack K., Coad J.P., Roberto J.B.
Journal of Nuclear Materials vol.145-147 February (II) 1987 (Procs. 7th Int. Conf. on Plasma-Surface Interactions in Controlled Fusion Devices, Princeton, 5-9 May 1986) pp.383-386.

207. Observation of fusion reaction gamma-rays in JET.
Sadler G., Jarvis O.N., van Belle P., Hawkes N., Syme D.B.
Controlled Fusion and Plasma Physics: 14th European Conference, Madrid, 22-26 June 1987. Contributed papers, part 3 European Physical Society, 1987. pp.1232-1235.
(Also as Report JET-P(87)23, pp.45-48.)

208. An electron cyclotron emission diagnostic for the edge region of the JET plasmas.
Salmon N.A., Bartlett D.V., Costley A.E.
JET papers presented to Workshop on High Temperature Plasma Diagnostics, Varenna, Italy, September 1986.
Joint European Torus, JET. 1986. pp.70-77.
Report JET-P(86)45

209. High resolution T(sub e) measurements in JET and their application to the study of the edge plasma and density limit disruptions.
Salmon N.A., Bartlett D.V., Costley A.E., Hugon M.
Controlled Fusion and Plasma Physics: 14th European Conference, Madrid, 22-26 June 1987. Contributed papers, part 3 European Physical Society, 1987. pp.1248-1251.
(Also as Report JET-P(87)23, pp.49-52.)

210. First results from the LIDAR Thomson scattering system on JET.
Salzmann H., Hirsch K., Nielsen P., Gowers C., Gadd A., Gadeberg M., Murmann H., Schrodter C.
Nuclear Fusion vol.27 no.11 November 1987 pp.1925-1928.
(Also as Report JET-P(87)16)

211. Experimental and theoretical studies of harmonic ICRF heating on JET.
Sand F., Cottrell G.A., Bhatnagar V.P., Bures M., Cordey J.G., Core W., Corti S.,

Hamnen H., Hellsten T., Jacquinot J., Start D.F.H., Thomas P.H., Watkins M.
Controlled Fusion and Plasma Physics: 14th European Conference, Madrid, 22-26 June 1987. Contributed papers, part 3 European Physical Society, 1987.
pp.801-804.
(Also as Report JET-P(87)23, pp.81-84.)

212. XUV Spectroscopy in JET during the Second Semester 1986
Saoutic B., Ramette J., Mattioli M., Denne B., Behringer K., Magyar G., Peacock N., Ravestien A., Schwob J.L., Sieweke F., Talbot A.
Joint European Torus JET
Report JET-R(87)14

213. Coulomb collision rates for slide-away distributions.
Schamel H.K., Duchs D.F.
Fusion Theory Meeting, Wepion, Belgium, 16-18 June 1986. Abstracts.
p.51.

214. The high voltage grid interface in present and future JET operational requirements.
Selin K.I., Ciscato D., Marchese V., Ashmole P., Jervis B.
Fusion Technology 1986, Procs. 14th Symposium, Avignon, 8-12 September 1986. Vol.1. Oxford, Pergamon for the Commission of the European Communities, 1986.
pp.867-874.

215. Hollow profiles during the H-mode in JET.
Smeulders P., Brusati M., Gottardi N., Lazzaro E., Nowak S., Rimini F.
American Physical Society. Bulletin.
vol.32 no.9 October 1987 (Program of the 29th Ann. Mtg. Div. Plasma Phys., San Diego, 2-6 November 1987. Abstracts.)
p.1837, 5V 7.

216. Locked n=1 modes in JET.
Snipes J.A., Campbell D.J., Lopes Cardozo N., Hugon M., Haynes P.S., Hender T.C.
Controlled fusion and plasma physics. 14th Euro. Conf., Madrid, 22-26 June 1987. Contributed papers. Part 1. European Physical Society, 1987.
pp.69-72.
(Also as Report JET-P(87)23, pp.1-4.)

217. Wall concepts and density control for JET.
Sonnenberg K., Dietz K.J., Kupschus P.
Fusion Technology 1986, Procs. 14th Symposium, Avignon, 8-12 September 1986. Vol.1. Oxford, Pergamon for the Commission of the European Communities, 1986.
pp.273-285.

218. Impurity influx behaviour in JET.
Stamp M.F., Behringer K.H., Morgan P.D., Summers H.P., Forrest M.J.
Journal of Nuclear Materials
vol.145-147February (II) 1987 (Procs. 7th Int. Conf. on Plasma-Surface Interactions in Controlled Fusion Devices, Princeton, 5-9 May 1986)
pp.236-240.

219. Edge probes.
Stangeby P.C.
Journal of Nuclear Materials
vol.145-147February (II) 1987 (Procs. 7th Int. Conf. on Plasma-Surface Interactions in Controlled Fusion Devices, Princeton, 5-9 May 1986)
pp.105-116.

220. Measurements of the Cross-Field Diffusion Coefficient $D_\perp$ in the Edge Plasma of JET
Stangeby P.C., Tagle J.A., Erents S.K.
Joint European Torus JET
Report JET-P(87)57

221. Monte Carlo Modelling of Impurity Ion Transport for a Limiter Source/Sink
Stangeby P.C., Farrell C., Hoskins S., Wood L.
Joint European Torus JET
Report JET-P(87)61

222. Interpretation of Langmuir, heat-flux, deposition, trapping and gridded energy analyser probe data for impure plasmas.
Stangeby P.C.
Journal of Physics D. Applied Physics
vol.20 no.1114 November 1987
pp.1472-1478.

223. Monte Carlo modeling of impurity transport for a limiter source/sink.
Stangeby P.C., Wood L., Hoskins S.
Controlled fusion and plasma physics. 14th Euro. Conf., Madrid, 22-26 June 1987. Contributed papers. Part 2.
European Physical Society, 1987.
pp.714-717.

224. Prolonged sawtooth-free periods in JET during central ICRH experiments.
Start D.F.H., Bartlett D.V., Bhatnagar V.P., Bures M., Campbell D.J., Cottrell G.A., Evrard M.P., Gambier D., Gormezano C., Hamnen H., Hellsten T., Jacquinot J., Kaye A.S., Lazzaro E., Morgan P.D., O'Rourke J., Sand F., Snipes J., Thomas P.R., Tubbing B.J.D., Wade T.J., Wesson J.A.
JET papers presented at the 7th APS Topical Conf. on Applications of Radio Frequency Power to Plasmas, Kissimmee, Florida, 4-6 May 1987.
Joint European Torus, JET. 1987.
pp.1-4.
Report JET-P(87)40

225. Momentum transport and scaling effects

observed in neutral beam heated rotating plasmas in JET.
Stork D., Boileau A., Bombarda F., Campbell D.J., Challis C., Core W.G., Denne B., Duperrex P., Giannella R., Horton L., Jones T.T.C., Kallne E., Pochelon A., Ramette J., Saoutic B., Schram D., Snipes J., Tallents G., Thompson E., Tonetti G., von Hellerman M., Wesson J.
Controlled fusion and plasma physics. 14th Euro. Conf., Madrid, 22-26 June 1987. Contributed papers. Part 1.
European Physical Society. 1987.
pp.306-309.
(Also as Report JET-P(87)23, pp.105-108.)

226. Overview and operation of the control, safety and interlock on the JET neutral beam injector.
Stork D., Jones T.T.C., Burt A., Cooper D., Davies J.F., Ewers D.T., Krom J.G., McCullen P., Nijman J.P., Stabler A., Starley K.D., Young D., Young I.D.
Fusion Technology 1986, Procs. 14th Symposium, Avignon, 8-12 September 1986. Vol.2. Oxford, Pergamon for the Commission of the European Communities, 1986.
pp.1451-1459.

227. Plasma measurements for JET.
Stott P.E.
Royal Society. Philosophical Transactions. Series A vol.322 no.1563 29 June 1987 (The JET Project and the prospects for controlled nuclear fusion: Discussion held 12-13 March 1986)
pp.47-65.
(Also as Report JET-P(86)48)

228. Recent results from the JET experiment.
Stott P.E.
American Physical Society. Bulletin. vol.32 no.4 20-23 April 1987 (Program of the 1987 Spring Meeting, Arlington, Virginia, 20-23 April 1987)
Abstract JC 2, p.1103.

229. Review of JET diagnostics and results.
Stott P.E.
Joint European Torus JET. 1986.
22p.
Report JET-P(87)04
Presented at the Course on Basic and Advanced Fusion Plasmas Diagnostic Techniques, Varenna, 1986.

230. Book review: Numerical simulation of plasmas, Springer series in Computational Physics, by Y.N.Dnestrovskii and D.P.Kostomarov.
Stringer T.E., reviewer
Plasma Physics and Controlled Fusion vol.29 no.9 September 1987
p.1169.

231. Thermography of carbon first walls and limiters in JET.
Summers D.
JET papers presented to Workshop on High Temperature Plasma Diagnostics, Varenna, Italy, September 1986.
Joint European Torus, JET. 1986.
pp.16-21.
Report JET-P(86)45

232. Interpretation of emission from ions out of ionisation balance.
Summers H.P., Behringer K.H., Boileau A., Horton L., Stamp M.F., von Hellerman M., Forrest M.J., Peacock N.J.
Joint European Torus JET. January 1987.
17p.
Report JET-P(86)42

233. Recombination of neon-like and adjacent ions in plasmas.
Summers H.P., Behringer K., Wood L.
Physica Scripta
vol.35 no.3 March 1987
pp.303-308.

234. Recombination and population structure.
Summers H.P., Behringer K.H., Denne B.
Joint European Torus JET. January 1987.
11p.
Report JET-P(86)43

235. Boundary layer conditions in JET during RF heating.
Tagle J.A., Brinkschulte H.W., Huld T., Stangeby P.C., de Kock L., Erents S.K., McCracken G.M., Fielding S.J.,
Journal of Nuclear Materials vol.145-147 February (II) 1987 (Procs. 7th Int. Conf. on Plasma-Surface Interactions in Controlled Fusion Devices, Princeton, 5-9 May 1986)
pp.231-235.

236. Diagnosis of the JET scrape-off layer using heat flux/Langmuir probes.
Tagle J.A., Brinkschulte H., Erents S.K., McCracken G.M.
JET papers presented to Workshop on High Temperature Plasma Diagnostics, Varenna, Italy, September 1986.
Joint European Torus, JET. 1986. pp.78-83.
Report JET-P(86)45

237. The effect of edge temperature on impurity production under a range of operating conditions in JET.
Tagle J.A., Erents S.K., McCracken G.M.Pitts R.A., Stangeby P.C., Lowry C., Stamp M.F.
Controlled Fusion and Plasma Physics: 14th European Conference, Madrid, 22-26 June 1987. Contributed papers, part 2 European Physical Society, 1987.

pp.662-665.
(Also as Report JET-P(87)23, pp.5-8.)

238. Errors in measuring electron temperatures using a single Langmuir probe in a magnetic field.
Tagle J.A., Stangeby P.C., Erents S.K.
Plasma Physics and Controlled Fusion vol.29 no.3 March 1987
pp.297-301.

239. Obtaining values of D from measurements of the edge scrape-off lengths in JET.
Tagle J.A., Lowry C., Erents S.K., Stangeby P.C.
Controlled fusion and plasma physics. 14th Euro. Conf., Madrid, 22-26 June 1987. Contributed papers. Part 2. European Physical Society, 1987.
pp.670-673.

240. X-Ray Spectroscopy of Tokamaks
Tallents G.J.
Joint European Torus JET
Report JET-P(87)56

241. Experimental studies in JET with magnetic separatrix.
Tanga A., Bartlett D.V., Behringer K., Bickerton R.J., Cheetham A., Cordey J.G.,Gibson A., Gottardi N.A., Gondhalekar A., Harbour P.J., Jaeckel H., Keilhacker M., Lazzaro E., Martens V., Noll P., Nowak S., Schuller F.C., Tagle A.J., Taroni A., Thomas P.R., Tibone F.
Plasma Physics and Controlled Nuclear Fusion Research, 11th Int. Conf., Kyoto, 13-20 November 1986. Volume 1. Vienna, IAEA. 1987.
pp.65-73.
(Also as Report JET-P(86)44)

242. Magnetic separatrix experiments in JET.
Tanga A., Behringer K.H., Costley A.E., Brusati M., Denne B., Edwards A., Gibson A., Gill R.D., Gottardi N., Granetz R., Harbour P.J., Jackel H., Keilhacker M., Lazzaro E., Malacarne M., Morgan P.D., Noll P., O'Rourke J., Stott P.E., Summers D.R., Tagle J.A., Thomas P.R.
Nuclear Fusion vol.27 no.11 November 1987
pp.1877-1895.
(Also as Report JET-P(87)11)

243. Plasma behaviour in L and H modes in JET.
Tanga A., Keilhacker M., Bartlett D., Behringer K., Christiansen J., Cordey J.G., Costley A., Gibson P., Harbour P., Lomas P., Smeulders P., Thomsen K., Watkins M.
American Physical Society. Bulletin.
vol.32 no.9 October 1987 (Program of the 29th Ann. Mtg. Div. Plasma Phys., San Diego, 2-6 November 1987. Abstracts.)
p.1837, 5V 6.

244. Simulation of transients in JET by means of predictive transport codes.
Taroni A., Tibone F.
Controlled fusion and plasma physics. 14th Euro. Conf., Madrid, 22-26 June 1987. Contributed papers. Part 1. European Physical Society, 1987.
pp.97-100.
(Also as Report JET-P(87)23, pp.165-168.)

245. A comparison between additional heating data and forms with model scale invariance.
Thomas P.R.
Joint European Torus JET. May 1987.
15p.
Report JET-P(87)17
Submitted to Nuclear Fusion

246. A simple model for hot ion plasmas.
Thomas P.R.
Japan Atomic Energy Research Institute. May 1987.
19p.
Report JAERI-M 87-064 Microfiche

247. Phenomenological and predictive studies of confinement and global heating in JET neutral beam heated limiter plasmas.
Thompson E., Bartlett D., Bombarda F., Bracco G., Campbell D.J., Challis C., Christiansen J.P., Cordey J.G., Corti S., Costley A., Duesing G., Giannella R., Goede A.P.H., Horton L., Jones T.T.C., Kallne E., Kaneko O., Lomas P.J., Muir D., Snipes J., Staebler A., Stork D., Stubberfield P.M., Tallents G., Thomas P.R., Thomsen K., von Hellerman M., Watkins M.L.
Controlled fusion and plasma physics. 14th Euro. Conf., Madrid, 22-26 June 1987. Contributed papers. Part 1. European Physical Society. 1987.
pp.310-313.
(Also as Report JET-P(87)23, pp.93-96.)

248. Confinement analysis of auxiliary heated JET discharges.
Thomsen K., Bhatnagar V., Callen J.D., Christiansen J.P., Cordey J.G., Evrard M., Gambier D., Gottardi N., Hellsten T., Muir D.G., Lomas P.J., Smeulders P., Thomas P.R.
Controlled fusion and plasma physics. 14th Euro. Conf., Madrid, 22-26 June 1987. Contributed papers. Part 1. European Physical Society, 1987.
pp.168-171.
(Also as Report JET-P(87)23, pp.109-112.)

249. Calibration methods for ECE systems with microwave sources -a feasibility study.
Tubbing B.J.D., Kissel S.E.
Joint European Torus JET. 1987.

32p.
Report JET-R(87)03

250. Electron cyclotron emission spectroscopy on thermonuclear plasmas. Instrumental aspects, calibration and applications.
Tubbing B. J. D.
Utrecht. Drukkerig Elinkwijk. 1987.
240p.
Ph.D. Thesis

251. Heat pulse propagation studies in JET.
Tubbing B. J. D., Lopes Cardozo N. J.
Joint European Torus JET. 1987.
51p.
Report JET-R(87)01

252. Tokamak heat transport - a study of heat pulse propagation in JET.
Tubbing B. J. D., Lopes Cardozo N. J., Van der Wiel M. J.
Nuclear Fusion
vol.27 no.11 November 1987
pp.1843-1855.
(Also as Report JET-P(87)12)

253. The computation of fusion product spectra from high temperature plasmas.
van Belle P., Sadler G.
JET papers presented to Workshop on High Temperature Plasma Diagnostics, Varenna, Italy, September 1986.
Joint European Torus, JET. 1986.
pp.50-57.
Report JET-P(86)45

254. CODAS: The JET control and data aquisition system
van der Berken H., Best C. H., Fullard K., Herzog R. F., Jones E. M., Steed C. A.
Fusion Technology, Vol.11 No.1 January 1987
(Special issue on design, construction, and first operational experience on the Joint European Torus (JET))
pp.120-137

255. Computer control and data acquisition at JET.
van der Beken H.
IEEE Transactions on Nuclear Science
vol.NS-34 no.4 August 1987 (5th Conf. on Real-Time Computer Applications in Nuclear, Particle and Plasma Physics, San Francisco, 12-14 May 1987).
pp.742-746.
(Also as Report JET-P(87)19)

256. Some aspects of operational reliability of the JET central interlock and safety system (CISS) in the period March 1984 to December 1986.
van Montfoort J.
Joint European Torus JET. 1987.
15p.
Report JET-R(87)04

257. Global wave calculation for the Alfven and ion-cyclotron range of frequencies in exact toroidal geometry.
Villard L., Appert K., Hellsten T., Vaclavik J.
Fusion Theory Meeting, Wepion, Belgium, 16-18 June 1986. Abstracts.p.55.

258. Present results of charge exchange recombination spectroscopy on JET and prospects for future alpha particle diagnostics.
von Hellermann M., Boileau A., Horton L., Peacock N., Schumacher U., Summers H.
Controlled Fusion and Plasma Physics: 14th European Conference, Madrid, 22-26 June 1987.
Contributed papers, part 3 European Physical Society, 1987. pp.1260-1263.
(Also as Report JET-P(87)23, pp.189-192.)

259. Charge exchange recombination spectroscopy on JET.
von Hellermann M. G., Boileau A., Horton L. D., Summers H. P., Peacock N. J.
JET papers presented to Workshop on High Temperature Plasma Diagnostics, Varenna, Italy, September 1986.
Joint European Torus, JET. 1986.
pp.64-69.
Report JET-P(86)45

260. Design and manufacture of water cooled electrostatic screens for JET ICRF antennae.
Walker C. I., Kaye A. S., Brinkschulte H., Horn R. A., Plancoulaine J., Sigournay D., Bevilacqua G., Anselmi F.
Fusion Technology 1986, Procs. 14th Symposium, Avignon, 8-12 September 1986.
Vol.1. Oxford, Pergamon for the Commission of the European Communities, 1986.
pp.807-814.

261. Non evaporable getter pumping for JET ICRF antennae.
Walker C. I., Kaye A. S., Horn R. A., Mazza F.
Fusion Technology 1986, Procs. 14th Symposium, Avignon, 8-12 September 1986.
Vol.1. Oxford, Pergamon for the Commission of the European Communities, 1986.
pp.815-820.

262. The JET project and material aspects of the machine.
Walravens M. J.
Joint European Torus JET. July 1987.
20p.
Report JET-P(87)33
Submitted to Metals and Materials

263. Sawtooth relaxations
Ward D. J.
Joint European Torus JET
Report JET-P(87)51

264. A model for pellet ablation in JET.
Watkins M. L., Houlberg W. A., Cheetham A. D., Gondhalekar A., Granetz R., Hendriks F., O'Rourke J., Stubberfield P. M.

Controlled fusion and plasma physics. 14th Euro. Conf., Madrid, 22-26 June 1987. Contributed papers. Part 1. European Physical Society, 1987.
pp.201-204.
(Also as Report JET-P(87)23, pp.121-124.)

265. A fast shutter system for the JET neutral injectors.
Watson M.J., Haange R., Stork D., Tivey R., Young D.
Fusion Technology 1986, Procs. 14th Symposium, Avignon, 8-12 September 1986. Vol.2. Oxford, Pergamon for the Commission of The European Communities, 1986.
pp.1145-1151.

266. Density perturbation at rational q-surfaces following pellet injection in JET.
Weller A., Cheetham A.D., Edwards A.W., Gill R.D., Gondhalekar A., Granetz R.S., Snipes J., Wesson J.
Controlled fusion and plasma physics. 14th Euro. Conf., Madrid, 22-26 June 1987. Contributed papers. Part 1. European Physical Society, 1987.
pp.25-28.
(Also as Report JET-P(87)23, pp.137-140.)

267. Persistent density perturbations at rational-q surfaces following pellet injection in the Joint European Torus.
Weller A., Cheetham A.D., Edwards A.W., Gill R.D., Gondhalekar A., Granetz R.S., Snipes J., Wesson J.A.
Physical Review Letters
vol.59 no.2016 November 1987
pp.2303-2306.

268. Sawtooth oscillations.
Wesson J.A., Nave M.F., Kirby P.
Plasma Physics and Controlled Nuclear Fusion Research, 11th Int. Conf., Kyoto, 13-20 November 1986. Vol.2.
Vienna, IAEA. 1987.
pp.3-10.

269. Sawtooth oscillations - understanding and control. 5th Euro. Tokamak Programme Workshop, Toledo, Spain, 17-19 December 1986.
Wesson J.A.
Joint European Torus, JET. 1987.
8p.
Report JET-P(87)14

270. Theory of sawtooth oscillations.
Wesson J.
Joint European Torus JET. November 1987.
30p.
Report JET-P(87)55
Paper presented at Workshop on Theory of Fusion Plasmas, Varenna, 24-28 August 1987.

271. Tokamaks.
Wesson J.A.
Oxford, Clarendon Press. 1987.
309p.
Oxford Engineering Science Series No.20.

272. Helium leak detection in JET in the presence of high deuterium partial pressure.
Winkel T., Hemmerich J.L.
Journal of Vacuum Science and Technology A: Vacuum, Surfaces and Films
vol.5 no.4 pt.IVJuly/August 1987 (Procs. 10th Int. Vacuum Congress, 6th Int. Conf. on Solid Surfaces, 33rd National Symp. of the American Vacuum Society, Baltimore, 27-31 October 1986).
pp.2637-2640.

273. Remote handling tools for JET.
Wykes M.
Fusion Technology 1986, Procs. 14th Symposium, Avignon, 8-12 September 1986. Vol.2. Oxford, Pergamon for the Commission of the European Communities, 1986.
pp.1839-1844.

274. JET papers presented at 12th Symposium on Fusion Engineering (SOFE), Monterey, U.S.A., 1987
Many JET Authors
Joint European Torus JET
Report JET-P(87)52

275. JET Annual report 1986. JET Joint Undertaking Abingdon, Joint European Torus JET. June 1987.
Edited by: Keen B.E., Lallia P.P., O'Hara G.W., Pollard I.E.
57p.
EUR 11114 EN(EUR-JET-AR9)

276. JET Progress report 1986. JET Joint Undertaking Abingdon, Joint European Torus JET. March 1987.
Edited and compiled by: Keen B.E.
595p.
EUR 11113 EN(EUR-JET-PR4)

277. JET papers presented at the 7th APS Topical Conference on Applications of Radio Frequency Power to Plasmas,
Kissimmee, Florida, Mat, 1987.
Many JET Authors
Joint European Torus JET
Report JET-P(87)40

278. JET contributed papers to the 14th European Conference on Controlled Fusion and Plasma Physics,
Madrid, Spain, June 1987,
Many JET Authors
Joint European Torus JET
Report JET-P(87)23

Appendix III

Reprints of JET papers

(a)	JET-P(87)04	Review of JET diagnostics and results (Invited paper at the Course on Basic and Advanced Fusion Plasma Diagnostic Techniques, Italy 1986);
(b)	JET-P(87)11	Magnetic Separatrix Experiments in JET;
(c)	JET-P(87)15	JET Latest Results and Implications for a Reactor (Invited paper presented to the 7th International Conference on Plasma Physics, Kiev, U.S.S.R., 6th -10th April 1987);
(d)	JET-P(87)21	Results of RF Heating on JET and Future Prospects (Invited paper presented to the 7th APS Topical Conference on Application of RF Power to Plasmas, Kissimmee, Florida, U.S.A., 4th -6th May 1987);
(e)	JET-P(87)23	JET Contributed papers to the 14th European Conference on Controlled Fusion and Plasma Physics, (Madrid, Spain, 22nd-26th June 1987);
(f)	JET-P(87)39	Particle Balance and Wall Pumping in Tokamaks (Invited paper at 14th European Conference on Controlled Plasma Physics, Madrid, Spain, 22nd-26th June 1987);
(g)	JET-P(87)37	Operational Limits and Confinements in JET (Invited paper presented at the 14th Conference on Controlled Fusion and Plasma Physics, Madrid, Spain, 22nd-26th June 1987);
(h)	JET-P(87)52	JET Papers Presented at 12th Symposium on Fusion Engineering (SOFE), (Monterey, U.S.A.);

Invited paper at the Course on Basic and Advanced Fusion
Plasma Diagnostic Techniques, Varenna, Italy, 1986

Review of JET Diagnostics and Results

P.E. Stott

1. Introduction

The Joint European Torus (JET) [1,2] is the largest single project of the coordinated fusion research programme of the European Atomic Energy Community (EURATOM). JET's main objective is to obtain and study plasmas in conditions and with dimensions approaching those needed for a fusion reactor (ie. $n_i \approx 2 \times 10^{20} m^{-3}$; $T_i \gtrsim 10$keV, and $\tau_E \approx 1$-2s).

Since the first operation of JET in June 1983 there has been steady progress in improving the plasma operating conditions [1]. Discharges with the full design value of the toroidal field $B_T = 3.4$T and with plasma current I_p up to 5.1MA are now obtained routinely. Experiments with ion cyclotron resonance heating (ICRH) started in 1985 with two antennas and coupled powers up to 6MW. A third antenna was added in 1986 and the coupled power is now being raised towards 9MW. These experiments use H and ^{3}He minority heating schemes in D plasmas [2,3]. Experiments with neutral beam injection heating (NBI) started in 1986 with a single beam line capable of operating at energies up to 80keV with either H° (up to 5MW) or D° (up to 9MW) of neutral beams injected into H+ or D+ plasmas [4]. The maximum total power input (ie. ohmic + ICRH + NBI)

(Invited lecture at the Course on Basic and Advanced Fusion Plasmas
Diagnostic Techniques, Varenna, Italy 1986)

into a single discharge is ~ 18MW.

With ohmic heating, peak ion and electron temperatures of 3keV and 4keV respectively are achieved with a plasma density ~ 4.2 $10^{19}m^{-3}$ and energy confinement time τ_E up to 0.8s. With ICRH the peak electron and ion temperatures are increased to about 5.5keV but the energy confinement time drops to about 0.3s. With neutral beam heating there is also a reduction in the energy confinement time but at low central densities $n_e(0) \lesssim 1.5 \times 10^{19}m^{-3}$ central ion temperatures $T_i(0) > 12.5$ keV are obtained. Improved confinement has been recently observed with neutral beam heating in discharges with a divertor-like configuration when the plasma boundary is defined by a magnetic separatrix so that the discharge is no longer in contact with the limiter.

JET started operating in 1983 with a minimum number of basic diagnostic systems. Further systems have been added progressively and the full set of JET diagnostics is now near completion. The present status is summarized in Table 1 which shows that out of a total of 39 systems, 24 are in routine operation, 10 are being installed or commissioned and a further 5 are still to be constructed. A schematic showing the location of diagnostics on the JET machine is shown in figure 1.

In this lecture I will review the present status of the JET diagnostics and give a brief review of recent experimental results.

2. Overview of JET Diagnostic Systems

The design of diagnostic systems for JET started in 1979 and was reviewed at the last Varenna diagnostics meeting in 1982 [5]. Since then there have been a few changes; some new systems have been added and a few systems cancelled, but the majority of the systems now installed and working on JET are those which were described at the meeting four years ago. The time scale to design, construct, install and bring into full reliable operation the diagnostics for a large fusion experiment like JET is substantial. It takes a minimum of two to three years and in some cases as long as six or seven years. Many of these diagnostic systems have been built by the other fusion laboratories who are partners in the JET project. These systems were specified and paid for by the JET project via a series of contracts and this formal relationship was needed

so that the work in the many different laboratories could be effectively co-ordinated and the complex systems could be built to uniform standards. This has been a particularly successful collaboration with the result that the diagnostic expertise of the European Fusion Programme has been concentrated at JET. Many skilled scientists, engineers and technicians have been involved and many people have worked at JET for varying periods to install and operate these systems.

A deliberate policy has been to use diagnostic methods whenever possible whose principals have already been demonstrated on other experiments. However, there are some exceptions where novel diagnostic techniques have been developed and applied on JET. What is new is the sophistication of the application of the established methods to JET and the complexity of the engineering. This has been necessitated by several factors including the large physical size of JET, the need to maintain compatibility with the very high standards of engineering of the other systems of the JET device and by the hostile radiation environment which will occur in discharges with deuterium and tritium. Considerable emphasis has been placed on achieving much higher standards of reliability and accuracy for these diagnostic systems than has previously been the norm in fusion research. All of the JET diagnostic systems are remotely controlled through a computer system and many can be operated automatically with a minimum of skilled operators.

In order to make the most efficient use of experimental time and to improve the self consistancy of the measurements, a complete set of data is measured simultaneously during every discharge. In general we find that the measurements are reproducible from shot to shot for discharges with the same conditions. A large number of spatial channels is needed to measure profiles of plasma parameters with adequate spatial resolution (generally 5-10cm) in these discharges with large poloidal cross-section (2.5 x 4.2m). As the poloidal cross-section of JET discharges is non-circular, those measurements which integrate along a chordal line of sight have to be unfolded by tomographic inversion methods and thus the plasma must be viewed simultaneously in orthogonal directions. In most cases the number and location of the lines of sight are severely constrained by the access to the plasma through the available ports in the vacuum vessel. There are similar considerations in determining the time scales on which data should be recorded. The plasma parameters related to quasi-equilibrium processes (eg.

the energy balance) need to be recorded on time scales which are up to an order of magnitude shorter than the characteristic equilibrium times, eg. recording on time scales of about 10ms is required for equilibrium time scales $\geq$ 100ms. Data is usually recorded at this rate throughout the 20 second period of the JET discharge, ie. typically 2 x 10^3 data points per spatial channel. There are however many transient plasma phenomena which take place on much shorter time scales (eg. instabilities and disruptions) and these data must be recorded on time scales of a few microseconds. Clearly it would not be feasible in terms of data storage to record data on all the measurement channels at a MHz rate for 20s and so the fastest data taking rates are usually switched on for a limited number of time windows centered around periods of interest. These windows may be pre- or post- triggered, in some cases by signals from other diagnostics.

Fairly stringent constraints have had to be applied to the data requirements of each diagnostic to keep the total data recorded per JET discharge within reasonable limits. Presently we record about 7 x10^6 data points per discharge and this is planned to increase to about 1.5 x10^7 when all of the diagnostics are operating. The data is recorded in local CAMAC memories during the discharge and then read into the memories of a network of NORD computers (NORD 500 series) which are used for diagnostic control and for immediate data analysis. Initial analysis and display of results is carried out by these computers in the interval between successive discharges and is used to guide the progress of the experiment. At the same time the complete raw data file is copied into the memory of a large main frame computer system (IBM 3084Q + CRAY XMP) where it can be used for higher level analysis and it is via these computers that the retrospective analysis of JET data is carried out. An important feature is that data for all JET discharges and from all the diagnostics are available to all members of the JET project via this main frame computer.

Magnetic Diagnostics

Measurements of the poloidal magnetic field outside the plasma are used to determine the discharge current, loop volts, ohmic power input, position and shape of the plasma boundary. More detailed analysis of these data yields information on the total plasma energy and pressure, plasma inductance and

the shape of the magnetic surfaces inside the plasma [6]. The magnetic measurement coils (KC1) are shown schematically in Figure 2. The components of the poloidal magnetic field perpendicular to the surface of the vacuum vessel are measured with a set of flux loops on the surface of the vessel [7]. There are two types of loops; full flux loops which make a single turn in the toroidal direction are used in locations where there are no obstructions from ports etc, whilst saddle loops are used in places where there are obstructions. The component of the poloidal field parallel to the vacuum vessel surface is measured with small pick-up coils which are located inside inconel protection tubes on the inside of the vacuum vessel. There are 18 of these pick-up coils distributed around the poloidal circumference and there are identical sets of coils on each of the octants. The signals from these coils are processed electronically and combined in various ways using both analog and digital techniques to yield the various plasma quantities. For example the plasma current is obtained by adding the signals from all the internal pick-up coils to simulate a continuous Rogowski coil. The plasma position and the shape of the outermost magnetic flux surface are determined to a typical accuracy of ±10mm by a numerical solution of the Laplace equation for the poloidal field outside the plasma with the boundary conditions fitted to the field components measured by the magnetic diagnostics. For plasmas with elongated cross-section the internal flux surfaces can be estimated by solving the Grad-Shafranov equation with the outer flux surface as a boundary condition. The integral plasma quantities such as the total kinetic energy, pressure and inductance are obtained from the Shafranov integrals. The coils and flux loops on two of the octants are dedicated for active feedback control of the plasma position, current, shape etc., whilst those on the other six octants are used for diagnostics purposes. The diamagnetic effect is used to determine the perpendicular plasma pressure using a set of coils which is supported on one of the toroidal field coils.

Electron Density

The electron density profiles are measured by interferometry and by reflectometry. The main interferometer is a Far Infra-Red instrument (KG1) with seven vertical and three lateral lines of sight [8,9]. This systems works at a wavelength of 195μm using DCN laser sources. The frequency shift for the reference arm is produced by means of a rotating grating. The optical components of the vertical channels are supported on a massive frame which is

mechanically independent of the rest of the JET machine in order to reduce the effect of vibrations. However, the lateral channels have mirrors which are mounted on the inside of the vacuum vessel and are thus sensitive to vibrations. These channels were designed to operate simultaneously with a second interferometer (wavelength = 3.39μm) in order to compensate for the effect of the mechanical vibrations but unfortunately this system has not worked satisfactorily due to difficulties with the alignment and reflectivity of the internal mirrors at the shorter wavelength. Modifications are in hand to change the second wavelength to 119μm. JET also has a 2mm Microwave Interferometer (KG2) with a single vertical line of sight which is used mainly as a back-up to the Far-Infra-Red Interferometer.

We are also developing Microwave Reflectometry (KG3) [10] as a diagnostic to improve the accuracy of the density profile measurements near to the edge of the discharge where the data from the Far-Infra-Red interferometer is rather sparse and where future changes to the JET machine configuration will cause us to loose one of the vertical channels. Results with a prototype reflectometer have been very encouraging [11] and a multichannel instrument [12] is now being constructed and will be installed on JET during 1987. This instrument will also be used to observe localised density fluctuations.

Electron Temperature

The main methods used for electron temperature measurements are electron Cyclotron Emission (KK1 and KK2) and Thomson Scattering (KE1 and KE3). In addition the X-ray Pulse Height Analysis System (KH2) [13] is used to measure fast electron distributions in runaway or slideaway discharges.

We have invested considerable effort into developing ECE [14] as the main electron temperature diagnostic in JET. A poloidal section of the plasma is viewed along ten different chords by an array of rectangular horn antennae. The ECE radiation (for typical JET parameters in the range 70 - 350GHz) is transmitted from these antennae by oversize rectangular microwave waveguides to the detectors which are located outside the Torus Hall. The distance along the route followed by the waveguides is of the order of 100m and the oversized waveguide is needed for low attenuation of the transmitted signals. Great care is required in the design of bends etc. to avoid serious problems with conversion between different waveguides modes.

Four types of detectors are used.

i) The complete spectrum of the ECE radiation over several harmonics is measured with scanning Michelson Interferometers (scan time ~15ms), and the relative amplitudes of the different harmonics are used to check that the emission is thermal.

ii) The spatial profile of temperature along different chords is measured with Fabry-Perot Interferometers which are scanned over the second harmonic emission in a time of ~3ms. Each scan gives a temperature profile along the chordal line of sight with a spatial resolution ~10cm. By combining the data from different chords a two dimensional distribution can be constructed. The Fabry-Perot instruments can also be operated at fixed frequencies so that the temperatures at selected positions in the plasma can be recorded as a function of time with a sensitivity about 5eV and time resolution about 10μs.

iii) A twelve channel Grating Polychromator (KK2) is used to record the time variation of temperatures at 12 selected positions along a single chord. This is particularly useful for measurements of the propagation of heat perturbations through the plasma following the collapse of an internal sawtooth instability and permits a measurement of the thermal conductivity.

iv) A superheterodyne receiver (KK3) [15] is being developed for measurements of the temperature profile near the plasma edge.

The ECE diagnostics are absolutely calibrated by means of specially developed thermal sources of known temperature and emissivity. These calibration techniques have now been developed to the point where the absolute accuracy of the ECE measurements on JET is estimated to be within ±10% and the relative accuracy between different spatial points on the same profile is within ±5%. These values are confirmed by comparison with the Thomson scattering measurements (Figure 3).

JET will have two Thomson scattering systems, one is already operating and the second is under construction. The first system, which we call the Single Point Thomson Scattering System (KE1), is of conventional geometry (Figure 4), ie. the scattered light is collected in a cone at 90° to the incident light.

The source is a ruby laser which can be operated in a variety of combinations of energy per pulse and repetition rate ranging from a single pulse of 25J to a series of ~25 pulses of 2.5J at 1Hz. The system is limited to a single spatial point measurement per discharge but can be moved to different major radii in between successive discharges. This system has been in operation for two years and has worked very reliably [16,17].

A new type of Thomson Scattering diagnostic (KE3) is being developed for JET and will be installed at the end of 1986. The system will use a laser with a much shorter pulse length (~250ps) than a conventional Thomson scattering laser (~20ns). The scattered light will be recorded continuously as the laser light pulse travels across the plasma. The spatial profile will be determined from the time of flight of the laser pulse whilst temperature and density will be determined respectively from the spectral width and intensity of the scattered light as in a conventional system. This system has been described in detail in another paper at this meeting [18]. The new system will use much of the existing optics of the Single Point system and both systems will be able to operate together.

Ion Temperatures

Ion temperatures are generally more difficult to measure than electron temperatures and all of the available methods encounter some problems and limitations. We have an array of five Neutral Particle Analysers (KR1) which view the poloidal section along different chords [19]. Each instrument has magnetic and electrostatic analysers which disperse the ions in both mass and energy onto on an array of channel multipliers thus measuring simultaneously the hydrogen and deuterium fluxes. These instruments can measure the temperature of the hydrogenic ions, the ratio D^+/H^+, and the fast ion distribution functions during additional heating. However, measurements at high densities are limited by the opacity of the plasma to neutrals escaping from the central plasma. Under these conditions the instruments usually do not measure the central ion temperature directly, and to extrapolate the data to the central region, it is therefore necessary to use a neutral atom transport code.

Two Neutron Spectrometers (KM1 and KM3) are used to measure ion temperatures in deuterium plasmas [20] with ohmic heating or hydrogen neutral beam

injection (they cannot measure temperatures during deuterium beam injection because the neutron production is then dominated by the beam-plasma interactions). At low yields in deuterium plasmas a ^{3}He ionization chamber has been used above the roof of the Torus Hall using a penetration hole through the roof as a collimator. This is a temporary installation and the ionization chamber will be moved later to a large concrete shield and collimator in the torus hall. In the Time-of-Flight Neutron Spectrometer (KM3) neutrons are scattered by protons in the first of a pair of scintillators which are separated by ~1m. The neutron energy is determined by the time-of-flight between the two scintillators. This instrument has higher resolution than the ionization chamber but lower sensitivity and therefore requires a higher neutron flux to be effective.

The velocity distribution of impurity ions is measured spectroscopically with several instruments. The High Resolution Crystal Spectrometer (KX1) is used to observe highly ionized nickel ions in the central core of plasma, typically out to a radius of ~0.5m [21]. It views tangentially and thus also measures the toroidal rotation velocity. The crystal and detector are located outside the Torus Hall on a Rowland circle whose diameter is 24m. Information on the temperature and rotation at the edge of the plasma can also be obtained from the Grazing Incidence Survey Spectrometer (KT4). The temperatures of light impurity ions are measured by Charge Exchange Recombination Spectrometry (KS4) [22] but this instrument can be used only during neutral beam injection heating. (JET does not have a dedicated diagnostic neutral beam). It is planned that the heating neutral beam sources will be modulated in order to improve the ratio of signal to background noise. The present instrument views perpendicularly in the plasma mid-plane and will be later extended to a tangential view over the whole cross-section.

For some discharge conditions there is good agreement between values of ion temperature measured with the different diagnostics (Figure 5), but there are also many discharges where the agreement is less satisfactory for reasons which are still not completely understood.

Impurities

As in most tokamaks, spectroscopic diagnostics are the main methods for identifying the impurities in the plasma and for measuring their

concentrations. The wavelengths of the emitted impurity line radiation cover a very wide spectral range from the visible (~6000A) through the ultraviolet to the soft x-ray region (~1A). Several different instruments are needed to cover this very wide spectral range and some overlap is desirable for cross calibration. The spectral survey is covered by three instruments: a VUV Broad Band Spectrometer (KT2), a Grazing Incidence Survey Spectrometer (KT4) and a Soft X-ray Pulse Height Analysis System (KH2). A Broad Band Crystal Spectrometer (KS1) with two crystals in a periscope-like arrangement with the detector outside the Torus Hall will be installed for the tritium phase of JET operation.

There are also three spectrometer systems which are designed to measure spatial profiles of impurities [23]. The VUV Spatial Scan Spectrometer (KT1) will cover the wavelength range from 2000 to 100A and is based on three identical duochromators. This instrument will view the plasma through rotating grazing-incidence mirrors, with two horizontally viewing instruments and one viewing vertically. Unfortunately the full implementation of this diagnostic has been delayed by a series of vacuum problems in the mechanisms of the rotating mirrors. A Spatial Scan Crystal Spectrometer (KS2) is being constructed and will cover the wavelength range 15 - 25A. This instrument uses two crystals which can be translated and rotated synchronously to scan in wavelength whilst the crystal nearer to the plasma can also be rotated about an orthogonal axis to scan the plasma spatially. This instrument will be installed during 1987. Information on spatial profiles of impurities is also obtained by Charge-Exchange Recombination Spectrometry (KS4).

The fluxes of impurities and hydrogenic atoms entering the plasma from the walls and limiters are measured with Visible Spectrometers (KT3) and H_α Monitors (KS3). The effective ionic change, Z_{eff}, is measured spectroscopically by visible bremstraahlung with a system (KS3) which includes a number of discrete channels and a poloidal array, and also from the intensity of the Soft X-ray Pulse Height Spectrum (KH2).

The power radiated by impurities is measured by two arrays of Bolometers (KB1) which view the plasma in orthogonal directions through small apertures (Figure 6). The horizontal camera has 20 channels and the vertical camera has 14

channels. Each detector consist of a pair of thin film, gold resistors evaporated on to a mylar foil. One resistor receives plasma radiation and the other is shielded from the plasma. The pair are connected in a bridge arrangement to cancel drifts in the substrate temperatures and this arrangement also cancels to first order the effects of neutron and hard x-ray radiation. The radiated power density is obtained by Abel inversion using the shape of flux surfaces derived from the magnetic diagnostics. The radiated power is also measured with an array of Soft X-Ray Diodes (KJ1) which are primarily intended for fluctuation and instability studies. The bolometer and diode arrays are in fact complementary since the X-Ray Diodes are more sensitive the hot central plasma core whilst the bolometers are more sensitive the cooler plasma edge regions.

Plasma Boundary

Direct measurements of the plasma interactions with material surfaces have been made by post-mortem surface analyses of samples removed from the limiter and walls whenever the JET vacuum vessel has been opened for maintenance [24]. These measurements necessarily give an integrated picture over many months of operation but have nevertheless allowed us considerable insight into the processes responsible in JET for impurity production and migration. Probe drive systems are used to expose surface collector probes in the plasma boundary region for single discharges or for a sequence of discharges. These probes have both time and spatial resolution. Two probe drives (KY3) are located on the top of the vacuum vessel and one of these contains a magazine of five interchangeable collector probes which may be removed via a vacuum cassette. There is also a more sophisticated transfer system (KY2) which can be used to expose probes in the horizontal mid-plane of the torus (close to the limiters) and then to transport the samples to a Surface Analysis Station (KY1) where they can be analysed immediately by a variety of techniques. These systems have given preliminary data during 1986 and will come into full operation in 1987.

The same probe drive systems are also used to introduce electrical probes into the boundary regions of the discharge to measure the local plasma densities, temperatures and heat fluxes [25]. These measurements are supplemented by fixed probes which are located in the protective carbon shield surrounding one of the RF antennas. The measurements of plasma densities and temperatures in the edge regions will be extended into the plasma by the new Microwave

Reflectometer (KG3) and Super Heterodyne ECE (KK3) diagnostic systems which have already been discussed.

The surface temperatures of the limiter antenna, inner wall tiles and separatrix plates are measured by infra-red cameras (KL1). Two camera systems are used. The first system is based on CCD cameras which have good spatial resolution [26,27]. This is used to monitor high surface temperatures which could result in thermal damage. However this system has a limited dynamic range and cannot be used to follow the full temperature excursion of the limiter surface during a high powered discharge. A new system is being developed based on an infra-red detector array (sensitive in the wavelength range 3 - 5μm) which will cover a wider temperature range but will have lower spatial resolution.

Neutron and Fusion Products

Considerable effort is being invested in neutron and fusion product diagnostics in view of JET's experimental programme in D-D and D-T plasmas. A particular requirement for the neutron diagnostics is to cover a very wide range of yields from ~10^{10} neutrons s^{-1} in hydrogen discharges (ie. from runaways) to ~10^{19} neutrons s^{-1} (in hot D-T plasmas). The total neutron yield is monitored routinely using ^{235}U and ^{238}U Fission Chambers (KN1) which are mounted in pairs on the JET machine structure. Two new neutron yield diagnostics are just being installed and commissioned. These are two arrays of Collimated Neutron Detectors (KN3) which will measure the spatial profile of the neutron yield and an Activation Transfer System (KN2) which will expose neutron foils close the plasma edge and transfer them pneumatically to a counting station [28].

The neutron spectrometers (KM1 and KM3) for ion temperature measurements in deuterium plasmas have already been described. When these measurements are made simultaneously with the total neutron yield it is possible to determine the deuterion density n_d. Typically we find $0.5 \leq n_d/n_e \leq 0.7$. Construction is now starting on two 14MeV spectrometers (KM2 and KM5) which will be required during the tritium phase of the JET experimental programme. A prototype fusion product diagnostic (KP1) has been tested and has given some very interesting data on the production of energetic protons during ICRH [29]. This development and related work on α particle diagnostics is continuing.

Fluctuations and Instabilities

Many of the diagnostics already discussed are also used with fast time resolution windows to study fluctuations and instabilities. In particular sawteeth are being studied with the ECE diagnostics (KK1 and KK2) and with the Soft X-ray Diode Arrays (KJ1). The diode arrays [30] are mounted inside the JET vacuum vessel in two cameras which view the plasma cross-section in orthogonal directions. The wavelength range of these detectors can be changed by means of thin foil filters which can be introduced in front of the detectors and this has the effect of changing the sensistivity of the system to respond to changes in the plasma temperature and density. Each detector integrates the emission along its line of sight but with such a large number of sight lines (62 horizontal and 38 vertical) it is possible to unfold the integral signals remotely using tomographic methods to produce contour maps of the local soft x-ray emission density. This diagnostic has proved particularly powerful in observing the mechanism of the sawtooth collapse [31].

3. Summary of Experimental Results

JET has now been operating for three years and there has been steady progress in improving plasma operating conditions [32]. Discharges are now run routinely at the full design value of the toroidal magnetic field B_T = 3.4T and with currents up to 5.1MA (Figure 8). The plasma current, position, elongation and shape are all controlled by feedback. The range of stable discharge conditions is summarized in table 2. Experiments concentrated initially on ohmically heated discharges and have now been extended to include powerful ion cyclotron resonance and neutral beam injection heating. The ion cyclotron resonance heating operates at frequencies in the range 25 - 55 MHz corresponding to the gyro frequency resonances of H^+ and $^3He^{++}$ ions which are added as minority species to deuterium plasmas (typically in concentrations <10%). The position of the resonance layer and thus the power deposition profile can be varied either by changing the toroidal magnetic field or the frequency of the heating wave. Experiments started during 1985 using two antennas which could be connected in different configurations (monopole, dipole or octopole) to study how the coupling efficiencies varied with the distance between the plasma edge and the antennas. The maximum power coupled into the plasma was ~ 5MW for 2s. A third antenna was added early in 1986 and the coupled power is now being raised to towards 9MW. The central electron temperature rises to ~ 7.4keV.

Experiments with neutral beam injection started in 1986 with a single injection line capable of injecting up to about 6MW of 80keV H° or about 9MW of 80keV D° into the plasma. The maximum plasma temperature obtainable with neutral beam heating depends on the plasma density. At medium to high densities the ions have been heated to about 6.5keV and the electrons to 4.8keV using 5.5MW of neutral beam power. At lower densities the ion temperature can greatly exceed the electron temperature and can reach about 12.5keV.

Energy Confinement

Systematic studies have been made of the dependence of the global energy confinement time τ_E on various plasma parameters. In ohmic discharges the full range of plasma dimensions and elongations permitted by the JET vacuum vessel has been explored. This has included elongated full bore discharges (R = 2.96m, a = 1.2m, b/a $\lesssim$ 1.65) and circular discharges limited on the inner wall (R_0 = 2.5m, a = 0.8m). The latter discharges are a close simulation of discharges in TFTR and because of the strong gradient in B_T, have $B_T \simeq 4T$ on the plasma axis. As in smaller experiments the general trend of these data is that in ohmic discharges the confinement improves with increasing plasma density $\bar{n}_e$ and limiter safety factor q_a however, the JET data show a much weaker dependence on $\bar{n}_e$ and q_a than in smaller tokamaks (typically in JET $\tau_E \sim \bar{n}_e^{0.4} \times q_a^{0.3}$) and in particular the confinement time saturates for $n_e \gtrsim 3\ 10^{19}\ m^{-3}$. The regression fit to the full JET ohmic data set is

$$\tau_E = 0.03\ \bar{n}_e^{0.4}\ q_a^{0.3}\ B_T^{0.6}\ a^{1.3}\ R^{1.7}$$

Note that this linear fit to the full data set hides the saturation in n which is apparent when the data is examined closely. There is clearly a very strong dependence on the plasma dimensions ($\sim R^3$ at fixed R/a) and on toroidal field ($\sim B_T^{0.9}$ if the B_T dependence on q_a is included explicitly). It is also worth noting that there is no explicit dependence on the elongation b/a beyond that included implicitly in q_a. The largest value of τ_E in an ohmic discharge is $\tau_E \sim 0.8$ (I_p = 3MA, B_T = 3.4T).

With additional heating the confinement time τ_E degrades with increasing input power as seen in a number of other experiments. The degradation is independent of the type of heating, whether ion cyclotron, neutral beam or a combination of both. Figure 9 shows the plasma energy W_k plotted against

the total heating power P_T and can be represented by an offset linear scaling of the form $W = W(o) + \tau_{inc} P_t$. Where W(o) and the incremental confinement time τ_{inc} are functions of the plasma parameters. Extrapolating to higher heating powers, the global confinement time τ_E will saturate in the range 0.1 to 0.3s.

Recent experiments have produced magnetic separatrix configurations in JET (fig 10) which have improved confinement with neutral beam heating compared to limiter discharges. These discharges with improved confinement have many of the characteristics of the so-called H modes seen in other tokamaks.

Plasma Purity

The JET vacuum vessel is fabricated out of inconel (mainly nickel and chromium) and is usually operated at a temperature ~ 300°C. There are now eight large carbon limiters (0.8 x 0.4m) on the mid-plane at the outer major radius. The ion cyclotron antennas are in similar positions to the limiters but at slightly larger major radii and are surrounded by protective frames of carbon tiles. The inner wall is also covered with carbon tiles to a height of ± 1m above the mid plane. There are also carbon tiles at the top and bottom of the torus in the vicinity of the X points of the magnetic separatrix. The standard conditioning procedure following exposure of the torus to atomosphere is to bake the torus to about 350°C followed by several days of continuous glow discharge cleaning in hydrogen or deuterium.

The main impurities are carbon ($2\% \leq n_c/n_e \leq 4\%$) and oxygen ($1\% \leq n_o/n_e \leq 2\%$) which enter the discharge from the walls and limiters. The most important metallic impurity is nickel and the concentration is in the range 0.001 to 0.3% depending on the plasma conditions. The original sources of the nickel are the inconel walls and the nickel screens of the RF antennas. The nickel from the antennas is observed to enter the plasma directly when power is applied to an antenna but there is no influx from an antenna to which no power is applied. The nickel from the walls appears to enter the plasma by a two step process: (i) the carbon limiters become covered in metal during glow cleaning and following discharges which have ended with disruptions; (ii) during subsequent tokamak discharges this metal is eroded and enters the plasma. Thus we see that nickel concentrations in the plasma are reduced

progressively during a sequence of stable discharges with ohmic or neutral beam heating but are increased during ion cyclotron heated discharges or following discharges which have ended in disruptions. However, it is important to emphasize that under most conditions the concentration of metallic impurities in JET is small and does not significantly cool the central core of the discharge as shown in the radial profiles of the radiated power which were already illustrated in Figure 7.

The large area of carbon on the inside wall has a strong pumping effect and is used to control the plasma density by moving the discharge into contact with the inside wall. The detailed mechanism of this pumping effect is not yet fully understood.

Disruptions

Figure 11 summarizes the limits of stable operation in JET. The limit to low q operation is $q_\psi = 2.0 \geq 0.1$ where q_ψ is the field line q. The cylindrical q at the limiter ~ 1.6.

Disruptions at the density limit in discharges with $q_\psi \geq 3$ are preceded by signs of deterioration up to 1s before the final energy quench. The radiated power rises to equal the total power [31] and although the ohmic power also increases due to increased plasma resistance, it fails to keep place with the increasing radiation. The temperature profile contracts and there is increased mhd activity. In a typical case an oscillatory mode (predominantely m = 2, n = 1) grows for about 30ms and then the mode stops rotating and locks in a fixed toroidal phase. After the mode locks it continues to grow in amplitude and the ECE diagnostics show that the temperature profile flattens slightly at the minor radius corresponding to the calculated position of the q = 2 surface. This is consistent with the growth of a non-rotating magnetic island (the ECE diagnostic views close to the calculated position of the 'O' point). There are indications of similar evidence from the soft x-ray diode diagnostics but the analysis is presently at a preliminary stage and there could be other interpretations. The spatial resolution of the ECE diagnostic (at present 40mm in the radial direction) is not quite sufficient to determine whether the 'O' point of the magnetic island is colder than the surrounding plasma as predicted by one model of disruptions. The new superheterodyne ECE diagnostic will have better spatial resolution and will be used for these

studies. The soft x-ray diode arrays give a very detailed picture of the displacement of the hot central core in the final few ms before the energy quench.

Sawteeth

Sawtooth oscillations occur in almost all discharges and have been studied extensively with a range of diagnostics [31]. In ohmically heated plasmas the modulation of the central electron temperature is up to 20% and the period is between 30 and 250 ms. In discharges with ion cyclotron heating (Figure 12) or co-injected neutral beams the modulation is increased up to 50% and the period extended up to 600ms, whereas with counter injected beams both the modulation and the period are reduced. With combined ion cyclotron and neutral beam heating we have sometimes seen sawteeth of very long duration lasting for more than 1s. These have been called "monster" sawteeth. The monster sawteeth were first seen in relatively low current discharges (I_p ~ 2MA) but similar long duration monster sawteeth have now been seen in discharges with an internal separatrix (I_p = 2MA) and at high currents I_p = 5MA (Figure 13). These are not simply sawteeth with particularly long periods but they are characterised by low levels of coherent mhd activity suggesting that the internal m = 1 mode has stabilized. However, after a monster sawtooth collapses the plasma remains in an unstable state which seems to prevent the growth of a second monster sawtooth in the same discharge although they may be several more normal sawteeth.

The collapse mechanism appears to be the same in all JET discharges although there is a range of different precursor activity. The collapse occurs on a much shorter time scale (typically about 100μs) than would be consistent with resistive reconnection models. Detailed studies with the x-ray and ECE diagnostics show that the collapse has an m = n = 1 structure and involves the displacement in minor radius of the hot central core of plasma. The displaced core spreads poloidally around the magnetic axis into a crescent shaped region [30] and at the same time there is a rapid outflow of plasma energy. The time scale of the collapse together with the detailed displacement and spreading of the hot core are in agreement with the predictions of a model where the sawtooth collapse is an ideal mhd instability.

4. Future Plans

The programme planned for JET includes a substantial increase in the additional heating power. During the next three years the ion cyclotron heating will be increased to 15MW for 20s. A second neutral beam line will be installed in 1987 to bring the total neutral beam power to about 10MW of 80keV H°, 160keV D° or about 18MW 80keV D°. This additional heating power will be tested in two discharge configurations: a) a magnetic separatrix at $I_p \leq$ 4MA, b) limiters at $I_p \leq$ 7MA (such a low q discharge has already been simulated at 3.5MA and B_T = 1.7T). The main aim of JET experiments during the next few years will be to reach maximum performance with full additional heating power in deuterium plasmas before proceeding to the final phase requiring the introduction of tritium. A number of other machine enhancements which might influence the confinement are also being considered. These include control of the current profile using lower hybrid resonance heating, beryllium limiters and gettering, feedback control of disruptions and repetitive hydrogen pellet injection.

Very few major diagnostics are planned for JET beyond those which are already in construction. However there are a few minor additions (including a laser blow-off system to inject trace impurities) and several modifications and upgrades to existing systems. Them include upgrading the Far-Infra-Red interferometer permit Faraday Rotation measurements (KG4), and various ideas for α particle diagnostics.

5. Conclusion

A considerable effort has been invested into providing the JET experiment with a comprehensive set of diagnostics. Particular emphasis has been placed on making measurements of the different plasma parameters simultaneously within a single discharge, in order to avoid problems of irreproducibility. Considerable care has been taken during the design and construction of these diagnostic systems to ensure that they are consistent with the high standards of engineering of other systems of the JET machine. Many of the systems described in this paper were operated in a preliminary version for the first operation of JET in 1983, and since then they have been refined and brought into full operation, allowing the scientific personnel to concentrate on interpretation of data. A few systems including the neutron diagnostics

specifically intended for the later phases of JET's programme are still in construction and will be installed within the next few years.

Acknowledgements

The successful implementation of the JET diagnostic systems is due to the efforts of many colleagues in the JET Team, and in the other European Fusion Laboratories. I am grateful for their contributions and hard work.

References

[1] The JET Team., IAEA Conf. on Plasma Physics and Controlled Nuclear Fusion Research, Kyoto, Japan, 1986. Paper CN-47/A-I-2.

[2] J Jacquinot et al, IAEA Conf. on Plsma Physics and Controlled Nuclear Fusion Research, Kyoto, Japan, 1986. Paper No. 28, 1 (1986).

[3] P P Lallia et al, IAEA Conf. on Plasma Physics and Controlled Nuclear Fusion Research, Kyoto, Japan, 1986. Paper No. 28, 1211 (1986).

[4] The JET Team, First Results of Neutral Beam Heating on JET., Plasma Physics and Controlled Fusion., Vol 28 No. 9A P.1429 (1986).

[5] P E Stott, Course on Diagnostics for Fusion Reactor Conditions, Varenna, Italy, 1982. Vol. II P517.

[6] J P Christiansen, Integrated Analysis of Data from JET, JET Report, JET-R(86)04.

[7] P E Stott, Course on Diagnostics for Fusion Reactor Conditions, Varenna, Italy, 1982. Vol.II P403.

[8] D Veron, Course on Diagnostics for Fusion Reactor Conditions, Varenna, Italy 1982. Vol.I P199.

[9] G Magyar & J O'Rourke, Operating the JET Multichannel FIR Interferometer, this Conference.

[10] A E Costley, Diagnosis of Fusion Plasmas Using Reflectometry, this Conference.

[11] A Hubbard et al, Electron Density Measurements on JET using a Microwave Reflectometer, this Conference.

[12] R Prentice et al, The JET Multichannel Reflectometer, this Conference.

[13] D Pasini et al, The X-ray Pulse Height Analysis System at JET, this Conference.

[14] A E Costley, Recent Developments and Applications of Electron Cyclotron Emission, this Conference.

[15] N Salmon et al, An Electron Cyclotron Emission Diagnostic for the Edge Region of the JET Plasma, this Conference.

[16] P Nielsen et al, The Single Point Thomson Scattering System for JET, (to be published).

[17] R Prentice et al, First Results from Thomson Scattering on JET. Proc. 5th Topical Conf. on High Temperature Plasma Diagnostics, Tahoe City, USA, Sept. 1984. Rev. Sci. Insts. Vol.56 No.5 ptII P1070 (1985) Abstract.

[18] C Gowers et al, The JET LIDAR Thomson Scattering System, this Conference.

[19] G Bracco, S Corti, V Zanza et al, First Results from JET Neutral Particle Analyser (NPA) (1984), JET-IR(84)04.

[20] O N Jarvis et al, Neutron Spectrometry at JET., 6th Topical Conf. on High Temperature Plasma Diagnostics. Rev. Sci. Instr. 57 (1986) 1717.

[21] S Bombarda, R Giannella, E Kallne, G Tallents, S Bly-daubah, P Faucher, M Cornille, J Dubah and A H Gabriel, Observations and Comparisons with Theory of Helium and Hydrogen - Like Spectra of Nickel from the JET Tokamaks, (to be published).

[22] M Von Hellermann, Charge Exchange Recombination Spectroscopy on JET., this Conference.

[23] K Behringer, B Denne & G Magyar, Space Resolved Measurment of Impurity Radiation on the JET Tokamak, this Conference

[24] R Behrisch et al, Contamination of the JET Limiters with Metals during the Different Operational Phases., 7th Int. Conf. of Plasma Surface Interactions in Fusion Devices, Princeton, USA (1986). (JET-P(86)35).

J P Coad et al, Depth Profiling Experiments on JET Wall Samples., 7th Int. Conf. of Plasma Surface Interactions in Fusion Devices, Princeton, USA (1986). (JET-P(86)35).

[25] T Tagle, Diagnosis of the JET Scrape-off Layer using heat flux/Langmuir Probes, this Conference

[26] D Summers, Thermography of Carbon Limiters, this Conference

[27] C Lowry, The Limiter as a passive Diagnostic, this Conference

[28] D B Syme, Neutron Diagnostics for JET, this Conference

[29] G. Sadler et al, Fusion Product Measurements on JET, 13th Euro. Conf. on Controlled Fusion & Plasma Heating, Schliersee, April 1986, Vol 10C (1986) 105.

[30] R Granetz, X-ray Tomography and the Physics Results from JET (Abstract only), this Conference

[31] D Campbell et al, IAEA Conf. on Plasma Physics and Controlled Nuclear Fusion Research, Kyoto, Japan, 1986. IAEA CN 47/A VII-5

[32] The JET Team, IAEA Conf. on Plasma Physics and Controlled Nuclear Fusion Research, Kyoto, Japan, 1986. IAEA CN 47/A-1-2.

Table 1

STATUS OF THE JET DIAGNOSTICS SYSTEMS, OCTOBER 1986

System	Diagnostic	Purpose	Association	Status (OCT. '86)	Compatibility with tritium	Level of automation
KB1	Bolometer Scan	Time and space resolved total radiated power	IPP Garching	Operational	Yes	Semi-automatic
KC1	Magnetic Diagnostics	Plasma current, loop volts, plasma position, shape of flux surfaces	JET	Operational	Yes	Fully automatic
KE1	Single Point Thomson Scattering	T_e and n_e at one point several times	Risø	Operational	Yes	Fully automatic
KE3	Lidar Thomson Scattering	T_e and n_e profiles	JET and Stuttgart University	Being installed Operational mid '87	Yes	Will be fully automatic
KG1	Multichannel Far Infrared Interferometer	$\int n_e ds$ on 7 vertical chords and 3 horizontal chords	CEA Fontenay-aux-Roses	Operational	Yes	Semi-automatic
KG2	Single Channel Microwave Interferometer	$\int n_e ds$ on 1 vertical chord	JET and FOM Rijnhuizen	Operational	Yes	Fully automatic
KG3	Microwave Reflectometer	n_e profiles and fluctuations	JET	(1) Prototype system operational (2) Multichannel system being constructed. Operational mid '87	Yes	(1) Not automatic (2) Will be fully automatic
KG4	Polarimeter	$\int n_e B_p ds$ on 6 vertical chords	CEA Fontenay-aux Roses	Operational early '87	Yes	Semi-automatic
KH1	Hard X-ray Monitors	Runaway electrons and disruptions	JET	Operational	Yes	Fully automatic
KH2	X-ray Pulse Height Spectrometer	Plasma purity monitor and T_e on axis	JET	Operational	Yes, after modification	Semi-automatic
KJ1	Soft X-ray Diode Arrays	MHD instabilities and location of rational surfaces	IPP Garching	Operational	No	Semi-automatic
KK1	Electron Cyclotron Emission Spatial Scan	T_e (r,t) with scan time of a few milliseconds	NPL, UKAEA Culham and JET	Operational	Yes	Fully automatic
KK2	Electron Cyclotron Emission Fast System	T_e (r,t) on microsecond time scale	FOM, Rijnhuizen	Operational	Yes	Fully automatic
KL1	Limiter surface temperature	Monitor of hot spots on limiter, walls and RF antennae	JET and KFA Jülich	Operational	No	Fully automatic
KL2	Limiter surface temperature	Temperature of belt limiters	JET	Under construction	No	Will be fully automatic
KM1	2.4MeV Neutron Spectrometer	Neutron spectra in D-D discharges, ion temperatures and energy distributions	UKAEA Harwell	Not yet fully operational	Yes	Will be fully automatic
KM3	2.4MeV Time-of-Flight Neutron Spectrometer		NEBESD, Studsvik	Not yet fully operational	Yes	Will be fully automatic
KM4	2.4MeV Spherical Ionisation Chamber		KFA Jülich	Not yet installed	Yes	Will be fully automatic
KM2	14MeV Neutron Spectrometer	Neutron spectra in D-T discharges, ion temperatures and energy distributions	UKAEA Harwell	Design completed	Yes	Not yet installed
KM5	14MeV Time-of-Flight Neutron Spectrometer		NEBESD, Gothenberg	Decision on construction under review	Yes	Not yet installed
KN1	Time Resolved Neutron Yield Monitor	Time resolved neutron flux	UKAEA Harwell	Operational	Yes	Fully automatic
KN2	Neutron Activation	Absolute fluxes of neutrons	UKAEA Harwell	Commissioning	Yes	Not yet implemented
KN3	Neutron Yield Profile Measuring System	Space and time resolved profile of neutron flux	UKAEA Harwell	Commissioning	Yes	Not yet implemented
KN4	Delayed Neutron Activation	Absolute fluxes of neutrons	Mol	Awaiting delivery	Yes	Not yet installed
KP1	Fusion Product Detectors	Charged particles produced by fusion reactions	JET	Prototype operational	Prototype - No	Prototype not automatic
KR1	Neutral Particle Analyser Array	Profiles of ion temperature	ENEA Frascati	Operational	Yes, after modification	Semi-automatic
KS1	Active Phase Spectroscopy	Impurity behaviour in active conditions	IPP Garching	Operational early '87	Yes	Not yet implemented
KS2	Spatial Scan X-ray Crystal Spectroscopy	Space and time resolved impurity density profiles	IPP Garching	Operational end '86	No	Not yet implemented
KS3	H-alpha and Visible Light Monitors	Ionisation rate, Z_{eff}, Impurity fluxes	JET	Operational	Yes	Semi-automatic
KS4	Charge Exchange Recombination Spectroscopy (using heating beam)	Fully ionized light impurity concentration, $T_i(r)$, rotation velocities	JET	Operational	Yes	No
KT1	VUV Spectroscopy Spatial Scan	Time and space resolved impurity densities	CEA Fontenay-aux-Roses	Operational	No	Semi-automatic
KT2	VUV Broadband Spectroscopy	Impurity survey	UKAEA Culham	Operational	No	Fully automatic
KT3	Visible Spectroscopy	Impurity fluxes from wall and limiters	JET	Operational	No	Semi-automatic
KT4	Grazing Incidence Spectoscopy	Impurity survey	UKAEA Culham	Operational	No	Semi-automatic
KX1	High Resolution X-ray Crystal Spectroscopy	Ion temperature by line broadening	ENEA Frascati	Operational	Yes	Fully automatic
KY1	Surface Analysis Station	Plasma wall and limiter interactions including release of hydrogen isotope recycling	IPP Garching	Operational	Yes	Automated, but not usually operated unattended
KY2	Surface Probe Fast Transfer System		UKAEA Culham	Operational	Yes	
KY3	Plasma Boundary Probes	Vertical probe drives for electrical and surface collecting probes	JET, UKAEA Culham and IPP Garching	Operational	No	
KZ1	Pellet Injector Diagnostic	Particle transport, fuelling	IPP Garching	Operational	Yes	Not automatic

Table II
Range of the Main JET Plasma Parameters

Parameter	Value
Toroidal field (plasma centre) B_t	1.7-3.4 T
Plasma current, I_p	1-5 MA
Flux safety factor at edge, q_ψ	2.2-16
Volume averaged density, $\bar{n}_e$	$0.5\text{-}5\times10^{19}\,m^{-3}$
Central electron temperature, $\hat{T}_e$	2-7.5 keV
Central ion temperature, $\hat{T}_i$	1.5-12 keV
Energy confinement time, τ_E	0.2-0.9 s

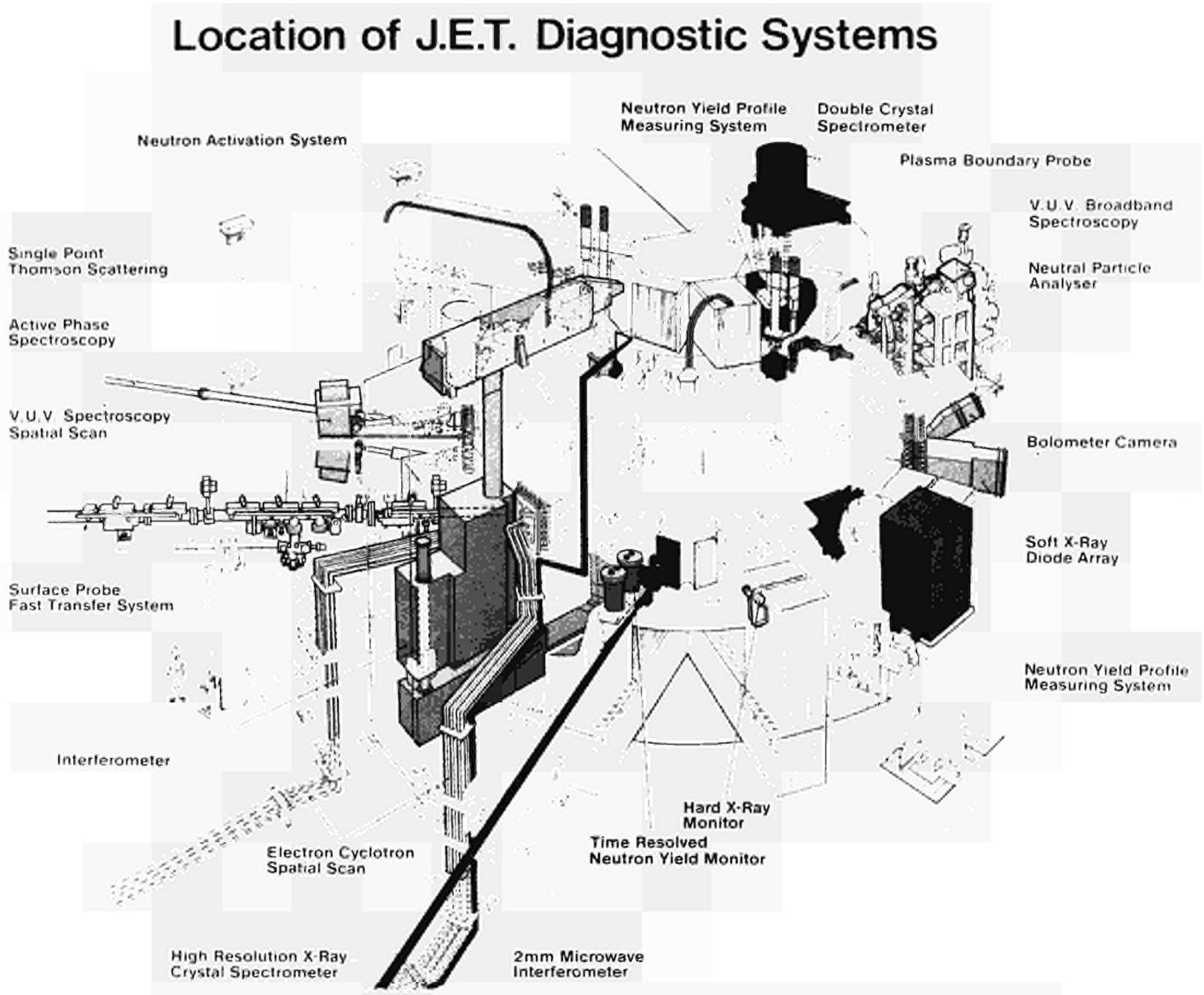

Figure 1 Schematic showing the location of some of the JET Diagnostic Systems.

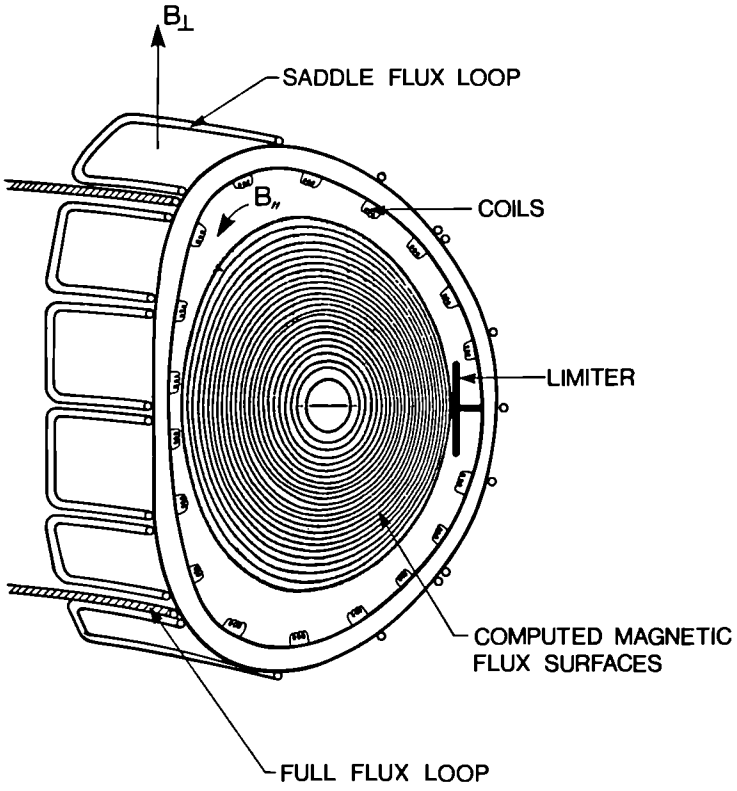

Figure 2 Magnetic diagnostics.

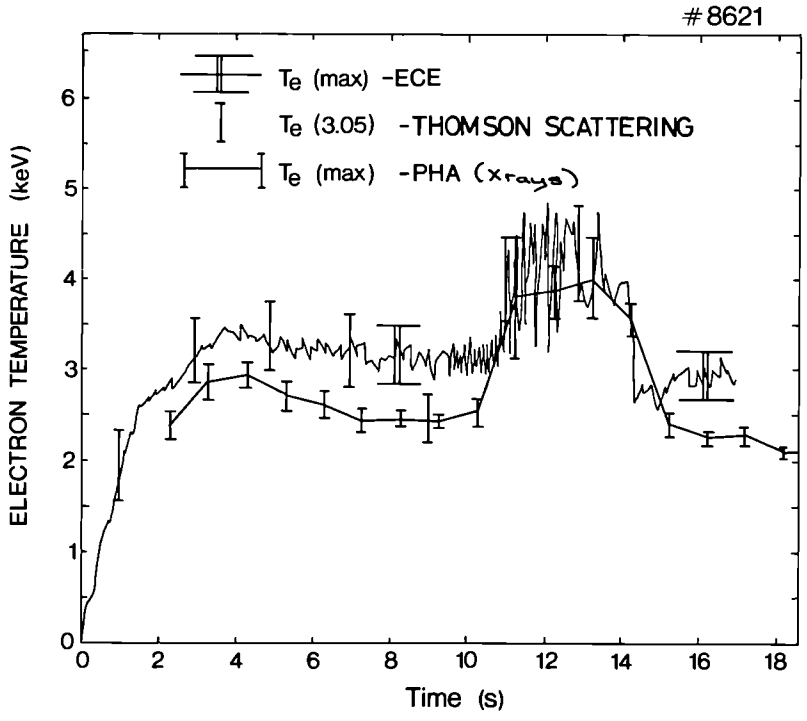

Figure 3 Comparison of Electron Temperature Measurements with different diagnostics.

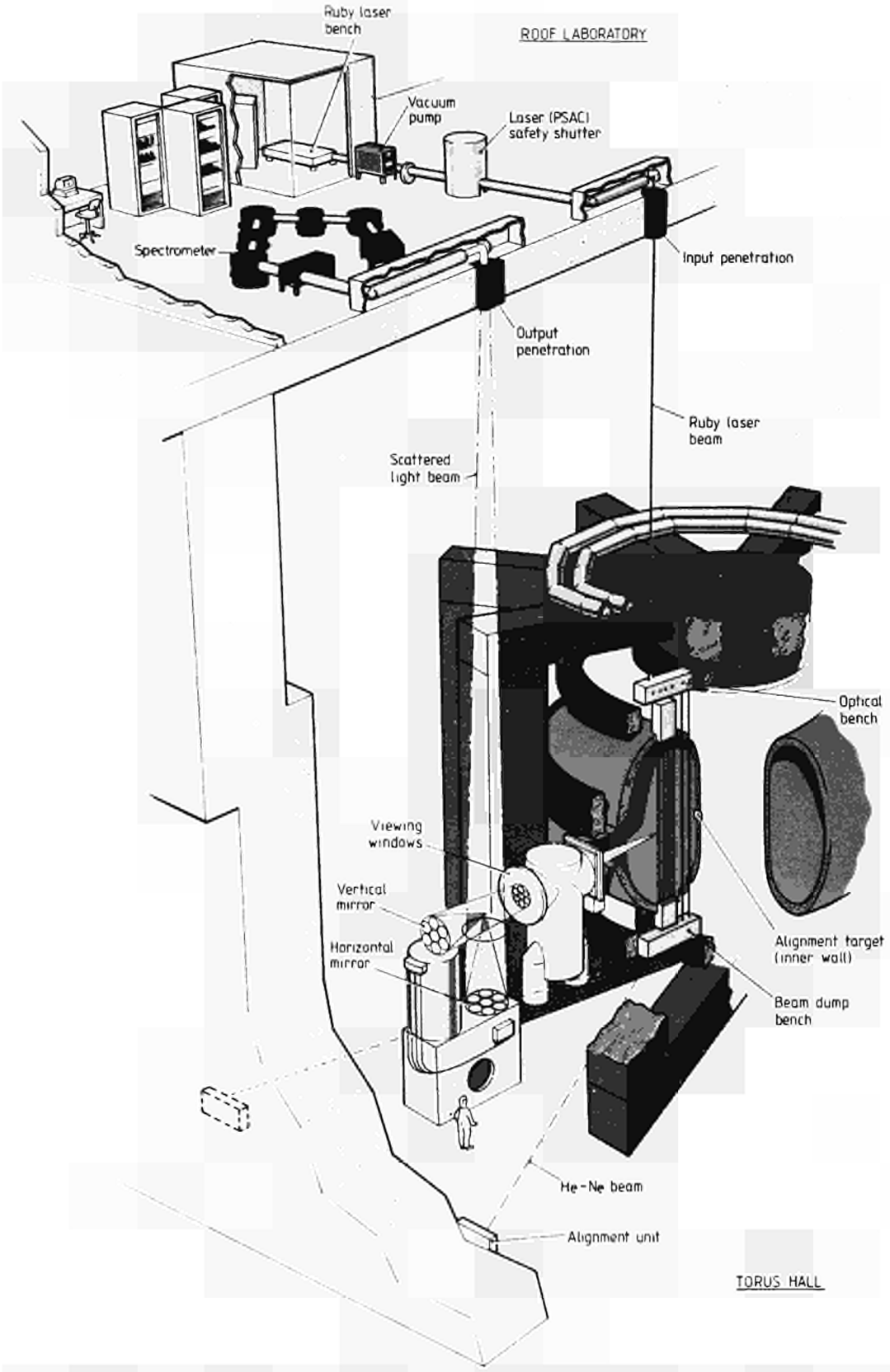

SINGLE POINT THOMSON SCATTERING SYSTEM KE1

Figure 4 Schematic of the Single Point Thomson Scattering Diagnostic.

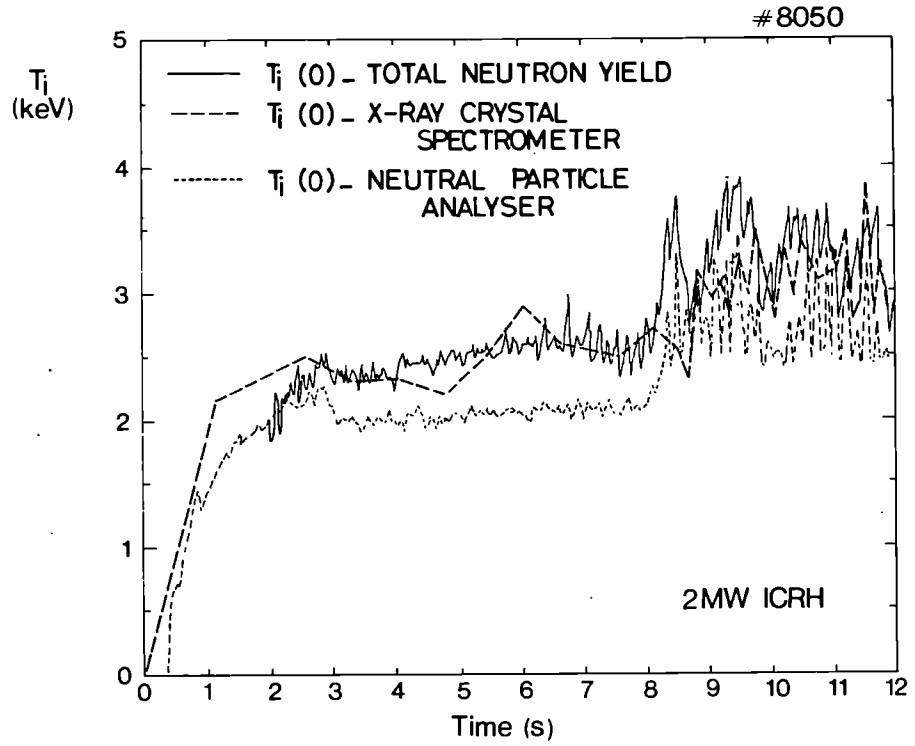

Figure 5 Comparison of Ion Temperature Measurements with different diagnostics.

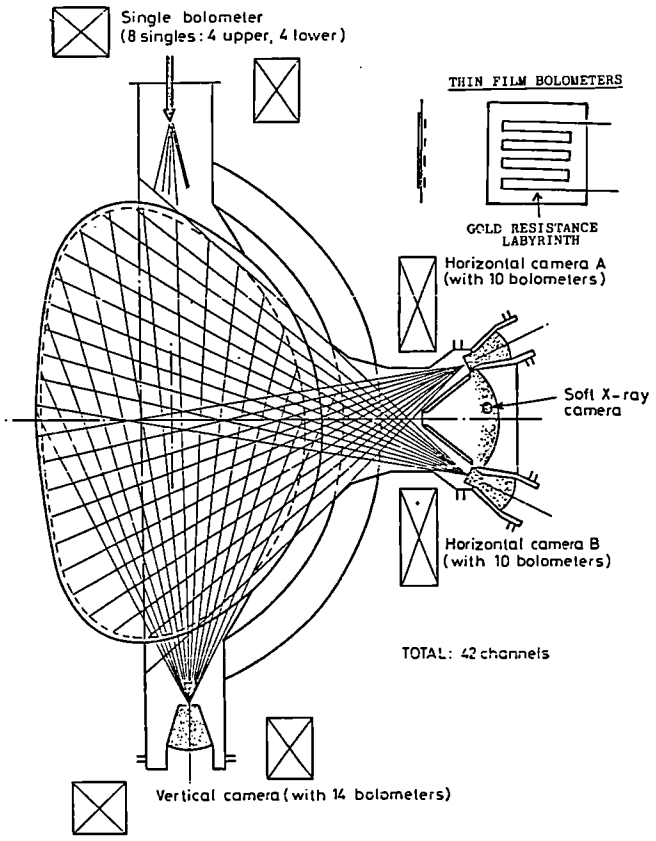

Figure 6 Lines of sight of the bolometer arrays.

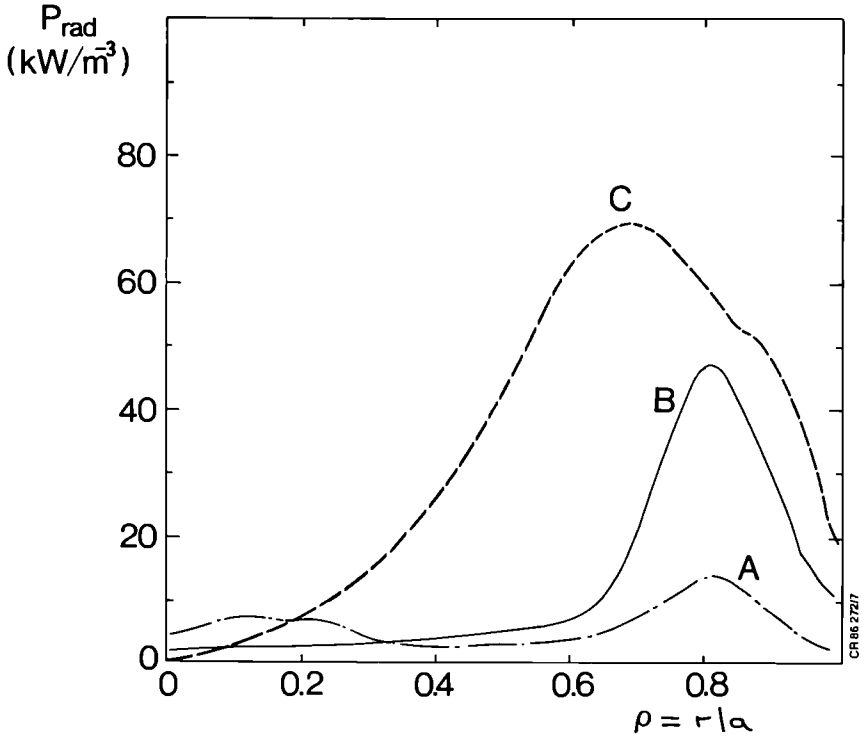

Figure 7 Profiles of radiated power density measured with the bolometer arrays.

A = a typical ohmic discharge

B = an NBI discharge located on the inner wall

C = a combined heating discharge on the limiter

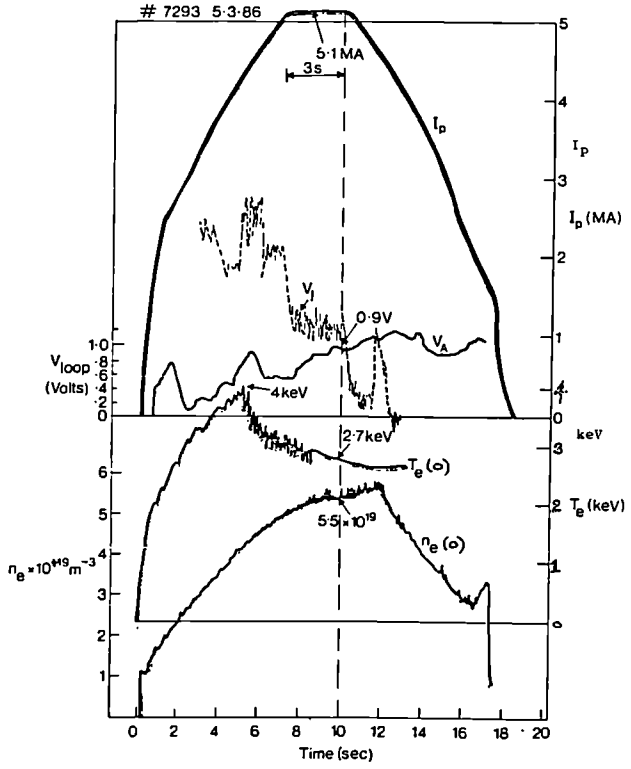

Figure 8 Waveforms of current, and central electron temperature and density in a high current ohmic discharge (B_T=3.4T, q_ψ=3.25, q_{cyl}=2.25, b/a=1.4).

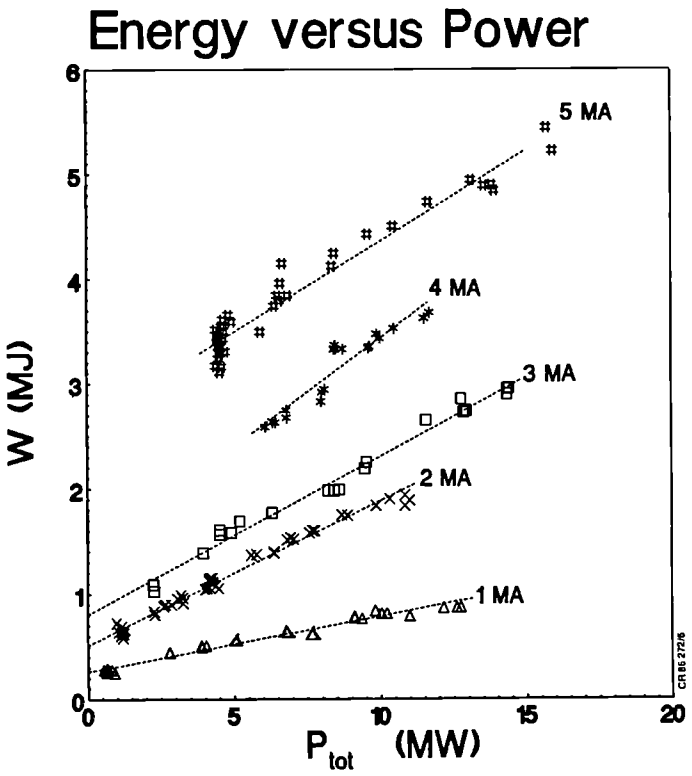

Figure 9 Total plasma energy versus total input power for discharges with different plasma currents (D_p 1 < I_p < 5MA) and additional heating.

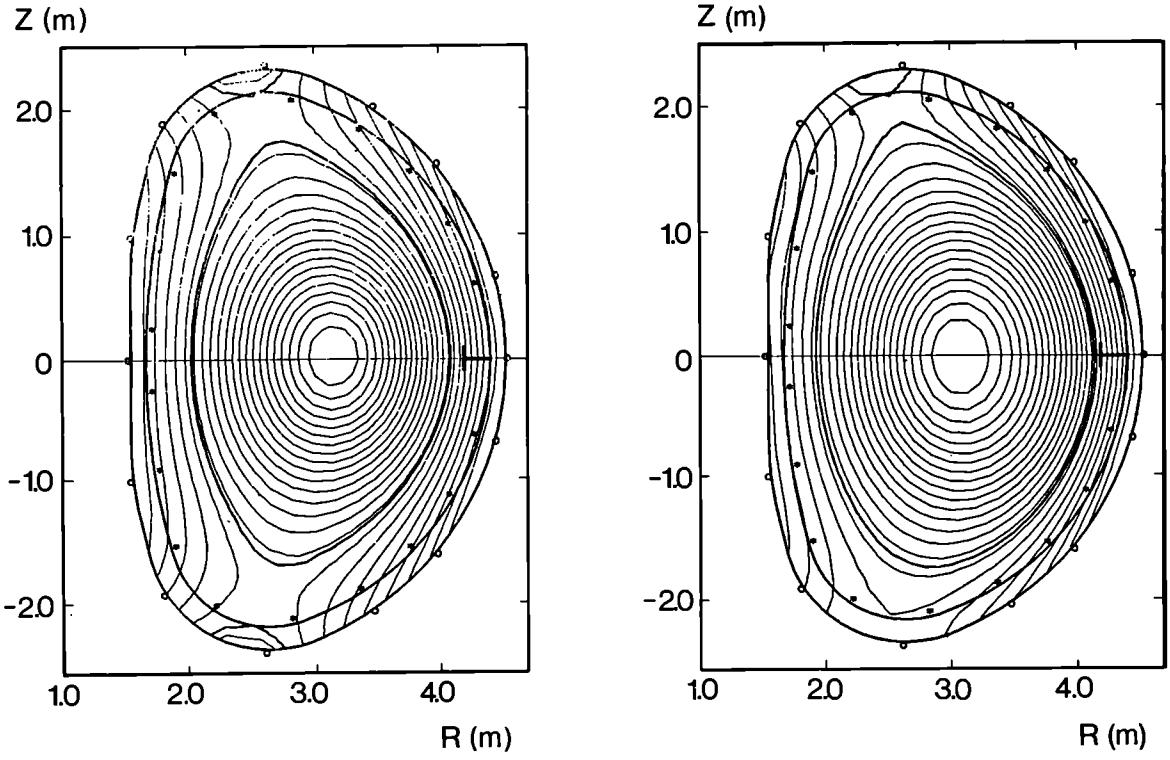

Figure 10 Magnetic flux surfaces for discharges with internal separatrices showing double and single null configurations.

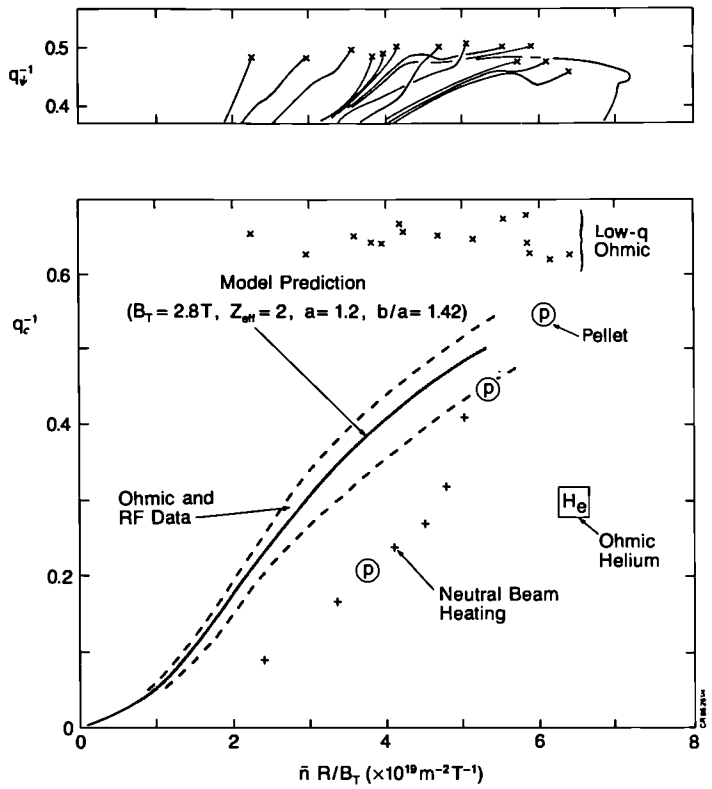

Figure 11 Hugill diagrams showing the limits of stable operation.

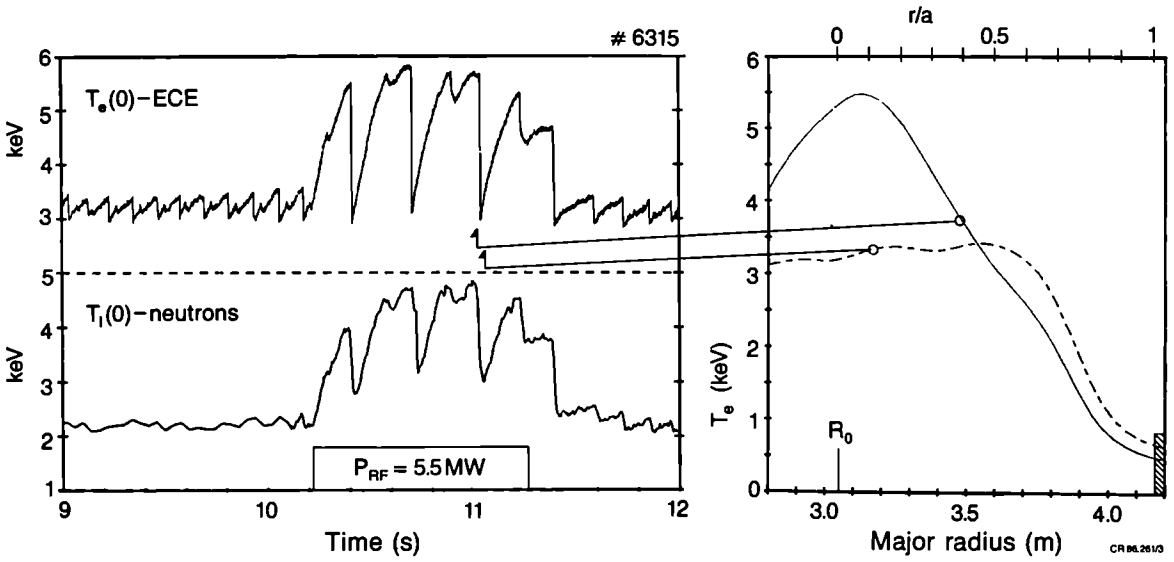

Figure 12 Sawteeth in a discharge with ion cyclotron heating.

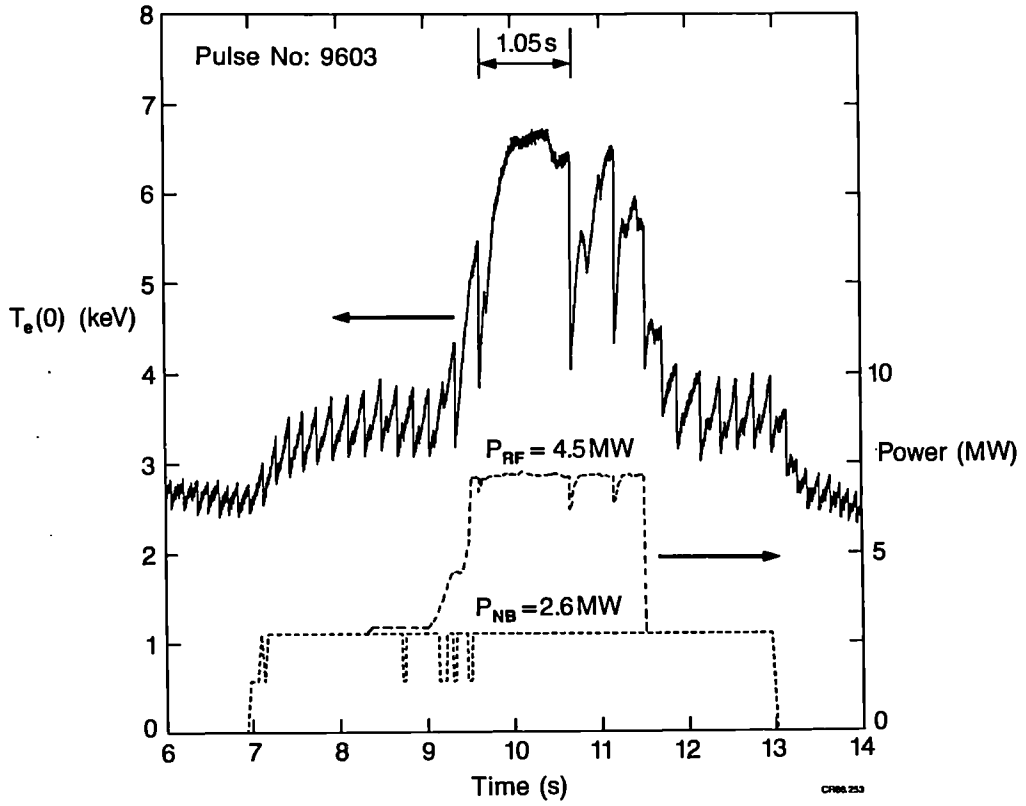

Figure 13 Monster sawtooth in a discharge with combined neutral beam and ion cyclotron heating.

Magnetic Separatrix Experiments in JET

A. Tanga K. Behringer M. Brusati B. Denne A. Gibson N. A. Gottardi
P. Harbour H. Jäckel M. Keilhacker E. Lazzaro M. Malacarne P. D. Morgan
P. Noll J. O'Rourke D. Summers J. A. Tagle P. R. Thomas A. Costley
P. E. Stott D. J. Campbell R. Gill R. Granetz A. Edwards

Abstract

Magnetic separatrix configurations have been produced in JET for plasma currents up to 3MA. Experimental results with these configurations show that some features common to divertor tokamaks can be achieved. In ohmic discharges high recycling regimes can be produced. In neutral beam heated discharges, substantial improvement of the energy confinement time is produced together with the characteristic signatures of an H mode. These characteristics include improved particle confinement, flatter density profile, and an increase in electron temperature especially at the edge leading to a characteristic pedestal feature. At higher neutral beam power, higher plasma densities are reached, with deterioration of beam penetration and strong radiation losses in the outer region of the plasma. The global energy confinement time in the H mode is observed to degrade with additional power. However, results of radial power balance analysis suggest that in the central region where the radiation is not important the degradation of confinement is small.

+ Permanent address: Max-Planck-Institut für Plasmaphysik,
D-8046 Garching/Munchen, FRG

Introduction

JET (Joint European Torus) was conceived as a tokamak with the ability to approach plasma conditions appropriate to a thermonuclear reactor. The achievement of this goal depends on the optimisation of all the fusion parameters: plasma density, temperature and energy confinement time.

Overcoming, or at least reducing, the deterioration of confinement with intense additional heating is crucial to the achievement of these objectives. A substantial improvement in the transport properties of the plasma has been an important feature of tokamaks with a poloidal divertor in the H-mode.

In these experiments the divertor configuration, whose important feature is the presence of a magnetic separatrix, was supplemented by either a divertor chamber as in ASDEX[1] and PDX[2], or by a large volume as in D-III[3]. JET can produce a magnetic separatrix configuration but without a divertor or large ballast vacuum region. The distance between the X-point and the target plates is at most only a few centimeters. However the experimental results reported here show that the plasma behaviour is changed in a similar way to divertor tokamaks. High recycling regime has been observed in ohmic high density discharges, and, with neutral beam heating power larger than 5MW, a regime of enhanced energy and particle confinement has been produced. Typical features of this regime are similar to those observed in ASDEX and PDX in the H-mode, such as the sudden reduction of recycling, as a consequence of improved particle confinement, build up of a temperature pedestal at the plasma edge and a

global reduction of thermal transport. The relative quiescence of the JET H-mode makes it much more akin to the Edge Localised Modes (ELM) free phase in ASDEX [4] and to the H-mode found in DIII-D [5] than to the behaviour of the normal H-mode observed in ASDEX [1] and in PDX [2].

The first section of this paper is devoted to the analysis of the magnetic separatrix configuration in JET. In section 3 and 4 global characteristics and the confinement properties of the H-mode are discussed. The presence of a magnetic separatrix changes the boundary conditions of the discharge and a section is devoted to these phenomena. The behaviour of impurities and particle transport is then analysed and the final section is devoted to a preliminary analysis of energy transport and to the problem of confinement degradation with additional heating.

2. Plasma Equilibrium

2.1 Plasma Shape

JET is a tokamak designed to produce plasmas with elongated and D-shaped cross-sections. This is achieved by feedback control of currents in the shaping coils P2 and P3, shown in Fig 1, the details of the feedback system have been described elsewhere [6].

The P2 and P3 coils produce a mainly quadrupole field which controls the plasma elongation. A net hexapole field, which controls the plasma triangularity, can also be produced by causing oppositely directed currents to flow in these two pairs of coils. In addition to the field produced by the shaping coils, the effects of small aspect ratio and the

attraction of the iron core causes the plasma to have a natural elongation of about 1.4 in the presence of a purely vertical field (such as that created by the equilibrium coil P4). A second source of hexapole field is the main transformer coil P1, due to the leakage field produced by the iron collars at the top and bottom of the central column. For a large current in the P1 coil (-22MA), the flux in the equatorial plane is:

$$\psi\ (R,\ Z=0) = -17 - 0.071\ \left[\frac{R-R_o}{a_\nu}\right]^2 - 6.8\ \left[\frac{R-R_o}{a_\nu}\right]^3 - 3.9\ \left[\frac{R-R_o}{a_\nu}\right]^4 . \qquad (1)$$

Where R(m) is the major radius coordinate, R_o = 2.96m, ψ is in Weber and a_ν(m) is the mean minor radius of the vessel. The hexapole moment is proportional to the coefficient of $\left(\frac{R-R_o}{a_\nu}\right)^3$ and the octupole moment is proportional to that of $\left(\frac{R-R_o}{a_\nu}\right)^4$. The source of the hexapolar field of the iron core can be identified as due to the particular slope of the unsaturated iron collars. From a calculation, made using a Schwarz-Christoffel transformation of the polygonal boundary of the iron core [7], the combined hexapolar moment contribution of shaping coils and the iron leakage field, proportional to the primary current I , can be evaluated as:

$$M_H = \frac{\mu_o I_H}{\pi R_c^3} - \frac{\mu_o I_1}{\pi R_c^3}\,\alpha \quad . \qquad (2)$$

Where α is typically 10^{-2}, I_1 is the current in the primary circuit, I_H is the shaping coils current, R_c is the distance between the coil and the magnetic axis of the plasma. The first term on the r.h.s. represents the effect of the shaping coils, the second term represents the contribution of the primary current leakage field of the coil P1, which, in its negative swing phase, produces a shaping effect in addition to that of the P2 and P3 coils.

2.2 The Formation of a Magnetic Separatrix

By increasing the multipolar fields at a given value of plasma current, it is possible to produce a D shaped plasma whose two stagnation points are pulled inside the vessel, corresponding to a double-null configuration. By unbalancing the up-down shaping currents, a configuration in which only one of the two stagnation points is inside the vessel can also be achieved, corresponding to a single null configuration.

Two typical flux plots for single- and double-null configurations are shown in Fig 2. The distance between the X-points and the protection plates is a roughly linear function of the shaping current, as is shown in Fig 3. Magnetic separatrix configuration experiments have been performed with a current ratio of -40/24 for P2 and P3 coils for double-null configuration, producing an elongation of ~ 1.8; and a ratio of -20/16, (upper coils P2 and P3 only), for single-null configuration, which has a lower elongation of 1.65. This lower value is due to the lower contribution of the quadrupole field proportional to the difference in currents between P2 and P3 compared to the hexapole field. The vertical

position was adjusted by varying the radial field coil current on a time scale of about one third of a second.

2.3 Stabilization of Vertical Plasma Position

The vertical plasma position is unstable in JET for plasma elongation larger than 1.2. The relation between the growth rate of the vertical instability and the plasma parameters has been described elsewhere [6]. In general terms, the destabilising force on the plasma, displaced by δZ_p from the original position, can be described by $F = 2A_{pp}'' I_p^2 \delta Z_p$; where I_p is the plasma current and the coefficient

$$A_{pp}'' = -\frac{\pi R}{I_p}\left\{\left[\left(\frac{\overline{\delta B}_R}{\delta Z}\right)\right]_{equil} + \left[\left(\frac{\overline{\delta B}_R}{\delta Z}\right)\right]_{iron}\right\} . \qquad (3)$$

Where $\left(\frac{\overline{\delta B}_R}{\delta Z}\right)_{equil}$ is the gradient of the quadrupole component of the equilibrium field, $\left[\left(\frac{\overline{\delta B}_R}{\delta Z_p}\right)\right]_{iron}$ δZ_p is the radial field change caused by the iron circuit when the plasma current is displaced by δZ_p. The radial field gradients and variations are averaged over the plasma cross-section. By using the Shafranov equation the parametric dependence of A_{pp}'' can be written:

$$A_{pp}'' \simeq \frac{\mu_o R}{a^2+b^2}\left[\frac{b-a}{b+a}\right]P_q - \frac{3\mu_o}{16R}\left[\left(\ell n \frac{8R}{\bar{r}_p} - \frac{17}{12}\right)\right].P_T + \frac{\mu_o R}{2\bar{r}_m^2} \quad . \qquad (4)$$

Here $\bar{r}_m$ is the average effective distance of the magnetic circuit from the

plasma centre, $\bar{r}_p$ is the average plasma minor radius, a is the minor horizontal plasma radius, b is the minor vertical plasma radius, the coefficients P_q and P_T take into account plasma current effects and are equal to 1 for a flat current profile. The first term describes the effect of non-circularity, the second term represents a toroidal stabilizing effect, and the last term describes the effect of the iron. The agreement between the values derived from formula 4 and those calculated by using a full equilibrium code is fairly good, and is within 20% for limiter, double-null and single-null configurations. Since the main coefficient A''_{pp} in the formula for the vertical destablising force depends essentially on plasma elongation, plasma current profile and geometrical factors, it can be concluded that magnetic separatrix configurations are no more vertically unstable than symmetric limiter configurations with the same size, elongation and plasma current profile.

The stabilisation of vertical plasma position during a disruption with fast current quench is, however, more difficult in single null configurations. In limiter discharges the vertical position is kept centred on the midplane. In the single null configuration, instead, the position of the effective current centre is usually displaced from the midplane by some value Z_o. Rapid change of the plasma current then induces voltages proportional to Z_o multiplied by the time derivative of the plasma current both in the radial flux measurement and in the radial field coil. Therefore the stabilising circuit receives a perturbation right from the beginning of the disruption. Consequently during the disruption the voltage limits of the radial field amplifier can be reached, so that the stabilisation is disabled and the disruption is

accompanied by an escalating vertical plasma displacement. The actual displacement is expected to depend on the ratio of instability growth time to the current quench time.

Moreover, even in single-null configuration discharges arranged to have $Z_o \simeq 0$, because the decay time phase of the plasma current is much faster than the decay time of the shaping coil current. This produces large values of the quadrupole and hexapole field, compared to plasma current, which exceed the stabilization limit. In all cases the vertical plasma movement is directed towards the X-point.

3. Effects of Magnetic Separatrix in Ohmic Discharges

The magnetic separatrix configuration is usually produced during the current flat top of well established limiter discharges. The current in the shaping coils is raised in about 1s. During this time the plasma elongation is increased until a magnetic separatrix configuration is produced. This configuration can then be maintained for several seconds. In order to achieve a magnetic separatrix configuration at the highest plasma currents, use must be made of the combined effects of the primary coil leakage fields and of the shaping coils. In this case, the magnetic separatrix configuration is produced for several seconds at the end of a plasma current flat-top when the current in the primary coil is large. The magnetic configuration is deduced from the equilibrium identification code IDENT B [8] suitably modified for accurate determination of field null location [9]. The precision of the magnetically determined position of the X-point is 3÷5cm and within this distance it coincides with the position deduced from TV camera observations. Both the radial and

vertical position of the X-point are held constant within a few centimetres by the position control system. The X-point location is only weakly sensitive to changes of internal plasma parameters produced, for instance, by additional heating. The time evolution of the main signals for an X-point discharge is shown in Fig 4. During the magnetic separatrix configuration the deuterium recycling (monitored by D_α light) shifts from the outer limiters to a small area around the X-point. Simultaneously, the value of Z_{eff} drops. The average plasma density tends to decrease, a deuterium gas puff of 50÷100mbar/ls is needed for the first couple of seconds to sustain the plasma density at a constant value. When the separation between the plasma and the outer limiter is larger than 7cm, the limiter recycling virtually disappears. Even in the double-null configuration, TV observations in the near infra-red show the formation of a bright region, of approximately 20cm across, coinciding with only one of the X-points. The X-point which emits large radiation is the same even if the plasma is moved vertically, by as much as 20cm, causing the nominal double null configuration to become a single null one, suggesting that this is not connected with slight up-down asymmetries of the poloidal field. The radiating X-point is the one in the ion drift direction although this drift direction was not changed in the experiments. Consequently the asymmetry may be due to neoclassical ion effects such as those observed in ASDEX [10], where it was found that the power threshold for the H mode was lower when the ion drift direction was toward the X-point. Accordingly in the single-null configuration in JET the X-point was chosen to be in the ion drift direction.

In ohmic magnetic separatrix discharges, the value of the global energy confinement time is somewhat larger than that of the corresponding limiter

discharges. In particular, for comparable plasma density and current, plasma temperatures are similar but the loop voltage is somewhat lower than in limiter discharges, so that the confinement times are longer. In Fig 5 the values of global confinement time for the double-null configuration are plotted together with that of limiter discharges with same current (2MA) and toroidal field. The horizontal axis is the scaling factor $n_e\ q_{cyl} R^2 a$, which roughly represents the JET ohmic confinement [11]. The difference in confinement between the X-point and the limiter discharges is beyond experimental error. However, one cannot at present exclude the possible effects of different elongation and Z_{eff} in the scaling.

The presence of a high density region, which is a key feature of divertor plasma experiments, has been clearly detected in the JET ohmic discharges. During the magnetic separatrix configuration, the number of fringes measured by the interferometer channel intercepting the X-point shows an increase, while the average plasma density is approximately constant. This can be used to estimate the local X-point density. Assuming that the radius of the high density plasma region is of the same order as the highly radiating region seen by the bolometer and TV camera (~20cm across), this leads to densities of the order of ~ 1 - $2 \times 10^{20} m^{-3}$. In high density discharges, the small area around the X-point is capable of radiating up to 50% of the input power. The power radiated from this region scales roughly with the square of plasma density and it is similar in double-null and in single-null configurations.

4. Neutral Beam Heating of Single-Null Discharges

4.1 Time Evolution

Heating experiments have been performed in single-null discharges with deuterium co-injection at energies up to 80keV per deuteron, in deuterium plasmas. The pulse length was limited to <4s to avoid thermal overloading of the graphite target tiles. Experiments were carried out at plasma currents of 1, 2 and 3MA and toroidal fields between 2.0T and 3.4T. The relative direction of toroidal field and plasma current was chosen to have the ion drift directed toward the X-point, which was in the upper part of the vessel. Typically, the time evolution of such a discharge shows three characteristic phases which are shown in Fig 6 for a 2.0MA discharge with ~7MW of total input power. In the first 0.5 s of neutral beam heating, the plasma density increases slowly, the total stored energy increases up to a value somewhat larger than that expected for a limiter discharge with similar parameters. This phase has been called the L-phase. In this phase the plasma does not show characteristic features of an H-mode: the D_α signal monitoring the particle flux to the wall is high, with a low value of the particle confinement time. This phase, described later, is also characterised by intense edge MHD activity and by rapid losses of particles, corresponding with edge relaxations, detected by the D_α array. The value of stored energy is somewhat larger than that of corresponding limiter discharges, indicated by a dotted line in Fig. 6

After 0.5 s, and often at a sawtooth crash, a transition occurs: the density starts to increase at a much higher rate and so does the total stored energy. The plasma density increases at a faster rate than the

beam fuelling. The D_α signal drops at both the plasma boundary and at the X-point, the edge temperature profile steepens and stays constant, (as shown at 10cm within the separatrix in Fig 6). The global energy confinement time increases to a higher value. This phase has been called the H-phase because it shows characteristic behaviour of the H-mode discharges found in other tokamaks [1,2,5] such as: a) the existence of a power threshold; b) a preceding L-phase; c) simultaneous improvement in energy and particle confinement; d) a drop in recycling signals and e) development of high edge electron temperatures. In JET the H-mode could be obtained only for power levels exceeding 5MW at a toroidal field of 2.1T. This level is practically independent of plasma current. The threshold power was 9MW for toroidal field of 2.8T and, with the power presently available, it has not been possible to produce an H-phase at toroidal fields of 3.4T. Magnetic separatrix discharges which fail to achieve an H-mode show L-phase behaviour for the entire duration of the beam pulse. At the transition to H-phase, MHD fluctuations and the edge relaxations stop (as described in Sect. 5). During the H-phase, the increase in density causes the beam particles and power to be deposited more and more in the outer regions of the plasma column. The impurity concentration, which increases slightly, causes build up of the radiated power mostly from the outer half plasma radius reducing the power conducted to the separatrix. When this power flow drops below threshold, the H-mode collapses, reverting back into an L-mode. The H to L transition is characterised by the release of plasma energy gained during the H-phase. This energy is mainly conducted to the separatrix dump plates in times of ~ 50ms causing large excursions of the surface temperature of the dump tiles. In this phase the plasma density falls rapidly and the radiated power is reduced. With sufficient neutral beam

power, subsequent further L-H transitions can take place. As described in sect. 5, during the H-mode there are no indications of the high recycling regime, which is observed in ohmic plasmas (c.f. section 3).

4.2 Global Energy Confinement

The main results achieved in the H-mode are summarised in Figs 7 and 8, which show the total stored energy and the global energy confinement time as a function of the total input power. The confinement data are shown for plasma currents of 1, 2 and 3MA for limiter, L- and H-phases. Fig 7 shows the total stored energy versus total input power for the same discharges as in Fig 8 with the addition of the values of the magnetic separatrix discharges in the L-mode. The latter were chosen among discharges with values of toroidal field of 3.0 to 3.4 Tesla for which, presumably, the threshold power for the transition to the H-mode is larger than that available. The energy confinement for the L-mode is between the limiter values and those of the H-mode.

In Fig 8, the H-mode points have energy confinement times more than a factor of two larger than limiter discharges at the same current. It is also evident that in the H-mode the energy confinement time scaling is approximately proportional to the plasma current.

The values for the H-mode points have been selected towards the end of the H-phase when the derivative of the plasma energy content is small compared to the total input power. However, the maximum value to which the plasma density climbs during the H-mode is a function of the input power itself and this is shown in Fig 9. The dependence can be approximated by a slope $(P-P_o)^{0.5}$. Input power and plasma density are then coupled and it is

difficult to extract a parametric dependence of the confinement time on plasma density. These densities correspond to values of the Murakami parameter 20% higher than those otherwise possible in ohmic or neutral beam heated limiter discharges.

In the H-mode the values of energy confinement time decrease with increasing power; the problem of confinement degradation in the H-mode is analysed in the final section of this paper.

4.3 Electron Temperature Profiles

A typical sequence of electron temperature profiles from electron cyclotron emission analysis is shown in Fig 10, where constant neutral beam power is applied and the discharge goes from the L to the H-phase. During the initial L-phase the temperature increases, with a roughly constant profile shape. The transition to the H-phase is characterised by an abrupt increase in the edge temperature, similar to the "pedestal" observed in ASDEX [1] and PDX [2]. The outermost point which can be measured by the second harmonic of electron cyclotron emission is at R = 4.0m so that the electron temperature at the separatrix radius (at R = 4.1 m), cannot be determined. During the H-phase, the plasma density increases continuously and the average electron temperature increases slightly, at the highest plasma densities the average electron temperature may fall slightly before the end of the H-phase.

The broadening of the electron temperature profile can be deduced also from the X-ray tomographic reconstruction shown in Fig 11. The emission in the edge region increases substantially and during the H-mode the volume

of plasma emitting X-rays increases to nearly the whole plasma cross-section. The change in profile shape is also clearly seen in the plot of the second moment (a measure of the profile width) of the X-ray data from the vertical camera shown in Fig 12. The second moment increases by 30-40% during an L to H transition and this change is a clear indicator of the existence of the H-mode. The observation of X-ray emission from close to the plasma boundary indicates that the electron temperatures in this region are roughly double those observed in the L-phase. After the H-mode transition, both the amplitude and inversion radius of sawteeth decrease, and the period also decreases.

4.4 Electron Density Profiles

The electron density profiles of both ohmically heated and L-mode neutral beam heated X-point discharges are similar to those obtained in limiter and inner-wall discharges, having a profile ($n_e = n_{eo} (1-\rho^2)^{0.5}$). The transition from L-mode to H-mode, is marked by a pronounced broadening of the density profile. A typical sequence of density profiles is shown in Fig 13. Spatially resolved measurements of the D_α light indicate that the total electron source decreases during the L-mode to H-mode transition. Thus the behaviour of the density profile must be attributed to a net decrease in the outward flux of particles during the transition to the H-mode.

Changes in particle transport can be analysed using a simple model in which the electron flux Γ_e can be described with an expression of the form [12]:

$$\Gamma_e = -D_p \nabla n_e - \Gamma_p \quad . \qquad (5)$$

Here D_p is the diffusion coefficient and Γ_p is an inward particle flux. For typical values of the diffusion coefficient, ($-0.6 m^2/s$), the flattening of the density profiles during the H-mode implies that the ratio Γ_p/D_p is doubled at r/a - 0.75. Toward the end of the H phase the density profiles are very flat ($n_e = n_{eo} (1-\rho^2)^{0.25}$). At the H to L transitions the density falls and the density profile rapidly reverts back to the more peaked shape characteristic of the L-mode, as shown in Fig 14.

4.5 Current Density Profiles

Indications of current density profile changes during the H-mode can be derived from the time evolution of internal inductance.
The values, calculated with the magnetic code [8], are shown together with the poloidal beta in Fig 15. The value of ℓ_i drops during the H-mode indicating a flattening of current profile distribution. A full reconstruction of the MHD equilibrium, by fitting the magnetic data shows that a good fit can be obtained only with current profiles which, instead of being typically bell shaped, have shoulders at the plasma edge. This is in agreement with the increase of edge temperature reported above.

5. Plasma Edge and Scrape-off

5.1 Edge plasma fluctuations

The H-mode has been associated with characteristic behaviour of the magnetic fluctuations at the plasma edge in D-III [13] and to Edge Localised Modes in ASDEX [4]. In JET the L-phase of the discharge is characterised by edge fluctuations extending along the full poloidal circumference. These fluctuation disappear at the L to H transition. The physical nature of the edge fluctuation described here is probably different from the ELM's observed in ASDEX [4]. Whilst the ELM's observed in ASDEX occur after a quiescent phase and are triggered by the edge pressure gradient reaching a limit value, the fluctuations observed in JET are associated with L-mode, they preceed the H-phase and the plasma pressure has a low value. These are present for the whole duration of the beam pulse in discharges with insufficient power for the L to H transition. The JET L-phase fluctuations are clearly visible on the soft X-ray, fast MHD signals, reflectometer and D_α multichannel signals. The level of magnetic turbulence, (in the frequency band 5-60kHz), is enhanced by the presence of neutral beam heating; whenever an L to H transition occurs signals of the magnetic pick-up coils close to the single-null show a marked and sudden drop, as shown in Fig 16. This figure shows the good time correlation existing between the level of magnetic turbulence (at about 40kHz) and the H and L phases of the discharge.

The L-H transitions are always preceded by regular disruptive-like events at the plasma edge. The mode is seen in most X-ray channels as a disruptive-like instability with a sudden drop in X-ray intensity. A more detailed study of these fluctuations, using data taken at 200kHz, shows that in the outermost channel the change in intensity occurs very rapidly (80μs) whereas in other channels at smaller radii the change is much

slower (800μs). This indicates a mode occurring in the edge region with its effects becoming slower as it propagates inwards.

The traces of the pick up coils, which detect the magnetic part of the fluctuations, during the L-phase, feature regular spikes which are correlated with each edge disruption observed by the X-ray signal. This is shown in detail in Fig 17(a),(b). Sawtooth crashes decrease the repetition frequency of these edge modes and generally the final transition coincides with one of these crashes as shown in Figs 18(a) and (b). The second example, in Fig 18c-d, shows the magnetic activity during a typical H-L transition. This transition is accompanied by a burst of broad band magnetic activity which lasts for times comparable to the relaxation of the density and temperature profiles.

5.2 Plasma Scrape-off Measurements

Scrape off parameters are measured by a Langmuir probe. The vertically moveable probe can scan a region on the top of the machine at a major radius R=3.2m. In discharges with additional heating a vertical scan can be performed up to a distance of 5 cm from the magnetic separatrix.

The temporal variation of the probe saturation current, i_{SAT}, is shown in Fig 19 with the D_α signal taken along a vertical chord. Beams were switched on at 9.5 seconds, the H-mode was achieved from 12 to 13.6 seconds. The scrape off electron density is approximately constant during the H-mode despite a three-fold increase in plasma density. This contrasts with limiter and L-mode discharges where the density, in the

scrape off, increases approximately with the square of the average electron density. There is a significant transient rise in i_{SAT} with the termination of the H-mode. This is associated with the rapid loss of confinement at the H to L transition.

5.3 Particle Balance and Recycling Coefficient

A common feature of H-mode observed in JET as well as in ASDEX [1], PDX [2], DIII-D [5] is the rapid increase in plasma density which takes place after its onset. In the H-mode the particle fluxes from the plasma are reduced as seen by the drop of D_α signals. Using the data from a poloidal array of D_α detectors the global particle balance equation has been solved [14]. The resulting time evolution for the global particle confinement time and global recycling coefficient is shown in Fig 20. In the ohmic discharges with magnetic separatrix the values of particle confinement time are lower than in the limiter configuration and during the L-phase there is a degradation of τ_p similar to that observed in limiter discharges. At the onset of H-mode the value of τ_p doubles stepwise and stays roughly constant throughout the H-phase. Since the rate of increase of plasma density is up to a factor two larger than the fuelling rate, the values of the recycling coefficient are larger than one, this effect is further enhanced by the increase of τ_p.

A comparative plot of τ_p for limiter, L and H mode discharges is shown in Fig. 21 versus average plasma density. The limiter discharges are characterised by values of particle confinement time that decrease with increasing density, essentially as a result of higher edge plasma densities. In contrast, with magnetic seperatrix, two regions exist: at

low densities, in the L mode, the value of τ_p is lower than in the limiter discharges while in the H mode it is higher. In the H-mode the particle fluxes from the plama, as measured by D_α array, are small. This is in agreement with small values of saturation current measured by the Langmuir probe. These observations, the indication of high edge temperatures (c.f. sect. 4.3) and the comparative low level of radiation from the X-point region (c.f. Fig. 6 and sect. 6.2) indicate that there is no high recycling region in the H-mode.

6. Behaviour of Impurities and Radiation Losses

Spectroscopic diagnostics (XUV, VUV, Visible and Charge Exchange Recombination Spectroscopy (CXRS) have been used for studying impurity behaviour in JET plasmas during magnetic separatrix operation. The main impurities in JET plasmas are carbon (from carbon limiters and protection plates) and oxygen. Metals (nickel and chromium from Inconel walls and antenna screens) generally contribute little to Z_{eff} and radiated power. Typical impurity concentrations (in % of the electron density, n_e) are [15]: 2-4% C, $\simeq$ 1% O, and 0.02%, or less, metals. During the period in which most of the X-point operation was carried out, the oxygen concentration in the plasma was, however, somewhat higher ($\simeq$ 2%) due to occasional vacuum leaks.

6.1 Ohmic Discharges

Compared to similar limiter discharges Z_{eff} was somewhat lower in X-point

plasmas (Fig 22 - filled circles), essentially due to a reduced carbon concentration (1-2% C during X-point). The reduction implies that less carbon was produced at the X-point graphite target plates than at the limiters. Metal concentrations were reduced too, although the dump plates were most likely covered by wall material. During previous operation with Inconel dump plates no increase was observed in metal concentrations in the plasma when changing from carbon inner-wall to X-point operation. These observations indicate a low plasma temperatue ($\tilde{-}$ 20eV) in front of the plates characteristic of the high recycling zone described above, resulting in a low sputtering yield. A change in the screening property of the boundary plasma is a less likely explanation, results on ASDEX [16] showing that the screening is comparable in divertor and limiter plasmas. The oxygen concentration, oxygen most likely originating from the vessel walls, was 1-2% n_e, similar to limiter palsmas for the same plasma conditions.

6.2 Discharges with Additional Heating

With Neutral-Beam Injection (NBI) both carbon and metal concetrations were higher than in the ohmic case, which is consistent with an observed increase in the edge electron temperature, although the metals might also have originated from CX sputtering. The C/O ratio increased during NBI, in contrast to what was observed in limiter plasmas, where oxygen was the dominating impurity during NBI at high $\bar{n}_e$. As shown in Fig 22 somewhat higher Z_{eff} values were found in X-point plasmas with additional heating - the general falling trend with increasing n_e, observed in ohmic cases,

being maintained. During Ion Cyclotron Resonance Heating (ICRH) and combined heating, increased levels of screen material (Ni and Cr) were found in the plasma as in the limiter cases [17].

During the H-mode, Z_{eff} did not decrease as normal at high $\bar{n}_e$ (see Fig 22), but remained similar to the lower-$\bar{n}_e$ values of 3-4. The high Z_{eff} values could be accounted for by the central concentrations of light impurities as measured by CXRS (Fig 23). The C/O ratio during H-mode was 1-2:1. An observed increase in metal density can be explained either by sputtering by CX neutrals or by the increased edge temperature. The metal concentration was relatively independent of $\bar{n}_e$ for H-mode plasmas which contrasts with the falling trend with increasing $\bar{n}_e$ seen in all other types of discharges (Fig 24). However, the metal concentration is still low: its contribution to Z_{eff} is ≤ 0.2 (Fig 25), and $\leq 10\%$ of P_{rad} is due to metals according to transport code calculations.

At the L-H transition the radiation from the peripheral ions (O IV- O VII lines) was essentially unchanged (or even decreased) after the L-H transition, whereas O VIII radiation, emitted from radial locations further in, increased roughly as $\bar{n}_e^2$. The behaviour of the lowly-ionised C and O is consistent with the observed change in edge parameters, and results in less total radiation per ion for these light impurities.

The bulk particle confinement increased by a factor ~3 in the L-H transition. The impurity confinement increased similarly. For carbon the improved confinement can be seen in Fig 23: the carbon concentration is

essentially constant, or increases somewhat in the H-mode, although the carbon influx (represented by the C III-line brightness) drops just as the hydrogen flux, ϕ_H (carbon production yield $\phi_C/\phi_H \sim 5\%$).

There is no indication of impurity accumulation in the neoclassical sense. Analysis of several metal ionisation stages as well as the soft X-ray emission profiles and bolometer show that the metal density profile is not peaked in the centre. The values of nickel concentration derived from Ni XXV, XXVI, (VUV spectrometer) and Ni XXVII (X-ray crystal spectrometer) line intensities agree to within a factor ~2, which is within the error bars. The absence of impurity accumulation might possibly be explained by the presence of sawteeth in the H-mode discharges.

The time evolution of radiation losses in an H-mode discharge is shown in the bottom traces of Fig 6. During the first L-phase the power radiated from the main plasma (P^{rad}_{bulk}) is of the order of 20% of the total input power. During the H-mode, the power radiated from the main plasma increases while the power radiated from the small region around the X-point is roughly constant (see Fig 6). When only neutral beam heating is applied the increase of the radiated power from the main plasma scales with the square of plasma density as is shown in Fig 25: the ratio of radiated power to square of the average plasma density is approximately constant during the H-phase while the average plasma density increases three times. This is in agreement with the result that Z_{eff} and the concentration of the main impurities are approximately constant during the H-phase. The increase in bulk radiation during the H-phase takes place essentially in the outer region of the plasma as is shown by the sequence

of Abel inverted radiation profiles shown in Fig 26, although the radiating shell penetrates more deeply inside the plasma at higher densities. The total radiated power can be accounted for by the radiation of oxygen and carbon, although the radiation profile is dissimilar to the usual light impurity edge shells. Metals should contribute little ($\leq$10%) unless their concentration was substantially underestimated, which is unlikely since all VUV and X-ray diagnostics yield consistently low results. Model calculations based on the usual transport coefficients fail to explain the broad shells seen by the bolometer, although a change in ionisation balance due to the presence of beam neutrals leads to some inward shift and broadening of light impurity radiation. It must be assumed that impurity transport is modified in the following way: a high inward drift velocity at the plasma edge leads to a steepening of impurity ion profiles and higher particle confinement. This profile change is confirmed by a comparison of nickel radiation from the plasma edge (Ni XVII, XVIII) and from the plasma interior (Ni XXV, XXVI). In the plasma centre, impurity ion profiles are hollow, probably due to the non-stationary nature of the H-mode discharges. On the basis of these assumptions, the bolometer profiles can be explained by the radiation of light impurities, essentially oxygen. The same transport model may explain the meausred density profiles during the H-mode. The power flow to the magnetic separatrix can be calculated from global power balance. The density related increase in radiation reduces the power flow to the magnetic separatrix, at the moment of H to L transition, this is found to be between 3.5 and 4.0MW, independent of the value of the input power. This indicates that the end of the H phase is connected to a threshold value for the power flow to the magnetic separatrix.

7. Transport Phenomena in H-mode discharges

Transport features of H-mode discharges in JET have been investigated using the 1½D time-dependent interpretation code JICS [18]. As experimental information on the ion temperature profile is not available, a large uncertainty exists in the evaluation of the electron-ion coupling power term which accounts for a non-negligible fraction of the power balance for both populations. The ion energy content can be modelled from the experimental information of the ion temperature on axis, provided by the X-ray crystal spectrometer and charge exchange spectroscopy and taking into account as a mild integral constraint the total plasma stored energy as measured by the diamagnetic loop. However, the strong electron-ion coupling which exists at the high flat profile electron density profiles typical of JET H-modes, suggests that the overall dynamics of these discharges is best dealt with using a single fluid approach.

It is found that the L to H transition triggers a reduction of transport losses over the whole plasma cross-section; this reduction is established during a time of the order of the confinement time and is then maintained for the whole H-phase. This is well correlated with the build-up of a thermal barrier at the plasma edge similar to that found on ASDEX [19].

In Fig 27, the total plasma stored energy is shown as a function of radius at different times during the H-mode. Two distinct phases can be observed: during the first phase a gradual build-up of the plasma energy content takes place, which can be attributed to reduced global losses; in the second phase increased radiation losses deplete the stored energy. As a result the total energy confinement time is affected, while the

confinement time in the inner transport dominated layers remains unaltered (Fig 28). Sensitivity analysis of τ_E on the ion temperature profile (not available experimentally) was carried out by varying T_i within a range ($\pm$ 20% locally) compatible with the strong electron-ion coupling, which occurs at these high densities.

The related uncertainty is found to be ~25%, i.e. less than the difference in behaviour of τ_E at <a> and <a>/2 as shown in Fig 28. No appreciable confinement degradation appears with increasing input power respect to ohmic values (Fig 29).

8. Conclusions

These experiments have focused on the study of physics parameters affected by operation with a magnetic separatrix. The analysis of plasma equilibrium shows that a magnetic separatrix configuration can be created in JET by suitable selection of currents in the coils used for control of the plasma elongation and triangularity and by the leakage field of the primary circuit.

The vertical stability of this configuration is not appreciably different from that of a limiter discharge with similar elongation. However, with magnetic separatrix configuration, plasma disruptions always tend to have a vertical instability component. Features typical of a divertor tokamaks have been observed in JET such as the formation of a high recycling regime in ohmic high density discharges. With neutral beam heating in the single null configuration an improved confinement regime has been observed when the total input power exceeded a threshold value of 5MW. This regime

shows typical signatures previously observed in H-mode discharges in ASDEX, PDX and DIII-D. Characteristics such as an increase of particle confinement and a quench of plasma edge instabilities measured by magnetic pick-up coils, soft X-ray, reflectometry and D_α emission have been observed. An improvement in global energy confinement by a factor of two compared to limiter discharges has been measured. During the L-phase confinement is somewhat improved over that in the limiter configuration but lower than the best confinement achieved in the H-phase.
In common with ASDEX, PDX and DIII-D H-mode, the JET H-mode shows a large increase in plasma density, flatter density profile, and an increase in electron temperature especially at the edge, leading to a characteristic pedestal feature. The dominant impurities are carbon and oxygen, and metal impurity concentrations, larger compared to limiter discharges, contribute only a small amount to the value of Z_{eff}. These relatively higher impurity concentrations may be explained by longer confinement times and/or by increased sources due to higher edge temperatures. In the lifetime of the JET H-mode, lasting at most 2 seconds, the radiation profile is characteristically hollow indicating no significant accumulation of impurities in the centre of the discharges. It should be noted however that the duration of the H-mode is much shorter than the time the incoming impurities need to reach the centre of the plasma, if the transport is purely neoclassical.

In the latter part of an H-mode the input power is deposited, and also radiated, increasingly in the outer layers of the plasma, due to the increase in plasma density and the higher concentration of impurities, until the H-mode collapses. The H-modes reverts to an L-mode when the power flowing to the separatrix falls below a threshold value.

Global energy confinement times degrade with power, but this degradation can be largely ascribed to poor beam penetration and to high radiation losses. Power balance calculations performed over the inner half only of the plasma radius, where radiative losses are still negligible, give indications that the central confinement does not suffer appreciable deterioration with power.

ACKNOWLEDGEMENTS

This paper contains experimental results which have been achieved by the dedication and efforts of all the JET Team. Particularly involved in the experimental work have been members of the Magnet and Power Supply Division, First Wall Division, the Neutral Beam Heating Division, Radio Frequency Heating Division and the Experimental Divisions. The efforts of J Christiansen in producing "Fast" code analysis of the magnetic configuration and K. Thomsen for the data management are acknowledged. We are grateful to R. J. Bickerton, J. G. Cordey, M. L. Watkins and A. Gondhalekar for the fruitful discussions, and to G Fussmann for preliminary analysis of spectroscopic data. Thanks are also due to P. Lomas and F. C. Schüller, for conducting experimental sessions, and to B E Keen for editorial work on the paper.

REFERENCES

[1] Wagner, F., Becker, G., Behringer, K., Campbell, D., Eberhagen, A., et al in Proceedings of the Ninth International Conference on Plasma Physics and Controlled Nuclear Fusion Research. Baltimore 1-8 Septemer 1982. IAEA-Vienna 1983, page 43; and Wagner, F., Becker, G., Behringer, K., Campbell, D., Eberhagen, A., et al Phys. Rev. Lett 49 1408 (1982).

[2] Kaye, S.M., Bell, M.G., Bol, K., Boyd, D., Brau, K., et al in Proceedings of the Symposium on Energy Removal and Particle Control in Fusion Devices Princeton, N.J., USA, 26-29 July 1983. North-Holland Physics Publishing Co, Amsterdam 1984, page 115.

[3] Ohyabu, N., Burrell, K., H., De Boo, J., Ejima, S., Groebner, R., Overskei, D., et al Nucl. Fus. 25 49 (1985).

[4] Keilhacker, M., Fussmann, G., Von Gierke, G., Janeschitz, G., Kornherr, M., et al in Proceedings of the Tenth International Conference on Plasma Physics and Controlled Nuclear Fusion Research London 11-19 November 1984, Vol I, page 71 (IAEA-Vienna 1985).

[5] Luxon, J., Anderson, P., Baity, F., Baxi, C., Bramson, G., et al "Initial results from DIII-D Tokamak" presented at Eleventh International Conference on Plasma Physics and Controlled Nuclear Fusion Research. Kyoto, Japan, 13-20 November 1986. Paper IAEA-CN-47/A-III-3. To be published.

[6] Bertolini, E., Mondino, P.L., Noll, P., Fusion Technology 11 (1987) 71.

[7] Bewley, L. V., in "Two dimensional fields in Electrical Engineering" - Dover Publ. N. York (USA) 1963.

[8] Brusati, M., Christiansen, J.P., Cordey, J.G., Jarret, K., Lazzaro, E., Ross, R., Comp. Phys. Rep. 7-8 (1984) 345.

[9] Tanga, A., Campbell, D.J., Denne, B.D., Gibson, A., Gottardi, N., et al in Proceedings of 12th European Conference on Controlled Fusion and Plasma Physics, Budapest 2-6 September 1985, Published by European Physical Society, (Budapest 1985), Vol I, page 19.

[10] Wagner, F., Bartiromo, R., Becker G., Bosh, H. S., Eberhagen, A. et al., Nucl. Fus. 25 1490 (1985)

[11] Bickerton, R. J., Alladio, F., Bartlett, D. V., Behringer, K., Behrish, R., et al. in Plasma Physics and Controlled Fusion, 28 (1986) 55.

[12] Coppi, B. and Sharky, N., in Physics of Plasma Close to Thermonuclear Conditions, Proceedings of the course held in Varenna, Italy 27 August - 8 September 1979. Commission of the European Communities, Brussels. Vol I, page 47; and Behringer, K., Engelhardt, W., Feneberg, W., Fussmann, G., Bull Amer. Phys. Soc., 25 (1980) 875.

[13] Ohyabu, N., Jahns, G. L., Stambaugh, R. D., Strait, E. J., Phys. Rev. Lett. 58 120 (1987).

[14] Tanga, A., Gowers, C.W., Hugenholtz, C.A., Morgan, P., Schüller, F.C., "Global Particle Balance and Recycling in First JET Discharges". JET Report: JET-P(84)09.

[15] Behringer, K., Boileau, A., Bombarda, F., Denne, B., Engelhardt, W., et al. "Impurity production mechanisms and behaviour during additional heating in JET" presented at Eleventh International Conference on Plasma Physics and Controlled Nuclear Fusion Research, Kyoto, Japan, 13-20 November 1986. Paper IAEA-CN-47/A-IV-1. To be published.

[16] Engelhardt, W., Becker, G., Behringer, K., Campbell, A., Eberhagen, A., et al. J of Nucl. Mater. 111&112 337 (1982).

[17] Behringer, K., Denne, B., Forrest, M. J., Hawkes, N. C., Kaye, A., et al, in Proc. of the 13th European Conference on Controlled Fusion and Plasma Heating, Schliersee, 14-18 April 1986. Published by European Physical Society, Vol 10C, Part I, p.176.

[18] Brusati, M. and Cordey, J. G., in Proceedings of 12th European Conference on Controlled Fusion and Plasma Physics, Budapest, 2-6 September 1985, Published by European Physical Society, (Budapest 1985), Vol I, p.34.

[19] Gruber, O., Jilge, W., Bernhardi, K., Eberhagen, A., Fussmann, G., et al in Proc. of 12th European Conference on Controlled Fusion and Plasma Physics. Budapest 2-6 September 85 Vol I, p.18 (Budapest 1985).

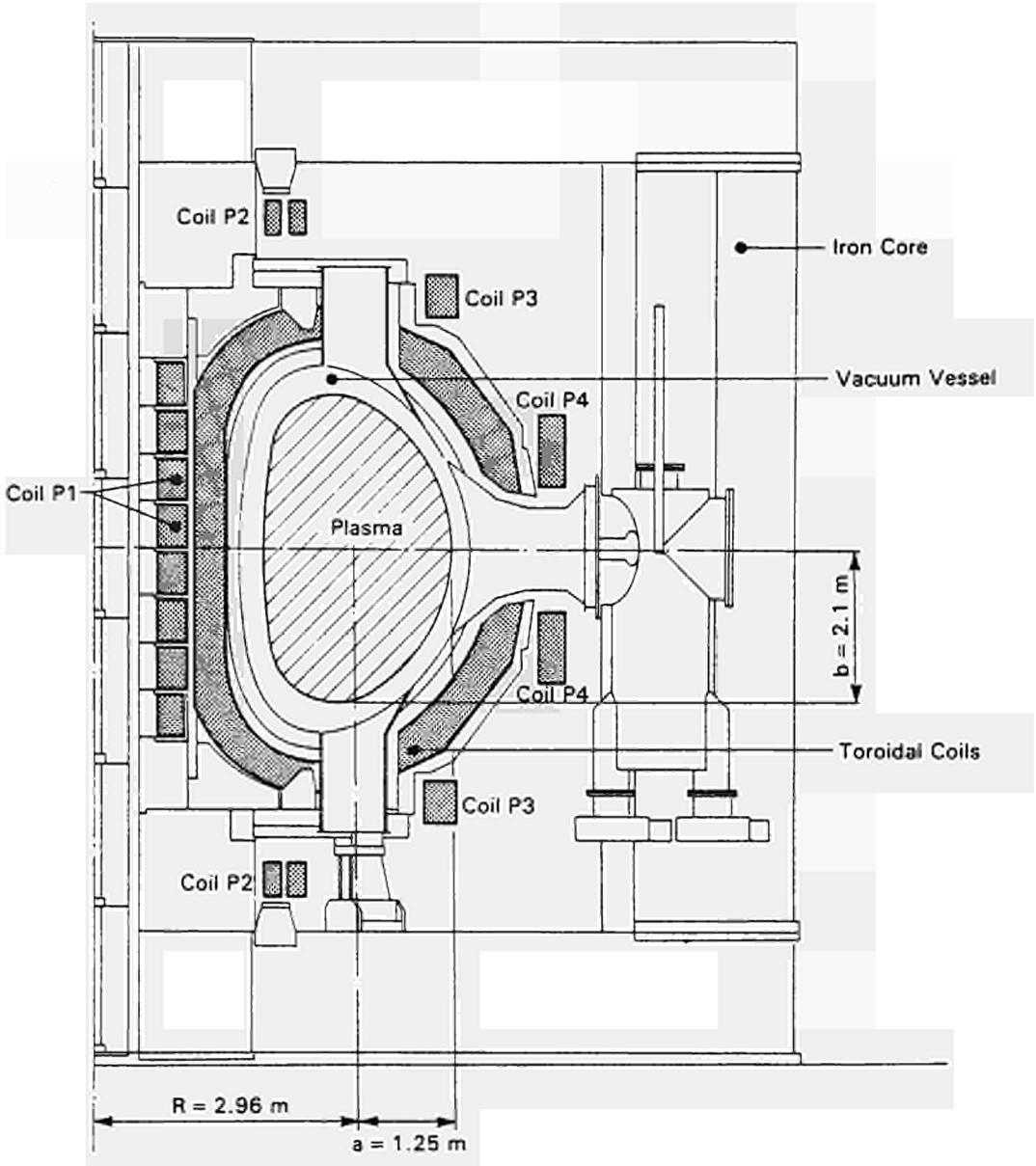

Fig 1 Cross-sectional view of JET showing the location of various coils.

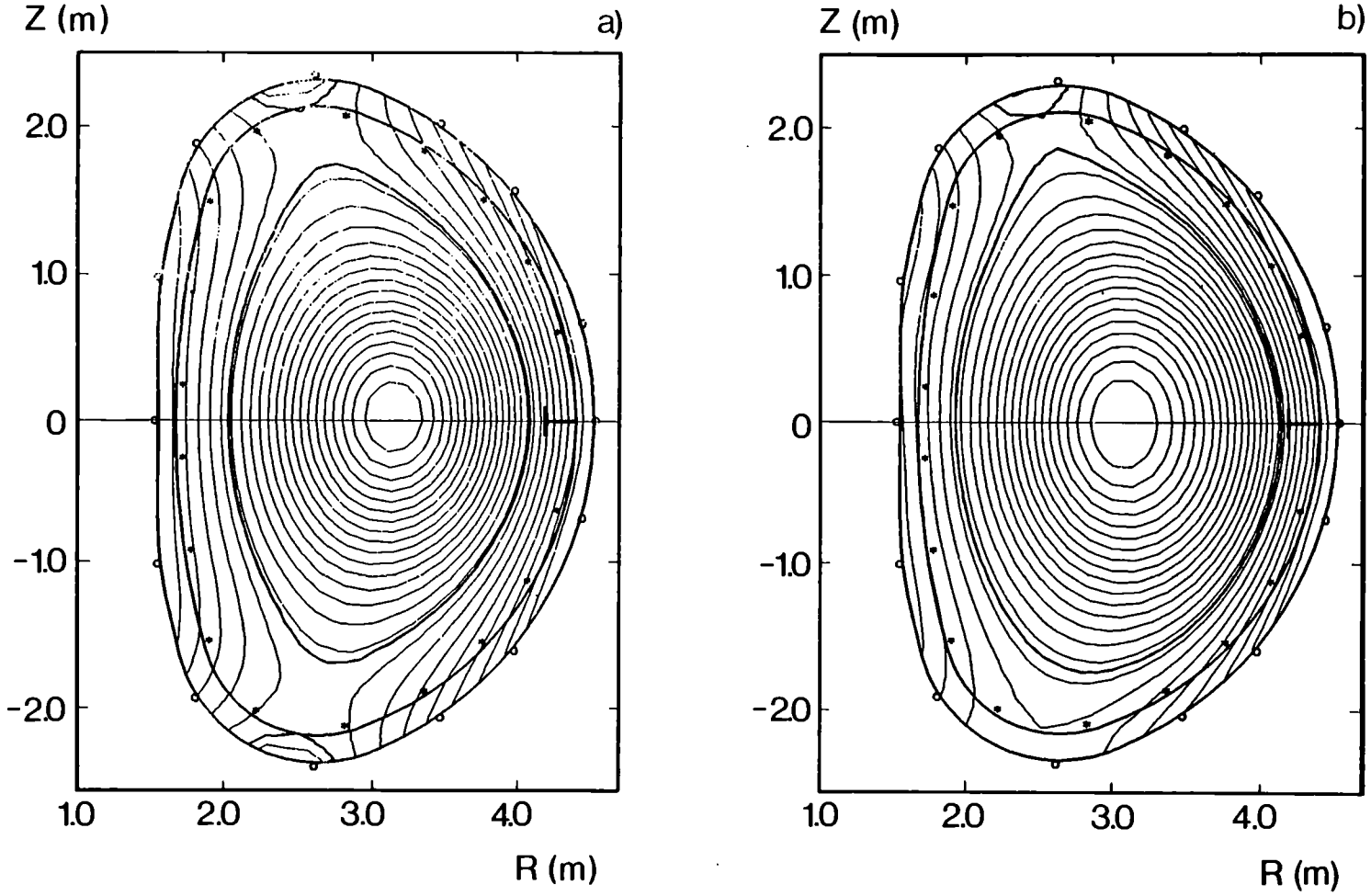

Fig 2 (a) Flux plot of a double null configuration. Plasma current = 2MA, toroidal field 2.8T, plasma electron average density = $3.10^{19}m^{-3}$, poloidal beta = 0.44, plasma elongation = 1.8.

(b) Flux plot of a single null configuration. Plasma current = 2.0MA, Toroidal field = 2.2T, plasma electron average density = $3.10^{19}m^{-3}$, poloidal beta = 0.6, (Pulse No 10237, t = 13.5s).

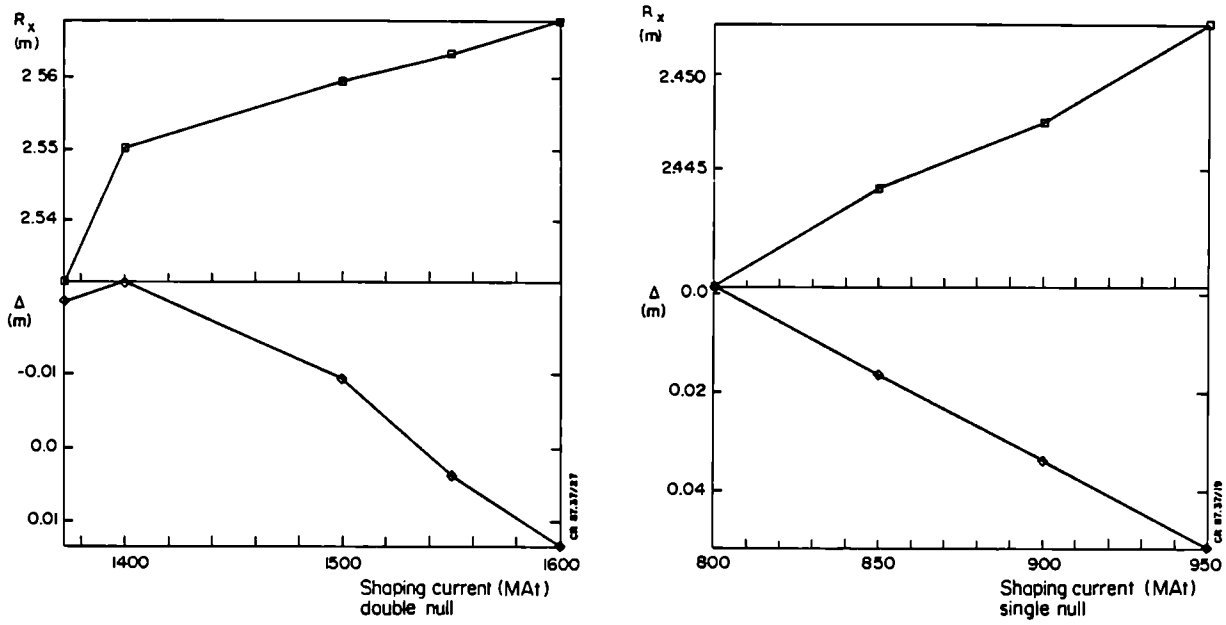

Fig 3 Calculated major radius of the X-point R_x, and Δ distance of the X-point from the target tiles versus the total shaping current in the coils P2 and P3 (with the turn ratio as in the text), at moderate primary current.

(a) Double-null configuration at plasma current of 2.0MA.

(b) Single-null configuration at plasma current of 2.0MA. The value of the major radius co-ordinate of the X-point is virtually independent of the shaping current. The sign of Δ is chosen to be positive for X-point within the vessel aperture.

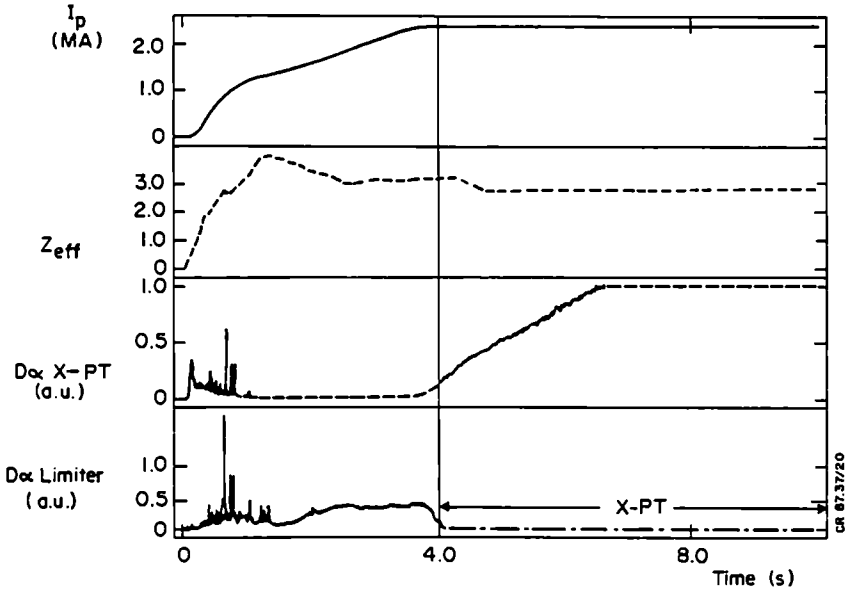

Fig 4 Time evolution of a typical ohmic discharge with magnetic separatrix. From the top, plasma current, ion effective charge measured by visible bremsstrahlung, intensity of D_α radiation from the X-point and from the limiter.

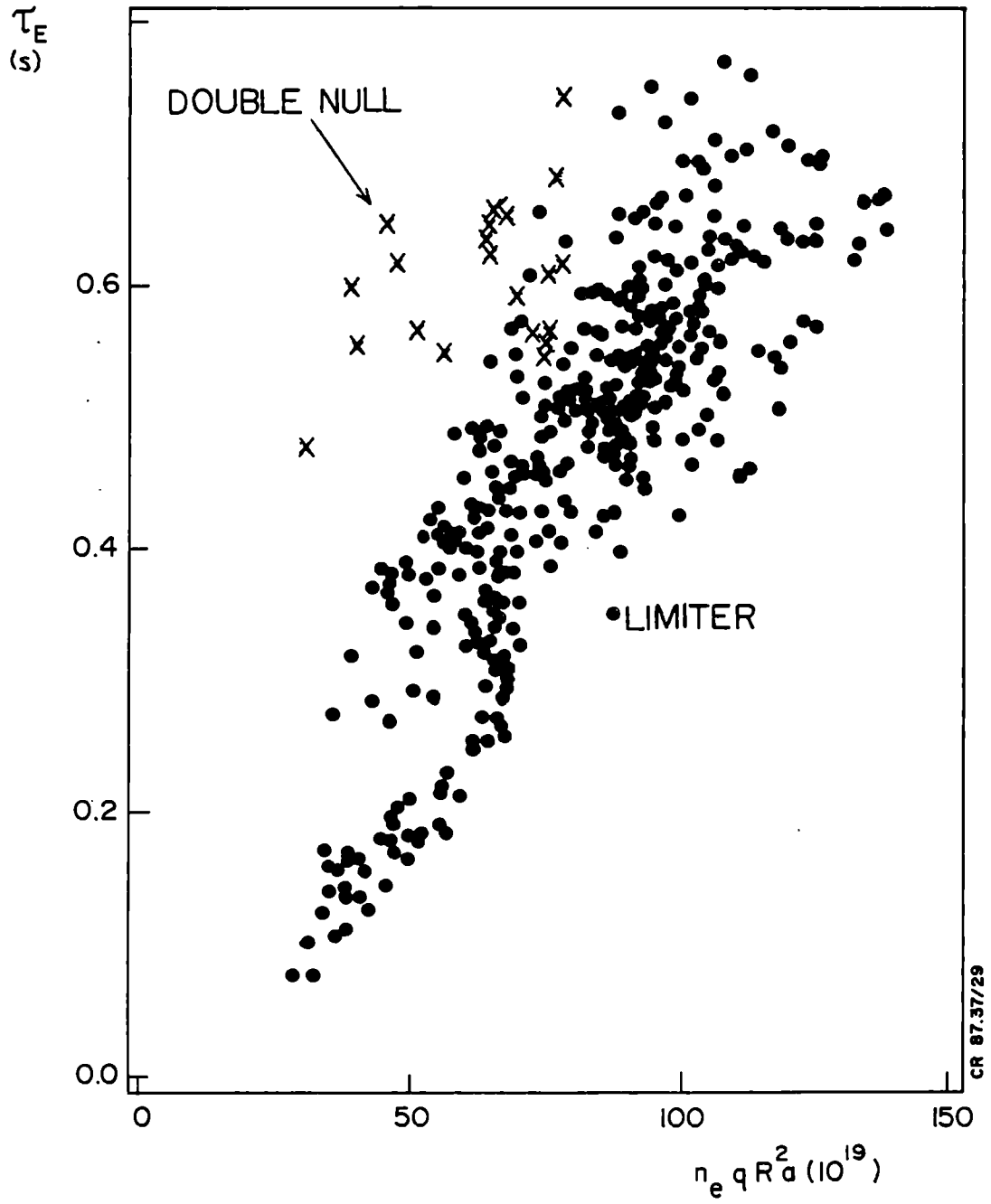

Fig 5 Energy confinement plot for magnetic separatrix and limiter ohmic discharges at plasma current of $2.0MA_T$ versus neo-Alcator scaling. Note that the best fit of JET ohmic data scales as $\tau_E \alpha\ R^{1.7}\ a^{1.3}\ q\ n_e^{0.4}$.

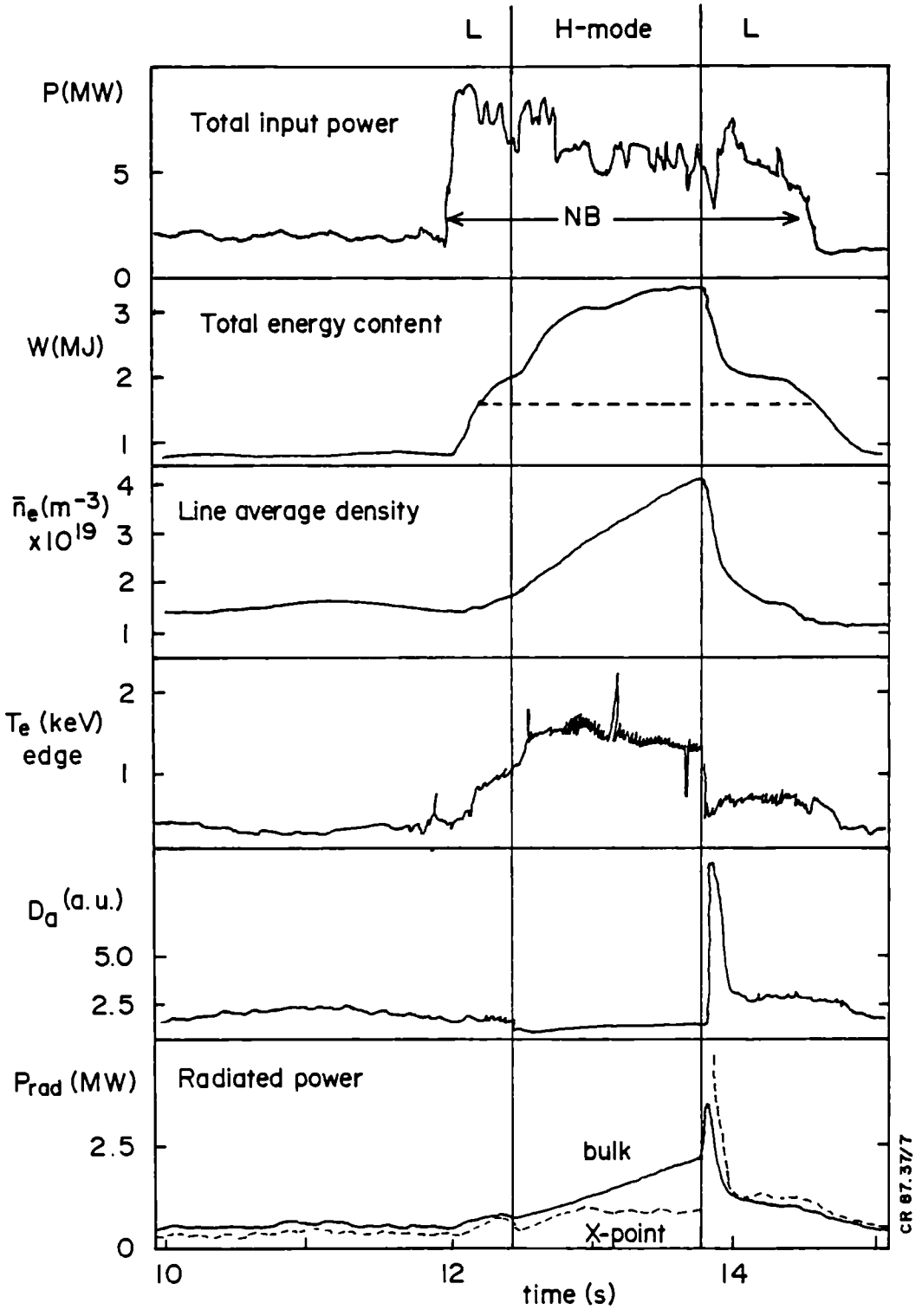

Fig 6 Time evolution of neutral beam heated single null discharge. Plasma current = 2.0MA, toroidal field = 2.2T (Pulse No 10645).

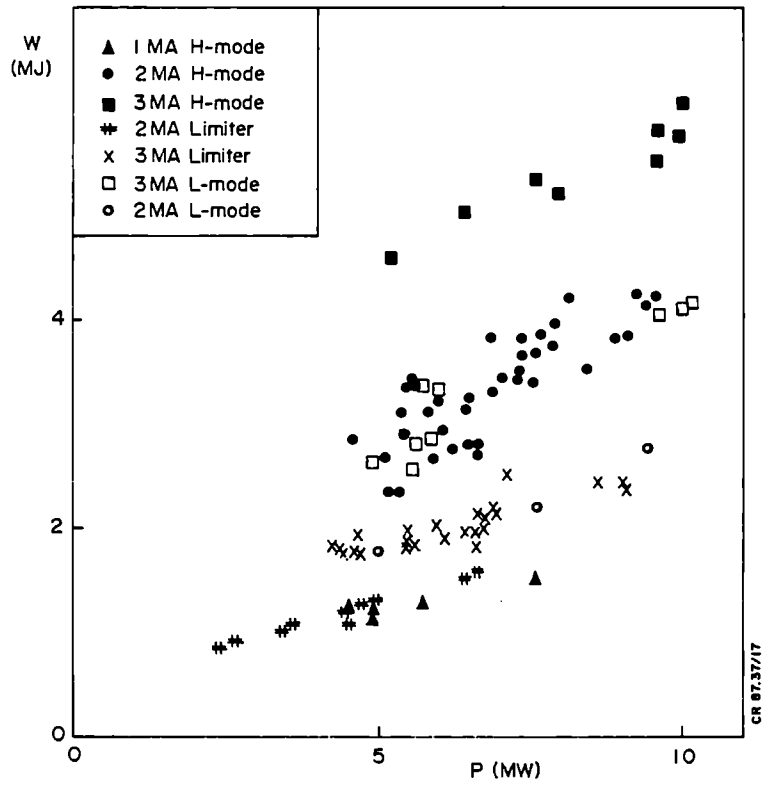

Fig 7 Total stored energy, as measured with diamagnetic loop, versus total input power for limiter and L and H-mode discharges, toroidal field = 2.2T.

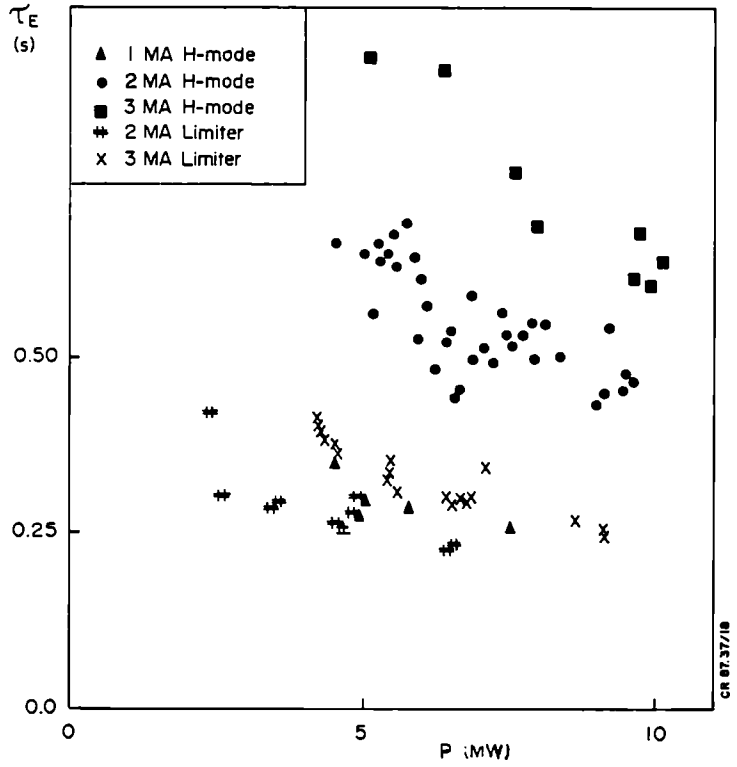

Fig 8 Global energy confinement time measured with diamagnetic loop versus total input power.

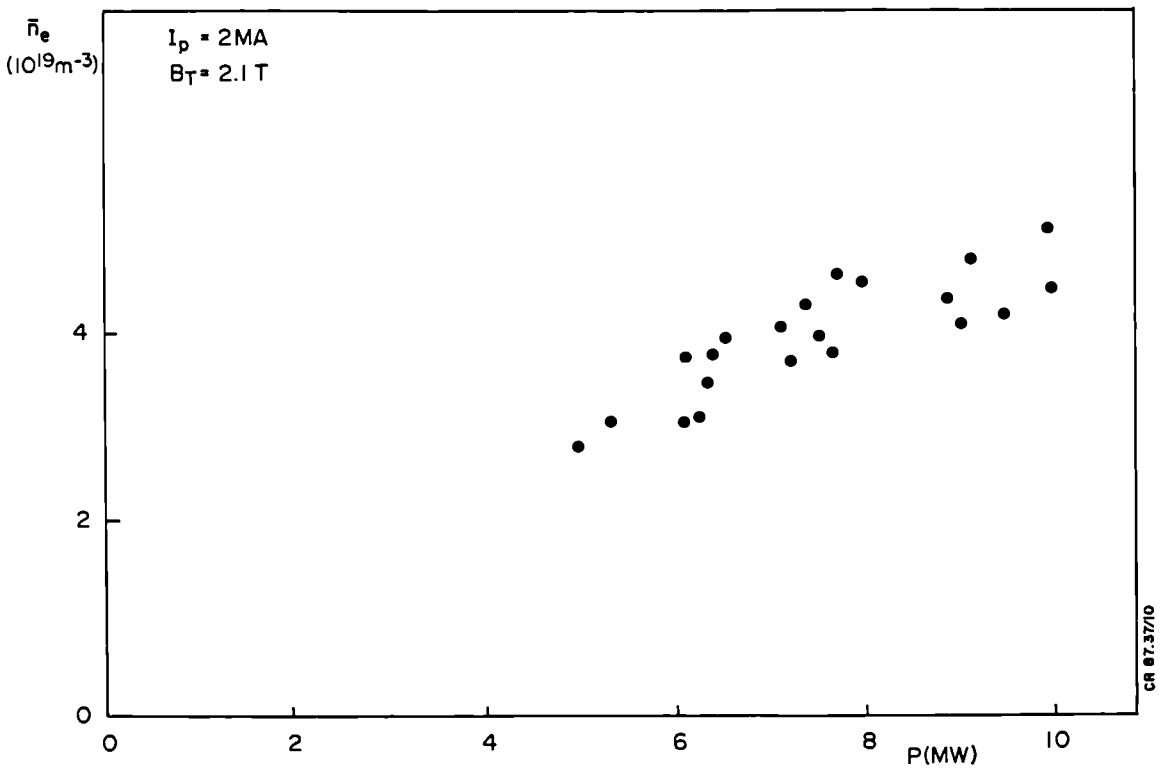

Fig 9 Maximum volume average electron density during the H-mode versus total input power.

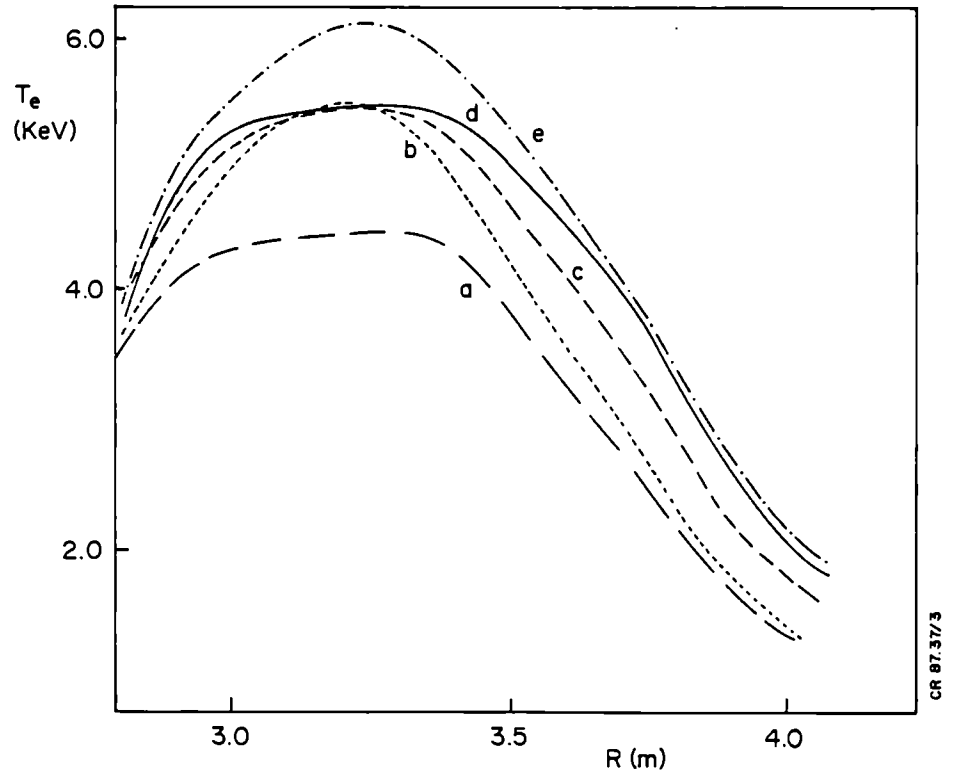

Fig 10 Sequence of ECE profiles showing the L-H transition,(a) is at t = 12.0s,(b) at t = 12.2s,(c) at t = 12.4s; this radial profile coincides with the transition L→H,(d) at t = 13.2s, and (e) at 13.3s. The average plasma density increases during this sequence from 1.7 to $3.5.10^{19}m^{-3}$. (Pulse No 10826, plasma current 2MA, toroidal field 2.8T).

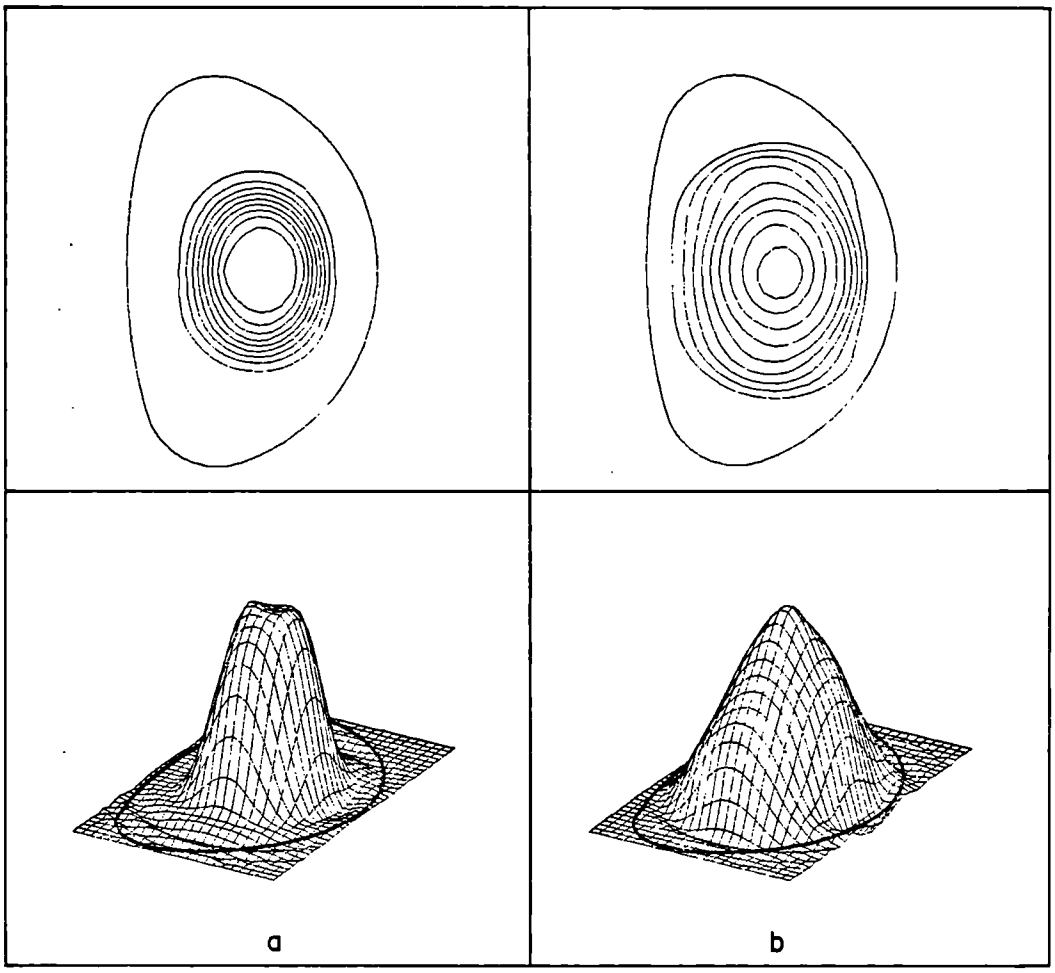

Fig 11 Profiles of soft X-ray emissivity for L and H-mode.

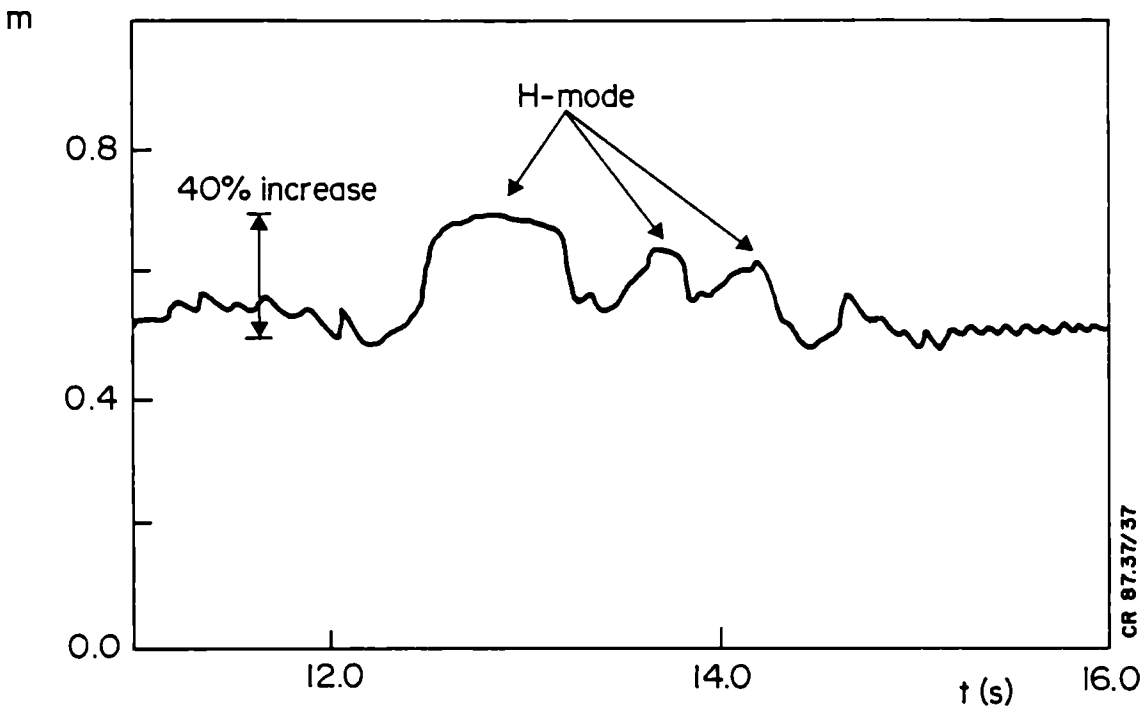

Fig 12 Time evolution of the second moment of the X-ray profile for a discharge with 7MW of total input power.

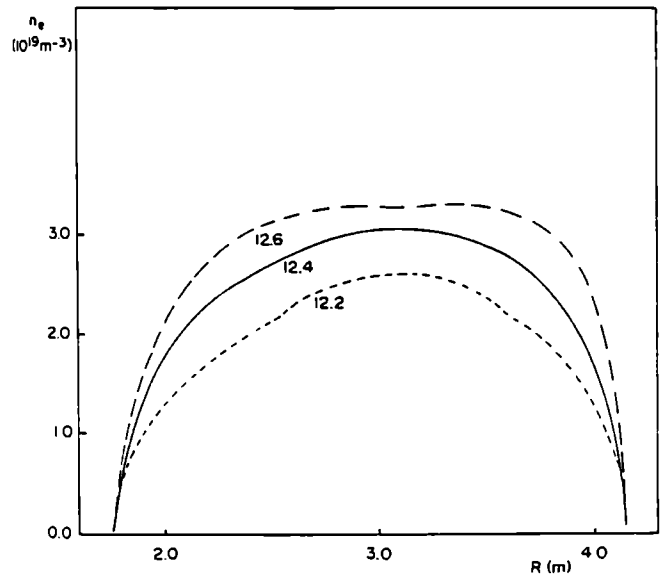

Fig 13 Sequence of electron density profiles from Abel inverted interferometric signals featuring a L-H transition. The profile at t=12.2s is taken in the L-phase, that at 12.6s is in the H-phase.

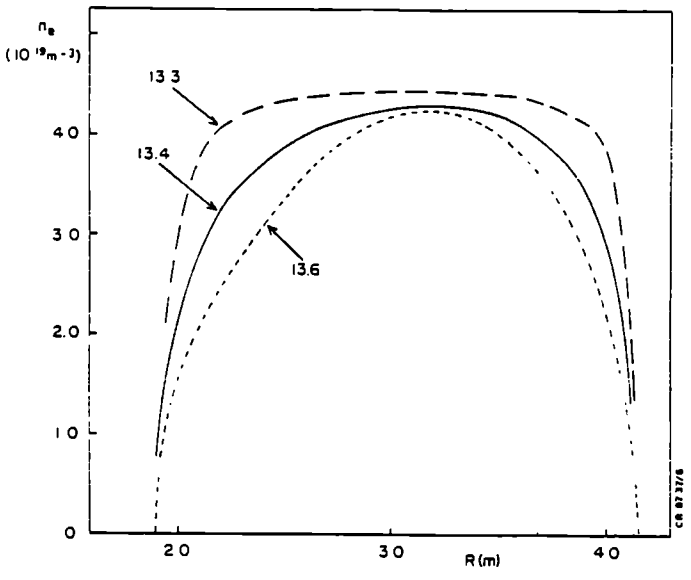

Fig 14 As from Fig 13 but featuring a H-L transition. The profile at t=13.3s is in the H-phase while at t=13.6s the discharge in the L-phase.

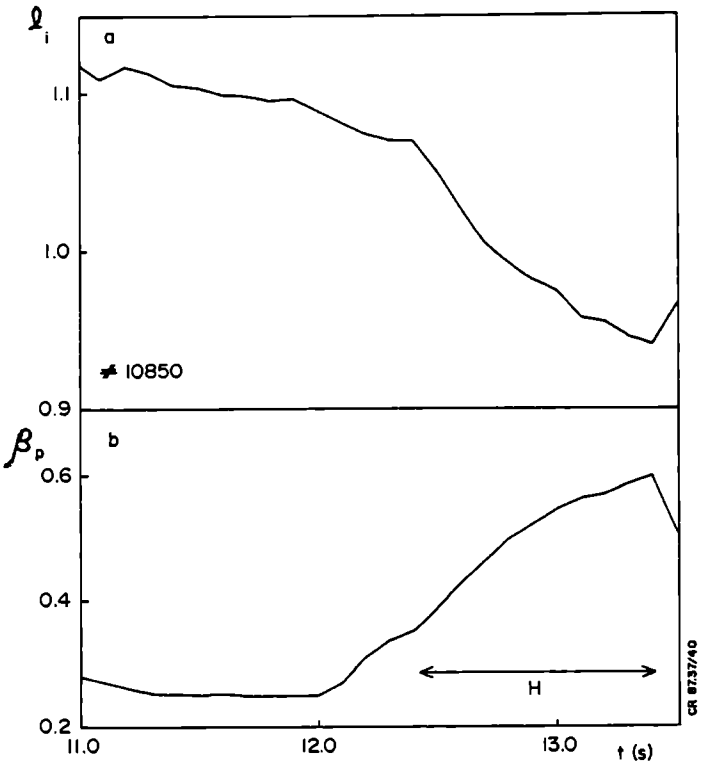

Fig 15 (a) Time evolution of internal inductance during L and H mode.
(b) Time evolution of poloidal beta.

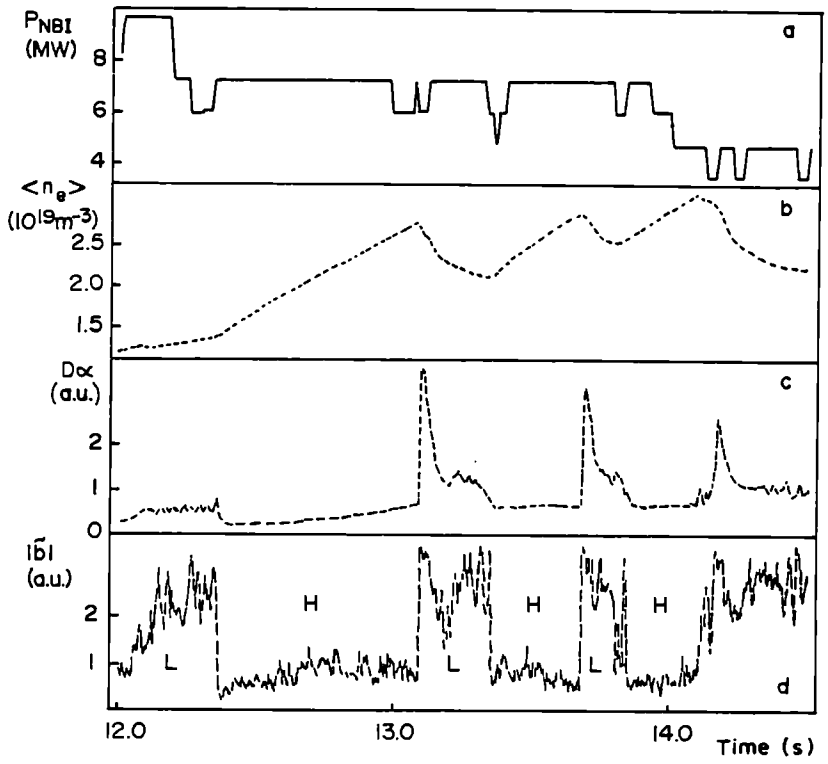

Fig 16 Time evolution of (a) Neutral beam power,(b) average electron density,(c) D_α chord integrated emission,(d) Magnetic fluctuation in a frequency band centred at f = 40kHz. A sequence of three L and H pnases is shown.

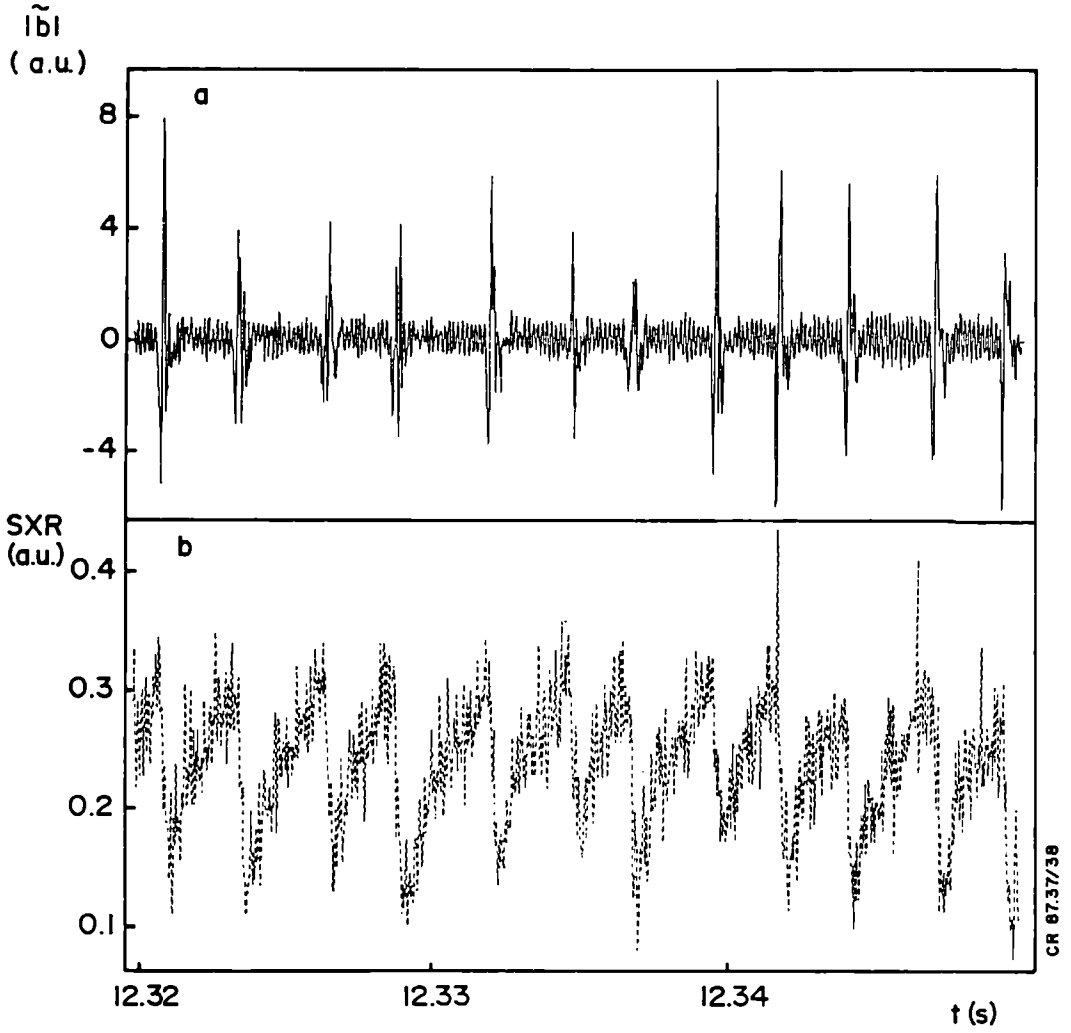

Fig 17 Time correlation between fluctuation from (a) magnetic pick up coil and (b) edge soft X-ray signal.

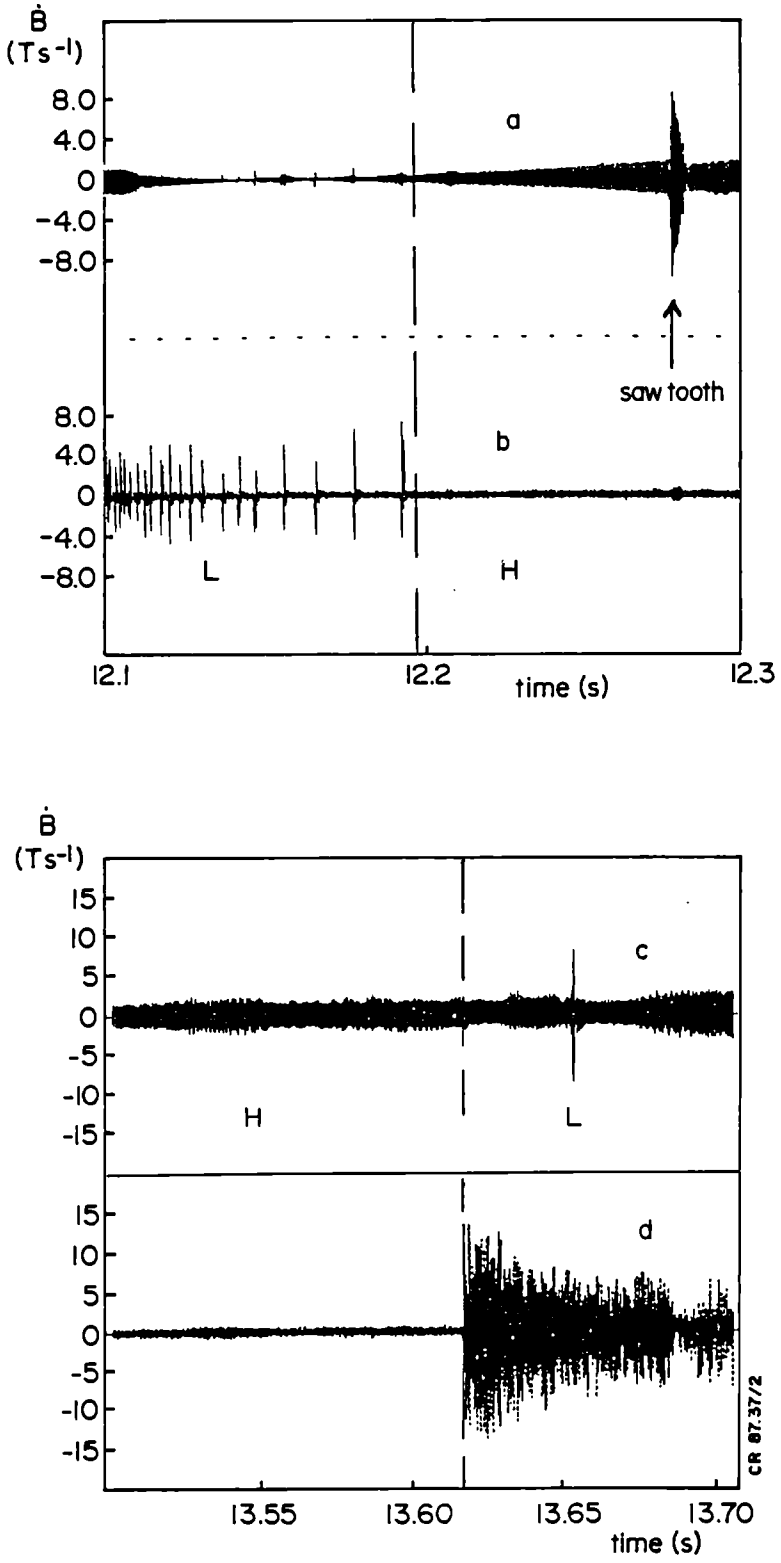

Fig 18 Magnetic fluctuations during the L to H transition;(a) pick up coil near the X-point;(b) pick up coil opposite to the x-point (bottom of the vessel. During H-to L transition: (c) pick up coil near the X-point;and (d) opposite the X-point.

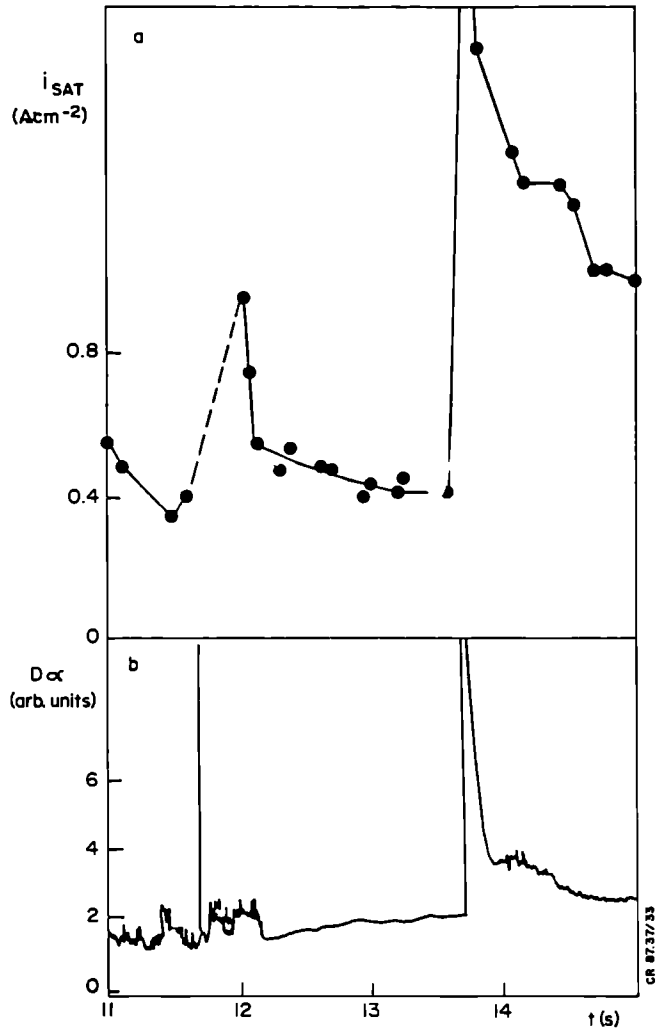

Fig 19 Temporal variation of (a) saturation current measured by a Langmuir probe and (b) D_α signal.

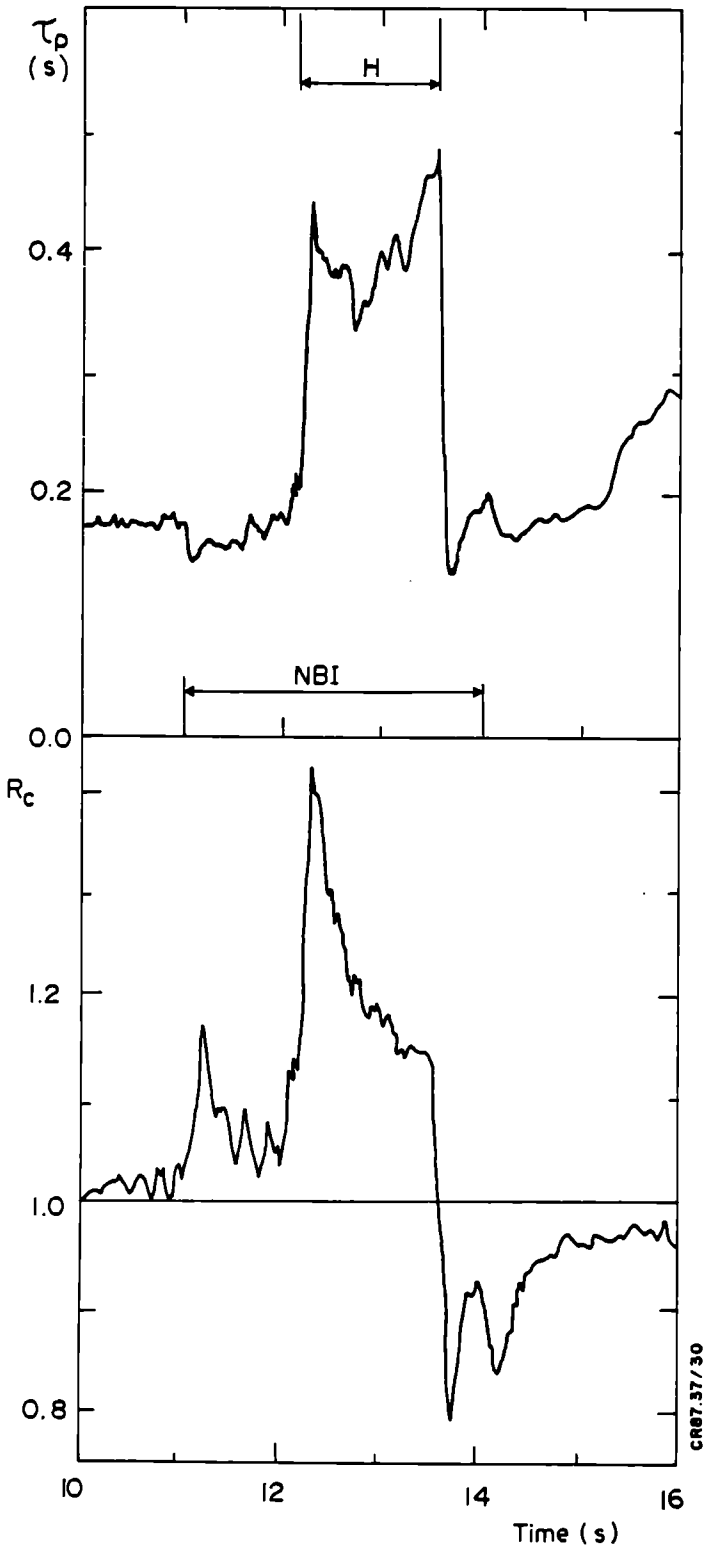

Fig 20 Temporal variation of (a) global particle confinement time during L-H-L mode, (b) Recycling coefficient (Pulse No 10789, plasma current: 3.0MA; total input power ~ 10MW).

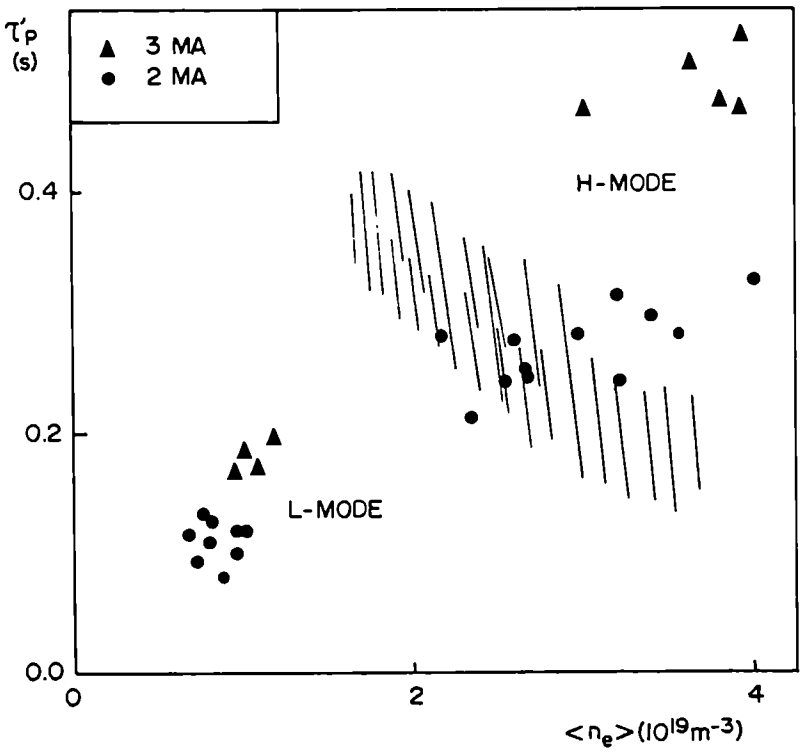

Fig 21 Global particle confinement time versus plasma density for L and H mode discharges. The dashed area is the reference limiter band of values.

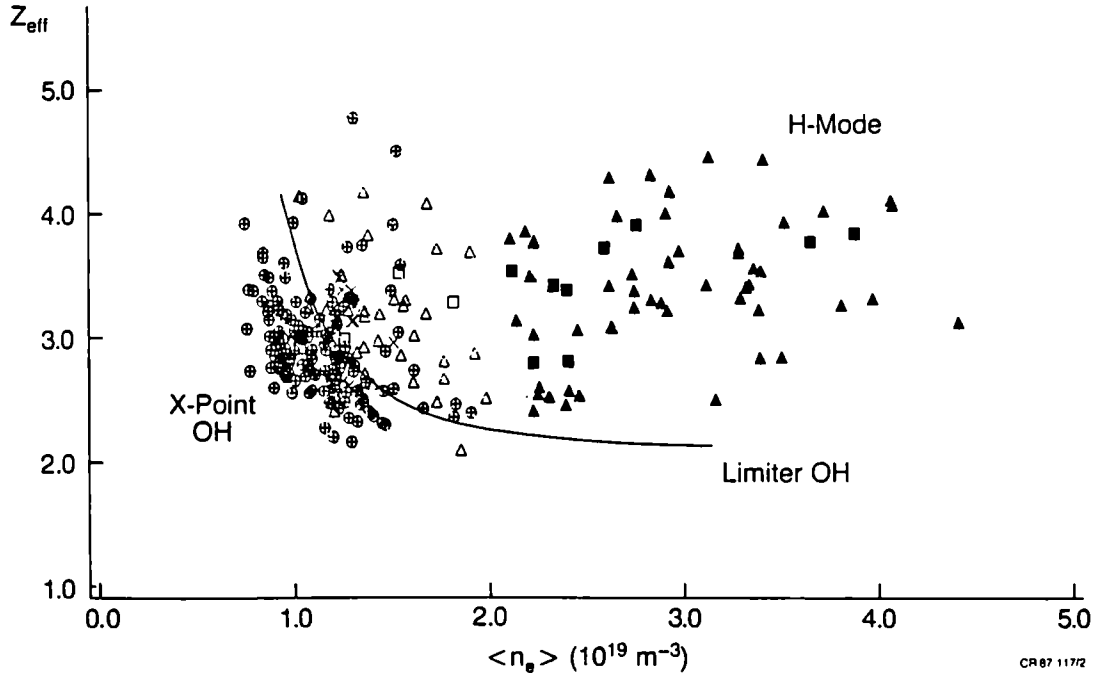

Fig 22 Z_{eff} vs $\langle n_e \rangle$ for X-point plasmas with ohmic heating (o), NB-heating (Δ) and combined heating ( ) (solid symbols denoting H-mode). For comparison the continuous line shows the typical behaviour of limiter plasmas with ohmic heating is shown. In the H-mode, Z_{eff} does not decrease as normal with higher $\bar{n}_e$.

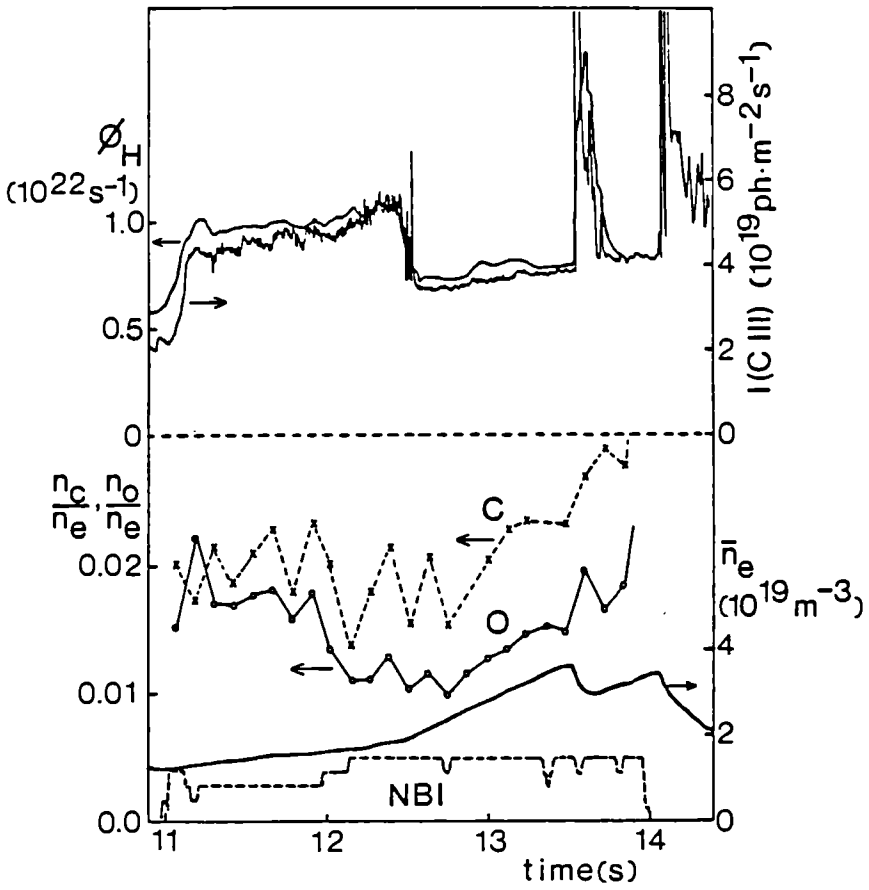

Fig 23 Behaviour of line average electron density ($\bar{n}_e$), carbon and oxygen concentrations (from CXRS), hydrogen flux (ϕ_H), and carbon influx, represented by the brightness of a C III-line (vertical viewing) during L- and H-mode in a NB-heated (5MW) X-point discharge. The L→H transition takes place at ~12.5s. The confinement of carbon is improved in the H-mode.

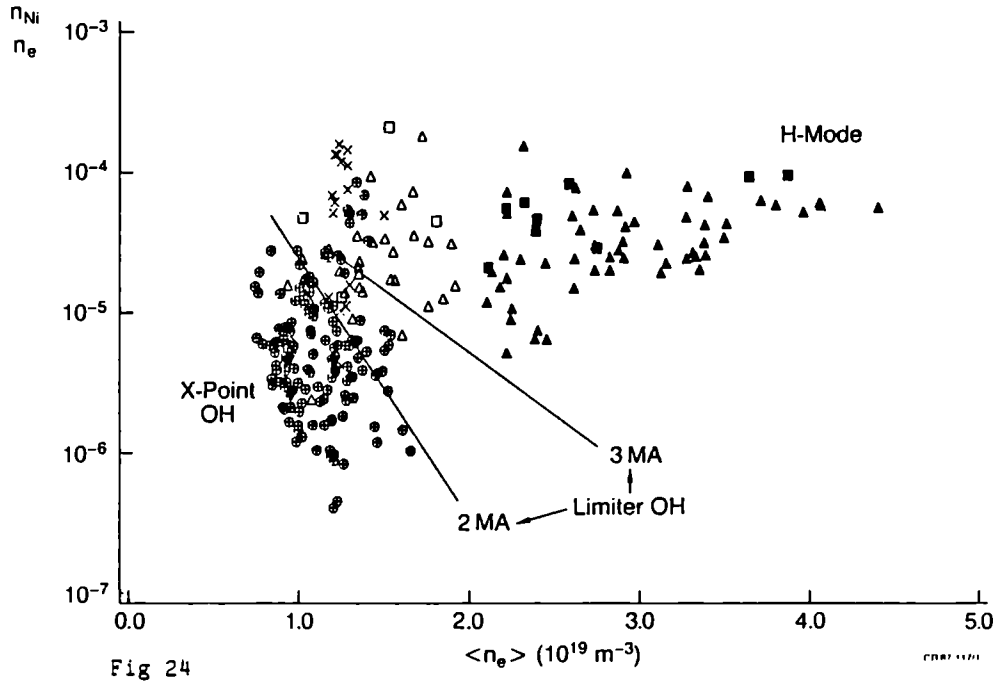

Fig 24 Comparative values of the nickel concentrations vs $<n_e>$. Same symbols are the same as in Fig 22. For comparison the lines show the trend for ohmic limiter discharges at 2MA and 3MA.

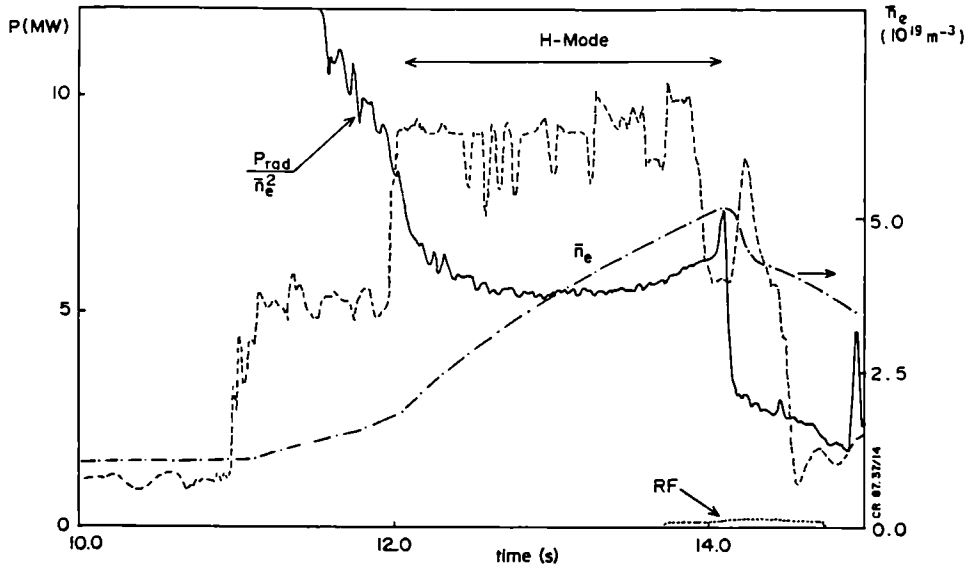

Fig 25 Time variation of the ratio of the radiated power from the main plasma to the square of the average plasma density during L and H-mode (#10755), P is the total input power, $\bar{n}_e$ is the line average density.

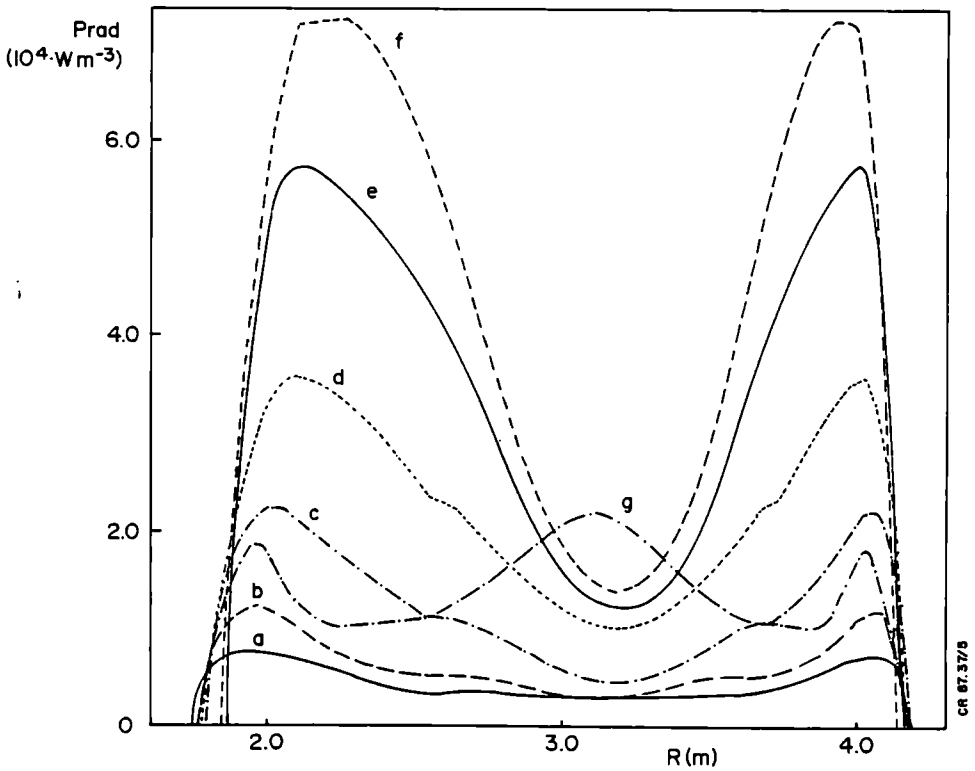

Fig 26 Sequence of Abel inverted radiation profiles for the same pulse of Fig 25. (a) is at 11.3s, (b) at 11.9s, (c) at 12.5s, (d) at 13.1s, (e) at 13.7, (f) at 14.0s at the end of the H phase, and (g) at 14.3 is just after the H→L transition.

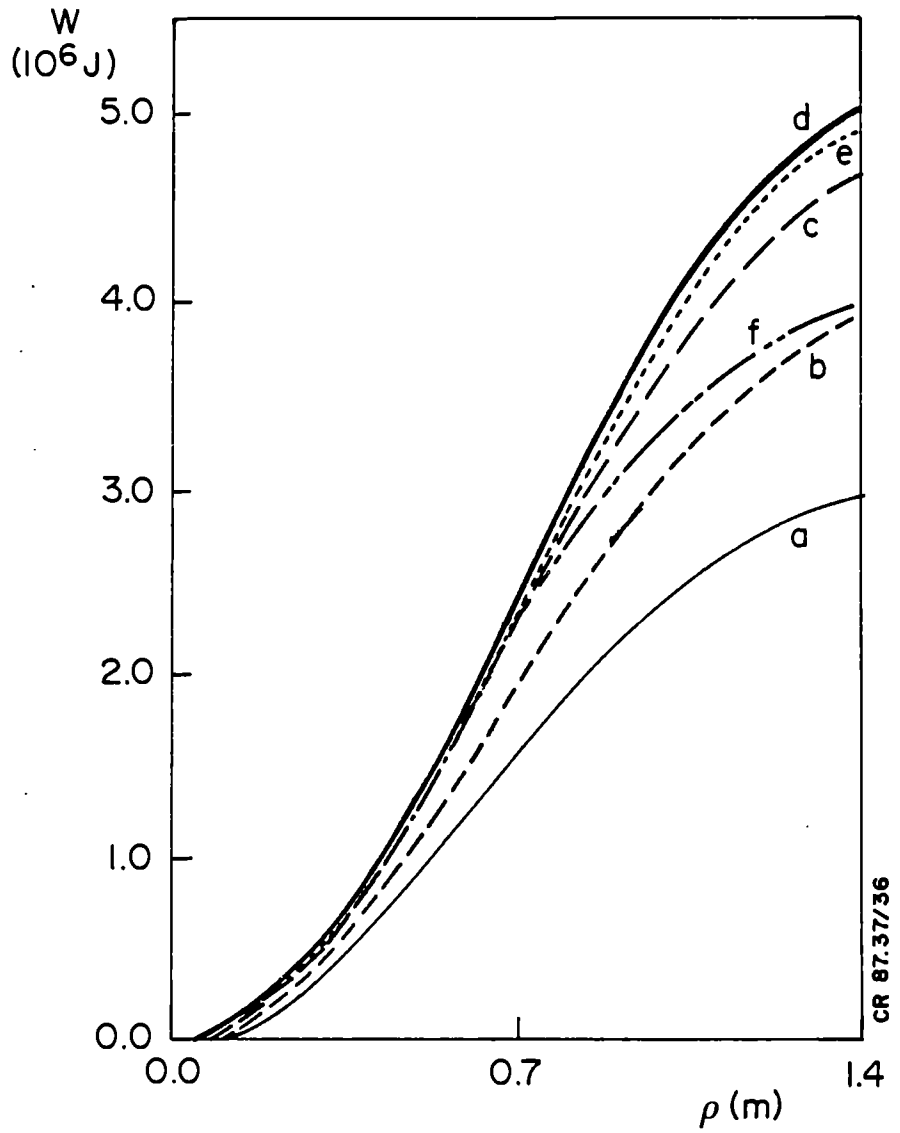

Fig 27 Radial profile of the total plasma stored energy for pulse 10755. Times: (a) t=12.2s; (b) t=12.5s; (c) t=12.8s; (d) t=13.0s; (e) t=13.4s and (f) t=13.7s. The horizontal axis is the average plasma radius over iso - ψ surfaces.

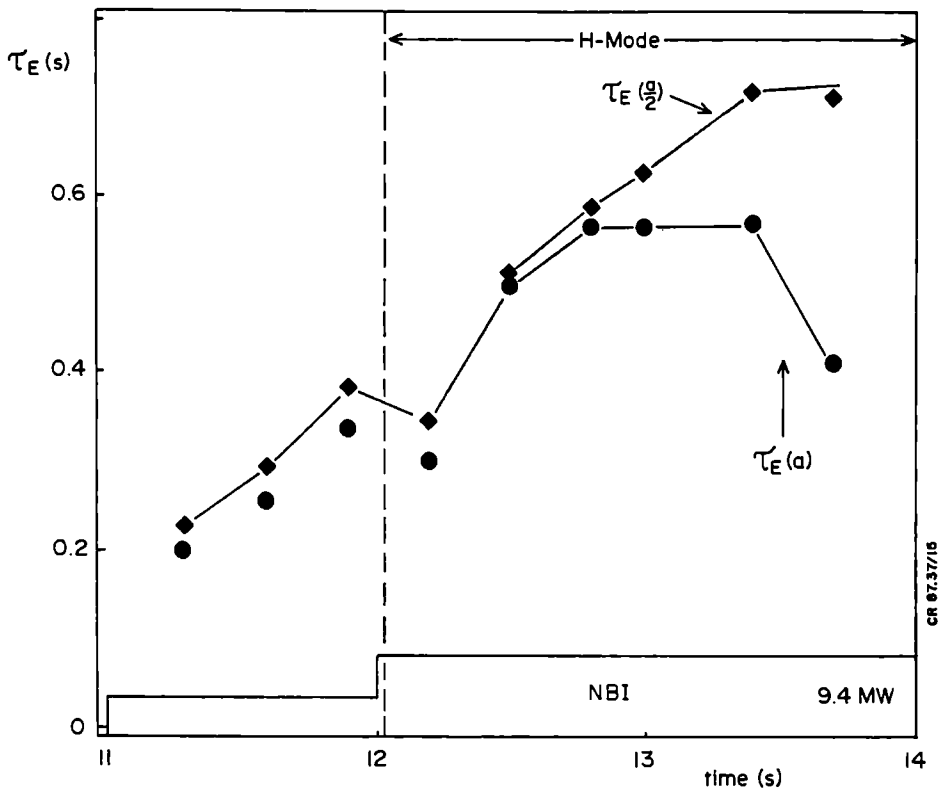

Fig 28 Comparison of time evolution of energy confinement time at half of the plasma radius and the global values, from kinetic data (# 10755).

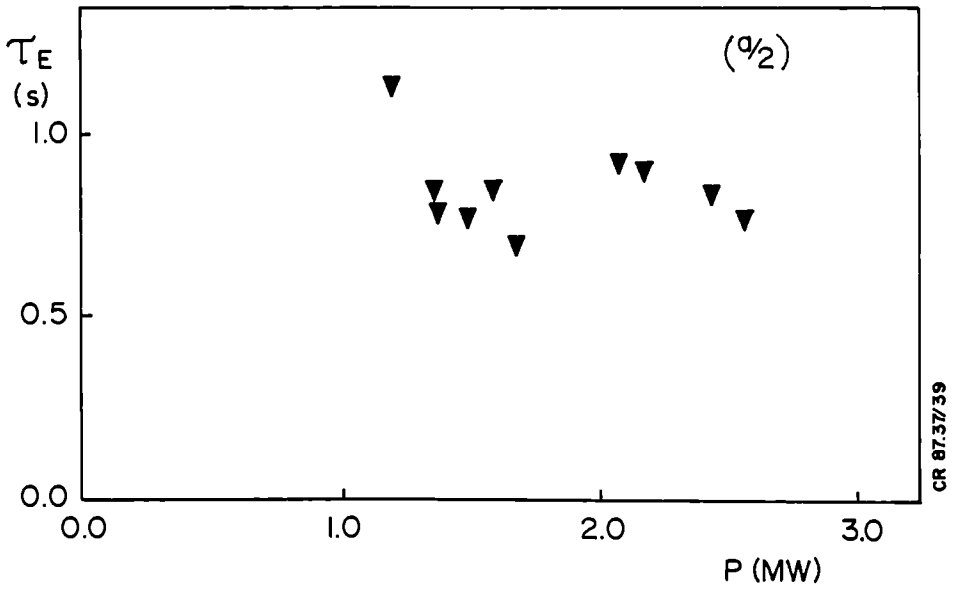

Fig 29 Confinement time at half plasma radius versus total input power calculated from kinetic data of a series of three discharges.

Invited paper presented to the 7th International Conference on
Plasma Physics, Kiev, U.S.S.R., 6th-10th April 1987

JET Latest Results and Implications for a Reactor

P-H. Rebut P.P. Lallia

ABSTRACT

In nearly four years of operation of the JET tokamak, experiments have been undertaken with input powers up to 7MW of ICRF, ~10MW of neutral beam and ~18MW during combined operation. JET results show many advances made during this period. With ohmic heating alone, good confinement (τ_E up to 0.9s), high temperatures ($\hat{T}_e$ up to 5keV) and a fusion product $\langle \hat{n}_i \tau_E \hat{T}_i \rangle = 10^{20} m^{-3}.s.keV$ have been achieved. Highly efficient ion heating has been observed ($\hat{T}_i > 12.5 \pm 1.5$keV) at moderate neutral beam injection levels ($P_{NB} \leq 8$MW) and at low average densities ($\bar{n}_i = 1-1.5 \times 10^{19} m^{-3}$). But with increasing additional heating, confinement is degraded and thus additional heating has little impact on the fusion product. However, a fusion product of $2 \times 10^{20} m^{-3}.s.keV$ has been achieved with a magnetic separatrix configuration in JET. Experimental results are examined in terms of possible scaling laws for electron energy confinement and implications for a reactor are considered.

1. INTRODUCTION

The main objective of the Joint European Torus (JET) is to obtain and study plasmas in conditions and with dimensions approaching those needed for a fusion reactor (i.e. $n = 2 \times 10^{20} m^{-3}$; $T \geq 10$keV, and $\tau_E = 1-2$s). The aims of the JET project remain those set out at the start of the design phase in 1974, which were to study: (i) the scaling of plasma behaviour as plasma parameters approach the thermonuclear reactor regime; (ii) plasma-wall interactions in these conditions; (iii) plasma heating and (iv) α-particle production, confinement and consequential plasma heating.

The last item requires that the machine operates eventually in a deuterium-tritium mixture, and therefore, it has been designed for remote maintenance and tritium compatibility. The design, construction and operation of the machine were achieved by the dedicated efforts of the JET Team and the details have been reported, previously [1,2].

2. MACHINE STATUS

(a) Machine Conditions

Machine conditions have been progressively improved since first operation and all machine systems have now met or exceeded stringent design specifications. The achieved parameters are compared with the design values in Table I.

TABLE I

PRINCIPAL PARAMETERS OF JET: DESIGN AND ACHIEVED VALUES

PARAMETER	DESIGN VALUES	ACHIEVED VALUES
Plasma minor radius (horizontal), a	1.25m	0.8-1.2m
Plasma minor radius (vertical), b	2.10m	0.8-2.1m
Plasma major radius, R_o	2.96m	2.5-3.4m
Plasma elongation ratio, ε=b/a	1.68	1.2-1.7
Flat-top pulse length	Up to 20s	Up to 20s
Toroidal magnetic field (plasma centre)	3.45T	3.45T
Plasma current:		
circular plasma	3.2MA	3.0MA
Elongated plasma	4.8MA	5.1MA
Flux Drive Capability	34Vs	28Vs
Additional heating power (in plasma)	1986 Values / Full Values	
RF Power	8MW (3 antenna) / 32MW (8 antenna)	<7MW
Neutral beam power	10MW (1 box) / 20MW (2 boxes)	<9MW

In most recent experiments, eight carbon limiters have been located symmetrically on the outer equatorial plane of the vessel. Since disruptions mostly terminate on the inner walls, these have been covered by carbon tiles to a height of ±1m around the mid-plane. Similar tiles also protect the frames of RF antennae, eight octant joints and the outer wall from neutral beam shine-through. Additional tiles have been installed at the top and bottom of the vessel to protect the vessel during X-Point (separatrix) operation. The surface area covered (~45m^2) corresponds to ~20% of the vessel area. The inner wall tiles, used as limiters, and those for X-point protection have provided powerful pumping (with speeds up to 100mbar.l.s^{-1}), allowing operation at low densities near the plasma edge and were also used to reduce the density after neutral injection, to avoid disruptions. Recently, helium discharges prior to normal operation have improved the inner wall tiles pumping capacity.

(b) RF Heating System

Since early 1985, three RF antennae have been located at the outer equatorial wall. Power is transferred to the plasma at a radiation frequency (25-55MHz) corresponding to the cyclotron resonance of a minority ion species (H or He^3). Each antenna is fed by a tandem amplifier delivering up to 3MW in matched conditions. The three units have been regularly operated up to 7.2MW for 2s pulses. ICRF experiments with 8s pulse duration have delivered ~40MJ to the plasma.

(c) Neutral Beam System

A long pulse (~10s) neutral beam (NB) injector with eight beam sources and one integrated beam line system has been operated on JET since early 1986. H beams with particle energies up to 65keV and a total beam power of ~5.5MW have been injected into D plasmas. D beams with particle energies up to 75keV and a total power up to 10MW have also been injected into D plasmas. Up to 40MJ have been delivered to the plasma during a pulse.

(d) Diagnostics

About 30 different diagnostics have been installed on JET, allowing cross checking of the main plasma parameters and detailed analysis of the main plasma features. The details have been described, previously (3).

3. EXPERIMENTAL RESULTS

(a) Plasma Parameters

Three main modes of operation have been employed on JET, in which plasmas have been bounded by:

(i) eight carbon limiters on the outer equatorial plane;

(ii) carbon tiles on the inner equatorial plane (small major radius side of vacuum vessel);

(iii) a magnetic separatrix with X-points at the top and bottom of the torus.

In these configurations, various heating scenarios have been used, ranging from ohmic heating alone to combinations of ohmic, RF and NB. The main JET parameters achieved are presented in Table II. Examples of typical pulses under various conditions are indicated in Fig.1, which show the density (n), electron temperature (T_e) and safety factor (q) profiles, with ion temperature (T_i) measurements, where available.

Under these different conditions, plasma parameters have been obtained, as follows:

(i) with ohmic heating only, $\hat{T}_i$ and $\hat{T}_e$ of 3keV and 4keV, respectively, were achieved with $\bar{n}$ ~$4.2\times10^{19}m^{-3}$ and τ_E up to 0.9s;

(ii) with RF heating, $\hat{T}_i$ and $\hat{T}_e$ reached 5.5keV with $\bar{n}=3.5\times10^{19}m^{-3}$, however, τ_E dropped to ~0.3s. $\hat{T}_e$ reached 8keV in He plasmas;

(iii) with neutral beam heating, $\hat{T}_i$ up to 6.5keV at $n=3\times10^{19}m^{-3}$ was produced. At lower densities ($n\sim1.5\times10^{19}m^{-3}$), $\hat{T}_i \geq 12.5$keV was observed (Fig.1(e)). Again, degradation in τ_E to 0.3-0.4s was seen. With ~7MW of neutral beam injection, current drive of

TABLE II

SUMMARY OF MAIN JET PARAMETERS
(NOT NECESSARILY IN THE SAME PLASMA PULSE)

PARAMETER			VALUE
Safety factor at Plasma boundary	q_{cyl}	$\geq$	1.5
	q_{ψ}	$\geq$	2.1
Vol. average Electron density	$\bar{n}(x10^{19}m^{-3})$	$\leq$	5.0
Central electron temp.	$\hat{T}_e$(keV)	$\leq$	8.0
Central ion temp.	$\hat{T}_i$(keV)	$\leq$	12.5
Global energy conf. time	τ_E(s)	$\leq$	0.9
Fusion performance Parameters	$\langle\hat{n}_i\hat{T}_i\tau_E\rangle$ $(x10^{19}m^{-3}.keV.s)$	$\leq$	20.
Input ICRF power	P_{RF}(MW)	$\leq$	7.0
Input NBI power	P_{NB}(MW)	$\leq$	9.0
Total input power	P_t(MW)	$\leq$	18.0
Stored plasma energy	W_p(MJ)	$\leq$	6.1

0.4MA was observed at $n=2x10^{19}m^{-3}$;

(iv) 15MW of combined RF and NB heating was coupled to the plasma in a 5MA discharge: the plasma energy content was ~6MJ (Fig.1(d));

(v) in single null "X-point" discharges, H modes have been obtained. At 3MA and with 8MW of NBI, a plasma energy content of 6MJ has been observed.

The JET impurity behaviour is similar to that observed in other ungettered tokamaks with graphite limiters [4]. In most cases, impurity radiation losses were mainly caused by carbon and oxygen and originated mainly near the plasma edge. In limiter discharges, metal concentrations were only significant (i.e. >0.1% n_e) when the carbon limiters were metal-coated following accidental melting and evaporation of wall material. The release of metals from the limiters can be explained by a combination of sputtering by deuterium and by light impurities. The metal fluxes decrease as the plasma density increases and the plasma current decreases. These fluxes are inversely

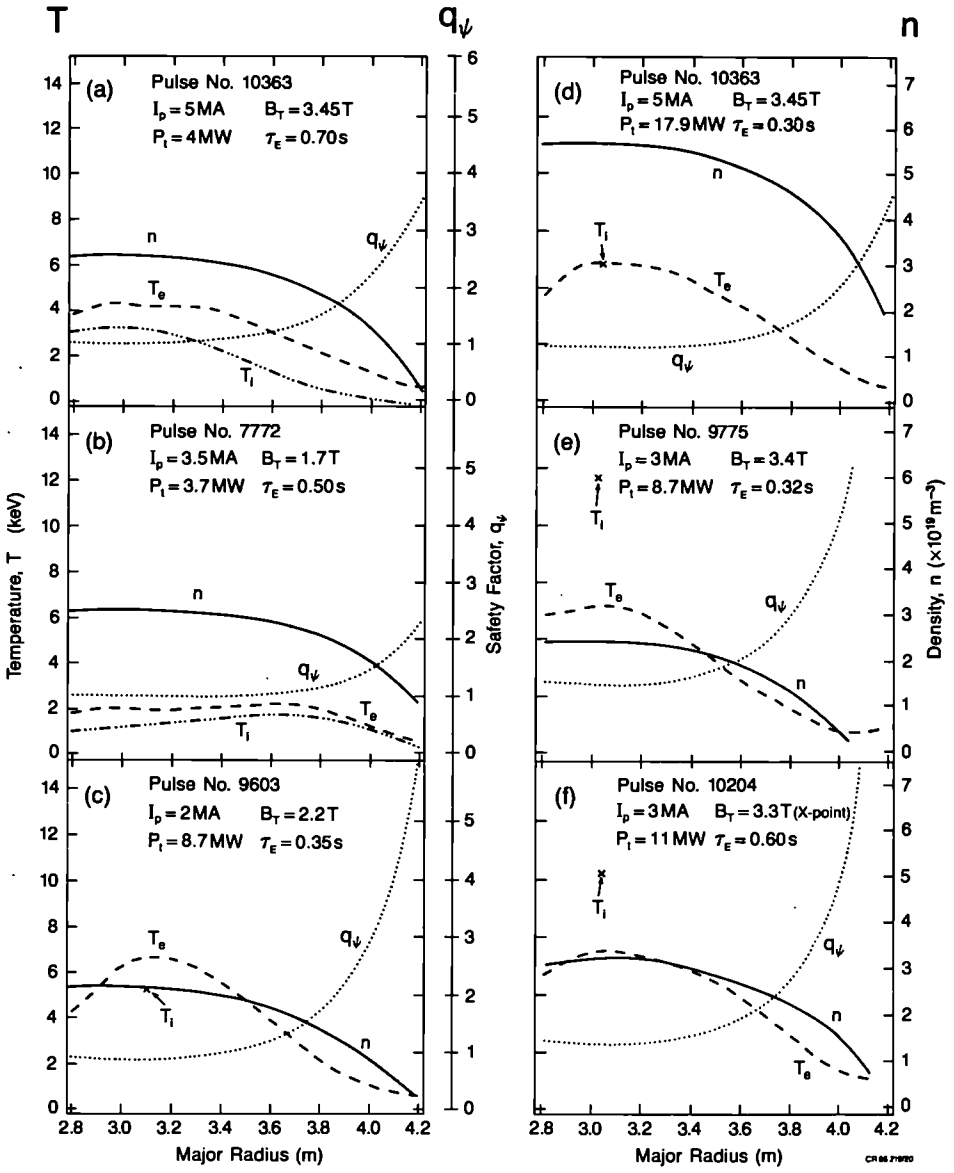

Fig.1 The density (n), electron temperature (T_e) and safety factor (q) as a function of major radius. The ion temperature (T_i) is shown where available. These profiles are indicated for the cases: (a) 5MA pulse (No:10363), Ohmic heating only, B_T=3.45T; (b) Low q pulse (No:7772), ohmic heating only, I_p=3.5MA, B_T=1.7T; (c) Monster sawtooth pulse (No:9603), P_{add}=6.1MW; (d) 5MA Pulse (No:10363) with 15.2MW of RF + NB power, B_T=3.45T; (e) High T_i pulse (No:9775) P_{add}=8MW; (f) X-Point configuration pulse (No:10204) I_p=3MA P_{add}=8.2MW;

correlated with the light impurity behaviour. At high plasma density, radiation losses were mainly caused by oxygen.

The effective plasma charge Z_{eff} ranges usually between 2 and 3 for $\bar{n}_e > 3 \times 10^{19} m^{-3}$. Z_{eff} was reduced and approached unity for a time duration exceeding 0.5s after injection of a deuterium pellet.

(b) Density Limitations

The operating diagram for JET is shown in Fig.2. For a given normalised current (1/q), there is a band of operating densities. Below a certain density, the discharge fails to breakdown, and above a critical density, the discharge is terminated by a disruptive instability. In ohmic plasmas, the density limit is $n_c(OH)(m^{-3}) = 1.2 \times 10^{20} B_T(T)/qR(m)$, and depends on plasma purity. In RF heated discharges, it is only slightly increased, possibly because the effect of extra power is cancelled by an impurity increase. In neutral beam heated plasmas, the limit is substantially increased (see Fig.2) to $n_c(NB)(m^{-3}) = 2 \times 10^{20} B(T)/qR(m)$. Switching off neutral beams at high density causes the plasma to disrupt, which indicates that the power input plays an important role in the disruption mechanism. Preliminary experiments with a single-shot pellet injector have also exceeded the OH density limit [5].

Density limit disruptions are always preceeded by an increase in the impurity radiation at the plasma edge [4], and a contraction of the electron temperature profile followed by the growth of coherent MHD activity (principally m=2, n=1). Alternative theoretical models predict that either the temperature profile contraction leads to an unstable current profile [6,7], or that the increased radiation losses at the q=2 surface lead to a thermal instability [8]. However, both effects might be involved. Both models predict growth of an m=2, n=1 island before the disruption. Both observations and theoretical considerations show that the central plasma density can be increased by deep fuelling.

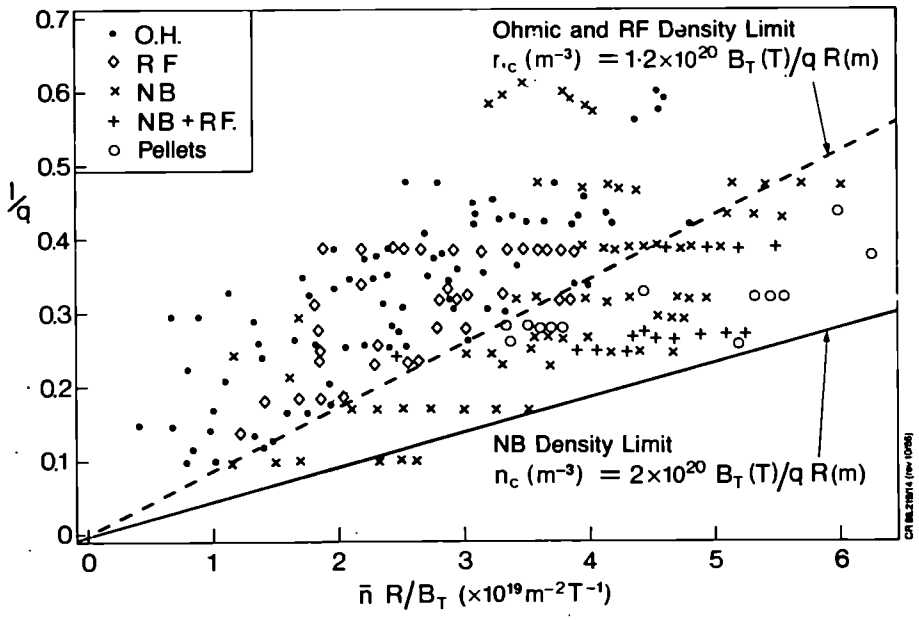

Fig.2 Normalized current [=1/q] versus normalised density [=$\bar{n}R/B_T$];

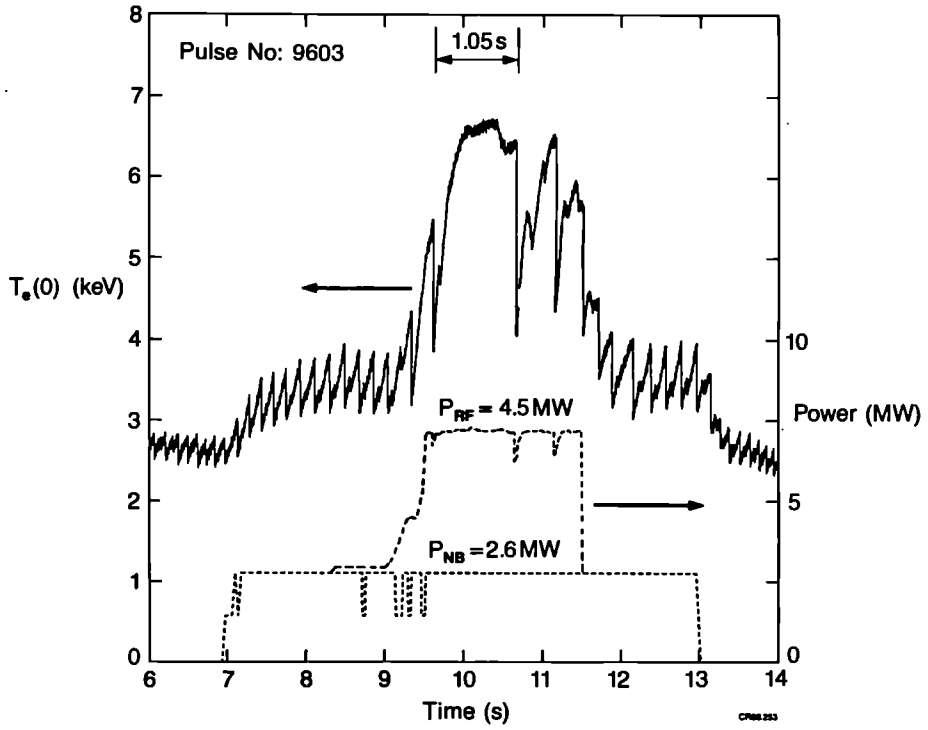

Fig.3 Sawtooth oscillations of the central electron temperature, showing the effects of NB and RF additional heating;

(c) Temperature Effects

Sawtooth oscillations are observed in most JET discharges. In general, these instabilities limit the T_e and T_i values, and in certain cases, the global energy confinement times. With central deposition of additional power, sawteeth may develop large amplitudes with up to 50% modulation in central electron temperature and long periods (up to 0.6s) [6]. In some cases, with NB and/or RF heating, 'monster' sawteeth have developed (see Fig.3), characterised by durations up to 1.6s and a strong reduction of the low m, n MHD activity.

The peak electron temperature $\hat{T}_e$ can be raised significantly with additional power above the value in the ohmic phase as shown in Fig.4(a). The dispersion seen in $T_e(0)$ is due to sawteething and to variations in profile deposition of the additional power. By contrast, the electron temperature at the inversion radius (q~1 surface) shows

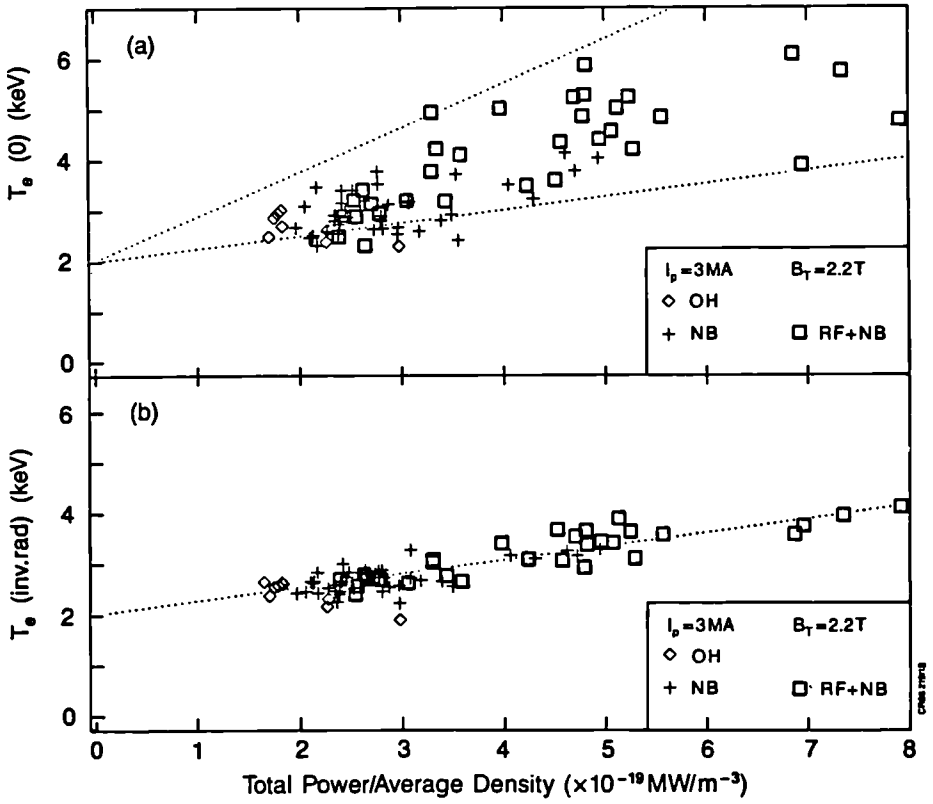

FIg.4 (a) electron temperature at the centre, (b) electron temperatures at the inversion radius (q=1);

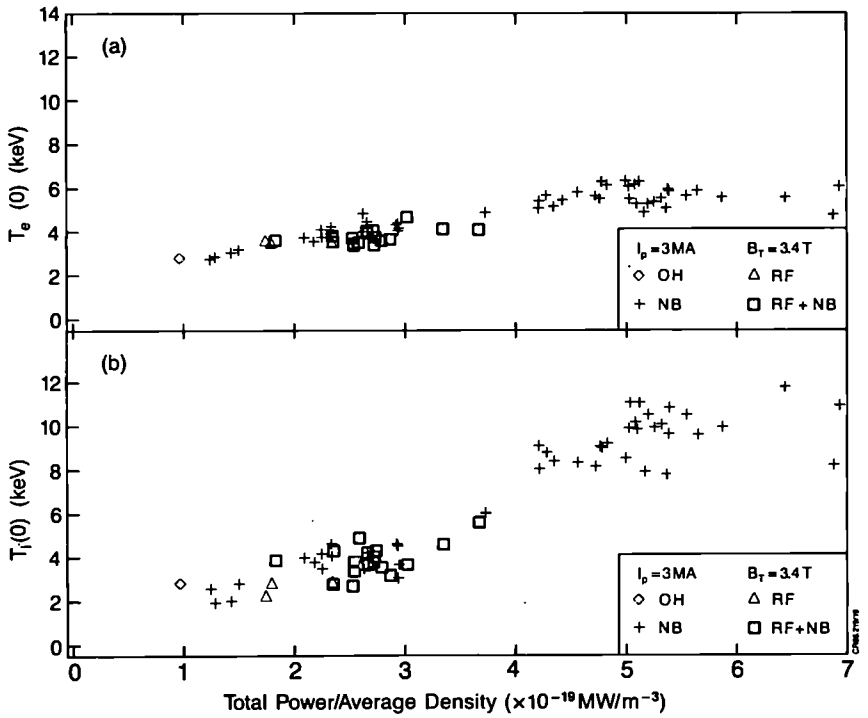

Fig.5 (a) electron temperature (T_e) at the centre and (b) ion temperature (T_i) at the centre as a function of power input per particle for various heating scenarios;

weak dependence with the power input per particle ($P/\bar{n}$) for a given plasma current and toroidal field (Fig.4(b)).

The ion temperature behaviour appears quite different; the peak ion temperature $\hat{T}_i$ is plotted in Fig.5(b) versus $P/\bar{n}$. Above 4×10^{-19}MW/m^{-3}, the ion temperature can greatly exceed the electron temperature and can reach ~12.5keV in JET.

(d) Confinement Degradation

The total energy confinement time on JET is defined by $\tau_E=W_k/[P_{tot}-dW_k/dt]$, where W_k is the kinetic energy and P_t is the total input power to the plasma without subtracting radiation losses. Reported values of τ_E are quasi-stationary.

With additional heating, the confinement time, τ_E, degrades with increasing input power (Fig.6(a)), as seen in a number of other experiments. The degradation is independent of type of heating,

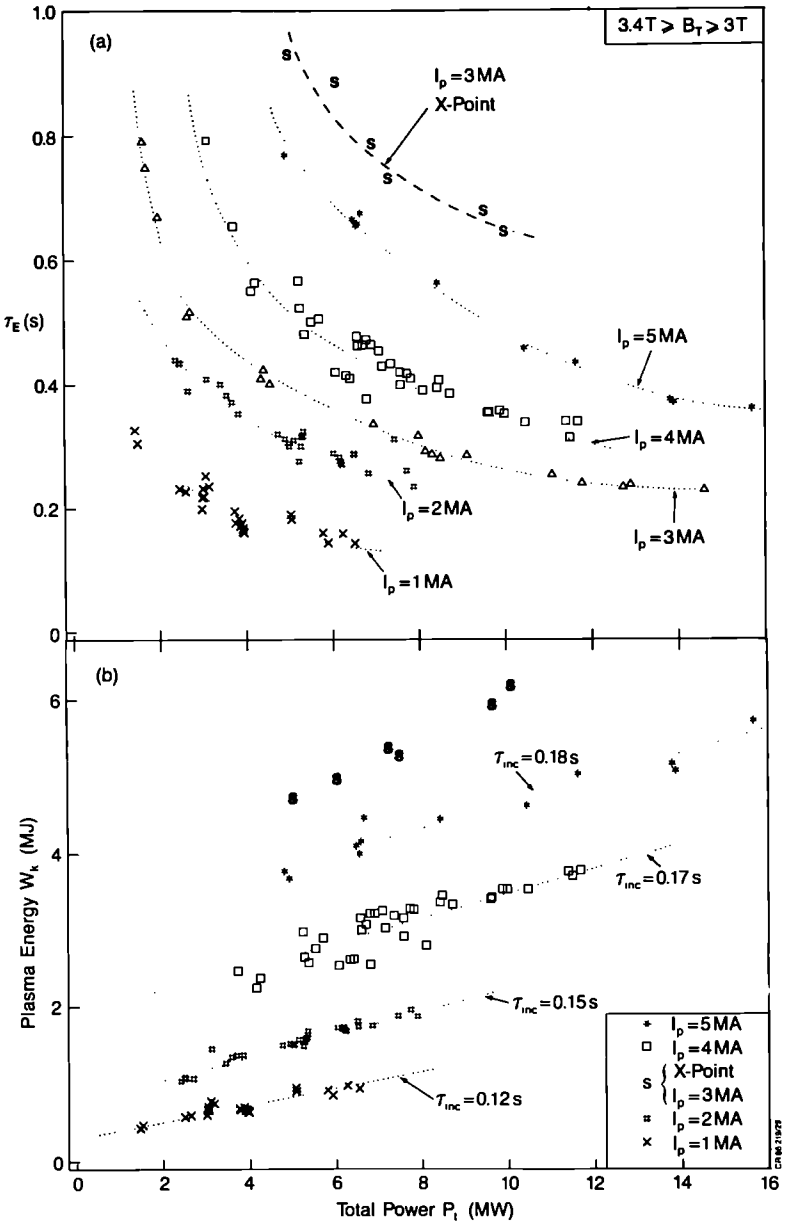

Fig.6 (a) the energy confinement time τ_E as a function of additional heating power (at I_p)=1,2,3,4 and 5MA; 3.4T$\geq B_T \geq$3.0T); (b) plasma energy content W_k versus the total input power P_t, with NBI or ICRF heating (I_p=1,2,4 and 5MA; 3.4T$\geq B_T \geq$3.0T);

whether RF, NB or combined. The rate of increase in W_k with P_t ($=\Delta W_k/\Delta P_t$) appears to reach a limit of 0.1-0.3MJ/MW(=s) at high powers (see fig.6(b)), independent of type of additional heating. Confinement time depends weakly on plasma density but scales favourably with plasma current.

Since the plasma energy is a function of n_i, T_e and T_i, the degradation in confinement time is consistent with the observation that the electron temperature at the inversion radius (q=1 surface) increases little with power input (see Fig.4(a) and (b)).

(e) Magnetic Separatrix Experiments

A better confinement regime with additionally heated plasmas has been observed (H-mode) in some Tokamaks with magnetic limiters or divertors. Stable discharges with a magnetic separatrix (or X-point) inside the vessel have been maintained in JET for several seconds, at plasma currents up to 3MA with a single null and up to 2.5MA with a double null [9]. The single null discharges have an elongation of 1.65 (see Fig.7) compared with 1.80 for the double null and are therefore more stable against vertical displacements. In these configurations, the plasma is detached from both the limiter and the inner wall; recycling occurs in an open divertor region near the X-point. While interaction

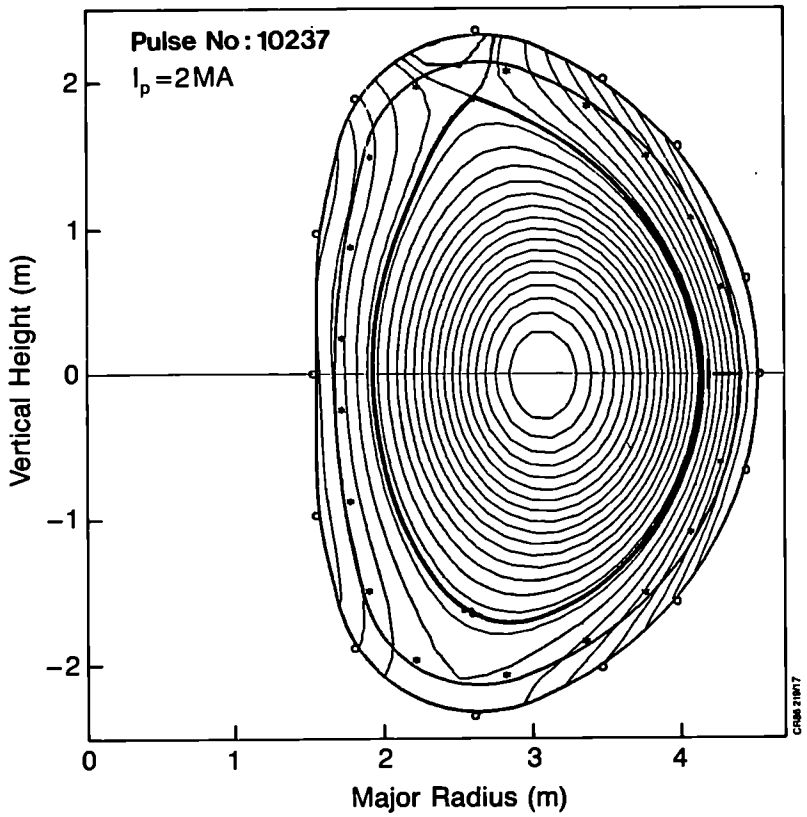

Fig.7 Single-Null X-Point configuration

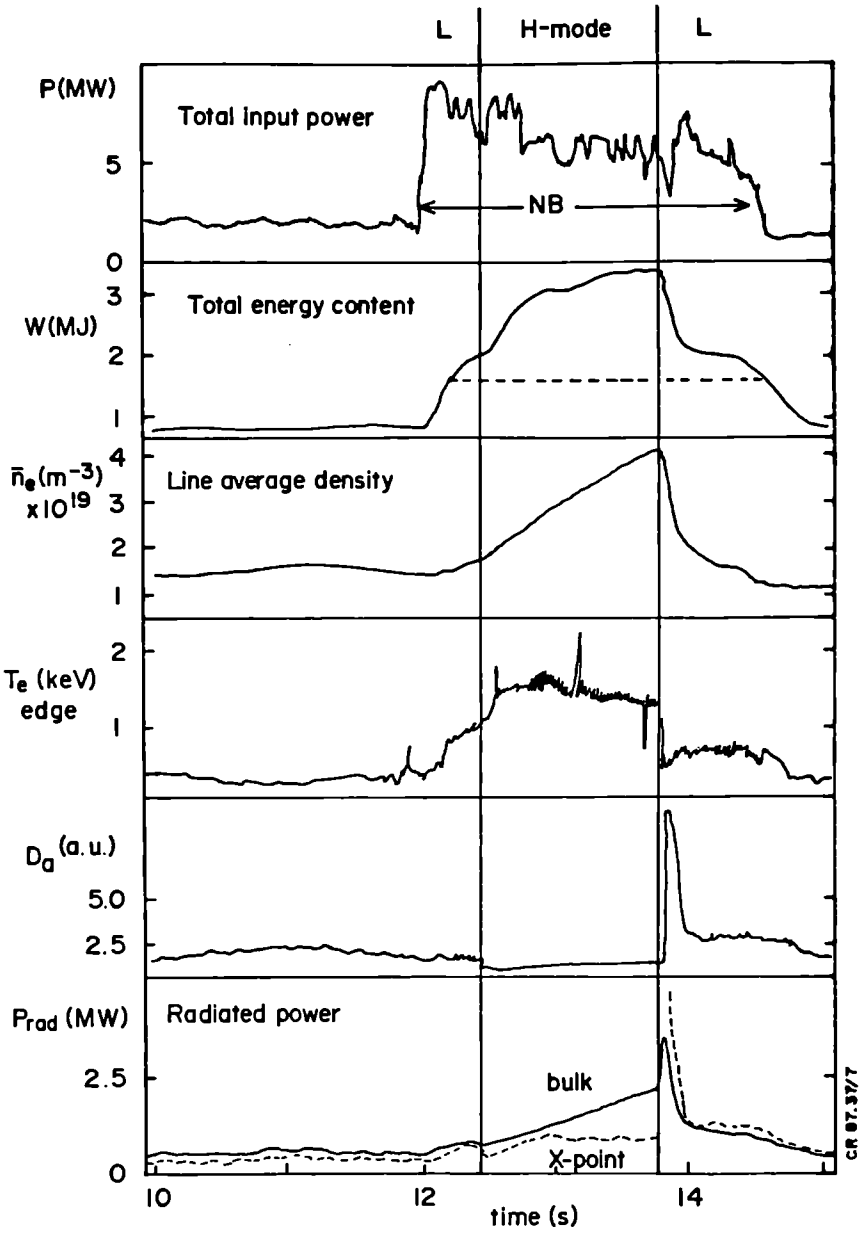

Fig.8 Single-Null X-Point experiment (Pulse No:10237) showing time evolution of:

(a) total input power, P_t;

(b) power to target plates ($P_t - P_{rad} - dW/dt$) (from bolometric analysis);

(c) total energy content W from the diamagnetic loop;

(d) line electron density, $\int n_e dl$;

(e) plasma edge temperature, T_e(edge);

(f) D_α signal from the plasma boundary.

of the discharges with the limiters was curtailed, the increased localised power deposition on the top and bottom target plates has, so far, limited the total input power to 10MW.

With neutral beam heating power greater than 5MW, a transition to enhanced plasma confinement (H-mode) was obtained in single null operation with B_T=2.2T. The usual H-mode features were observed (see Fig.8); decreased D_α light emission at the plasma boundary, reduced broadband magnetic fluctuations near the X-point, a rise in plasma density and in energy content, a sudden increase of electron temperature near the separatrix producing a pedestal to the temperature profile (see Fig.9b)and a flat density profile with a steep gradient near the separatrix (see Fig.9a). The H-mode phase could be sustained for durations approaching 2s. The continuous density rise increased the radiated power from the bulk plasma and is the likely cause for termination of this phase. There was no indication of a peaking of the impurity profile. While the energy content reached a quasi-steady state for times approaching 1s, the electron temperature could reach a maximum before the end of the H-mode phase. In these conditions, a plasma energy content of 6MJ was obtained with 8MW NB heating in addition to ohmic power of 2MW at I_p=3MA. The global confinement time in this mode exceeded by more than twice that value obtained with limiter or inner wall discharges. Increasing the magnetic field raised the power threshold required to switch to an H-mode, and has so far prevented a transition occurring with B_T>2.8T. H-modes have not yet been achieved with a double null configuration.

Separatrix operation appears to induce substantial changes in the plasma behaviour compared to limiter operation. This is possibly a result of the high shear at the boundary of the plasma, consistent with H modes obtained with a separatrix almost on the wall.

(f) Progress Towards Breakeven

A record value of the fusion product $\langle \hat{n}_i \tau_E \hat{T}_i \rangle$ of $2\times10^{20} m^{-3}.s.keV$ has been achieved with 10MW neutral beam heating during X-point operation

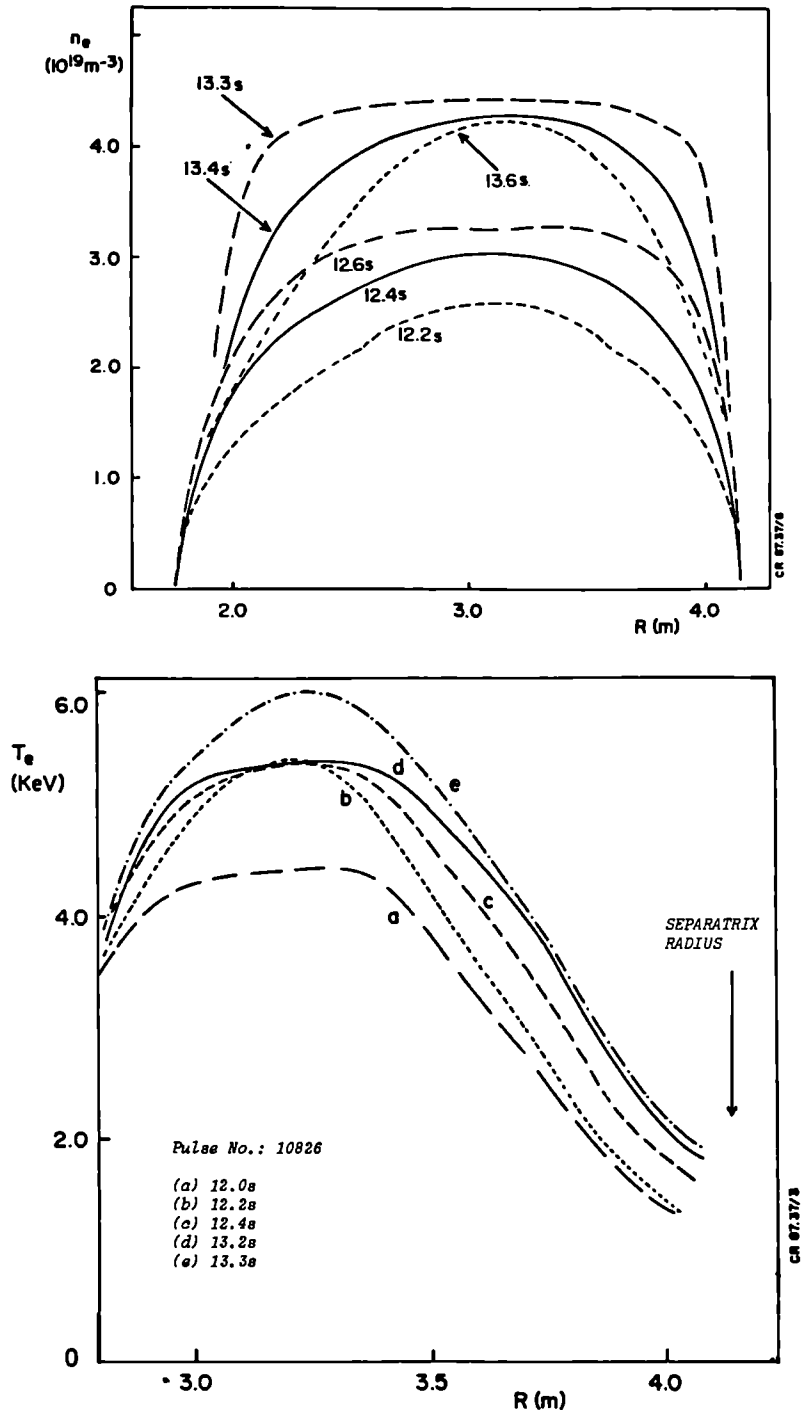

Fig.9 (a) Density profiles during L→H→L transition (times are marked on the diagram);
(b) Temperature profiles during L→H transition (times are marked on the diagram).

in the H-mode. For limiter discharges, the values of the fusion product are similar for ohmic, RF, NB and combined heating methods. This is caused by degradation in confinement time offsetting gains made in other parameters. The maximum values of the fusion product and the corresponding values of plasma temperature, density and energy confinement time are given in Table III for differing operating scenarios.

TABLE III

MAXIMUM VALUES OF $\langle \hat{n}_i \tau_E \hat{T}_i \rangle$

EXPERIMENTAL PROGRAMME	PEAK DENSITY	ENERGY CONFINEMENT TIME	ION TEMPERATURE	FUSION PARAMETER	Q_{DT} EQUIVALENT	PLASMA CURRENT
	$\hat{n}_i$ ($\times 10^{19} m^{-3}$)	τ_E (s)	$\hat{T}_i$ (keV)	$\langle \hat{n}_i \tau_E \hat{T}_i \rangle$ ($\times 10^{19} m^{-3}$.s.keV)	Q_{DT}	I_p (MA)
Ohmic (4.6MW)	4.2	0.8	3.0	10	0.010	5
ICRF (7MW)	3.7	0.3	5.4	6	0.012	3
NBI (6MW)						
High n_i	4.4	0.4	4.0	7	0.10*	3
Low n_i	1.5	0.4	10	6	0.20*	3
Combined NBI + RF (14MW)	5.0	0.4	3.5	7	0.10*	3
X-point (NB-10MW)	5	0.65	6	20	0.15*	3

*Beam-Plasma reactions are dominant

Neutron yields up to $3 \times 10^{15} s^{-1}$ have been obtained with NB heating, mainly from deuterium-deuterium reactions occurring between the deuterium particles in the heating beams and the plasma. The best ratio of fusion power to input power obtained was $Q_{DD}=3.5 \times 10^{-4}$ which is equivalent to $Q_{DT}=0.2$, if tritium was introduced into the machine under

these conditions and would correspond to a fusion power production of above 1MW.

4. SUMMARY OF JET RESULTS

A summary of JET results is given, as follows:

(a) both ICRF and neutral beam (NB) injection methods are effective in delivering power into the JET plasma with the expected profile depositions. Large central electron and ion temperature increases have been observed; $\hat{T}_e$ and $\hat{T}_i$ have reached values of 7.5keV at densities of $3\times10^{19}m^{-3}$. At lower density ($\sim1.5\times10^{19}m^{-3}$), $T_i \geq 12.5$keV has been measured;

(b) with both these heating methods, the plasma energy has increased with input power. About 6MJ energy has been achieved in JET plasmas with ~18MW of total power input. However, the rate of energy increase with power ($\Delta W_k/\Delta P_t$) ~0.1-0.3s is smaller than the corresponding ohmic confinement times (τ_E~0.6-0.8s). The fusion product $\langle \hat{n}_i \tau_E \hat{T}_i \rangle$ has reached values exceeding $10^{20}m^{-3}$.s.keV, both in ohmic plasmas at 5MA and with additional heating: the degradation in confinement offsets the gains in density and temperature;

(c) a higher fusion product value of $2\times10^{20}m^{-3}$.s.keV has been obtained in the X-point configuration at lower current (~3MA). Values of $\tau_E \approx 0.6$-0.7s and $\hat{T}_i$ up to 10keV were achieved with neutron production $\sim3\times10^{15}ns^{-1}$ equivalent to a thermal $Q_{DT}=0.1$, the total Q_{DT} being ~0.15;

(d) in the central region (inside the inversion radius) between sawtooth collapses, additional heating is effective in increasing the plasma electron temperature (cf monster sawteeth);

(e) outside this region, electron heating is poor. The electrons seem to be the main energy loss channel, which appears related to confinement properties and not to the heating process;

(f) good prospects exist on JET for production of several MW of α-particle power at a value $Q_{DT}\approx1$;

(g) α-particle heating is expected to behave in a similar fashion to

other heating methods. Therefore, a reactor must either: (i) work at moderate currents with sophisticated control of the central region; or (ii) work at high currents without the need for complex control and additional heating.

5. AN INTERPRETATION OF CONFINEMENT AND CONSEQUENCES FOR A REACTOR

JET data have been used to assess the status of theoretical understanding of heat transport. Local fluxes have been derived from measurements and compared with presently available theoretical values. No acceptable agreement has yet been found [10]. Heuristic scaling laws can be derived by using dimensionless parameters [11,12,13]. Dimensionless parameters can be categorized into two groups.

(a) Shape Parameters: defined as ratios of two components of the same physical quantity and which describe either the geometry of the plasma (such as q; R/a; r/a; b/a; $r(\partial q/\partial r)$; $r(\nabla T/T)$ etc.) or its composition (i.e. m_e/m_i; n_e/n_i; T_e/T_i; Z_{eff}).

(b) Structural Parameters: constructed from different physical quantities. The relationships between the structural parameters reflect the underlying physics. When atomic processes, such as ionisation, line radiation and charge exchange are excluded, it is sufficient to introduce six structural parameters to describe a Tokamak plasma in a steady state; these are shown in Table IV. In this table, the subscripts t and p refer to the toroidal and poloidal component, respectively, η is the resistivity, v_s is the sound velocity, v_A the Alfven velocity, v_E the velocity at which energy flows out of the system, v_{th} the electron thermal velocity and v_{dia} the component of the diamagnetic drift velocity resulting from the temperature gradient. The other symbols have their normal meaning.

When quasi-neutrality exists, i.e. when the Debye length does not play a role, the parameters Γ and ζ are used only to define the collisions between charged particles. For instance, the Spitzer resistivity ($\eta \sim T^{-3/2}$) is defined by the relationship $\Delta = \zeta\Gamma^{-2}$. The parameter Φ is

TABLE IV

STRUCTURAL PARAMETERS DESCRIBING A TOKAMAK PLASMA

DESCRIPTION	PARAMETER
Ideal MHD	$\beta = \frac{P}{B_t^2/2\mu_o} = (\frac{v_s}{v_A})^2$
Resistive MHD	$S = \frac{B_p v_A}{\eta j} = \frac{v_A}{v_{pinch}}$
Power flux balance	$\Phi = \frac{\text{Power flux}}{\text{Energy density x } v_s} = \frac{v_E}{v_s}$
Finite Larmor radius or two-fluid MHD	$\Omega = \frac{2m_e kT_e}{e^2 B_t^2 r^2} = (\frac{v_{dia}}{v_{th}})^2$
Relativistic effects	$\Gamma = 2kT/m_e c^2 = (\frac{v_{th}}{c})^2$
Granular effects	$\zeta = e^2/rm_e$

required by the fact that the system is an open one: a continuous flow of energy to the plasma is provided by the various heating systems. Here only the dependence between structural parameters will be considered. This means that the expressions given in the following must be multiplied by a shape parameter function, which may not necessarily be known. Note that the magnetic Reynolds number S and Φ are ratios of velocities, while β and Ω are ratios of the square of velocities. In any relation between these parameters, it is anticipated that Φ and S will be affected by integer exponents, while β and Ω will be at a half power exponent. Also, the relationship between structural parameters should be relatively simple. Other well known dimensionless plasma physics parameters can be written in terms of previous ones. For instance, the drift parameter ($=j/env_{th}$) is $\xi = \Omega^{1/2}/\beta$

The power balance equation with ohmic heating only is $\Phi_\Omega = 1/S\beta^{3/2}$ while the classical and neoclassical perpendicular transport are

described by $\Phi_{\perp} = \beta^{1/2}/S$ and the plateau regime by $\Phi_p = \Omega$. Parallel transport would be described by $\Phi_{\parallel} = \Omega S/\beta^{1/2}$.

The JET experimental results (in particular, the behaviour of the electron temperature profile) strongly suggest that there is no fundamental difference between ohmic and auxiliary heated discharges: the mechanisms responsible for confinement degradation already seem at work during the ohmic phase. A formulation of the electron radial heat flux ϕ_e, reflecting this behaviour could be:

$$\phi_e = n\chi_{an}\nabla T.g\left(\left|\frac{\nabla T}{(\nabla T)_c}\right|\right) + \phi_{neo}$$

where χ_{an} is the anomalous heat diffusivity responsible for the observed incremental confinement time and g is a function of the temperature gradient which goes to zero when ∇T is smaller than a critical value $(\nabla T)_c$. ϕ_{neo} reflects the neoclassical transport and is only significant when g=0. A possible form for g is:

$$g = \left[1 - \frac{(\nabla T)_c}{\nabla T}\right] \cdot H\left[\left|\nabla T\right| - \left|\nabla T\right|_c\right]$$

Such a form of the function g is supported by the JET results[14].

One hypothesis proposed is that $(\nabla T)_c$ corresponds to the establishment of a chaotic magnetic topology involving small islands [15]. The resulting flow of energy should then be a combination of parallel and perpendicular transport. Written in terms of dimensionless parameters, this means

$$\Phi_{an} = \Phi_{\perp}^{u} \cdot \Phi_{\parallel}^{v} \qquad \text{with } u + v = 1$$

The simplest form is u=v=½ and correspondingly, $\Phi_{an} = \left[\frac{\beta^{1/2}}{S} \cdot \frac{\Omega S}{\beta^{1/2}}\right]^{1/2} = \Omega^{1/2}$. Note that, except for missing shape parameters, this relation shows a sort of Bohm like diffusivity.

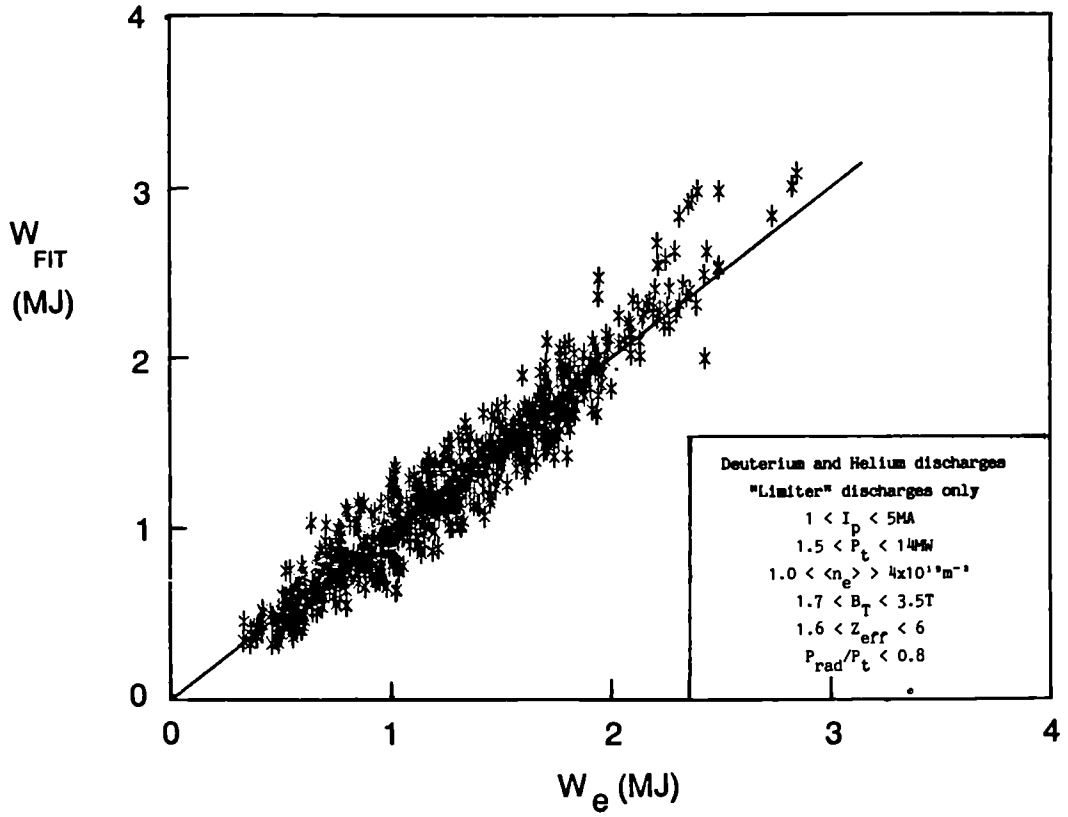

Fig.10 Total stored electron energy W_e versus the fit proposed in Eq.(1). Data include ohmic heating only, NBI only, ICRF only and combined heating.

The comparison between the fitted and calculated values is shown in Fig.10, where the range of the experimental data is indicated. While the JET plasma size is almost unchanged in all the data presented and some shape factors are still likely to be missing, the scaling provides the size dependence and fits quite well the results of smaller Tokamaks where the electron energy content is four orders of magnitude smaller.

If proven to be correct, the scaling proposed has direct consequences on the ignition margin and on the size of future devices. Note that the critical electron temperature, would vary as $(BI^2)^{1/4}$ at the density limit ($n \propto B/L$). As any increase above the critical temperature is very consuming in input power, it seems better to be close to the required ignition temperature already in the ohmic heating phase. A current and size increase in a Tokamak machine could achieve ignition <u>without</u> additional heating. The resulting simplification of

The expression for the critical electron temperature gradient should be deduced from the mechanism sustaining the perturbed magnetic topology. A non-proven but plausible one involves a balance between the pressure exerted on the islands, either by an acoustic wave (Ω_{c1}) or by a torsional Alfven wave (Ω_{c2}), and the resistive dissipation of the induced currents. In terms of dimensionless parameters, it reads

$$\Omega_{c1} = 1/S\beta^{3/2}$$

$$\text{or} \quad \Omega_{c2} = 1/S\beta$$

The heat flux equation becomes

$$\Phi = [\ \Omega^{1/2} - \Omega_c^{1/2}\ ]\ H(\Omega - \Omega_c) + \text{Neo-classical terms}$$

Another term may enter the right side of equation when describing the boundary of the discharge where atomic physics becomes dominant.

With the help of empirical scaling of JET results [16], it has been possible to deduce some but likely not all the involved shape parameters and to propose here a heuristic scaling. The global electron energy content W_e can be deduced from the flux equation by solving for temperature and introducing the total input power, P_t, independent of the heating method (ohmic, NBI or ICRF).

$$W_e = \alpha_1 Z^{1/4} n^{3/4} B^{1/2} I^{1/2} L^{11/4} \left\{1 + \alpha_2 \frac{M^{1/2} P_t}{n^{1/2} Z^{1/2} B L^{3/2}}\right\}^{1/2} \qquad (1)$$

where the critical temperature gradient is defined by $\Omega_{c1} = 1/S\beta^{3/2}$; M is the atomic number, Z the effective charge, n the volume averaged density ($10^{19} m^{-3}$), I the plasma current (in MA), B the toroidal field (in T) and L an average size of the plasma (in m): ($L = \sqrt[3]{Rab}$). The coefficients α_1 and α_2 are found by a regressional fit on about 1,200 JET "limiter" data points. The result is $\alpha_1 = 2.3 \times 10^{-2}$ and $\alpha_2 = 3.0$ when W_e is in MJ and P_t in MW.

the overall system could well compensate for the larger size. The above scaling suggests that in a Tokamak with a major radius of ~x2.5 that of JET, a magnetic field close to 4.5T and a plasma current near 25MA, a deuterium-tritium plasma would ignite with ohmic and α-particle heating only. The thermonuclear output of such a machine could be increased by injecting fuel pellets: the thermal insulation should degrade as the additional heating provided by the α-particles increased without a strong variation of temperature. Burn control would be performed entirely through density control.

ACKNOWLEDGEMENTS

The JET achievements are the result of the work of the JET Team. In addition, we are pleased to acknowledge the help of Dr. K. Thomsen in handling the JET data resulting in Fig.10 and of Dr. B. Keen in reading carefully the manuscript.

7. REFERENCES

(1) Design, Construction and First Operational Experience of JET, Special Issue of Fusion Technology, 11, 43, (1987);

(2) P.H. Rebut et al, Proceedings of the 11th IAEA Conference on Plasma Physics and Controlled Nuclear Fusion Research (Kyoto, Japan, November 1986);

(3) P.E. Stott, Proceedings of the Workshop on High Temperature Plasma Diagnostics (Varenna, Italy, September 1986);

(4) K. Behringer et al, Proceedings of the 11th IAEA Conference on Plasma Physics and Controlled Nuclear Fusion Research (Kyoto, Japan, November 1986);

(5) A. Gondhalekar et al, Proceedings of the 11th IAEA Conference On Plasma Physics and Controlled Nuclear Fusion Research (Kyoto, Japan, November 1986);

(6) D.J. Campbell et al, Proceedings of the 11th IAEA Conference on Plasma Physics and Controlled Nuclear Fusion Research (Kyoto, Japan, November 1986);

(7) J.A. Wesson et al, Proceedings of the 11th IAEA Conference on Plasma Physics and Controlled Nuclear Fusion Research (Kyoto, Japan, November 1986);

(8) P.H. Rebut and M. Hugon, 10th IAEA Conference on Plasma Physics and Controlled Fusion Research (London, U.K.), (1984) Vol.II, p197;

(9) A. Tanga et al, Proceedings of the 11th IAEA Conference on Plasma Physics and Controlled Nuclear Fusion Research (Kyoto, Japan, November 1986);

(10) D.F. Düchs et al, Proceedings of the 11th IAEA Conference on Plasma Physics and Controlled Nuclear Fusion Research (Kyoto, Japan, November 1986);

(11) B.B. Kadomtsev, Fiz Plazmy, 1, (1975) 531; [Sov. Phys.-J. Plasma Phys., 1 (1975 295];

(12) J.W. Connor and J.B. Taylor, Nuclear Fusion, 17 (1977) 1047;

(13) P.H. Rebut and M. Brusati, Plasma Physics and Controlled Fusion, 28, 113 (1986);

(14) J.D. Callen, J.P. Christiansen, J.G. Cordey, P.R. Thomas and K. Thomsen, Modelling of Temperature Profiles and Transport Scaling in Auxiliary Heated Tokamaks, to be published in Nuclear Fusion, and N. Lopes Cardozo, this Conference;

(15) P.H. Rebut, M. Brusati, M. Hugon and P.P. Lallia, 11th IAEA Conference on Plasma Physics and Controlled Nuclear Fusion Research (Kyoto, Japan, November 1986) and M. Hugon et al, this Conference:

(16) J.G. Cordey et al, Proceedings of the 11th IAEA Conference on Plasma Physics and Controlled Nuclear Fusion Research (Kyoto, Japan, November 1986).

Invited paper presented at the 7th APS Topical Conference on
Application of RF Power to Plasmas, Kissimmee, Florida, U.S.A.,
4th-6th May 1987

Results of RF Heating on JET and Future Prospects

J. Jacquinot V. P. Bhatnagar G. Bosia M. Bures G. A. Cottrell
Ch. David M. P. Evrard D. Gambier C. Gormezano T. Hellsten
A. S. Kaye S. Knowlton D. Moreau F. Sand D. F. H. Start
P. R. Thomas K. Thomsen T. Wade

ABSTRACT

Ion Cyclotron Resonance Heating (ICRH) has been applied to various JET plasmas with net coupled powers reaching 7 MW for several seconds. Conditioning with helium discharges is shown to be effective in controlling the density and in reducing the total radiated power to about 25% of the input power. On axis heating invariably results in long sawteeth of large amplitude. In most high power cases, a sudden bifurcation to monster sawteeth as long as 1.6 s is observed. The monster sawtooth is accompanied by an improvement in energy confinement time (+20%) and by an increase in density. Central electron and ion temperatures of 7 and 5.5 keV respectively have been achieved with 6.5 MW of ICRF power. The heating rate is reduced with off-axis heating in agreement with diffusive heat transport models.

The future RF programme on JET includes upgrading the ICRF power to 20 MW and the development of current drive methods using a phased ICRF array of 8 antennae and later on a Lower Hybrid Current Drive system at 3.7 GHz with a 10 MW launcher.

1. INTRODUCTION The JET RF programme now consists of two distinct activities:

(i) Ion Cyclotron Resonance Heating (ICRH), which started operation in 1985. The first stage of this programme has recently been completed.

(ii) Lower Hybrid Current Drive (LHCD). Studies started in 1986 and approval for the construction of a first stage of the 3.7 GHz equipment has been obtained.

ICRH and NBI will ultimately (c. 1988) inject 40 MW of power in the plasma (20 MW each). LHCD is aimed at controlling the current profile in order to suppress the sawteeth and possibly to achieve higher confinement regimes.

This article, which follows several previous reports [1a, b, c,], summarizes the main experimental results obtained with ICRH.

Power accountability has been deduced from the stored energy response to a step power increase [1a]. The power deposition profile has been analysed using power modulation of long pulses [1c].

As expected in large Tokamaks with short antennae located near the equatorial plane about 80% of the power is deposited in a narrow zone (± 10 cm for off-axis heating, ± 30 cm for on-axis heating) defined by the iou-iou hybrid resonance. The 20% remaining power seems to appear at the edge producing serious modifications of the scrape off layer. These edge effects can be suppressed by phasing coupling elements toroidally [3] so that most of the power is radiated at a high $k_{//}$ ($\simeq 7\ m^{-1}$). The heating rate in this case was higher (+ 25%) presumably because all the power was now available for plasma core heating. These experiments were limited to low power (~ 1.5 MW) due to a low coupling resistance but suggested a redesign of the antennae to allow this mode of operation with improved coupling for the next stage of the ICRH programme.

Earlier plasma heating studies [1a,b,4] have shown that the increase of plasma stored energy is rather insensitive to the method of heating (ICRH, NBI). More extensive studies have demonstrated the interest of local heating [1b,c,5] in the plasma centre due to the diffusive nature of heat transport [5]. Another major difference between NBI and ICRF using a minority species is that NBI dominantly heats the ions and ICRF heats the electrons via a highly energetic minority. At low density NBI creates a "hot ion" mode and ICRF a "hot electron" mode.

This article is organized in the following manner. The ICRF data base is first presented with particular attention to the localisation of the heating zone and to conditions of very low plasma radiation. The resulting scaling of confinement with plasma current is discussed. We then compare the various heating scenarios using the same plasma current but different minority species or magnetic configuration (in particular X-point). Finally we discuss future prospects of RF in JET examining specific RF scenarios capable of producing a high fusion yield without significant activation.

2. EXPERIMENTAL CONDITIONS, HELIUM CONDITIONING Experiments were performed with 3 antennae, all phased (unless stated) in the toroidal monopole mode (e.g. with a radiation spectrum peaked at $k_{//}=0$). Operation just after the installation of the antennae resulted in a high fraction of plasma radiation (e.g. $p = P_{rad}/P_{tot} \simeq 0.7$) of the input power. The density increase with RF was high and density disruption would set a RF power limit at low plasma current. The situation improved remarkably with high current, high power pulses which apparently carbonized the interior of the vessel. However, p stayed above 0.5 (Fig 1). Discharges in Helium were performed at the end of the operating period. The increase of density with RF was low e.g. no more than 25% for P_{RF} = 7 MW and p decreased from typically 0.55 with ohmic heating to 0.25 at maximum RF power (7.4 MW). These improved conditions remain unchanged after a return to Deuterium plasmas. Fig. 1 illustrates the effect of Helium conditioning for 2 MA plasmas both with Deuterium and Helium species.

3. SCALING OF ENERGY CONFINEMENT WITH ICRF Figs. 2 and 3 summa-

rize the available confinement data of plasmas heated by ICRF heating alone using outboard limiters (in one series of experiments the outboard limiters were removed and the plasma was limited by the side protections of the 3 antennae). The plasma current was varied from 1 MA to 5 MA. This scan was normally done with a constant ratio of the wave frequency to the vacuum toroidal field (ν/B_ϕ). Paramagnetic shift of the resonance (R_c) resulted in a variation of the resonance layer (as much as 25 cm). Fig. 2 gives the stored energy for all limiter discharges with $|R_o - R_c| < 0.55$ m. Note that on axis heating of 5 MA plasmas have only been performed with a 50 cm displacement of the resonance layer. In Fig. 3 the incremental confinement $\tau_{inc} = \Delta W/\Delta P_{tot}$ is plotted for the entire data set as a function of the resonance position. For each data subset the heating efficiency decreases as the resonance is moved out. The data is well represented by a law

$$\tau_{inc} = \tau_o \, (1 - (r_c/a)^2)^2 \; ; \; r_c = R_c - R_o \qquad (1)$$

This result has now been obtained in the following conditions: (i) in a single shot by ramping down the toroidal magnetic field during the pulse[1b] ; (ii) by changing the frequency from shot to shot [1c], (iii) as in (ii) but in Helium discharges with Hydrogen minority heating. In this third series of experiments, the total radiated power was a factor 2 to 3 smaller than in the two other series. The fact that the τ_{inc} (r_c/a) is similar in all these series despite significant changes in radiation, suggests this data should be analyzed in terms of heat transport models.

Rebut et al [6] have proposed an anomalous transport model in which the heat flux can be described by

$$q = n \, \chi \, (\nabla T - \nabla T_c) \, H \, (\nabla T - \nabla T_c) \qquad (2)$$

Here, the anomalous heat diffusivity χ is "switched on" by the step function H when the electron temperature gradient ∇T rises above a critical value ∇T_c.

Callen et al [5] have analysed in detail the consequences of general diffusion laws and shown that Eq. (2) belongs to a functional form which best represents the following phenomenae observed with additional heating:

(i) the heat pulse propagates with a velocity independent of additional heating power [12];

(ii) the off-set linear law of $W = W_o + \tau_{inc} P$ which is a direct consequence of Eq. (2) assuming that χ does not have a strong dependence on ∇T. The 2 MA data in Fig 2 is a good illustration of the offset linear law;

(iii) the decrease of heating efficiency with off-axis ICRF heating. Calculations [5] shows that Eq. (1) is obtained provided that χ is assumed to be independent of ∇T but increases with radius approximately as

$$\chi(r) = \chi_o/(1-r^2/a^2) \qquad (3)$$

We now use Eq. (1) and the off-set linear law to deduce, experimentally, the importance of the plasma current. We write:

$$W = W_o + \tau_o P^*_{tot} \; ; \; P^*_{tot} = 0.85 \, P_{OH} + (1-r_c^2/a^2)^2 P_{RF} \qquad (4)$$

P^*_{tot} draws its significance from the diffusive heat transport model: P^*_{tot} is the power which when deposited entirely on axis would give the same increase in W as the spatially distributed P_{OH} and the off-axis P_{RF}.

Representation of the data versus P^*_{tot} (Fig 2) shows that:

for 2 MA ; τ_o = 180 ms, W_o = 0.55 MJ

for 5 MA ; τ_o = 310 ms, W_o = 1.45 MJ

Using the diffusive heat transport model, it is also possible to correct P^*_{tot} for radiation losses. Including the full profile effects of the radiation following the prescription of [5], we find no changes of τ_o and W_o in the 2 MA data but in 5 MA it amounts to a 10% reduction of P^*_{tot} (τ_o = 340 ms).

A consequence of Eq. (2) is a relation between an averaged critical gradient $\overline{\nabla T_c}$ and W_o : $\overline{\nabla T_c} \approx W_o/2\pi^2 R_o a^3 n$. We find that $\overline{\nabla T_c} \approx 1.7$ keV $m^{-1} \pm .4$ for both the 2 MA and 5 MA data.

The physical significance of the critical gradient $\overline{\nabla T_c}$ is the expectation of a reduced heat transport in regions where $\nabla T < \overline{\nabla T_c}$. Such a situation can arise with high power off-axis ICRH. Indeed the heat transport coefficient appear significantly reduced for this case [7]. The reduction concerns only the central zone located inside the heated shell and the overall effect is a loss of heating efficiency.

4. HEATING SCENARIOS, MONSTER SAWTEETH, X-POINT DISCHARGES Recent high power experiments confirm previous conclusions that there is hardly any observable differences in stored energy between scenarios using a He^3 or a H minority. In agreement with minority slowing down physics [8], He^3 minority heating, particularly at low or moderate power, is more efficient at heating ions than the H minority but at the expense of a smaller electron heating rate. Using high power on-axis heating with $n_{H,He^3}/n_D \approx 0.05$, electron heating via the minority species dominates. The ions are slowly heated by electron collisions. An example of this delayed heating is apparent on Fig. 4.

A common feature of high power on-axis heating is the sudden transition [9] from the regular sawteeth behaviour (period ≈ 300 ms) to long MHD quiescent periods of up to 1.6 s ("Monster" sawteeth). The electron temperature (Fig 4) saturates after 200 ms but the density, the stored energy (Fig 5), and the ion temperature keep increasing during the quiescent period. The monster has beneficial effects (gain of a factor of 2 to 3 on the reaction rate and of ≈ + 20% on the stored energy). However, its crash may induce a locked MHD mode which deteriorates confinement. In several cases this mode lasted for the rest of the pulse.

On the contrary when the resonance is located outside the q=1 surface the sawteeth become smaller and shorter [1b].

ICRF heating of single null X-point discharges has only been performed at 2MA with P_{RF}<6MW and 6cm separating the antenna from the plasma (Figs. 4 and 5). No clear transition to an "H mode" regime has been observed. However, the confinement is better than in limiter discharges with the same plasma current. τ_{inc} reaches 350 ms and the confinement degradation is small. The edge MHD activity is smaller than in limiter discharge. This improvement of energy confinement is also accompanied by increased impurity levels. The total radiated power fraction p increases from 0.25 (limiter) to 0.5 (X-point) and Z_{eff} from 2.5 (limiter) to 4.5 (X-point).

5. ICRF SCENARIOS PRODUCING A HIGH YIELD OF D-He^3 FUSION REACTIONS

In this section, we consider ICRH scenarios capable of producing a significant amount of fusion yield from non thermal reactions between energetic Deuterium and Helium3 ions. The basic reactions are

$$D + He^3 \rightarrow H \quad (14.7\ MeV) + He^4\ (3.6\ MeV)$$
$$D + He^3 \rightarrow L_i^5 \quad + \gamma\ (16.6\ Mev)$$

The second reaction only occurs with a much smaller probability and is mentioned here as a diagnostic of the process since the γ production can be monitored [10]. The cross-sections for both reactions have maxima at 440 keV. We are interested in producing a significant number of these reactions in order to study the confinement of fusion products without large neutron activation of the Tokamak.

The following ICRF scenarios have been considered:

(S1) He^3 minority heated by ICRF in a D plasma, a standard JET operating regime.

(S2) Harmonic Deuterium heating, $2\omega_{cD}$, in a He^3 plasma with NBI. In this scenario, the parameters are optimized to maximize the damping of ICRF on the Deuterium beam ions to increase their energy to the optimum of the D-He^3 cross section. Fundamental damping on a H minority is to be avoided in this scheme and therefore an H concentration smaller than 1% is required. In preliminary studies [11] up to 10% of the RF power was absorbed in this manner as deduced from observed beam acceleration above the injection energy.

(S3) $2\omega_{C\ He^3}$ scenarios in a D plasma. The 2nd harmonic damping of He^3 will become a dominant process when the ion temperature reaches 7 keV. This will be best achieved in the hot ion mode generated by NBI at low or moderate densities. Again in this scheme, fundamental damping by an H minority can occur on the high field side of the Tokamak, and thorough conditioning of the Tokamak will be required to remove Hydrogen contamination.

A Fokker-Planck calculation in these three situations has been performed [2] assuming an isotropic distribution, $T_e = T_i$ and $Z_{eff} = 1$. Figure 6 gives the fusion amplification factor $Q = P_{Fusion}/P_c$ versus P_c, the power effectively coupled to He^3 in S1 and S3 scenarios or to the beam ions in the S2 scenario.

Scenario S1 appears to give the highest Q which reaches 0.06 for JET parameters with full ICRF heating. It is also the most effective scenario from the point of view of coupling to the desired species since the damping per pass is expected to be high (≈ 70%) and no other competing damping (to H for instance) can occur. The Fokker-Planck code predicts that minority velocity distribution will become highly anisotropic with a "parallel temperature" ($T_{//}$) not exceeding 20 keV, which defines, from Döppler effects, an absorption layer of ±30 cm. However, it is likely that a velocity space instability will relax the anisotropy, increase $T_{//}$ and broaden the deposition profiles.

The production of 16 MeV γ's has already been observed in JET [10] in conditions corresponding to S1. The observed flux corresponds to about 15 kW of D-He^3 fusion reaction power or to $Q \approx 3 \times 10^{-3}$. With $T_e \sim T_i \sim 5$ keV and $Z_{eff} \approx 2$, this value corresponds to $P_n \sim 0.1$ MW m^{-3} which implies a deposition profile extending to $r \simeq .6$ m. No attempt has yet been made to optimize the He^3 concentration to reach the maximum Q value.

6. THE LOWER HYBRID CURRENT DRIVE PROJECT The large temperature collapses which are observed during sawteeth with high additional power deteriorates the fusion yield and can generate a locked MHD modes with a decrease of confinement time (-25%) and, in some cases can cause a major disruption. JET has proposed a Lower Hybrid Current Drive system in order to permanently stabilize the sawteeth. The main parameters are given in Table 1.

Table 1

Frequency	3.7 GHZ - Avoid coupling to NBI ions - Reach $n_o \approx 10^{20}$ m^{-3}
$n_{//}$	$1.2 < n_{//} < 2.4$ 48 multijunction units
Coupled Power	1.6 MW (stage 1), 10 MW (stage 2)
Current Drive	0.1 to 0.25 MA/MW, with $n_e = 5 \times 10^{19}$ m^{-3}

The construction of Stage 1 has started and a prototype launcher is expected to be ready in mid 1988.

7. CONCLUSION The first stage of the JET ICRF heating programme has been completed and the main objectives have been achieved. Net coupled powers in excess of 7 MW, $T_{eo} = 7$ keV and $T_{io} = 5.5$ keV have been obtained. The total radiated power is less than 25% of the input power when Helium conditioning is used.

Off-axis heating suggests that the heat transport is diffusive. On-axis heating is always more efficient and slows down, rather unexpectedly, the internal sawteeth relaxation. The quiescent period lasts no more than 1.6 s but has a beneficial effect on the fusion yield. The best incremental confinement time has been

obtained in X-point discharge although a transition to an H mode has not yet been observed.

The JET HF programme is being vigorously pursued with the upgrading of the ICRH to 20 MW with 8 antennae, the preparation of high fusion yield scenarios, and the development of a Lower Hybrid Current Drive system capable of driving up to 2.5 MA.

REFERENCES

[1a] J. Jacquinot et al, Plasma Phys. and Contr. Fusion 28 1 (1986)
[1b] J. Jacquinot et al, JET-P (86) 18, to be published in the Philosophical Transactions of the Royal Society
[1c] JET team, "RF Heating on JET" 11th Int. Conf. on Plasma Physics and Controlled Fusion Research, IAEA-CN-47/F-I-1 (1986)
[2] T. Hellsten, K. Appert, W. Core, H. Hamnén, S. Succi, Proc. of the 12th Eur. Conf. on Contr. Fusion and Plasma Phys. Budapest (1985)
[3] M. Bures et al, accepted for publication in Plasma Physics and controlled Fusion
[4] P.P. Lallia et al, Plasma Phys. and Conf. Fusion, 28 1211 (1986)
[5] J.D. Callen, J.P. Christiansen, J.G. Cordey, P.R. Thomas, K. Thomsen, JET P (87) 10, submitted to Nuclear Fusion
[6] P.H. Rebut, M. Brusati, M. Hugon, P.P. Lallia, 11th Int. Conf. on Plasma Physics and Cont. Fusion Research, IAEA-CN-47/E.III 4 (1986)
[7] M. Brusati, private communication
[8] V.P. Bhatnagar et al, to be presented at the EPS Conf. Madrid (1987)
[9] D.F.H. Start et al, this conference
[10] G. Sadler et al, to be presented at the EPS Conf. Madrid (1987)
[11] G.A. Cottrell et al, this conference
[12] B.J.D. Tubbing, N.J. Lopes Cardozo, JET-R(87)01.

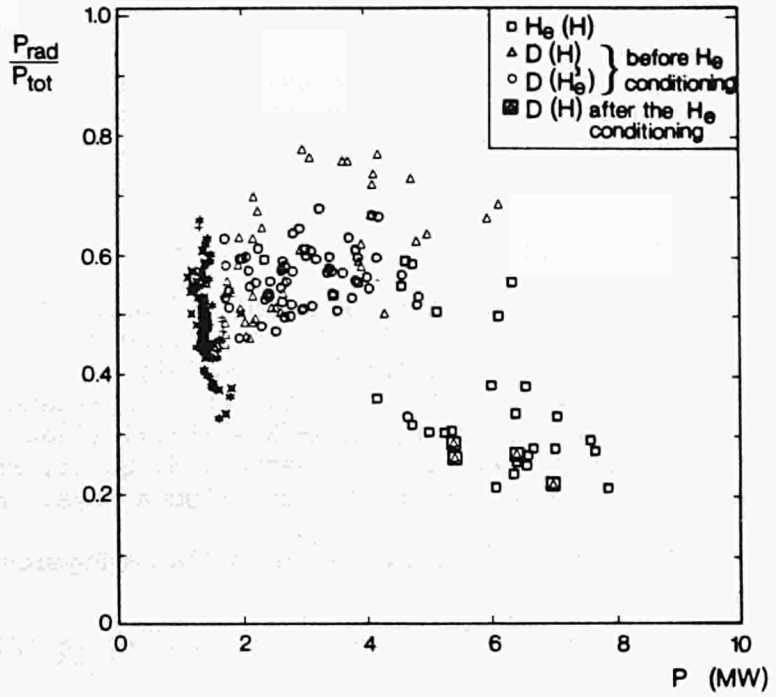

Fig. 1 Total radiated power normalised to the total input power (RF + ohmic) versus total input power. 2 MA discharges with $1 < \bar{n}_o \times 10^{-19} < 2.5$

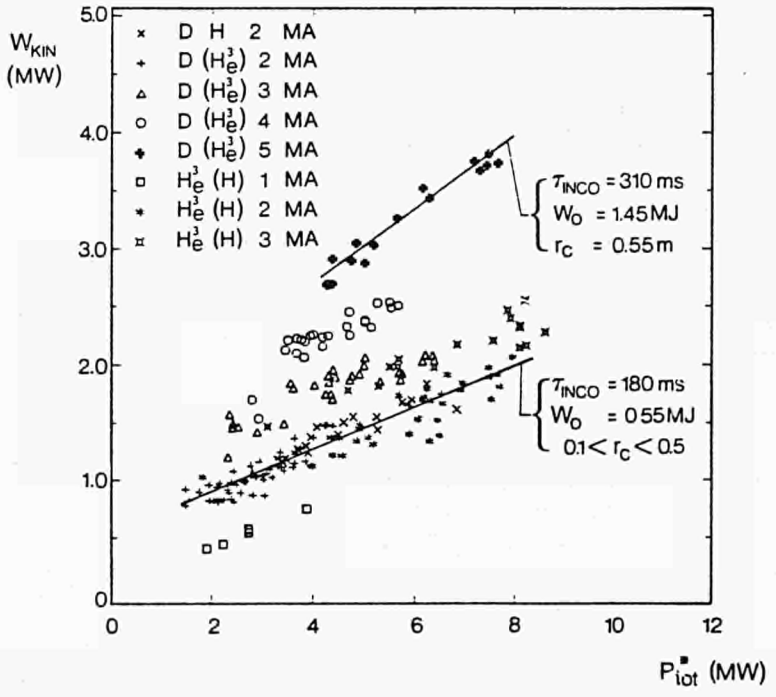

Fig. 2 Plasma stored energy versus effective input power $P^*_{tot} = 0.85\ P_{OH} + (1 - \chi^2)\ P_{RF}$; $\chi = (R_c - R_o)/a$. In the diffusion heat transport model with constant $\chi(VT)$, the deposition of P^*_{tot} exactly on the magnetic axis produces the same increase of W than the distributed power P_{OH} and P_{RF}.

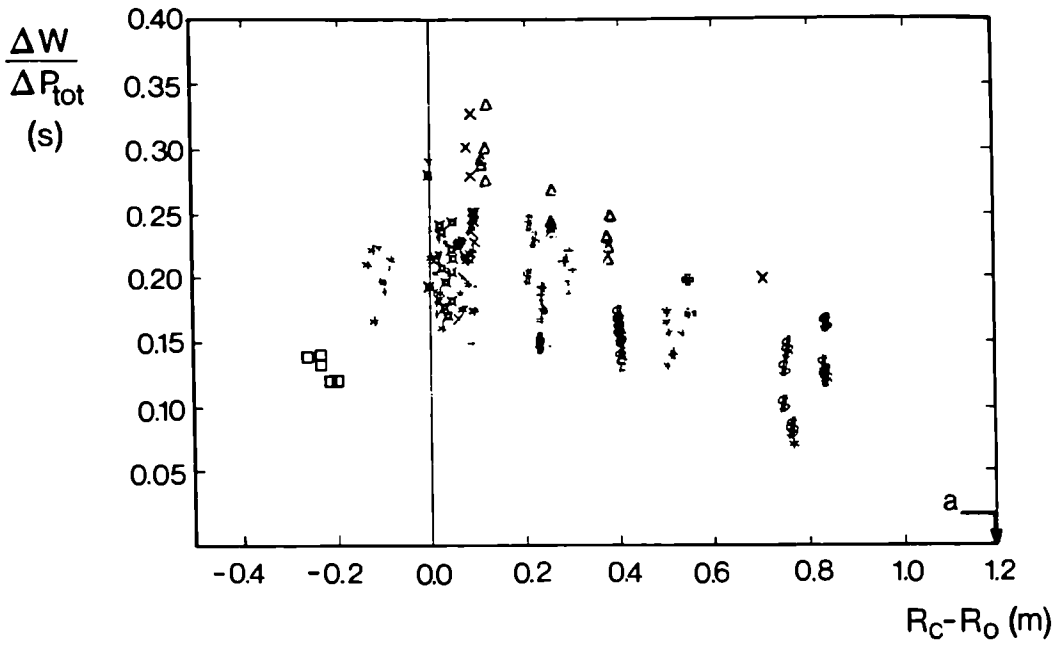

Fig. 3 Incremental confinement time $\Delta W/\Delta P_{tot}$ with $P_{tot} = P_{OH} + P_{RF}$ versus the position of the cyclotron resonance (R_c) with respect to the magnetic axis (R_o) for all JET limiter data. The symbols are explained on Fig. 2, in addition 2.5 MA data points are represented by $. Note the general decrease of the heating efficiency with off-axis heating which can be represented by a law $(1 - \chi_e)$

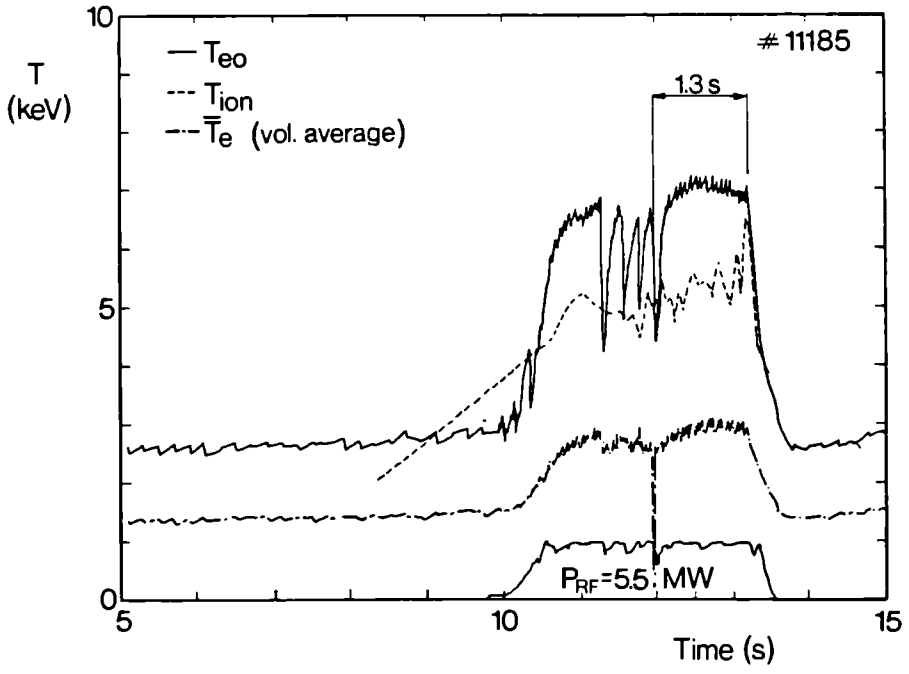

Fig. 4 Evolution of the electron and ion temperatures during 5.5 MW heating pulse (3.5 sec) in an X-point discharge (Helium plasma). 2 monster sawteeth are separated by normal sawteeth.

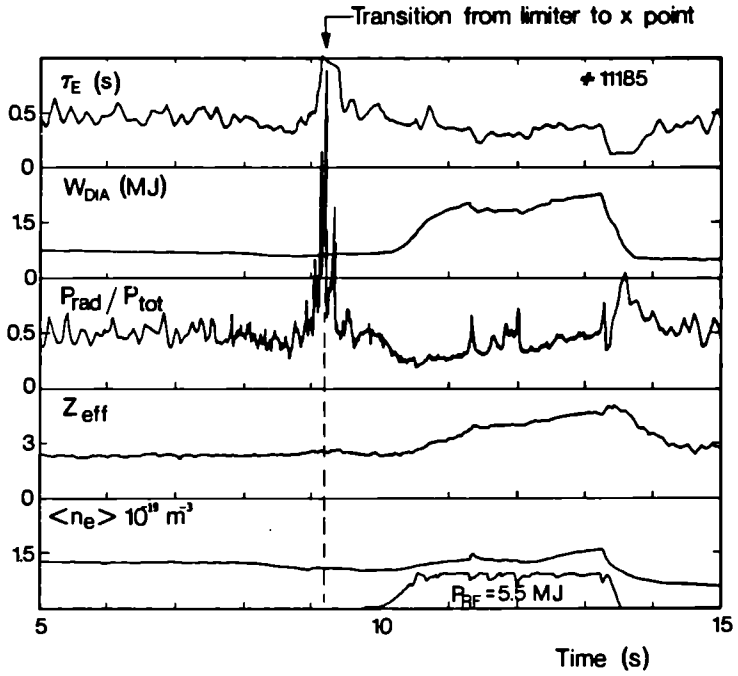

Fig. 5 Evolution of plasma parameters during a 5.5 MW heating pulse in an X-point discharge. Note the increase of density and stored energy during the monster sawtooth.. The high Z_{eff} and P_{rad}/P_{tot} is typical of the high power X-point discharge.

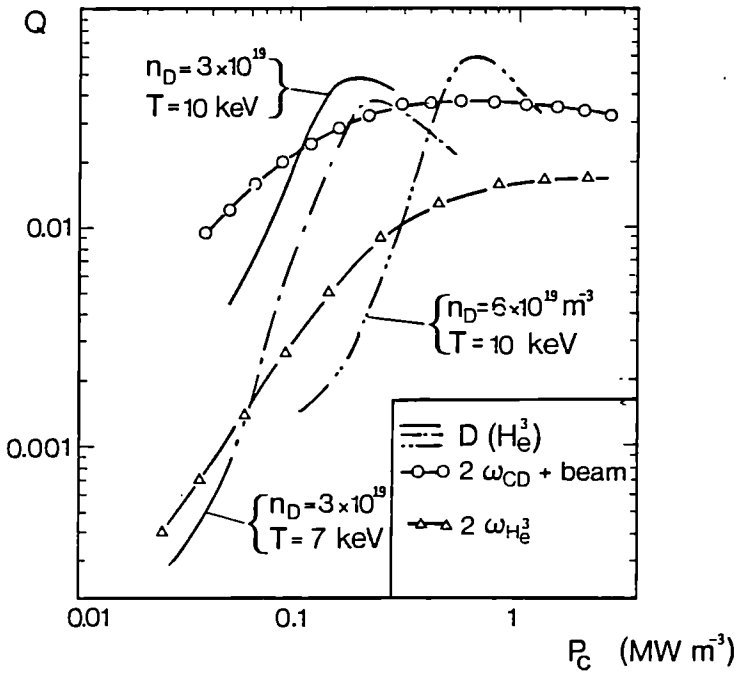

Fig. 6 Fusion amplification factor for D-He³ reaction versus the power damped in the resonating species. 3 scenarios are considered (i) D(He³), He³ resonating minority with n_{He^3}/n_D = 0.02 (ii) $2\omega_{CD}$, Harmonic resonance with Deuterium beam ions, E_{inj} = 80 keV, n_{He^3}/n_D = 1 (iii) $2\omega_{C\,He^3}$, Harmonic resonance with Helium3, n_{He^3}/n_D = 0.5. In all cases Z_{eff} = 1

JET Contributed papers to the 14th European Conference on Controlled Fusion and Plasma Physics, Madrid, Spain, 22nd-26th June 1987

JET Authors

May 1987

LOCKED n=1 MODES IN JET

J A Snipes, D J Campbell, P S Haynes*,
T C Hender*, M Hugon, N Lopes Cardozo@, F C Schuller

JET Joint Undertaking, Abingdon, Oxon, OX14 3EA, UK

*(UKAEA/Euratom Fusion Assn)Culham Laboratory, Abingdon, Oxon, OX14 3DB, UK
@Association Euratom-FOM, FOM-Instituut voor Plasmafysica, Rijnhuizen, Nieuwegein, The Netherlands

Introduction MHD oscillations in JET are often observed to slow down as they grow and lock when the amplitude exceeds $\tilde{b}_\theta$(wall) $\sim$ 10 G, then continue to grow to large amplitude ($\tilde{b}_r/B_\theta$(wall) $\sim 0.6 - 1.2 \times 10^{-2}$). Such locked modes occur before all density limit disruptions and most current rise disruptions and can also develop after pellet injection, as well as after 'monster' [1] sawteeth and remain at a large amplitude throughout the discharge. They have a dominant toroidal mode number of n=1 and poloidal mode numbers of m=2, 3, or 4. These large amplitude modes can have profound effects on the plasma affecting sawteeth, the electron temperature profile, plasma rotation, particle losses and in some cases may be responsible for a decrease in the plasma stored energy.

Calculations with two MHD codes [2,3] indicate that interaction of the growing oscillating mode with a resistive wall or a small ($\sim$ 10 G at the wall) external field asymmetry may be responsible for mode locking.

Detection of Locked Modes Integrating the difference of signals from saddle coils about the outer midplane from the same signals 180° apart toroidally measures the odd n component of the radial field perturbations in the plasma. Two of these predominantly n=1 signals, at toroidal angles of 45° and 135° (relative to Octant 1) provide the sin and cos components of the mode so that the amplitude and phase of the locked mode can be determined.

Location of Locked Mode O and X Points Under most conditions, the mode locks in the same position and remains in that position throughout the discharge. Figure 1 shows a view of Octant 3 (ϕ = 90°) of JET for the standard locked mode position as calculated by an MHD code [2]. The X point of the m=2, n=1 mode lies in the midplane. This corresponds to having the 45° locked mode signal negative and equal and opposite to the 135° signal. In some cases, especially after the plasma current and toroidal field were reversed for counter injection operation, the mode locks in other locations or changes phase after it has locked, suggesting that if a field asymmetry is responsible, it changes with conditions.

Pre-disruptive Locked Modes Oscillating growing MHD precursors with predominantly m=2, n=1 (or sometimes m=3) are observed before most disruptions. The frequency of oscillation usually lies between 200 Hz and 1 kHz, but increases with NB power to > 5 kHz. The oscillations may last for only a few msec or for as long as 200 msec before the mode locks. When locking occurs, the tangential field amplitude at the wall is 4 - 20 G and the radial field is 0.25 - 1.5 G. After locking, the mode grows to an amplitude of $\tilde{b}_r/B_\theta$(wall) $\sim 0.6 - 1.2 \times 10^{-2}$ just before disruption. The

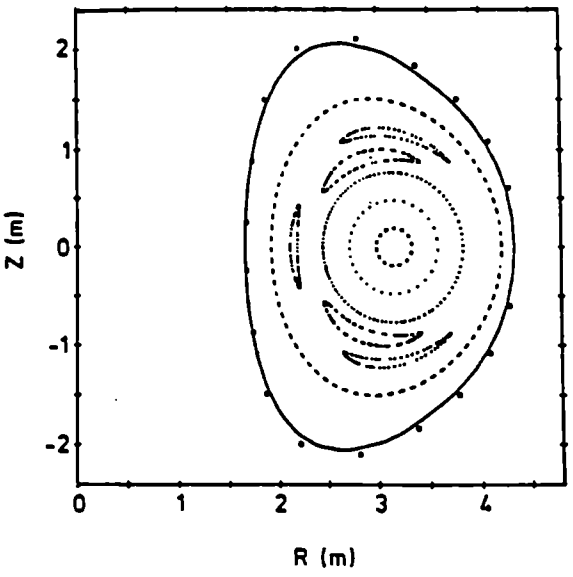

Figure 1. Simulation of locked mode just before disruption ($\tilde{b}_\theta/B_\theta = 1\%$).

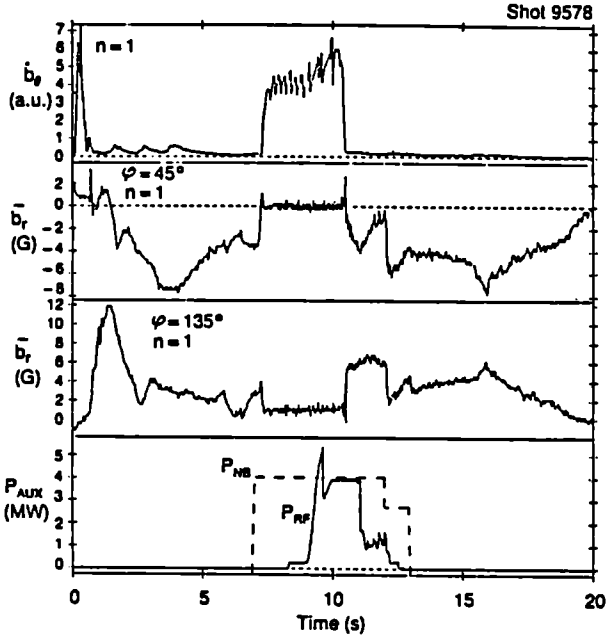

Figure 2. Early locked mode unlocks during NB, then locks again after a sawtooth collapse.

duration of the locked mode phase before disruption is normally about 100 msec, but can be shorter than 10 msec at very low q or longer than 1.5 sec at intermediate or high q. At very low q, the usual precursor oscillations are absent leaving only a rapidly growing n=1 displacement about 20 msec before the disruption.

Current Rise Locked Modes Locked modes often develop during the current rise even as early as 400 msec into the discharge reaching an amplitude of $\tilde{b}_r/B_\theta$ (wall) $\sim 2 - 6 \times 10^{-3}$. Depending on the evolution of $q_\psi(a)$, the locked mode can decay after 0.5 - 2 sec, continue to grow until disruption, or persist throughout the length of the discharge. It is observed that the chance of having a disruption following a current rise locked mode is greatly enhanced when $q_\psi(a)$ lies between 3 and 4. By modifying the evolution of $q_\psi(a)$ through changing the plasma aperture, the current rise rate, the toroidal field, or indirectly through changing the density, current rise locked modes can be reduced in amplitude or even eliminated. Skin current effects may play a role in mode locking during the current rise. Figure 2 shows a locked mode that begins in the current rise, then unlocks with the NB and oscillates for several seconds before it locks again after a sawtooth collapse and remains locked throughout the remainder of the discharge. The top trace is a rectified and smoothed n=1 combination of poloidal field pick-up coils. The second and third signals are the locked mode monitor signals. Poloidal analysis of the mode structure of current rise locked modes indicates that the dominant mode number can be at least as high as m=4, n=1. It is possible that the driving mode is still m=2, n=1 through toroidal mode coupling.

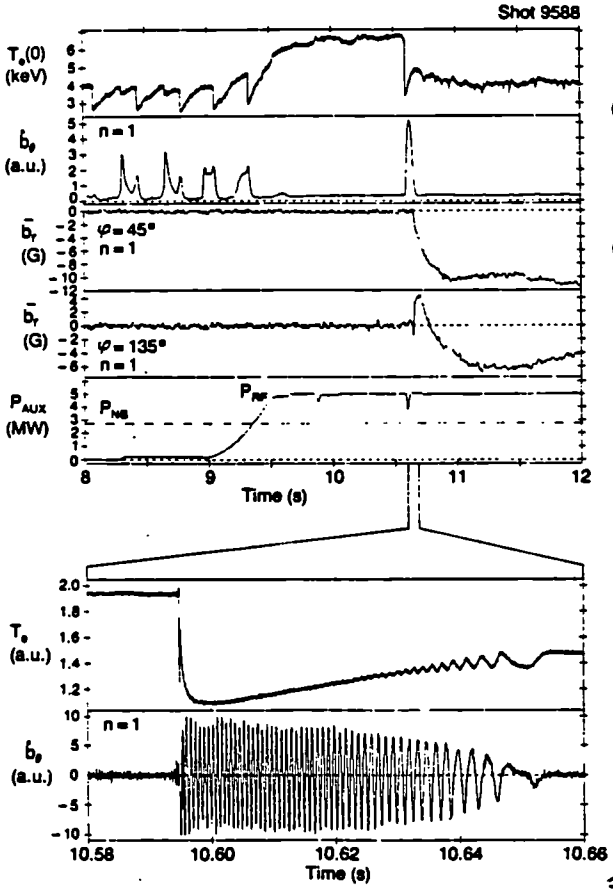

Figure 3. Mode locking occurs after a monster sawtooth during combined ICRH and NB heating. The expanded T_e signal looks just inside the sawtooth inversion radius.

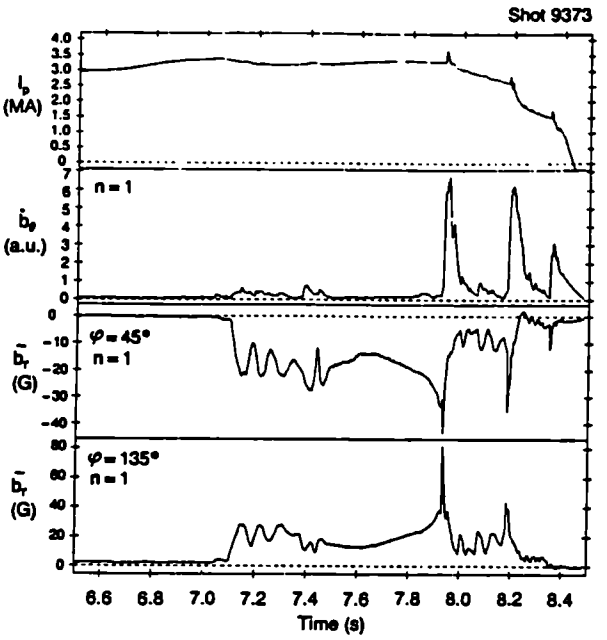

Figure 4. Pellet injection (7.0 sec) induces a locked mode that leads to a disruption.

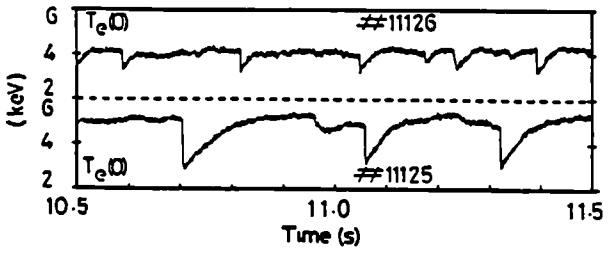

Figure 5. Effects of locked modes on sawteeth. The top trace is during a locked mode, while the bottom trace has no locked mode.

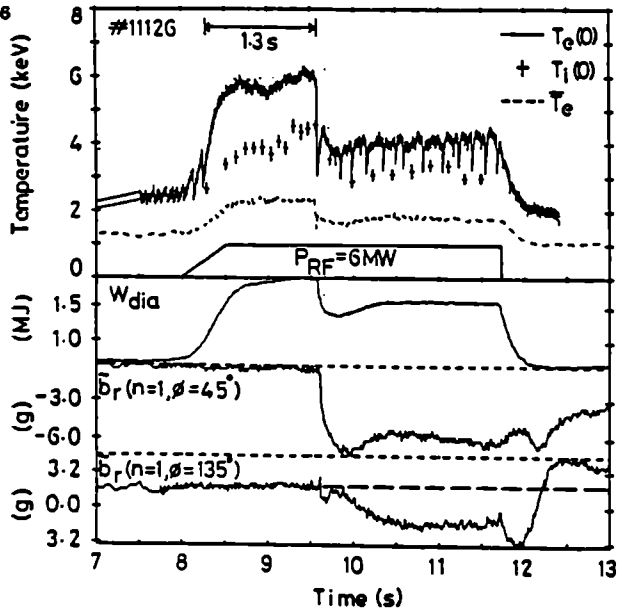

Figure 6. Reduction in diamagnetic stored energy during a locked mode after an ICRH only monster sawtooth.

Locked Modes After Monster Sawteeth Figure 3 shows a locked mode induced by a monster sawtooth collapse during combined ICRH and NB heating. The expanded time traces show the mode locking on both the ECE and n=1 poloidal pick-up coil combination signals. Normally, after a combined heated monster sawtooth there is a large ($\tilde{b}_\theta / B_\theta \sim 7 \times 10^{-4}$) oscillating m=3, n=2 mode that persists for several seconds [1], but when the oscillating mode locks, the m=2, n=1 can be dominant and oscillate for only 60 msec before locking.

Locked Modes After Pellet Injection In many cases, just after the injection of a pellet there arises a large locked mode that can persist for several seconds or result in a disruption. Figure 4 shows such a pellet induced locked mode that eventually leads to a disruption. The pellet was fired at 7.0 sec into the discharge. The density decays much more rapidly if the pellet induces a locked mode, suggesting that such large MHD modes can increase particle losses. The 'snake' oscillations [4] often observed after pellet injection can persist in the presence or absence of oscillating and locked MHD activity observed on the magnetic diagnostics.

Discussion Large MHD modes can have profound effects on the plasma. Figures 3 and 5 show that sawteeth during such large modes are reduced in amplitude by more than a factor of two and saturate much faster. Before density limit disruptions, the electron temperature profile about the q_ψ=2 surface is rapidly flattened over a region of 10-15 cm just after the mode locks [1]. The spatial distribution of the neutral influx due to recycling can also be affected during large MHD modes near the density limit.

A very prominent effect of locked modes is that they can actually stop the observed central plasma ion toroidal rotation despite intense input momentum from the NB [5]. This follows the general trend that the central ion velocity compares well with that calculated from the frequency of edge MHD oscillations. The strong effects on sawteeth and the central plasma rotation suggest that magnetic perturbations measured at the wall can affect the center of the plasma when they reach sufficient amplitude.

In some cases, particularly after monster sawteeth, the onset of a large MHD mode ($\tilde{b}_r/B_\theta \sim 2.4 \times 10^{-3}$) coincides with a 20 - 25% drop in the stored energy (Figure 6). In the previous shot, which was similar but without a locked mode, the temperature reached 5.5 keV at the sawtooth peaks (Figure 5), suggesting that the large MHD mode may have kept the temperature low perhaps by increasing plasma losses.

Since large amplitude MHD modes can affect the plasma momentum, particle balance, and in some cases, appear to affect the energy content their effects need to be better understood and taken into account when these basic plasma properties are analyzed.

References

[1] D J Campbell, et al, Proc 11th Int Conf on Plasma Physics and Contr Nucl Fusion Research, (Kyoto, 1986).
[2] T C Hender, D C Robinson, and J A Snipes, Proc 11th Int Conf on Plasma Physics and Contr Nucl Fusion Research, (Kyoto, 1986).
[3] M F Nave and J A Wesson, this conference.
[4] A Weller, et al, this conference.
[5] D Stork, et al, this conference.

THE EFFECT OF EDGE TEMPERATURE ON IMPURITY PRODUCTION UNDER A RANGE OF OPERATING CONDITIONS IN JET

J A Tagle, S K Erents*, G M McCracken*, R A Pitts*,
P C Stangeby+, C Lowry° and M F Stamp

JET Joint Undertaking, Abingdon, Oxon OX14 3EA, UK
* Culham Laboratory, Abingdon, Oxon OX14 3EA, UK
+ Institute for Aerospace Studies, University of Toronto, Canada
° Imperial College of Science and Technology, London, UK

1. INTRODUCTION

The radial distribution of electron temperature and density in the edge of a Tokamak determines impurity production and transport. The impurity production by sputtering of the limiter and wall material is controlled by the particle fluxes and their energies. The subsequent transport of these impurity atoms back into the main plasma is controlled by the probability of ionization, which is again a function of the edge temperature and density. Finally this data allows one to convert the spectroscopically measured photon output from ionization states of the neutral impurity entering the edge plasma into atomic influx rates[1]. In this paper we show how the electron temperature and density in the scrape-off layer (SOL) of JET for ohmically heated plasmas in D and He^+ scale with plasma currents I_p = 1-5 MA, toroidal field B_T = 2.1-3.5 T and line averaged density $\bar{n}_e$ = 1-4 x 10^{19} m^{-3}. These data are then used to calculate the carbon impurity production by physical sputtering from the limiter.

2. TEMPERATURE AND DENSITY SCALING

The results were obtained using Langmuir probes situated on an ICRH

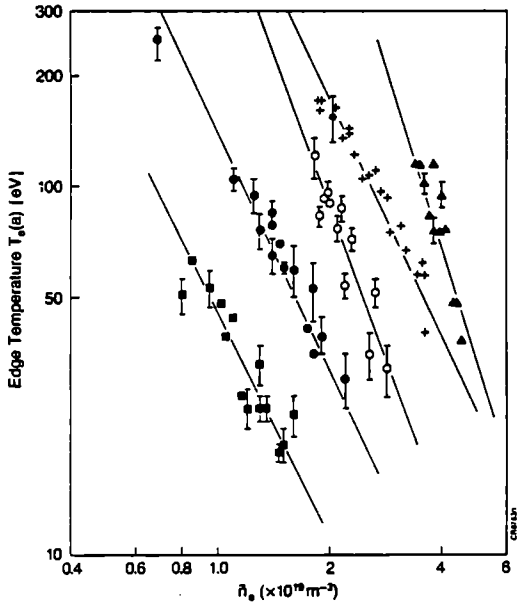

Fig. 1 Effect of line average density $\bar{n}_e$ on temperature T_e at LCFS.

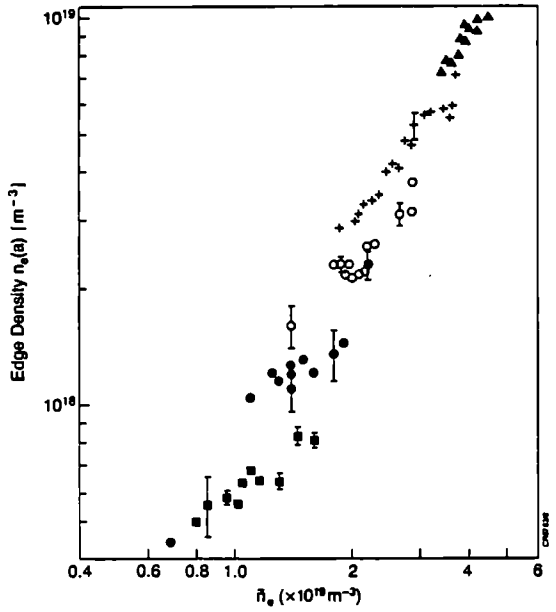

Fig. 2 Effect of $\bar{n}_e$ on density n_e at LCFS.

(■ = 1MA,2.1T; ● = 2MA,2.1T; o = 3MA,3.4T; + = 4MA,3.5T; ▲ = 5MA, 3.5T)

antenna protection tile, close to the torus midplane. Details of the diagnostic were reported elsewhere[2]. Assuming an exponential decay of the edge parameters in the SOL[1], the density and temperature profiles are extrapolated 15 mm to the last close flux surface (LCFS), defined by the carbon limiter. The scalings of edge temperature $T_e(a)$ and density $\bar{n}_e(a)$ with line averaged central density ($\bar{n}_e$) for plasma currents 1 MA - 5 MA are shown in figure 1 and 2. Each data point represents steady state conditions during separate discharges and the parameters measured were averaged over a few seconds before the end of the plasma current flat top. Although the data were collected over several months, all are ohmic, limiter discharges in deuterium with fairly constant loop volts. The fraction of power radiated, (P_{RAD}/P_{OHM}) was ≈ 0.5. $T_e(a)$ falls with increasing $\bar{n}_e$ and increases with increasing input ohmic power ($P_{OHM} \alpha I_p^{0.8}$). The fitted lines in figure 1 gives us an approximate empirical scaling for the complete data set

$$T_e(a) \alpha \{I_p/\bar{n}_e\}^2 \quad (1)$$

For a fixed I_p, the edge density $n_e(a)$ scales almost linearly with central density, $\bar{n}_e$. From figure 2

$$n_e(a) \alpha I_p \bar{n}_e \quad (2)$$

An analytical model which considers particle diffusion and cooling of the edge by impurity sputtering [3,4] predicts that $n_e(a) \alpha \bar{n}_e^2$, and that $T_e(a) \alpha P_{OHM}/\bar{n}_e^2$. However this model assume a constant electron impact ionization rate ($\overline{\sigma v_i}$). In fact, ($\overline{\sigma v_i}$) $\alpha \bar{n}_e^{-1}$ over the temperature range shown in figure 1, hence the linear dependence of $n_e(a)$ on $\bar{n}_e$ is in agreement with the model. An exception to this scaling is the case of the 5 MA data which could be due either to the non-steady state plasma conditions (very short current flat-top) or to the close proximity of the plasma to the inner wall, causing the power to be shared between the outer toroidal limiter and the inner wall tiles.

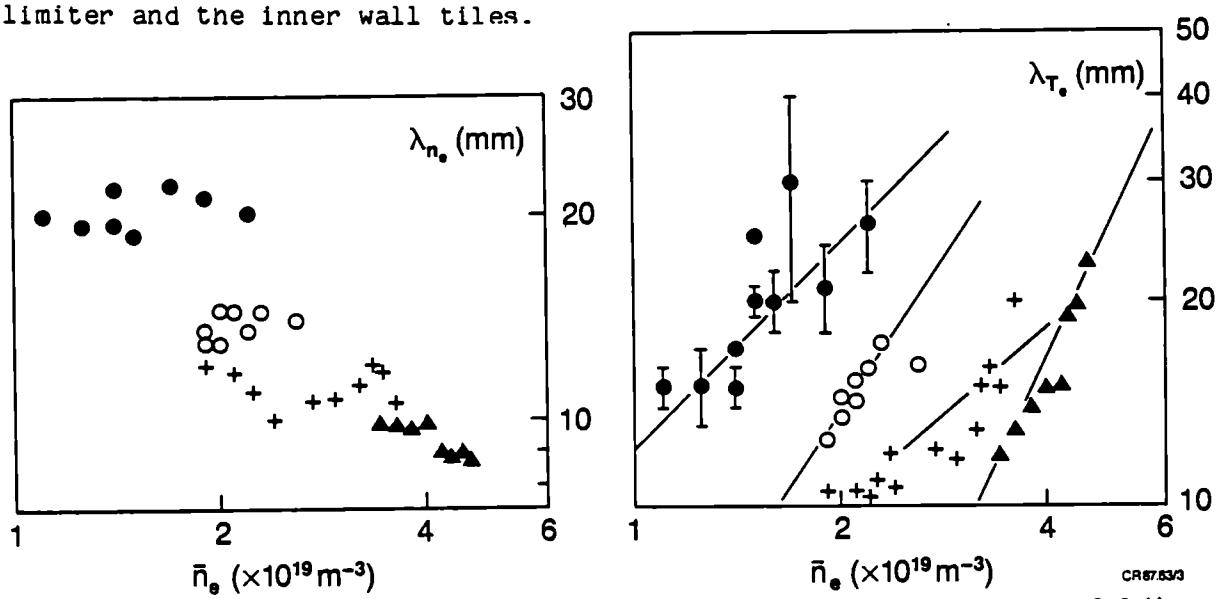

Fig. 3 The effect of $\bar{n}_e$ and I_p on density λ_n and temperature λ_T e-folding length in the SOL.
(● = 2MA,2.1T; o = 3MA,3.4T; + = 4MA,3.4T,▲ = 5MA,3.4T)

3. CHANGES IN THE SOL THICKNESS AND RADIAL DIFFUSION

In figure 3 we present the scaling of SOL thickness for edge temperature and density with $\bar{n}_e$ and I_p. The density e-folding length, λ_n, is practically independent of central density $\bar{n}_e$, but is almost inversely proportional to plasma current for a fixed toroidal field B_T. However, λ_T is rather less well defined due to scatter in the data points, but in general shows an increase with $\bar{n}_e$ and a decrease with I_p. Using the λ_n values and a formulation for the cross-field diffusion coefficient, $D_\perp$, deduced by Stangeby[5] we caluclate $D_\perp$ ($\bar{n}_e$). This is shown in figure 4 (for 2 MA and 3 MA discharges only), and the scaling

$$D_\perp \propto \bar{n}_e^{-1.3} \qquad (3)$$

is found. Since $D_\perp \propto \lambda_n^2 \, T_e(a)^{0.5}$, and λ_n is almost independent of $\bar{n}_e$, it follows that the inverse dependence of $D_\perp$ on $\bar{n}_e$ is largely due to the change of edge temperature with density. In fact we found that $D_\perp \propto T_e(a)^{0.7}/B_T^{1.5}$, although the power law dependence on B_T is only approximate because of a limited data set at different B_T. Nevertheless, it appears that the cross-field diffusion is not very different from Bohm.

4. IMPURITY PRODUCTION

The measured values of the ion flux and temperature have been used to calculate the local physical sputtering rate at the limiter as a function of radius, which after integration over the radial coordinate, gives the total carbon flux. The ion energy was deduced from the sum of the ion thermal energy plus the acceleration across the sheath potential, V_s ie. $E = 2T_e + qV_s$; where q is the charge state. To calculate V_s we use the value of the secondary electron emission coefficient $\bar{\gamma}(E)$ measured on typical limiter samples exposed to the JET plasma[4]. It is then assumed that all sputtered carbon is ionized, (q=4), and available for self-sputtering of the limiter. The total flux of carbon is then

$$\Gamma_c = \Gamma_D Y_D/(1 - Y_c) \qquad (4)$$

where Y_D and Y_c are the deuteron and carbon self-sputtering yields. The results of these calculations are presented in figure 5. The total carbon influx rate decreases with $\bar{n}_e$ for fixed plasma current, and increases with I_p for a constant $\bar{n}_e$. Even though $Y_D(E)$ only falls slightly with decreasing $T_e(a)$ over the energy range of interest (550 > E > 150 eV for D^+ ions), the fall in

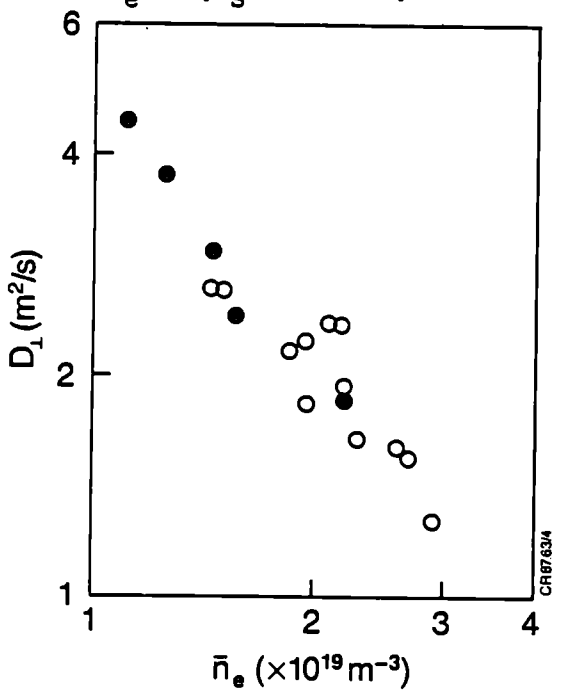

Fig. 4 Effect of $\bar{n}_e$ and I_p on cross field diffusion coefficient. (● = 2MA,2.1T,o = 3MA,3.4T).

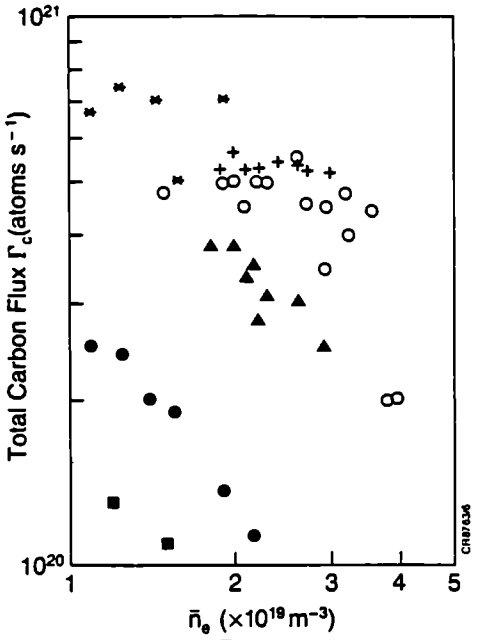

Fig. 5 Effect of $\bar{n}_e$ and I_p on total carbon flux sputtered from the limiter [■ = 1MA,2.1T; ● = 2MA,2.1T; ▲ = 3MA, 3.4T] [o = 2 MA,2.1T in He^4 plasma] [CIII flux (arb units): ✱ = 2MA,D; ✚ = 2MA He]

self-sputtering $Y_c(E)$ is greater (over a higher energy range) and the combination in equation 4 results in the pronounced decrease of Γ_c with $\bar{n}_e$. We include a comparison for similar data for discharges in He^4, (2 MA, 2.1 T) and also with the spectroscopically determined CIII flux. Here $Y_{He^4} = 4\ Y_D$ at a given energy. There is also an increase in the ion energy due to a slightly higher sheath potential and because the helium ion is doubly ionised. The Γ_c calculated is ≈ 4 times higher than in the D case, but remains quite flat for He^4 over the measured $\bar{n}_e$ range. This is due to the self-sputtering yield being almost constant over the He^4 ion energy range. The spectroscopy data are in good agreement for discharges in He^4. However in the case of D discharges the spectroscopically measured Γ_c remains constant with $\bar{n}_e$ and is higher than in He^4 discharge. Our calculations can not take into account the oxygen sputtering of carbon, charge-exchange and the screening of impurities due to ionization in the SOL, which could explain these differences.

CONCLUSIONS

- Empirical laws relating edge parameters and global plasma parameters have been found in JET for ohmically heated limiter discharges. The relations given in equations (1) and (2) determine a lower limit for density and upper limit for temperature ($P_{RAD}/P_{OHM} \to 0$) for a given input power (P_{OHM})
- The empirical laws can be explained by a simple a global power balance model.
- The limiter sputtering and total carbon release rates increase with input power for a given density, and decrease with increasing density. The model predicts that $\Gamma_c \propto T_e(a)^{0.6}$ for D discharges.

REFERENCES

1. S K Erents, J A Tagle, G M McCracken, P C Stangeby and L de Kock, Nuclear Fusion 26 (1986) 1591.
2. J A Tagle, S K Erents, G M McCracken and H Brinkschulte, Workshop on High Temperature Plasma Diagnostics, Varenna, Italy, 3-13 September 1986 (in press).
3. W Engelhardt et al, J Nucl Mater, 111-112 (1982) 337.
4. S K Erents, J A Tagle, G M McCracken, P C Stangeby et al, 'The dependence of tokamak edge conditions on global plasma parameters in JET', to be published.
5. P C Stangeby, J A Tagle, S K Erents and C Lowry (these proceedings).

CARBON EROSION AND DEPOSITION AT THE JET LIMITERS

J P Coad, R Behrisch*, J Roth*, L de Kock, J Ehrenberg**, G Israel, D H J Goodall+, W Wang* and M Wielunski*

JET Joint Undertaking, Abingdon, Oxon OX14 3EA, UK
* Max-Planck Institut für Plasmaphysik, 8046 Garching-bei-München, FRG
+ Culham Laboratory, Abingdon, Oxon OX14 3DB, UK
** on attachment to JET from the Max-Planck Institut für Plasmaphysik

INTRODUCTION

Carbon is the major impurity in the JET plasma, and may limit the ultimate temperatures and densities obtained. To understand the carbon levels observed it is important to assess the production mechanisms at the limiters and walls, and transport in the plasma. This paper describes studies of carbon erosion and deposition at the carbon limiters in JET in 1986, performed by marker experiments. The pattern of erosion from and deposition observed on the limiters represent a starting point for impurity transport calculations and are also important for predictions about erosion in future plasma machines with higher temperatures and larger pulses.

EXPERIMENTAL

Before the 1986 operations a carbon limiter tile was implanted with ^{13}C at 1.4 MeV to a mean depth of ~ 2 μm at a number of points on the surface facing the plasma. The shape of the limiter tile was also accurately measured using a coordinate measuring machine to show up larger changes in dimensions (>a few microns). The limiter tile was placed adjacent to the plasma midplane on the limiter in octant 1D. Altogether there were eight limiters in operation for almost all 3200 discharges of the 1986 campaign, the limiters being effectively 12mm in front of the protection tiles of the three RF antennae.

While the investigation of limiter erosion can only give a global result after many discharges, erosion in one discharge was also investigated with a special limiter probe which was also implanted with ^{13}C, however at 40keV (0.1μm mean depth). The limiter probe was a 50mm diameter cylinder of POCO graphite mounted on one of the manipulators of the Fast Transfer System (FTS) which allows samples to be inserted into the shadow of the limiters just above the outer midplane of the vessel (in Octant 7) (Fig.1a). From this position, the probe has a short connection length on the electron drift side of ~2.5m to a graphite limiter in octant 6D, whilst on its ion-drift side it has a long connection length of either ~25m to the inner wall or ~55m to a limiter, depending on the size of the plasma.

After exposure the limiter tile and the probe were analysed by Secondary Ion Mass Spectroscopy (SIMS) to determine the depth of the ^{13}C marker.

In addition nuclear reaction techniques were used to measure deuterium, and Rutherford Backscattering (RBS) and Proton Induced X-ray Emission (PIXE) were used to determine metallic deposits.

RESULTS AND DISCUSSION

On the limiter tile the ^{13}C marker had disappeared in the central part, while it could still be detected on the edges. On the ion drift side ^{13}C was discovered 22μm beneath the surface, being covered by a deposited layer of ^{12}C containing of the order of 0.5% Ni impurity and several per cent of hydrogen isotopes (5% H, 1% D). On the electron drift side even heavier deposition was observed with some flaking of the deposit: flake thicknesses were about 100μm. This is consistent with the physical measurement of the limiter tile (Fig.2). It shows that over the central region of the tile erosion of over 200μm occurred. Fig.2 includes the results from three scans across the tile, each of which gives a similar profile. Three tiles of another limiter have also been measured yielding similar depths of erosion. Computer calculations of erosion and redeposition on limiter surfaces predict large erosion and redeposition ([1]). However, the net changes appear to be small, so that the 200 μm observed here may only be a small fraction of the total erosion.

The erosion of the limiter tile is the result of about 3200 discharges including many different modes of operation and other events such as glow discharge cleaning and disruptions. In order to determine the erosion and deposition during a well-defined discharge the special probe was exposed using the FTS. The probe was inserted to within 10mm of the last closed surface for two identical 5MA shots with 5 secs flat tops: a section of this limiter probe is shown in Fig. 1b. The surface at all points on the section of the probe marked in Fig. 1b with circles was analysed for D, Ni and Cr by nuclear techniques, and points also marked with squares were profiled with Secondary Ion Mass Spectroscopy (SIMS) to look for the ^{13}C marker, and study the depth distribution of other elements. The probe shows a similar erosion pattern to that at the main limiter. At points furthest from the plasma the marker was present at a depth larger than prior to exposure, while nearer the plasma

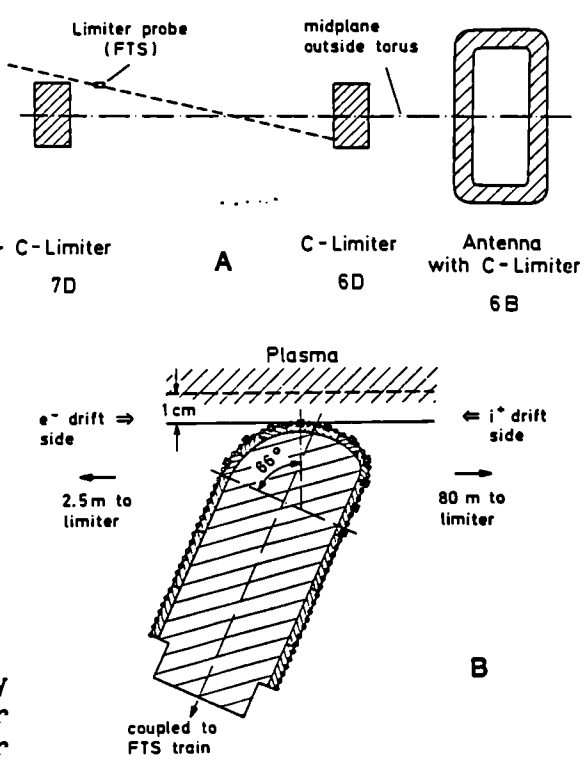

Fig. 1(a) Relative positions of components in the JET vessel.
(b) Geometry of the limiter probe.

the markers could not be detected. However, at the surface tangential to the field lines ^{13}C was detected but in a somewhat modified distribution. Fig.3 shows the results of the nuclear analyses of the probe. For each analysis point the areal elemental concentration is plotted against the distance from the plasma, taking into account the angle between the surface normal and magnetic field lines. Large fluences of deuterium are observed of up to 10^{18} atoms cm^{-2}, disregarding the anomaly at the centre which is due to the angle correction. The Ni and Cr are plasma impurities and on the ion side are in total about 0.5% of the collected deuterium. The amounts collected on the electron-drift side are considerably less, probably due to the shorter connection length. From the large amount of D observed even in the eroded regions it has to be assumed that after erosion, codeposition of carbon and deuterium plus hydrogen occurred in a later phase of the discharge. A trapped D fluence of 8×10^{17} atoms cm^{-2} cannot be due to ion implantation ([2]) at a plasma edge temperature of about 100-200 eV ([3]), but indicates a deposited layer of about 0.2 μm of saturated carbon ([4]).

CONCLUSIONS

The JET limiters show both large amounts of erosion and deposition, according to the proximity to the plasma. Close to the plasma ~ 200 μm have been eroded in 1986, corresponding to about 60 nm (net) per discharge, whilst a few centimetres from the plasma up to 100 μm has been deposited onto the original surface: this is the cumulative result of exposure throughout the 1986 campaign.

The limiter probe was exposed to just two identical 5 MA discharges to show what happens at the limiter on a much shorter timescale. It is found that erosion and deposition patterns are very similar to the main limiters in that erosion of > 0.1 μm occurs near the plasma edge, and deposition occurs a few centimeters away from the edge. However, there is also as much deposition on the surface in the eroded zone as elsewhere: this must occur in a later part of the discharge. It is therefore necessary to investigate this on a smaller time scale, so that one can ascertain within a single discharge when erosion and deposition occur.

Globally, one finds that most of the carbon from the limiters (and from the inner wall) is deposited on the sides of the limiters and on the RF antennae, whilst a relatively thin layer of carbon (with some co-deposited D and H, and a low concentration of metals) covers the vessel walls. This layer was not maintained on the inner half of the vessel in 1985, and carbonisation was found to reduce the metallic impurities in the plasma. However, the thin layer of carbon on the vessel wall in 1986 may simulate an all-carbon wall in JET, explaining the low metal concentrations found in the plasma.

ACKNOWLEDGEMENTS

The authors are indebted to staff at the Chalk River Laboratory, Canada for the high energy ^{13}C implants.

REFERENCES

1. J N Brooks, J Nuclear Materials 111/112 (1982) 457.
2. W R Wampler, D K Brice and C W Magee, J Nuclear Materials 102 (1981).
3. S K Erents, J A Tagle et al, J Nuclear Materials 145-147 (1987) 231.
4. W R Wampler and C W Magee, J Nuclear Materials, 103/104 (1981) 509.
5. J Roth et al, J Nuclear Materials 145-147 (1987) 383.

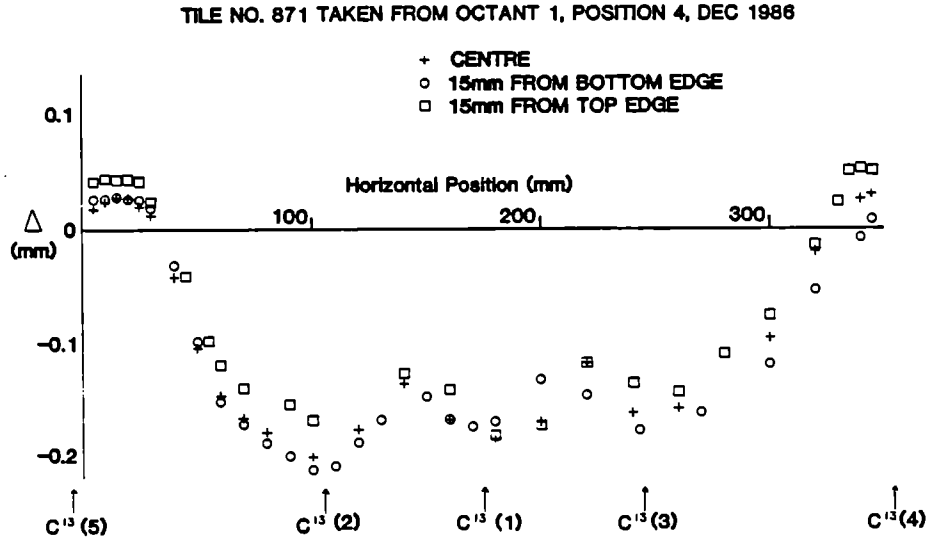

Fig. 2 Topographical changes in a limiter tile after use in 1986.

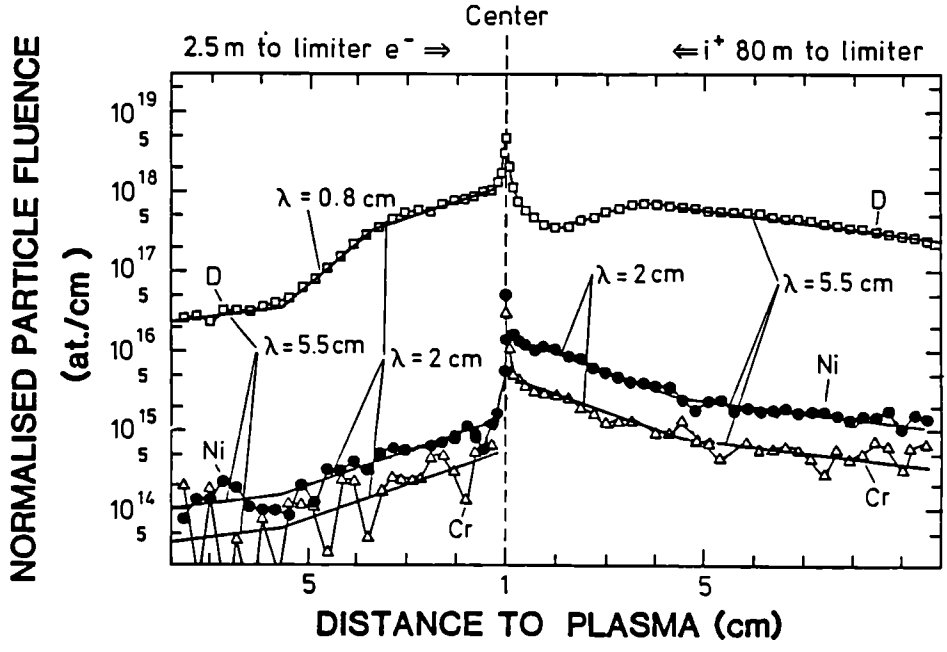

Fig. 3 Nuclear analysis of the limiter probe.

PRELIMINARY MEASUREMENTS OF IMPURITY FLUXES USING TIME RESOLVED COLLECTOR PROBES IN JET

H Bergsaker*, J P Coad, L de Kock, B Emmoth*,
J Hancock, A Stevens and J Vince

JET Joint Undertaking, Abingdon, Oxon OX14 3EA, UK
* Research Institute of Physics, 10405 Stockholm 50, Sweden

1. INTRODUCTION

Two probe systems have been developed to collect impurities in the boundary region during selected tokamak pulses, the Fast Transfer System (FTS) which exposes probes near the outer midplane and the Plasma Boundary Probe System (PBPS) which inserts probes near the top of the vessel. The preliminary results of the first exposures with each of these systems are presented here, and the results are compared with Langmuir probe data obtained from similar shots.

2. EXPERIMENTAL

The PBPS is a vertical shaft mounted on top of the torus in Octant I, the probe entering the vessel at a major radius of 3.25 m, just outside the plasma centre (at 3.15 m). The probes are cylinders (initially of graphite) which can rotate within a carbon shield with two slits, one on the ion drift side and one on the electron drift side of the probe axis. Connection lengths on the electron drift side were about 9 metres, and on the ion drift side were about 60 metres, for the types of pulses considered below.

The first PBPS probe was exposed during shots 9657 to 9661 (inclusive). The shots were 3 MA, 2.8 T pulses, with 10 second flat tops. The plasma was in contact with the limiters during the flat-top, but was pushed onto the inner wall at the start of the rampdown. The probe did not rotate for pulse 9657, but for the others it rotated at constant angular velocity during 8 seconds of the flat top.

The FTS enters the torus horizontally 385 mm above the median plane, and uses the same collector probes as the PBPS. The connection length on the electron-drift side is 2.5 m to a graphite limiter in octant 6D, and on the ion-drift side is typically 55 to 80 metres if the field lines clear the inner wall, or 25 to 35 metres if they do not. The probe was exposed without rotation to eight 3 MA discharges (8927 to 8934), so that deposition only occurred under the two slits, whilst two other probes were exposed to single pulses when the collector was rotated throughout the pulse.

3. RESULTS

The analysis of the deposit in the flat-top region of the PBPS probe as a function of vertical distance from the plasma is shown in Fig. 1. The area analysed was exposed for a total of 2.2 secs(- ½ sec from each of four discharges) approximately half way through the flat top period The observed amounts of deuterium, oxygen and metal (small amounts of the elements Cr, Fe and Ni are not separately resolvable by the technique

used, Rutherford Backscattering Spectroscopy) decrease exponentially with distance into the scrape-off layer (SOL). Careful analysis of the deposits on this probe, the first silicon probe and various shields indicates that the deuterium is not related to the incident deuterium flux, but to the amount of carbon collected. This conclusion is reached from analysis of the thicker deposits, eg. in the two slit images wherein deuterium and oxygen are found to be at a constant level of about 20 and 5% respectively, the remainder being carbon. Thus, the collected amounts of carbon, oxygen and metal impurities are at approximately, 20, 1 and 0.1% of the total ion fluence at a vertical distance of 64 mm from the plasma boundary, the flux being taken from Langmuir probe data measured for these shots. Also on figure 1 are shown as dashed lines similar plots of concentration versus distance from the plasma for the rampdown image. The distributions are much flatter than for the flat top and the amounts of deposit much larger.

The first probe exposed on the FTS was not rotated so gave integrated data from eight similar discharges. It showed much greater amounts of deposition on the ion drift side than on the electron-drift side, so the latter is probably affected by the short connection length. To gain more direct information on the relative amounts of carbon and deuterium collected in the SOL, the second probe exposed on the FTS was made from silicon (the collector) and inconel (the shield). The probe was rotated throughout a single 5 MA pulse(10903) in a step-wise manner, each point being exposed for 1.33 seconds. Figure 2 shows the analyses of deuterium and carbon as a function of distance from the plasma from a part of the collector exposed to the ion-drift direction at the beginning of the flat-top: the amount of deuterium is approximately a constant fraction of the amount of carbon (at 25 to 30%). The metal impurity levels are a similar proportion of the deuterium concentration to that found on carbon probes, but at these low levels could also be influenced by local sputtering from the sides of the inconel shield. On this probe the greatest deuterium and carbon levels were found on areas exposed during the flat-top, the levels falling away from these values in both the ramp-up and ramp-down phases. If the Langmuir probe data recorded much nearer the plasma boundary at the midplane are extrapolated to this distance from the boundary they suggest the ion saturation current is similar to the deposition rate of carbon as deduced from figure 2. Clearly there is an inconsistency here which requires ellucidation.

The last rotating collector probe to be exposed in 1986 was exposed using the FTS to a 2 MA plasma (flat-top from 45 to 55 secs) with 4 MW of auxiliary RF heating from 48 to 51.5 seconds (shot 11149). Carbon and deuterium concentrations found on the collector 66 mm from the plasma boundary as a function of time in the pulse are shown in Figure 3. The area was exposed through the ion-side slit and each point was exposed for 1.33 secs. Prior to rotation during shot 11149 the probe was parked in position in the torus during shots 11143 to 11148 (some of which disrupted). Thus deposits accumulated at the zero positions during these pulses, which accounts for the high apparent levels near 40 and 60 seconds in Fig. 4 (the image points for the ion and electron-side slits, respectively). Although there is some scatter in the data, the carbon level is higher than the deuterium level as usual except during the period of RF heating. During RF heating the deuterium level greatly

increases (by a factor of about 10) and then clearly exceeds the carbon concentration, which only increases marginally. Langmuir probe data ([1]) suggest that closer to the plasma the ion density increases and the ion temperature does not fall off as rapidly as one moves out into the SOL during RF heating. If the Langmuir probe data is extrapolated to 66 mm from the boundary (ie. the distance at which the data of Fig. 3 is taken) then one might expect a greater ion (deuterium) flux and temperatures of ~ 20 eV rather than ~ 5 eV.

4. DISCUSSION

During the flat top phases impurity fluxes decrease radially into the SOL with e-folding lengths of typically 10-20 mm. Differences in folding lengths have been observed between carbon (as inferred from deuterium where necessary) and other impurities (oxygen and metals), and between ion side and electron side. However, not enough measurements have been made to be sure these differences are systematic, and connection length effects have not been evaluated. A clearly different folding length was observed during rampdown (combined with moving to the inner wall) using the PBPS. As two probes exposed using the FTS have not shown such effects during simple rampdowns, it seems reasonable to assume a strong flux of carbon which is almost constant in the region probed (from 60 to 120 mm vertically above the plasma) associated with the move to the inner wall. This may be of relevance to the phenomena of "wall pumping" and will be investigated further.

For all the probes exposed during ohmic heating there is no evidence of implantation of deuterium into the probes. All the deuterium levels observed can be explained by trapping within the associated carbon deposits, for example by co-deposition, and in many cases the deuterium concentrations are too high to have occurred by implantation. The situation during RF heating is totally different, however. The deuterium concentration suddenly increases and exceeds the carbon level while the RF heating is on. The majority of this deuterium must be implanted into the silicon substrate, or else be combined on the surface with some element which is undetected. In order to implant ~ 2.5 x 10^{16} atoms cm^{-2} of deuterium at the fluence of ~ 10^{18} atoms cm^{-2} predicted from Langmuir probe data, an ion temperature of 30-50 eV is required, assuming a Maxwellian distribution, or an ion energy of ~ 180 eV for monoenergetic ions ([2],[3]). During ICRH the predicted average ion temperature is ~ 20 eV at 66 mm from the boundary, so average ion energies of ~ 80 to ~ 120 eV might be expected, allowing for the sheath potential ([4]): this approaches the order of magnitude needed and the energies deep in the boundary may be sufficient to explain the implantation observed.

5. CONCLUSIONS

Four collector probes were exposed using either the PBPS or FTS systems at JET towards the end of the 1986 campaign, of which three gave time-resolved information. As a variety of plasma parameters and conditions were involved, the results merely provide a foretaste of the information that may be gained in more comprehensive studies.

It is already clear that important information can be obtained relating to wall pumping, connection lengths, diffusion and RF heating effects in the SOL.

ACKNOWLEDGEMENTS

The authors are indebted to D Wilson, M Green and K Slavin for software support, the Culham and GEC staff involved in the installation of the FTS, the JET teams which provide technical support and the JET operations team who permitted exposure of the probes. The probes were designed by C Dorn and J Ehrenberg (Max-Planck Institut für Plasmaphysik, 8046 Garching-bei-München, FRG).

REFERENCES

1. S K Erents, J A Tagle et al, J Nuclear Materials, 145-147 (1987) 231.
2. G Staudenmaier et al, J Nuclear Materials 84 (1979) 149.
3. S Cohen and G McCracken, ibid, p157.
4. R Chodura, J Nuclear Materials 111 and 112 (1982) 420.

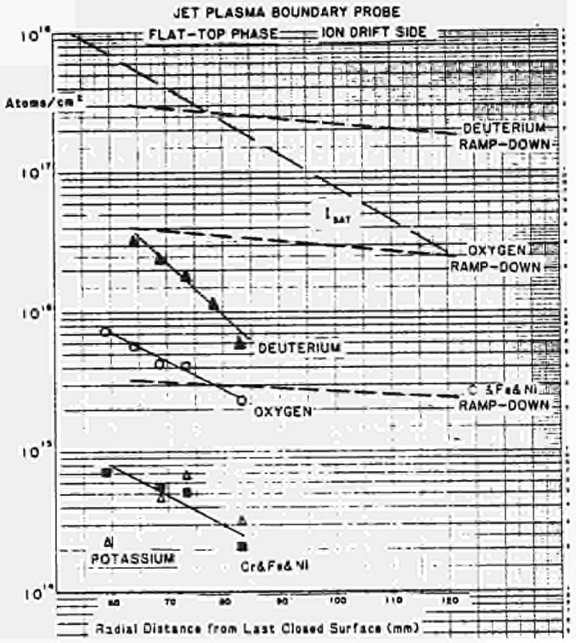

Fig. 1 PBPS probe results.

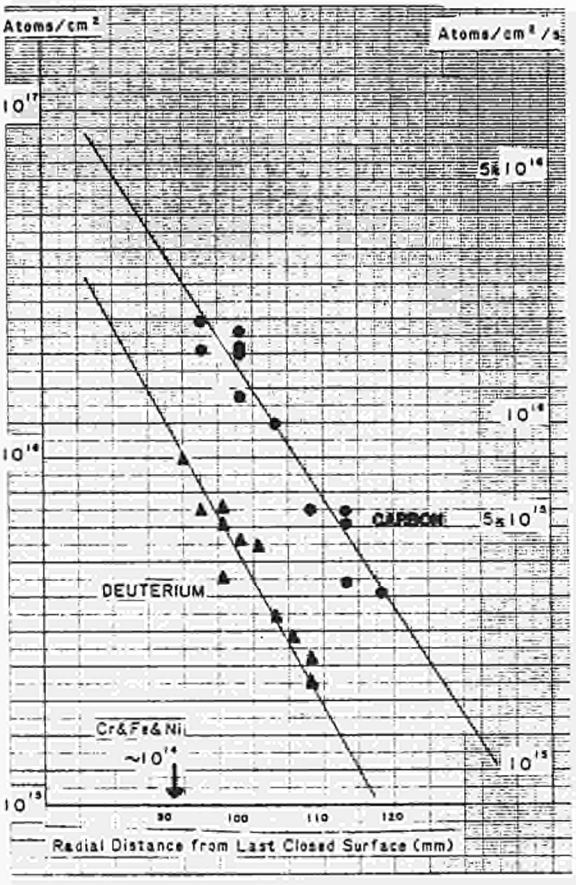

Fig. 2 D and C during a 5 MA flat top.

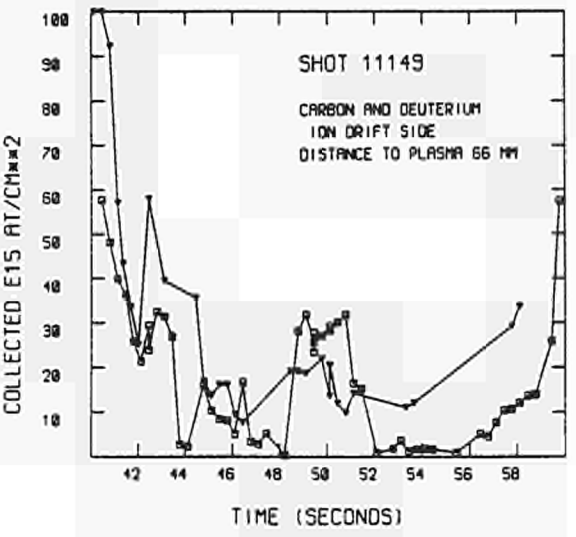

Fig. 3 D and C during an RF heated discharge.

EDGE DYNAMICS IN PELLET-FUELLED INNER-WALL JET DISCHARGES

S.A. Cohen*, J. Ehrenberg**, D.V. Bartlett, D.J. Campbell, A.D. Cheetham, L. de Kock, A. Gondhalekar, N. Gottardi, R. Granetz, W. Houlberg***, H. Jaeckel**, E. Lazzaro, P. Morgan, J. O'Rourke, M. Pick, M.F. Stamp, D.D.R. Summers, E. van der Goot, M. Watkins, and A. Weller**

JET Joint Undertaking, Abingdon, Oxon OX14 3EA, UK
* Visiting scientist, Plasma Physics Laboratory, Princeton University, Princeton, NJ, 08544, USA
** On attachment from Max-Planck-Institut fur Plasmaphysik, 8046 Garching bei Munchen, FRG
*** Oak Ridge National Laboratory, Oak Ridge, TN, 37831, USA

I. Introduction

Pellet fuelling has shown itself to be an effective means for obtaining low Z_{eff} peaked density profiles in ohmic plasmas [1]. Further uses of pellet fuelling may develop when tokamaks enter their DT burning phases. Then the above factors and the correct species mix become crucial for achieving the largest Q value. A necessary corollary for the success of sustained pellet fuelling is good hydrogen removal from the plasma edge. Methods to control the edge exhaust have included various wall conditioning techniques and special limiter or divertor configurations. For any of these approaches to be optimized, an understanding of the basic processes of hydrogen transport in the plasma and in the walls must be developed.

In this paper we report on the density behaviour in JET during pellet-fuelled inner-wall discharges without auxiliary heating. Certain discharges, characterized by minor disruptions at the q=2 surface, show a ten times more rapid decay of the plasma density than previously observed. We show that this is related to the combined effects of plasma and wall properties.

The time evolution of the plasma density is simulated by a 1-d plasma transport code which includes the effects of minor disruptions on both particle transport in the plasma and recycling behavior at the wall. As a starting point for the analysis we use transport coefficients from previous studies of the density profile evolution of neutral-beam and ICRF- heated JET outer-limiter discharges [2]. Several-fold changes in the particle transport and reflection coefficients during the minor disruptions are required to fit the present experiment. The detailed description of hydrogen transport in JET walls and limiters is in a companion paper [3].

II. Experiment

Deuterium pellets (4e21 atoms) were injected into deuterium discharges formed with JET in the inner-wall configuration [1]. The target plasmas had central electron densities and temperatures of 2e19 m^{-3} and 3 keV, respectively. Immediately after injection the plasma parameters were: B_ϕ =2.8T, I_ϕ =3.0-3.5 MA, R_0=3.00 m, a=1.15 m, b=1.61 m, $q_{cyl}(a)$=5.0, $T_e(0)$=1 keV, and $\langle n_e \rangle$=4-5e19 m^{-3}. The distance from the last closed flux surface to the outer limiter was 7 cm. The time evolution of the volume-average electron density (from a 5-chord IR interferometer array) and edge electron temperature (from 2-nd harmonic ECE) are shown in figure 1 for two discharges, 9226 and 9238, which had similar macroscopic plasma

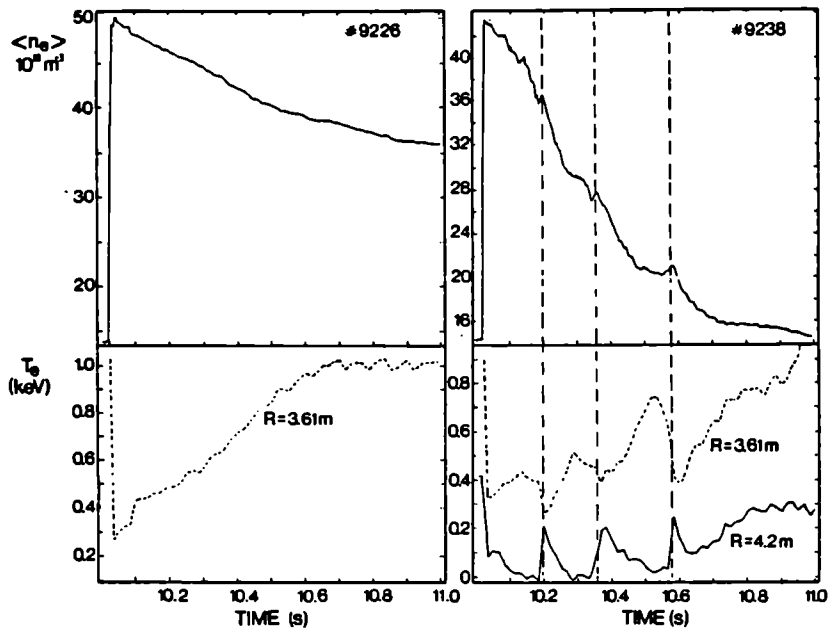

Fig. 1. Time evolution of the volume-average electron density, $<n_e>$, and the electron temperature at R=3.61 and 4.2 m for two discharges, 9226 and 9238. The latter was characterized by minor disruptions at the q=2 radius, R=3.85 m. The high edge temperature for 10.05>t>10.7 s is an artifact, known to be due to 2-nd harmonic overlap in ECE.

parameters. The first discharge is typical of those which did not have minor disruptions. The electron density decays smoothly with about a 2 s e-folding time. The electron temperature falls when the pellet is injected, and recovers slowly, in about 1 s.

In contrast, the density in discharge 9238 decays in a scallop-like manner, with an overall e-folding time of 0.25 s. As ascertained from both ECE and soft x-ray measurements, this discharge undergoes several minor disruptions (at t=10.195, 10.355, and 10.58 s) with phase inversion radii at R=3.85 m. This position is coincident with the location of the q=2 surface calculated from magnetics. The rapid decay of plasma density- at rates up to 3e21 atoms/s- occurs only if the disturbance from the disruption propagates to the inner-wall radius. Within 15 ms after the initiation of each disruption, the edge temperature has risen above 100 eV where it remains for about 50 ms. It is typical that a series of 3-4 such minor disruptions occurs following pellet injection into discharges of this type and that during each disruption $<n_e>$ falls about 0.7e19 m^3. The electron density on axis falls about 15% during the first 15 ms after each disruption. Concurrent with the rise in $T_e(a)$ is a rise in $n_e(r>.8a)$, as shown in fig 2. However, the D-α emission from the inner wall decreases during the disruptive phase, indicating a decrease in deuterium reemission from the inner wall in spite of the expected increase in flux to the wall due to the increases in edge density and temperature.

Other mhd activity occurred in both types of discharges. Sawteeth preceded and followed pellet injection. "Snake" oscillations [4] were also present after the pellet but ended before the disruptions. No precursor

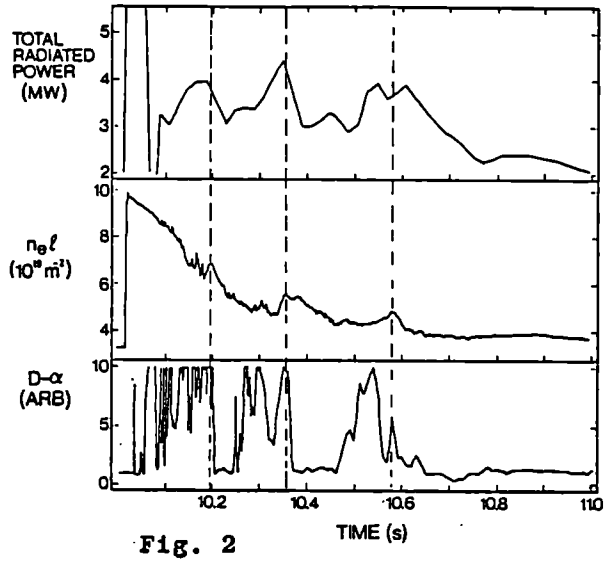

Fig. 2

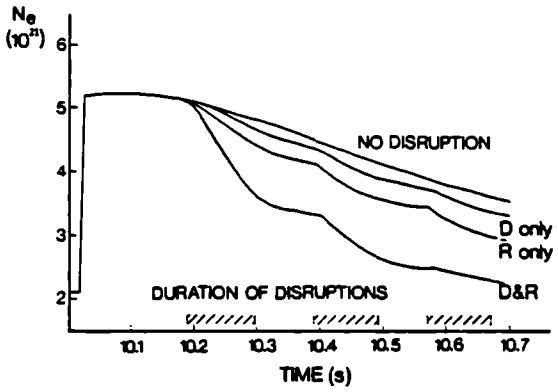

Fig. 3

Fig. 2. Line-integral electron density, $n_e l$, at R=3.75 m, D-α emission from the inner wall, and total radiated power for discharge 9238.
Fig. 3. Calculated time evolution of N_e for four cases: no disruptions; particle reflection,r, changed from 0.85 to 0.07 for 100 ms during the three disruptions; D changed a factor of 3 for 100 ms during the three disruptions ; and changing both r and D during the disruptions.

oscillations to the disruptions were observed, though minor sawteeth at q=1 immediately preceded many.

III. Modelling Plasma Behaviour

Previous studies of density evolution in JET showed the need for both diffusive and convective terms in the particle transport equation. The diffusion coefficient varied with radius from 0.3 m^2/s on axis to 1.0 m^2/s at the edge, and the convective term (inward) increased from 0 m/s on axis to 0.6 m/s at the edge. These combine to give a calculated global confinement time of about τ_p=0.35 s. The confinement of pellet-fuelled particles is 50% longer due to their (calculated) deposition near the plasma core. The apparent confinement time, $\tau_p^* = \tau_p/(1-R)$, due to the finite reycycling, R, is about 2 s, giving R=0.82. The observed rapid decay of density in the plasma core during the minor disruptions shows the need to increase the transport rate of particles out of the plasma. As noted earlier, the drop in D-α emission shows that the recycling (which includes direct particle reflection) drops. In all the models we have tried, agreement with the experiment is only obtained when R drops to $\leq$0.15.

We have considered two classes of models for particle transport by the disruptions. The first assumes an instantaneous rearrangement of the density. For this class we achieve reasonable agreement between the calculated and measured volume-average densities if either of two rearranged density profiles are used: a 15% drop on axis with those particles placed outside the q=2 surface; or a flattening of the density profile for $\pm$30 cm around the q=2 surface. However neither of these

satisfies the observed 15 ms decay time of density on axis. The second class of models (fig 3) involves the increase of outward transport for about 100 ms after the disruption. To obtain good agreement with the density decay, either the diffusion coefficient, D, must be raised about a factor of three across the entire plasma cross-section or the convection must be made outward.

IV. Discussion

The reduction in particle recycling at the inner wall is a necessary, but not sufficient, condition to explain the experimental observations of both the decrease in D-α light and the decay of density. Without the drop in R any increased transport to the wall would result in increased D-α emission. The cause of the reduced R could be the increased energy of the impacting deuterium ions due to the increased sheath potential ($\simeq 4.2T_e$) associated with the increased electron temperature at the edge. It is known from beam-solid studies [5] that the reflection coefficient of D on carbon does drop from about .7 to .1 as the ion energy increases from 20 eV to 500 eV. These energetic ions are then implanted about 10 nm into the carbon tiles of the inner wall. If the carbon there is sufficiently cool (T<400 C) the implanted deuterium will remain trapped until its concentration exceeds 0.1-0.4 of the carbon density. If the temperature of the carbon is slightly higher then it may serve as a temporary reservoir only [3], releasing the implanted deuterium at a rate determined by the diffusion of D in carbon.

Minor disruptions occur in JET in a variety of configurations including outer limiter discharges. In that case no drop in density is observed and the D-α emission is seen to rise. We speculate that the cause for this difference is the limiter temperature which is measured to be > 700 C. In contrast the temperature of the inner wall is < 350 C.

Theories of minor disruptions, under development [6], have magnetic reconnection only within the islands located at the q=2 surface. The islands are thought to be only a few cm in width. Hence these theories offer no explanation for the particle loss from the plasma core.

Discharges with minor disruptions do not have particularly good energy confinement. It thus does not appear desirable to provoke minor disruptions as a way to enhance pumping. However, the apparent connection between high sheath potentials and better wall pumping does suggest that edge plasma heating, or alternatively negative biasing of large area limiters, may provide a suitable solution, at least in the short term, to the problem of hydrogen exhaust at the plasma edge.

V. References

1. A. Gondhalekar, A. Cheetham, M. Bures, et al., Proc. 11-th Int. Conf. on Plasma Physics and Contr. Fusion, Kyoto, 1986.
2. A. Cheetham, J.P. Christiansen, S. Corti, et al., Proc. 13-th Eur. Conf. on Contr. Fusion and Plasma Physics, Schliersee, V.1, (1986) 420.
3. J. Ehrenberg, S.A. Cohen, L. de Kock, et al., this conference.
4. A. Weller, A.D. Cheetham, A.W. Edwards, et al., this conference.
5. G.M. McCracken and P.E. Stott, Nucl. Fusion 19 (1979) 889.
6. J. Wesson, private communication.

Power Balance in the Bulk Plasma and in the Scrape-off Layer during H and L Mode Divertor Discharges in JET

H J Jaeckel[a], P J Harbour, N Gottardi,
E B Deksnis, P D Morgan, D D R Summers, J A Tagle
JET Joint Undertaking, Abingdon, Oxon OX14 3EA, United Kingdom
[a] *Permanent address : EURATOM-IPP Association, Garching, W. Germany*

Introduction – In JET a magnetic separatrix can be formed inside the vacuum vessel at plasma currents up to 3 MA with one ("single null", SN) or two ("double null", DN) stagnation points ("X-point") [1,2]. In SN discharges a transition from L- to H-mode has often been observed with neutral beam (NB) heating in the range 5–10 MW. A significant fraction of the total radiation power loss is dissipated from the the X-point region(s). Using bolometer measurements an attempt is made to estimate the power radiated from the confinement region and the divertor region(s). The radial emissivity profiles of the confined plasma show broad radiation shells during the H-mode. The poloidal distribution of the radiation flux near the X-point is compared with the poloidal distribution of the D_α emission. The power flow to the divertor target tiles is estimated using infrared thermography. The occurence of the H-mode appears to be related to the heating of the plasma edge.

Experimental Setup: The relationship between the JET X-point null, the divertor target tiles and the relevant diagnostics is shown in Fig. 1 in plan view. The eight sets of carbon target tiles were installed as protective tiles for the octant joints.

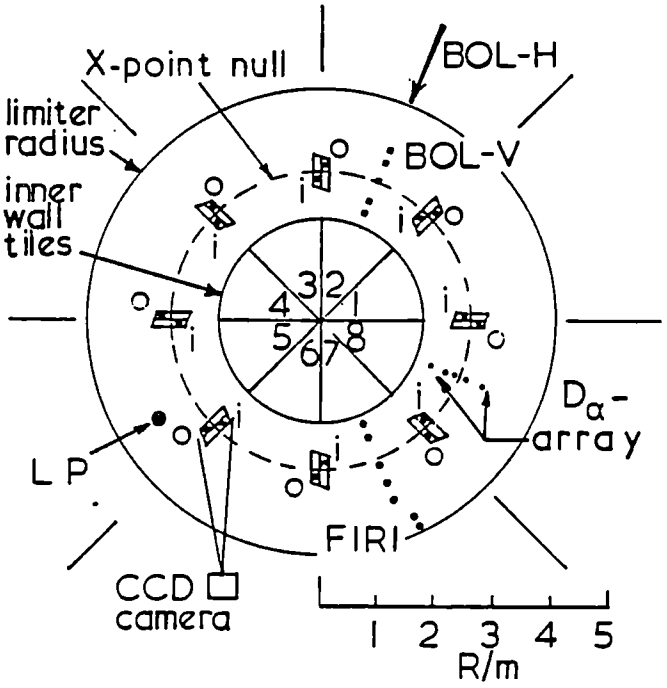

Fig. 1 : Schematic plan-view of the JET vacuum vessel showing the relationship of the diagnostics to the eight sets of divertor target tiles. The scrape-off layer impinges at a glancing angle of 9.5 ° on an outer (o) and an inner (i) location of each set. The horizontal (BOL-H) and vertical (BOL-V) bolometer cameras, the D_α array, the far infrared interferometer (FIRI) and the moveable Langmuir probe (LP) are all located in mid-octant as shown. The CCD camera, mounted midplane, views directly the top target tiles on octant joint 5/6.

The total radiation power is measured by two bolometer camera systems, located in mid-octant, one horizontal the other vertical [3]. Camera chords looking into the X-point regions at the top and/or the bottom of the plasma show enhanced radiation. The detection range of the bolometers is $3 \leq E_{ph}[eV] \leq 9000$, so that all radiation which might contribute substantially to the total power loss is detected. By choosing channels not affected by the X-point radiation and assuming toroidal symmetry one can estimate the radiation P_{rad}^{bulk} from

the bulk plasma (confinement region). The radiation from the X-point region P_{rad}^{xp} is defined as $P_{rad}^{xp} = P_{rad}^{tot} - P_{rad}^{bulk}$. Fig 2 shows P_{rad}^{bulk}, P_{rad}^{tot} and P_{rad}^{xp} for a discharge with H-mode.

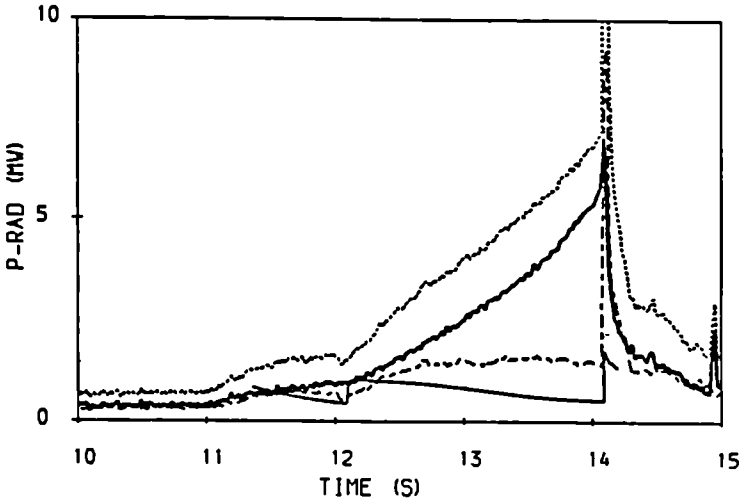

Fig. 2 : Radiation power P_{rad}^{bulk} (bold solid curve), P_{rad}^{xp} (dash-dotted) and P_{rad}^{tot} (dotted) for a SN-discharge with H-mode from 12 to 14.1 s (JET pulse 10755). Also shown is the power flow to the outer divertor target P_t^{outer} (thin solid curve).

One set of target tiles is viewed directly with an infrared CCD camera (Fig.1), filtered to be sensitive from 0.98 – 1.02 μm. For many pulses the camera had insufficient dynamic range to measure the surface temperature of the tiles ($\leq 1800\ ^\circ C$) throughout the pulse. However it has been possible to estimate both the power flux to the outer (electron side) tiles P_t^{outer} (Fig. 2), and the area of the SOL. The power to the inner (ion side) tiles P_t^{inner} was difficult to estimate but it was $\leq P_t^{outer}/2$ in all H-mode discharges.

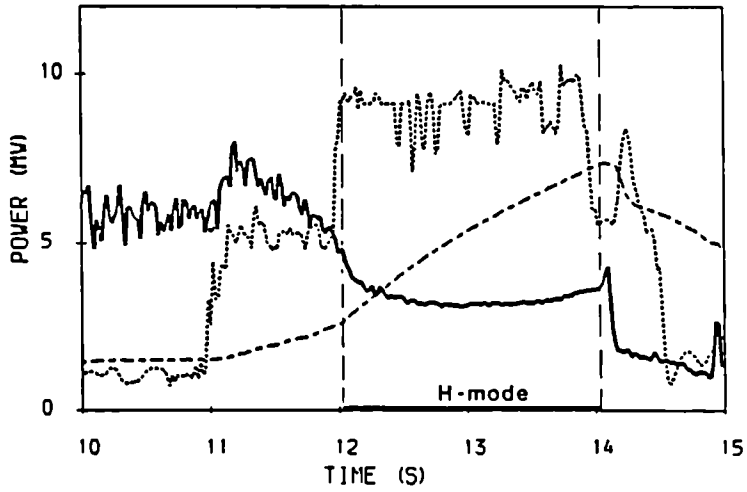

Fig. 3 : Evolution of $P_{rad}^{bulk}/<n_e>^2$ (solid curve; arb.units) during the L-mode and H-mode for a NB-heated discharge. The volume averaged density $<n_e>$ (dash-dotted; $6\times10^{19}\ m^{-3}$ full scale) steadily increases during the H-mode. The dotted curve shows the evolution of the total input power, P_{heat}^{tot} (JET pulse 10755).

Bulk Radiation Loss: During the L-mode P_{rad}^{bulk} and P_{rad}^{xp} are nearly equal (Fig. 2). The bulk radiation power is about linearly proportional to the volume averaged density up to $<n_e> \leq 1.5\times10^{19}\ m^{-3}$, achieved in the L-mode. During the H-mode when $<n_e>$ increases steadily up to $\leq 4\times10^{19}\ m^{-3}$ a strong increase in P_{rad}^{bulk} is observed, roughly proportional to $<n_e>^2$ in pure NB heated discharges (Fig. 3). Disregarding changes in temperature and in profiles of density and of impurities this implies constant impurity concentration. In the few cases when the H-mode was sustained for some time with the addition of slight RF-heating ($P_{ICRH} \leq 2\ MW$) a more rapid increase of P_{rad}^{bulk} with $<n_e>$ was observed.

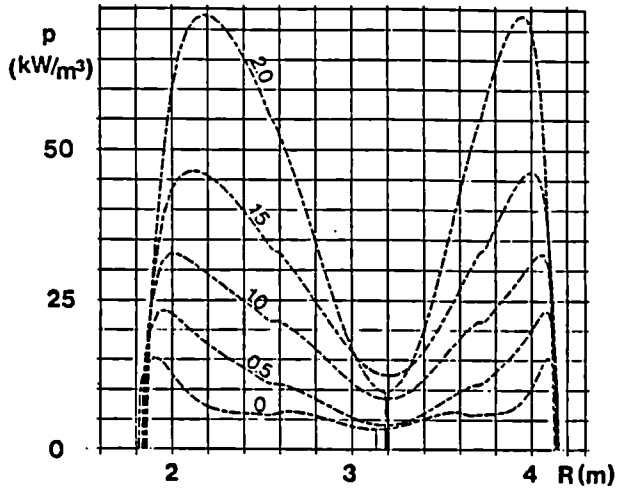

Fig. 4 : Evolution of the radial emissivity profile during the H-mode. Although the main impurity species are carbon and oxygen, very broad radiation shells are observed. The number at each curve gives the time of the profile with respect to the start of the H-mode. Curve 0 shows the profile during the preceding L-mode (JET pulse 10755).

The dominant impurities in purely NB heated discharges are carbon and oxygen; metals are negligible [4]. Radial emissivity profiles derived from the bolometer measurements show a radiation shell much broader than predicted by coronal equilibrium. Furthermore the width of the radiating shell broadens during the H-mode although the plasma density in the outer region grows faster than in the centre. This behaviour is not understood at present. Fig. 4 shows the evolution of radiation emissivity profiles during one of the longest H-modes ($\sim 2.1\ s$) achieved so far in JET.

Power Flow and Radiation in the Scrape-off Layer: The power conducted into the SOL (the heating power of the SOL) is given by

$$P_{heat}^{SOL} = P_{heat}^{tot} - dW_p/dt - P_{rad}^{bulk} - P_{cx}^{bulk} .$$

The charge exchange losses P_{cx}^{bulk} are not measured and are neglected thus overestimating P_{heat}^{SOL} which is typically 40 to 60 % of P_{heat}^{tot} and does not vary significantly during the H-mode. The power loss from the SOL is given by

$$P_{loss}^{SOL} = P_{rad}^{xp} + P_t^{inner} + P_t^{outer} + P_{cx}^{SOL} + P_{cx}^{xp} + P^{lim} .$$

An upper bound for the charge exchange loss may be estimated, using the measured D_α-influx from the walls ($\leq 10^{22}\ s^{-1}$), to be $P_{cx}^{SOL} \leq 0.3\ MW$; P_{cx}^{xp} is estimated to be smaller. Using data from the Langmuir probes the power conducted to the limiters and wall, P^{lim}, is negligible. The largest power losses measured from the SOL are by radiation and conduction to the target tiles, and these are maintained during the H-mode, in contrast to observation in ASDEX [6]. At the onset of the H-mode in JET, P_{rad}^{xp} usually decreases suddenly and then increases with $<n_e>$ until it reaches $\sim$ 15% of P_{heat}^{tot} and then becomes stationary, although both $<n_e>$ and P_{rad}^{bulk} grow steadily. In contrast P_t^{outer} appears to show an increase to about 15% of P_{heat}^{tot} at the onset of the H-mode and then decreases to $\sim$10% before termination. Immediately after the H-mode is terminated, there is a remarkable increase in P_{rad}^{xp}, P_t^{outer} and P_{heat}^{SOL} (Fig. 2) for $\leq$ 40 ms. The poloidal distribution of P_{rad}^{xp} shows a maximum at the inner wall side of the X-point in its immediate vicinity (Fig.5). This distribution deviates appreciably from the D_α distribution [5] indicating that Lyman-α emission (to which the bolometers are still sensitive) only partially accounts for the observed emissivity. With carbon target tiles, C is expected to be mainly responsible for the radiation loss in the divertor region. The observed maximum mean emissivities lie between 1 and 5 $MW\ m^{-3}$. An estimate on the basis of coronal equilibrium gives the lower limit of the possible carbon

concentration, showing that it must be at least 5 to 10% at (assumed) local densities of $5\times10^{19}\ m^{-3}$ to account for the observed radiation levels, assuming a SOL thickness of about 2 cm at the maximum of P_{rad}^{xp}. However the local poloidal resolution of the bolometers ($\sim 0.4\ m$) may lead to a flattening of the poloidal profile. With a steeper profile the peak emissivity may be larger, suggesting local densities $\leq 10^{20}\ m^{-3}$ at the target tiles. This is consistent with the observed power flux ($\leq 1\ kW\ cm^{-2}$)to the outer tiles if $T_e \leq 10\ eV$ locally. The fast poloidal decay of the X-point radiation indicates high gradients of T_e and n_e, as have been observed in other tokamaks [6,7]. These high gradients would be more probable with the higher value of n_e ($10^{20} m^{-3}$). It is worth noting that in the inner divertor region, where P_{rad}^{xp} and D_α radiation are high and so the flux of recycling atoms must be high, P_t^{inner} is low. The opposite is true in the outer divertor region where the recycling flux must be lower.

Triggering and Termination of the H-mode: There is experimental evidence that the H-mode is triggered by increasing the heating power conducted into the plasma edge, and that this can be achieved by increasing the power input, or possibly by the decay of a sawtooth, or alternatively by decreasing the edge radiation loss by reducing local impurity sources. At present it is not quite clear if an increase of P_{heat}^{SOL} triggers the L/H-transition. In many cases an increase of P_{heat}^{SOL} preceded an H-mode but there were also cases observed where the H-mode was achieved at constant P_{heat}^{SOL}. Apart from those cases where the additional heating power was switched off the termination of the H-mode always occured when $P_{rad}^{bulk}/P_{heat}^{tot}$ reached about 60%.

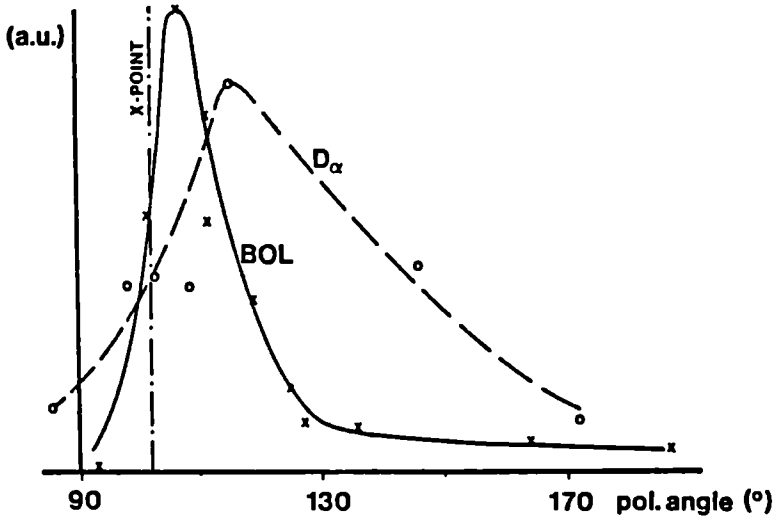

Fig. 5 : Poloidal distribution of P_{rad}^{xp} and of the D_α radiation in the X-point region. The graph covers the upper half of the plasma cross section for a SN discharge (JET pulse 10755) during the H-mode ($\theta = 0$ at the outer midplane).

References

[1] A Tanga et al., Proc. 12th European Conf. on Contr. Fus. and Plasma Phys., Vol I P 267, Budapest 1985

[2] A Tanga et al., Proc. 11th Int. Conf. on Plasma Phys. and Contr. Nucl. Fus. Res., Kyoto, IAEA-CN-47/I-6, (1986)

[3] K F Mast and H Krause, Rev. Sci. Instr. 56(5)(1985)969

[4] B Denne et al., this conference

[5] P D Morgan et al., this conference

[6] F Wagner, M Keilhacker et al., J. Nucl. Mat. 121(1984)103

[7] S Sengoku et al., Nucl. Fusion 24(1984)415

DENSITY AND TEMPERATURE CHANGES IN THE JET EDGE PLASMA DUE TO NEUTRAL BEAM INJECTION

S K Erents,* J A Tagle, and G M McCracken*

JET Joint Undertaking, Abingdon, Oxon OX14 3EA, UK
* Culham Laboratory, Abingdon, Oxon OX14 3DB, UK
(Euratom/UKAEA Fusion Association)

1. Introduction

A knowledge of the scaling of edge parameters with neutral beam power is important for predicting the plasma behaviour as the beam power is increased.
In ohmically heated discharges in JET it has been found that the edge temperature and density vary in a predictable way with the line average density and the input power[1,2]. In this paper the effects of neutral beam heating on the edge parameters has been investigated. The edge temperature and density have been measured over a wide range of conditions using the Langmuir probes in the scrape-off layer (SOL). The temperature and density profiles are normally exponential falling with e-folding lengths of between 5 and 50 mm. From these measurements estimates have been made of the total carbon sputtering yield from the limiters. Scaling of the impurity production to higher beam powers is discussed.

2. Experiment

The mode of operation of the Langmuir probes in JET to obtain ion current density ($I_s(r)$), and electron temperature ($T_e(r)$) is described in previous publications. From these measurements the electron density ($N_e(r)$) is obtained.
Data are taken from an extensive neutral beam heating campaign in which various NBI powers were injected into 1-5 MA reference plasmas. Measurements were made as close to steady state as possible, during the plasma current flat-top just before NBI, and one second into NBI when the temperature is near to a maximum (for 2 MA discharges) and the internal energy is no longer changing, ($\dot{W} = 0$). However, the mean plasma density and the radiated power is still changing rapidly at this time, so a true steady state has not been reached.

3. Results

Results for average plasma density (n_e), ion current density (I_s) and temperature (T_e) at the first Langmuir probe position are plotted as a function of time in figure 1. The edge density 15 mm behind the LCFS (last closed flux surface) calculated from I_s and T_e, is also shown. A NBI power level of 5.3 MW is injected at 9 seconds during the plasma current (2 MA) flat-top. This figure illustrates the type of result which is obtained for a high NBI power injected into a low ohmic power (1.2 MW) discharge. The edge temperature, which before injection is falling due to a slowly rising density, increases immediately after injection with a time constant of ~ 0.3 to 0.5 seconds, then falls again as the edge density continues to rise. Very little increase in T_e is observed when the ohmic and NBI power are of a

similar level; indeed one second after NBI, T_e is often lower than that during the ohmic phase of the discharge.
Data extrapolated to the LCFS is plotted as a function of total power input (ohmic + NBI) in figure 2, for plasma currents of 2 MA and 4 MA. The mean plasma density, which rises due to particle fuelling by the beams, is also shown. The edge temperature data is more scattered at the higher plasma currents (4 MA), but has clearly fallen below its ohmic value one second after NBI switch on, for the higher NBI power levels. Both particle flux and edge density continue to rise with increasing total input power.
The effect of neutral beam heating on the edge profiles is presented in figure 3. The e-folding length of both density (λ_n) and temperature (λ_T) remain almost constant as the NBI power is increased for a given plasma current. This is in contrast to both ohmic heating [2] and ICRH [4]. In ohmic heating as the plasma current is increased the profiles become progressively steeper i.e. λ_n decreases. For ICRH the profiles become flatter as the heating power is increased.

4. Discussion

The slow increase in edge parameters at NBI switch-on, ($\tau \approx 0.3$ to 0.5 seconds, figure 1), demonstrates that the disturbance is due to particles diffusing from the core plasma rather than a directly induced edge effect as observed with ICRH, (4).

The edge temperature increases, but then quickly falls again as the edge density rises. The rise is due to the instantaneous power input at constant density. There are two possible explanations for the falling edge temperature. The first is that as the plasma density rises due to beam fuelling, the particle flux and edge density (via re-cycling) rise. As the particle flux to the limiter rises the average energy per particle, and the edge temperature, decrease. The second explanation is that when the edge temperature rises for a given flux the number of impurity atoms sputtered from the limiters increases. This initial increase is mainly due to carbon self-sputtering - the sputtering yield due to deuterons is almost constant for ion energies corresponding to the T_e range shown in figure 2. The impurity density then increases, and so even at constant density the total radiation increases. This feed back mechanism results in less power being conducted to the edge and so the temperature reaches a new equilibrium.
Both these processes are likely to occur when the neutral beam heating is turned on: An analytical model of these processes has been proposed, [2] and an approximate expression is derived that

$$T_e(a) \propto \frac{P_{TOT}}{\langle n_e \rangle^2}$$

Where P_{TOT} is the total power input. This is in reasonable agreement with the neutral beam heating results.
Both particle flux and density show an increase with total power input, (figure 2), and each show an almost linear increase with plasma current.

The total power conducted to the edge, P_c is given by

$$P_c = (P_\Omega + P_{NBI} - P_{RAD}) = \int_{r=a}^{r=wall} L_w \cdot \gamma_s \cdot I_s \ (a) . e^{-r/\lambda_I} . T_e(a) \ e^{-r/\lambda_T} . dr \quad (1)$$

where a is the radius of the LCFS, γ_s is the sheath energy transmission factor and L_w is the wetted height of the limiters.
The power conducted to the limiters has been calculated using the experimental density and temperature profiles. It has been found that $P_c + P_R$ is directly proportional to P_{TOT} and that the data is in good agreement with the data for ohmically heated discharges, (2).
The total impurity production rate resulting from physical sputtering of the limiters has been calculated using the measured particle flux and temperature profiles. It was assumed that the deuterium energy was the sum of the thermal energy plus that resulting from acceleration in the sheath potential. Physical sputtering only was assumed since no evidence of chemical sputtering has been observed in JET, (5). The results are shown as a function of NBI power in figure 4. Both deuteron sputtering and carbon self sputtering have been included assuming that all carbon atoms enter the plasma and return in an average charge state 4. It is seen that the carbon impurity influx increases roughly linearly with total power input. This increase is predominantly due to the increase in edge density.

5. Conclusion

Measurements of the edge parameters have been made over a range of neutral beam heating powers and a range of plasma operating conditions. A reasonable energy balance between the heating power and the power radiated and convected to the limiters has been established. Initially when neutral beam heating is turned on the edge temperature rises but it quickly falls again as the plasma mean density and edge density rise. A notable feature of the edge condition during NBI is that the edge profiles do not change significantly. This is in contrast to the situation during ohmic heating and ICRH.
From the measured edge profiles calculations of the flux of carbon sputtered from the limiter have been made. The impurity flux increases approximately linearly with the neutral beam power. This is expected to lead to a less than linear increase in the impurity density due to increased screening of the impurity flux at higher plasma densities.

References

1. J.A. Tagle, S.K. Erents, G.M. McCracken, R. Pitts, P.C. Stangeby, C. Lowry and M.F. Stamp. These proceedings.
2. S.K. Erents, J.A. Tagle, G.M. McCracken, P.C. Stangeby, et al, 'The dependence of Tokamak edge conditions on global plasma parameters in JET', to be published.
3. S.K. Erents, J.A. Tagle, G.M. McCracken, P.C. Stangeby and L. De Kock. Nuclear Fusion 26 no 12 (1986) 1591-1603.
4. H. Brinkschulte, J.A. Tagle, M. Bures, S.K. Erents, P.J. Harbour, T. Huld, A.S. Kaye, C. Lowry and G.M. McCracken. Proc. 13. Eur. Conf. on Controlled Fusion and Plasma heating, Schliersee, April 14-18 1986.
5. M.F. Stamp et al, J. Nucl. Mat. 145/147(1987) 236-240.

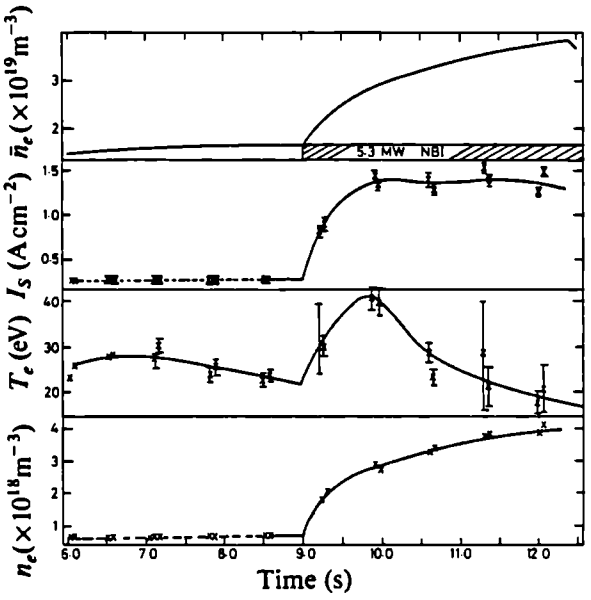

Fig.1 Time dependence of edge parameters 15 mm behind LCFS. $I_p = 2$MA, $B_T = 3.4$T.

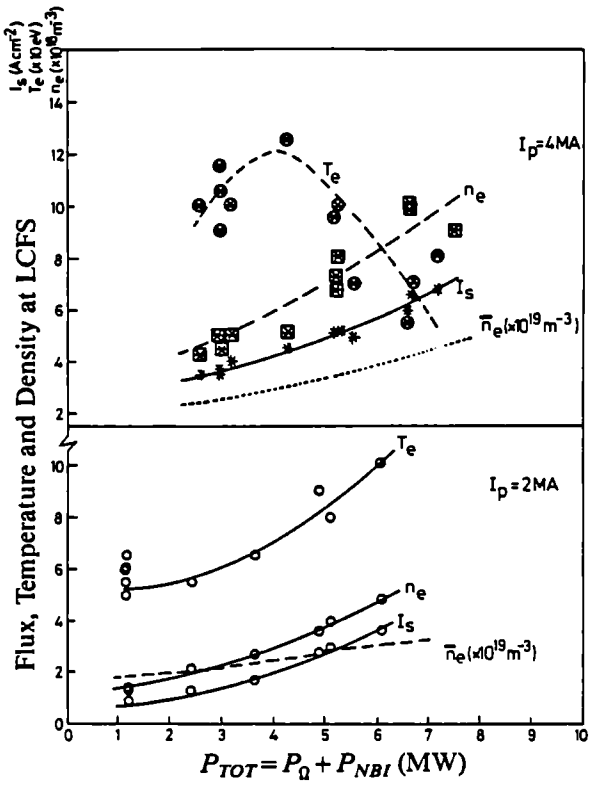

Fig.2 Effect of total input power on edge parameters at LCFS. The average plasma density is also shown.

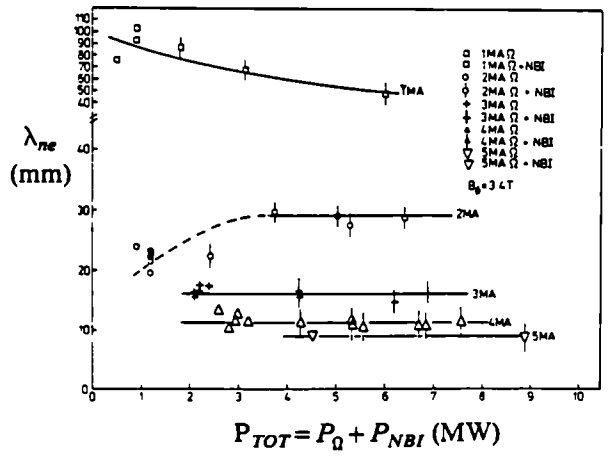

Fig.3 Effect of total input power on density e-folding length for plasma current $I_p = 1$-5MA.

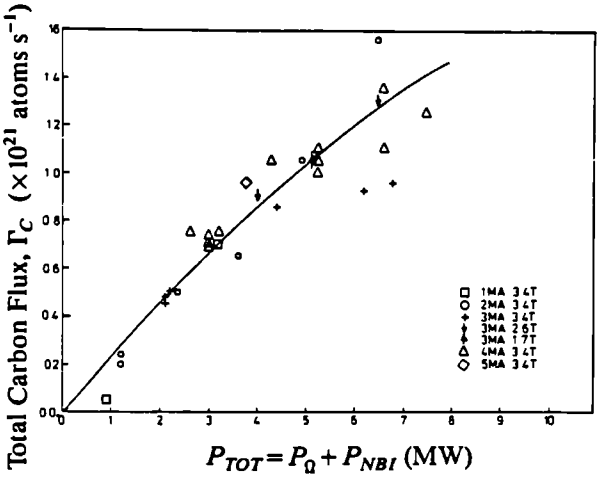

Fig.4 Effect of total input power on total carbon flux sputtered from all limiters.

CR87.77

THE EFFECTS OF WALL AND LIMITER MATERIAL PROPERTIES ON HYDROGEN RECYCLING IN JET

J Ehrenberg°, S A Cohen*, L de Kock, P J Harbour,
P D Morgan, M F Stamp and D D R Summers

JET Joint Undertaking, Abingdon, Oxon OX14 3EA, UK
° On attachment from Max-Planck-Institut für Plasmaphysik,
8046 Garching bei München, FRG
* Visiting scientist from Plasma Physics Laboratory,
Princeton University, Princeton NJ 08544, USA

I INTRODUCTION

The recycling of hydrogen at the limiters and walls of a fusion machine is important in controlling the particle and power balance of the plasma.

The problem may be subdivided into two parts: the transport of particles in the plasma and the transport of particles in the limiters and walls. In this paper we concentrate on the transport in the limiters and walls, treating plasma transport in a global way.

We present a numerical model which predicts, as a function of time during a simulated plasma discharge, the number of plasma particles and the particle fluxes to and from limiters and walls. We study with this model a JET discharge in which the plasma was moved from the outer limiter onto the inner wall and back to the limiter. We find good agreement between experiment and simulation.

II EXPERIMENTAL ASPECTS OF RECYCLING IN JET

JET limiter discharges are initiated with a hydrogen or deuterium gas prefill. A subsequent dosing raises the density. When the dosing valve is closed the density stays approximately constant /1/. The number of particles found in the plasma, compared to the number admitted into the machine (the fuelling efficiency) depends on the conditions of the limiters and walls. However, the walls and limiters soon reach a steady state in which the fuelling efficiency is below one.

In some JET discharges, the plasma is moved from the outer carbon limiter onto the inner carbon wall. Subsequently the plasma density drops. This pumping at the inner wall is not reduced after a series of similar discharges, excluding the saturable trapping of hydrogen implanted into carbon as a pumping mechanism. Also, we estimate that pumping due to deuterium/carbon codeposition /2,3/ contributes less than 30%, otherwise the required erosion rate of carbon would have to exceed that from known processes by a factor of three. When the plasma is moved back to the outer limiter, the density rises again. An example is shown in Fig. 1. This indicates that changes in the plasma position may be considered as changes in the balance between the particle fluxes out of the plasma and those out of walls and limiters.

III THE RECYCLING MODEL

The walls and limiters in a fusion machine are a reservoir for hydrogen atoms in the same way as the plasma is a reservoir for ions /4,5/. The neutral gas phase is unimportant as a reservoir because its confinement time for neutrals is of the order 10^{-3} s and thus much smaller than the particle confinement time τ_p in the plasma. Walls and limiters, in order to be an important reservoir, must have a particle confinement time τ_w similar to the plasma particle confinement time. The plasma is the source for energetic ions and neutrals which impact the walls. τ_w can be considered as the time these particles need to diffuse back to the surface and to desorb into the plasma. This effect is well-known for the case of hydrogen in metals and is called transient or dynamical retention /6/. However JET has carbon limiters, carbon inner walls and inconel vessel walls which are covered with a carbon layer (> 10 nm) /7/. In addition the carbon is saturated with deuterium, contaminated with metallic impurities and may have cracks at the surface. Little is known about dynamical retention in such materials. Nevertheless, we use the concept of hydrogen diffusion in solids and develop a model to calculate the number of plasma particles as well as particle fluxes from walls and limiters.

We assume that the change in the number of plasma particles (N_p):

$$\frac{dN_p}{dt} = - \frac{N_p}{\tau_p} + f \cdot \phi, \qquad (1)$$

where ϕ is the total flux of deuterium atoms from walls and limiters and f is a factor taking into account that part of this flux returns directly to the limiters and walls due to atomic processes, ionisation in the scrape-off layer, or due to the escape of neutrals. The magnitude of f has to be estimated.

Plasma losses, N_p/τ_p, are assumed to stream either to the outer-limiters or to the inner wall, depending on where the plasma resides. The flux $(1-f)\phi$, which is that part which does not fuel the plasma, is shared between the limiter, the inner wall, and the rest of the vessel wall. It is assumed that 50% of this flux goes to the surface where the plasma resides (limiter or inner wall) and 50% to the rest of the wall and the inner wall or limiter (i.e. depending on where the plasma is not). The latter 50% is assumed to be shared according to the ratio of the respective surface areas. The partition is somewhat arbitrary, however it simulates roughly the situation that the probability of creation of "daughter"-neutrals by charge exchange processes is largest near surfaces where recycling is large. Thus "daughter"-neutrals have a good chance to return to that surface where the initial neutrals have been born.

The particles which impinge onto surfaces are either reflected (with reflection coefficient, r) or penetrate into the material up to a depth d. r and d depend on the impact energy of particles, which is derived from Langmuir probe measurements in the plasma boundary of JET /8/. For simplicity we assume monoenergetic particles. The penetrating particles are the source for the diffusion in walls and limiters. The diffusion equation is solved numerically, using an assumed diffusion coefficient, a

recombination coefficient, and appropriate boundary conditions. The diffusive losses as well as the reflected flux from all surfaces then fuel the plasma (see equ 1). From the dependence of the experimental fuelling efficiency on the number of particles admitted to the machine, it can be shown that the release of particles from JET limiters and walls is most likely determined by diffusion. Thus we have to know the diffusion coefficient only. We also have to know whether diffusion takes place within the entire wall thickness ($\leq 10^{-2}$ m) or only within a surface layer with a thickness L. Assuming a simple triangular concentration profile of diffusing particles in limiters and walls (peaked at the range d and zero at either surface of the layer L) it can be shown that the wall confinement time τ_W is approximately:

$$\tau_W \sim \frac{d \cdot L}{D} \text{ if } L > d \text{ and } L \ll (t_{max} \cdot D)^{1/2} \qquad (2)$$

where t_{max} is the duration of particle bombardment. If $L \geq (t_{max} \cdot D)^{1/2}$, τ_W is larger than in (2) and depends on time. In this case (or when d > L) it can be shown that the plasma is still pumped by the walls, however, the number of particles cannot increase during a discharge as is shown to occur in Fig. 1. Good agreement between experiment and calculation was found by taking L to be around 20 nm. This suggests that the material structure of wall and limiter surfaces prevents the diffusion of a significant fraction of deuterium into the bulk material.

IV RESULTS

For the calculation presented in Fig. 2 we took a reflection coefficient, r, of 0.3 and a particle range, d, in walls/limiters of 5 nm corresponding to an impact energy of about 100 eV for deuterium on carbon. According to previous investigations /1/ τ_p was taken to be proportional to $1/N_p$. To simulate the higher temperature at the limiter (> 700°C) compared to the walls (300°C) and the different materials (carbon, carbonized inconel), we assumed the diffusion coefficient D to be different on these surfaces. D and the factor f (see Fig. 2) were varied until satisfactory agreement with the experiment was achieved. The discharge scenario simulated in Fig. 2 is as follows: an external gas source with 10^{21} particles/s for the first 4 s, fills the plasma while it rests at the limiter. The total particle input is the same as in the experiment of fig. 1. At 6 s the plasma interaction is shifted from the limiter to the inner wall. At 10 s this is reversed. To simulate the detached plasma phase at 6 s and 10 s the plasma particle confinement at these times was enhanced for 0.2 s by a factor of 2. Good agreement between calculation and experiment was achieved with $D = 2.10^{-11}$ cm²/s at the limiter, $D = 1.10^{-11}$ cm²/s at the inner wall, and $D = 1.10^{-12}$ cm²/s at the rest of the wall. The set of values for d, L, D and f is not unique. The limiter flux, deduced from the data in Fig. 1 agrees within a factor of 2 with that in Fig. 2. However the measured inner wall D_α-signals show toroidal variations, probably caused by non-uniformities in the surface of the inner wall, making a quantitative comparison difficult.

V CONCLUSION

A model has been developed to describe the complementary processes of pumping and fuelling of plasma by diffusion of deuterium in limiters and walls. Also account is taken of non-fuelling processes which increase particle fluxes to walls/limiters and subsequently the particle inventory therein. Comparison with experimental results shows good quantitative agreement. The model indicates the importance of plasma and wall properties for the balance of particle fluxes.

VI REFERENCES

/1/ P Morgan et al, Proceedings 12th Europ Conf Contr Fus Plasma Phys, Budapest, 2-6 September 1985, Vol II, 535.
/2/ R Behrisch et al, Journal of Nucl Mat, 145+147 (1987) 723.
/3/ H Bersaker et al, Journal of Nucl Mat, 145+147 (1987) 727.
/4/ G M McCracken and P E Stott, Nuclear Fusion, Vol 19, No 7 (1979) 889.
/5/ T Jones et al, this conference.
/6/ F Waelbroek et al, Journal of Nucl Mat, 111+112, (1982) 185.
/7/ P Coad et al, Proceedings 12th Europ Conf Fus Plasma Phys, Budapest, 2-6 Sept 1985, Vol II, 571.
/8/ T Tagle et al, this conference.

FIGURES

Fig. 1 Plasma current I_p, total number of electrons N_e, and D_α signals from limiters and inner wall of a JET discharge which was moved onto the inner wall at t=6s and removed back to the limiter at 10 s and again moved to the inner wall at 14 s. To compare N_e with N_p of fig. 2, N_e has to be reduced by approximately 20% due t o Z_{eff} = 2, assuming carbon as the only impurity.

Fig. 2 Calculated number of plasma particles N_p and particle fluxes from limiter, Γ_L and inner wall, Γ_{IW} for a discharge with a similar total particle inventory as in Fig. 1.

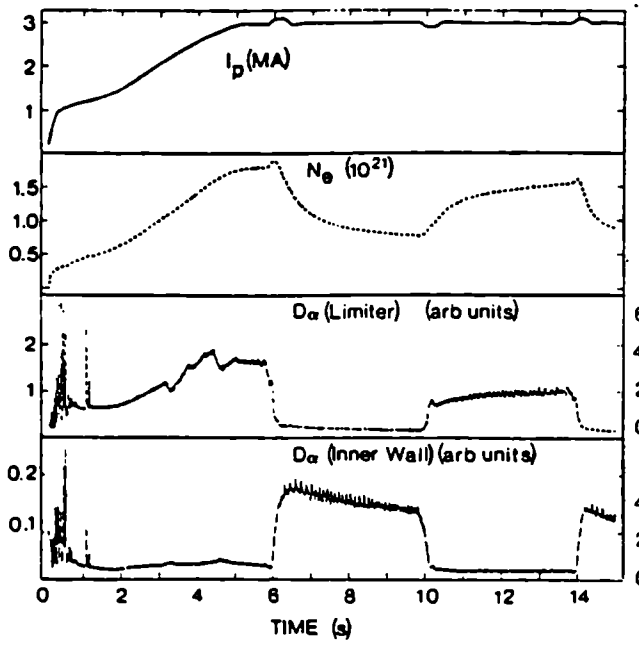

Fig. 1

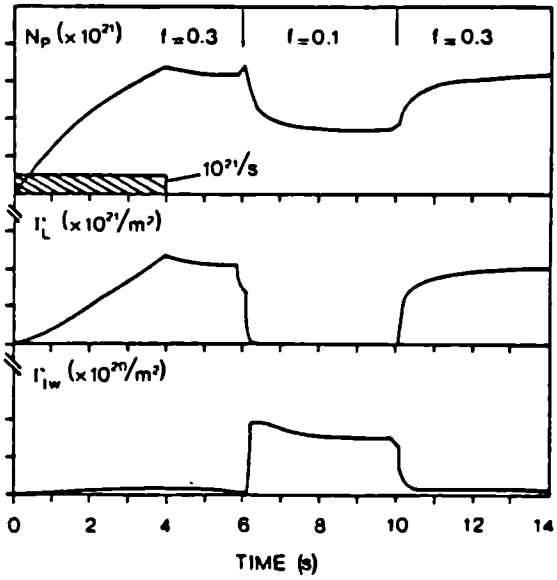

Fig. 2

ION TEMPERATURE MEASUREMENTS USING NEUTRON SPECTROMETRY

O N Jarvis, S Corti, M Hone, G Gorini, J Källne, V Merlo,
P D Morgan, G Sadler and P van Belle
JET Joint Undertaking, Abingdon, Oxon, OX14 3EA, UK

ABSTRACT

Neutron spectrometry has been used at JET to measure the central ion temperature in deuterium discharges under conditions of Ohmic heating, ICRF heating and Neutral Beam heating with hydrogen beams. The ion temperatures measured with neutron spectrometry agree well with temperatures obtained from Neutral Particle Analysis and impurity X-ray spectrometry line broadening techniques. By combining ion temperature and total neutron yield data, the central deuterium to electron density ratio $\hat{n}_d/\hat{n}_e$ can be obtained. For typical JET plasmas Ohmically heated to T_i = 3 keV, $\hat{n}_d/\hat{n}_e$ is found to be less than 0.4.

* * *

Neutron spectrometry was proposed [1]) many years ago as a particularly direct method of determining the majority species ion temperature in deuterium or deuterium-tritium plasmas but it was only recently when high-current, long duration, tokamak plasmas become available that the potential of this technique could be realized in practice. Even now, with JET providing 3 MA, ten second duration, discharges it is only exceptionally possible to obtain an accurate (± 10%) temperature measurement in a single discharge. More commonly, it is necessary to aggregate the spectra for a few (not more than seven) similar discharges before acceptable statistical accuracy is obtained. This is because the ^{3}He ionization spectrometer employed at JET for neutron spectometry has until recently been used in the Roof Laboratory at a distance of over 20 m from the plasma and the neutron flux at the spectrometer has been correspondingly low. The experimental arrangement and typical energy spectra have been presented previously [2]). With stronger neutron yields (ie. above 10^{13} n/sec), or a reduced separation between plasma and spectrometer, the statistical uncertainty can be reduced until the counting rate limit of a few kHz is reached; it should be possible in principle to make one useful temperature measurement in a two-second counting period.

The essential condition for neutron spectrometry to provide a useful temperature measurement is that the plasma ion energy distribution be Maxwellian. For this reason the method is limited to plasma heated Ohmically, by ICRF with either ^{3}He or H minority heating and by Neutral Heating with hydrogen beams. For JET plasmas so heated there is no evidence that the deuterium ions show any departures from a Maxwellian energy distribution.

The first step towards acceptance of neutron spectrometry as a diagnostic technique is to demonstrate that it provides results which are in

agreement with those obtained by more conventional methods. One of the virtues of neutron spectrometry is that the uncertainties can be clearly stated, being mainly statistical with an overall normalization uncertainty about ± 5%. However, because of the long measuring time needed by the spectrometer, it is necessary to average the measurements from the other diagnostics over the relevant interval. In figure 1 we compare ion temperatures obtained with the neutron spectrometer with those obtained through Neutral Particle Analysis on deuterium atoms. The agreement between the two techniques is well within the ± 15% uncertainty associated with the NPA technique. It should be noted, however, that to obtain this result the NPA data must be subjected to the full analysis for plasma opacity etc; ie the simple linear extrapolation technique cannot be used for the higher densities. In figure 1 we also compare the neutron spectrometer results with those from Ni^{26+} impurity X-ray line broadening [3]. For these last measurements no plasma related corrections are needed since the emission is strongly localized at the plasma centre. Unfortunately, the X-ray emission becomes unusably low for temperatures below 2.5 keV for the present data set. Once again the agreement between the two techniques lies well within the expected range of uncertainties. The overall agreement found here constitutes firm evidence that the ion energy distributions are Maxwellian since the three techniques are sensitive to differing portions of the energy distribution.

The total neutral emission from JET plasmas is routinely measured to ± 10% absolute normalization accuracy with a set of fission chambers [4]. A knowledge of the central ion temperature can be used in combination with the neutron emission strength to obtain the deuterium ion to electron density ratio, $\hat{n}_d/\hat{n}_e$, provided information on electron temperature and density profiles are available from other diagnostics and that the shape of the temperature and density profiles for ions are assumed to be the same as for electrons [5]. It is not essential to use the ion temperature derived from neutron spectrometry for this purpose but it is preferred because both measurements, of temperature and yield, are characteristic of the same portion of the ion energy distribution (the mean energy of ions undergoing fusion reactions is about $3T_i$ for T_i= 4 keV) and, moreover, the purely plasma physics complications are minimal. The total of 50 Ohmically heated and ICRF heated discharges studied were grouped in sequences of consecutive similar discharges and the statistics aggregated as necessary to give acceptable statistical accuracy. This gave 11 groups, for which the $\hat{n}_d/\hat{n}_e$ ratios are shown plotted against $\hat{T}_i$ in figure 2. A sharp fall from $\hat{n}_d/\hat{n}_e$ ~ 0.8 at 2 keV to 0.3 at 3 keV is fairly clear, despite the relatively large uncertainties at low $\hat{T}_i$. It should be recognized that useful data can only be obtained from discharges with sufficiently high neutron emission; that we show no results with low $\hat{n}_d/\hat{n}_e$ around 2 keV is probably no more than a consequence of this, whereas high $\hat{n}_d/\hat{n}_e$ at high temperature would be easily detectable. We conclude that high ion temperatures are achieved in JET Ohmically heated plasmas as a consequence of the impurity level being high. It is noteworthy that the addition of ICRF heating does not lead to a further decrease in $\hat{n}_d/\hat{n}_e$ and so the impurity level is definitely not a direct consequence of the ion temperature being high.

The $\hat{n}_d/\hat{n}_e$ values can be combined with the available information on the impurity content of the plasma assuming that the main impurity is carbon (as would be expected for a tokamak lined with graphite tiles), to provide estimates for Z_{eff}. These 'neutron' Z_{eff} values are compared in figure 3 with the directly measured average Z_{eff} from visible bremsstrahlung radiation and with that calculated from the axial resistivity. Bearing in mind the possibility of a 25% peaking in the Z_{eff} profile, it is seen that the agreement with the bremsstrahlung data is, on average, acceptable whilst the agreement with the resistivity data is excellent. It should be noted that the reverse procedure of extracting $\hat{n}_d/\hat{n}_e$ ratios from Z_{eff} is very imprecise for high Z_{eff} due to the ± 15% associated uncertainty when carbon is assumed to be the major impurity.

In conclusion, we have shown that neutron spectrometry provides ion temperature data which agree well with temperatures from more conventional techniques and that in combination with the neutron yields, the temperatures permit values for $\hat{n}_d/\hat{n}_e$ to be obtained which are disturbingly low but nonetheless compatible with other information concerning impurity levels in JET for the discharges studied.

ACKNOWLEDGEMENT
The authors are grateful to E Källne for providing the nickel X-ray data.

REFERENCES

1. G Lehner, Z Phyzik 232 (1970) 174.
2. O N Jarvis et al, Rev Sci Instr 57 (1986) 1717.
3. R Giannella, F Bombarda, E Källne, L Panaccione and G Tallents, Bull Am Phys Soc 31, 1590, 1986.
4. M T Swinhoe and O N Jarvis, Nucl Instrum Meth in Physics Research 221 (1984) 460.
5. O N Jarvis et al, European Conference Abstracts, Vol 9F, Part 1, p223, 1985.

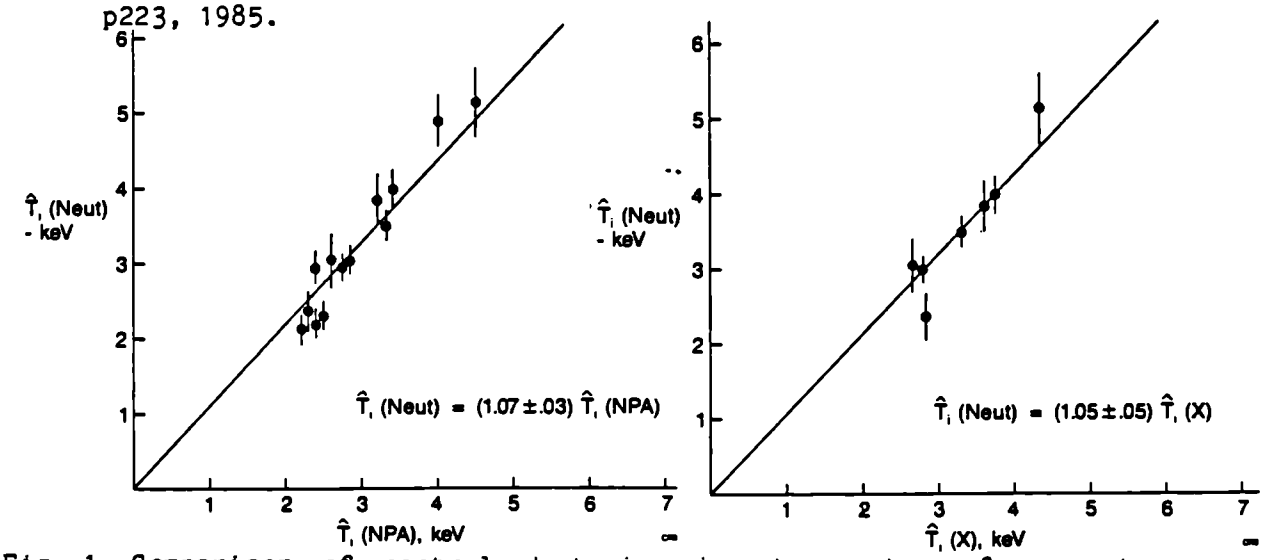

Fig. 1 Comparison of central deuterium ion temperature from neutron spectrometry (Neut) with values obtained from Neutral Particle Analysis (NPA) and Nickel Impurity X-ray line broadening (X).

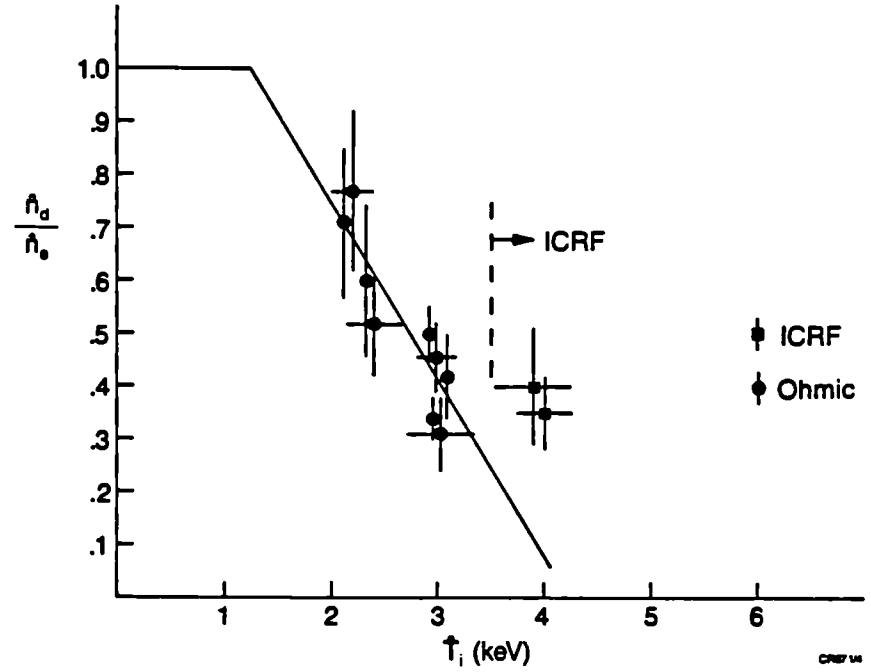

Fig. 2 Variation of $\hat{n}_d/\hat{n}_e$ with central ion temperature for Ohmic and ICRF (^{3}He) heating.

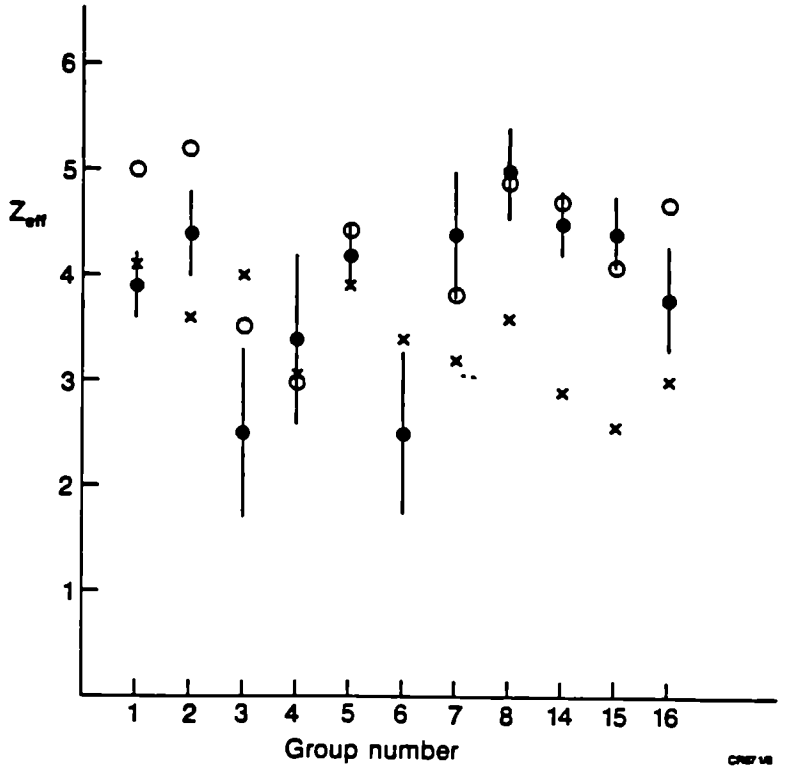

Fig. 3 Comparison of Z_{eff} values obtained from neutron measurements (♦) with values from axial resistivity (o) and visible bremsstrahlung (x) measurements.

FIRST MEASUREMENTS OF NEUTRON EMISSION PROFILES ON JET

J M Adams[+], O N Jarvis, J Källne, G Sadler, D B Syme[+], M T Swinhoe[+], N Watkins[+], P van Belle and K Verschuur*

JET Joint Undertaking, Abingdon, Oxfordshire, OX14 3EA, UK
[+] AERE Harwell, Didcot, Oxfordshire, OX11 ORA, UK
* ECN, Petten, The Netherlands

ABSTRACT

A multichannel neutron collimator system has been installed on the JET tokamak for the measurement of neutron emission profiles from deuterium plasmas. In preliminary measurements, the development of the emission profile with time for Ohmically heated plasmas is seen clearly, and the profiles for Ohmic, Neutral Beam and ICRF heated plasmas are examined. The neutron signals show the sawtooth inversion effect so familiar from electron temperature profile measurements.

* * *

A neutron emission profile measurement diagnostic has recently been installed on JET to sample the spatial distribution of neutron emissivity from a poloidal section through the plasma. The diagnostic is still in the early stages of commissioning but nevertheless much interesting data has been collected under diverse plasma operating conditions.

The diagnostic comprises two multichannel collimator arrays, a 32 tonne horizontal camera possessing 10 channels to measure the vertical profile, and a 10 tonne vertical camera with 9 channels (only 7 operational) to measure the horizontal profile. The experimental layout is illustrated in fig. 1.

The width of the poloidal viewing area for each channel in the central region of the torus is about 10 cm. The neutrons are detected with NE213 liquid scintillators coupled to photomultipliers and the signals are processed using Pulse Shape Discrimination to separate neutrons from gamma-rays. The necessity for pulse processing introduces a counting rate limitation of about 300 kHz, but of this rate only 30 kHz is useful because of the necessity to apply energy discrimination to reject neutrons of less than 2.0 MeV which form the background of wall scattered neutrons that must inevitably be present in any system which views the central column of the tokamak through the plasma. Detailed neutron transport calculations have been performed to elucidate the fraction of wall scattered events which exceed the chosen discrimination level: it is found that this background is rather flat (ie. similar for all data channels) and is no more than 3-4% of the count-rate in the central channel. Since this background can be calculated reasonably well, it is seen that the radial profiles can be measured down to 1% of the central channel count-rate.

An examination of the time traces (not shown here) for the seventeen data channels for a 5 MA, 3.4 T discharge shows very clearly how the plasma discharge begins as a narrow channel (not quite centred in the vacuum vessel) which heats very strongly at first and then cools a little as the heated channel broadens. The plasma current holds its flat-top of 5 MA for only 4 seconds. It is clear that the neutron emission profile does not quite reach equilibrium conditions before the current decay commences.

The neutron emission profiles can be predicted from a knowledge of the magnetic flux surfaces, assumed to be surfaces of constant temperature and density, and of the radial profiles for the deuterium ion temperature and density. Since JET plasmas are D-shaped, a functional form for the spatial dependence of temperature and density is adopted:

$$T_e(R,Z) = T_{eo}\ \psi^p\ (R,Z),\ \text{etc},$$

where ψ is a suitable parameterization for the magnetic flux surfaces valid for low β plasmas. For circular plasmas, $T_e(R,Z) = T_{eo}\ (1-r^2/a^2)^{2p}$, where a is the limiter radius. The peaking factor p for the electron density is known from the multichannel Far Infra-Red Interferometer [1]) and is assumed to describe also the ion density. The peaking factor for the ion temperature is obtained by fitting the predictions to measurement, as illustrated in fig. 2 for the 5 MA, Ohmic heated discharge. The predictions are subject to the constraint that the total neutron emission agrees with that measured with the neutron yield monitor diagnostic (a set of fission counters). It is seen that the neutron emission data are fitted remarkably well by an ion temperature peaking factor of 1.0, with the single point for channel 14 providing the sole exception. (The reason for this discrepancy is not known, but is should be remembered that this diagnostic is not yet fully commissioned and there may well be hidden problems such as effects of magnetic fields and high operating temperatures on the photomultipliers). This peaking factor has been selected mainly on the basis of comparison of absolute counting rates; a more careful analysis would permit the absolute scaling to be adjustable and may well lead to a somewhat smaller peaking factor. It is interesting to note that the peaking factor which approximately fits the electron temperature for this discharge is p = 0.3, representing a much broader profile. The statistical accuracy of the data shown in fig. 2 is quite good, the error bars essentially representing the uncertainty in detector efficiency for each channel; consequently, small changes in the profile can easily be detected. Rather surprisingly, it is found that the profile changes very little when 6 MW of D° neutral beam heating or 8 MW of ICRF heating is applied. The electron temperature profile is similarly little changed for these 5 MA discharges; however, profile changes are known to occur for 3 MA discharges.

Finally, it is interesting to note that sawteeth oscillations are clearly to be seen in the signals from the multichannel collimator provided the neutron emission is sufficiently strong. A typical discharge (3.0 MA,

2.2 T, 6 MW D° neutral beam heating) provides the results shown in fig. 3, where the traces from three channels of the horizontal camera are displayed: the line-of-sight for channel 6 passes below the centre of the plasma by about 10 cm, channel 8 by 50 cm and channel 9 by 70 cm. Channel 6 shows the normal sawteeth, channel 8 shows no discernable sawteeth whereas channel 9 displays inverted sawteeth for which the rise in neutron emission coincides with the fall for the inner channels.

REFERENCES

1. G Braithwaite et al, "The multichannel far infra-red interferometer (KG1) on JET", JET Internal Report JET-IR(85)06.
2. A E Costley et al, Europhysics Conference Abstract Vol 9F, Part 1, (1985), 227.

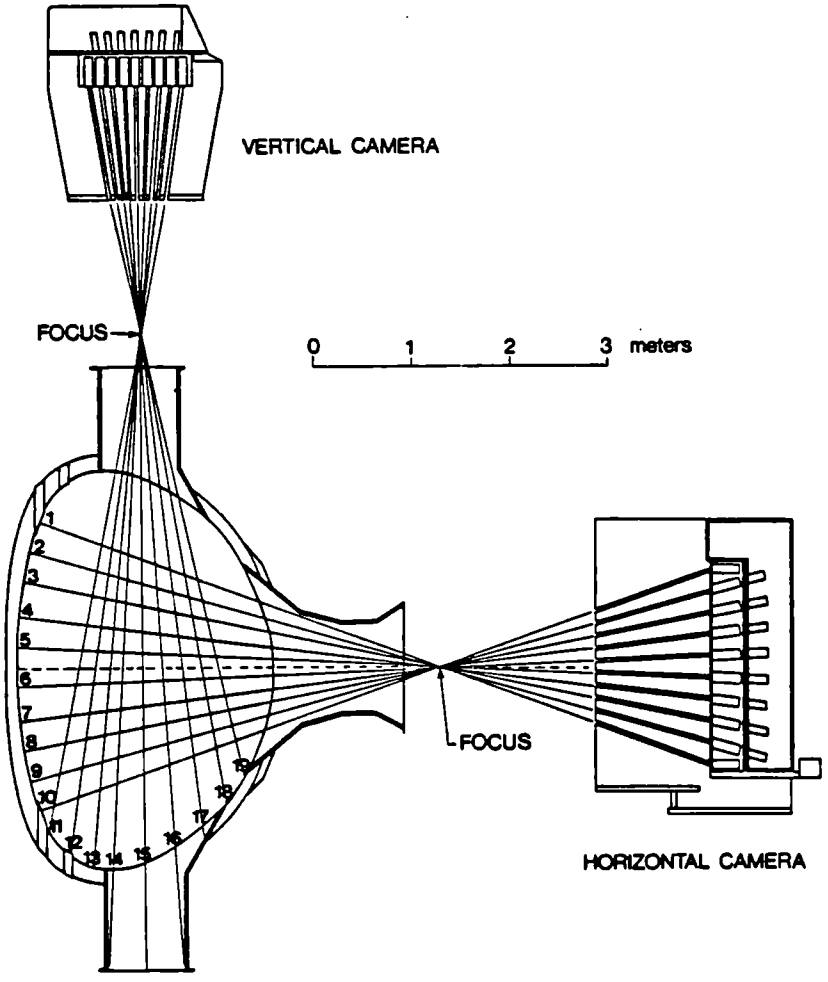

Fig. 1 KN3 NEUTRON PROFILE MONITOR
DETECTOR CHANNEL LINE-OF-SIGHT SCHEMATIC

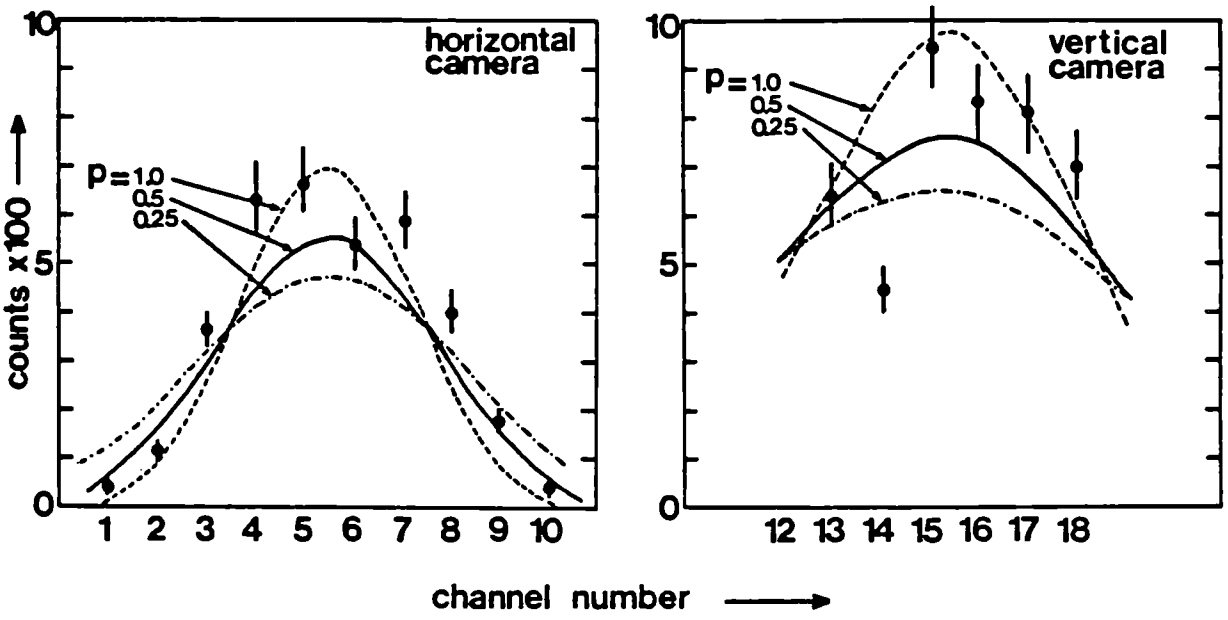

Fig. 2: Determination of the temperature profile peaking factor for discharge 10936 at the end of the 5 MA current-flat-top.

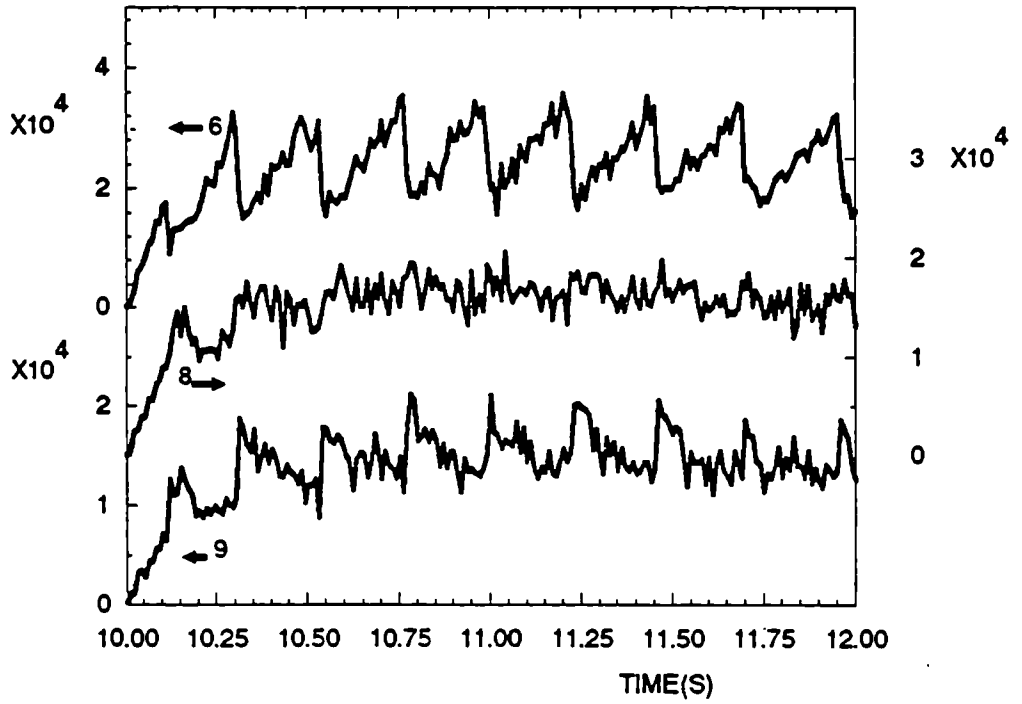

Fig. 3: Neutron count rates as recorded by three channels for discharge 10822 (3 MA, 2.2 T, 6.5 MW NBI). The sawteeth invert with increasing distance from the plasma centre (channels 6 to 9, see text).

STUDIES OF TRITIUM BURN-UP IN JET DEUTERIUM DISCHARGES

P Batistoni[1], M Martone[1], M Pillon[1], M Rapisarda[1],
J Argyle[2], G Huxtable[2], D B Syme[2], E Bittoni[3], K Verschuur[4],
G Gorini[5], O N Jarvis, J Källne and G Sadler

JET Joint Undertaking, Abingdon, Oxon, UK
[1] Association EURATOM-ENEA, CRE Frascati,
CP 65-00044 Frascati (Rome), Italy
[2] AERE, Harwell, Oxon, UK
[3] ENEA, Via Mazzini 2, Bologna, Italy
[4] Netherlands Energy Research Foundation ECN, PO Box 1,
1755 ZG Petten, Holland
[5] Scuola Normale Superiore, Pisa, Italy

ABSTRACT

The 14 MeV neutron production has been measured in JET deuterium discharges using the activation technique. These data were combined with the routinely measured 2.5 MeV neutron yield to determine the burn-up fraction of fast tritons. Information on the triton confinement and slowing down is derived by comparison with the calculated classical particle behaviour in the plasma. The experimental technique is discussed and the first results on triton burn-up in JET are presented for different plasma conditions of Ohmic, ICRF and NBI heated discharges.

x x x

A pneumatic rabbit system has been installed at JET for transportation of neutron activation samples between irradiation positions at the plasma and γ-activation measuring stations [1]). This system has been used to measure the total time integrated neutron yield from deuterium discharges at JET for plasmas of different conditions and additional heating scenarios. The first experiments have been devoted to measurements of the yield of 14 MeV neutrons using activation of Copper. These neutrons arise from the burn up of fast tritons through the reaction $d + d \rightarrow t + p$ with the same source strength as the $d + d \rightarrow {}^3He + n$ reactions responsible for the dominant 2.5 MeV neutron yield in deuterium plasmas. The total neutron yield was measured using activation of indium but is also routinely available from accurately calibrated fission chamber measurements. The 14 MeV to 2.5 MeV neutron intensity ratio, $\zeta = I_{14.1}/I_{2.5}$, is of interest as a direct measure of the fraction of fast tritons that burn up while they are confined and slowing down in the plasma [2]). In a wider context, the information gained from fast triton studies has a bearing on the individual particle behaviour of 3.5 MeV alpha-particles from d-t reactions under similar plasma conditions because of the similarities in Larmor radii. In this Conference report, we present the first results on the triton burn-up fraction in JET

deuterium discharges of various plasma conditions using Ohmic, ICRF and NBI heating.

The measurements are compared with theoretical burn-up ratios calculated using a classical model for the particle slowing down and confinement. The tritons are born at 1 MeV and slow down to thermal energies by Coulomb interactions with electrons and ions on a time scale much longer than the particle confinement time in JET; the burn-up contribution from thermal reactions is insignificant. The orbits of tritons born in different volume/pitch-angle elements of the plasma are calculated within the guiding centre approximation but neglecting pitch-angle scattering during the slowing down; the triton production is assumed to be isotropic and toroidal symmetry is assumed as well.

The present experiment was performed with the newly installed pneumatic system for the transport of activation capsules between four irradiation positions at the JET vacuum vessel (but inside the massive shielding surrounding it) and detection stations far removed from the torus. The energy spectrum of the induced γ-activation was measured with a high purity germanium detector (HPGe) or a NaI detector, and the neutron fluence received by the activation samples was determined from the measured γ-decay rate using known cross sections and half-lives ($T_{1/2}$). Copper samples were used to determine the 14 MeV neutron fluence by measuring the 511 keV γ-line ($T_{1/2}$ = 9.73 m) resulting from the $^{63}Cu(n,2n)^{62}Cu$ reactions (E_{th} = 10.9 MeV). The fluence of low energy neutrons, predominantly 2.5 MeV neutrons, was measured using the reaction $^{115}In(n,n')^{115}In$ with a threshold of about 1.0 MeV; this reaction results in γ-emission of 0.335 MeV ($T_{1/2}$ = 4.5 h). The relationship between the neutron fluence seen by the activation sample and the source of primary fusion neutrons from the plasma was determined [3]) by modelling the JET torus and calculating the fluence and the energy distribution of scattered neutrons. The calculated response of the activation samples to a given source strength of virgin plasma neutrons is estimated to have an accuracy of better than 25%. This estimate is consistent with the agreement we have found between the results on the neutron yield as obtained from the present indium activation measurements and those of the neutron flux measurements performed with fission chamber with a known calibration [4]) uncertainty of ±10%. Until we have refined the calculations for the activation calibration response we use the 2.5 MeV neutron intensity from the fission chamber and the 14 MeV intensity from the Cu activation to determine the intensity ratio, ζ.

Measurements of the burn-up ratio were made for JET plasmas in the parameter ranges I_p = 1-5 MA, B_T = 2.2-3.4 T, $\bar{n}_e$ = 1-4 $10^{19} m^{-3}$ and T_e = 3-6 keV. The peak neutron production rates were in the range 2-30 10^{14} n/s and Cu activation data were obtained with good statistical accuracy for neutron yields larger than 5.10^{14} neutrons (or fluences of 5.10^{8} neutron/cm^2 or larger) using samples of less than 20 g. Most discharges were performed with an open magnetic field configuration having a single vertical separatrix (X-point) and with H-mode achieved in one case. Only

one of the discharges studied so far was with Ohmic heating only while all others were with ICRF ($P \leq 2$ MW) and/or NBI ($P \leq 8$ MW) additional heating.

For the Ohmic discharge (pulse number 10661 with $B_T = 3.4$ T, $I_p = 3$ MA, $T_e = 3.7$ keV and $Z_{eff} = 2.6$) the burn-up ratio was determined to be $\zeta = 8.1\ 10^{-3}$ with a statistical error of $\pm$ 0.7. The calculated classical value is $\zeta = 1.1\ 10^{-2}$ taken as the time average for a discharge during which the plasma parameters were but slowly changing; the triton confinement fraction was > 98% for the part of this discharge where the neutron yield was significant with ζ varying in the range 9.7-12.2 10^{-3} due mainly to the variation in Z_{eff} and T_e, this calculated value has an estimated uncertainty of about 20%. The observed value is thus consistent with the expected classical particle behaviour of tritons for these plasma conditions.

The experimental burn-up fractions obtained for the additionally heated plasmas are presented in Fig. 1. For these discharges a calculation of the kind performed for discharge 10661 is not at present possible, for a number of reasons: the triton birth profiles are not known, the high Z_{eff} values (up to 5.5) introduce a large uncertainty in the deuterium concentration ratio, n_d/n_e, and the use of a steady-state model is inappropriate for discharges in which the plasma parameters vary strongly with time. Nevertheless, the data can be analyzed in an approximate manner using the well-known scaling $\zeta \sim (n_d/n_e)T_e^{3/2}$ to convert all discharges to standard reference conditions, $T_e = 5.0$ keV and $Z_{eff} = 3.0$, where we have used the central value for T_e and derived n_d/n_e from Z_{eff} on the assumption that the major plasma impurity is carbon. Since this last assumption is questionable, attention was restricted to discharges with Z_{eff} falling in the range 2.0 to 4.0.

With this approach, it is found that the burn-up fractions for additionally heated plasmas may attain a value as high as that obtained for the ohmic discharge discussed earlier, or fall to values 40% lower. A somewhat random scatter in the results is undoubtedly introduced through the uncertainty in n_d/n_e whereas some systematic trends due to profile effects and low triton confinement at the lower plasma currents can be expected. However, from the results it is not possible to discern clear trends of burn-up with plasma current, toroidal field, nature of the additional heating or magnetic field configuration. Nevertheless, these results are encouraging as the simple classical model does appear to reproduce the experimental burn-up fractions adequately.

In the future we plan to extend the measurements to examine more closely the plasma parameter dependence of the triton burn-up fraction, to improve the absolute normalization of the 2.5 MeV and 14 MeV neutron measurements and to perform more careful comparisons with classical calculations taking into account the rapid time variation of plasma parameters associated with additional heating.

REFERENCES

1. E Lees et al, "Neutron detection techniques for plasma diagnostics at the Joint European Torus", Radiation Effects 95 (1986) 1259.

2. J D Strachan et al, "Confinement of fusion products in tokamaks, Course and Workshop on Basic Physical Processes of Toroidal Fusion Plasmas, Varenna, August 1985.

3. K Verschuur, "Furnace calculations for JET neutron diagnostics", ECN-146 (1983).

4. O N Jarvis et al, "Further calibrations of the time resolved neutron yield monitor (KN1)", JET-IR(85)06.

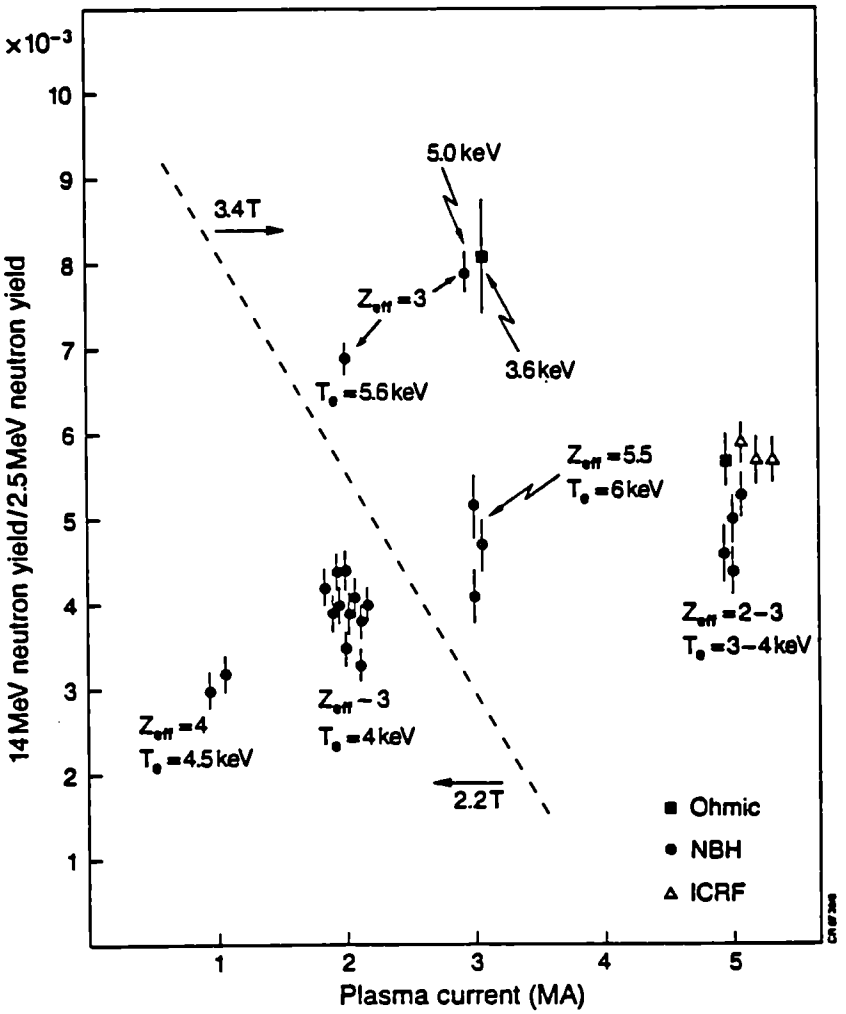

Fig. 1 Experimental values obtained for the triton burn-up fraction for various values of plasma current (1-5 MA) and toroidal field (2.2 and 3.4 T). The variation in T_e and Z_{eff} may obscure other dependencies.

OBSERVATION OF FUSION REACTION γ-RAYS IN JET

G Sadler, O N Jarvis, P v Belle
N Hawkes* and B Syme*

JET Joint Undertaking, Abingdon, Oxon, OX14 3EA, UK
* AERE Harwell, Didcot, Oxon, OX11 ORA, UK

ABSTRACT
Gamma-rays from the fusion reactions $D(^3He,\gamma)^5Li$ (E_γ=16.6 MeV) and $D(p,\gamma)^3He$ (E_γ=5.5 MeV) have been observed in JET discharges. During ^3He minority ICRF heating of deuterium plasmas the intensity of the 16.6 MeV γ-ray exceeded 250 c/s from which a generated fusion power of 9.4 kW can be deduced leading to a Q value of $1.5\ 10^{-3}$, the highest ever achieved. Under conditions of H minority heating the shift and width of the 5.5 MeV line yields information on the energy distribution of the very fast reacting protons. Finally, the observation of 4.4 MeV γ-rays from the decay of the first excited state of ^{12}C indicates the presence of C as a plasma impurity as well as the presence of exceptionally energetic ions required for the excitation.

INTRODUCTION

The use of γ-ray emission as a diagnostic tool for fusion reactions from plasmas was first proposed by Medley et al [1]. First attempts to detect such γ-rays have been reported by Newman and Cecil [2] for the D,p reaction and more recently by Cecil et al [3] for the D,^{3}He reaction. Here we present the first unambiguous measurements of fusion γ-rays in large quantities, thus demonstrating the viability of the technique.

The experimental set-up is depicted in fig. 1. Two different detectors were used: a 125 diameter by 125 mm long Sodium Iodide (NaI) scintillator and a 75 mm by 75 mm Bismuth Germanate (BGO) crystal. Both detectors were operated simultaneously on similar lines of sight. The intrinsic detection efficiencies were taken from the literature, either directly [4] (BGO) or by interpolation [5-6] (NaI). The systematic error on the total deduced efficiencies taking into account the geometry as well as any absorbing material in the line of sight is estimated to be less than ± 30%. When tested by comparing results from the two systems, typical discrepancies of less than 10% are found. For the energy calibration a set of standard γ-ray sources was used as well as an Am-Be (4.4 MeV) and a Pu-^{13}C (6.1 MeV) source.

16.5 MeV γ-RAYS

Gamma emission from the D (^{3}He, γ)^{5}Li reaction proceeds through both the ground state (γ_0) and excited state (γ_1) of ^{5}Li at ~ 3 ± 0.5 MeV. Both levels are broad (1.5 MeV and 5 MeV respectively) and the lines are not resolved. This, together with the limited detector resolution, explains the shape of the experimental spectra (fig. 2b) as observed during ^{3}He minority heating of D^+ plasmas.

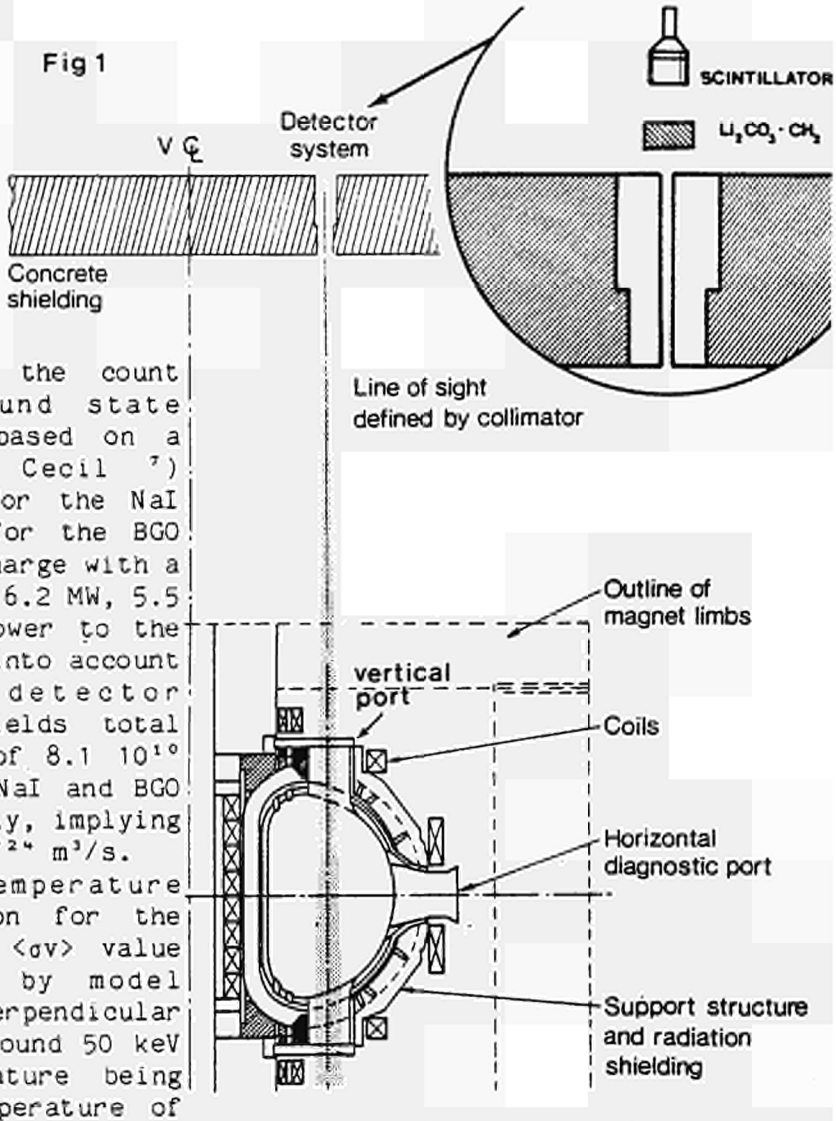

Fig. 1 Experimental arrangement showing the well shielded location of the γ-ray detectors in the JET Roof Laboratory.

The determination of the count rate from the ground state transition has been based on a recent analysis by Cecil [7] leading to 265 c/s for the NaI detector and 85 c/s for the BGO detector during a discharge with a total heating power of 6.2 MW, 5.5 MW of which was RF power to the ^{3}He minority. Taking into account the respective detector efficiencies, this yields total gamma emission rates of 8.1 10^{10} and 7.9 10^{10} for the NaI and BGO detectors. respectively, implying a $\langle\sigma v\rangle$ value of 4.4 10^{-24} m^3/s. Assuming a two temperature Maxwellian distribution for the heated ^{3}He ions this $\langle\sigma v\rangle$ value can be reproduced by model calculations with a perpendicular temperature tail of around 50 keV (the parallel temperature being set equal to the temperature of the bulk of the plasma). The mean energy of the reacting ^{3}He ions is calculated to be 200 keV. At this energy the branching ratio $^3He(D\gamma_0)^5Li/^3He(D,p)^4He$ is 2.5 10^{-5} from which we deduce a total charged particle reaction rate of 3.2 10^{15} or a fusion power of 9.4 kW. With a total power of 6.2 MW applied, the power multiplication factor is deduced to be Q = 1.5 10^{-3}, tne highest value yet achieved in a Tokamak.

5.5 MeV γ-RAYS

During H minority heating of D^+ plasmas the 5.5 MeV γ-line from the $D(p,\gamma)^3He$ reaction can be clearly seen as shown in fig 2c. A similar analysis of the line intensity to that carried out above leads to a perpendicular temperature of the H minority of slightly above 100 keV. The reacting protons are found to have an average energy of ~ 200 keV and the expected corresponding γ line width and shift are 100 keV and 150 keV respectively.

At 5.5 MeV the NaI detector resolution is ~ 180 keV and its response consists mainly of a full energy (FE) peak plus a single photon escape

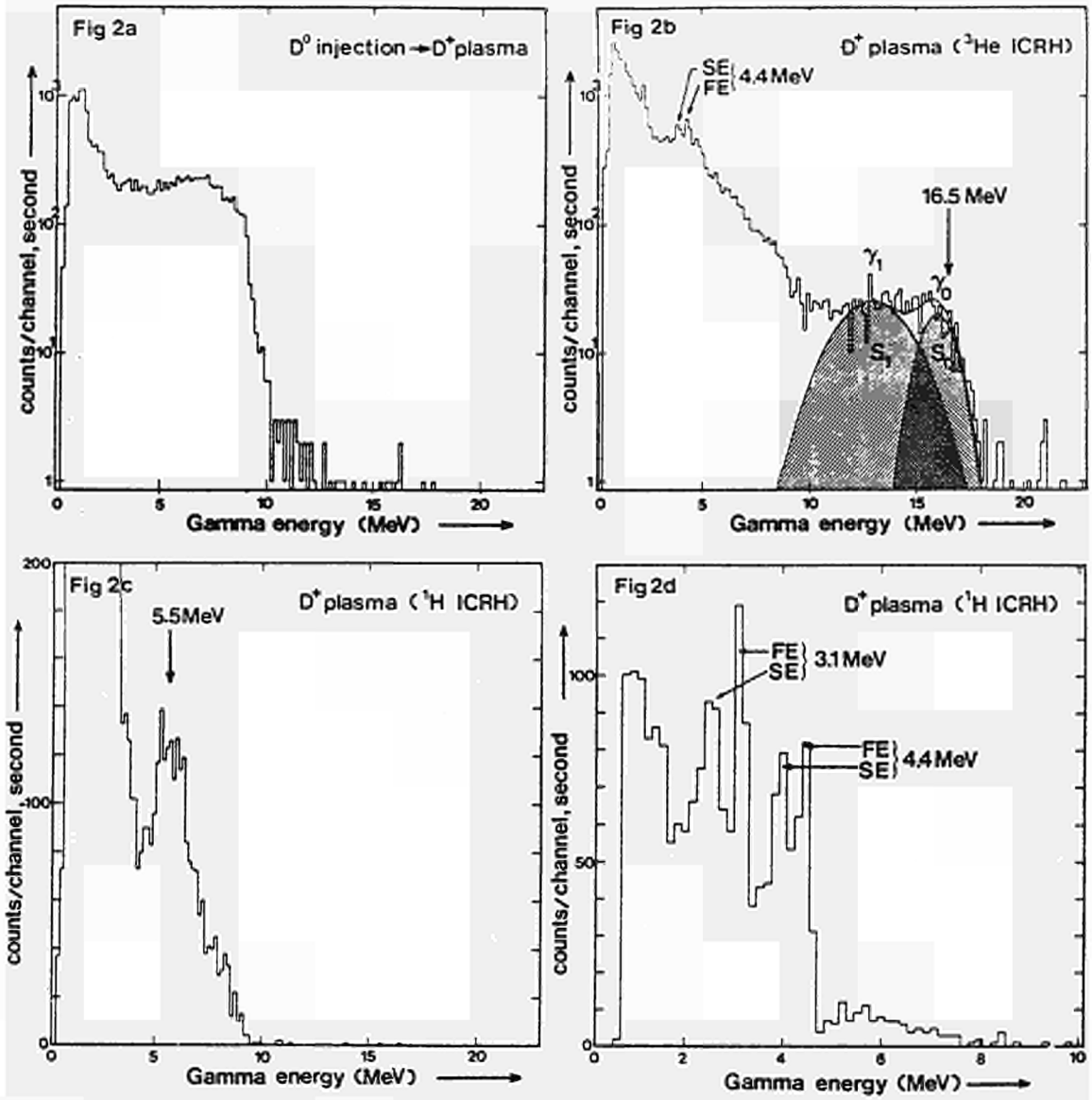

Fig. 2 γ-ray spectra as observed with the NaI detector for various plasma conditions. a) spectrum from a D° beam heated D^+ plasma demonstrating the count rate capability of the system. Only a very few counts are recorded above 10 MeV. b) Spectrum obtained under conditions of ^{3}He minority heating. Count rates in both cases are comparable but the spectrum shape now clearly shows the γ_0 and γ_1 lines from the D(^{3}He,γ)^{5}Li reaction. c) Spectrum showing the broadened D(p,γ)^{3}He 5.5 MeV line and d) the narrow impurity lines at 3.1 MeV and 4.4 MeV during H minority heating. Discharge parameters for 2b are I_p = 2 MA, B_T = 3.4 T, $\hat{T}_e$ = 5.1 keV, $\hat{T}_i$ = 5.0 keV, $\hat{n}_e = 3.7 \cdot 10^{19}$ m^{-3} and P_{rf} = 5.5 MW. The parameters for case 2c are I_p = 2 MA, B_T = 2.1 T, $\hat{T}_e$ = 6.6 keV, $\hat{T}_i$ = 4.7 keV, $\hat{n}_e = 2.7 \cdot 10^{19}$ m^{-3} and P_{rf} = 5.6 MW.

(SE) peak located 511 keV below the FE peak. The observed spectrum however only shows a single very broad peak indicating that the FE peak and SE peak overlap due to line broadening and shift. The calculated line shape mentioned above appears to be slightly narrow to explain the experimental observation. In order to exploit the line shape information completely more detailed calculations are required including folding of the calculated non Gaussian line shape with the detector response as well as the use of a more realistic distribution function.

IMPURITY LINES

A few narrow gamma lines could be observed on many occasions. Their occurrence is clearly correlated with the application of RF power. Careful checks demonstrated that these lines are not due to neutron induced background or to charged particle excitation of vacuum vessel material. One of these lines is at 4.4 MeV and can clearly be identified as emanating from the first excited level of ^{12}C. In the D-^{3}He case (fig 2b), the total number of 15 MeV protons generated and confined in the plasma is sufficient to explain the line strength by inelastic scattering if the ^{12}C concentration in the plasma lies between 3 and 8% of the electron density.

However, the 4.4 MeV line is also observed during H minority heating when energetic protons (E > 4.4 MeV) are not created by fusion reactions (fig 2d). Moreover a further line at 3.1 MeV appears very often either in isolation or together with the 4.4 MeV line (fig 2d). A possible explanation here could be provided by the existence of a very energetic RF driven H minority tail (4.4 MeV line) as well as a moderately energetic deuterium tail from second harmonic heating (3.1 MeV line) as predicted recently on theoretical grounds [8]. The 3.1 MeV line would then originate in the ^{12}C (D,pγ) ^{13}C reaction . The relative intensities of the lines would depend on the details of the H and D distributions as both reactions have rather different cross sections.

CONCLUSION

Gamma-radiation emitted from fusion and nuclear reactions in a tokamak plasma have been definitively observed. Observation of fusion gamma-rays is uniquely important for reactions such as D,^{3}He for which there is no accompanying neutron emission and the charged particles are fully confined in the high current JET plasmas.

REFERENCES

1. S S Medley, F E Cecil, D Cole, M A Conway and F J Wilkinson, Rev Sci Instrum 56 (5) 975 (1985) and references therein.
2. D E Newman and F E Cecil, Nucl Inst Meth 227, 339 (1984).
3. F E Cecil, S S Medley, S L Liew, L P Ku and J Kolibal, Bull Am Phys Soc, 31 (9) 1627 (1986).
4. N R Roberson, S A Wender and D M Drake, Nucl Instr Meth, 214,541(1983)
5. D M Drake, L R Nilsson, J Faucett, Nucl Instr Meth, 188, 313 (1981).
6. F E Cecil, F J Wilkinson, R A Ristinen, R Rieppo, Nucl Instr Meth A234, 479 (1985).
7. F E Cecil, D M Cole, R Philbin, Phys Rev C32 (5) 690 (1985).
8. T Hellsten, JET Joint Undertaking, private communication.

HIGH RESOLUTION T_e MEASUREMENTS IN JET AND THEIR APPLICATION TO THE STUDY OF THE EDGE PLASMA AND DENSITY LIMIT DISRUPTIONS

N A Salmon*, D V Bartlett, A E Costley and M Hugon

JET Joint Undertaking, Abingdon, Oxon OX14 3EA, UK
* Imperial College of Science and Technology, University of London, UK

1. INTRODUCTION

This paper describes a new electron cyclotron emission (ECE) diagnostic for measurements of the electron temperature (T_e) on JET [1]. The distinguishing feature of this diagnostic is the combination of excellent spatial resolution (about 2 cm in the radial direction), good time response (about 10 μs), and the ability to resolve temperature changes down to a few eV. Results are presented for two applications: measurements of the temperature profile in the edge region for a particular JET plasma, and measurements of temperature oscillations preceding density limit disruptions.

2. SYSTEM DESCRIPTION AND CALIBRATION

Radiation from the plasma is coupled into a ~ 40 m long overmoded waveguide system and transmitted to the receiver, figure 1. The latter is based on heterodyne detection and the design is similar to that used by Hartfuss and Tutter [2]. The local oscillator operates at 67 GHz and the mixer is sensitive over the band 73 to 79 GHz. A power divider splits the signals into eight channels and each channel contains a narrow band filter of width ~ 250 MHz. The eight frequencies are equally spaced in the range 73 to 79 GHz. The detectors are Silicon Schottky barrier diodes and the video amplifier chain has a variable bandwidth up to 100 kHz. A rotary waveguide switch permits viewing of a reference plasma noise tube for checking stability.

The system is calibrated by chopping between large area microwave absorbers at the temperature of liquid nitrogen (77 K) and at room temperature. The microwave absorbers are placed in the vacuum vessel during JET shutdown periods. During JET operation, the calibration is checked by cross calibration against a standard ECE Michelson interferometer.

Electron temperature measurements can be made by measuring optically thick ECE in either the fundamental ordinary mode polarization, or second harmonic extraordinary mode polarization, of the electron cyclotron frequency. The receiving frequencies have been chosen so that for o mode observation at B_T = 3.4 T and I_p = 5.0 MA the observed region of the plasma is $3.9 < R < 4.15$ m, ie the outer edge region ($R_{limiter}$ = 4.174m). The spatial resolution is ~ 2 cm in the radial direction and ~ 8 cm in the transverse direction. With the video bandwidth set at 10 kHz the signal/noise is typically 150/1. Different regions of the plasma can be

explored by changing B_T or I_p (because of the poloidal field).

3. MEASUREMENTS OF THE EDGE TEMPERATURE

Measurements of T_e in the core region $R < 3.8$ m, are made routinely on JET using the standard ECE diagnostic. Similarly, measurements in the scrape-off layer $R > 4.2$ m are obtained routinely using Langmuir probes. Measurements in the intermediate edge region are not routinely available and so an attempt was made to measure T_e in this region using the multichannel heterodyne radiometer.

The first attempt was made in the o mode with $B_T = 3.4$ T and $I_p > 4.0$ MA. Substantial non-thermal emission was observed in the low frequency (ie. outer) channels, making the T_e measurements unreliable. Details of this emission will be presented in the poster. By operating at $B_T = 1.7$ T, $I_p = 1.5$ MA, and with a slightly increased aspect ratio = 3.0 (to avoid harmonic overlap), and by measuring the e mode emission in the second harmonic, reliable measurements of the edge T_e profile were obtained, figure 2. The optical depth is < 1 in the edge region and so a correction has been applied using an assumed density profile and simple reflection model [1]. This profile is a reasonable continuation of the T_e profile at $R < 3.8$ m measured by the Michelson interferometer, but shows an increasing deviation as one moves towards the limiter position. This may be due to reduced accuracy in the Michelson measurement in the edge region at this low toroidal field.

4. DENSITY LIMIT DISRUPTIONS

In the second application, the heterodyne radiometer was used to measure the T_e profile with good spatial and temporal resolution, preceding a density limit disruption. The plasma conditions were chosen such that the observation channels spanned the $q = 3$ and $q = 2$ rational surfaces. Specifically, $3.0 < B_T < 3.4$ T and $I_p = 2.0$ MA, and the measurements were made in the O mode fundamental so the observation region was $3.17 < R < 3.99$ m. Other relevant plasma parameters were $R_o = 3.05$ m, $R_{Limiter} = 4.174$ m, $q_\psi = 7.0$, elongation $k = 1.33$ and the maximum volume average electron density was $\sim 1.25 \times 10^{19}$ m^{-3}.

The observations confirm earlier work [3,4], which showed a number of distinct phases leading up to the disruption: firstly a contraction of the temperature profile which leads to a series of growing temperature (and magnetic) oscillations followed by a series of temperature collapses (or soft disruptions) at irregular intervals ultimately leading to the final disruption (figure 3). There are usually 2 successive oscillatory periods. The first, which the magnetic diagnostics identify as predominantly m=3, n=1, is seen by the ECE diagnostic to be localised in a region ~ 8 cm wide centred on R = 3.95 m which is approximately the calculated radius of the q=3 rational magnetic surface. The second, identified by the magnetics as predominantly m=2, n=1, is localised to a region ~ 10 cm wide centred on R = 3.77 m which is within 4 cm of the calculated position of the q=2 rational surface. (This agreement is

within the accuracy of the magnetic equilibrium code calculations). Temperature profiles corresponding to the maxima and minima of the m=2 oscillation are shown in figure 4. There is a periodic localised depression of the T_e profile which develops into a significant localised flattening. The flattening corresponds to the 'O' point of a rotating magnetic island as interpreted from the magnetic diagnostics. Further analysis and measurements will be needed before the driving mechanism for the growth of the island can be identified [3,5].

After the oscillating phase, the magnetic diagnostics show that the island stops rotating and locks in a fixed toroidal position such that the 'O' point of the island is close to the location of the ECE viewing antenna [6]. As shown in figure 3, there are repeated changes in the temperature profile in which localised flat regions develop and disappear as the discharge undergoes soft disruptions.

We would like to acknowledge the co-operation of E Lazzaro, S Nowak and J Snipes in obtaining and interpreting the magnetic signals, and D J Campbell for providing useful comments.

[1] N A Salmon, D V Bartlett and A E Costley, Proc. Workshop on Basic and Advanced Fusion Plasma Diagnostic Techniques, Varenna 1986, JET-P-(86)45 (to be published).
[2] H J Hartfuss and M Tutter, Rev Sci Inst 56, 1703 (1985).
[3] J Wesson et al, Proc. 12th European Conference on Controlled Fusion and Plasma Physics, Budapest 1985, I 147.
[4] D J Campbell et al, Paper IAEA-CN-47/A-VII-5, Proc. 11th International Conference on Plasma Physics and Controlled Nuclear Fusion Research, Kyoto 1986.
[5] P H Rebut and M Hugon, in Plamsa Physics and Cont Nucl Fusion Res (Proc 10th Int Conf, London, 1984) 2, IAEA Vienna (1985) 197.
[6] J Snipes et al, this conference.

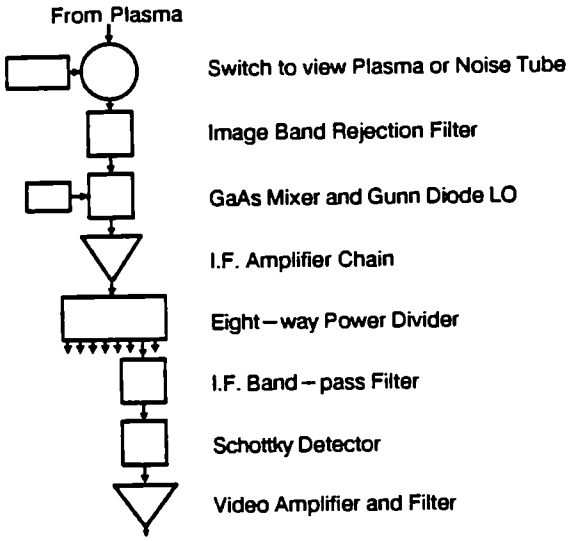

Figure 1: Block diagram showing the essential components in the Heterodyne Radiometer.

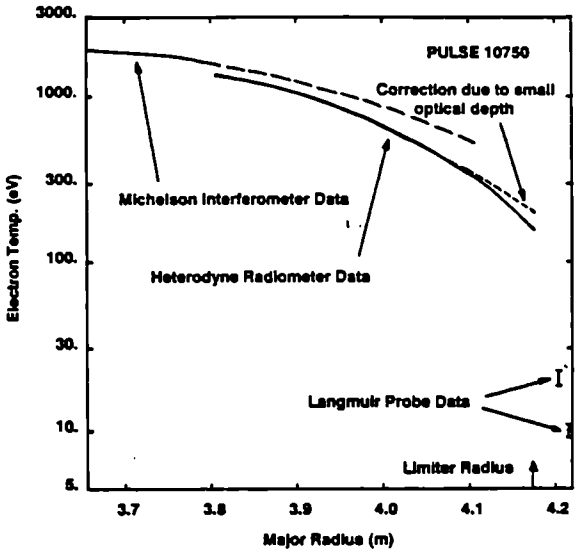

Figure 2:
Temperature profile in the edge region of JET, measured by two ECE diagnostics and the Langmuir Probe.

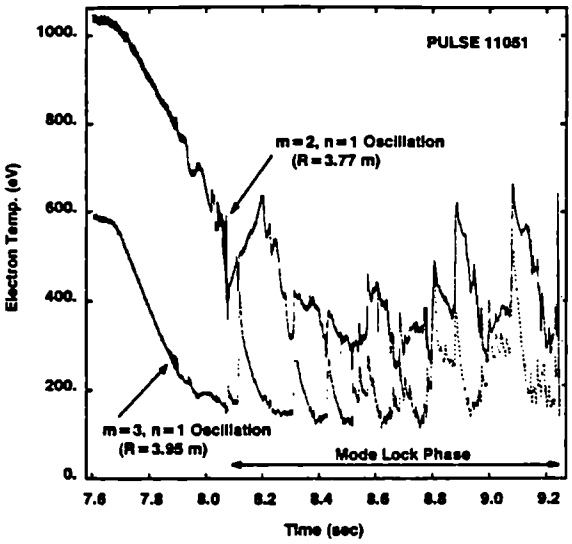

Figure 3:
Two channels of the Radiometer showing temperature oscillations and the mode lock phase leading up to a density limit disruption.

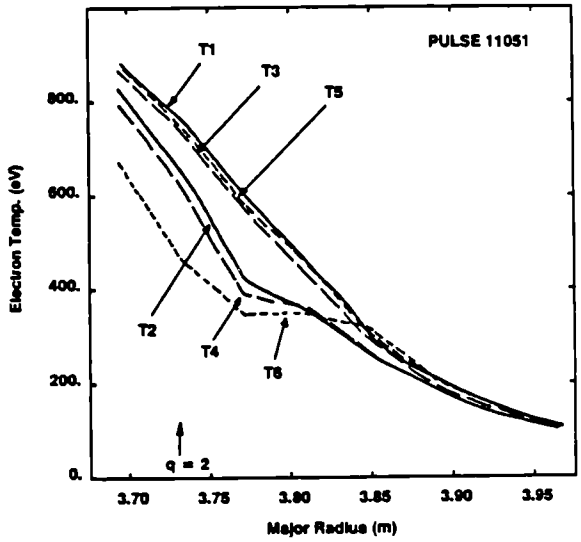

Figure 4:
Temperature profiles during the m=2, n=1 oscillation, at the times marked on fig. 5.

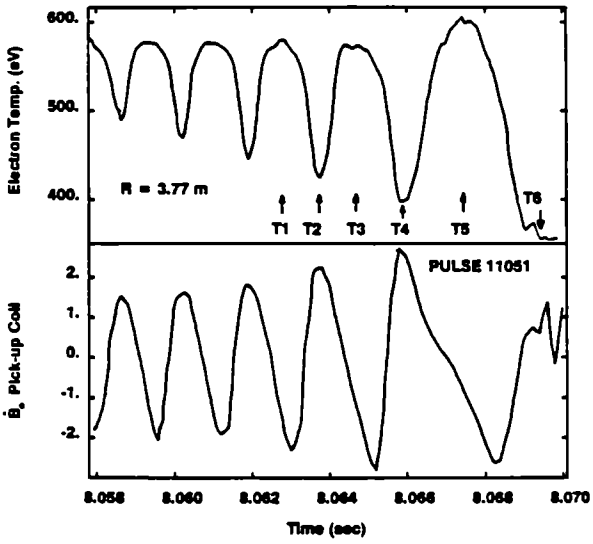

Figure 5:
Temperature near the q=2 surface and the $\dot{B}_\theta$ signal during the m=2, n=1 MHD oscillation.

MEASUREMENT AND ANALYSIS OF TWO-DIMENSIONAL ELECTRON TEMPERATURE PROFILES IN JET USING ECE

D V Bartlett, D J Campbell, A E Costley, S E Kissel
S Nowak, M Brusati and E Lazzaro

JET JOINT UNDERTAKING, ABINGDON, OXON OX14 3EA, UK.

1 Introduction

The JET electron cyclotron emission (ECE) diagnostic employs twelve spectrometers viewing the plasma along ten sightlines which are distributed poloidally in a fan-shaped array [1,2]. This enables the diagnostic system to be optimised for various studies relating to such topics as plasma transport and mhd activity. It is particularly important in an elongated geometry such as JET's to confirm that the calculated poloidal flux surfaces are isotherms. Therefore, four sightlines are devoted to broadband spectral measurements with a system of Michelson interferometers. Analysis of second harmonic extraordinary mode ECE has enabled us to construct two-dimensional temperature contours and compare them with flux surfaces derived from the JET equilibrium codes [3].

2 Measurement System

Details of the JET ECE Diagnostic may be found in [1,2]. The sightlines used for the observations reported here are shown in figure 1: a horizontal channel 13 cm below the torus midplane and three channels which view the upper half of the plasma at angles of 17.5^{o}, 25.5^{o} and 33^{o} to the midplane. Rapid-scan Michelson interferometers measure the ECE spectrum in the range $70 < f < 600$ GHz with a frequency resolution of ~10 GHz and a time resolution of ~15 ms. The absolute spectral response of each channel is determined by means of a portable large area hot body [4] which is placed inside the JET vacuum vessel [5]. Uncertainties in the calibration of the system response are the dominant source of uncertainty in the measured electron temperature profiles. It is estimated that the uncertainty in the level of the derived temperatures is $\pm$ 10%, and the uncertainty in the shape of the temperature profiles is $\pm$ 5%.

The time and spatial dependence of the electron temperature is derived using second harmonic extraordinary mode emission. Overlap with the third harmonic limits the region in which the temperature can be determined unambiguously to $2.8 < R < 4.2$ m. As the JET plasma fills the region $1.7 < R < 4.2$ m, just over half the electron temperature profile can be obtained. Antenna pattern width and spectral resolution average the temperature information over a volume ~15 cm along the line of sight and ~15 cm perpendicular to the line of sight. The signal to noise ratio in the measurements is $\geq$ 100:1.

In small aspect ratio, high current tokamaks such as JET, corrections to the total magnetic field, due to paramagnetism ($\beta_p < 1$) or diamagnetism ($\beta_p > 1$) and the poloidal field profile, play a significant role in the frequency-to-space conversion necessary for the interpretation of the emission spectra as temperature profiles. Previous analyses [2] have employed cylindrical, low-β approximations for these corrections, which

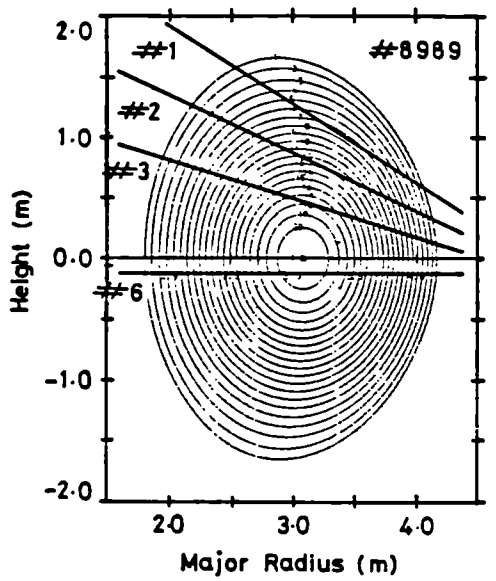

Fig 1: Cross-section of JET plasma showing sightlines used for two dimensional temperature measurements.

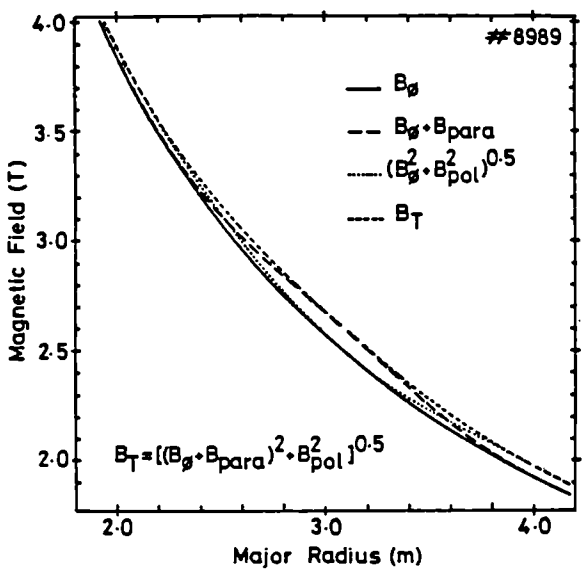

Fig 2: Spatial dependence of calculated corrections to vacuum toroidal field and resultant total field.

have, in the main, proved adequate. However, the extension of the system to two-dimensional measurements and the increasing plasma performance achieved with powerful additional heating have necessitated the use of a more accurate calculation of the internal magnetic field derived from the full solution of the magnetic equilibrium which calculates an optimum fit to the magnetic measurements [3]. Note that this does not constrain the isotherms derived from the ECE measurements to follow the calculated flux contours. Figure 2 shows the contributions to the total magnetic field, derived from the equilibrium calculation. This point is further illustrated in figure 3, which shows temperature profiles from three of the four channels. The solid lines show profiles obtained using the cylindrical approximations, and the symbols show profiles calculated using the full solution for the total magnetic field. Typically there is a shift of 5-10 cm in the radial location of the profiles (compared to the typical error of ~30 cm which results if only the toroidal vacuum field is used).

3 Analysis

Two-dimensional temperature measurements have been obtained under a wide range of plasma conditions, both in ohmic and additionally heated discharges, and in limiter and internal separatrix (X-point) plasmas. It is found that, in general, results from the most extreme poloidal channel (#1 at 33^o) are unreliable due to the fact that the plasma is optically thin over a large part of the radial viewing range, and radiation from the hot central region of the plasma may be reflected into the line of sight of the antenna. A sophisticated emission code [6] is being developed to allow further interpretation of these measurements, but these are not incorporated in the present analysis.

Temperature profiles from the remaining three channels, projected onto the major radius coordinate, are shown in figure 3 - the individual symbols indicate the profiles derived using the full calculation of the magnetic

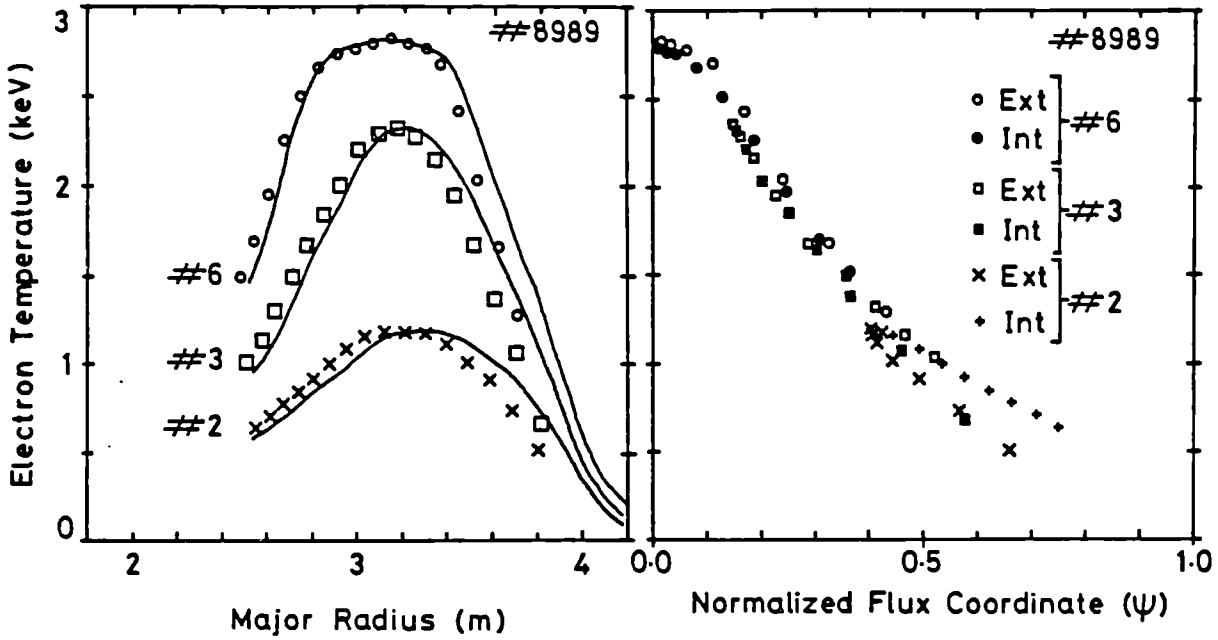

Fig 3: Temperature profiles along three sightlines, projected onto the major radius coordinate.

Fig 4: Temperature profiles along three sightlines as a function of the calculated flux coordinate ψ.

field. These were obtained during the ohmic phase of a JET discharge with I_p=2.5 MA, B_ϕ=2.6 T, $\bar{n}_e(0)=2.6.10^{19}$ m^{-3}, κ=1.45. As expected, the maximum temperature along each sightline decreases with increasing poloidal angle. The fact that the flux surfaces derived from the magnetic equilibrium codes are indeed isotherms is illustrated in figure 4, where the temperature profiles from the three channels are plotted as a function of the flux coordinate ψ. In addition, the profiles are folded about the magnetic axis to emphasise their symmetry in ψ-space. It is found that temperatures derived from channel #2 (25.5°) are routinely too low by ~15%, ie they lie close to the limit of the estimated systematic uncertainties in the absolute calibration. A final conclusion from figure 4 is that the ECE is localised both in the horizontal plane (due to the magnetic field gradient) and in the vertical plane (due to the narrow acceptance angle of the diagnostic viewing optics).

To facilitate the derivation of isothermal contours in the poloidal cross-section with the present limited number of viewing channels, an assumption of up-down symmetry for the horizontal channel is made, and the sightline is reflected in the torus midplane. The two-dimensional contours derived are shown in figure 5, where they are superimposed on flux surface contours derived from the calculation of the magnetic equilibrium. The good agreement obtained over the region of plasma currently accessible to the ECE diagnostic is typical for the majority of plasma conditions investigated to date. These extend over a substantial fraction of the JET operating regime: $1 \lesssim I_p \lesssim 3$ MA, $2 \lesssim B_\varphi \lesssim 3.4$ T, $2 \lesssim n_e \lesssim 3.10^{19}$ m^{-3}, $1.3 \lesssim \kappa \lesssim 1.7$; both in ohmic and additionally heated (NBI and ICRH) discharges; and in limiter and X-point configurations in the L-mode confinement regime. A significant discrepancy has been found in the X-point configuration in the H-mode regime, and it is thought that the

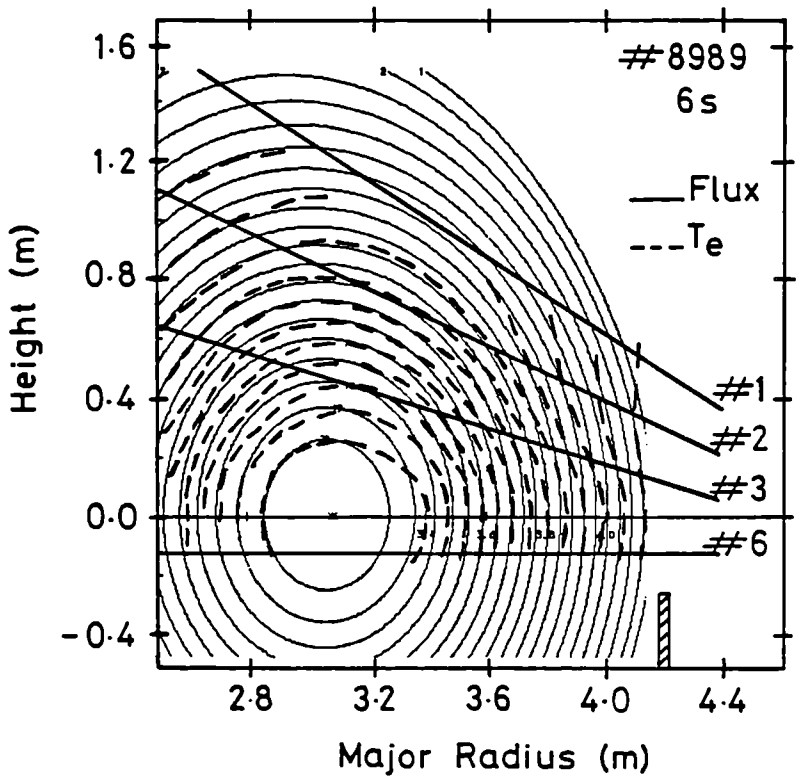

Fig 5: Two-dimensional temperature contours (broken lines) plotted in the poloidal cross-section of JET. Within experimental uncertainties, these are in good agreement with the calculated magnetic flux surfaces which are shown as solid lines.

differences may be due to anisotropies in the pressure distribution which are not yet properly accounted for in the equilibrium codes.

4 Conclusions

Derivation of two-dimensional electron temperature profiles from ECE measurements in JET have established that, in the region accessible to the ECE diagnostic and within the experimental uncertainties, the magnetic flux surfaces are isothermal contours under most operating conditions. As a final point it should be noted that refraction of the ECE is not a significant problem at the densities for which this analysis has been made. At higher densities a more sophisticated analysis will be made using the simulation/interpretation codes currently being developed [6].

5 References

[1] A E Costley et al, Proc EC-4, 4th Int W'shop on ECE and ECRH, Rome, March 1984, 1-10.
[2] A E Costley et al, Bull Am Phys Soc 30 1361 (1985).
[3] D J Campbell et al, JET Preprint JET-P(86)46 (to be published).
[4] E A M Baker, National Physical Laboratory, U K, private communication.
[5] S E Kissel et al, Proc EC-5, 5th Int W'shop on ECE and ECRH, San Diego November 1985, 65-73.
[6] G Ramponi et al, ibid, 10-17.

FIRST T_e PROFILE RESULTS FROM THE JET LIDAR-THOMSON SCATTERING SYSTEM

C Gowers, B Brown, A Gadd, M Gadeberg, K Hirsch+, H Murmann*
P Nielsen, H Salzmann+, C Schrödter°
JET Joint Undertaking, Abingdon, Oxon OX14 3EA, UK
+ On attachment from Institut für Plasmaforschung, Universität Stuttgart, 7000 Stuttgart 80, FRG
* Max-Planck-Institut für Plasmaphysik, 8046 Garching, FRG
° Max-Planck-Institut für Quantenoptik, 8046 Garching, FRG

INTRODUCTION - The application of 180° Thomson scattering using short (~ 300 ps) laser pulses for measuring electron temperature and density profiles in large fusion devices was proposed in /1/. With the short laser pulse method, spatial resolution along the laser beam is achieved by high-speed detection techniques allowing time-of-flight measurements /2/. This LIDAR (Light Detection and Ranging) technique was applied for the first time on the JET tokamak. The JET LIDAR Thomson Scattering diagnostic is described in outline below. The first electron temperature profiles obtained with the system are presented and compared with those obtained using other JET diagnostics.

THE LIDAR THOMSON SCATTERING SYSTEM - Figure 1 shows the optical set-up of the diagnostic. A ruby laser pulse of 220 ps duration is directed radially into the tokamak vessel in the equatorial plane and dumped on a carbon tile at the inner torus wall. The laser beam inside the vessel has a constant diameter of 50 mm. During the measurements described here, the laser (JK LASERS (Lumonics) Rugby, UK), capable of 5 J operation at up to 0.5 Hz repetition rate, was operated at 2 J and single shot.

a) Laser - The laser consists of an actively mode-locked oscillator, two single pulse selectors (Pockels cell shutters) in series to attenuate spurious background pulses and four stages of amplification. Two vacuum spatial filters are also included in the amplifier train.
b) Input Optics - In the initial set up described here the laser beam was directed to the Torus 60 m away by a simple mirror system. Imaging optics and a vacuum pinhole system will be used in the future.
c) Collection Optics - The backscattered light is collected by a folded spherical mirror system through an array of six windows surrounding the central laser input window on the JET vessel. Its effective solid angle of collection is 5.5×10^{-3} sr. The collection optics and the labyrinth mirror system, which transmits the collected light through the 2.2 m thick biological shield, is shared with the single spatial point 90° Thomson scattering system on JET /3/, for which it was constructed. The two collected light beams are separated from each other in the entrance slit plane of the polychromator of the single point scattering system. The entrance slit is surrounded by a broadband mirror which directs approximately 95% of the scattered light from the LIDAR laser beam into the LIDAR polychromator.
d) Polychromator - The three main features of the LIDAR polychromator are extremely high optical throughput of 1 cm^2sr, high average

transmission of the six spectral channels (about 70%) and rejection of ruby laser stray light by a factor greater than 10^5. This performance is achieved with a filter polychromator in which the incident light is shone onto a stack of short wave pass interference edge filters with decreasing cut-on wavelengths, the filters being tilted slightly with respect to each other /4/. The transmission bandwidth of a spectral channel observing reflected light from this filter stack is defined by the cut-on wavelengths of two adjacent filters of the stack and by a suitably chosen coloured glass filter in front of each detector. Additional short wave pass filters in front of each detector improve further the rejection of stray ruby laser light. The collection mirrors, which are illuminated homogenously by scattered light during the passage of the laser pulse through the plasma, are imaged onto the filter stack. In this way slight variations of the cut-on wavelengths across the surface of the 200 mm diameter edge filters are averaged in the same way when the scattering volume moves through the plasma. In the course of the first measurements, reported here, only four of the available six spectral channels were used. Their transmission bands were 660-626 nm, 639-601 nm, 598-534 nm and 530-480 nm, respectively.

e) Detectors and Digitizers - The high speed detection of the backscattered light pulse is accomplished using proximity focused MCP photomultipliers (ITT F 4128) with 20 mm diameter photocathodes. The output signals are registered by TEK 7912 AD transient digitizers with 7 A 29 vertical amplifier plugs-in. The overall bandwidth of the complete detection and registration system is approximately 700 MHz.

f) Stray Light Suppression - Ruby laser stray light pulses arriving at the detectors before the scattered signal are suppressed very effectively (by a factor of 10^{13} /4/) by gating the photocathode to MCP gap of the detectors. The flat top of the gate is about 30 ns long and the ringing, coupled to the detector output by the 10 ns risetime/150 V amplitude gating pulse, is kept below 10 mV. An intense stray light pulse occurs after the measurement when the laser pulse strikes the carbon tile dump at the Torus inner wall. This stray light burst causes a 300 V/0.5 ns electrical pulse at the output of the detectors and a high speed, pulse clipping diode circuit in the signal lead is used to protect the vertical amplifier plug-ins of the digitizers /5/.

RESULTS - Figure 2 shows an overlay of the detector signals recorded by the digitizers both when the laser was pulsed a) during a JET pulse (full curve) and b) with no plasma present in the JET vacuum vessel (dashed curve).

The base lines prior to gating on the detector appear in region 1. For region 2, as the detectors were gated on, a 'switch on' peak was observed due mostly to the presence of some spurious laser stimulated fluorescence from a (temporary) mask surrouding the laser input mirror figure 1. This spurious source of stray light will be avoided in the future when the imaging input optics is installed. The difference between the continuous and dashed curves in region 3 shows the expected low plasma light level, a merit of the LIDAR system resulting from the short integration time in the detection system. Thus, the difference between the two curves in region 4 is predominantly due to the scattered light from the laser pulse as it propagates through the plasma.

The signal traces are effectively terminated by the arrival of the stray light burst caused by the laser pulse striking the carbon dump tile at $t \simeq 48$ ns. No stray light pulses from the main laser pulse were observed during the 17 ns scattering record, region 4, but the effect of a low level (10^{-*}) laser pre-pulse striking the dump - 2 ns before the main pulse can be seen on digitizer 1 at - 46 ns. The pre-pulse has since been removed by more careful setting up of the laser oscillator.
The scattered light signals from figure 2 have been time correlated using the data obtained from a test experiment in which the peak of the stray termination pulse was displayed by using optical attenuation in front of each detector. The time marker so obtained is also indicated in figure 2. In this first analysis, the electron temperature has been fitted to each 500 ps time averaged segment of the channel data in region 4. The resultant T_e profile is shown in figure 3a where it is compared with the partial T_e profile obtained from the JET ECE diagnostic /6/. At this time during the discharge - 6 MW of RF heating power were being applied to the plasma, producing a moderately high central electron temperature.
In contrast figure 3b shows a low T_e case just after pellet injection in which a central electron temperature of a factor of 4 lower is indicated. Once again good agreement between the profile data from the two diagnostics is obtained. In fact the LIDAR system to date has been used successfully over the 0.2-5.0 keV temperature range. Also from figure 3b, the steep temperature gradient around 2.6 to 2.8 m indicates that the spatial resolution of the diagnostic is 0.10-0.15 m as expected.

CONCLUSION - The first electron temperature profiles have been obtained with the LIDAR Thomson Scattering diagnostic on the JET Tokamak.
The full T_e profiles are in good agreement over a wide range of plasma conditions with partial profiles obtained by the ECE technique.
A spatial resolution for the diagnostic of 0.10-0.15 m is indicated with this preliminary data set.

ACKNOWLEDGEMENT - It is a pleasure for the authors to acknowledge the support and encouragement received from all their colleagues at JET, Risø National Laboratory, Denmark, Stuttgart University and MPQ Garching FRG. We are also indebted to the JET ECE group for the use of their temperature profile data.

REFERENCES

/1/ H Salzmann, K Hirsch, Rev Sci Instr 55 (84), 457.
/2/ R Kristal, Diag. for Fusion Exps, Varenna 1978, p 617, EUR 6123.
/3/ P Nielsen, Course on Diagnostic for Fusion Reactor Conditions, Varenna 1982, Vol 1, p 225, EUR 8351-1EN.
/4/ C Gowers, M Gadeberg, K Hirsch, P Nielsen, H Salzmann et al, Course and Workshop on Basic and Advanced Fusion Plasma Diagnostic Techniques, Varenna 1986, page 205, Vol 2.
/5/ J Bundgaard et al, private communication, Risø National Laboratory.
/6/ A E Costley et al, in Controlled Fusion and Plasma Physics (Proc 12th European Conference, Budapest 1985) 9F-I (1985) 227.

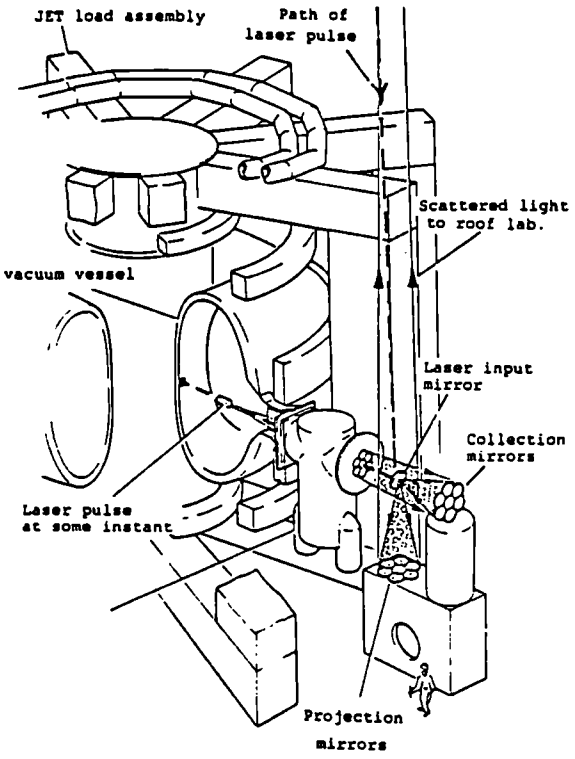

FIG 1. SCHEMATIC OF LIDAR THOMSON SCATTERING DIAGNOSTIC ON JET

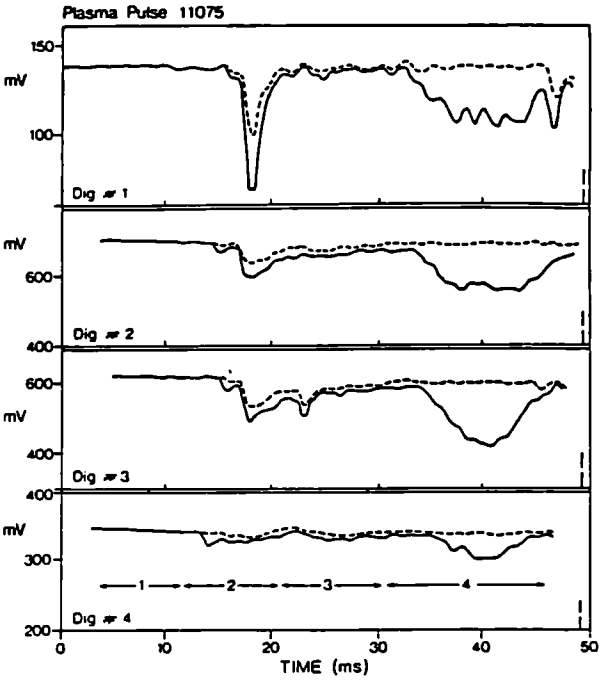

Signals output by the digitisers (a) During a Plasma pulse (full curve)
(b) During Laser only shot - no plasma (dashed)
Region 1 - Detector output prior to gating on (baseline)
Region 2 - Detector output during gating on
Region 3 - Detector output due to Plasma light
Region 4 - Detector output during period laser pulse traverses plasma

The vertical bar indicates the fiducial marker for each digitiser signal

Fig 2

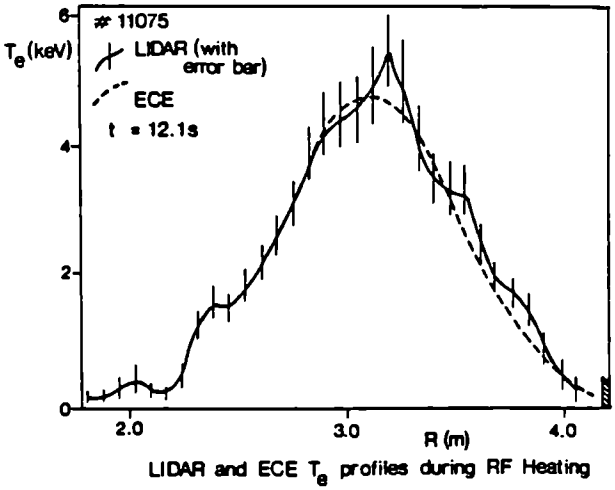

LIDAR and ECE T_e profiles during RF Heating

Fig 3a

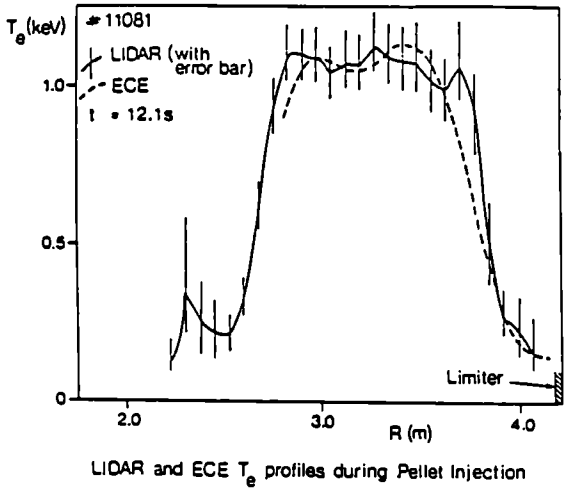

LIDAR and ECE T_e profiles during Pellet Injection

Fig 3b

TRANSIENT STABILIZATION OF SAWTEETH BY ADDITIONAL HEATING IN JET

D J Campbell, D V Bartlett, V P Bhatnagar[1], M Bures, G A Cottrell, P A Duperrex[2], C D Challis, J G Cordey, A W Edwards, C Gormezano, C W Gowers, R S Granetz, J H Hamnen[3], T Hellsten, J Jacquinot, E Lazzaro, P J Lomas, N Lopes Cardozo[4], P Mantica[5], J A Snipes, D F H Start, D Stork, P E Stott, P R Thomas, E Thompson, K Thomsen, G Tonetti[2] and J A Wesson

JET JOINT UNDERTAKING, ABINGDON, OXON OX14 3EA, UK.
[1] EUR-EB Association, LPP-ERM/KMS, B-1040 Brussels, Belgium.
[2] CRPP/EPRL, 21 Avenue des Bains, CH1007 Lausanne, Switzerland.
[3] Swedish Energy Research Commission, S-10072 Stockholm, Sweden.
[4] FOM Instituut voor Plasmafysica, 3430 Be Nieuwegein, The Netherlands.
[5] EURATOM-CNR Fusion Association, Milan, Italy.

1 Introduction

During additional heating in JET, sawtooth activity normally dominates the evolution of the plasma core, limiting plasma temperature and density. However, in some experiments with auxiliary powers of above 5 MW (ICRH plus NBI, ICRH alone, or NBI alone), the plasma undergoes a transition to a new regime in which the sawtooth instability is suppressed for periods of up to 1.6 s and the level of long wavelength coherent mhd activity is very low. The long quiescent period (3-5 energy replacement times) allows plasma transport and confinement to be studied in a regime free from mixing due to sawteeth, and permits an evaluation of the possible benefits of sawtooth stabilization for near-ignition conditions.

2 Experimental Observations

Experiments with additional heating have been carried out in JET at total power levels of up to 19 MW, using an NBI system capable of delivering up to 10 MW of 80 keV deuterons into the torus, and an ICRH system which has injected up to 8 MW into the plasma [1]. The experiments reported here utilised NBI co-injection and on-axis ICRF resonance heating. Under such conditions, the sawtooth and mhd activity exhibit two distinct types of behaviour. In the more usual [2,3], the sawtooth period increases by a factor of 2-3 relative to the ohmic phase of the discharge, ie up to ~0.5 s, and the relative modulation $T_e(max)/T_e(min)$ increases to ~2 compared to 1.1-1.2 during ohmic heating. A variety of mhd activity accompanies the sawteeth.

The second, newly observed and significantly different type of behaviour is illustrated in fig 1. The rise of the 'sawtooth' beginning at 9.6 s exhibits weak mhd activity. In a number of cases, a small partial sawtooth also occurs. However, after 300-400 ms the mhd activity becomes quiescent ($\tilde{B}_\theta/B_\theta \lesssim 5.10^{-5}$). In many cases both the density and stored plasma energy rise continuously until the sawtooth collapse occurs, although the central electron temperature saturates. This saturation lasts for ~0.7 s (and can last for up to 1.4 s), during which no low m,n number mhd activity is

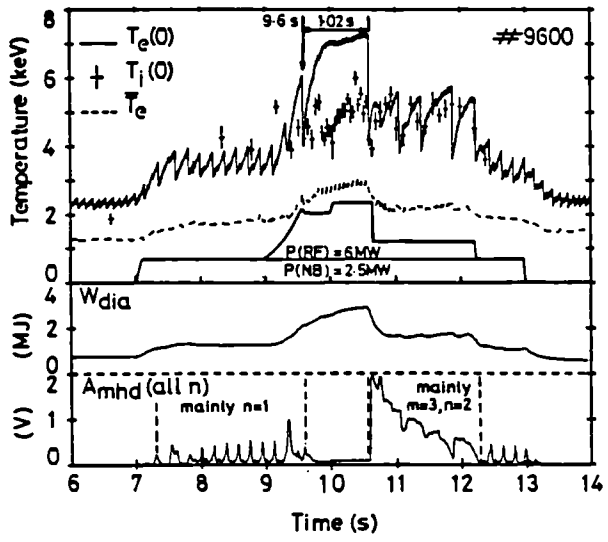

Fig 1: Evolution of a JET discharge in which sawtooth stabilization occurred.

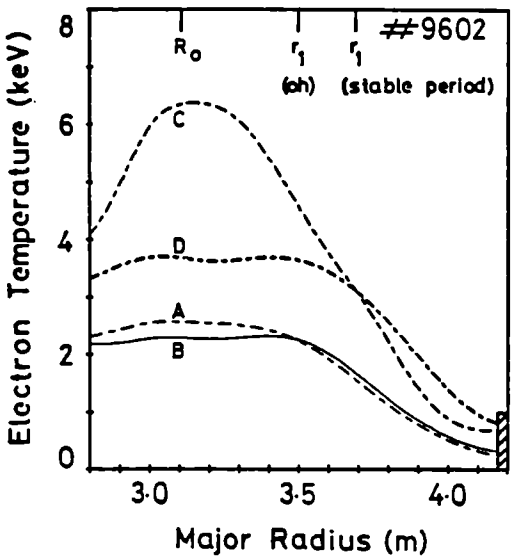

Fig 2: Electron temperature profiles before (A) and after (B) an ohmic sawtooth, and before (C) and after (D) the collapse terminating a stable period such as that in Fig 1.

observed by ECE, soft X-ray diagnostics, or magnetic pick-up coils. Throughout this period, therefore, the m=1 mode appears to be stabilized. A significant consequence is that the global energy confinement time can improve by up to 20% relative to the normal sawtoothing regime.

The stable period is terminated by an m=n=1 instability which exhibits the dynamics of the normal sawtooth collapse in JET [4], but, in addition, an m=3,n=2 mode is often destabilized, as shown in fig 1. This may be due to changes in the current profile during the stable period which could lead to a steep current gradient at the q=3/2 surface at the sawtooth collapse (note that the edge value of q remains virtually constant). The observed expansion of the sawtooth inversion radius r_1, from ~40 cm during the normal sawtoothing regime to 50-60 cm at the collapse terminating the quiescent period, provides further evidence for changes in the current profile during this time. Fig 2 illustrates the expansion of the inversion radius as observed in the electron temperature profiles. More precise measurements with an ECE polychromator and soft X-ray tomography confirm this result. In discharges where the (3,2) mode is quenched during the auxiliary heating phase, or is not excited, subsequent long stable periods can occur (up to 1.6 s in duration). However, a mode with n=1 (usually m=2) may also be destabilized [5]. In these cases, the mode locks after ~50 ms, leading to a significant deterioration in central temperatures, and a degradation of ~25% in global energy confinement time.

The quiescent regime has been obtained under a wide range of conditions in JET (I_p=2-5 MA, B_φ=2-3.4 T, q_ψ=3.4-6, $\bar{n}_e$=1.5-4.$10^{19}m^{-3}$), but no crucial parameter has yet been identified. The regime occurs in plasmas limited on

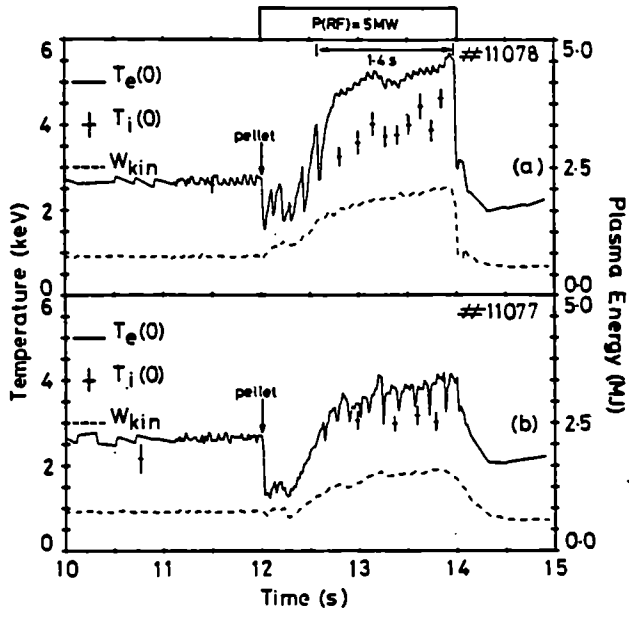

Fig 3: (a) Sawtooth stabilization following pellet injection.
(b) Similar discharge with 'locked' n=1 mode. Note lower stored energy.

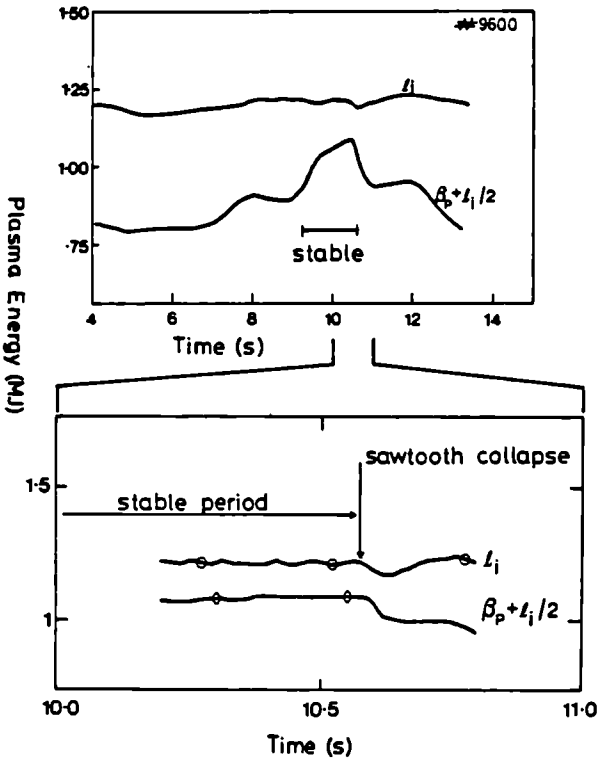

Fig 4: Behaviour of l_i and $\beta_p+l_i/2$ during a discharge in which stabilization occurred.

the outer limiter, the torus inner wall, or by a magnetic separatrix. It was first observed during combined heating (NBI plus ICRH), but has subsequently been attained with ICRH alone, in He^3(H), D(H), and D(He^3) minority heating schemes, and with NBI alone. Sawtooth stabilization has also been observed following pellet injection into ICRF heated discharges, and such a case is shown in fig 3a. Significantly, in similar discharges where stabilization did not occur (fig 3b) a locked n=1 mode was observed accompanied by substantially degraded confinement.

3 Analysis

Detailed measurements of the current profile j(r) in ASDEX have shown that sawtooth stabilization by lower hybrid current drive is due to a broadening of the current profile which raises q(0) above 1 [6]. We have investigated the evolution of j(r) during the quiescent period in JET by analysis of magnetic measurements using the JET equilibrium codes [7]. While the analysis indicates that q(0) lies in the range 0.9–1.0 during this time, the systematic uncertainty (~20%) in the derived value of q(0) makes it impossible to determine unambiguously whether q(0) is above or below 1. The most significant result obtained is that the plasma inductance l_i remains constant, or decreases slightly (fig 4), indicating that j(r) is not peaking, in spite of the strong peaking of T_e.

The good agreement between observations of the sawtooth collapse in JET [4], and the predictions of an ideal instability model [8] suggests that a

mechanism involving a broadening of j(r), so that q(0)>1, is the most likely explanation of the sawtooth suppression. The substantial mhd activity which follows the quiescent period, in particular the destabilization of the (3,2) and (2,1) modes, further suggests that a current profile modification is occuring. However, since the calculated beam-driven current profile is too peaked to maintain q(0)>1, and since ICRH is not expected to drive currents, explanations involving non-inductive current drive seem to be excluded. Calculations of the bootstrap current profile using the measured temperature and density profiles in JET predict that the total bootstrap current should increase, from ~50 kA during the ohmic phase of the discharge, to over 100 kA during the quiescent period. However, resistive diffusion calculations show that this would be insufficient to maintain q(0)>1 for the required period. As yet, therefore, there is no mechanism for curent profile broadening which would quantitatively explain the stabilization.

Alternative explanations involving energetic particles cannot be eliminated conclusively, but the density of such particles appears insufficient to produce stabilization on the basis of current theoretical understanding. A further possibility is that a change in the impurity profile could directly affect the rate of current diffusion. However, the extreme peaking of the temperature profile would necessitate a substantial change in the central impurity density of, perhaps, a factor of 3, which is far greater than actually observed.

The most significant aspect of these results is that it may be possible to suppress sawteeth without active stabilization measures. However, the present transient stabilization, can be followed by a deterioration of the plasma behaviour at the sawtooth collapse. A further important point is that the long stable period (3-5 energy confinement times) allows potential advantages of full sawtooth stabilization to be evaluated. It is found that the energy confinement time can be 15-20% higher than in the normal sawtoothing regime, but this appears to be the result of allowing the plasma to approach equilibrium rather than an improvement in transport. The major advantage is expected to be a significant enhancement of the D-T fusion yield which, in the near-ignition regime, is approximately proportional to $n_i^2 T_i^2$. Our calculations predict a substantial gain in fusion power production if the appropriate profiles can be achieved.

4 References

[1] P H Rebut et al, Proc 11th Int Conf on Plasma Phys and Contr Fus Res, Kyoto, Japan, 1986.
[2] D J Campbell et al, ibid.
[3] R D Gill et al, Proc 13th EPS Conf, Schliersee, W Germany, 1986, 1 21.
[4] A W Edwards et al, Phys Rev Lett, 57 210 (1986).
[5] J A Snipes et al, this Conference.
[6] K McCormick et al, Phys Rev Lett, 58 491 (1987).
[7] D J Campbell et al, JET Preprint JET-P(86)46 (to be published).
[8] J A Wesson, Plasma Phys Contr Fus 28(1A) 243 (1986).

HEAT PULSE PROPAGATION IN RELATION TO THE ENERGY CONFINEMENT IN JET

N.J. Lopes Cardozo[+], B.J.D. Tubbing[+], D.J. Campbell, A. Cheetham, A. Gondhalekar.

JET JOINT UNDERTAKING, ABINGDON, OXON, OX14 3EA, UK.

+ On attachment from: FOM Instituut voor Plasmafysica, Nieuwegein, The Netherlands.

INTRODUCTION

Heat Pulse Propagation (HPP) studies [1-3] have in general resulted in values for the heat diffusivity χ_e of the electron channel that exceed the estimates based on the evaluation from the power balance. No satisfactory explanation for these discrepancies has been given yet. In this paper (see also [4]), which summarises the main results of heat pulse studies in JET, we set out to resolve these discrepancies. We examine the relation between the static (power balance) and dynamic (HPP) methods of assessing χ_e.

THE INCREMENTAL HEAT DIFFUSIVITY

Fig.1a is a plot of total stored energy W versus total input power P (n_e=2.5 $10^{19}m^{-3}$, B_T=3T, I_p=3MA). The plot shows that $\tau_E \equiv W/P$ decreases with increasing input power. In JET, as in many other machines, these W(P) plots can be described by an offset straight line, the slope of which is called the incremental energy confinement time $\tau_{E,inc} \equiv dW/dP$.

From the energy confinement time we derive a value $\chi_{e,pb}$ for the heat diffusivity at a radius r = 2/3 a, using the well-known relation $\chi_{e,pb} = ab/4\tau_E$ (Eq1), where a,b are the horizontal and vertical minor radii. This expression is derived assuming that the heat flow per unit area in the electron channel, q_e, can be expressed as $q_e = - n_e \chi_e \nabla_r T_e$ (Eq2). Since χ_e may depend on $\nabla_r T_e$, a change of q_e induced by a variation of $\nabla_r T_e$ is governed by the incremental heat diffusivity $\chi_{e,inc}$, defined by $\chi_{e,inc} \equiv (1/n_e) dq_e/d\nabla_r T_e$. It can be shown that $\chi_{e,inc}$ is related to $\tau_{E,inc}$ by the analog of Eq1, $\chi_{e,inc} = ab/4\tau_{E,inc}$. From Fig.1a we derive $\tau_{E,inc}$ = 210 ms, and $\chi_{e,inc}$ = 2.5 m^2s^{-1}, for the discharge conditions concerned.

The concept $\chi_{e,inc}$ can be further illustrated by evaluating a local power balance at r=2/3 a. This is the radius at which the HPP measurements are done. Fig.1b shows the local temperature gradient ∇T_e versus the power P_e transported by the electrons through the flux surface (of area S), with P_e normalised on local density. The plot has again the character of an offset straight line, the slope of which yields the incremental heat diffusivity. The fitted line in the plot corresponds to $\chi_{e,inc}$ = 2.5 m^2s^{-1}, consistent with the value derived from $\tau_{E,inc}$. It is important to observe that the χ_e relevant to a perturbation of the temperature gradient is $\chi_{e,inc}$ and not $\chi_{e,pb}$.

ANALYSIS OF HEAT PULSE PROPAGATION

The fast collapse of the sawtooth instability flattens the electron temperature profile from the centre up to the mixing radius r_{mix} on a timescale of ≈100 μs. After the collapse, the

profile relaxes to the unperturbed profile of just before the next collapse. At radii outside r_{mix}, we observe the heat pulse signals. Fig.2 shows two typical examples of the electron temperature signal vs. time for six radial positions. From the measured heat pulse traces a value for χ_e can be derived, which we denote by $\chi_{e,hp}$

The heat pulse perturbs, in first order, only the temperature and the temperature gradient. The perturbed heat flow is then $\tilde{q}_e = n_e \chi_e \nabla\tilde{T}_e + n_e \tilde{\chi}_e \nabla T_e$ (Eq3) , where χ_e is not a constant, but a function of the perturbed quantities, T_e or ∇T_e. As we have shown in [5], a T_e dependence would hardly affect the evaluation of $\chi_{e,hp}$. Hence we consider here only a functional dependence on ∇T_e. Then, the heat diffusivity relevant to the perturbation is by definition

$$\chi_{e,hp} = \frac{1}{n_e} \frac{\partial}{\partial \nabla T_e} q_e = \chi_e + \left(\frac{\partial}{\partial \nabla T_e} \chi_e\right) \nabla T_e \qquad \text{(Eq4)}$$

in which χ_e represents the equilibrium value. Depending on the form of $\chi_e(\nabla T_e)$, $\chi_{e,hp}$ will be larger than $\chi_{e,pb}$. Under the condition that the offset linear behaviour of $q_e(\nabla_r T_e)$ shown in Fig.2 is valid on a time scale faster than the heat pulse, $\chi_{e,hp}$ should be equal to $\chi_{e,inc}$.

INSTRUMENTATION AND DATA PROCESSING

The HPP signals are measured with a twelve channel ECE grating polychromator [2], with a radial line of sight in the median plane and a radial resolution of ± 3 cm. The heat pulse signals are characterised by a delay time t_p and an amplitude A (see Fig.2). From the t_p and A values, we derive a heat pulse velocity $v_{hp} = dr/dt_p$ and a radial damping rate $\alpha = ad(\log A)/dr$, as the characteristic parameters. As is shown in [6], $\chi_{e,hp}$ can be derived from v_{hp} and α ; $\chi_{e,hp} = 4.2\, v_{hp}/\alpha$.

RESULTS FOR ADDITIONALLY HEATED DISCHARGES

We limit the discussion here to a set of auxiliary heated limiter discharges with I_p = 3 MA, $2.9 < B_T < 3.5$ T, with total power varied from 2.1 to 13.5 MW. Fig.3 shows the $\chi_{e,hp}$ values and the $\chi_{e,pb}$ values (from Eq1) as a function of total input power. While the increase of $\chi_{e,pb}$ with power represents the deterioration of confinement, $\chi_{e,hp}$ is a constant within the experimental error. Its value is $\chi_{e,hp} = 2.5 \pm 0.5\ m^2 s^{-1}$. A further illustration of the constancy of $\chi_{e,hp}$ under increasing power is given in Fig.2, where signal traces of two different discharges with 2.5 and 10.4MW resp. are shown to be almost identical.

DISCUSSION

On the basis of the constancy of $\chi_{e,hp}$ with respect to the input power and on the basis of the numerical agreement between $\chi_{e,hp}$ ($2.5 \pm 0.5\ m^2 s^{-1}$) and the estimates for $\chi_{e,inc}$ ($2.5 \pm 0.5\ m^2 s^{-1}$) we conclude that indeed the identification $\chi_{e,hp} = \chi_{e,inc}$ is correct. It then follows that the heat diffusivity χ_e is a function of ∇T_e on a timescale much faster than the heat pulse (ie. a few ms). We propose a specific dependence of the type given in Fig.4. This 'critical gradient' model is consistent with both the observations of $\chi_{e,pb}$ and $\chi_{e,hp}$. The model can be interpreted to represent a micro instability that starts to grow above a

threshold value of ∇T_e. At high ∇T_e, the instability saturates, and $\chi_{e,pb}$ goes to its asymptotic value $\chi_{e,hp}$. The ratio $\chi_{e,hp}/\chi_{e,pb}$ is largest just above the critical gradient, which is the normal operating range for ohmic discharges. We speculate that below the critical gradient χ_e has a low, eg. Alcator-Intor, value.

A different interpretation of the offset linear behaviour [3,7] is that the total heat flow is the net result of the outward diffusive flow, governed by a heat diffusivity of value $\chi_{e,inc}$ and an inward heat pinch, the mechanism of which is unexplained.

If χ_e increases with ∇T_e, this will naturally give rise to a certain rigidity of the electron temperature profile. Our model is thus capable of explaining a certain degree of 'profile consistency', without invoking non-local transport (see also [7]).

FIRST RESULTS DURING PELLET INJECTION

HPP measurements were performed on two discharges (B_t=3.4T, I_p=3MA), in which the sawtoothing continued normally after injection of a deuterium pellet. Table 1 shows the results. $\chi_{e,hp}$ is given before injection, in an interval between 0.1 and 0.5 s after injection, and in an interval 2 s after injection of the pellet.

Table 1

time	48.4-50	50.1-50.5	52-53 s
11014	2.2±0.5	1.7±0.4	2.2±0.4
11016	1.6±0.5	0.9±0.3	2.2±0.5
pulse		$\chi_{e,hp}$ (m^2/s)	

The trend is a substantial drop of $\chi_{e,hp}$ after injection of the pellet. The low value persists for about 0.5 s. Thereafter $\chi_{e,hp}$ returns to its pre-pellet value. It is interesting to note that the reduction of $\chi_{e,hp}$ goes together with a decrease ∇T_e after the pellet injection. ∇T_e (at r = 2/3 a) is reduced from 4 keV/m to 2.6 keV/m in the interval between 0.1 and 0.5 s after the pellet. The latter value is lower than the lowest obtained in ohmic heating steady state conditions, ie. $\geq$ 3 keV/m. This observation is consistent with the critical gradient model. However, because the plasma is far from the steady state, these results should be treated with care.

REFERENCES

1 Callen J D, Jahns G L, Phys. Rev. Letters 38 (1977) 971

2 Tubbing B J D ea., Proc. 12th. Europ. Conf. Budapest, 9F1 (1985) 138

3 Frederickson E D, ea., Nucl. Fusion 26 (1986) 849

4 Tubbing B J D, Lopes Cardozo N J, JET report JET-R(87)01

5 Tubbing B J D, Lopes Cardozo N J, Wiel M J van der, subm. to Nucl. Fusion.

6 Lopes Cardozo N J, ea., to be published.

7 Callen J D, ea., JET report JET-P(87)10, subm. to Nucl. Fusion

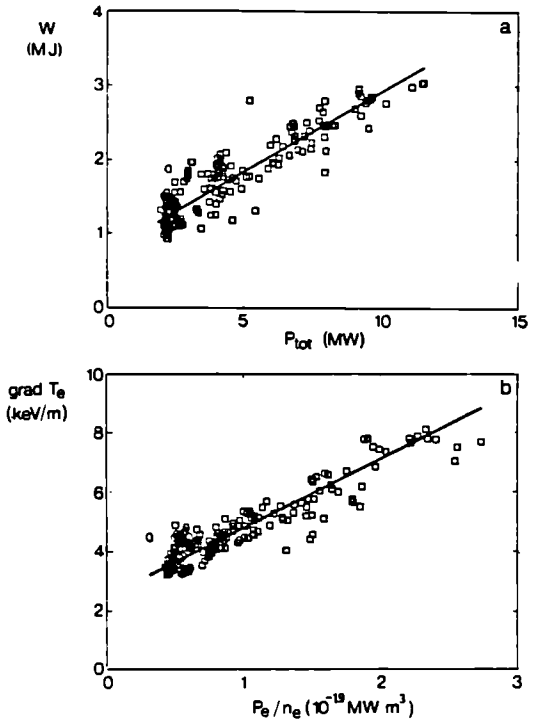

Fig.1 Global and local power balance.
a) The total kinetic energy content W as a function of the total input power P, for a selection of JET data: I_p = 3MA, B_T = 3.4 T, n_e=2.5 10^{19} m^{-3}.
b) $\nabla_r T_e$ vs P_e/n_e (P_e is the power transported by the electrons), evaluated at r = 2/3 a for the same selection of data.
The full lines correspond to $\chi_{e,inc}$=2.5 m^2/s.

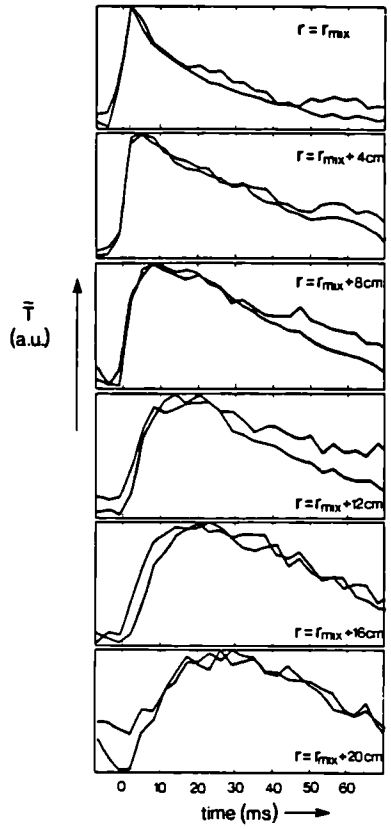

Fig.2 Heat pulse signals in two discharges, with P=2.7 and 10.4 MW resp. Note that while the input power is quadribled the pulse shapes have not changed.

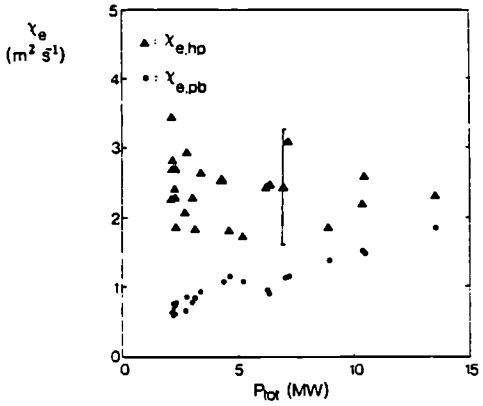

Fig.3 The measured values of $\chi_{e,hp}$ and the corresponding values of $\chi_{e,pb}$ as a function of input power. While $\chi_{e,hp}$ is constant, $\chi_{e,pb}$ increases with increasing power, thus showing the deterioration of the global confinement.

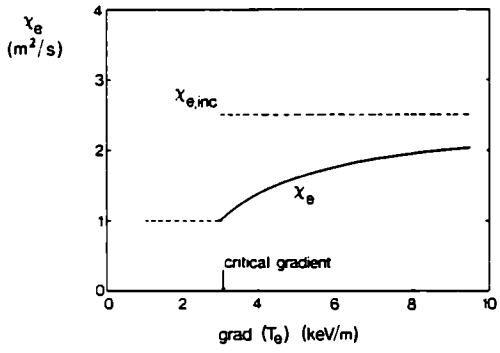

Fig.4 Sketch of the critical gradient model. This dependence of χ_e on $\nabla_r T_e$ allows a unified description of the heat pulse results and the power balance analysis.

FLUCTUATIONS AND CONFINEMENT IN JET

P A Duperrex[+], P Cripwell[x], A W Edwards, R D Gill, R S Granetz, A Hubbard[x], M Malacarne, G Matthews*, F Simonet[l], J Snipes, A Weller[o]

JET Joint Undertaking, Abingdon, Oxfordshire, OX14 3EA, UK
On attachment from: [+] CRPP, Lausanne, Switzerland,
[x] Imperial College, London, UK
* Culham Laboratory, Abingdon, Oxfordshire, UK
[l] CEA, Cadarache, France
[o] IPP, Garching, FRG

ABSTRACT

Fluctuation measurements in JET are presented and their correlation with the confinement is discussed for limiter and X-point discharges.

I INTRODUCTION

Measurement of turbulence in tokamak is motivated by the fact that anomalous transport is often attributed to micro-instabilities. The results presented here concern fluctuations analysis in JET using different diagnostics: edge located pick-up coils for poloidal magnetic fluctuations ($\tilde{b}_\theta$), diodes for fluctuations of soft X-ray and visible light emission, a reflectometer for density fluctuations and Langmuir probes for electrostatic fluctuations.

II LIMITER DISCHARGES

Magnetic pick-up coils in JET detect the usual Mirnov activity (f ~ 0.3 → 7 kHz) [1], events linked with the internal disruption (the so-called gong [2]) and fluctuations [3]. The signal is either recorded with relatively fast ADC (sampling frequency: 40 kHz) or monitored by 8 hardware band-pass filters (from 5 to 56 kHz). The amplitude decreases with frequency: $\tilde{b}_\theta \alpha f^{-1.5 \pm 0.5}$ above 2 kHz. The total normalised amplitude is typically: $\tilde{b}_\theta / B_\theta \sim 10^{-4} - 10^{-5}$. Cross correlation techniques have been used to determine the spatial characteristics of these fluctuations. Two different types of activity can be observed in the frequency range 0 to 20 kHz. The first, dominant at frequencies up to 10 kHz, is observed to propagate in the electron diagmagnetic drift velocity direction (also with Neutral Beam Injection). On the contrary, the second type (dominant from 10 kHz) appears to be stationary even during NBI with n=1 and m equal to the outermost integral q_ψ value. Both types are strongly correlated along a direction parallel to the equilibrium magnetic field ($\underline{B}_o$) (fig. 1). The corresponding correlation length is larger than the major radius (R). The phase shift between 2 magnetic probes along this direction is very close to zero for all frequencies indicating $\underline{k} \cdot \underline{B}_o \sim 0$ for the broadband spectrum.

The $\tilde{b}_\theta$ level depends strongly on the plasma-probe distance and increases when additional heating is applied. This enhancement is observed for all pick-up coils and therefore is not due to a simple shift of the plasma. It also increases with I_p and decreases with B_T though it is not possible to determine if it is a genuine enhancement or is due to the closer location of the resonant layer at lower $q_\psi(a)$. However, taking these effects into account by multiplying $\tilde{b}_\theta$ by $q_\psi(a)$ (or B_T/B_p) the normalised level is shown in Fig. 2 (for f = 40 kHz in this example) to increase with τ_E^{-1} (τ_E = energy confinement time).

Fluctuations from visible light emission were measured by 2 arrays of soft X-ray diodes without foils. Tomographic reconstruction confirms that the measured emission is essentially located at the plasma edge. Cross-correlation analysis shows the presence of high m wave numbers. In the frequency range 15-20 kHz the measured m numbers are about 25 - 35 and for the frequency range 40-60 kHz the corresponding m numbers are m ~ 70-100.

Density fluctuations have been measured with a reflectometer. Coherent oscillations are sometimes seen which correlate well with the magnetic signals. However no correlation between broadband density and magnetic fluctuations has yet been found. Langmuir probes in the scrape-off layer can also detect fluctuations in the range 0 to 20 kHz. Preliminary results indicate that the correlation length is shorter than the distance (10 cm) between the 2 probes. No correlation has been obtained either with the magnetic or the reflectometer data as far as the broadband spectrum is concerned.

III FLUCTUATIONS DURING X-POINT DISCHARGES

During X-point discharges, visible light fluctuations are seen to correlate with the first type of magnetic activity (the propagating type) measured with a coil which is near the X-point and very close to the plasma for this configuration, whereas the n=1 low m magnetic standing fluctuations do not have any visible counterpart.

A new type of edge activity in JET has also been observed. Perturbations appear to dominate in the phase preceding the transition from a low confinement regime (L-mode) to a high confinement regime (H-mode) (fig. 3): regular spikes are observed on the magnetic, reflectometry (when probing the edge density) and visible light emission signals. They are correlated with a sudden flattening of the soft X-ray emission at the edge. The repetition frequency of these spikes is slowed down by sawtooth disruptions, one of which often marks the final transition to the H-mode. In contrast H→L transitions (which are preceded by a large increase of edge radiation) are characterised by a sudden burst of broadband (turbulent) activity with $m \geq 6$-8 and $n \geq 1$, (fig 4a). Coherent oscillations resonant on surfaces deeper inside the plasma are apparently unaffected by the transitions (fig 4b). The X-ray emission drops at the edge and H_α radiation from the single X-point region shows a

large increase; very often spikes reappear after this initial burst. During the H-mode, edge turbulent fluctuations are still present, though at a much lower level.

IV DISCUSSION AND CONCLUSION

Turbulence up to 50 kHz has been observed with different diagnostics. Magnetic fluctuations have a very long correlation length ($\geq$ R). This could confirm that the magnetic connection length is of the order of ~ qR.

No correlation has yet been found between the broad-band fluctuations of the different diagnostics for limiter discharges. During X-point discharges the light emission exhibits some correlation with a magnetic coil near the X-point for which edge fluctuations dominate the signal. The enhancement of $\tilde{b}_\theta$ during additional heating proportionally to τ_E^{-1} points out a possible link between $\tilde{b}_\theta$ and the anomalous transport. Edge perturbations appear to play an important role in the physics of the high confinement regime (H-mode).

REFERENCES

[1] Snipes J et al: EPS Schliersee 1986, Vol I, p152.
[2] Duperrex P A, Keller R, Malacarne M, Pochelon A: EPS Budapest 1985, Vol I, p126.
[3] Malacarne M, Duperrex P A: JET Report JET-P(86)31.

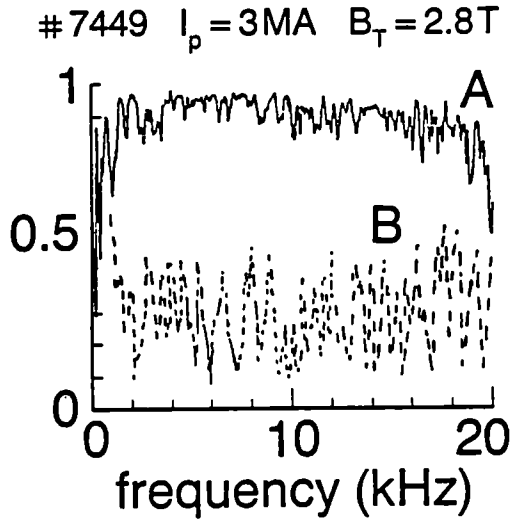

Fig. 1: Coherence spectrum between 2 magnetic coils A) along $\underline{B}_0$, B) across $\underline{B}_0$.

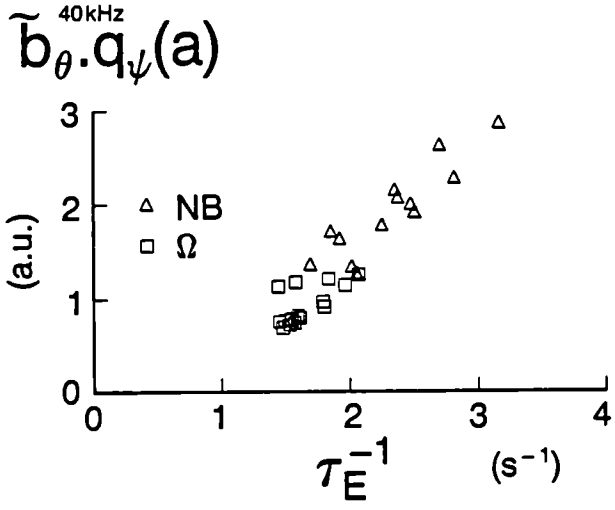

Fig. 2: Normalised level $\tilde{b}_\theta$ (at 40 kHz) versus τ_E^{-1}. Ip = 2, 3, 4 MA, B_T = 2.5, 2.8, 3.4 T.

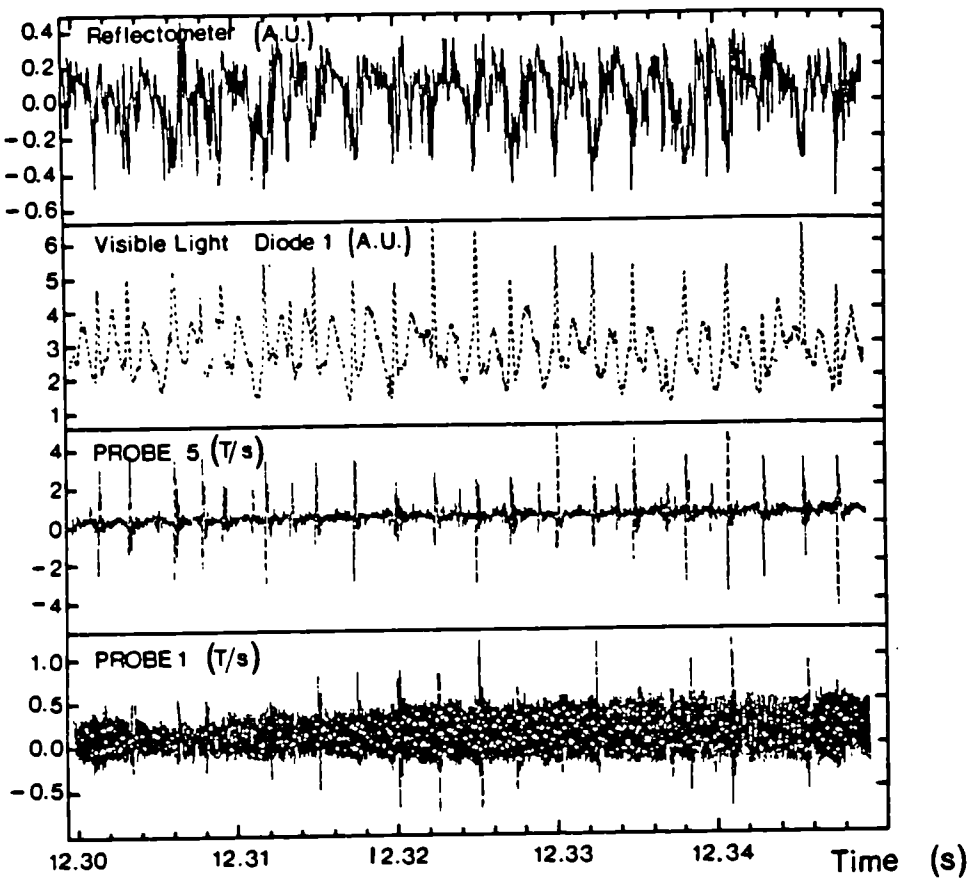

Fig. 3: "spike" activity at the edge during the L phase prior to an H mode transition. # 10850

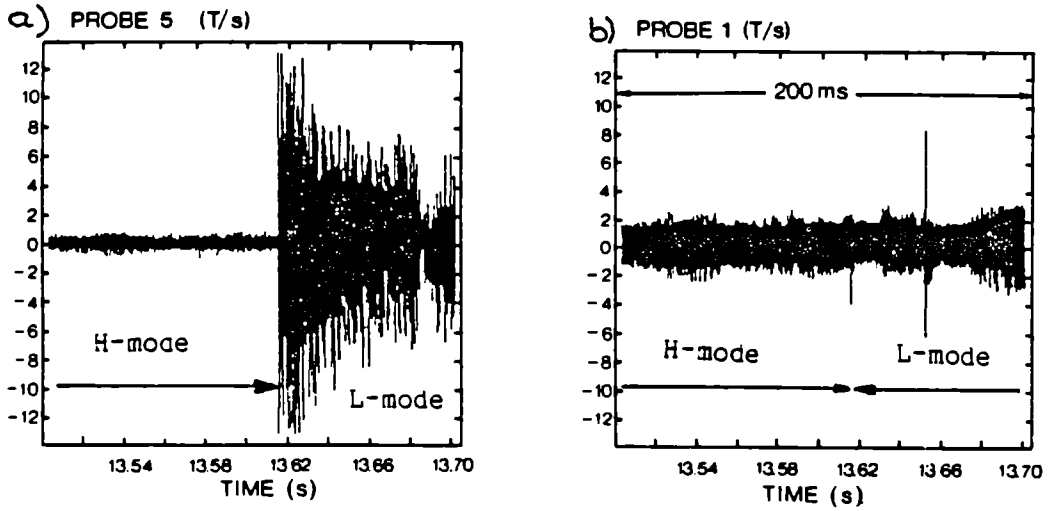

Fig. 4: Magnetic signals at the H-L transition. # 10789
a) probe 5 near the X-point for which edge fluctuations signal dominates.
b) probe 1 behind the limiters, dominated by coherent oscillations resonant deeper inside the plasma.

H-MODE CONFINEMENT IN JET

M Keilhacker, C M Bishop*, J G Cordey, D G Muir, M L Watkins

JET Joint Undertaking, Abingdon, Oxon, OX14 3EA, UK
*EURATOM-UKAEA Association, Culham Laboratory, Abingdon, Oxon, OX14 3DB

1. OPERATIONAL LIMITS AND CHARACTERISTICS OF JET H-MODES

H-mode confinement has been observed in JET discharges employing magnetic separatrix configurations with a single null X-point [1]. The experiments discussed in this paper have been carried out with neutral beam heating (NB) with up to 10MW power (80kV D° injected into a deuterium plasma) and at plasma currents I_p of 1, 2 and 3MA. Above a power threshold a clear transition from L- to H-mode is observed. This threshold is practically independent of plasma current (in the range 1 to 3MA) but has a strong dependence on toroidal magnetic field (~5MW at 2.2T and ~10MW at 2.8T). It is noteworthy that H-mode behaviour has been obtained in JET for very modest separation between the X-point and the target plates (a few centimetres), whereas conditions on the distance between the separatrix and the outer limiter (wall) were found to be rather more stringent (≥ 5cm).

All characteristics typical of an H-transition are exhibited in JET discharges: a sudden drop in the D_α emission, reduction of power flow into the scrape-off layer, sharp increase in the edge electron temperature and - most important - sudden changes in the slopes of the signals representing the particle and energy contents of the plasma, indicating improved particle and energy confinement. Unlike H-mode discharges in divertor experiments such as ASDEX, those in JET are free of edge localised modes (ELMs) and do not reach stationary conditions. Concomitant with a continuous rise in density during the H-mode is an increase in bulk plasma radiation, roughly proportional to $\langle n_e \rangle^2$. In contrast, the radiation from the X-point region stays more or less constant during the H-mode. The H-mode reverts to an L-mode after typically 1 to 2s due to a thermal collapse in the plasma boundary or X-point region.

Energy confinement in L- and H-modes is examined using global and local transport analyses (Section 2) and an interpretation of the confinement behaviour is suggested in Section 3.

2. ENERGY CONFINEMENT IN L- AND H-MODES

Figs 1a and b show the global energy confinement time $\tau_E(a)=W/(P-\dot{W})$ as a function of the total net input power $(P-\dot{W})$ for the L- and H-modes of 1, 2 and 3MA X-point discharges. W is the diamagnetic measurement of the stored energy. The data set has been restricted to $\dot{W}/P < 0.2$, close to steady state conditions. The H-mode confinement times are more than a factor of 1.5 higher than the L-mode data, which themselves are a factor of about 1.5 higher than those for corresponding limiter discharges (see Reference [1]). For both L- and H-modes, τ_E increases roughly linearly with I_p but decreases with power. Plotting $\tau_E(a)$ versus $(P-\dot{W})/\langle n_e \rangle$ shows that Ohmic, L- and H-mode data all fall onto a single curve for data both near steady-state for a wide range of discharges (Figure 2a) and further

away from steady-state for data accumulated during the evolution of a limited number of discharges (Figure 2b, using a local transport analysis and the kinetic stored energy). While the data suggests an underlying improvement of confinement with density and a degradation with power it is not possible to justify this fully since the density and power have not been controlled independently: the density influx exceeds initially the beam fuelling component, but is dependent on the input power (Figure 3).

In Figure 4 the heat flux through surfaces at half and three-quarter radius are plotted against $n_e \nabla T_e$ at different times through a representative pulse in which the input power is approximately constant. It is to be noted that there is little to distinguish the energy transport at the two radii. In particular, the transition from L- to H-mode is gradual, with improved confinement corresponding to higher density. There is little data which could allow the power dependence at constant density to be determined, but an indication of degradation with power is seen with the two H-mode points (marked o on Figure 4), which correspond to the same density as those marked Δ, but at twice the power level. Furthermore, removing the density dependence from the data in Figure 4 indicates that the temperature gradient is independent of power in the range of power examined. The improved confinement of H-modes compared to L-modes results therefore in the plasma interior from the increased density achievable and, in addition, from improved edge confinement as manifested by the establishment of a pedestal in the electron temperature.

3. INTERPRETATION OF ENERGY CONFINEMENT IN L- AND H-MODES

Improved edge confinement in H-modes may be interpreted in terms of the special MHD ballooning stability properties of a plasma close to a separatrix [2]. For lower values of the input power the edge pressure gradient lies in the first stable region, at or below the marginally stable value given by the pressure gradient parameter, $\alpha \sim 0.4$. This corresponds to the L-mode. At higher values of the input power the edge pressure gradient near the separatrix lies in the second stable region and is no longer determined by the ballooning mode transport. This pressure gradient is connected to the rest of the profile (which is again in the first stable region) at a critical value, $\Lambda_c \sim 0.7$, of the edge current density, $\Lambda = \mu_o a V / 2\pi R B_p \eta$. This is the H-mode profile with its characteristic steep edge gradient. The existence of a minimum threshold power to achieve the H-mode (being the power needed to place the edge gradient just above the second stability boundary) arises automatically in this picture. For a typical JET X-point equilibrium, the edge temperature profiles can be constructed as shown in Figure 5, where zero temperature is assumed at the separatrix. It should be noted that the temperature gradients (8keV/m) associated with the first stable region are similar in both the L- and H-modes and in reasonable agreement with experiment. It is not possible to resolve experimentally at present the steep gradients associated with the second stable region. However, the predicted temperature ~1.7keV at the top of this gradient (corresponding to $\Lambda \sim \Lambda_c$) agrees well with experiment.

4. CONCLUSIONS

Global and local transport analyses of JET X-point discharges indicate a deterioration of confinement with increasing ratio of input power to density. This trend is continuous from ohmic through to L- mode and H-mode phases. In the plasma interior improved confinement is linked to higher density, thereby masking the degradation of confinement with power. In addition, H-modes have improved edge confinement as manifested by an edge pedestal in the electron temperature. Such a heat barrier arises automatically from the predictions of ballooning mode theory, corresponding to the transition to the second stable region above a certain power threshold.

An alternative mechanism for such a barrier limiting the transverse heat flux is provided by the critical temperature gradient model of reference [3]. High edge temperatures could also arise by limiting the parallel heat flux outside the separatrix as in reference [4].

H-modes in JET terminate with a radiative collapse before reaching stationary conditions. Provoking the occurrence of ELMs may alleviate these problems.

ACKNOWLEDGEMENTS

The authors are pleased to acknowledge discussions with members of the JET team, and in particular Drs M Brusati, N Gottardi, H Jaeckel, T Tagle and A Tanga.

REFERENCES

[1] Tanga, A et al, in Plasma Physics and Controlled Nuclear Fusion Research (Proc 11th Int Conf, Kyoto, 1986), paper IAEA-CN-47/K-I-1.

[2] Bishop, C M, Nucl Fusion 26(1986)1063 and Culham Laboratory Preprint, CLM-P815(1987).

[3] Rebut, P H et al, this Conference.

[4] Ohkawa, T et al, Phys Rev Lett 51(1983)2101.

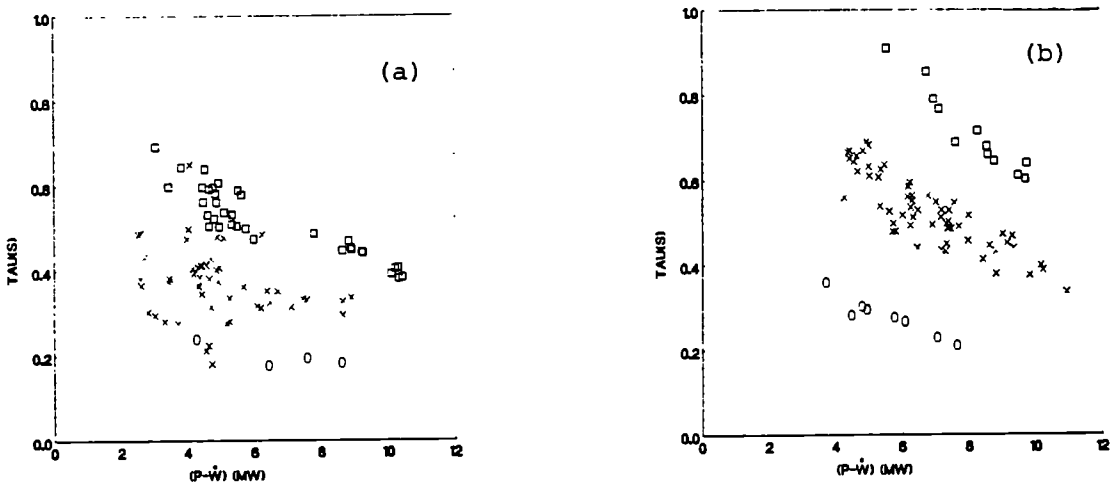

Fig 1: Global energy confinement time versus total net input power for currents of 1,2 and 3MA (o,x,□ respectively) in (a) L-mode and (b) H-mode.

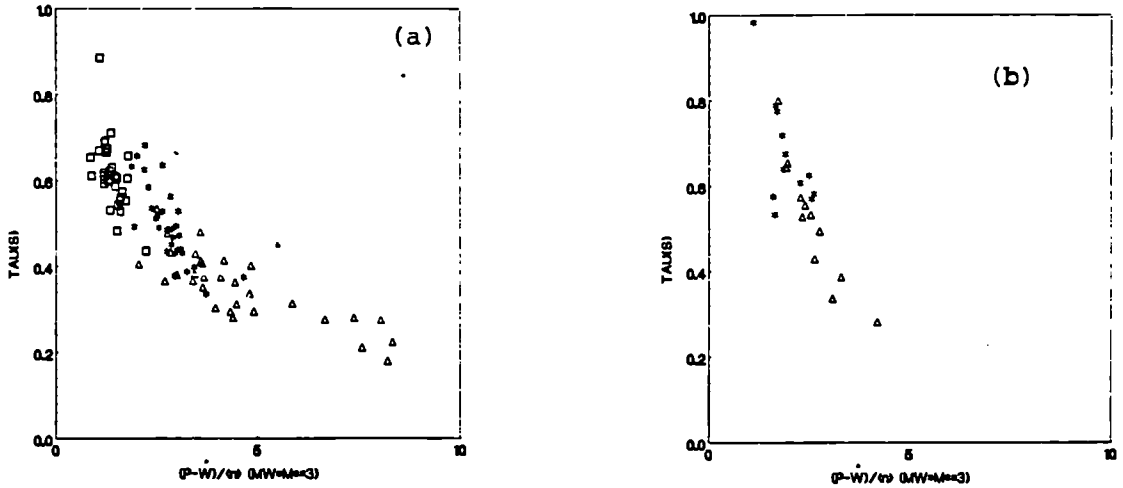

Fig 2: Global energy confinement time versus total net input power/volume-averaged electron density in OH-(□), L-(Δ) and H-(*) phases of 2MA discharges from (a) global and (b) local transport analyses.

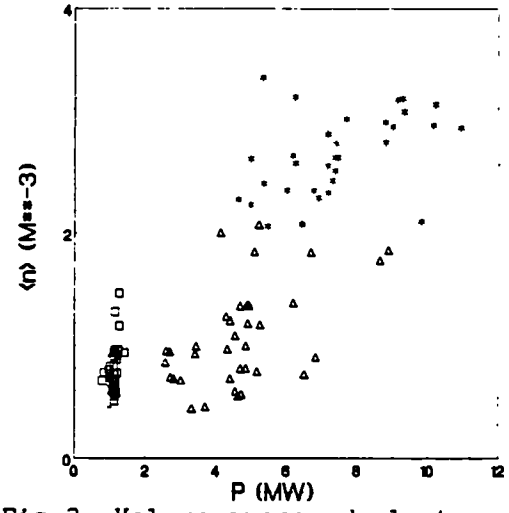

Fig 3: Volume-averaged electron density as a function of total input power in OH-(□), L-(Δ) and H-(*) mode phases of 2MA discharges.

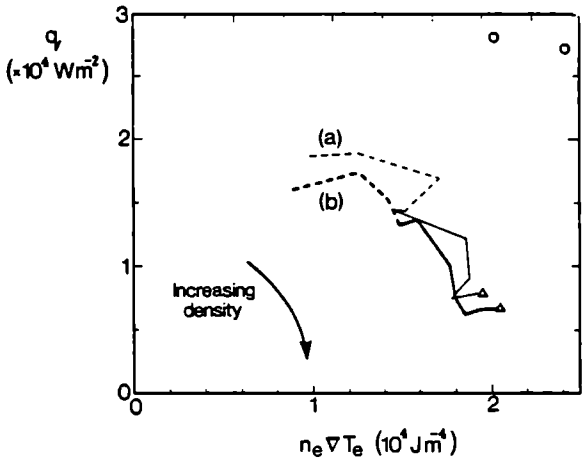

Fig 4: The time variation during JET pulse #10237 of the power flow versus $n_e \nabla T_e$ through magnetic flux surfaces at (a) half and (b) three-quarter radius: (---) corresponds to the L-mode and (—) to the H-mode.

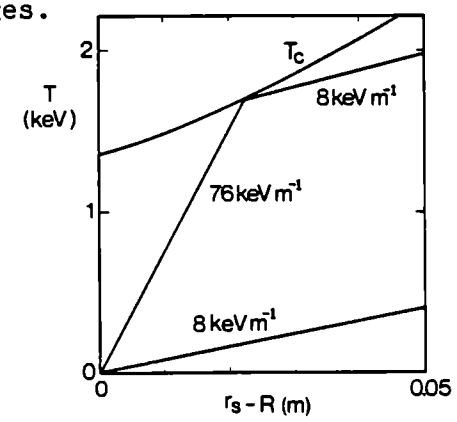

Fig 5: Temperature profiles constructed inside the separatrix on the basis of ballooning mode theory

BEHAVIOUR OF PARTICLE INFLUXES AND EDGE RECYCLING DURING ICRF HEATING ON JET

M. Bureš, V.P. Bhatnagar*, M.P. Evrard*, A. Gondhalekar, J. Jacquinot, T.T.C. Jones, P.D. Morgan, D.F.H. Start

JET Joint Undertaking, Abingdon, Oxon, OX14 3EA, UK
* LLP-ERM/KMS; EUR-EB Association, 1040 Brussels, Belgium

INTRODUCTION

During ICRF heating in JET, the main species and the impurity neutral influxes always increase. The magnitude of influxes and also the density increase is proportional to the RF power. The important parameter is the number of neutral atoms available for desorption from the wall and limiters. This depends strongly on the conditioning of the vessel and after glow discharge cleaning or carbonisation the neutral influxes are substantially enhanced. The global particle confinement, which is the ratio of the electron content and the total influxes, is thus always decreasing with the input power.

The density evolution is appropriately described by the incremental confinement time τ_p^{RF} of the additional density and by the time dependent additional influxes $\Delta\phi^T$.

NEUTRAL INFLUXES AND DENSITY EVOLUTION

The neutrals are released typically with two time scales. The flux from the wall is seen to rise rapidly ($\tau \lesssim 10$ msec). The flux from the

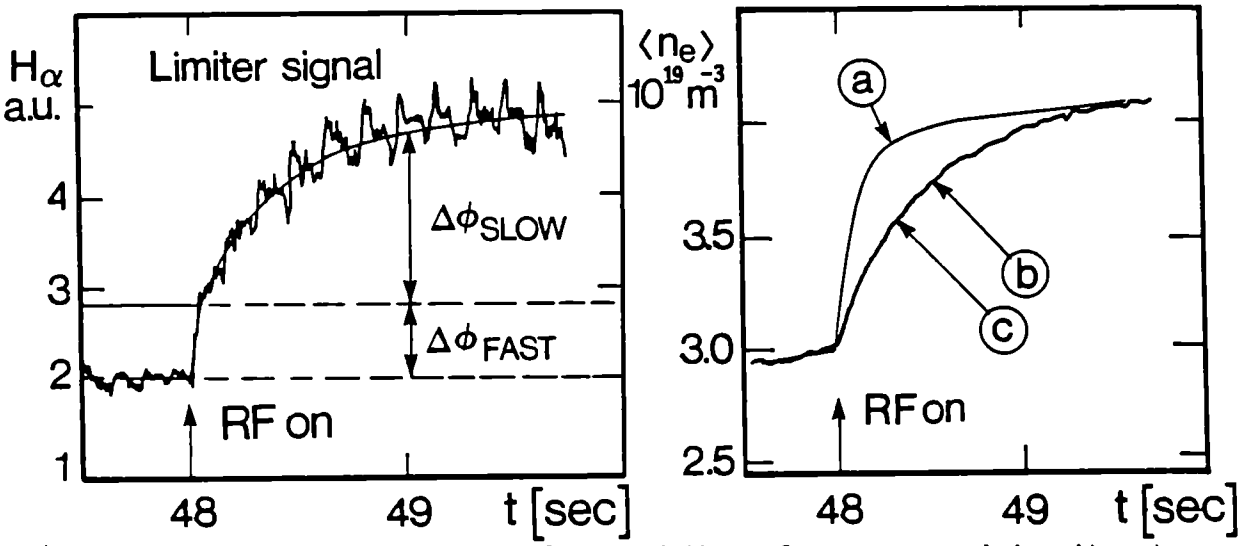

Fig. 1 Evolution of the limiter flux and the volume averaged density at the onset of the RF power. (c) and (b) curves represent the measured and simulated (eq. 1) density traces. Curve (a) shows the evolution if the total neutral influx is assumed to vary as a step function.

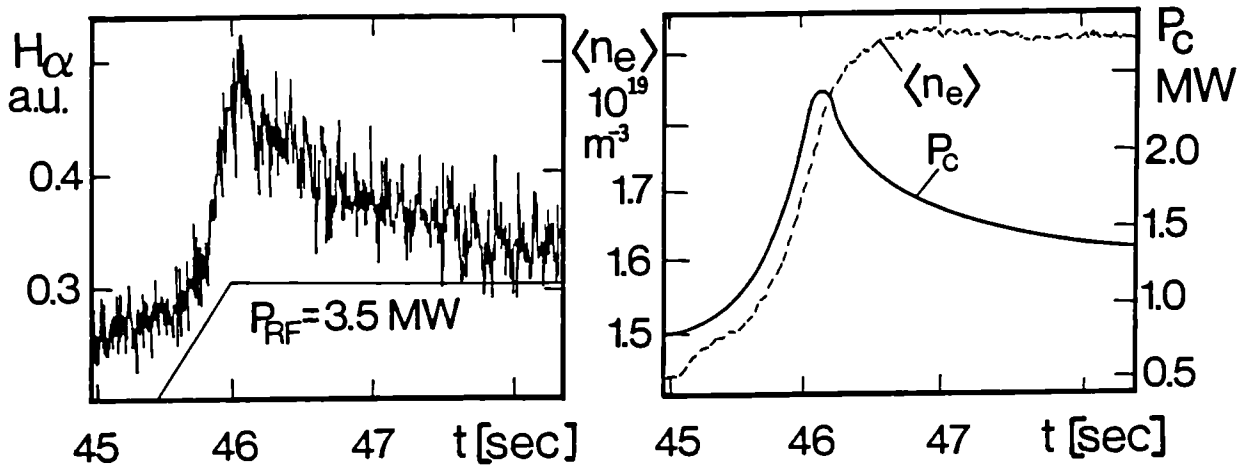

Fig. 2 Time evolution of the conducted power into the SOL, H_α signal from limiter and the average density.

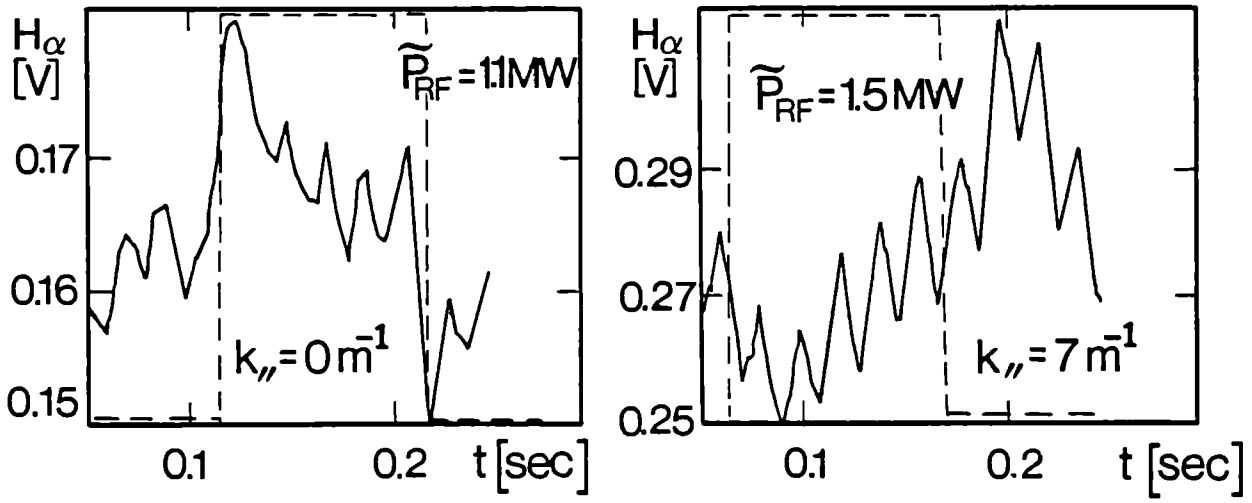

Fig. 3 Boxcar averaged limiter flux signal with the RF power modulated by 5 Hz in D(H) scenario. The signals are shown for the cases of the dipole and quadrupole phasing of the antennae.

limiter also rises rapidly but its final value approaches on approximately the confinement time scale for energy. An example of limiter flux is shown in Fig 1.

The fast flux from the wall is ≈ 40% of the fast limiter flux. The particle balance then becomes

$$\dot{N} + \frac{N}{\tau_p^{RF}} = \Delta\phi^T = \Delta\phi \left(1 + \frac{Z_{eff} - 1}{Z_I + 1 - Z_{eff}}\right) [s^{-1}] .$$

$\Delta\phi = \Delta\phi_F + \Delta\phi_s$ are the particle fluxes deduced from the absolute H_α measurements. The typical values of Z_{eff} measured by the visible bremsstrahlung are in the range 2.5 - 3.5. $Z_I = 7$ is assumed in simulation, which represents well the JET dataset on Z_{eff}. Assuming the fast flux to vary as a step function and taking $\Delta\phi_s\,(t) = \Delta\phi_s\,(1-\exp(-t/\tau_1))$ the evolution of the total electron content from the ohmic value can be expressed

$$N(t) = \Delta\phi^T \tau_p^{RF}(1-\exp(-t/\tau_p^{RF})) - \Delta\phi_s^T \tau_p^{RF} \tau_1 (\exp(-t/\tau_p^{RF}) - \exp(-t/\tau_1)) \,/(\tau_p^{RF} - \tau_1) \quad (1)$$

Here $\tau_p^{RF} = \Delta N/\Delta\phi^T$. The measured and calculated densities are shown in Fig 1, curves c and b. We conclude that the density evolution is determined not only by the confinement time τ_p^{RF} but also by the evolution of fluxes. Eq. 1 can be used to define the recycling coefficient $R = \frac{\Delta\phi(t)}{N(t)/\tau_p^{RF}}$. It always increases at the onset of RF power indicating a rapid neutral desorption. The importance of the flux evolution for the density build-up is also observed in cases where the RF power is ramped up. Correspondingly the influxes become slower and the density build-up longer.

CORRELATION OF INFLUXES WITH RF POWER

Already during the early high power experiments on JET [1] it was concluded that 20-30% of RF coupled power which could not be accounted for and therefore had to be dissipated at the edge or the scrape-off layer (SOL) of the plasma. As indeed all the fluxes are proportional to the RF power, it is suggested that the fast influx is correlated to the unaccounted RF power P_{RF}^A while the slow influx from limiter is due to the RF power diffusing from the central parts of the plasma $P_{RF}^1(t) = (P_{RF} - P_{RF}^A)(1-\exp(-t/\tau_{RF}))$ corrected for the increase of radiation. Here $P_{RF} = P_{RF}^1 + P_{RF}^A$ and $\Delta W = P_{RF}^1 \tau_{RF} = P_{RF} \tau_{inc}$. P_{RF} is the power radiated by the antenna and ΔW is the increase of plasma energy. τ_{inc} is the incremental confinement time which is usually used to describe the efficiency of the additional heating of the plasma. It was observed during the 5 MA discharges that the fast portion of the limiter influx scales indeed with P_{RF}^A. The importance of the power conducted into the SOL is shown in Fig 2. The influx from the limiter is not proportional to the plasma density, as observed in OH cases [2].

EFFECTS OF THE ANTENNA PHASING

The 5 MA high RF power discharges show the fast limiter influx. At low power levels the fast influxes are often masked by the fluctuations due primarily to sawteeth activity. The modulation of RF power and signal averaging to improve the signal to noise ratio clearly demonstrate that limiter signal contains a fast portion even at lower power levels. Fig 3 shows the boxcar averaged normalised signals for the dipole and quadrupole [1] phasing. The level of the fast signal correlated with the RF power represents 10-15% of the total limiter signal with dipole antennae. The fast limiter influxes with the quadrupoles were not observed. Also the incremental confinement time for energy increases typically by ≈ 25% [3]. Experiments were performed in deuterium with the hydrogen minority.

SCALING OF INFLUXES WITH THE RF POWER

The neutral influxes from the limiter and wall are routinely measured on JET. The main results of scaling with the power in RF equilibrium can be summarised as follows:

(a) both limiter and wall influxes increase roughly linearly with the RF power up to the maximum levels achieved so far, $P_{RF} \approx 8$ MW.

(b) the density increase is correspondingly also linear, except for the lower power levels, where it increases faster.

(c) the ratio of wall to limiter flux scales with the plasma current and is independent of the RF power in accordance with the expected evolution of the SOL profiles.

CONCLUSIONS

The time evolution of density during the RF heating on JET can be explained in terms of fast and slow neutral influxes. The conducted power into the SOL is an essential factor for the neutral flux release. The fast influx at the onset of the RF power is correlated to the unaccounted RF power. The limiter signal contains a non-negligible fraction of the fast influx which disappears when the antennae are phased as quadrupoles.

ACKNOWLEDGEMENTS

We wish to thank our colleagues in the JET team, especially the tokamak operating teams and those operating the diagnostics used in the experiments reported in this paper.

REFERENCES

[1] J. Jacquinot et al, Plasma Phys. and Contr. Fusion, Vol. 28, No 1A, pp.1-15, 1986

[2] P. Morgan et al, 12th Europ. Conf. on Contr. Fusion and Plasma Phys., Budapest 1985, Vol. 9F, Part II, p. 535

[3] M. Bureš et al, submitted for publication.

EXPERIMENTAL AND THEORETICAL STUDIES OF HARMONIC ICRF HEATING ON JET

F. Sand, G.A. Cottrell, V.P. Bhatnagar, M. Bures, J.G. Cordey, W. Core, S. Corti, H. Hamnen, T. Hellsten, J. Jacquinot, D.F.H. Start, P.H. Thomas, M. Watkins

JET Joint Undertaking, Abingdon, Oxon, OX14 3EA, UK

ABSTRACT

Experiments have been carried out on JET to study harmonic heating by ICRF. In the first set of experiments, RF power was coupled to D^+ beam ions (65 keV < E_b < 85 keV) with the $2\omega_{cD}$ resonance in the plasma centre. Accelerated ions in the range E_b < E < 120 keV were seen together with, typically, a twofold enhancement in the DD reactivity. The results are compared with Fokker-Planck calculations which are also used to predict reactivity enhancements at the higher heating powers available to JET in future experiments. A second set of experiments used H minority heating to preheat a He^3 plasma before switching on power at $2\omega_{cHe^3}$. Preliminary estimates indicate that ~ 10% of the harmonic heating power was absorbed at $2\omega_{cHe^3}$ with most of the power being deposited at the complementary off-axis H-minority resonance.

INTRODUCTION

ICRF minority heating on JET produces mainly electron heating due to highly energetic (> 200 keV) tail formation and has achieved central electron temperature in excess of 7 keV [1]. Similar bulk ion heating could, in principle, be attained by direct coupling at $2\omega_{ci}$. Recent transport analysis of JET data [2] suggest that such a localized source would provide optimum ion heating efficiency and consequently high thermal fusion reactivity. Experiments have been made to test the feasibility of first harmonic heating which relies on finite ion Larmor radius (ρ_i) effects with the power absorption scaling as $P_{ab} \sim (k_\perp \rho_i)^2$. These experiments attempted to maximize this factor by using a) combined ICRF and neutral beam injection (NBI) with the RF power coupled to the D^+ beam ions and b) H-minority heating to raise the temperature of a He^3 plasma prior to harmonic heating at $2\omega_{cHe^3}$.

ICRF + NBI EXPERIMENTS

Deuterium beam ions with energy in the range 65-80 keV were injected into a D^+ plasma and ICRF applied with the $2\omega_{cD}$ resonance close to the magnetic axis. The effect on the beam distribution function of 6 MW of RF power and 3.6 MW of NBI is shown in Fig 1 which is data from a neutral particle analyser (NPA) viewing at 15° to the radial direction in the median plane. Without RF the slope of the tail above the injection energy is T_t = 5.6 ± 1.4 keV (≈ $T_e(o)$) whereas with RF the slope increases to T_t = 18 ± 7 keV whereas $T_e(o)$ has increased to 6 keV. Fig 1 also shows

the H^+ spectrum due minority heating of residual H^+ ions at ω_{cH} which is coincident with $2\omega_{cD}$.

The enhancement of the DD reaction rate when ICRF is applied is typically a factor of 2-3. This is due to acceleration of the beam ions and to bulk ion heating by direct absorption at $2\omega_{cD}$ and by indirect (H)D minority heating. To assess the relative contributions the ratio B of observed reactivity with RF to that without RF is plotted in Fig 2 against the predicted ratio A for no RF acceleration of the beam ions but including both beam-plasma and thermal reactivities. The observed ratio exceeds the predicted ratio except at low RF power showing that the beam ion acceleration produces a substantial reactivity enhancement factor, $\varepsilon = B/A$, which increases with P_{RF}. Also shown in Fig 2 are data for central ^3He minority heating for which the $2\omega_{cD}$ resonance is outside the plasma. In this case there is no beam acceleration mechanism and the measured and predicted ratios are the same. On the assumption that the reactivity increase due to beam acceleration is due to an RF-generated increase in the number of D^+ ions close to the injection energy, the enhancement is expected to scale as $\varepsilon = (1+ P_D/P_B)$. In this expression P_B is the beam power and P_D is the RF power absorbed by the beam and is given by $P_D = P_H \beta_D/\eta_H$. The quantities β_D and η_H are the perpendicular fast ion beta and hydrogen to deuterium ratio respectively and P_H is the power absorbed by the H^+ minority. The data fit this linear dependence (Fig 4) with $\eta_H = 0.02 \pm 0.01$ consistent with $\eta_H = 0.03 \pm 0.01$ from NPA data.

As the ICRF power on JET is increased for future experiments the power coupled to the beam ions will produce substantial distortions to the beam distribution function which must be taken into account in calculating both the coupled power and the fusion yield. Such calculations have been made using the code described by Hellsten et al[3] to solve the non-linear, time dependent Fokker-Planck equation for the beam distribution. For example under the conditions of the above experiments the ratio of power absorbed by the deuterium ions to that absorbed by the H^+ minority, averaged over the plasma volume, is typically 0.25 if no distortion of the beam distribution is taken into account. However this ratio increases to 0.36 when the ICRF induced distortions are included.

We have also calculated the incremental fusion energy gain defined as $\Delta Q = n^2_D(\langle\sigma v\rangle - \langle\sigma v\rangle_{th})/(P_D+P_{NBI})$ where $n^2_D\langle\sigma v\rangle$ and $n^2_D\langle\sigma v\rangle_{th}$ are the steady state fusion yields obtained for RF + NBI and for a Maxwellian respectively. Results for DD are plotted in Fig 4 against RF power for parameters typical of the present experiments, namely $n_e = 3\times10^{19}$ m^{-3}, $n_D/n_e = 0.5$, $E_o = 80$ keV, $T_e = T_D = 4$ keV and 6 keV. The present experiments were carried out at power densities close to 0.15 Wcm^{-3} so that a factor of three increase in power could significantly increase the value of ΔQ. It is worth noting at this point that the experiments had not reached steady state and so the gain could be larger than that shown in Fig 4. Also shown in Fig 4 is the enhancement for a DT plasma with $n_D = n_T = 2\times10^{19}$ m^{-3}, $Z_{eff} = 1$, $T = 5$ keV and 10 keV and $E_o = 140$ keV. The value of ΔQ is reduced as the RF power is increased because more ions are heated beyond the peak in the fusion cross section.

COMBINED ω_{cH} + $2\omega_{cHe^3}$ EXPERIMENTS

These experiments were carried out in a He^3 plasma using ICRF frequencies of 28.3 MHz (ω_{cH}) and 31.7 MHz ($2\omega_{cHe^3}$). The toroidal field was 1.8T so that both resonances were close to the plasma centre. Power at ω_{cH} (~ 2.5 MW) was switched on for 2 sec to produce a plasma with a central ion temperature, ($T_i(o)$), of 3.4 keV and a volume average density $\langle n_e \rangle = 1.35 \times 10^{19}$ m^{-3}. After 1 sec of minority heating, 2.2 MW of power at $2\omega_{cHe^3}$ was applied and $T_i(0)$ was raised to 3.8 keV. The density increased slightly to $\langle n_e \rangle = 1.5 \times 10^{19}$ m^{-3} but the electron temperature remained constant at $T_e(o) = 3.7$ keV. The interpretation of the results is complicated by the fact that, during the combined heating phase, there is an H-minority resonance on the inboard plasma edge (R = 2.1 m) for f = 31.7 MHz. However, preliminary analysis indicates that ~10% of the power at 31.7 MHz is producing harmonic heating at $2\omega_{cHe^3}$.

CONCLUSIONS

Harmonic heating experiments have demonstrated coupling of RF power at $2\omega_{cD}$ to D^+ beam ions. Enhanced fusion yields have been observed and calculations predict that significant increases in Q can be achieved as the RF power is raised in future experiments. Preliminary studies of harmonic coupling to bulk ions have given encouraging results but further experiments at higher values of T_i to achieve better absorption are needed to fully define the feasibility of this scheme.

ACKNOWLEDGEMENTS

We wish to thank our colleagues in the JET team, expecially the tokamak and NBI operating teams and those operating the diagnostics used in the experiments reported in this paper.

[1] J. Jacquinot et al, Proc of 7th APS Topical Conf. on Application of RF Power to Plasmas, Kissimmee, 1987, to be published

[2] J.D. Callen, J.P. Christianse, J.G. Cordey, P.R. Thomas and K. Thomsen, JET Presentation, DPA(04)87, to be published

[3] T. Hellsten, K. Appert, W. Core, H. Hamnén, S. Succi, 12th Conf. on Contr. Fusion and Plasma Physics, Budapest, 1985 Vol 2 p 124

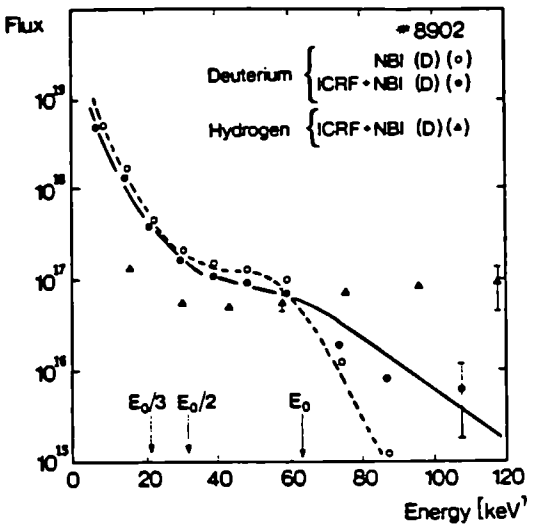

Fig 1 Deuterium NPA spectra during NBI (3.6 MW) and NBI (3.6 MW) + ICRF (6 MW) phases of the same discharge. The hydrogen spectrum during the combined heating phase is also shown.

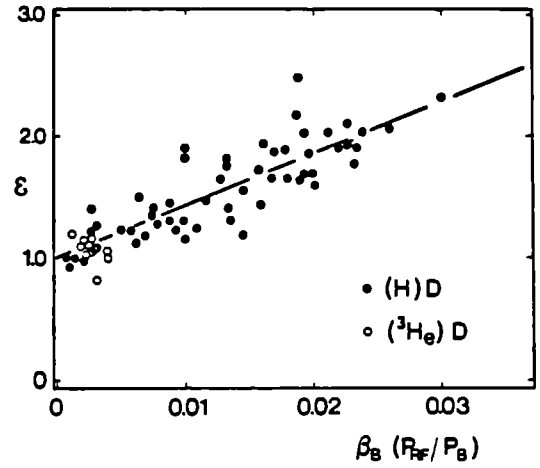

Fig 3 Experimental reactivity enhancement parameter versus the model scaling law.

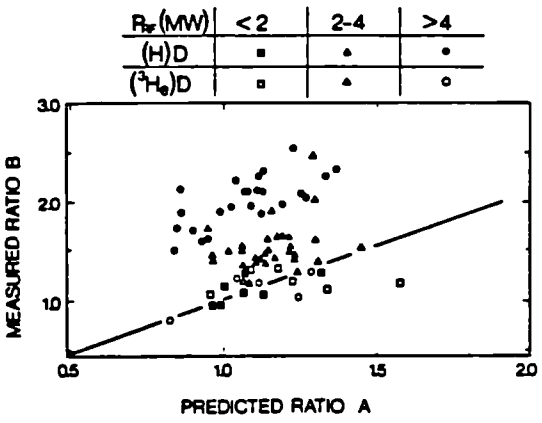

Fig 2 Measured versus predicted DD reaction rate ratios for different conditions of both ^{3}He and H minority schemes with $D^0 \rightarrow D^+$ NBI.

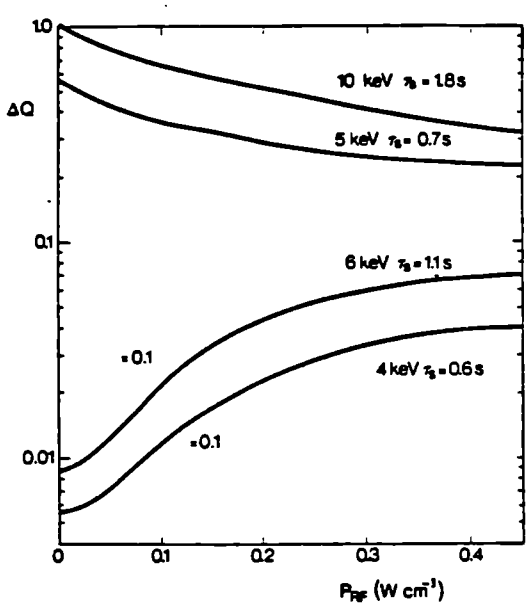

Fig 4 Incremental ΔQ plotted versus RF power density assuming $T_e = T_i$. Lower curves: DD reactivity; Upper curves: DT reactivity. Steady-state conditions are reached after approximately one Spitzer slowing-down time, τ_S.

EXPERIMENTS WITH DIVERSE ICRH SCENARIOS ON JET

V.P. Bhatnagar*, J.J. Ellis, J. Jacquinot, D.F.H. Start

JET Joint Undertaking, Abingdon, Oxon, OX14 3EA, UK
*From LPP-ERM/KMS, EUR-EB Association, 1040 Brussels, Belgium

1. INTRODUCTION

During the last ion-cyclotron resonance heating (ICRH) experiments on JET, RF power exceeding 7 MW for several seconds, has been coupled to the JET plasma (f ~ 32 MHz) in a variety of conditions: Limiter, Inner-Wall and X-Point Configurations in (H)-D, (He^3)-D and (H)-He^3 plasmas, where the symbol in the parenthesis represents the minority species. Also, the combined neutral-beam and ICRH experiments have been carried out with D^0-beam injected in D-plasmas both with He^3 and H as minority species. The latter scheme also produces significant acceleration of D^+-beam at the 2nd-harmonic frequency which coincides with H-minority cyclotron frequency. Preliminary experiments at $2\omega_{ci}$ of He^3 have also been done which remove such a degeneracy.

In this paper, we attempt to make a comparison of the plasma heating and confinement results, hitherto, obtained in limiter discharges with minority ICRF heating in the above mentioned three plasma compositions. Also ICRF experiments with an X-point configuration are discussed.

2. RESULTS

In order to make good scaling studies with plasma current and a comparison of minority heating with two minority species (H and He^3) and two majority species (D and He^3), for the results presented below, we include the data of JET limiter discharges extending over a period of one year. The plasma parameters under ICRF heating are in the following ranges: $0 \leq P_{RF}(MW) \leq 7$; $0 \leq W_{RF}(MJ) \leq 35$; generally, f~33 MHz but for off-axis heating $24 \leq f(MHz) \leq 47$; $2 \leq B_\phi(T) \leq 3.5$; $1 \leq I_p(MA) \leq 5$; $0.7 \leq P_{OH}(MW) \leq 4.5$; $1 \leq \bar{n}_e x 10^{-13}(cm^{-3}) \leq 5$; $2 \leq T_{eo}(keV) \leq 7$; $1.5 \leq T_{io}(keV) \leq 5$; $0.2 \leq P_{rad}/P_{tot} \leq 0.8$; $2 \leq Z_{eff} \leq 5$.

(a) Confinement A plot of stored kinetic energy vs total power input P_T is shown in Fig 1 where we have identified both the minority and majority species, at different plasma currents. It is clearly seen that the stored energy increases linearly with the applied power but, the lines do not go through the origin and follow the so-called "off-set linear" law. This behaviour is also predicted by the theoretical heat pinch or the critical temperature gradient model[1] and fits well the JET ICRH experimental data when the heat diffusion coefficient $\chi(r)$ is taken to vary as $\chi_0/(1-r^2/a^2)$ where a is the plasma radius. Note that there is little difference in the energy confinement time in the various minority species heating carried out in the two majority species (see 2 and 3 MA data).

The incremental confinement time τ_{inc} is given by the slope of a line in the W-P_T plot where the scan is carried out at constant density.

To obtain such data in the experiment is tedious. For individual shots, τ_{inc} can be obtained by $\tau_{inc} = (W-W_{OH})/\Delta P_T$ where W_{OH} during RF is determined by a projection of the OH-data which has its inherent assumptions and leads to larger error bars. Since the density rise during RF is small in JET, we can deduce $\tau_{inc}=(W-W_{OH})/\Delta P_T$ in terms of the directly measured quantities where W_{OH} is the stored energy just before the ICRH pulse [2]. The results obtained by the two procedures are nearly the same especially when the Δn_e and ΔP_{OH} are small [3] and here we illustrate the results by the latter procedure. In addition to the data contained in Fig 1, we also include other off-axis heating data in Fig 2 to plot τ_{inc} as a function of the cyclotron layer position (r_c) from the magnetic axis. The r_c has been calculated by including the corrections of poloidal field and paramagnetic effects to the vacuum field which can be significant at higher currents [4]. It is seen from Fig 2 that τ_{inc} degrades as we move r_c away from the magnetic axis. A broken line has been drawn through the 2 MA, He^3(H) data points which extend over a larger range of r and we note that the degradation varies as $(1-r_c^2/a^2)^2$ which is predicted by the heat pinch model [1] for the $\chi(r)$ variation mentioned above. The τ_{inc} data in Fig 2 has been replotted as $W-P_T$ plots at several fixed r_c positions and slopes of these lines vary in accordance with the broken line shown in Fig 2.

We now proceed to fit the W vs P_T data at different I_p given in Fig 1 with r_c appropriately accounted for. The total stored energy can be written as $W = W^o + \tau_{inc} \cdot (P_T-P^o)$ where W^o is the initial plasma energy (or W_{OH}) and P^o is the initial heating power (or P_{OH}). Though in Ref [1], τ_{inc} is split into a "heating efficiency" and τ_χ, we choose to include the degradation in confinement with off-axis heating in τ_{inc} itself to plot the data in terms of measured quantities and find that a good fit to the data in Fig 1 (solid lines) can be described by the above expression of W where

$$\tau_{inc} = \tau^o_{inc}[s] \cdot I_p^\alpha\,[MA] \cdot (1 - (r_c/a)^2)^2$$

and $\tau^o_{inc} = 0.15$ s and $\alpha = 0.5$ [3]. The same data can be fitted equally well by using a W_{OH} that has been corrected for the density rise during RF [5] and the value of $\tau^o_{inc} = 0.18$ and $\alpha = 0.25$. Corrections for the radiation profiles increases α by ~ 0.1. The τ_{inc} in ICRF heating of JET does not show a linear current scaling as opposed to TEXTOR [5] but is more in line with JFT-2M data [6]. However, the scaling advocated by JFT-2M i.e. $\tau_{inc} \sim 0.12\, a_p^2\, I_p^0\, n_e^0$[7] should also include the degradation when heating is carried out off-axis, the so-called profile effects described above.

(b) Heating For a comparison of the heating efficiency $\eta = \Delta T/(P_{RF}/\bar{n}_e)$ of different combinations of minority and majority species, we have selected 2 MA data and we plot ΔT_e and ΔT_i, in Fig 3 and 4 respectively, as a function of $P_{RF}/\bar{n}_e$ where $\bar{n}$ is the line average density. Note that at lower values of $P_{RF}/\bar{n}_e$, the increase of ΔT_e is much weaker (especially for He^3 minority) as compared to that of ΔT_i. However, at larger values of $P_{RF}/\bar{n}_e$, the ΔT_e rises faster whereas the ΔT_i has a tendency to flatten out. This behaviour is found to be consistent with the Stix [8] theory, in which at lower power densities, the weaker

minority ion tail formed relaxes on the bulk ions especially in the He^3 minority case due to stronger ion-ion coupling between He^3 and bulk deuterons. At higher power densities, the strong tail formed in the case of H-minority relaxes on electrons heating them preferentially. However, due to relatively smaller equilibration time between electrons and ion species compared to the confinement time in JET, there is a considerable heating of ions as well in the high power minority heating.

(c) X-point discharges A series of X-point discharges were made in which attempts were directed to achieving a transition to H-mode with ICRF alone using He^3(H) plasma composition. In order to couple significant amount of power, the ICRF antenna-plasma distance was kept to about 6 cm (compared to 10 cm in NBI X-point discharges). RF power up to a level of 6.5 MW was coupled but no sharp transition akin to an H-mode could be demonstrated. However, in these ICRF heated X-point discharges, 20% larger τ_{inc} was obtained than in Limiter discharges possibly due to higher plasma elongation. In some X-point discharges as in Limiter discharges improved confinement times were coincident with the appearance of an ultralong (monster) sawtooth which are accompanied by an increase in density, stored energy and quiescent MHD activity etc [9].

3. SUMMARY AND CONCLUSIONS

The stored energy in ICRF heated discharges follows an off-set linear law which is predicted by the heat pinch or critical temperature gradient model [1]. The W-P_T data can be fitted by taking $\tau_{inc} = \tau_{inc}^{[s]} \cdot I_p^{\alpha}$ (MA). $(1-(r_c/a)^2)^2$ where $\alpha = 0.25$ to 0.5. Similar values of τ_E were found in heating with different minority and majority plasma compositions. At low power densities, ion heating efficiencies are better especially in the He^3 case whereas at higher power densities, improved electron heating is produced. Though it has not been discussed, in (H)-He^3 plasmas, it is easier to control the density and the radiated power and Z_{eff} are lower. Ultra long (Monster) sawteeth are also found to occur in (H)-He^3 X-point discharges in which τ_E is about 20% better than the limiter discharges. However the production of a fullfledged H-mode with ICRF alone was not attained presumably due to insufficient RF power when the plasma had to be kept significantly detached from the antenna in the X-point configuration.

REFERENCES

[1] J.D. Callen et al, JET-P (87)10, P-H Rebut et al, as in [2], CN-47/E-III-4.
[2] J. Jacquinot et al, 11th IAEA, Kyoto, Japan, 1986 CN-47/F-I-1.
[3] V.P. Bhatnagar et al, JET Report under preparation.
[4] V.P. Bhatnagar, JET-JDN(87)3, Internal Note, unpublished.
[5] P.E. Vandenplas et al, as in [2], CN-47/F-I-4.
[6] K. Odajima et al, Phys. Rev. Lett. 57, (1986) 2814.
[7] Y. Shimomura et al, Comments on Plasma Phys. Controlled Fusion 10 (1987) 207.
[8] T.H. Stix, Nucl. Fusion 15 (1975) 737.
[9] J. Jacquinot et al, Invited paper, 7th Topical Conf. on RF, Kissimmee, Florida (1987).

ACKNOWLEDGEMENTS

We wish to thank our colleagues in the JET team, especially the tokamak operating teams and those operating the diagnostics used in the experiments reported in this paper.

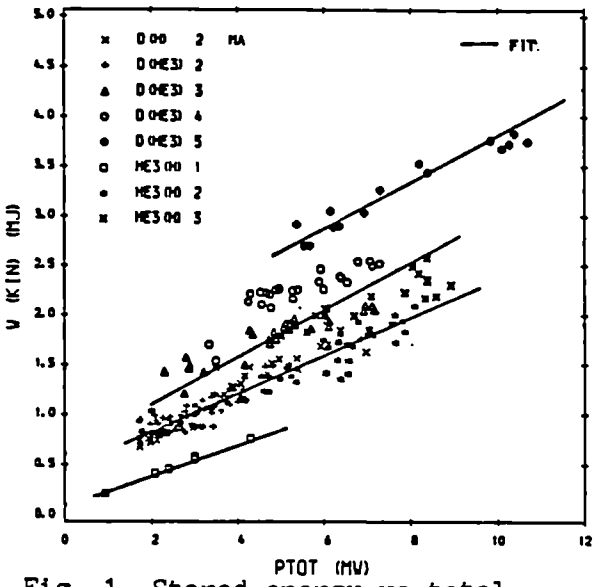

Fig. 1 Stored energy vs total input power during ICRH for different I_p and plasma compositions

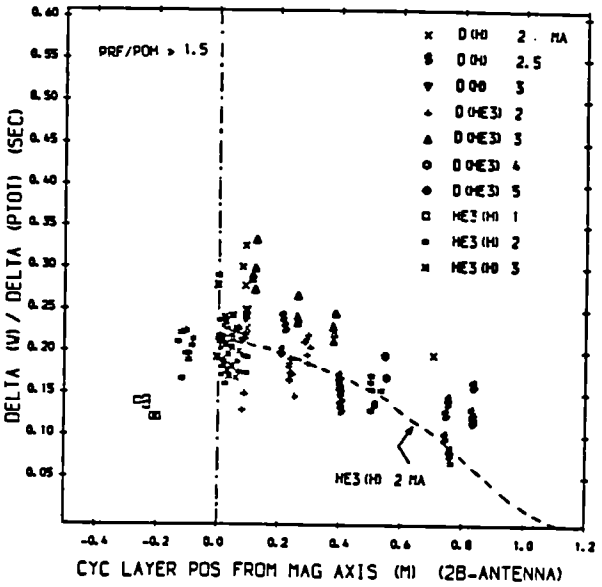

Fig. 2 τ_{inc} vs cyclotron layer position from the magnetic axis during minority heating

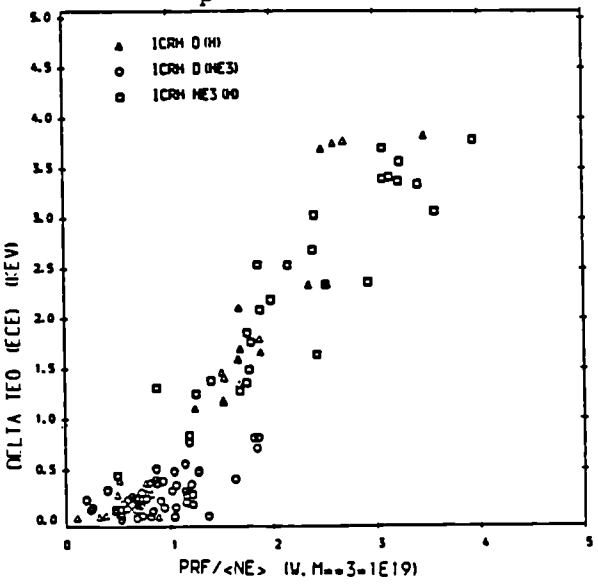

Fig. 3 ΔT_{eo} vs $P_{RF}/\bar{n}_e$ for different plasma compositions. I_p = 2 MA and $1 < \bar{n}_e < 2.5$ - $0.1 \leqslant r_c$ (m) $\leqslant 0.25$ in Fig. 3 and 4

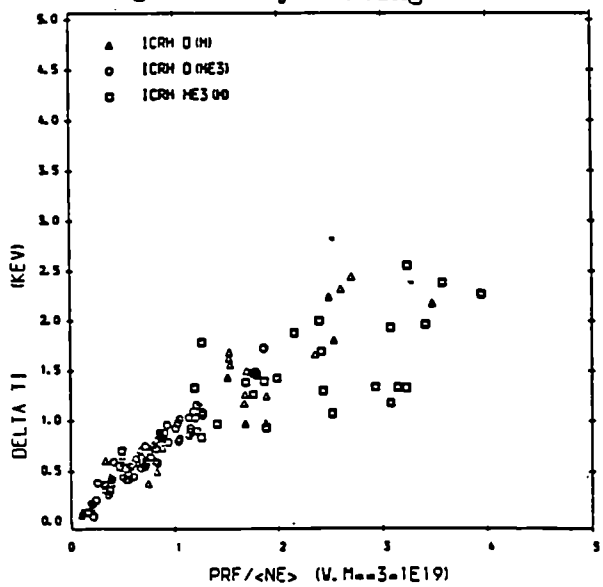

Fig. 4 ΔT_i vs $P_{RF}/\bar{n}_e$ as in Fig. 3

RFK/SK10/DR

PLASMA CURRENT PROFILE CONTROL IN JET BY LOWER HYBRID CURRENT DRIVE

S. Knowlton*, C. Gormezano, D. Moreau**, R.J. Anderson, V.P. Bhatnagar***, G. Bosia, H. Brinkschulte, C. David**, J.A. Dobbing, J. Jacquinot, A.S. Kaye, M. Pain, D.F.H. Start.

JET Joint Undertaking, Abingdon, Oxon, OX14 3EA, UK.

* From Plasma Fusion Centre, M.I.T. Cambridge, Mass. 02139 USA.
** From EUR-CEA Association, CEN Cadarache, 13108 St. Paul lez Durance, France.
*** From LPP-ERM/KMS; EUR-EB Association, 1040 Brussels, Belgium.

INTRODUCTION

Recent studies on several tokamaks have shown that the sawtooth instability can be suppressed by lower hybrid current drive (LHCD). The stabilization generally results from a broadening of the plasma current profile [1]. A number of improvements in plasma parameters are associated with the current profile broadening by LHCD. Under certain conditions, the suppression of sawteeth has led to peaked electron temperature profiles with a corresponding increase in central energy confinement [1,2]. Improvement of energy confinement in NBI-heated plasmas as a result of broadening of the current profile by LHCD has been observed [3], and the control of disruptions by LHCD current profile modification of low q discharges has also been reported [4]. It is also expected that the confinement of energetic fusion products will be significantly improved in the absence of sawteeth. In general, active tailoring of the current profile is considered to be a useful tool to optimize the performance of tokamaks. The benefits of sawtooth suppression and current profile control for increased fusion yields will be examined in a large scale LHCD experiment presently being prepared for JET. The explicit purpose of this experiment is to broaden the current profile of NBI and ICRF heated JET plasmas in order to achieve fusion grade central parameters, e.g. $T_{eo} = T_{io} = 10$ keV at $n_{eo} = 10^{20}$ m^{-3}.

EXPERIMENTAL PLANS

A 3.7 GHz lower hybrid system capable of 10 MW injected power for a maximum pulse length of 20 seconds has been proposed for installation on JET. The RF power will be coupled through a single port by a multi-junction-type phased waveguide array [5]. A sketch of the proposed launcher is shown in Fig. 1. The antenna consists of 48 separate modules, each of 2 rows by 4 columns of waveguides. The entire grill is moveable via a double bellows assembly; thermal expansion of individual waveguides is permitted by a separate bellows on each waveguide feed. The RF power is supplied by 24 klystrons. Within each module, the power is split to feed the two rows of E-plane multijunctions. The maximum incident power density at the grill mouth is $P_{rf} = 4.1$ kW/cm^2 which, based on empirical scalings from previous LHCD experiments, is achievable at this frequency. Passive waveguides shown in Fig 1 in the inset at

left reduce the reflection coefficient in the edge modules. The waveguide dimensions at the grill mouth are 7.2 x 0.9 cm, and the wall thickness is 0.2 cm. The overall reflection coefficients of the multijunction grill are in the range of 1 - 5%. The multijunction is constructed such that the relative phase between adjacent waveguides in the module is $\Delta\phi = 90°$. The launched parallel wave number spectrum can be varied by changing the relative phase $\delta\phi$ between the 8 modules in a horizontal row. The n// spectra launched by the grill, as predicted by a multijunction coupling code [6], is shown in Fig. 2 for the phase settings $\delta\phi = -90°$, 0°, and +90°. For the phase $\delta\phi = 0°$, the spectrum exhibits a narrow peak at $n_{//} = 1.9$ which contains approximately 70% of the total coupled RF power. Another 20% of the injected power is located in a narrow peak at $n_{//} \simeq -5.5$ (off the figure to the left). Waves in this spectral range do not contribute significantly to the net RF driven current because of the high collisionality of electrons resonant with these waves. The narrow spectrum permits a concentration of power at relatively low values of n// for efficient current drive, but still above the accessibility limit for conversion to the fast wave. The average $n_{//}$ can be varied in the range $n_{//} = 1.4 - 2.3$ to provide some control of the RF deposition profile under different plasma conditions.

Because of the elongation of the JET plasma and the high currents (I_p - 7MA) forseen for future JET operations, the angle α between the local magnetic field at the grill mouth and the RF electric field in the waveguides may be as large as $\alpha = 20°$. The question of slow wave coupling with a non-zero poloidal field is investigated with a simple model of coupling to a monochromatic wave of finite poloidal wave number in a homogeneous plasma. The angle β in the vertical plane between the wavevector and the horizontal is varied to find the optimal coupling condition, as given in this model by the plasma surface admittance of the monochromatic wave. For values of $\alpha = 15°$-30°, the reflection coefficient exhibits a broad minimum over a range of $\Delta\beta = 30°$, with optimal values at $\beta \sim 5°$-10°. Such small values of β can be imposed by phase differences between the horizontal rows of modules. Thus for the range of plasma currents envisaged for JET, the finite poloidal field is not expected to impede efficient coupling.

WAVE PROPAGATION

The wave propagation and damping within the plasma is modelled with the use of the Bonoli-Englade combined lower hybrid toroidal ray tracing and Fokker-Planck analysis code [7]. The calculated coupled power spectra illustrated in Fig. 2 are divided into approximately 50 separate n// components which are launched from the outer midplane of the torus. The trajectory and evolution of the wave vector components of each ray are calculated by geometric optics in toroidal geometry for realistic JET temperature and density profiles. At present, the magnetic equilibrium is taken to be Shafranov-shifted circular flux surfaces with the minor radius corresponding to the JET minor radius along the horizontal midplane. Wave damping along the ray is calculated self-consistently in the presence of the RF-generated fast electron tail from the numerical

solution of the one-dimensional Fokker-Planck equation incorporating an enhanced effective perpendicular temperature. Appropriate moments of the distribution function give the radial profiles of the RF driven current density and the absorbed RF power. Examples for JET parameters are shown in Fig. 3 for B_T = 3.4T, I_p = 3MA, n_{eo} = 4.5 x $10^{19}m^{-3}$ (parabolic profile) and temperature profiles of the form $T=T_o(1-r^2/a^2)^3$. For such plasmas in JET, the sawtooth inversion radius is located approximately at r = 0.4 m. In the simulations shown, the spectrum for $\delta\phi = 0°$ ($n_{//}$ - 1.9) was used, and P_{rf} = 5 MW. Cases for (i) T_{eo} = 5 keV and T_{io} = 4 keV; and (ii) T_{eo} = 10 keV and T_{io} = 7 keV are illustrated. The low temperature case exhibits centrally peaked RF deposition and current profiles. Although the rays do not penetrate inside r/a < 0.4 on their initial pass, the eventual upshift in $n_{//}$ allows propagation to the central region where damping subsequently occurs. At higher electron temperatures, the tail formation and quasi-linear absorption take place at larger radii (r/a > 0.35). In both cases, a very small amount of negative RF current is generated at large radii due to the damping of relatively high parallel wave number rays on the negative side of the spectrum. The localization of the RF driven current outside the inversion radius in the higher temperature case is clearly desirable for sawtooth stabilization and current profile broadening. The RF driven current profile is narrow as a result of the narrow spectrum and efficient damping accorded by the high temperatures although radial diffusion of fast, current-carrying electrons has not been taken into account. Furthermore, the calculated RF current drive efficiency η=0.5 MA MW^{-1} 10^{20} m^{-2} in this case is approximately 15% higher than in the lower temperature plasma, in part due to lower superthermal electron collisionality at mid-radius. We remark that such an improvement of current drive efficiency with increasing electron temperature has been reported from LHCD experiments on NBI-heated JT-60 plasmas [3].

SUMMARY

A LHCD system for current profile modification is being designed for JET. The design makes use of the multijunction grill concept to improve the coupling and to reduce the overall complexity of the system. The grill couples a narrow spectrum to the plasma for localized current drive. The present calculations indicate that the RF deposition is indeed localized well off-axis for conditions expected in JET under high power ICRF and NBI heating, thus providing significant broadening of the total current density profile.

ACKNOWLEDGEMENTS

We thank Dr. P. Bonoli for kindly providing us with a version of the ray tracing and Fokker Planck code and for further assistance.

1. F.X. Söldner et al., Phys. Rev. Lett 57(1986
2. T.K. Chu et al. Nucl., Fusion 26(1986)666)1137
3. K. Ushikusa et al., JAERI-M 87-012(1987)
4. D. Van Houtte et al., Nucl. Fusion 24(1984)1485
5. C. Gormezano et al., Nucl. Fusion 25(1985)419
6. D. Moreau and T.K. N'guyen, EUR-CEA-FC 1246 (1984)
7. P. Bonoli and R. Englade, Phys. Fluids 29 (1986)2937

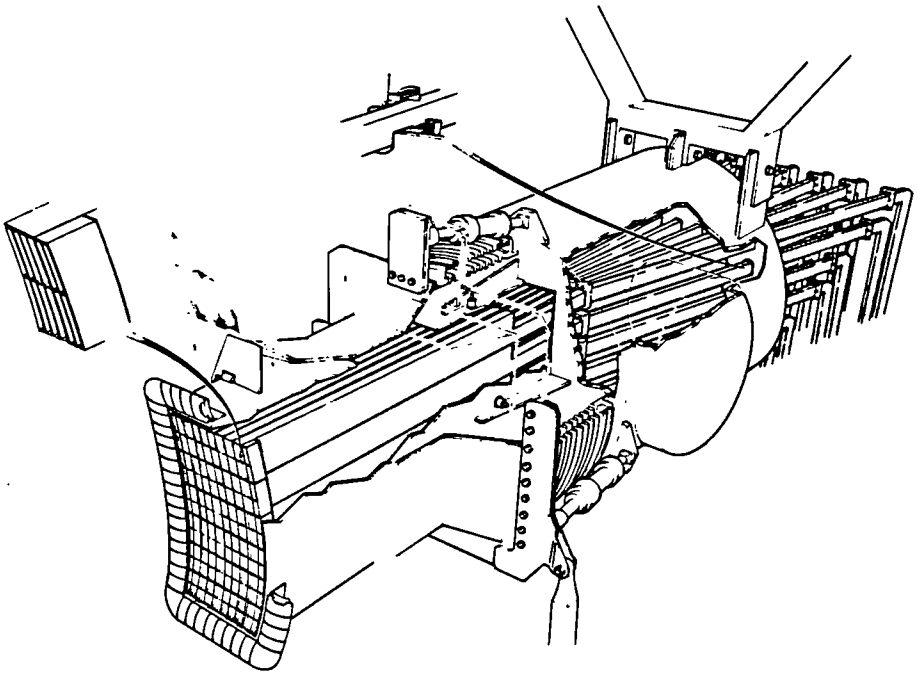

FIG. 1. Sketch of the proposed JET lower hybrid grill.

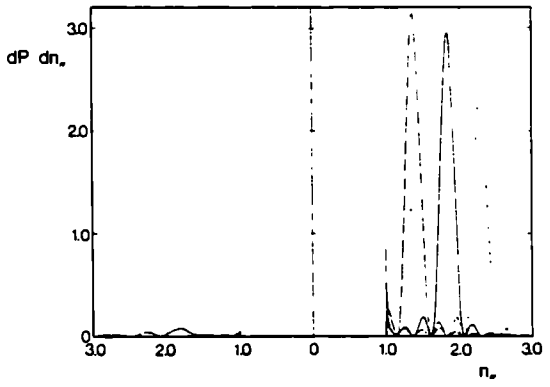

FIG. 2. Detail of calculated power spectra for $n_{//} \leq 3$; $n_e = 1.4 \times 10^{18}$ m^{-3} and $\nabla n_e = 1.4 \times 10^{20}$ m^{-4} at the grill mouth. The phase between adjacent modules is $\delta\phi = -90°$ (dashed line); 0° solid line; and +90° (dot-dashed line).

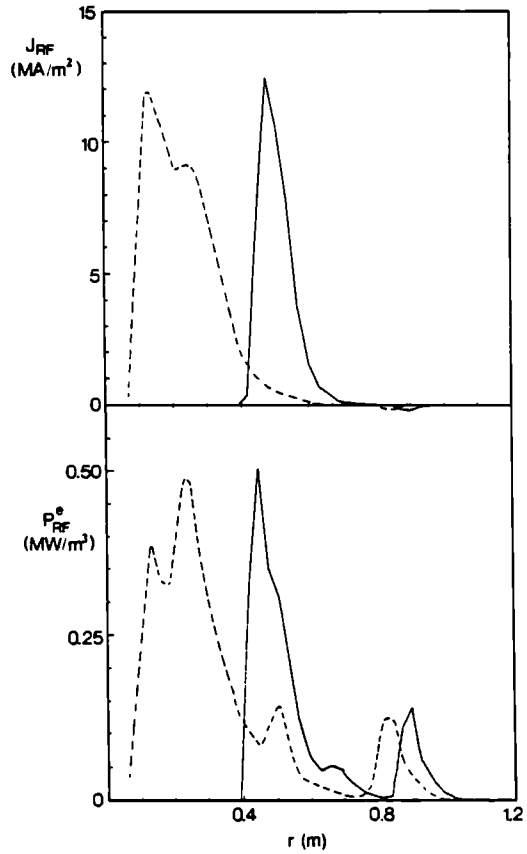

FIG. 3. (a) Calculated RF current density profile in JET for $T_{eo} = 5$ keV, $T_{io} = 4$ keV (dashed line); and $T_{eo} = 10$ keV and $T_{io} = 7$ keV (solid line). (b) RF power profile on electrons for the same conditions.

PHENOMENOLOGICAL AND PREDICTIVE STUDIES OF CONFINEMENT AND GLOBAL HEATING IN JET NEUTRAL BEAM HEATED LIMITER PLASMAS

E Thompson, D Bartlett, F Bombarda(1), G Bracco(1), D J Campbell, C Challis, J P Christiansen, J G Cordey, S Corti, A Costley, G Duesing, R Giannella(1), A P H Goede, L Horton, T T C Jones, E Kallne, O Kaneko(2), P J Lomas, D Muir, J Snipes, A Staebler(3), D Stork, P M Stubberfield, G Tallents, P R Thomas, K Thomsen, M von Hellerman and M L Watkins.

JET Joint Undertaking, Abingdon, U.K., (1) EURATOM-ENEA Association, Frascati, Italy, (2) Institute of Plasma Physics, Nagoya, Japan, (3) IPP Garching, FRG.

INTRODUCTION

NBI experiments have been performed using a wide range of target plasmas to establish the scaling of the global energy confinement with plasma current (I_p), toroidal magnetic field (B_T) plasma density (n_e) and input power (P_{TOT}) for both H°(≤65 keV) & D°(≤80 keV) injection into D plasmas. This paper describes results obtained with the plasma boundary defined by either the 8 outboard graphite limiters, or by the graphite inner wall protection tiles. The results of NBI experiments in X-point plasmas are presented elsewhere [1].

The JET vacuum vessel and graphite surfaces are conditioned by baking and glow discharge cleaning. They were maintained at 290°C during these experiments. The plasma density behaviour during NBI varied according to limiter configuration and is described in [2]. In summary the onset of NBI led to a transient density increase under all conditions. For outboard limiters the density rises linearly during NBI. On the inner wall tiles, a much lower density increase was obtained. This pumping was further improved during the 'hot-ion' campaign by conditioning the inner wall surfaces using Helium Ohmic discharges prior to NBI discharges.

GLOBAL ENERGY CONFINEMENT

The total plasma energy content from diamagnetic loop measurements (W^{DIA}) of all NBI plasmas is well described by a linear function of P_{TOT} when all other controllable parameters are constant [3]. Energy contents determined from poloidal field measurements and kinetic pressure profiles show similar behaviour and the three stored energy measurements are in reasonable agreement. The energy contents are roughly proportional to plasma current. These dependences have been built into an offset linear scaling law [3] of the form (figure 1)

$$W^{DIA} = 0.225\ n_e^{0.6}\ I_p^{0.5}\ B_T^{0.4} + 0.047\ I_p\ P_{TOT} \qquad (1).$$

The scaling of the energy content of Ohmic discharges is reproduced by the scaling of the intercept in (1). The dependence of W on the relevant parameters is described equally well by a power law fit, which is shown in figure 2

$$W^{DIA} = 0.27\ P_{TOT}^{0.37}\ I_p^{0.67}\ \langle n_e \rangle^{0.41}\ B_T^{0.24} \qquad (2)$$

The data is also well described by L-mode scaling [5].

From local transport analysis [4] which includes the NBI power deposition profile it can be concluded that the plasma thermal conductivity apparently depends upon the poloidal field only.
The 3 MA data obtained after He conditioning were not used in the above fitting procedure and they exhibit higher values of τ_{inc} ($= \delta W/\delta P_{TOT}$) than high density pulses. The measured density profiles of these discharges also show a tendency towards being slightly more peaked than other types of NI discharges.

Heating Efficiency with NBI

NBI electron heating efficiency on JET has been constrained by the relatively low values of injection energy (30-60 keV/AMU). The electron heating efficiency (figure 3) tends to saturate at electron temperature values 5-6 keV where the total power input to the electrons (NBI + Ohmic + Equipartition) has fallen to a low level.
In contrast, ion heating efficiency increases with the power per particle (figure 4). The spectroscopic N_i^{26+} temperature measurements shown in figure 4 are calculated to be at most 1-2 keV higher than the deuterium temperature at the highest values. The discharges following helium conditioning show the best ion heating, partly because lower densities are accessible than in limiter discharges. This results in the decoupling of the ions from the electrons as the equipartition time (τ_{ei}) becomes larger than the energy confinement time.
These 'High T_i' discharges gave the highest neutron rate obtained on JET ($2.8\ 10^{15}\ s^{-1}$) of which approximately half can be attributed to beam-plasma reactions.

Enhanced Confinement in Inner Wall Discharges

The energy content of the inner wall (3 MA, 3.4 T) plasmas falls into 2 groups ('A' and 'B' in figure 5). The type A plasmas were those immediately following helium conditioning. They showed reduced recycling evidenced by a steady-state density and the lowest values of deuterium-α light during NBI.
The measured electron energy contents (W_e) in the two groups were identical within errors so the difference in W^{DIA} must reside in the ions. The calculation of stored energy using the measured central ion temperature and dilution factor from the measured Z_{eff} indicates that the ion temperature profile was more peaked than that of the electrons in these shots. This is confirmed by preliminary results obtained by a neutral particle analyser array.

Power Balance in Hot Ion Plasmas

The data for 3.0 MA/3.4 T plasmas with $5.0 < P_{TOT} < 7.0$ MW has been compared with results from a simple 0-D model. The model uses characteristic times based on L-mode scaling for loss rates in both channels and classical equipartition between them. The predictions of this model reproduce the data tolerably well (figure 6). This indicates the energy confinement is no different in character between hot ion and high density regimes.
Local transport analysis is limited by the preliminary nature of ion temperature profiles, nevertheless the available data does show that, in

contrast to high density plasmas, the ion loss channel dominates within the central half minor radius in hot ion plasmas. Ion convection and conduction have comparable magnitudes in the centre and equipartition returns a large power fraction to the electrons in the outer plasma. In these respects JET hot ion plasmas are similar to TFTR supershots [6].

REFERENCES

[1] Keilhacker M, et al, these proceedings.
[2] Jones TTC, et al, these proceedings.
[3] Cordey JG, et al, 11th Int. Conf. on Plasma Phys. & Contr. Nucl. Fus. Research (Kyoto 1986), IAEA-CN-47/QA-II-3.
[4] Callen J, et al, 'Modelling of temperature profile responses to Heating Profiles in JET', these proceedings.
[5] Goldston RJ, Plasma Phys. & Contr. Fus. 26,1A,87-103 (1984).
[6] Hawryluk RJ, et al, 11th Int. Conf. on Plasma Phys. & Contr. Nucl. Fus. Research (Kyoto 1986), IAEA-CN-47/A-I-3.

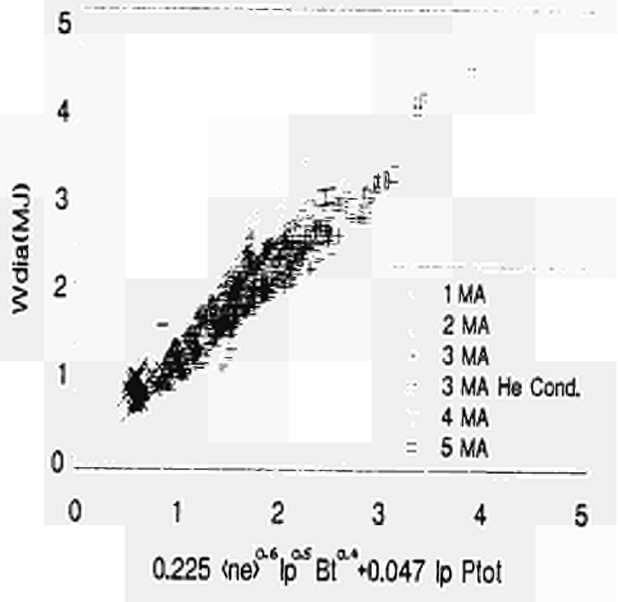

Figure 1 : Offset linear scaling law plotted against JET NBI stored energy measured by diamagnetic loop (W^{DIA}).

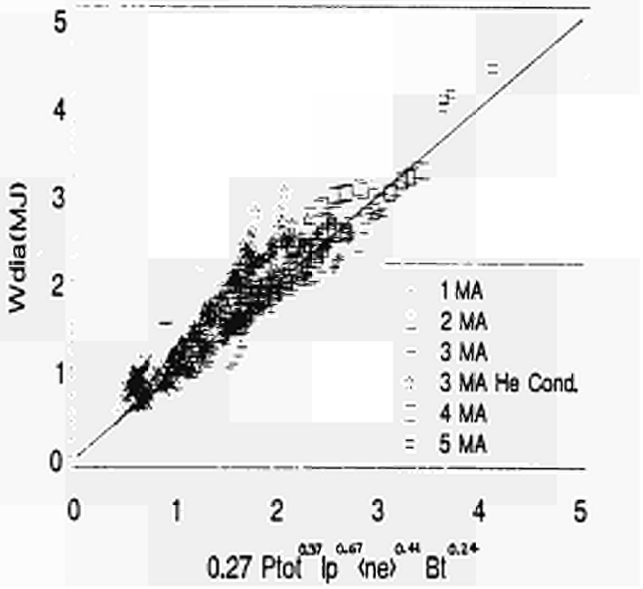

Figure 2 : Power law fit to NBI W^{DIA} measurements.

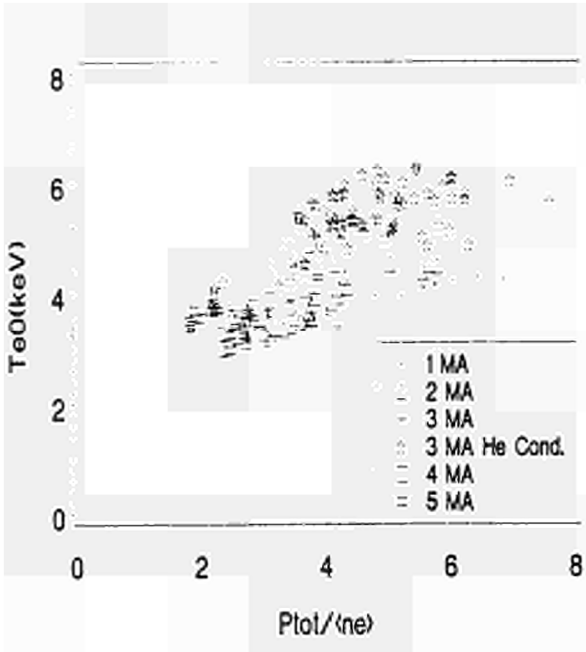

Figure 3 : Central electron temperature from ECE measurements for NBI discharges as a function of total power (P_{tot}) normalised by volume averaged density ($\langle n_e \rangle$).

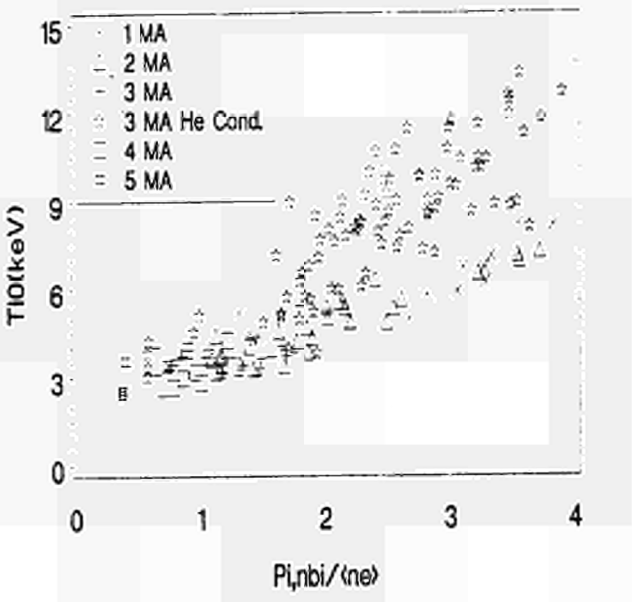

Figure 4 : Central ion temperature ($T_i(o)$) for Ni^{26+} ions in NBI discharges measured by Doppler shift of the NiXXVII line as a function of calculated power to the ions (P_{bi}) normalised by volume averaged density ($\langle n_e \rangle$).

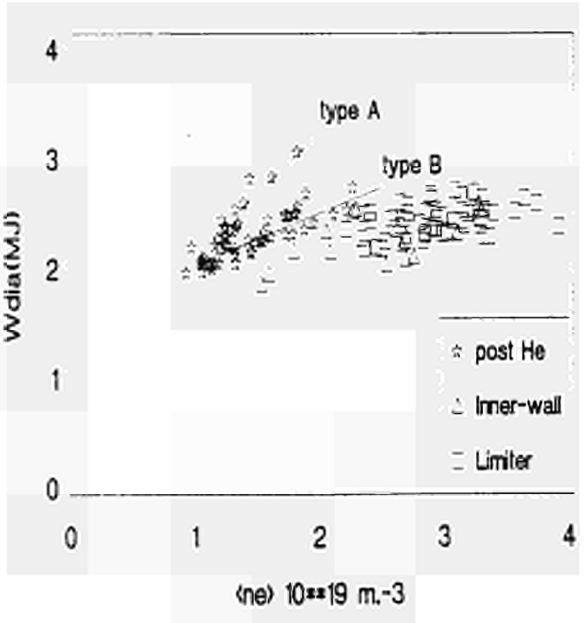

Figure 5 : Diamagnetic stored energy measured as a function of volume averaged density for 3 MA/3.4 T NBI discharges.

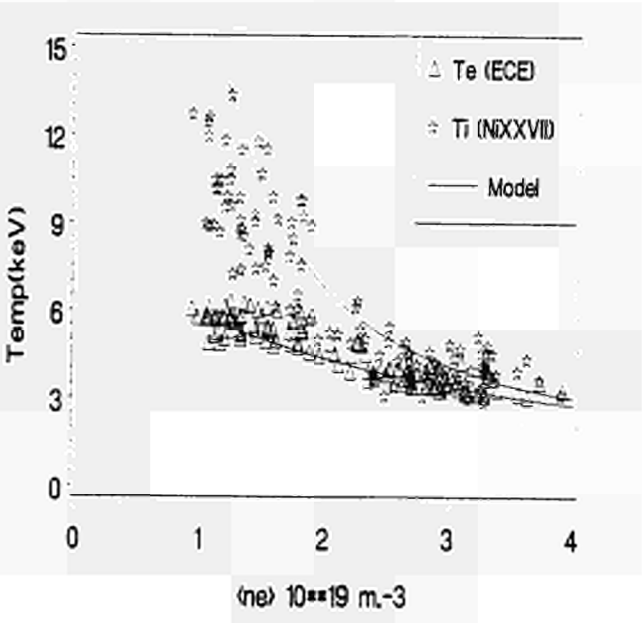

Figure 6 : Measured $T_i(o)$ and $T_e(o)$ for NBI discharges compared to predictions from the simple 0-D code (see text).

NEUTRAL BEAM CURRENT DRIVE STUDIES AT JET

C. Challis, J.G. Cordey, H.Hamnén, D. Campbell, J. Christiansen, M. Cox, E. Lazzaro, D. Muir, D. Stork, P. Stubberfield, E. Thompson.

JET Joint Undertaking, Abingdon, Oxon., OX14 3EA, UK

Introduction

The JET neutral injection system consists of two injection boxes, each designed to operate up to injection energies of 80keV in H or 160keV in D. To date, only one box has been in operation, with the second box scheduled to operate in the second half of 1987. The injected power per box is up to 10MW. The neutral beam trajectory is shown schematically in Fig.1.

During neutral beam heating (co-injection) in low plasma current discharges, the loop voltage drops to levels substantially below the values that would be expected from the changes in the electrical conductivity. For the corresponding counter-injection cases, the drop in the loop voltage is less than would be expected from the changes in conductivity. We attribute these differences to neutral beam current drive. A typical loop voltage trace for a co-injection case is shown in Fig.2 (curve d). Also shown are the traces that would be expected from the changes in conductivity alone (a), from conductivity plus the effect of the predicted beam current (curve b, cf below) and finally, curve c, from conductivity plus beam current plus the neo-classical bootstrap current [1]. The predicted bootstrap current typically turns out to be rather small(~50-150kA) and both the latter curves reproduce the measured experimental loop voltage rather well.

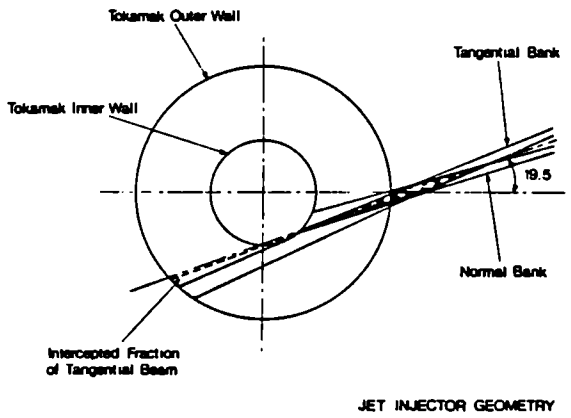

Fig.1 Schematic view of the JET injection geometry.

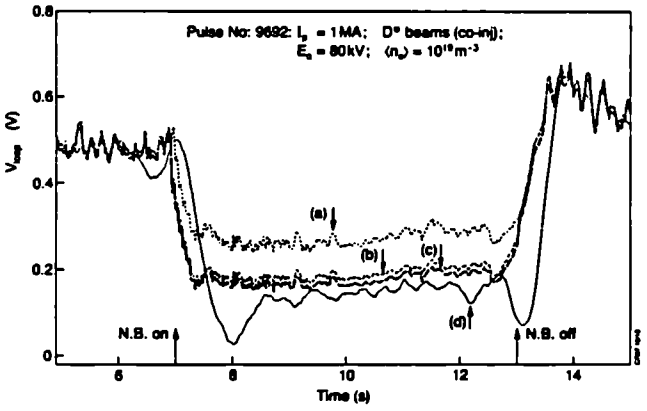

Fig.2 a) Prediction for V_{Loop} from conductivity change only.
b) Conductivity plus beam driven current
c) as in b) but plus bootstrap current
d) V_{Loop} experimental trace.

Analysis and Results

To predict the beam power deposition and the beam driven current the code PENCIL is used. PENCIL uses an analytical solution of the bounce-averaged Fokker-Planck equation, with the experimentally measured plasma parameters as input variables. This solution includes collisional slowing-down and pitch-angle scattering. The effects of energy diffusion, acceleration of the fast ions by the electrical field and bulk plasma rotation are neglected as they are small for typical JET conditions.

To determine the magnitude of the current which is driven by the beam, the difference between the actual plasma current and the ohmically driven current is formed:

$$I_b = I_p - \int \sigma E dA$$

Here, σ is the neoclassical conductivity, E is the inductive field strength and the integration is carried out over the plasma cross section. In carrying out this integral, two assumptions are made:

i) Z_{eff} as calculated from visible bremsstrahlung is constant over the cross section, and

ii) $E = E_{surface}$ over the cross section.

The limited information we have about impurity profiles tends to uphold the first assumption. The second assumption of course, invalidates any attempts to study transient phenomena. Instead we are limited to cases where the beams are held at a constant power for a sufficiently long time, typically about 5 seconds, in order for the plasma to reach a steady state in which transient inductive effects have disappeared.

Interpreting the beam driven current according to the prescription described above for the experimental loop voltage trace shown in Fig.2, we find the result shown in Fig.3. All the 1MA NBI shots have been studied in this way and a data-base has been set up. In Fig.4 is shown a comparison between interpreted and predicted beam driven currents. Each point

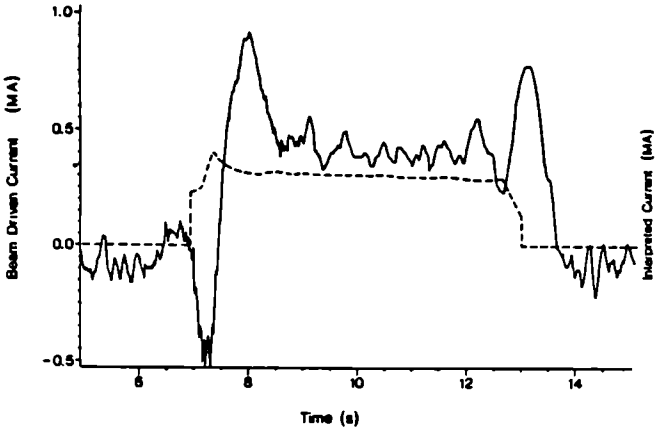

Fig.3 Interpreted (solid line) and predicted (dashed) beam driven current.

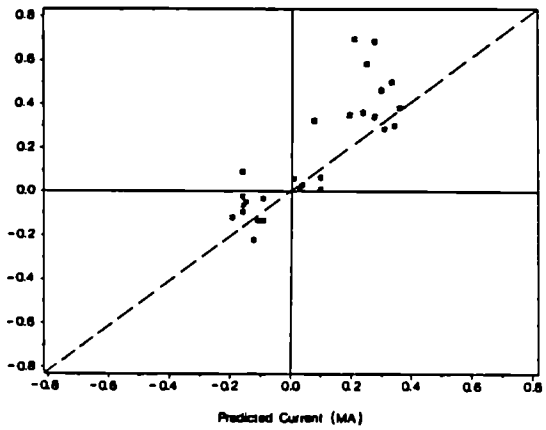

Fig.4 Comparison between interpreted and predicted currents.

corresponds to a time-average over one pulse, in every pulse excluding from the average the first 1.5 sec after beam turn on and the last 1 sec before beam turn off to avoid transient effects. There is a reasonable agreement between predicted and interpreted current although more counter-injection data is needed. Typically, the beam driven current in these low density discharges is ~ 400kA.

Discussion

Apart from the interpretative study summarised above, we have also carried out a predictive study, in order to clarify the physical processes involved and to be able to extrapolate to future performance.

According to the results of this predictive study, the magnitude of the beam driven current in JET is almost entirely determined by the plasma density and rather insensitive to other parameters such as temperature, Z_{eff} and injection energy. The scaling with density, assuming $n_e = n_o\sqrt{1-\rho^2}$, for two different injection energies is shown in Fig.5.

The unfavourable scaling with density is a result of the JET injection geometry, see Fig.1. The geometry, with beams nearer to perpendicular than to parallel with respect to the current direction, has the effect that fast-ion trapping is very important in the outer regions of the plasma. The predicted beam driven current decreases rapidly with increasing density and resultant poorer beam penetration, due to the fact that a larger and larger fraction of the injected ions are "born" in trapped orbits. This effect, which practically nullifies the beam current outside roughly half radius, together with the r-dependence of the volume element, also makes the profile shape of the beam current rather insensitive to changes in plasma parameters. In Fig.6 the normalised current profile shape is compared with the neoclassical inductive current profile. Being so similar, it appears difficult to significantly change the total current density profile using beam current drive with the JET injection geometry. However, it must be borne in mind that sawtooth activity may substantially

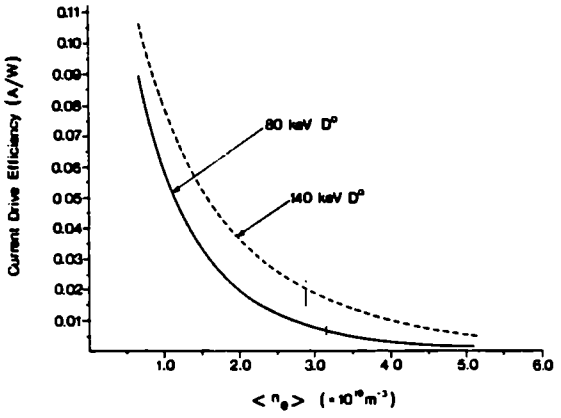

Fig.5 Predicted scaling of current drive efficiency with plasma density.

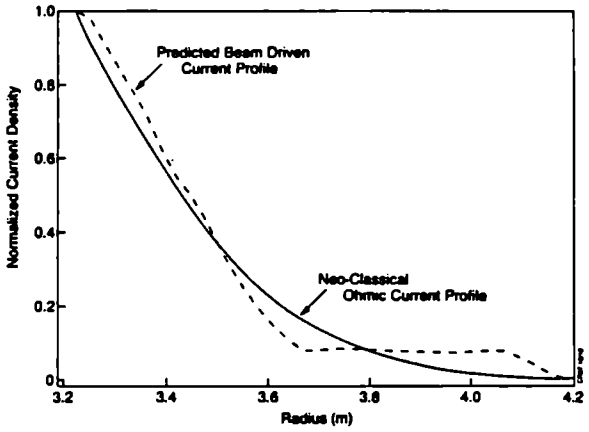

Fig.6 Normalised neoclassical (solid line) and beam current (dashed) profiles.

flatten the neoclassical profile, in which case the beam current would probably narrow the total profile in the case of co-injection and broaden it for counter-injection.

Based on these model predictions, the following could be expected for two injection boxes using D-injection with $\langle n_e \rangle = 1.2 \times 10^{19} m^{-3}$ and $T_e(0) = 5keV$:

E_o	80keV	140keV
P_{inj}	20.5MW	15.2MW
I_{beam}	0.85MA	0.85MA

where the lower injected power at 140keV is due to decreased neutralisation efficiency of the fast ions extracted from the beam sources.

Conclusions

Based on this study it appears as if:

i) Currents driven by the beams have reached around 0.5MA in low density discharges.

ii) There is a reasonable agreement between interpreted and predicted beam driven current.

iii) Fast ion trapping is a very important effect in reducing the beam current with the JET injection geometry.

iv) The magnitude of the driven current is rather insensitive to all plasma and injection parameters apart from the plasma density, on which the dependence is strong and unfavourable.

v) The beam driven current profile is determined almost exclusively by the geometry. Compared to neoclassical ohmic current profiles, the beam current profile is probably somewhat more peaked.

Reference

[1] F.L. Hinton, R.D. Hazeltine, Rev. Mod. Phys. 48 (1976), 239.

NEUTRAL BEAM AND EDGE FUELLING EFFECTS IN JET DISCHARGES

T T C Jones, E Thompson, A Gondhalekar, P J Lomas, P D Morgan, J O'Rourke, D Stork.

JET Joint Undertaking, Abingdon, UK.

1. INTRODUCTION

Understanding recycling is of considerable importance for Neutral Beam Heating (NBH) since there is strong additional edge fuelling from the limiter. Significant density increase is also observed during RF heating [1]. Density control during NBH depends on the ability of the limiter to pump (recycling coefficient $R < 1$) and low recycling may also help in obtaining favourable edge plasma conditions necessary for good energy confinement. The density behaviour of high power ($\lesssim 10$ MW) NBH JET plasmas has been compared with the predictions of a simple model describing the beam fuelling, and recycling at the various graphite surfaces of the machine (conventional outer limiters, inner wall and X-point protection tiles). The comparison supports the validity of the model, and the consequences for the material properties are described. Since, in principle, it should be possible to derive the parameters of the model rigorously from particle transport within graphite (and in the plasma) the results may provide a useful constraint for the more materials-oriented recycling modelling in tokamaks currently in progress, e.g. [2,3].

2. DENSITY BUILD UP WITH NBH FOR OUTER LIMITER DISCHARGES

Figure 1 shows the typical behaviour of volume averaged electron density $\langle n_e \rangle$, edge recycling fluxes ϕ_L and ϕ_W at the limiter and vessel wall respectively (from H_α measurements), and recycling coefficient R for an outer limiter NBH plasma. Figure 1 defines the asymptotic beam fuelling efficiency ε; the gas and beam fluxes ϕ_g and ϕ_b are also shown. The principal features are: (i) recycling takes place mainly at the limiter; (ii) there is a transient increase in recycling flux on application of NBH ($R>1$) resulting in an initial beam fuelling efficiency >1; (iii) an asymptotic fuelling efficiency $\varepsilon < 1$ which implies R must tend to a value < 1, but since $\phi_b \ll \phi_L$ the asymptotic value of R must remain close to 1. The behaviour suggested applying a model based on dynamic equilibrium between the plasma particles and particles retained on the limiter for some finite time before being re-emitted. The initial transient influx from the limiter can be explained by a disturbance of equilibrium established prior to application of NBH, towards a new equilibrium favouring the plasma. Ignoring losses, the equations describing this exchange can be written:

$$\dot{N}_p = -\alpha(1-r)N_p + \beta N_s + \phi_b \qquad (1)$$

$$N_s + N_p = N_o + \phi_b t$$

where N_p = plasma electron content; N_s = H + D content of limiter surfaces

$N_o = (N_s + N_p)$ (t=0); ϕ_b = beam atom flux;

$\alpha^{-1} = \tau_p$ = plasma particle confinement time;

$\beta^{-1} = \tau_s$ = limiter surface residence time;

r = limiter surface prompt reflection coefficient.

The solution of (1) subject to the boundary condition $N_p(t=0) = N_p^o$ is:

$$N_p = N_p^o + \Delta N_p^\infty (1-\exp -t/\tau) + \varepsilon\phi_b t \qquad (2)$$

where $\varepsilon = \beta/[\beta + \alpha (1-r)]$; $\tau = 1/[\beta + \alpha (1-r)]$;

and $\Delta N_p^\infty = \varepsilon N_o + \alpha(1-r)\phi_b/(\alpha(1-r) + \beta)^2 - N_p^o$

The function (2) was fitted to the experimentally measured N_p for many outer limiter discharges and hence best-fit values for $\alpha(1-r)$ and β obtained. The fits were generally very good (eg. fig 2). The total recycling flux can be written:

$$\phi_R = \alpha r N_p + \beta N_s \qquad (3)$$

The first term is the prompt reflected flux and the second the re-emitted particle flux. The initial increase in ϕ_L as measured (eg. fig 1) is not instantaneous at t=0, but typically has a rise time of ~ 200 ms; if power flux into the scrape-off layer is responsible for enhanced re-emittance, the finite beam slowing down time (~ 100 ms) has to be taken into account. The fitted values of τ are typically ~ 0.8 s and during the main transient characterized by τ, ϕ_L always 'turns over' as the density ie. the second time derivatives of N_p and ϕ_L are of the same sign. It can be proved using (3) that necessary and sufficient conditions for the latter are that $\alpha r > \beta$ and $r > \varepsilon$. Figure 3 shows plots of $\tau_p^* = 1/\alpha(1-r)$ and $\tau_s = 1/\beta$ versus ε obtained by fitting (2) to the measured $N_p(t)$. The asymptote for τ_p^* as $\varepsilon \to 1$ supports the fact that $r > \varepsilon$, as expected. Also, when r was calculated using values of τ_p from the standard global particle balance equation, using $\tau_p^* = \tau_p/(1-r)$, it was again found that $r > \varepsilon$. Thus the variations in ε are largely explained by changes in r.

3. DENSITY RISE AT ONSET OF H-MODE

Equation (2) well describes the density increase observed at the onset at t = 0 of the H-mode [4]. The initial fuelling rate is typically ~ 2-3 times ϕ_b, asymptotically approaching a value of $\varepsilon \leq 1$. Here, the initial increase is considered to be due to an instantaneous increase in τ_p, and ϕ_R measured at the X-point tiles instantaneously drops, consistent with the drop in the reflected flux $\alpha r N_p$ [5].

4. DENSITY CONTROL USING He CONDITIONED INNER LIMITER

The foregoing discussion assumes that the limiters are 100% saturated, i.e. all the strongly binding traps (~ 4 eV) are occupied. Such strongly bound H or D atoms can only be displaced by incident ions and the displaced atoms repopulate all available traps, including those of lower binding energies, on a statistical basis. A model based on this process [6] predicts an inversely temperature dependent saturation H + D content

N_{SAT} for graphite; at saturation for each incident ion exactly one H or D atom is promoted from the trapped population (N_T) to a weaker trap from which thermal detrapping is possible, and adds to the mobile, diffusing population (N_{free}). Assuming the build-up to saturation is approximately exponential with total fluence the probability of an incident ion adding to N_T is:

$$P_{trap} = 1 - N_T/N_{SAT} = 1 - (N_s - N_{free})/N_{SAT} \quad (4)$$

and a modified set of particle balance equations may be written:

$$\begin{aligned} \dot{N}_p &= \alpha(1-r)N_p + \beta N_{free} + \phi_b \\ N_s &= N_T^o + N_{free}^o + \phi_b t - N_p \\ \dot{N}_{free} &= \alpha(1-r)N_p(1-P_{trap}) - \beta N_{free} \end{aligned} \quad (5)$$

where N_T^o, N_{free}^o refer to $t = 0$

Integrating equations (5) shows that (i) for sufficiently depleted surfaces ($N_T^o/N_{SAT}<1$) the asymptotic beam fuelling efficiency $\varepsilon \to 0$; (ii) $\dot{N}_p/\phi_b > 1$ for small t, depending on the value of N_{free}^o established by the target plasma; (iii) for 100% saturation ($N_T^o/N_{SAT} = 1$) this model reduces to that described in section 1. These features are observed in the density behaviour of NBH discharges run on the inner wall tiles after He discharge conditioning, and in L-mode X-point discharges (figure 4).

5. CONCLUSIONS

The density rise observed with NBH and at the onset of the H-mode can be satisfactorily described using a simple particle balance model. The fitted parameters show that H or D atoms retained on graphite plasma limiters have a characteristic residence time $\geq$ 1 s. The magnitude of the density increase is largely dependent on the transient influx from the limiter, and not simply on the beam fuelling rate. Density control can be obtained by sufficient depletion of the H + D content of the limiters and other surfaces interacting with the plasma, e.g. by He discharge conditioning. This method has been successfully employed in JET for the inner wall tiles which present a larger area and operate cooler than the outer limiters.

REFERENCES

[1] M Bures et al, contributed paper, this conference.

[2] J Ehrenberg, S A Cohen, L deKock et al, contributed paper, this conference.

[3] D Heifetz, private communication.

[4] A Tanga, XI IAEA Conference on Plasma Physics and Controlled Nuclear Fusion Research, Kyoto, Japan, 1986.

[5] P D Morgan and J O'Rourke, this conference.

[6] D K Brice, B L Doyle and W R Wampler, J.Nucl.Mater. 111/112 p.598.

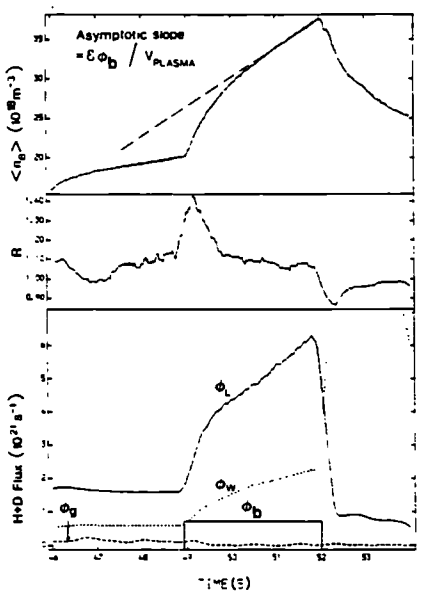

Figure 1 Input fluxes and evolution of plasma density for 5.2 MW H° injection into a 4 MA, 3.4 T D plasma, and definition of asymptotic beam fuelling efficiency ε, where V_{PLASMA} = plasma volume.

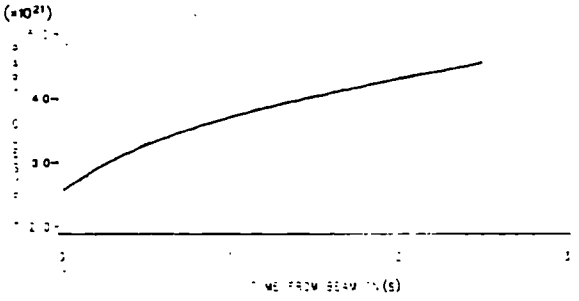

Figure 2 Time evolution of measured plasma electron content during NBH with function (2) fitted for an outer limiter discharge.

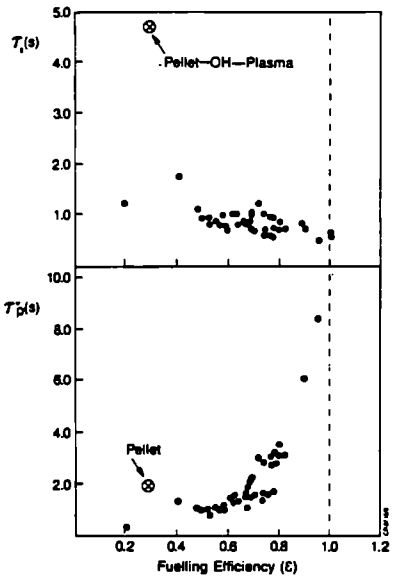

Figure 3 Dependence of best fit values of τ_p^* and τ_s on ε for outer limiter NBH discharges, plus one pellet injection case, calculated setting $\phi_b = 0$ in (2) and assuming α, β, r do not change after the pellet.

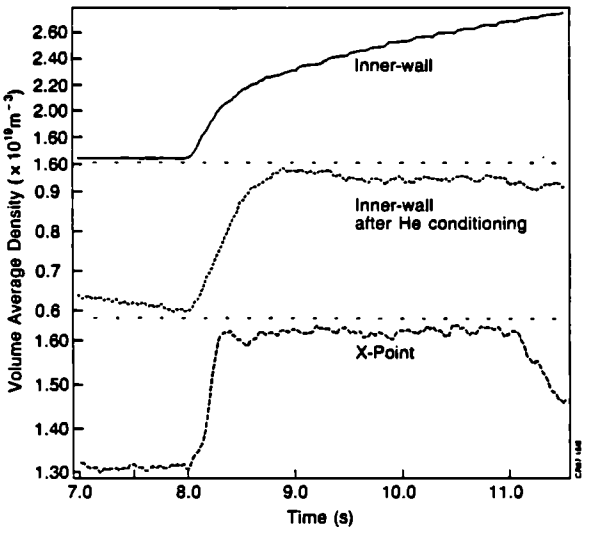

Figure 4 Density response for an unconditioned inner wall, He discharge conditioned inner wall, and double null separatrix plasma on application of NBH at t = 8.0 s in each case.

MOMENTUM TRANSPORT AND SCALING EFFECTS OBSERVED IN NEUTRAL BEAM HEATED ROTATING PLASMAS IN JET

D Stork, A Boileau, F Bombarda(1), D J Campbell, C Challis, W G Core, B Denne, P Duperrex(2), R Giannella(1), L Horten, T T C Jones, E Källne, A Pochelon(2), J Ramette(3), B Saoutic(3), D Schram(4), J Snipes, G Tallents, E Thompson, G Tonetti(2), M von Hellerman and J Wesson.

JET Joint Undertaking, Abingdon, UK.
(1) EURATOM-ENEA Association, Frascati, Italy.
(2) EURATOM-CRPP Association, Lausanne, Switzerland.
(3) EURATOM-CEA Association, CEN Cadarache, France.
(4) Eindhoven University of Technology, Eindhoven, The Netherlands.

1. INTRODUCTION

Rotational phenomena have been studied in JET discharges with plasma currents from 1-3 MA and high power (≤10 MW) neutral Beam Injection (NBI). Deuterium beams at energies up to 80 keV and hydrogen beams at energies up to 65 keV have been applied. The simultaneous effects of NBI and high power (≤7.5 MW) ICRF on rotation, the dependence of central rotational velocity on NBI power, and temporal and profile effects in rotational velocity have been studied.

2. DIAGNOSTICS

Toroidal rotation on JET has been measured using several diagnostics.

a) Central (major radius R=3.1m) angular velocities ($\omega_\phi(0)$) were determined from the Doppler shift of the He-like NiXXVII resonance line observed by an x-ray crystal spectrometer [1]. This measured ω_ϕ averaged over a region centred on zero minor radius (r) with half-width ≈0.4 m.

b) MHD diagnostics used were pickup coils to measure $\tilde{B}_\theta$ and a Fabry-Perot interferometer detecting electron cyclotron emission (ECE). The rotation of the activity was inferred from frequency measurements. The coils [2] detected the m=2,3 components of n=1 MHD activity at the plasma edge. The ECE diagnostic [3] measured m=1, n=1 activity at normalised minor radius r/a ≈ 0.3.
These diagnostics were of use when MHD activity was significant ($\tilde{B}_\theta/B_\theta(a) \sim 1\text{-}3 \times 10^{-5}$).

c) For some shots additional spectroscopic measurements were made. An XUV spectrometer [4] measured Doppler shifted lines of ionised states of Nickel and Carbon and angular velocity profiles were obtained.
A Charge Exchange Recombination Spectroscopy (CXRS) diagnostic was also used on Doppler shifted light from excited C^{6+} and O^{8+} ions. This measured rotation at R=2.3 m (inboard) and at r/a ~ 0.6. [5].

3. SCALING PROPERTIES OF CENTRAL ROTATIONAL VELOCITIES

On application of NBI to the plasma, a strong toroidal rotation was observed on all diagnostics. The rotation took between 0.5-1.0 second to reach quasi-steady values.
The quasi-steady state values of $v_\phi(0)$ derived from the Ni XXVII Doppler shift are plotted in figure 1 against the beam power per particle $P_b/\langle n_e \rangle$.

$v_\phi(0)$ tends to saturate with increasing $P_b/\langle n_e\rangle$ and to increase slightly with increasing plasma current. The highest values of $v_\phi(0)$ were slightly below half the fluid sound speed (C_s). H° and D° injection induced similar rotations. Counter injection data are similar to co-injection data once the Ohmic plasma rotation (measured by the MHD diagnostics) is taken into account. This rotation was ~ 2-2.5 10^4 ms^{-1} counter to I_p and has been corrected for in figure 1.
The data have been compared with the scaling predictions for $v_\phi(0)$ based on the gyroviscous theory of Stacey et al [6].
Gyroviscous theory predicts $v_\phi(0)$ scales as:

$$v_\phi(0) \simeq \frac{f_p(o)}{V_p} \cdot \frac{\langle n_e\rangle}{n_d(o)} \cdot \frac{\overline{2m_b}}{E_b} \cdot \frac{2\,R_o^2 eZ_{eff} B_T(o)}{T_{i,OH}(0)+C(P_b/\langle n_e\rangle)} \cdot \frac{(1-f_T)P_b/\langle n_e\rangle}{} \quad (1)$$

where $f_p(o)$ is the peaking factor for the NBI momentum deposition on axis; V_p is the plasma volume; $\langle n_e\rangle$ is the volume averaged density; $n_d(o)$ is the axial deuteron density; $T_{i,OH}(0)$ is the central Ohmic ion temperature; C is the ion heating efficiency $[\Delta T_i(0)/P_b/\langle n_e\rangle)]$; f_T is the fraction of injected particles injected in trapped orbits contributing no net momentum to the plasma.
Using the JET ion heating data [7], gyroviscosity predictions as in fig. 1 are obtained for two values of trapped particle fractions. These discharges have closer to 40% trapped beam but the data are well above the '40% trapped' prediction from gyroviscosity. The gyroviscous prediction is within a factor of ~ 2-5 of the data but the scaling with I_p is in the opposite direction to any which might be inferred from JET data.
Gyroviscosity is also not affected by plasma collisionality and this conflicts with the observation of strong rotational velocity sawteeth on JET. These are shown in figure 2 with the crystal spectrometer at temporal resolution ~20 ms. The sawteeth correlate well with variations in electron temperature suggesting that the decreasing collisionality of the plasma between sawteeth affects the central momentum transport.

4. MHD AND PROFILE EFFECTS IN MOMENTUM TRANSPORT

The sudden decrease of $v_\phi(0)$ at a sawtooth collapse is suggestive of the importance of MHD effects in momentum transport.
In extreme cases such as locked modes, MHD activity appears to play a strong role. At the appearance of a locked mode in the plasma, the rotation of the ions is seen to stop on a ~ 100 ms timescale in spite of the continued presence of the driving beams [8].
Where 'high' ($\delta B_\theta/B_\theta \geq 10^{-4}$) MHD activity was present, the rotational angular velocity determined from edge MHD activity was equal to the central toroidal angular velocity determined from the crystal spectrometer. This is shown in figure 3 and could be taken as evidence of a momentarily flat ω_ϕ profile during periods of high MHD activity. It is also possible that it merely indicates toroidal mode coupling driving the edge mode from a mode resonant on a rational q_ψ surface nearer the plasma centre and rotating with the central velocity [2]. The second possibility would lead to an MHD rotational 'profile' which was sheared relative to that of the bulk plasma.
On some shots in which XUV rotational profiles were taken the profiles of

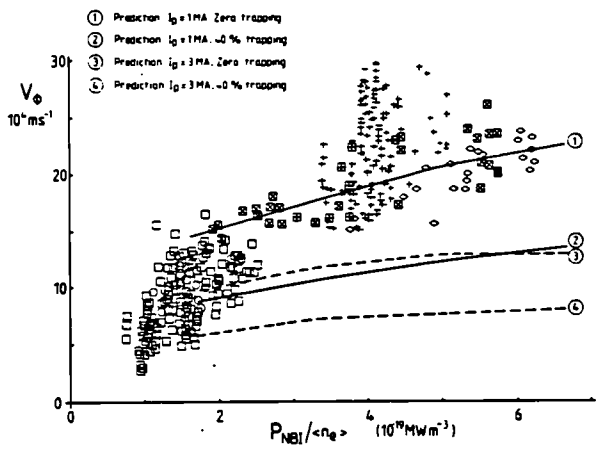

FIGURE 1: CENTRAL ROTATIONAL VELOCITY COMPARISON WITH GYROVISCOUS SCALING.

□	3MA	OUTER LIMITER	D° - D Co AND COUNTER INJECTION
○	3MA	OUTER LIMITER	H° - D Co INJECTION
◇	3MA	INNER WALL LIMITER	D° - D Co INJECTION
▽	2MA	X POINT	D° - D Co INJECTION
▽	2MA	X POINT	D° - D COUNTER INJECTION
◇	1MA	INNER WALL LIMITER	D° - D Co INJECTION

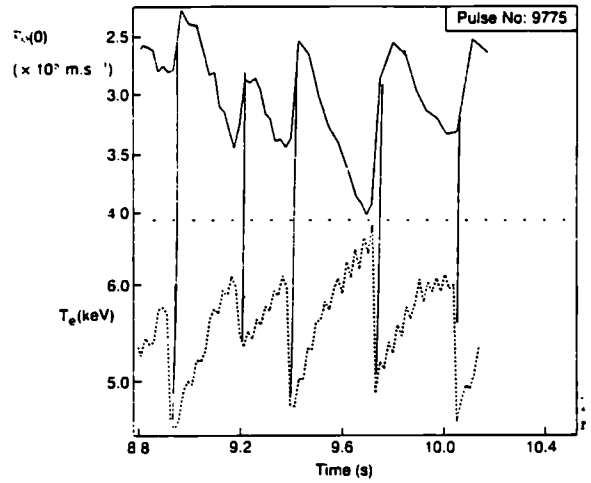

FIGURE 2: SAWTEETH EFFECTS ON ROTATIONAL VELOCITY AS MEASURED BY NIXXVII DOPPLER SHIFT

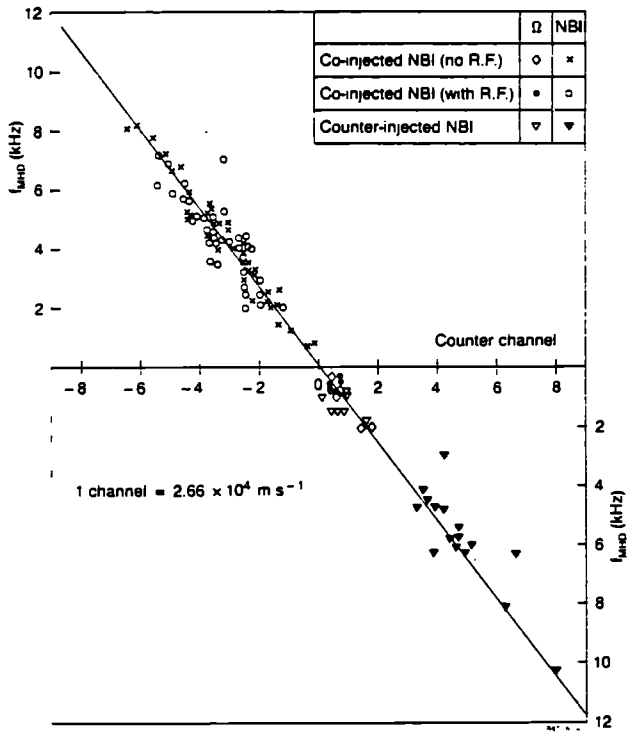

FIGURE 3: CORRELATION BETWEEN EDGE MHD MEASUREMENT OF ROTATION AND CENTRAL ION DOPPLER SHIFT MEASUREMENT (IN TERMS OF SPECTROMETER CHANNEL SHIFT). LINE IS

$2\pi f^{MHD}(R+a) = R.V_\phi{}^{MHD}(R)$.

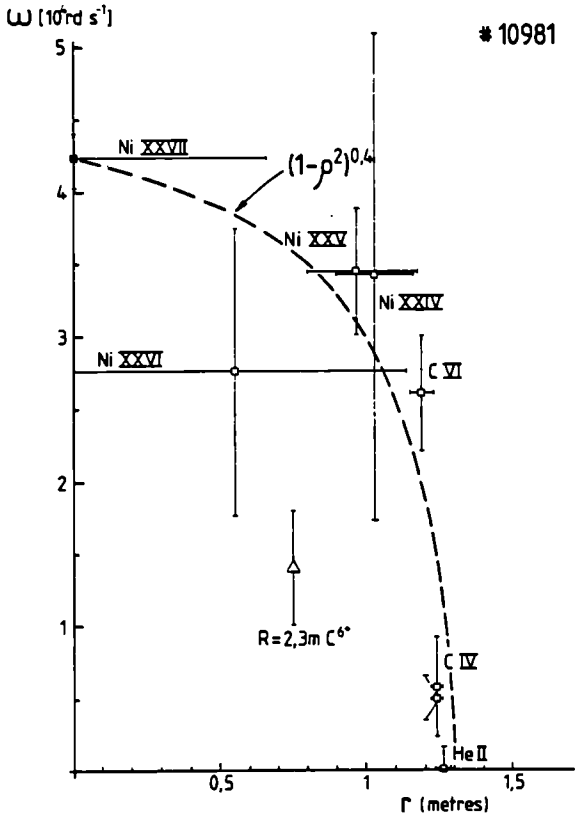

FIGURE 4: ROTATIONAL PROFILE MEASUREMENT (5MA PLASMA)

■ CRYSTAL SPECTROMETER
△ CXRS DIAGNOSTIC
□ XUV SPECTROMETER

the impurity ions appeared fairly flat. In figure 4 a parabolic function with γ_ϕ value = 0.4 can be drawn through data from the XUV spectroscopy and the crystal spectrometer. These diagnostics assume ω_ϕ is uniform on a flux surface when fitting, which is backed up by recent measurements on Doublet III [9]. Gyroviscosity predicts breaking of this uniformity to $O(\varepsilon)$ and some evidence that $\omega_\phi(\rho)$ is not uniform comes from the CXRS diagnostic. This is shown in figure 4 where a γ_ϕ value of ~ 2 would seem more appropriate for the inboard variation of ω_ϕ. The CXRS diagnostic generally gives $1 \leq \gamma_\phi \leq 2$.

5. EFFECTS OF RF ON NBI-INDUCED PLASMA ROTATION

ICRF was applied to JET discharges with rotation driven by NBI. ICRF tuned to ^3H_e minority in the plasma was largely ineffectual in altering rotation but when tuned to H minority in the plasma the RF caused a sharp drop of up to a factor 2 of rotational velocity. The central rotational velocity clamped (no sawteeth), often for long periods in the case of the so-called 'monster sawtooth' [10] shots where sawteething on the other plasma parameters (eg: $T_e(0)$) was also absent. The change in rotational velocity occurred over a period of 0.5-1.0 secs.
A possible explanation is that ICRF coupled to H minority is able to couple to the beam ions at $2\omega_{CD}$ for deuterium beams. The effects of this have been calculated and observed in other JET discharges [11]. Coupling imparts perpendicular momentum to the beams and preferentially scatters beam particles into trapped orbits where they impart negligible momentum to the plasma. With this reduction in the momentum driving term the rotational velocity drops. The RF also causes a density rise which decreases the penetration of the beam neutrals and deposits more fast ions in trapped orbits in the outer plasma. The cumulative effects of these two sources have been calculated using value measured post-RF increase in neutron yield from the plasma. Within an accuracy ~ 10-20% it is found that the change in rotational velocity can be accounted for by a change in the driving term (from the parallel momentum) from the effect of ICRF beam coupling in this manner.

REFERENCES

[1] Gianella R, et al, Bull. Am. Phys. Soc. 31(9),1590 (1986)
[2] Snipes JA, et al, 13th EPS Conf. on Contr. Fus. & Plasma Htg.(1986), (Europhysics Conference Abstracts) Pp 152-155
[3] Campbell DJ, et al, JET-P(86)05 (1986)
[4] Behringer K, Ramette J, et al, these proceedings.
[5] Horton LD, et al, Bull. Am. Phys. Soc. 31(9),1590 (1986)
[6] Stacey WM Jr, et al, Nucl. Fus. 26(3),293-302, (1986)
[7] Thompson E, et al, these proceedings
[8] Snipes JA, et al, these proceedings
[9] Burrell KH, et al, submitted for publication to Nuclear Fusion (1987)
[10] Campbell DJ, et al, 11th IAEA Conf. on Plasma Phys. & Contr. Nuc. Fus. Research (Kyoto, 1986) IAEA-CN-47/A-VII-5
[11] Anderson D, et al, 13th EPS Conf. on Contr. Fus. & Plasma Htg. (1986), (Europhysics Conference Abstracts), Pp.97-99.

CONFINEMENT ANALYSIS OF AUXILIARY HEATED JET DISCHARGES

K Thomsen+, V Bhatnagar++, J D Callen*, J P Christiansen, J G Cordey, M Evrard++, D Gambier**, N Gottardi, T Hellsten, D G Muir, P J Lomas, P Smeulders, P R Thomas

JET Joint Undertaking, Abingdon, Oxfordshire, OX14 3EA, UK
+Risø National Laboratory, Denmark, ++LPP-ERM/KMS, 1040 Brussels, Belgium,
*University of Wisconsin, Madison, WI 53706, USA,
**CEA, Fontenay-aux-Roses, France

1. INTRODUCTION

Up to 9MW of neutral beam heating (NBI) and up to 7MW of ion cyclotron resonance heating (ICRH) and up to 16MW of combined heating have been applied to JET discharges. In NBI experiments, both H and D beams have been injected into D discharges. ICRH heating scenarios with H or ^{3}He minority ions in D discharges and H minority ions in ^{3}He discharges have been tried. This paper reports experiments in which the plasma was limited by an outboard limiter or the inner wall.

The dependence of stored energy W on total input power P is approximately the same for all combinations of heating methods (ie, the degradation of the global energy confinement time τ_E is approximately independent of heating method). Power scans at constant plasma current I_p show that the best data representation is a scaling with W increasing linearly with P (offset linear), in which the slope $\Delta W/\Delta P$ is the incremental confinement time, τ_{inc}. Whereas W clearly increases with I_p for fixed P, the scaling of τ_{inc} with I_p is not as apparent. This is mainly due to the lack of sufficient data with fixed plasma parameters. The plasma density n increases both with I_p and additional heating power, which makes it difficult to perform proper power scans at fixed density. A scaling law for W was obtained from early NBI results at I_p = 1, 2 and 3MA using standard regression techniques. This showed $\tau_{inc}[s] = 0.047\ I_p\ [MA]$ [1], which when applied to all data exhibits a substantial scatter. The scatter in W versus P for fixed currents is thought to be due to differences in the power deposition and radiation profiles, and in density.

A way of including these effects in analyses of confinement properties has been proposed [2]. There is strong evidence that the energy transport is diffusive [3]. By assuming that the heat flux is given generally by heat conduction plus convection in the form $\underline{q} = -n\chi\nabla T + \underline{q}_{conv}$, the heating effectiveness η and the ideal incremental confinement time τ_χ have been derived. Thus an effective power input, $P_{eff} = \eta P$, can be calculated from power deposition profiles and radiation profiles for a certain form of the heat diffusivity χ. The incremental confinement time can be written as $\tau_{inc} = \eta\tau_\chi$. Results from analyses utilising this method will be discussed.

2. DENSITY SCAN WITH NBI

A closer examination of data scatter from NBI heating experiments (D° into D^+) at fixed I_p = 3MA and B_T = 3.4T reveals that τ_{inc} is decreasing with increasing density. At low density ($n < 1.7 \times 10^{19} m^{-3}$) τ_{inc} = 0.28s, while at high density ($n > 1.7 \times 10^{19} m^{-3}$) τ_{inc} = 0.14s as shown in Fig 1. We have analysed these data in two steps with a constant n and χ model.

The penetration depth of the neutral beams decreases with increasing density, which means that the power deposition profiles are less peaked than the ohmic heating profile at low densities while they are quite flat at high densities. The correction due to different heating effectiveness η of the differing deposition profiles are indicated by the letter B in Fig 1. The remaining difference in slopes disappears when the effective power lost by radiation is also taken into account (letter A in Fig 1). The offset W(o) is different for low and high density (0.5MJ and 0.9MJ) while τ_χ is independent of density (0.57s).

3. ON/OFF-AXIS HEATING WITH ICRH

Narrow power deposition profiles ($\Delta r \lesssim a/5$) have been observed in experiments with ICRH heating of minority ions [4]. By modelling the heating profile with a δ-function located at the minority ion cyclotron resonance position, information about the heating effectiveness η can be obtained from experiments in which the resonance position was varied. The variation of τ_{inc} with the heating resonance position r_h is shown in Fig 2, for ^{3}He-plasmas with H minority ions at I_p = 2MA (using different frequencies 28.4 -37.2MHz and toroidal fields 1.7 - 2.35T).

An attractive feature of these experiments was the low level of radiation experienced in ^{3}He-discharges, in which corrections for radiation losses could be ignored. The ICRH heating effectiveness depends on r_h. To explain the variation of τ_{inc} shown in Fig 2, it is necessary to introduce a χ that increases with radius. With $\chi = \chi_o/(1 - r_h^2/a^2)$, the model gives $\eta(r_h) = (1 - r_h^2/a^2)^2$, which is shown by the dashed line in Fig 2. The mean value of τ_{inc} for on-axis heating has been used for τ_χ (= 0.2s).

4. CURRENT SCANS WITH ICRH

All ICRH scenarios give similar confinement scaling properties. Similarly, the toroidal field plays a minor role in the scaling of τ_{inc}. The immediate conclusion from power scans at different currents is that τ_{inc} = 0.2 sec and independent of I_p.

The poloidal and paramagnetic corrections to the vacuum field are much larger than originally anticipated. Thus, especially the 5MA experiments can be regarded as off-axis heating experiments. Using the heating effectiveness $\eta = (1 - r_h^2/a^2)^2$ in Sec 3, the power input has been corrected for heating profile effects and have greatly improved the 5MA data (see Fig 3). A scaling with $\tau_\chi \propto I_p^{0.5}$ was obtained, after correction [5]. Finally correction of the 1 and 5MA data for radiation losses provide a further improvement of τ_χ (~0.37s) at 5MA and the 1MA results were only slightly changed to τ_χ ~ 0.19s, (see Fig 3). The radiation correction to the other the data remains to be carried out. However, the 1MA data still seems better than would be implied by the $\tau_\chi \propto I_p$ scaling derived from the NBI data.

5. CURRENT SCANS WITH COMBINED HEATING

Combined NBI and ICRH heating up to 16MW has been successful in increasing the total stored plasma energy. Power scans at different currents have shown an improvement in τ_{inc} with increasing current. These results have been corrected for radiation losses and power deposition

profile effects using a constant χ model and are shown in Fig 4. A regression analysis yields $\tau_\chi[s] = (0.12 \pm 0.03)\ I_p\ [MA]$. Even though the change from total input power P to P_{eff} increases the slopes of the lines substantially, there is still a non-zero offset, (ie, $W = \tau_\chi\ P_{eff} + W(0)$ with $W(0) > 0$).

6. CONCLUSION

Analysis has shown that the observed dependences of incremental confinement time $\tau_{inc} = \eta\tau_\chi$ with density and resonance position are mainly due to power deposition profile effects on the heating effectiveness η. The data scatter is greatly reduced when corrected for radiation losses. After correction for both radiation and heating profile effects ICRH results show an improvement in τ_χ with plasma current. However, this is still not as strong as the NBI and combined heating data which show $\tau_{inc}, \tau_\chi \propto I_p$. Future higher power and current experiments should clarify this dichotomy.

7. REFERENCES

[1] Cordey J G et al, IAEA-CN-47/A-II-3, Plasma Physics and Controlled Fusion, Kyoto, Japan, 1986.

[2] Callen J D, Christiansen J P, Cordey J G, Thomas P R, Thomsen K, JET Preprint P(87)10, submitted to Nuclear Fusion.

[3] Tubbing B J D, Lopez-Cardozo N J, JET Report R(87)01.

[4] Jacquinot J J et al, IAEA-CN-47/F-I-1, Plasma Physics and Controlled Fusion, Kyoto, Japan, 1986.

[5] Bhatnagar V P et al, this Conference.

Fig 1: W (magnetic) vs P from NBI experiments (3MA, 3.4T) with corrections due to heating profile effects (B) and radiation losses (A) indicated.

Fig 2: τ_{inc} (diamagnetic) vs normalised plasma radius from On/Off axis ICRH experiments ((H)^{3}He, 2MA) with $\eta = \tau_\chi(1-\rho^2)^2$ shown by the solid line.

Fig 3: W (kinetic) vs P with and without corrections from ICRH current scans ((^{3}He)D, 5MA, 3.4T and (H)^{3}He, 1MA, 2.2T).

Fig 4: a) W (magnetic) vs P from current scans with combined heating. The symbols are defined in b) where W (magnetic) vs P corrected for heating profile effects are shown for the same data set.

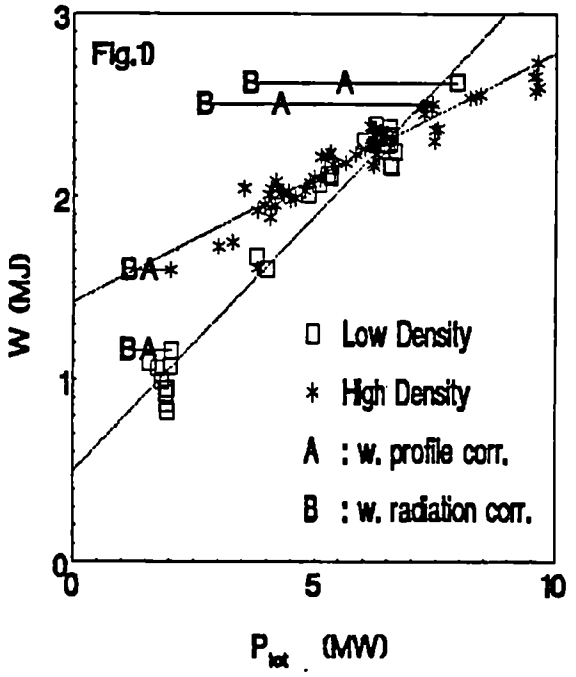

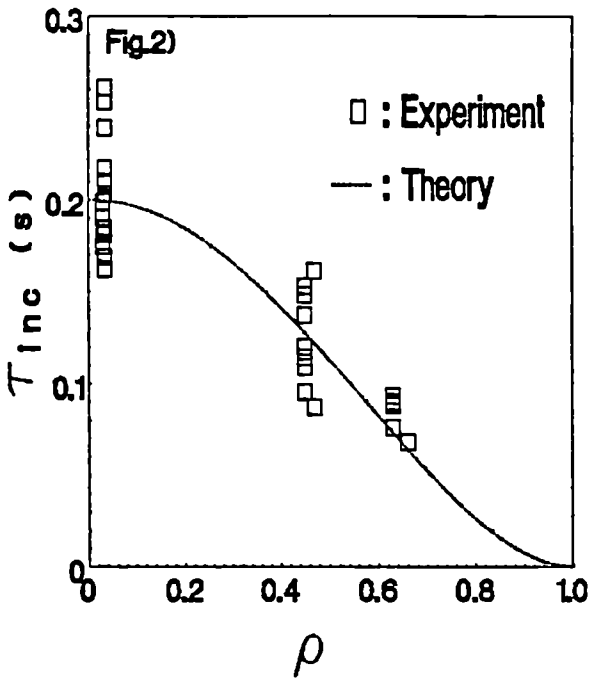
Fig.2)
□ : Experiment
— : Theory
τ_{inc} (s)
0.3
0.2
0.1
0
0
0.2
0.4
0.6
0.8
1.0
ρ

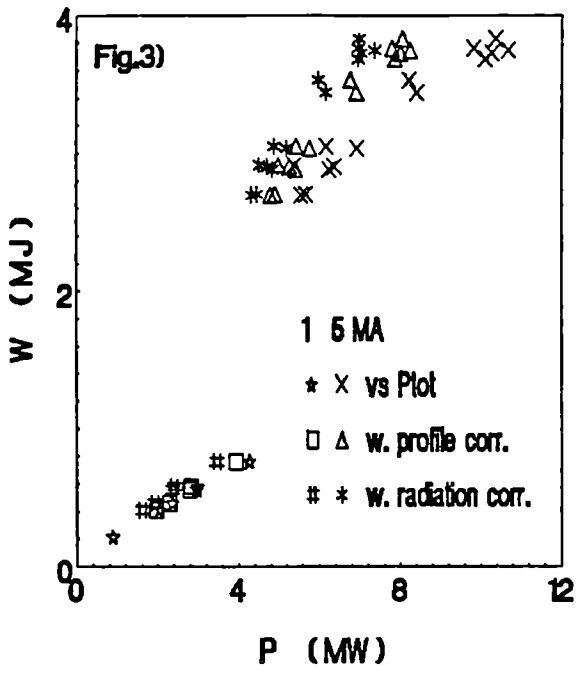
Fig.3)
1 5 MA
* X vs Plot
□ Δ w. profile corr.
* w. radiation corr.
W (MJ)
4
2
0
0
4
8
12
P (MW)

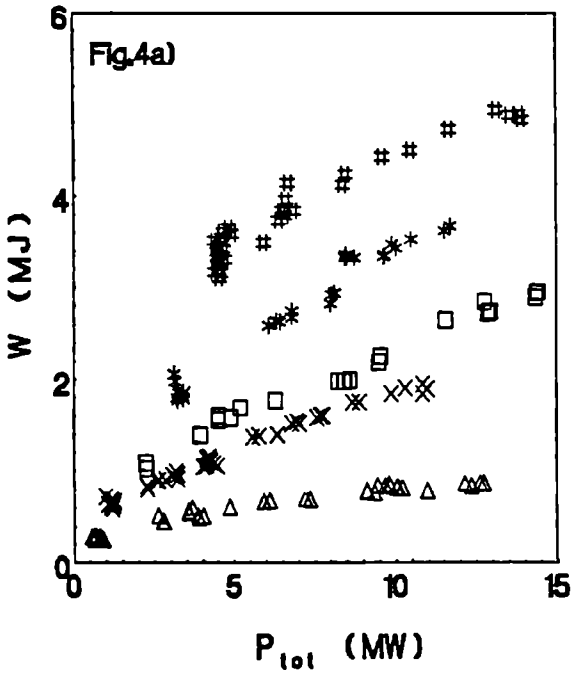
Fig.4a)
W (MJ)
6
4
2
0
0
5
10
15
P_{tot} (MW)

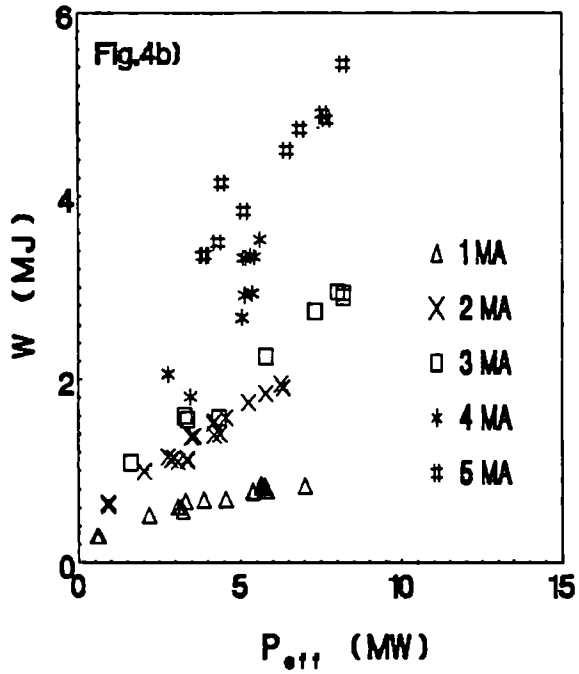
Fig.4b)
Δ 1 MA
X 2 MA
□ 3 MA
* 4 MA
# 5 MA
W (MJ)
6
4
2
0
0
5
10
15
P_{eff} (MW)

HEAT FLUX ANALYSIS OF AUXILIARY HEATING DATA FROM JET

J P Christiansen, J G Cordey, J D Callen* and D G Muir

JET Joint Undertaking, Abingdon, Oxon, OX14 3EA, UK
*University of Wisconsin, Madison, WI53706, USA

ABSTRACT

A new method for analysing local heat transport has been applied to data from neutral beam heated discharges in JET. Estimates of heat diffusivity obtained by this method are found to agree with results from heat pulse propagation studies and results deduced from empirical scaling laws for global confinement.

1. INTRODUCTION

A new method has been proposed [1] for interpreting measurements of the spatially resolved electron temperature profile by examination of the parametric dependence of the heat flux through a given flux surface. In this paper we describe the results obtained by applying this method to data from neutral beam heating power scan experiments on JET. The power scans have been performed over a range of plasma currents (1 to 5MA) and the beam power has been increased in steps of approximately 1MW up to 9MW. In the analysis the total heat flux q is compared with local plasma parameters, eg, density, temperature, current and their gradients. The analysis suggests the following relationship:

$$\underline{q} = -\chi\, en\nabla T + \underline{q}_{pinch} \quad , \qquad (1)$$

where χ is a heat diffusion coefficient and q_{pinch} represents a heat pinch. SI units are used with temperatures in eV and currents in units of MA.

2. CALCULATION OF HEAT FLOW

In a steady state plasma configuration the power balance equation for electrons and ions is:

$$\langle \nabla \cdot \underline{q} \rangle = \langle Q_\Omega + Q_{NB}^e + Q_{NB}^i \rangle = \langle Q \rangle \quad , \qquad (2)$$

where $\langle\ \rangle$ denotes a flux surface average. Q is the total heating rate and includes ohmic heating and power deposition from the neutral beam to electrons and ions. The radiation loss rate is not included in (2). A preliminary analysis of selected JET pulses shows Q_{RAD} to be highly peaked in the outer region $0.9 < x < 1$. The flux surface label x used in the analysis varies from 0 to 1 and we integrate equation (2) from $x = 0$ up to 3 representative radii $x = {}^1/_2, {}^2/_3, {}^3/_4$. This integration yields for the heat flux:

$$q(x) = \frac{a}{\frac{dV}{dx}} \int_0^x Q(x') \frac{dV}{dx'}\, dx' \quad , \qquad (3)$$

where a is minor radius and V is the volume enclosed by a surface x. The ohmic contribution to Q is $E_\phi/\eta_\parallel$, $E_\phi = V_o/2\pi R$ where V_o is the loop voltage calculated from magnetic measurements. The neoclassical resistivity is determined from the electron temperature profile. The neutral beam power deposition is computed from Fokker-Planck equations using electron density and temperature data; the computation assumes the slowing down of injected ions to be complete. The q(x) heat flux data thus obtained is now analysed together with density and temperature data from approximately 350 observations. Each observation involves a time average over 0.4 sec of the data and typically 2-4 observations per plasma pulse are used. Figure 1 shows radial profiles of the heat flow q(x) before (full curves) and during neutral beam heating (dashed curves) for 3 pulses with 1, 3 and 5MA. It can be seen that a substantial change (by a factor 20) occurs for the 1MA pulse.

3. DEPENDENCE OF HEAT FLOW ON LOCAL PARAMETERS

Standard linear regression analysis has been applied to the heat flux data by fitting it to an empirical expression like:

$$q_{fit} = - C\, e\, n^{\alpha}\, \nabla n^{a}\, T^{b}\, \nabla T^{\beta}\, I^{\gamma}\, J^{c} - q_{pinch}. \qquad (4)$$

The heat pinch term labelled q_{pinch} may depend on n, ∇n etc in a way different from the first term of (4). The data at 1MA eliminates any ∇n dependence and the data as a whole eliminates any current density J dependence. Since T and ∇T are strongly related either but not both, may be used. In the 1MA data alone the ∇T dependence is stronger than the T dependence. The best fit to all the data is thus:

$$q_{fit} = - C\, e\, n^{\alpha}\, \nabla T^{\beta}\, I^{\gamma} + q_{pinch}. \qquad (5)$$

In (4) and (5) I denotes the current flow inside a surface x. The values of the exponents ± their standard deviations are:

$$\alpha = 0.75 \pm 0.11, \quad \beta = 0.74 \pm 0.12, \quad \gamma = -0.78 \pm 0.11.$$

Also $$C = 11.34 \pm 2.31, \qquad q_{pinch} = 9.1 \pm 3.5 .$$

The large uncertainty in q_{pinch} is due to the scatter in the data as shown in Figure 2. By constraining two of the 3 exponents to be equal to 1 in 3 separate regression analyses the standard deviations drop and

$$\alpha = 1.01 \pm 0.02, \quad \beta = 1.02 \pm 0.04, \quad \gamma = -0.99 \pm 0.02 .$$

This result strongly suggests that

$$q = -C_o/I\ en\ \nabla T_e - q_{pinch}, \quad C_o = 8.0 \pm 0.2, \quad q_{pinch} = 4.3 \pm 0.6 , \qquad (6)$$

represents the best fit to the data on q. Figure 3 shows a plot of values of q against q_{fit} all evaluated at x = ¾. The different symbols refer to the plasma current (as in Figure 1): open circles (1MA), full circles (2MA), triangles (3MA), squares (4MA), asterisks (5MA). Additional attempts to allow for density and temperature dependence of q_{flow} either fail or

increase the standard deviations of the fitting parameters beyond the confidence level.

4. HEAT DIFFUSIVITY

The heat diffusion coefficient inferred from (6) is:

$$\chi = 8.0/I(x)m^2/sec \qquad (7)$$

This estimate shows that χ would decrease as x and $I_\phi(x)$ increase. When the analysis of 3 is carried out at $x = {}^1/_2$ and $x = {}^2/_3$ we find that the best estimate of C_o decreases to about 4.0 at $x = {}^1/_2$. The value of χ obtained from (7) for $I_\phi(x={}^3/_4) = 2.75$MA is $2.9m^2$/sec and this agrees well with the result $\chi_{HP} = 2.4 \pm 0.7m^2$/sec obtained from heat pulse propagation measurements [2]. Figure 4 shows values of q (full triangles) and q_e (open triangles) against $n\nabla T$ for a range of 3MA pulses; q_e is that part of q delivered directly to the electrons. The shaded area in Figure 4 represents the relationship between q and $n\nabla T$ which follows from the heat pulse propagation measurements.

From (7) we can derive an incremental confinement time [1] using an average χ.

$$\tau_{inc} = \eta \bar{\tau}_\chi = \eta \frac{3ab}{8\bar{\chi}} (1 + \xi) \qquad (8)$$

where a and b are the semi-axes of the elliptic plasma cross-section; η is the heating efficiency [1] of neutral beam heating and varies for JET from 0.3 to 0.6; ξ is the ratio ion to electron energy content and is typically 0.4-0.5. From (8) we find $\tau_{inc} = (0.04 - 0.08)$ I(sec), which compares favourably with the scaling law $\tau_{inc} = 0.047$ I(sec) obtained from JET data on global confinement [3].

5. SUMMARY

Several approximations have been made in this study of heat flux in JET: omission of radiation loss, ion-electron energy exchange, radial variation of safety factor, departures from equilibrium etc. Such approximations mitigate against a further analysis of the detailed dependence of χ upon local parameters, but do leave scope for future work. The difference between the fitted expressions (5) and (6) is such that it is difficult to extract more than the dependence (7) of χ from the data. This dependence of χ upon $I_\phi(x)$, or the average poloidal field, is very pronounced in the JET data. It indicates the highest incremental confinement to occur at high plasma currents.

6. REFERENCES

[1] CALLEN J D, CHRISTIANSEN J P, CORDEY J G, THOMAS P R, THOMSEN K, JET Preprint P(87)10, submitted to Nuclear Fusion.

[2] TUBBING B J D, LOPEZ-CARDOZO N J, JET Report R(87)01.

[3] CORDEY J G et al, Paper IAEA-CN-47/A-II-3, Plasma Physics and Controlled Fusion, Kyoto, Japan, 1986.

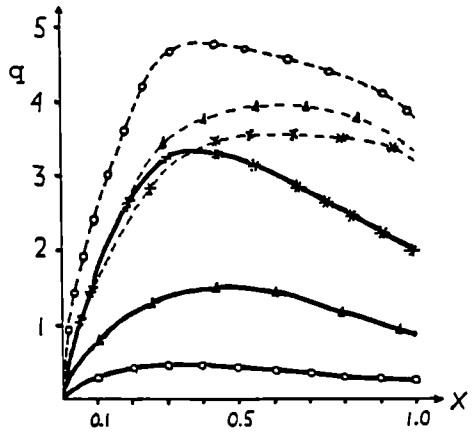

Fig 1: Radial profiles of heat flow for 3 pulses of 1MA(o), 3MA(Δ), 5MA(*). Units of q are $10^4 Wm^{-2}$ in all Figures.

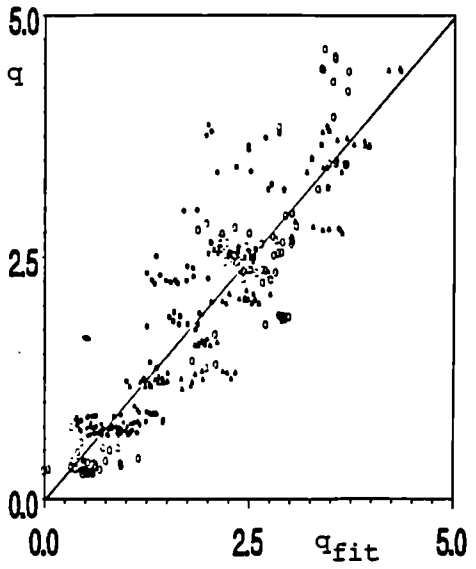

Fig 2: Values of q plotted against values of q_{fit} given by (5). The symbols are explained in the text.

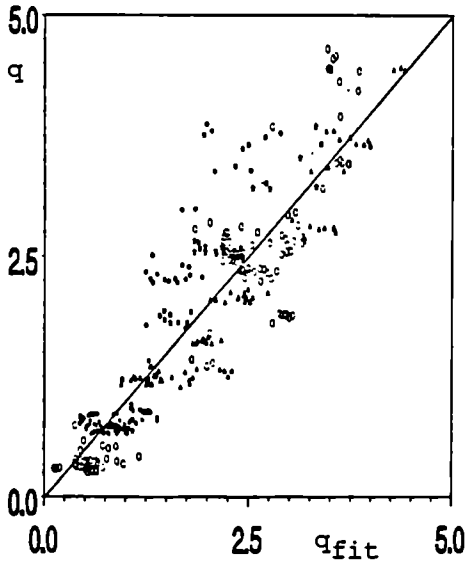

Fig 3: Values of q plotted against q_{fit} given by (6).

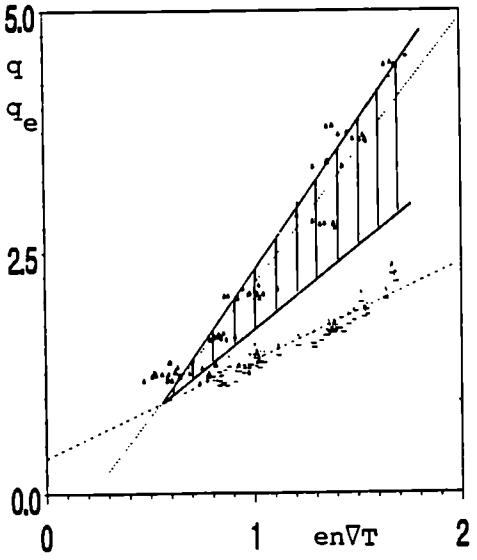

Fig 4: q(▲) and q_e(Δ) vs enΔT. The shaded area is the range given by heat pulse propagation measurements. Units of enΔT are 10^4 Jm^{-4}.

MODELLING OF TEMPERATURE PROFILE RESPONSES TO HEATING PROFILES IN JET

J.D. Callen*, J.P. Christiansen, J.G. Cordey

JET Joint Undertaking, Abingdon, Oxon. OX14 3EA, UK
*University of Wisconsin, Madison, WI 53706, USA

1. Introduction

Temperature profiles in tokamak plasmas have been characterised as exhibiting a high degree of "profile consistency" [1]. However, some variation in the temperature profiles have been observed with changes in the heating profile [2]. In this work [3] we seek to explain the temperature profile variations and global transport scaling due to changes in the heating profile using local heat transport models that are consistent with other, local measurements of heat transport in JET.

Global indications of changes in the temperature and current profiles in JET are shown in Figs.1,2. Figure 1 shows that the equilibrium ratio of the average temperature to the peak temperature increases as the heating profile broadens with decreasing safety factor q. Figure 2 shows that neutral beam broadens the electron temperature profile after injection. The current profile broadens on a longer time scale which is of the order of the magnetic diffusion time scale, as expected. Ref.[3] provides full details of the work presented here.

2. Local Heat Transport Models

Two recent developments [4,5] have helped to clarify the form of local models appropriate for describing heat transport in JET. First [4], the heat diffusion coefficient derived from heat pulse propagation measurements (χ_{HP}) has been shown to be independent of auxiliary heating power and to be approximately equal to that deduced from the incremental energy confinement time τ_{inc} [6]. Second, the total (electron plus ion) heat flux through the confinement zone of the plasma has been shown to be fit best [5] by

$$\underline{q} = - n\chi\underline{\nabla}T + \underline{q}_{flow} = - n\chi\underline{\nabla}T - \underline{q}_{pinch}. \qquad (1)$$

The nondiffusive flow term q_{flow} is found [3-6] to be negative, which indicates a heat pinch [7] or critical temperature gradient onset phenomenon [8]. Possible interpretations of it are discussed in [3].

Two specific local heat transport models [7] based upon Eq.(1) are used below to predict the temperature profiles for given heating profiles:
1) Constant heat pinch model: $\chi(r)$ and $q_{pinch}(r)$ are assumed to have given spatial profiles, but to be independent of parameters like T, input power.
2) Nonlinear χ model: $q_{flow} = 0$ and $\chi \sim (\underline{\nabla}T)^{\beta}$.

3. Temperature Profiles Induced by Various Auxiliary Heating Profiles

Temperature profiles for given heating profiles $Q(\underline{x})$ are calculated from the flux-surface-average equilibrium heat balance equation $\langle\underline{\nabla}\cdot\underline{q}\rangle = \langle Q\rangle$. Using Eq.(1), the heat balance equation can be integrated once to yield an equation for the radial temperature gradient. To solve for the temperature profile we must choose a particular local heat transport model.

In what follows we use for simplicity n(r) = constant and a cylindrical geometry approximation.

Constant heat pinch model. The predicted temperature profiles are given by a double radial integral of the heating profile Q(r) and hence relatively insensitive to small changes in Q. Such profiles induced by a variety of heating profiles Q(r) ranging from peaked on axis (dotted line) through flat (solid dark line) to peaked at the plasma edge (dashed line) are indicated in Fig.3. The temperature profiles are plotted on a logarithmic scale normalised at the half radius [9]. Fig.3 shows that only very modest temperature profile variations are expected for physically relevant changes in the heating profile. The ratio $\langle T\rangle/T(0)$ for these profiles are in agreement with the ranges indicated in Fig.1.

Nonlinear χ model. The predicted temperature profiles depend on a double radial integral of the $1/(\beta+1)$ fractional power of the heating profile Q(r); they are even less sensitive to variations in Q than those shown in Fig.3.

JET data for centrally peaked heating. The experimental temperature profiles that result from a variety of JET auxiliary heating profiles are shown in Fig.4. Comparing Fig.4 with Fig.3 we see that the weak temperature profile variations caused by changes in the heating profile are in reasonable agreement with the theoretical predictions. The best agreement occurs for $\beta<<1$ and for χ increasing radially.

Localised off-axis heating. In JET experiments the ICRH heating profile is highly peaked ($\Delta r \leq a/5$) near the radial location of the cyclotron resonance r_h. Both the heat pinch and nonlinear χ models predict the $\Delta T(r)$ due to ICRH to be constant inside the heating radius. However, the magnitude of $\Delta T(0) = \Delta T(r_h)$ and the radial fall off of ΔT with r outside of r_h depends on the model chosen. Comparisons of the ΔT obtained experimentally with the theoretical predictions in hydrogen minority ^{3}He majority plasmas are shown in Fig.5. Again, we find that there is best agreement between the experimental data and the local transport model predictions for $\beta<<1$ with χ increasing radially.

3. Global Transport Scaling

The stored energy $W=(3/2)\int d^3x\, n(T_e+T_i)$ derived from the constant heat pinch model is expressed as

$$W = \tau_\chi(1+\xi)\,\{[P_{in}]_{eff} + P_{pinch}\} = \tau_{inc}\,P_{in}(a) + W(0), \qquad (2)$$

where

$$\tau_{inc} = \eta\tau_\chi(1+\xi)/2,\ \tau_\chi = 3ab/4\bar{\chi},\ \xi=\langle n_iT_i\rangle/\langle n_eT_e\rangle,\ [P_{in}]_{eff} = \eta P_{in}(a). \qquad (3)$$

The heating effectiveness parameter η defined in [3] is unity for delta function heating on axis and zero for edge localised heating.

The global transport scaling law given in Eq.(2) has the offset-linear form that has been found [6] to characterise JET data quite well. The energy confinement time $\tau_E=W/P_{in}$ exceeds τ_{inc} for low power levels (e.g. ohmic heating), but approaches it for high input power levels. The

incremental confinement time τ_{inc} approaches the ideal incremental energy confinement time τ_χ when $\eta \to 1$ (central heating) and $\xi \to 1$.

4. Discussion and Conclusion

The temperature profiles predicted by local heat transport models have been shown to be in good accord with JET experimental results. The weak temperature profile responses to changes in the heating profiles explain "profile consistency", at least to the extent it is observed in JET. The local transport model which best characterises JET data is based on a heat pinch (or excess ∇T) model with a heat diffusion coefficient $\chi(r)$ that increases with radius. The global transport scaling law derived from this model exhibits a linear-offset form and provides definitions for the incremental energy confinement time τ_{inc} and the heating effectiveness η. These latter definitions provide a basis for taking account of heating profile effects in determinations of the energy confinement scaling in auxililary heated tokamaks.

References

[1] B. Coppi, Comments on Plasma Phys. and Cont. Fusion 5, 261 (1980).

[2] D.V. Bartlett et al., EPS Schliersee conference, Vol.10C, part I, p.236; J. Jacquinot et al., Phil. Trans. R. Soc. Lond. (to be published 1987); J. Jacquinot et al., 1986 Kyoto IAEA meeting paper F-I-1.

[3] J.D. Callen et al., JET-P(87)10, March 1987 (submitted to Nuclear Fusion).

[4] B.J.D. Tubbing, N.J. Lopes Cardozo, JET-R(87)01 (abridged version submitted to Nuclear Fusion; see also N.J. Lopes Cardozo et al at this conference).

[5] J.D. Callen, J.P. Christiansen, J.G. Cordey, D. Muir (at this conference).

[6] J.G. Cordey et al., 1986 Kyoto IAEA meeting paper A-II-3.

[7] E.D. Fredrickson et al., Nuclear Fusion 26, 849 (1986).

[8] P.H. Rebut et al., 1986 Kyoto IAEA meeting paper E-III-4.

[9] R.J. Goldston et al., 1986 Kyoto IAEA meeting paper A-II-1.

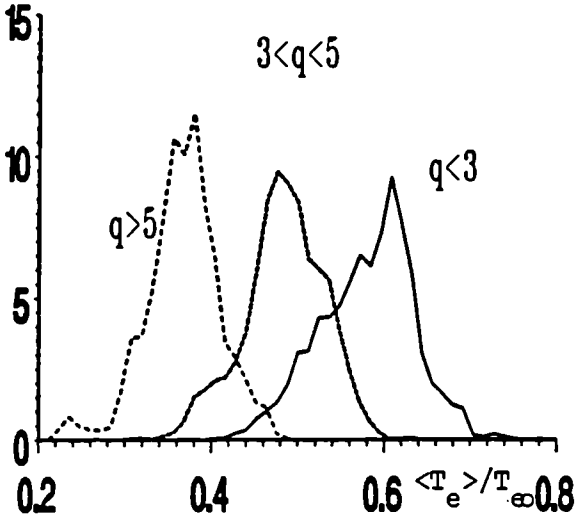

Fig.1 Normalised histogram of occurrences of average to peak temperature ratios for various safety factor ranges.

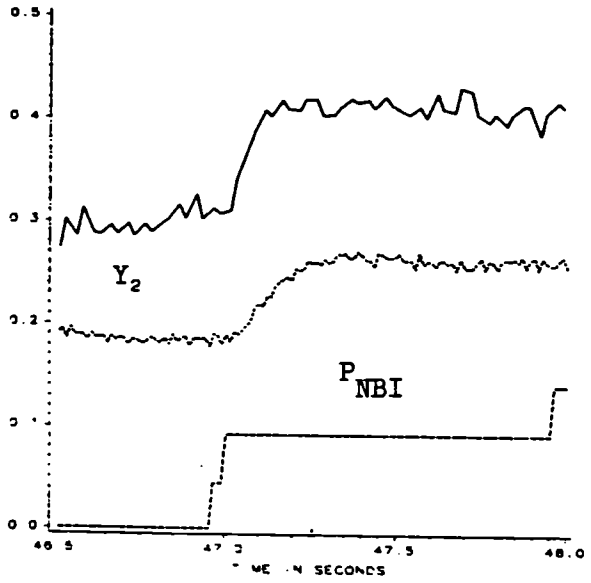

Fig.2 Temporal change of average to peak temperature ratio and a measure of current profile width Y_2 as neutral beam heating is applied.

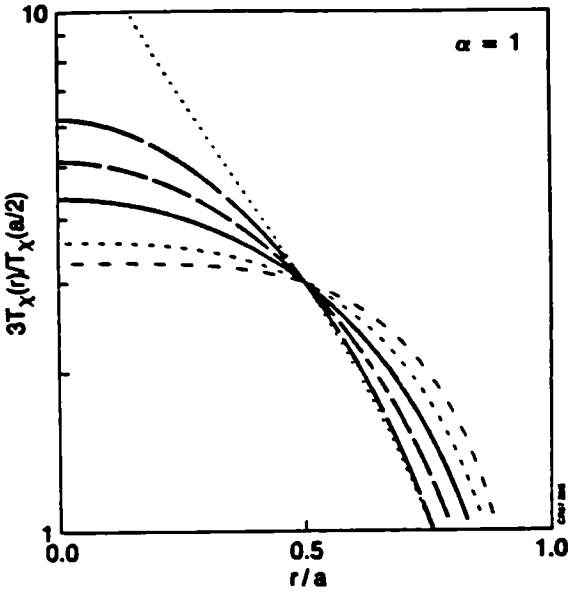

Fig.3 Temperature profiles induced by by various heating profiles for heat pinch model.

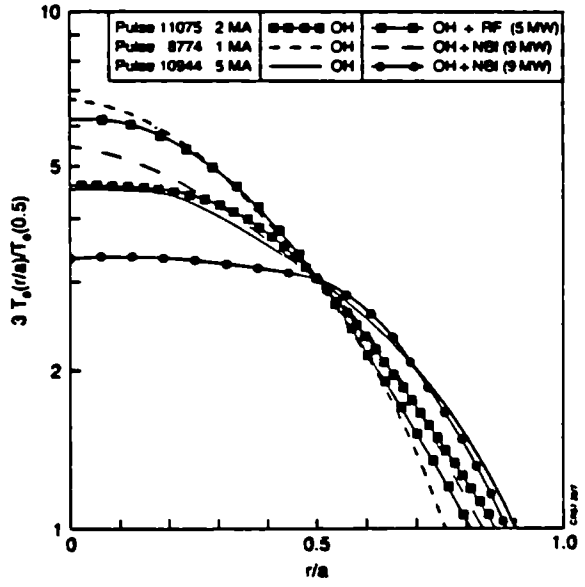

Fig.4 Temperature profiles induced by various heating profiles.

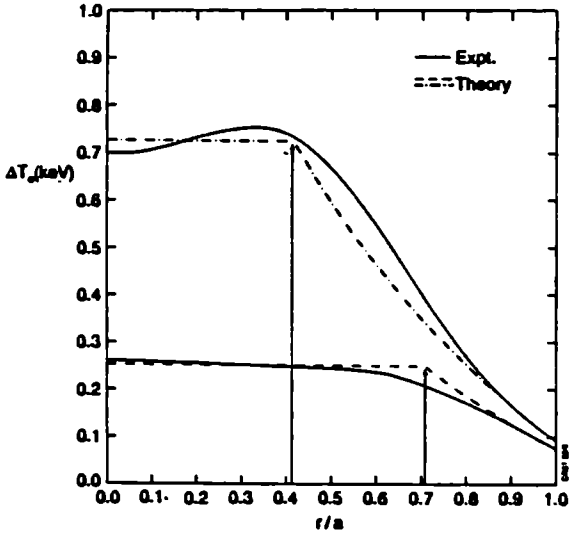

Fig.5 Comparison of the temperature change due to localised ICRH in JET with local transport model predictions

A MODEL FOR PELLET ABLATION IN JET

M L Watkins, W A Houlberg*, A D Cheetham, A Gondhalekar,
R Granetz, F Hendriks, J O'Rourke, P M Stubberfield

JET Joint Undertaking, Abingdon, Oxon OX14 3EA, UK
*Oak Ridge National Laboratory, Oak Ridge, TN 37831, USA

1. INTRODUCTION

Solid deuterium pellets have been injected into JET discharges for a wide variety of plasma conditions (including limiter, inner wall and X-point discharges) with ohmic heating alone, and in combination with ICRF (up to 6MW) and NBI (up to 8MW of 75kV deuterium injection). The pellets are injected in the mid-plane along a major axis of the plasma. The penetration of these pellets is compared with that determined by the neutral gas shielding (NS) model [1] and the neutral gas and plasma shielding (NGPS) model [2]. A suitable model is proposed for the effective ionisation radius in the NGPS model which determines the ionised shield parameters. For present JET experiments penetration is found to be consistent with electron ablation alone. The lack of fast ion effects is interpreted in terms of expected energy and power thresholds.

2. EXPERIMENTAL DETERMINATION OF PENETRATION

An array of soft X-ray diodes viewing horizontally behind the pellet yields a qualitative view of the time-dependent pellet ablation rate and an accurate measurement of the time at which the ablation process ends (Figure 1). The structure is similar to that exhibited by the D_α light viewed along the pellet path. Pellet penetration depth is determined from this data together with data from an array of soft X-ray diodes viewing the pellet trajectory vertically (Figure 2). These signals also provide the pellet speed in the plasma (0.75-1.2km/s) which may be compared with the speed deduced from time-of-flight measurements in the pellet launcher. Pellets, nominally 3.6mm and 4.6mm cylinders of equal diameter and length, penetrate a distance 0.5-1.2m, the distance between the limiter and the magnetic axis being about 1.1m.

3. NEUTRAL GAS AND PLASMA SHIELDING MODELS

In the NS model monoenergetic electrons are shielded from the pellet by a layer of dense molecular hydrogenic gas. A fit to the numerical solution of the hydrodynamic equations of mass, momentum and energy in the neutral shield, assuming uniform volumetric heating, leads to a relationship between the energy flux and the thickness of the neutral shield. An energy balance at the pellet surface provides a second relation between the energy flux and the ablation rate. The NGPS model extends the solution of the neutral shield by treating the electrons as having a Maxwellian distribution and adding contributions from fast ions with both of these effects increasing ablation. A cold plasma shield extending along the magnetic field is also present, increasing the shielding of incident electrons and thus decreasing ablation. The effective ionisation radius is considered as the only free parameter in our applications of the NGPS model.

The plasma response during pellet ablation is represented by adiabatic mixing of the ablatant plasma with the plasma electrons in the NS model (collisional plasma), whereas the incident electron distribution function is depleted in the NGPS model (collisionless plasma) which is more appropriate for JET plasmas.

4. COMPARISON BETWEEN EXPERIMENT AND THEORY

JET geometry and plasma parameters (electron density profiles from 7 vertical chords of an FIR interferometer and temperature profiles from 2nd harmonic ECE data) are used to assess variations in the ablation model. The data set used for the comparison between the experimentally determined penetration distance and that obtained by modelling is considerably extended beyond that of Ref [3] and now contains about 100 discharges. Integration of the FIR chordal data indicates that the smaller pellets contain about 85% of the mass of a 3.6mm cylinder while the larger pellets contain about 70% of the mass of a 4.6mm cylinder. This mass discrepancy appears to be systematic and likely arises during pellet formation and acceleration rather than during the ablation process. We use 85% of the mass for all of the 3.6mm diameter pellets (spherical radius of 1.95mm assumed) and 70% of the mass for the 4.6mm diameter pellets (spherical radius of 2.34mm assumed).

The pellet velocities determined from time-of-flight and vertical soft X-ray data agree to within about 10% - this yields no significant difference in calculated penetration depths. Variation of the pellet size from 60-95% leads to less than ±5cm in the calculated penetration depths around the reported values. Uncertainties in the electron density and temperature data is greatest in the outer edge of the plasma; sensitivity to the density variation is weak while variation of the electron temperature in the expected range leads to an error of ±5cm in the calculated values. Measured penetration depths are accurate to within half the separation between vertical soft X-ray chords or ±3cm.

4.1 Ohmic Heating Alone

The NS model does not reproduce very well the penetration in ohmic discharges, especially for deeper penetration (Figure 3a). This is because the neutral shield solution for monoenergetic incident electrons does not adequately represent the penetration of electrons from the tail of the distribution when the electron temperature exceeds about 1keV [2]. The agreement between theory and experiment is improved but consistently low with the NGPS model and an ionisation radius fixed at r_o = 3.5mm independent of pellet radius, r_p (Figure 3b), the model used in earlier predictive calculations for JET[4]. This agreement can be further improved by fixing the thickness of the ionised shield at 1mm, that is, an ionisation radius of $r_o = r_p$ + 1mm (Figure 3c).

4.2 Additional NBI and ICRF Heating

With additional heating the NS model again shows discrepancies between calculated and experimental depths comparable to those for ohmic discharges. The NGPS model with a 1mm thick ionised shield and ignoring any fast ion contributions to the ablation process gives an adequate fit to the data (Figure 3d) with a spread comparable to that found in ohmic

discharges. From this we conclude that fast ion effects are not important at the present power levels. During high power NBI shots, the electron temperature in the outer plasma rises above 450eV where the shield thickness to stop electrons becomes greater than that to stop 80kV deuterium ions [2]. Furthermore, even with 8MW of NBI injection the fast ion energy flux in JET is an order of magnitude lower than the electron energy flux at all radii.

5. CONCLUSIONS

It is found that the NGPS model, which includes both a dense neutral gas shield and a cold plasma shield extended along the magnetic field lines, reproduces the JET experimental data for pellet penetration when the effective thickness of the neutral gas layer is set at 1mm. Good agreement is found on the basis of electron ablation alone indicating that fast ion effects during NBI and ICRF heating are not important for the present levels and densities of fast ions. Detailed theoretical models of the spatial and energy distribution of fast ions during ICRF heating have not yet been developed for evaluating their effect on pellet ablation.

REFERENCES

[1] Milora S L, Foster C A, IEEE Trans on Plasma Sci PS-5 (1978) 12.

[2] Houlberg W A, Milora S L, Attenberger S E, "Neutral and Plasma Shielding Model for Pellet Ablation", submitted to Nuclear Fusion.

[3] Gondhalekar A, et al, in Plasma Physics and Controlled Nuclear Fusion Research (Proc 11th Int Conf, Kyoto, 1986) IAEA, Vienna, to be published.

[4] Watkins M L, Houlberg W A, Kupschus P, Stubberfield P M, Taroni A, Proc 13th Eur Conf on Cont Fusion and Plasma Heating, Schliersee, 1986, 10c(I), EPS (1986) 156.

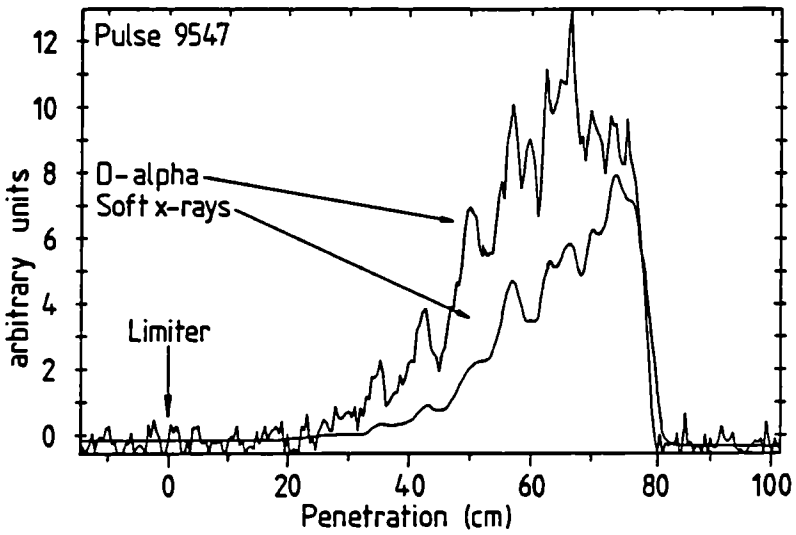

Fig 1: Typical D_α and soft X-ray signals as a function of the distance of the pellet from the outer limiter

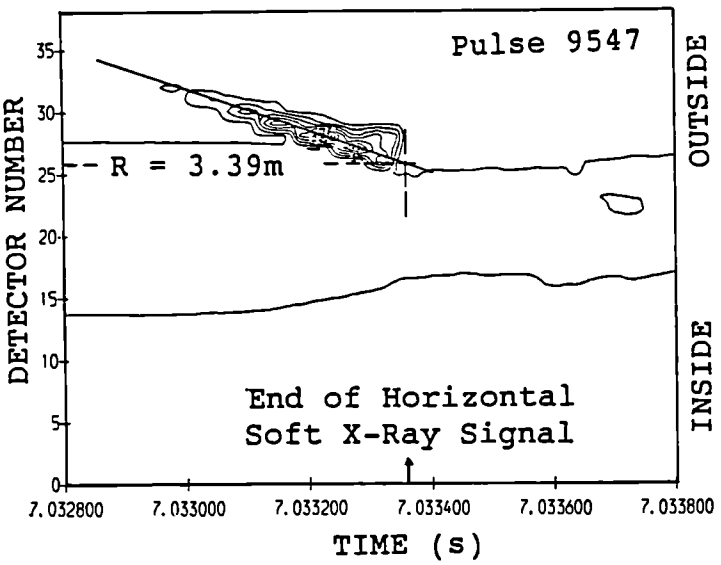

Fig 2: Intensity contours of vertical soft X-ray data during pellet injection. The slope of the curve passing through the peaks determines velocity and the end point is the maximum penetration depth.

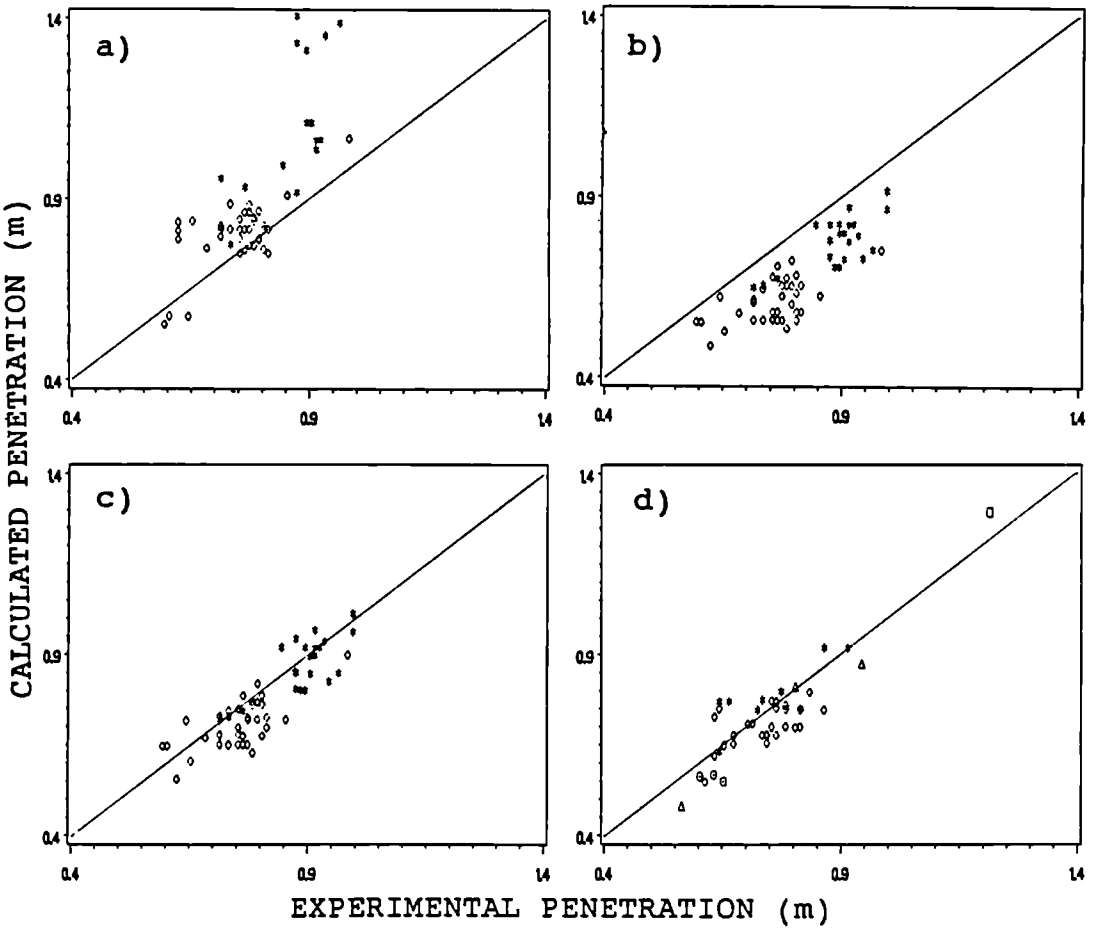

Fig 3: Calculated penetration depth vs experimental penetration depth for: a) NS model in OH; b) NGPS model in OH with r_o = 3.5mm; c) NGPS model in OH with $r_o = r_p$ + 1mm; and d) NGPS model in NBI and ICRF with $r_o = r_p$ + 1mm. Distances are measured from the limiter.

ELECTRON HEAT TRANSPORT IN TOKAMAKS

P H Rebut, M L Watkins and P P Lallia
JET Joint Undertaking, Abingdon, Oxfordshire, OX14 3EA, UK

1. INTRODUCTION

Earlier work [1-4] on the role of the magnetic field topology in determining tokamak behaviour, such as anomalous electron heat conduction and degradation of confinement with additional heating, relies on an equilibrium being established between laminar surfaces, magnetic islands and ergodic domains in a plasma. This concept leads to a change in the plasma behaviour when the interaction of sets of magnetic islands produces a surrounding ergodised region. An analysis, based on the non-dimensional structural parameters which describe the dominant physical processes and the non-dimensional shape parameters which generally describe the geometry of the plasma or its composition, is summarised in Section 2. This analysis can be interpreted in terms of a critical temperature gradient, a specific form of which (together with the heat flux which results when this gradient is exceeded) is consistent with a plausible physical mechanism for the sustainment of the magnetic islands. This mechanism relies on the directed kinetic energy of electrons compensating the resistive dissipation of the induced currents needed to maintain the topology (Section 3). The resulting model is found to agree with JET experimental data in terms of the global scaling of the stored electron energy (Section 4) and the detailed profile analysis using transport code simulations of JET discharges (Sections 5 and 6).

2. DIMENSIONAL ARGUMENTS

Heuristic scaling laws have been derived on the basis of non-dimensional parameters [3]. The dominant physical processes are described by normalised structural parameters representing the plasma pressure, β, the resistivity, Δ, the power flow, ϕ and the diamagnetic thermal drift speed, Ω. Granular and relativistic effects are ignored for the present discussion. Taking account of the number of independent variables which can be constrained externally, a single relationship must exist between the parameters. This must be of the general form:

$$\phi = \phi(\beta, \Delta, \Omega) \quad \text{where} \quad \phi = \frac{F}{nkTv_s}$$

and

$$\beta = 2\mu_o nkT/B_t^2 \quad ; \quad \Delta = \eta J/B_p v_s \quad ; \quad \Omega = (2m_e/kT)(k\nabla T/eB_t)^2 \tag{1}$$

applicable to all tokamaks and, given the geometric and magnetic configurations, the input power and the plasma density, serves to define the plasma temperature. The ohmic heating power can be written as $\phi = \Delta/\beta$ and in ohmically heated plasmas equation (1) becomes :

$$g(\beta, \Delta, \Omega) = 0 \tag{2}$$

JET experimental results strongly suggest a large resilience to changes in the electron temperature profile in the conduction zone. It is therefore reasonable to interpret equation (2) mainly as defining a critical temperature gradient. We propose that:

$$\Omega = \Omega_c(\Delta,\beta) \quad \text{and} \quad \Omega_c(\Delta,\beta) \propto \Delta/\beta \tag{3}$$

We suggest that this form for the critical temperature gradient applies for all forms of input power. Of course, with strong heating, further departures from the critical temperature profile are to be expected. We propose as a form for equation (1):

$$\phi = -\Omega_c^{\alpha}[\Omega^{1/2} - \Omega_c^{1/2}]H[\Omega^{1/2} - \Omega_c^{1/2}] + \phi_{neo} \quad , \quad \alpha = 0, \tfrac{1}{2}\ldots \tag{4}$$

where ϕ_{neo} represents all the normal heat losses through the electron channel and H is a function which is zero (or unity) for $\Omega <$ (or $>$) Ω_c.

3. PHYSICAL MODEL

Consistent with the concept of a chaotic magnetic topology involving small magnetic islands being responsible for the transport properties, we present a plausible argument to define the temperature gradient and the electron heat flow. The power balance between the directed kinetic energy of electrons and the resistive dissipation of the induced currents, $\tilde{J}$, needed to maintain the magnetic topology of the islands may be expressed:

$$\tfrac{1}{2} m_e n \left(\frac{\nabla T}{2eB_t}\right)^2 v_{the}\, \sigma_{erg} \propto E\, \tilde{J}\, \sigma_{erg}\, L \tag{5}$$

or

$$\tfrac{1}{2} m_e n\, v_{the} \left(\frac{\nabla T}{2eB_t}\right)^2 \propto E\, B_t\, \gamma^2 \tag{6}$$

where σ_{erg} is the cross-section of the ergodic magnetic flux and L is the length needed to cross one chain of islands. Thus the temperature gradient is related to the overlapping parameter γ. For low collisionality, γ exceeds a certain critical value, $\gamma_c \sim 0.9$, in which case equation (6) reduces to equation (3). The heat flux is then:

$$F = -\nu \frac{\delta^2}{R} v_{the}\, n_e k \nabla T_e\, (\gamma - \gamma_c) + F_{neo} \quad \text{with} \quad \gamma = \gamma_c\, \nabla T_e / \nabla_c T \tag{7}$$

δ is related to the interspace between the chain of islands and ν is a numerical factor. Equation (7) could be written in the form:

$$F = -\chi\, n_e k(\nabla T_e - \nabla_c T) H(|\nabla T_e| - |\nabla_c T|) + F_{neo} \text{ with } \chi = \nu\gamma \frac{\delta^2}{R} v_{the} \tag{8}$$

Specifically, $\alpha = 0$ gives the following expressions for $\nabla_c T$ and χ:

$$\nabla_c T = \nu_c \left[\frac{EB_t^3}{n_e \sqrt{T_e}}\right]^{1/2} \frac{1}{q} \qquad \chi = \nu_H \frac{\nabla T_e}{B_t} \frac{q^2}{q'} \tag{9}$$

where $\nu_c = 3.5$ and $\nu_H = 4.0$ with E in Vm^{-1}, B_t in T, n_e in $10^{19} m^{-3}$ and T_e in keV. These expressions are used in Section 4-6. However, a more suitable form for equation (8) may be with $\gamma\delta \propto (\nabla T_e / 2eB_t) q^2/q'/v_{thi}$ (corresponding to $\alpha = \tfrac{1}{2}$).

4. GLOBAL SCALING

Expressed in terms of the input variables of electron density, n_e, toroidal magnetic field, B_t, plasma current, I (MA), the average size of the plasma, ℓ, and the input power, P (MW) (independent of the heating method, namely, ohmic, NBI or ICRF), the global electron energy content, W_e (MJ), can be deduced from equations (3) and (4) and written as:

$$W_e = \alpha_1 Z^{1/4} n_e^{3/4} B^{1/2} I^{1/2} \ell^{11/4} \left\{1 + \alpha_2 \frac{M^{1/2} P}{n_e^{1/2} Z^{1/2} B \ell^{3/2}}\right\}^{1/2} \qquad (10)$$

M is the atomic number and Z is the effective charge. From a regressional fit to about 1200 data points from JET limiter discharges, the coefficients α_1 and α_2 are found to be respectively 2.3×10^{-2} and 3. The comparison between the fitted and calculated values is shown in Figure 1, where the range of the experimental conditions is also shown. A more refined treatment requires the direct simulation of the plasma profiles.

5. SIMULATION OF ELECTRON ENERGY TRANSPORT

A simplified 1-D electron energy transport code which uses equations (8) and (9), ohmic and additional input power and experimental density profiles (but ignores ion transport and radiated power) has been used to compare computed and experimental data. For two values of the plasma current the comparison in terms of the global energy content is shown in Figure 2. Simulations also show the possibility of a pedestal in the electron temperature when a high shear is introduced at the edge, thereby simulating an H-mode.

6. FULL TRANSPORT CODE SIMULATIONS

A range of JET discharges has also been simulated using the above model for electron transport (equations (8) and (9)) in the 1-1/2D predictive transport code, ICARUS. Other features of the model are basically those used previously [5].

Computed electron temperature profiles are compared with the experimental ones after the collapse of the sawtooth in various ohmic discharges with different electron densities and currents (Figure 3). Other characteristics of the discharge, for example, ohmic power, radiated power, confinement times, are also well represented.

With neutral beam injection the observed degradation in confinement is obtained without changing the transport model. The electron temperature profiles at the end of the ohmic phase and the L-mode are well simulated, as also is the temporal behaviour for the central electron temperature during the transient between the OH and L-mode (Figure 4).

7. CONCLUSIONS

A model for electron heat transport in tokamak plasmas which in a single formulation accounts for both the anomalous behaviour in ohmic plasmas and the degradation of confinement with additional heating has been proposed. Some shape parameters (such as, T_e/T_i, r/R, $T\nabla n/n\nabla T$) are possibly hidden in the evaluation of ν_c and ν_H. While this model does not yet have an established theoretical basis, it is nontheless consistent with the theory of ergodic magnetic fields and JET experimental results.

ACKNOWLEDGEMENTS

We are pleased to acknowledge the assistance of Dr K Thomsen in preparing the JET data used in Figures 1 and 2.

REFERENCES

[1] Rebut, P H and Lallia, P P, Proceedings of the 7th International Conference on Plasma Physics (Kiev, USSR, April 1987).

[2] Rebut, P H et al, in Plasma Physics and Controlled Nulcear Fusion Research (Proc 11th Int Conf, Kyoto 1986) paper IAEA-CN-47/E-III-4.

[3] Rebut, P H and Brusati, M, Plasma Physics and Controlled Fusion, 28 (1986)113.

[4] Rebut, P H and Hugon, M, in Plasma Physics and Controlled Fusion Research (Proc 10th Int Conf, London, 1984), 2(1984)197.

[5] Watkins, M L et al, Proc 13th Eur Conf on Cont Fusion and Plasma Physics, Schliersee, 1986,10C(I), EPS(1986)156.

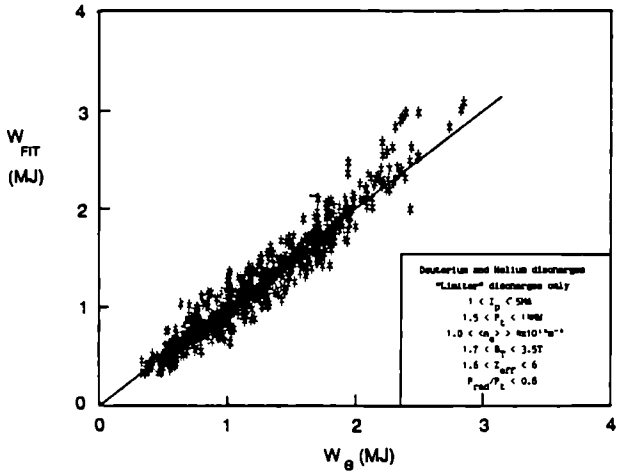

Fig 1: Total stored electron energy versus the fit proposed in Eq(10).

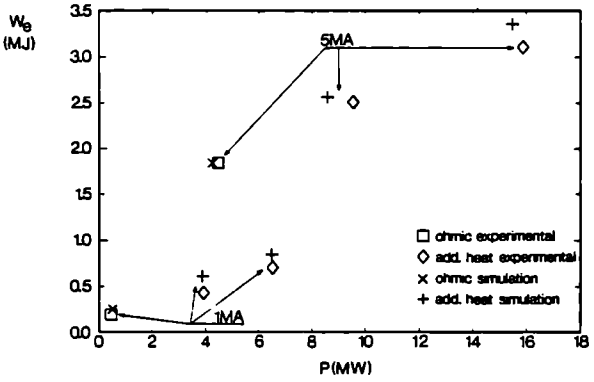

Fig 2: Total stored electron energy versus total input power for 1&5MA.

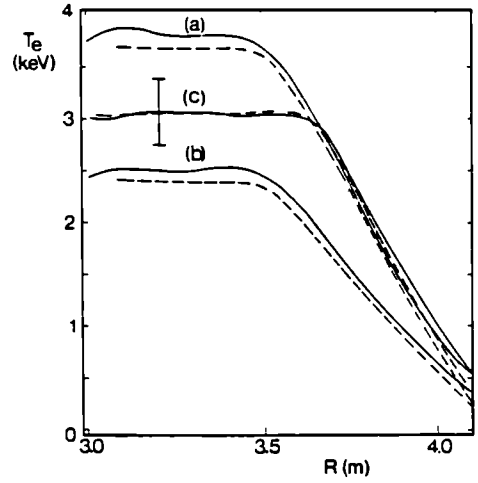

Fig 3: Experimental (—) and computed (---) electron temperature profiles for a)3MA,1.6x10^{19}m^{-3}; b)3MA,3.2x10^{19}m^{-3};c)5MA,3.2x10^{19}m^{-3}

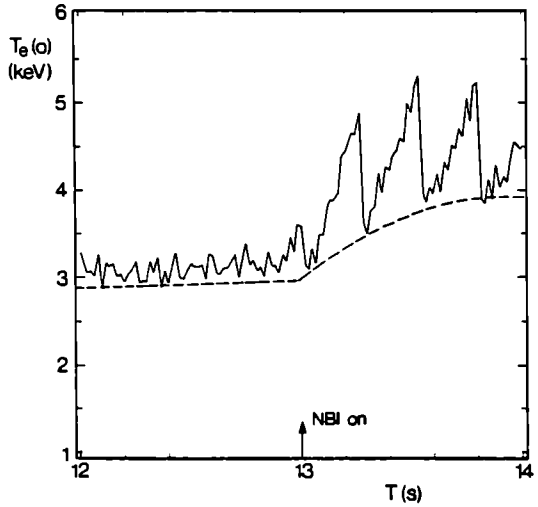

Fig 4: Experimental (—) and computed (---) central electron temperature for a 2MA X-point discharge in OH and L- mode with NBI.

VISIBLE RADIATION STUDIES ON JET USING A MULTI-CHORD POLOIDAL ARRAY

P D Morgan and J J O'Rourke

JET Joint Undertaking, Abingdon, Oxon, OX14 3EA, UK

INTRODUCTION

Visible radiation from the JET plasma has been routinely monitored since the beginning of operation in mid 1983. Absolute measurements are made of H_α or D_α emission, continuum radiation at 523.5 nm and the intensities of lines from such species as C III, O II and Cr I. These provide information on particle confinement and recycling, the temporal behaviour of Z_{eff} and the influxes of impurities, respectively. The measurements are made using typically 12 discrete telescopes distributed around the vacuum vessel, which view limiters, antennae, the inner wall and the upper/lower wall [1].

Recently, a 13-telescope array has been added which permits the study of the spatial variations of optical emission in a poloidal cross-section of the plasma. In this paper we describe the application of the array to measure continuum radiation and D_α emission. Analyses of the data have yielded the temporal evolution of the $Z_{eff}(r)$ profile and of particle confinement and recycling; the results reported herein pertain to discharges fuelled by pellet injection and to discharges limited by a magnetic separatrix, respectively.

APPARATUS

Figure 1 shows a schematic diagram of the array. Thirteen telescopes collect light through 3 quartz windows in a main vertical port, giving a total field of view of ~55° and covering $\gtrsim$95% of the plasma cross-section. Each telescope has a collection cone of full angle ~1.2°, resulting in a spot size of diameter ~12 cm at the top wall for channel no.6. The upper and lower port flanges are ~6.5m apart.

A total of 13 optical fibres of core diameter 0.6 mm and length ~100 m (Quartz et Silice PCS 600) is used to connect the telescopes to 13 EMI 9658R photomultipliers. The system covers the spectral range between ~350 and 750 nm. Isolation of the required spectral feature is achieved using 13 interference filters with appropriate pass-band, of width ~1 nm FWHM. The time response of the system is 200 μs.

RESULTS AND DISCUSSION

(a) Continuum Measurements

Figure 2 shows 3 continuum traces at 523.5 nm obtained with the array. The 3 signals gradually rise, following breakdown, reflecting an increasing plasma density. At 7.0s there is an abrupt increase in the continuum intensities, following the injection of a D_2 pellet containing ~4.5×10^{21} atoms into the plasma. The plasma initially loses particles rapidly, as evidenced by the decreasing continuum signals, before reaching equilibrium at a density higher than before injection.

The local continuum emissivity is given by

$$\varepsilon(r) \propto n_e^2(r) Z_{eff}(r) / \sqrt{T_e(r)}$$

and determination of $\varepsilon(r)$ will permit the evaluation of $Z_{eff}(r)$, provided $n_e(r)$ and $T_e(r)$ are known. However, the 13 optical channels measure the continuum brightness along the various chords, ie the line integral of the emissivity. $\varepsilon(r)$ is evaluated by the procedure of Abel inversion [2], by assuming that the magnetic flux surfaces are also surfaces of constant emissivity.

The emissivity profile for an ohmic discharge at t=6s is shown in Figure 3, which was obtained using the raw data shown in part in Figure 2. Multiplying this profile by the variable $(\sqrt{T_e(r)}/n_e^2(r))$ yields the radial profile of Z_{eff}, as shown by the solid line in Figure 4. In addition, $Z_{eff}(r)$ is shown 0.25s after a D_2 pellet was injected. The latter profile is considerably flatter, with the central value $Z_{eff}(o)$ having been reduced by a factor of >3. At this time $n_e(r)$ has completely filled in, following its perturbation. The reduction in Z_{eff} by pellet injection can be explained by the impurity content not changing and being further diluted by the D ions. Within ~3s of injection Z_{eff} rises to a value typical of that in gas-fuelled discharges at the new density [3].

(b) D_α Measurements

In figure 5, D_α emission recorded by 3 telescopes in the array is shown as a function of time. At -4s the plasma was expanded inwards, the signal in channel 1 rising as the D_α emitting shell moves into tangency with the viewing chord and the plasma briefly touches the inner wall. At -8s the plasma was contracted off the inner wall and outer limiters and at -9s a magnetic separatrix was established, resulting in increased wall emission as recorded by the other 2 channels. A 3s NBI pulse of peak power 9.3 MW was applied at 11s, inducing the H-mode of confinement for ~1.4s at t=12.3s. This is reflected by a reduction in D_α emission except at the X-point zone (which is in the vicinity of the end of chord 5), despite the rapidly-increasing plasma density. The H→L-mode transition at ~13.7s results in an abrupt loss of particles and increased D_α emission through recycling. At ~16s the plasma is again expanded, to touch inner wall and limiters at 18-20s.

From the particle balance equation,

$$\frac{dN_e}{dt} = \Phi_{in} + \Phi_{gas} + \Phi_{NBI} - \frac{N_e}{\tau_p} ,$$

where N_e is the total electron content and Φ_{in} is the flux of recycled neutrals which are ionised, the global particle confinement time τ_p may be calculated. Φ_{in} is deduced from D_α measurements using the array and single telescopes viewing the limiters. Since $\Phi_{in} = R\, N_e/\tau_p$ $(=R\Phi_{out})$, the recycling coefficient R may also be obtained [4]. The effects of impurities are taken into account.

Figures 6(a) and 6(b) show the temporal variation of τ_p and R during the discharge for which Figure 5 shows the raw data in part. The substantial drop in τ_p at ~9s is probably due to the formation of the separatrix, although it cannot be entirely excluded that a previously-hidden source has moved into view. This is followed by an abrupt increase at ~12.3s due to the L→H-mode transition with improved particle confinement. Contemporaneous with this behaviour, the recycling coefficient, which has a value close to 1 in equilibrium, decreases at separatrix formation, as particles are lost from the plasma, before

recovering. Following a perturbation to R at switch-on of NBI, 11s, it rises dramatically at the H-mode onset at ~12.3s; the improved particle confinement resulting in much lower particle efflux. At the H→L-mode transition, R drops to below 1 as the plasma rapidly loses particles. The change in sign of (1-R) at the end of the H-mode, wrt the onset, corresponding to a switch from fuelling to pumping, is in qualitative agreement with the model of Jones et al [5]. As the plasma is moved back to the outer limiters, beginning at -16s, τ_p rises and R recovers to ~1.

SUMMARY

A 13-telescope array has been used to study poloidal variations in continuum radiation and in D_α emission from JET plasmas, yielding the temporal evolution of $Z_{eff}(r)$ and of particle confinement and recycling, respectively. Reductions of $Z_{eff}(o)$ by >3 have been observed following D_2 pellet injection into OH discharges. In plasmas limited by a magnetic separatrix, increases in τ_p by ≤2.5 have been observed at L→H-mode transition.

REFERENCES

[1] P D Morgan et al, Rev.Sci.Instrum. 56, (5) part 2, 862 (1985)
[2] N Gottardi et al, Proc.12th Europ.Conf. on Controlled Fusion and Plasma Phys. 9F, part 1, 30 (1985)
[3] A Gondhalekar et al, 11th Int. Conf. on Plasma Phys. and Controlled Nuclear Fusion Research, paper IAEA-CN-47/I-I-6 (1986)
[4] P D Morgan et al, Proc.12th Europ.Conf. on Controlled Fusion and Plasma Phys. 9F, part 2, 535 (1985)
[5] T T C Jones et al, this conference.

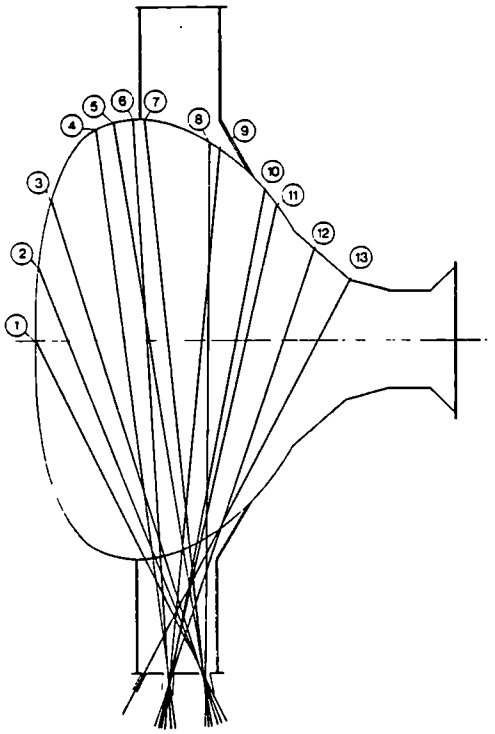

FIGURE 1: Arrangement of the 13 lines-of-sight of the array.

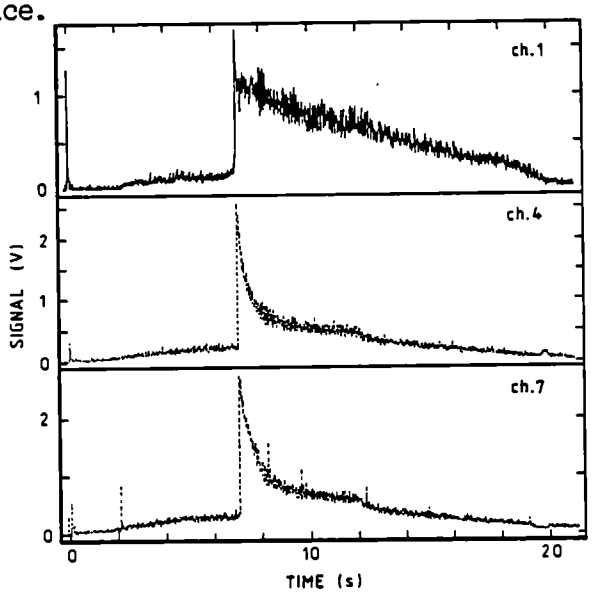

FIGURE 2: Continuum signals from 3 channels, cf Fig.1, during an OH discharge. At 7 s a D_2 pellet was injected. Pulse #9376, I_p =2.5-3.4 MA, B_ϕ =2.1 T.

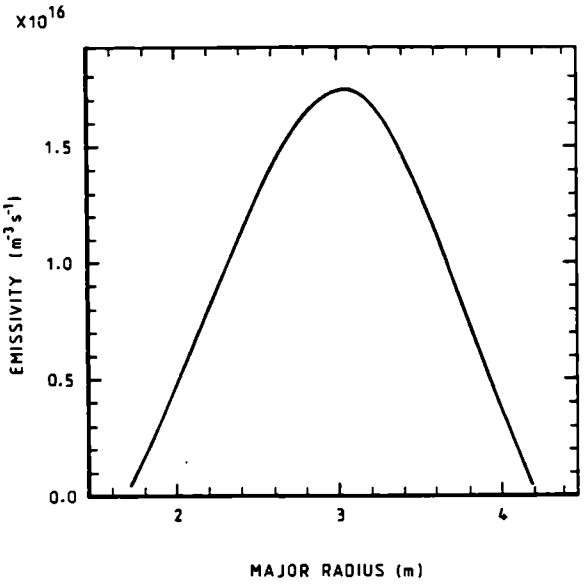

FIGURE 3: Photon emissivity profile as a function of major radius at 6s for pulse #9376. Plasma centre is at 3.07 m.

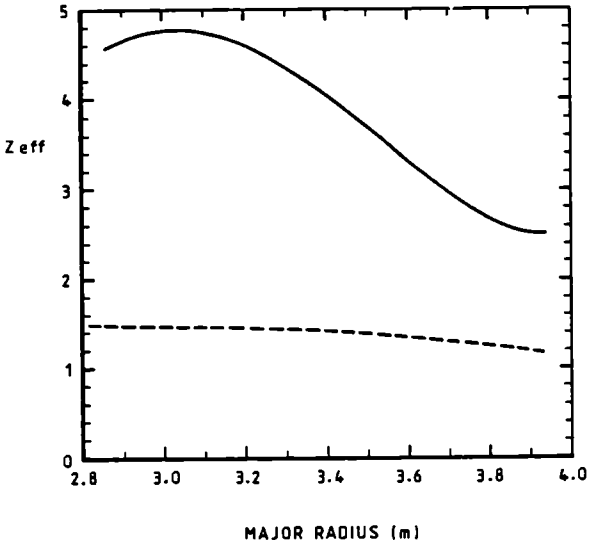

FIGURE 4: Radial profiles of Z_{eff} for pulse #9376. Solid line - profile at 6s. Dashed line - profile at 7.25s, 0.25s after the injection of ~4.5×10^{21} D atoms.

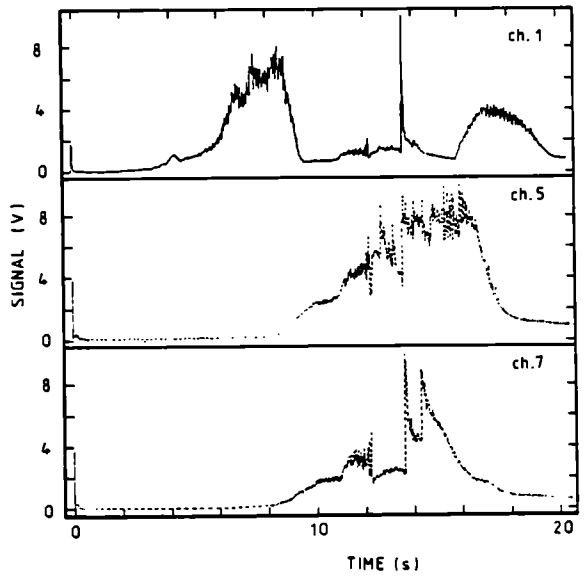

FIGURE 5: D_α emission from 3 chords (see Fig.1). At ~ 9s a magnetic separatrix formed. At 11s 9.3MW of NBI was applied for 3s. At ~12.3s an L→H-mode transition occurred. Pulse #10789, I_p=3 MA, B_ϕ=2.2 T.

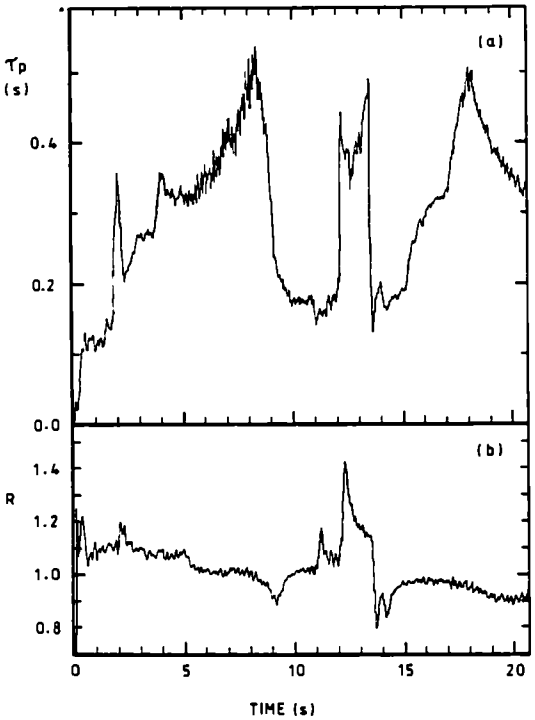

FIGURE 6: Pulse #10789. (a) Temporal variation of global particle confinement time, τ_p. (b) Temporal variation of recycling coefficient, R.

JET XUV SPECTROSCOPY : FIRST RESULTS

J Ramette*, K Behringer, B Denne, W Griffin+, N C Hawkes+, G Magyar, M Mattioli*, N J Peacock+, B Saoutic* and J L Schwob°

JET Joint Undertaking, Abingdon, OX14 3EA, UK
+ Culham Laboratory, Abingdon, OX14 3DB, UK
* Association EURATOM-CEA, CEN Cadarache, 13115 St Paul lez Durance, France
° Racah Institute, Hebrew University of Jerusalem, Israel

I INTRODUCTION

For understanding impurity radiation, transport and energy balance, XUV spectroscopy is one of the most powerful techniques. In earlier stages of JET operation the VUV spectra were recorded by a multichannel spectrometer operating in survey mode, ie in a wide wavelength range (100-1700 A) but at low resolution (FWHM - 2.3 A). Plasma spectroscopy on various tokamaks has shown that practically all particle transport and power loss estimates are affected by the lack of good spectral resolution. For this reason an up to date version of the Schwob-Fraenkel extreme grazing incidence duo-multichannel XUV spectrometer [1] previously used on PLT, TFTR and TFR has been installed on JET during the spring of 1986. The first results are reported below.

II EXPERIMENTAL

The JET XUV spectrometer is a time resolved spectrograph covering the wavelength range 10-340 A. The basic instrument is a high resolution, interferometrically adjusted 2 m, 600 grooves/mm grating spectrometer operating at an extreme grazing incidence angle (1.5°). The gold coated ruled Bausch and Lomb grating is blazed at 1.31°. Two parts of the spectrum are recorded simultaneously by two scanning detectors. They consist of a MgF_2 coated funneled microchannel plate coupled to a phosphor screen image intensifier. Its output is conducted by a flexible optical fibre to a 1024 element photo diode array, controlled and read out by an optical multichannel analyser (EGG/PAR). The simultaneous spectral coverage is 20 to 40 A with one detector operating between 10 and 140 A, and the other between 140 and 340 A. With a 20 μ entrance slit the spectral resolution (FWHM) is 0.2 A. A full spectrum may be recorded in 16 ms, but the minimum read out time for selected pixels may be 1 ms. Under JET plasma conditions an exposure time of 160 ms is routinely used.

Following the grating equation and the spectrometer geometry a wavelength calibration was carried out using the intrinsic impurity lines in JET. It was necessary to add empirical small corrections function of the screw position and of the image distortion in the fibre optic chain [1,2]. The estimated accuracy of the peak wavelengths is ± 0.05 A corresponding to an uncertainty of ± 1 pixel. This is a pessimistic estimate for strong lines, the peak of which can be located to better than ±.1 pixel.

The observed instrumental function is very close to a Gaussian, its width is increasing slightly with the detector position along the Rowland

circle. A best fitting procedure is used, based on a least square method; it allows to fit up to 5 Gaussian profiles with a constant background level. The accuracy of the measured relative position and width of a line is strongly statistic dependent. For high count rates ($\geq$ 5000 counts) accuracies of a few x 10^{-3} A are obtained.

The spectrometer is located in the torus midplane and views a horizontal chord at a slight angle (α=11.35°), thus allowing Doppler shift measurements due to toroidal rotation.

III HIGH RESOLUTION XUV SPECTRA

High resolution XUV spectra have been obtained under a variety of JET operating conditions. Detailed studies can be found in [2]. As an example a spectrum of a 5 MA-NBI-RF discharge (shot #10981) is shown in figure 1.

IV DOPPLER SHIFTS AND WIDTHS MEASUREMENTS

If a collective velocity of the plasma particles is superimposed on the thermal velocity the whole broadened line is shifted. Assuming that the angular velocity of the plasma $\omega(r)$ is constant over the same magnetic surface this shift is given by: $\Delta\lambda / \lambda = R\omega(r)\sin\alpha/c$ where R is the major radius of the plasma and α is the angle between it and the line of observation. For R=3 m this leads to: $\Delta\lambda_D/\lambda_o = 2 10^{-9}\omega(r)$ [rd s^{-1}].

In fig.2 the time evolution of Ni XXVI ion temperature and of angular rotation velocity are given for shot #9776. Angular rotation velocities up to 10^5 rd S^{-1} and ion temperatures up to 10 keV are measured during the 7 MW NBI phase. Using several ions in combination with impurity transport code calculation assuming usual JET transport coefficient ($D=1.m^2s^{-1}$, S=1) and excluding the charge exchange effects, radial ion temperature profiles (fig.3) and angular rotation velocity profiles (fig.4) are inferred. These profiles are generally flat in the centre, dropping steeply at the edge within a few cm (the horizontal error bars being assumed equal to the thickness of the emission shells as given by the code).

V LINE INTENSITY RATIO STUDIES

Study of the spectral lines emitted by He-like ions plays a very important role in the evaluation of the characteristics of laboratory and astrophysical plasmas. In particular the ratio $G=E_I/E_R$ (E_I and E_R are the emissivities of the intercombination ($1s^2\ {}^1S_0$-$1s2p\ {}^3P_1$) and resonance ($1s^2\ {}^1S_0$-$1s2p\ {}^1P_1$) lines respectively) has been used to determine the electronic temperature T_e of tokamak plasmas [3]. Neglecting charge exchange and recombination from H-like ions, the calculations of [3b] have been used. An example of the estimated T_e value is given in fig.5. The most striking effect is obtained during X-point discharge where the temperature of the emitting shell of CV, located near the limiter radius, is increasing from 160 eV up to 320 eV. No other modification was observed during X-point plus H-mode plasmas.

REFERENCES

[1] Schwob J L, Wouters A W, Suckewer S and Finkenthal M, PPPL Report 2419 (1986); accepted for publication in Rev. Sci. Instr.

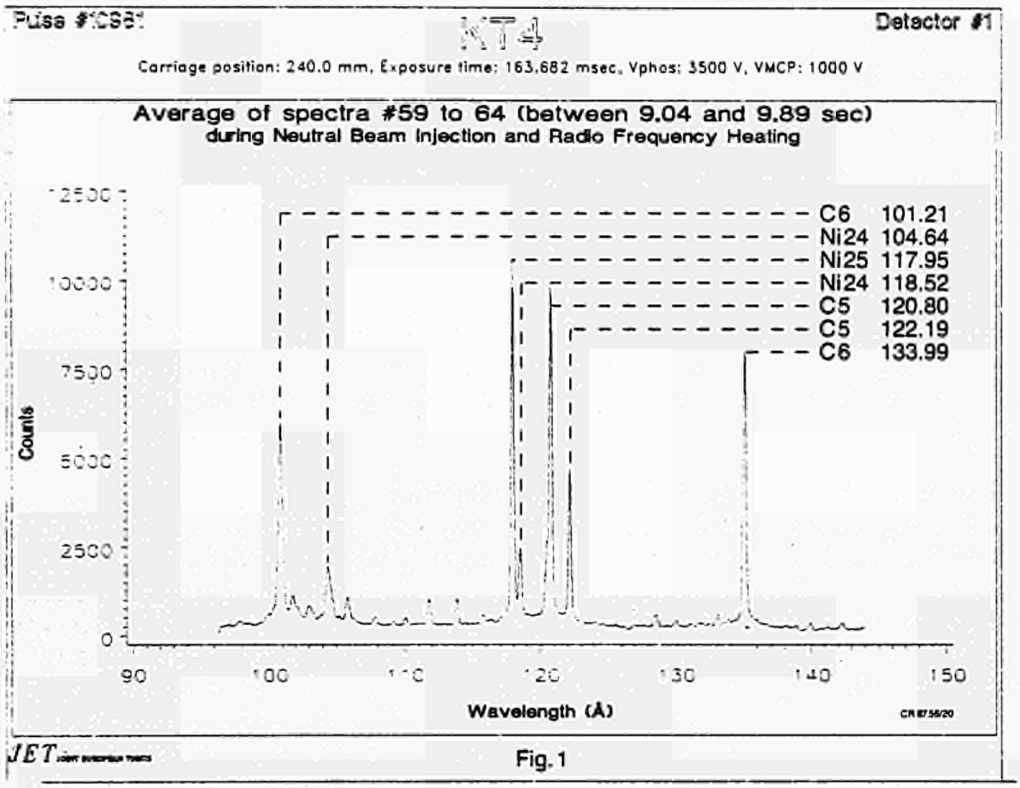
Pulse #10981
KT4
Detector #1
Carriage position: 240.0 mm, Exposure time: 163.682 msec, Vphos: 3500 V, VMCP: 1000 V
Average of spectra #59 to 64 (between 9.04 and 9.89 sec)
during Neutral Beam Injection and Radio Frequency Heating
C6 101.21
Ni24 104.64
Ni25 117.95
Ni24 118.52
C5 120.80
C5 122.19
C6 133.99
Counts
Wavelength (Å)
JET

Fig. 1

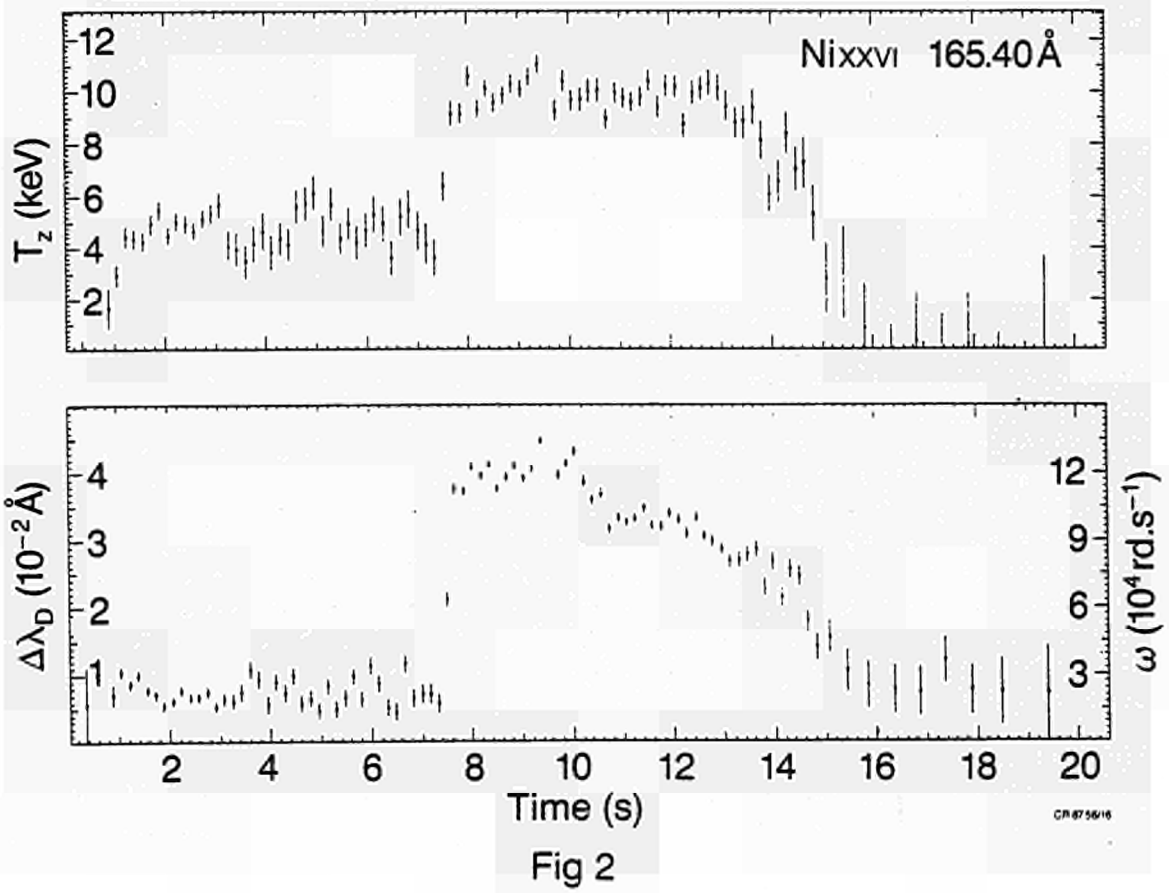
Nixxvi 165.40Å
T_z (keV)
$\Delta\lambda_D$ (10^{-2}Å)
ω (10^4rd.s^{-1})
Time (s)

Fig 2

[2] Behringer K, Denne B, W Griffin et al., JET Report (1987) "JET XUV Spectroscopy: Report of the first measurements during 1986 (second half) operations" (to be published)

[3] a) Peacock N J, Hughes M H, Summers H P et al., Proceed. 7th Int. Conf. on Plasma Physics and Controlled Nuclear Fusion Research, Innsbruck 1978, IAEA, Vienna 1, 303 (1979)
b) TFR Group, Doyle J G and Schwob J L J. Phys. B 15, 813(1982)

ACKNOWLEDGEMENT
The authors gratefully acknowledge the technical help given by A Ravestein and F Sieweke.

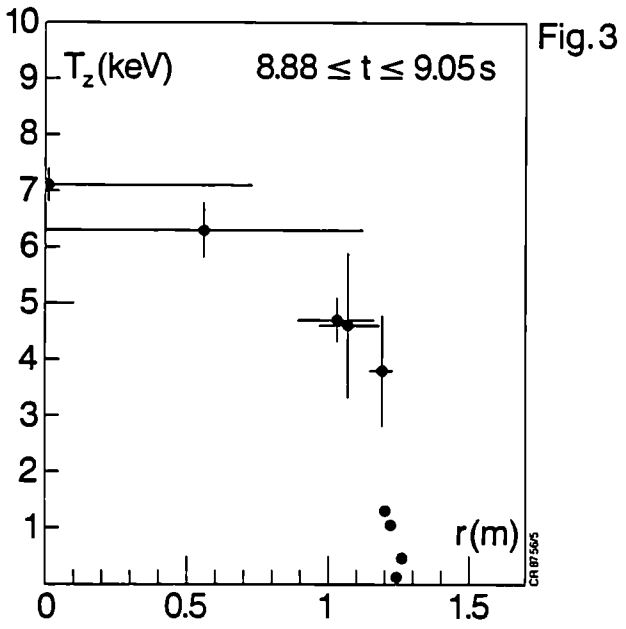

Fig.3

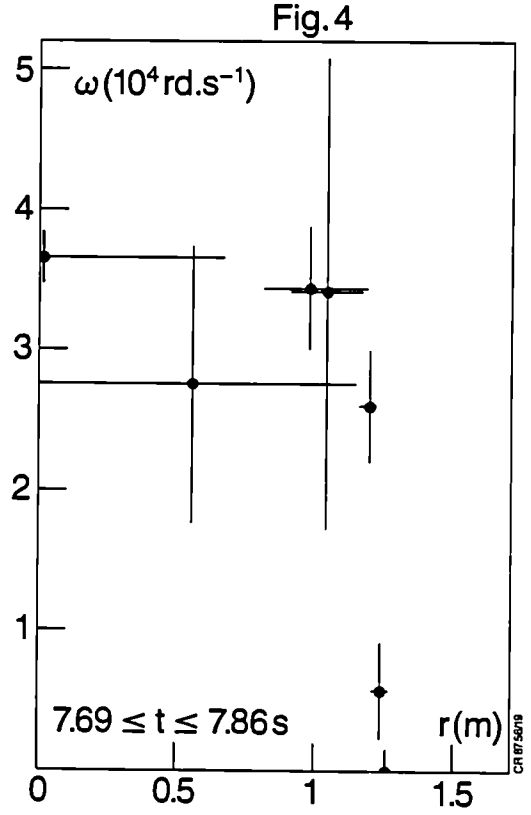

Fig.4

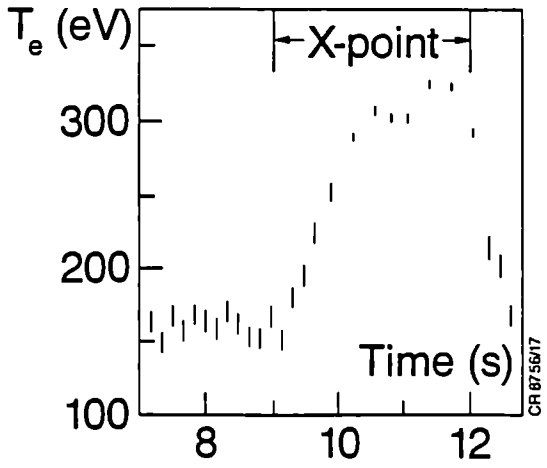

Fig.5

Fig.3 & 4: From left to right data points refer to Ni XXVII (from X-ray spectroscopy) Ni XXVI, Ni XXV, Ni XXIV, Ni XVIII, C VI, C V, C IV and He II (from XUV spectroscopy)

DENSITY PERTURBATIONS AT RATIONAL q–SURFACES FOLLOWING PELLET INJECTION IN JET

A. Weller[a], A. D. Cheetham, A. W. Edwards, R. D. Gill,
A. Gondhalekar, R. S. Granetz, J. Snipes, and J. Wesson
JET Joint Undertaking, Abingdon, Oxon OX14 3EA, United Kingdom

[a] *Permanent address : EURATOM-IPP Association, Garching, W. Germany*

Introduction – The ablation of pellets injected in JET [1] produces a pronounced resonance effect at rational q – values of 1 and 3/2. After ablation, $m = 1, n = 1$ and $m = 3, n = 2$ structures are observed as compact snake-like perturbations [2] by the soft x-ray cameras. The "snake" oscillation is caused by a rotating localised region of higher density, which can persist for $\geq 2\ s$. The observed effect can be used to measure the dynamic behaviour of the $q = 1$ and $q = 3/2$ surfaces. In particular, new information on the evolution of the q – profile during sawtooth collapses is obtained. The characteristics of these perturbations, their relationship to rational q – surfaces, and possible explanations for the existence of the "snake" are presented.

Observation of the snake oscillation – Two soft x-ray cameras[3,4] containing 100 detectors view the plasma with a spatial resolution of $\approx 7\ cm$ in orthogonal directions at the same toroidal position as the D_2 pellet injector. Pellets of 2.2×10^{21} or 4.5×10^{21} atoms are injected in the horizontal plane into ohmically heated JET plasmas ($2 \leq B_T(T) \leq 3$, $3 \leq I_p(MA) \leq 3.6$) with velocities of $\sim 1\ km/s$. Their penetration and ablation is deduced by observing the intense bremsstrahlung emission from interactions of plasma electrons with pellet particles, using the vertically mounted soft x-ray camera (fig. 1).

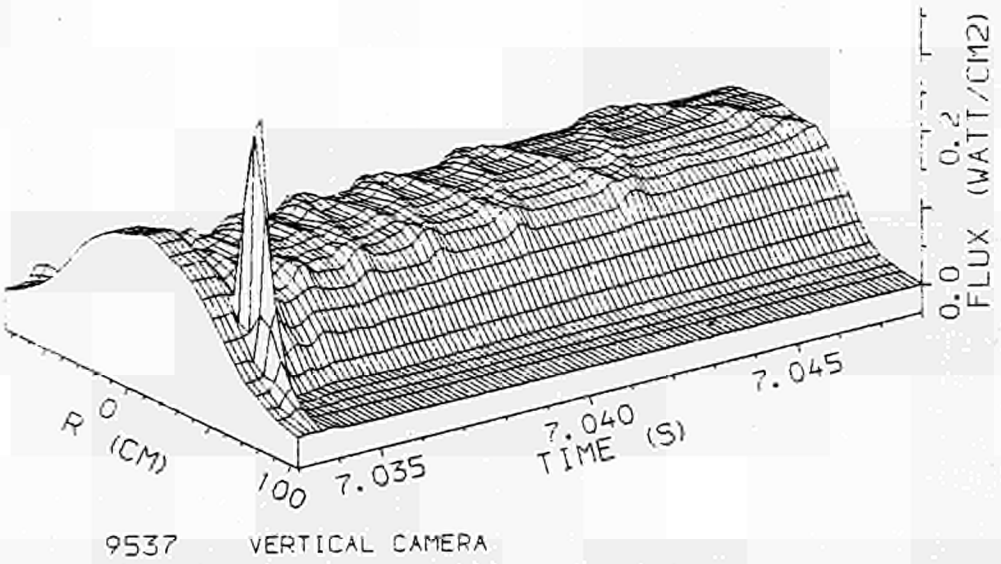

Fig. 1 : Soft X–ray flux (vertical camera, 140 μm Be – filter) around the time of pellet injection showing the initial peak from ablation and the subsequent "snake" oscillation.

Immediately after pellet ablation, the x-ray emission decreases due to the cooling of the plasma. The most striking remaining effect is the observation of a snake-like modulation superimposed on a

symmetric emission profile. The snake is caused by the rotation of a small region of plasma with usually enhanced x-ray emission. The dimensions of this region and its position in the plasma can be accurately determined both directly from the experimental data, and also by tomographic reconstruction techniques. A typical snake has dimensions of of ~ 15 *cm* (FWHM) in radial and of ~ 25 *cm* in poloidal direction.

Plasma parameters in the snake region – The temperature and density in the snake region are determined from an ECE polychrometer and a 2 *mm* microwave transmission interferometer (fig. 2).

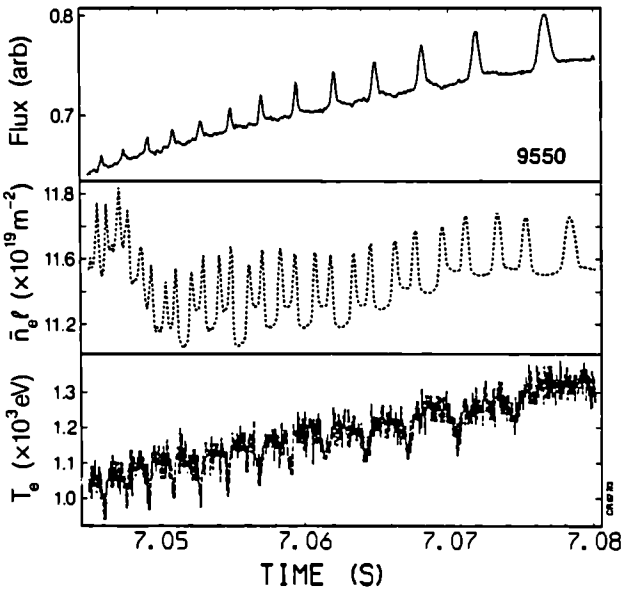

Fig. 2 : Correlation of soft X-ray signal (top, non central channel) with line density and T_e at the snake radius. Different signal phases are due to different measuring locations.

Large density perturbations $\delta n_e/n_e \leqslant 1$ are deduced from the line integral measurements of the density using the dimensions of the snake region. The corresponding temperature drop is smaller, indicating increased pressure in the snake region. The temperature perturbation reduces after ~ 100 *ms*, although the density perturbation remains unchanged.

The interferometer is displaced toroidally with respect to the x-ray cameras by 135° and the phase between the signals of the line density and the soft X-ray emission show that the snake has a topologically $m = 1, n = 1$ structure.

Relation to rational q-values – The snake oscillation seen in fig. 1 is clearly an effect associated with the $q = 1$ surface because of its $m = 1, n = 1$ topology and because its radial location coincides with the sawtooth inversion radius (derived from tomographically inverted signals). Moreover, at this same radius a characteristic dip in the D_α emission from the ablating pellet is seen. At the $q = 1$ radius the ablation rate is expected to drop, because only the plasma particles in a narrow flux tube, which intersects the ablating pellet, can contribute to the ablation.

Another observation is that the snake oscillation is more frequently seen, when the pellet is injected just before a sawtooth collapse. At this time the $q = 1$ radius has probably grown to its maximum value and the $q = 1$ surface is more easily accessible to the injected pellet, as shown later.

Occasionally, in addition to the snake at $q = 1$, a perturbation of higher symmetry is also seen. Analysis of the complicated soft X-ray signal patterns reveal a $m = 3, n = 2$ structure. A clear correlation with $m = 3$, $n = 2$ magnetic signals is also found, and the location of the perturbation coincides with the calculated position of $q = 3/2$.

Lifetime of the snake – The local density enhancement at $q = 1$ can persist for $\geq 2\ s$ without a significant decay or spreading during that time. This is even seen after several sawteeth which leave the structure unaffected. Fig. 3 shows the snake modulation during two 100 *ms* time intervals of the same discharge. Generally, the rotation slows down after some 100 *ms* and the snake is locked between sawtooth collapes (fig. 3 b, ~ 0.9 *s* after pellet ablation). During the sawtooth collapse a rotation is initiated for a short time.

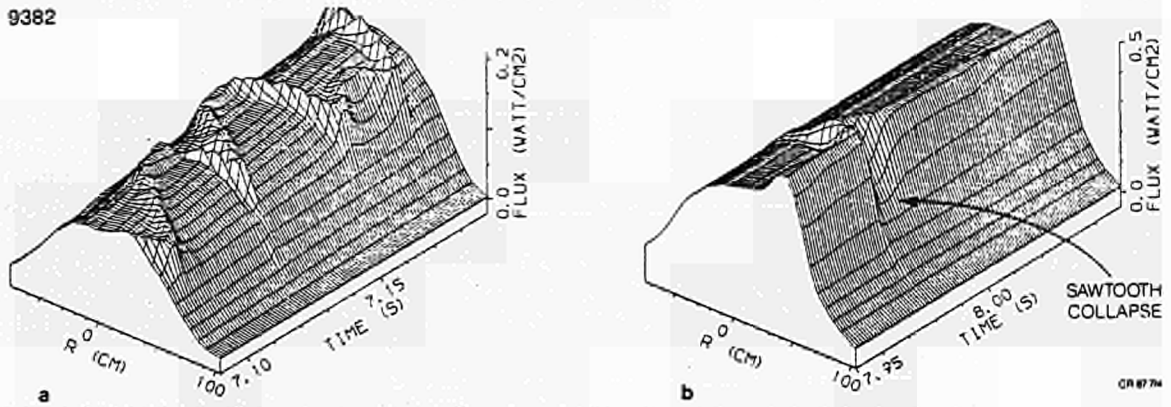

Fig. 3 : X – ray emission (vertical camera) showing a long lasting snake. In the later phase (b) the oscillation has locked. The sawtooth does not change the snake.

The long lifetime of the snake can be used to make a continuous determination of the position of $q = 1$. In particular, a large rapid inward shift of the $q = 1$ radius is seen during the sawtooth collapse phase followed by a slow expansion of the $q = 1$ surface after the collapse (fig. 4).

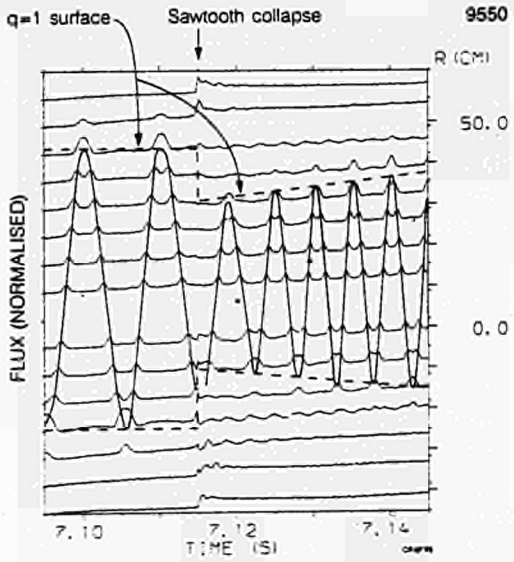

Fig. 4 : X – ray signals during a sawtooth crash, which shows the inward shift of $q = 1$ derived from the snake oscillation.

Discussion – In the case of an axisymmetric equilibrium, perturbations of temperature δT and density δn are expected to spread out poloidally by collisional diffusion along the magnetic field lines. Around $q = 1$, the spreading times scale like :

$$t_{spread} \sim \frac{1}{(1-q)^2}$$

Given the plasma parameters in the "snake" region, these values are found to be

$$t_{spread} \sim 100\ \mu s \text{ for } \delta T \quad \text{and} \quad t_{spread} \sim 10\ ms \text{ for } \delta n$$

These are times for the perturbations to fall below a 10 % level outside a very narrow region with $|\ 1-q\ | < 10^{-2}$.

The observed long persistence of the density perturbation therefore implies the *formation of a magnetic island* at $q = 1$ due to the local cooling and the associated current perturbation along a helical flux tube. We estimate that a magnetic island of several centimeters width would grow within a time of $\sim 100\ \mu s$ due to the initial temperature perturbation $\delta T/T \geq 0.2$. During this time ablated particles are continuously deposited at $q = 1$, which later are confined effectively in the island.

The *persistence* of the particles in the magnetic island, however, is difficult to understand. First, neoclassical (banana diffusion regime) particle confinement times in the snake region are only $\sim 0.3\ s$; and second, the toroidal precession of trapped particles would lead to drift of the particles out of the snake region on a time scale of only $\sim 15\ ms$. A plausible explanation for the persistence of the snake may then be given in terms of a new non-axisymmetric stationary equilibrium, which has been accessed by the pellet injection. The higher density in the snake region could be maintained by inward convection, in a similar but not understood manner to the inward convection of particles in the bulk of the tokamak plasma.

Another observation is that the temperature perturbations become very small after $\sim 100\ ms$. However, calculations show, that an *island* with the dimensions of the snake can be *maintained* by $\delta T/T \approx 10^{-2} - 10^{-1}$, which is too small to be detected. The required current perturbation could also be produced by a local change of Z_{eff} due to the electric potential associated with the locally enhanced deuteron pressure.

The observed effect gives information about the q – *profile* : First, the radial position of $q = 1$ (and $q = 3/2$) are derived, and secondly estimates of the central q value can be made from the radial shift of $q = 1$ during a sawtooth collapse. Because the change in q caused by sawteeth in JET is $\Delta q \sim 0.02$ only[5] , a smooth q – profile has to be very flat inside $q = 1$ with $q(0) \sim 0.97$ before the sawtooth crash in order to produce the large observed shift of $r_{q=1}$ ($\Delta r_{q=1}/r_{q=1} = -1/3$, fig. 4). For the discussion of sawtooth models it is also important to note, that $q = 1$ exists throughout the sawtooth cycle, and that a sawtooth collapse does not seem to cause a large rearrangement of the magnetic topology (eg. complete reconnection at $q = 1$).

References

[1] A. Gondhalekar et al., Proc. 11th Int. Conf. on Plasma Phys. and Contr. Nucl. Fusion Research, Kyoto, IAEA-CN-47/I-I-6, (1986)

[2] A. Weller et al., submitted to Phys. Rev. Lett.

[3] A.W. Edwards et al., Rev. Sci. Instrum. 57 (8), 2142 (1986)

[4] A.W. Edwards et al., Phys. Rev. Lett. 57 (2), 210 (1986)

[5] D.J. Campbell et al., Proc. 11th Int. Conf. on Plasma Phys. and Contr. Nucl. Fusion Research, Kyoto, IAEA-CN-47/A-VII-5, (1986)

[6] J.A. Wesson et al., Proc. 11th Int. Conf. on Plasma Phys. and Contr. Nucl. Fusion Research, Kyoto, IAEA-CN-47/E-I-1-1, (1986)

STUDY OF MHD PHENOMENA IN JET WITH SMALL-SIGNAL X-RAY IMAGING

R. S. Granetz[a], A. W. Edwards, R. D. Gill, A. Weller[b]
JET Joint Undertaking, Abingdon, Oxfordshire, UK, OX14 3EA

[a] *Permanent address: MIT, Cambridge, MA, USA*
[b] *Permanent address: IPP, Garching, West Germany*

Introduction

Many of the interesting MHD phenomena observed with the JET soft X-ray imaging arrays are characterised by relatively small (a few percent or less) oscillations and/or transients in the chord-integrated signals. After the 2-dimensional local emissivity is reconstructed using tomography, useful information about the MHD perturbations is contained in the images, but it is nearly totally obscured by the much greater background equilibrium emission. Therefore in order to extract detailed knowledge of the size, structure, and growth of these instabilities, we have applied several image enhancement and analysis techniques. Our findings, as well as the imaging methods, are described in this paper.

$m = 2$ Disruption Precursor

Density-limit disruptions in JET are always preceded by a growing $m = 2$ oscillation as seen in Fig. 1. As the amplitude grows, the rotation frequency gradually decreases until the mode locks, usually a few tens of milliseconds before the first of several disruptions. The absolute amplitudes of the $m = 2$ oscillations displayed in Fig. 1 are quite small—no more than ~2% of the central chord signal, and they are difficult to discern after tomographic reconstruction. Fig. 2a shows the emissivity at $t = 8.5482$ sec (indicated by the arrow in Fig. 1). In order to enhance the MHD perturbation a 'baseline' image is subtracted from it. This 'baseline' image is the average of all the reconstructed images occurring during the time span in-

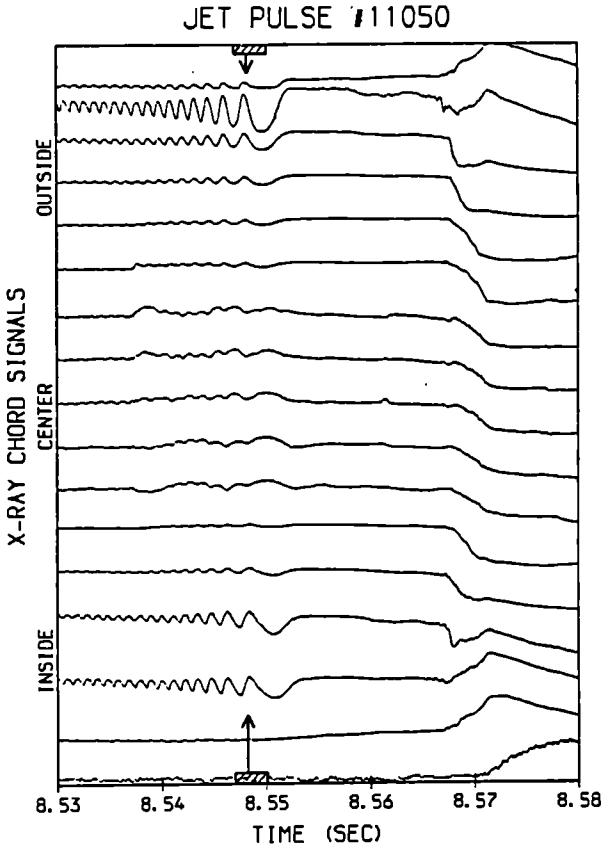

Fig. 1—Signals from a few of the detectors in the vertical X-ray array during a typical JET disruption. Growing oscillations are visible on the inner and outer chords prior to the first disruption at $t \simeq 8.57$ sec. Note: relative amplitudes are not to scale.

dicated by the hashed bars in Fig. 1. Since this corresponds very closely to one complete oscillation, the 'baseline' image. represents the unperturbed background emission. Subtracting it from the image at the indicated time yields the 2–d structure of the perturbed emission shown in Fig. 2b.

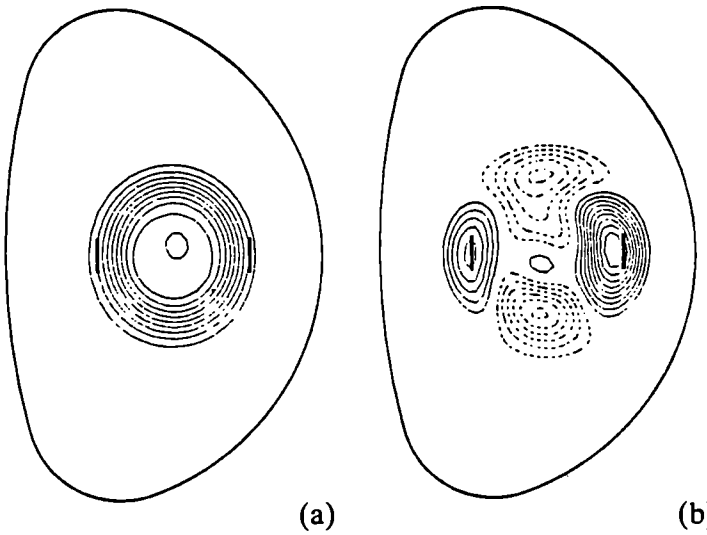

Fig. 2—Tomographic reconstruction during the $m = 2$ disruption precursor. The calculated $q = 2$ radii on the midplane are also shown.
(a) Actual image. Maximum emission is 2700 W/m^3.
(b) After subtraction of 'baseline' image. Maximum is 90 W/m^3. Dashed contours represent negative emissivity. The size of any possible magnetic island cannot be deduced from this plot.

In most cases there is also simultaneously an $m = 1$ perturbation near the plasma center. The peak amplitude of the $m = 2$ structure in Fig. 2b is located near the calculated $q = 2$ radius and is equal to just 3% of the central emission.

Because tomography using a relatively small number of chords can be prone to error, one should initially be cautious when looking at such low amplitude features. We have verified our results in this study by utilising the fact that the tomography transformation is linear. If $\mathcal{F}(\mathbf{s}_1)$ represents the tomographic inversion operator applied to the set of X–ray chord signals measured at time t_1, then ideally: $\mathcal{F}(\mathbf{s}_2 - \mathbf{s}_1) = \mathcal{F}(\mathbf{s}_2) - \mathcal{F}(\mathbf{s}_1)$. In other words, if one first subtracts 'baseline' raw chord signals from the chord signals at the time of interest, and then directly reconstructs just this difference of signals, the resulting image should be identical to Fig. 2b. In practice, however, this will only be true if the numerical algorithm used to implement the inversion operator, $\mathcal{F}$, is sufficiently accurate, and if the signal-to-noise ratio is good. For this particular example the two methods give virtually identical results, thus verifying the credibility of the analysis.

Although the $m = 2$ structure in Fig. 2b covers a large radial extent of more than 50 cm and is not localised on the $q = 2$ surface, the perturbation of the mhd fluid (and therefore the size of any underlying perturbation such as a magnetic island) is very much smaller and may be calculated as follows. If it is assumed that the local X–ray emissivity is carried along with the moving fluid, then the displacement vector $\xi(R,Z)$ can be calculated from the reconstructed X–ray images $X(R,Z)$. To first order, $\Delta X \approx -\xi \cdot \nabla X$ and therefore on the horizontal midplane $\xi_R \approx -\Delta X(R)/X'(R)$. Obviously even a very small fluid displacement occurring in a region of large X–ray gradient can give rise to measurable perturbations. This is indeed what we find, as shown in Fig. 3. The spatial displacement due to the $m = 2$

instability just before locking is typically only a few centimeters. Inside the $q = 2$ radius this result agrees well with magnetic island calculations using data from the $\dot{B}_\theta$ loops[1], but the phase reversal expected outside of the $q = 2$ surface has not been observed yet in the reconstructed X–ray images. This may be due to lack of X–ray signal from beyond the $q = 2$ region, insufficient radial resolution, or higher m–modes in the plasma edge which cannot be distinguished by the two-array system. Or perhaps the magnetic island model is not the correct explanation of the $m = 2$ instability.

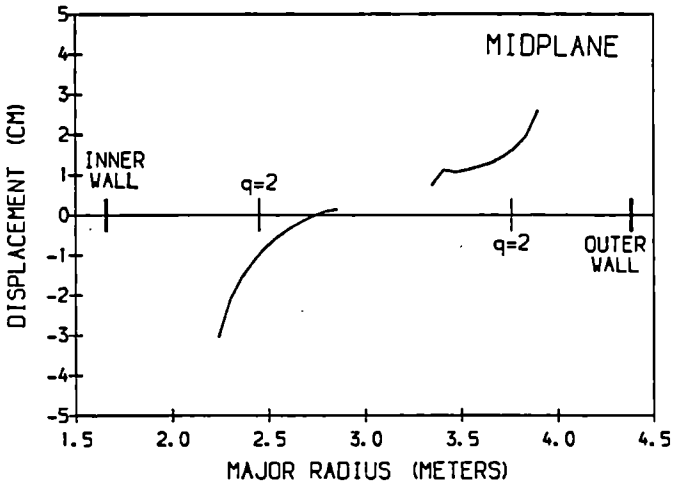

Fig. 3—Radial displacement on the horizontal midplane due to the $m = 2$ mode. The emissivity is too low in the edge regions to calculate ξ_R reliably.

Sawtooth Inversion Radius

The technique of image subtraction can also be used to study a host of other MHD phenomena such as the eigenfunction of the instability responsible for the sawtooth crash, the structure of the $m = 1$ precursor oscillations, and differences between partial and full sawteeth. Due to space limitations these cannot be discussed in this paper but will be presented in the poster. On a slower timescale (~5 msec) the method can accurately give the location of the sawtooth inversion radius, which presumably is an indicator of the $q = 1$ surface. A reconstruction is done a few milliseconds after a sawtooth crash and then subtracted from a similar reconstruction done a few milliseconds before the crash. The locus of all zero-valued points defines the 2–d inversion surface. In the past this radius has been approximated by visual examination of the raw chord-integrated signals. In practice we find that this leads to an unacceptable value (>30% too small) for the actual inversion radius. Knowledge of the $q = 1$ surface has helped in our understanding of the 'snake'[2] perturbation seen immediately after pellet injection. After confirming the $m = 1/n = 1$ structure, we hypothesised that the 'snake' was a resonant phenomenon on the $q = 1$ surface. This was substantiated by comparing the location of the 'snake' with the inversion surface of the sawtooth immediately prior to pellet injection, and showing that the two coincide, as seen in Fig. 4. Analysis of 'snakes' occurring in plasmas having different q_ψ (and therefore different $q = 1$ radii) confirm the hypothesis.

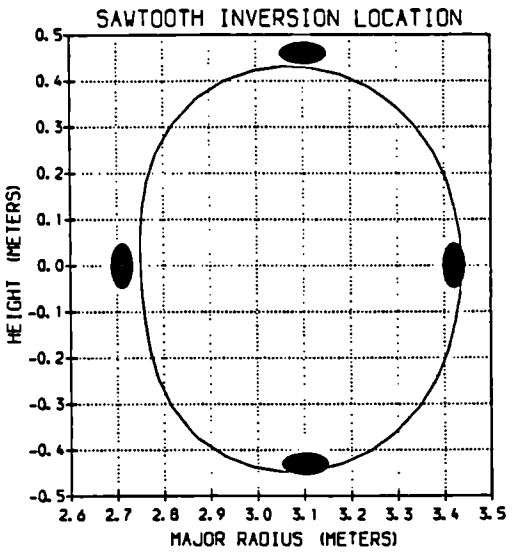

Fig. 4—Comparison of sawtooth X-ray inversion surface with the 'snake' location. The large black dots indicate the position of the 'snake' at four times during its oscillation cycle.

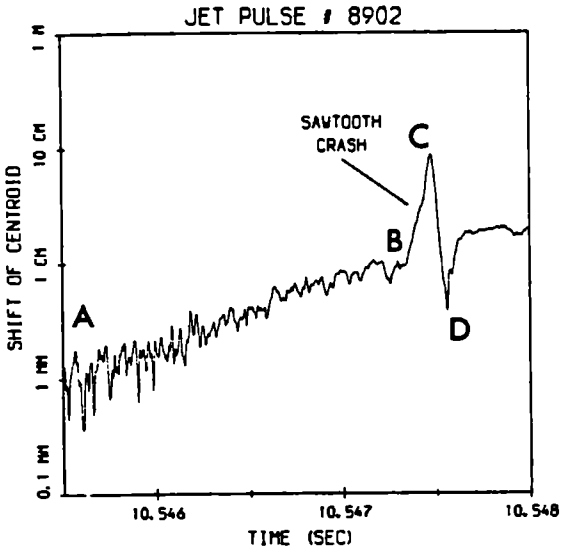

Fig. 5—Logarithmic plot of the shift in X-ray centroid versus time during a sawtooth crash. The noise level is of order $O(0.5$ mm). The shift is measured relative to the time-averaged centroid location ~3 msec before the crash.

Sawtooth Instability Growth Rate

The last topic discussed concerns the sudden growth of the instability responsible for the sawtooth crash observed in JET. It has been proposed[3] that linear ideal MHD theory may explain the fast collapse time, as long as the q-profile is quite flat and near unity in the central core of the plasma. Of course, in a linear theory the growth rate, γ, is constant in time, and therefore the eigenfunction amplitude should increase exponentially. This predicted behavior can be sensitively tested for experimentally by calculating the centroid of the tomographically reconstructed X-ray emission versus time and plotting the magnitude of its shift from the plasma center on a logarithmic scale. In principle, one should see just a single straight line rising out of the noise level, with a slope equal to γ. In Fig. 5 the centroid shift is shown for a sawtooth with a growing precursor oscillation from A to B, followed by the rapid displacement phase from B to C and the re-arrangement to a final symmetric state from C to D (the last two phases are described in detail in Ref.4). It can be seen that the the precursor and rapid collapse phases cannot be described by a single growth rate and it follows that the overall behaviour cannot be explained by a linear theory. We therefore still do not understand the sawtooth 'trigger' mechanism and, in addition, the relationship between the $m = 1$ precursor and the sawtooth crash, if any, is also unclear.

References

[1] J.A. Snipes et al, Proc. 13th Europ. Conf. on Controlled Fusion and Plasma Heating, Schliersee, 1985, Part I, 152–155.
[2] A. Weller et al, to be published.
[3] J.A. Wesson et al, 11th Int. Conf. Plasma Phys. and Contr. Nucl. Fus. Res., Kyoto, 1986, IAEA-CN-47/E-I-1-1.
[4] A.W. Edwards et al, Phys.Rev.Lett. 57(1986)210.

MEASUREMENT AND SIMULATION OF SLOWING DOWN SPECTRA OF FAST IONS DURING NEUTRAL BEAM INJECTION IN JET

S Corti, G Bracco+, W Core, A Giannelli+, V Zanza+

JET Joint Undertaking, Abingdon, OX14 3EA, UK
+ ENEA-Euratom Association, Frascati, Italy

Introduction

An array of four passive neutral particle analysers (NPA) looking at different poloidal angles (Fig.1) has been used for the measurement of neutral spectra, of both H and D simultaneously, during NBI in JET. The beam system has been operated up to 80 KeV for co- and counter-injection, and neutral spectra have been obtained up to 100 KeV with the analysers line-of-sight set at different toroidal angles.

The NPA simulation code /1,2/ has been extended to include the energy distribution of slowing down fast ions obtained as an analytical solution of the Fokker-Planck equation /3/.

The geometry of both the injected beams and the NPA detectors is shown for two extreme cases: in the polar diagram of Fig.2 the case of co-injection with quasi-perpendicular toroidal viewline of the analysers is shown; the case of counter-injection with the analysers in the most tangential location is shown in Fig.3. The polar angle on these diagrams represents the pitch-angle while the radial coordinate is the distance between the magnetic surface intersected by a beam (or by a NPA) viewline and the magnetic axis, as measured on the equatorial plane of the torus. The computation of the pitch-angle has been performed taking into account the real plasma geometry obtained with an equilibrium code /4/ and includes the effect of the plasma current. It can be seen that in the case of counter-injection the NPA and injectors pitch-angles are in closer alignment than in the co-injection case.

The Model

The measured neutral flux at energy E is computed as

$$\phi(E) = \int_0^{\ell} n_0[n_i(E)+n_b(E)]\langle\sigma v\rangle_{cx}\, e^{-\int_0^{\ell} d\ell'/\lambda}\, d\ell \qquad (1)$$

where n_0 is the neutral density, $n_i(E)$ is the bulk ion maxwellian distribution function, $n_b(E)$ is the distribution function of the slowing down beam ions, $\langle\sigma v\rangle_{cx}$ is the charge exchange reaction rate and λ is the neutrals mean-free-path. The quantity $n_b(E)$ has been computed using the analytical solution /3/ of the Fokker-Planck equation, which for energies smaller than the injection energy E_0 is:

$$n_b(E) = \frac{S\,\tau_{s\ell}\sqrt{E}}{2(E^{3/2}+E_c^{3/2})} \sum_{J=0} \left(\frac{E_0^{3/2}+E_c^{3/2}}{E^{3/2}+E_c^{3/2}}\right)^{\frac{\rho\,J(J+1)+d}{3}} \cdot \left(\frac{E}{E_0}\right)^{\frac{\rho\,J(J+1)}{2}} \cdot K_J P_J(\mu) \qquad (2)$$

where: $\rho = m_i Z/(2\, m_b)$; $d=[3+(m_b/m_i)^{3/2}\, E_c^{3/2}\, T_i\, E^{-5/2}]$; E_c is the critical energy, $\tau_{s\ell}$ is the electron slowing down time, S the beam ion deposition rate, $Z=Z_{eff}$, m_i and m_b the ion masses of the plasma and the beam respectively and $P_J(\mu)$ is the Legendre polynomial of order J. The angular shape of the source function is given through its Legendre coefficient K_J.

In order to have a good angular description of the distribution function, considering that the beam angular spread is very small (<1°), a large number of Legendre polynomials has to be used to define the solution and is unsatisfactory. In order to avoid this difficulty the following expression for the angular dependence of the slowing down distribution function has been used:

$$f(\mu,E) = \frac{1}{\sqrt{\pi}\ \sigma}\, e^{-\left(\frac{\mu-\mu_o}{\sigma}\right)^2} \qquad (3)$$

where $\sigma^2 =$

$$\begin{cases} \dfrac{Z}{m_b}\, \ell n\, \left(\dfrac{1+(E_c/E)^{3/2}}{1+(E_c/E_o)^{3/2}}\right) & \text{for } E<E_o \\ \dfrac{Z}{m_b}\, \ell n\, \left(\dfrac{1+(E_c/E_o)^{3/2}}{1+(E_c/E)^{3/2}}\right) & \text{for } E>E_o \end{cases}$$

and μ_o is the source pitch-angle. This expression is an approximated solution of the Fokker-Planck equation down to the energy

$$E_{lim} = E_c \Big/ \left\{ \left[1+(E_c/E_o)^{3/2}\right] \cdot \exp\, \left[\frac{m_b}{Z}\, \left(\frac{1-|\mu_o|}{2}\right)^2\right] - 1 \right\}^{2/3} .$$

The matching between solutions (2) and (3) is obtained using $F(\mu,E_{lim})$ as the source function to be developed in Legendre polynomials and to be used in eq.(2).

For energies $E>E_o$ the solution given in /3/ decreases with an e-folding length E_D:

$$E_D = \left(E_o^{3/2}\, T_e + E_c^{3/2}\, T_i\right) / \left(E_o^{3/2} + E_c^{3/2}\right) \quad . \qquad (4)$$

Equations (1), (2), (3) and (4) have been included in the NPA code and used in the present simulation.

Results

Two simulations are presented for the two cases whose geometry is shown in Figs.2 and 3, ie co- and counter-injection of D beams into D plasma at beam energies of 62 and 75 KeV respectively. The results are shown in Figs.4 and 5.

In both cases H and D spectra have been measured, the H coming from the walls as 3% of the total D density.

From the maxwellian H spectra the ion temperature profile is obtained using eq.(1), with $n_b=0$, in a fitting procedure /2/. The neutral density profile is also computed with a 1-D cylindrical code similar to the one described in /5/. The edge neutral density has been assumed different for different analysers to allow for a certain poloidal asymmetry.

Using the ion temperature and neutral density profiles thus obtained, the D spectra due both to the bulk and the slowing down distributions are then evaluated.

In both cases the agreement between the computed spectra and the experimental data is rather good, especially if the fact that no free parameters are used in the procedure is taken into account.

The counter-injection case (Fig.5), where the beams and the analysers have practically the same pitch-angle (Fig.3) is somewhat critical as much of the slowing down neutral flux is coming from the very edge of the plasma where all main plasma parameters are rapidly varying. Nevertheless the computed results reproduce well the qualitative different D spectra obtained in this case.

We can then conclude that the slowing down spectra of injected deuteron can be reproduced in JET by the solution of the classical Fokker-Planck equation.

Moreover, the spectra at $E>E_o$ are also well reproduced (Fig.4). Since this part of the spectra depends essentially on both T_e and T_i [eq.(4)], the fact that they are reproduced in the present model is showing a good consistency between T_e and T_i measured values.

References

/1/ G Bracco et al - 'First results from JET-NPA' - JET-IR(84)04 - 1984

/2/ S Corti et al - 13th Europ. Conf. on Controlled Fusion and Plasma Heating, Schliersee, 14-18 April 1986, 1, 109

/3/ J Cordey, W Core - Phys. of Fluids, 17, 8, (1974)

/4/ M Brusati et al - Computer Physics Reports 1, 7/8, 345, (1984)

/5/ S Tamor - J. of Comput. Physics, 40, 104, (1981)

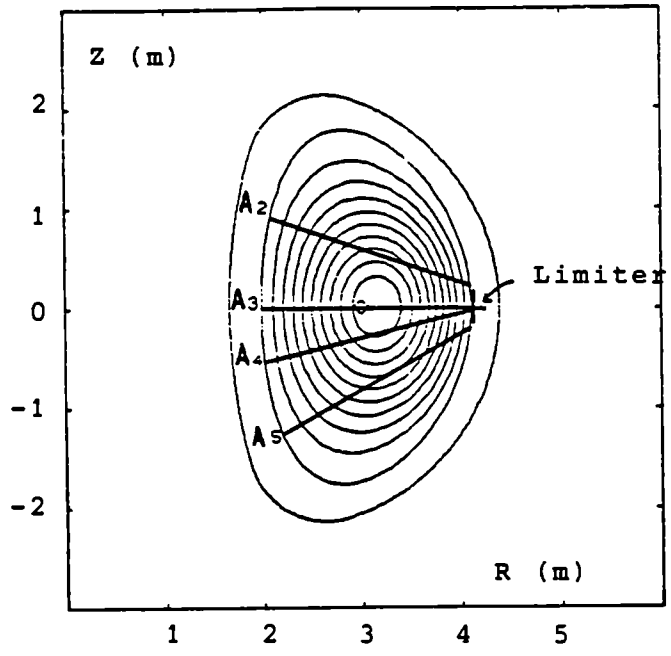

FIGURE 1
Poloidal lines of sight of the four analysers used in JET for the measurement of the slowing down spectra

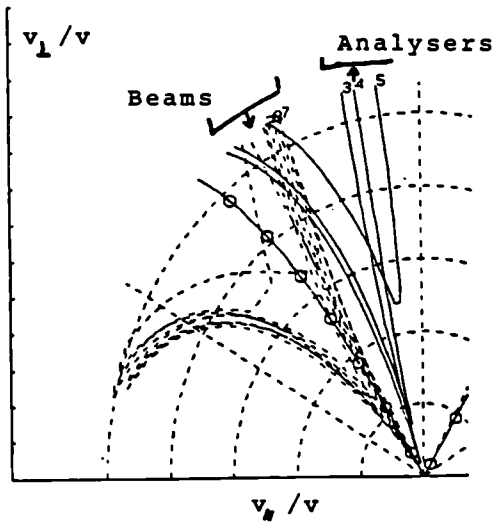

FIGURE 2 - Pitch-angles of Beams (dashed lines) and Analysers for co-injection with analysers quasi-perpendicular.

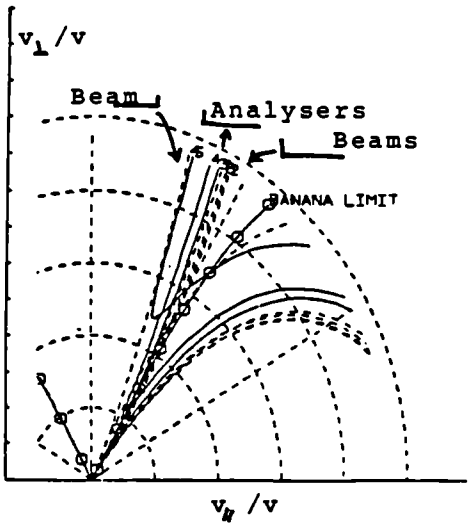

FIGURE 3 - Pitch-angles of Beams (dashed lines) and Analysers for counter-injection with analysers in most tangential location.

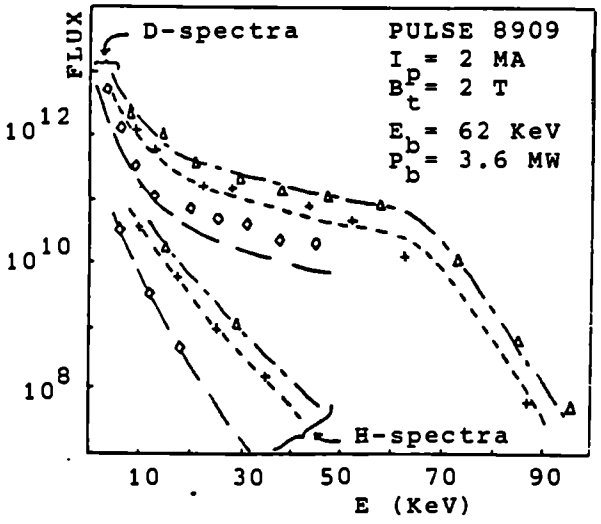

FIGURE 4 - Measured and simulated H- and D-spectra in the case of Fig. 2 (- —Δ- — an. 3 ; --- + --- an. 4 ; —— ◇ —— an. 5)

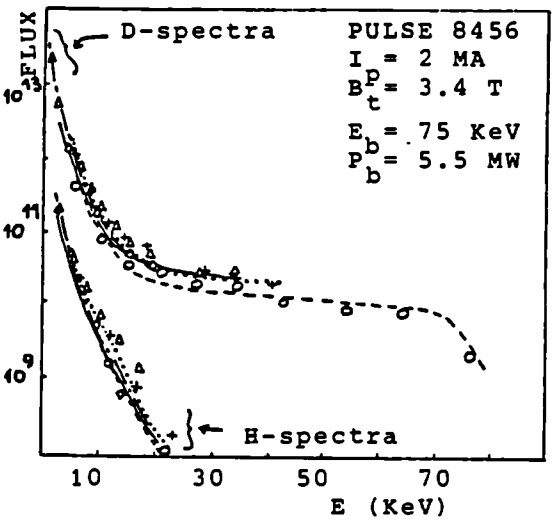

FIGURE 5> - Measured and simulated spectra in case of Fig.3 (--- o ---an. 2;- — Δ- —an. 3; ..... + ...an. 4;—— ◇ ——an. 5)

IMPURITY BEHAVIOUR IN X-POINT PLASMAS ON JET

B Denne, K Behringer, A Boileau, G Fussmann+, M v Hellermann, L Horton, J Ramette*, B Saoutic*, M F Stamp and G Tallents

JET Joint Undertaking, Abingdon, OX14 3EA, UK
+ IPP-Garching, D-8046, FRG
* EURATOM-CEA Association, CEN Cadarache, France

INTRODUCTION

The magnetic separatrix (X-point) configuration has been successfully established in JET /1/. Spectroscopic diagnostics (XUV, VUV, visible and Charge Exchange Recombination Spectroscopy (CXRS)) have been used for studying impurity behaviour in these discharges.

The main impurities in JET plasmas are carbon (from carbon limiters and protection plates) and oxygen. Metals (nickel and chromium from Inconel walls and antenna screens) generally contribute little to Z_{eff} and radiated power. Typical impurity concentrations (in % of the electron density, n_e) are /2/: 2-4% C, ≈1% O, and 0.02%, or less, metals. During the period in which most of the X-point operation was carried out, the oxygen concentration in the plasma was, however, somewhat higher (≈2%) due to occasional leaks.

X-POINT PLASMAS WITH OHMIC HEATING

During ohmic X-point operation, the carbon concentration was observed to be only 1-2% n_e, a reduction compared to similar limiter discharges, implying that less carbon was produced at the X-point graphite target plates than at the limiters. Metal concentrations were reduced, too, although the plates were most likely covered by wall material. During previous operation with Inconel target plates no increase was observed in metal concentrations in the plasma when changing from carbon inner-wall to X-point operation. These observations indicate a low plasma temperature (≈20 eV) in front of the plates, resulting in a low sputtering yield. The oxygen concentration, oxygen most likely originating from the vessel walls, was 1-2% n_e, similar to limiter plasmas for the same plasma conditions. As a result, for given $\bar{n}_e$, Z_{eff} was somewhat lower in X-point as compared to limiter plasmas (see Fig.1). The total power radiated, P_{rad}, was ≈40% of the input power at the lowest electron densities, increasing with n_e and approaching 100% at $\bar{n}_e$ ≈ 2×10^{19} m^{-3}. This includes the power radiated from the X-point region which was 30-40% of the total power radiated in all cases.

ADDITIONAL HEATING (L-MODE)

During additional heating a modest increase in n_e was observed. With Neutral Beam Injection (NBI) both carbon and metal concentrations were higher than in the ohmic case, which is consistent with an observed increase in the edge electron temperature, although the metals might also have originated from CX sputtering. The C/O ratio increased during NBI, in contrast to what was observed in limiter plasmas, where oxygen was the dominant impurity during NBI at high $\bar{n}_e$. Somewhat higher Z_{eff}-values were found in X-point plasmas with additional heating - the general

falling trend with increasing n_e, observed in ohmic cases, being maintained. During Ion Cyclotron Resonance Heating (ICRH) and combined heating, increased levels of screen material (Ni and Cr) were found in the plasma as in the limiter cases /2/. The total power radiated from the bulk of the plasma was typically ~25% of the total input power.

H-MODE

During H-mode, n_e increased steeply (Fig.2). The electron density profile was quite flat. Langmuir-probe data /3/ showed that n_e in the scrape-off layer was approximately constant throughout the duration of the H-mode despite ~3x increase in bulk density. The electron temperature profile became broader and the edge temperature was high (a few 100 eV). Radiation emitted from peripheral carbon and oxygen ions (C III - C V and O IV - O VII lines) was essentially unchanged (or even decreased) after the L→H transition, whereas C VI and O VIII radiation, emitted from radial locations further in, increased, reflecting the increasing bulk electron density. The behaviour of the lowly-ionised C and O is consistent with the observed change in edge parameters, and results in less total radiation per ion for these light impurities. After the H-mode was established, the total power radiated from the bulk plasma increased approximately as $\bar{n}_e^2$ /4/, except when ICRF was applied, in which case it increased more steeply due to some metal contribution. Eventually the radiation losses lead to the termination of the H-mode. No ASDEX-type edge-localised-modes (ELM's) (see e.g./5/) were observed, probably because of the high radiation levels.

The bulk particle confinement increased by a factor ~3 /6/ in the L→H transition. The impurity confinement increased similarly. For carbon the improved confinement can be seen in Fig.2: the carbon concentration is essentially constant, or increases slightly in the H-mode, although the carbon influx (represented by the C III-line brightness) remains unchanged with respect to the hydrogen flux, ϕ_H (carbon production yield $\phi_C/\phi_H \approx 5\%$). Towards the end of the H-mode the impurity confinement deteriorated as τ_E (deduced from the decay of the nickel concentration). There is no indication of impurity accumulation in the neoclassical sense. Analysis of several metal ionisation stages as well as the soft X-ray emission profiles and bolometer profiles show that the metal density profile is not peaked. The absence of impurity accumulation might be explained by the presence of sawteeth in the H-mode discharges.

The bolometer profiles are hollow with a broad radiating shell /4/. Transport code modelling for carbon and oxygen reproduces the measured peak radiated power, but the measured radiating shell extends further in radially than predicted by the code. This discrepancy is presently not understood.

During the H-mode, Z_{eff} did not decrease as normal at high $\bar{n}_e$ (see Fig.1), but remained similar to the lower-$\bar{n}_e$ values of 3-4. The high Z_{eff} values could be accounted for by the measured central concentrations of light impurities. The C/O ratio during H-mode was 1-2:1. An observed increase in metal density can be explained either by sputtering by CX neutrals or by the increased edge temperature. The metal concentration is rather independent of n_e for H-mode plasmas which contrasts with the falling trend with increasing $\bar{n}_e$ seen in all other types of discharges.

However, the metal concentration is still low: its contribution to Z_{eff} is ≤ 0.2, and $\leq 10\%$ of P_{rad} is due to metals according to transport code calculations. For the discharge shown in Fig.2, e.g., the metal concentration at the end of the H-mode was 0.002%.

SUMMARY AND CONCLUSIONS

In ohmic X-point plasmas Z_{eff} is reduced somewhat compared to similar limiter discharges as a result of lower carbon and metal concentrations. This indicates a low plasma temperature in front of the neutraliser plates.

In additionally heated, L-mode, X-point plasmas, carbon and metal concentrations are higher, consistent with the observed increase in edge temperature. ICRH and combined heating results in higher levels of screen material (Ni and Cr) in the plasma like in the limiter cases.

During H-mode, particle confinement improves by a factor of ~3; impurity confinement improves similarly. No impurity accumulation, in the neoclassical sense, has been observed.

During H-mode, Z_{eff} does not decrease as normal with higher $\bar{n}_e$, but remains at values of 3-4, typical of lower-$\bar{n}_e$ plasmas. Measured carbon and oxygen concentrations (from CXRS) can account for the measured bulk radiated power and Z_{eff}, metals contributing only little.

No ASDEX-type ELM's have been observed. ELM's could allow control of the plasma density and impurity contamination. It might be possible to achieve longer H-modes in JET by reducing the impurity content of the plasma, in order to obtain ELM's, or to provide some efficient density pumping mechanism.

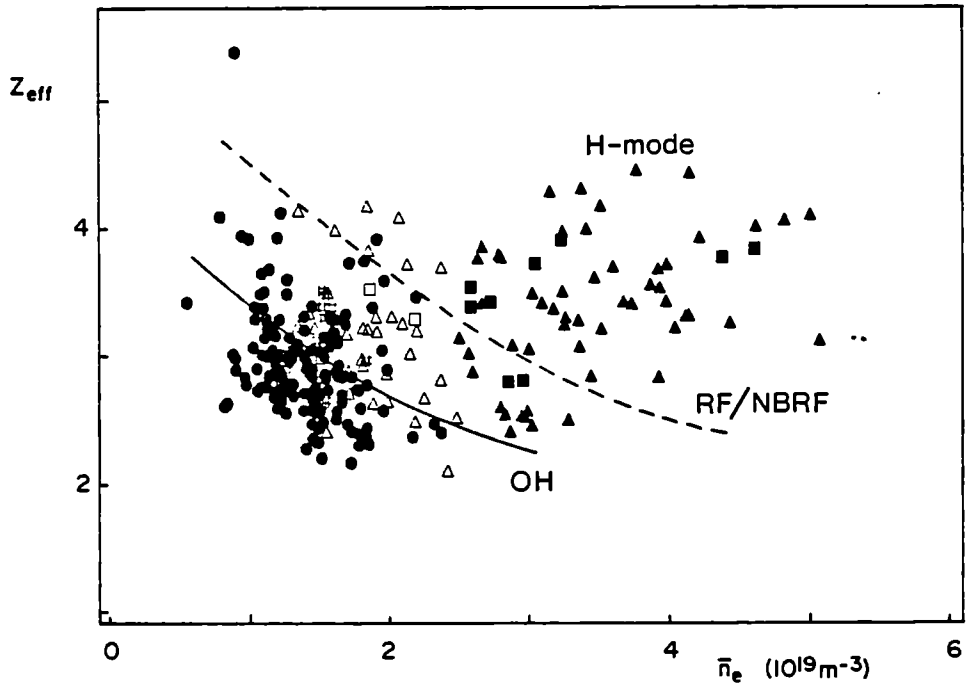

FIG.1 Z_{eff} vs $\bar{n}_e$ for X-point plasmas with ohmic heating (●), NB-heating (Δ) and combined heating (□) (filled symbols denoting H-mode). For comparison the typical behaviour of limiter plasmas with ohmic heating (——) and with RF/combined heating (----) are shown.

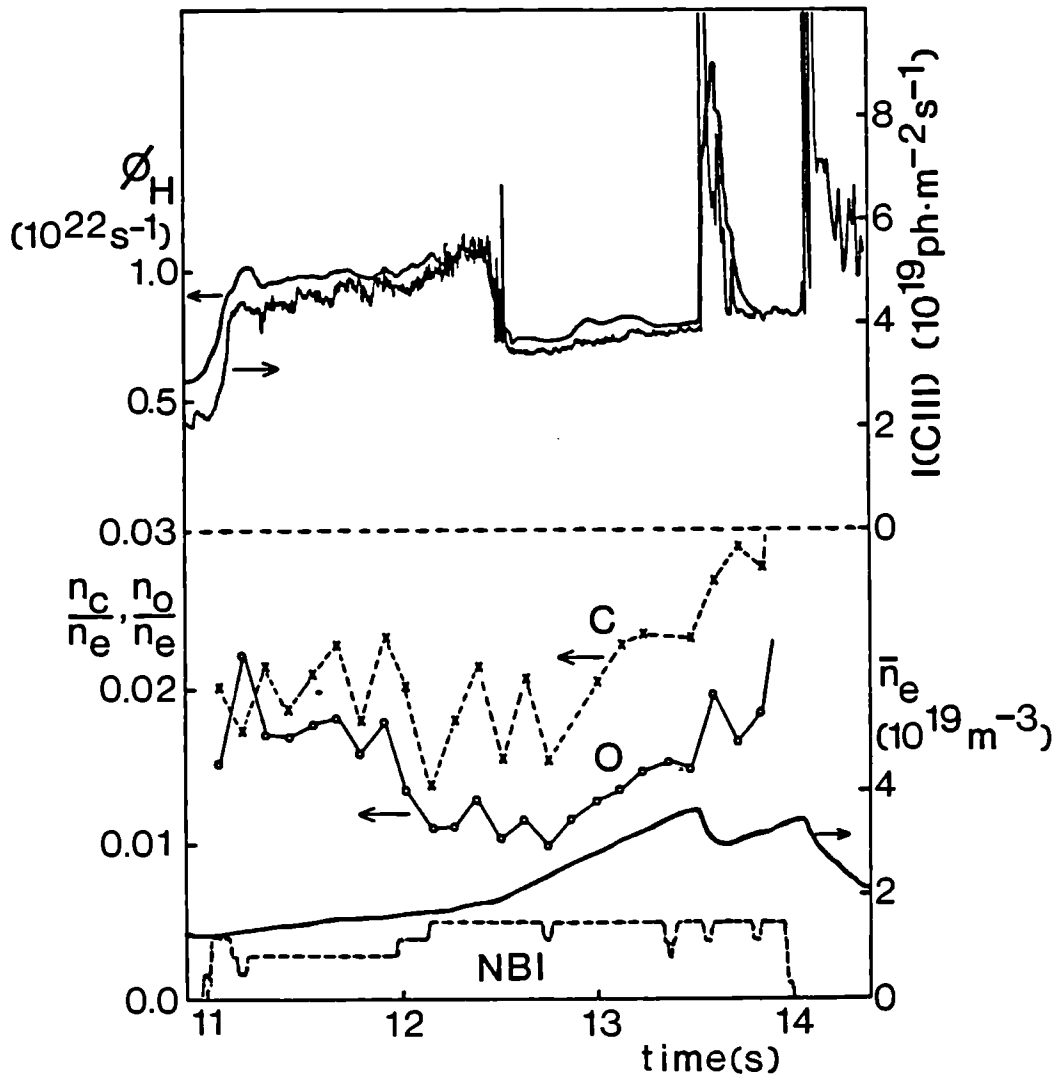

FIG.2. Behaviour of line average electron density ($\bar{n}_e$), carbon and oxygen concentrations (from CXRS), hydrogen flux (ϕ_H), and carbon influx, represented by the brightness of a C III-line (vertical viewing) during L- and H-mode in a NB-heated (5MW) X-point discharge. The L→H transition takes place at ~12.5 s.

REFERENCES

[1] Keilhacker, M, et al, (this conference)
[2] Behringer, K et al, IAEA, Kyoto 1986
[3] Tagle, A J (private communication)
[4] Jäckel, H, et al (this conference)
[5] Keilhacker, M, et al, Plasma Phys.and Contr.Fusion 26, 49(1984)
[6] Morgan, P D and O'Rourke, J J, (this conference)

ION ENERGY TRANSPORT IN JET DISCHARGES

G. Bracco+, M. Brusati, S. Corti, F. Rimini, F. Romanelli+
C. Sack, A. Taroni, F. Tibone, V. Zanza+

JET Joint Undertaking, Abingdon, Oxon., OX14 3EA, UK
+Associazione ENEA-Euratom sulla Fusione, Frascati, Italy

Introduction

Simulation of JET experimental results with predictive transport codes have always shown a tendency to require rather large (3-8) "anomaly factors" for the neoclassical ion thermal conductivity χ_{ineo} in order to reproduce the measured central value of the ion temperature T_{io} [1]. However, no firm conclusion on the radial (not to mention the functional) dependence of χ_i was possible in the absence of reliable measurements of T_i-profiles.

Interpretation of passive charge exchange (NPA) data has led to the determination of JET ion temperature profiles [2] in both ohmic and auxiliary heated discharges at low and moderate density [$\bar{n} \leq 2\times10^{19}m^{-3}$]. These discharges have been analysed with an interpretative transport code (JICS) and simulated with a predictive transport code (JETTO) in order to assess both magnitude and radial dependence of χ_i. The anomalous character of χ_i has been confirmed and results are similar to those reported for Doublet III [3]. A revised expression of χ_i based on η_i-modes has also been derived and its range of validity assessed.

Interpretative Code Analysis

In this analysis, χ_i is derived from the ion energy balance equation where the experimental profiles of ion and electron temperatures and Z_{eff} are supplied as input. A fundamental assumption, adopted also in the case of predictive code simulations, is that the electron-ion energy coupling be classical, with impurity corrections taken into account via Z_{eff}. Only ohmic and RF heated discharges have been considered so far, since in these cases a reliable T_i profile is provided by the NPA diagnostic under the assumption that the departure of the ion distribution function from thermal is negligible [2]. RF power deposition profiles are also given as input data to JICS when required and have been computed by means of a ray tracing code [4].

The ion heat diffusivity χ_{iexp} derived from JICS at $r = 0.6\,a$ for a few representative cases is shown in Fig.1. The values are in the range $(1\text{-}3)m^2/sec$, also typical for χ_e in the same cases. Both the numerical value of χ_{iexp} and its radial dependence are different from χ_{ineo} [5]. This is illustrated by Fig.2, where the ratio χ_{iexp}/χ_{ineo} is shown as a function of radius for one representative case. The value χ_{iexp}/χ_{ineo} in the so-called confinement zone ($0.3 \leq \frac{r}{a} \leq 0.7$) varies from 5 to more than 10.

The scatter in the data reflects the uncertainty associated with the experimental values and the numerical determination of ∇T_i, and not surprisingly it becomes very large in the external region.

Predictive Code Simulation and Theory

In the predictive approach to the problem of determining χ_i, various models for χ_i are introduced in the code and the resulting ion temperature profiles are compared with the experimental ones. In the examples considered here all the relevant quantities are either simulated by the code well within the experimental error bars (e.g. T_e, see [6]) or taken from JET data banks to which the JETTO code is linked (e.g. radiation profiles). This ensures that uncertainties in the modelling of other phenomena do not affect the determination of χ_i more than experimental uncertainties.

Results from the predictive code confirm the findings of the interpretative code. In particular, it is clear that at least at low density ($\bar{n} \approx 10^{19} m^{-3}$) the usual approach with $\chi_i = \alpha \chi_{ineo}$, $\alpha \approx 5$ does not allow a good simulation of JET T_i profiles, either in ohmic or in RF heated discharges. A typical example of results is shown in Figs.3,4. The same figures show that better simulations can be obtained with $\chi_i \approx \chi_e$, χ_e being an electron thermal conductivity that allows reproduction of T_e-profiles [6]. Such a choice for χ_i has been found to determine in transport codes a central value of T_i and an ion energy content consistent with experimental observations also in cases at higher density where no T_i profile is yet available and the usual approach $\chi_i = \alpha\, \chi_{ineo}$ cannot be excluded.

Comparison of these results on χ_i in JET discharges, characterised by rather flat density profiles, as well as those reported in other devices (e.g. [3]) with theoretical models suggests that a major role in determining χ_i could be played by the so-called η_i-mode ($\eta_i = d\ell n\, T_i / d\ell n\, n_i$). Previous tests on an expression of $\chi_{i\eta_i}$ failed in reproducing ion thermal fluxes available at the time in JET [7]. The derivation of $\chi_{i\eta_i}$ has been recently reviewed [8] leading to a reduction of the coefficient $\chi_{i\eta_i}$ used in [7]. In addition, a theoretical expression of the threshold η_{ic} for the instability derived in [8] has been introduced in place of the assumption $\eta_{ic} = \text{const} \approx (1\text{-}1.5)$.

The new expressions in the code are:

$$\chi_i = \chi_{ineo} + \alpha\, \chi_{i\eta_i}, \quad \chi_{i\eta_i} = \omega_{*i}\, \rho_i^2\, \Omega_i / b_i = 2.6\times10^{19}\, \frac{T_i^{3/2}}{B_t^2}\, \eta_i^{1/2} f\left(1 - \frac{\eta_{ic}}{\eta_i}\right) \varepsilon_n^{1/2}.$$

Here standard notations are used [8], $b_i = 0.1$ and $\Omega_i = 0.8\, \varepsilon^{1/2} \eta_i^{1/2} f(1-\eta_{ic}/\eta_i)$. $f = (1-\eta_{ic}/\eta_i)^{1/2}$ is derived in [8] for $\eta_i \geq \eta_{ic} = 1 + 2.5(\varepsilon_n - 0.2)$ if $\varepsilon_n > 0.2$, $\eta_{ic} = 1$ elsewhere ($f=0$ for $\eta_i < \eta_{ic}$); $\varepsilon_n = (\nabla \ell n n)^{-1}/R$ and α is a numerical coefficient to be determined from simulations and hopefully close to 1.

Results from the code show that reasonable ion thermal fluxes and χ_i values are obtained in all tested cases inside the so-called transport region if $\alpha \approx 0.5\text{-}1.0$. However, central values of T_{iexp} require that $\chi_{i\eta_i}$ should not be switched off when η_i falls below η_{ic}. This happens mainly in the central region where η_{ic} becomes rather large ($\gtrsim 4$). An empirical working prescription seems to be to replace the threshold function $f(1 - \eta_{ic}/\eta_i)$ with a function $(\eta_i/\eta_{ic})^{\beta}$, $\beta \approx 1\text{-}1.5$.

In the external region the available experimental information, albeit less reliable than elsewhere, does seem to require a χ_i increasing with radius. This is not consistent with the T_i dependence of χ_{in_i} and would require some further modification to χ_{in_i} or an additional mechanism at work. Results of simulations with χ_{in_i} are also shown in Figs.3 and 4.

Conclusions

Results of interpretative and predictive transport codes show that both the magnitude and the functional dependence of χ_{ineo} are not consistent with the available experimental profiles of T_i (and T_e) at least at low density.

A better term of comparison than χ_{ineo} for χ_i seems to be the electron thermal conductivity; $\chi_i \simeq \chi_e$ is generally a better prescription for JET simulation than $\chi_i \simeq 5\ \chi_{ineo}$, especially at low density.

Reasonable results for T_i in the central and intermediate plasma region are provided if $\chi_i \simeq \chi_{ineo} + \chi_{in_i}$ is used in a transport code; χ_{in_i} needs, however, some modifications from the theoretical expression derived in [8].

References

[1] Taroni, A. et al, 12th European Conference on Controlled Fusion and Plasma Physics, Budapest, 2-6 September 1985, Vol.I, p.22.

[2] Corti, S. et al, 13th European Conference on Controlled Fusion and Ploasma Heating, Schliersee, 14-18 April 1986, Vol.I, p.109.

[3] Groebner, R.J., et al, Nucl. Fus. 26, 543 (1986).

[4] Bhatnagar, V. et al, Nucl. Fus. 24, 955 (198).

[5] Chang, C.S., Hinton, F.L. Phys. Fluids, 25, 1515 (1986).

[6] Taroni, A., Tibone, F. paper presented at this conference.

[7] Düchs, D.F. et al, Eleventh International Conference on Plasma Physics and Controlled Nuclear Fusion Research, Kyoto, 13-20 Nov. 1986.

[8] Romanelli, F., JET report in press.

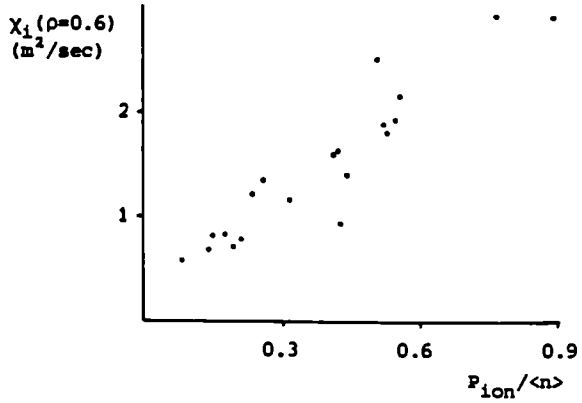

Fig. 1 : χ_{iexp} in the confinement zone as a function of input power per particle (in MW $/10^{19}$ ions m^{-3}).

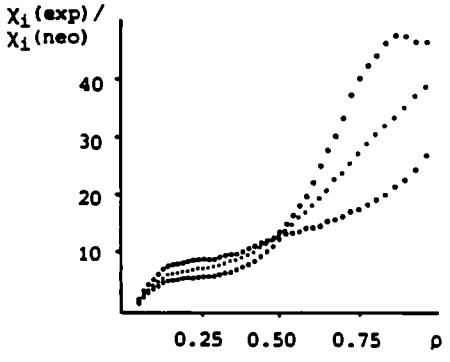

Fig. 2 : The ratio χ_{iexp}/χ_{ineo} as a function of radius at three times during the flat-top of a "monster" sawtooth (#11133, B_t= 2.2T, I_p=2.0MA, $<n_e>$=1.5 $10^{19}m^{-3}$, P_{RF}=4.5MW).

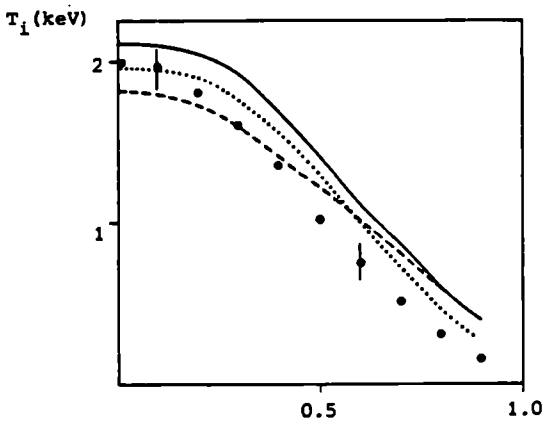

Fig. 3: Comparison of experimental (full circles) and computed T_i-profiles in an ohmic case. The models used are χ_i= 5 χ_{ineo} (solid line), $\chi_i=\chi_{ineo}$ + χ_e (dotted line) and χ_i= χ_{ineo} + χ_{ini} (dashed line). In χ_{ini} we have used $f=n_i/n_{ic}$ (#8961, B_t= 2.5T, I_p=2.5MA, $<n_e>$=1.7 $10^{19}m^{-3}$).

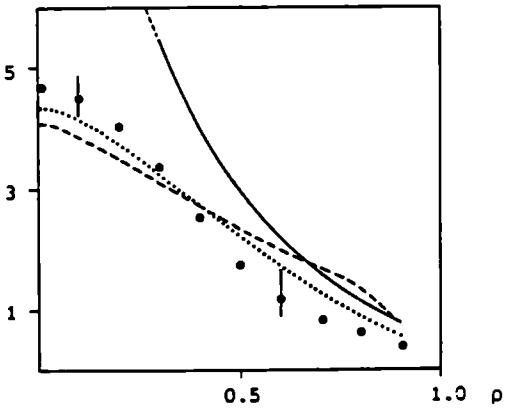

Fig. 4: Comparison of experimental and computed T_i-profiles at the end of the flat-top of a "monster" sawtooth. Symbols and models are as in Fig. 3. The RF-heated plasma is that of Fig. 1.

BEAM-PLASMA FUSION YIELD IN ROTATING TOKAMAK PLASMAS

W.G.F. Core, P. van Belle, G. Sadler

JET Joint Undertaking, Abingdon, Oxon., OX14 3EA, UK

1. Introduction

In the neutral injection heating of tokamak plasmas, fast ions are initially injected as neutrals, which after ionisation, slow down on the background plasma to thermal energy. During this relaxation process, the fast ions, in addition to heating the plasma directly, can undergo thermonuclear reactions, and even in the case of balanced injection, impart momentum to the system. This input of momentum gives rise to plasma rotation preferentially in the toroidal direction, and for uni-directional injection, velocities in excess of the sound speed have been predicted [1]. These bulk plasma rotational velocities may have important consequences for the beam heating efficiency, the thermonuclear reactivity of the system, and in the interpretation of the measured fusion yields.

In this paper we first consider the effect of bulk plasma toroidal rotation on the beam-plasma reactivity rates, and in particular, the thermonuclear power amplification factor Q of systems close to ignition [2]. Then the modification to the fusion charged particle birth profiles due to the combined effects of rotation and orbit trajectory is examined. Finally, results of calculations done using actual measured plasma parameters for the JET D→D injection experiments in which large rotational velocities have been observed are compared with the measured neutron fluxes.

2. Preliminary Considerations

Some obvious points regarding the injected ions as viewed in the laboratory and plasma frames are worth mentioning. Fast ions deposited in passing orbits moving in a co-rotational direction in the laboratory frame will in the rotating plasma frame suffer an apparent reduction in energy, and conversely, passing ions moving in a counter-rotational direction will have their energy increased. Accordingly, the fast ion slowing down time and consequently their density is then either reduced or increased. The transformation of particle velocity v, and pitch variable ξ ($=v_{\parallel}/v$), from the laboratory to the plasma frame $(v,\xi)\rightarrow(v_R,\xi_R)$ is: $v_R^2=v^2-2v\xi v_{\parallel_o}+v_{\parallel_o}^2$, $\xi_R=(v\xi-v_{\parallel_o})/v_R$, where $v_{\parallel_o}$ is the component of the bulk plasma ion velocity along the magnetic field. If, under this transformation, orbit distortions are small, and $f(v,\xi)\rightarrow f(v_R,\xi_R)$, where $f(v,\xi)$ is the flux surface averaged fast ion distribution function, then the relaxation of the injected ions can be most conveniently described by the Fokker-Planck equation,

$$\frac{\partial f}{\partial t} = C(f) + S, \qquad \ldots (1)$$

where C(f) is the usual Coulomb scattering operator valid in the velocity range $v_i \ll v \ll v_e$, where now v_i, v, and v_e are the thermal ion, fast ion, and electron velocities in the plasma frame respectively. S is the number of

fast ions produced per unit phase space volume per second with initial velocity v_o on a particular magnetic surface.

The thermonuclear reactivity $\langle\sigma v\rangle$ is then

$$\langle\sigma v\rangle = 4\pi \int_0^\infty v^2 dv\, a_o(v)\, (\sigma v),$$

where (σv) is the reaction rate for fast ions interacting with a warm Maxwellian target plasma, and a solution to Eq.(1) has been obtained in the form of an expansion in Legendre polynomials P_n, viz $f(v,\xi) = \Sigma a_n(v) P_n(\xi)$. Similarly, the "figure of merit", or amplification factor for such a system is defined by

$$Q = \frac{\langle\sigma v\rangle Y}{\bar{S}\, E_o},$$

where Y is the total fusion energy release per reaction, $\bar{S}$ is the number of fast ion produced per unit volume per sec., and E_o is the injection energy.

Using these model simplifications the effects under consideration here can now be examined by invoking the well developed techniques appropriate to the study of injection into stationary plasma systems [3].

3. Effect of Rotation on Local $\langle\sigma v\rangle$ and Q-Factor

For this purpose, and in view of its importance in achieving ignition in present and future tokamaks, we consider the beam-plasma system T(D,n)^{4}He, and in particular the two limiting cases of co-and counter-rotational injection. In the former, and for the range of injection energies $E_o < 120$keV, the rotation of the plasma gives rise to a reduction in the beam-target interaction energy, leading to a reduced reactivity rate and Q-value. In the latter, an increase in the fusion yield will occur. For fast ions in trapped orbits, and due to the increase in thermonuclear cross section with energy, there will be a net gain in yield for these particles.

The results for typical values of electron temperature and injection energies are shown in Figs.2,3. The asymmetry in $\langle\sigma v\rangle$ and Q are clearly indicated. Unbalanced injection leads to a decay in the neutron production during the heating phase. For 80keV deuterium injection into a $T_e = T_i = 10$keV, $n_e = 3\times10^{13}$cm^{-3} tritium plasma rotating with velocity $v_\phi \approx 0.5C_s$, where C_s is the ion sound speed, a decay in the neutron production due to the fast ions in passing orbits of 40% is predicted. However, this loss in neutron production will be partially compensated by the trapped ion contribution. This point will be discussed in the next section.

4. Modifications to the Fusion Product Birth Profiles

As previously mentioned, for trapped beam ions, the effect of plasma rotation leads for this class of particle, to a net gain in the thermonuclear reactivity and local Q of the system. Since the fraction of fast ions in trapped orbits increases with distance from the toroidal axis, the occurrence of hollow fusion yield profiles in beam-plasma configurations where the fast ion deposition is broad is then expected.

In order to examine this situation we again consider the aforementioned system of 80keV deuterium injection into the $T_e=T_i=$ 10keV, $n_e=3\times10^{13}cm^{-3}$ tritium plasma rotating at various toroidal velocities. In addition we assume a small aspect ratio ($\varepsilon=r/R_o<<1$) cylindrical plasma with minor radius a = 1.25m, major radius R_o = 2.96m, and a flat fast ion deposition profile. The effective fusion reaction rate $\langle\sigma v\rangle \approx \langle\sigma v\rangle_+ + \sqrt{2\varepsilon}(\langle\sigma v\rangle_- - \langle\sigma v\rangle_+)/2$, where the subscripts (+,-) are the calculated, Fig.1, co- and counter-rotation reaction rates respectively. The results of these calculations are shown in Fig.3. It is to be noted that everywhere within the plasma volume the reactivity is reduced. This reduction, which is typically 60% when $v_\phi \approx C_s$, is greatest on or near the toroidal axis where the fraction of fast ions in trapped orbits is least. However, current large tokamaks (JET, TFTR) have measured $v_\phi < C_s$.

5. Comparison with Measured Neutron Yields during D→D Injection Heating Experiments

We consider #8902 of the current JET database. The decay of the neutron production during the neutral beam heating phase, represented by the bold straight line, is shown in Fig.4. The plasma rotational velocity was observed to be $v_\phi = 1.5\times10^7 cms^{-1}$ after 2 seconds of beam heating alone. for these particular plasma parameters of $T_e=$ 3.63keV, $n_e=2\times10^{13}cm^{-3}$, injection energy $E_o=$ 65keV, and assuming that the principle contribution to the measured neutron yield is from the centre of the discharge, where the fast ions are in passing orbits we obtain $\Delta\langle\sigma v\rangle/\langle\sigma v\rangle \approx 6\%$. However, Fig.4 gives, for constant deuterium density, $\Delta\langle\sigma v\rangle/\langle\sigma v\rangle = 9\%$. This discrepancy between measurement and theoretical prediction is probably due to the uncertainty in deuterium density.

6. Concluding Remarks

The build-up of toroidal momentum during uni-directional neutral injection heating of tokamak plasmas leads to:

i) A reduction in the beam-plasma reactivity and local thermonuclear Q-value.

ii) For the T(D,n)^{4}He system considered this reduction which is greatest at the centre of the discharge is typically 70% for rotation velocities at or near the ion sound speed.

iii) The effect of plasma rotation on fusion reactivity rates can be reduced by increasing the fraction of fast ions in trapped orbits which will be the case during ICRF heating of the beam ions.

iv) Finally, it is worth mentioning that measurements of plasma rotational velocities in current large tokamaks (JET, TFTR) are less than the ion sound speed.

Results of calculations done using actual measured plasma parameters for the JET D→D experiments in which large rotational velocities have been observed are in reasonably good agreement. The possibility of deducing the plasma rotational velocity from the neutron yield measurements should not be excluded.

References

[1] CALLEN, J.D., CLARKE, J.F. Bull. Am. Phys. Soc., 16 (1971).

[2] DAWSON, J.M., FURTH, H.P., TENNEY, F.H. Phys. Rev. Letts., 26 (1971).

[3] CORDEY, J.G., CORE, W.G.F. Phys. of Fluids 17 (1974).

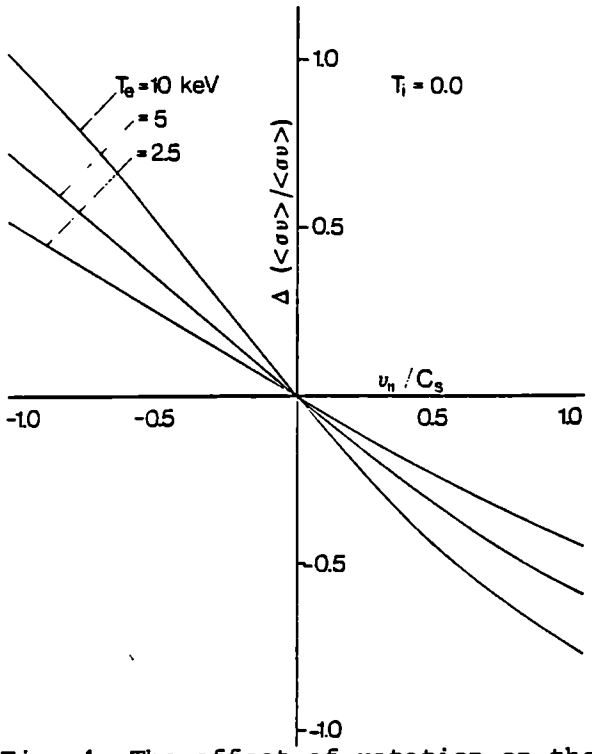

Fig. 1: The effect of rotation on the reactivity rate of fast ions injected in the co- ($v_\phi/c_s > 0$) and counter-rotation ($v_\phi/c_s < 0$) directions are shown.

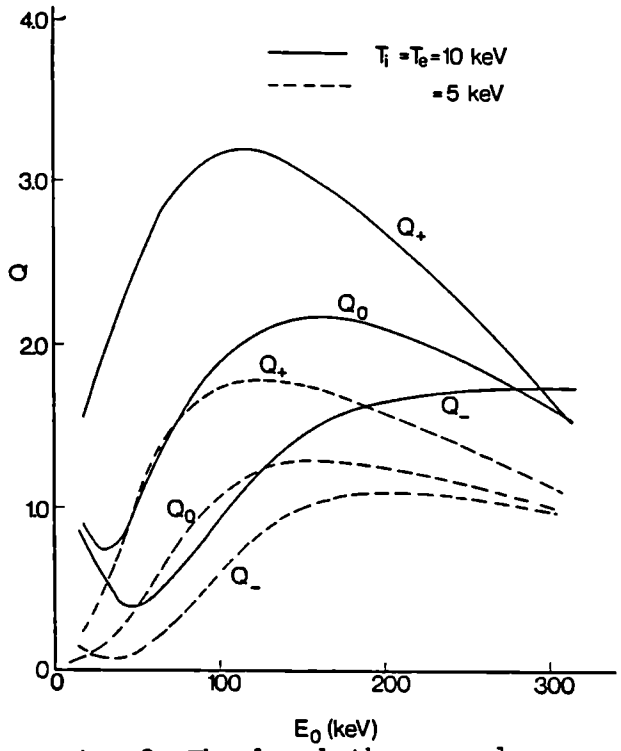

Fig. 2: The local thermonuclear amplification factor Q as a function of deuteron injection energy. Q_+ is the value for counter-rotation and Q_- for co-rotation. Electron density $n_e=3\times10^{13}cm^{-3}$, $v_\phi \simeq 0.5c_s$, Y=17.6MeV.

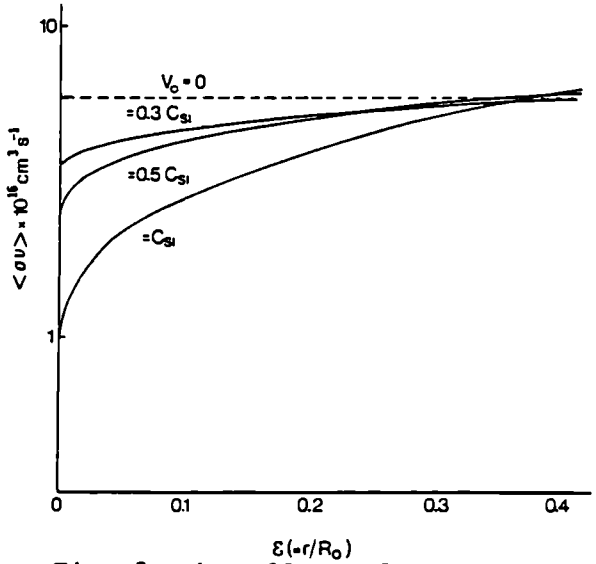

Fig. 3: The effect of rotation on the fusion yield profile is shown. Rotation leads to a reduction in the reactivity which is greatest on or near the toroidal axis where the fraction of fast ions in trapped orbits is least.

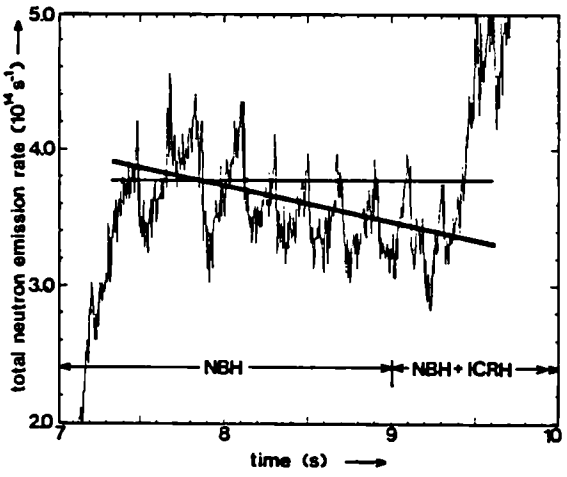

Fig. 4: #8902, D→D injection. The measured neutron yield during the beam heating phase is shown. E_o= 65keV, $n_e=2\times10^{13}cm^{-3}$, T_e=3.6keV.

SIMPLIFIED MODEL FOR ICRH POWER DEPOSITION IN LARGE TOKAMAKS

T. Hellsten and L. Villard*

JET Joint Undertaking, Abingdon, Oxon. OX14 3EA, UK
*CRPP École Polytechnique, Fédérale de Lausanne, Switzerland

1. Introduction - To calculate the power deposition during ion cyclotron heating (ICRH) in tokamak plasmas, ray tracing codes and global wave codes have been developed. The basic problem to solve is a complicated wave equation in a non-trivial geometry having only one ignorable coordinate. Both methods require long computational times making them less suitable for implementation in transport codes and data interpretation. In this report we present a simplified formula for the flux surface averaged power deposition which is based on calculations with the global wave code LION [1]. The formula relates the power deposition to the damping coefficient, the variation of the absorption coefficient along the cyclotron resonance and the Doppler width of the cyclotron resonance. The formula agrees well with the calculations with the LION code, but it is restricted to the case where the absorption occurs along a single ion cyclotron resonance going through the magnetic axis and to a particular equilibrium. However, the formula is found to be not too sensitive to small variations in aspect ratio or cross section.

For large power densities the velocity distribution of the heated ions develops a high energy tail which in its turn may modify the absorption coefficient. A change in the absorption coefficient will then lead to a corresponding change in the power deposition. Thus the power deposition becomes a non-linear function of the launched power. This is particularly important for heating at the first harmonic cyclotron resonance where the absorption coefficient can be substantially enhanced. In section 3 the power deposition and the velocity distribution is solved in a self consistent way by iterative calculations by using the above mentioned formula.

2. Analysis of the Power Deposition Profiles - The presence of cavity resonances leads to spatial fluctuations of the power deposition depending on the position of maxima and minima of the wave field. For heating scenarios with at least a moderately strong damping, the antennae couple to a large number of eigenmodes such that these fluctuations become less important. For such situations one does not need to know the exact field but it is sufficient to know the mean value. The corresponding power deposition in the poloidal cross-section is then characterised by its vertical and horizontal extension. The horizontal extension is determined by the Doppler broadening of the cyclotron resonance. The vertical extension is determined by the focusing of the wave field which depends on the geometry and strength of the damping.

We have focused our study to typical JET equilibria having an ellipticity of 1.4, a triangularity of 0.19 and an aspect ratio of 2.6, and for which the absorption occurs through a single ion cyclotron resonance passing through the magnetic axis. To analyse the power deposition it is more convenient to study the Poynting flux integrated over the magnetic surfaces, $\bar{P}(s)$, where s denotes a parameter such that $s \propto \sqrt{\psi}$ and $s = 0$ at

the magnetic axis and 1 at the plasma boundary. The flux surface averaged power density is obtained by differentiating $\bar{P}$ with respect to the enclosed volume.

We first analyse strongly and weakly damped scenarios. For strongly damped scenarios the wave is focused to the centre of the plasma. As an ansatz for the flux surface averaged Poynting flux we take

$$\bar{P}_1(s) = P_o\{1 - \exp[-(s/s_o)^2 \ln 2]\}/[1 - \exp[-(1/s_o)^2 \ln 2]] \qquad (1)$$

The half width, s_o, is related both to the geometry and the Doppler broadening of the cyclotron resonance. The Doppler broadening is proportional to $2n\sqrt{\langle v_{\parallel}^2\rangle}/\omega\Delta R$, where n is the toroidal mode number, $\langle v_{\parallel}^2\rangle$ is the averaged parallel velocity squared of the heated ions, $\omega/2\pi$ is the wave frequency and ΔR is the horizontal extension of the cross-section. The relation between s_o and $2n\sqrt{\langle v_{\parallel}^2\rangle}/\omega\Delta R$ is obtained with the LION code (Fig.1).

In the case of weakly damped scenarios the structure of the wave field varies considerably for small changes of the equilibrium parameters depending on which eigenmodes the antennae couple to. We have not found any correlation between the toroidal mode number or coupling resistance with the power deposition. We then take the mean value of the flux surface averaged Poynting flux for some randomly chosen toroidal modes. We define this mean value, $\bar{P}_2(s)$ as the expected Poynting flux. The power deposition is given by $d\bar{P}_2/ds$, which is proportional to the flux surface averaged absorption coefficient a(s). We define a function f(s) such that

$$a(s)\, f(s) = \frac{1}{\bar{P}_2(1)} \frac{d\bar{P}_2}{ds} \int_o^1 a(s)\, f(s)\, ds \qquad (2)$$

f(s) is related to the averaged amplitude of the electric field along the cyclotron resonance and to the geometry. In Fig.2 we show f(s) for a few different density profiles. By varying a(s) along the cyclotron resonance, we found that f(s) stays roughly constant as expected.

For the general case of a medium strong absorption we decompose the flux surface averaged Poynting flux, $\bar{P}$, into $\bar{P}_1$ and $\bar{P}_2$ such that

$$\bar{P} = P_o(\alpha\, \bar{P}_1 + (1 - \alpha)\, \bar{P}_2) \qquad (3)$$

In Fig.3 we compare α with a damping coefficient, a_{IS}, as calculated with the ISMENE code [2]. This coefficient is related to the damping coefficient for a single pass, a_s, $a_s = 1 - \sqrt{1 - a_{IS}}$. The power absorbed at the first pass, P_s, is given by $P_s = (1 - \sqrt{1 - a_{IS}})\, a_{IS}\, I$, where I is the incidenting Poynting flux. P_s/I is a good approximation to $\alpha(a_{IS})$. These calculations have been done for heating scenarios having constant density and temperature to make a(s) constant. The absorption coefficient is varied by varying the concentration.

As a formula for the integrated Poynting flux, $\bar{P}$, we use Eq.(3) where P_1 is defined by Eq.(1) and P_2 by Eq.(2) and $\alpha = a_{IS}(1 - \sqrt{1 - a_{IS}})$. This model has been compared with the LION code and good agreement is obtained. In Fig.4 we show the comparison for the following heating scenarios: $\omega = \omega_{CH}$ in ^{3}He where $a_{IS} = 0.35$, $\omega = \omega_{CH}$ in D where $a_{IS} \sim 0.90$.

3. Iterative Calculations of the Power Deposition Profile - When the absorption coefficient is modified due to tail formation of the heated species, the power deposition and the velocity distribution have then to be calculated self consistently. This can be done by iterations. The damping coefficient of a Maxwellian plasma is calculated with the ISMENE code. For first harmonic heating $a(s) \propto k_{\perp}^2 n_R T_R \propto n_e n_R T_R$ where R stands for the resonating ion species and e for electrons. The enhancement of the absorption, γ for a steady state distribution compared to what a Maxwellian one absorbs for the same electric field is calculated with a Fokker-Planck code [3]. The modified absorption coefficient is calculated from $a = 1 - \exp(-a^*\gamma)$ where a^* is defined by $a^* = -\ln(1-a_M)$ and a_M is the absorption coefficient for a Maxwellian velocity distribution. The iterations are then performed in the following way. The power deposition is first calculated for a Maxwellian velocity distribution. The enhancement factor γ is then calculated for the previously obtained power density. The next power deposition is then calculated with the previously obtained absorption coefficients etc. The flux surface averaged Poynting flux obtained for a Maxwellian velocity distribution and a steady state velocity distribution is compared in Fig.5 for the case of $\omega = 2\omega_{CT}$, $n_D = n_T = 2 \cdot 10^{13} cm^3$, B = 3.4T and 10MW launched power. For this case γ varies from 10 in the centre to 1 at the boundary.

References

[1] VILLARD, L., et al. Comp. Phys. Reports 4 (1986) 95.

[2] APPERT, K., et al. Comp. Phys. Communications 40 (1986) 73.

[3] HELLSTEN, T., et al. 12th European Conf. on Contr. Fusion and Plasma Heating, Budapest (1985). Proc. Contributed Papers Vol.II, p.124.

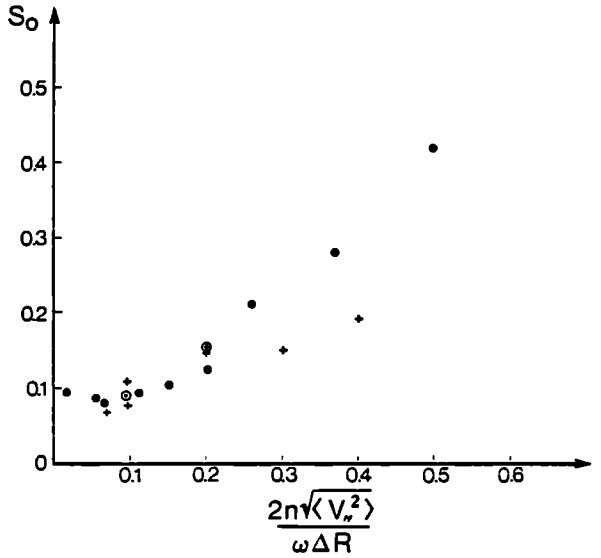

Fig.1 Relation between S_o and the Doppler width of the resonance (• elliptic, + circular plasma cross section).

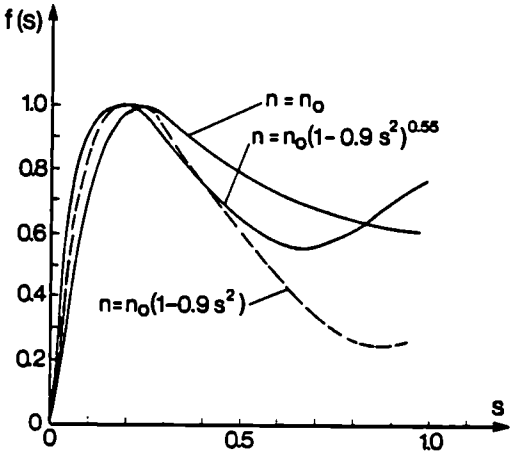

Fig.2 The function f(s) for various density profiles.

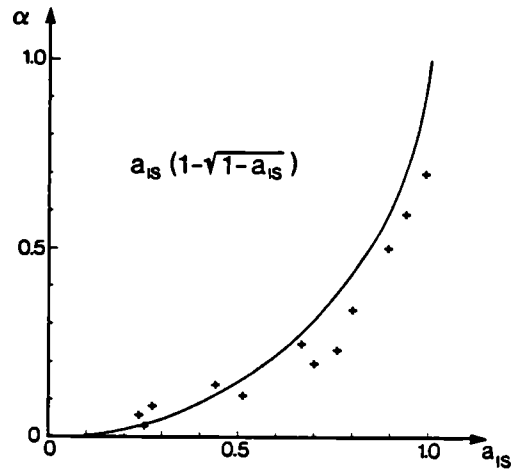

Fig.3 The relation between α and a_{IS}.

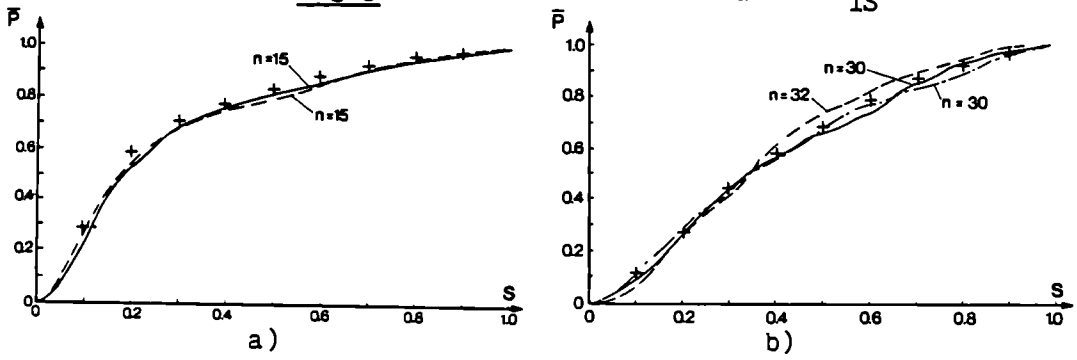

Fig.4 Comparison between the simplified formula (+) and calculations with the LION-code, n is the toroidal mode number.
a) $\omega = \omega_{CH}$ in D-plasma. b) $\omega = \omega_{C^3He}$ in D-plasma.

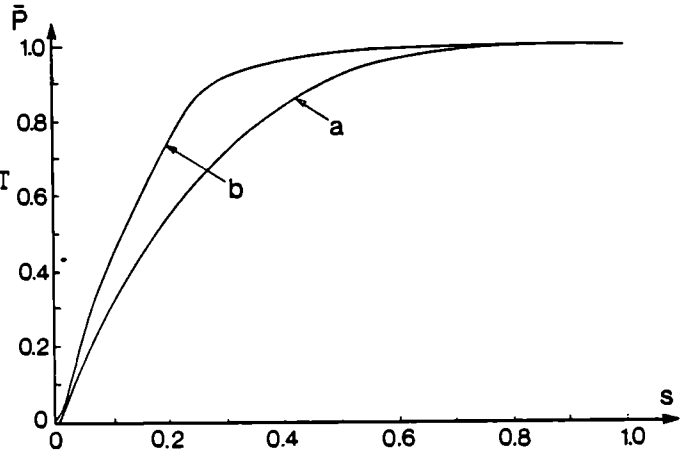

Fig.5 Flux averaged Poynting flux for different velocity distributions during $\omega = 2\omega_{CT}$ heating in a D-T-plasma.
a) Maxwellian velocity distribution, b) a steady state velocity distribution during ICRH-heating.

SIMULATION OF TRANSIENTS IN JET BY MEANS OF PREDICTIVE TRANSPORT CODES

A. Taroni and F. Tibone

JET Joint Undertaking, Abingdon, Oxon., OX14 3EA, UK

Introduction

An empirical electron heat conduction coefficient χ_e constraining the electron temperature profile to asymptotically reach observed "consistent profiles" was proposed in [1]. In this paper we summarise the results of simulations of several JET discharges in a variety of situations. The cases considered are felt to be particularly significant and to constitute a much more demanding test for a transport model than standard steady state or slowly evolving cases. They allow to assess clearly merits and limitations of our model that has to be modified in order to take into account fast time scale phenomena such as the heat pulse propagation after a sawtooth crash.

Computational Results

We have used the expression for the electron heat diffusivity first derived in [1]:

$$\chi_{ePC}(r) = F(r) \cdot \frac{\int_0^r [P_{in}(r) - P_{out}(r)]\, r dr}{n_e(r)\, T_e(r)}$$

where $P_{in}(P_{out})$ represents all of the source (sink) terms in the electron energy balance, while F(r) is a shape factor which determines the detailed shape of the exponential temperature profile that will be reached in steady-state (e.g. for a Gaussian profile $T_e(r) = T_{eo}\exp(-\alpha_T r^2/a^2)$ one will have $F(r) = a^2/(2\alpha_T r^2)$).

This model has been used to simulate, by means of a 1½D predictive transport code, the following plasma regimes experimentally observed in JET.

Localised off-axis heating experiments - RF heating experiments have been performed in JET by shifting the minority resonance layer position away from the plasma centre. Ray tracing calculations predict that heating occurs in a narrow radial range ($\Delta r \sim 20$cm), and that electron heating is largely dominant in the H-minority cases we have studied [2].

During off-axis heating, the shape of the electron temperature profile remains essentially unchanged, with its magnitude increased (Fig.1).

While the Ohmic profile can be reproduced acceptably using various different models (Fig.1a), we find that during RF heating one has to prescribe $\chi_e(RF) > \chi_e(OH)$ in the external region, while $\chi_e(RF) < \chi_e(OH)$ in the inner core, where no auxiliary power is deposited (Fig.1b). This behaviour is a natural outcome of the definition of χ_{ePC}.

The result is similar to that reported in [3] for TFTR edge heating experiments with neutral beam injection.

"Monster" sawtooth evolution - The "monster" sawtooth regime, with up to 1.5 sec long sawtooth-free intervals, offers an opportunity to study the evolution of the central portion of the electron temperature profile towards a steady-state configuration without the effect of sawtoothing.

In JET, such transition is observed to occur on a relatively fast time scale (0.2-0.3sec), and is characterised by a sudden saturation of the central temperature (Fig.2).

When trying to simulate this behaviour, we find that a transport model is needed that predicts a strong increase of heat diffusion when T_e gets close to the steady-state, "limit" profile.

One way of doing this is provided by χ_{ePC}, by virtue of its implicit profile constraint (Fig. 2).

Heat pulse propagation - Full transport code simulations where the Kadomtsev model is used to simulate sawteeth (with the sawtooth period prescribed from experiment) give realistic predictions as to the sawtooth amplitude and to the size of the "mixing" region, and can therefore also be used to follow the time evolution of the computed sawtooth-induced heat pulses.

We have compared computed and measured results for one representative discharge for which heat pulse propagation measurements were available during both the Ohmic and a strong auxiliary heating ($P_{tot} > 10MW$) phase. During the latter, computed and measured times required for the heat pulse to reach the boundary region are in reasonable agreement. For the Ohmic plasma the experimental time is about three times faster. Here, it does not seem to be possible to make the agreement any better by using a purely diffusive model, if this is bound to reproduce the global confinement and the steady-state temperature profile.

One effective way of tackling the problem seems to be the introduction of a substantial "heat pinch" along the lines suggested in [4,5]. We have added to the electron thermal flux q_e an inward term linear in the minor radius. Thus one has:

$$q_e = - n_e \chi_{ePC} \nabla T + q_{avv} - rh.$$

Here q_{avv} is the usual convective term and h is a constant such that the total heat pinch related source in the plasma volume V_p is $\int_{V_p} h dV \approx (1-2) P_{OH}$. Notice that one can interpret rh/χ_{ePC} as a "critical gradient" [6,7].

This modification of the model, as shown in Fig.3, actually provides the required speeding up of heat pulses, while leaving the global confinement unchanged. The effect is small during the auxiliary heated phase, and does not change the previous picture significantly there.

Discussion and Conclusions

Results obtained so far show the following:

The tendency of T_e profiles to relax in steady state to the same shape independent of the power deposition profiles is consistent with an empirical electron heat diffusion coefficient increasing locally with the power deposited inside a given radius. This dependence of χ_{ePC} and its local inverse dependence on n_e and T_e also provide an automatic improvement of the confinement in the central region of the plasma when off axis auxiliary heating is applied, as experimentally observed. However, this does not imply that the electron heat flux must really be dependent on non

Figure Captions

Fig 1: Experimental and computed T_e-profiles plotted versus a normalised flux surface coordinate ρ for a JET discharge with off- axis RF heating (#8961, B_t=2.5Tm I_p=2.5MA, $\langle n_e \rangle_{OH}=1.7\cdot10^{19}m^{-3}$, $\langle n_e \rangle_{RF}=2.2\cdot10^{19}m^{-3}$, P_{RF}=4.8MW). Figure 1a refers to the ohmic phase, Fig 1b to the RF-heated phase. Full circles represent the experimental profiles. The computed ones are obtained using χ_e(Alcator-Intor) [solid lines] and χ_{ePC} [dotted lines]. During RF heating, the power deposition profile is peaked around ρ = 0.6 with a width $\Delta\rho$ = 0.1. χ_{eAI} is increased in order to reproduce the degradation in global confinement, by 50% over the whole plasma cross-section.

Fig 2: Results of the simulation of the time evolution of T_{eo}^{EXP} during a monster sawtooth (solid curve) with χ_{ePC} (dotted curve) and χ_{eAI} (dashed curve). In both computations the experimental confinement time is reproduced.

Fig 3: Heat pulse propagation as computed without (dashed) and with (solid line) a heat pinch term included in the electron energy balance, as discussed in the text.
The plasma is ohmically heated, and $\int hdV$ ~ 3.5MW. The experimental time for the heat pulse to travel from ρ = 0.4 to ρ = 0.7 is 30 msec.

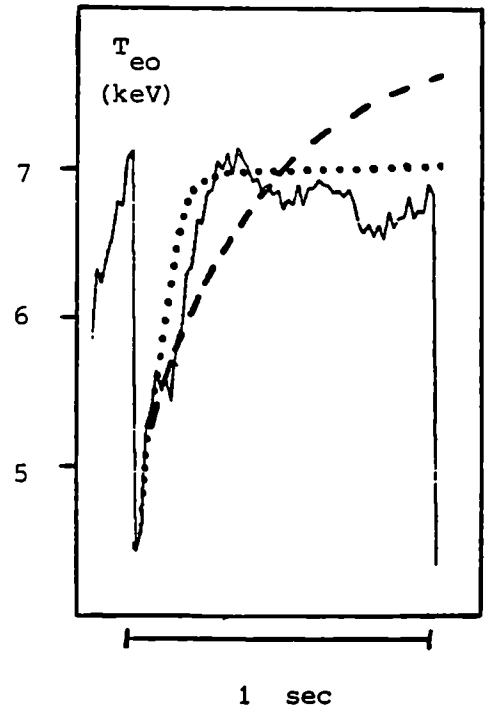

Figure 3

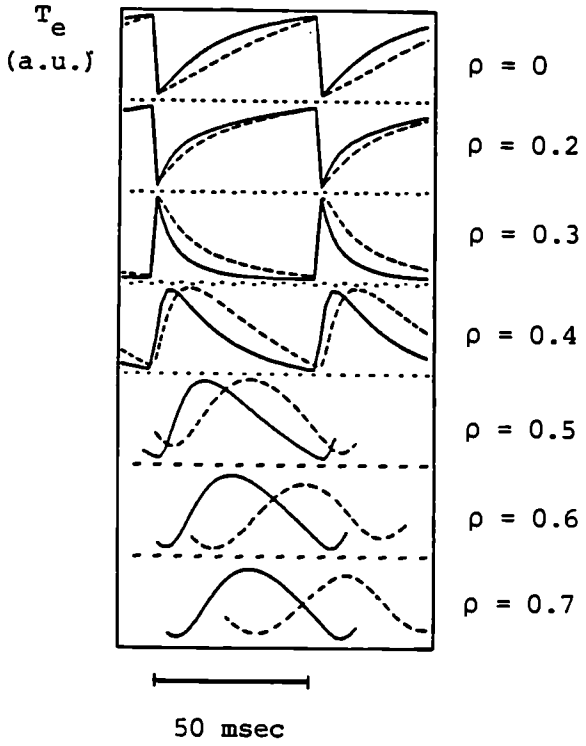

Figure 4

local quantities. Most probably, it simply shows that one must look for a plausible physical mechanism that can provide effects equivalent to the ones produced by χ_{ePC} in our computations. We notice that a coefficient χ_e with a suitable non linear dependence on ∇T_e and other local quantities could in practice produce steady-state results non distinguishable from those obtained with χ_{ePC} [8].

- Results with χ_{ePC} based on Gaussian or other exponential profiles are sensitive to the value of T_e at the boundary of the region where χ_{ePC} is applied [1]. Thus the scaling of the electron energy content is strongly coupled to the power handling capability of the plasma boundary region. However this is not the only possible way to "normalise" χ_{ePC}. An alternative way is to provide the required normalisation through a proper internal microinstability, as proposed in [9]. The same microinstability should provide the correct radial dependence of χ_e, which remains unexplained in [9].
- χ_{ePC} seems to be consistent with the time evolution of the central value of T_e in "monster" sawteeth.
- The main features of the heat pulse propagation following a sawtooth crash cannot be simulated by a transport model including χ_{ePC} alone. A simple modification of the transport model including a so-called "heat pinch" does allow simulation of heat pulse diffusion. However the "heat pinch" prescription, while having some theoretical basis in the critical gradient approach [7], is far from being uniquely defined at present.

References

[1] A. Taroni, F. Tibone, Proc. 13th EPS Conference (1986) 10c, p.160.
[2] V.P. Bhatnagar et al, Proc. 13th EPS Conference (1986) 10c, p.193.
[3] R.J. Goldston et al, Proc. 13th EPS Conference (1986) 10c, p.41.
[4] N. Lopez-Cardozo, B. Tubbing, JET-R(87)01 to be published in Nucl. Fus.
[5] J.D. Callen et al, JET-P(87)10, to be published in Nuclear Fusion.
[6] P.H. Rebut, M. Brusati, Pl. Phys. Contr. Fus. 28 (1986) 113.
[7] P.H. Rebut et al, This conference.
[8] A. Taroni, F. Tibone, JET-IR(87)02.
[9] W.M. Tang, Nucl. Fus. 26 (1986) 1605.

Fig. 1a

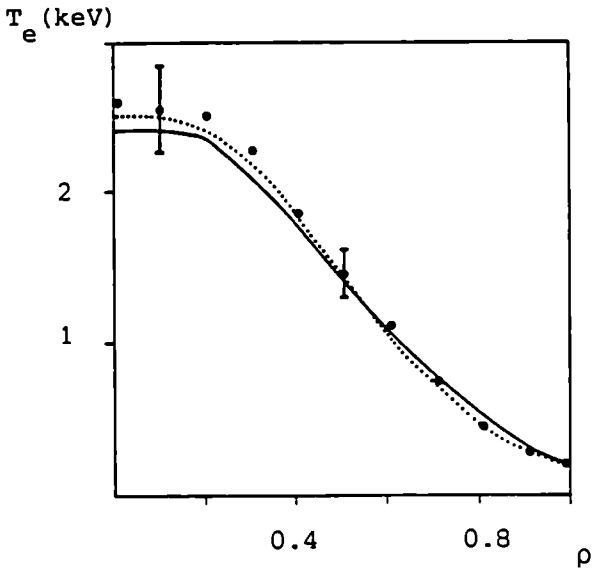

Fig. 1b

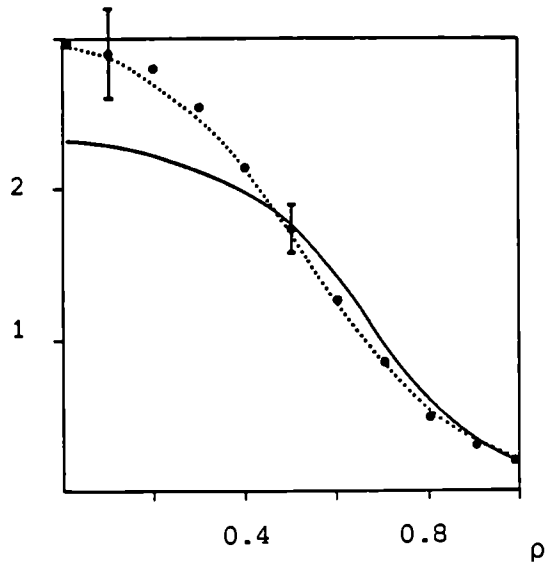

PROFILE EFFECTS ASSOCIATED WITH PELLET FUELING OF JET

A D Cheetham, D J Campbell, A Gondhalekar, N Gottardi,
R Granetz, P D Morgan and J O'Rourke

JET Joint Undertaking, Abingdon, OX14 3EA, UK

ABSTRACT

Pellet fueling experiments have been performed on JET using a single-shot pneumatic injector giving 4.6 mm (4.5×10^{21} atoms) or 3.6 mm (2.2×10^{21} atoms) diameter cylindrical deuterium pellets with velocities between 0.8 and 1.2 $km\cdot s^{-1}$[1]. In this paper the effects of pellet fueling on the density and temperature profiles of OH discharges are described. In particular the consequences of pellet penetration into the $q<1$ region are examined. It is shown that for significant modification of the density profile in JET, the pellet must penetrate the $q=1$ surface and major deposition must occur within the $q<1$ region. During pellet injection, the peak electron temperature drops by a large factor. But no evidence is found in JET for a low temperature front travelling faster than the pellet, in the plasma outside the sawtooth inversion region. However, when the pellet reaches this region very rapid (<50 μs) equalization of T_e occurs throughout the sawtooth inversion domain.

ELECTRON DENSITY PROFILE, $n_e(r)$

During pellet fueling there are three timescales to consider: (a) pellet ablation and penetration (<1ms), (b) inward transport of the ablated pellet material and peaking of the density profile (<500ms), (c) relaxation back to pre-pellet conditions (≥1s). Pellet ablation and penetration in JET have been modelled successfully using a modified neutral gas shielding model [1,2]. Immediately after ablation the density profile is hollow, fig.1a, the degree of hollowness depending on the penetration of the pellet, which in turn depends on the target plasma parameters. The density profile recovers to a peaked shape in ~200ms, with a central density 1.5 - 2 times larger than the pre-pellet value. Evolution to a peaked profile is discontinuous when sawteeth occur. Analysis of the density profile and its evolution for pellet fueled discharges has been made using a model of electron flux $\Gamma_e = -D\nabla n_e + Vn_e$. The diffusion coefficient $D(r)$ and the convection velocity $V(r)$ thus deduced are similar in magnitude to those for gas fueled discharges which showed a large scatter but no systematic dependence on $\bar{n}_e$, I_ϕ, B_ϕ or heating mode [3,4].

Analyses of individual pellet cases show that in the outer limiter configuration, V/D changes from $-0.2\ m^{-1}$ before pellet injection to $-0.4\ m^{-1}$ immediately after, reverting to $-0.2\ m^{-1}$ about 1s later, as evidenced by the more peaked density profile after pellet injection, which subsequently returns to its original form. In JET, significant peaking of the density profile does not take place unless pellet deposition within the $q<1$ region occurs. The peakedness of the density profile can be quantified by an effective minor radius, $r_e(t)$, of a torus of major radius R equal to that of the plasma column, and uniform density equal to the peak density $n_e(0,t)$, and containing the same total number of

electrons as in the plasma, $N_e(t)$, where

$$r_e(t) = (N_e(t)/n_e(0,t)\ 2\pi^2 R)^{1/2}.$$

Fig.2a shows how $r_e(t)$ (normalized to the pre-pellet value, $r_e(0)$) evolves after pellet injection, for three pellets penetrating to different distances r_p from plasma center. We see that the profiles take ~0.5s to reach maximum peakedness, minimum $r_e(t)/r_e(o)$, then return to the pre-pellet shape after another 0.5s. The minimum value of $r_e/r_e(o)$ (corresponding to maximum peakedness) is plotted against pellet penetration (deduced from X-ray camera observations) in fig.2b. The graph shows clearly that deeper the penetration, greater is the peakedness of the density profile. Also, significant peaking occurs only if the pellet penetrates beyond the sawtooth inversion radius r_c. For the discharges examined here $40 \leq r_c(cm) \leq 50$. The most peaked profiles obtained in JET, with $n_e(o)/\bar{n}_e \sim 2$ and $n_e(o) \sim 1.2 \times 10^{20}$ m^{-3}, have been observed in the magnetic separatrix configuration formed during single-null X-point operation. The target plasma conditions were such that the pellet penetrated to the center of the plasma, fig.1b.

ELECTRON TEMPERATURE PROFILE, $T_e(r)$

In Alcator-C [5] and TFR [6], the presence of a low temperature front propagating faster than the pellet, cooling the plasma ahead of the pellet, is inferred from high speed measurements of electron temperature at different plasma radii during pellet injection. The velocity of the cool front is deduced to be typically about twice that of the pellet. The observations have been interpreted as evidence of enhanced electron termal diffusivity, χ_e, and an increase of a factor ≥ 100 above the normal value has been deduced for OH plasmas. Further speculations about dependence of χ_e on the electron temperature profile have also been made [6]. Measurements of temperature front propagation in JET have been made using the 38 chord soft X-ray array that views the plasma diameter from above at the same toroidal location as the pellet flight path, and a 12 channel ECE array located 135° toroidally away from the pellet. Fig.3a is a plot of position (X-ray chord number) against time. The path of the pellet and the penetration depth are shown for three pulses, and the time at which the chord integrated X-ray signal starts to decrease, indicating cooling (corresponding to t_1 in [6]) is plotted. We see that at radii $r > r_c$ the signal starts to decay 10→50 μs before the pellet arrives, but there is no evidence of a cold front travelling much faster than the pellet (V~1 Km/s). When the pellet reaches the sawtooth inversion radius r_c, as determined from tomographic reconstruction of the X-ray data, immediately (<50 μs) the electron temperature over the whole central region decreases. Fig.3b shows a similar plot for a series of pulses with a higher value of q(a) such that the $q<1$ region is smaller. The same behaviour is seen again. The observations of figs.3a and 3b, which are based on chord integrated soft X-ray measurements, are confirmed by ECE measurements of local T_e. The extremely fast timescale of the profile collapse is comparable to that seen during the sawtooth collapse phase in JET, and implies a χ_e far in excess of the value determined by heat pulse propagation, $\chi_e \sim 2.5$ $m^2 . s^{-1}$ [7], for OH JET discharges. Thus there is evidence for enhanced χ_e inside the sawtooth inversion region, but not in the region $r > r_c$ as claimed elsewhere [6].

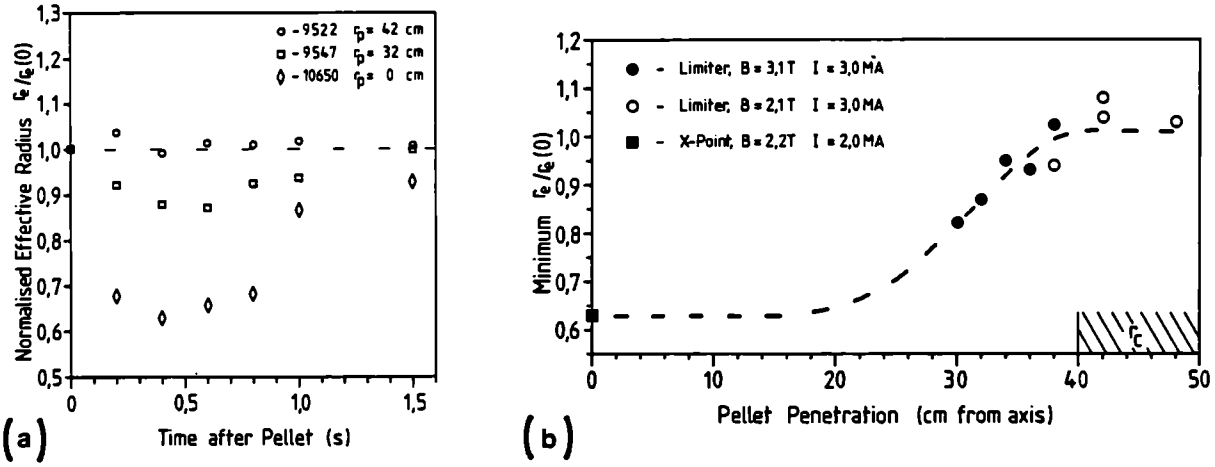

FIG 2: (a) $r_e(t)/r_e(0)$ for three different pulses.
(b) Minimum $r_e(t)/r_e(0)$ taken from (a), as a function of pellet penetration.

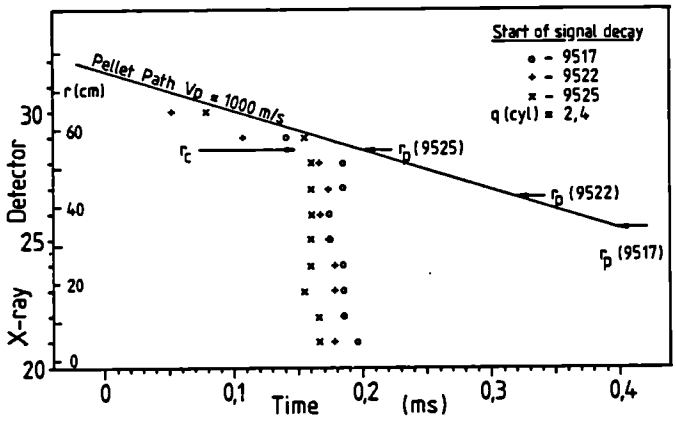

FIG 3:

X-ray detector (radial position) Vs. time, showing the pellet path and the start of the decay of the chord integrated X-ray flux for that detector.

(a) I_ϕ=3 MA, B_ϕ=2.1 T, q(cyl)=2.4
(b) I_ϕ=3 MA, B_ϕ=3.1 T, q(cyl)=3.5

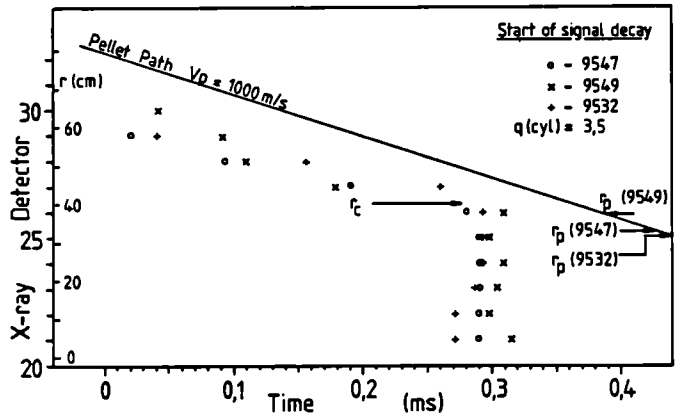

The duration of pellet ablation (<1 ms) is much shorter than the sawtooth period in JET (~100 ms). The pellets are injected randomly at different stages of the sawtooth cycle, from shot to shot. The anomalously high value of χ_e, however, is independent of the phase of the sawtooth with respect to pellet injection. The similarity between the enhanced central transport which is observed during pellet injection, and that seen at a sawtooth collapse suggests a common origin for the rapid thermal loss in the two processes. Furthermore, it underlines previous observations in JET that during sawtooth collapses, thermal transport can take place on a timescale much faster than that predicted if macroscopic magnetic reconnection were to occur and cause it [8].

REFERENCES

[1] A Gondhalekar et al., 11th IAEA Conference on Plasma Physics and Controlled Nuclear Research, Kyoto, Japan, 1986. Paper IAEA-CN-47/I-I-6.

[2] M L Watkins et al., "A Model for Pellet Ablation in JET". This conference.

[3] A Gondhalekar et al., Bull. Am. Phys. Soc., 30 (1985) 1525.

[4] A Cheetham et al., 13th European Conf. on Contr. Fusion and Plasma Physics, Schliersee 1986, Europhysics Conference Abstracts, 10c I (1986) 240.

[5] C Gomez et al., Bull. Am. Phys. Soc., 29(1984)1320.

[6] L Laurent et al., Plasma Physics and Controlled Fusion, 28, 1A (1986) 85.

[7] B J D Tubbing et al., "Heat pulse propagation in relation to the energy confinement in JET". This conference.

[8] D J Campbell et al., Nuclear Fusion, 26(1986)1085.

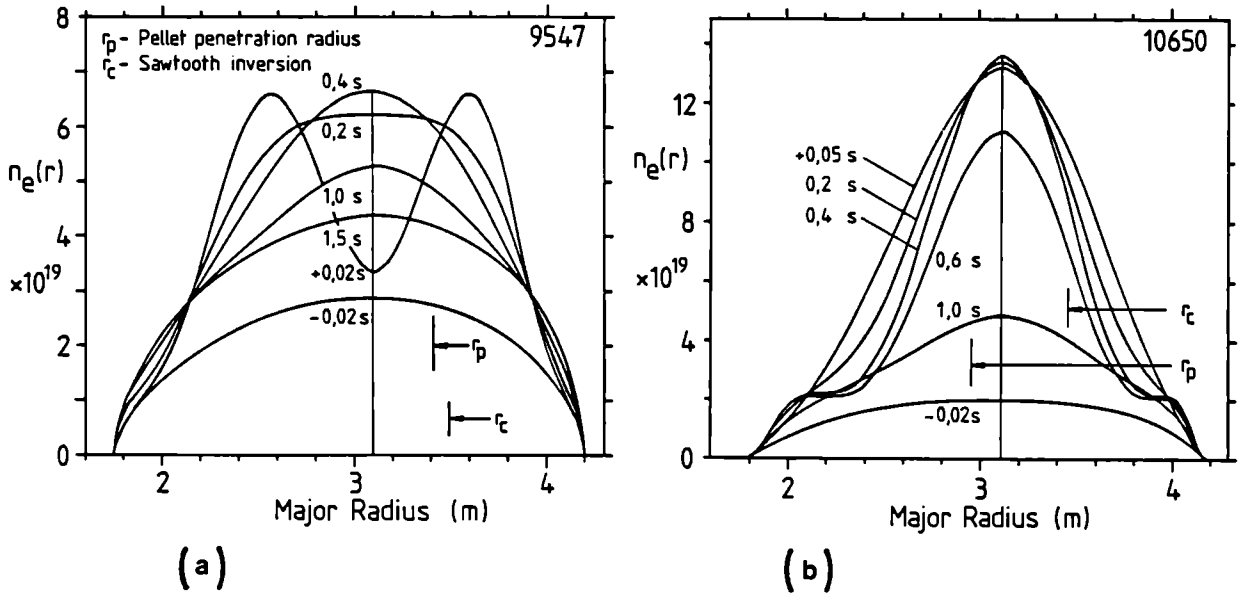

FIG 1: Temporal evolution of the density profile for 1.5s after pellet injection in (a) Limiter discharge, I_ϕ=3 MA, B_ϕ=3.1 T, q(cyl)=3.5; (b) X-point discharge, I_ϕ=2 MA, B_ϕ=2.2 T, q(cyl)=3.3

MOMENT APPROACH TO FLOWS, CURRENTS AND TRANSPORT IN AUXILIARY HEATED TOKAMAKS

Y. B. Kim[1,2], J. D. Callen[2] and H. Hamnén
JET Joint Undertaking, Abingdon, Oxon, OX14 3EA, UK.
[1]Culham Laboratory, UKAEA, Abingdon, Oxon, OX14 3DB, UK.
[2]University of Wisconsin, Madison, USA.

Introduction

In the most prominent auxiliary heating schemes for tokamaks (NBI and ICRF) the plasma is heated through collisional interaction of an anisotropic, but low density fast ion tail with the background plasma. In this paper the moment approach to neoclassical transport [1] is utilized to develop a unified theory of flows, currents and neoclassical cross-field transport induced by these fast ion tails. The fast ion distributions are calculated in the usual way for NBI [2,3] and ICRF [4]. The parallel components of the background $\vec{V}$, $\vec{q}$, etc. moment equations are solved in the next section to derive the parallel flows and an Ohm's law that includes the neoclassical electrical conductivity (Spitzer plus trapped-particle effects), the bootstrap current, and the fast ion currents [5], including trapped-particle effects. The parallel flows also determine the parallel viscous forces [1] and result in neoclassical transport. The additional radial transport fluxes induced by the fast ion momentum and heat flow inputs are calculated next. They are similar to those derived previously for NBI[2,3], but more accurate and complete. The magnitudes of these additional transport fluxes are compared with the usual transport fluxes and estimated for the upcoming high power heating experiments in JET. The final section summarizes the results obtained.

Modified Ohm's Law

$\langle \vec{B}\cdot \int d\vec{v} m_a \vec{v} L_j^{3/2} \rangle$ moments of the background Kinetic equation for j=0,1 yield the flux-surface-averaged parallel momentum balance equation and the heat flux balance equation. At equilibrium, they become

$$\begin{bmatrix} \langle \vec{B}\cdot\nabla\cdot\underline{\underline{\Pi}}_a \rangle \\ \langle \vec{B}\cdot\nabla\cdot\underline{\underline{\Theta}}_a \rangle \end{bmatrix} = \begin{bmatrix} \langle \vec{B}\cdot\vec{F}_{a1} \rangle \\ \langle \vec{B}\cdot\vec{F}_{a2} \rangle \end{bmatrix} + \begin{bmatrix} \langle \vec{B}\cdot\vec{F}_{af1} \rangle + n_a e_a \langle \vec{B}\cdot\vec{E} \rangle \\ \langle \vec{B}\cdot\vec{F}_{af2} \rangle \end{bmatrix} \qquad (1)$$

where $\vec{F}_{af1}$ and $\vec{F}_{af2}$ are momentum and heat flux inputs due to fast ion respectively. Now we use the constitutive relations for the parallel viscous stresses in terms of poloidal flows and the friction-flow relations for the parallel friction vectors in terms of parallel flows to obtain a closed set of matrix equations for the flux surface averaged parallel flows (or the poloidal flows) [1]

$$\frac{n_a m_a}{\tau_{aa}} [\mu^a] \begin{bmatrix} u_{\theta a} \langle B^2 \rangle \\ \dfrac{2 q_{\theta a}}{5 P_a} \langle B^2 \rangle \end{bmatrix} = \frac{n_a m_a}{\tau_{aa}} [\nu^a] \begin{bmatrix} \langle (V_{\parallel e} - V_{\parallel i}) B \rangle \\ \dfrac{2}{5 P_a} \langle q_{\parallel a} B \rangle \end{bmatrix} + \begin{bmatrix} \langle \vec{B}\cdot\vec{F}_{af1} \rangle + n_a e_a \langle \vec{B}\cdot\vec{E} \rangle \\ \langle \vec{B}\cdot\vec{F}_{af2} \rangle \end{bmatrix} \qquad (2)$$

where $[\mu]$ and $[\nu]$ are the dimensionless viscosity matrix and friction matrix respectively.

The Onsager symmetry between the Ware flux and the bootstrap current transport coefficients can be seen directly from Eqs. (4) and (7) since the $[\nu^e]$ and $[\mu^e]$ matrices are symmetric. If we focus our attention on the large aspect ratio limit (but in all collisionality regimes), the additional fluxes $\Delta\Gamma$ and Δq are written as follows

$$\begin{bmatrix} \Delta\Gamma_{re} \\ \dfrac{\Delta q_{re}}{T_e} \end{bmatrix} = \begin{bmatrix} \mu_1^e \\ \mu_2^e \end{bmatrix} \frac{Z_f^2}{Z^2} \frac{m_e c n_f V_{\|f} \nu_e}{eB_p} \tag{8}$$

In the banana regime $\Delta\Gamma_e$ agrees well with the previous kinetic calculation [3]. The ion particle flux $\Delta\Gamma_i$ satisfies the ambipolarity condition $Z_i\Delta\Gamma_i = \Delta\Gamma_e$ and the additional ion heat flux is $\Delta q_i/T_i = (\mu_2^i/\mu_1^i)\Delta\Gamma_i$

Conclusions and Discussions

The moment approach is used to develop a unified theory of flows, currents and neoclassical cross-field transport in auxiliary heated tokamaks. A 2x2 matrix approximation gives very good agreement with previous kinetic and numerical calculations. For the upcoming high power NBI heating (20 MW) experiments in JET (D^+/T^+ plasma with tangential D^o injection, $n_e \sim 0.5\times10^{14}cm^{-3}$, $T_e \sim 5keV$, $E_{bo} \sim 80keV$, $Z \sim 2$) the estimated beam driven current is about 1MA. The additional particle transport and the electron heat transport induced by the fast ion tails are comparable to the usual fluxes ($\Delta\Gamma/\Gamma \equiv \Delta q_e/q_e \sim 1$) for $n_f V_{\|f}/n_e V_{Te} \sim 10^{-3}$ and $\rho_{\theta e}/a \sim 10^{-3}$. However, it is very unlikely to see these additional fluxes since the particle diffusion and the electron heat diffusion are anomalously higher than neoclassical values. Fast ion tails have negligible effect on the ion heat transport in JET($\Delta q_i/q_i \sim 10^{-2}$).

Acknowledgement

Two of the authors gratefully acknowledge the hospitality of Culham (Y.B.K.) and JET(J.D.C.). This work is partially supported by the U.S. Department of Energy through Grant No. DE-FG02-86ER53218.

Table 1. - Values of A(Z) given by Eq.(6)

	Z=1	1.2	2.0	4.0	8.0
Eq.(6)	1.642	1.545	1.343	1.182	1.094
From Ref.[7]	1.667	1.563	1.349	1.180	1.092

References

[1] S.P.Hirshman and D.J.Sigmar, Nuclear Fusion 21, 1079 (1981)
[2] J.D.Callen et al., in Plasma Phys. and Cont. Nuc. Fus. Research (Proc. 5th Int. Conf. Tokyo, 1974) 1, IAEA, Vienna 645 (1975)
[3] J.W.Connor and J.G.Cordey, Nuclear Fusion 14, 185 (1974)
[4] D. Anderson et al., JET Report (86) 09
[5] J.G.Cordey et al., Plasma Physics 24, 73 (1982)
[6] S.P.Hirshman and D.J.Sigmar, Phys. Fluids 20, 418 (1977)
[7] D.F.H.Start et al., Plasma Physics 22, 303 (1980)

Explicit expressions for the matrix elements [1] are given as follows:

$$[\nu^a]=\begin{bmatrix} -\ell_{11}^a & \ell_{12}^a \\ \ell_{21}^a & -\ell_{22}^a \end{bmatrix} \text{ with } \begin{cases} \ell_{11}^e=Z, \ \ell_{12}^e=\ell_{21}^e=\frac{3}{2}Z, \ \ell_{22}^e=\sqrt{2}+\frac{13}{4}Z \\ \ell_{11}^i=-Z, \ \ell_{12}^i=-\frac{3}{2}Z, \ \ell_{21}^i=0, \ \ell_{22}^i=\sqrt{2} \end{cases}$$

The above friction matrix is valid regardless of collisionality regime and the viscosity matrix which is valid in all collisionality regime is given in Ref. [6]. In the banana regime the viscosity matrix is given explicitly as follows,

$$[\mu^a]=\begin{bmatrix} \mu_1^a & \mu_2^a \\ \mu_2^a & \mu_3^a \end{bmatrix} \text{ with } \begin{cases} \mu_1^e = f_t f_c^{-1} \{Z+\sqrt{2}-\ell n(1+\sqrt{2})\} \\ \mu_2^e = f_t f_c^{-1} \{-3Z/2-4/\sqrt{2}+5\ell n(1+\sqrt{2})/2\} \\ \mu_3^e = f_t f_c^{-1} \{13Z/4+39/4\sqrt{2}-25\ell n(1+\sqrt{2})/4\} \end{cases}$$

where $f_c=1-f_t=\frac{3}{4}\langle B^2\rangle\int_0^{B_m^{-1}} \lambda d\lambda \langle(1-\lambda B)^{1/2}\rangle^{-1}\cong 1-1.46\sqrt{\varepsilon}$ and μ^i can be obtained from μ^e by substituting 0 for Z.

The parallel, poloidal and perpendicular flows are related through geometric relations in an axisymmetric system as follows

$$\begin{bmatrix} \langle V_\parallel B\rangle \\ \frac{2}{5P_a}\langle q_{\parallel a} B\rangle \end{bmatrix} = \begin{bmatrix} u_{\theta a}\langle B^2\rangle \\ \frac{2q_{\theta a}}{5P_a}\langle B^2\rangle \end{bmatrix} - \frac{cIT_a}{e_a}\begin{bmatrix} \frac{\partial}{\partial\psi}\ell nP_a + \frac{e_a}{T_a}\frac{\partial}{\partial\psi}\Phi_o \\ \frac{\partial}{\partial\psi}\ell nT_a \end{bmatrix} \tag{3}$$

Eqs. (2) and (3) can be solved together to obtain the parallel transport fluxes in terms of all thermodynamic forces

$$\begin{bmatrix} -\frac{1}{n_e e}\langle J_\parallel B\rangle \\ \frac{2}{5P_e}\langle q_{\parallel e} B\rangle \end{bmatrix} = [\mu^e-\nu^e]^{-1}[\mu^e]\begin{bmatrix} \frac{cIT_e}{e}A_p - u_{\theta i}\langle B^2\rangle \\ \frac{cIT_e}{e}A_{Te} \end{bmatrix} + \frac{\tau_{ee}}{n_e m_e}[\mu^e-\nu^e]^{-1}\begin{bmatrix} \langle\vec{B}\cdot\vec{F}_{ef1}\rangle - n_e e\langle\vec{B}\cdot\vec{E}\rangle \\ \langle\vec{B}\cdot\vec{F}_{ef2}\rangle \end{bmatrix}$$

where $A_p=\frac{\partial}{\partial\psi}\ell nP_e+\frac{T_i}{Z_i T}\frac{\partial}{\partial\psi}\ell nP_i$ and $A_{Ta}=\frac{\partial}{\partial\psi}\ell nT_a$ (4)

The first term on the right side is the bootstrap current and the second term is the current driven by the applied electric field and the fast ion tails. Eq. (4) is valid for all collisionality regimes and axisymmetric geometries of arbitrary cross section. So we have obtained the detailed expression for the surface-averaged total current in auxiliary heated tokamaks,

$$\langle J_\parallel B\rangle_{total}=\langle J_\parallel B\rangle_B+\langle J_\parallel B\rangle_E+\langle J_\parallel B\rangle_f+\langle J_\parallel B\rangle_H$$

where $\langle J_\parallel B\rangle_B = -cIP_e(L^e_{31}A_p + L^e_{32}A_{Te} + L^i_{32}A_{Ti})$, $\langle J_\parallel B\rangle_E = \sigma_{NC}\langle \vec{B}\cdot\vec{E}\rangle = \frac{n_e e^2}{m_e \nu_e}\Lambda_o^{NC}\langle \vec{B}\cdot\vec{E}\rangle$

$$\langle J_\parallel B\rangle_f = n_f e_f \langle \vec{B}\cdot\vec{V}_f\rangle \ , \quad \langle J_\parallel B\rangle_H = -\frac{e}{m_e\nu_e}\{\Lambda_o^{NC}\langle \vec{B}\cdot\vec{F}_{ef1}\rangle + \Lambda_1^{NC}\langle \vec{B}\cdot\vec{F}_{ef2}\rangle\}$$

where $\langle J_\parallel B\rangle_B$ is the bootstrap current, $\langle J_\parallel B\rangle_E$ the neoclassical Spitzer current, $\langle J_\parallel B\rangle_f$ the current of fast ions and $\langle J_\parallel B\rangle_H$ the background neoclassical current driven by fast ion tails. Each transport coefficients are written explicitly in terms of 2x2 matrix elements as follows:

$$L^e_{31} = \{\mu^e_1(\mu^e_3+\ell^e_{22}) + \mu^e_2(\ell^e_{12}-\mu^e_2)\}/D \ , \quad L^e_{32} = (\mu^e_2\ell^e_{22} + \mu^e_3\ell^e_{12})/D$$

$$L^i_{32} = L^e_{31}\cdot\ell^i_{22}\mu^i_2/\{\mu^i_1(\ell^i_{22}+\mu^i_3) - (\mu^i_2)^2\}, \quad \Lambda_o^{NC} = Z(\mu^e_3+\ell^e_{22})/D, \quad \Lambda_1^{NC} = Z(\ell^e_{12}-\mu^e_2)/D$$

with $D = (\mu^e_1+\ell^e_{11})(\mu^e_3+\ell^e_{22}) - (\mu^e_2-\ell^e_{12})^2$

Note that in the limit that μ goes to zero, which is the case for a collisional limit or in a straight tokamak, the bootstrap current disappears and the rest of currents assume their classical forms. If we focus our attention on the current driven by NBI in the banana regime large aspect ratio limit with $V_{bo} \ll V_{Te}$, we obtain

$$\langle J_\parallel B\rangle_{NBI} = n_b e_b \langle V_{\parallel b} B\rangle \left\{1 - \frac{Z_b}{Z} + \frac{f_t}{f_c}\frac{Z_b}{Z}A(Z)\right\}, \quad A(Z) = \frac{Z^2+2.21Z+0.75}{Z(Z+1.41)} \qquad (5)$$

in which the term $-Z_b/Z$ is the classical response of background plasma (no trapping) and the term with $A(Z)$ is the neoclassical correction with trapped particle effect. In table 1, Eq.(5) is compared with the previous numerical result [7], which shows good agreement.

Neoclassical Cross-Field Transport

Eqs. (3) and (4) can be solved explicitly for poloidal flows which are directly related to neoclassical cross-field particle flux $\Gamma_{\psi a} = \langle \vec{\Gamma}_a\cdot\nabla\psi\rangle$ and heat flux $q_{\psi a} = \langle \vec{q}_a\cdot\nabla\psi\rangle$

$$\begin{bmatrix}\Gamma_{\psi a}\\ q_{\psi a}\\ \hline T_a\end{bmatrix} = -\frac{cI}{q_a\langle B^2\rangle}\begin{bmatrix}\langle \vec{B}\cdot\nabla\cdot\underline{\underline{\Pi}}_a\rangle\\ \\ \langle \vec{B}\cdot\nabla\cdot\underline{\underline{\Theta}}_a\rangle\end{bmatrix} = -\frac{cI}{q_a\langle B^2\rangle}\frac{n_a m_a}{\tau_{aa}}[\mu^a]\begin{bmatrix}u_{\theta a}\langle B^2\rangle\\ 2q_{\theta a}\langle B^2\rangle\\ \hline 5P_a\end{bmatrix} \qquad (6)$$

Straightforward matrix manipulation of Eq.(2) for electrons and ions gives the additional fluxes due to the fast ion momentum and heat flux inputs.

$$\begin{bmatrix}\Delta\Gamma_{re}\\ \Delta q_{re}\\ \hline T_e\end{bmatrix} = \frac{n_e c B_T}{B_p\langle B^2\rangle}[\mu^e][\mu^e-\nu^e]^{-1}\begin{bmatrix}\frac{1}{n_e e}\langle \vec{B}\cdot\vec{F}_{ef1}\rangle\\ \frac{1}{n_e e}\langle \vec{B}\cdot\vec{F}_{ef2}\rangle\end{bmatrix} \qquad (7)$$

MODE LOCKING IN TOKAMAKS

M.F.F. Nave and J.A. Wesson

JET Joint Undertaking, Abingdon, Oxon. OX14 3EA, UK.

1. Introduction

In tokamaks the growth of tearing modes with their associated magnetic islands leads to helical magnetic field perturbations, $\tilde{B}$, outside the plasma. These perturbations are observed to rotate with a frequency typically ~1-10kHz. Thus at an external conductor these magnetic perturbations are oscillatory and the induced electric fields produce fluctuating currents, $\tilde{j}$. The field penetration is small at high frequencies but increases with decreasing frequency.

The induced currents give rise to a force $\tilde{j}\times\tilde{B}$ in the conductor. Similar $\tilde{j}\times\tilde{B}$ forces arise in the plasma and the result is a transfer of momentum from the plasma to the conductor. This causes a slowing of the plasma and a reduction in the frequency. This leads in turn to an increased penetration of the fields into the conductor and to a strengthening of the interaction. The consequence is an increasingly rapid transfer of momentum from the plasma, which finally brings the magnetic islands to rest. This phenomenon is observed in tokamaks and is called mode-locking.

The following sections describe a theoretical model for a plasma with a resistive shell and give analytic and numerical solutions.

2. Theoretical Model

For a large aspect-ratio tokamak the equation governing the magnetic perturbations due to a tearing mode is [1]

$$\frac{1}{r}\frac{d}{dr}\,r\,\frac{d\psi}{dr} - \frac{m^2}{r^2}\,\psi - \frac{dj/dr}{B_\theta(1 - nq/m)}\,\psi = 0 \qquad (1)$$

where ψ is the helical flux function with $\tilde{B}_r = (1/r)\partial\psi/\partial\theta$ and $\tilde{B}_\theta = -\partial\psi/\partial r$. The solutions of this equation give the growth of the magnetic island through [2]

$$\frac{dw}{dt} = \frac{\eta}{\mu_o}\,\Delta'(w) \qquad \text{where} \qquad \Delta'(w) = \psi'\Big|_{r_s-w/2}^{r_s+w/2} \Big/ \psi(r_s), \qquad (2)$$

η is the resistivity at the resonant surface r_s, and the island width w is related to the magnetic perturbation through

$$w = 4(q|\psi|/q'B_\theta)^{1/2}_{r=r_s} \qquad (3)$$

where q is the safety factor.

In the presence of a thin resistive shell of radius d, thickness δ and conductivity σ, the boundary condition for equation (1) at the surface of the plasma is

$$\frac{\psi'}{\psi} = -\frac{m}{a}\,\frac{1 + f(a/d)^{2m}}{1 - f(a/d)^{2m}} \qquad \text{where} \quad f = \frac{1}{1 + (im/\omega\tau)} \qquad (4)$$

ω being the frequency, and $\tau(=\mu_o\sigma d\delta/2)$ being the characteristic resistive time constant of the shell. For $\omega\tau\to\infty$, f=1 and for $\omega\tau\to 0$, f=0.

The force on the plasma due to the perturbations causes an acceleration which changes the frequency seen by the wall. The precise way in which

this occurs depends on the details of the plasma response. For purposes of illustration it is assumed that the plasma moves "rigidly". The change in the observed frequency is then given by the equation

$$\frac{d\omega}{dt} = \frac{m\int F_\theta r dV}{\int \rho r^2 dV} + \frac{n\int F_\phi dV}{R\int \rho dV} \tag{5}$$

where F_θ and F_ϕ are the poloidal and toroidal components of the force perpendicular to the perturbation helix, given by

$$F = \bar{J}\bar{B}_r = \frac{1}{\mu_o}\nabla^2\psi \frac{1}{r}\frac{\partial\psi}{\partial\theta}. \tag{6}$$

Substitution of equation (6) into equation (5) leads to

$$\frac{d\omega}{dt} = \frac{aJ}{2\mu_o} \mathrm{Im}(\psi^*\psi')_{r=a} \qquad \text{where} \quad J = \frac{m^2}{\int \rho r^3 dr} + \frac{n^2}{R^2\int \rho r dr}. \tag{7}$$

The first term in J is much larger than the second but it is possible that in some circumstances the poloidal motion is prevented by damping. In this case the first term in J is removed.

The complete time evolution is now described by equations (1)-(4) and (7), and solutions are described in the following two sections.

3. Analytic Approximations for Mode Locking

The island growth is given by equation (2) and using the approximation

$$\Delta'(w) = \Delta'(0)(1 - w/w_s)$$

where w_s is the saturated island size the solution is

$$w = w_s(1 - \exp(-t/\tau_I)) \qquad \text{where} \quad \tau_I = \mu_o w_s/n\Delta'(0) \tag{8}$$

To calculate the time development of the frequency we consider the case where the resistive shell is at the surface of the plasma, that is b=a. Then, using equations (3),(4) and (7) we obtain

$$\frac{d\omega}{dt} = -c\frac{1}{\tau_A^2}\frac{\omega\tau}{\omega^2\tau^2 + m^2}\left(\frac{w}{a}\right)^4 \tag{9}$$

where $$c = \frac{m^2}{256}\left(\frac{r_s}{a}\right)^{2m}\left(\frac{aq'}{q}\right)^2_{r_s} g \qquad \text{and} \quad \tau_A^2 = \mu_o/Ja^2B_\theta^2(r_s)$$

g is a numerical factor of O(1) depending on the particular equilibrium and varying with ω. To avoid complexity and to illustrate the basic behaviour we shall regard g as a constant.

In the case where locking occurs before saturation, the solution for w given by equation (8) can be expanded to give

$$w = w_s t/\tau_I$$

and the solution of equation (9) is then

$$(\omega_o^2 - \omega^2)\tau^2 - 2m^2 \ell n \frac{\omega}{\omega_o} = \alpha \frac{\tau\, t^5}{\tau_A^2 \tau_I^4} \tag{10}$$

where $$\alpha = \tfrac{2}{5}c(w_s/a)^4$$

Equations (8) and (10) show the basic features of mode-locking. The island grows to saturation on a timescale determined by the resistivity of the plasma and the strength of the instability. The frequency change described by equation (10) occurs in two phases. In the first phase the first term on the left dominates. During this phase the t^5 dependence means that the change in frequency is slow initially but becomes

increasingly rapid after a time characterised by

$$\tau_1 = \left(\omega_o^2 \tau\ \tau_A^2\ \tau_I^4/\alpha\right)^{1/5}.$$

In the final phase of the locking the second term in equation (10) dominates and the residual frequency decays as $\exp-(t/\tau_d)^5$ with

$$\tau_d = \left(2m^2\tau^{-1}\ \tau_A^2\ \tau_I^4/\alpha\right)^{1/5}$$

4. Numerical Solutions

Numerical calculations have been carried out to obtain solutions of the equations given in section 2, to illustrate the interaction of tearing modes with a resistive shell.

Figure 1 gives the saturated island width for an m=2 tearing mode as a function of $\omega\tau$. The current profiles are taken to have the form $j=j_o(1-(r^2/a^2))^\nu$ with $q_o=0.8$, and the resistive shell is at the surface of the plasma. For $q_a \geq 4$ ($r_s/a \leq 0.7$), the resonant surface is sufficiently far from the shell that the stabilising effect of high frequency is negligible. The reason, of course, is that even a perfectly conducting shell is ineffective in such cases. For lower q_a, the resonance is closer to the shell and the effect of high frequencies is more marked. For $q_a<2.75$ ($r_s/a > 0.85$), the change from zero frequency to high frequency completely stabilises the mode.

Figure 2 shows the results of two time-dependent calculations of mode-locking, both for the m=2 mode. The plasma has a=1.0m and $q_o=1.0$. The initial frequency $\omega=2000\ s^{-1}$ and $\tau=5$ms. The first calculation is for $q_a=4.0$. The island saturates at w=16cms, but the mode locking occurs for $w \simeq 2$cm. The magnetic signal, $\hat{B}_\theta$, grows initially in response to the growing instability. It reaches a maximum and begins to fall when the coupling to the wall starts to reduce the frequency (since $\hat{B}=\omega\bar{B}$). The increased amplitude then strengthens the deceleration and the frequency ω is finally reduced to zero with a strong exponential decay. This is the mode lock.

The results of the second calculation are shown in Fig. 2(b). This case has $q_a=2.25$ and consequently the resonance is close to the conducting shell ($r_s/=0.94$). As a result the shell has a stabilising influence at high frequencies. This is clearly seen on the graph of the island width where an abrupt increase in the growth rate occurs when the shell loses its stabilising effect at the onset of the mode-locking.

5. Summary

A theoretical model of mode-locking through the effect of a resistive shell has been described. This model has been used to obtain both analytic and numerical solutions. At high frequencies the resistive shell behaves like a perfect conductor, but generally this does not prevent the growth of tearing modes. As the magnetic island grows there is a transfer of momentum between the plasma and the shell which reduces the frequency. This allows further penetration of the oscillating magnetic field into the shell. The reduction in frequency and the increased penetration each enhance the other, leading finally to a complete locking of the mode.

Acknowledgement

The authors would like to thank Dr E. Lazzaro for helpful discussions.

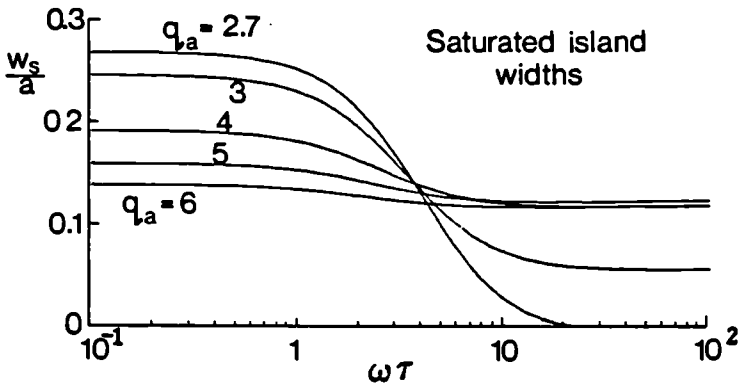

Fig.1 Graphs of saturated m=2 island width, w_s, against $\omega\tau$ for different values of q_a.

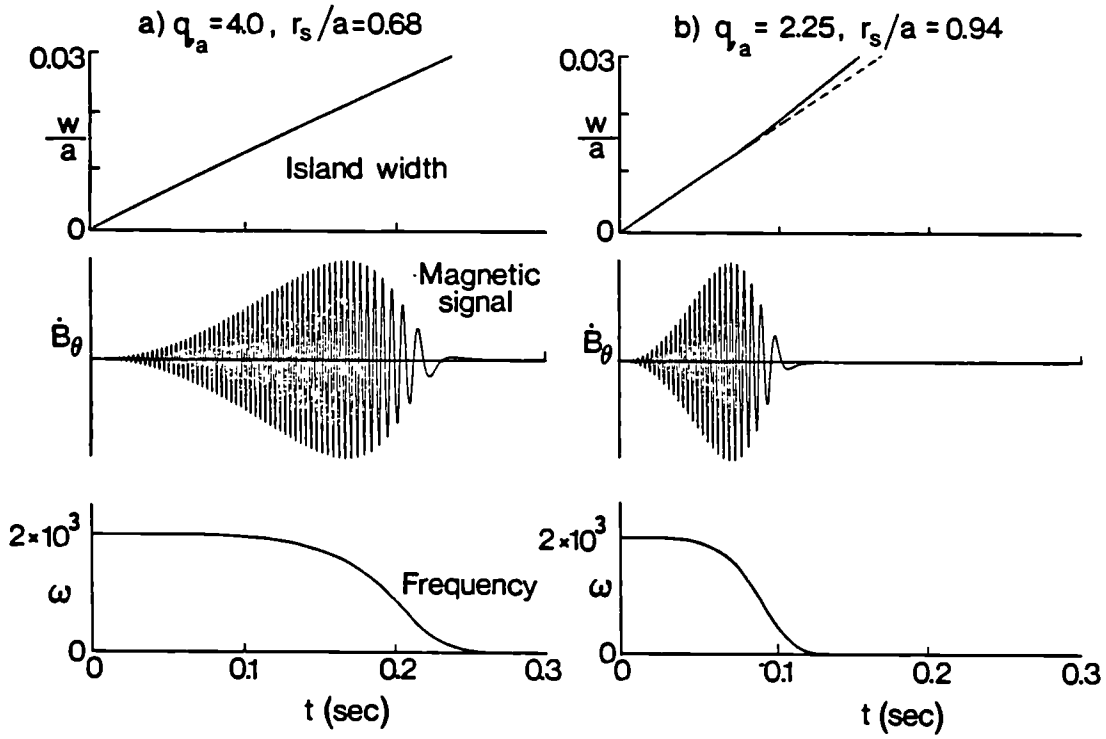

Fig.2 Mode-locking for two values of q_a. Graphs show the time development of the island width w, the magnetic signal $\dot{B}_\theta$ and the frequency ω.

References

[1] Wesson, J.A. Nuc. Fus. 18, 87 (1978).

[2] White, R.B. et al. Phys. Fluids 20, 800 (1977).

HEAT TRANSPORT IN JET

M. Brusati, A. Galway, H. Hamnén, F. Rimini, T. Stringer

JET Joint Undertaking, Abingdon, Oxon, OX14 3EA, UK

Introduction - A number of JET pulses, representative of the different regimes of operation, have been analysed using the 1½-D time dependent JET transport analysis code, JICS. This evaluates the components of the electron and ion energy equations in flux surface coordinates, using as input the experimental profiles of electron density and temperature, and the effective Z from Bremsstrahlung; the ion cyclotron (ICRH) and neutral beam injection (NBI) power deposition profiles are computed from ray tracing and pencil beam codes respectively.

When the bulk ion velocity distribution is thermal, its temperature profile is obtained from the neutral particle analyser (NPA) diagnostic, and the local ion diffusivity χ_i is then calculated directly from energy balance. In general χ_i is found to follow a radial scaling well approximated by $\chi_i \sim 1/n_e$, substantially different from the neoclassical value. When the majority ions have a high energy tail due to neutral beam slowing down, the central value of the ion temperature is provided by X-ray crystal and/or charge-exchange recombination spectroscopy. The profile is then evaluated assuming $\chi_i \sim \alpha/n_e$, and adjusting its absolute magnitude iteratively to produce satisfactory agreement between the resulting total stored plasma energy and the stored energy measured by the diamagnetic loop.

Of the OH and ICRH pulses only those for which the NPA ion temperature profile is available have been analysed. The philosophy was to concentrate on a limited number of pulses which are fully diagnosed, rather than including a large number of incompletely diagnosed ones. Because of the limited number of pulses the conclusions reached are preliminary.

Results - We have explained ohmic NB heated plasmas with inner wall limiter, SN X-point (L,H mode), and plasmas with on and off axis ICRF heating.

The temperature profiles show a fair degree of "profile consistency". In Fig.1 $T_e^{-1} \cdot dT_e/dr$, measured at 60% of the plasma radius, is plotted against the input power to the electron, divided by the electron density, for a number of additionally heated plasmas. The temperature gradient was extracted from the ECE data without smoothing, and so is sensitive to small random variations in T_e.

The ion and electron heat loss rates are found to be comparable in all cases. The electron thermal diffusivity, evaluated at radii where transport dominates the balance, scales linearly with the input power/particle up to $P/n \sim 1.5\times10^{-19} Wm^3/10^{19}$, with no evident scaling with plasma current or magnetic field. This result was already obtained analysing JET ohmic plasmas [1].

In Fig.2 the electron and ion diffusivities χ_e, χ_i are plotted versus P/n. The ion values are related to regimes where the ion temperature profile is available experimentally. The ion diffusivity shows no correlation with neoclassical theory, as found also by Bracco et al [2]. It is almost an order of magnitude larger and its radial variation and parameter scaling appear to be different (Fig.3).

The behaviour of χ_e and $T_e^{-1} \cdot dT_e/dr$ leads naturally to the electron con-

finement time degradation. The local rate of change of the electron stored energy is small compared with the other terms in the electron balance but it is a substantial fraction of the total in the ion case.

A consequence of the electron and ion response to heating is that preferential heating is lost mostly via the species which is heated directly. This is shown in Fig.4 where the ratio of ion to electron flux losses is plotted against the ratio of ion to electron input power. The initial slope (~.6) indicates that with preferential electron heating (Ohmic and ICRF) and preferential ion heating up to 70% of the input power coupled directly to the ions, ~30% of the power is exchanged between electrons and ions, as a result of variations in temperature differences balancing the variations in density. At highly selective ion heating the ratio of ion to electron losses saturates at $\sim 1+(\nu_{ei}\tau_E)^{-1}$, where ν_{ei} is the electron-ion coupling rate and τ_E the plasma energy confinement time.

The availability in JET of different heating schemes (NBI, ICRF) and scenarios (H, D injection up to 80keV/H, 160keV/D, on and off axis (H, H^3) minority heating and mode conversion) allows a wide variation of power deposition profiles. It is found experimentally that the electron temperature response to different heating profiles is much faster (<20ms) than diffusion time scales would predict (~.3s). Similar effects have been observed in JET pellet injection experiments, where the cooling induced by the pellet propagates rapidly to the plasma inside the ablation radius ($r_{ab}\sim r_q=1$) [3]. Confinement degradation is observed where the coupled power can be dissipated through effective radial diffusion due to temperature and density gradients. This is the case of NBI heating and ICRF on axis heating, where the degradation of confinement with power is uniform across radius.

The fast, non diffusive response of the electron temperature profile to localised power deposition leads to improvement in confinement in the plasma core during ICRF off axis heating; the global confinement still degrades.

In both cases the degradation is well described by an offset linear dependence of the plasma energy on the input power ($\tau_{inc}\sim .2s$). This fact is consistent with the behaviour shown above and can be explained by a transport mechanism based on the critical temperature gradient model [4].

Comparison with Theory - Within the mixing radius, typically 0.5m to 0.6m in low q JET pulses, energy transport is generally dominated by sawtooth relaxations, which periodically flatten the temperature and density profiles. In the edge plasma, typically r<1.2m, radiation may dominate the energy transport. To explain the anomalous transport between these radii, several different instabilities have been proposed. The most commonly invoked are the dissipative trapped electron mode (DTEM), the ion temperature gradient mode, and the η_e mode [5].

In Fig.5 the theoretically predicted electron thermal diffusivity for the DTEM [6] is plotted against the experimental local diffusivity derived by JICS. The prediction is for the collisional or the collisionless forms of the DTEM, whichever is appropriate for the experimental parameters. The predicted values tend to be higher than those measured, by about an order of magnitude. The predicted diffusivity should include an undetermined numerical factor, arising from uncertainty in the saturated fluctuation amplitude. This factor, which is set to unity in Fig.5, could possibly explain the discrepancy in magnitude. However, the lack of any correlation between the predicted and experimental diffusivities is more difficult to explain and supports the earlier conclusion [7] that the DTEM is not the main source of

anomalous transport in JET pulses. A similar comparison, using the predicted thermal diffusivity for the η_e mode [5], again showed no correlation.

The ion temperature gradient mode is frequently referred to as the η_i mode, because it becomes unstable only when $\eta_i = d\ell nT_i/d\ell nn_i$ exceeds a critical value. The anomalous transport predicted for this mode is large, larger even than for the DTEM. This has led to the expectation that this high anomalous transport will prevent η_i from exceeding its critical value by much. Because of its complex dependence on plasma parameters, in prediction codes the critical value is commonly taken to be 1.5, a mean value. The threshold has been recently found to increase linearly with $\varepsilon_n = n/(R\, dn/dr)$ when $\varepsilon_n < 0.3$ [8]. Fig.6 shows the ratio of the measured η_i to Romanelli's predicted threshold, as a function of radius. While the correlation is far from convincing, it is not inconsistent with a rapid increase in diffusivity when η_i exceeds the threshold, bearing in mind the error bars on the measured η_i.

Another clue to the local transport process is given by the JET "monster sawteeth" [9]. During the sawtooth rise phase, the central temperature rises almost adiabatically, with small transport losses. The sawtooth rise is then abruptly terminated by a sharp "knee". This is consistent with a strong loss process which is switched on when the local temperature gradient exceeds a threshold value [4].

It should be pointed out that the JET pulses used for comparison with theory are mostly additionally heated. Publications which found experimental evidence for DTEM transport [6,10] also concluded that the η_i mode provides the dominant loss mechanism when η_i exceeds its threshold. It appears from Fig.6 that additionally heated plasmas in JET generally do exceed this threshold, which may be why no evidence for the DTEM is seen.

Conclusions - A number of representative JET pulses have been studied from the point of view of local transport properties. Based on this preliminary study, it appears that: i) The electron and ion loss channels are of comparable importance. ii) The ion thermal diffusivity does not appear to be neoclassical, either in magnitude, radial scaling or parameter dependence. iii) The temperature profile shapes are rather independent of heating method and location. Changing the heating profile alters the thermal diffusivity profile so as to maintain the same temperature profiles. The change in the diffusivity profile occurs on a timescale much faster than would be expected from the energy confinement timescale. iv) The thermal diffusivities show no obvious correlation with prediction for either the dissipative trapped electron mode or the η_e-mode. A correlation may exist between the measured η_i and the predicted critical value for the η_i mode.

References

[1] M. Brusati, G. Cordey, 12th Proc. EPS Conf. Budapest I (1985) 34.

[2] G. Bracco, et al, this conference (1987).

[3] A.D. Cheetham et al, this conference.

[4] P.H. Rebut, et al, this conference.

[5] P.N. Guydar, et al, Phys. Rev. Lett. 57 (1986) 2818.

[6] R.E. Waltz et al, 11th IAEA Conf. Kyoto, paper A-VI-1-3 (1986).

[7] D.F. Düchs, et al, ibid, paper A-VI-1-1 (1986).

[8] F. Romanelli, to be published.

[9] D.J. Campbell, et al, this conference.

[10] F. Romanelli, W.M. Tang and R.B. White, Nucl. Fusion 26 (1986) 1515.

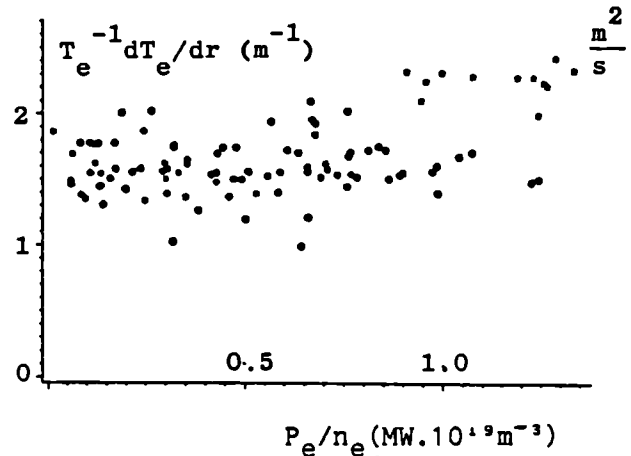

Fig.1 $T_e^{-1}dT_e/dr$ at r=.6a vs input power/electron

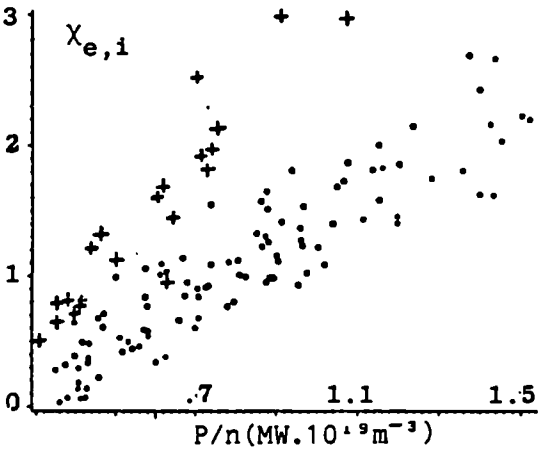

Fig.2 $\chi_e(\cdot)$, $\chi_i(+)$ at r=.6a vs input power/particle

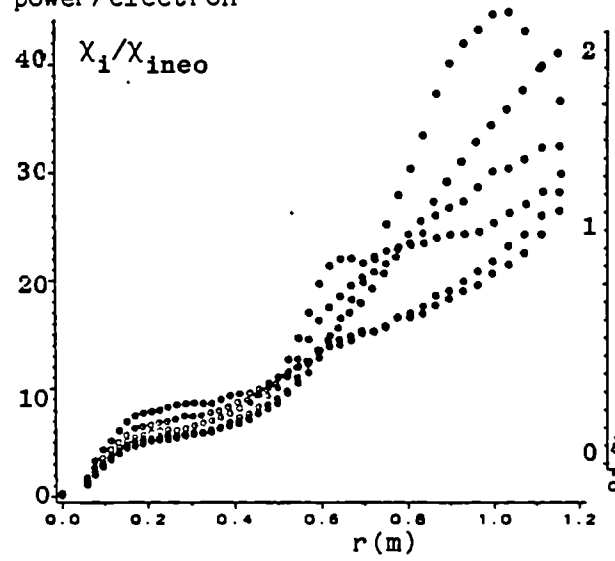

Fig.3 χ_i/χ_{ineo} vs radius for an ICRH JET discharge.

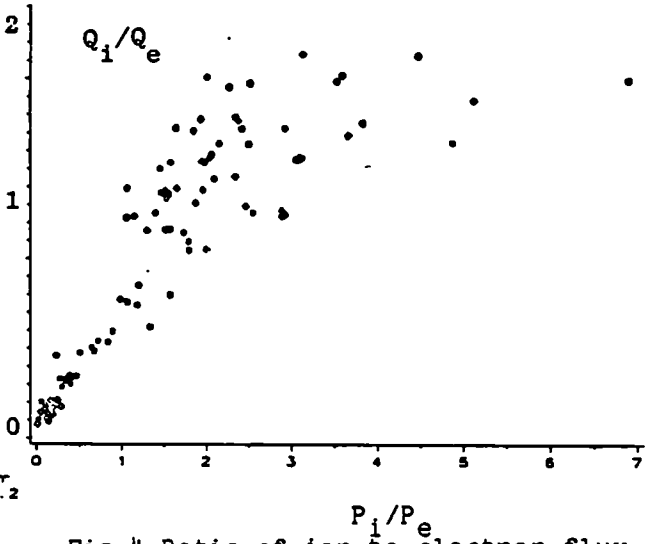

Fig.4 Ratio of ion to electron flux losses vs ion to electron input power (r=.6a)

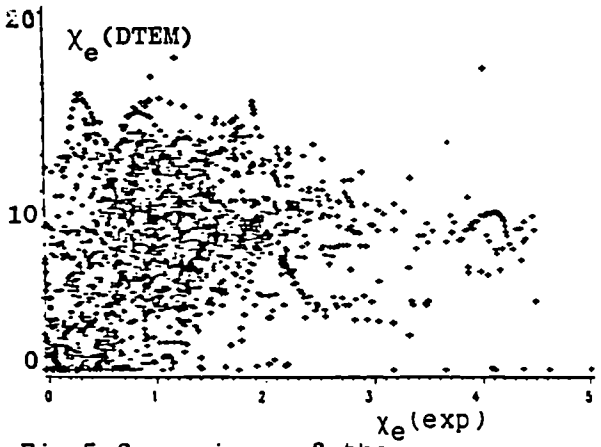

Fig.5 Comparison of the experimental χ_e with that predicted for the DTEM

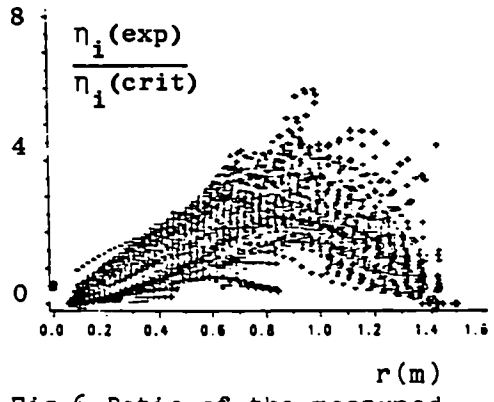

Fig.6 Ratio of the measured n_i to the critical value vs radius for additionally heated pulses

FEEDBACK CONTROL OF AMPLITUDE AND FREQUENCY OF DISRUPTIVE MODES

E. Lazzaro, M.F.F. Nave

JET Joint Undertaking, Abingdon, Oxon., OX14 3EA, UK

Introduction

The operation of tokamaks at high current and high plasma density is limited by the occurrence of disruptions, often believed to be related to the nonlinear evolution of resistive modes driven by unfavourable current gradients. Several techniques have been proposed where, by using external helical windings, it should be possible to provide the magnetic field which would control the growth of the magnetic islands [1-2].

We present an analytic and numerical study (in cylindrical approximation) of the non-linear response of the instability to the feedback currents in presence of a wall of finite conductivity. Control of amplitude and frequency of the modes is discussed.

Outline of the Model

Experimental evidence [3] in JET shows that the magnetic perturbation signals of the unstable modes are related to a bulk fluid toroidal rotation and growing radial field. Interaction with the resistive wall [4] eventually brings the mode to lock allowing the field perturbation $\tilde{B}_r$ (proportional to the square of the island size) to grow to disruption conditions.

These observations are considered in a standard model, of a straight cylindrical plasma of mass M, radius a, within a resistive vessel of radius d and thickness δ. At radius b, $a \lesssim b \sim d$ we consider an ideal system of helical conductors with pitch $\frac{m}{n} = \frac{2}{1}$, carrying a time varying control current $I_A \exp(i\phi_A(t))$. The magnetic field of the mode is expressed in terms of the helical flux perturbation ψ as

$$\tilde{B} = \mathrm{Re}\left[\underline{\nabla}\psi \times \underline{e}_z\right] e^{i\phi(t)} \tag{1}$$

where $\phi(t) = \int^t \Omega(t')dt'$ and Ω is the mode (island) rotation frequency which evolves accordingly with the momentum exchange with the wall, as

$$\ddot{\phi} = \frac{1}{MR} \int dV \, (\underline{j}\times\underline{\tilde{B}})_\phi = -\frac{2n\pi^2}{MR\mu_o} \mathrm{Im}\left(a\psi_a^* \psi_a'\right) \tag{2}$$

which can then be related to an apparent poloidal rotation by $\dot{\theta}_w = \frac{n}{m}\Omega$. The measurable perturbation field $\underline{\tilde{B}}$ is related by the non-linear tearing mode theory to the square of the island width W which evolves as

$$\frac{dW}{dt} = \frac{n}{\mu_o} \Delta' \tag{3}$$

$$\text{where } \Delta' = \lim_{\varepsilon \to 0} d \left. \frac{\ell n\, r\tilde{B}_r}{dr} \right|_{r_s-\varepsilon}^{r_s+\varepsilon}, \quad r_s = r\left(q=\frac{m}{n}\right) \tag{4}$$

We have embodied analytically the forcing term I_A in the boundary conditions of the equations for the perturbed flux and have solved them in the intervals $0<r<r_s$, $r_s<r<a$, $a<r<b$, $b<r<d$, $d<r<d+\delta$, $d+\delta<r<\infty$, with the appropriate interface conditions. The resulting dynamic equations exhibit explicitly the dependence on the control parameters I_A and ϕ_A. In the case $a<d$, $b\sim d$ we have

$$\frac{dW}{dt} = \frac{n}{\mu_o}\left\{\Delta'_\infty - \left[f_R + Z_A\left(1-\left(\frac{b}{d}\right)^{2m} f_R\right)\cos\Theta + Z_A\left(\frac{b}{d}\right)^{2m} f_I \sin\Theta\right](\Delta'_\infty - \Delta'_W)\right\} \tag{5}$$

$$\frac{d^2\theta_W}{dt^2} = \frac{n^2\pi^2}{MR\mu_o}\left(B_\theta \frac{q'}{q}\right)^2_{r_s} \frac{W^4}{64}\left(\frac{a}{d}\right)^{2m}\left\{f_I\left[1-\left(\frac{b}{d}\right)^{2m} Z_A\cos\Theta\right]+\left[1-\left(\frac{b}{d}\right)^{2m} f_R\right] Z_A\sin\Theta\right\} \tag{6}$$

where, with $\tau_V = \mu_o\sigma\delta d/2$, $\omega = \dot{\theta}_W$ $\quad \Theta = \frac{m}{n}(\theta_W - \theta_A)$

$f_R = \dfrac{\omega^2\tau_V^2}{\omega^2\tau_V^2+m^2}$, $\quad f_I = \dfrac{-m\omega\tau_V}{\omega^2\tau_V^2+m^2}$ in the high frequency $\left(\omega\tau_V >> \dfrac{\delta}{d}\right)$ approximation,

$Z_A = \dfrac{8\mu_o I_A}{m(B_\theta q'/q)_{r_s} W^2}\left(\dfrac{d^2}{ab}\right)^m = \dfrac{I_A}{GW^2}$, and Δ'_∞, Δ'_W are the Δ' for the case with no wall and superconducting wall. Here the terms $\left(1 - \left(\frac{b}{d}\right)^{2m} f_R\right)$ account for the image currents in the vessel, which reduce the effect of I_A, and cause dephasing.

Using the freedom afforded by the two control parameters I_A, ϕ_A in principle it is possible to select appropriate feedback equations closing system (5),(6), by mapping the right hand sides into stabilising terms

$$\dot{W} = -\alpha W$$

$$\ddot{\Theta} = -\beta^2\Theta$$

where α^{-1} is the desired island damping time and β^{-1} is the desired oscillation time of the phase difference Θ of the mode and the applied current around the value $\Theta=0$. In the case of a perfectly conducting wall the necessary condition for island stabilisation is then

$$I_A = \frac{GW^2[\Delta'_W + \frac{\mu_o \alpha W}{n}]}{[\Delta'_\infty - \Delta'_W][1 - (\frac{b}{d})^{2m}]} \qquad (7)$$

i.e. proportional to the measured signal $\tilde{B}_\theta$. The second condition, to keep the necessary small phase difference between the mode and the control current requires changes of the control frequency on a time β^{-1} shorter than the characteristic time scale

$$\tau \sim 0.2 \frac{m}{n} (\frac{b}{a})^m \frac{(\mu_o \rho)^{1/2}}{\bar{B}_\theta} R$$

If good phase matching is not kept an initial small phase difference $\Theta(0)$ growth flips the system to an unstable state ($\cos\Theta<0$ in eq.5 with $f_I \sim 0$).

The equilibrium condition $\hat{W}=0$ obtained from (7) for $\alpha=0$ ($\beta=0$) and shown in Fig.1, allows an estimate of the control current I_A necessary to stabilise a given island size for a plasma with $I_p=1.5$MA, $\frac{b}{a} = 1$, $\frac{d}{a} = 1.2$, $n_{sp}(T_e=1\text{keV})$, $q(a)=4$. Fig.2 shows the island size evolution in the uncontrolled (unstable) case (curve 1) with $I_A=0$, in the controlled case with perfect phase matching $\Theta=0$ (curve 2) and in the case of a flip instability (curve 3) occurring when a phase difference $\Theta=14°$ is introduced at $t=1.5$ on the stabilised case of curve 2. Fig.3 shows the time behaviour of the controlling current for the case of Fig.2.

Conclusions

Feedback control of m=2, n=1 tearing mode islands appears feasible with moderate control currents, if accurate phase tracking can be provided.

References

[1] V.V. Arsenin et al., IAEA-CN-37/N-1, p. 237, Plasma Phys. and Contr. Nucl. Fus., Innsbruck 1978.

[2] D.A. Monticello, R.B. White, Phys. Fluids 23 366 (1980).

[3] D. Stork et al., Bull. Am. Phys. Soc. 31 1503 (1986).

[4] M.F.F. Nave, J.A. Wesson, This conference.

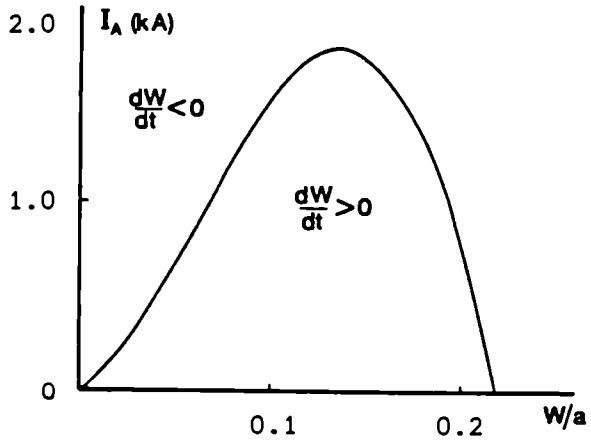

Figure 1

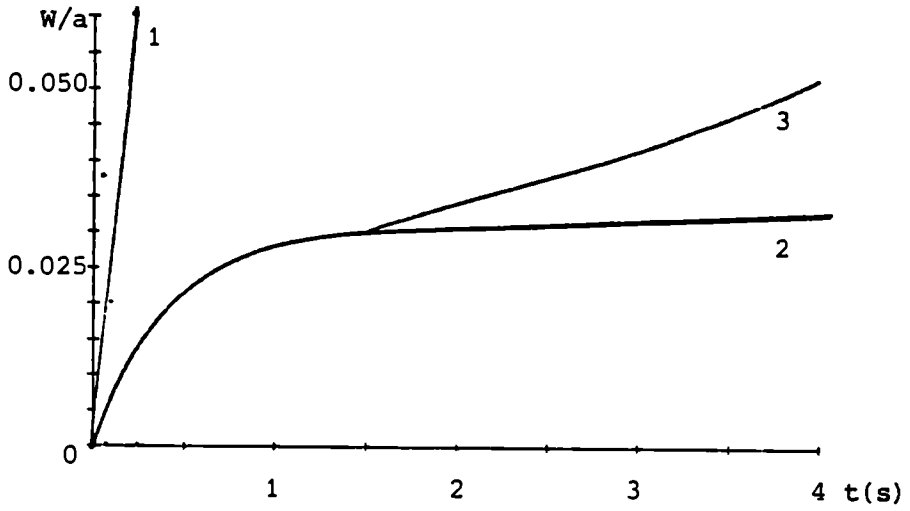

Figure 2

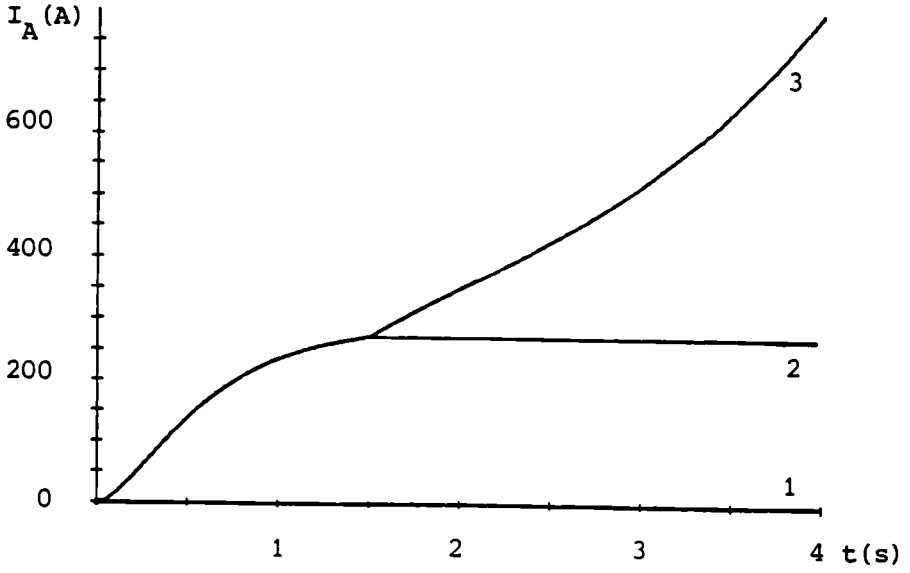

Figure 3

PRESENT RESULTS OF CHARGE EXCHANGE RECOMBINATION SPECTROSCOPY ON JET AND PROSPECTS FOR FUTURE ALPHA PARTICLE DIAGNOSTICS

Manfred von Hellermann, Alain Boileau, Lorne Horton, Nichol Peacock *, Uwe Schumacher **, Hugh Summers

JET Joint Undertaking, Abingdon OX14 3EA GB, *UKAEA Culham Laboratory, Abingdon OX14 3DB GB, **MPI f. Plasmaphysik, 8046 Garching, FRG

Introduction: The charge exchange recombination spectroscopy diagnostic provides local values of low-Z ion densities and ion temperatures of fully stripped atoms such as **deuterium, helium, carbon and oxygen.** Those particles represent the bulk of a JET plasma. The diagnostic uses the JET heating neutral beams as a source of fast neutrals with beam energies up to 80 keV (40 keV/amu for deuterium injection) . Doppler widths and Doppler shift of the observed charge exchange spectra enable measurement of ion temperature and bulk plasma velocity. Absolutely calibrated intensities and local neutral beam particle densities give values of the dominant low-Z impurity concentration and allow therefore the determination of localized Z_{eff} data and its temporal development. The effective excitation rates for charge capture and subsequent cascading and l-mixing are corrected for given local ion density and temperature [1].

Experimental: The CXR diagnostic has employed during the first year of neutral beam heating on JET three viewing lines, two of them intersecting the neutral beams in the plasma centre (R=3.05m) and at a radius of R=2.3m respectively (FIG 1). A third, passive viewing line in the adjacent octant next to the injector box provides background spectra. The collected light in a spectral range between 400 and 700 nm is transferred via 120m quartz fibres into a remote diagnostic area to be analysed by two spectrometers and linear detector arrays (FIG.2). A beam splitter arrangement enables simultaneous investigation of two recombination spectra emitted from the same active volume.

Results: Ion temperatures were measured in a wide range of plasma parameters. In high electron density cases the observed ion temperatures during neutral beam heating are raised to levels comparable to the central electron temperatures (FIG.3a) and follow its sawteeth oscillations. During hot ion modes of low density plasmas the ion temperatures can exceed electron temperatures by factors of 2 to 3 (FIG 3b). Five different CX lines from helium, carbon and oxygen were analysed and have shown agreement of resulting ion temperatures within 5 to 10% (cf. FIG 4). No systematic mass dependence within in the investigated range of M=3amu to M=16amu was found. The observed low-Z temperatures are

however systematically lower than simultaneously measured central Ni^{26+} temperatures [2]. Further clarifications are intended.

The dominant light impurities of a JET plasma are carbon and oxygen. Typical measured values are 0.5 to 2 % oxygen and 2 to 5% carbon . The temporal development during neutral beam injection appears to depend on several parameters such as electron density and operation mode. During limiter discharges the concentration of carbon tends to decrease and that of oxygen to increase slightly with increasing electron density. In so called x-point, L-mode configurations the carbon concentration is usually markedly increased and that of oxygen remains almost constant (FIG 5). During H-mode operations carbon and oxygen both go up, but the resulting Z_{eff} is only enhanced slightly due to a significant increase of confinement. Deduced Z_{eff} values based on oxygen and carbon (FIG 6) are in rough agreement with independant measurements based on visible Bremsstrahlung[3]. In helium discharges the oxygen concentration is usually less than 1% and CXRS Z_{eff} values determined by carbon and helium concentrations alone are comparable to $Z_{eff,vis}$.

A new 8 chord viewing line system is presently commissioned. It will allow measurement of radial profiles of ion temperature, low-Z ion density and toroidal rotation velocity. In addition to present results a systematic investigation of hydrogen charge exchange spectra and that of excited beam particles is planned.

<u>Application to alpha particle diagnosis:</u> In the active phase of JET the neutral beam heating system will be operated at 160 keV of deuterium. It is therefore of considerable interest to investigate the feasibility of using the existing CXR diagnostic facilites for alpha particle diagnosis. Numerical calculation of expected recombination radiation spectra created by a slowing down alpha-particle population show that a relativeley broad spectrum (FIG 7) of approximately 100 A width is to be expected for the helium transition 4 to 3 at 4686 A. The width of the energy range for charge capture which is in the order of 150 keV/amu with a maximum at 60 kev/amu determines the effective fraction of slowing down alpha particles contributing to the excited spectrum. It appears to be feasible to use curve fitting procedures to determine slowing down parameters from measurements of the spectral shape and deconvolving the CXR dependance.

[1] A.Boileau et al. to be published, [2] M.von Hellermann et al. Workshop on Advanced Fusion Plasma Diagnostic Techniques, Varenna 1986, [3] P.D.Morgan et al. this conference

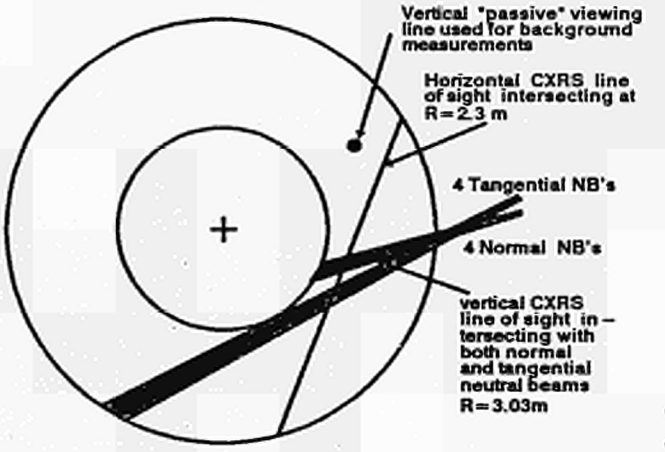

Fig. 1 LAYOUT OF VIEWING LINES AND NEUTRAL BEAMS

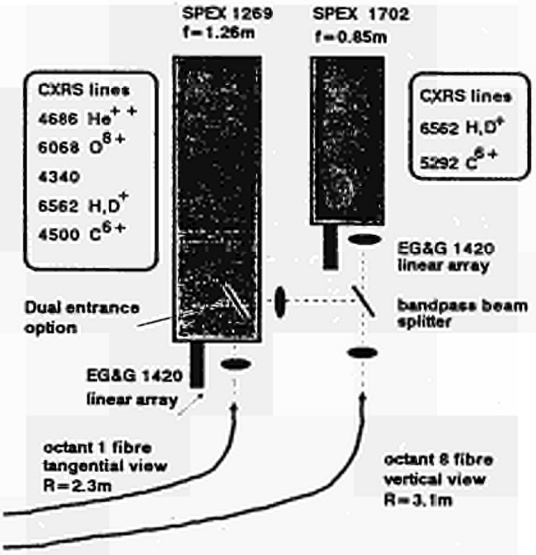

Fig. 2 Dual Spectrometer Layout of CXR Diagnostic

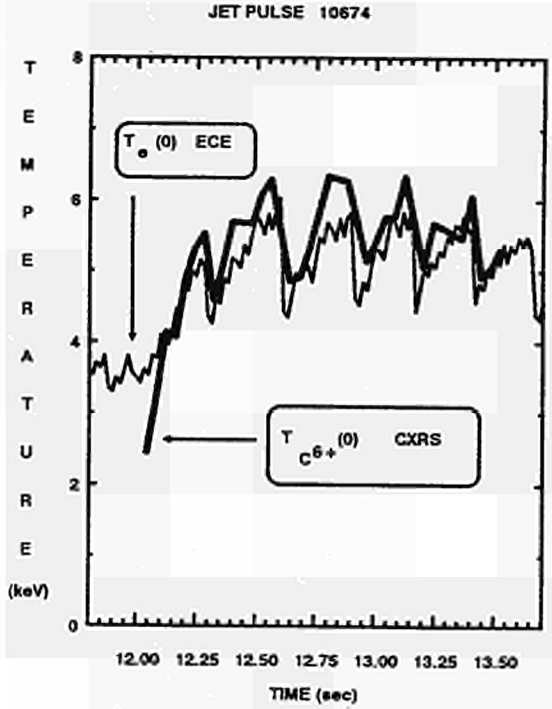

Fig. 3a Central ion and electron temperature

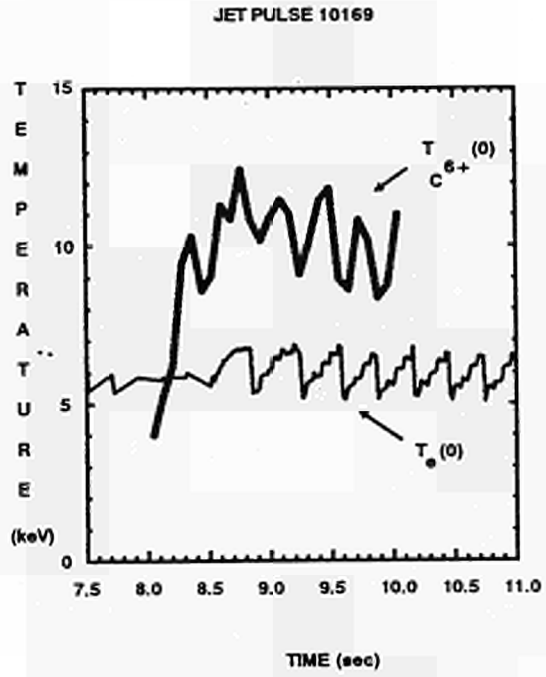

Fig. 3b Comparison of central ion and electron temperature during a hot ion mode pulse

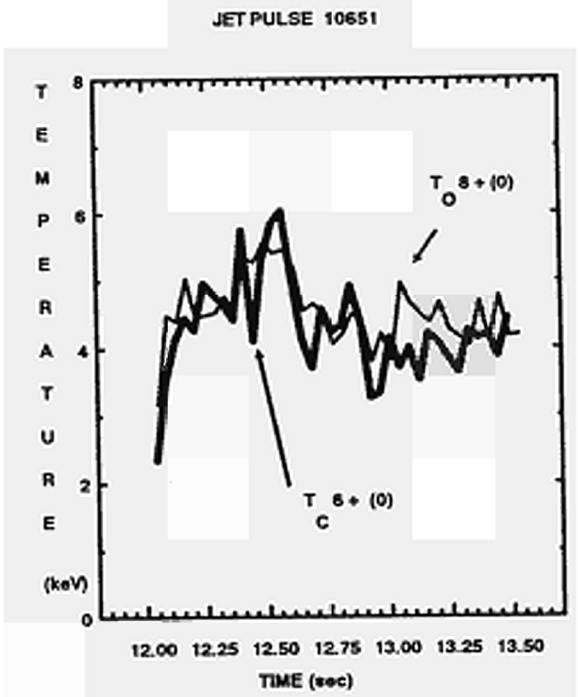

Fig. 4 Central oxygen and carbon ion temperature

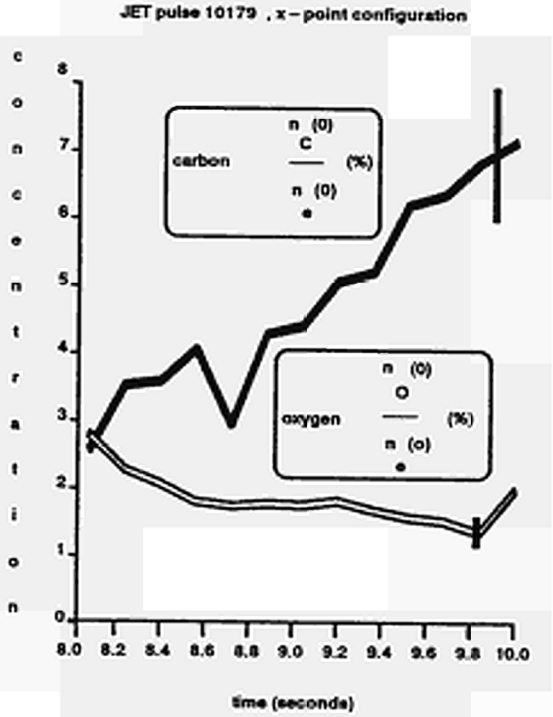

Fig.5 Central carbon and oxygen concentration

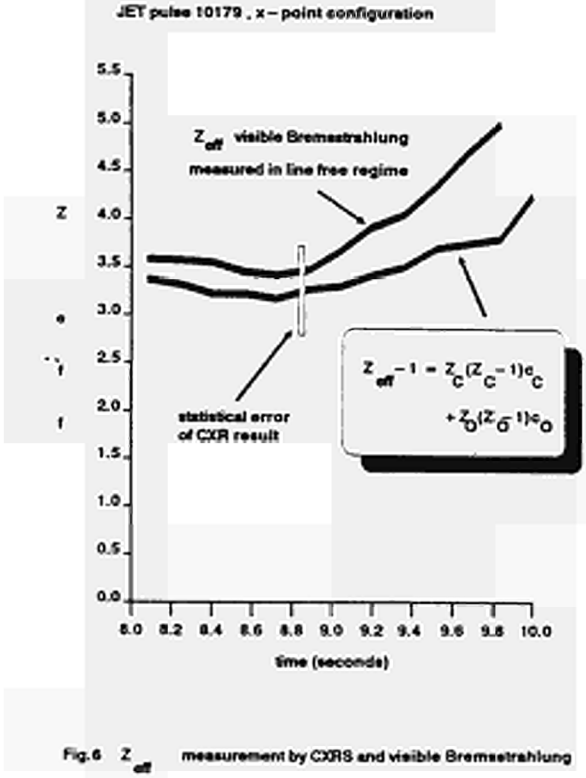

Fig.6 Z_{eff} measurement by CXRS and visible Bremsstrahlung

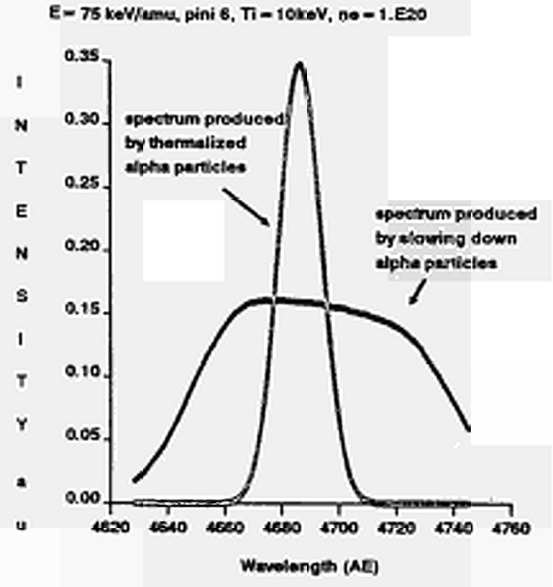

Fig. 7 Expected alpha particle CXR spectrum

Invited paper at 14th European Conference,
Madrid, Spain, 22nd-26th June 1987

Particle Balance and Wall Pumping in Tokamaks

S.A.Cohen K.Erents J.Ehrenberg P.Harbour T.T.C.Jones
P.D.Morgan A.Gondhalekar J.O'Rourke M.Bureš J.A.Tagle
P.Coad M.Watkins L.de Kock and the JET Team

ABSTRACT

The properties of carbon, with respect to its ability to absorb and release hydrogen, are reviewed and applied to the interpretation of density behaviour in Ohmic-, NBI- and ICRF-heated tokamak discharges. Based on the experimental observations, improvement of H-mode parameters in JET due to reduced hydrogen re-emission from the walls is predicted with a numerical model. The particle removal rates required for Q=1 in JET are estimated.

KEYWORDS

Tokamaks; hydrogen; carbon; fuelling; wall pumping; particle confinement; auxiliary heating.

1. INTRODUCTION

Hydrogen gas introduced into tokamak discharges will be deposited into the plasma and the material structures surrounding it. Both act as temporary reservoirs. Hydrogen may leave one reservoir by stimulated or spontaneous processes and then enter the other. The detailed hydrogen density profiles in each reservoir are determined by coupled transport equations. Thus the global particle confinement times in the materials and in the plasma affect the total particle content in each.

The term 'particle balance' refers to the relative and absolute amounts of hydrogen in the two reservoirs. 'Wall pumping' is the act in which the materials (limiters and walls) absorb hydrogen from the plasma.

Fuelling methods, plasma transport coefficients, and hydrogen recycling will control the plasma density and its profile. Their importance is illustrated by the following examples: any fuelling technique requires removal of hydrogen from the edge plasma to avoid exceeding the density limit; the record ion temperatures achieved in neutral-beam heated PLT (Eubank and co-workers, 1979) and TFTR (Hawryluk and co-workers, 1987) required gettering or wall conditioning to obtain the lowest initial density of the target plasma; the Alcator-C record $n\tau$ (Greenwald and co-workers, 1984) required pellet fuelling; the H-mode requires control of hydrogen recycling (Wagner, Keilhacker, and co-workers 1984); and the ratio of D to T and the impurity content (including helium ash) in D-T burning devices will strongly affect the Q attainable. For reasons of safety, these latter devices must also have accurate accountability and control of their tritium inventories.

Density control was first achieved by a series of pragmatically developed techniques, specifically wall and limiter conditioning by tokamak discharges. Then coatings with passive or getter films were tried and other wall-conditioning plasma processes tested (Cohen, 1984). Further methods for removing hydrogen from the plasma edge developed simultaneously and include various pump limiter (Mioduszewski, 1984) and divertor (Wagner and Lackner, 1984) configurations. Recently pumping by carbon walls (de Kock and co-workers, 1987) has gained attention.

The importance of density profiles in this and the next generation of tokamaks (e.g. Rebut and Lallia, 1987) demands scrutiny of the above-listed measures and additionally of the control of fuelling and of plasma transport coefficients. We focus on the newest phenomenon, wall pumping.

Reviews already exist for wall conditioning, pump limiters, divertors, and pellet fuelling. And success in modifying the particle transport in a favourable way may be as elusive as similar efforts to improve the plasma's thermal insulation.

In this paper we first review material properties which establish the boundary conditions for the plasma. Carbon properties are chosen as being representative because many structures in present tokamaks are manufactured from graphite, and because carbonaceous layers are known to form on the walls as a result of plasma operation (Cohen and co-workers, 1978). Measurements of the amount of hydrogen left in the tokamaks walls and limiters are then presented. The next section notes the importance of wall temperature to density control and also speculates on the mechanisms responsible for wall conditioning by low-current helium discharges (Dylla and co-workers, 1987). We then describe the density evolution in JET during Ohmic, ICRF and NBI operation to connect the material and edge plasma properties to overall tokamak behaviour. The final section is on future work. It lists the physics studies of material properties needed to elucidate the present tokamak results. This is followed by an evaluation of the density control and particle removal rate required to achieve Q=1 in JET, and the proposition that improved plasma parameters in H-modes may be attained by reducing hydrogen re-emission from the walls.

2. CARBON PROPERTIES

Pure solid carbon exists in three basic forms: diamond, graphite and amorphous. Carbon in tokamaks contains a mixture of these, but is also impure (containing hydrogen and heavier atoms), and porous. Most carbon properties were obtained in laboratory studies of pure samples, unexposed to tokamak plasmas; some data on exposed carbon samples are available. An accurate model of carbon's role in density control requires that all properties be measured for plasma-irradiated carbon.

A most important property is erosion by sputtering. For room temperature graphite the sputtering yield Y below ~ 500 eV is approximately independent of the energy E of the impacting hydrogen (Roth, 1987), in contrast to most materials. This is attributed to chemical effects such as formation of volatile hydrocarbons. Above 500eV the sputtering yield falls with increasing energy. (At 500°C the yield increases a factor of 2 as the energy increases from 20 eV to 300 eV and then falls for E $\gtrsim$ 500 eV.) For monoenergetic deuterium impacting graphite, the maximum sputtering yield is 0.03 at room temperature and 0.2 at 550°C, again due to chemical synergy. The physical sputtering yield changes little with impurity content of the carbon while the chemical yield decreases (Behrisch, 1987).

For a fixed power loss from the plasma through the conduction channel, the maximum carbon production rate, ΓY, by hydrogen impact (fig.1) occurs at a low energy, below 20 eV. For carbon ions impacting carbon limiters, the maximum rate, again for fixed power loss, is at about 150 eV, where the physical sputtering yield is proportional to energy (Lackner and co-workers, 1984). Therefore tokamak operation at edge temperatures above ~ 50 eV should result in lower carbon influx by ion sputtering.

Direct and immediate kinematic reflection will occur for a fraction of hydrogen atoms which impact solid carbon. The measured reflection coefficient (for normal incidence deuterium on graphite) is also shown in fig. 1 (Behrisch and Eckstein, 1984; Chen, Scherzer, and Eckstein, 1984). No data exists below 300 eV where the reflection coefficient is ~ 0.3. Calculations indicate that the reflection continues to increase down to about 10 eV (Eckstein and Heifetz, 1987). These data too point to the benefits of a high edge temperature, in this case to reduce reflection of the impacting

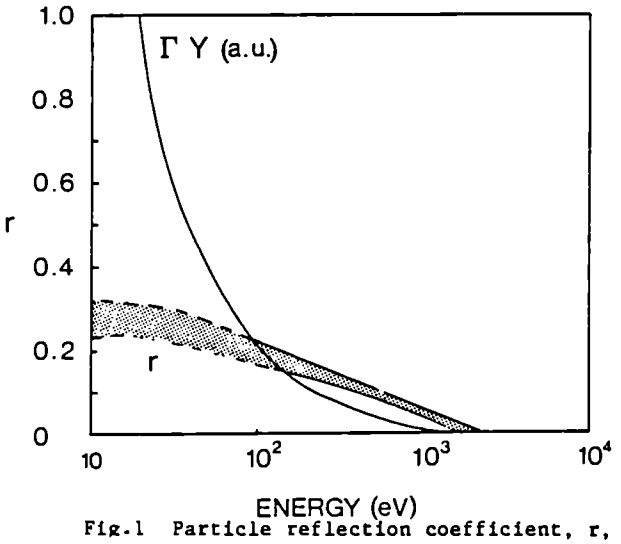

Fig.1 Particle reflection coefficient, r, and impurity generation rate, ΓY, at fixed power loss for normal incidence deuterium impact on room temperature graphite.

hydrogen by the graphite. No change in reflection coefficient occurs for hydrogen-loaded carbon surfaces while an increase in reflection occurs for surface contamination by heavy impurities such as iron.

Particles impacting the carbon lattice create damage by breaking bonds and displacing carbon atoms. The damage acts as trapping sites of about 4.6 eV depth for hydrogen (Wilson and Hsu, 1987). At room temperature the density of the hydrogen in the traps can reach 40% of the bulk carbon number density. Intrinsic traps, ~ 4 eV deep, occur in unirradiated bulk graphite at a level of about 20 ppm. The penetration of energetic hydrogen ions into bulk carbon (Andersen and Ziegler, 1977) is about 2×10^{-11} m/eV in the energy range 20 eV < E < 20 keV. In beam-solid experiments, the beam is first strongly absorbed by the graphite target. But the amount of retained hydrogen increases towards a saturation value (Staudenmaier and co-workers, 1979) approximately as $[1-\exp(-F/N_s)]$, where N_s is the energy-dependent saturation value (~ 2×10^{21} $E^{0.8}$ (keV) m^{-2}) and F the fluence. The saturation level decreases with increasing temperature from 40% at temperatures below 300°C to about 5% at 700°C.

The impact of any type of energetic ion or neutral onto hydrogen-loaded carbon can result in release of the hydrogen from the traps. The initial cross-section (Wampler and Doyle, 1987) for such release is shown in fig. 2, where the abscissa is the nuclear energy loss rate from the impacting particle to the carbon lattice. From the straight-line model we estimate that for a 0.5 keV proton the cross-section is about 5×10^{-21} m^2 (Andersen and Ziegler, 1977). As the energy of the impacting proton decreases, it eventually becomes ineffective in desorbing trapped gas because of its reduced range and reduced available energy. Once released from the traps, hydrogen is observed to leave the lattice and enter the gas phase as molecules (Scherzer, Borgesen, and Möller, 1987). In beam-solid experiments when the retained hydrogen approaches the saturation value, further bombardment results in 100% re-emission, initially with the trapped particles leaving the graphite and the bombarding particles replacing them in the traps. If a room temperature graphite sample is saturated by bombardment with keV hydrogen and then heated to ~ 600°C during continued bombardment, initially the re-emission will exceed 100%. Except for this case, no ion-induced desorption experiments have shown re-emission greater than unity. Of course, room temperature unconditioned materials, e.g., hydrocarbon-contaminated, will show desorption yields greater than unity, but this has not been observed for hot, T > 300°C, conditioned graphite. Desorption by light particles, electrons or photons, is expected to be less important. However, this needs direct verification in an intense radiation environment typical of tokamaks.

Once beam irradiation has ceased, a hydrogen-implanted carbon sample has its hydrogen density distribution determined by its temperature-dependent diffusivity and the boundary conditions, including the internal porosity. This is about 1 m^2/gm for unirradiated POCO graphite (Causey,

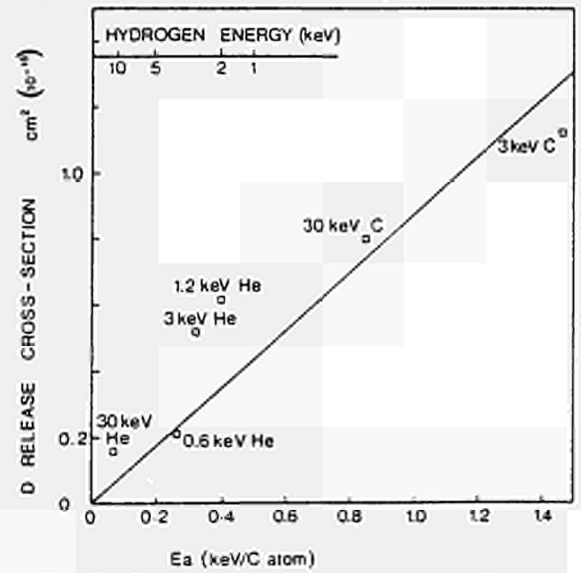

Fig.2 Deuterium release cross-section versus energy into atomic collisions for various particles impacting deuterium-saturated room temperature graphite.

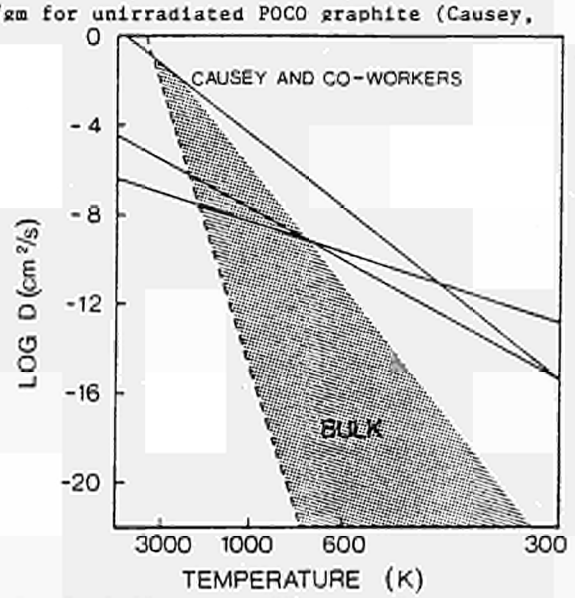

Fig.3 Diffusion coefficient of deuterium saturated room temperature graphite. The solid lines are estimates of surface diffusivity.

Baskes, and Wilson, 1986). Microscopic examination of graphite exposed to hydrogen plasmas shows that an open porous structure develops to depths in excess of 10 microns (Goebel and co-workers, 1987). The structure is sponge-like, with typical voids of 1-10 microns diameter and walls less than 1 micron in thickness. Based on these micrographs, a crude lower limit of the porosity is 20 m^2 of microscopic area per m^2 of macroscopic surface. Nakamura and co-workers (1986) measured surface roughness factors as high as 100 for graphite irradiated by 1.5×10^{18} cm^{-2} 3 keV D.

Causey, Baskes and Wilson (1986) categorize two main types of hydrogen diffusion in unirradiated graphite, fig.3. Diffusion through the bulk becomes important for temperatures above ~ 1000 K. The activation energy is between 2 and 5 eV. This process is poorly understood, so the grey-hatched area in fig.3 should only be considered as an estimate. The other diffusion process, characterized by traps of depth 0.4 - 0.9 eV (and possibly as low as 0.15 eV (LaMarche and co-workers, 1986)), is thought to occur on the surface of graphite microcrystallites. This can affect the hydrogen density distribution at temperatures as low as 100°C. It is expected that impurities, hydrogen content, porosity, and radiation damage will change the diffusion and recombination of hydrogen in carbon (Amemiya, 1987).

Thermally activated release of implanted hydrogen shows (Nakamura and co-workers, 1987) that at fluences above 10^{16} cm^{-2} molecular hydrogen is thermally released at temperatures as low as 100°C. The peak release rate is at about T ~ 600°C, in agreement with Philipps and co-workers (1987).

The final process relevant to wall pumping is the build-up of hydrocarbon films on cool surfaces near a warm plasma-irradiated graphite sample (Hsu and Causey, 1987). This phenomenon, termed 'co-deposition', is ostensibly due to chemical sputtering. It is a non-saturable mechanism for pumping hydrogen. Diffusion of hydrogen into bulk graphite would also effectively show no saturation because of the huge capacity of the bulk.

3. HYDROGEN IN TOKAMAK WALLS

The aforementioned phenomena show several ways by which hydrogen may be incorporated within the carbonaceous structures found in tokamaks. There are two methods to measure the hydrogen left behind in the walls and limiters of a tokamak after a discharge. The first is to measure directly the hydrogen in the walls. Using ion-beam techniques capable of probing to 1 micron depth, several hundred such measurements on JET components and samples of wall and limiter areas (Behrisch and co-workers, 1987: Bergsåker and co-workers, 1987) were performed. Note that hydrogen which has diffused further into the bulk remains undetected by this analysis method. In the pre-ICRF, pre-NBI 1985 operating period, the retained hydrogen isotopes concentrations reached levels as great as 2×10^{22} m^{-2}, corresponding to carbon layers saturated to depths of 0.5 microns. This depth rules out direct implantation of plasma ions as the cause of the high concentrations. (Energies of 70 keV are required to penetrate 0.5 micron.) Averaging over the entire interior surface area of JET, the total amount of retained deuterium within the first micron was about 10^{24} atoms. Co-deposition during tokamak discharges is a possible cause. But our model of co-deposition during discharge steady state fails by a factor of 10 to reproduce such high hydrogen deposition rates. We believe a more likely cause was the extensive use of glow discharge carbonization during this period. In support of this view are results from the 1986 campaign, which included ICRF and NBI and little carbonization. Ion beam analysis showed that the total retained amount of deuterium was about 5 times less than in 1985 (Behrisch, 1987) and corresponded to about 1% of the gas fuelled during the 1986 period. (Hydrogen was not measured but was expected to be small because few discharges were fuelled with hydrogen.) The concentration was highest on structures near the plasma edge, but not those subject to the most intense particle and heat flows. In 1985 deuterium was found approximately uniformly around the walls; in 1986 it was concentrated on the inner wall, in agreement with the more extensive use then of the carbon-tiled inner wall as a limiter.

The second method is to measure the gas pumped out of the tokamak after a discharge and compare it with that puffed in during the discharge. Fig.4 shows such a measurement performed in JT-60 (Nakamura and co-workers, 1986). Immediately after the discharge most of the gas was trapped in the walls. Several seconds after the discharge the pressure rose to a peak and then decayed, in proportion to 1/t. For Ohmic discharges, the JT-60 team found the pumped deuterium ranged from 40% to 80% of that introduced in the pulsed gas feed. Assuming a continued 1/t re-emission, it would take about 10^4 s (for the 80% case) to 10^9 s (for the 40% case) to re-emit all the deuterium. Experiments on ASDEX, a machine with no carbon components, showed about 90% of the

injected gas pumped away in the 15 minutes after each discharge (Wang, Poschenrieder, and Venus, 1986). Measurements on TFTR (a machine with tens of square meters of graphite components and cool walls) after helium conditioning show the pumped deuterium to be initially 12% of that introduced into a discharge (Dylla and co-workers, 1987). After about 12 shots the walls were de-conditioned, but the pumped amount increased to the asymptotic value of only 25%. This has been taken as evidence of co-deposition, which may occur during discharge start-up, steady state, or termination.

The pressure after a discharge in JET is also shown in fig.4, along with the pressure with a gas puff only (no plasma). From these we can get a measure of the characteristic time during which hydrogen leaves the vessel walls after being implanted by the plasma. This is seen to be $\gtrsim$50 s.

For the upcoming tritium experiments ways to remove this retained hydrogen are being developed which rely on thermal, erosion, replacement, and desorption mechanisms described in section 2.

4. WALL CONDITIONING

Numerous reviews have been written on impurity control by wall conditioning methods (Dylla, 1980; Cohen, 1984), including the new technique of carbonization (Winter, 1987a). Density control can also be effected by wall conditioning. Two new results are noted here, the first pertains to wall temperature, the second to desorption.

Figure 5 shows the time evolution of two series of discharges in TEXTOR, with each series interrupted by 20 minutes of rf glow discharge cleaning (rfgdc) in pure deuterium (Winter, 1987b). (One month prior to these experiments, TEXTOR had been extensively carbonized.) In the first series, a), the wall temperature was 150°C. With the same gas feed into each discharge, the post-rfgdc discharges (22821-26) displayed a higher density, indicating an increase in the global recycling coefficient, presumably due to wall loading with deuterium. In contrast, the second series of discharges, with the wall temperature at 350°C, showed a reduction in the density of those discharges after the rfgdc (23346-52), clearly indicating a decrease of deuterium in the carbonized film near its surface. The conclusion is that a carbon wall temperature in excess of ~ 300°C will result in appreciable wall pumping. Presumably, the lattice stores the hydrogen for a few seconds during a discharge; then thermally activated diffusion and desorption empty the near-surface carbon lattice between discharges.

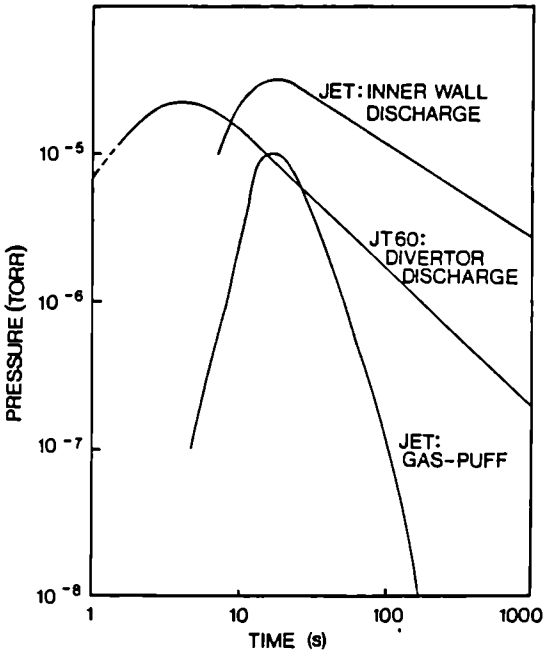

Fig.4 Pressure versus time after Ohmic discharges in JT-60 and JET. Also shown is JET data for a gas puff only.

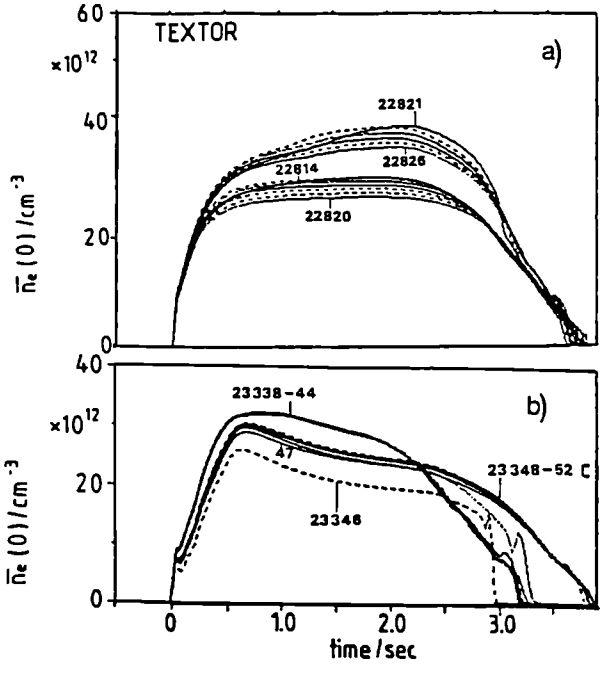

Fig.5 Plasma density versus time for two sets of discharges in TEXTOR. The wall temperature was 150°C in a) and 350°C in b).

The success of low current (I_p < 1 MA) helium conditioning pulses in producing low density target plasmas has been attributed to helium and carbon ion-induced desorption (IID) of the hydrogen occupying the deep damaged-induced traps (Dylla and co-workers, 1987). Continuing the IID line-of-reasoning we first note that the scrape-off distance is longer at lower plasma currents (Tagle and co-workers, 1987). It is important that the helium ions reach (scour) more distant surfaces which are exposed to charge-exchange neutrals during hydrogen discharges. Furthermore, an optimal energy exists where the impacting ions penetrate far enough into the carbon and still have a high enough desorption cross-section. This energy is about 500 eV for helium impact, requiring an edge electron temperature of ~ 65 eV. Tagle and co-workers (1987) have shown that this occurs in JET only at low plasma currents and at a density of about 10^{19} m^{-3} for helium. A subtle reason for the superiority of helium over hydrogen (or deuterium) in the conditioning discharges is that the ion density in the edge in helium discharges is higher than in hydrogen discharges. (The most likely cause for this is the lack of Franck-Condon events for helium keeps the ionization source nearer the plasma edge.) Hence the flux onto surfaces is higher. And obviously, hydrogen cleaning is less effective than helium because it reloads the lattice.

Another reason is the delicate balance between ion induced desorption and thermal diffusion. Ehrenberg (1987) and others (Causey, Baskes, and Wilson, 1986; LaMarche and co-workers, 1986) have shown that there is a large reservoir of hydrogen within the bulk of the carbon. When the plasma current is high, the power into the plasma increases, increasing the thermal load on the limiter (McCracken, 1987). Then hydrogen desorbed from the near-surface region may be replenished by hydrogen diffusing out of the bulk. Another contributing factor to the benefits of low current operation for wall conditioning is the better confinement of the desorbed hydrogen in the lower density plasma causing less prompt reimplantation.

5. DENSITY BEHAVIOUR IN JET

Efforts have been made on JET to compare the plasma density evolution with numerical models (Ehrenberg and co-workers, 1987; Jones and co-workers, 1987; Bures and co-workers, 1987) based on the previously described properties of carbon and of the plasma. Concerning the latter, experiments (Cheetham and co-workers, 1986; Hubbard, Ward, and Stringer, 1986; Gondhalekar and co-workers, 1987; Cohen and co-workers, 1987; Stangeby and co-workers, 1987) under a variety of JET conditions have shown nearly the same plasma particle transport coefficients. These are a diffusivity of 1 m^2/s at the edge and 0.3 m^2/s on axis, and an inward convection proportional to minor radius equal to ~ 0.1 m/s at the edge. The equations describing density evolution are the local flux and conservation equations. Insight may be gained by recasting these equations into the global form of the two reservoir model.

$$\dot{N}_p = -(1-r_w)\frac{N_p}{\tau_p} + (1-r_p)\frac{N_w}{\tau_w} + \phi \qquad (1)$$

where N_p = total hydrogen content of the plasma,
τ_p = global particle confinement time in the plasma,
r_w = kinematic reflection coefficient of the wall,
N_w = total hydrogen content in the walls,
τ_w = global particle confinement time in the walls,
r_p = reflection coefficient of the plasma, and
ϕ = the fuelling source.

The definition of a residence time in (or on) the walls clarifies its role as a reservoir. In steady-state, i.e., no fuelling and 100% recycling, the particles will divide themselves between the two reservoirs proportional to their effective confinement times in each, where the effective confinement time includes the reflection coefficient factors.

In the actual numerical evaluations of the flux equations, separate carbon properties are used for the inner wall, wall, and limiters. The diffusion equation of hydrogen in carbon is solved, including a source term dependent on impact energy, and boundary conditions appropriate to first- or second-order release from the surface. Impurities are taken into account using the measured Z_{eff} to modify N_p. The flux out of the walls back into the plasma consists of three

terms, two prompt (the kinematically reflected and the desorbed) and one slow (the diffusing/recombining) part. The two prompt terms are proportional to N_p/τ_p, the first term on the RHS of eqn.(1). The essence of the slow part is embodied in the global particle confinement time in the wall, τ_w, defined in the same way that the global plasma particle confinement time is defined, thus $\Gamma_w A_w = N_w/\tau_w$, where Γ_w is the flux out of the wall into the plasma and A_w the wall area. Particles entering the plasma may be 'reflected' (Voss, 1980) by charge exchange or Franck-Condon processes, summarized by the probability factor r_p, which is estimated to be 0.5.

The flux equation in the entire plasma may be solved in each interval of time using transport coefficients and fuelling profiles obtained from plasma and atomic physics codes, or the plasma particle confinement time may be treated as an explicit function of plasma parameters. From H-α measurements we find for ohmically heated deuterium plasmas

$$\tau_p = 2 \times 10^3 \; R(cm) \; a(cm)^2/n(cm^{-3})^{0.8} \; sec. \qquad (2)$$

The density dependence agrees with that predicted by Engelhardt and Feneberg (1978) for gas-fuelled discharges and with that noted by Stangeby (1987). In these Ohmic discharges there is no strong dependence on B_T or I_p. The dependence on the mass of the background gas is relatively weakly documented - both helium and hydrogen having somewhat shorter confinement then deuterium. During auxiliary heating, the particle confinement time decreases a factor of 2 in L-mode discharges and increases about a factor of 2 in H-mode discharges. Fuelling on axis, as by NBI, only alters the particle confinement time in a transient manner because edge recycling occurs at a high rate compared to the central fuelling rate.

For diffusion-dominated release of hydrogen from the wall, the particle confinement time in the wall may be estimated from the diffusivity and range data in section 2. For the surface diffusivity, τ_w is about 1 s at 200°C. But the rate will depend strongly on temperature, changing a factor of 10 as the temperature changes 100°C. We again point out that the diffusivity through carbon in tokamaks may be quite different from that in unirradiated samples. One might suggest that the best measure of τ_w is that derived from the release of gas after a discharge. But the > 50 s value of τ_w is inconsistent with the fuelling efficiency and particle balance to be described in the next section. We conclude that the processes occurring during discharge termination, the so-called 'soft landing', are different than during the steady state.

5.1 Ohmic Heating

To study the role of material and plasma properties in determining the density in ohmic plasmas discharges of various initial densities were formed on the outer carbon limiters (macroscopic area ~ 1 m^2) then moved to the carbon-tiled inner wall (macroscopic area ~ 20 m^2) (Ehrenberg and co-workers, 1987). During each discharge the plasma was shifted back and forth between the limiters and inner wall twice. The movements took 400 ms each, and the residence time on each surface was 4 seconds between moves. The time evolution of the gas feed, N_D, and H-α emission from the limiters and the inner walls is shown in fig.6 for five discharges in the series. Only in the first discharge (11019) was the plasma not shifted. A deuterium pre-fill was introduced into the vessel about 0.5 s before each discharge. Note that in discharges 11020, 11022 and 11023 the subsequent dosing gas feed was shut off at 4 s, while in 11024 the dosing feed was never turned on. In spite of no gas feed during the time 0 to 4 s, the density in 11024 still rose, indicating a continuous fuelling of that discharge for at least those first four seconds. The source of the fuelling is predominantly the release of hydrogen from the walls and limiters.

The number of electrons in the plasma of 11024 represents at most (at t = 4 s) 50% of those introduced with the gas feed. The fuelling efficiency decreased with increasing density, which Ehrenberg and co-workers show is indicative of diffusion-limited (or another first-order process) release of the hydrogen from the walls. This considerably eases solution of eqn.(1) by eliminating a free parameter, the recombination coefficient.

When the plasma is moved to the inner wall the density drops. The density asymptotically approaches a lower level, consistent with a new balance between wall pumping and outgassing or between τ_p and τ_w. The maximum decay rate measured was 2×10^{21}/s in this experiment. On repositioning the plasma on the outer limiter the density rises, approximately back to its value at 5 s. The initial rate of rise is typically 6×10^{20}/s.

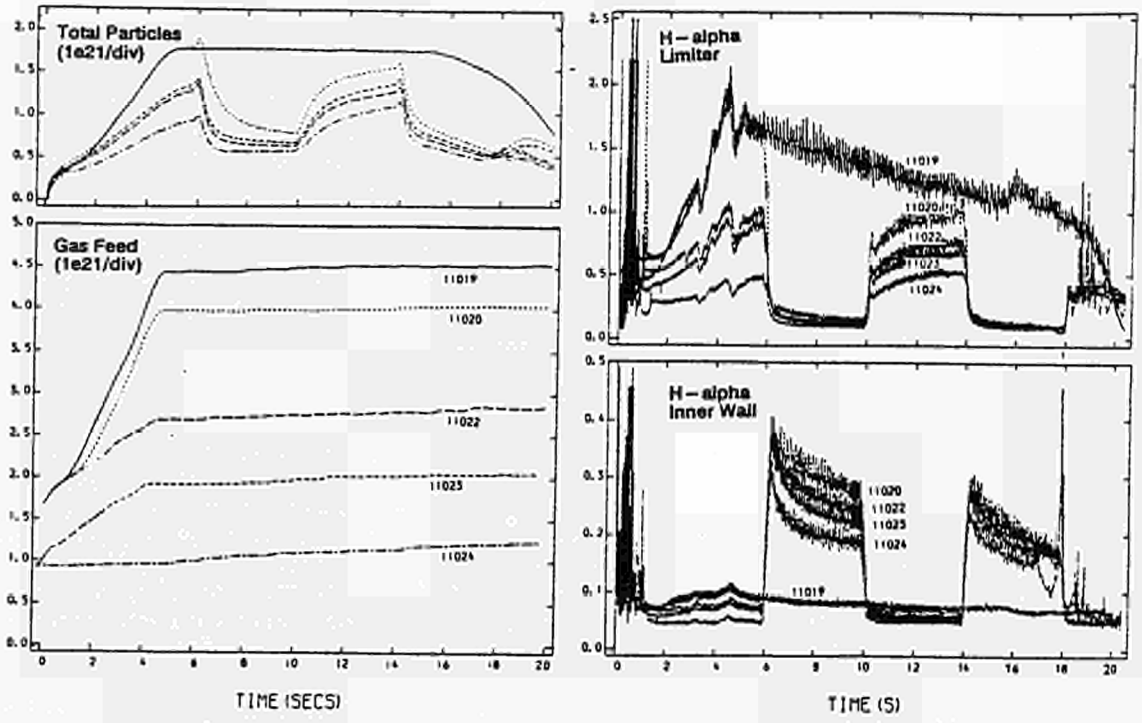

Fig.6 Time evolution of 4 parameters for 5 discharges: 11019, 11020, 11022, 11023 and 11024. 11019 was always positioned on the outer limiters; the others were started on the outer limiter, moved to the inner wall at 6 s, moved back to the limiter at 10 s, back to the inner wall at 14 s, and back to the limiter at 18 s.

The pumping ability of the inner wall showed no saturation after 10 such discharges in the sequence. Had bombardment-induced deep traps been responsible for the pumping, these would have saturated in 2 seconds, based on the particle fluxes, or in 2 discharges, based on the gas fuelled. These estimates allow for an edge plasma temperature of up to 200 eV, the entire inner wall being completely free of hydrogen, and a wall temperature below 300°C. We conclude that this mechanism is unimportant in this pumping experiment.

The continuous outgassing of the walls is demonstrated by the non-zero value to the H-α radiation from the inner and upper wall during the time the plasma resides on the limiter. A quantitative evaluation of the electron source rate from the H-α brightness gives 6×10^{20}/s. The initial source for this outgassing is the discharge initiation which loads the walls with 50-70% of the prefill gas. As this source empties it is replaced by hydrogen implanted by charge exchange. Note that a fuelling efficiency of 50% implies $\tau_p \sim \tau_w \sim 0.5$ s, indicating the inapplicability to analysis of the steady state of τ_w determined from post-discharge outgassing.

The initial rapid rise of density when the plasma is repositioned on the outer limiter is mainly the result of wall outgassing and the inability of the outer limiters to absorb (more) hydrogen. Ion-induced desorption of hydrogen from the near-surface of the limiter (replenished from deep within by thermally activated diffusion) may contribute up to ~ 20% in the initially rapid rise, as estimated from H-α. We have shown by probe measurements that when the plasma is on the inner wall very few ions impact the outer limiters. Hence the density rise is not due to release of the hydrogen ions implanted in the limiters when the discharge was on the inner wall. The salient point is that the density rise is most closely connected to the amount of gas injected by the dosing and prefill for that discharge only.

Why the inner wall configuration pumps so well compared to the limiter is still a matter of speculation. The H-α signals indicate that a significant (> 30%) part of the 're-fuelling' comes from the top/bottom walls. It has been suggested that different diffusion coefficients exist because of different materials (possibly temperatures) at the walls and limiters. Ehrenberg achieves excellent agreement between the experiment and numerical integration of eqn.(1) using

diffusion coefficients of order $10^{-11,-12}$ cm^2/s and a finite thickness to the material of about 50 nm. The layer thickness L is related to the diffusion coefficient D, such that $\tau_w \sim L/D$. The layer thickness may be related to structure Goebel and co-workers observe. The global particle confinement in the wall calculated by Ehrenberg is about 1.25 s, and is amplified by the recycling and reflection processes near the plasma edge to about 4 s. The confinement time is shorter in the warmer limiter by a factor of 10. The kinematic reflection coefficient in this model is 0.3.

Another model depends on the different carbon areas. This requires a porosity of 15 m^2/m^2 to sorb 5×10^{21} atoms in each discharge. Using the entire area of the inner wall, either surface adsorption (to a maximum areal density of 2×10^{15} cm^{-2}) or supersaturation of the carbon lattice (to 10% above the 0.4 value described in section 2) would require a surface roughness factor in excess of 15, which is expected. But neither a supersaturated bulk or surface layers of such high areal density for deuterium on carbon have been reported. And the correct residence time for deuterium in or on the carbon is required.

Also different edge plasma parameters may occur because of its different configuration. A two-fold drop in τ_p when the plasma is moved onto the inner wall would explain the density behaviour. We do not have sufficiently accurate H-α data to rule out changes in τ_p.

Thus, we know wall outgassing is important. Though good simulations of the density behaviour in Ohmic discharges have been achieved we must conclude that there is not yet data to select between the various plausible mechanisms for temporary hydrogen storage by carbon. However, an important parameter, τ_w, has been measured and future experiments should clarify the relevant processes.

5.2 Neutral-Beam Injection

The density rises during NBI by an amount that depends on wall conditions and plasma configuration (Jones and co-workers, 1987). In fig.7 are shown three cases. For unconditioned inner wall or x-point operation the density rises at an initial rate that is about twice the beam fuelling rate. The thermal part of the edge plasma (Erents, Tagle and McCracken 1987) does not respond as quickly as the density rise, indicating that it is not responsible for desorbing atoms. Heating the walls and limiters is estimated to be too slow to account for the density rise. And the loss of fast ions is not expected to result in a great desorption yield both because of the small losses and the small cross-section, e.g. fig.3. One possible cause is neutral-impact desorption by the charge exchange flux resulting from thermal plasma ions charge exchanging with the neutral beam. As indicated in section 2, greater than unity desorption yields require hydrocarbon (not carbon) films. After conditioning with helium, the best inner wall discharges show an initial rate of density rise equal to the beam current.

Jones has modelled the density behaviour in these discharges. He assumes a global model of the solid, using τ_w instead of a separate diffusion term. The best fit to his data results with $\tau_w = 1$ s, in good agreement with the Ohmic JET models. The asymptotic density rise in the unconditioned inner wall discharges is found from his model to be the beam-fuelling rate times $\tau_p/(\tau_p + \tau_w(1-r_w)/(1-r_p))$.

After termination of NBI into limiter plasmas, the density in a discharge remains above its preinjection value, as in most gas-and pellet-fuelled discharges (Cohen and co-workers, 1987). This is explained by the ratio of confinement times in the Jones model equations. NBI with conditioned walls results in the post-injection density reverting to its preinjection value because of the availability of deep traps to the 'hard' charge exchange neutral spectrum during NBI.

During the H-mode, the plasma particle confinement time doubles and the edge temperature increases above 1 keV about 5 cm inside the separatrix. The drop in H-α light at the divertor plate is then due to the decreased hydrogen ion flux, the decreased kinematic reflection coefficient at the divertor plate, and the decreased desorption cross-section. The initial density rise during the H-mode transition is at about 2.5 times the beam current. The same factors contribute to this density rise as in the case of the unconditioned inner wall, namely outgassing, ion- and neutral-induced desorption, and beam fuelling.

5.3 ICRF Heating

The application of ICRF power to tokamaks results in an instantaneous (t < 0.2 ms) change in the edge plasma (Cohen and co-workers, 1984). The scrape-off layer broadens, causing an increase in ion flux to the wall. The ions neutralize, re-enter the plasma, and cause charge exchange events. Probably the subsequent neutral flux to the walls causes desorption of hydrogen, hence the density rise. Once again a desorption mechanism must be found with greater than unity yield. The density rise during ICRF heating is less at higher currents. Then the walls are proportionally less important than the limiters as sources of gas.

In early JET operation (Cheetham and co-workers, 1986) the density rise associated with ICRF heating increased linearly with power. But continued JET operation has reduced the density rise by a factor of 3, (fig.8) with saturation evident. More recently, helium conditioning has further reduced the density rise another 30-50%. Additional decreases in density rise occur using different antenna configurations (Bures and co-workers 1987).

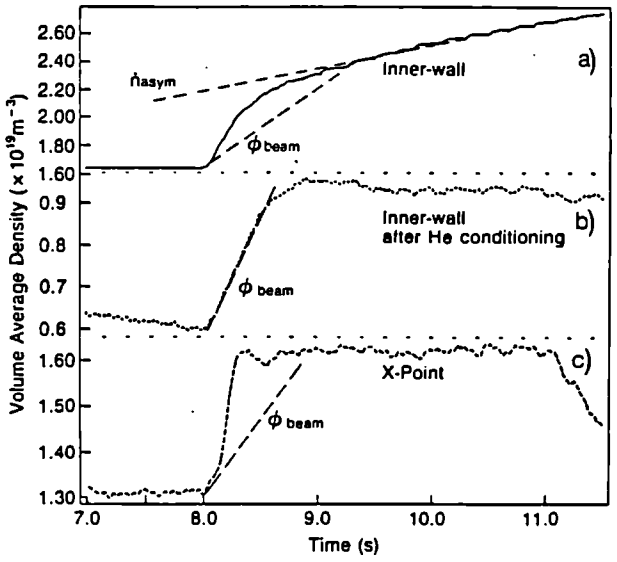

Fig.7 Density rise during NBI for three cases. Also shown is the fuelling rate, Φ_{beam}, and the asymptotic density rise.

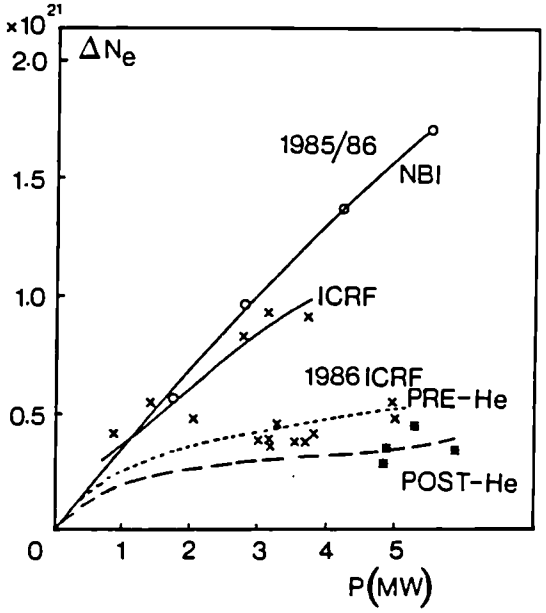

Fig.8 Density rise versus auxiliary heating power for two different operational periods, 1985/1986 and 1986. Reduced density rise was attained during 1986 both by ordinary conditioning (.....) and helium conditioning (-----).

Bures and co-workers (1987) have modelled the evolution of density during ICRF heating. They find the most important term in eqn.(1) is the desorption, which is characterized by two different time scales. Rapid desorption is due to the rapid edge modification caused by RF power absorbed in the edge plasma. A slower desorption occurs, driven by the diffusion of heat out of the core of JET. Again, there is a need to find a process involving carbon bombardment that results in the liberal (greater than unity) release of absorbed hydrogen atoms.

6. FUTURE PLANS

Certain basic materials properties of tokamak-plasma-irradiated carbon must be measured to fully understand the present results and predict future behaviour. The main questions concern hydrogen transport through the damaged and impure lattice. Does hydrogen transport occur between or across graphite planes, along free surfaces, or through stacked faults? What is the thermal activation energy for the transport? Does a supersaturated state exist? Is diffusion in the graphite lattice hindered at high hydrogen concentrations? What is the accessible porosity of irradiated graphite? Are there really only two depths to the hydrogen traps in damaged graphite? Where does recombination to molecules occur? Is desorption in tokamaks spontaneous (thermally activated) or

stimulated by particle impacts? These questions can be answered in the laboratory and must be verified on the tokamaks. In addition, a larger database must be formed of measurements of the hydrogen left in tokamak walls so that the tritium issue and desorption yields can be properly addressed. Detailed post-discharge wall outgassing studies must be made for a variety of discharges. And suggested techniques for removing tritium from the walls should be tried.

The success of low current helium discharge conditioning reopens the question of how to obtain optimum conditioning. One way is with helium glow discharges. In this manner all surfaces are bombarded, not just those nearest the edge plasma. In addition no thermal load - which might act to enhance diffusive repopulation of the depleted surface - is placed on the structures.

As previously described, wall pumping is a desirable if not an essential capability for long pulse operation. How much then is required? We can use the Q=1 case described by Bickerton and co-workers (1987) as a baseline for JET. The average density must be kept at or below 4×10^{19} m^{-3} to have a high enough temperature with the maximum available heating power, 20 MW of NBI and 20 MW of ICRF. If the fuelling were all by neutral beams and the particle confinement time were L-mode, one can readily calculate the particle losses using eqn.(2). This gives a required recycling coefficient of about 0.98, equivalent to 1.5×10^{21}/s of pumping. This has been achieved with the inner wall for a few seconds. For longer duration NBI, both the sorption and power handling capabilities of the inner wall may be stressed. With this high recycling at the edge, a broad profile will result. If a peaked density profile is required to optimize Q, then the location of the fuelling must be better controlled. Core fuelling, as with pellets, must augment the beam fuelling and the wall pumping increased to reduce the edge source. Fig.9 shows the peakedness in the density profile obtainable by altering the ratio of edge, S(a), to central, S(0), fuelling. By decreasing the recycling coefficient to 0.89 and injecting 4.5×10^{21} atoms/s in pellets, the peakedness can be increased to 3 in steady state. The total pumping now required is 6×10^{21}/s, a value never attained. However a pump limiter could be used. Dietz and co-workers, (1987) have designed for JET a pump limiter with an estimated pumping speed equivalent to a recycling coefficient of 0.9. If a higher peakedness is desired, based on our present understanding of wall pumping, pump limiters, and plasma transport, it could only be accomplished in a transient manner. In fig.10 is shown the time evolution of the peakedness and τ_p for a discharge (with standard plasma transport coefficients) heated by NBI and fuelled by pellets. Of

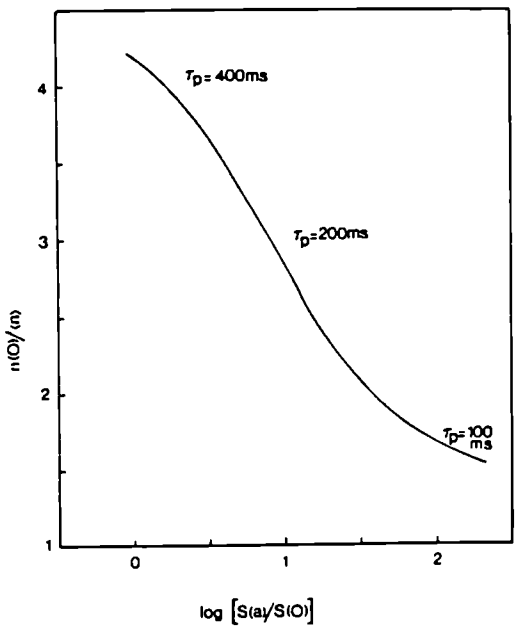

Fig.9 Density profile peakedness, n(0)/<n>, versus location of the electron source. S(a) and S(0) are respectively the electron creation rates near the limiter radius and near the plasma axis.

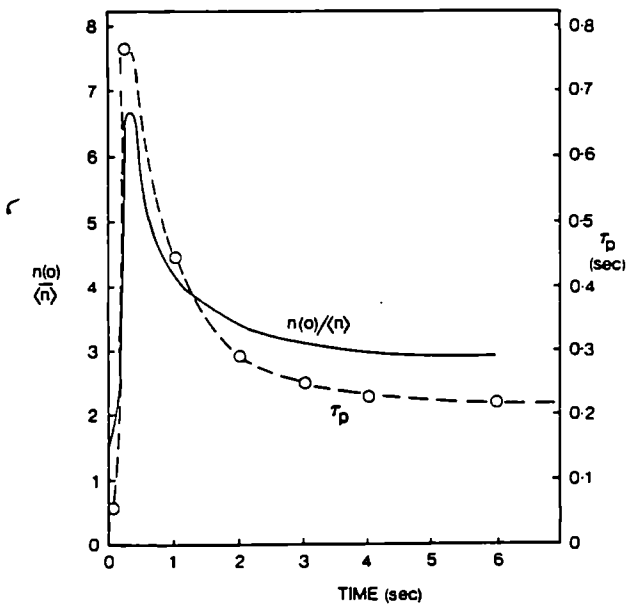

Fig.10 Computed time evolution of the density peakedness and particle confinement time for a JET discharge fuelled with a pellet containing 4×10^{21} atoms at t = 0.05 s and then continuously with 20 MW of 120 keV NBI. The recycling coefficient was set to 0.9.

course, a lowering of the particle diffusivity on the JET axis to increase τ_p there to 10 seconds would also increase the peaking for a longer duration.

The outgassing of the walls observed in JET discharges provides an unwanted and an as-yet-uncontrolled fuelling with cold gas. Better discharge initiation and wall conditioning could eliminate this in the future. What benefits would occur? We examine the effect on H-modes by the following 1 1/2-d simulation of JET discharges with auxiliary heating. Good simulations of Ohmic and L-mode phases are obtained using the critical temperature gradient model for electron energy transport (Rebut, Watkins, and Lallia, 1987). If in these calculations the edge particle transport is modified by reducing the particle diffusion coefficient to 1/4 its standard value in the vicinity of the separatrix, pedestals on the edge temperature reminiscent of the H-mode form. This ansatz of a reduced particle diffusivity is consistent with the experimental observations of reduced recycling fluxes during H-modes. If the additional gas fuelling due to outgassing, 6×10^{20}/s, is shut-off in the calculations, even higher pedestals in temperature occur (fig.11), leading to increased stored energy and higher central temperatures. We also speculate that an influx of cold gas leads to the termination of H-modes by its adverse effect on the edge temperature. Hence reduced edge fuelling by reduction of wall outgassing will result in a longer duration of the high edge temperature and the H-mode itself.

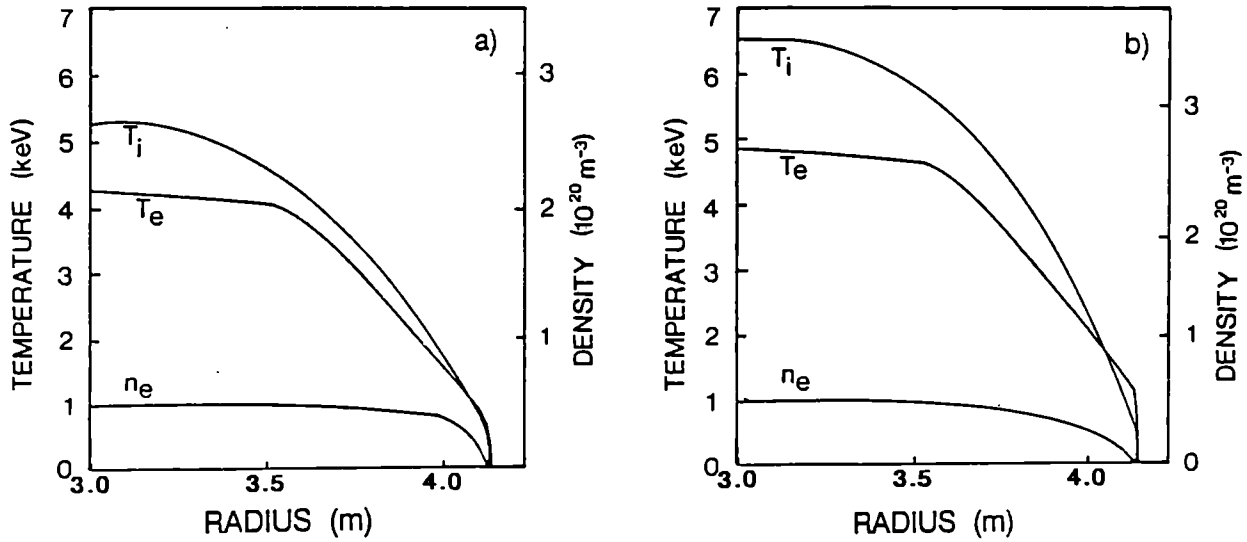

Fig.11 Calculated density and temperature profiles for two JET-like plasmas. The transport coefficients are described in the text. The wall outgassing was set to 6×10^{20}/s in a) and 0 in b). Note the higher central and edge temperatures in b) for these H-mode simulations.

ACKNOWLEDGEMENTS

We thank Dr R Behrisch and Prof P C Stangeby for their comments and Drs H F Dylla, H Kishimoto, W Poschenrieder, M Redi, B Wampler, P Wienhold, J Winter and M Yoshikawa for unpublished data.

REFERENCES

Amemiya, S. (1987). In T. Yamashina (Ed.), Characterization of Graphite as a First Wall and Evaluation of the Stability Against Plasma, Hokkaido University, Sapporo, pp.52-60.

Andersen, H.H. and J.F. Ziegler (1977). The Stopping and Ranges of Ions in Matter, Vol.3, Pergamon Press, New York.

Behrisch, R. and W. Eckstein (1984). In D.E. Post and R. Behrisch (Ed.), Physics of Plasma-Wall Interactions in Controlled Fusion, Plenum Press, New York, pp.413-438.

Behrisch, R. (1987). Private communication.

Behrisch, R., J. Ehrenberg, M. Wielunski and co-workers (1987). J. Nucl. Mater. 145-147, 732-726.

Bergsåker, H., R. Behrisch, J.P. Coad, and co-workers (1987). J. Nucl. Mater., 145-147, 727-730.

Bickerton, R.J., and the JET Team (1987). Plasma Physics & Controlled Fusion. This volume.

Bures, M., V.P. Bhatnagar, M.P. Evrard, and co-workers (1987). Proceedings 13th European Conference on Controlled Fusion and Plasma Physics, Madrid, Vol.11D, Part II. pp.722-725.

Causey, R., M.I. Baskes, and K. Wilson (1986). J. Vac. Sci. and Technol., A4, pp.1189-1192.

Cheetham, A., J.P. Christiansen, S. Corti, and co-workers (1986). Proceedings 12th European Conference on Controlled Fusion and Plasma Physics, Schliersee, Part I. pp.240-243.
Chen, C.K., B.M.U. Scherzer, and W. Eckstein (1984). Appl. Phys. A. 33, pp.265-268.
Cohen, S.A., H.F. Dylla, S. Rossnagel, and co-workers (1978). J. Nucl. Mater, 76/77, pp.459-471.
Cohen, S.A., D. Ruzic, D.E. Voss, and co-workers (1984). Nucl. Fusion 24, pp.1490-1494.
Cohen, S.A. (1984). In D.E. Post and R. Behrisch (Ed.), Physics of Plasma-Wall Interactions in Controlled Fusion, Plenum Press, New York. pp.773-854.
Cohen, S.A., J. Ehrenberg, D.V. Bartlett, and co-workers (1987). Proceedings 13th European Conference on Controlled Fusion and Plasma Physics, Madrid, Vol.11D, Part II. pp.694-697.
Dietz, J. and co-workers (1987). Private communication.
de Kock, L. and the JET Team (1987). J. Nucl. Mater., 145-147, pp.26-40.
Dylla, H.F. (1980). J. Nucl. Mater., 93 & 94, pp.61-70.
Dylla, H.F., P.H. LaMarche, M. Ulrickson, and co-workers (1987). Nucl. Fusion, in press.
Eckstein, W. and D. Heifetz (1987). J. Nucl. Mater., 145-147, pp.332-338.
Ehrenberg, J. (1987). J. Nucl. Mater., 145-147, pp.551-555.
Ehrenberg, J., S.A. Cohen, L. de Kock, and co-workers (1987). Proceedings 13th European Conference on Controlled Fusion and Plasma Physics, Madrid, Vol.11D, Part II. pp.706-709.
Engelhardt, W. and W. Feneberg (1978). J. Nucl. Mater., 76-77, pp.518-520.
Erents, S.K., J.A. Tagle, G.M. McCracken, and co-workers (1987). Proceedings 13th European Conference on Controlled Fusion and Plasma Physics, Madrid, Vol.11D, Part II. pp.740-743.
Eubank, H.P., R.J. Goldston, V. Arunasalam, and co-workers (1979). Phys. Rev. Lett. 43, 270-274.
Goebel, D.M., Y. Hirooka, R.W. Conn, and co-workers (1987). J. Nucl. Mater., pp.61-70.
Gondhalekar, A., M. Bures, D. Campbell, and co-workers (1987). In Plasma Physics and Controlled Fusion Research, IAEA, Vienna. IAEA-CN-47/I-I-6.
Greenwald, M., D. Gwinn, S. Milora and co-workers (1984). Phys. Rev. Lett., 53 p.352.
Hawryluk, R.J., V. Arunasalam, M.G. Bell, and co-workers (1987). Plasma Physics and Controlled Nuclear Fusion Research, IAEA, Vienna. IAEA-CN-47/A-1-3.
Hsu, W. and R. Causey (1987). J. Vac. Sci. and Technol. A5 (6). In press.
Hubbard, A., D. Ward and T.E. Stringer (1986). Proceedings 12th European Conference on Controlled Fusion and Plasma Physics, Schliersee, Part I. pp.232-235.
Jones, T.T.C., E. Thompson, A. Gondhalekar, and co-workers (1987). Proceedings 13th European Conference on Controlled Fusion and Plasma Physics, Madrid, Vol.11D, Part I. pp.17-19.
LaMarche, P., H.F. Dylla, P.J. McCarthy, and co-workers (1986). J. Vac. Sci. and Technol. A4, pp.1198-1202.
Lackner, K., R. Chodura, and M. Kaufmann (1984). Plasma Physics & Controlled Fusion, 26, 105-115.
McCracken, G.M. (1987). Plasma Physics & Controlled Fusion. This volume.
Mioduszewski, P. (1984). In D.E. Post and R. Behrisch (Ed.), Physics of Plasma-Wall Interactions in Controlled Fusion, Plenum Press, New York. pp.891-930.
Nakamura, H., T. Ando, S. Niikura, and co-workers (1986). JAERI-M 86-173.
Nakamura, K., S. Fukuda, T. Hino, and co-workers (1987). J. Nucl. Mater., 145-147, 301-304.
Philipps, V., E. Vietzke, M. Erdweg, and co-workers (1987). J. Nucl. Mater., 145-147, 292-296.
Rebut, P.H. and P.P. Lallia (1987). JET Preprint-P(87)15.
Rebut, P.H., M. Watkins and P. Lallia (1987). Proceedings 13th European Conference on Controlled Fusion and Plasma Physics, Madrid, Vol.11D, Part I. pp.172-175.
Roth, J. (1987). J. Nucl. Mater., 145-147, pp.87-95.
Scherzer, B.M.U., P. Borgesen and W. Möller (1987). IPP-JET-Report No.32.
Stangeby, P.C. (1987). J. Nucl. Mater., 145-147, pp.105-117.
Stangeby, P.C., J.A. Tagle, S.K. Erents and co-workers (1987). Proceedings 13th European Conference on Controlled Fusion and Plasma Physics, Madrid, Vol.11D, pp.670-673.
Staudenmaier, G., J. Roth, R. Behrisch, and co-workers (1979). J. Nucl. Mater. 84, 149.
Tagle, J.A., S.K. Erents, G.M. McCracken, and co-workers (1987). Proceedings 13th European Conference on Controlled Fusion and Plasma Physics, Madrid, Vol.11D, Part II. pp.662-665.
Voss, D.E. (1980). Ph.D. Thesis, Princeton University.
Wagner, F., M. Keilhacker and the ASDEX and NI Teams (1984). J. Nucl. Mater., 121, 103.
Wagner, F. and K. Lackner (1984). In D.E. Post and R. Behrisch (Ed.), Physics of Plasma-Wall Interactions in Controlled Fusion, Plenum Press, New York. pp.931-1004.
Wampler, B. and B. Doyle (1987). Private communication.
Wang, Y.G., W.P. Poschenrieder and G. Venus (1986). J. Vac. Sci. and Technol. A4, pp.2520-2525.
Wilson, K. and Hsu, W. (1987). J. Nucl. Mater., 145-147, pp.121-130.
Winter, J. (1987a). J. Nucl. Mater., 145-147, pp.131-145.
Winter, J. (1987b). J. Vac. Sci. and Technol., A5(6). In press.

Invited paper presented at the 14th European Conference on
Controlled Fusion and Plasma Physics, Madrid, Spain, 22nd-26th June 1987

Operational Limits and Confinement in JET

R. J. Bickerton (The JET Team)

ABSTRACT

Operational limits on JET in terms of density, current and plasma beta are described. The results for various heating schemes are displayed in the $\hat{n}\,\tau_E\,\hat{T}_i$ vs $\hat{T}_i$ plane against the contours of constant thermonuclear gain Q. The confinement data is compared with several scaling laws and the eventual performance of JET predicted. Finally the likelihood of ignition in the enhanced version of NET is assessed.

KEYWORDS

Tokamak; Fusion.

INTRODUCTION

JET is a large tokamak with the parameters listed in Table 1. It has been operated with plasma currents up to 5MA in limiter bounded mode and 3MA with a single null magnetic separatrix. The additional heating capability has been up to 10MW of neutral beam injection and 8MW of ion cyclotron resonance heating (ICRH). The machine has recently been modified in such a way that the above numbers will be increased to 7MA (limiter), 4MA (single null), 20MW (neutral beam) and 20MW (ICRH) respectively. A further modification planned for 1990 is the addition of 10MW of lower hybrid power for current drive studies.

In this paper we outline the operational limits already encountered together with the performance levels achieved. The theoretical MHD stability limits on β are then discussed and the existing experimental data presented. Several different scaling laws for the energy confinement time have been proposed on the basis of JET and other tokamak data. These are compared and the eventual JET performance is estimated. Scaling from the JET data the prospects for NET are considered.

TABLE 1

JET PARAMETERS

MAJOR RADIUS, R_o(m)	3.0
MINOR RADIUS OF PLASMA, a(m)	1.2
ELONGATION OF PLASMA CROSS-SECTION, K	≤1.8
TOROIDAL FIELD STRENGTH AT R_o, (T)	3.4
PLASMA CURRENT (MA)	
(a) LIMITER BOUNDED	5.0(7.0)
(b) SINGLE NULL X-POINT	3.0(4.0)
NEUTRAL BEAM HEATING POWER(MW)	10(20)
ICRF HEATING POWER (MW)	8(20)

(Bracketted figures are the anticipated performance levels for the 87/88 campaign.)

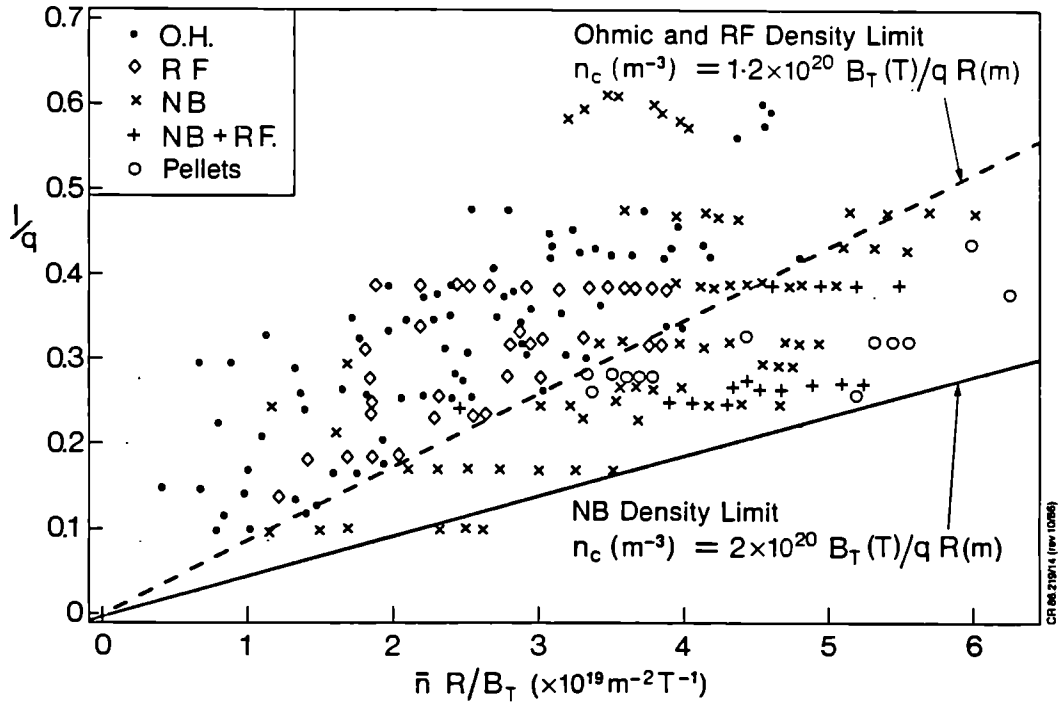

Fig. 1. Plot of operating conditions in normalised current, normalised density plane. $q_{CYL} = 5AB/\pi RI$ where A is the cross-sectional area of the plasma (m^2), B_T the toroidal field strength (T), R the major radius (m) and I the plasma current (MA). $\bar{n}$ is the average electron density (m^{-3}).

DENSITY AND CURRENT LIMITS

The density and current limits experienced on JET are presented in normalised form in Fig. 1.

Here q_{CYL} is defined as

$$q_{CYL} = \frac{5AB}{\pi RI}$$

where A is the cross-sectional area of the plasma, R the major radius, B the toroidal field strength and I the plasma current. Units are m, T, MA. The Murakami parameter M is defined as

$$M = \frac{\bar{n}R}{B}$$

where n is the average electron density in units of $10^{19}m^{-3}$.

The data in figure 1 shows that the operating regime is bounded on three sides. There is a working low density limit set approximately by $M<(1/q)$. This limit is complex and depends on the time history of the discharge. During the current rise phase the neutral particle influx and correspondingly the density must be above a minimum level to avoid MHD mode-locking and disruptions (J. Snipes et al, 1987) or the creation of runaway electrons with $\varepsilon>1$MeV. Once the flat-top in total current is reached the density can be progressively reduced by switching off gas input and moving the discharge on to a surface with a high particle pumping capacity such as the carbon tiles on the small major radius side of JET (referred to henceforth as the "inner wall"). In this way slide-away discharges can be created with densities down to $1.5\times10^{18}m^{-3}$ and with no sign of a lower limit other than the time available for pumping. Note that in the normalised plot, lines of constant ratio between $(1/q_{CYL})$ and M are lines of constant electron drift velocity, V_d

$$V_d = 1.6\times10^6\left(\frac{1}{Mq_{CYL}}\right)\ m/s$$

Another limiting line is the density limit above which the discharge disrupts. For normal Ohmic

and RF-heated discharges this is a fairly well defined boundary given by

$$(n_c)_1 = \frac{1.2\times10^{20}\ B}{q_{CYL}\ R}$$

while with neutral beam injection at powers up to 10MW the limit is considerably higher at

$$(n_c)_2 = \frac{2\times10^{20}\ B}{q_{CYL}\ R}$$

With ohmic heating alone the limit $(n_c)_1$ can be significantly exceeded by the injection of a single deuterium pellet.

A third line bounding stable operation is given by $1/q_{CYL} \sim 0.6$. Careful experiments have shown that this "low q" boundary is precisely given by $q_\psi=2$, where q_ψ is the actual field line safety factor at the plasma boundary. (Campbell et al, 1986)

Note that the achievable values of M in JET have a maximum at 6-7 for low q_{CYL} while the design value for NET is 16 (Engelmann, 1986) and for an economic reactor $\sim$ 30. Thus it is important to understand the mechanism of high density disruptions.

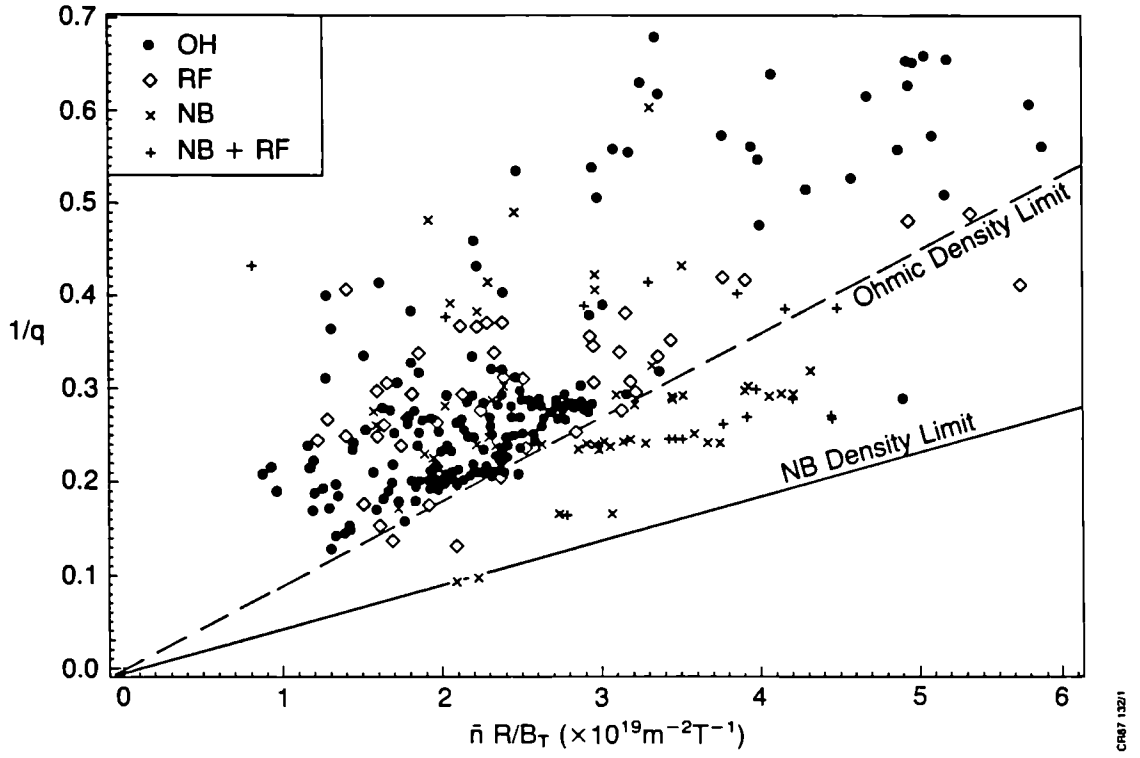

Fig. 2. Plot of operating conditions in the normalised current, $(1/q)$ normalised density $(\bar{n}R/B_T)$ plane for the 1986 disruptions which occurred during the current flat-top.

Figure 2 shows the disruption data in the density-current plane for the flat-top phase of the plasma current waveform. Most of the points are well inside the so-called stable zone of Fig. 1. For $q_{CYL}>2.5$ these disruptions are nearly all preceded by a rise in the radiated power P_{RAD} to equal the input power. For $q_{CYL}<2.5$ the majority of the disruptions are not preceded by such a rise. These low q disruptions reflect the high sensitivity of discharges when the resonant surface $q_\psi=2$ approaches the plasma boundary. In fact detailed study shows that high density disruptions are preceded by a rise in the radiated fraction followed by a shrinking of the temperature profile and of the current channel (Campbell et al, 1986). Thus some of the unpredictability of disruptions is related to varying contamination of the discharge. Increasing the power input into the discharge increases the density limit unless as in the RF case the increase in power is accompanied by an increase in the edge density. Deuterium pellet injection raises the density but reduces Z_{eff} while increasing the Ohmic input.

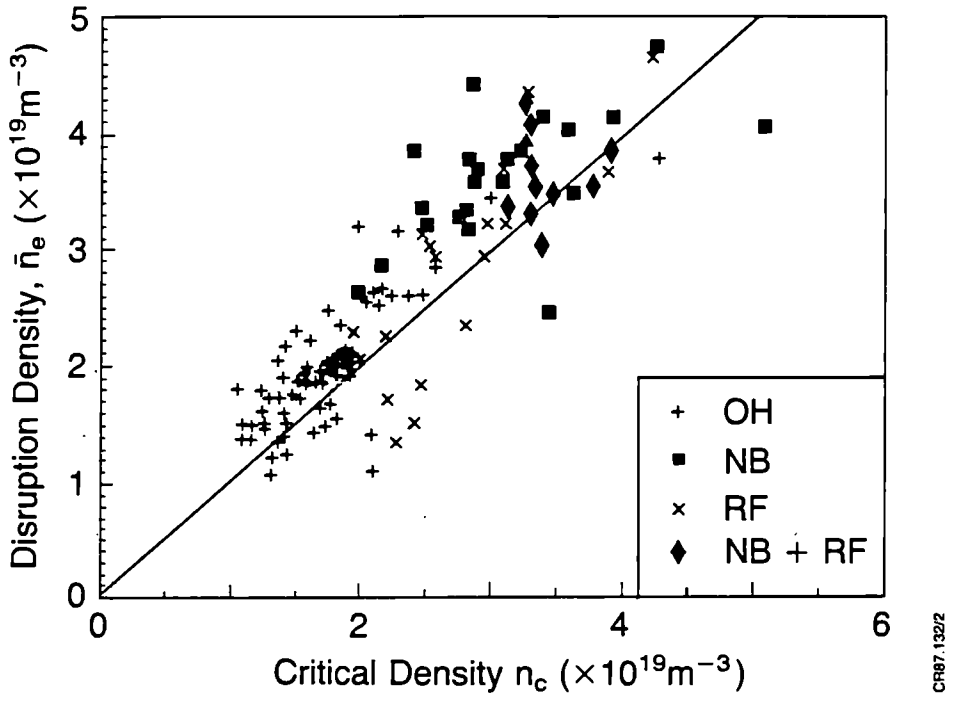

Fig. 3. Comparison between the density at disruption and the critical value predicted by the expression $n_c = 3.5 \left\{ \frac{P_{IN}\, q_{CYL}}{(Z_{eff}-1)\, R\, ab\, (q_{CYL}-2a/b)} \right\}^{1/2}$

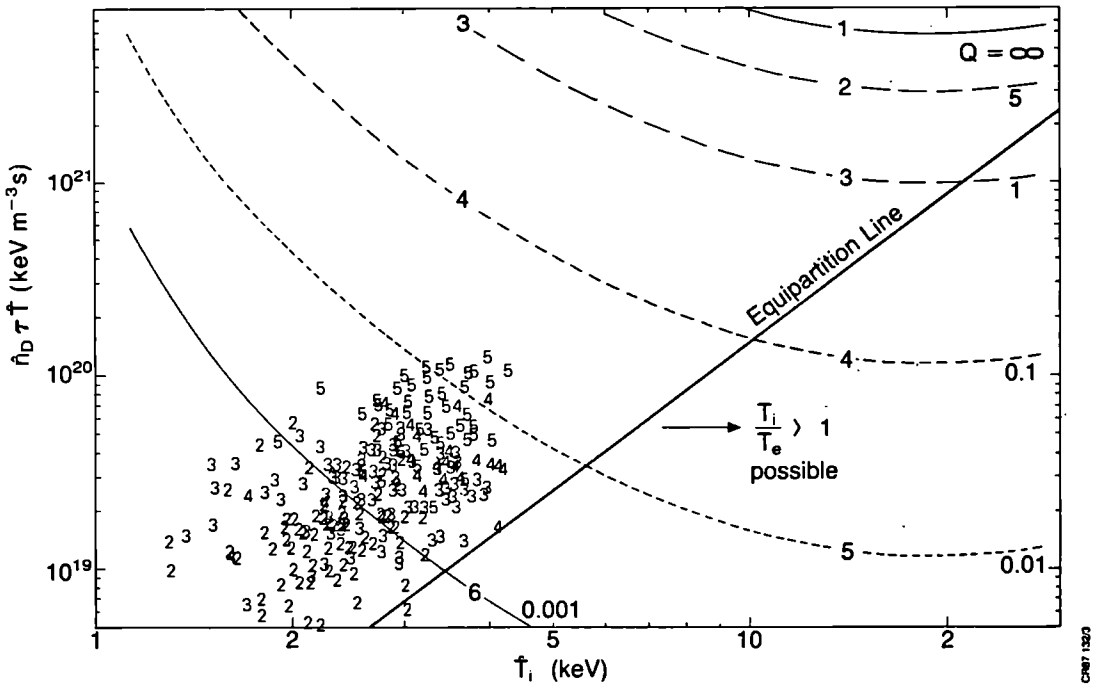

Fig. 4. Data for ohmic heating only discharges plotted in the $\hat{n}_D\, \tau_E\, \hat{T}_i - \hat{T}_i$ plane. Numbers refer to the current level in MA. Equipartition line shows $\hat{n}\, \tau_E\, \hat{T}_i = 4.5 \times 10^{17}\, \hat{T}_i^{5/2}$. Contours show lines of constant Q (Q=thermonuclear power output/power input). Discharges bounded by limiters or inner wall.

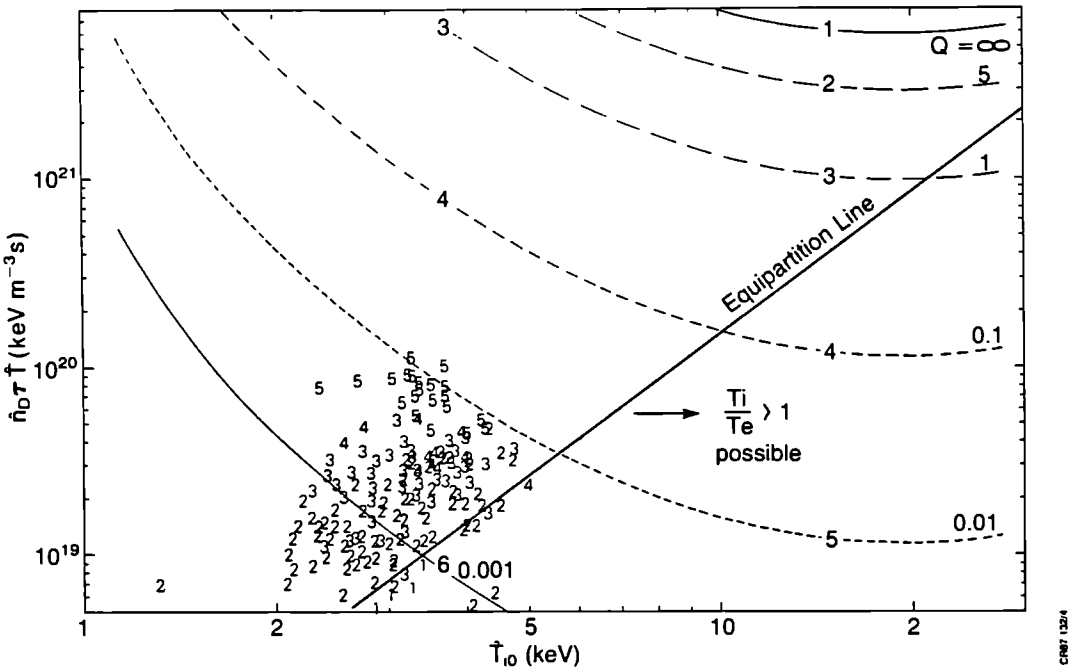

Fig. 5. Data for RF heating only discharges plotted in the $\hat{n}_D \tau_E \hat{T}_i - \hat{T}_i$ plane. Numbers refer to the current level in MA. Equipartition line shows $\hat{n} \tau_E \hat{T}_i = 4.5 \times 10^{17} \hat{T}_i^{5/2}$. Contours show lines of constant Q (Q=thermonuclear power output/power input). Discharges bounded by limiters or inner wall.

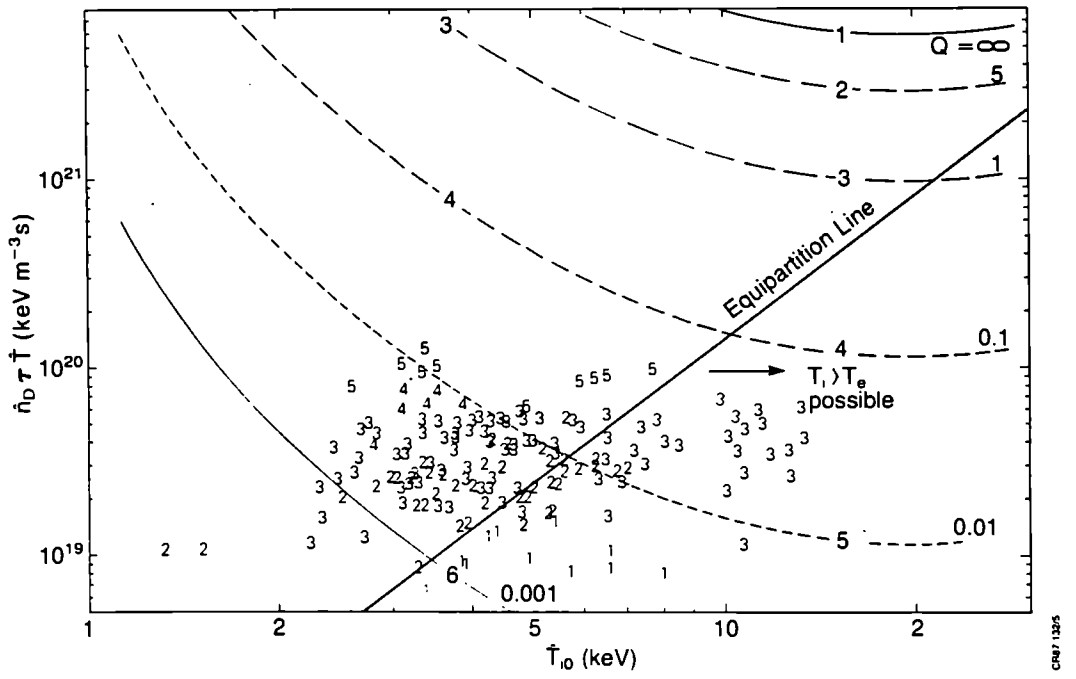

Fig. 6. Data for neutral beam heating only discharges plotted in the $\hat{n}_D \tau_E \hat{T}_i - \hat{T}_i$ plane. Numbers refer to the current level in MA. Equipartition line shows $\hat{n} \tau_E \hat{T}_i = 4.5 \times 10^{17} \hat{T}_i^{5/2}$. Contours show lines of constant Q (Q=thermonuclear power output/power input). Discharges bounded by limiters or inner wall.

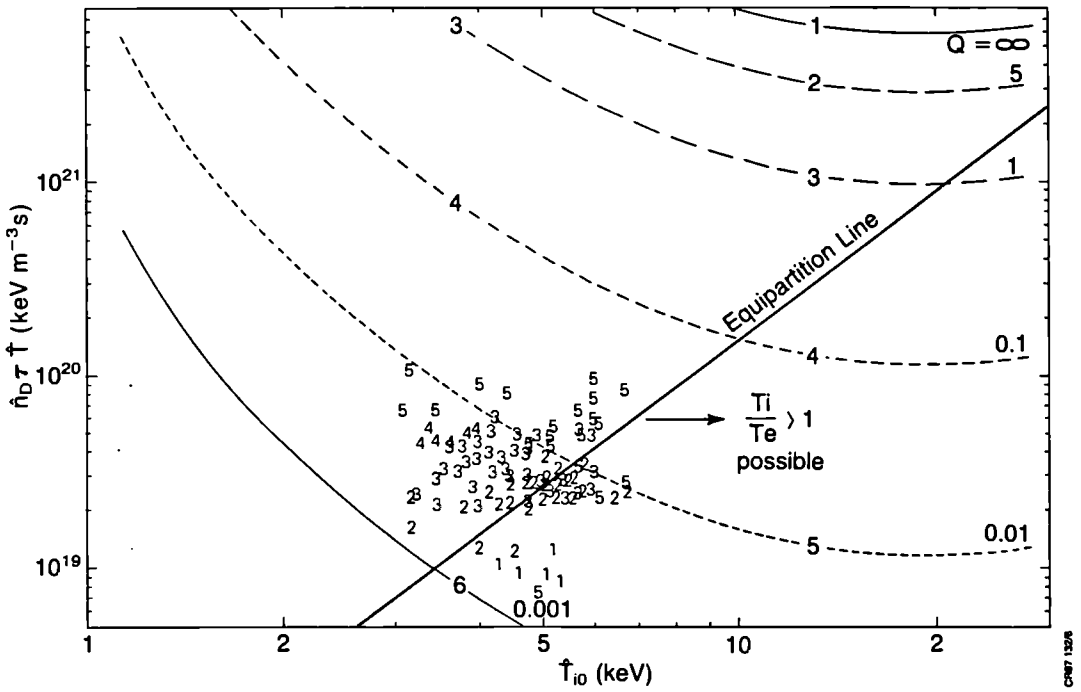

Fig. 7. Data for combined neutral beam and RF heating discharges plotted in the $\hat{n}_D \tau_E \hat{T}_i - \hat{T}_i$ plane. Numbers refer to the current level in MA. Equipartition line shows $\hat{n} \tau_E \hat{T}_i = 4.5 \times 10^{17} \hat{T}_i^{5/2}$. Contours show lines of constant Q (Q=thermonuclear power output/power input). Discharges bounded by limiters or inner wall.

A simplified model (Campbell et al, 1986) for low Z dominated discharges (ie valid for $Z_{eff} \neq 1$) based on the triggering of disruption as $P_{RAD}/P_{IN} \rightarrow 1$ gives

$$M = \frac{3.5}{B} \left\{ \frac{P_{IN} \; R \; q_{CYL}}{(Z_{eff}-1) \; a \; b \; (q_{CYL}-2a/b)} \right\}^{1/2}$$

where the units are m, MW and the term $(\frac{q_{CYL}}{q_{CYL} - 2a/b})$ is approximately the ratio of the total volume to the volume outside the $q_\psi = 2$ surface.

This gives good agreement with JET data Fig. 3 and suggests that to achieve high M in future machines will require a substantial increase in the power input per unit length and a reduction of Z_{eff} compared with JET. This latter improvement is required in any case to reduce the depletion of the reacting fuel.

EQUIVALENT THERMONUCLEAR Q VALUES

Q is defined as, $Q = \frac{P_{th}}{P_{input}}$

where P_{th} is the total thermonuclear output power for a D-T plasma.

$$P_{th} = \int dV \; n_D n_T \; (\overline{\sigma v}) \; Y$$

where $\overline{\sigma v}$ is the velocity cross-section product averaged over a Maxwellian ion distribution for temperature $T_i(r)$ and Y = 17.6MeV is the energy yield per reaction.

In steady state $P_{INPUT} = P_{LOSS} - P_\alpha = P_{LOSS} - \frac{P_{th}}{5}$

where P_{LOSS} is the total power loss from the system and P_α is the α-power input which is assumed to be all deposited in the plasma.

$$P_{LOSS} = \frac{W}{\tau_E}$$

where W is the total energy content in the plasma and τ_E the global energy confinement time.

The JET results are plotted in the $\hat{n}\ \hat{T}_i\ \tau_E$ vs $\hat{T}_i$ plane in Figs. 4-7. In this plane are also plotted the contours of constant Q assuming $T_e=T_i$, the density and temperature profiles typical of the experiments and $n_D=n_T=\frac{1}{2}(n_D)_{Expt}$ where $(n_D)_{Expt}$ is the experimental deuteron density (determined from the measured Z_{eff} and the assumption that the depletion is due to carbon and oxygen).

The results for four different heating scenarios are shown in Figs. 4-7, namely for ohmic heating only, RF heating, neutral beam heating and combined RF and neutral beam heating. This data is for plasmas bounded on either the outer limiters or the inner wall. It is evident that the highest Q values (close to 0.1) are reached with 3MA discharges on the inner wall with neutral beam heating. The highest ion temperatures are reached in these same discharges where the strong pumping action of the carbon tiles enables the density to be kept low ($1\text{-}2\times10^{19}m^{-3}$). In these plasmas $T_i/T_e \sim 2$, giving the so-called hot ion mode. This means that the Q values derived from the contours are underestimated by a factor of $\frac{(1+T_e/T_i)}{2}$. The ability to increase the ratio T_i/T_e depends on two conditions,

(1) the additional heating system must predominantly heat the ions directly.
(2) the equipartition time τ_{equ} must be significantly longer than the global confinement time.

Classically

$$\tau_{equ} = \frac{0.084\ T_e^{3/2}\ (keV)}{n_{e19}}$$

If we define $T_i/T_e>1.5$ as a hot-ion mode then in the $\hat{n}\ \hat{T}_i\ \tau_e$ vs $\hat{T}_i$ plane the line

$$\hat{n}\ \tau_E\ \hat{T}_i = 4.5\times10^{17}\ \hat{T}_i^{5/2}$$

divides the regime where the hot ion mode is possible from that in which equipartion ensures $T_e \sim T_i$. This line is shown on Figs. 4-7 where we see that the neutral beam results at high ion temperature are all in the hot ion regime. Note that the hot ion mode criterion intersects the ignition requirement at $\hat{T}_i \sim 50keV$. Thus it is not the optimum route all the way to ignition but it is certainly a promising approach to $Q \sim 1$.

Figure 8 shows the X-point results in the same plane. Evidently $Q \sim 0.1$ conditions are reached in the H-mode single null discharges even at 2MA (A Tanga, Kyoto, Nuclear Fusion etc.). These results were obtained with neutral beam heating only.

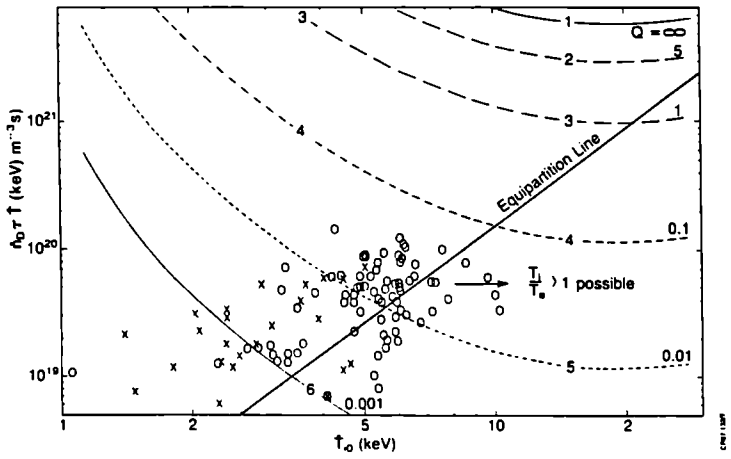

Fig. 8. Data for separatrix bounded plasmas, all heating schemes. X - Double null results (2MA), O Single null results (2&3MA). Upper single null results are H-modes all with only neutral beam heating. Contours of constant Q as in figures 4-7.

LIMITATIONS ON ADDITIONAL HEATING SYSTEMS

Neutral Beam Injection

The main limitations are on the plasma density. The density must be high enough to avoid excessive shine through and low enough to maintain a power deposition profile peaked in the central core of the plasma.

For JET with 120kV deuterium beams these limits are

$$1.10^{19}cm^{-3} < \bar{n} < 4x10^{19}\ cms^{-3}$$

Other factors notably limitations on confinement time mean that this is a fully acceptable operating range.

Ion Cyclotron Resonance Heating (ICRH)

ICRH has the proven advantage of very localised power deposition depending primarily on the choice of magnetic field, frequency and minority species. However there is a serious limitation due to the need to have the plasma boundary sufficiently close to the antenna screen in order to achieve good coupling. Figure 9 shows the theoretical and experimental variation of coupling resistance with plasma distance for the antennae used in the past. There is quite good agreement. Also shown are the theoretical values for the new design of antenna, eight of which are now installed on the machine. It is clear that it should be possible to couple significant power to the plasma in the promising scenario of X-point operation. In this case it is important that the plasma-antenna distance exceeds some critical value, at present unknown but probably ≥5cms. The importance of increasing the voltage hold-off capability of the antenna-feeder combination is also evident.

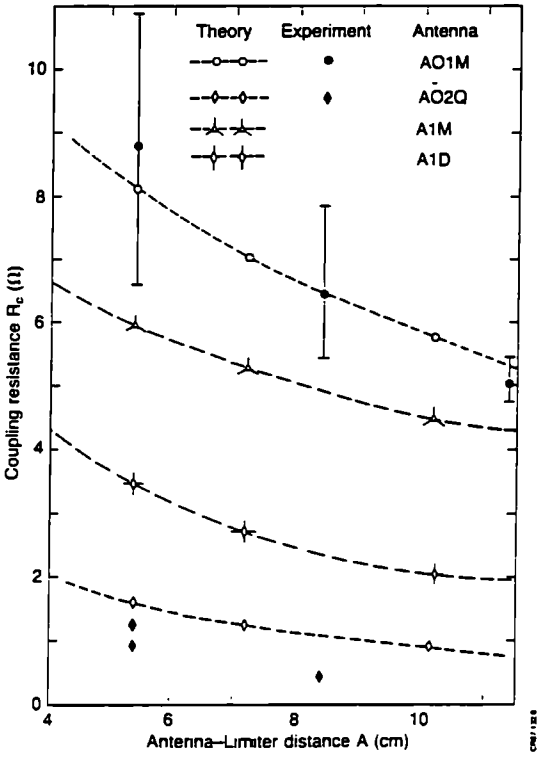

Fig. 9. Variation of coupling resistance R_c with antenna - plasma distance. A01M and A02Q are the antennae used in the 1985/1986 campaign in the monopole and quadrupole configurations. A1M and A1D are the newly installed antennae of different design operating in the monopole and dipole configurations. Coupled power is proportional to V^2R_c where V is the voltage on the antenna. A1D should have the same favourable properties as A02Q in that it has no component with $K_{||}$ =0. At the same time it should have a higher coupling resistance.

β - Limits

The theory of limiting β due to MHD instabilities (Troyon et al, 1984) has been remarkably successful in predicting the operating limits which are observed experimentally. The Troyon limit is,

$$\bar{\beta} = 2.8 \frac{I}{Ba} \quad \% \qquad (\bar{\beta} \text{ is the value of } \beta \text{ averaged over the plasma volume})$$

and is derived by optimising the pressure profile. Hender et al (1987) have studied the MHD stability of a wider range of pressure profiles. For JET at 7MA and full field 3.5T they find the limits on $\bar{\beta}$ and β_o vs $P_o/\langle p \rangle$ shown in Fig. 10 for a given q_ψ profile with q_ψ=3.6 at the boundary. Evidently the more peaked the pressure profile the lower the permissible values of both β_o and $\bar{\beta}$ in this case. The thermonuclear Q depends very weakly on this profile provided $7<T_i<20$keV but depends linearly on central values of $\hat{n}\,\hat{T}_i\,\tau_e$, ie on $\beta_o\,\tau_E$. For JET with B=3.5T a thermonuclear Q=1 requires $\beta_o\tau_E$=9%s. Taking the maximum β_o from Hender et al (=15%) gives a simple requirement on τ_E, τ_E>0.6s for a profile in which $P_o/\langle p \rangle$ = 3.

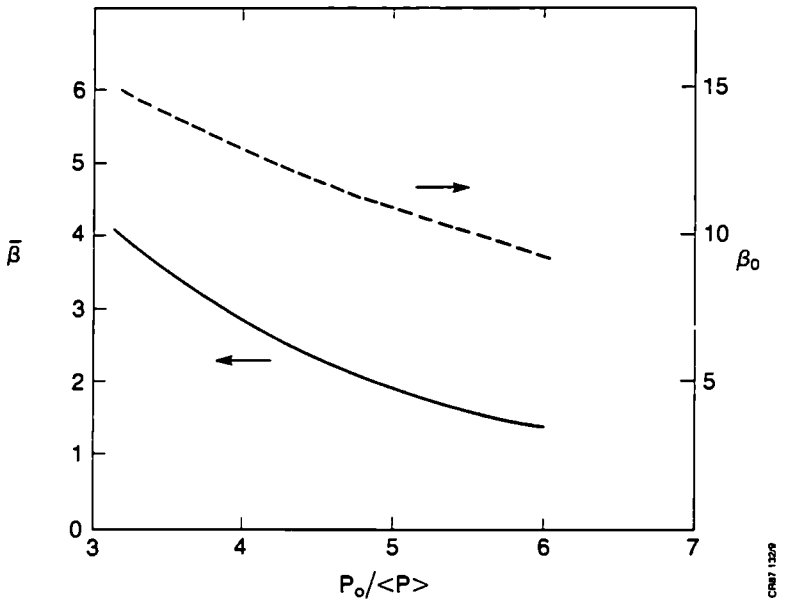

Fig. 10. Variation of ideal MHD stable values of $\bar{\beta}$ and β_o with the pressure peaking factor $p_o/\langle p \rangle$. Calculation is for q_ψ ranging from 1.2 on the axis to 3.6 at the boundary corresponding to 7MA in JET with B_T=3.5T.

In Fig. 11 the present experimental results on $\bar{\beta}$ are plotted vs $I/_{Ba}$. The line represents the Troyon limit. Evidently we have achieved ∿ 0.6 x the limit in H-modes at currents of 2-3MA. As we will see later the combination of available input power and confinement time degradation is likely to be more limiting to JET performance than MHD modes.

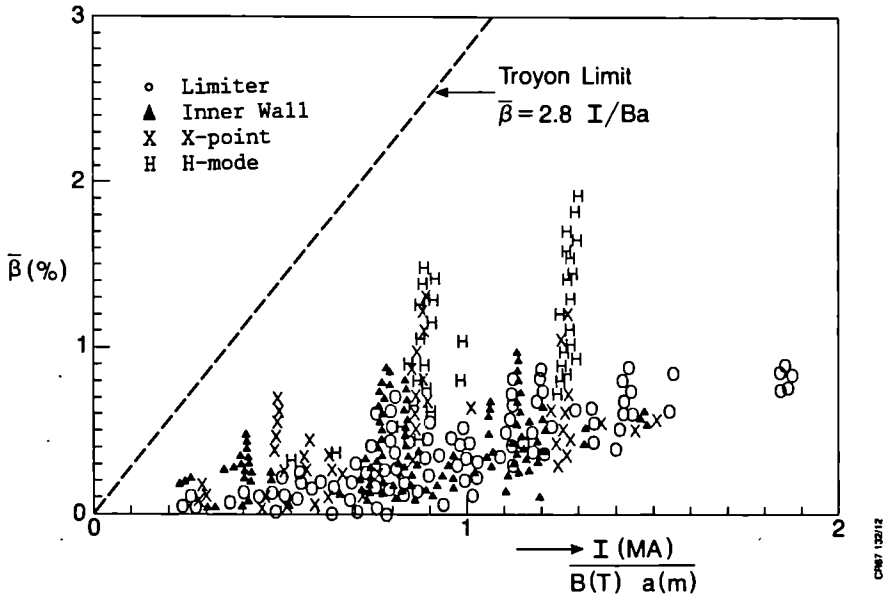

Fig. 11. The values of $\bar{\beta}$ derived from diamagnetic data versus the parameter I/Ba. Dotted line shows Troyon limit with K_T=2.8

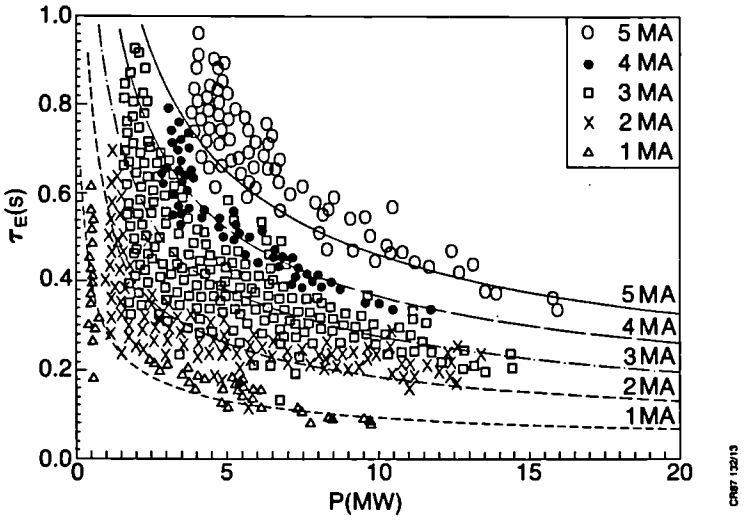

Fig. 12a. Confinement time τ_E versus input power for plasmas bounded on the inner wall or outer limiters. Lines are the predictions of the Goldston L-mode formula for an elongation of 1.4.

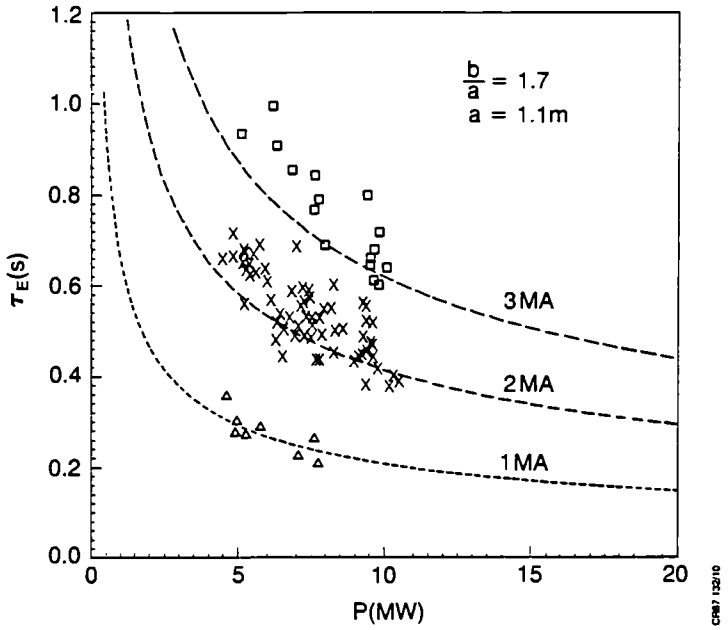

Fig. 12b. Confinement time versus input power for H-mode discharges with single null magnetic separatrix boundary. Lines are 2 x the predictions of Goldston L-mode scaling with the appropriate elongation. (=1.7)

ENERGY CONFINEMENT TIME

Figure 12a shows the confinement time vs power for all JET data excepting that for X-point operation. The lines plotted correspond to the scaling developed by Goldston (1984) namely,

$$\tau_E(s) = 3.7\text{x}10^{-2}\ I_p\ P^{-\frac{1}{2}}\ R^{1.75}\ a^{-0.37}\ K^{\frac{1}{2}}$$

It is remarkable that this expression with unchanged constants fits JET data so well since it was derived from tokamaks smaller in physical scale by a factor 3 and smaller in maximum current by a factor 10.

The H-mode results (Tanga et al) show a similar degradation with power but an important improvement over the L-mode by just over a factor 2 as shown in Fig. 12b. These discharges do not reach a steady state, the density rises continuously so that the beam power is progressively deposited in the outer regions. Consequently the degradation of confinement time may not be an intrinsic feature of JET H-modes. (Keilhacker - this conference)

P. Thomas (1987) has used Connor-Taylor variables to derive a power law scaling fitting the JET data, for limiter discharges he finds

$$\tau_E(s) = 3.4\ (\tau_R\ \tau_A)^{0.5}\ \beta_I^{-1}$$

where τ_R is the resistive penetration time, τ_A the poloidal Alfven transit time and $\beta_I=(\frac{1+\epsilon^2}{2\epsilon}).\frac{2.12W}{I^2R}$ where W is the plasma energy content. (MJ).

Guided by a model in which a critical electron temperature gradient exists for the development of magnetic islands embedded in regions of stochastic field Rebut et al (1987) have derived an expression for the electron energy content of the plasma W_e,

$$W_e = \alpha_1\ Z^{\frac{1}{4}}\ n_e^{\frac{1}{4}}\ B^{\frac{1}{2}}\ I^{\frac{1}{2}}\ \ell''/4\ \left(1+\alpha_2 \frac{M^{\frac{1}{2}}_i P}{n_e^{\frac{1}{2}}\ Z^{\frac{1}{2}}\ B\ell^{3/2}}\right)^{\frac{1}{2}}$$

with $\alpha_1 = 2.3\text{x}10^{-2}$, $\alpha_2 = 3$, $\ell = (abR)^{1/3}$ and units MJ, MA, MW, T, m, $10^{19}m^{-3}$

These three formulations show $\tau_E \propto P^{-\frac{1}{2}}$ at high power, they differ mainly in the dependence on n and I. Callen et al (1987) have analysed JET data in detail considering a balance between an inward

heat pinch and outward thermal conduction. They find an offset linear variation for the plasma stored energy versus input power. For high input power this leads to,

$$\tau_E(s) = 0.12\eta\ I$$

where η is a heating effectiveness which is a defined function of the power deposition and thermal diffusivity profiles. For typical present JET cases η=0.45 giving

$$\tau_E = 0.05\ I$$

For the expected JET parameters I_p=7MA, B=3.4T, a=1.2m, b=1.9m, P=40MW, $\bar{n}$=5x10^{19}m^{-3} the predictions for τ_E are,

Goldston L - mode	0.33s
Thomas model	0.43s
Rebut et al model	0.37s
Callen et al	0.32s

As might be expected for the relatively small extrapolation from present experiments the results do not differ very much. However since $Q \propto P\ \tau_E^2$ the predicted Q values will show more variation.

PERFORMANCE AND DEVICE EXTRAPOLATION

For the purpose of extrapolation we use the L-mode expression and characterise τ_E as $\tau_E = \gamma_g\ \tau_{EL}$ where τ_{EL} is the L-mode value. The central fusion parameter $X=\hat{n}\ \hat{T}\ \tau_E$ is then given by

$$X = 3.33 \times 10^{18}\ \frac{\gamma_n\gamma_T\gamma_g^2\ a^{1.26}\ R^{0.5}\ \varepsilon^2\ B^2}{q^2} \qquad (m^{-3},\ keV,s)$$

$$\gamma_n = \frac{\hat{n}}{\bar{n}}\ ,\ \gamma_T = \frac{\hat{T}}{\bar{T}}$$

This expression shows that X is a fixed characteristic of the device with the only possible variations through the γ values.

If we combine the L-mode scaling with the Troyon β limit then there is a condition on the heating power required,

$$P_1 = \frac{10.5\ a^{2.74}\ \varepsilon\ B^2\ K_T^2}{\gamma_g^2\ R^{1.5}} \qquad MW$$

where $\bar{\beta} = K_T\ I/B_a$ is used as the Troyon limit.

Combining the L-mode scaling with the Murakami parameter M gives a different condition on the power required,

$$P_2 = \frac{30\ M^2\ a^{0.74}\ q^2}{\gamma_g^2\ R^{1.5}\ \varepsilon}\ \left(\frac{\bar{T}}{10}\right)^2 \quad MW$$

where $\bar{T}$ is the average temperature (keV)

From these formulae with P for JET fixed at 40MW, q=1.8, $\gamma_n\gamma_T$=3, $\bar{T}$=5keV, we find

$$X = 2\times10^{20}\ \gamma_g^2$$
$$K_T = 0.8\ \gamma_g$$
$$M = 3.4\ \gamma_g$$
$$Q = 0.2\ \gamma_g^2$$

Since K_T<<2.8 we see that JET is confinement rather than β limited, that for γ_g=1, X $\sim$ 2x10^{20} correspond to Q $\sim$ 0.2 and that to reach this performance the tokamak must be operated with a relatively low value of M corresponding to $\bar{n}_e \sim 4\times10^{19}$m^{-3}. For the H-mode with γ_g=2 the predictions for 40MW input are

	I_p = 4MA	I_p = 6MA
X	2.6×10^{20}	6×10^{20}
K_T	1.6	1.6
M	3.4	5.0
Q	0.26	0.6

Since $K_T<2.8$ it is clear that the normal critical β is not exceeded.

If we apply these expressions to the parameters of 'enhanced NET' (Engelmann, 1986) we find for the parameters, R=5.4m, a=1.7m, ε=2.2, B=4.8T, I=14.8MA a consistent set for ignition with $X=5\times10^{21}m^{-3}$ keV seconds, P=100MW, τ_E=2.8s, $p/\bar{p}$=3, γ_g=2.2 (requiring H-mode) $\bar{n}=7\times10^{19}m^{-3}$(M=8). These figures are all plausible on the basis of the present JET data. The Rebut-Lallia scaling is more pessimistic and requires an H-mode type improvement of $\sim$ 2.5 in the confinement time for ignition. Callen-Cordey scaling, assuming a (size)^2 dependence is more optimistic and predicts ignition without an H-mode improvement.

NON THERMAL CONTRIBUTIONS TO Q

With neutral beam heating we can expect contributions to Q due to reacting collisions between the fast beam ions themselves Q_{bb} and between beam and background 'plasma' ions, Q_{bp}. The contribution due to Q_{bb} is dominant at low plasma densities and high input power since

$$Q_{bb} \propto \frac{P_b\,\varepsilon_b}{n_e^2}\quad\frac{1}{\text{volume}}$$

while $Q_{b-p} \propto \varepsilon_b^{1/2}$ where ε_b is the energy of the injected beam ions.

This is for the case where $\varepsilon_b<\varepsilon_c$ the critical energy ($\sim 20T_e$) below which the fast ions slow down by collisions with background ions. Figure 13 shows the predicted Q values with 20MW of RF, 20MW of NBI and confinement times in the range extrapolated from present experiments. Evidently the maximum total Q is achieved at low density and contains a significant non-thermal contribution.

Taking into account the earlier evidence on confinement time we see that it should be possible to achieve a total Q $\sim$ 1 in 7MA limiter or 4MA X-point operation. With 6MA X-point operation total Q $\sim$ 1.5 should be possible.

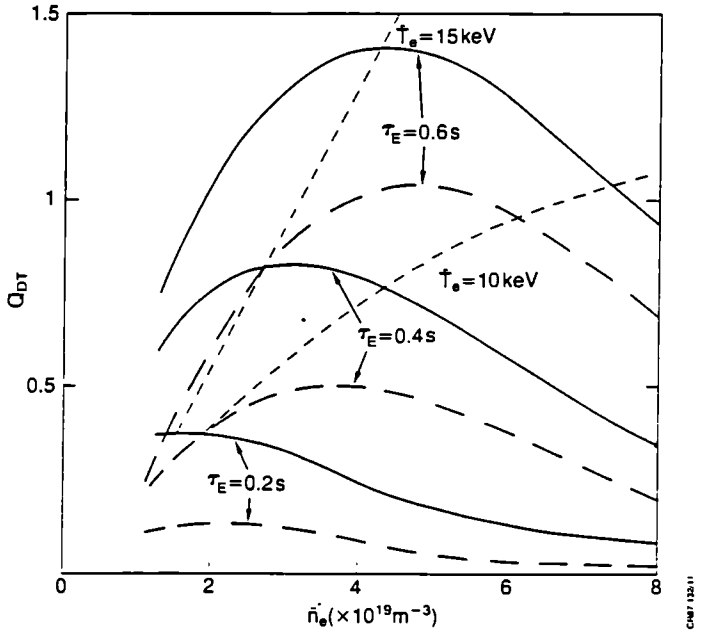

Fig. 13. Predicted Q values for various values of confinement time. Power input is 20MW ICRH and 20MW neutral beam injection. Dashed lines show thermonuclear Q. Continuous lines show total Q values including beam plasma contributions. (1:1 D-T mixture without depletion)

CONCLUSIONS

(a) JET operation is limited in the normalised density vs normalised current plane in much the same way as all other tokamaks but with a maximum Murakami parameter $\sim$ 6 at $1/q_{CYL} \sim 0.6$. High density disruptions are due to current channel shrinkage as the radiated power in the periphery rises.

(b) Conditions have been achieved in deuterium corresponding to a thermonuclear Q $\sim$ 0.07 in a D-T mixture.

(c) JET performance has been well below the β-limit so far. It is likely to remain so with limiter operation but with higher current H-modes the Troyon limit may be approached.

(d) All JET operation shows severe confinement degradation as the heating power is increased.

(e) Different interpretations of the existing data lead to much the same predictions for operation at the extended parameters of current and power that will be used in the future.

(f) To achieve thermonuclear Q $\sim$ 1 requires $\tau_E > 0.6$s due to the MHD stability limitations on β_o.

(g) A total Q $\sim$ 1.0 is a realistic prediction when thermonuclear and beam-plasma contributions are included.

(h) The presently accessible values of M are fully adequate. Indeed with 40MW of input power the average density must be kept below $4 \times 10^{19} m^{-3}$ in order to get a high enough average temperature.

(i) On the basis of present JET data a machine with the parameters of 'enhanced NET' should ignite provided H-mode type confinement is achieved.

REFERENCES

Callen, J. D., J. P. Christiansen, J. G. Cordey, P. R. Thomas and K. Thomsen (1987). JET Preprint - P(87)10.

Campbell, D. J. et al (1986). 11th International Conference on Plasma Physics & Controlled Nuclear Fusion Research, Kyoto, IAEA-CN-47/A-VII-5.

Engelmann, F. (1986). NET Report. EUR-FUI/XII - 80/86/64.

Goldston R. (1984). Plasma Physics & Controlled Fusion, 26, 87.

Hender, T. C., P. S. Haynes, D. C. Robinson and A. Sykes (1987). Proceedings 13th EPS Conference on Controlled Fusion & Plasma Physics, Madrid.

Keilhacker, M. (1987). Proceedings 13th EPS Conference on Controlled Fusion and Plasma Physics, Madrid.

Rebut, P. H. and P. P. Lallia (1987). 7th International Conference on Plasma Physics, Kiev.

Snipes J. et al (1987) Proceedings 13th EPS Conference on Controlled Fusion & Plamsa Physics, Madrid.

Tanga, A. et al (1986). 11th International Conference on Plasma Physics and Controlled Nuclear Fusion Research, Kyoto, IAEA-CN-47/K-I-1.

Thomas P. Resistive MHD Scaling paper. JET Preprint P-(87)17.

Troyon F., R. Gruber, H. Sauremann, S. Semenzato and S. Succi (1984). Plasma Physics & Controlled Fusion, 26, 209.

APPENDIX I

THE JET TEAM

JET Joint Undertaking, Abingdon, Oxon, OX14 3EA, U. K.

J. M. Adams[1], H. Altmann, R. J. Anderson, D. V. Bartlett, W. Bailey, K. Behringer, E. Bertolini, P. Bertoldi, C. H. Best, V. Bhatnagar[2], R. J. Bickerton, A. Boileau[3], T. Bonicelli, S. J. Booth, A. Boschi, G. Bosia, M. Botman, G. Bracco[4], H. Brelen, H. Brinkschulte, M. L. Browne, M. Brusati, T. Budd, M. Bures, H. Buttgereit, D. Cacaut, C. Caldwell-Nichols, J. Callen[5], D. J. Campbell, J. Carwardine, G. Celentano, C. D. Challis, A. Cheetham, J. Christiansen, C. Christodoulopoulos, P. Chuilon, R. Claesen, J. P. Coad, S. Cohen[6], S. Conroy[14], M. Cooke, J. G. Cordey, W. Core, S. Corti, A. E. Costley, G. Cottrell, M. Cox[7], P. Cripwell[14], D. Cross, C. David[18], E. Deksnis, A. de Matteis[8], J. Deng[9], G. B. Denne, G. Deschamps, K. J. Dietz, J. Dobbing, S. E. Dorling, D. F. Düchs, G. Duesing, P. Duperrex[10], H. Duquenoy, L. de Kock, A. Edwards, J. Ehrenberg[15], W. Engelhardt, S. K. Erents[7], B. T. Eriksson, H. Falter, M. Forrest[7], C. Froger, K. Fullard, M. Gadeberg[11], A. Galetsas, A. Gibson, R. D. Gill, A. Goede, A. Gondhalekar, G. Gorini, C. Gormezano, N. A. Gottardi, C. Gowers, R. Granetz, B. J. Green, F. S. Griph, R. Haange, J. H. Hamnén[12], C. J. Hancock, P. J. Harbour, P. Haynes[7], T. Hellsten, J. L. Hemmerich, R. Hemsworth, F. Hendriks, R. F. Herzog, K. Hirsch[15], J. Hoekzema, L. Horton[13], J. How, M. Huart, A. Hubbard[14], M. Hugon, M. Huguet, B. Ingram, H. Jäckel[15], J. Jacquinot, Z. Jankowicz[16], O. N. Jarvis, E. Joffrin, E. M. Jones, T. T. C. Jones, P. D. Jones, E. Källne, J. Källne, A. Kaye, B. E. Keen, M. Keilhacker, S. Knowlton, A. Konstantellos, M. Kovanen[22], P. Kupschus, P. Lallia, J. R. Last, L. Lauro-Taroni, E. Lazzaro, R. C. Lobel, P. Lomas, N. Lopes-Cardozo[17], M. Lorentz-Gottardi, C. Lowry[14], G. Magyar, D. Maisonnier, M. Malacarne, V. Marchese, P. Massmann, G. McCracken[7], M. J. Mead, P. Meriguet, S. F. Mills, P. Millward, A. Moissonnier, P. L. Mondino, D. Moreau[18], P. Morgan, H. Morsi[15], G. Murphy, M. F. Nave, L. Nickesson, P. Nielsen, P. Noll, S. Nowak, W. Obert, D. O'Brien, K. Odajima[19], J. O'Rourke, T. Oyevaar[17], M. G. Pacco, J. Paillere, M. Pain, S. Papastergiou, D. Pasini[21], M. Paume, N. Peacock[7], M. Pick, J. Plancoulaine, J-P. Poffé, R. Prentice, T. Raimondi, J. Ramette[18], C. Raymond, P. H. Rebut, J. Removille, W. Riediker, F. Rimini, D. Robinson[11], A. Rolfe, R. T. Ross, G. Rupprecht[15], R. Rushton, H. C. Sack, G. Sadler, J. Saffert, N. Salmon[14], H. Salzmann[15], A. Santagiustina, M. Schmid, F. C. Schüller, K. Selin, R. L. Shaw, K. Shibonuma[19], R. Sillen[17], R. Simonini, P. Smeulders, J. Snipes, L. Sonnerup, K. Sonnenberg, M. Stamp, P. Stangeby[20], D. Start, C. A. Steed, D. Stork, P. E. Stott, T. E. Stringer, D. Summers, H. Summers[21], J. Tagle, H. Tamnen, A. Tanga, A. Taroni, A. Tesini, P. R. Thomas, E. Thompson, K. Thomsen[11], F. Tibone, P. Trevalion, M. Tschudin, B. Tubbing[17], E. Usselmann, H. van der Beken, M. von Hellermann, J. E. van Montfoort, T. Wade, C. Walker, B. A. Wallander, M. Walravens, K. Walter, D. Ward, M. L. Watkins, M. Watson, J. Wesson, E. Westerhoff[15], J. Wilks, T. Winkel, C. Woodward, M. Wykes, D. Young, L. Zannelli, J. W. Zwart

PERMANENT ADDRESS

[1] UKAEA, Harwell, Nr. Didcot, Oxon, UK.
[2] EUR-EB Association, LPP-ERM/KMS, B-1040 Brussels, Belgium.
[3] Institute National des Recherches Scientifique, Quebec, Canada.
[4] ENEA-CENTRO Di Frascati, I-00044 Frascati, Roma, Italy.
[5] Dept. of Physics, University of Wisconsin, Madison, U.S.A.
[6] Princeton Plasma Physics Laboratory, New Jersey, U.S.A.
[7] UKAEA Culham Laboratory, Abingdon, Oxfordshire, U.K.
[8] ENEA-CRE, Bologna, Italy.
[9] IPP, Hefei, China,
[10] CRPP/EPFL, 21 Avenue des Bains, CH-1007 Lausanne, Switzerland.
[11] Risø National Laboratory, DK-4000 Roskilde, Denmark.
[12] Swedish Energy Research Commission, S-10072 Stockholm, Sweden.
[13] Natural Sciences and Engineering Research Council, Ottawa, Canada.
[14] Imperial College of Science and Technology, University of London, U.K.
[15] Max Planck Institut für Plasmaphysik, D-8046 Garching bei Munchen, F.R.G.
[16] Institute for Nuclear Studies, Swierk, Poland.
[17] FOM Instituut voor Plasmafysica, 3430 Be Nieuwegein, The Netherlands.
[18] Commissiariat a L'Energie Atomique, F-92260 Fontenay-Aux-Roses, France.
[19] JAERI, Tokai Research Establishment, Tokai-Mura, Naka-Gun, Japan.
[20] Institute for Aerospace Studies, University of Toronto, Downsview, Ontario, Canada.
[21] University of Strathclyde, 107 Rottenrow, Glasgow, U.K.
[22] Dept. of Physics, Lapeenranta University, Finland.

JET Papers Presented at the 12th Symposium on Fusion Engineering (SOFE), Monterey, U.S.A.

Many Authors

PREPRINT
Proceedings of 12th Symposium on Fusion Engineering, Monterey, Oct, 1987

JET Project Technical Development dictated by the Recent Scientific Results and Prospects for Extensive D-T Plasma Studies in Break-even Conditions

by E. Bertolini, M. Huguet and the JET TEAM.

JET Joint Undertaking, Abingdon, Oxon. OX14 3EA, U.K

Abstract

DURING the first four years of operation, JET, the largest Fusion Facility of the Fusion Programme of the European Community EURATOM, has performed experiments on a wide range of plasma parameters. It has reached central ion temperatures above 12 keV, central ion density up to $5 \times 10^{19} m^{-3}$, and global energy confinement times up to 0.9 s, at plasma currents up to 5 MA in material limiter configuration and up to 3 MA in magnetic limiter configuration. Up to 15 MW of combined ion cyclotron resonance heating (ICRH) and neutral beam injection (NBI) heating power have been injected into the plasma. The record fusion parameter achieved ($\bar{n}_i . \tau_E . \bar{T}_i$) is 2×10^{20} m^{-3} s keV, a mere factor of five below that required for break-even conditions.

To bridge that gap a comprehensive development programme is underway with a view to better control the parameters of the discharge and extend the operational space: plasma currents up to 7 MA with material limiter and up to 4 MA with magnetic limiter, additional heating with ICRH and NBI up to 40 MW, lower hybrid current drive (LHCD), high speed multipellet injection, pumped limiters and saddle coils to control disruptions.

With full implementation of these features, by 1990, it is expected that break-even conditions would be sufficiently close or perhaps reached, thus allowing a start on a meaningful active phase (for which remote handing tools and the tritium plant are being prepared), i.e. extensive studies of a D-T reacting plasma in or near break-even conditions, which is the main goal of the JET Project.

1. Introduction

JET (Joint European Torus), the major experiment of the Fusion Programme of the European Community EURATOM, began operation in June 1983; its key aim is to prove the scientific feasibility of nuclear fusion by means of extensive studies of a deuterium-tritium (D-T) reacting plasma in break-even conditions.

The technical achievements and the scientific results of JET have been reported in detail at most major fusion engineering and physics Conferences, worldwide, establishing the key role of JET at the forefront of fusion research today.

For two years, the machine has been working at its full design performance, i.e. toroidal magnetic fields up to 3.45 T and plasma currents up to 5 MA with flat-top duration of 4 s that can be extended at lower currents. The early technical and experimental results have shown the soundness of the JET design, both in terms of technical capability and of physics performance.

Subsequently, with the start of the plasma heating programme, using ion cyclotron radio-frequency and neutral beam injection systems, it was clearly shown that, while the peak plasma temperature could be substantially increased with additional heating, the associated degredation of the energy confinement time was likely to impair the full achievement of JET goals.

A comprehensive set of measures, to both develop a better understanding of underlying physics and to counteract this adverse effect has been conceived. This calls for the addition of new features to JET, which, together with the already planned development, led to the 'JET New Development Plan', which has been vigorously pursued, and is well underway at present. The wisdom of such a plan has been shown by the 1986 JET results, which have shown the beneficial effect of an increased plasma current on the energy confinement time and permitted establishment of H-mode operation with magnetic limiter.

The suitability of the JET development plan is further supported by the consensus, now developing worldwide, on the key features of JET, that, to a different degree, appears to be included in the design of all major tokamak experiments of reactor relevance, including the 'next steps' such as NET and the newly born ITER.

The aim of this paper is to present the status of the present JET development plan and to give further evidence of the exciting expectations of the JET D-T phase.

2. JET Experimental Results and Main Implications

Although the focus of the 1986 experimental campaign was on plasma heating studies, the flexibility of the JET apparatus and its major subsystems has allowed trials, necessarily on a limited scale, but at plasma parameters of real significance, of some of the key features of the engineering development programme now underway. Experiments have been conducted on a wide range of machine and plasma parameters (see Table I), allowing to quantitatively assess their relative influence on the overall performance. Among these parameters is routine operation at plasma currents of 5 MA which is a unique feature of JET on the world scene.

5987/95

TABLE 1
JET machine and plasma parameters during the 1986 experimental campaign

Parameters		Design Value	Achieved Value
Major Radius	(m)	2.96	2.5 – 3.4
Minor Radius	(m)	1.25	0.8 – 1.2
Plasma Elongation	–	1.68	1.2 – 1.7
Plasma Current	(MA)	4.8	5.1
Flat Top Pulse Length	(s)	up to 20	up to 20
Toroidal Magnetic Field	(T)	3.45	3.45
Flux Swing Capability	(Wb)	34	28
Neutral Beam Power	(MW)	20	10.0
ICRH Power	(MW)	20	7.0
Total Input Power	(MW)	> 40	18
Central Plasma Density	(m^{-3})	$\geq 10^{20}$	5×10^{19} (*)
Central Electron Temperature	(keV)	≥ 10	8.0 (*)
Central Ion Temperature	(keV)	≥ 10	12.5 (*)
Global Energy Confinement Time	(s)	~ 1	0.9 (*)
Fusion Parameter	(m^{-3} s keV)	$0.5 \div 1 \times 10^{21}$	2.10^{20}

(*) Not necessarily in the same pulse.

0006 CR 87 1725

2.1 Machine Conditions (1986 Campaign)

The temperature of the double-walled (eight octants) **vacuum vessel** was controlled up to 300°C, the typical operating temperature (**Fig.1**). Eight uncooled graphite limiters were located on the outer equatorial plane of the vessel. The inboard wall of the vessel was protected by graphite tiles since most disruptions terminate there. The high pumping speed of the hot graphite has been used to control the plasma density during a discharge and to ramp down the density at the end of the discharge, thus minimizing the risk of disruptions upon switching off the neutral injection beams. Such density control has been achieved in a controlled way by pushing the plasma towards the inboard wall. Other graphite tiles also protected the frames of the ICRF antennae, eight octant joints in the poloidal direction, and the outer wall from neutral beam shine-through. Additional tiles were also mounted to partially protect the walls in the vicinity of the X-points. About 1/5 of the vessel inner wall (~ 45m^2) was thus covered with graphite tiles.

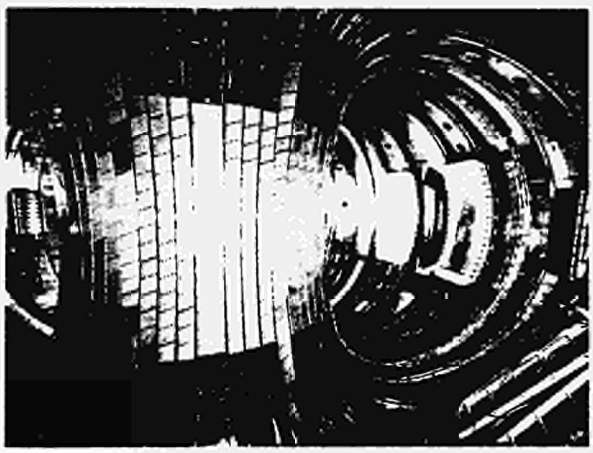

Fig.1 Vacuum vessel configuration during 1986 experimental campaign showing two of the eight graphite limiters, two of the three RF uncooled antennae and the extent of the vessel graphite tiling.

The **tokamak electromagnetic system** allowed toroidal fields of 3.45 T with a 10 s flat-top, and a transformer flux swing of 28 Wb. Typical pulses were from 3 MA, 10 s flat-top up to 5 MA with 4 s flat-top (where up to 30 Wb were made avaliable with an 'ad-hoc' plasma start up scenario). Independent circuits (but not fully separated) provided plasma current feedback control, radial position control, vertical position control and plasma shape control. An operational limit was set on the plasma elongation as a function of the plasma current in order

to limit the vessel displacement in case of vertical instability to values compatible with the existing vessel supports.

Additional heating (on top of the 3-5 MW of ohmic heating) was provided by 3 radiation-cooled **RF antennae** each supplied by two 1.5 MW generators in the frequency range 25-55 MHz, (up to 7 MW and up to 40 MJ were injected into the plasma) and by an array of 8 **neutral injection beams**, supplying up to 10 MW of deuterium beam power at 75 kV and up to 40 MJ of energy per pulse, through the port located at Octant No. 8 of the vacuum vessel.

A complete set of 30 diagnostics allowed cross checking of measurements of the most relevant plasma parameters. These include a **single pellet launcher**, installed to study plasma edge effects, which was also used for preliminary plasma fuelling experiments.

2.2 Key Experimental Results (1986 Campaign)

The JET results [1] will be briefly reviewed only to the extent necessary to highlight motivations for the new development plan.

The main plasma parameters of one of the best pulses (No.10363) with material limiter are shown in **Fig 2.** By increasing the input power by a factor of 4.5 (by means of RF and NB heating), both the plasma temperature and density are substantially increased in the plasma central region, but the global energy confinement time is considerably reduced; thus limiting increases in the fusion parameter ($\hat{n}_i . \tau_E . \hat{T}_i$).

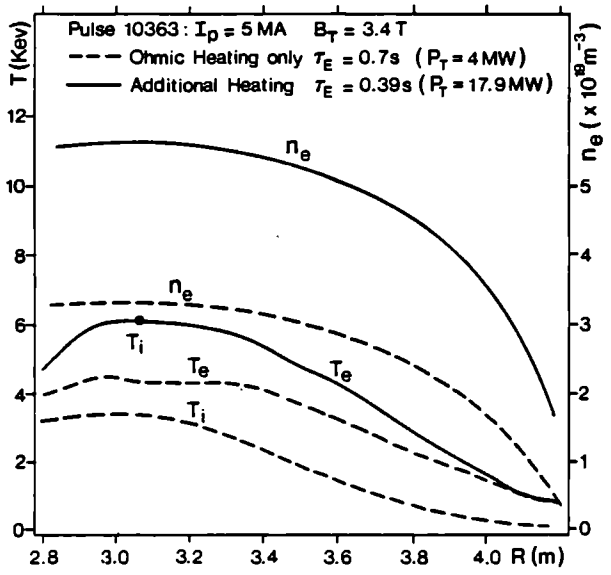

Fig.2 Electron densities (n_e), electron temperatures (T_e), ion temperatures (T_i) profiles and energy confinement times (τ_E): a comparison between ohmic heating only and NB+RF additional heating.

Both double or single X-point magnetic limiter configurations have been established up to 3 MA, by exploiting the local saturation of the iron of the magnetic circuit, thus allowing the achievement of H-mode operation [2,3].

Results obtained by operating with a wide range of plasma currents, with both material and magnetic limiter configurations are summarised in **Fig.3.** These allowed first important conclusions to be drawn on the JET development plan. The energy confinment time degrades with plasma heating power but improves by moving to higher plasma current (1 to 5 MA) and, at a given plasma current

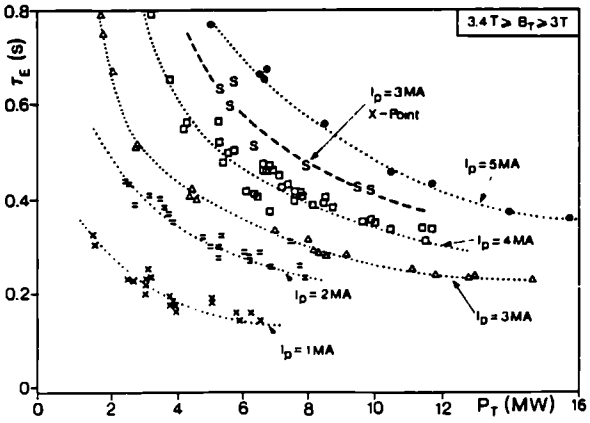

Fig.3 Summary of the 1986 results: energy confinement times (τ_E) as a function of the total input power (P_T) in the plasma current range 1 to 5 MA in material limiter discharges and at 3 MA in magnetic limiter discharges.

(3 MA), it also improves up to a factor of 2 when H-mode operation is achieved in the magnetic limiter configuration.

Other important results are shown in **Fig.4.** It has been possible to suppress sawteeth for periods up to 1.5 s with radio frequency heating in excess of 4.5 MW and with combined NBI and RF heating in excess of 6 MW. Although, due to the lack of specific measurements, it cannot be claimed that this favourable behaviour is due to modification of the current density profile, it is however expected that sawteeth can be eliminated or at least drastically reduced, by properly controlling this profile.

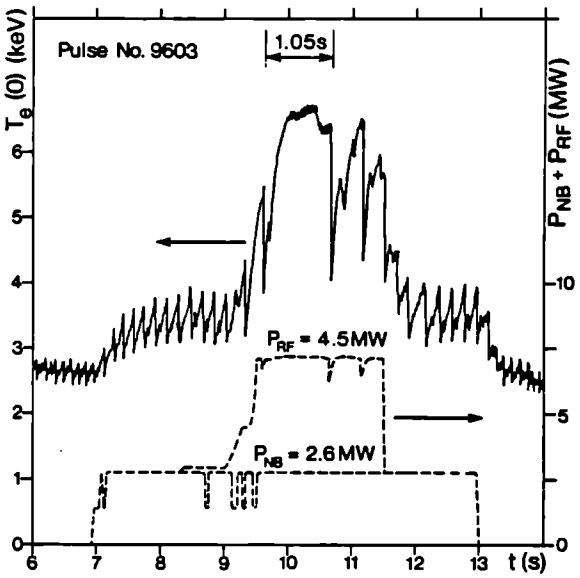

Fig.4 Suppression of the sawteeth ('monster' sawtooth) for 1.05 s with combined NB and RF additional heating.

Preliminary experiments with single pellet injection at velocities of 1.2 km/s have shown that the central density can be substantially increased, leading also to a transient improvement of the global energy confinement time. Moreover Z_{eff} which with graphite tiling of the vessel has been as low as 2, can reach values close to unity with pellet injection [4].

Finally, experiments conducted at 3.5MA and at half of the toroidal field (1.7T), simulating 7 MA operation, have shown safe operation (i.e. no disruptions) with the safety margin q_ψ close to 2.

3. The New JET Development Plan

The record values of the fusion parameter ($\hat{n}_i . \tau_E . \hat{T}_i$) (where $\hat{n}_i$ is the central ion density, τ_E the global energy confinement time and $\hat{T}_i$ the central ion temperature) so far achieved are $10^{20} m^{-3}$ s keV, with ohmic heating only (I_p = 5MA, $\hat{n}_i = 4.2 \times 10^{19} m^{-3}$, τ_E = 0.8s, $\hat{T}_i$ = 3 keV) and $2 \times 10^{20} m^{-3}$ s keV, in single X-point configuration and with additional heating (I_p = 3 MA, $\hat{n}_i = 5 \times 10^{19} m^{-3}$, τ_E = 0.65s, $\hat{T}_i$ = 6 keV). In order to reach thermal break-even conditions this product has to be increased by a factor of ~5 to reach $10^{21} m^{-3}$ s keV and the plasma temperature must be in excess of 10keV.

The New JET Development Plan [5] is directed toward this goal, within the limits imposed by the possible level of engineering upgrading of the JET tokamak and its major subsystems, by the tight lifespan of the Project, by the constraints in the budget, and last but not least, by the ingenuity and the capability of the JET Team.

In simple terms, we have to increase each one of the key plasma parameters: density, temperature and energy confinement time, by a factor of about 1.5-2. In addition, the facility to control the profiles of the density, temperature and current should be also provided. Profiles shown in **Fig. 5** have been proposed as targets [1].

Sections 3.1, 3.2 and 3.3 summarise the physics motivation of the new JET Development Plan. It will be seen that most of the measures which are planned affect more than one of the above parameters (for instance neutral beam injection tends to increase both the temperature and the density). However, each measure is mainly directed at one parameter alone.

3.1 Density

Pellet injection has proven to be a viable tool to increase the central density. In JET, deep fuelling is made difficult by the large size, the high density and temperature of the plasma: high speed (5 – 10 km/s) pellets are thus required. The density of the plasma boundary must be kept relatively low and therefore effective edge pumping must be provided. This can be achieved with **pump limiters**, which will also allow effective control of the density decay at the end of the pulse, thus removing one of the major causes of disruptions.

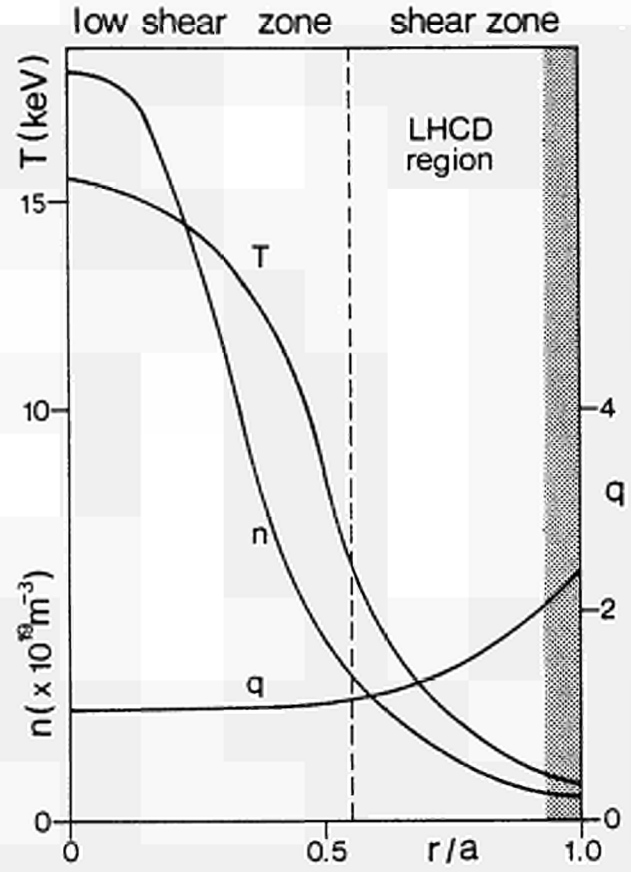

Fig.5 A scenario of plasma density (n), temperature (T) and MHD safety factor (q) profiles, suitable for break-even conditions.

The increase of fraction of vessel wall area covered by **graphite tiles**, should also have a beneficial effect on the plasma purity. Already the increased tiling from 4% to about 20% has shown a substantial reduction of the metal impurities, leaving only carbon and oxygen to account for Z_{eff}. Since this reduction of impurity content has allowed safe operation at higher densities (Murakami Limit), **beryllium** would be even a more appropriate material for plasma facing components, due to its lower Z and to its gettering properties for oxygen.

Disruptions represent an unacceptable risk for a fusion reactor and it is therefore necessary to learn how to control them. Experiments in JET have shown that disruptions are characterised by a precursor magnetic activity which is essentially an $m = 2$, $n = 1$ mode. A scheme to stabilize disruptions is to provide counter magnetic perturbation by means of **saddle coils** inside the vacuum vessel.

In summary, the plasma density control and plasma purity issues will be tackled with extensive vessel wall tiling (graphite and/or beryllium), active edge pumping (pump limiters) deep fuel injection (pellet and NB injection) and active control of disruptions (saddle coils). Gas injection will of course be retained as an additional density control knob. It is expected, through all the above measures, to reach the required enhanced density control, density profile, plasma purity ($n_e \sim n_i$, i.e. $Z_{eff} = 1$) and to drastically reduce the number of disruptions.

3.2 Temperatures

Both electrons and ion central temperatures increase with plasma heating. Therefore, the primary source of further plasma heating should come from completion of the already planned **ICRH system** (from 3 to 8 antennae) and **NB system** (from 8 to 16 injectors at 80 kV and 160 kV). This will bring the total power available from 17 MW to 40 MW.

It has been shown that suppression of sawteeth can bring about higher electron temperatures and a somewhat higher plasma energy content. If this was possible for the whole duration of high performance discharges in JET, it would contribute to increasing the plasma central temperature and energy confinement time, because the temperature would continue to increase instead of undergoing a sudden drop every period.

A **lower hybrid radio frequency system** has been used to reduce the peaking in current density profile on Tokamaks such as PLT, ASDEX, PETULA, JT60 and, to some extent, decouple the current density from the electron temperature. This makes peaked temperature profiles compatible with flatter current density profiles, thus allowing stabilization of sawteeth, while maintaining high performance at the plasma centre.

3.3 Energy Confinement Time

From the JET experimental results there is clear evidence that the confinment time increases with the plasma current. If the scaling law of **Fig.3** is confirmed, then the beneficial effect of **higher plasma currents** (7 MA with a material limiter and 4 MA with a magnetic limiter) would counter the degradation of the energy confinment due to the much larger additional heating power. Confinment times in the range of at least 0.35 – 0.4 s should be achieved with a total external heating power as high as 40 MW. More optimistic predictions indicate a possible saturation of the degradation of the energy confinment time. This has been neither confirmed nor contradicted by the JET results and would lead to higher values of the energy confinment time.

4. The 7 MA and X-Point Study

While operation at 5 MA is already above the maximum design value of 4.8 MA, extending the operating range much further, would require reconsideration of design of the JET machine and of the power supplies, in great detail. Two goals have been set: **7 MA, 10 s flat-top, in material limiter configuration** and **4 MA, 10 s flat-top, with single or double null magnetic limiter configuration.** These values are the result of a compromise between two contradictory aspects: only a substantial plasma current increase would allow achievement of a meaningful increase in performance, but, at the same time, modifications on the machine and other systems had to be kept to a minimum in order to remain within the specified time scale and budget constraints. The relatively large values of the current flat-top times are suggested by the desire to reach steady state conditions to such a degree as to make the term dW/dt negligible in the formula for global energy confinment time, $\tau_E = W/(P_{IN} - dW/dt)$.

An ad hoc group has been set up with the following terms of reference:

(a) Is it reasonable to consider an extension of JET operating range to 7 MA limiter and to 4 MA X-point?
(b) What are the modifications/additions required?
(c) If the answer to question (a) is yes, progressively implement the modifications/additions defined in (b).

The key issue is the detailed study of the **mechanical and thermal behaviour of the machine components** under the new operating conditions, including the effect of radial disruptions and vertical instabilities. The analysis must be carried out for in-vessel components (limiters, RF antennae, graphite protection tiles, X-point dump plates, pump limiters, etc.) for the vacuum vessel itself, and for the toroidal and poloidal field coils and the mechanical structure. Since this represents a large amount of work, requiring both analytical and computer analysis, substantial outside support has been arranged including the Engineering Analysis Division of Princeton Plasma Physics Laboratory. The NET Team has carried out computer calculations of the forces on the vessel in the event of vertical instabilities and radial disruptions, since suitable computer codes were either available there, or in the late phase of development. Although the major forces acting on the structural components of JET are electromagnetic, thermal effects give also rise to serious problems due to the combination of enhanced machine parameters and long pulses.

On **power supplies**, analysis must be directed towards achieving larger flux swings to produce and sustain larger plasma currents, the implementation of new schemes for enhancing the current in magnetic limiter configuration and the redefinition and design of the plasma current, position and shape control systems. Moreover any new power supply equipment required must take into account the constraints included in the supply contract between the UK Central Electricity Generating Board and JET. All JET loads, except the ohmic-heating coils and part of the toroidal coils, are directly supplied by the Grid at 400 kV.

Finally, since the tokamak and its power supplies are required to operate beyond original design specifications, an accurate analysis of the effect of the fault conditions must also be performed. A reference scenario, as shown in **Fig. 6**, has

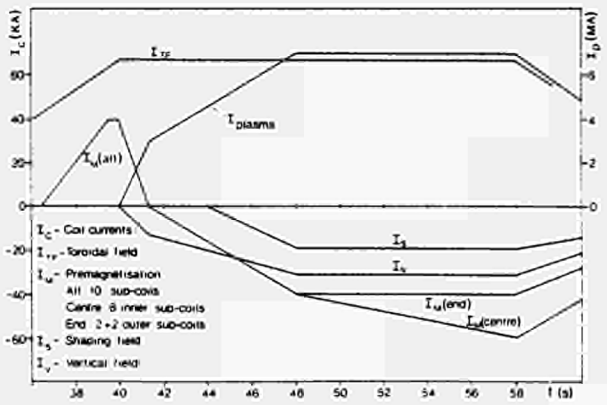

Fig.6 Currents in the toroidal and in the poloidal coils versus time for a 7 MA, 10 s plasma pulse, used as reference scenario for the '7 MA Study'.

been taken for the key aspects of the engineering analysis of the 7 MA study and a similar one for the 4 MA X-point study has been used.

5. Status of the JET Development Plan

While the physics requirement for break-even have dictated the need of these additional features, it is the imaginative JET design with its inbuilt flexibility, which has allowed a coherent technical development to bring the JET facility into an operating range well beyond design specifications, at the expense of only minor modifications to the JET assembly. Implementation of the new additions and the consequent upgrading of the experimental programme have required, however, an extension of the life of the Project of two and a half years, i.e. until the end of 1992. In fact, only after Spring 1990 will the JET facility be in its final configuration.

A brief account of the status of the JET development is given in the following.

5.1 The Tokamak Assembly

The new development programme calls for modification and additions to the magnet system and to the vacuum vessel.

5.1.1 Magnetic System

Enhancement of the **electromagnetic system** [6,7] requires an increase in length of the P1 coil stack (ohmic heating) from 8 to 10 subcoils to reduce stray fields at breakdown and also to supply the new stack with four busbars (instead of two) to allow a substantial increase in flux swing capability and to establish and control magnetic limiter configurations up to 4 MA (and possibly above). Such an important change is made possible by the topology of the machine and the special design of the P1 coil stack. The modification involves supplying the central 6 subcoils of P1 with larger currents (up to 60 kA instead of the nominal value of 40 kA), which is, in principle, possible because the increased outward force will still be compensated by the centering force of the toroidal field coils (see **Fig. 7**), [7].

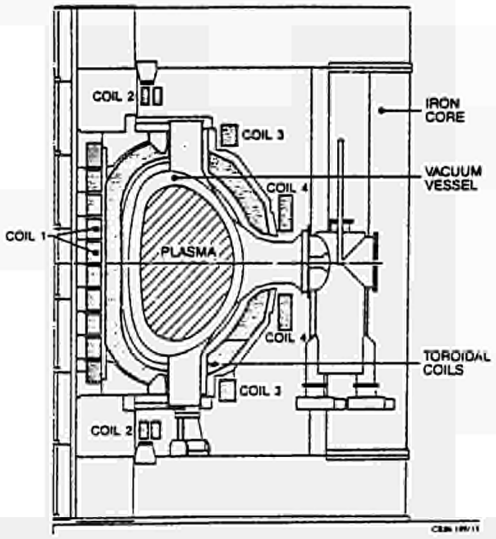

Fig.7 Cross-section of the JET tokamak showing the new configuration with ten P1 subcoils where the six central subcoils are mechanically supported by the centering force acting on the toroidal coils.

This work, which has required disassembly of the top part of the machine, was successfully completed during the 1986-87 shutdown, but has also uncovered a problem due to the mechanical interface between the P1 coil stack and the toroidal field coils. As a result of the combination of the centering forces and torque acting on the toroidal field coils, the P1 stack twisted during the pulse but did not fully return to its initial position. New locking keys, fitted with springs, have been machined on the P1 subcoils, to ensure that all subcoils return to their positions after a pulse.

The extensive **stress analysis** performed both on the poloidal and on the toroidal field coils, as part of the mentioned 7 MA study have shown the following:

(a) The **P1 coil stack** can take the electromechanical load resulting from operation at 60 kA in the central six coils. However, a high thermal stress arises due to the thermal gradients during cooldown after the pulse. The temperature rise for a 10 s, 7 MA plasma current flat-top, would be 67 °C, while a safe value should be around 25 °C. A new water cooling loop design is under consideration to reduce the thermal gradient.

(b) The **outer poloidal field coils**, P2, P3 and P4 would still operate within their design limits: peak shear stresses up to 15 MPa in the insulation have been calculated and are considered acceptable. Only the P4 coils require strengthening of supports to cope with vertical loads during vertical instabilities. This is already implemented;

(c) On **toroidal field coils**, the critical and most highly stressed regions are at the top and bottom of the coils, particularly in X-point configuration, where the transverse poloidal flux is highest. Finite element analysis has shown that the shear stress in the insulation is of the order of 20 MPa, which is high but, in principle, acceptable for a limited number of pulses. Full scale fatigue tests, using the prototype toroidal field coil are planned, to better assess these critical points. The long flat-top required (18 s) at the design value of the magnetic field (3.45 T) implies the temperature to rise to an excessive level in the toroidal field coils. This limitation will be eliminated by the end of 1987 by chillers, which will reduce the cooling water input temperature to 7 °C.

(d) The existing shell **mechanical structure**, designed to take the torque of the toroidal coils in both normal and fault operating conditions, should still be adequate.

5.1.2 Vacuum Vessel

Due to currents induced in the vessel during normal and abnormal (disruption) working conditions, a careful assessment of the new stress levels to which the vessel should be subjected has been considered. Since the early phases of the JET operation, one of the most severe conditions (and more severe than expected during the design phase) has proven to be a **vertical instability** [8]. The vertical forces experienced by the vessel can be inferred from force balance calculations and also from the measured displacements of the vessel. The experimental values found at plasma currents in the range of 1-3 MA cannot be easily extrapolated up to 7 MA since the force depends in a complex way on the plasma current ($\propto I_p^2$), elongation and safety factor, q. In the worst case, the total vertical load on the vessel should not exceed 1000 tonnes. Finite element calculations have shown that the stress level should be acceptable everywhere (at least, for a small number of vertical instabilities), when the vessel is adequately supported.

The temporary vessel supports which were installed in 1984 (with 350 tonnes vertical forces capability), and have allowed operation up to 5MA with plasma elongation of 1.35, have been replaced, during the 1986/87 shut-down. The **new supports** are specified to resist vertical forces up to 1600 tonnes, and have been conceived and designed as purely passive systems to eliminate the need for interventions during the active phase of JET. This means that the supports should allow free expansion of the vessel during heating up to 300-400 °C and cooling down (vertical excursions up to 10mm are experienced), while limiting the vessel displacement to 1-2mm for the sudden forces applied during the pulse (where the vertical disruption will be the most severe condition). The supports based on an inertial system (which blocks the displacement only for accelerations above a certain value, typically $-4 m/s^2$) have been installed and now are being tested (**Fig. 8**).

Calculations are underway, in conjunction with NET, to assess the level of stress in the vessel, both for **vertical** and **radial disruptions**.

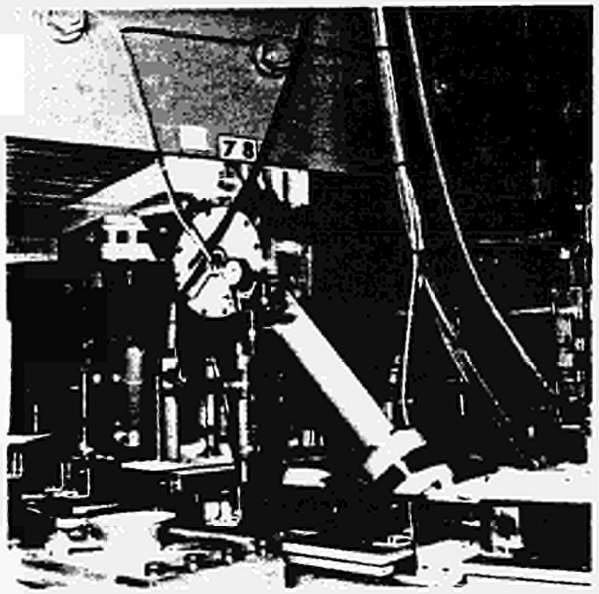

Fig.8 Two of the 32 (16 top, 16 bottom) inertial supports due to prevent major displacements of the vacuum vessel during vertical instabilities.

5.1.3 Plasma Facing Components

The new inner wall configuration of the vessel is shown in **Fig. 9** [9]. All 32 bellows inconel protection plates have been covered with graphite tiles, giving a total of **40 graphite rings**; the 8 discrete (uncooled) graphite limiters have been replaced by two **toroidal belt limiters** (15 m^2 total surface) consisting of a water

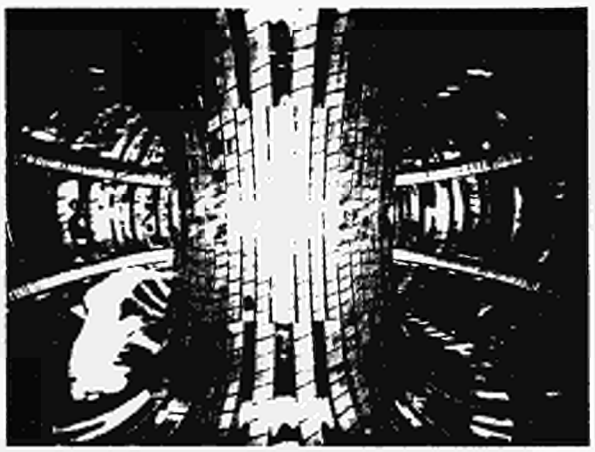

Fig.9 Present configuration of the vacuum vessel showing the graphite belt limiters, two of the eight water cooled RF antennae (right) and the enhanced graphite tiling.

ooled inconel structure covered by graphite tiles and capable of absorbing 40 MW if power for 10 s; the 3 A_0 (uncooled) **ICRH antennae** have been replaced with new A_1 (water cooled) antennae with graphite tiles protection frames. Up to 0% ($\sim 100\,m^2$) of the vessel surface is now covered by graphite tiles. Fibre reinforced tiles have been installed in the most critical points (e.g. at the neutral beam hine-through locations).

Further enhancements of the vessel inner wall will take place in the future (**Fig. 0**). Energy **dump plates** will be installed at the top and bottom of the vessel, s a protection against the heat load in the vicinity of the X-points. Although he basic design is different from that of the belt limiter, the dump plates still asically consist of a water-cooled inconel structure covered with graphite (or eryllium) tiles. The **8 saddle coils** aiming at controlling plasma disruptions will e installed in the same area. They will be radiation cooled and protected with raphite tiles. Each coil consits of inconel conductors to be supplied with curents of 5-10 kA able to create a perturbation magnetic field of 5-10 gauss. There vill be **2 water cooled pump limiters** to control the plasma density. They will be

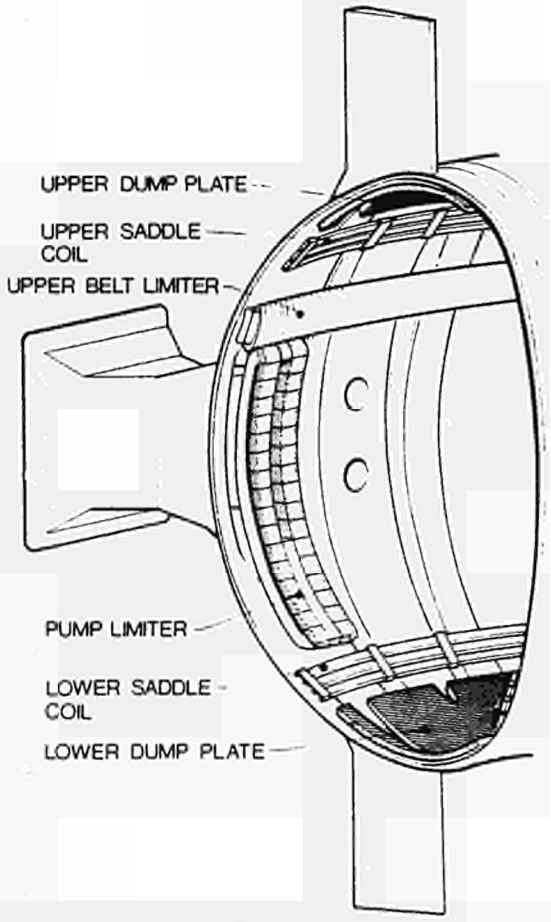

Fig.10 Future additions to the vacuum vessel configuration: magnetic separatrix, dump plates, belt limiters and saddle coils.

installed between the toroidal belt limiters at the outboard wall and will use 2 horizontal ports for the pumping of the neutral gas; 6 out of 32 sections of the belt limiters will have to be removed to allow the particle flux to reach the pumping limiters. Pyrolitic graphite components are planned for the limiter blades. These limiters are expected to remove 5-10% of the total particle flux at the plasma boundary. Consideration is being given to **bumper limiter** using fibre reinforced tiles to allow long duration inner wall limited plasma discharges.

Although the experimental results obtained with the vessel in the configuration of **Fig. 1** have shown almost total disappearance of metallic impurities, (with Z_{eff} of 2–4, from only O_2 and C impurities), it is believed that the replacement of graphite tiling with beryllium tiling and/or coating will further improve plasma purity. Therefore the toroidal belt limiter, the ICRH antennae and the X-point energy dump plates have been made compatible with future installation of **beryllium tiles**, now under manufacture. While, at present, the vessel walls can be covered with carbon (by glow discharge with a methane-hydrogen mixture), the beryllium coating will be performed by four **beryllium evaporators**, now ready for installation when a decision is made to use beryllium as plasma facing material.

5.2 The Power Supplies

The JET New Development Plan calls for power supply development in three areas: the tokamak electromagnetic system, the auxiliary systems and the interface with the 400 kV grid.

5.2.1 Electromagnetic System

A new **modulation circuit** [6] must be integrated in the existing poloidal circuit to allow operation of the tokamak at the enhanced parameters. A simplified schematic of the poloidal circuit is shown in **Fig. 11**. Besides the previous key functions of establishing and controlling plasma current, the circuit fulfils the following new functions:

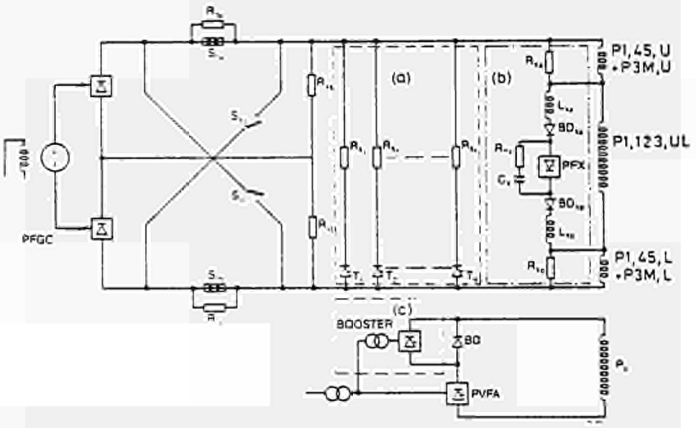

Fig.11 A simplified schematic of the poloidal circuit power supplies, showing the new additions: (a) switching network, (b) PFX unit, (c) booster amplifiers.

(a) active **control of stray fields** at breakdown by supplying the 6 central subcoils of P1 with a current a few kA lower than the premagnetisation current of 40 kA, which flows in the top and bottom subcoils;

(b) control of the **derivative of the plasma current** during the early phase (< 1 s) of the pulse, by means of the switching network which achieves optimum balance between a high value plasma current at the end of the initial phase (fast rise phase) and the undesirable hollow current density profiles due to skin current effects. This is complemented with the upgrading of the voltage capability from 2.8 to 12 kV (booster amplifier) of the vertical field amplifier to control the plasma radial position during the early phase of the discharge when high breakdown voltages (> 30 V) are used;

(c) **enhancement of the flux swing** from the present maximum of 28 Wb to 40 Wb, to allow a long flat-top at high plasma current (10 s for a 7 MA current), by supplying the inner 6 P1 subcoils with 60 kA while 40 kA flows in the top and bottom subcoils. This function is performed by the PFX (Poloidal Field X-point) unit.

(d) actively **establish X-point configurations** up to 4 MA (or above if possible), by a currents up to 60 kA in the 6 inner P1 subcoils and 40 kA lower in the top and bottom subcoils.

The switching network and a temporary booster amplifier (the latter to enhance the open circuit voltage capability for plasma radial position control, from 2.8 to 5.6 kV) are now operational; the PFX unit is being commissioned: the full capability of the booster amplifier, together with the upgrading up to 40 kA for 15 s, (presently 25 kA, 25 s) of the vertical and shaping amplifiers, will be available in March 1988; the active control of the stray fields will become a JET feature after the 1988 shutdown. Moreover new busbars have been installed to restore

complete electrical separation of the tokamak poloidal subsystem (ohmic heating, radial position control, vertical position control and plasma shaping) [10]. During 1988, the plasma position feedback will use digital control (as the plasma current control does already) and it will be progressively upgraded to cope better with enhanced JET performance.

As part of the 7MA study, extensive calculations are underway to analyse the effect of fault conditions in the new electromagnetic configuration of the machine and power supplies.

5.2.2 Other Systems

The eight power supplies for the second **neutral beam injection system** have been commissioned so that 16 NB injectors at 80kV, 60A are now operational. One 160kV, 30A NB line has shown reliable operation in the Test bed. Therefore, during the 1988-89 shutdown, a system of 8×160kV, 30A injectors will be installed.

Each **ICRH power supply unit** has been upgraded by 25% to cater for the new 2MW generator tetrodes, by providing new power supplies for the driver and using the full capacity of the exising system for the RF generators.

The **LHCD power supplies** for the 24×500kW klystrons have been ordered, and one third of the system should be available for installation during the 1988-89 shutdown, while completion is scheduled for the following shutdown.

A study is underway aimed at design of the **feedback amplifiers for disruption stabilisation** due to supply currents in the kA range at 1−2kV to the saddle coils inside the vacuum vessel, with a frequency response variable from zero to several kHz.

5.2.3 Interface with the 400kV Grid

With power supplies upgrading, the additional systems becoming progressively available and the new operating scenarios being established, the demands on the 400kV grid as power source have had to be reassessed. A computer code, which simulates all power supplies and the grid has been developed, to assess new demands with particular attention to the contractual limits on voltage drops (mainly related to the reactive power demand) and to the power step (mainly related to the profiles of the active power demand).
Analysis (part of the 7MA study) performed in cooperation with the Central Electricity Generating Board [11] has shown that the existing limits can be extended to 2.5% voltage drop (from the present 1.5%) and to a 150MW step (from the present 50MW) for a limited number of pulses per year. While a full analysis is still underway, preliminary computations indicate that both active and reactive compensation may be required, in the range up to 100MW and 100MVAR respectively, to meet the requirements of the JET operating scenarios for 1990. The design of the **compensation network** has been completed and technical specification for tendering are being prepared.

5.3 Plasma Heating and Fuelling Systems

The **8 ICRH generators** are being upgraded by replacing each 1.5MW tetrode with new 2MW tetrodes, allowing each of the 8 antennae to be supplied with 4MW power (at 25-55 MHz) for periods greater than 10s and a total capablility of injecting 20MW into the plasma [12]: 3 antennae are already supplied by the new tubes and completion is expected within a few months.

The second box of 8×80kV, 60A **neutral injector** has been installed and commissioning has started. A total amount of neutral beam power of 20MW with deuterium beams will be soon be available. The injector design has been modified from a four to a three grid system and the prototype has been successfully commissioned at 160kV, 30A [13].

The **LHCD system** (Lower Hybrid Current Drive) has been designed and most orders placed: it is planned to have the full system available by 1990. The goal is to drive up to 2MA current in the outer region of the plasma, at densities up to $5\times10^{19}m^{-3}$, by making use of 24 klystrons at 3.7GHz, each capable of delivering 500kW for up to 20s; the supply voltage will be 60kV [14].

The **pellet injectors** for injecting several pellets per pulse, with a diameter up to 6mm and speeds of 5−10km/s, considered necessary for central fuelling of the plasma, are under development. With 6mm foam polystyrol pellets (close to the specific density of deuterium), speeds up to 4.3km/s have been reached [15]. A 1 to 5Hz three barrel system, where the speed is limited to 1.5km/s (2.6,4 and 6mm pellet diameters) has been installed during the 1987-88 shutdown through cooperation between the US Department of Energy and Euratom. Experiments should provide useful information on the final configuration of the JET pellet injection system and will provide early physics results about density control.

5.4 Diagnostics

An extensive range of diagnostics has been installed on JET for the measurement of the important plasma parameters: electron temperatures and densities, ion temperatures, magnetic fields, impurities, neutrons, fusion products, plasma boundary parameters, fluctuations and instabilities [16]. Approximately 30 systems are in routine operation while a further 10 systems are nearing completion. Most of the systems operate automatically and require minimum maintenance. diagnostics are compatible with D-T phase of operation. Two new **diagnostics** have been recently acquired, the **LIDAR** (Thomson Scattering) for electron density and electron temperature measurements with spatial and time resolution and a **polarimeter** (Faraday rotation) for poloidal field (hence, safety factor q) spatial and time resolved measurements.

Feasibility studies are in progress on some additional diagnostics aimed particularly at studying the alpha particle population and, if approved, these diagnostics would be installed during the shutdowns preceding the Phase IIIA and Phase IIIB operations.

Such extensive development requires a significant upgrading of **CODAS** (Control and Data Acquisition System), to cater for the new plants and for the modification of the existing ones, to cope with the expected growth of the JET Pulse File (JFP) size to 15MBytes per pulse (now 9MBytes) and to improve the available operational facilities in the control rooms [17]. A fully dedicated IBM 3090 (200VF) computer is now available for JET data processing.

5.5 Preparation for the D-T phase

The two main areas of development specific to the active phase of JET are remote handling and tritium handling. Although the work in these fields involve the installation of new complex systems it should be reminded that the whole design of JET includes already, in every subsystem, specific features only necessary for an extended D-T experimental phase [18,19].

5.5.1 Remote Handling

Three of the four **main transporters**, the 150 tonnes crane, the articulated boom for in-vessel work and the low level transporter are already routinely used. The articulated boom with the capability to carry 1 tonne over ¼ circumference (~5m), thus servicing half vessel from one port and 350kg over ½ circumference (~10m), thus servicing the whole vessel from one port, has been widely used during the installation of the belt limiters (**Fig. 12**) and the ICRH antennae during the 1987 shutdown. The Articulated and Telescopic Arm (**TARM**) with carrying capabilities up to 3 tonne over 3m, which will work around the machine, will be ordered soon.

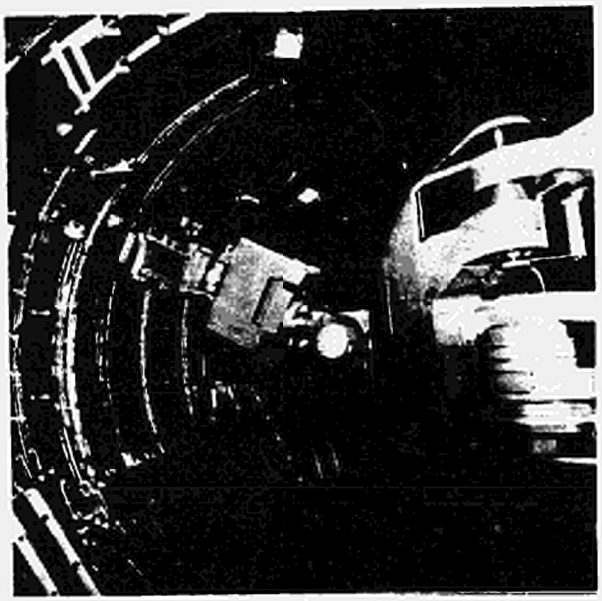

Fig.12 Installation of the belt limiters making use of the articulated boom.

As far as the **end effectors** are concerned, one of two multipurpose servomanipulators (Mascot) has been delivered and is being commissioned, the second one will be delivered soon. The other end effectors, such as the belt limiter gripper and the RF antenna grabber, have been used on the articulated boom for the in-vessel work. A number of **special tools** have already been used. These include cutters and welders for the lip octant joints, for various flanges, for the circular diagnostic ports (90 to 155mm in diameter), and special tools for installing the vessel wall tiles.

The first version of **IVIS** (In-Vessel Inspection System) has been used widely during the past two years. It is installed at 4 top ports symetrically disposed around the vessel. Since the TV camera is assembled at the lower end of the viewing probe, the IVIS can be used only at vessel temperatures below 50°C. A new system has now been designed to allow viewing with a vessel temperature up to 350°C where the camera (in the same position but without zoom) will be kept below 30°C by water cooling and glass radiation shields. Moreover, the lighting system will be improved and complemented with light pipes entering the vessel through four independent vertical ports.

Finally the TAC (Torus Access Cabin) has been in full use during the recent shutdown to control access to the vessel. It will be an essential feature when beryllium tiles are installed and the vessel walls are moderately radioactive due to the neutron fluxes and to the tritium produced by high plasma performance in deuterium. The TAC will be of no use in the D-T phase, when access to the Torus Hall is prohibited.

5.5.2 Tritium Plant

The basic design of the **tritium recycling plant** is well advanced [20]. The plant will receive all gases from the torus, the neutral injectors and pellet injectors, purify them from impurities, separate the hydrogen isotopes and store them for reuse. The design philosophy calls for double confinement around primary components. Cryodistillation and gas chromatography as an auxilliary system will be used for isotope separation. Key components testing is being done on a special test rig.

Major orders will be placed from late 1987 onwards. A new tritium building to be located on the West side of the Torus Hall has been designed. Plant operation is expected to start in early 1990 but introduction of tritium into the plant is not expected before late 1990.

6. Future Experimental Prospects

The JET enhancement described in Section 5 should allow the following scenarios.

Phase IIB (1987-88)

It is expected to achieve currents up to 7MA for 10s with material limiter and 4MA with magnetic limiter for flat-tops limited by the uncooled graphite protections in the vicinity of the X-points. Full NB power at 80kV and full ICRH power for up to 10s, multipellet injection at 1.5km/s, current density control, within the limited capabilities of ICRH and NBI, will all be available.

It is expected to increase the central plasma temperature and the central plasma density by a factor 1.5 to 2 and to increase by a factor 1.5 the global energy confinement time at a given plasma power input, thus allowing an increase of the fusion parameter $\hat{n}_i.\tau_E.\hat{T}_i$ by a factor $\times 2$.

Phase IIIA (1988-89)

During this phase, the wall material may be beryllium thus allowing a higher purity plasma. The key machine parameters should be as in the previous phase. Better control of plasma start-up should be achieved due to the availability of active control of stray fields. Better plasma density and profile control should be achieved with deep fuelling obtained with the 8 NB injectors at 160kV and the prototype high speed pellet injector. Moreover, $m = 2$, $n = 1$ instability mode suppression should be studied when the required power supplies are available.

Phase IIIB (1990-91)

During this phase, the machine and its auxiliary systems should be in their final configuration and therefore simulated break-even conditions in deuterium should be achieved. Plasma density and temperature control should allow studies of peaked profiles using the high speed multipellet injector and the pump limiters; NB injectors should be operated up to 160kV with deuterium (in the next phase one box with tritium). Therefore deep plasma heating and fuelling should be possible. The cooled energy dump plates should allow high energy (high input power and long flat-top) magnetic limiter configuration experiments to assess performance of the H mode.

Preliminary evaluations extrapolated from present results [21] indicate that if an energy confinement time of about 0.6s can be maintained at central plasma temperatures close to 15keV and with peaked temperature profiles, even with not too peaked plasma densities, Q (thermal) ~1 could be achieved (**Fig. 13**). The same result could be achieved with more peaky density profiles at lower values (~0.4s) of the global energy confinement time (**Fig. 5**) [1].

Phase IV (1991-92)

Following the 1990 shutdown, where the ultimate preparation of all specific equipment and tools for the active phase will be carried out, D-T operation will start, eventually tackling the unique goal of JET, that of real fusion experiments in break-even conditions. The alpha particle release, their plasma heating properties and the fusion neutron production will be studied in great detail, without technical limitation on the number of pulses ($\geq 10^3$), provided the machine proves reliable and the large variety of remote handling tools and procedures prove suitable for this mammoth task.

7. CONCLUSIONS

The experimental results so far obtained with JET have shown that the key plasma parameters have already reached values of reactor relevance ($\hat{T}_i = 12.5$ keV, $\tau_i \sim 0.9$s, $\hat{n}_i \sim 5 \times 10^{19} m^{-3}$) and have put JET in the forefront of fusion research today. With a better understanding of the underlying physics, a number of measures have been taken to counteract degradation of global energy confinement time with heating power and to further enhance the presently achieved value of fusion paremeter, by a factor of up to 5, necessary to reach break-even conditions. This includes: the upgrading of the electromagnetic system to increase the plasma current capability in both material (~7MA) and magnetic limiter (~4MA) configurations; control of the plasma current density to suppress sawteeth and allow peaked temperature profiles (with a 10MW LHCD system); control of the density profiles using 5-10km/s pellet injection, deep NB fuelling and pump limiters; control of the plasma purity with low Z-wall material (graphite and/or beryllium); and high power (~40MW) central heating of the plasma for up to 10s pulse duration.

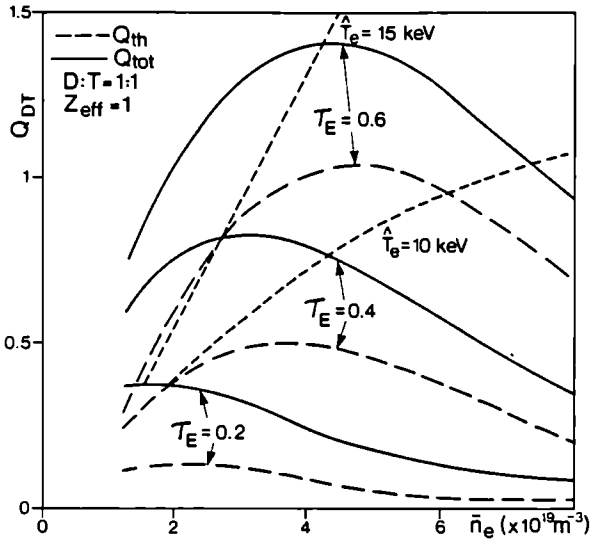

Fig.13 Scenarios for thermal (Q_{th}) and total (Q_{tot}) break-even conditions in JET, showing the central electron temperature (T_e), average electron density ($\bar{n}_e$) and required energy confinement time (τ_E) dependence.

Predictions extrapolated from JET experimental results, indicate that thermal break even conditions (i.e. $\hat{n}_i.\tau_E.\hat{T}_i = 10^{21} m^{-3}$s keV) can be approached (i.e. $Q_{th} = 1$, at $\hat{T}_i \sim 15$ keV, $\hat{n}_i = 1\text{-}2 \times 10^{20} m^{-3}$ and τ_E ~0.6-0.4s). These exciting prospects are made possible thanks to the imaginative initial design concept of JET and to its inbuilt flexibility, which have allowed extension of the machine operating range well beyond design specifications, with limited modifications and additions to machine components and auxiliary systems.

Experiments performed during the short period following the latest shutdown have already given preliminary indications of the success of enhancements introduced so far.

The reduction of stray fields of more than a factor of 2, the doubling of the voltage capability for plasma radial position control and the control of the plasma current derivative have already allowed improved discharge start-up conditions, permitting good breakdown at larger premagnetization currents (up to 40kA) [10]. In these conditions plasma currents of 5MA with 10s flat top have been achieved.

Heating experiments with the new ICRH antennae and 10MW coupled to the plasma have shown long monster sawteeth (up to 2.45s) during the full duration of the RF power pulse, together with a substantial increase of plasma density and temperature and peaked electron temperature profile with $\hat{T}_e \sim 7$ keV (**Fig. 14**).

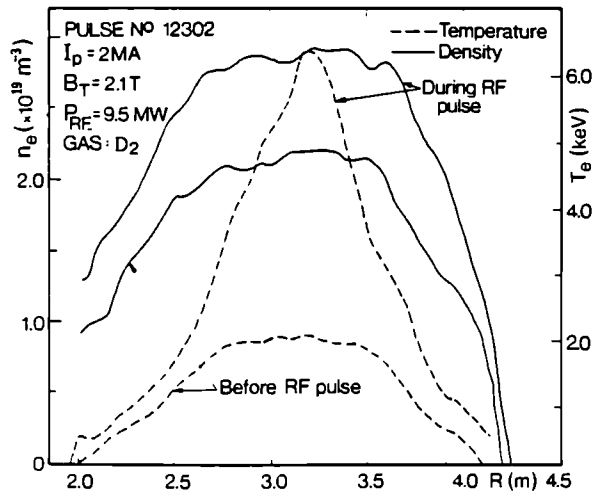

Fig.14 Latest RF heating results, showing electron density and temperature increase and peaked temperature profiles, due to the suppression of the sawteeth.

The degree of flexibility of the JET assembly may not have been fully exhausted with the implementation of the Development Plan described. If more substantial modifications of the machine were taken into consideration, it would would not be inconceivable to extend further the single X-point current capability to 6-7MA. This would require to increase by a factor of about 3 the ampere-turns of the upper P2 coil, and by a factor 1.5 of the ampere-turns of upper P3 coil. The most critical aspect would be the need for an additional upper structure to support the toroidal coils against the substantially increased torque.

If results already obtained with H-mode operation can be extrapolated according to the scaling of **Fig. 3** up to plasma currents of 6-7MA, JET should then easily reach the thermal break-even regime.

However, the unique contribution of JET to the worldwide fusion research effort will be the extended D-T active phase, where not only a real thermonuclear plasma will be carefully studied in reacting conditions, but some of the key fusion technologies, such as remote maintenance and repairs and fuel exhaust reprocessing in the tritium plant, will be operational for the first time.

Acknowledgements

The authors wish to acknowledge the hard work of the technical staff of JET for their contribution to the operation and development of JET to fulfill the aims of the JET Experimental Programme.

References

[1] P.H. Rebut and the JET Team, 'JET Latest Results and Future Prospects', Invited Paper, **Proceedings of the 11th International Conference on Plasma Physics and Controlled Nuclear Fusion Research** Vol 1, pp 31-49—Kyoto (Japan), November 1986.

[2] A. Tanga et al, 'Experimental Studies in JET with Magnetic Separation Configuration', **Proceedings of the 11th International Conference on Plasma Physics and Controlled Nuclear Fusion Research** Vol 1, pp 65-73—Kyoto (Japan), November 1986.

[3] M. Keilhacker et al, 'H Mode Confinement in Tokamaks', Invited Paper, **Proceedings of the 14th European Conference on Controlled Fusion and Plasma Physics**, Madrid (Spain), June 1987, to be published in Plasma Physics and Controlled Fusion.

[4] A. Gondhalekar et al, 'Pellet Fuelling of JET Plasmas during Ohmic, ICRF and NBI Heating', **Proceedings of the 11th International Conference on Plasma Physics and Controlled Nuclear Fusion Research**, Vol 3, To be published, Kyoto (Japan), November 1986.

[5] M. Huguet, 'Technical Aspects of the New JET Development Plan', Invited Paper, **Proceedings of the 14th Symposium on Fusion Technology (SOFT)**, Vol 1, pp 253-262, Avignon (France), September 1986.

[6] E. Bertolini et al 'The Development of the JET Electromagnetic System', **Proceedings of the 14th Symposium of Fusion Technology (SOFT)**, Vol 1, pp 263-271, Avignon (France), September 1986.

[7] J. Last et al, 'The JET Magnets: Operational Experience and Plans for Upgrade', **Proceedings of the 14th Symposium on Fusion Technology (SOFT)**, Vol 2, pp 1643-1648, Avignon (France), September 1986.

[8] P. Noll et al, 'Stabilisation of Vertical Position and Control of Plasma Shape in JET', **Proceedings of the 11th Symposium on Fusion Engineering**, Vol 1 pp 33-40, Austin (U.S.A.), November 1985.

[9] K. Sonnenberg et al, 'Wall Concepts and Density Control for JET', Invited Paper, **Proceedings of the 14th Symposium on Fusion Technology (SOFT)**, Vol 1, pp 273-285, Avignon (France), September 1986.

[10] P.L.Mondino et al, 'The Poloidal Field System Enhancement in JET to Produce Plasma Current up to 7MA with Material Limiter and up to 4MA with Magnetic Separatrix: a Report on the Electrical Study', **This Conference.**

[11] K.I. Selin et al, 'The High Voltage Grid Interfaces on Present and Future JET Operational Requirements', **Proceedings of the 14th Symposium on Fusion Technology (SOFT)**, Vol 1, pp 867-874, Avignon (France), September 1986.

[12] T.J. Wade et al, 'The Technology of the Upgraded JET ICRF Heating System', **Proceedings of the 7th Topical Meeting on Technology of Fusion Energy**, Reno (USA), June 1986, Fusion Technology Journal, November 1986, Vol 10, N^0 3, pp1398-1403.

[13] R.S. Hemsworth et al 'Characteristics of the JET 140kV, 30A Ion Beam Source and Operational Tests of the Second JET Neutral Beam Injectors System in the JET Test Bed in Hydrogen and Deuterium using both the 80kV and the 160kV Beam Sources', **This Conference.**

[14] C. Gormezano et al, 'Plans for Current Profile Control in JET', Invited Paper, **Proceedings of the 14th Symposium on Fusion Technology (SOFT)**, Vol 1, pp 287-298, Avignon (France), September 1986.

[15] P. Kupschus et al 'The JET Multi-Pellet Injector Launcher—Machine Interface', **This Conference.**

[16] P. Stott 'Plasma Measurements for JET' **Phil. Trans. Roy. Soc. London**, Vol 1. A322, pp47-66, 1987.

[17] H van der Beken 'Computer Control and Data Acquisition of JET', **Proceedings of the 5th Conference on Real Time Computer Applications in Nuclear, Particle and Plasma Physics**, San Fransisco (USA), May 1986, to be published.

[18] M. Huguet, E. Bertolini, 'Main Features Implemented in the JET Facility for D-T Operation', Invited Paper, **Proceedings of the 7th Topical Meeting on Technology of Fusion Energy**, Reno (USA), June 1986, Fusion Technology Journal November 1986, Vol 10, N^0 3, pp 1398-1403.

[19] J. Dean et al 'Preparation for the D-T Phase Operation in JET', Invited Paper, **Proceedings of the 14th Symposium on Fusion Technology (SOFT)**, Avignon (France), September 1986.

[20] H. Hemmerich et al 'Tritium System for JET, Concept and Status', **This Conference.**

[21] R.J. Bickerton and the JET Team, 'Operational Limits and Confinement in JET', Invited Paper, **Proceedings of the 14th European Conference on Controlled Fusion and Plasma Physics**, Madrid (Spain), June 1987, to be published in Plasma Physics and Controlled Fusion.

THE JET 10 MW LOWER HYBRID CURRENT DRIVE SYSTEM

C. Gormezano, G. Bosia, H. Brinkschulte, C. David, J.A. Dobbing, A.S. Kaye,
J. Jacquinot, B. Lloyd, S. Knowlton, D. Moreau, M. Pain, J. Plancoulaine,
T. Wade, C. Walker
JET Joint Undertaking, Abingdon, Oxon, OX14 3EA, UK

1. Abstract

A Lower Hybrid system to control the plasma current profile is being prepared so that a higher central electron temperature can be obtained. The proposed system is designed to launch 10 MW of power at f = 3.7 GHz through a single port in JET, producing between 1 and 2 MA of RF driven current at an average density of 5 x 10^{19} m^{-3}. Current drive efficiency is maximized by using a low value of the parallel wave number spectrum (N// ~ 1.3 - 2.3). The final launcher will be made of 48 multijunctions fed by 24 klystrons with the proper phasing. Dynamic matching of the launcher will be optimized by moving the launcher in real time during the pulse. A first stage (2 MW) is presently under construction. The full system is being designed to be in operation in 1990.

2. Introduction

Active tailoring of the current profile in tokamak plasmas is generally considered to be a useful tool to optimise their performance. A broadening of the current profile by means of Lower Hybrid Current Drive (LHCD) has been observed in many experiments resulting in the suppression of internal instabilities in NBI and ICRF heated plasmas. Control of disruptions by current profile modification of low q discharges by means of LHCD has likewise been observed. As a result of broadening of the current by means of LHCD, improvement of the energy confinement has been obtained in JT-60. Therefore a large Lower Hybrid system is being designed whose explicit purpose is to broaden the current profile of JET for NBI and ICRF heated plasmas in order to achieve fusion grade central parameters, e.g. $T_{eo} = T_{io} > 10$ keV at $n_{eo} = 10^{20}$ m^{-3}. LHCD can be associated with other non inductive current drive methods (ICRH, NBI, bootstrap) in order to achieve the required current profile in JET /1/ for plasma current up to 7 MA.

The choice of frequency is a compromise between various technical and scientific considerations: losses in the transmission line, density limit for current drive, avoiding coupling to energetic ions created by the other heating methods, etc.. A frequency of 3.7 GHz has been chosen, based on the above considerations and the availability of klystrons with large output power per unit (0.5 MW).

The grill technology to be applied in JET is based on the multijunction grill which provides a good match to the klystron over a wide range of plasma conditions, and thus provides flexibility in the acceptable position of the grill relative to the plasma surface.

The main features of the design are the following:

- feedback control of the phasing between multijunctions in order to achieve the narrow wave spectrum required from physics considerations. Moreover this wave spectrum should be varied between 1.3 and 2.3 by proper phasing adjustment within a JET pulse.
- active control of the launcher radial position during a JET pulse in order to operate the system in matched conditions, i.e. to couple the maximum allowable power during significant variations of the scrape-off plasma density.
- operation during the tritium phase of JET which requires built-in safety systems preventing tritium leakage outside the torus, remote handling capabilities and emphasis on the reliability of the system.

The LH system is scheduled to be installed in JET during the major shutdown at the beginning of 1990. An intermediate step is planned in which a prototype system of 4 klystrons with the corresponding launcher will operate on a testbed and possibly be placed in JET by the end of 1988. Most of the various subsystems: the generator (24 klystrons), the transmission line (40 m long), the launcher (384 waveguides into 48 units), the control command logic and data acquisition, are in the phase of detailed design and construction of prototypes. High power tests of critical items are under way.

3. The Launcher

The RF power will be coupled through a single large horizontal port of JET (octant 3) by a multijunction-type phased waveguide array. A sketch of the proposed launcher is shown in fig. 1. The antenna consists of 48 separate modules, each of 2 rows by 4 columns of waveguides. The entire grill is moveable by up to 300 mm via a bellow assembly in order to maintain the density at the grill mouth in the required range for a proper matching. Thermal expansion of individual waveguides is permitted by separate bellows on each waveguide feed.

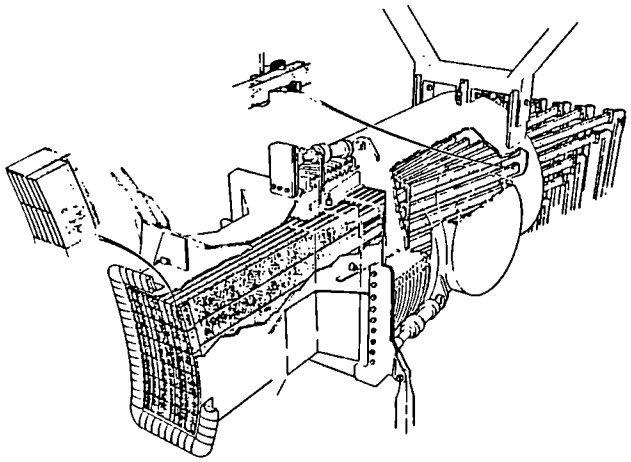

Fig. 1 Sketch of the proposed JET lower hybrid grill.

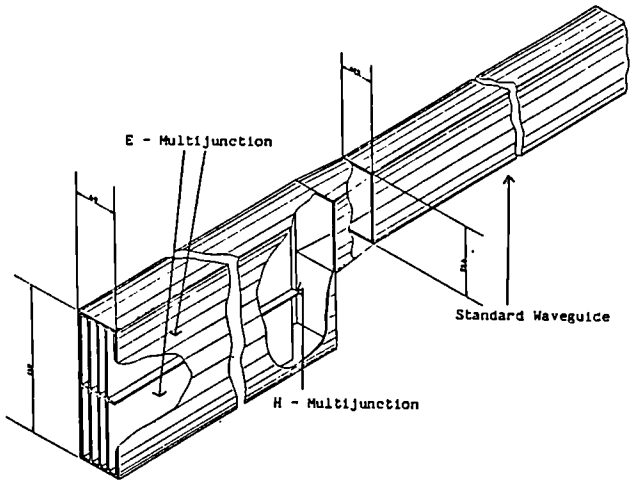

Fig. 2 Schematic of the JET multijunction.

The RF power is supplied through 24 splitting networks allowing 48 modules to be fed by 24 klystrons. Within each module, the power is split to feed two rows of E-plane multijunctions as sketched in fig. 2.

The waveguide dimensions are 72 x 9 mm at the grill mouth with a wall thickness of 2 mm. These dimensions are a compromise between requirements of the physics of Lower Hybrid Current Drive and the physical constraints of the JET port. The resulting incident power density of 4 kW/cm² for 10 MW incident power appears achievable at this frequency without cumbersome and lengthy conditioning procedures. Passive waveguides at the sides of the antenna reduce the reflection in the edge modules and strengthen the mechanical assembly of the launcher.

The material of the launcher has been chosen to be stainless steel mainly due to its mechanical properties when heated to high temperature (500°C) and under disruption-induced stresses. The waveguides will be machined out of stainless steel bars. The multijunction module is machined in several pieces which will be assembled afterwards. The assembly plane is at the centre of the long side of the waveguide so that HF currents are not interrupted. V shaped joints on the walls and precise machining will permit the pieces to be well-aligned, whereupon they will be brazed or permanently clamped together. Initial high power testing has shown the practicality of the latter technique.

A hybrid junction in vacuum splits the power from the main waveguide to feed the two E-plane multijunctions. A vacuum load, capable of sustaining several kW of power, will be placed on the fourth port of the hybrid junction to optimise the power balance in the two output arms. Nonetheless, the junction is designed to couple most of the reflected power to the main waveguide in order to minimise the power requirements of the vacuum load. The total length of the multijunctions is about 3 meters in order to locate the EC resonance zone, which is susceptible to multipactor breakdown, in an area where the RF field is minimum. A standard waveguide made from copper coated stainless steel will connect the multijunctions to the RF windows as shown in fig. 3. Copper sheets inserted between the modules will enhance radiation cooling and assist in module bakeout conditioning.

The final coating of the launcher has not yet been chosen. Initial testing of the rough gold coating developed for antimultipactor coating /2/ has shown prohibitive resistive losses. Other coatings in addition to copper coating such as carbon, Ti C, Ti N, etc ... are under consideration.

The RF windows separating the torus from the transmission lines pressurised with SF6 constitute one of the critical items of the system. A failure of one of these windows could lead to a release of tritium into the main transmission line and from these eventually to the outside, as well as to a pollution of the torus. To avoid that risk, double RF windows of the same type as the output windows of the klystrons will be used. They will form a compact unit comprising 2 suitably spaced thick BeO windows with a pumped interspace between the two ceramics. In the event of failure of one window, tokamak operation is still possible although RF power may not be able to be transmitted through the faulty window. The vacuum waveguides will be connected to the windows via a remotely handleable flange which is being designed.

The major item of the vacuum tank is the large bellows which permits the radial displacement of the launcher. A double bellow made from Inconel-600 (1 mm wall thickness, 1.25 m inner diameter, stroke ± 150 mm) with an evacuated interspace and able to sustain 10^4 full stroke movements has been designed and is in the prototype development phase. Similar requirements apply to the small bellows (stainless steel, ± 25 mm stroke, 104 mm inner diameter) which allows the thermal expansion of the vacuum waveguides. To the end plate of the vacuum tank is attached a support which is connected to the launcher at the grill mouth.

In order to maintain a pressure of about 10^{-5} torr in the waveguides during an RF pulse, a cryopump system with a pumping speed of 10^5 ℓ/s is being designed. The use of getter pump is not feasible due to restrictions on total JET tritium inventory. The required pumping of the modules will be obtained via holes in the vacuum waveguides.

For optimal coupling, the grill mouth should lie on a surface of constant density. Moreover, the grill mouth should also be tangent to the local toroidal field line in order to launch the desired narrow spectrum. Accordingly, the face of the grill will be contoured to the shape of the flux surface in both toroidal and poloidal directions. The density will almost be constant along a field line which will be bounded by a picture frame limiter of the same type as the one used for ICRH antennae in JET.

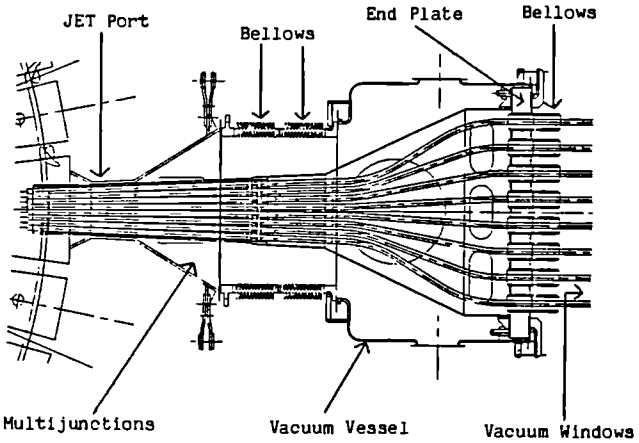

Fig. 3 Top view of the launcher.

In the poloidal direction, the grill will follow a magnetic surface corresponding to a 7 MA limiter discharge. The estimated deviation from these cases

(major radius of 4.1 m), either when the grill is displaced or during an X-point discharge is in the range of 5 mm. The corresponding change in matching due to a density variation [$\Delta n_e/n_e$~50%] could be accommodated by the multijunction system.

The side limiters are located so as not to interrupt the resonance cones. Heat loading studies have been performed with the use of detailed edge physics and calculations based on previously measured experimental edge parameters in JET. A maximum heat load of 0.6 MW ($\bar{n}_e$=2.10^{19}m^{-3}, I_p=3 MA, T_e(a)=100eV, P_{Lim}=20 MW) has been found corresponding to a power density of 3.3 MW/m^2 on the limiter. This heat can be removed by radiation cooling to fins located between the limiter and the wall. The heat load will be taken either by carbon or beryllium tiles.

Initial calculations of the disruption-induced stresses indicate that the main load is a torque whose value is about 100 kNm for a 7 MA, 10 ms disruption. A more sophisticated code operated by Culham /3/ has given similar results. These forces will be directed against a structure located in the torus port by means of the honeycomb structure of the grill mouth and the support structure carrying the waveguides. More detailed analysis is proceeding for assessing the movement of the grill induced by the torque and the fatigue on the welds between waveguides at the launcher mouth and on the waveguides themselves.

The launcher array is matched to the plasma by adjustment of its horizontal position during a pulse. The match will change with the local density at the grill mouth. Variations of the density and of the density gradients at the grill mouth are caused by changes in the target plasma induced by the various scenarios foreseen for JET, for instance:

- strong additional heating
- changes in the plasma current
- transition from inner wall to limiter plasma
- transition from L to H mode
- pellet fuelled plasmas

The motion of the grill during the shot will be achieved by moving the launcher with hydraulic rams acting between a reaction flange on the fixed Torus port and thrust pads on the LHCD launcher vacuum vessel. The reference position required will be defined in real time by a control command signal derived from a preset signal or from a suitably processed diagnostic such as a double Langmuir probe system located in the picture frame, which is being designed. Design values are the following: Mass to be moved: 8 tonnes, stroke length: 300 mm, acceleration: ± 2m/s^2, velocity limited to 0.3m/s, response time: up to 30 mm in 220 ms (with a 3 mm overshoot), accuracy: ± 1 mm. The complete launcher assembly is supported on external pivots linked to JET core vertical limbs. The front of the launcher is free to roll between bearings mounted in the torus port. Prototype of these bearings, operating at up to 500°C with loads of up to 45 kN in vacuum, with effective coefficients of friction less than .05 are being life tested.

4. Generator and Waveguide Transmission Line

The 24 klystron constituting the 12 MW RF plant will be housed on two floors in 6 modules of 4 klystrons each (see fig. 4). In order to coordinate the operation of the various ancillary equipment, the high voltage power supply, the crowbar system, the low power RF drive, as well as to protect the klystron in the event of a fault, a protection and control system based on programmable logic controllers (PLC) is used. This system will also handle the generator interface to CODAS with each controller handling one module of 4 klystrons. Simple operating modes, such as conditioning and operation on test loads, can be handled by the controller alone.

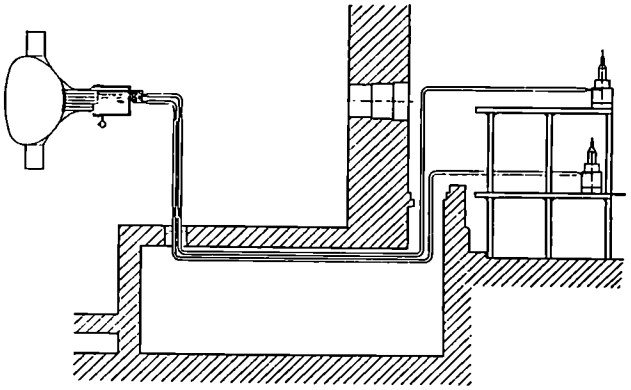

Fig. 4 Lay-out of the transmission line.

The klystrons are specified to deliver 500 kW for 20 sec with 2% reflected power and are of the same type as those delivered to Tore Supra /4/. First series tubes have already been produced with the required specification. In fact, because of the large size of the collector, it appears that higher output powers will be possible, albeit at a lower VSWR. High power tests aiming at delivering 700 kW for 10 sec at a VSWR of 1.1 are scheduled for the near future. The entire RF system has been designed to handle the higher power levels which may be achieved with upgraded klystrons.

Accordingly, the use of circulators at the klystron output is envisaged. A set of 4 circulators will be used with the prototype launcher in order to explore the operation of the system in extreme matching conditions. However, their major benefit will be to increase the output power of the klystrons by lowering the VSWR seen by the klystron, as discussed above.

Control of the phase is a very important feature of the system since a well defined spectrum in parallel wave number is required in order to obtain a good localization of the non inductive current drive. Reliable measurements of the phase of the wave as close as possible to the grill mouth are essential. Conventional techniques (HF probes, diodes, coaxial cables, ...) are impractical near JET due to the high neutron flux expected during the tritium phase. An overall system aiming at ±5°accuracy in phase control between klystrons has been designed. It makes use of the cross talking between two adjacent multijunctions. Cross coupled power of 1 to 2% is predicted by computation of the scattering matrix of the grill in the presence of the plasma. In order to recognize the contribution of the reflected power in a given module, the frequency in each multijunction is periodically (few ms every 500 ms) shifted by a small amount (2 MHz). Therefore changes in relative phase due to thermal expansions will be determined by comparing the phase of the frequency shifted component in a given waveguide and two adjacent ones. Phase and power control will be made using heterodyne techniques from signals collected in the transmission line.

In order to improve the reliability of the system, the klystrons can be tested on individual dummy loads in the klystron hall, prior to feeding the JET launcher by means of high power switches. The transmission line is composed of waveguide runs approximately 40 m long from the klystron down through a sealed penetration into the basement area then through another penetration into the torus hall.

In order to obtain insertion losses and VSWR as low as possible (.9 dB between the klystrons windows and the launcher vacuum windows VSWR:1.1:1) a slightly oversized waveguide (77.2 x 38.6 mm) has been chosen. This decreases the losses by 16% as compared with a standard waveguide while still keeping single mode propagation. These losses are kept close to the theoretical values which is possible by a careful choice of the copper material, by fixing a maximum value to the roughness of the guide inner surface and by using high quality flanges and bends. A full oversized waveguide run (10 modes) would have increased the cost by a very large factor (~ 2) without decreasing significantly the losses (2 to 3%) due to the complicated path of the transmission line.

The heat ($\Delta T \sim 20°$ C during a pulse) will be removed by circulating SF_6 at a small flow. As shown in Fig. 5 each waveguide is split by a hybrid junction into two arms in order to feed the 48 units. Phase compensating elements will be inserted so that most of the reflected power will be directed towards a load located in the fourth arm of the hybrid junction. Flexible elements allow the stroke of the launcher to be accommodated. Remote handling flanges at each end of the splitting network are being designed.

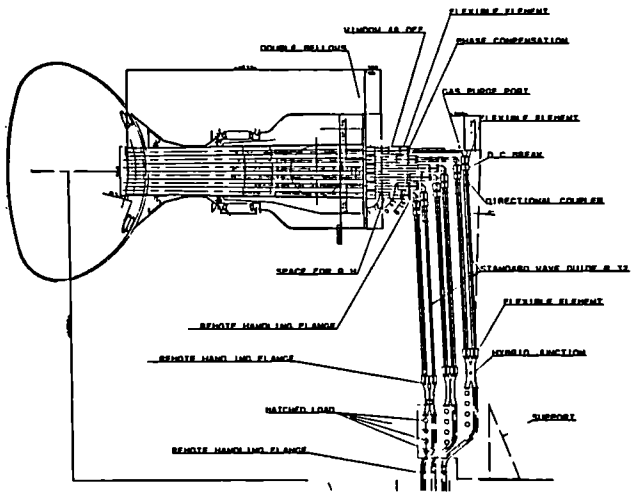

Fig. 5 Lay-out of the splitting network.

Summary

The main features of the Lower Hybrid Current Drive system which is being built for JET are summarized in the next table. Low power and high power tests of the critical items are under way. The low power testing of the main microwave components: Power splitter, phase shifters, etc. have been completed. Completion of the milestones for the construction of the system: end of 1988 for a first stage (2 MW) and 1990 for the full system appears to be feasible.

Lower Hybrid System for JET

Frequency		3.7 GHz
Power (generator)		12 MW
No of klystrons		24
No of waveguides		384
" "	horizontal	32
" "	vertical	12
Waveguide dimension		72 x 9 mm
Power density		4 kW/cm^2
Maximum Reflected power		
without circulators		2%
with circulators		8%
Waveguide material		Copper Coated Stainless Steel
Maximum temperature		500°C
Stroke		300 mm
Total weight of the launcher		~ 8t
Pressure (during a pulse)		10^{-8}torr
Pumping speed		10^5 l/sec
Phase control		10°
Length of the transmission line		~ 40 m
Estimated insertion losses		~ 1 dB
Central N// Value		1.8
Range of N//		1.3-2.3
Estimated driven current at ne =	$2 10^{19}$ m^{-3}	3-5 MA
" " " "	$5 10^{19}$ m^{-3}	1-2 MA

Acknowledgements

It is a pleasure to acknowledge the Instituto Superior Technico at Lisbon for their help in the theoretical estimate of LHCD in JET. We are very grateful to the Tore Supra team for allowing JET to use their high power test bed and for their help in operation and in interpretation of these tests.

References

1. C. Gormezano et al, in Proc. 14th Symposium on Fusion Technology, Avignon (1986).
2. H. Derfler et al, in Proc. 4th Varenna-Grenoble Symp. on Heating in Toroidal Plasma, Roma II (1984) 1261.
3. N.A. Mitchell, G.H. Harding, Code Electra. Technical note (Culham)
4. R. Magne et al, in Proc. 14th Symposium on Fusion Technology, Avignon (1986).

EARLY OPERATING EXPERIENCE WITH THE JET NEUTRAL INJECTOR POWER SUPPLIES, RELIABILITY AND IMPROVEMENTS

J A Carwardine, R Claesen, C Christodoulopoulos, P Bertoldi, J Deng (1), R Rushton
JET Joint Undertaking, Abingdon, UK. (1) Institute of Plasma Physics, Hefei, China

ABSTRACT

The JET Neutral Beam Power Supplies consist of Accelerating Grid power supply and associated protection system, Arc and Filament power supplies, Gradient grid resistive divider, Suppression grid power supply, Snubber Bias power supply, and Deflection Magnet power supply.

Operation of the first eight Injectors started independently from the machine in mid-1985, with the first injection taking place early in 1986. The experience gained has been used to improve the operation and reliability of the power supplies. Injection from the second group of eight injectors is due to start before the end of 1987.

Reliability has improved considerably, as problems have been highlighted and eliminated. Some examples are given of major problems experienced during operation, together with some of the solutions implemented. The paper will discuss, in the main, the experience of the 1986 operating phase, since the most data is available for this period. Statistical fault analysis will be presented for two periods of operation.

REMOTE OPERATION OF THE POWER SUPPLIES

The JET Neutral Injection System is separated into two groups of eight injectors on opposite sides of the machine (at Octants 4 & 8). The two groups are essentially identical and are operated independently, each having its own computer control system. Figure 1 shows the interfaces between the main computer system and the power supplies.

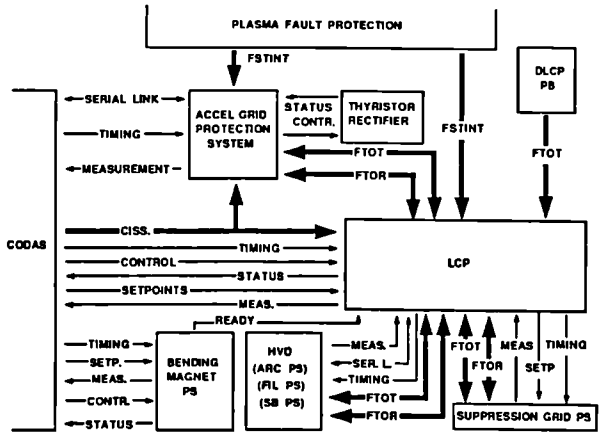

FIG.1 NEUTRAL INJECTION POWER SUPPLY INTERFACE

Control of the power supplies from the main computer can be performed at two levels through touch-sensitive panels and mimic screens:

- LEVEL 3 control allows operations on individual power supplies, regardless of whether they are selected for beam operation.
- LEVEL 2 control allows operations to be carried out simultaneously on all supplies selected for operation. Selection of the power supplies (Injectors) and their parameters, is performed by the Neutral Injection Operator, through a series of setting screens [Ref.1]. The Power Supply Operator is unable to change the selection of power supplies or the parameters fed to them. This is done deliberately to ensure that the correct parameters are loaded for the beam power levels required and to ensure the safety of the beam line.

A facility provided by the LEVEL 2 software, for the auxiliary power supplies, is the TEST OF SETPOINTS. Parameters loaded into the power supplies are routed through the control electronics and sent back to the central computer as an analogue signal. This signal is then compared to the requested value loaded from the setting screen. If there is a discrepancy of 5% or more, an error is registered and the pulse is inhibited.

Parameters loaded into the G1 power supplies are echoed by the protection system and are continually monitored by the serial link software.

The status of the power supplies is displayed on a series of mimics, on the computer console. An overview mimic shows the status of all power supplies for one group of injectors (Octant 4 or Octant 8). The overall status, selection of power supplies, indication of any alarms, and the main pulse parameters are shown on this mimic. Detail mimics can be called directly from this overview, using a tracker ball.

INTERFACE TO THE CENTRAL COMPUTER

Two modes of communication are used between the power supplies and the central computers.

For the accelerating grid power supply and protection system there is a hardwired RS232 serial link running between each Grid Protection System and CODAS (Control and Data Acquisition System - the JET computer system) (Fig.1). This provides information on the status of the power supply, and sends commands and set-points from CODAS.

In the case of the auxiliary power supplies (ARC, FILAMENT, SUPPRESSION GRID, SNUBBER BIAS and DEFLECTION MAGNET power supplies), each individual command or status bit is wired separately from a Local Control Panel to digital interface modules in the CODAS local cubicles.

The two methods offer different advantages. The serial link is less prone to breakdowns because there are fewer components involved. It does however, rely on software in the controllers. Problems are still occasionally experienced during operation. These can principally be attributed to incompatibility between the two.

The hardwired approach offers ease of commissioning and fault finding, since all signals are individually accessible. However, the very large number of components involved, increases the frequency of breakdowns. (In the case of each pair of auxiliary power supplies, the interface is achieved using 25 printed circuit cards, providing some 400 channels).

ORGANISATION OF POWER SUPPLY OPERATION

Operation of the neutral Injection system generally follows that of the JET machine; that is on a two shift basis covering the hours 06.30 to 22.30, five days per week. Every six weeks of operation is followed by one week of maintenance and one week of commissioning.

So far, only the Injectors on Octant 8 have been in routine operation. Operation of the power supplies for these injectors requires one operator for each shift. The duties of the operator include start up and shutdown of the supplies. To assist in fault-finding, an expert is available on an on-call basis. Operation of the overall beamline requires an additional operator and a physicist.

It is proposed that in the future, the injector power supplies will be operated by the magnet power supply operator. Combined operation was tried for several weeks at the end of the 1986 operating phase with mixed success. During Neutral Injection experiments, both main Magnet and Neutral Beam power supplies could be successfully operated by the one team. However, during independent operation of the injectors, combined operation was not very successful.

SYSTEM RELIABILITY

Operational experience has already highlighted some weak areas in the system. Many problems have been overcome as a result of this experience. Two particular aspects of the system reliability will be discussed - that of early pulse terminations, and that of system down-time.

Early Termination of Pulses

Figures 2 & 3 summarise beam operation for weeks 17 & 18, during 1986. It can be seen that the majority of pulses terminated by the power supply can be attributed to a relatively small number of interlocks.

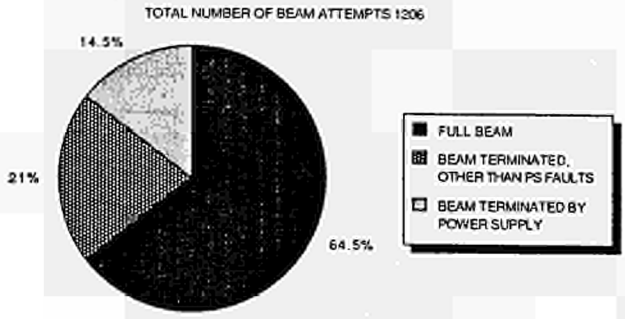

FIG.2 SUMMARY OF BEAMS FOR WEEKS 17 & 18

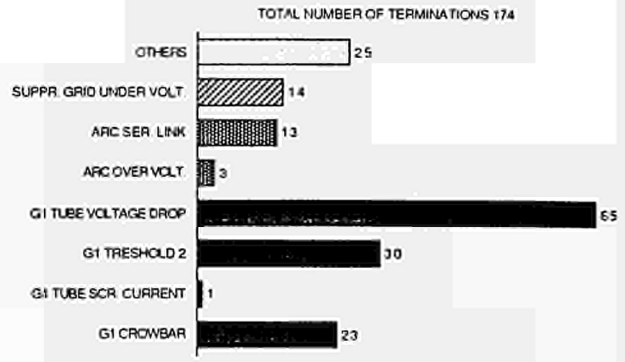

FIG. 3 BREAKDOWN OF POWER SUPPLY TERMINATIONS WEEKS 17 & 18

During this period, particular problems were experienced with the grid protection system crowbar, and the tetrode voltage drop. During the following maintenance week, efforts were made to resolve these problems. Data for the following operating period (figures 4 & 5) shows the improvement.

Problems with the serial link to the arc power supplies were also resolved. The interlock 'G1

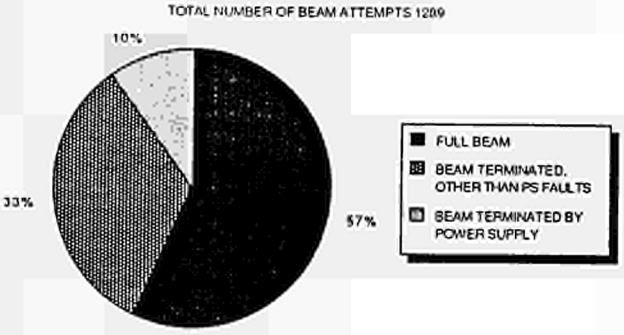

FIG.4 SUMMARY OF BEAMS FOR WEEKS 21 TO 24

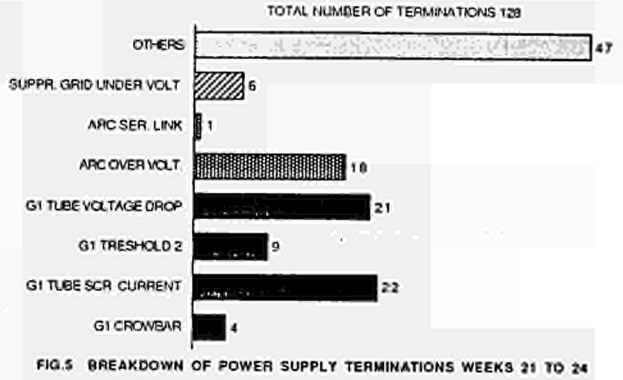

FIG.5 BREAKDOWN OF POWER SUPPLY TERMINATIONS WEEKS 21 TO 24

THRESHOLD 2' results from excessive load current, as a result of a breakdown. It appears frequently during conditioning of the injectors and indicates that the tetrode has failed to block

Experience has shown that pulsing of a well conditioned injector is much more reliable than that of an injector which frequently breaks down. In order to improve reliability, it therefore seems necessary to concentrate on the power supply elements involved in blocking and reapplication.

One element which has been studied in detail, is the Arc Power Supply Notcher, comprising a bank of switching transistors which sink the plasma-source current during a reapplication [Ref 2]. The switching transistor fault detector, which detects short circuit transistors, proved very unreliable. In some cases, pulses were terminated consistently, even when it was clear that there was no real fault. The problem has been almost entirely eliminated by improved matching of the detector analogue signal to the true voltage waveform.

System Down-Time

Figures 6 & 7 show the availability of power supplies for the operating periods above.
The length of time out of service is not shown. This data would be misleading, since immediate repair of a fault is not always possible due to the inaccessibility of the plant during operation. Two factors effect this:
Two grid protections systems are enclosed in the same cabinet, so repair of one means that the other unit must be withdrawn from service.
Repair of a fault on one of the high voltage decks

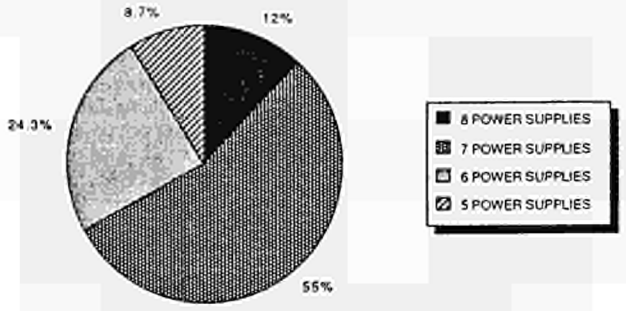

FIG.6 SUMMARY OF POWER SUPPLY AVAILABILITY FOR WEEKS 17 & 18

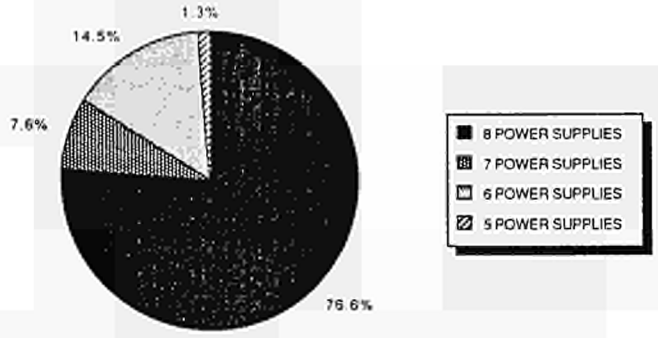

FIG.7 SUMMARY OF POWER SUPPLY AVAILABILITY FOR WEEKS 21 TO 24

(Auxiliary Power Supplies) necessitates the shutdown of eight injector power supplies, in order to allow safe access to the area.
The difficulties in gaining access to equipment often means that a simple fault can remove an injector from service for a complete day, if the other injectors are required continuously. It should also be noted that one fault can remove two injectors from service, since most of the control and interface electronics is common to two power supplies.

Failure of Electronics on Auxiliary Power Supplies: There have been a large number of random component failures on printed circuit cards, in the auxiliary power supply local control panels and high voltage decks. At first, no explanation could be found, but it was discovered that the air temperatures inside the electronics cubicles was exceeding 40 degrees celsius (some 20 degrees above ambient). This was offered as one explanation for the failures. Cooling fans have since been installed in both the local control panel and to each electronics chassis inside the high voltage decks, and the operating temperatures inside the local control panels have fallen to about 30°C. The number of failures has now fallen.

Grid Protection System Input Crowbar: The circuit of the ignitron stack consists of 5 ignitrons in series with cascade triggering [Ref 5]. The trigger pulse is applied to the lowest ignitron, cascading of the stack providing triggers to successive ignitrons.

Two problems have been encountered:

1. Self-firing

If the ignitron elements in the stack are not well conditioned, the stack has been seen to self-fire (breakdown prematurely). Conditioning involves the removal of mercury drops from the inner surfaces of the tube. These would otherwise cause the ignitron to break down when voltage is applied between anode and cathode.

The procedure used for conditioning the ignitrons in the JET protection systems incorporates both thermal and electrical conditioning, such that each tube just withstands about 30kV (giving a stack withstand voltage in the order of 150kV). The tubes can be conditioned to much higher levels, but the withstand voltage is deliberately limited, in order to give some degree of self protection. The maximum voltage expected on the stack is 120kV.

2. Failure to fire

The crowbar stack fails to close when a trigger is applied. This fault has far more serious consequences and has been more difficult to cure. The precise cause of the failure to fire is not known, but measurements have shown that the trigger pulse does not always cascade to the topmost ignitrons. Calculations proved that the energy available in the trigger pulse is considerably less than recommended for reliable firing. Furthermore, the energy was not being shared equally amongst the five ignitrons.
Two actions have been initiated:
a) The sharing of the trigger energy has been improved by changing of passive components on the crowbar stack.
b) Investigations are underway to increase the size of the storage network in the trigger supply.

The failure-to-fire was not experienced during initial testing of the prototype unit, nor in the commissioning of the other units at JET. It is likely that the problem has become apparent only as the ignitrons have aged (ignitor wetting), which results in a lower resistance between the ignitor and the mercury pool. The lower resistance of the ignitor-cathode junction causing even worse sharing of the available energy between the five devices.
In order to combat the problem, the ignitrons will be checked during every maintenance period (once every two months) for aging. Any ignitron whose ignitor-cathode resistance falls below 20 ohms will be replaced. In addition, each crowbar stack is checked for reliable firing before the start of each week's operation.

Tetrode Oscillations: From the earliest commissioning of the Protection systems, problems were experienced with oscillations in the series tetrode [Ref 3]. The oscillations were solved by putting damping material in the anode cathode area. The latest version installed, damps oscillations for currents up to 80A and voltage drops across the tube of between 7 and 15kV.
Problems were also encountered with the seals between tetrode hood and anode-cathode area:
a) The filament contact ring is forced air cooled. This means that hot air is blown over one of the seals. This was causing premature aging of the seal through

oxidation; the rubber compound became very brittle and fractured. The composition of the rubber has been changed to cure this problem.

b) The seals had some damping effect on the parasitic oscillations. Energy was therefore absorbed by the seals which eventually caused failures resulting in almost knife-like cuts in the seal. More effective damping material has reduced the energy absorbed by the seal to safe levels.

High Voltage Power Supply Filter: Problems have been encountered with excessive peaks and dips in the high voltage power supply. These cause either a tetrode screen grid overcurrent or an excessive voltage drop across the tetrode.

At the start of the pulse, all of the energy is taken from the capacitor in the output filter, until the commutation of the freewheel thyristor to the main bridge is completed [Ref 6]. Because of the high resistor value (100 ohm) in the filter, the voltage drops instantly and continues dropping as a capacitor is discharged. In order to prevent the voltage dropping too low (resulting in a tetrode screen overcurrent), an additional 16% is added to the voltage set-point during the precharging of the inductor, and during the reapplication time. In addition, there is a large differential component in the controller, in order to push up the voltage as quickly as possible. If the Injector breaks down immediately, almost no current is drawn from the supply, and part of the energy in the filter inductor is transferred to the capacitor, so pushing up the voltage. If this happens several times in succession, then the voltage across the tetrode exceeds the threshold and the pulse is terminated.

This problem was not experienced during commissioning on dummy resistive load, because an immediate injector breakdown was not simulated [Ref 4]. A study has been initiated with a view to increasing the size of the filter components.

Plasma Source Current Controller Optimisation: The controller for the plasma source current has been well document [Ref 2]. A closed loop controller acts on the filament power supply to control the temperature of the filaments. The ionisation of the gas in the plasma source is then emission limited. Some time was spent during the latter half of 1985 optimising the current controller. A spare injector was temporarily installed close to the power supplies, together with a gas system, vacuum pump and cooling.

Local operation of the arc and filament power supplies allowed analysis of the control system with the real load. In order to reduce the error between demanded current and actual current obtained, the loop gain of the controller was increased by a factor of six. This initially had a destabilising effect on the current, resulting in a large overshoot and several periods of oscillation. The addition of phase advance in the feedback path stabilised the controller. It is now possible to acheive a wide range of source currents from a single value of filament preheating.

Fires in Grid Protection Crowbar Stack: In the past 12 months, we have suffered two fires in the protection system crowbar stacks. In both cases the crowbar was totally destroyed and approximately 65cm³ of mercury was deposited into the surrounding area. The resulting contamination has had far more serious consequences than the fire damage itself. The first fire happened after the first application of voltage following a maintenance period, when the ignitrons were removed for conditioning. The cause of the second fire is currently under investigation.

FAULT FINDING

Many difficulties have been encountered when trying to trace faults in the power supplies.

Often, the symptoms of a fault has given no clue as to the nature of the fault. For example, a small power supply was found to be oscillating - the fault showed up as spurious firing of the Suppression Grid power supply.

A fault may not be seen because of other overriding factors. A fault which developed in the timing system to a suppression grid supply caused the injector to break down. This was not noticed immediately, since the injectors were not well conditioned and were expected to break down.

Much of the electronics is at high voltage making fault finding difficult and time consuming.

In order to simplify location of faults, further diagnostic facilities are under construction, allowing remote monitoring of several signals at the same time. A 'Wiseman' guide is also under preparation. This will detail faults seen previously, together with their symptoms.

CONCLUSIONS

Whilst reliability of the injector power supplies has improved dramatically since the first operation in 1985, there is still a lot of work to do. Particular effort is needed in studying the elements involved in the blocking and reapplication of the supplies injector breakdown. It is hoped that the improvements on the power supplies can be extended during the next periods of operation.

ACKNOWLEDGEMENTS

The authors would like to thank all members of the Additional heating Power Supply Group for their continued support during commissioning and operation of the Injector power supplies. Thanks are also extended to E Bertolini for his contribution during the operation and for his help in the preparation of this paper.

REFERENCES

1. D Stork et al., "Overview and Operation of the Control Safety and Interlock on the JET Neutral Beam Injector". Proc. 14th Symposium on Fusion Technology, Avignon, Sept 1986.

2. G L Basile et al:"The Neutral Injector Auxiliary Power Supply System in JET:Design, Manufacture and Tests". Proc. 13th Symposium Fusion Technology, Varese, Italy, Sept 1984, p834.

3. L Egerszegi et al. A model for the parasitic oscillations in power tetrodes, Int. J. Electronics, 1986, Vol 61, no.5, pp575 - 582.

4. R Claesen et al., "Commissioning and Early Operation of the Power Supply and Protection System for the Extraction Grid of the JET Neutral Injectors at 160kV". Proc. 14th Symposium Fusion Technology, Avignon, France, Sept 1986, pp 933-939.

5. United States Patent 4,232,351 High Voltage Crowbar circuit with Console Triggered Series Ignitrons.

6. R Claesen and P L Mondino: "Neutral Beam Injection and Radio Frequency Power Supplies". Fusion Technology, vol. 11 Jan 1987, pp 141 -162.

THE ADDITIONAL SWITCHING NETWORK, A NEW PART OF THE POLOIDAL FIELD SYSTEM OF JET: DESIGN AND EARLY OPERATION

T. Bonicelli, V. Marchese, P.L. Mondino
JET Joint Undertaking, Abingdon, Oxon, OX14 3EA, U.K.

ABSTRACT

The Additional Switching Network became part of the JET Poloidal Field system after the 1986-1987 shutdown. This paper describes the main features of the various components of the Additional Switching Network and the results of factory tests and of tests performed at JET site are reported. Finally, an assessment of the first three months of operation is presented.

1. Introduction

The Additional Switching Network (ASN) was installed and commissioned during the JET 1986-1987 shutdown and is now fully operational as a part of the JET Poloidal Field (PF) system (Fig 1).

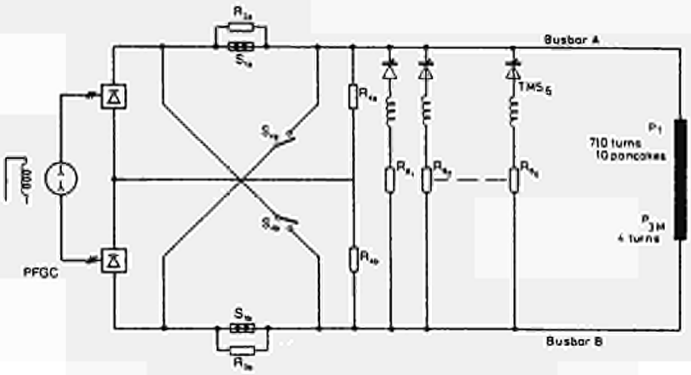

Fig 1 - Ohmic Heating Circuit Diagram.

The scientific background which led to the decision to procure the ASN has already been described [1]. The purpose of the ASN is to reduce quickly the voltage across the magnetizing coil during the plasma fast-rise phase by switching in commutating resistors R8 to control to some extent the rate of rise of the plasma current and to optimize plasma start-up conditions. A reduction of the MHD activity and a better exploitation of the available flux swing should in this way be achieved. The reduction of the loop voltage after the breakdown phase helps, moreover, to control the plasma radial position. This is critical in JET at higher premagnetisation currents due to a lack of voltage capability across the vertical field coils (this problem is being tackled by increasing the voltage capability of the relevant power supply).

2. Description of the Main Components of the ASN

The ASN consists of six identical branches connected in parallel with the JET magnetizing coil between the two busbars A and B. Each branch is composed of a Commutating Resistor (R8) and of a Thyristor Make Switch (TMS). A Limiting Inductor and a Current Transducer can be considered as part of the Thyristor Make Switch. Each branch has a nominal resistance of 0.9Ω, thus the total parallel resistance is 0.15Ω.

2.1 Commutating Resistors

Each commutating resistor (nominal value 0.9Ω) has an energy capability of 135MJ every ten minutes (nominal JET duty cycle) but a 50% overload (200MJ) would not cause damage. The resistors are forced air cooled with air-to-water heat exchangers. The overall dimensions of each resistor are 3200 x 1680 x 2500mm; the weight is 3400kg. The nominal voltage is 24kV r.m.s. Each resistor is internally arranged in twelve elementary banks of 1.2Ω each and, by means of bolted connection links, two different resistance values of 0.9Ω and 1.6Ω can be obtained.

A sketch of a resistor elementary bank is shown in Figure 2. The desired ohmic value is attained by assembling together 228 stainless steel strips (440 x 50 x 1.5 mm); two consecutive strips are joined together by means of three welding spots. The mechanical assembly exerts pressure in the same area as the welding spots.

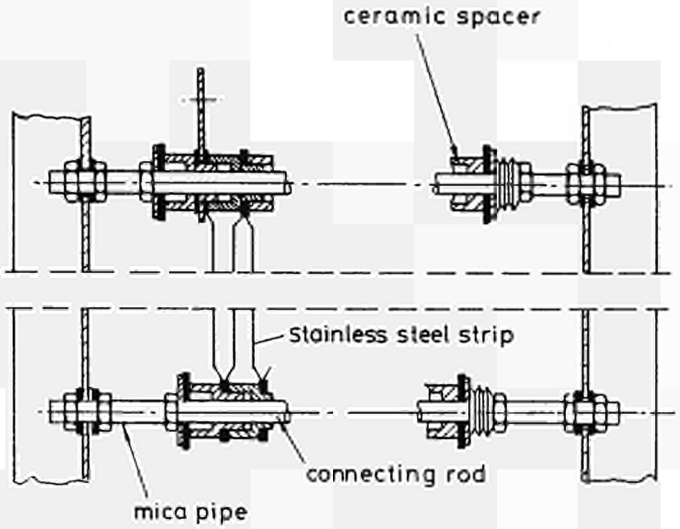

Fig 2 - Resistor elementary bank.

The insulation between active material and connecting rods is given by ceramic spacers and mica pipes. The active material is stainless steel AISI 310, whose main features are:

- low thermal coefficient of resistivity ($\sim 0.5 \times 10^{-3} °C^{-1}$ in the range 20 - 400°C);
- high maximum working temperature (~700°C).

Actually, the design maximum average working temperature attained during a nominal pulse is only 400°C.

2.2 Thyristor Make Switches

The Thyristor Make Switches (TMS) are required to close under a maximum voltage of 25kV and to carry a nominal current pulse as shown in Fig 3.

The TMS design is based on the following main features:

- use of the larger thyristor presently available (100mm silicon base material, VDRM = 4200V, ITAV = 3000A) without paralleling, and are water-cooled on both sides;
- the voltage safety factor is 1.5, plus one redundant thyristor. Such a safety factor is considered adequate, taking into account the conditions of installation and operation of the equipment (indoor and without direct connections to outdoor electrical networks). Each thyristor stack is thus arranged in 10 levels;

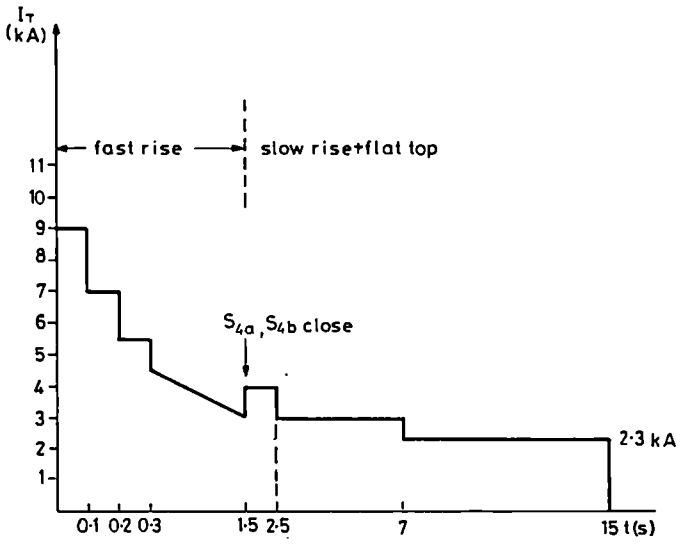

Fig 3 - Nominal current pulse.

- a limiting inductor of 1.25mH, air cooled in series connected to limit the maximum di/dt at a conservative 20 A/µs, thus avoiding the danger of "hot spots" in the wafer;
- the triggering signals are generated for each individual thyristor in a Local Control Cubicle (LCC) at earth potential and are sent, through optical fibres, to the high voltage thyristor stacks. Each thyristor level is provided with a firing module on a printed circuit board (pcb) standing at high potential, which converts the light signal coming from the LCC into a current pulse applied to the gate of the thyristor itself. At the same time, an answer back signal is generated and sent, through an optical fibre, to the LCC for monitoring purposes (Fig 4).

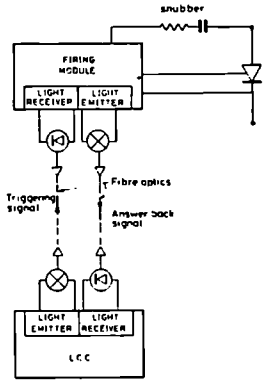

Fig 4 - Firing circuit schematic.

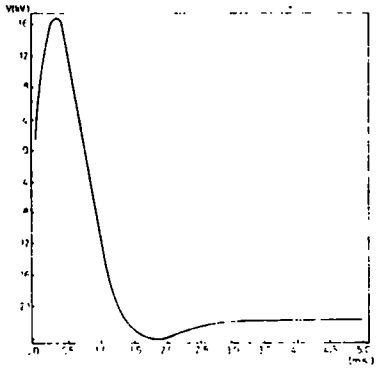

Fig 5 - Transient voltage across P1 at the opening of S1a and S1b.

The energy necessary to fire each thyristor is taken directly from the main busbars through the RC snubber circuit, taking advantage of the transient voltage (Fig 5) produced by the discharge of the Commutating Capacitors at the beginning of the fast rise. A self-firing protection is implemented in the firing module.

If for any reason, the voltage across an individual thyristor exceeds ~4000V in the forward direction, the thyristor itself is immediately fired, via the discharge of a BOD element, as protective action;

- a RC snubber, R=22Ω, C=1.8µF, is connected across each thyristor in order to assure good voltage sharing among the thyristors in series;
- the mechanical design of the stack is well assessed and has been used in several previous projects. The overall dimensions of each stack (post insulators included) are 1063 x 750 x 810mm.

After discussions with the Manufacturer, it was decided to limit the maximum junction temperature for normal operation to 120°C, even if the thyristors are not required to block any voltage after the current zero at the end of the pulse, in order to avoid long-term variation in the doping of the base material. The junction temperature rise has been limited at 80°C in order to avoid long-term mechanical problems arising from differential dilatations.

To comply with these limitations, the switching sequence is subjected to the constraint that, as a first step, at least three branches must be switched in simultaneously. This is not felt as a limitation from the operational viewpoint, since a large voltage step-down is required anyway, after the first breakdown phase. Nevertheless, each Thyristor Make Switch is capable of withstanding stresses coming from the application of the current waveform, shown in Fig 6, corresponding to the firing of only one switch, which is regarded as a fault condition.

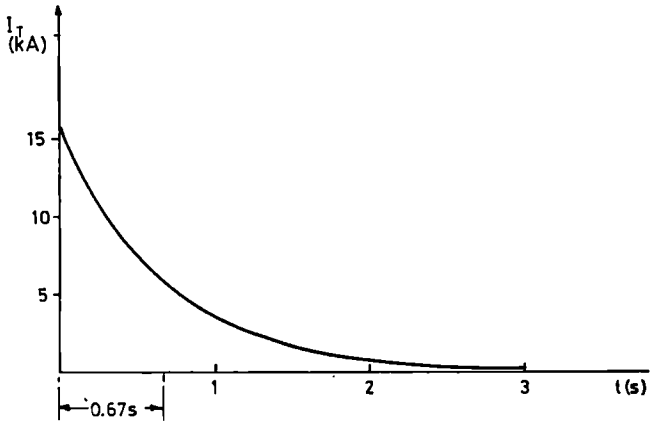

Fig 6 - Fault current flowing in one branch when none of the other branches is switched in.

The current in each branch is measured by a Hall effect current transducer with measuring range up to 40kA [2].

3. Control and Protection

Two LCCs perform the control, monitoring, protection and interfacing functions either locally, for commissioning, or remote, for normal operation. The choice of two independent LCCs is due to contractual reasons.

The firing command to each thyristor switch (see Fig 4) is generated by the Central Timing System (CTS) within an enabling window of 1.5s. This command is routed by the Switch Controller inside the LCC to the firing modules standing at high voltage, with a negligible delay, using ten independent fibres. An equal number of fibres are used as handshake. If, after a fire command, one or more answer-back signals are not received an Inhibit Pulse (IP) request to the Central Interlock and Safety System(CISS) is issued, which prevents the trigger of the next pulse until the fault is repaired. In addition, if after a selectable time delay set at about 1ms, the switch is not conducting (current larger than 100A), a firing command is sent to all the remaining switches and an Emergency Shutdown (ES) request is issued to CISS, which stops the pulse.

The TMS Measurement System monitors currents, inlet and output cooling water temperatures of each switch. Two overcurrent trip levels have been set: when the first threshold, set at 10kA, is reached, a firing command to all the remaining switches and an ES request to CISS are issued; when the second one, set at 16kA,

is reached, the excitation circuit breaker of the poloidal FGC is tripped and the CTS is stopped (direct interlock). The TMS system is also fired, via direct interlock, if a fault is detected in other parts of the PF system (eg current in the neutral at interruption).

The junction temperature rise of each switch is simulated in analogic form using, as input signal, the power losses, calculated starting from the currents, which feed an operational amplifier with 6 RC networks in the feedback loop representing the thermal time constants of thyristor and heat sink. The absolute junction temperature is then computed, summing up the average water temperature, which is obtained averaging inlet and outlet water temperatures. If the absolute junction temperature of any switch exceeds 120°C an ES request to CISS is issued together with the firing of all the remaining switches. If the water flow of any thyristor switch is below a minimum level of 25 l/min an ES request to CISS is issued and the pulse is stopped.

The demineralising cooling plant is controlled by the local PLC (Simatic S5 115U). The PLC is also interfaced with the Local Control Panel (LCP), with the Protection Logics, with CODAS and CISS. 96 digital inputs and 128 digital outputs are processed by the PLC in about 115 ms which is consistent with the CISS cycle time of 125ms.

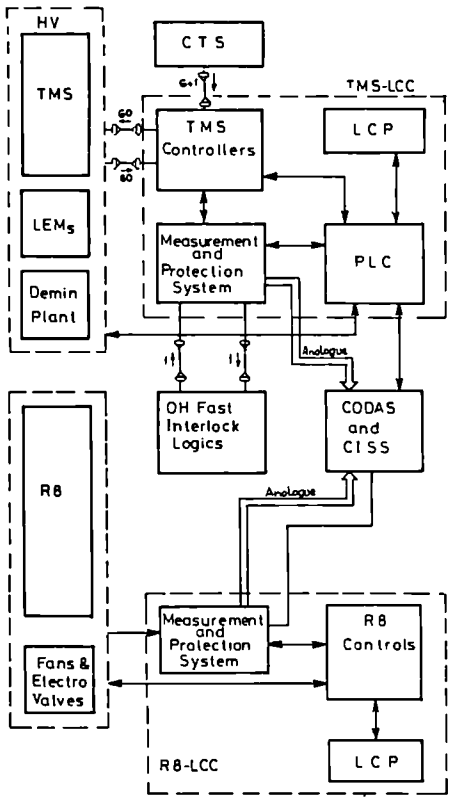

Fig 7 - ASN Control and Protection System.

The control of R8 is performed with traditional relay logic. As shown in Fig. 7 the cubicle is interfaced with CODAS, CISS and the cooling plant (fans and electrovalves). Cooling water and air temperatures are monitored by six independent electronic modules. An IP request to CISS is generated if water or air temperatures exceed 60°C and 200°C respectively. Since the resistors are designed to withstand the energy of one pulse in case of water flow below a minimum level of 150 l/min, the required interlock to CISS is to inhibit the next pulse.

All the alarms, as general policy, are latched inside the two LCCs. If the fault cannot be repaired in a reasonable time, the possibility to put one branch off-line has been provided. In this case, the CISS interlock from the faulty branch is overriden. At least three branches should be on line in order to operate the system safely.

4. Factory Tests

All the components of the ASN were extensively tested in factory before despatch, to check their compliance with the JET Technical Specifications. A list of the tests performed on thyristor stacks and commutating resistors is reported in Table 1.

TABLE 1 - FACTORY TESTS

Component	Test	Test Conditions	Comments
Thyristor Stack	1 Short duration a.c. voltage test between terminals	24.5kV rms 1 min	Routine test
	2 Short duration a.c. voltage test to ground	38kV rms 1 min	Type test leakage current < 1.6 mA
	3 Voltage sharing test	20kV rms between terminals	Routine Test Maximum voltage difference < 5%
	4 Firing check	Trigger pulse 1A/50µs	Routine test on each thyristor
	5 Lightning impulse to ground	75 kV peak 5 pulses each polarity	Type test
	6 Switching impulse between terminals	34.5 kV peak 135/2000 µs 5 pulses each polarity	Type test
	7 Self firing Protection	34.5 kV peak 135/2000µs Trigger signal to one thyristor disconnected	Type test
	8 Firing test	The thyristor stack is fired under 18.5kV, a current pulse of 4kA peak follows	Type test
	9 Firing test under minimum voltage	The thyristor stack is fired under 2kV	Type test
Commutating Resistor	10 Lightning Impulse test to ground	95 kV 5 pulses each polarity	Type test
	11 Short duration a.c. test to ground	50 kV rms	Routine test
	12 Current impulse on a resistor bank section	7.5 kA rms 140 ms	Type test A third of a resistor bank was subjected to test (0.4Ω)
	13 Load test on bank	630 A rms 25s and 35s	Type test The test lasting 35s corresponds to an overload of 40%
	14 Short duration voltage test on a resistor bank	11 kV rms 1 min	Routine test Voltage applied between resistor grid and supporting rods

During all the tests on the thyristor stacks, demineralised cooling water was flowing in the pipes and the heatsinks.

During the switching impulse test between terminals - test 6 in Table 1 - the voltage across the thyristor nearest to ground level was monitored and found to be

consistent with a correct sharing of the voltage amongst the ten thyristors in series in the stack.

Test 7 was performed to check the proper functioning of the self firing protection. A thyristor stack, with one of the fibre optics leading the trigger signal to one thyristor disconnected, was subjected to a 34.5kV switching impulse. The stack was fired in correspondence of the peak of the applied voltage. Fig 8 shows the voltage across the disconnected thyristor: when the stack is fired the voltage starts increasing until it reaches 4.1kV when the self firing protection becomes active and the thyristor is immediately fired via the BOD.

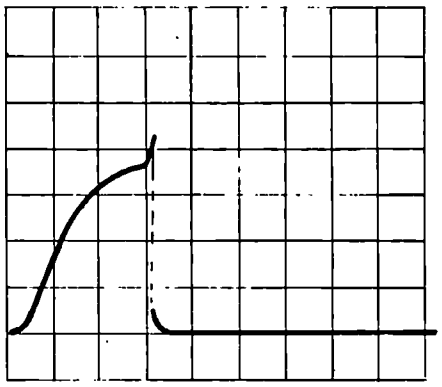

Fig 8 - Voltage across the disconnected thyristor during the self-firing test.

Test 9 was performed to check the functioning of the firing circuits under the specified most stringent conditions. The thyristor stack was successfully fired under 2kV at a maximum delay of 650ms (specified 500ms) after the charge of the firing capacitor.

The tests 12 and 13 were performed in an early stage of the project to assess the soundness of the proposed design for the resistor banks, which was modified compared with the previous commutating resistors installed at JET. The tests showed an improvement in the exploitation of the active material, more uniformly utilised, and the temperature was always kept within the acceptable limits (less than 600°C when a 40% overload was applied).

TABLE 2 - TESTS AT JET SITE

Component	Test	Test Conditions	Comments
Resistor	1 H.V. test to ground	50kV d.c. 1 min both polarities	
	2 Heat run test	Nominal energy pulses at nominal duty cycle	The pulses were repeated until thermal steady state conditions were attained
Thyristor Stack	3 H.V. test to earth	42kV d.c. 1 min	Cooling system running
	4 H.V. test between terminals	31kV d.c. 1 min	as above

5. Tests at JET Site

The commutating resistors and the thyristor stacks were high voltage tested to check the soundness of the insulation after delivery and installation at the JET site (see Table 2).

The commutating resistors were then subjected to a heat-run test which was carried out making use of the Poloidal Field Generator. The rated energy was repetitively applied to the resistors and thermal steady state conditions were reached. The cooling air and water temperature was checked and found to be according to design values (see Fig 9), thus confirming efficient functioning of the heat exchanger.

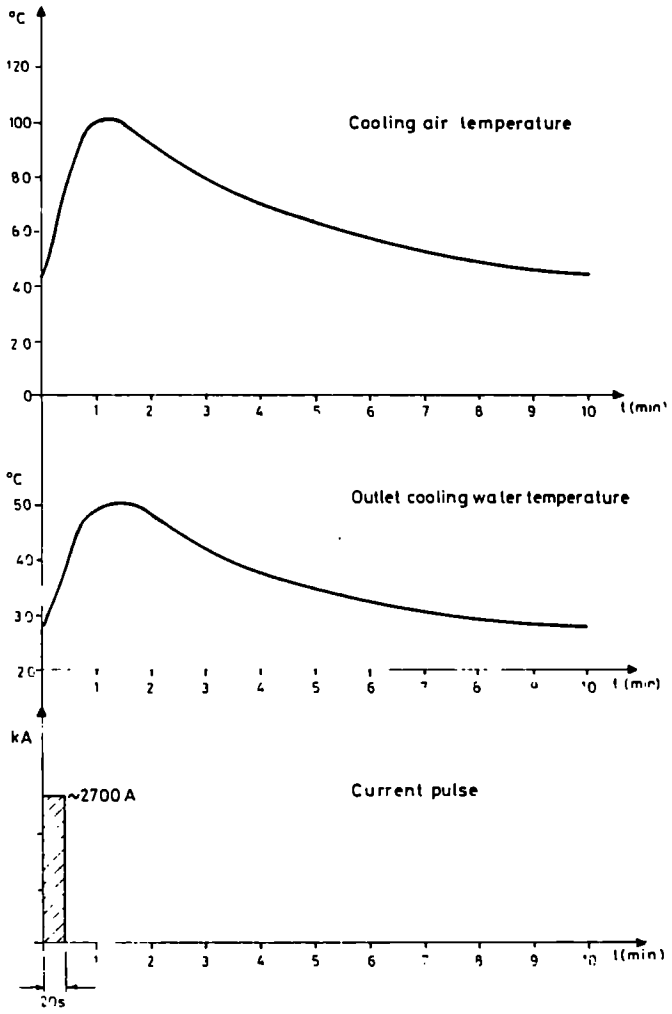

Fig 9 - Cooling air and water temperatures during the heat-run test on the commutating resistors.

The complete ASN was then subjected to a series of integrated commissioning tests. These tests were performed making use of the Ohmic Heating Circuit in full operating configuration under remote control from CODAS. In this way, the equipment was tested up to the design values in the same conditions of operation with plasma.

The test sequence was as follows:

* Firing Tests: A current of 10kA was driven in the JET magnetizing coil P1 and then transferred to the commutating resistors R3 and R4 with the circuit breakers S1 open. One thyristor switch was fired and a

current with a peak value of 4kA was therefore commutated in the series connected R8. The test was repeated on all the thyristor make switches.

* Test of Protections: The overcurrent protections (both thresholds, see Section 3) and the absolute junction temperature protection of all the switches were individually tested, adjusting the thresholds at levels lower than operational ones. The Firing Sequence protection (see Section 3) was tested withdrawing the relevant firing pcb. All the protective actions proved to be working properly. Fig 10 shows, for instance, the results of the test on the overcurrent protection of the Thyristor Make Switch 4. When the threshold value (~ 7.5kA) is reached, the protection becomes active and all the other switches are fired, thus relieving the faulty switch from part of the current which drops at 3kA.

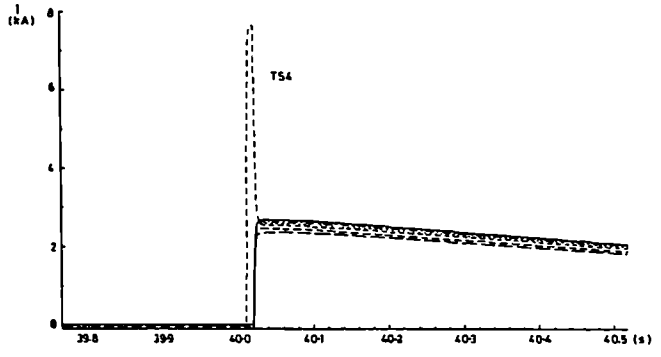

Fig 10- Currents in the Thyristor Make Switches during the overcurrent protection test on TS4.

* Test of Normal Operation up to the Design Values: The current in the magnetising coil was then progressively increased up to 40kA, and the "nominal" firing sequence of the Additional Switching Network was performed. Three thyristor make switches were fired at 40.01s, whereas the other three were fired at 40.23s. The results are reported in Fig 11a and 11b which show the trend of currents and simulated junction temperatures, respectively. The maximum current in a switch was about 8.7kA and the maximum junction temperatures, attained at 40.23s, was about 87°C ($\Delta\Theta$~67°C), well within the design values.

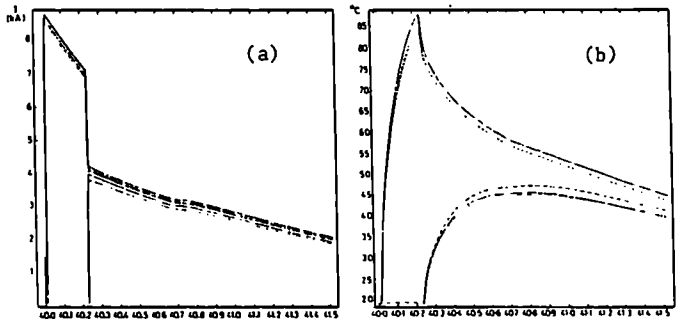

Fig 11- Current (a) and simulated junction temperature (b) during a "nominal" pulse.

* Test of Minimum and Maximum Time for Firing: In the Technical Specification, it was required that the Thyristor Make Switches should be fired at any instant between 40.002s and 40.500s. A check of this requirement was carried out and was found that the switches can be actually fired in the time window 40.001s ÷ 41.300s.

During these commissioning pulses, only two failures in the control electronics were recorded.

6. Early Operation

Since July 1987, the ASN has been service and it is now regularly used during plasma operation. Fig 12a shows the beginning of a discharge with a premagnetisation current of 30kA, when no R8 commutating resistor is switched in. A voltage of about 17.2kV is produced across the magnetising winding and the plasma current starts rising quickly (~3 MA/s during the first 300ms), the vertical amplifier tries to maintain the radial position control and goes to full voltage. Actually, since the voltage capability of the vertical amplifier is presently not sufficient, the error signal $\delta\psi R$, which gives an indication of the error on the plasma radial position control, becomes somewhat high, even if, due to the decreased voltage across the magnetising coil, the radial position is later recovered.

Fig 12b shows the plasma start up when three R8 commutating resistors are switched in at 40.1s. The error signal $\delta\psi R$ is now much reduced and the vertical amplifier recovers the radial position control much earlier.

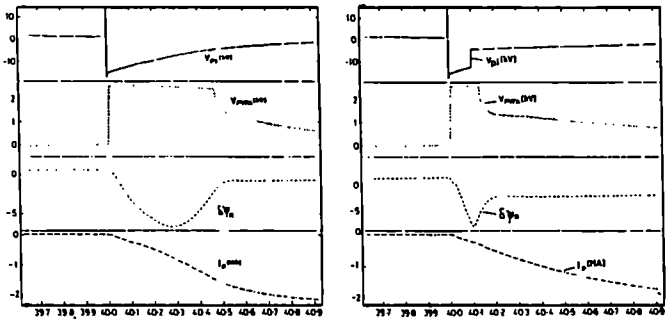

(a) (b)

Fig 12- Fast-rise phase: primary voltage Vp_1 vertical field amplifier voltage VPFVA, radial position error $\delta\psi R$, plasma current IP.
(a) without switching of the ASN.
(b) three R8 resistors are switched in at 40:1.

It is still too early to draw any conclusions about the effect on the plasma behaviour of the switching-in of the commutating resistors R8. Anyway, it seems certain that the slowing down of the rate of rise of the plasma current after the first phase of plasma formation leads to a strong reduction of the MHD activity, resulting in a more reliable plasma discharge. Improvements in the flux consumptions are still to be assessed and quantified. Another positive "side effect" of the Additional Switching Network is, as seen before, a reduced error on the plasma radial position during operation at the higher premagnetisation currents.

The utilisation of the ASN, together with the improvements of the magnetic configuration of JET which led to a reduction of the stray fields inside the vessel, has allowed more reliable operation at 30 kA of premagnetisation current and, for the first time in JET, plasma operation with a premagnetisation current of 40kA, making the nominal flux swing thoroughly available. Fig 13 shows the beginning of one of these discharges. When the premagnetisation current is interrupted a voltage of about 22kV is applied across P1. At 40.04s, after plasma breakdown, three R8 commutating resistors are switched in, and the voltage across the magnetising winding shows a reduction to about 6.7kV and the radial position is recovered. The remaining three resistors are inserted at 40.23s, further controlling the rate of rise of the plasma current.

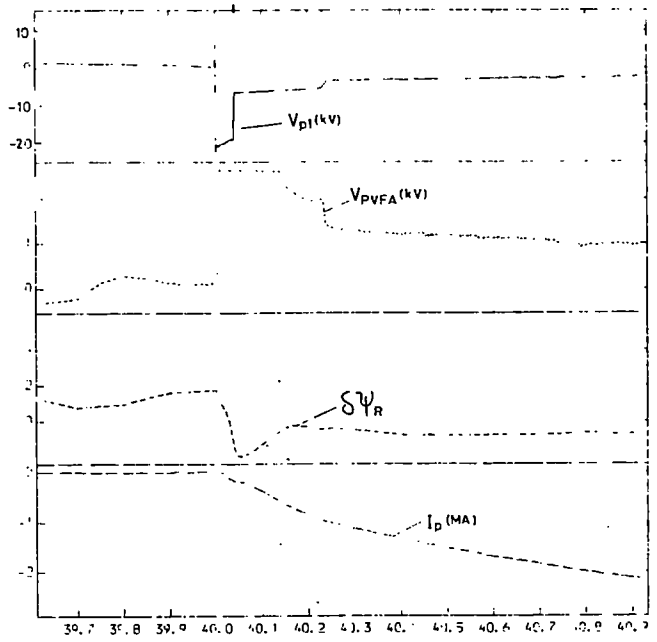

Fig 13- Fast-rise phase: primary voltage Vp_1, vertical field amplifier voltage VPFVA, radial position error $\delta\psi R$, plasma current IP during a 40kA premagnetization current pulse.

Anyway, operation of the premagnetisation current at 40kA is possible only in a narrow window of parameters, mainly due to the high stray fields still present at 40kA. Active Stray Field Compensation is now under study [3] to overcome this problem.

From the technical point of view, only one failure has been recorded during the first three months of operation: the power supply module of the PLC in the Local Control Cubicle was found to be faulty, probably due to a bad connection.

7. Conclusion

The Additional Switching Network has been satisfactorily in service for three months, without problem.

The choice to make use of thyristor rather than more traditional electromechanical switches has been rewarding and, even over a short period of time, the reliability of the system seems to be higher: no fault in any of the power components has been recorded so far.

From the plasma operation viewpoint, greater flexibility has been achieved and the start-up scenario has been improved.

8. Acknowledgements

The authors would like to thank E Bertolini for his technical and managerial supervision; D Hrabal and P Baigger (Siemens, Erlangen, FRG) for the work done on the Thyristor Make Switches and F Jaselli (Microelettrica Scientifica, Milano, Italy) for the work done on the Commutating Resistors.

We gratefully acknowledge the dedication of A Keymer and S Shaw during installation, commissioning and early operation of the ASN.

References

[1] P L Mondino, T Bonicelli, M Huart, A Santagiustina, "The Development of the JET Poloidal Field Power Supplies to Reach the Nominal Flux Swing Capability". Proc 14th Symposium Fusion Technology, Avignon, 8-12 September 1986, vol. 1, p. 859.

[2] T Bonicelli et al., "Comparison among different current transducers used in JET for the Magnet Power Supplies in the current range 4-100 kA", presented at the 12th Symposium on Fusion Engineering, Monterey, USA, 12-16 October, 1987.

[3] P L Mondino et al., "The PF System Enhancement in JET to Produce Plasma Current up to 7MA with Material Limiters and up to 4MA with Magnetic Separatrix: a Report on the Electrical Study", presented at the 12th Symposium on Fusion Engineering, Monterey, USA, October 12-16, 1987.

AN INTEGRATED CONTROL SYSTEM FOR REMOTE HANDLING EQUIPMENT AT JET

A Galetsas, A C Rolfe, C A Steed

JET Joint Undertaking, Abingdon, Oxfordshire OX14 3EA, UK

Abstract

This paper describes and discusses the interconnection and control of all JET Remote Handling equipment comprising end-effectors, transporters, viewing and control equipment.

The focal point of the JET Remote Maintenance System (RMS) is the Remote Handling Control Room (RHCR) from which all Remote Handling equipment is monitored and controlled. This comprises 5 general purpose Remote Handling Work Stations (RHWS), two real-time 3D Graphic Work Stations (GWS), and two Servomanipulator Master Stations (SMMS).

These have ergonomically designed to maximise human operator efficiency.

All Remote Handling work is performed with the aid of the viewing systems which consists of 70 TV cameras and the real-time GWS. The outputs of the TV cameras can be switched by any RHWS to display at any of the 40 monitors in the RHCR.

The integration of the RMS involves a 3 level hierarchical structure, comprising the Remote Handling equipment, their intelligent controllers and a supervising minicomputer which provides an adaptive man-machine interface function. These units are interconnected through point-to-point serial links and two local Area Networks. This architecture was adopted in order to utilize as much as as possible existing JET-CODAS software and hardware.

Introduction

A requirement of the JET machine is that it should be remotely maintainable.

To meet this objective, design effort is required in two basic areas.

Firstly, in the design of an extensive series of Remote Handling (RH) equipment, comprising of robotic arms and vehicles, servomanipulators, special end-effectors and viewing systems.

Secondly, in the integration of all the above equipment into a centrally monitored and controlled system. In this way a remote maintenance intervention involving the simultaneous use of many Remote Handling equipment could be organized and executed safely from the Remote Handling Control Room (RHCR) by a few human operators.

This paper concentrates on the second design problem.

Short Description of the Remote Handling Equipment

The Remote Handling equipment is classified into the following categories:

1 End-effectors and special tools including two force-feedback servomanipulators (MASCOT 4).

2 Transporters for the above end-effectors.

3 Viewing equipment (TV and graphics).

4 Control and monitoring equipment.

Each Remote Handling equipment has its own intelligent local controller and can be controlled in isolation of the other equipment through a local control panel. All local controllers have serial and/or parallel ports and few have Ethernet ports as well.

End-effectors and Special Tools

The main end-effector is a MASCOT 4 two-arm master-slave servomanipulator. It is a highly dextrous force-feedback manipulator capable of handling 20 kg loads.

Each arm has seven 7 degrees of freedom and is electrically actuated.

The local controller of MASCOT 4 is a multiprocessor-based system (zilog) housed in two cubicles. These cubicles are connected with a high speed serial link. Separate CPUs handle the left and right arms, so that only one arm could be utilized if required. Six RS232 ports are available for communications with other computers.

The Mascot local controller, provides master-slave operation of the arms plus special functions such as teach-and-repeat, static load compensation and wrist constraint in a plane.

Several other end-effectors have been specially designed for the handling of particular components like belt limiters, R F Antennae etc. These have several motorised motions plus sensors. These motions and sensors are controlled by the local controller of the robotic arm (articulated boom) to which they are attached.

Many special Remote Handling tools have been designed including TIG welding, cutting, and handling tools [1].

The local controller for the welding tools is a microcomputer-based (Intel 8085) programmable welding source capable of remote operation through an RS232 serial link.

The local controller for all other tools is an 8085-based microcomputer controlled through an RS232 serial link.

Transporters

The transporters are robotic equipment which can carry or place in position and hold the end-effector which includes the slave servomanipulator arms.

Each transporter is controlled through its own local intelligent controller.

Four types of transporters have been developed.

Firstly, the articulated boom is an 8 degree of freedom

robotic arm capable of lifting 1000 kg. Various end-effectors could be attached to the end of the articulated boom including three 4 degree of freedom camera arms. The articulated boom is used for in-vesel maintenance, and has a local controller consisting of a GE series six multi-CPU programmable controller. This provides for control and monitoring of the boom plus teach-and-repeat facilities [2].

The second transporter is a crane-mounted telescopic arm (TARM) intended for ex-vessel maintenance. It has 9 main degrees of freedom and its horizontal section is similar to the articulated boom. Its local controller is a multiprocessor system with RS232 and Ethernet ports for communication to the external world.

The third transporter is called low-level transporter (LLT) and it is intended for handling heavy components near the bottom of the JET machine like turbomolecular pumps and associated vacuum valves. It is a modified electric fork-lift truck with specially designed end-effectors. It has a maximum vertical and horizontal extension of 2 m and 4 m respectively and load-capacity of 450 kg. Its local controller is still under design.

The forth type of transporters are radio-controlled vehicles fitted with small manipulators, end-effectors and cameras. The local controllers for remote operation are being designed.

Viewing Equipment

All the remote maintenance work depends on standard colour TV video feedback information complemented by colour 3D real-time graphics. Approximately 70 TV camera locations which are placed on the Remote Handling equipment and fixed to the walls of the Torus hall and hot cell provide the required TV surveillance. The video output of these camera is fed to a cross-bar video/audio matrix so that any TV output could be connected to the TV screens situated in the Remote

Handling Control Room. The cross-bar matrix is controlled from a microcomputer-based system through RS232 ports for command and feedback information transfer. This microcomputer controls and also monitors the cameras which are attached on the walls of the Torus and assembly hall. All the other cameras are controlled from the local controller of the Remote Handling equipment which carries them.

In addition to the TV video feedback, two 3D real-time graphics systems (GWS) provide computer generated views of the JET machine and its environment. These pictures show the current position of Remote Handling equipment, and provide collision warnings. The graphics systems are stand-alone Silicon Graphics 3020 work stations with RS232 and Ethernet communication ports.

Control and Monitoring Equipment

The main control and monitoring equipment is the Remote Handling Workstation (RHWS). Through the RHWS, any Remote Handling equipment, except MASCOT 4, can be controlled.

The RHWS is the main building block of the Remote Handling Control Room (RHCR).

The RHWS is a general purpose work station designed at JET using as much existing hardware and software building blocks as possible. This reflects in its appearance and functions. It consists of two 20" colour screens, two 9" colour screens, two 9" black and white sreens, two sets of push buttons and one analogue 3-axis joystick. A keyboard and tracker ball are also available.

Human factors were taken into account in the design of the RHWS. The main features of the RHWS are:

- The general operating procedure of the RHWS is identical irrespective of which Remote Handling equipment is controlled. The work station software configures the workstation according to which equipment is controlled and guides the human operator with menus and error instructions.

- The number of control devices were limited as much as possible and the prototype design has one joystick, one set of 20 programmable push buttons for Remote Handling equipment control and another set of 20 programmable push buttons for TV camera control. Separate push buttons for equipment and camera control exist in order to allow for simultaneous control of Remote Handling equipment and cameras.

- The reuse of the programmable input devices is achieved through a Touch Panel (TP). The special feature of this TP is that it can produce graphics for easier selection of options. Also its data tree has few branches for each Remote Handling equipment. This facilitates easy reallocation of control devices, particularly important for the real-time control of robotic equipment.

An ergonomic Servomanipulator Master Station (SMMS) has been designed, including mobile and fixed in space TV screens, one RHWS, one GWS and the servomanipulator master arms. Two human operators will man the SMMS, one for the manipulator control and one for the camera and transporter control.

The SMMS layout resulted after detailed Remote Handling task analysis and it will be tested extensively with mock-up test before its actual use on the JET machine.

The JET Remote Maintenance System (RMS)

This section will describe the integration of all Remote Handling equipment into one centrally controlled and supervised Remote Maintenance System (RMS).

Functional Requirements of the JET Remote Maintenance System

The required integration of all the Remote Handling equipment should result in a Remote Maintenance System with the following characteristics.

- All Remote Handling equipment (except MASCOT) to be controlled from any general purpose RHWS.

- The MASCOT will have its own master controls.

- Maximum of two Remote Handling tasks requiring the MASCOT in parallel with up to two additional Remote Handling equipments also controlled.

- Real-time operation: ie the delay for the operator's inputs to the Remote Handling equipment actuators to be less than 300 ms.

- Hardware or software failures should not result in uncontrolled motions of Remote Handling equipment.

- Human factors should be taken into account in the design of control stations.

- Existing JET hardware and software modules should be used as much as possible.

Remote Handling Equipment Integration

An overall diagram of the RMS interconnections is shown in Fig 1.

The blocks on the top of the page represent the control room equipment and the blocks on the bottom of the page represent the intelligent controllers of each Remote Handling equipment.

Two local area networks plus point-to-point serial links are employed for the data transmission, plus individual cables for the transmission of standard colour TV and audio signals. This architecture was adopted in order to utilize existing JET-CODAS software and hardware and at the same time fulfil the real-time requirement of the RMS.

Thus the non-time critical information is transmitted via the CAMAC serial highway and when a guaranteed response is required the data is transmitted through the point-to-point RS232 serial links or Ethernet.

An overall diagram of the RMS software architecture is shown in Fig 2.

For the control and monitoring of each Remote Handling equipment there is an RT-program which runs on the NORD-100 and configures the RHWS accordingly. A lot of JET standard software is available on the NORD-100 in order to help implementing the above function. For example, the "mimic" package helps in the generation of graphics to be used on any RHWS colour screen or touch panel. The communication of the RT programs and the 5 RHWS hardware is done via the CAMAC serial highway.

Although the CAMAC serial highway link is fast (5 M bits/sec) the overloading of NORD-100 which controls CAMAC, delays the data transfer appreciably. Thus the dedicated serial links were provided for transmission of commands to the Remote Handling local controllers.

The communication software for the serial links runs on distributed microcomputers (Texas TMS 99000) which are called CAC (CAMAC-Auxiliary Controller) (Fig 2). In this way the commands from the RHWS input devices are transmitted directly to the appropriate Remote Handling equipment local controller within the required 250 ms.

A cross-bar switch provides the required switched-circuit service since 5 RHWS could be connected to many local controllers.

The serial port of all local controllers has been standardized as RS232 with optical modems and the link layer protocol has been defined by JET. In this way some simplicity has resulted in the interconnection of these multiventor local controllers.

The above desribed utilization of CAMAC and dedicated serial links result in difficult hardware and software implementation especially as the system is expanded.

To alleviate these problems a little, an Ethernet LAN is introduced for the following two applications [3].

a. The collection of graphics data.

b. The TV camera control and monitoring.

The Graphics Work Stations (GWS) require measured data in real-time for the production of graphic images of the Remote Handling equipment in relation to their environment. Such data is typically joint angles of robotic arms which are available from the local controller of the appropriate Remote Handling equipment.

Two GWS will be employed, one for in-vessel modelling and one for ex-vessel.

The second Ethernet application is the TV camera control and monitoring. This involves the transmission of data to the camera local controllers from the 5 RHWS and vice versa.

The CCTV system through its 3 serial links controls and monitors the fixed cameras plus the cross-bar video/audio matrices. However, the cameras which are carried on individual Remote Handling equipment are controlled by separate local controllers. Again Ethernet will provide for the required interconnections.

An initial data traffic analysis has shown that a raw data load of 31 KBauds is expected for these applications, thus Ethernet is appropriate for this and also future applications.

Conclusions

In this paper the integration of all the Remote Handling equipment into a centrally controlled system has been described.

The implementation of this system is proceeding in stages because of the time and effort required in designing and integrating the prototype Remote Handling equipment required for the JET remote maintenance.

The integrated Remote Maintenance System architecture has been strongly influenced by the desire to use, in JET, available software and hardware building blocks and at the same time satisfying the special Remote Handling requirements.

This architecture will integrate present and future Remote Handling systems with minimum interference on the actual design of the local controllers of each equipment.

Acknowledgements

We would like to thank all the people in Remote Handling and CODAS, whose work made the implementation of the JET Remote Maintenance System possible.

References

[1] S Mills : "A Practical Experience of Using Special Remote Handling Tools on JET" Proc. this symposium.

[2] L Galbiati : "Control and Operation of JET Articulated Boom" Proc. this symposium.

[3] A Galetsas : JET Joint Undertaking, Abingdon, UK. Unpublished information.

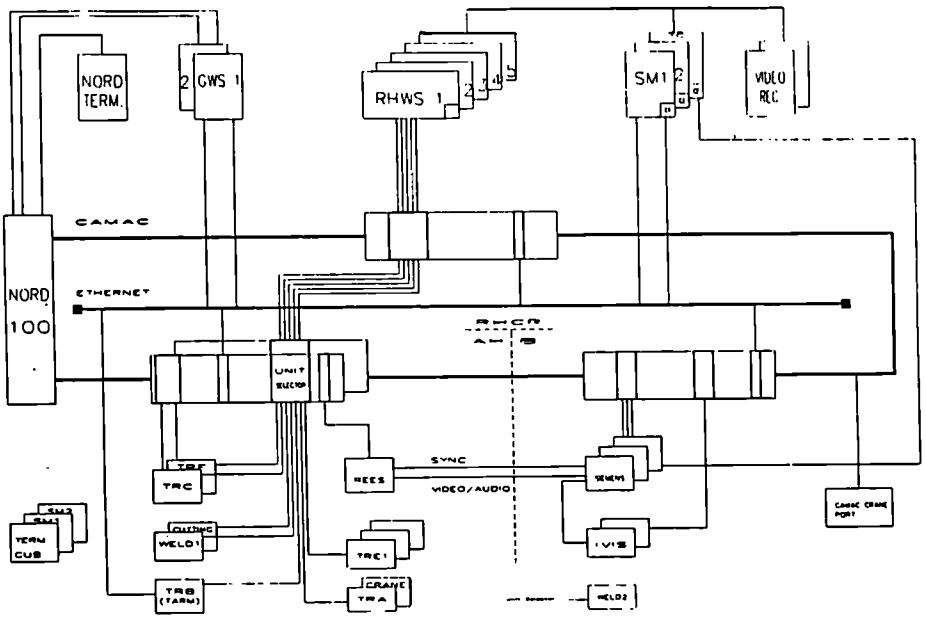

FIG 1 : JET Remote Maintenance System

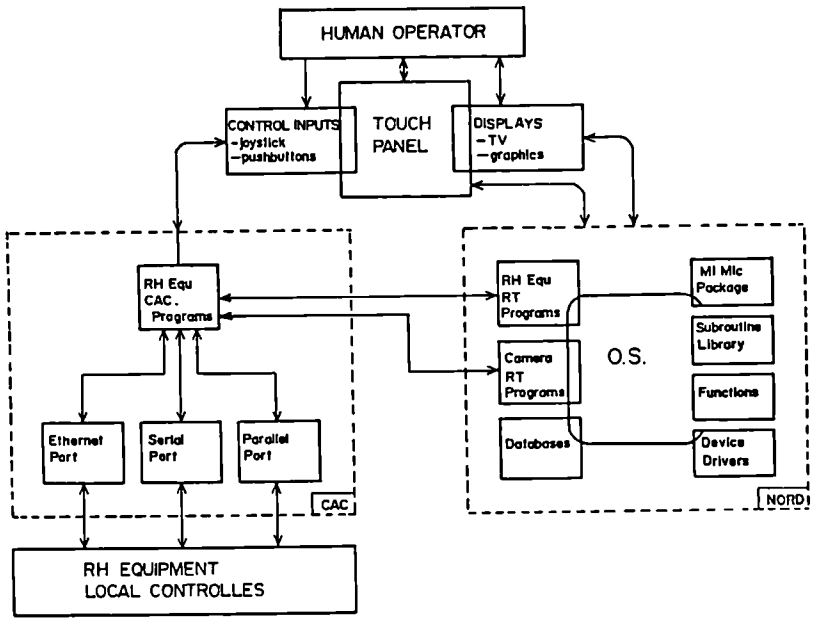

FIG 2 : Remote Handling Workstation Software Architecture

COMPARISON AMONG DIFFERENT CURRENT TRANSDUCERS USED IN THE JET MAGNET POWER SUPPLIES IN THE CURRENT RANGE 4-100kA

T Bonicelli, T Eriksson, M Huart, A Moissonnier, P L Mondino, C Raymond
JET Joint Undertaking, Abingdon, Oxon, OX14 3EA, U.K

Abstract

Three types of high current transducer are installed on the DC side of the JET Magnet Power Supplies: coaxial shunts, Hall effect current transducers and zero-flux current transformers. After a review of the basic working principles of the three current transducers, this paper reports the operational experience gained in JET, so far.

1. Introduction

The JET magnet power supplies can be subdivided into two main systems:

- the Toroidal Field System
- the Poloidal Field System

The former consists of the Toroidal Flywheel Generator Convertor (TFGC) and of two Toroidal Field Static Units (TFSU1 and TFSU2) series connected to the TFGC (Fig. 1). These power supplies feed the toroidal field coils, which represent a large inductive load (L = 660mH, R=61.7mΩ), with currents up to 67kA.

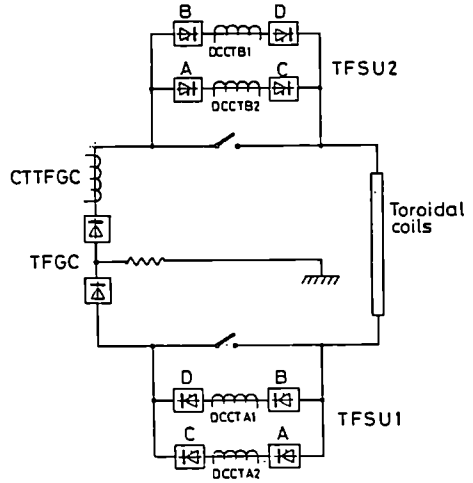

Fig 1 - Toroidal Field System Schematic

The latter, which includes the Ohmic Heating Circuit, is a fairly complicated system feeding four different sets of coils (Fig 2):

- The magnetising coils (L = 230mH, R = 40mΩ), are fed by the Poloidal Flywheel Generator Convertor (PFGC) and, from the end of 1987, by a two quadrant thyristor convertor (PFX) connected in parallel to the six central subcoils. Currents up to 40kA flow in the external subcoils and up to 60kA in the six inner subcoils.
- The plasma radial position coils (typ. L = 290mH, R = 27mΩ) connected to a two quadrant thyristor convertor (PVFA3,4) with currents up to 35kA.
- The plasma shaping coils (typ. L = 15mH, R = 6mΩ), where currents up to 35kA flow, fed by a two quadrant thyristor convertor (PVFA1).
- The plasma vertical position coils (L = 43mH, R = 24mΩ) with currents up to 3kA, fed by two four quadrant thyristor convertors (PRFA1,2 and PRFA3,4).

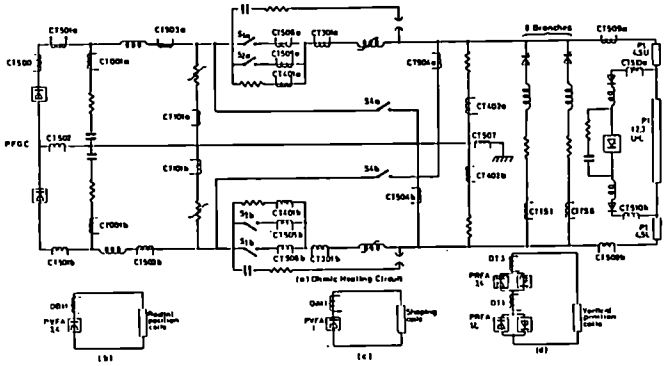

Fig 2 - Poloidal Field System Schematic (Configuration at the end of 1987)

A thorough description of the JET magnet power supplies has been given in [1], whereas the latest developments of the Poloidal Field System are reported in [2] and [3].

2. Current Transducers in JET

Several current transducers are installed for monitoring, control and protection on the DC side of the JET magnet power supplies. The main requirements for these current transducers are:

- capability of measuring current pulses lasting about 20s, with maximum values in the range -1-100kA, with bandwidth extending from DC to -5-10kHz, at a duty cycle of one pulse every ten minutes;
- good electromagnetic insensitivity, since the environment is rather noisy due to the presence of circuit breakers, spark gaps, thyristor convertors;
- high reliability, since the current transducers are often an essential part of the protection of very expensive components;
- high availability, to minimise delays and stops of the experimental programme.

A list of the current transducers presently installed in the JET magnet power supplies (DC side) and their main characteristics are given in Table 1.

Three types of current transducers are presently used:

- coaxial shunts;
- Hall effect (zero flux) current transducers;
- zero flux current transformers with sensing winding.

The current transducers are part of a more extensive measuring and data acquisition system. The simplified block diagram (Fig 3) shows a typical pattern of the signal conditioning.

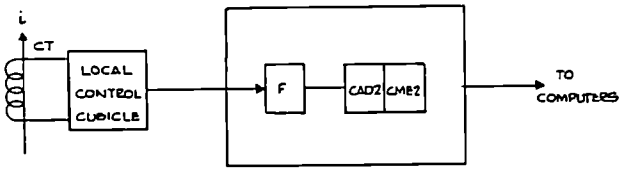

Fig 3 - Typical signal processing diagram

Table 1
DC Current Transducers in JET Magnet Power Supplies

	Current Transducers	System	Type	Irat (kA) (Max)	I^2t (A^2s)	Dimensions (approx) (mm)	Weight (kg)	Accuracy	BW (kHz)	Cooling	Remarks
A	CT501a/b CT503a/b CT504a/b CT509a/b CT510a/b	Ohmic Heating Circuit	coaxial shunt (R=20μΩ)	200	10^{11} (repetitive)	ϕ700 ℓ1400	400	(*) ± 1% (Shunt) ± 1.5% (electro-optic link - 100 kHz channel)	(**) 0-8	Forced air	
B	CT506a/b CT301a/b	Ohmic Heating Circuit	coaxial shunt (R=20μΩ)	200	$3.6\ 10^{10}$ (repetitive)	ϕ500 ℓ900	190	As above	(**)0-22	Forced air	Compensated
C	CT401a/b CT402a/b CT505a/b CT508	Ohmic Heating Circuit	coaxial shunt (R=20μΩ)	200	$3.6\ 10^{10}$ (repetitive)	ϕ500 ℓ900	190	As above	(**) 0-8	Natural air	A larger resistance variation is allowed compared with type B
D	CT502 CT507 CT001a/b	Ohmic Heating Circuit	coaxial shunt (R=40μΩ)	100	$2\ 10^{8}$ (repetitive) $6\ 10^{9}$ (on Fault)	ϕ280 ℓ550	30	As above	(**) 0-8	Natural air	
E	CT101a/b	Ohmic Heating Circuit	coaxial shunt (R=2mΩ)	100	10^{7} (repetitive) 10^{8} (on Fault)	ϕ200 ℓ600	3	(*) ± 3.5% (Shunt) ± 1.5% (electro-optic links)	(**) 0-800	Natural air	
F	CTTS1 CTTS2 CTTS3 CTTS4 CTTS5 CTTS6	Additional Switching Network	Hall effect	10kA 40kA-1.5s	Continuous 2.4 10^{9}	445x575x140	60	(**) 0.1% (Direct Current) < 1% (I = 700 A 85 kHz)	(*) 100 small signal	Natural air	
G	CT500 CTTFGC	PFGC TFGC	Hall effect	65kA	Continuous	900x900x216 (measuring head) 420x360x120 (signal converter)	136 73	(**) 0.1% (2500A - 60Hz)	(*)>10	Natural air	
H	DCCT A1 DCCT A2 DCCT B1 DCCT B2	TFSU1 TFSU2	Zero-flux current Transformer	50	$2.5\ 10^{10}$	350x350x250	NA	(*) 0.2%	(*) 10 small signal	Natural air (power transistor forced air coolod)	
I	OA11 OB11	PVFA1,2 PVFA3,4	As above	40	$2.5\ 10^{10}$	350x350x250	NA	(*) 0.2%	As above	As above	
J	DT 1 DT 3	PRFA1,2 PRFA3,4	As above	4	10^{8}	NA	NA	(*) 0.2%	As above	Natural air	

(*) Manufacturer's data
(**) Test data

The signal generated by the transducer is sent to the Local Control Cubicle (LCC) of the Local Unit (e.g. TFSU1 or PVFA3,4). In the LCC, the signal is processed for monitoring control and display purposes and fast protective action, if applicable, is taken.

The LCC interfaces with a CODAS (Control and Data Acquisition System) cubicle. After optional filtering the analogue signal is digitized by, for instance, a 32-channel 12-bit analogue/digital convertor (CAD2 module) with sampling rate ranging from 6kHz (when 32 channels are used) to 40kHz (only 4 channels used) and stored in a memory (CME2 module).

The data is transferred after each pulse to the computer system where it is archived and made available for later display [4].

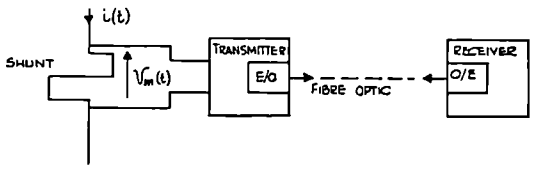

Fig 4 - Electro-optical signal transmission

3. Coaxial Shunts

The coaxial shunt is a well known and widely used method of measuring high impulse currents. In JET, an electro-optical link is associated with each shunt, to provide the required insulation between shunts, connected to high voltage busbars, and low voltage control and monitoring equipment (Fig 4).

A schematic of a coaxial shunt is shown in Fig 5.

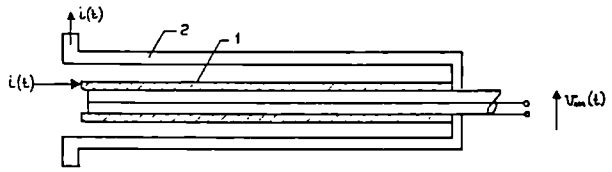

Fig 5 - Coaxial Shunt

The current i(t) flows through the inner cylinder (1) made of resistive non-magnetic material and returns through the external cylinder (2). The space inside the inner cylinder is magnetic field free, so the output voltage signal $v_m(t)$, theoretically proportional to the current i(t), is not affected by inductive voltage drops. Limitation of the bandwidth is mainly due to skin effects, which, for a given resistive material, depend on the thickness of the inner cylinder. The response time of a coaxial shunt can be evaluated to a first approximation [5] as:

$$T = \frac{\mu_0}{6} \frac{d^2}{\rho}$$

where: $\mu_o = 4 \times 10^{-7}$H/m, d = thickness of resistive cylinder (m), ρ = resistivity of resistive material (Ωm) and the bandwidth is :

$$B = \frac{1}{2\pi T} = \frac{3}{\pi} \frac{\rho}{\mu_o d^2} \quad \text{(Hz)}$$

The thickness d strongly depends on the rated I^2t of the shunts, where:

$$I^2t = \frac{c\gamma\Delta t S^2}{\rho} \quad (A^2s)$$

Where: c = specific heat of the resistive material (J/kg°C), γ = density of the resistive material (kg/m³), Δt = temperature rise (°C), and S = cross section of the resistive cylinder (m²)

Thus for a given material and a maximum allowed Δt, the following relation can be obtained:

$$I^2t \propto D^2d^2$$

where D = average diameter of inner cylinder (m) and, finally, once D has been determined on the basis of mechanical and manufacturing considerations:

$$I^2t \propto 1/B$$

Shunts designed to absorb the energy of large current pulses normally have a reduced bandwidth, unless provision is made for some sort of compensation.

The inner cylinder of the shunts installed at JET is made of cupronickel, whose main characteristics are: $\rho = 0.37 \times 10^{-6}$ Ωm, c = 370 J/kg°C, γ = 8900 kg/m³, and $\alpha = 0.016 \times 10^{-3}$ 1/°C (temperature coefficient)

To reduce the resistance variation and the mechanical stresses due to thermal expansion, the maximum temperature of the resistive material is limited to about 250°C, when the nominal pulse is applied. If D is 0.394m (e.g. CT506, CT301, CT401, CT402, CT505, CT508), a thickness d of about 6mm is required for the necessary thermal capacity. By using the previous relations, one can obtain an estimate of the bandwidth:

$$B = \frac{3}{\pi} \frac{\rho}{\mu_o d^2} = 7.8\text{kHz}$$

The shunts of type B are actually frequency compensated by means of an arrangement of measuring leads, experimentally optimised [6]. From the mechanical view point, the shunt is mounted in vertical position. The inner resistive cylinder of cupronickel is brazed to two copper support tubes with silver alloy, to assure good electrical contact. The inner cylinder can move freely with respect to the external one so that no stress due to differential expansion arises.

Cooling with forced air is used for the heavy duty shunts, when a smaller resistance variation is desired. The measuring arrangement is completed by an electro-optical link (Fig 4). The voltage signal $v_m(t)$ from the shunt modulates the frequency of a carrier (f=550kHz), which controls the emission of a light-emitting diode. The frequency modulated light impulses are sent through a multi-mode fibre from the transmitter, set a high voltage potential, with respect to the grounded receiver. Here the modulated light is converted into electrical signals by a photo-diode, then is demodulated and made available for further processing. The transmitter is powered by a battery standing at the same potential and constantly under charge through a high voltage isolation transformer.

4. Hall Effect Current Transducers

The Hall-effect current transducers used in JET are of compensating current (zero-flux) type. A basic schematic is shown in Fig 6.

The conductor carrying the current i(t) (to be measured) is surrounded by an iron-cored magnetic circuit. The Hall detector is placed in an air-gap of

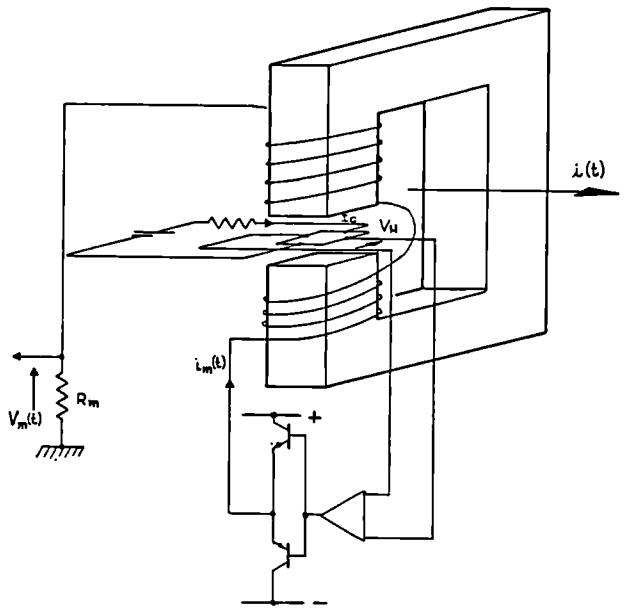

Fig 6 - Hall effect (zero-flux) current transducer

the magnetic circuit. A coil with N turns symmetrically disposed with respect to the air gap is wound around the iron core. The Hall-effect current transducer senses the magnetic field in the gap, which is proportional to $i(t) - Ni_m(t)$, neglecting the magnetising current, and, in the presence of a constant "excitation" current (continuous or alternate depending on the saturation), gives an output voltage V_H proportional to the magnetic field. The voltage V_H is used as a feedback signal to control the current $i_m(t)$ to obtain a magnetic null in the gap, which is achieved when $i_m(t) = i(t)/N$. The current $i_m(t)$ is finally passed through a burden resistor R_m, thus giving an output voltage $V_m(t)$ proportional to the current i(t). Since the current transducer always operates close to a zero-flux condition a good linearity is assured throughout the whole range of measured currents.

In practice, several Hall detectors are used in the same transducer and each of them is provided with an individual coil independently controlled. The resulting current $i_m(t)$ is obtained summing up the individual feedback currents in each coil. In this way, good insensitivity to the external magnetic fields and towards the position of the primary busbar is attained. High insulation levels can be easily achieved between the primary and the secondary circuits by making use of insulating busbars.

Eight Hall-effect (zero-flux) current transducers are installed at JET. Six of them (named F, in Table 1) are part of the Additional Switching Network, commissioned in July 1987 and now in service. Each is provided with eight Hall detectors, placed in air gaps distributed symmetrically along the iron core. A 10000 turn coil is associated with each Hall detector, thus giving a transformer ratio of 1/10000.

The nominal current of the transducers is 10kA, for which continuous operation is allowed, but the measuring range extends up to 40kA (1.5s); the limitation on I^2t comes, firstly, from the rating of the output power transistors and, secondly, from the heat dissipation in the compensating coils.

The electronic circuits are part of the measuring heads so that a compact solution is attained. The measuring head can be split in two pieces thus allowing easy mounting of the current transducer. The insulation level of the current transducer is 12kV, but in the actual installation a busbar insulated for the full voltage (24kV rms) has been fitted.

Tests show that the current transducers are able to

correctly measure an a.c. current at 85kHz, peak value 1kA, with limited phase shift (~ 0.8μs) and error well below 1%. Other tests executed with impulse current with peak value of 42kA showed that the current transducers are able to follow (di/dt) higher than 200A/μs.

Two other Hall-effect (zero-flux) current transducers, (G in Table 1) are installed at the output of the PF and TF generator converters and have been in service since the beginning of JET operation. The measuring heads, hexagonally shaped, are provided with six Hall detectors, whereas the control electronics are placed in a separate unit. The transformer ratio is 1/5000. The nominal continuous current is 65kA but the measuring range extends to about 120kA.

5. Zero Flux Current Transformers with Sensing Winding

Similar to the Hall-effect transducer described above, the zero-flux current transformer uses a toroidal core of ferromagnetic material provided with a compensating winding fed from a high gain amplifier which balances the flux on the transformer to zero.

However, the high gain amplifier is regulated by the integrated signal from a sensing winding on the transformer core. Assuming infinite gain of the amplifier and neglecting drift and offset, the system would be a perfect closed loop where no flux variation could occur and the high gain amplifier current would always be proportional to the primary current.

Fig. 7 shows a block diagram of a practical circuit which will allow for non-ideal circuit elements.

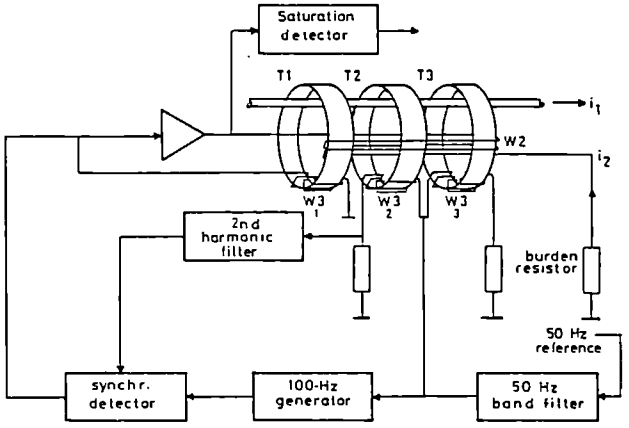

Fig 7 - Zero flux current transformer with sensing winding

The key component to avoid drift is a magnetic modulator and a second harmonic filter. The cores T2 and T3 are alternatively positively and negatively saturated through the windings W3 via a harmonic free 50Hz modulation supply.

If the total flux is balanced, the modulation current will contain only odd harmonic components. If, however, the total flux is different from zero there will be a difference in the interval of positive and negative saturation at T2 and T3. Hence the modulation current will contain even harmonics, dominated by the second harmonic.

The second harmonic is filtered out and fed to a synchronous demodulator. The polarity and value of the demodulator output gives a measurement of the sign and magnitude of the total flux imbalance and is added to the compensating current amplifier in order to restore an overall zero flux situation. To achieve high accuracy, a highly stable and accurately calibrated burden resistor is used. The burden resistor is normally mounted on a heat sink, which for extremely high accuracy can be temperature controlled with forced water cooling. In the event of inability to achieve flux balance, for instance, in case of fault or high primary current, the transducer is fitted with saturation detection, which also operates in case of an auxiliary power loss.

Eight high current transucers of this type have been in operation, since the start of JET operation, with only two faults recorded in the control electronics and in the auxiliary power supply.

The sizes used at JET have been set up with a nominal current of 4,40 and 50kA pulsed DC current. Smaller models (1A) have been used extensively connected via a series resistor to provide voltage measurement at an insulation levels of 20kV rms for 1 min.

6. Operational Experience

6.1 Shunts and signal transmission

Faults on the current transducers type A, B, C, D, and E represent 5% of the total number of faults in the Ohmic Heating Circuit. Three types of problem have been experienced, so far (4.5 years of operation) amongst the 27 shunts installed:

(a) The voltage signal from the shunt is sent to the control protection equipment through a transmitter, an optic fibre and a receiver. This electro-optical system is the least reliable part by far (95% of faults), mainly because of noise and abnormal drifting of the voltage-to-frequency and frequency-to-voltage convertors. Moreover, some replacement spares are difficult to obtain. Consequently, it has been decided to install new electro-optical links with stable and improved characteristics. For channels used as part of protection circuits, we are presently assessing a different electro-optical link, whereas, for channels used only for monitoring, we are developing our own system;

(b) From the mechanical view point, the CTs with forced air cooling have a weakness in the flow detectors, which must be inspected and adjusted regularly. Substitution of this component with a more reliable type is now under consideration;

(c) Overheating of the connections between shunt and busbars on three shunts have been experienced due to bolts not being properly tightened (this reminds us that connections of a heavy current circuit should be checked regularly).

6.2 Hall-effect current transducers

Since 1981, when two current transducers G (Table 1) were installed, no faults have been detected, neither on the head nor in its controls. The only necessary intervention to keep the devices in good working order was an annual calibration, which is performed by comparison with other current transducers inserted in the same circuit.

No significant data is available about the 6 current transducers installed in the Additional Switching Network (type F) due to the very short (3 months) period of service. No problem has been recorded, so far.

6.3 Zero-flux current transformers (H,I,J in table 1)

Eight current transducers of this type are installed. Two faults have been recorded since the start of JET operation. In this case, as for the Hall-effect devices, the only intervention really necessary to keep the equipment in good working condition is an annual calibration.

Table 2 - Comparative Table

Type	Dimensions	Weight	Installation Constraints	Galvanic Insulation	Aux PS Requirements	BW	Accuracy	Electro-magnetic insensitivity	I^2t capability	Reliability	Maintenance Requirements	Cost
Coax. Shunts (electro-optical link included)	Large, for heavy duty shunts	Heavy	Heavy, if forced cooling is required	Very high insulation levels are achievable with electro optic links	Low (a few watts for the transmitter).	Wide for small shunts, it decreases for heavy duty shunts	~2.5%	Good	Limited, but very high peak currents can be measured without saturation	Good for the shunts, poor for the electro-optic links	High current connection checks. Cooling. Battery for the transmitter	1
Hall Effect (zero-flux)	Compact solution	Medium	Easy to install	Easy to attain using insulating busbars	Medium (~ 0.5 kW peak for type F)	Wide ~100kHz small signals	< 1%	Good	High	Good	Minimal	0.65
Zero-flux Current Transformer	Compact, electronic and transformer completely separated	Medium	Easy to install	Easy to attain using insulating busbars	Medium (~1.5kW peak for types H,I)	Medium ~10kHz small signals	< 1%	Good	High	Good	Minimal	1

7. Comparison Among the Three Types of Current Transducers

Table 2 reports some comparative assessments on the three types of current transducers considered in the paper.

This comparison is made on the basis of experience gained in JET, so far, and is therefore restricted to the models installed.

7.1 Installation Constraints

Hall-effect current transducers and zero-flux current transformers are relatively easy to install, due to the limited dimensions and the absence of high current connections. The mounting arrangement should be such that heavy current busbars are not too close to the measuring head (at a distance of at least twice the diameter of the heads), to avoid magnetic interference. Coaxial shunts have larger dimensions and, especially, if forced air-cooled, entail some constraints on installation.

7.2 Galvanic Insulation

Very high insulation levels are achievable combining a shunt with an electro-optic link. Insulation for medium voltages is easily achieved for the other two types of current transducers. In principle, insulation for the highest voltages is possible, but the accuracy of the measuring system decreases as the size of the hole passing-through increases.

7.3 Auxiliary Power Supplies Requirements

The transmitters presently installed in the electro-optic link for the shunts requires about 5W. The required auxiliary power supply for the Hall-effect current transducers, which has to provide the compensating current $i_m(t)$, is 500W (type F) peak. Higher requirements come from the zero-flux current transformers (~1.5kW) peak.

7.4 Bandwidth

All the transducers installed have a bandwidth which suits the JET requirements. For the next generation of tokamak experiments, when much longer current pulses are expected [7], some limitation could arise for the shunts, (as shown in Section 3) unless efficient cooling systems are adopted.

7.5 Accuracy

The accuracy of all the current tranducers considered here meet JET requirements. No particular problem has arisen due to electro-magnetic interference.

7.6 Reliability and Maintenance Requirements

Experience gained in JET, so far, is basically positive for all the three types of transudcers. Coaxial shunt solution has been somewhat penalised by the relatively low reliability of the electro-optical transmission chain.

Acknowledgements

Thanks are due to the Manufacturers of the current transducers presented in this paper who have made information and data available to the authors: Passoni e Villa (Milano, Italy) for the coaxial shunts, Halmar Electronics (Columbus, Ohio, USA) and LEM (Geneva, Switzerland) for the Hall-effect current transducers and Holec (Hengelo, Holland) for the zero-flux transformers.

References

[1] E Bertolini, P L Mondino, P Noll: "The JET Magnet Power Supplies and Plasma Control Systems", Fusion Technology, Vol 11, p. 71, January 1987

[2] P L Mondino, T Bonicelli, M Huart, A Santagiustina: "The Development of the JET Poloidal Field Power Supplies to Reach Nominal Flux Swing Capability" Proc. 14th Symposium Fusion Technology, Avignon, Sept '86, Vol 1, p.859

[3] P L Mondino et al: "The PF System Enhancement in JET to Produce Plasma Current up to 7MA with Material Limiters and up to 4MA with Magnetic Separatrix: a Report on the Electrical Study", presented at the 12th Symposium on Fusion Engineering, Monterey, USA, October, 1987.

[4] H van der Beken et al: "CODAS: The JET Control and Data Acquisition System"; Fusion Technology, Vol 11 p. 120, January 1987

[5] IEC 60-4 (1977): "High Voltage Testing Techniques. Part 4: Application guide for measuring devices"

[6] E Rinaldi, A Zingales, P Tietz: "High Energy Shunt". 4th International Symposium on High Voltage Engineering, Athens, Sept 1983.

[7] J B Hicks, N Mitchell, E Salpietro: "NET Plasma Engineering and Poloidal Field Coil Power Supplies". Proc. 14th Symposium Fusion Technology, Avignon, Sept 1986, Vol 1, p 707.

THE PF SYSTEM ENHANCEMENT IN JET TO PRODUCE PLASMA CURRENTS UP TO 7MA WITH MATERIAL LIMITERS AND UP TO 4MA WITH MAGNETIC SEPARATRIX: A REPORT ON THE ELECTRICAL STUDY.

P.L.Mondino, T.Bonicelli, T.Eriksson, M.Huart, V.Marchese
P.Noll, F.Petree, C.Raymond, A.Santagiustina, L.Zannelli.
JET Joint Undertaking, Abingdon, Oxon, OX14 3EA, U.K.

1. Abstract

After a review of various modifications already made as part of the Poloidal Field (PF) system enhancement, this paper describes the current modulation circuit that causes different currents to flow in two parts (six central pancakes and four end pancakes) of the JET magnetizing windings.

The extra magnetomotive force of the central pancakes increases the flux variation from 34Wb to 40.6Wb to sustain plasma currents up to 7MA. The extra leakage flux between the central and the end pancakes permits a magnetic separatrix configuration with plasma currents up to 4MA.

The current modulation circuit with active stray field compensation will finally allow good plasma start-up with nominal 40kA premagnetization. Other modifications are described and the plan of the PF system enhancement is reported.

2. Introduction

The Poloidal Field (PF) power supplies of JET are described in detail in [1]. The configuration of the JET PF system used during the experimental campaign from March 1985 to November 1986 is shown in Fig 1.

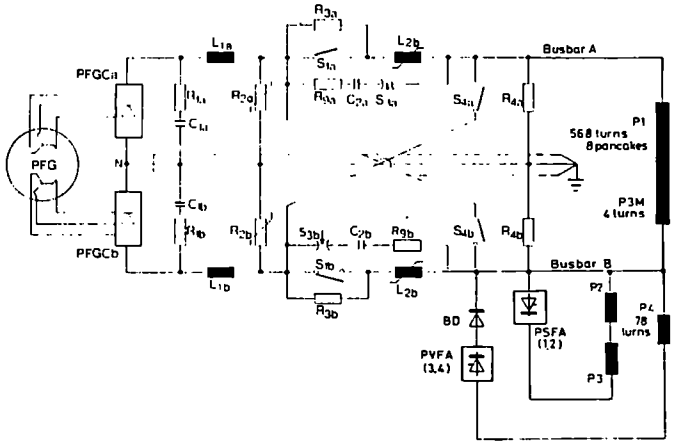

Fig. 1 PF System Configuration from March 1985 to November 1986.

The Poloidal Flywheel Generator supplies, through two Diode Converters (PFGC), the Ohmic Heating (OH) Circuit which modulates the flow of power from the generator to the magnetizing winding of JET. This consists of the coil P1, made up of eight series connected pancakes, plus a few turns (4-8) of the outer coils P3m. The shaping field coils, P2s and P3s, and the vertical field coils P4 are supplied by two identical AC/DC thyristor converters. All power supplies and coils are connected together by a common busbar. With this configuration, it was possible, during 1986, to exceed the design value of plasma current (4.8MA) and to establish record performance of 5MA constant for 4s.

A limitation in the PF system was on the current at the end of premagnetization, due to high stray fields at breakdown: the nominal 40kA could not be reached, therefore, the flux variation available to sustain the plasma current was lower than the nominal 34Wb [2]. Gas breakdown, plasma formation and current rise were all coupled because the voltage waveform across the magnetizing winding was almost wholly determined by the premagnetization current and the Commutating Resistors. The generator voltage was too low to influence the natural exponential decay of the circuit during Fast-Rise (S1 and S4 open). Moreover, the pattern of stray fields, at breakdown, was largely determined by the level of iron saturation; the amplitude increased approximately with the square of the premagnetization current. As a consequence, reliable plasma start-up was obtained with only 20-25kA premagnetization, giving available flux variations of 26.5 - 28.5Wb, respectively; the commutating resistors were kept at the high value of 0.6Ω to provide high electric field [2]. A narrow parameter range was found for the 30kA premagnetization due to high stray fields and insufficient voltage from the Poloidal Vertical Field Amplifier (PVFA), which became heavily saturated during the beginning of fast-rise (300-400ms). With 40kA premagnetization, it was not possible to start the discharge.

The common busbar, connecting electrically the magnetizing, shaping and vertical field systems, did not limit the performance but severely restricted maintenance, installation and commissioning. When one system was alive for commissioning, no easy access was possible to the others. Moreover, the various power supplies could only be tested under load, when connected to the respective coils, limiting the commissioning time available and restricting access to the machine. Finally, the nominal voltage of the shaping field amplifier was higher than required causing high reactive power consumption.

3. Planned development and new requirements identified in 1986.

The need to shape the voltage across the magnetizing winding during fast-rise was identified as early as 1980 [3]. Restrictions on budget delayed procurement until the beginning of the JET Operation Phase. Experimental evidence was progressively accumulated on the need for some means of voltage shaping to decouple gas breakdown, plasma formation and current rise by reducing, in steps, the induced loop voltage. During the same time, good radial equilibrium is required. The Additional Switching Network (Fig 2) installed during the 1986-1987 Shutdown has allowed proper shaping of the voltage across the magnetizing winding [4]. The Booster Amplifier, now being manufactured, will be installed in early 1988: connected in series with the existing amplifier PVFA 3,4 it will supply the necessary additional voltage across the coil P4 to provide good radial equilibrium during early fast-rise.

The four units of the amplifier 1, 2 have been reconfigured; PVFA 1 (two units in parallel) now supplies (as PSFA) the shaping field coils (nominal voltage V = 1.15kV at nominal current I = 25kA for 25s; 35kA can be supplied for 12.5s), PVFA 2 (two units in series) is connected as a temporary booster (Fig. 2) to provide 2.8kV at no load and 2.3kV at 12.5kA but the cable that connects it in parallel with the bypass diode BD in series with PVFA 3,4, has limited I^2t (6kA, 1.0s). With this modification, the voltage available across P4 during fast-rise has been doubled (5.6kV with $I \leq 6kA$). This has allowed further improvements to plasma start-up and, more importantly, the number of turns of P4 has been increased from 78 to 122. During

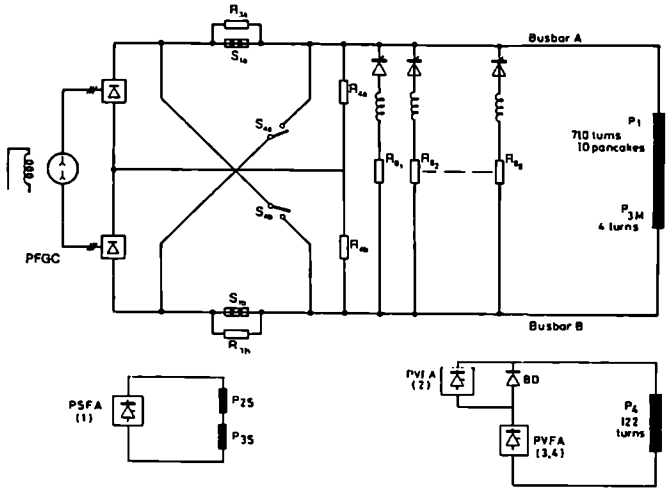

Fig.2 PF System Configuration from September to November 1987.

the 1986 5MA campaign with additional heating, the maximum current in P4 (78 turns) was 33kA, just below the limit (35kA). More magnetomotive force is now available, with the same current limit to sustain plasma currents higher than 5MA with full additional heating.

Moreover, the inner coil P1 has been increased during the last shutdown from eight to ten pancakes for Passive Stray Field Compensation and two more busbars have been added to allow supplying different currents to the two portions of P1. The stray fields (B_s) produced by the new magnetizing winding are lower than those of the previous eight pancake configuration. With 40kA premagnetization, B_s~25mT has been measured at the vessel inboard side, on the equatorial plane, whereas previously the value was B_s~55mT. Nontheless, start-up at 40kA is still rather difficult. At 30kA, the combined effect of the passive stray field compensation, of the additional switching network and of the temporary booster has allowed reliable start-up [4].

New PF busbars have been installed to provide galvanic separation between the various subsystems, and temporary connections to a dummy load are now available.

In parallel with this planned development, new requirements have been put forward. The plasma current will be increased above 5MA aiming towards 7MA, with material limiters, increasing the flux variation from the nominal 34Wb to 40.6Wb. The corresponding increase in the magnetomotive force could, in principle, be obtained by increasing the nominal current, in the central six pancakes of P1, from 40kA to 60kA during plasma flat-top, when the central pancakes are compressed by the toroidal field coils [5].

The plasma current will increase from 3.0MA to approximately 4.0MA when the plasma surface is defined by a magnetic separatrix. This aim could, in principle, be obtained by increasing the stray flux between the central six pancakes and the two end ones at the top and bottom of P1.

4. The Current Modulation Circuit

4.1 Description

The Current Modulation Circuit [6] shown in Fig 3, will supply the six central pancakes of P1, independently from the four end pancakes at the top and bottom. The main components are: The Poloidal X-point Field Amplifier (PFX), two additional busbars connecting PFX to the intermediate connections of P1 coil (Busbar A2 and B2), the PFX Blocking Diodes BDX, and the PFX Filter (the Capacitor C3 and the Resistor R13). The Active Stray Field Compensation Network is also shown, made up of the Resistors R12 and the Inductors L4.

The current modulation circuit has been designed to allow its implementation in two steps: without and with the active stray field compensation network. This approach was followed, since it was not known at the time of design, whether the stray fields produced by the ten pancakes of P1 and by the optimum number of turns of P3m were low enough to allow reliable plasma start-up at 40kA premagnetization. Sufficient experimental evidence has been collected soon after operation started, in July 1987, to decide that the active stray field compensation network is indeed necessary only at full premagnetization. Lower stray fields are expected, from magnetostatic field calculations, with 40kA in the end pancakes and slightly lower current (~38kA) in the central pancakes of P1. The optimum value of current difference will be determined experimentally with the current modulation circuit, without active stray field compensation, as soon as available for operation in November 1987.

The PFX Amplifier is an AC/DC thyristor converter: it will initially consist of the Amplifier 5,6 already installed and fully tested (identical to existing PVFA 3,4: 2.3kV at 25kA for 25s; 35kA for 12.5s). It is planned to connect, during the 1988 shutdown, the existing PVFA 2 in series to PVFA 5,6 to increase the overall voltage capability. During premagnetization, slow-rise and flat-top, PFX will actively control the currents in the central and end pancakes of P1 as described in section 4.5.

The Blocking Diodes (BDX) consist each of 108 large diodes, 18 in parallel, 6 in series: each parallel group has its own parallel snubber (capacitor and resistor connected in series). BDX will take most of the voltage applied during fast-rise across the six central pancakes of P1. Therefore, PFX is only rated for the voltage required during premagnetization (PFX in inversion) and during slow-rise and flat-top (PFX in rectification). The PFX filter has been designed to protect PFX against transient overvoltages when the

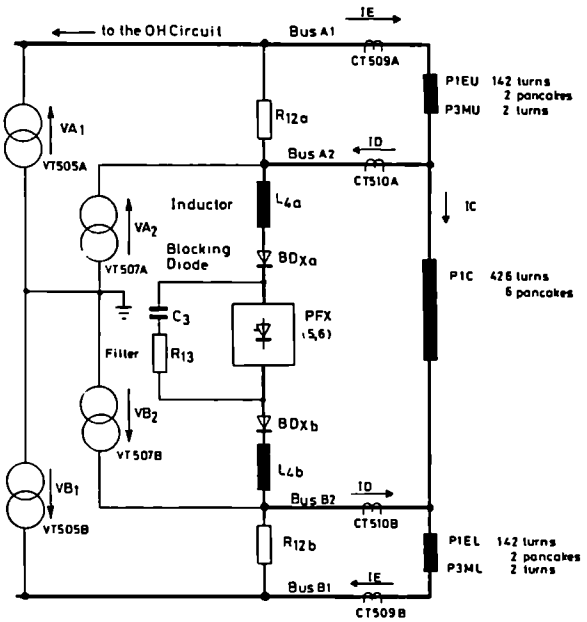

Fig.3 The Current Modulation Circuit.

commutating capacitors C2 are discharged at the beginning of fast-rise and to reduce the output voltage ripple. The fast transients caused by the discharge of the commutating capacitors have been analysed using a

computer model. Extensive computer simulations have allowed the identification of the nominal values of the various components (see Table 1).

Table 1

CURRENT MODULATION CURCUIT: NOMINAL VALUES

PFX Amplifier PVFA 5,6 ONLY
V = +2.8, -2.2kV No load
I = 35kA 12.5s
40kA 15s
PFX Amplifier PVFA 5,6+PVFA 2
V = +4.2, -3.2kV No Load
I = 40kA for 15s.
L4a, L4b PFX Protective Inductor (each)
L = 0.3mH
I = 40kA for 15s
V = 12kV
BDX, BDXb PFX Blocking Diodes (each)
V_{rev} = 12kV
I = 40 kA for 15s.
R12a, R12b Resistors (each)
R = 2Ω
V = 12kV
E = 5MJ
C3 Filter Capacitor
C = 15mF
V = 5kV
R13 Filter Resistor
R = 80mΩ
P = 10kW continuous

4.2 Fast Transients

The behaviour of the circuit during the early phase of fast-rise (discharge of the commutating capacitors) strongly depends on whether the active stray field compensation network is present or not.

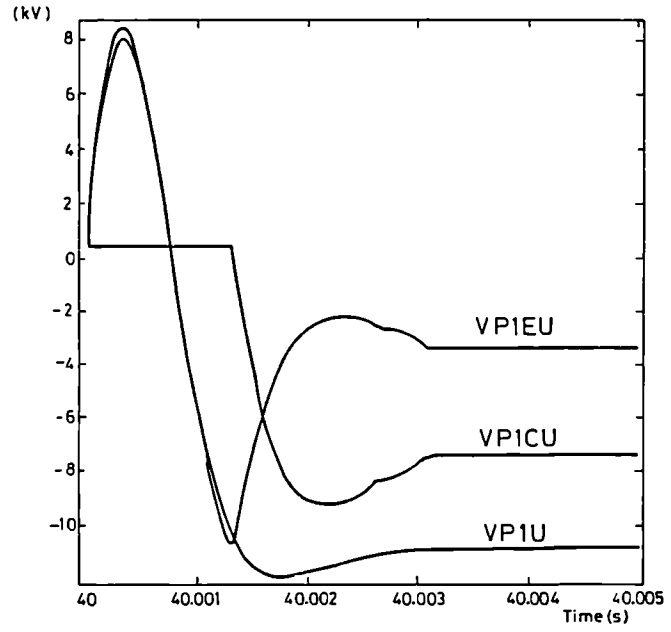

Fig.4 Voltage waveforms without active stray field compensation: IE = IC = 40kA, ID = 0, R3 = R4 =0.6Ω VP1U = voltage between P1 coil terminal (busbar A1) and neutral VP1EU= voltage across upper end coils (between busbar A1 and A2) VP1CU= voltage between P1 coil terminal (busbar A2) and neutral.

In its absence, Fig 4 show the voltage transients assuming 40kA premagnetization, with a value of 0.6Ω for all commutating resistors. According to the calculation, 10kV peak appears, across two end pancakes. If current is flowing through PFX at the end of premagnetization, the blocking diodes will continue to conduct for a longer time and the voltage across the two end pancakes will easily reach the maximum of 12kV. The accuracy of the model, estimated to be - ±10% is validated by comparison with the experimental results.

If the active stray field compensation network is present, the current ID (current difference between central and end pancakes), needed to compensate stray fields, flows in the two intermediate busbars A2, B2 (see Fig 3). At the beginning of fast rise the current ID is progressively transferred from PFX to the resistors R12. When the process is completed the blocking diodes withstand the negative voltage; the voltages across the magnetizing winding are shown in Fig.5. The value of the resistors R12 will be chosen

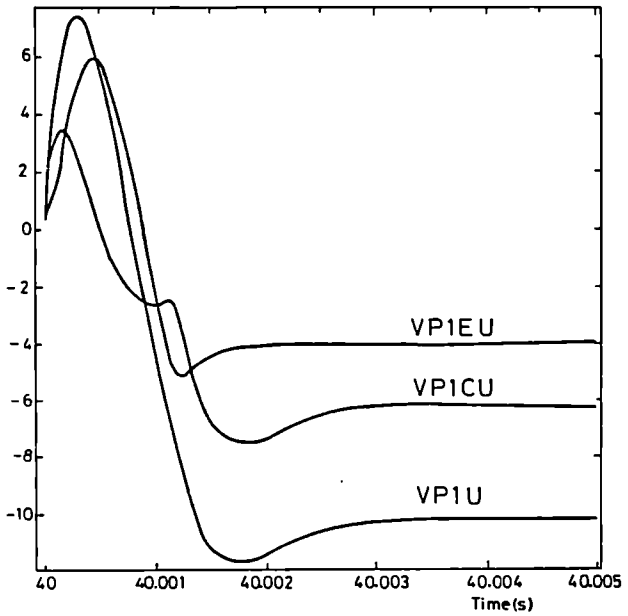

Fig.5 Voltage waveforms with active stray field compensation.
IE = 40kA, IC = 38kA, ID = 2kA, R3 = R4 =0.6Ω

to maintain the natural voltage distribution between the end and central pancakes of P1, during the early phase of fast-rise. Moreover, the current ID should decay more or less proportionally to the average of IE and IC. When the additional switching network is switched on, the matching between R12 and the total equivalent resistance is destroyed and ID will decay faster.

In conclusion, the transient analysis shows that, although overvoltages could be easily generated across the two end pancakes of coil P1, with both versions of the circuit, these are well within the nominal voltage (10kV per pancake).

4.3 Scenarios

The 7MA scenario has been evaluated assuming 40.6Wb flux variation available from the magnetizing winding. From calculations, it appears that 4s flat-top will be available with a resistive loop voltage of 1V. A longer flat-top up to 10s could be reached with lower resistive loop voltage down to 0.5V. Figs 6 and 7 show current and voltage waveforms.

During premagnetization, the generator converter applies positive voltage to the magnetizing winding (busbars A positive) through the closed circuit breakers S1; positive current starts rising. Without active stray field compensation network, PFX (in inversion) prevents current (ID = 0) flows in the

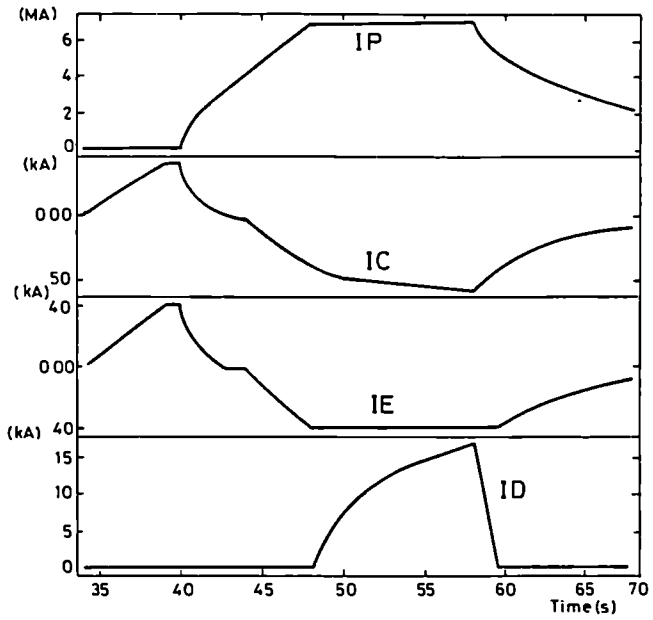

Fig.6 7MA scenario: loop voltage 0.5V, flat top length 10s, R3 = R4 = 0.6Ω, R8 =0.15Ω, 40kA premagnetisation: IP = plasma current
IC = current through the central pancakes of P1
IE = current through the end pancakes of P1
ID = IE - IC current difference.

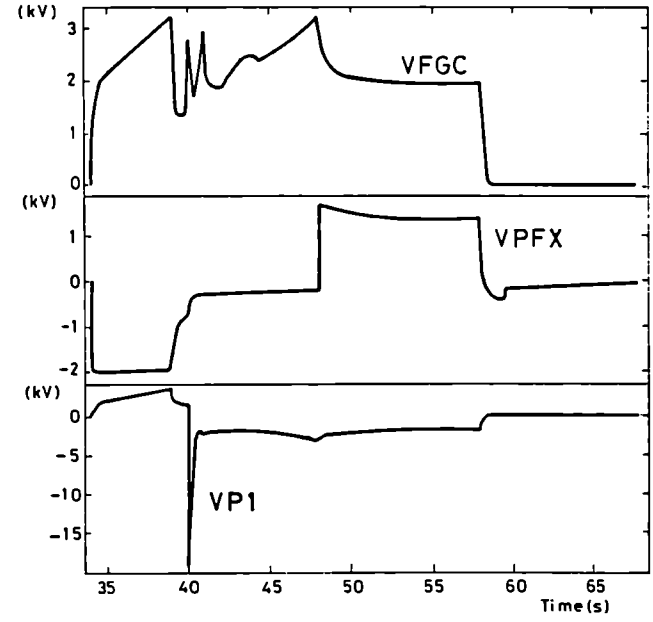

Fig.7 7MA scenario (as in Fig.6): VFGC voltage at the output of the PF generator convertor, VPFX voltage at the output of PFX, VP1 voltage across the magnetizing winding.

busbars A2, B2. When the active stray field compensation network is implemented (after the shutdown planned for 1988), PFX (still in inversion) will control the current ID to ≈2kA. The premagnetization lasts 6s approximately in both cases due to the limitation of the voltage in inversion, of PFX consisting of PVFA 5,6 only. With PVFA 2 connected in series with PVFA 5,6 a shorter premagnetization can be used. During slow-rise and flat-top, currents in the central and end pancakes of P1 are equal until the limit ≤40kA is reached in the end pancakes: PFX is in inversion and a negative voltage is applied across the blocking diodes, so no current can flow in this branch. The generator-converter controls the current rise through the magnetizing winding according to the demand of the plasma current controller. When the limit ≤ 40kA is reached, PFX starts to increase ID in order to maintain constant current (≤ 40kA) in the end pancakes. The current in the central pancakes is increased, under PFGC control, up to the maximum allowed value of 60kA.

Simulations have been performed to consider various cases: the commutating resistors with values of 0.6 and 0.34Ω, operation of the additional switching network, etc. Table 2 shows the requirements for the main parameters. An asterix indicates that requirement is higher than the nominal performance, also given in the table. The thermal limitations to the central pancakes of P1 coil will be increased from 32 to 46 GA²s by a modification, under design, to its cooling system [7]. The limitation coming from PFGC can be removed reducing the plasma current derivative during the last 1-2s of slow-rise.

Table 2

JET PF SYSTEM REQUIREMENTS

		NOM.VAL					
PLASMA CURRENT	(MA)	4.8	7	7	4	7	7
FLAT TOP TIME	(s)		10	4	10	10	4
RISE TIME	(s)		8	6	7	8	6
LOOP VOLTAGE	(V)		0.5	1.0	0.6	0.5	1.0
R4 RESISTANCE	(Ω)	0.6	0.6	0.6	0.6	.34	.34
R3 RESISTANCE	(Ω)	0.6	0.6	0.6	0.6	.34	.34
R8 RESISTANCE	(Ω)	.15	.15	.15	-	.15	.15
PFGC ENERGY	(GJ)	2.6	2.4	2.0	.62	2.8*	2.2
R4 ENERGY	"	480	139	136	67	222	215
R3 ENERGY	"	800	351	341	194	606	577
R8 ENERGY	"	810	628	606	-	627	593
PFX I**2*T	(GA²s)	16	1.6	.95	14.2	1.9	.9
PFGC I**2*T	"	90	65	46	11	82	56
P1E I**2*T	"	32	31	21	7.2	32	20
P1C I**2*T	"	32	43*	28	35*	45*	27
MAX PFGC CURRENT	(kA)	85	75	83	27	87	97*
AT:PFGC VOLTAGE	(kV)	5	3.3	4.0	0	3.4	4.2
PFGC SPEED	(rpm)	225	184	182	201	178	173
MAX PFGC EXC CUR	(kA)	5.6	4.1	4.7	1.2	4.8	5.7
MAX PFX CURRENT	(kA)	35	17	18	35	17	19
MAX PFX VOLTAGE	(kV)	2.8	2	2.1	2.1	2	2.1

The 4MA X-point scenario does not need all of the available flux variation. Therefore, the resistive loop voltage is not critical. Figs. 8 and 9 show the current and voltage waveforms for the 4MA X-point scenario. Most likely the current required at the end of premagnetization will be only 20-25kA, so that the active stray field compensation is not required. During slow-rise and flat-top, the leakage flux produced by ID is controlled by PFX. The generator convertor controls the voltage increasing all P1 currents on demand from the plasma current controller to reach and maintain the required plasma current.

4.4 Fault Analysis and Protection

Possible faults caused by malfunction of the current modulation circuit are described below: the expected protective actions are also mentioned.

A short circuit between busbars A1 and A2, for instance, could happen during the early fast-rise, as a consequence of a flashover across the resistor R12a. The upper end pancakes of P1 are shortcircuited when negative voltage is supplied across P1 by the OH circuit. If the fault takes place with 40kA in P1, the current in the upper end pancakes will rise, reaching 47.5kA in approximately 300ms. The fault will be detected by the protection P1E overcurrent: the R8

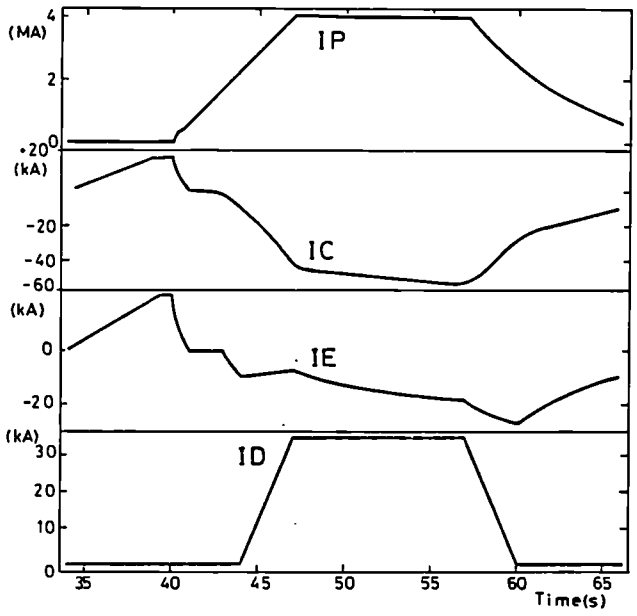

Fig.8 4MA, X-point scenario: loop voltage 0.6V, flat top length 10s, R3 = R4 = 0.6Ω, R8 = 0.15Ω, 20kA premagnetization.

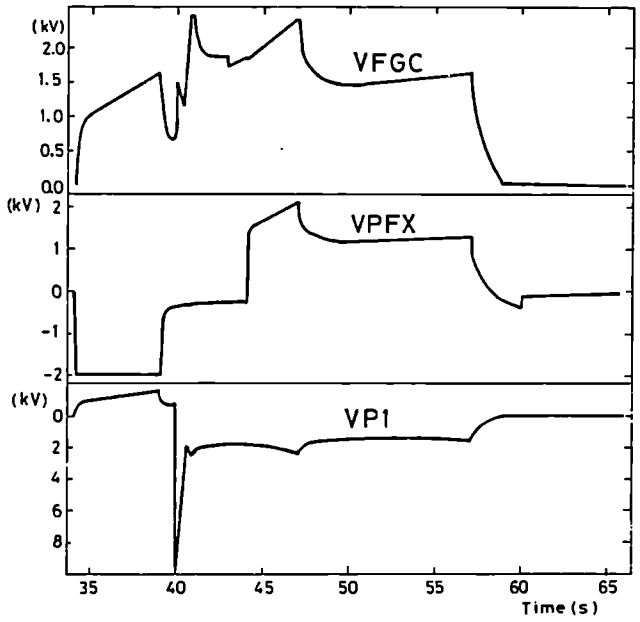

Fig.9 4MA, X-point scenario (as in Fig.8).

resistors will be switched on reducing the overcurrent substantially.

A short circuit between busbar A2 and B2 requires PFX to be designed to withstand it. Overcurrents up to 130kA could flow through PFX, the blocking diodes and the inductors L4 when present. These components are designed to withstand this overcurrent for 100ms, the expected time needed for the PFX overcurrent protection to open the PFX 33kV circuit breaker.

An earth fault from busbar A2, for instance, during fast-rise causes a voltage of approximately 12kV across the resistor R12a when present and across the upper end pancakes of P1. The resistor R12 will be designed to withstand that voltage (Table 1). The fault will be detected by the protection P1E overvoltage and, possibly, by overcurrent in the neutral: the R8 resistor will be switched on reducing the overvoltage substantially.

Full excitation to the generator convertor during premagnetization could provide up to 10kV across P1. Since PFX with the other components (BDX and L4) shows low impedance, compared to the central pancakes of P1, high current could be reached quickly in the end pancakes of P1. This fault should be detected by the protection ID overcurrent during premagnetization: the generator will be de-excited.

Full excitation of the generator or of PFX during flat-top could raise the current both in the end and in the central pancakes of P1 above the new nominal limits. This fault will be detected by P1E overcurrent or P1C overcurrent or ID overcurrent: in all cases, the generator will be de-excited. PFX voltage will also be brought down to zero as described below.

Other faults directly related to the presence of the active stray field compensation network are being considered: since this facility will only be implemented during the 1988 shutdown, the related protective actions are not yet finalized.

A new measurement and protection cubicle has been built and will be operational with the current modulation circuit in November 1987. Fig 3 shows the various current and voltage transducers available as part of the current modulation circuit. The current in the central pancakes of P1 and the voltages across the upper and lower end pancakes will be available through electronic manipulation. Given the symmetry of the circuit, each parameter is measured twice. A high degree of redundancy will be available in the protection. Table 3 gives the complete list of each protection with its main purpose.

Table 3

No	PROTECTION	AIM
1	P1E overcurrent	To avoid coil overstresses
2	ID overcurrent	To protect against possible PFX run-away that could lead to TF coil overstress due to P1 leakage field.
3	P1C overcurrent	To avoid coil overstress
4	ID overcurrent during premagnetisation	To protect against a possible PFGC run-away in premag that could lead to P1E and PFX overvoltages at interruption and too high a current in P1E.
5	P1 coil currents in opposite direction	Should prevent over large repulsion forces between P1E and P1C.
6	P1E overvoltage	To detect abnormal operations of the switching network
7	P1C overvoltage	As above
8	P1E I^2T Limit Exceeded	To avoid P1E thermal overstresses
9	P1C I^2T Limit Exceeded	To avoid P1C thermal overstresses

All interlocks will be backed up by the PF Central Interlock and Safety System (CISS) which acts with a cycle time of 125ms.

4.5 Control

The new control circuit is a part of the plasma position and current control system (PPCC). It represents an enhancement of the present digital control system of the plasma current. The heart of this circuit is a TM99000 micro processor (CAMAC module). All computations are performed in integer arithmetic to ensure sufficient speed (updating time ≤ 5ms). The vectors determining reference waveforms are downloaded before the plasma pulse. During the pulse,

the reference waveforms are generated by linear interpolation. AD and DA converters are used for analog inputs and for the generation of the control signals for the power supplies.

Analog input signals are IP = plasma current, IE, ID and ITF = current of the TF coil, analog output signals are VI and VX. VI controls the excitation of the generator, and VX controls the output voltage of PFX (in voltage control). The control circuit is linked with the JET Pulse Termination Network. A "SOFT STOP" request is raised by the control system when the plasma current error exceeds a preset limit during periods where plasma current feedback is active. The basic control modes are outlined below. During the premagnetisation phase IE is feedback controlled through the PFGC, using a PID algorithm. The difference current ID is feedback controlled through PFX, using proportional control, to reduce the stray magnetic field, if required.

During the fast-rise phase, the generator control signal VI and the reference (= desired value) for the difference current ID are set to zero. The actual current ID decreases in a similar way as IE, depending on the choice of R12 (Fig 3).

During the subsequent slow-rise, flat-top and current decay phases (after closure of the Reversing Make Switches S4), the plasma current is normally controlled via the PFGC using a PID - feedback algorithm, in much the same way as in the present current control system. The difference current ID is controlled via PFX using proportional control and a preprogrammed reference current waveform. However, when IE reaches a nominal limit IEN ($\leq$40kA), then the PFX control is changed to feedback control of IE to keep IE=IEN for as long as required. At the same time, the plasma control algorithm is modified to take care of the changed characteristics of the PFGC load.

When IC reaches a nominal limit ICN ($\leq$ 60kA), then the PFGC is controlled to keep IC at this limit until the plasma current has decreased either to some selectable value IPMIN or reaches the desired current reference value of the current decay phase. In this way, one can obtain a more gentle current decrease than by a SOFT STOP action (setting VI=0), reducing thereby the probability of a density disruption.

The TF current signal ITF is used to reduce the limit of IC from 60kA to some smaller value $\geq$40kA in a continuous way when ITF is smaller than the nominal maximum current of 67kA:

ICN = 40kA if ITF $\leq$ 27kA

ICN = 26.7 + 33.3 (ITF/67)kA if ITF>27kA

This serves to limit the radial expansion force at the central pancakes of P1, in cases where the compression force from the TF coils are insufficient.

5. Plan of the Enhancement

The different components needed for the PF system enhancement are becoming available at different times. A carefully thought plan was set up in the beginning of 1987 to make the best use of the equipment as soon as available. Table 4 shows the plan of the PF system enhancement divided into five phases. The improvements available within phases 1 and 2 have been described in section 3.

With phase 3, experiments above 5 MA with material limiters, and above 3 MA with magnetic separatix will be possible. With phase 4, the lack of power supply voltage across P4 during plasma start-up will be removed completely. Finally with phase 5, the active stray field compensation network will be available to optimise plasma start-up at 40kA premagnetization. The flux lost at plasma start-up will be reduced to a minimum and the nominal premagnetization will be available (nominal flux variation). All amplifiers will be upgraded in current (40kA, 15s) to match the design value of the coils (shaping field, vertical field and X-point field). PFX will be upgraded also in voltage, if necessary.

Table 4

Plan of the PF System Enhancement

Phase 1	- P1 from 8 to 10 pancakes
July 87	- Additional switching network
	- Galvanic separation among different systems
Phase 2	- PVFA 2 in series to PVFA 3,4 to act as
September 87	temporary booster amplifier
Phase 3	- Current modulation circuit without
November 87	active stray field compensation
Phase 4	- Final booster amplifier in series to
March 88	PVFA 3,4
Phase 5	- PVFA 2 in series to PVFA 5,6 to upgrade
End of 1988	PFX in voltage
shutdown	- Current upgrade to all amplifiers
	- Active stray field compensation network

6. Conclusion

The operational range of JET will be extended well above design values due to the enhancement report. With full additional heating, the last phase in the life of JET, the active phase, will start in the best possible conditions to make it successful. Substantial alpha-particle production is expected to study their confinement and heating. Comparison of 7MA material limiter plasmas and 4MA magnetic limiter plasmas will be made in fusion relevant conditions.

7. Acknowledgements

The authors would like to thank E. Bertolini for technical and managerial supervision; F.C. Schueller for many helpful discussions on physics requirement; a special appreciation is due to P.H. Rebut for his leading contribution in the choice of the new PF system configuration.

References

[1] E. Bertolini, P.L. Mondino and P. Noll, "The JET Magnet Power Supplies and Plasma Control Systems", Fusion Technology Journal, Vol. 11, No. 1, pp.71-119, January 1987.

[2] P.L. Mondino et al., "The Development of the JET Poloidal Field Power Supplies to Reach the Nominal Flux Swing Capability", Proceedings of the 14th Symposium on Fusion Technology, pp.859-866, Avignon, F, September 1986.

[3] F.C. Schueller, JET Joint Undertaking, Abingdon, U.K., Private Communication, 1980.

[4] T. Bonicelli, V. Marchese and P.L. Mondino, "The Additional Switching Network, a new Part of the Ohmic Heating Circuit of JET: Design and Early Operation", presented at the 12th Symposium on Fusion Engineering, Monterey, USA, October, 1987.

[5] J.R. Last D. Cacaut and J.W. Zwart, "The JET Magnets: Operational Experience and Plans for Upgrade", Proceedings of the 14th Symposium on Fusion Technology, pp 1643-1648, Avignon, France, September 1986.

[6] E. Bertolini et al., "The Development of the JET Electromagnetic System", Proceedings of the 14th Symposium on Fusion Technology, pp. 263-271, Avignon, F, September 1986.

[7] J.R. Last, JET Joint Undertaking, Abingdon, U.K, Private Communication, 1987.

REIONISED PARTICLES AND DUCT WALL PROTECTION OF THE JET NEUTRAL BEAM INJECTION SYSTEM

A P H Goede, S Papastergiou, J Simkin*), C Challis, G Duesing,
R Haange, T T C Jones, D Stork, E Thompson.

JET Joint Undertaking, Abingdon, Oxon, OX14 3EA, UK.
*) Vector Fields Ltd, 24 Bankside, Kidlington, Oxford, OX5 1JE, UK.

ABSTRACT

Experimental and computational data are presented of the reionised neutral beams in the duct of the JET neutral injector. The new duct protection system has been shown to successfully transmit 10 MW D° beams at 80 keV energy for several seconds pulse length. The measured power, power density and D-α light emission has led to increased understanding of the gas evolution in the duct and the importance of wall conditioning to avoid excessive beam reionisation.

1. INTRODUCTION

Neutral beams, having passed the ion deflection magnet, are subject to reionisation through collision with the background gas. Typically, in the JET Neutral Injector [1], about 4% of the 80 keV D° neutral beam is reionised depending on gas pressure and beam energy, comprising a total power of approximately 400 kW [2]. The reionised fractions are gradually peeled off and deflected onto the walls of the beam line due to the action of the poloidal stray magnetic field of the Tokamak. In the duct this leads to high localised power densities.

In the horizontal plane the power concentration arises because the trajectories of ions, created at different positions along the beam meet up near the walls of the duct. In the vertical direction the finite angle of incidence of the ions with respect to the poloidal fringe field produces fringe field focussing. A plan view of the JET neutral beam line is shown in Figure 1. Typical trajectories of the reionised particles are shown in Figure 2a (plan) and in Figure 2b (elevation), illustrating the reionised beam focussing effects.

During high power, long pulse neutral injection experiments the reionised power densities have exceeded the original design specifications [1] leading to failure of the water cooled duct protection panels. The high peak loads encountered followed a pressure excursion in the duct, possibly caused in one instance by the evaporation of gas condensed on the cryopumps and in another instance possibly by the excessive outgassing of an unconditioned duct wall.

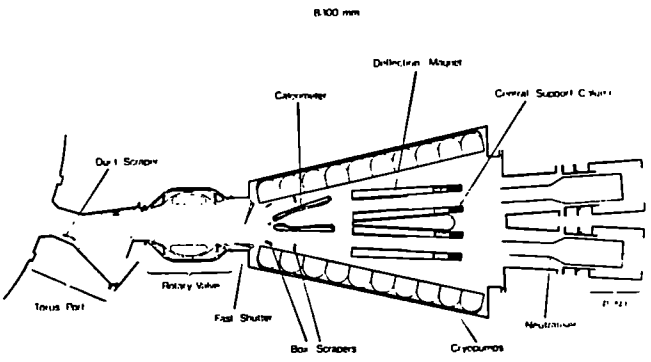

Figure 1 PLAN VIEW OF JET NEUTRAL INJECTOR

In this paper we present measurements and new 3 D-computations of the reionised beam power loading of the duct, measurements of the D-α light emitted by the beam-excited background gas in the duct, analysed in terms of surface and thermal gas desorption from the bulk material for various duct wall materials used (Ni,C,Cu). Also, the maximum neutral beam power that can be transmitted through the duct (beam-blocking effect) is discussed and predictions are made for the reionised particle loading during the future 7 MA operation of JET.

During the last 1986 operation period of JET, it has been demonstrated that a duct wall protection system consisting of high thermal capacity copper tiles, cooled between pulses, is adequate to transmit 10 MW D° beam power for several seconds. The recently implemented duct wall protection system for 7 MA operation is based on this principle. The mechanical design and the design calculations are presented in this paper.

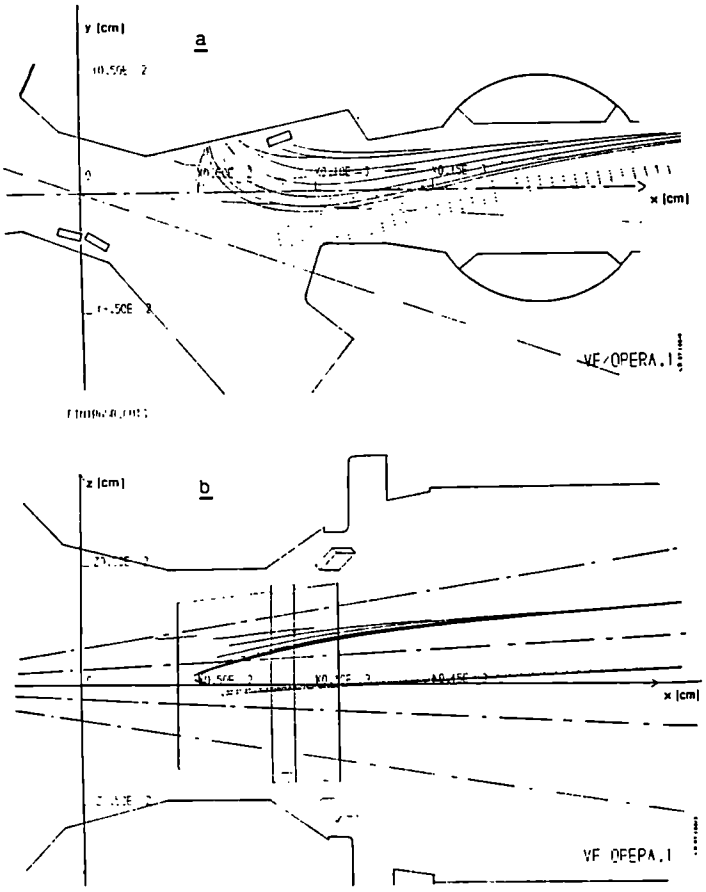

Figure 2 Computed 3D reionised particle trajectories in the JET duct in (a) plan and (b) elevation. Traced are the 50% beam contours. From these data together with the calculated gas profile the reionised power density at the duct wall has been calculated for Tokamak plasma currents ranging from 1 to 7 MA.

2. MECHANICAL DUCT PROTECTION SYSTEMS

The duct walls are protected from direct neutral beam interception by actively cooled beam scrapers. Originally, the walls were lined with thin-walled (1.6 mm) quilted nickel panels, which were actively water cooled (water flow rate ≈ 3.5 ℓ/s, pressure drop ≈ 2.5 bar). The calculated burn-out power loading was ≈ 300 W/cm², whilst a second failure mode through thermal stress is encountered at ≈ 1 kW/cm².

The rotary valve between torus and injection box was protected by a series of nickel tubes (8 mm dia., 1 mm wall) hydraulically connected in parallel (flow rates 1.4 ℓ/s and 4.2 ℓ/s for entry/exit port and rotor respectively). The calculated maximum safe power density was 390 W/cm².

In this configuration over 450 neutral beam pulses were transmitted through the duct at a power level in excess of 1 MW and pulse lengths longer than 1 sec, which includes a combined value of injected power and energy of 8.3 MW and 40 MJ respectively [2].

At the first accident (shot # 9777) a small hole of size 1.4 x 4 mm² was melted in the liner. The hole was repaired by welding and carbon tiles were placed in front of it covering a limited area of the liner only. At the position of the hole, one tile was equipped with a thermocouple. The graphite used is the same as the Tokamak inner wall protection (CL 5890 PT, manufactured by Le Carbone Lorraine).

The second accident (shot # 10363) resulted in a more violent burst of the liner (area not covered by carbon) producing an L-shaped tear of size 60 x 30 mm and melt marks elsewhere. Subsequently, the entire r.h.s. liner was protected by OFHC copper tiles of 15 mm thickness, blackened at the rear side (Al_2O_3 + TiO_2 plasma spray) to enhance radiation cooling. More extensive thermocouple instrumentation was also fitted.

3. TOTAL POWER LOADING

The total power to the duct liners and rotary valve has been measured by waterflow calorimetry. This power results from reionised particle impact only, direct beam interception being prevented by beam scrapers. In Table I the power is listed as a percentage of the extracted power IV (I = beam current, V = extraction voltage).

The power to the duct liners is predominantly to the r.h.s. in co-injection, and to the l.h.s. in counter injection, consistent with the calculated particle trajectories (Figure 2a). At higher Tokamak plasma currents the calculated reionised power deposition shifts upstream with the increase of the stray magnetic field strength. This fact is consistent with the last series of measurements in Table I, where the power to the rotary valve is shown to increase from 0.19% to 0.73% IV with the plasma current, whilst the power to the duct liner reduces.

The absolute value of the measured reionised power is in good agreement with theory based on molecular gas flow calculations. The calculated pressure in the duct is typically 2 to 3 x 10^{-5} torr [1]. Calculations show that about 4% of the 80 kV - D° beams are reionised, corresponding to 1.6% IV. The measured reionised power is respresented by the sum of the power to the rotary valve and the duct liner (columns 1 and 3 Table I) and ranges between 1.2 and 2.2% IV.

The reionised power measurements listed in Table I cover the entire operation period from February to November 1986 and include hydrogen and deuterium beams. They show a remarkable consistency in their absolute values, irrespective whether the original nickel panels or the carbon tiles or the copper tiles were installed in the duct. This is also the case for the two shots #9777 and #10363 in which the nickel liner was damaged. The following conclusions can be drawn from this observation:

- The phenomenon giving rise to the high power densities required for melting the liner, must occur on a very short time scale, too fast to influence the water flow calorimetry. A time scale consistent with this would be 100ms or less.
- For conditioned walls the gas desorption coefficients are reduced to similar levels, irrespective whether copper, nickel or carbon is used as a duct wall material.

TABLE 1 Summary of Duct Power Loadings in % IV

Beam and plasma parameters		ROTARY VALVE	DUCT TOTAL	DUCT liner only
65 kV H° CO	2-4 MA	0.25-0.5%	2.0-2.5%	1.0-1.3%
75 kV D° CO 5-7 PINIs	3 MA	0.25%	2.3-2.5%	1.05%
75 kV D° COUNTER (inc 8 PINI shots)	1-3 MA	-	2.1-2.9%	1.1-1.6%
75 kV D° CO	5 MA	0.56%	2.1-3.0%	1.5%
8 PINIs # 8852		-	4.65%	3.4%
80 kV D° CO # 9777 (6 PINIs)	3 MA	0.22%	2.1%	1.03%
Carbon tiles installed (correction tile shielding)	3 MA	0.26-0.3%	1.7-2.6% (2 - 3%)	0.7±0.3% (1%±0.4)
80 kV D° CO (1-6 PINIs)	5 MA	0.61%	1.8-4.8%	0.8-3.0%
8 PINIs # 10363	5 MA	0.56%	3.2%	1.1%
Copper tiles installed	1 MA	0.19%	1.4-1.7%	0.30-0.40%
∿ 75 kV D° CO	2 MA	0.37%	1.3-1.7%	0.25-0.38%
(all 8 PINIs)	3 MA	0.48%	1.3-1.6%	0.20-0.30%
	5 MA	0.73%	1.0-1.4%	0.10-0.20%

4. POWER DENSITY

After the installation of the carbon and copper tiles in the duct, limited information on the local power density could be obtained. In a conditioned duct the peak power densities range from 150 to 200 W/cm² both for the carbon and copper tiles, the higher value referring to 5MA operation.

These values are consistent with new 3D power density calculations where the vertical focussing and the higher power transmitted through the duct are taken into account. Shown in Figure 3 are the measured and the calculated distributions of reionised power density on the copper duct wall plotted for a range of plasma currents I_p. Also indicated are the locations of the liner damage at 3MA (# 9777) and 5 MA (# 10363) operation respectively. A sample ion trajectory calculation for I_p = 3 MA is also shown. Only qualitative agreement is found for the location of the reionised power deposition.

Calculations show that the vertical focussing is strongest (factor two) for beam sources situated in the tangential bank, top and bottom position, because the angle of incidence with respect to the torus stray field is largest both in plan view as well as in elevation. Vertical focussing effects are weakest for beam sources situated near the equatorial plane of the Tokamak in the normal injection direction. The Calculations are found to be sensitive on the coil currents of the poloidal magnetic field, in particular

the radial and shaping fields. This result implies that any new design of duct wall protection must accommodate a wide power deposition area.

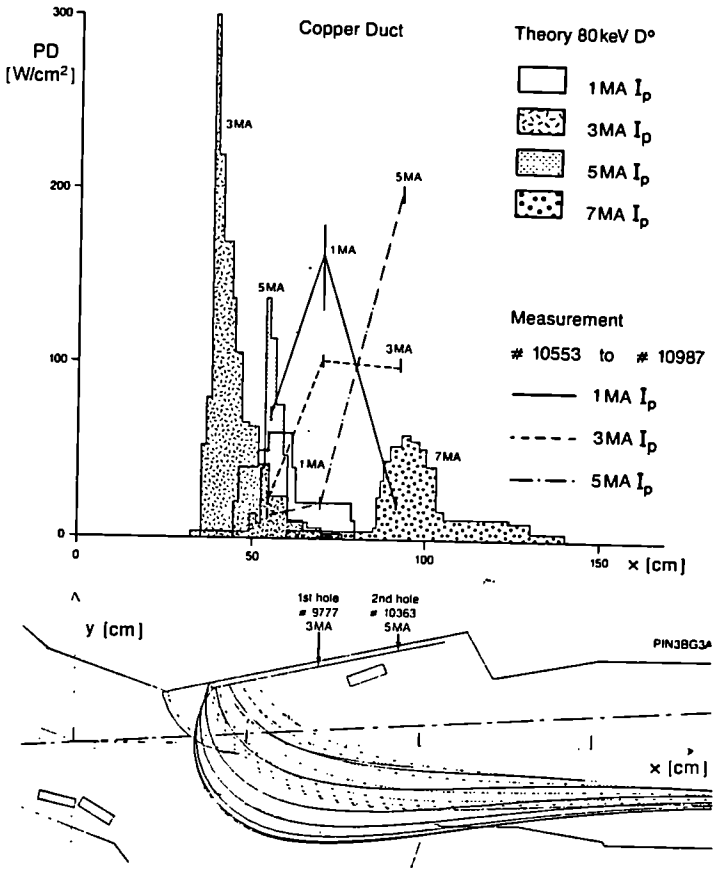

Figure 3 Measured and calculated power density profile along the r.h.s. duct wall (x-direction) of reionised particles for Tokamak currents ranging from 1 to 7 MA. A sample reionised trajectory at 3 MA plasma current is also shown.

5. DUCT CONDITIONING AND D-α LIGHT MONITORING

Information on the gas pressure in the duct is derived from the Balmer D-α light emitted by the background gas upon beam excitation. Monitoring the D-α light has proved a most useful indicator of the duct conditioning status and the fast phenomenon leading to melting and damage to the duct liner. The diagnostics consist essentially of a D-α interference filter of bandwidth ≈ 30 Å and transmission ≈ 70% connected by fibre optics to a photomultiplier.

For a constant number of beams (PINI's) transmitted through the duct, the D-α light emitted provides a localised pressure measurement. This is so because the excited Balmer states are short-lived; it can be shown that 75% of the light received by the monitor derives from excitations which occur within a 20 cm thick slab of the beam.

Figure 4a (lhs) shows that the first conditioning pulse on the carbon tile generates a large D-α signal which reduces in time sharply during the pulse. After three 0.5 sec conditioning pulses the light output has become stationary at a factor ≈ 20 lower level (Figure 4a rhs). At the same time the power density measured on the tile has dropped by a factor 5. The total power in the duct has dropped by a factor 3. A similar phenomenon is observed with the copper duct tiles, however conditioning periods are shorter, i.e. 0.2 sec.

These processes are interpreted as desorption of the weakly bound surface gas under reionised particle bombardment of the duct wall.

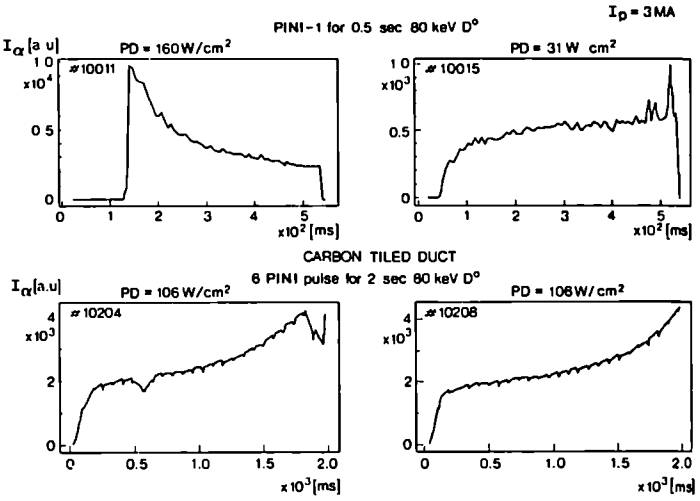

Figures 4a (top) and b (bottom) (see text)

In a well-conditioned duct a slow rise in the D-α light is observed consistent with a thermal time constant, see Figure 4b carbon tiled duct. A stationary condition develops in which the light output has the same magnitude and shape, whilst the temperature of the tile cycles between the same minimum and maximum values. The same phenomenon is observed for a copper tiled duct, see Figure 4c. This figure refers to an 8 beam pulse from time 1 to 2.5 sec whilst the rest of the time 4 tangential beams only are injected.

This phenomenon is interpretated as thermal desorption of gas from the bulk material as the temperature of the material increases during the pulse.

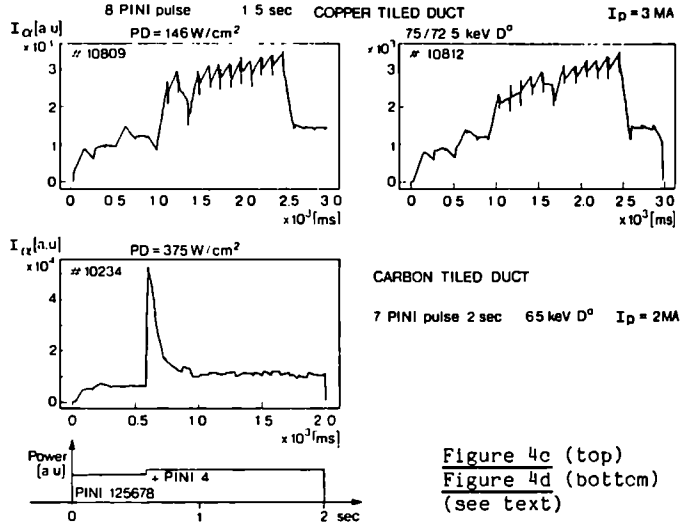

Figure 4c (top)
Figure 4d (bottom)
(see text)

Figure 4d shows the result of a beam source (PINI) brought in for the first time in an otherwise fully conditioned carbon tiled duct. A sharp rise (~ x 10) in the D-α light intensity is observed, decaying in typically 100 ms. This is interpreted as surface gas desorption upon reionised beam impact on an unconditioned part of the carbon wall, leading to a pressure surge of about a factor 10. The local power density increased by a factor 5 in this instance. The total power increased by a factor 1.5.

The conditioning process is illustrated by Figures 5a (carbon) and Figure 5b (copper) where the evolution of the D-α light emission is plotted for subsequent neutral injection pulses. To start with the individual beam sources (identified P-1 to P-8) are brought in one at the time for a short pulse length until the duct light emission has reduced to a stationary level (downward arrow). This level is similar for all duct materials employed. Carbon, however, has proved a difficult material to condition. The main cleaning requires approximately three 0.5 sec individual beam (PINI)-pulses, whilst a stationary condition is reached after ~ 60 beam secs. Change in Tokamak current required a full reconditioning programme. Copper requires only 0.5 sec conditioning pulses and the build up of power can be achieved much quicker (maximally 10 Tokamak pulses are required) as illustrated by Figure 5b.

Once the duct has been conditioned, the D-α light intensity reduces to similar levels for the nickel, carbon and copper duct materials, as is illustrated by Figure 5c and d. The upward arrow indicates the slow rise in D-α light emission during the pulse. No enhanced carbon or copper impurities were observed spectroscopically inside the Tokamak in either case.

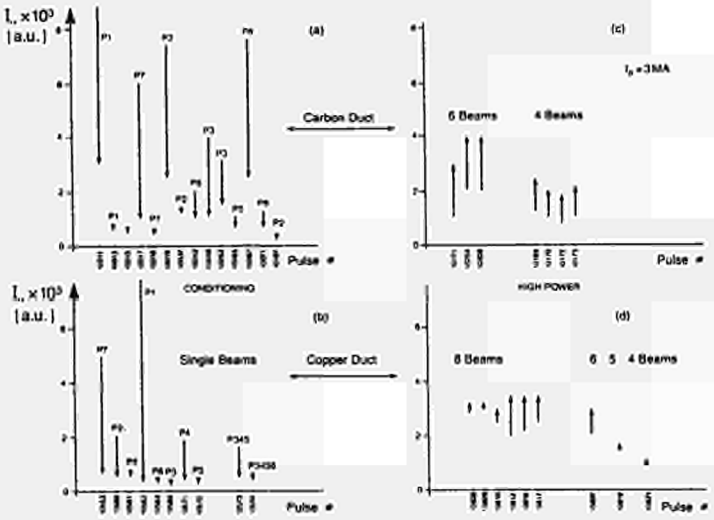

Figure 5a and b (l.h.s.) shows the duct wall conditioning process (a = carbon, b = copper) in terms of the D-α light intensity reduction (downward arrow) as a function of subsequent pulse number.
Figure 5c and d (r.h.s.) shows the gradual D-α light intensity increase for a conditioned duct for subsequent pulses. The light intensity is the same for copper or carbon duct material and rises gradually during the pulse (upward arrow).

6. BEAM BLOCKING

Beam blocking can occur when the total neutral beam flux I^o exceeds a limiting flux I_m [3]. This limiting flux $I_m/e = C / Y L \sigma_{01}$ is dependent on the gas desorption coefficient Y, the conductance of the duct C, the reionisation path length L and the reionisation cross section σ_{01}.

In case $I^o > I_m$ the pressure in the duct will exponentiate in a typical vacuum time constant $\tau \propto V/C$ where V is the volume of the duct chamber. In our case $I_m = 714/Y\ A_{eq}$ depending upon values of conductance and reionisation length chosen (but note that other expressions are possible [4] which would lead to a factor two higher values). For 8 beams of 80 keV D^o the equivalent current $I^o = 130\ A_{eq}$. Hence, for Y = 5 to 10, the maximum possible beam current will be reached. The time scale in which a pressure surge develops is in our case τ = 5 msec.

A desorption coefficient Y = 5 to 10 is not unrealistic for an unconditioned duct (see Figure 4d). We know that the phenomenon giving rise to duct liner melting takes place on a fast time scale (< 100 ms) as evidenced by the D-α light intensity increase and temperature spikes on the fast thermocouples and the lack of response in water flow calorimetry. Power densities well over 1 kW/ cm² are necessary to explain the observed melting on this short timescale.

Beam blocking could explain the bursting of the liner and the surface melting of the beam scraper in pulse # 10363, both in timescale and in power density levels triggered by reionised particle impact on an unconditioned area of the duct wall. In pulse # 9777 the duct was well conditioned. We assume here that beam blocking was triggered by a pressure rise observed in the duct (by D-α light increase towards the end of the pulse) possibly caused by a (partial) regeneration of the cryopumps which were in an unhealthy state during the pulse (pressure rise > 10^{-6} torr in neutral injection box).

7. NEW DUCT PROTECTION SYSTEM

In order to deal effectively with the peak power loads from reionised particles occurring during duct conditioning and other possible adverse operation conditions, the duct wall protection should consist of high thermal capacity elements as opposed to the originally installed high heat transfer, low thermal capacity elements. In the case of the JET duct, required to transmit 10 MW of 80 keV D^o beams for 10 sec pulse lengths and 10 minutes duty cycle, this can be realised with copper-tiles cooled during the off-duty period. Our experience during the last JET operation period has shown that 15 mm thick, radiation-cooled copper tiles are adequate for the transmission of ≥9MW D^o- beams for ≤3 sec. The total operation experience with the copper tiled duct comprises 155 pulses, 54 of which were at more than 7MW for more than 1 sec.

For the 1987-1988 operation period a new system has been installed based on OFHC Cu tiles, watercooled by 8 mm dia nickel plated stainless steel coolant tubes brazed onto the back. This system can deal with power densities of 500 W/cm², 10 sec pulse duration and a 5 mm strip power loading of ~ 4 kW/cm². Cu was preferred over Mo because of the faster cooling time and slightly better hot-spot handling capability (to avoid Mo recrystallisation). Water cooling is used as opposed to radiation cooling in order to reduce the maximum temperature by a factor two and the duty cycle by a factor 3 (to 10 mins). Draining the system allows vacuum bake out to 300°C followed by gas cool down. Brazing as opposed to clamping also resulted in faster cooling times. The maximum calculated copper temperature is ≈ 400°C. The tile support system is designed such as to cope with eddy current moments of 1500 Nm generated by a 7 MA, 10 ms plasma disruption.

REFERENCES

[1] G Duesing, H Altmann, H Falter, A P H Goede, R Haange, R S Hemsworth, P Kupschus, D Stork, E Thompson. Fusion Technology 11 (1987) 163.

[2] A P H Goede, C Challis, T T C Jones, A Stäbler, D Stork, E Thompson, Proc. 14th SOFT, Avignon (1986), Pergamon Press (1986) Vol 2, p.1139.

[3] A C Riviere, J Sheffield. Nucl. Fus. 15 (1975) 944.

[4] R S Hemsworth Culham Report CLM-R162 (1977).

THE DESIGN OF AN ISOTOPE SEPARATION SYSTEM FOR JET

Robert H Sherman
Tritium Science and Technology
Los Alamos National Laboratory
Los Alamos, New Mexico, USA

Abstract

Cryogenic distillation is planned as one of the processes to be used for isotope separation at JET. Three possible configurations of columns for this service are presented and discussed. The ability to easily control a system of columns must weigh heavily in the final selection of a process for construction.

Introduction

The decision by JET to install a major tritium handling facility as part of their later phase of operations presents some interesting problems in the design of isotope separation systems.

The hydrogen isotope separation system (ISS) for the Tritium Systems Test Assembly (TSTA) was designed on the assumption of basically a 1 : 1 D-T feed, with ca.1% of protium ingrowth, and D_2 neutral beam injectors running on a continuous cycle. JET, on the other hand, plans for the eventuality of D_2 and/or T_2 neutral beams, and D_2 and/or T_2 pellet injection operating on a 12 hour duty cycle.

In Table I the various input flow streams for a JET isotope separation plant are summarized. Feed stream #1 results from the pellet injector which will use H_2 as a propellant for either D_2 or T_2 pellets. The second stream is a combination of torus exhaust and neutral beam exhaust streams. The feed streams emenate from the fuel reprocessing system (Active Gas Handling System) which receives the various exhaust streams during operation and glow discharge cleaning, processess them to remove impurities, and then supplies them on a controlled basis to the cryogenic distillation system. The various feed stream cases represent different operating or glow discharge cleaning conditions.

The design of the fuel storage and purification system is discussed in another paper at this conference /1/.

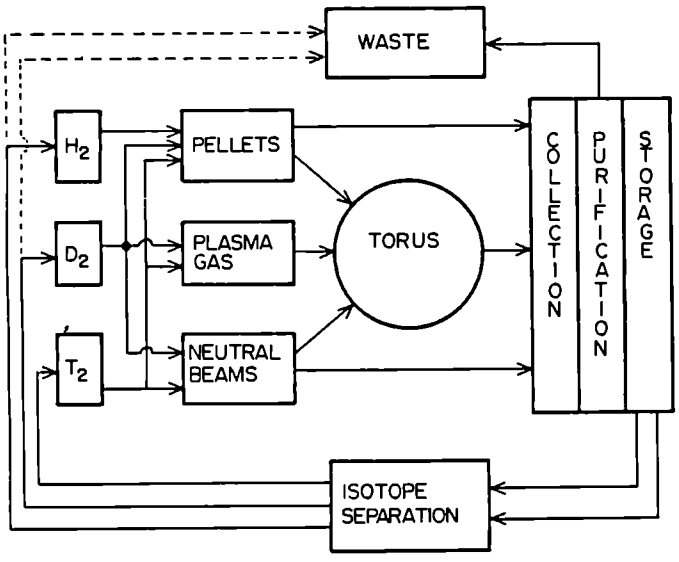

Fig 1 Basic Fuel Flow Path for JET

TABLE I

Input Fuel Stream for Isotope Separation

Case	Feed #	Rate m/s	Composition H	D	T	Remarks
1	1	1.8×10^{-3}	.989		.001	Nominal
	2	4.7×10^{-4}	.005	.709	.286	Max rate of T
2	1	1.8×10^{-3}	.969	.020	.011	Max rate of H
	2	4.7×10^{-4}	.050	.664	.286	
3	1	1.8×10^{-3}	.980	.020		Max rate of D
	2	4.7×10^{-4}	.005	.945	.050	
4	1	1.8×10^{-3}	.969	.020	.011	Max rate of H + D
	2	4.7×10^{-4}	.050	.900	.050	

In Table II the output fuel stream requirements of the ISS are summarized. These, in general, are easily met by a plant which utilizes cryogenic distillation as the primary means of effecting isotope separation if JET chooses to recycle both the H_2 and D_2 product streams. If the H_2 (and D_2) product streams are discarded, rather than recycled, a more stringent set of product purity requirements must be met, which are given in Table III.

TABLE II

ISS Output Fuel Stream
Requirements for Product Recycle

	Tritium Product	Deuterium Product	Protium Product
H	.001	.001	.989
D	.010	.998	.010
T	.989	.001	.001

TABLE III

ISS Output Fuel Stream
Requirements with Product Discharge to Atmosphere

	Tritium Product	Deuterium Product	Protium Product
H	.001	N/A	Balance
D	.010	Balance	N/A
T	.989	5×10^{-9}	5×10^{-9}

These basic fuel flow streams are indicated in Fig 1.

It is possible to arrive at a wide variety of plant designs to accomplish the stream purity requirements. Three of these will be discussed here.

Design

The basic principles for designing and cryogenic distillation plant for the separation of hydrogen isotopes have been enumerated in an earlier paper /2/. In the situation considered here, we are presented with feed streams comprising all 6 of the diatomic isotopic molecules and desire relatively pure products of H_2, D_2 and T_2, hence 3 undesirable species, HD, HT, and DT must be decomposed. The use of a large internal cycle stream of D_2, such as used at TSTA for decomposing HT (into HD and DT) will not work here. Instead, systems of several cascaded columns with recycle flows must be employed to deplete these species.

Scheme 1

In the 4-column scheme shown schematically in Fig 2, two recycle cascades are utilized to reduce unwanted species. In the cascade of columns A and B, DT and D_2 are obtained as the distillate from column A. This is then fed through equilibrator E_2 which produces a mixed stream including D_2, DT, and T_2. Column B separates the D_2 (to distillate) and yields a reboiler product of DT and T_2. The DT is again broken up in equilibrator E_1 and fed to column A. In this cycle DT can be reduced to a relatively low value (~ 1%).

The recycle loop of columns B, C, and D has a similar duty to reduce both HD and HT simultaneously.

Feed 1 which is mostly H_2 is fed into column D and the tritiated species are recovered in the reboiler and eventually find their way to column A. It is quite easy to provide a protium product of high purity since the key components in column D are H_2 and HD. Tritiated species can be depleted in the distillate to any desired level.

While HD and HT can be depleted from the D_2 reboiler product of column C to any desired level, such is not the case with DT. Essentially all DT carried from column B to column C will appear as a containment in the D_2 product. Thus the efficiency of separation of DT in column B is the most critical factor to overall product purity. This separation may be increased by increasing the number of stages (height) or the reflux ratio (reboiler power), but at the expense of increased tritium inventory.

The basic design parameters for this scheme using the nominal feeds for case 1 (Table I) are summarized in Table IV. Similar computations have been made for other feed cases and the resultant design parameters are quite similar.

TABLE IV

CALCULATED PARAMETERS FOR FIRST SCHEME

Column	A	B	C	D
Total Stages	90	90	90	90
Rectifying	42	69	75	28
Intermediate	0	0	0	46
Stripping	46	19	63	14
Light Key	DT	D_2	HT	H_2
Heavy Key	T_2	DT	D_2	HD
Feed 1	4.98×10^{-4}	9.30×10^{-4}	4.32×10^{-4}	1.8×10^{-1}
Feed 2				9.82×10^{-1}
Total Feed, mol/s	4.98×10^{-4}	9.30×10^{-4}	4.32×10^{-4}	1.90×10^{-1}
Distillate Flow	3.42×10^{-4}	4.32×10^{-4}	9.82×10^{-5}	1.78×10^{-1}
Reboiler Flow	1.56×10^{-4}	4.98×10^{-4}	3.34×10^{-4}	1.12×10^{-2}
Top Fraction	.686	.465	.227	.939
Light Key Recovery Fr	.993	.9000	.999978	.999
Heavy Key Recovery Fr	.0058	1.01×10^{-3}	1.11×10^{-5}	1.35×10^{-7}
Pressure, mbar	1080	1147	1080	1013
Temperatures				
Top	24.41	23.86	22.67	20.39
Feed 1	24.73	24.34	23.79	20.39
Feed 2				20.43
Bottom	25.26	24.87	23.89	22.84
Packed Section Meters	4.47	4.47	4.47	4.47
Diameter cm	1.044	1.780	1.069	3.068
Condenser Duty, Watts	5.3	15.5	5.5	16.0
Reboiler Duty, Watts	1.6	14.1	5.5	16.8
Reflux ratio	12.00	30.0	50.0	10.0

Inventories					Sum
H_2 (grams)	.0	.3	1.4	13.1	14.9
D_2 (grams)	4.9	20.8	11.6	1.9	39.1
T_2 (grams)	15.2	6.3	1.3	2.2	25.0

Product Streams			
H	0	5.3×10^{-4}	1.000
D	5.6×10^{-4}	0.99998	1.3×10^{-5}
T	0.994	1.1×10^{-4}	1.5×10^{-10}

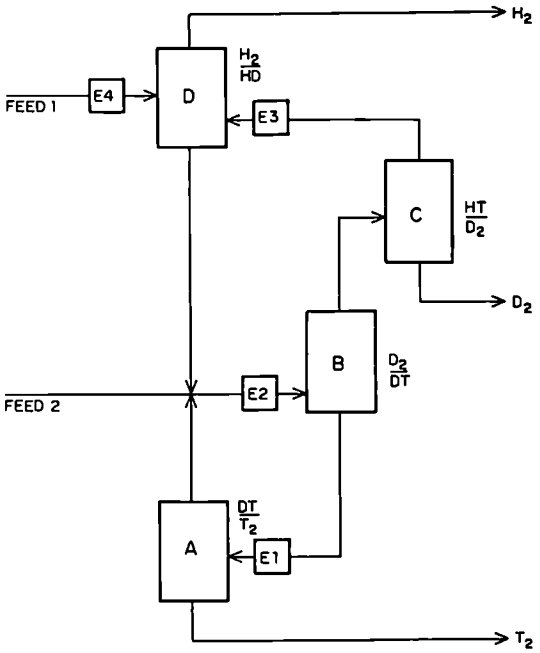

Fig 2 First Separation Scheme

Scheme 2

A different configuration was conceived by A Dombra /3/ and the detailed design, completed by A Everett, V Goyette and A Miller /4/ is shown in Fig 3.

In this scheme there are 3 separate recycle loops, each devoted to depleting one of the unwanted species - HD, HT, or DT. Columns A and B work together through the reboiler stream of B in such a recycle loop for the removal of DT in an identical manner to scheme 1. Similarly, columns B and C operate together through the distillate stream of B for the destruction of HT. This scheme has an advantage over scheme 1 in that, by a suitable choice of parameters, the stream of H_2 + HD effluent as the distillate of column C may be made arbitrarily low in tritium. Hence, if it is decided not to provide separate streams of H_2 and D_2 for refuelling by recycle, this mixed stream could be discharged directly to the atmosphere.

The operation of the recycle loop in column D may be understood by referring to Fig 4 which shows typical concentration profiles in a multicomponent column with a feed of equilibrated H_2 + HD from column C. It is clear that the separation of H_2 is satisfactory, but the reboiler product is mostly HD. If a side stream is withdrawn and equilibrated, then some of the HD is destroyed and more D_2 created. This stream can be reinserted into the column, as per scheme 2 and the resultant profile for column D is shown in Fig 5. It is clear that the HD profile has sharpened, and also moved upwards in the column. With more stripping plates active, the D_2 product is much purer.

An alternative to the recycle pattern proposed for column D is to use the technique employed by Sulzer in plants such as Grenoble, Darlington and Chalk River where the entire vapor stream is withdrawn, equilibriated and reinserted in the column on the next higher stage utilizing a liquid tray/vapor barrier.

The important design parameters for this scheme are given in Table V.

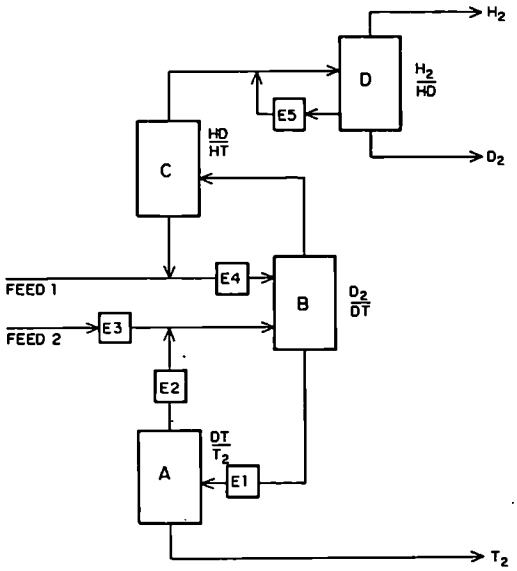

Fig 3 Second Separation Scheme

TABLE V

CALCULATED PARAMETERS FOR SECOND SCHEME

Column	A	B	C	D	
Total Stages	50	60	90	55	
Rectifying	5	39	79	19	
Intermediate	0	12	0	0	
Stripping	43	7	9	34	
Light Key	DT	D_2	HD	DT	
Heavy Key	T_2	DT	HT	T_2	
Feed 1	9.72×10^{-4}	2.43×10^{-3}	2.75×10^{-3}	6.00×10^{-3}	
Feed 2		1.29×10^{-3}			
Total Feed, mol/s	9.72×10^{-4}	3.72×10^{-3}	2.75×10^{-3}	6.00×10^{-3}	
Distillate Flow	8.17×10^{-4}	2.75×10^{-3}	2.12×10^{-3}	1.78×10^{-3}	
Reboiler Flow	1.55×10^{-4}	9.71×10^{-4}	6.30×10^{-4}	3.34×10^{-4}	
Top Fraction	.841	.739	.771	.297	
Light key Recovery Fr	.996	.681	.908	.597	
Heavy Key Recovery Fr	.298	9.35×10^{-3}	8.03×10^{-3}	7.39×10^{-4}	
Pressure, mbar	1147	1107	1107	1132	
Temperatures					
Top	24.65	22.01	21.32	20.78	
Feed 1	24.80	23.76	22.56	21.39	
Feed 2		24.30			
Bottom	25.47	24.61	23.65	24.06	
Packed Section					
Meters	2.44	2.95	4.47	2.69	
Diameter					
cm	1.219	2.804	2.672	1.788	
Condenser Duty, Watts	7.11	35.14	30.95	11.19	
Reboiler Duty, Watts	4.33	35.61	32.42	16.83	
Reflux ratio	6.80	12.00	15.00	7.00	
					Sum
Inventories					
H_2 (grams)	.0	2.6	11.9	5.4	19.9
D_2 (grams)	4.1	27.7	21.0	8.9	61.7
T_2 (grams)	18.5	6.7	1.8	.0	22.6
Product Streams					
H	0		0.843	.9995	4.2×10^{-4}
D	6.90×10^{-3}		0.157	5.0×10^{-4}	.9996
T	0.993		2.0×10^{-8}	1×10^{-13}	1×10^{-9}

Scheme 3

A third possible configuration of 4 columns has been proposed by Arthur D Little, Inc /5/ in a copyrighted design illustrated in Fig 6. Columns A and B perform just as in schemes 1 and 2. Column C and D form a simple recycle loop in which both HD and HT are decomposed. As in scheme 1, meeting the criterion for residual tritium in the D_2 product stream is the most difficult design problem. And here too, columns may be made arbitrarily large, but at the expense of tritium inventory.

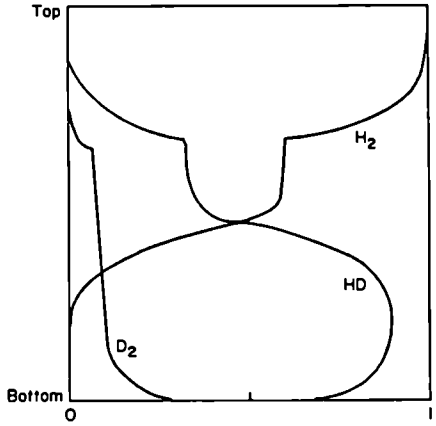

Fig 4 Typical Three-component Profile

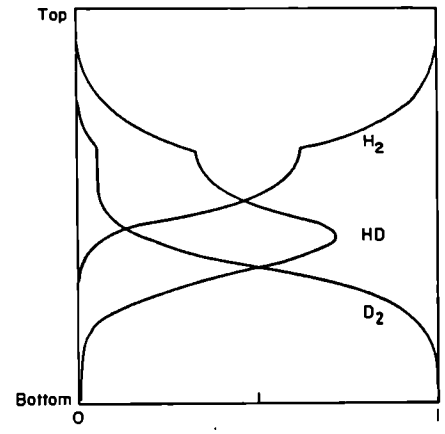

Fig 5 Modification of Profile from Sidestream Extraction and Equilibration

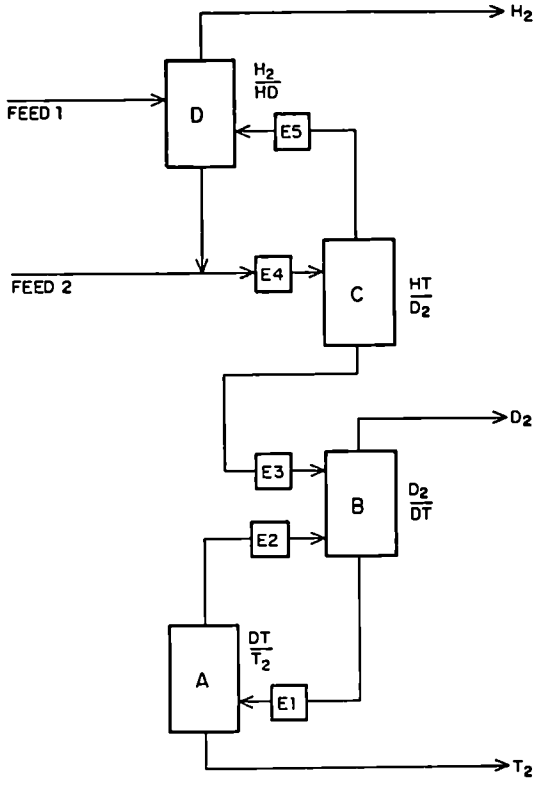

Fig 6 Four-column Scheme of Arthur D Little, Inc (C)

TABLE VI

PARAMETERS FOR ARTHUR D LITTLE, INC SCHEME

Column	A	B	C	D	
Product Purity					
H	0		3.3×10^{-5}	1.000	
D	9.8×10^{-3}		.9994	5×10^{-10}	
T	.990		2.7×10^{-3}	3×10^{-11}	
Column Pressure					
mbar	1013	1067	1107	1147	
Inventory					Sum
H_2	0	0	1.7	14.4	16.1
D_2	4.3	24.9	8.5	22	39.9
T_2	14.7	9.5	4.7	2.9	31.8

Control

Typical industrial processes endeavour to operate at a steady state whereas the JET operating scenario calls for many charges in feed stream concentration. While these may be clamped to some degree by the Active Gas Handling System, major fluctuations will occur and it is to be expected that about 12 hours will be necessary to approach a steady state. Therefore, stability and ease of control of the isotope separation system must be of major concern to JET.

A drawback of scheme 2 lies in the control of the system. As both the DT and HT recycle loops feed into column B, an upset in either loop will induce an upset in the other loop. This can significantly increase the time to steady state after a change in operating condition.

The first scheme is also subject to these same reservations but to a lesser degree since the recycle flows are smaller.

The third scheme is by far the easiest to control since each of the 2 recycle loops are effectively decoupled and well established control procedures may be utilized. The trade off is a somewhat larger tritium inventory.

Currently, gas chromatography is used for analytical control of many cryogenic distillation systems. This is really an unsatisfactory method because of the half hour time delay required to obtain the result. More rapid techniques, such as Raman spectroscopy must be employed to achieve adequate system stability.

References

/1/ "The JET Active Gas Handling System: Concept and Status" IEEE 12th Symposium on Fusion Engineering Paper 34-02 - J L Hemmerich.

/2/ "Cryogenic Hydrogen Isotope Separation for the Fusion Fuel Cycle" Fusion Technology, 8, 2175-83 (1986) - R H Sherman.

/3/ "Private Communications" - A Dombra.

/4/ "Cryogenic System #2: Isotope Separation Systems Design for JET" Report TTF-R-4. August 1987. This is an unpublished report with the source of copies being "Scientific Document Distribution Office", Atomic Energy of Canada Limited, Chalk River, Ontario, K0J 1J0 - A E Everett, V Goyette and A L Miller.

FRONT END EMBEDDED MICROPROCESSORS IN THE JET COMPUTER-BASED CONTROL SYSTEM, PAST, PRESENT AND FUTURE

CA Steed, H van der Beken, ML Browne, K Fullard, JET (UK),
K Reed, M Tilley, System Designers (UK), V Schmidt, RFX Padova (I),
JET Joint Undertaking, Abingdon, Oxfordshire OX14 3EA, England

SUMMARY

A brief history of the use of Front End Microprocessors in the JET COntrol and Data Acquisition System (CODAS) is presented. The present expansion in their use from 2 or 3 in 1983 to 27 now, is covered along with the reasoning behind their present usage.

Finally, their future planned use in the area of Remote Handling is discussed and our present views on the use of Front End processing in future large distributed control systems are presented.

1. INTRODUCTION

The computer based Control and Data Acquisition System (CODAS) for JET is based on the use of a hierarchical distributed system of NORSK DATA NORD-100 and NORD-500 computers. From its early conception [1] the use of intelligent front end microprocessors was always envisaged, however, when the early system became operational in July 1983 only three applications were in use, namely that of the waveform generator task used to control excitation of the flywheel generators, gas inlet dosing valves and to provide waveforms used by the analogue control system for Plasma Position and Current Control and two low level multiplexer applications.

It is intended in this paper to try to present the current position in terms of microprocessor applications both implemented and planned and, in so doing, to explain the rationale behind the heavy use which is now being made of microprocessors and to try to draw some conclusions based on our present and planned use, of particular relevance to the implementation of such large distributed control systems in the future.

2. GENERAL

The JET computer based control system (CODAS) is shown schematically in Fig 1.

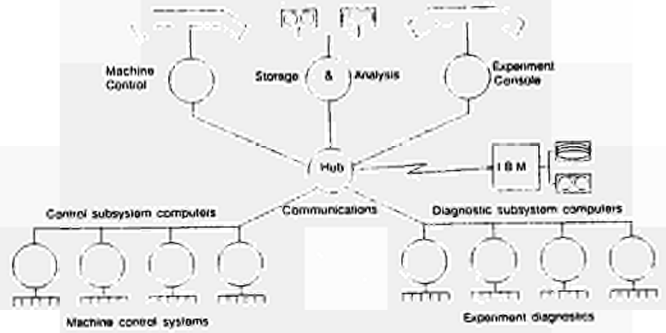

Fig 1 CODAS Computer Organisation

The design and implementation of CODAS has been described fully elsewhere [2] and will therefore only be covered briefly here. The operation of JET requires the fully integrated control of more than 20 computers. These computers are configured hierarchically and are all connected via a communication hub computer. The overall control of JET is divided functionally, vacuum, general services, toroidal field power supplies, etc and one computer is assigned to each function or subsystem. Each subsystem computer controls a CAMAC serial highway and all interfacing to experiment hardware is done through CAMAC crates distributed along this serial highway, which in some cases is in excess of one kilometre in length. Since the interface between the experiment hardware and the CODAS system is based entirely on the use of CAMAC, the front end microprocessors in use within CODAS are intelligent programmable CAMAC Auxiliary Crate Controllers (ACCs) based on the Texas Instruments TMS99000 series microprocessor. The use of this ACC serves five main purposes:

1. It allows the various applications to take advantage of the wide variety of available CAMAC I/O Hardware and, indeed in many cases, to share signals with software running on the subsystem computers.

2. It provides a ready-made two-way communication path at high speed via the CAMAC dataway and serial highway into the subsystem computer. This communication path is made use of both in downline loading of programs and data into the microprocessor memory and in ON-LINE monitoring of subsequent operations.

3. It allows data to be presented in a uniform way to other general purpose tasks running on the subsystem computers. These tasks include mimic displays, trend curve presentation, data logging, etc.

4. We are able to separate in these applications the real time aspects (front/end) from the general purpose computer operation.

5. The ancillary burden of handling special protocols and data formats can be removed from the subsystem computers.

The number of front end microprocessor applications in use on JET has grown from the initial applications in 1983 running on 8 ACCs to the present level of 27 different applications running on more than 50 ACCs.

3. Software Support and Engineering

As stated earlier, all our microprocessor applications have been based on the use of Texas Instruments TMS99000 incorporated into a CAMAC module. This has enabled us to concentrate our software support on this microprocessor (see Fig 2).

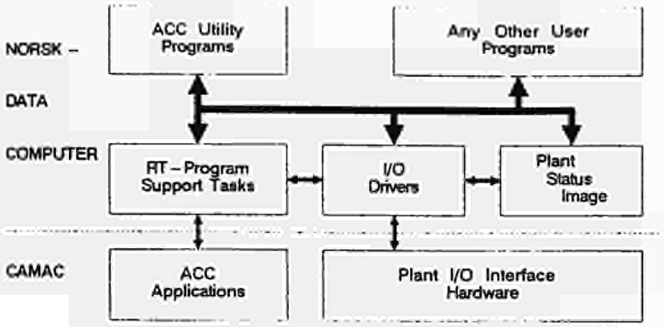

Fig 2 General Software Environment

Facilities provided within our environment are:

- Cross software support, developed at CERN, running on the NORSK-DATA NORD-100 computers including: Cross assembler, linkage editor, librarian, pusher for down line loading, and software for ON-LINE debugging via the CAMAC serial highway.
- A basic Real-time monitor for the ACC which controls one or more tasks executing in its memory as well as conversion routines and communication mechanism with the NORD-100.
- System routines allowing Real-time programs running on the NORD-100 to communicate with tasks executing in the ACC using a Mailbox technique with fixed pointers to buffer areas and trigger words held in the high part of the ACC memory, directly addressed by CAMAC commands from the NORD-100 programs.
- A simple "High Level Language" which compiles easily into the TMS99000 assembly code but which allows fast coding of applications and use of libraries whilst producing efficient assembly code, trapping many of the more common syntactical errors at the compilation stage.

4. APPLICATIONS

Low Level Signal Multiplexer

This application was developed to allow the handling of the very large number of thermocouple signals (700) distributed around the JET vacuum vessel and its various attachments. The control of the multiplexer hardware and DATRON digital voltmeter including cold junction compensation, was done within this processor. The calibrated data was then put into a standard format for access by all other software on the subsystem computers. This formed an important part of the bakeout control software for the vacuum vessel.

Waveform Generators

This application was one of the first implemented and involves the generation of waveforms, using either digital to analogue converters or just digital outputs, for excitation of the flywheel generators or for controlling the inlet gas flux into the vessel in real time for density feedback control.

Lidar Thomson Scattering Diagnostic

This diagnostic is a Thomson scattering system based on the time of flight or Lidar principle. The scattered light is dispersed through a six-channel polychromator onto photomultipliers where signals are recorded and digitised by fast (800MHz bandwidth) Tektronix 7912AD transient digitisers. These are interfaced to CODAS through an IEEE488 interface. For every laser pulse, each 7912 module will acquire data which needs to be read out before the laser pulses again. With a cycle rate of 2 secs between laser pulses, a microprocessor is needed to control the read out and storage of this data.

NORD to Micro-VAX Data Link

The Pellet injector hardware provided by the Oak Ridge National Laboratory is controlled by a DEC micro-Vax computer independently of the CODAS system. There is a requirement, however, to transfer data between the micro-Vax and the CODAS subsystem computer for collection and archiving during a JET pulse. To do this, a parallel data link is implemented under control of a microprocessor which once again handles the buffering of data thus allowing access by standard software running on the CODAS computers.

Residual Gas Analyser Control

This application illustrates well our present use of Front End microprocessors in two main areas:

a. Preprocessing of data into a standard format compatible with standard CODAS software running on the subsystem computers.

b. Intelligent handling of instruments and additional data collection hardware to allow more efficient spectrum scans.

The Balzers QDP101 mass spectrometer controller uses a DEC LSI-11 microprocessor. This is programmed to provide all local control of the mass spectrometer and additionally, via a serial RS232 link, provides facilities for the spectrometer to be controlled via a terminal or host computer. In the initial implementation, the CODAS control of this instrument was performed only through this serial link and using software running on the subsystem computer. This approach, however, had two major drawbacks:

a. Handling spectrum scans and transferring data through the serial link alone resulted in a mass scan taking approximately 5 minutes.

b. The software handling the mass spectrometers imposed an unacceptable CPU load when extrapolated to the simultaneous handling of 5 instruments.

For these reasons, it was decided to embark on the use of an ACC devoted to the control of each instrument and to use alternative hardware for collecting the mass scan data allowing the operation of the mass spectrometer in a faster mode which is not available through the serial link. This new approach is shown schematically in Fig 3.

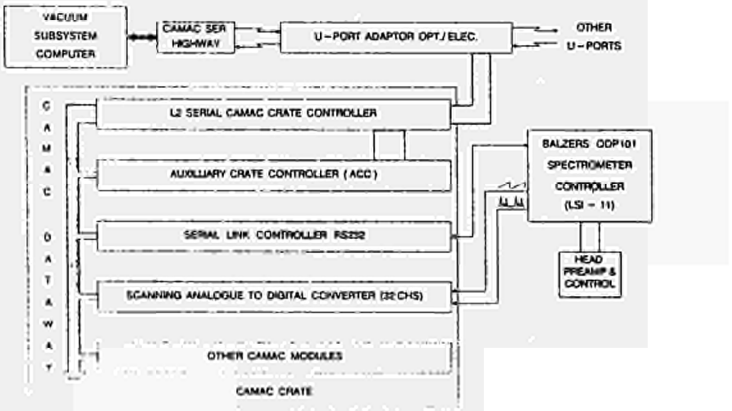

Fig 3 RGA Mass Spectrometer Schematic

The ACC is used to handle all serial link communications and, in addition, to control the spectrometer as if the QDP101 were driving an X-Y plotter. The plotter outputs for mass and intensity are then routed to analogue to digital converter channels which are sampled by the ACC synchronously with the spectrum scan and the data stored in the ACC memory. This approach allows a mass scan to be taken in a few seconds (5-15) which would previously have taken 5 minutes. In addition, the data for the last scan is always available until a new scan is completed (double buffered) thus a spectrum is made available for display on the subsystem computer without delay.

Plasma Control and Protection Systems

It is in this area of JET that the most significant changes are taking place, involving the use of many front end processors; these are shown schematically in Fig 4. When operations began in 1983, all feedback control of plasma current and position was performed by analogue methods. Whilst all the control systems implemented for control of plasma current, radial and vertical position, operated quite satisfactorily, it quickly became apparent that a number of problems existed. These problems were mainly concerned with the required flexibility of operation as different configurations of field coils and turns ratio were used. The result was a need to hold many different electronic modules with modified components selected for the configuration in use. In addition, the scope for errors increased with the increasing number of modules. In order to simplify the situation, it was decided to investigate the use of digital feedback control for the current in the poloidal field (PI) coils and the plasma. This system was implemented using an ACC and is described in detail in [3]. A number of significant improvements were incorporated:

a. The number of non-standard electronic modules used in the implementation were greatly reduced, most of the functions now being performed within the microprocessor.

b. The various reference waveforms previously used were all embedded within the same program thus avoiding the requirement for separate waveform generators.

c. With the availability of buffer memory within the microprocessor application it was possible to incorporate the facility to store diagnostic information to enable rapid diagnosis of hardware problems which may occur and to perform some level of data validation in real time to protect against erroneous operation, ie cross-checking output waveform values for validity.

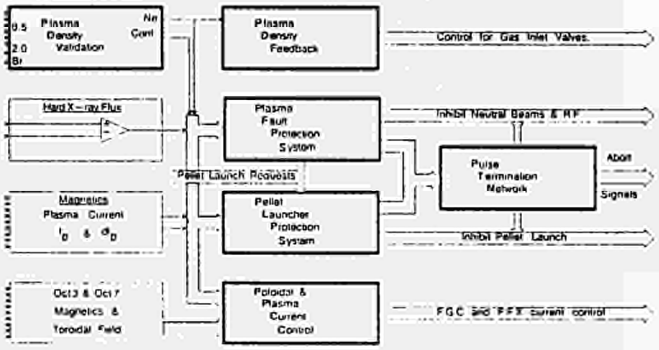

Fig 4 Plasma Control and Protection Systems

Further applications under consideration include the replacement of the present analogue control of radial position of the plasma. The diagram in Fig 4 shows the present microprocessor applications implemented or in the process of being implemented, highlighted by bold black boxes. A detailed description of each individual application is outside the scope of this paper and for detailed information the reader is referred to Refs [4, 5, 6]. To summarise the present position, however, the two Plasma protection systems PFPS and PLPS are provided to protect the JET machine against the possibility of injecting either beams of neutral atoms or high velocity pellets of deuterium, when plasma conditions are such that to do so would cause severe damage of the vessel wall opposite the injectors. Towards this end both microprocessors maintain an active pulse train at 1kHz only if a) the measured plasma density is above a threshold value for injection of neutral beams in the case of PFPS and b) if the measured electron temperature in the plasma is such that the ablation length for the deuterium pellet is less than the plasma width, for the pellet launch protection system PLPS. Additionally, other checks on plasma current, Hard x-ray flux and rate of change of plasma current provides protection against other adverse effects within the plasma. Any of these effects detected will result in the change in pulse train frequency to 0.5Hz. This use of an active pulse train for control purposes enables detection of all but very obscure failure modes within the microprocessor and provides a very high level of fail-safe operation.

Since the reliable operation of these two systems relies heavily on the use of measured plasma density, in order to carry the level of reliability and fail-safe operation through to these diagnostic signals whilst not at the same time losing too much operation time, particularly when pellets are injected, the Plasma density validation application is used to provide an analogue density signal validated from a combination of up to 3 input signals selected from 7 possible signals, and a confidence signal which may be high, low or invalid depending on the degree of match found between the selected input signals.

Finally, if the PFPS or PLPS system detect a serious abnormality in the real time plasma signals, it is desirable to try to terminate the plasma in a controlled way without causing a disruption. Towards this end a hardwired system of logic is implemented, known as the Soft or Pulse Termination Network. This system takes a variety of input signals and after applying appropriate conditioning logic closes down parts of the JET system in a controlled manner. The logic currently used in this network is shown in Fig 5.

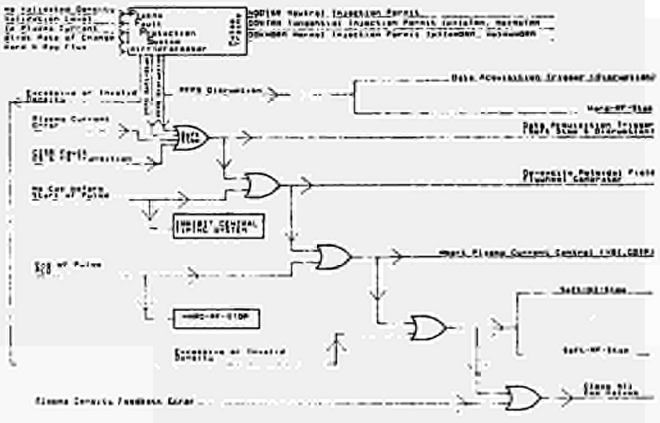

Fig 5 Pulse Termination Network Logic

Once again, the problem of flexibility whilst retaining operational reliability have been found to be apparently conflicting requirements in this

hardwired system and making changes to the logic as required during operations can be dangerous. The logic of this network is again, therefore, being replaced by a microprocessor application as indicated in Fig 4. The logic will be hard coded into the application but in a way which enables it to be changed with a minimum of effort and without any change in the hardware. Also the active pulse train approach will be adopted and will allow a gradual changeover in the operation of all hardware connected to this network in a controlled way to take advantage of the improved reliability and fail-safe operation.

Remote Handling Application

Perhaps the heaviest combined use of Front End processors by CODAS is in the area of remote handling.

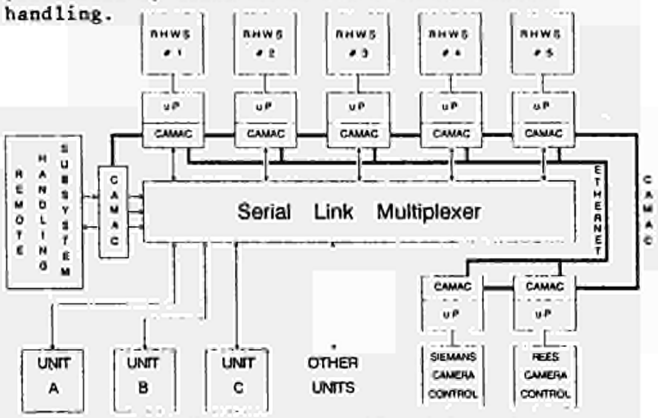

Fig 6 Remote Handling Schematic

When JET finally moves into the Tritium phase of operation, all maintenance operations on the experiment will have to be done using remotely controlled transporters and manipulators. Towards this end, therefore, a remote handling control room is being prepared to allow operation of this equipment [7]. Control of any single system hinges around the use of a remote handling workstation (RHWS) which, by means of monitor screens, touch panels, switches and closed circuit TV cameras, will allow the operator to perform all the necessary tasks. Each transporter will be provided with a local control unit which will be connected to the host computer via a serial RS232 link. The problems to be solved in the control of these transporters from the workstation are as follows:

a. Each workstation may control any of the available units.

b. A response time of 200ms is required from any operation on the workstation to visual feedback confirming execution.

Requirement b. above precluded the use of the general purpose subsystem computer and it was therefore decided to use a microprocessor application with the remote handling workstation built around a CAMAC crate using the same design philosophy as that adopted for the CODAS control room consoles and mobile control consoles. The main difference being in the incorporation of a CAMAC ACC to provide real time control of most of the features of the workstation. The customisation of the individual workstations to the transporter under its control being implemented by the ACC program. This means that requirement a. can be met by using the subsystem computer to control the RHWS customisation by down loading the ACC memory through the CAMAC serial highway with the application program required. The overall schematic in Fig 6 shows the general approach. As well as loading the appropriate application the subsystem computer selects the relevant serial link via the multiplexer to the system to be controlled and all subsequent operations are then handled by the ACC directly to the transporter local control unit. The remote handling workstation customisation will result in 7 separate microprocessor applications.

Two additional applications are implemented to allow real time control of closed circuit TV cameras. These are of two classes, those which are fixed at many different positions around the Torus Hall and basement (SIEMENS) and those which are mounted on the manipulators or transporters and are used to provide visual feedback during operation (REES). Each of these controllers must also be connected to each workstation in order that any workstation may control the cameras relevant to the transporter under its control. In this case, however, the connection is between the two ACC camera applications and the workstation applications and it was therefore decided that, in order to minimise the point to point connections that would have been necessary had a serial link been adopted for communication, a local area network (LAN) based on ETHERNET should be used.

5. CONCLUSION

In the four years since the start of operations on JET, the overall trend in the use of front end microprocessors has followed two main paths. The first has been in the use of front end intelligence to a) reduce CPU load on the subsystem control computers, whilst at the same time b) acting as a general translator in handling the very wide and varied link types, RS232, IEEE488, parallel links and the equally varied protocols in use in the different local control equipment and converting these to a standard form acceptable to general purpose software on the host computer. The second path has been in the expansion in the use of loosely linked applications as seen in the control and protection systems and even more closely linked as in the Remote Handling control system, which provides a level of autonomy at the microprocessor level whilst retaining supervisory control within the subsystem computer.

Our experience on JET indicates that this latter trend towards more autonomy at the front end microprocessor level must be an essential consideration in the design of future large scale control systems and it should also embody, wherever possible, the real-time validation of operational parameters and set points as lying within permitted limits both from the point of view of equipment and personnel safety as well as contractual obligations as for example in controlling the turn on and off of Neutral Beam and RF generators to avoid exceeding permitted transient loads on the National Grid.

6. REFERENCES

[1] The JET Project EUR-JET-R10, EUR 6831

[2] CODAS: The JET Control and Data Acquisition System, H van der Beken et al, Fusion Technology, VOL II, Number 1, January 1987

[3] Plasma Position and Current Control, K Reed, JET Divisional Note JDN/H(86)28

[4] Plasma Density Validation specification, SB Parker, K Reed, JET Divisional Note JDN/H(86)16

[5] Real Time Plasma Fault protection system for JET, A Gondhalekar et al, 13th SOFT, Varese (1984)

[6] The JET Pulse Termination Network, J How et al, 14th SOFT, Avignon (1986)

[7] An Integrated Control System for Remote Handling Equipment at JET, A Galetsas, A Rolfe, CA Steed, 12th SOFE, Monterey (1987), Paper 06-04

Testing of Beam Stopping Elements Using Hypervapotron Cooling

R B Tivey, H D Falter, R Haange, R S Hemsworth,
P Massmann, A Stäbler*.

JET Joint Undertaking, Abingdon, Oxon, OX14 3EA.

* IPP D8046, Garching, FRG.

ABSTRACT

Beam stopping elements using the hypervapotron cooling technique have been tested by JET to evaluate their peak power and total power handling capacities.

INTRODUCTION

Neutral beam injection systems require beam stopping panels to act as dumps for the unwanted unneutralised ions (ion dumps) and to act as scrapers to correctly shape the neutral beam so that it fits through the injector ports into the torus [1]. Because of limited space in the beamline the angles to which the surfaces intercepting the beams can be inclined are restricted, giving rise to high power densities on the beam stopping elements of ~ 10 MW/m². The hypervapotron structure developed by Thomson CSF of France for the cooling of their cylindrical anodes in power tubes, was chosen as the basis of the JET beam stopping element [2,3].

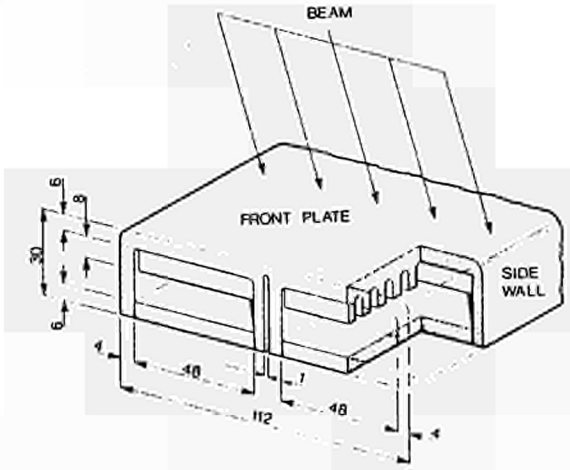

Fig 1: Schematic showing JET hypervapotron geometry

DESCRIPTION OF THE JET BEAM STOPPING ELEMENT

JET have adapted the 'hypervapotron' cooling technique to the rectangular geometry of their beam stopping element shown schematically in figure 1. This type of geometry is more suitable for use as a 'building block' for the various structures handling high specific heat fluxes within the neutral injectors. The beam stopping elements have been fabricated from a solution heat treated CuCrZr alloy (1.0% Cr, 0.07% Zr) using electron beam welding and then precipitation hardened at 480°C for 2 to 3 hours, to achieve both high strength and high thermal conductivity. The mechanical properties are:

Ultimate tensile strength	> 300 N/mm²
0.1% yield strength	> 200 N/mm²
Rupture elongation	> 15%
Thermal conductivity	> 333 W/m°k

The fin structure of the hypervapotron creates a stable boiling heat transfer into the water for very low flow velocities (3 m/s) and hence requires a low driving head. Optimisation of the fin geometry leads to a 3 mm wide fin alternating with a 3mm wide 8mm deep slot [4].

A 6mm plate in front of the fin structure includes a 1 mm allowance for sputter erosion. The heat capacity of this front plate provides a useful safety feature of the hypervapotrons. Thermocouples are positioned in the central web 3 mm below the surface of the front plate (see Fig 2).

The 250 beam stopping elements of the JET beamlines are operated with coolant flow velocities of 2.5 to 3.5 m/s, and coolant static pressures of 5 to 7 bar.

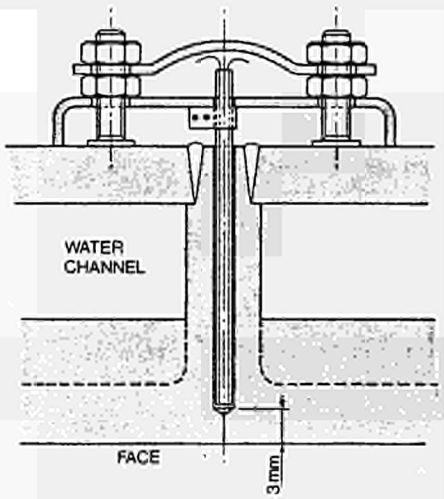

Fig 2: Schematic of thermocouple in the central web

The specified operational temperature limits monitored by the thermocouple is 400°C. This limitation is imposed to avoid over precipitation of the copper alloy and the consequent degradation of the mechanical properties of the copper.

A design study carried out by Thomson CSF for JET gave the peak power limitation of the hypervapotron structure as 20 MW/m², and stated that coolant velocities should not exceed 3 m/s [4].

The mechanical design and manufacture of the JET beam stopping element is discussed in detail in [2, 3].

INITIAL TEST ON JET HYPERVAPOTRON

Prior to commissioning the beam stopping elements into systems on the neutral injection beam lines, two elements were tested at LBL [5]. The results of the tests are summarised as follows:

1. An element is capable of intercepting a steady state specific heat flux of up to 15 MW/m². This was for a total power onto the element of ~ 200 kW.

2. The above is true for coolant flow rates over the range used, 2 ℓ/s to 3 ℓ/s, equivalent to 2 to 3 m/s coolant velocity.
3. In order not to exceed central web thermocouple temperatures of 400°C, the peak power limit is 13 MW/m².
4. Flow instabilities observed at inlet pressure of 3.3 bar disappeared when the inlet pressure was increased to 6.5 bar.
5. Apart from the instability at low pressure the hypervapotron action showed no change with variation of the overall flow rate.

TEST OF A HYPERVAPOTRON ELEMENT WITH SIDE LOADING

For a number of beam stopping elements along the beamline in particular in the full energy ion dumps it could not be avoided to have their side walls subjected to heat flux. Because of the design the hypervapotron effect is not expected to occur at the side wall (Fig 1).

An element was installed in the neutral injection test bed so that the angle at which the element intercepted the beam was adjustable. This adjustment was used to vary the loadings on the front plate and the side wall. We have:-
$P_{side} = P_{max} \sin\alpha$ and $P_{front} = P_{max} \cos\alpha$, where P_{max} is the power density measured normal to the beam, α is the angle between the element side wall and the beam axis, and P_{side} and P_{front} are the loadings on the side wall and the front plate.

Element surface temperatures were measured with an infra red camera calibrated by means of 6 inertial copper blocks adjacent to the test hypervapotron. For signals above 600°C the temperatures were extrapolated assuming no change in the emissivity of the copper.

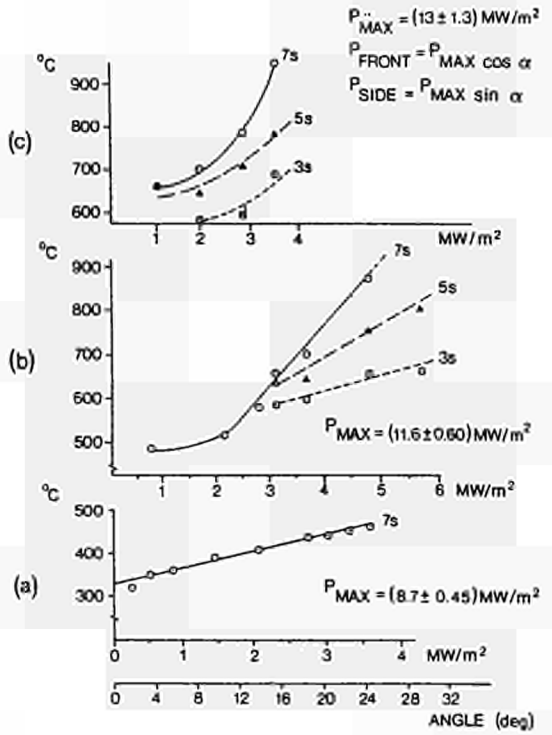

Fig 3: Side load test of the hypervapotron. Peak surface temperatures of the test element as a funtion of the front and side loading.

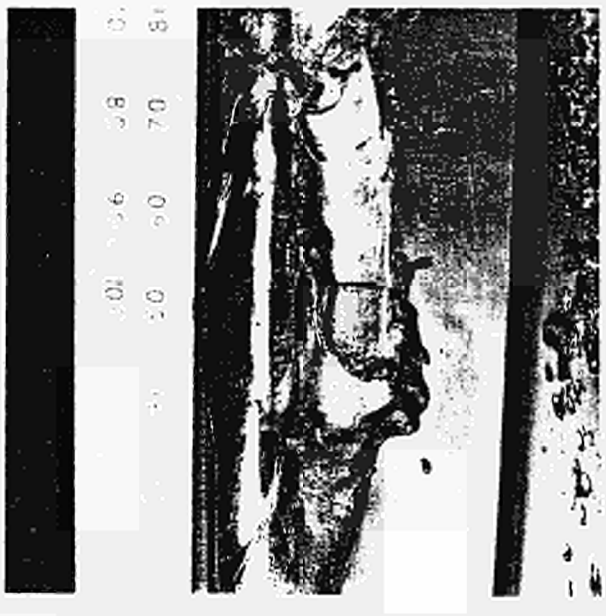

Fig 4: Side load test of the hypervapotron Photographs of the failure due to melting of the exposed radius joining the side wall and the front plate.

Fig 3a shows the measured peak surface temperatures for P_{max} of 8.7 MW/m². For side loads of up to 3.5 MW/m² the element reached equilibrium in 3 to 4 seconds. The peak temperatures were measured on the exposed radius joining the side wall and the front plate. Fig 3b gives the curves for an increased power loading, P_{max} = 11.6 MW/m². At less than 2 MW/m² on the side wall the element reached equilibrium with a maximum surface temperature of 500°C. However for increased values of P_{side} the maximum temperature rose rapidly at the exposed radius and did not achieve equilibrium. When the beam power density was increased further to P_{max} = 13 MW/m², Fig 3c, the temperature rise was more rapid and there was no sign of thermal equilibrium being reached.

Fig 4 shows the failure of an element along the exposed radius. It is estimated that the element was subjected to a front face load of 13 MW/m² and a side wall load of 7 MW/m². Melting of the copper occurred within 1 second of the power being applied.

In conclusion the limit of operation of the hypervapotron with side loading can be summarised as:

where $P_{front} = 13$ MW/m² $- P_{side}$

$P_{side} = 1$ to 4 MW/m².

TEST OF CURVED HYPERVAPOTRON ELEMENTS (MINIDUMP)

As part of a neutral injection upgrade investigation, the full energy ion dump was redesigned to incorporate several features intended to give increased power handling capabilities and improved reliability. A test rig modelling two pairs of beam stopping elements from this proposed dump is shown in Fig 5. The coolant flows through the twin channels of the hypervapotron in series, so called hairpin flow. This has the advantages of halving the total amount of coolant required in a dump. By clamping the elements at the end where the coolant enters and leaves the element the need for bellows is eliminated. According to the Thomson design study [4] the higher exit water temperatures are acceptable providing they remain 10 to 20°C below the saturation temperature.

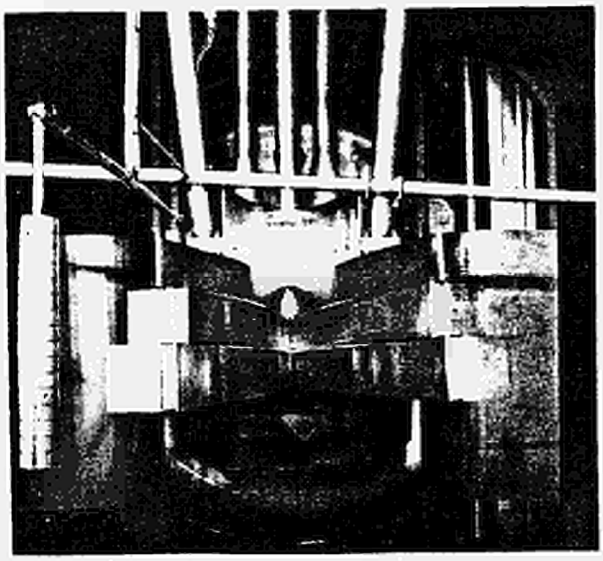

Fig 5: Photograph in the neutral injection test bed of the apparatus for testing the curved hypervapotrons.

Copper inertial calorimeters which were swung into position to intercept the beam during short pulses were used to evaluate the vertical beam profile and thermocouples inserted into the central web of the elements were used to estimate the horizontal beam profile. The coolant return temperature was monitored to give the total power incident on the elements. Linear displacement transducers measured the bending of the element brought about by the high heat flux. Thermocouples inserted through the back plate of the element into the hypervapotron fins at various depths were used to obtain a temperature profile through the fins.

From the testing of these elements the following conclusions were drawn:

1. There is a bend radius of 0.5M/MW/m² along the JET geometry hypervapotron.
2. For a given specific heat flux the temperature of the copper front plate of the element increases with an increase in the total power on the element.
3. Increasing the coolant flow rate reduces the temperature of the front plate, measured over the range of 1.25 to 5.0 m/s. This is contrary to the Thomson CSF prediction.

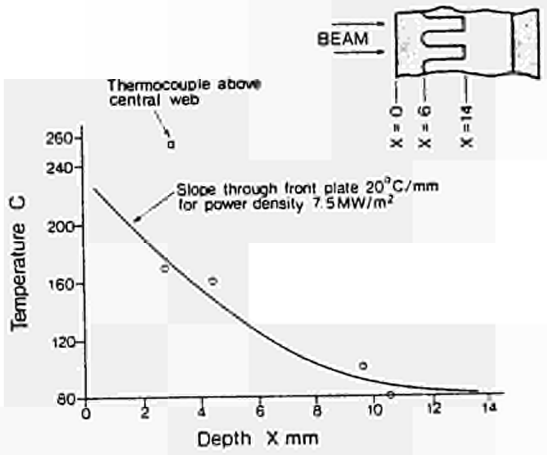

Fig 6: Temperature profile through the hypervapotron fin obtained during the testing of the minidump.

4. The temperature profile obtained through the fins is shown in Fig 6. Significant is the difference in the temperatures recorded by the thermocouple in the central web and the temperature of the copper above the hypervapotron structure.

   This effect was first observed in the testing of the hypervapotron at LBL, see Fig 7. Note that the values shown in Fig 6 for the minidump test are for a total power on the element of ~ 300 kW, whereas those in Fig 7 are for total powers up to 200 kW.

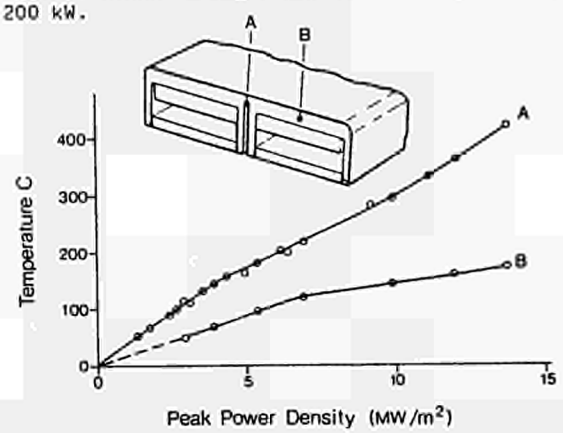

Fig 7: Temperature as a function of power density. Curve A at 3mm below the exposed surface of the element in the region of the central web. Curve B at 4mm +0.7mm below the exposed surface of the element in the region above the hypervapotron structure.

TOTAL POWER TEST OF STRAIGHT HYPERVAPOTRON

This test was designed specifically to investigate the total power handling capability of a beam stopping element. An element was suspended immediately beneath the minidump described above with the element angled to intercept the beam at 15°. The coolant was fed in parallel down the twin hypervapotron channels, the return water from the element was monitored using an ultrasonic flow meter and a thermocouple to determine the total power incident on the elements. Inertial copper calorimeters were used to determine the horizontal and vertical beam profiles. The total incident power calculated using these profiles was in good agreement with the values obtained from water calorimetry.

1. Fig 8a shows the profile of the beam incident on the beam stopping element, the spacing of thermocouples along the 930 mm element, and the direction of the coolant flow.
   Fig 8b shows a plot of the temperature of the element, again 3 mm below the surface of the front plate, against the specific heat flux. It is clearly shown that the points downstream of the peak flux have a consistently higher temperature per given power density than those upstream. Eventually there is a recovery in the performance of the hypervapotron indicated by the coming together of the upstream and downstream curves.

2. In a series of pulses 56 kV, 30A, the test element intercepted 540 kW total power, whilst the coolant flow rate and static pressure were varied. Fig 9 shows that the front plate temperature varies with both the static pressure and the flow rate, i.e. the temperature is a function of 1/PV. This indicates a power limitation caused by the proportion of vapour in the water channel behind the finned structure.
   The curve is for a specific heat flux of 9.4 MW/m².

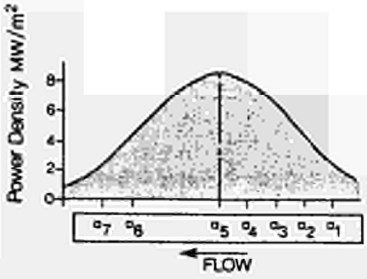

Fig 8a: Schematic showing position of thermocouple with respect to beam profile.

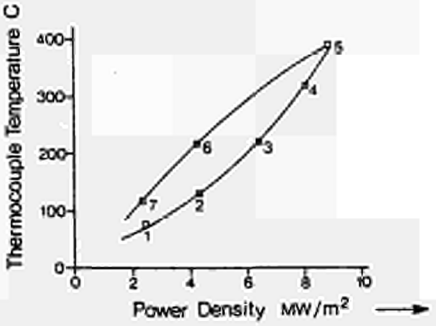

Fig 8b: Response of the central web thermocouples plotted against power density for the beam profile in Fig 8a.

3. The maximum total power applied to an element was 630 kW, with a peak load of 11 MW/m²: with a coolant flow of 4.7 m/s and static pressure of 5.8 bar. The central web thermocouple gave a reading of 530°C. This is well above the 400°C limit at the thermocouple imposed to avoid over precipitation of the copper alloy.

The operating conditions achieved during the test nearest to those occurring in the JET beam stopping elements in the beam line , were at 3.1 m/s and 6 bar where with a total power of 540 kW and peak power of 9.5 MW/m², the peak thermocouple temperature was recorded as 450°C. This suggest that at present the maximum total power the elements in the neutral injector beam lines will handle, without exceeding 400°C at the thermocouple, is < 500 kW with a peak power density of 10 MW/m².

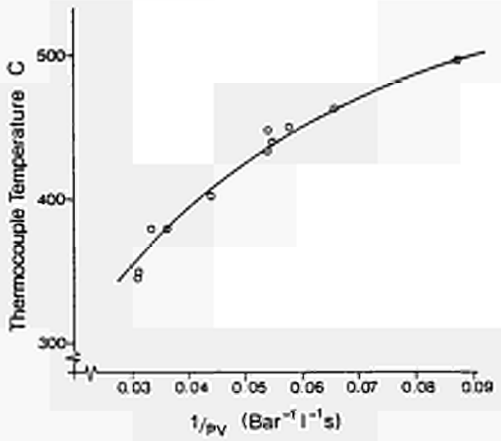

Fig 9: Peak central web thermocouple temperature as a function 1/PV for the coolant.

Table 1: Summary of JET Hypervapotron Tests

Test/Study	Limits
Thomson CSF Design Study	Peak Power ≤ 20 MW/m² Water Velocity ≤ 3 m/s Water outlet temp < T_{sat} -20°C
JET Design	Nominal design peak power = 10 MW/m² Surface temp. < 500°C T/C temp. < 400°C
LBL Hypervapotron Test	Peak power ≤ 15 MW/m² Water Velocity ≤ 2 to 3 m/s Operating Limit Peak power < 13 MW/m² for T/C temp < 400°C
JET Side Load Test	P_{front} = 13 MW/m² - P_{side} where 1 MW/m² < P_{side} < 4 MW/m²
Minidump Test of Curved Hypervapotrons	Indication of total power limitation. Performance improves with water velocity up to 5 m/s Bend radius = 0.5 m/MW/M²
Total Power Test on Straight Hypervapotron	Performance improves with both increased water velocity and pressure ...T/C temp = f(1/pv) At 4.7 m/s., 6 bar element handles 620 KW. T/C temp 500°C. Operating Limits Total power ∿ 500 Kw for peak power 10 MW/m², T/C temp 400°C Coolant 3 m/s and 6 bar.

CONCLUSION

Progress made in defining the JET hypervapotron performance limits is summarised in Table 1. To increase these limits it is planned to:

1) Reduce the proportion of vapour in the main water channel by varying flow rate, pressure and channel size.
2) Evaluate the implications of operating with the copper alloy at a higher temperature than 500°C.

ACKNOWLEDGEMENT

The authors are indebted to G Lundqvist and J Jensen for their input into the design of the test equipment, the JET Test Bed-Team for conducting the tests at JET, and K Berkner at LBL for the initial JET hypervapotron test.

REFERENCES

[1] Duesing G. JET Neutral Beam Injection System, Construction and Components Tests. Proc. 13th Symposium on Fusion Technology, Varese (1984).
[2] Haange R. Components for the Neutral Injection Beam Lines of JET, Proc. Instn, Mech. Engrs. Vol 200 (1986).
[3] Haange R, et al. JET Neutral Injection Beamline System Manufacture and Assembly. Proc. 11th Symposium on Fusion Engineering, Austin (1985).
[4] Thomson CSF. Technical Report to JET Contract JC 110 VHXX. Application of Hypervapotron Techniques to source of the JET cooling problems. (1980).
[5] Falter H D. Test of Two Hypervapotron Beam Stopping Panels at LBL Berkley. JET Internal Communication (1983).

AUTOMATIC ICRH POWER COUPLING TO ANY PLASMA IN JET

T.J. Wade, G. Bosia, M. Schmid, A. Sibley, JET Joint Undertaking, Abingdon, Oxon, OX14 3EA, UK.

Abstract

A new system of tuning the JET ICRH Plant has been devised, in which the existing system can be automatically matched to large antenna load variations.

Introduction

The JET 32 MW Ion Cyclotron Resonance Heating Plant is rapidly approaching completion. The present power capability of the eight generator-antenna units at the generator outputs is 27 MW and will reach full power when the remaining upgrade of 5 generators from 3 to 4 MW per unit is completed. (Ref. 1).

Each antenna-generator unit can deliver 70-90% of its full power to the plasma if the load presented by the plasma at the antenna is matched to the generator. (The remaining percentage is lost in the transmission line and antenna screen).

Two matching systems are installed. The main system uses one variable tuning stub at the generator together with small frequency variations to match any load to the generator. The second system uses a prematching stub near to the antenna to operate in the region of 34 MHz at low values of antenna load. Its function is to reduce the high voltage and current standing waves and thus the resulting losses

In both matching systems variations of antenna loading outside the design range results in reduction or loss of power from the generator. Recent operations on JET have shown that large antenna load variations are produced by 'H' mode transitions, pellet-injection, the start of neutral beam injection, and RF Eigen modes in the plasma.

A new system of tuning has been devised, in which both tuning systems are combined and adjusted so that RF power can be coupled continuously to any varying plasma load despite these transitions during a pulse. The adjustment to minimum reflection is still performed automatically with the frequency alone correcting the matching, with the stubs remaining in preset positions. The improved dynamic range of this system is approximately a factor 10 in coupling resistance.

The ICRF plant can thus automatically handle the transitions without any discontinuity in the heating power. Additionally no operator intervention is required to readjust the matching elements between shots which range from high coupling resistance in limiter discharges, to very low coupling resistance in X-point or inner wall discharges.

Generator - Antenna Load Matching

Each antenna generator unit can deliver maximum power to the plasma if the coupling presented by the plasma at the antenna ie. the antenna load, is matched to the generator. The RF coupling between the plasma at the antenna, (depending on plasma edge density, position and other factors) presents itself as an impedance at the antenna end of the transmission line, the resistive component of which is transformed into the 'Load' for the generator. If this coupling resistance is low there is a further constraint that under matched conditions high voltage and current standing waves appear on the RF transmission line connecting the generator to the antenna, and the antenna itself.

The maximum specified voltage of the system is 55 kV. It can be achieved but with some difficulty unless under perfect conditions. The routine maximum voltage of 30 kV is readily obtainable, representing 1 MW per generator/antenna per 'ohm' of coupling.

The generator end stage amplifier can produce full power into a load of VSWR 1:1.5 ie. a voltage reflection coefficient of 0.2 with any phase angle. The capabilities of the tetrode itself are somewhat larger to allow for the increased reactive components in the end stage output filter at the frequency band edges. (Ref. 1) The boundaries of the tube's range are set by the anode dissipation of the tube and by the varying high voltage supply. End stops exist at the tube maximum voltage swing and maximum current.

Present Matching Systems Fig. 1.

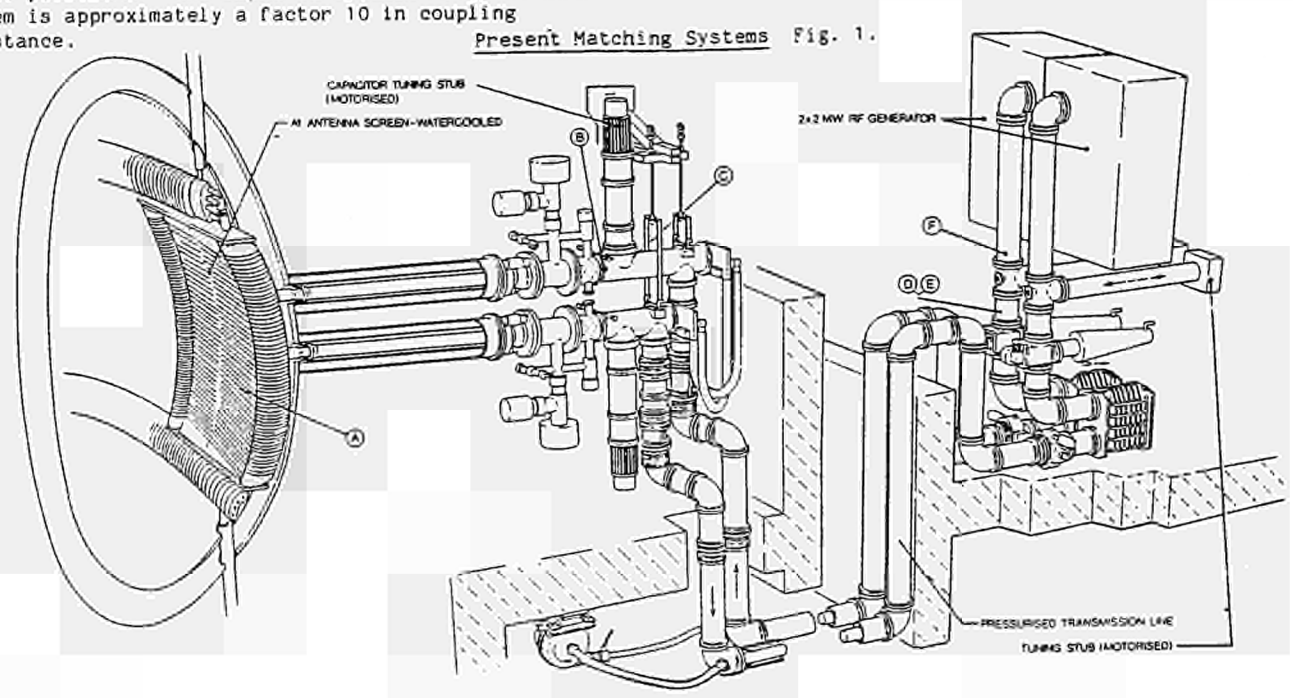

Present Matching Systems Fig. 1.

The JET ICRH plant is housed in an area adjacent to the TORUS hall with 30 ohm coaxial transmission lines connecting the generator to the Antenna. These lines have all been equalised to the same length - some 80 metres each to ensure symmetrical operation.

The plant is equipped with two matching systems:-

1) A moveable inductive stub close to the generator together with precision adjustable frequency allows any impedance presented by the antenna to be matched. The exact tuning frequency is obtained by a frequency control feedback loop. A 50 KHz frequency modulation on the carrier gives bipolar error signal when demodulated, minimising the reflection coefficient (ρ). "a.g.c" on the depth of modulation minimises the deviation when ρ is zero and a match is formed.

The transmission line length of 80 m, some 6.5λ at the lowest frequency, allows a complete reflection coefficient rotation of 2π within 0.9 MHz. Normally $\pi/4$ adjustment is sufficient for any match varying between 0 and 100% reflection.

The matches found are multiples of the line and antennae fundamental resonance, and are thus spaced at ~ 1.87 MHz intervals. These operational frequencies are covered by the almost continuous range of the generators in which the 23-57 MHz is divided into 8 channels each 4 MHz wide.

A second 'pre-matching' stub can be installed at the antenna to reduce the high standing wave on the line thus reducing losses and high peak voltage and currents in the case of low coupling to the plasma. However, unlike the generator stub its use is limited to two close frequencies near 34 MHz, a figure determined by its position some 2.6 metres from the antenna. More recently this fixed stub has been terminated with a high performance variable vacuum capacitor capable of providing adjustment during operation (Ref. 2). These two stub systems are independent in action.

The generator stub and frequency can be adjusted for optimum at any time during an operating session, normally at the beginning. If the preset parameters of the plant have not been previously ascertained, a frequency sweep is applied on a low power pulse with a plasma load on each generator, from which the optimum stub length and frequency are obtained. From then on, the automatic frequency control is used. The stub needs re-adjustment at higher powers since antenna coupling or loading is power dependent. The fixed prematching stubs however, initially had to be predetermined with some accuracy to match a predicted plasma coupling, as they could not easily be adjusted.

Experiments to improve this situation, to widen the acceptable range of plasma couplings that could be matched without stub adjustment led to be the development of a new system, dependent only on varying the frequency to adjust the match to varying load.

The wide range matching system

Instead of using the antenna prematching stub for perfect matching to one load value, it is set instead to obtain a 'partial match' VSWR bewtween 4:1 and 7:1 with the property that load variations either side of this value of coupling are transformed to variations in the phase of the reflection coefficient, ρ whilst its modulus remains substantially constant.

A small variation of frequency by the existing frequency matching system either side of the transformation allows a range of impedances of factor 8 or 10 to one to be matched to within the VSWR 1.5 circle at the generator by one value of the generator stub.

The antenna is modelled as a variable load at the end of the antenna line. Fig.2. The antenna line therefore consists of the vacuum feed through line (Zo=30 ohm) plus the actual antenna's equivalent length in 30 ohm line. (The series of various JET antennae have all in fact been different physical configurations, with different equivalent lengths. see Ref.3

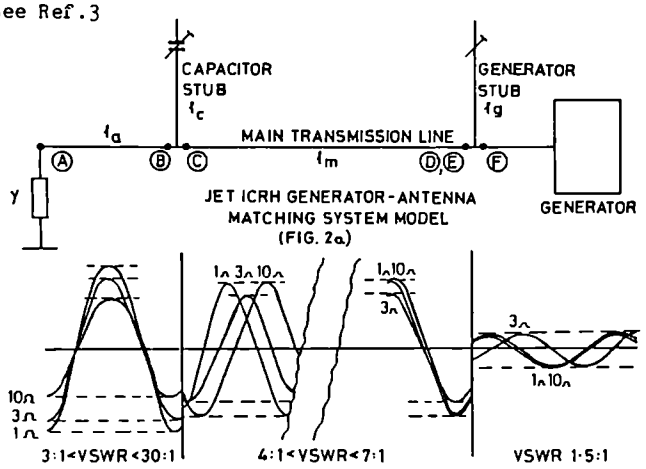

VSWR AT VARIOUS POINTS ON THE TRANSMISSION SYSTEM (FIG 2b)

Plotting the transformation on a Smith Diagram Fig.3a, a range of coupling impedances A-A' (1-10Ω) measured at the antenna is transformed as follows:

- B - B' before the capacitor stub,
- C - C' by the stub (this operation is substantially independent of small frequency changes),
- D - D' at the generator stub which collapses to the range
- E-Em-E' by changing frequency and hence the electrical length of the long line.
- The generator sees F-Fm-F'

The corresponding variation and phase of the voltage standing wave along the line is shown in Fig.3b, and the change in frequency with load in Fig.4.

The analysis of this transformation is given in appendix A

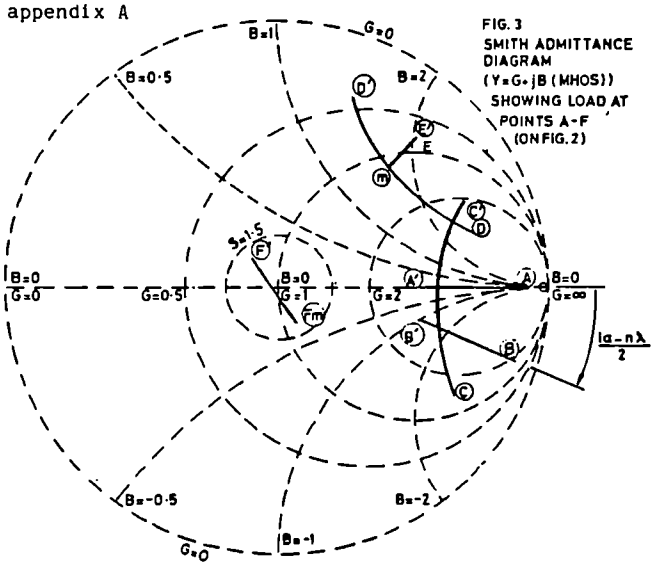

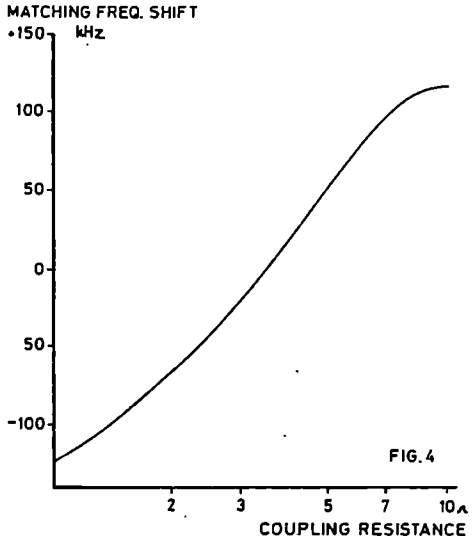

Fig.5 Antenna Stub Positions, Frequencies and Performance.

la	Frequency	M	N	Cap or ind	Comment	Dynamic range of complete system
4.419	0.356E+08	19	1	C	Existing	0.9 - 11 Ω
4.470	0.319E+08	17	1	1	Position	1.2 - 10 Ω
2.223	0.374E+08	18	3	C	Near	
2.347	0.480E+08	23	4	1	Torus Hall	
12.350	0.249E+08	12	2	C	Floor	
18.472	0.410E+08	18	5	C		1 - 12 Ω
18.514	0.571E+08	25	7	C		1.2 - 10 Ω
18.586	0.319E+08	14	4	1		- 1.5 - 10 Ω
18.598	0.480E+08	21	6	1	In	- 1.3 - 8.5 Ω
18.840	0.481E+08	21	6	C	Basement	
18.903	0.551E+08	24	7	1		
18.950	0.320E+08	14	4	C		
19.019	0.390E+08	17	5	1		

At present the stub position at the torus allows two close operating frequencies with the present A1 antenna, of 32 and 36 MHz in Monopole. In dipole these are approximately 2MHz higher. Referring to Fig 2, so long as the antennae line length la is short compared with the main transmission line length lm, multiple positions exist at which a prematching stub can be placed to accommodate more than just one frequency. The antenna line and the antenna stub act as a transformer from load variation to phase variation. The length of the antenna line to the first stub to perform the transformation, and the length of the main transmission to match this must add up to a constant - the existing installation. Both these quantities as a function of frequency are given in appendix A. A table (Fig.5) lists possible antenna stub positions, in order of distance from the antenna. A wideband match can be found within a tolerance of approximately ± 200 KHz at each frequency, thus each potential stub position will perform the wideband matching at a number of frequencies (adjacent on the list) which increases with the distance from the antenna. However, the dynamic range decreases as the antenna line length become more frequency sensitive.

Examining the existing installation (in which the practical layout of all apparatus around JET has to be considered) a position can be found in which the electrical length (in wavelengths) of antenna line to the prematching stub is equal in all 16 cases.

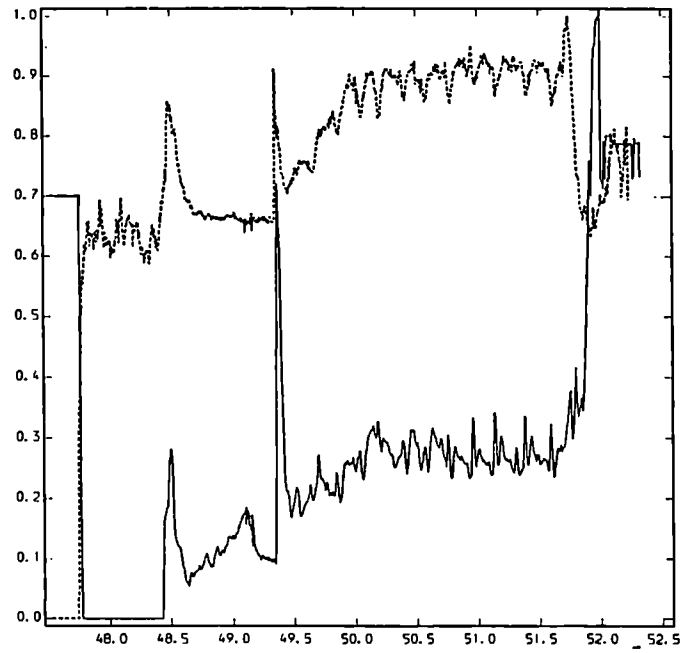

Pulse N° 11130
Fig. 6
—— Variation in coupling resistance R_c measured on Gen 6B (0-12.6Ω)
--- Variation in matching frequency of Gen 2B (-200 kHz to + 100 kHz)

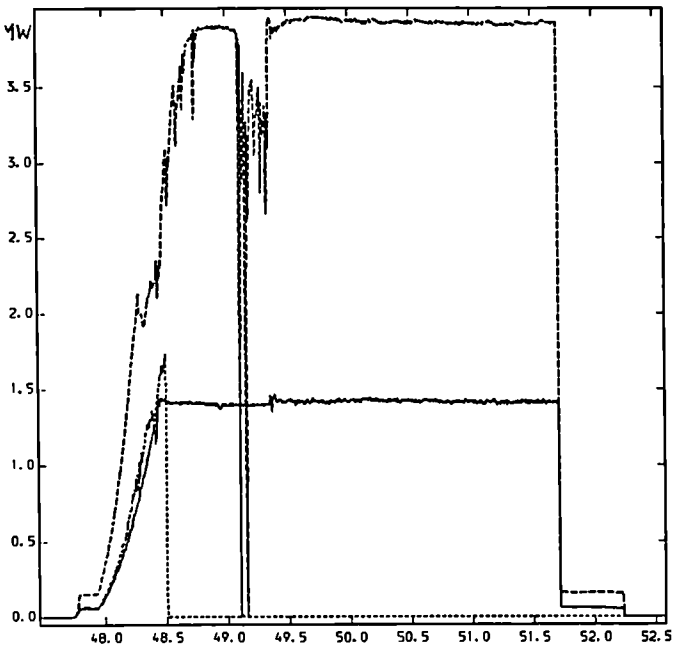

Fig. 7
—— Gen 2B power output (unaffected by R_c change)
... Gen 2D power output (tripped)
--- Combined output of Gen 6B & 6D on one antenna (note some effect of R_c change, buffered by combining unit)

Experimental results with Existing antennae prematching stub position

Tests of the system on JET have shown the improvement in generator tolerance of varying loads. For comparison generator 2B was equipped with additional stubs (Figs. 6, 7, 8.)

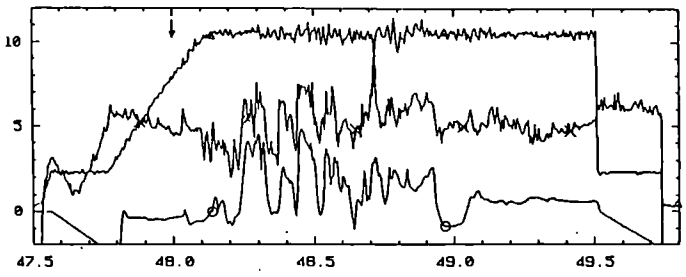

Pulse N° 11140
Fig. 8. ↓ Injection of pellet
X Variation in coupling resistance measured on Gen 2D (0.5Ω/div)
Ø Variation in matching frequency of Gen 2B (40 kHz/div)
Δ Output of generator 2B (low power only)

Conclusion

Antenna load variations outside the instantaneous matching range of the JET ICRH generators cause a reduction or total loss of heating power during the pulse.

Calculations and experimental results at 32 MHz have shown that a substantially wider dynamic range of matching (factor 8 - 10 in antenna loading) can be set up within the existing plant using both generator and antenna stubs in combination, to operate at 32 - 36 MHz. (Used for B_T=3.4T with ^{3}He minority species heating).

The antenna stub is used to convert load variations into variation of the standing wave phase on the transmission line which is then corrected and matched by the existing frequency control system, at the generator. The present system is limited to one nominal operating frequency by the existing atenna stub position in the transmission line.

An alternative positon for the antenna stub will enable the system to be operated at several (3 - 4) other frequencies, notably 48 MHz (used for B_T 3.4T with Hydrogen minority species). However the dynamic range may be slightly reduced (Factor 7).

References:-

(1) The Technology of the Upgrades JET ICRF Heating System. T.J. Wade et al. 7th topical meeting on the Technology of fusion energy. Reno Nevada 1986. Proceedings pp 1398-1403.

(2) Overview of the JET ICRF Power Plant and Development, R. J. Anderson et al. 14th SOFT. Avignon 1986.

(3) Engineering Design of the JET ICRF system. A. S. Kaye et al. 11th SOFE Austin Texas 1985 pp 1204-1209.

Appendix A (refers to Figs 2 and 3)

The antenna normalized admittance y is usually real and equal to $\frac{Zo}{rc}$ at (A).
The admittance before the antenna stub (B) is given by

$$Y_B = \frac{y + j \tan \beta la}{1 + jy \tan \beta la} \quad \text{where } \beta = \frac{\omega}{c} \qquad ..(1)$$

ω = angular frequency
c = velocity of light

tan βla is abbreviated to t.

$$Y_B \text{ becomes } = \frac{y(1+t^2)}{1+y^2t^2} + \frac{jt(1-y^2)}{1+y^2t^2} \qquad ..(2)$$

After the stub
$Y_C = Y_B - jb_c$; b_c = stub suseptance ..(3)

Y_C is of form = g + jb

The reflection coefficient measured at C,

$$\rho_C \text{ is given by } = \frac{g^2 - 1 + b^2}{(g+1)^2+b^2} + j\,\frac{2b}{(g+1)^2 + b^2} \qquad ..(4)$$

ρ_C = u + jv (where u, v are smith diagram coordinates.)

The modulus of ρ_C $[\rho_C] = \sqrt{u^2 + v^2}$.
$= [\rho_D] = [\rho_E]$ if la << lm.

Using the suffix m as a midrange match at the generator stub where gm = 1; bm is given by substitution in Ye.

$$bm = \sqrt{\frac{2[P]_C}{1 - [\rho_C]^2}} \qquad ..(5)$$

The final matched reflection coefficient $[P]_F$ is given by substituting bm
in $[P]_F = \sqrt{\frac{bm - bg}{4 + (bm-bg)^2}}$ when bg is the susceptance of the generator stub. ..(6)

The stub position is given by satisfying (7) and (8)

$$lm = \frac{m\lambda}{2} - 0.068\lambda \qquad \lambda \text{ in metres.} \qquad ..(7)$$

$$la = \frac{n\lambda}{2} \pm \alpha\lambda \text{ where + signifies a capacitive stub..(8)}$$
- signifies an inductive stub

la + lm = 83.8m

Using the values of t that give a reasonable dynamic range of coupling resistance R_c; $0.13 < \pm t < 0.3$

α is in the range $0.020 < \alpha < 0.046$.

m + n is in the range $13 < m + n < 32$
n is in the range $1 < n < 10$

Table 5 gives la, the corresponding frequency, m, n and the sign of α.

CONTROL AND OPERATION OF JET ARTICULATED BOOM

L Galbiati, T Raimondi JET
Joint Undertaking Abingdon
Oxfordshire, OX14 3EA

Abstract

During the 1987 shutdown 32 toroidal limiters and 8 antennae have been installed using the JET articulated boom under visual control.

Trials were done simulating remote conditions. This involved positioning of components up to 350 kg at a distance of 10 m, with 1 mm accuracy.

The boom has 8 main and 11 additional degrees of freedom for 3 TV camera articulated arms.

The control system, microprocessor based, includes teach and repeat and resolved motion facilities.

A dynamic simulation of the boom behaviour, including inertia cross coupling and elasticity of the joints has been validated on the real system.

Introduction

Remote maintenance inside the vacuum vessel is carried out by an articulated boom [1] able to position where required either heavy duty end effectors for handling particularly large components or dexterous force reflecting servomanipulators for more complex operations such as connection of services, bolting, welding and cutting. A quick connection device facilitates the change over [2].

The articulated boom, built to JET design, has been used during the 1987 shutdown to install all belt limiters and antennae with the purpose of gaining experience for the future remote operations. It consists of 5 segments articulating on the horizontal plane. The terminal one can also be tilted to reach the top and the bottom of the vessel and wall (Fig 1). The end effector can reach any part of the vessel from only one entrance port.

The tasks required include the positioning of components weighing up to 350 kg at a distance of 10 m from the first hinge, with a repeatibility of the order of 1 mm.

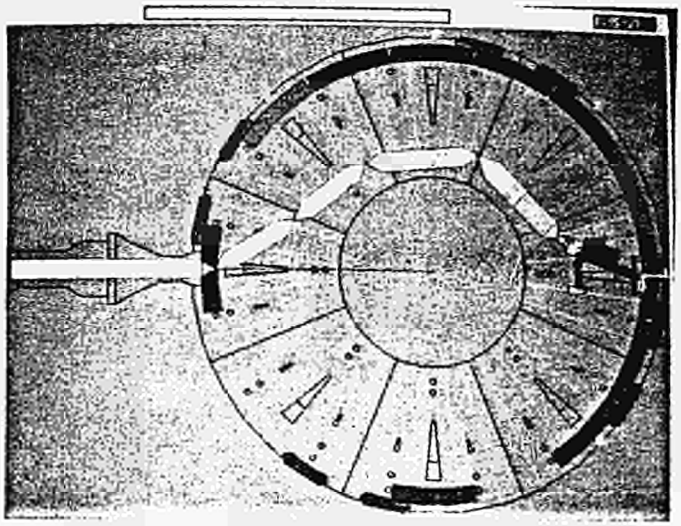

Fig 1 Articulated Boom In-vessel Plan View

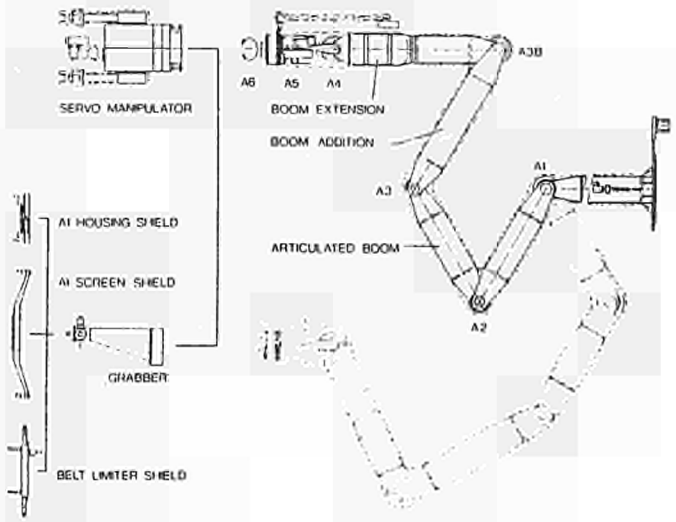

Fig 2 Articulated Boom Equipment

System Description

As shown in Fig 2, the boom consists of 4 motorised joints connected by hollow box sections to a trolley. After joint A3B (see Fig 2) there is a flange where the boom extension is affixed. The boom extension consists of 3 further joints with orthogonal axes, 2 TV cameras on articulated arms and a flange (A6) to which various end-effectors, including the servomanipulator, can be attached.

The control system is microprocessor based (Fig 3) and provides the following functions:

i) Close loop control of all joints, plus open loop control of adjustment jacks and various end-effector motors

ii) Control of the boom from either a Remote Handling Working Station (RHWS) or the local handbox

iii) Safety interlocks to prevent joint runaway, gross servo error, software programmable stops, etc.

iv) Sensor information to both RHWS and handbox

v) 3 modes of operation are available:

   a) Single joint - one or 2 joints can be selected and moved in rate control from a joystick or position control from a keyboard.

   b) A point of reference (POR) connected either to the end effector or other segments of the boom can be defined by the operator and can then be moved via joystick in a rate controlled resolved motion in 2 different preselectable co-ordinate frames. These are:

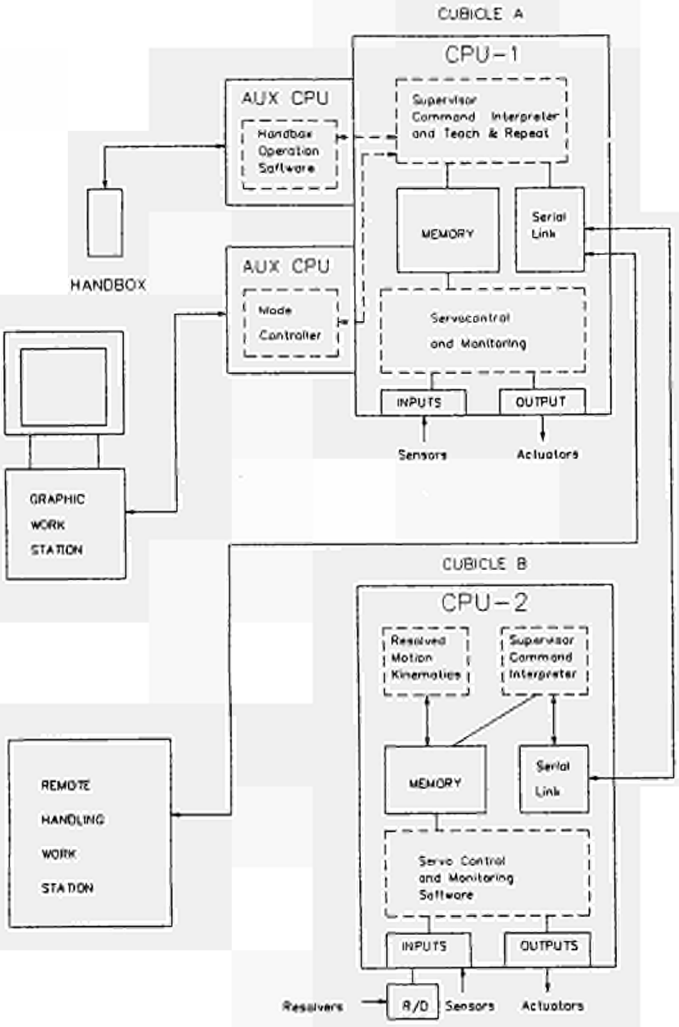

Fig 3 Control System Configuration

- Tool coordinate frame, with origin on the POR and orientated parallel to the relevant segment.

- Global co-ordinate frame, with origin on the centre of the machine and fixed orientation in space.

c) Teach-repeat which allows a previously taught sequence to be automatically repeated.

Each of the main joints A1, A2, A3, A3B, A4 and the translation of the support trolley A0 are controlled with a servo loop configuration shown in Fig 4.

The position error, calculated via software is applied as an input signal to hardwired velocity servo controlling dc torque motors with PWM (pulse with modulation) amplifiers.

The operator interacts with the system via:

- A Remote Handling Working Station, provided with touch screen to select allocation of joints to joystick, rocker switches allocated to various functions, proportional 3 DOF joystick, and 2 colour monitors.

- A handbox, small and portable mainly for commissioning purposes, provided with a 3 DOF joystick. A keyboard allows selection and actuation of all commands and error reports.

- A Graphics Workstation [3], which offers as powerful visual aid showing in real time the position of the boom relative to the environment.

Dynamics

Due to the exceptional dimensions, the inertias of the boom and the elasticity of the joints, dynamic cross coupling between the joints is to be taken into account.

A computer model has been set up [4] and validated. A comparison of step responses of real boom and model is shown in Fig 6. In each of the single joint models (Fig 4), the torque T developed by each gear box depends - through its elasticity, backlash and efficiency in both direct and backdriven modes - on the angular difference Δ between input and output shafts of the gear box.

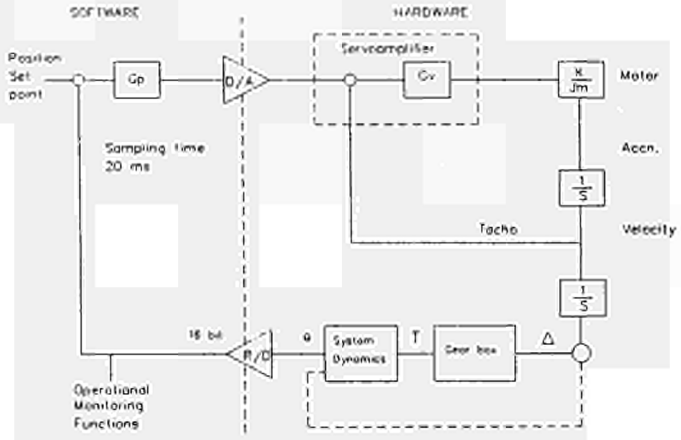

Fig 4 Control Loop Configuration

The single joint block diagrams are reciprocally coupled through the inertia matrix. This has a dimension 5 since only the 5 vertical hinge motions are considered to be relevant.

The computer program used is the CSMP running on IBM computer.

The actuators consist of Harmonic drive gear boxes, directly coupled to Inland DC torque motors, incorporating a DC tachogenerator.

This solution offers the desired compactness for the high torque required, fast response and negligible backlash. This in turn allows the installation directly on the joint of a resolver position sensor, coupled to a 16 bit resolver to digital converter, thus achieving the required repeatibility.

The main shortcoming of the Harmonic drive gear is a certain degree of elasticity. This however offers a beneficial compliance to the environmental constraints, while still achieving a satisfactory dynamic response and can be therefore considered a reasonable trade off.

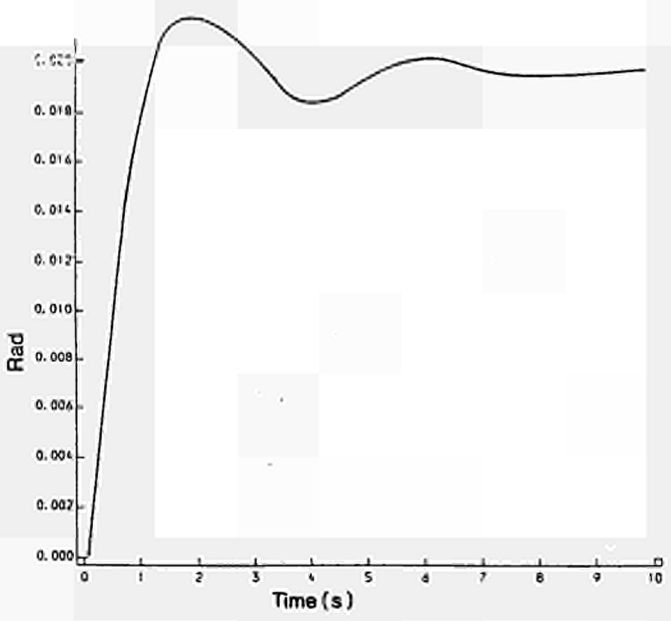

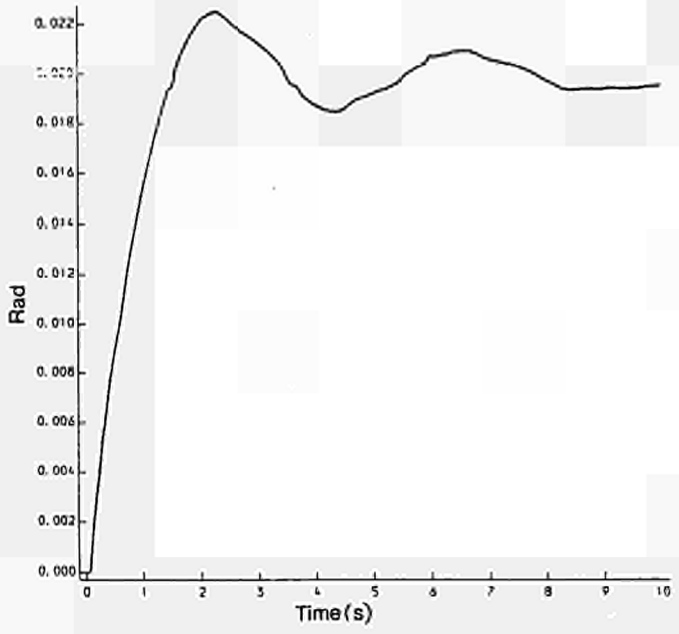

Fig 6 Step Response

Tasks Performed

32 "Belt" limiter sectors and 8 RF antennae were installed, during the 1987 shutdown. Installation was carried out using a "handbox" control inside the vacuum vessel.

Belt limiter installation

The limiters consist of 2 toroidal belts, each of which is composed of interchangeable sectors, each weighing 80 kg located above and below the equatorial plane of vacuum vessel. Each sector is basically a structure of fins welded onto water pipes, with graphite or beryllium tiles mounted in the fin interspaces.

The installation sequence is the following:

The limiter sectors are offered up to the articulated boom by a turret truck approximately 6 m above the floor. It is picked up by the boom end effector, consisting of a "shield" provided with 4 hooks. (Fig 7).

A sequence of movements of the hinges then takes place bringing the boom from the starting configuration through the port and up to the requested position of the limiter in proximity of the wall (Fig 1).

With a tilt motion T combined with a radial adjustment r the limiter then follows a trajectory virtually tangent to the vessel with a precision of $\pm$ 2 mm, so that its cooling pipe can be positioned behind the adjacent sector while the support plate engages the top hook fixed to the vessel. For the last limiter sector, which closes the belt ring, the positioning precision needed in plan view is in the order of 2 mm. The support plate is lifted above the lower hook fixed on the vessel and then tilted close to the vessel and lowered down onto the hook itself. The articulated boom end effector is then disengaged from the limiter by lowering it by a further small amount so that its hooks can slip out of the engagement holes in the support plate. Photos (7) and (8) show details of the final positioning.

Antennae installation

Each antenna consists of 2 parts:

- The antenna "housing", weighing approximately 350 kg, is to be installed on the wall in equatorial positions by inserting the 2 coaxial feedthroughs used as guiding dowels in the corresponding holes of the VV (Fig 9). Once positioned, the antenna housing is secured by a bayonet engagement manoeuvred outside the VVO.

- The electrostatic "screen", weighing also approximately 350 kg to be positioned on guiding pins previously installed on the housing. The screen is finally slid into contact with the housing and fastened to this using the servomanipulator.

Fig 7 Limiter Installation above Entrance Port

Fig 8 Limiter approaching Hooks of Vacuum Vessel Octant The Cooling Pipe is to be positioned behind Adjacent Segment, when present

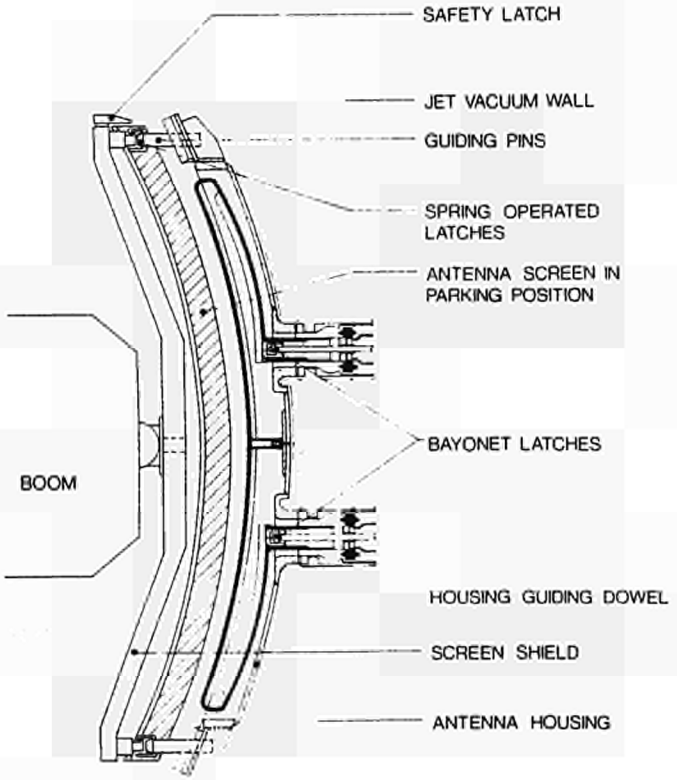

Fig 9 Scheme of Housing and Screen Attachment to Shield and Vacuum Vessel

Operational Experience and Enhancement Program

Difficulties were encountered in the following phases:

- Insertion of the boom into the port due to the narrow gaps (approximately 5 mm) left.

To avoid this problem the control software is being improved so that 'teach' can be done in resolved motion using any 3 adjacent joints. This, results in a very precise trajectory, and is then repeated with the same resolved motion algorithm, thus achieving satisfactory repeatibility (approximately 1 mm).

It was found difficult to guarantee that the hooks of the shield were totally disengaged from the limiter before retracting the shield, in which case the shield would catch on the limiters causing a jerk with potential danger to the tile integrity.

To avoid catching, the present passive hooks will be replaced with actuated ones.

- Dynamic repeatibility of known trajectory can be improved with the use of advanced control algorithms, which compute the effect of the inertia crosscoupling and introduce a correction on the input signals [6].

References

(1) P D F Jones, D Maisonnier, T Raimondi - Design and Operation of the JET articulated boom - SOFT, Austin 1985.

(2) T Raimondi - Design and Operation of the Remote Maintenance System in JET - Remote Systems and Robotics - ANS Meeting, Pasco, WA - April 1987.

(3) U Kühnapfel - Graphics Support for JET Boom Control, Remote Systems and Robotics - ANS Meeting, Pasco, WA - April 1987.

(4) D Maisonnier - Modelling and Control of a large Robot for Teleoperation System. Proc. of 1987 IEEE International Conference on Robotics and Automation.

(5) J Y Simon Luh, M W Walker, R P C Paul - Resolved Acceleration Control of Mechanical Manipulators. IEEE Transactions on Automatic Control. Vol AC-25.

(6) J Hewit - Active Control. I M E - London 1984.

THE FAST BEAM INTERLOCK SYSTEM FOR JET NEUTRAL INJECTION

D Cooper, D Stork, M J Mead, D Young

JET Joint Undertaking, Abingdon, Oxon. OX14 3EA

ABSTRACT

The JET Neutral Beam Injection (NBI) system poses severe interlock problems with the possibility of unsafe conditions arising on a fast timescale (≤ 100 ms). In order to cope with this the high-security Fast Beam Interlock System (FBIS) has been developed. It is used to turn off the beams in a failsafe manner when a condition arises which could damage the beam line or torus on a timescale too short to be dealt with by the JET Central Interlock and Safety System (CISS). FBIS interfaces signals from many JET safety systems and processes them to act directly on the Neutral Beam power supplies. The interfaces and the fail safe operation of FBIS are described. It is presently planned to upgrade the system to include a real-time comparison of the ion beam deflection magnet currents and the beam extraction voltage and a system which will compensate for the effects of the Tokamak stray fields on the NBI beamlines.

INTRODUCTION

The JET Neutral Beam Injection (NBI) system [1] consists of two beamlines, each with 8 ion sources (PINI's) and capable of delivering 10 MW of Deuterium beam (full energy 80 kV/atom) or 5.8 MW of Hydrogen beam (70 kV/atom) to the JET plasma. The NBI system is a long pulse ($t_p \leq 10$ sec) device and as there are many fault conditions which develop on a rapid time scale, it was necessary to develop a fail-safe system for rapid termination of the high power beams (power densities in the range 10-100 MW/m^2). This system is known as the Fast Beam Interlock System (FBIS).

The FBIS is designed to protect against the following situations arising:

1) Injection of beams with insufficiently dense plasma, too high beam power loading on the Tokamak inner wall.
2) Injection of beams into JET whilst the beamline fast shutter is not open.
3) Extraction of beams from the (PINIs) during excessive pressure transients.
4) Extraction of beams from the PINIs where the field setting of the Beamline Deflection Magnet and the beam voltage are not consistent.
5) Injection of beams into JET where the stray field from the Tokamak is not correctly compensated at the PINIs and would hence adversely affect their beam direction [2].

With the FBIS the aim was to design a fail safe interlock system with high reliability which in normal operation requires no user intervention and was interfaced to the JET Computer System (CODAS) [3].

Network Overview

The FBIS is distributed around the JET site, see Fig.1 and 2, with as much as 200 metres between nodes. Some systems interfacing with the FBIS are "smart" eg. the PFPS (Plasma Fault Protection System) [4] and some are passive eg. the Fast Shutter [6] and vacuum alarms. A signalling philosophy was developed to accommodate these variations. Signals are passed as pulse trains, smart systems must produce a pulse train by repeatedly setting and resetting a bit, but passive systems are sent a pulse train which is returned to the FBIS. The

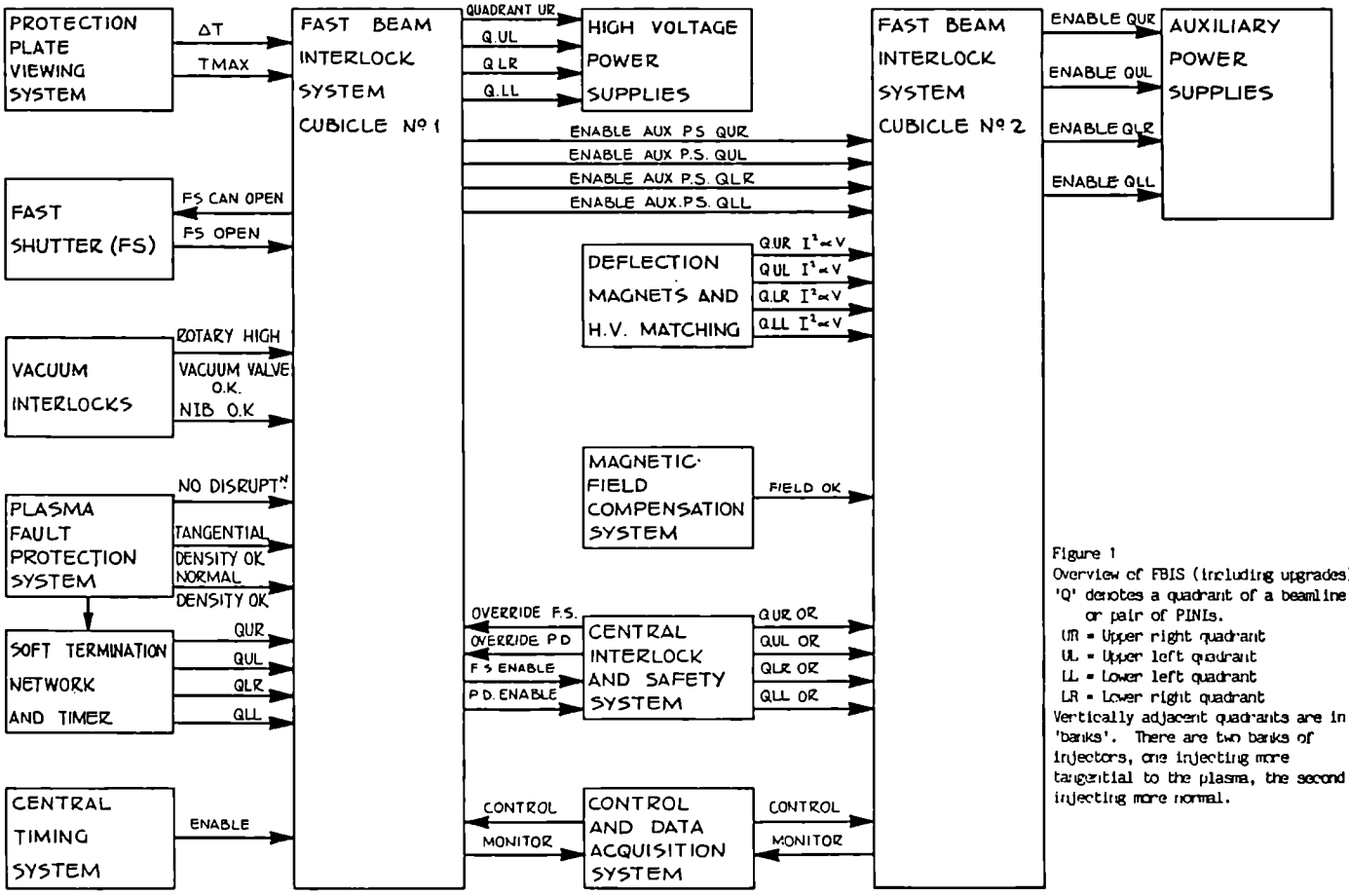

Figure 1
Overview of FBIS (including upgrades).
'Q' denotes a quadrant of a beamline or pair of PINIs.
UR = Upper right quadrant
UL = Upper left quadrant
LL = Lower left quadrant
LR = Lower right quadrant
Vertically adjacent quadrants are in 'banks'. There are two banks of injectors, one injecting more tangential to the plasma, the second injecting more normal.

power supply system is in four groups, one for each pair of PINIs. Each group must receive a pair of pulse trains before the beams can start. The removal of a pulse train leads to the switch-off of the high voltage and/or arc power supplies. Fusion experiments and particularly NBI systems present a hostile environment to electronic systems therefore optical fibre connections are used for all long distance signal paths. Particular attention was paid to reliability with high quality components being used throughout the system. The failure modes of individual devices such as fast relays, semiconductors and integrated circuits were considered in the design of the fail safe circuits. The remote checkability of the system under CODAS control was an important factor in the design.

INTERFACES WITH OTHER SYSTEMS

The FBIS interfaces with the following systems (see Fig.1):

Central Timing System (CTS)

The pulse sequence of the NBI beamlines consists (in chronological order) of powering the PINI filaments; introducing gas into the PINIs; striking arcs in the PINIs; filling the PINI gas neutralisers; applying gridstack voltages to cause the extraction of beams. This pulse sequence is described in more detail in [7] and is started by a branch of the JET Central Timing System (CTS).

The CTS also produces an enabling pulse window which starts a short time before the beams are required. Until this window is opened the FBIS will not allow beam operation.

Plasma Fault Protection System [4]

The PFPS provides three pulse trains at 500 Hz produced by a microprocessor repeatedly setting and resetting output bits each measurement cycle. When this processor is initialised the three optical outputs are illuminated (set to '1') therefore informing the FBIS that PFPS is ready and the optical links are in order. The three signals are:

1) "Nodisruption" (NODISR) which indicates adequate plasma current, low plasma hard X-ray flux and low plasma current derivative. If any of these conditions are not satisfied the plasma is deemed to have disrupted and the NODISR pulse train is removed. If this signal is removed in a neutral injection pulse all beams are stopped and the fast shutter is closed. The fast shutter is not allowed to be opened until this signal becomes valid. This signal is passed on to the other beam line with a 100 ms delay to prevent large power transients.
2) "DOKT" which indicates adequate plasma density for the four tangential beams on each beamline.
3) "DOKN" which indicates adequate plasma density for the four normal beams on each beamline.

PFPS is preprogrammed before the NBI pulse with the plasma current and density levels which will keep beam 'shine-through' power on the Torus walls to acceptable levels.

Another function of PFPS is to trigger the Soft Termination Network (STN). If the JET plasma density is above a defined limit or the density measurements are unreliable then the STN triggers a controlled ramp down of the additional heating power. The soft termination trigger to the neutral injection system is at present a single pulse on a optical fibre, and therefore not fail safe. This pulse triggers a CAMAC programmable timer situated in the NBI control system which in turn produces four trigger pulses normally at half second intervals. These four pulses are transferred by fibre to the FBIS and are latched in the four optical output modules. See Fig.3. This system produces a ramp down of the beams in pairs over 1.5 seconds. The STN is effectively backed up by the hard stop signals (DOKT, DOKN and NODISR) which stop all beams. The STN is being converted to a microprocessor based system providing fail safe 500 Hz pulse trains.

Central Interlock and Safety System (CISS)

CISS is a dual-processor programmable logic controller-based system which provides the basic safety of the NBI system [7] for faults of slow (> 125 ms) timescale, the FBIS handles all interlocks requiring fast response. CISS is the only system allowed to override some functions of the FBIS, (see Fig.1) there being no functions which can be overridden by the NBI operator. There are three operational modes of CISS:

1) Asynchronous mode where the beamline is pulsed independently of JET with its vacuum system isolated. In this mode the three interlocks from PFPS and also the interlocks from the Fast Shutter [6] and the injection duct Penning vacuum gauge are overridden.
2) Synchronous Test mode where short pulse (t_p < 500 ms) injection into JET without adequate plasma is possible, in this mode the PFPS interlocks are overridden.
3) Synchronous mode where full injection is possible, in this mode there are no interlocks overridden.

Fast Shutter

The Fast Shutter [6] provides a very low conductance between the NBI vacuum box and the torus between JET machine pulses in both synchronous modes of the system. This prevents gas backstreaming from the torus to the injection box cryopumps. The Fast Shutter is opened by the CTS - 850 ms before the beams are required but only if it is receiving an enabling pulse train signal from the FBIS. This pulse train is derived from the NODISR signal in synchronous mode. The pulse train is returned to the FBIS only when the shutter is fully open. A fault causing premature shutter closing would interrupt the returned pulse train and stop the beams, thus preventing damage to the fast shutter.

Fast Vacuum Gauges

There are two Fast Penning Gauges connected to the FBIS. The first is operational in all modes of the injector and measures the NBI box pressure. The second which is overridden in Asynchronous mode measures the injection duct pressure.

These Penning gauges are interfaced to the FBIS through window detectors. If the measured pressure is above a high set point (in practice ~ 5 10^{-4} mbar) the pulse train is interrupted. Also if the pressure is below the low set point the pulse train is also interrupted because of the risk that the gauge head might have been disconnected, switched off or suffered contamination.

Protection Plate Viewing System (PPVS) [5]

PPVS is an Infra-Red diode viewing system which observes the Tokamak inner wall protection tiles at

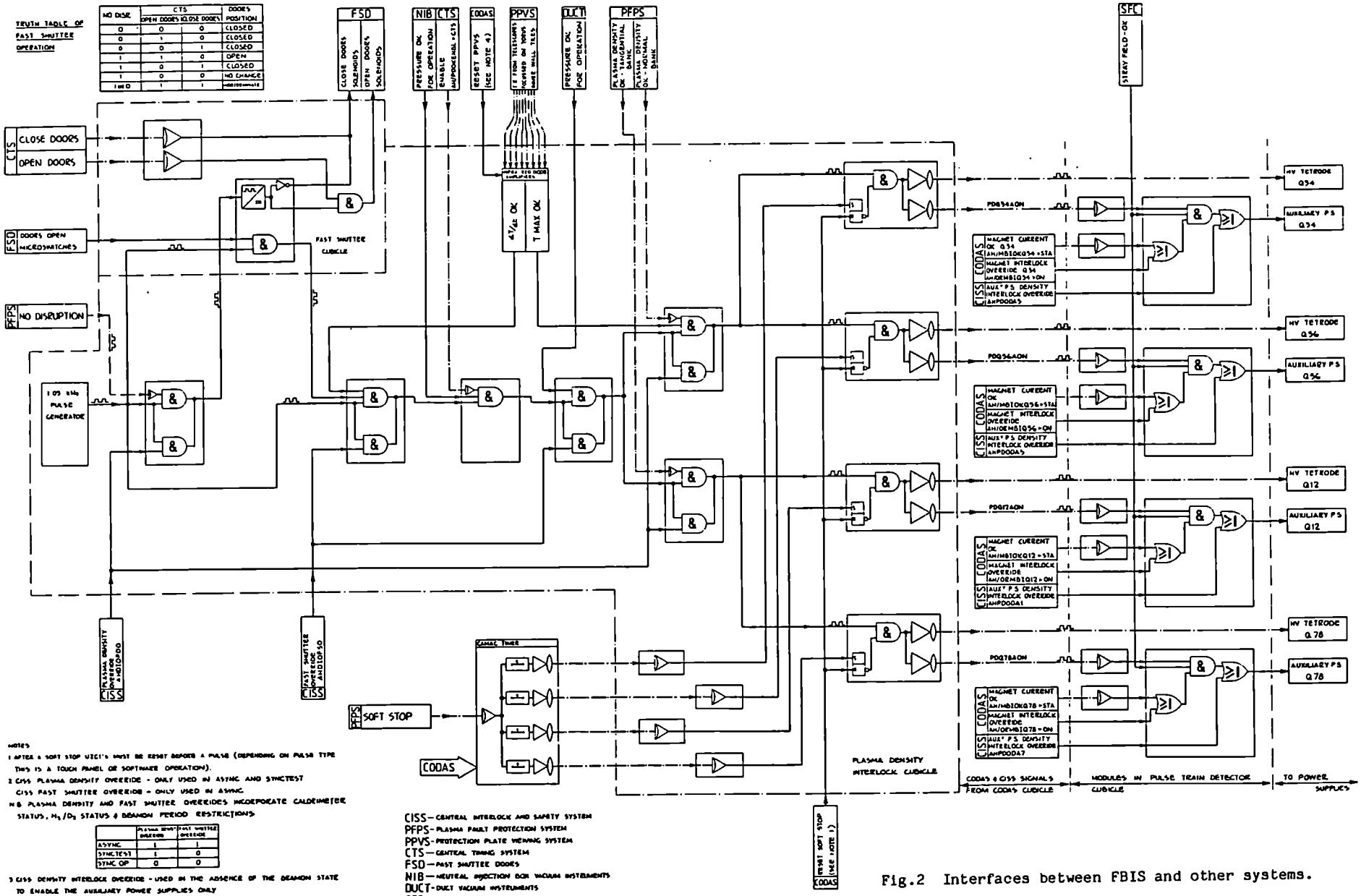

Fig.2 Interfaces between FBIS and other systems.

the points where the neutral beams impinge [7]. The diodes' electronics provide trip signals if the NBI shine through power is too high ie. the tiles get too hot (temperature > 1200°C) or if the time derivative of tile temperature is observed above a certain threshold. These trip signals interrupt the pulse trains through to the NIB power supplies and stop the beams. PPVS acts essentially as a 'back up' to the PFPS signals in this respect.

Interface with the NBI Power Supplies

The FBIS acts to switch off the NBI Power Supplies by two parallel routes for each PINI. One acting through the High Voltage supply system for the PINI grids, the other through the arc power supply for the PINI discharge chamber.

The High Voltage beam acceleration is applied to the PINI via a tetrode protection system unit [8] which acts under the control of CTS. This tetrode has within its control system a retriggerable monostable circuit which requires the input of the FBIS pulse train. If this pulse train is absent the HV power will not be switched on to the PINI. If the pulse train disappears during beam extraction the tetrode control acts to switch off the PINI HV via its Fast Turn Off (FTO) network [8]. This ensures a time response to FBIS commands - 1 ms.

In addition the FBIS pulse train is used to operate an external trip relay (figure 2) which acts to trip the arc power supplies of a PINI [9] via the FTO network. The disappearance of the arc makes beam extraction impossible and thus provides a parallel safety path. To enable arc-only operation on a PINI this safety trip from FBIS is overridden by CISS except in the periods defined by the timing system as 'BEAMON' periods, which are communicated to CISS [7].

SYSTEMS TO BE INTERFACED IN FUTURE

Deflection Magnet Interlock

Each quadrant of the NBI beamline consists of two vertically adjacent PINIs, run at the same extraction voltage with a deflection magnet in front through which the beams pass. The deflection magnet current is set algorithmically to match the extraction voltage [7] and the magnet is powered up before the pulse and a live check is done by the prepulse check software to establish that the desired setting is achieved [7]. During the pulse a hardwired interlock acts to terminate the PINI power supplies if the magnet current deviates by > 1% from the desired setting.

Although the deflection magnet itself is rated DC and is water cooled there are ancillary components such as bus bars and vacuum feedthroughs whose duty cycle will become more severe if the NBI system is upgraded to run Tritium beams (higher deflection current). To avoid having to power the magnets before the pulse (which can now lead to several minutes waiting with power on during a JET countdown sequence) an operation via the Timing System with a real time Deflection Magnet Interlock (DMI) is being added to FBIS.

The DMI will provide four pulse trains at 500 Hz produced by a microprocessor system as PFPS. Using the power supply data acquisition system this processor tests the square of the deflection magnet current against the output of the high voltage extraction power supply for consistency. Each measurement cycle updates the output pulse train which is gated onto the PINI arc supplies during the BEAMON period.

Magnetic Field Compensation System

The stray vertical field from the Poloidal Field coils of the JET device is higher than was anticipated during the design phase of the NBI system. This stray field is in excess of that catered for by the passive magnetic shielding of the beamline [1] and interferes with the beams before they are neutralised leading to beam deflection. Although only small deflection angles are involved, severe power loadings can result in the injection duct [2]. The problems are within normal operating bounds for plasma currents up to 3-3.5 MA but extension of JET operation to 7 MA [10] will require an active compensation of the stray fields. This active compensation system consists of coils wound around the NBI beam box at the ion source end. The coil currents will oppose and cancel the Tokamak stray field. The cancelled field will be measured by 3 gauss meters equipped with window detectors. The field must be within all 3 windows for the beam sustaining pulse train to be returned to the FBIS.

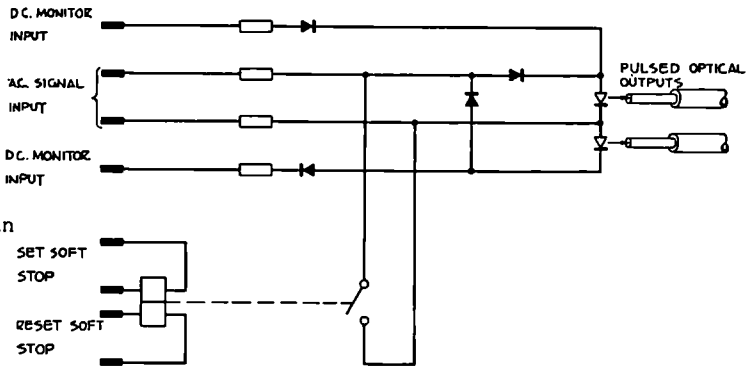

Fig.3 Optical Output Module

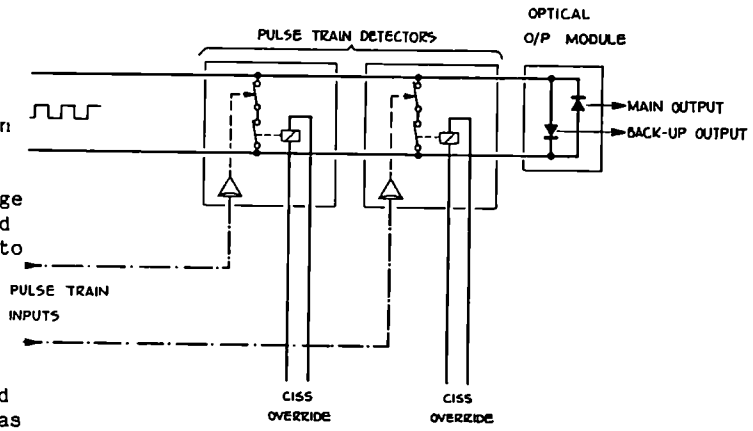

Fig.4 Example of the failsafe signalling philosophy

FBIS COMPONENTS

Optical Output Module

This module converts pulsed electrical signals into pairs of optical signals, each optical output is on alternately, one output for positive input half cycles and the other for negative half cycles (see Fig 3 and 4). Both optical signals must be received by the power supply system for the injectors to operate. One optical signal is sent directly to the high voltage power supply and the other sent to the arc power supply via the second interlock cubicle. The output of this module can be enabled or disabled, this function is used by the soft termination system.

Relays

The relays used in the FBIS were chosen for high reliability, long life time, 1500 V r.m.s coil-contact isolation and small size. The device used was tested for its immunity to external magnetic fields as parts of the system are close to high current bus bars etc. This relay also has a sealed and gettered housing. When two or more signals (pulse or D.C.) are to be gated together the relay contacts are connected in parallel. The safe state for the relays in this system is contacts closed and coils deenergised. Therefore contacts short out signals which can switch on the neutral injection power supplies. So when FBIS is allowing injection to proceed all relay contacts are open and all coils are energised. There are three advantages to this scheme:

1) The major failure mode for contacts is in the closed position.
2) The failure mode for coils is open circuit.
3) The dropout time is half the contact pickup time, ~ 2 ms.

Pulse Train Detector

This module is used in all parts of the system where a pulse train is to be tested for validity and combined with other pulse trains or signals. The module is designed to be fail safe for the signalling path and also includes a monitoring path, (used in test mode) see Fig.5. The signal input is a standard SMA optical fibre connector with a silicon p.i.n. diode detector. The detector current is amplified in a low noise saturating pre-amp with a small amount of hysteresis. This amplified signal is divided three ways, first is a band pass filter with approximately 400 to 1100 Hz pass band. Second is a first order high pass filter followed by a charge pump producing a d.c. voltage proportional to frequency. This d.c. voltage is added to the output of the band pass filter and passed to a saturating amplifier which is capacitively coupled to a rectifier and fast relay. This forms the signalling path through the module which is capacitively coupled throughout with self healing capacitors. The third output of the pre-amp is low-pass filtered and connected to a comparator with a trip level set at 45% of the peak pre-amp output. This comparator also has a relay at the output and with the low-pass filter form the monitoring path.

SYSTEM PERFORMANCE

This system has been very reliable with no non-safe failures to date. About 36 injection pulses have been terminated by a plasma disruption or soft stop whilst the beams were on and on one occasion the fast Shutter failed to open. The beam interlock correctly terminated the pulse. The only failures have been two optical fibre terminations.

USER INTERFACE

The system has not distracted the attention of the neutral injection operator therefore the beamline can be controlled by one operator.

The FBIS normally has a low profile for the JET NBI operator and occupies only a small area of the standard alarm system colour display. The alarm system alerts the operator to a system failure or premature termination of the beams. A touch screen is also available to the operator where a detailed mimic can be called up which displays all major F.B.I.S. states and the continuity of all fibre optic links. From this touch screen the operator can:

1) Put the system in test mode.
2) Clear the "soft stop" latches.

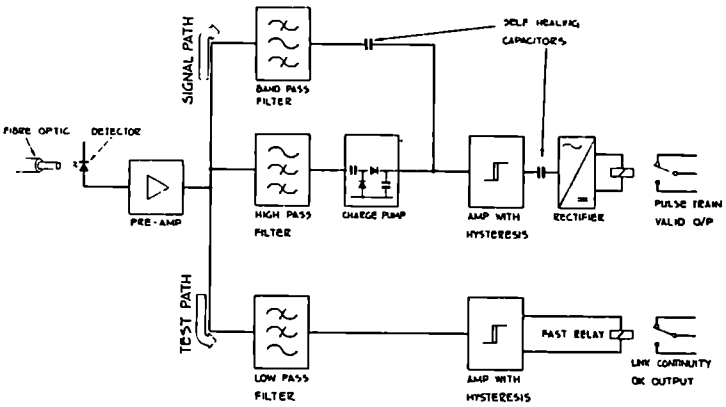

Fig.5 Pulse Train Detector

3) Call the FBIS state mimic.
4) Call the PPVS state mimic [5].

These functions are also under CODAS control when the NBI timing system is in synchronism with the JET CTS. [7].

ACKNOWLEDGEMENTS

It is a pleasure to acknowledge the contribution of Mr T Norman and Mr A Browne to the success of this work.

REFERENCES

[1] G Duesing et al. Fusion Technology 11 (1), 163-202 (1987).
[2] A P H Goede et al. Proc 14th SOFT, Avignon (1986) published in 'Fusion Technology 1986' vol 2, 1139-1144.
[3] F Bombi et al. 10th SOFE, Philadelphia, PA (USA) (1983).
[4] J How et al. 14th SOFT, Avignon (1986), ibid, pp 1421-1426.
[5] D Cooper, D Stork and A Stäbler. These proceedings. (Paper 38-05).
[6] M J Watson et al. 14th SOFT, Avignon (1986), ibid, pp 1145-1152.
[7] D Stork et al. 14th SOFT, Avignon (1986), ibid, pp 1451-1460.
[8] R Claesen et al. Proc 13th SOFT, Varese (1984) published in 'Fusion Technology 1984' vol 2, 829-834.
[9] G L Basile et al. Proc 13th SOFT, Varese (1984), ibid, pp 835-842.
[10] E Bertolini. These proceedings.

TESTING OF THE UPGRADED JET NEUTRAL INJECTOR

R S Hemsworth, G H Deschamps, H D Falter, and P Massmann

JET Joint Undertaking, Abingdon, Oxon, OX14 3EA.

INTRODUCTION

The JET beam sources (PINI's) were designed with a four grid (tetrode) extraction system for operation at 80 kV with a perveance matched current of 60 A when operating in H_2[1]. These sources are to be upgraded to a three grid (triode) configuration operating at 140 kV, 30 A with D_2 as the working gas. The same JET 'bucket' plasma sources will be used as are presently in operation with the tetrode extraction systems. The modification of one source to operate at these parameters and the subsequent testing of that source is described in this paper.

The test of the main section (magnet, beam dumps and beamline calorimeter) of the first JET injector in the JET Neutral Injection Test Bed with the tetrode (80 kV) sources set safe operating limits on the present JET injectors[2]. Similar tests have now been carried out with the second injector using both a tetrode (80 kV) PINI operating in H_2, and an upgraded (triode) PINI operating in D_2 at up to 160 kV. The JET injector incorporates eight PINI's, and measurements have been made with PINI's in both of the possible locations within one quadrant in the upper half of the injector. Particular attention has been paid during this 'Quadrant Test' to the profile of the deflected deuteron (proton) beams on the Full Energy Ion Dumps (FEID's), the determination of the safe operating limits of the system and the measurement of the neutralisation of the 140 kV deuterium beams.

TEST OF THE UPGRADED PINI

Modification of the PINI

A standard JET PINI was modified to the triode configuration[3] by the removal of the second (gradient) grid, the replacement of the first (plasma) grid and by increasing the extraction gap. The extraction gap was increased to 27.2 mm (metal to metal) by placing stainless steel discs under the ceramic post insulators which support the ground grid from the gradient grid holder. Details of the PINI construction can be found in reference 1.

The new plasma grid has the same basic hole pattern, but the aperture shape was changed[3]. The tetrode used offset apertures in the third (decel) grid to achieve the required focussing of the beam. As the electrostatic lens formed by the decel grid aperture in the triode is weaker than in the tetrode, the apertures in the new plasma grids need to be offset to give the net relative aperture displacements needed to obtain the desired focusing.

Results

Perveance Measurements: The perveance matched currents were measured at various voltages up to 160 kV with the system operating in D_2. Perveance match was defined in several ways, the principal ones being the determination of the current giving the minimum beamlet divergence for a given extraction voltage, or the maximum transmission to the Test Bed Beam Dump (TBBD). Alternatively it was taken as the current at a given voltage giving the minimum power to the scrapers at the side of the beam. The beamlet divergence was deduced from beam profiles measured by thermocouples buried in the vapotron elements making up the TBBD[4]. The power transmitted to the TBBD and the power loading on the beam scrapers were determined by water flow calorimetry. These three techniques agree within the experimental errors of ± 1 A; typical data are shown in Fig.1. The perveance was also measured with H_2 and He as the working gas. The resulting 'perveance' curves are shown in Fig.2.

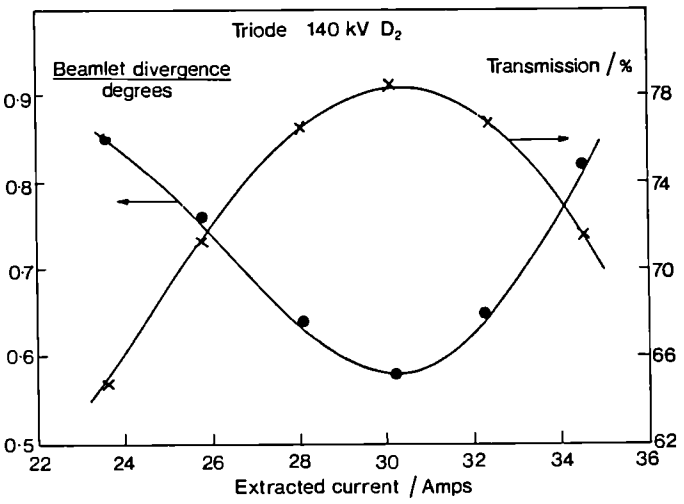

Fig.1: Beamlet Divergence and Transmission versus Extracted Current for the JET Triode PINI Operated at 140 kV in D_2.

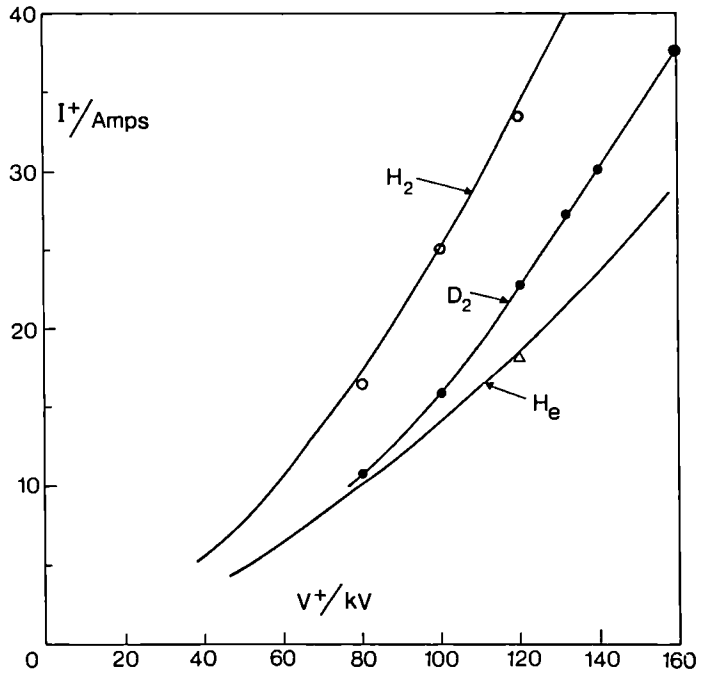

Fig.2: Perveance curves for the JET Triode. The solid curves are predicted curves - based on species measurements for H_2 and D_2; for He it is assumed that only He^+ is extracted.

PINI Power Loadings

The power loadings on the different components of the PINI have been measured (using waterflow calorimetry) as a function of perveance at various extraction voltages. Typical results are shown in Fig.3. As can be seen, the power loadings expressed as a fraction of the extracted power, with the exception of the second stage neutraliser (ie. the half of the neutraliser furthest from the grids) are not a strong function of either the perveance or the extraction voltage. All the loadings are within the power handling capability of the PINI components.

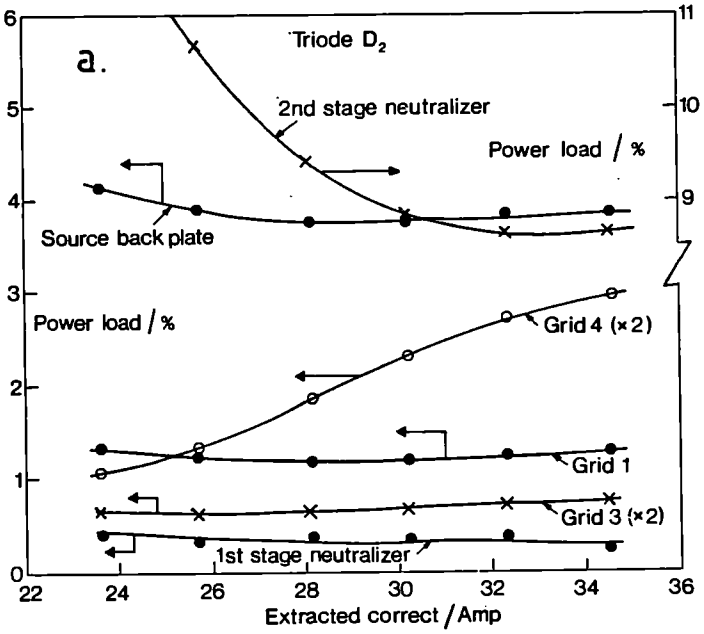

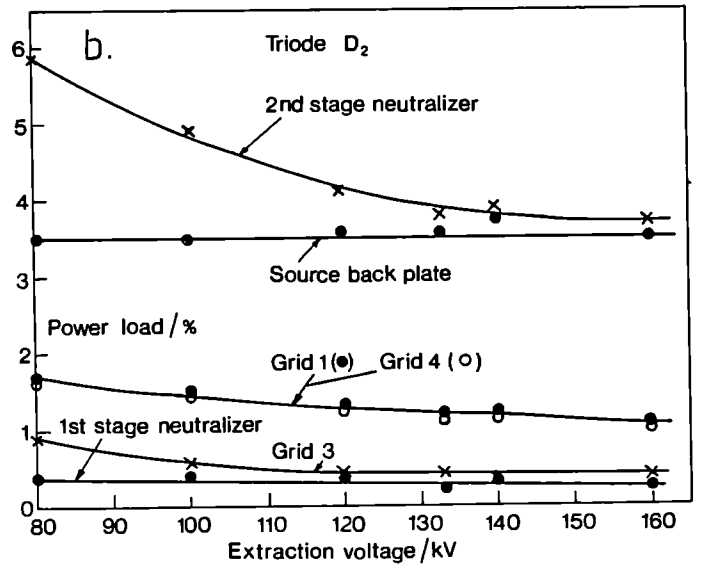

Fig.3: Power Loadings on the Components of the JET Triode PINI Expressed as a Percentage of the Extracted Power.
a) Versus the Extracted Current for 140 kV Operation in D_2
b) Versus Extraction Voltage under Perveance Matched Conditions - D_2 Operation.

For this Figure: Grid 1 is the Plasma Grid, Grid 3 the Decel Grid and Grid 4 is the Ground Grid. There is no Grid 2.

The PINI power loadings have also been measured as a function of the gas flows. With the JET system, gas is introduced both through the plasma source (Qs) and at the midpoint of the neutraliser (Qn). Fig.4a shows the loading on the source backplate as a function of these gas flows, and Fig.4b shows the same data but as a function of the residual pressure in the plasma source. These data indicate that the variation in the power loadings with the gas flow arise from reactions between the extracted beam and the gas in the extraction gap. The non zero intercept shown in Fig. 4b may be interpreted as being due to direct interception of beam particles on the decel grid leading to secondary electron emission, with the electrons being accelerated back through the extraction grid and onto the source backplate. It should be noted that due to uncertainties in the arc contribution to the power loading during beam extraction, the measured value of this intercept is subject to large errors (< ± 40%).

The data of Fig.4 may be used to optimize the distribution of gas flow to give the minimum power loading consistent with the required neutralisation target.

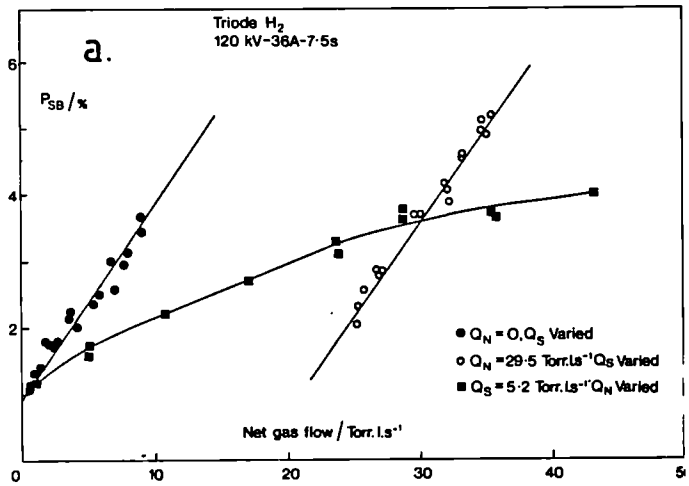

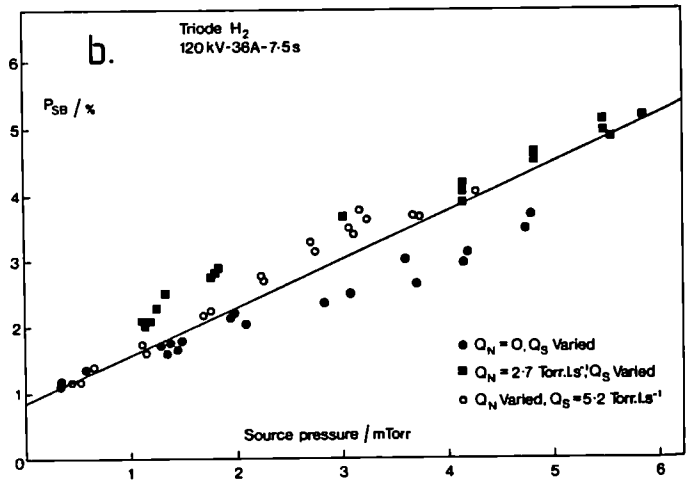

Fig.4: Power Loading on the JET Bucket Plasma Source (P_{SB}) Expressed as a Percentage of the Extracted Power

(a) Versus the Source and/or Neutraliser Gas Flow

(b) Versus the Residual Source Pressure, i.e. the Plasma Source Filling Pressure for the Set Gas Flows, After Allowing for the Removal of the Beam Particles.

TEST OF THE SECOND JET INJECTOR

The main components of a JET injector, i.e. the beam deflection magnets and their liners, the beamline calorimeter and the various ion dumps, are all mounted on the Central Support Column which is itself suspended from the lid of the Neutral Injection Box[5]. The Central Support Column is hollow and provides the main water distribution to the components it supports. As a standard JET Neutral Injection Box forms part of the JET Test Bed, the Central Support Column and the components it carries are readily mounted in the Test Bed. The Central Support Column and the associated components of the first JET injector were installed and tested with 80 kV PINI's operating in both H_2 and D_2 during the first half of 1985[2]. In order to improve the safe limits of the FEID defined by those tests, the magnets of the second injector have been modified using shims consisting of 2 cm thick parallel strips of soft iron added to the input and exit faces of the lower half of the magnet. The effect of these shims should be to give relatively more deflection to the beam from the lower PINI for a given magnet current. A tapered field correction shim was also added to the upper part of the exit face of the magnet, which is intended to correct possible over focussing of the upper beam if the magnet were operated at above the nominal setting for a given beam energy.

The objective of this second 'Quadrant Test' was to determine the safe operating limits with the upgraded PINI's and to evaluate the effect of the magnet shims.

Full Energy Ion Dump Instrumentation

One limitation of the first Quadrant Test was the degree of instrumentation used to determine the footprint of the dumped ion beams on the FEID. The basic instrumentation, which is unchanged for the second injector, consists of thermocouples buried in the vapotrons making up the FEID. These are sparsely distributed in three of the four FEID's of one injector. Although the fourth FEID is much better instrumented, this has proven inadequate for an accurate determination of the dumped beam footprint[2]. Also this instrumentation does not measure the power which falls onto the exposed sides of some of the vapotrons making up the FEID, which is important as regards defining the safe operating limits[2,6]. Therefore for this Quadrant Test, an extensive array of inertial calorimeter blocks, which give reasonably unambiguous data, were mounted onto the FEID to be tested. The FEID is constructed from staggered V's each made from two vapotrons (see refs. 2 and 5). The "calorimeter strips" were mounted on the surface of one V and against the exposed side of the lower V. The basic design features are shown in Fig.5. Each calorimeter block is actually part of a rectangular copper strip, which is slotted to inhibit thermal conduction along its length. The temperature of each block is measured with a sheathed thermocouple peened into the block. The strip is machined at the rear to provide a channel for the thermocouple leads and the face of the strip is machined to avoid high power densities at the corners created by the slots. Additional shaping at the side ensures that some blocks receive power only on the front face or from particles moving at an angle greater than 10° wrt the side of the block. This angle is significantly greater than the angular spread introduced in this plane by the deflection magnet or the beamlet divergence. By comparing adjacent blocks either receiving power from the side or not, the side loading may be deduced. When no side loading is present, these adjacent blocks allow the local rate of change of the power density along the strip to be accurately determined. The instrumentation was laid out on the FEID in a pattern which allows a relatively simple contouring routine to determine the overall beam footprint.

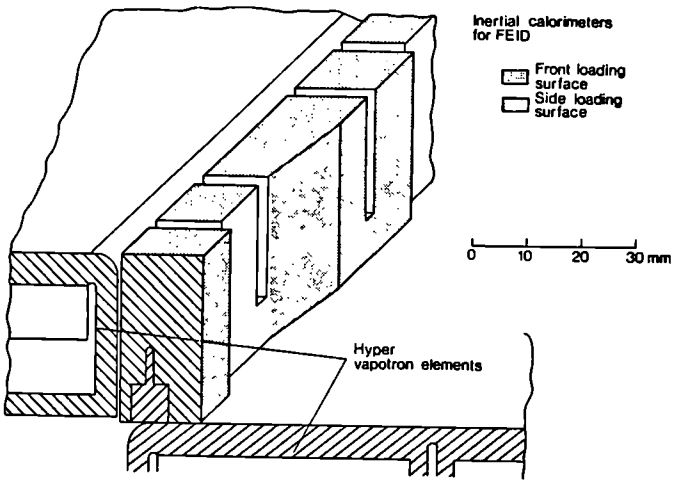

Fig.5: Schematic of the Calorimeter Block/Strip Installed on the Full Energy Ion Dump for the Second Quadrant Test.

Beam Profile Data

Triode (140 kV) System: Fig.6 shows the beam profile along the calorimeter strips from a 140 kV, 30 A (D_2) beam on the FEID. The insert shows a typic thermocouple response. Fig.7 shows the overall beam footprint from the same pulse. The solid dots on Fig indicate the calorimeter block locations.

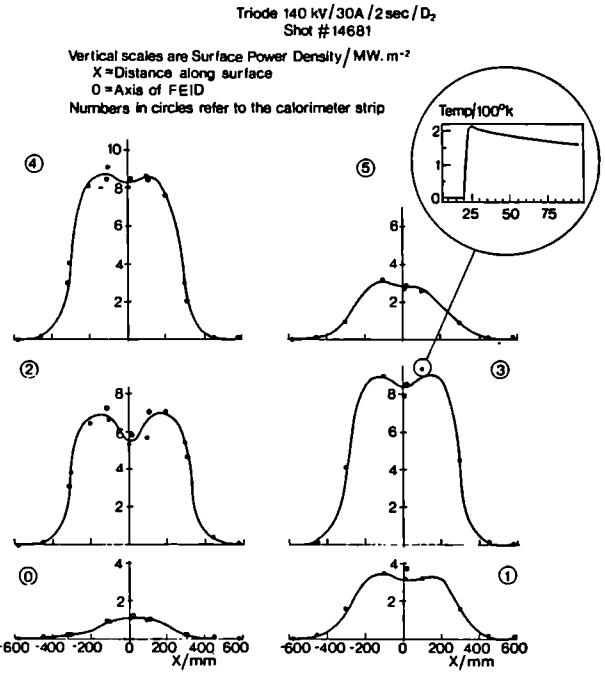

Fig.6: Beam Profiles along the Calorimeter Strips for a 140 kV, 30 A Deuterium Beam from the Lower PINI. The Insert Shows a Typical Thermocouple Response.

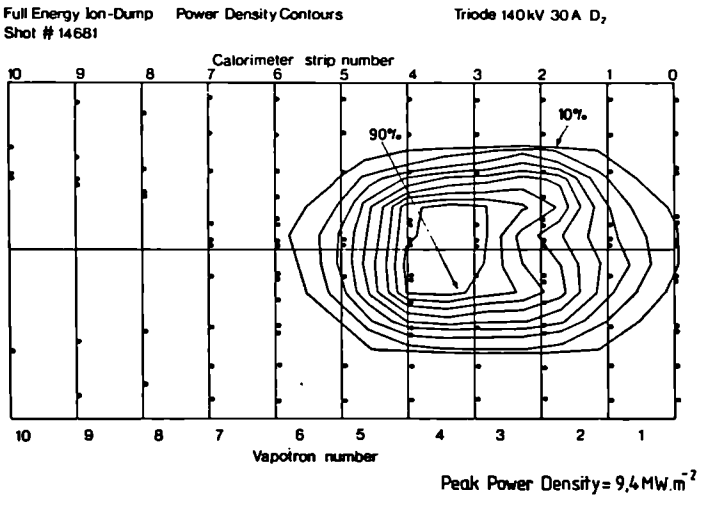

Fig.7: Beam Footprint derived from the data of Fig.10. The Peak Power Density for this Shot was 9.4 MW m^{-2}. The Outer Contour is 10% of the Peak; Subsequent Contours Increase in 10% Steps.

Careful evaluation of the data has shown that the side loading is always < 10% of the front loading. As the highest side loading occurs where the front loading is relatively low, it may be neglected as regards the safe operating limit. This is a surprising result from the viewpoint of both theoretical prediction and in light of the results of the first quadrant test. This is discussed further below.

The data show that at the nominal maximum beam parameters of 140 kV, 30 A, the power loading on the vapotrons is within the design limit of ~ 11 MW.m^{-2}, and that the beam is well contained within the dump. The beam is significantly narrower than was found for the tetrode system operating in H_2 at > 60 kV during the first Quadrant Test[2].

To assess the safety margins of the system, systematic scans have been made in gas flow and beam perveance. The beam has also been deliberately misaligned by up to +0.2° and -0.15°. With 140 kV deuterium beams, the beam profile is found to become broader at the highest perveance (37 A) reached and at the lowest gas flows achievable with 30 A extracted, which gave a calculated neutralisation target of ~ 4.10^{19} molecules.m^{-2}. However the beam is always well confined within the FEID and the power density is within the safe operating limits over the expected range of operations.

Tetrode (80 kV) System: Measurements with the tetrode system were restricted to a maximum extraction voltage of 70 kV and operation in H_2 because of time limitations. The beam at 70 kV was found to be well contained within the FEID, and significantly narrower than found at similar operating parameters during the first Quadrant Test[2]. This difference is somewhat difficult to quantify exactly as the diagnostics used were not the same. However the difference is quite clear in the wings of the profile where essentially identical diagnostics were installed for both sets of tests. The profiles are compared in Fig.8.

Neutralisation Measurements

During the first Quadrant Test, the neutralisation of the extracted beams was measured to be below theoretical expectations[7]. Measurements with the 140 kV system using deuterium beams during the present tests give the same result. This is illustrated in Fig.9.

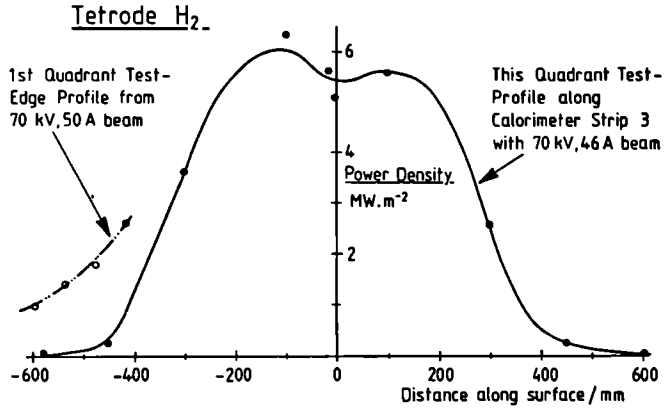

Fig.8: Power Density Profile Along Calorimeter Strip 3 for a 70 kV, 46 A hydrogen beam. The data from the First Quadrant Test for a 70 kV 50 A Hydrogen Beam Measured Using Essentially Identical Diagnostics are shown for Comparison.

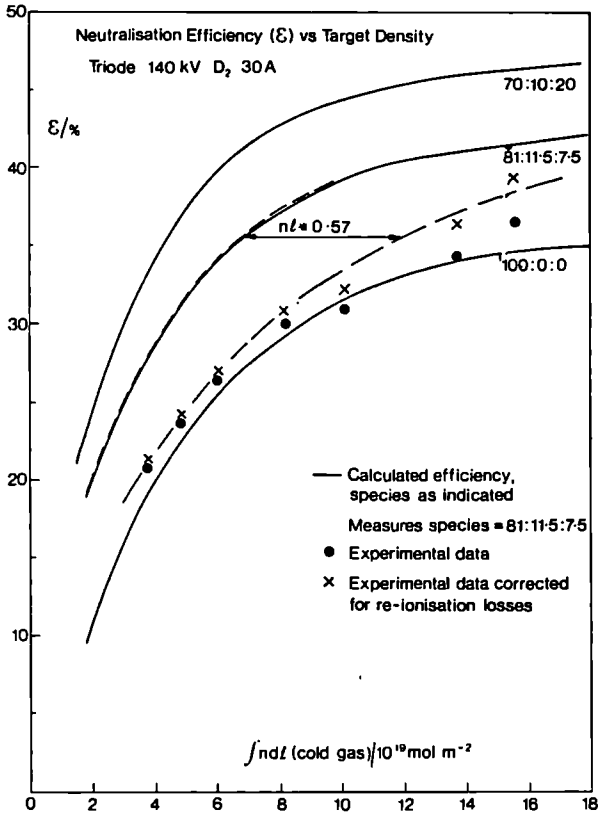

Fig.9: Neutralisation Efficiency (ε) of 140 kV, 30 A Deuterium Beams.

The basic neutralisation data are obtained simply by measuring the power to the TBBD (using waterflow calorimetry) with and without the deflection magnet energised. In order to compare with simple predictions these data have to be corrected for reionisation losses from the neutral beam as it traverses the magnetic field of the deflection magnet (particles re-ionised in this region do not reach the TBBD). The corrected data shown in Fig.9 fall well below the theoretical curve for the measured beam species mix. This result means that the neutral power to JET will be below the original expectations. The predicted power to JET derived from the experimental data are given in Fig.10.

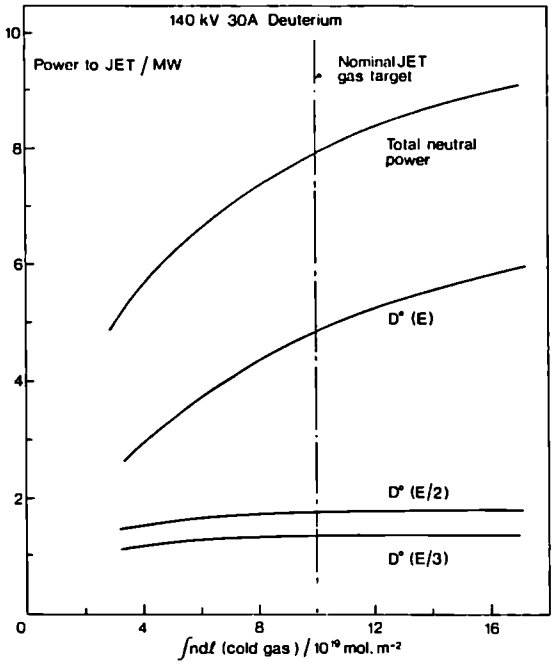

Fig.10: Predicted Power to the JET Plasma from One Upgraded Injector (8 PINIs) Operating at 140 kV.

DISCUSSION

PINI Upgrade

The performance of the JET PINI upgraded to give operation at 140 kV has been measured. The perveance matched current with D_2 at 140 kV is found to be the desired 30 A. The beam transmission and beamlet divergence are found to be similar to those for the present JET 80 kV tetrode system, and the source is acceptable as the basis of the upgrade of the JET injectors. As the beamlet divergence is found to be greater than that measured with the tetrode system operating at approximately half the energy per nucleon, but with very similar plasma source conditions, the divergence is obviously not governed by the temperature of the extracted ions. The power loadings (expressed as a fraction of the extracted power) on the various components of the PINI are all found not to be strong functions of the perveance or of the extraction voltage. All the loadings are within acceptable limits. As might be expected because of the longer extraction gap, the load on the source backplate from back streaming electrons is appreciably above that measured with the tetrode system. Although within acceptable limits, the measurements presented here of the variation of the loading with the source and neutraliser gas flows would allow a reduction in the loading by a re-arrangement of the gas flows, whilst maintaining the neutralisation target.

Second Quadrant Test

The testing of the main components of the second injector has shown that the system is safe for operation with deuterium beams at 140 kV, 30 A. The FEID is also safe with beams of 70 kV, 50 A from the present tetrode system operating in H_2. As this is the safe operating limit set for the first system, the addition of the shims to the magnet has neither improved nor degraded the safety of the system. Extrapolations from these data clearly show that the system would be unsafe for operation with either 80 kV, 60 A hydrogen beams or with 160 kV, 30 A deuterium beams (from a re-optimized PINI). Long pulse operation at these parameters would require upgraded dumps. However, operation at these parameters is possible with the present system for pulse lengths of up to 2 s because of the thermal response of the vapotrons.

Unlike the findings of the first Quadrant Test, the dumped beam is found not to give any significant side loading on the vapotrons of the FEID. This is ascribed to a number of factors, most important of which is direct interception of the deflected beam by the diagnostic used in the first Quadrant Test leading to a serious overestimate of the side loading. With the present measurements, as there is no discrimination against particles arriving at > 10° with respect to the side of the blocks, there is an underestimate of the side loading, but an overestimate of the sum of side and front loading, hence a conservative assessment of the safety of the system [6].

Also unlike the first Quadrant Test, the deflected beams do not show any significant broadening and they are well confined within the FEID. Some broadening is observed at high perveance and with very low neutralisation targets (both with 140 kV, deuterium beams) and, with hydrogen beams (tetrode operation), the width increases with beam energy. Extrapolation to 80 kV, 60 A, hydrogen operation suggests severe broadening at these beam parameters. The difference with the first Quadrant Test is only qualititively understood: The addition of the shims to the magnet moves the position of the magnet exit lens, with respect to the beam crossover in the non-bend plane, which should lead to a narrower beam footprint on the FEID.

The neutralisation of the high energy deuterium beams is measured to be below that predicted assuming the neutraliser gas is at room temperature. A similar result was found for hydrogen and deuterium beams at ≤ 80 kV per nucleon during the first Quadrant Test. The effect is presently assumed to be caused by heating of the gas in the neutraliser by the beam [8]. Extrapolation to operation on JET, allowing for reionisation losses in the NIB and the torus duct, gives a total neutral power to the plasma from one injector operating at 140 kV (D_2) of 7.9 MW.

REFERENCES

[1] A P C De Vere et al. "Engineering Design and Manufacture of Prototype Neutral Injector for JET". Proc 9th Symp on Eng Problems of Fus Res, Chicago, USA, 1981, pp 1534-1537.
H Altmann. "Manufacture of Beam Sources and Neutralisers for JET Neutral Injection". Proc 13th Symp on Fus Tech, Varese, Italy, 1984, pp 579-585.

[2] H D Falter et al. "Operational Test of the JET Neutral Injection System in the JET Test Bed". Proc 11th Symp on Fus Eng, Austin, USA, 1981, pp 786-790.

[3] M Fumelli et al. "Operation of a 160 kV, 37 A Neutral Deuterium Injector". Proc 13th Symp on Fus Tech, Varese, Italy, 1984, pp 617-623.

[4] H D Falter et al. "The JET Neutral Beam Test Bed Facility and First Results". Proc 13th Symp on Fus Tech, Varese, Italy, 1984, pp 571-578.

[5] G Duesing et al. "Neutral Beam Systems". Fusion Technology, January 1987, pp 163-202.

[6] R Tivey et al. "Testing of Various Types of Beam Stopping Elements Using Hypervapotron Cooling". This conference, Paper 32-08.

[7] R S Hemsworth et al. "Neutralisation Measurements for the JET Injector". Proc 13th Conf on Contr Fus and Plasma Heating, Schliersee, FDR, 1986, pp 297-300

[8] J R Paméla. "Gas Heating Effects in the Neutralisers of Neutral Beam Injection Lines". Rev Sci Inst 57 (6), 1986, pp 1066-1068.

THE THERMOCOUPLE DATA ACQUISITION SYSTEM FOR JET NEUTRAL BEAM INJECTION

M J Mead, A Browne, D Ewers, K Fullard, T T C Jones, D Stork.

JET Joint Undertaking, Abingdon, Oxon. OX14 3EA

ABSTRACT

Each of the JET Neutral Injection beamlines has a thermocouple data acquisition system designed to take signals from 400 thermocouples mounted in beamline components. These data acquisition systems are specially designed to suit a 10 MW long-pulse beamline operating in a radioactive environment. The signals which are used to calculate beam power densities from transient analysis come from special thermocouples and are sampled once every 40 ms. Thermocouple readings are also used to calculate total power absorbed by beamline components using water flow calorimetry or by the temperature rise of the component.

INTRODUCTION

The two JET Neutral Injection (NI) beamline systems [1] which are installed on the JET Torus are each designed to deliver 10 MW of beam power for 10 seconds. These systems require components able to handle very high beam powers for the long pulse length required. The development of these components has required extensive testing within the NI Test Bed Facility [2][3] using a JET designed thermocouple data acquisition system to gather signals from up to 400 thermocouples. The performance of each of the torus NI beamlines is also monitored using identical thermocouple data acquisition systems. The development and safe operation of these beamlines has depended heavily on the data taken by the thermocouple data acquisition systems.

SYSTEM SPECIFICATION

Each of the NI thermocouple data acquisition systems has to collect and process signals from 400 thermocouples mounted in beamline components and their cooling water circuits. The thermocouples which are all type K (nickel-chromium/nickel-aluminium) have earthed hot junctions so as to respond quickly to temperature changes. In order to survive during the active phase of JET, all electronic equipment is located outside the JET Torus hall and connected by cables up to 100 metres in length to the thermocouples on the beamline. The system is also expected to withstand transient voltages of up to 1 kV which could be induced into the cable system by plasma disruptions or a short circuit on a poloidal field coil. The system was specified to measure beam power density or total beam power falling on a component and the three types of thermocouples installed for this purpose are described in the following sections.

HYPERVAPOTRON THERMOCOUPLES

The high power beamline components like the calorimeter and ion dumps are made using hypervapotron beam stopping elements [4]. Bare wire thermocouples are mounted in these elements via rear holes such that the thermocouple tips are 3 mm from the front face (figure 1). The hypervapotrons can absorb beam powers of up to 12 MW/m² on their front faces. These hypervapotron thermocouples were designed to measure beam power density by using the rate of change of temperature during the first 300 ms after the beam is turned on (figure 2a). During this time the heat flow can be considered as a one dimensional diffusion process in a semi-infinite slab of copper. For this analysis to be usable, the thermocouple signal needs to be sampled at least once every 40 ms. Also the thermocouple junctions need to be formed at a precisely controlled depth down a 1.6 mm diameter hole. Initially the hot junctions were brazed in using a gold-indium braze but more recently a spot welding technique has been developed. The quantity of gold-indium used for the brazed type of hot junction was kept small so that the junction locations were well defined.

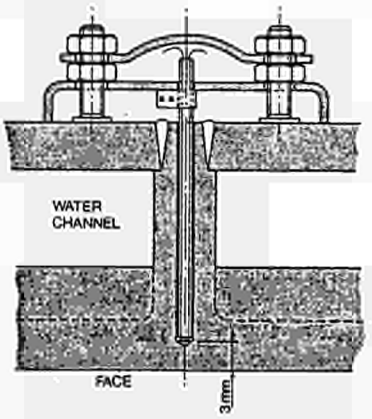

Figure 1 : Thermocouple Mounting in Hypervapotron

INERTIAL THERMOCOUPLES

Low power beamline components like the bending magnet liners, have small cooling water pipes attached or rely on cooling by conduction and radiation. These components heat up as they absorb power during a pulse and then cool down slowly between pulses. If the rate of heat loss during the pulse is sufficiently low then the thermocouples mounted in these components can be considered to be inertial and the energy absorbed from the beam is equal to the temperature rise ΔT of the component multiplied by its thermal capacity (figure 2b).

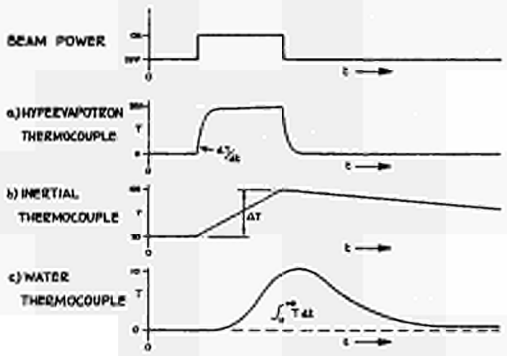

Figure 2 : Idealised Thermocouple Waveforms

WATER THERMOCOUPLES

Most of the beamline components have thermocouples fitted in their cooling water outlet pipes. This enables the total energy absorbed during a pulse to be calculated by integrating the area under the temperature waveform and multiplying this by the water flow (figure 2c). The water thermocouples fitted

outside the vacuum are of the conventional sheathed type with earthed hot junctions. Those inside the vacuum are of similar construction to the hypervapotron thermocouples. They are made using glass fibre insulated twisted pair type K thermocouple wire which is woven without lubricants so that it is vacuum compatible.

DESIGN PHILOSOPHY

While the design of the first NI beamline components was underway the basic parameters of the thermocouple data acquisition system were defined as follows:

1) Cold junction compensation is not required because the system need only measure temperature rises during a pulse and for one minute afterwards.
2) Multiplexers would be used to reduce by a factor of 8 to 1 the number of signals taken to the Analogue to Digital (A to D) converters.
3) Reed relay switching has to be used in the multiplexer to withstand 1kV transients. These relays could be switched fast enough to sample one signal every 5 ms so with an 8 to 1 multiplexer each hypervapotron thermocouple signal could be sampled once every 40 ms.
4) The signals from the multiplexers have to go into isolation amplifiers to provide good common mode rejection, to isolate the A to D converters from 1 kV transients and amplify the signals to suit the 10 volt range of the A to D converters.
5) Two CAMAC transient recording A to D converters are required to record and store in local memory the data from each pulse. One A to D converter would take data for 10 s from the fast thermocouples (hypervapotron) and the other would take data for 40 s from the slow thermocouples (inertial or water).

ELECTRONIC MODULES

The fast thermocouple signals are taken to cubicles containing racks of electronic modules connected up as shown in figure 3. The slow thermocouple signals go into an identical arrangement of modules running at a slower speed. The 32 channel 12 bit A to D converters and memory modules are standard commercial CAMAC units. All the other modules were specially designed in-house for use in this and other JET data acquisition systems.

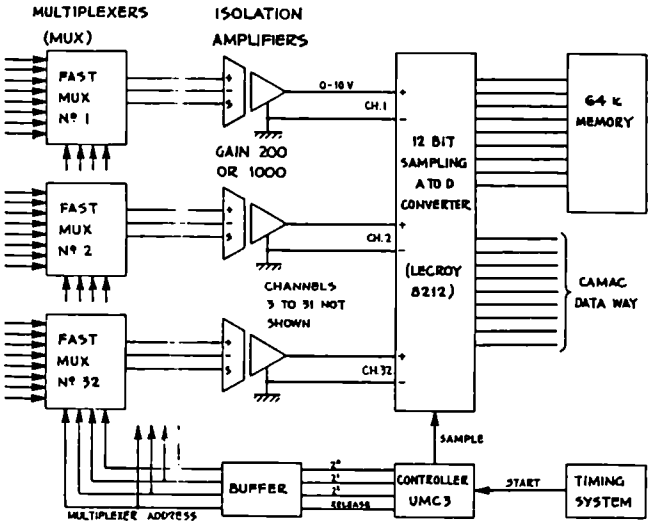

Figure 3 : Block Diagram of Data Acquisition System

The multiplexers (figure 4) use three-pole mercury wetted reed relays to switch one of the eight input signals to the output. The screen connections are switched as well as signal leads to avoid forming earth loops through cable screens. A passive filter is fitted to remove high frequency noise. The multiplexers have automatic open circuit detection circuits consisting of 10 MΩ resistors which drive the A to D converter input above + 10 volts if either of the thermocouple leads is open circuit. This has been found to be invaluable because broken wires are the most common type of fault and if inputs are left open circuit then they can pick up voltages from adjacent channels which look like real signals. The open circuit detection circuits introduce a small dc offset but with good thermocouples which have a lead resistance of less than 50 ohms the temperature offset is less than 1°C.

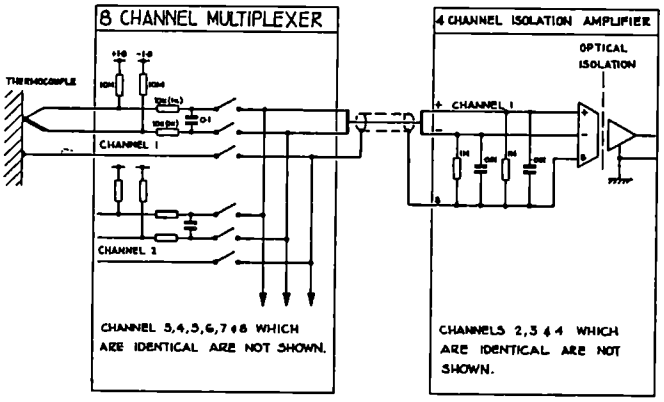

Figure 4 : Multiplexer and Isolation Amplifier

The isolation amplifier modules (Figure 4) have four optical isolation amplifiers in each unit. The gains of the amplifiers are normally set to 1000 for water thermocouples and to 200 for inertial or hypervapotron thermocouples. Each isolation amplifer has a low drift bipolar transistor instrumentation amplifer as a pre-amplifer. The inputs require bias currents of from 5 to 20 nA which flow via the screen and signal leads of the thermocouple when the multiplexer relay is closed.

PERFORMANCE

The performance of the system has proved to be satisfactory. Despite having sampling A to D converters and very long cables, the noise of the system is about one bit at the A to D converter (see figure 5). Interference or mains pick up is rarely a problem if thermocouples and cabling is properly installed using twisted pairs with only one earth point at the thermocouple hot junction. No attempt has been made to limit the signal bandwidth to less than half the sampling frequency since this would give a false dT/dt. The passive filter in the multiplexers has too high a cut off frequency for this. Sampling frequencies which are harmonically related to the 50 Hz mains are avoided so that any mains pick-up coming from badly wired thermocouples is recorded as an interference signal which is high enough in frequency to be removed by software signal processing techniques.

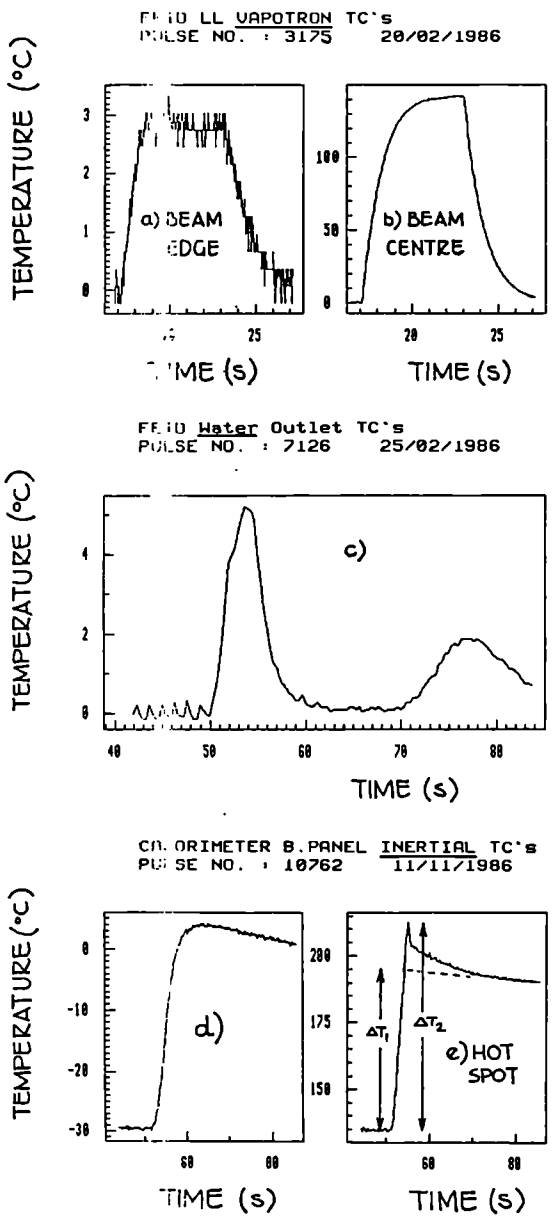

Figure 5 : Example of Thermocouple Signals

Most of the signal noise arises because the three poles of the multiplexer reed relays do not break and make at exactly the same time. For a short while the bias current to one of the inputs of the isolation amplifier may be flowing through a 10 MΩ resistor while the bias current to the other input is flowing through the thermocouple. The differential signals generated in this way are random and they disturb the amplifier while the multiplexer is changing channels. These transients decay exponentially but are still significant when the A to D converter takes its sample. The effect is much smaller with the slow thermocouples because a much longer settling time can be allowed. The problem could have been eliminated if a field effect transistor instrumentation amplifier had been used instead of one with bipolar transistor inputs.

SIGNAL INTERPRETATION

The interpretation of thermocouple signals is not always straightforward as previously suggested by figure 2. For example beam power does not fall uniformly on the larger inertial components and so the temperature across the component takes time to equalise. This effect is clearly seen with the thermocouple shown in figure 5e which is mounted at the centre of a component where the beam power is greatest. Clearly it is the temperature rise ΔT_1 and not ΔT_2 which should be multiplied by the total thermal capacity of the component to give the total energy absorbed.

The unprocessed signals from water thermocouples do not start exactly at 0°C as shown in figure 2c unless the temperature of the hot and cold junctions are the same. Before a signal can be integrated to give the energy absorbed from the beam pulse the initial water temperature or baseline has to be found and subtracted from the signal. This is calculated by averaging ten or so samples before the pulse. The baselines have already been subtracted from the water and hypervapotron thermocouples shown in figure 5. The baseline is not subtracted from inertial thermocouple signals because they may need to be monitored to ensure the components do not get too hot. The negative temperature of the calorimeter back panel thermocouple signal shown in Figure 5d implies that the component is 30°C below the cold junction temperature of about 20°C. This is to be expected since it is close to the beamline cryopump.

Hypervapotron thermocouple signals have been used to calculate beam power densities using samples taken during the first 0.3 s of beam-on time. Software has been developed to fit the temperature samples to a one dimensional model of the heat flow from the hypervapotron face and hence deduce the power density and effective thermocouple depth (figure 6). It is essential for the depth to be considered as an unknown in order to get a good fit for signals from some thermocouples (figure 7). On some beamline components up to half the thermocouples have effective depths of more than 4 mm despite careful dimensional checks during assembly. This is believed to be due to bad thermocouple brazing giving a poor thermal contact between the thermocouple junction and the copper material of the hypervapotron. Power densities derived from these 'bad' thermocouples may still be correct but further experiments are required to establish this. Full agreement between powers derived from inertial, water and hypervapotron thermocouples is not always obtained; one reason for this is that the beams can move during a pulse.

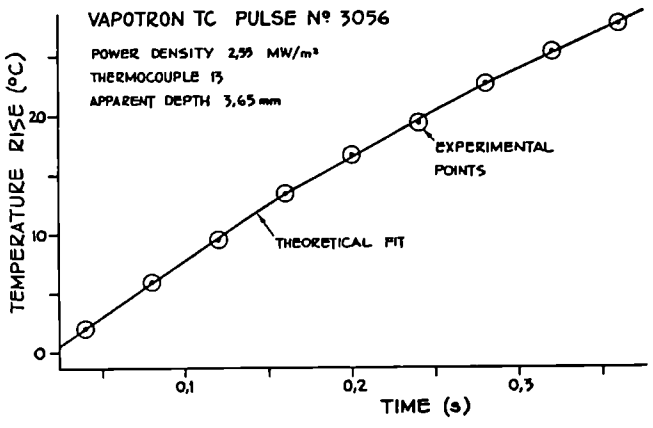

Figure 6 : Response Fitting giving 'Good' Depth.

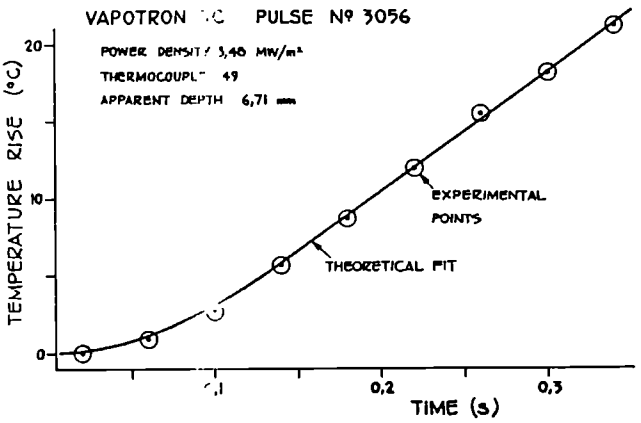

Figure 7 : Response Fitting giving 'Bad' Depth

THERMOCOUPLE FAULTS AND PROBLEMS

It is important to ensure that thermocouple wiring within a vacuum vessel containing an ionised gas is properly screened otherwise signals like that shown in Figure 8a may be obtained. This type of pick-up is generally a negative pulse coincident with the beam-on period due to an electron current pick-up.

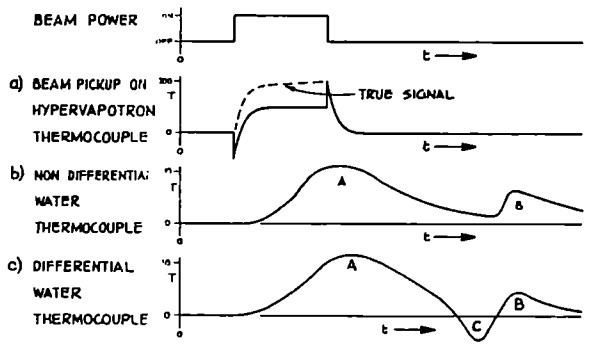

Figure 8 : Examples of Problems with Thermocouple Signals

Signals from water thermocouples must be used carefully when calculating total energy absorbed because they usually have a double response as shown in figures 8b and 5c. The response A comes from the beam energy absorbed by the component. The response B comes from the hot water passing right round the cooling water loop through a heat exchange system which does not remove all the beam energy the first time round. When A and B are well separated then the integration of response A, which gives the true energy falling on the component, can be stopped before B. When A and B overlap a second thermocouple has to be fitted to measure the inlet water temperature. Then the differential signal (figure 8c) can be integrated to give a more accurate estimate of the energy because the response C from the input thermocouple cancels the contribution due to the response B. When thermocouples are connected in series to form a differential pair, one of them must have an insulated hot junction in order to avoid partially short circuiting the signal. The second response B provides a useful check for faulty thermocouples because its height is almost exactly the same for all water thermocouples.

SYSTEM LIMITATIONS

With the benefit of experience in building and running this system a number of limitations have become apparent. The system was never intended to measure absolute temperature and so cold junction compensation was not fitted. The transitions from thermocouple wire to copper wire are usually made inside a remote handling connector which is often inside the vacuum vessel. These transition points which are the cold junctions are stable in temperature over the 40 s measurement time but their temperatures cannot be measured. There have been occasions when it would have been useful to know the absolute temperature of the beamline components close to the cryopumps which are at risk of damage by freezing if the cooling water flow is stopped.

The data acquisition system does not have an automatic calibration facility which could have been incorporated into multiplexer modules. This is not a problem because the electronic modules used in this system are reliable and do not require a gain calibration check more than once a year. The offset voltages of the amplifiers have been found to change significantly because of occasional high temperatures within the electronic cubicles. If the system was to be used for absolute temperature measurement then an automatic calibration facility would be needed to avoid frequent checks on amplifier offset drift.

Beamline components which are well designed to handle the power falling on them often make bad diagnostics. Water flow calorimetry can only be used if most of the heat from a component is removed by the water within half a minute of the pulse. Inertial calorimetry can only be used if the components cools down slowly which means that the component will probably get too hot if the system is pulsed at its maximum rate for a full working day. Some of the components used in the JET NI beamline fall between the two conditions under which accurate calorimetry is possible. This has led to the fitting of small copper blocks for accurate power density measurement during component tests carried out in the NI Test Bed. These inertial blocks usually have to be removed before components are installed on the Torus because otherwise they would be destroyed when the system is pulsed at full power at the normal repetition rate.

REFERENCES

[1] G Duesing, et al, "Neutral Beam Injection System", Fusion Technology, vol 11(1), pp 163-202, January 1987.

[2] G Duesing, "JET Neutral Beam Injection System: Construction and Component Tests", in Proceedings of 13th SOFT Varese, 1984, pp. 59-75.

[3] H D Falter et al, "The JET Neutral Beam Test Bed Facility and First Results", Proceedings of 13th SOFT Varese, 1984, pp. 571-578.

[4] R S Hemsworth, et al, "Testing of the Upgraded JET Neutral Injector", presented at these proceedings.

[5] R Tivey, et al, "Testing of Various Types of Beam Stopping Element Using Hypervapotron Cooling", presented at these proceedings.

THE NEUTRAL BEAM PROTECTION PLATE VIEWING SYSTEM ON JET

D Cooper, A Stäbler[1] and D Stork

JET Joint Undertaking, Abingdon, Oxon. OX14 3EA

(1) EURATOM - IPP, D8046, Garching, FRG

ABSTRACT

The diode viewing array and its control electronics, which together form the Protection Plate Viewing System for the JET Neutral Injectors, are described.

INTRODUCTION

Each of the Neutral Beam Injection (NBI) beamlines on JET is capable of delivering a total power of 10.4 MW (80 keV D° beams) or 5.8 MW (70 keV H° beams) [1]. There are 8 beams in 2 vertical banks of 4 and the bank at a more 'normal' injection angle impinges on the inner wall of the Tokamak after only one pass through the plasma (figure 1).

The unattenuated power density of the beams impinging on the inner wall can be as high as 31 MW/m² (for 80 keV D°) and to protect against shine through from the long pulse neutral beams the JET tokamak vessel is lined with graphite tiles. The tiles are observed using an external diode viewing array - the PROTECTION PLATE VIEWING SYSTEM (PPVS).

PPVS signals are used to provide interlocks which terminate the neutral beams if tiles are observed to be too hot or to have an excessive time-derivative of temperature.

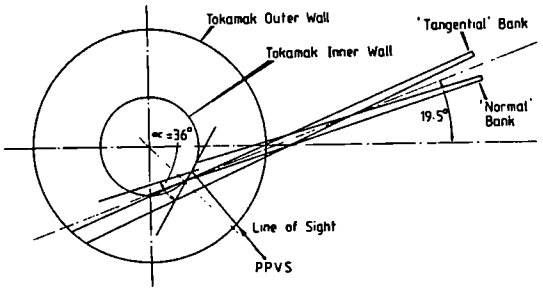

Figure 1 : Schematic Plan view of NBI beamline

SYSTEM SPECIFICATION FOR THE PPVS

As an interlock system the PPVS had to have redundancy in detection mechanisms; robustness and high integrity mechanically and optically; computer checkable integrity and stability; a high signal to noise ratio and individual channels with very similar response. Also because the device had to survive during the active phase of JET the torus end of PPVS had to have remote-handleability for urgent repairs. The PPVS signal processing electronics and optical detectors also had to be situated remotely (~ 50 m distance) from the Torus to avoid radiation damage.

Specific features

The graphite protection tiles have Inconel supports and the bulk temperature of the (tiles plus supports) should not exceed 650°C between pulses. This keeps the supports at a temperature below the downturn in their strength v's temperature curve and hence minimises the possibility of tiles being ripped from the wall in a disruption. With the 1:60 duty cycle of JET NBI system and a 10 second pulse length this translates to a maximum tile front face temperature $T_{FF(max)}$ around 1200°C. The PPVS had to be capable of detecting this temperature with a wide margin of safety.

To detect injection in a 'no plasma' situation PPVS had to be capable of detecting tile temperature derivatives ($\dot{T}_{FF}$). In order not to be tripped at the start of any beam pulse (when $\dot{T} \propto d/dt(t^{1/2}) \to \infty$ as $t \to 0$) the trip mechanism had to be filtered over a 20 ms period.

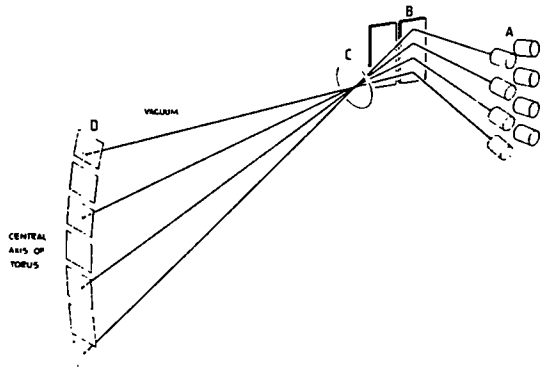

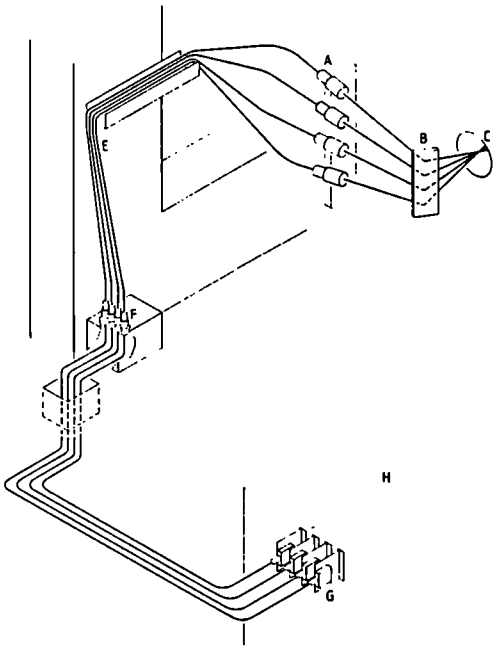

Figure 2 : Schematic of PPVS. Key: A - Optic Head Assembly
B - Mirror; C - UHV Window; D - Carbon Tiles
E - Fibre Optic; F - Bulkhead Connectors;
G - Diode Housing Modules.

No feasible routine calibration source for the PPVS was available inside the JET vacuum vessel. The only facility for checking the deterioration of the window through which the PPVS views the tiles is the firing of test beam pulses onto the tiles with no plasma present (interlocks overridden). The NBI Safety System [2] limits the pulse length in this test mode to ≤ 400 ms and the resulting tile temperatures of T_{FF} - 700°C had to be detectable by PPVS with an accuracy - ±20°C.

DESIGN FEATURES OF THE PPVS

Optical and Mechanical Features

The PPVS consists of 8 Germanium diodes which view the Infra Red (IR) radiation from the tiles via a head optics - optical fibre arrangement (see Figure 2).
The large (5mm diameter) diodes at the reception end are sensitive in range 0.7 μm < λ < 2.0 μm. Blocking filters in front of Ge diode remove effects of plasma light below λ = 800 nm and each beam hot spot is viewed by 2 independent diodes for redundancy.
The PPVS head optics (figure 3) collect IR radiation from an area - 20 cm diameter at the tile and contain miniature lights which are illuminated before each NBI shot to check out the combined performance of the fibre optic, diode and electronic circuit.
The head optics mirrors can be swung simply out of line for remote-handling repairs to the Sapphire UHV window.
This system is equipped with specially designed remote handling (RH) optical connectors and bulkhead connectors (see figure 4). The connectors' design ensures repeatability of signal when disconnection or reconnection takes place and the bulkhead connector loss is ≤ 1 db. The special front-end 'jumper cable' fibres will be removed for RH repairs. These fibres are low-loss mono-filament radiation-resistant quartz fibres.

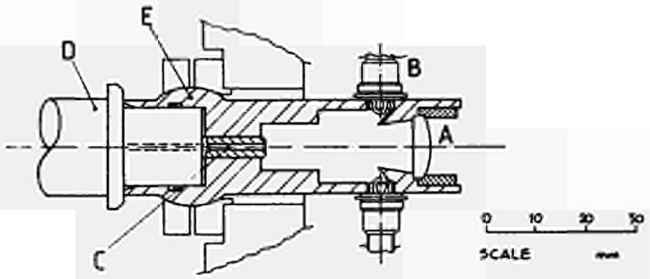

Figure 3 : PPVS Head Optics unit. Key: A - Input Lens; B - Test Lights; C - Fibre Optic; D - RH Connector; E - Adjustment Bearing.

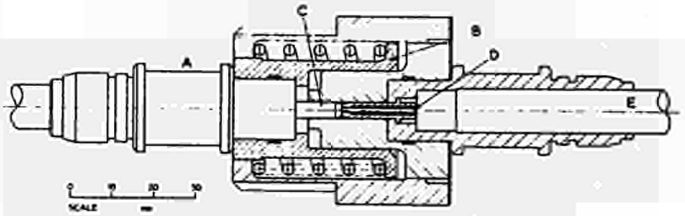

Figure 4 : Bulkhead Connector. Key: A - RH Plug; B - Spring loaded housing with precision-ground surfaces; C - Precision nose cone for fibre optic; D - Low loss fused quartz fibre optic; E - Armoured Cable.

Electrical Design Features

The Ge diodes are Peltier cooled to enhance signal to noise ratio. Each diode signal is amplified (current to voltage amplification) by a JET designed UZL3 trip amplifier, a schematic circuit for which is shown in Figure 5. The amplifier has a circuit which enables the diode signal, (which varies as T_{FF}^4 to T_{FF}^6 (T_{FF} = tile temperature), to be accurately linearised. This ensures a near-constant time derivative trip. The linearising circuit is detailed in figure 5 and contains special "Zener diode" equivalent IC's which provide a temperature independent voltage reference operating at uniquely low currents (μA range).

Figure 5 : Circuit diagram for UZL3 Diode trip amplifier

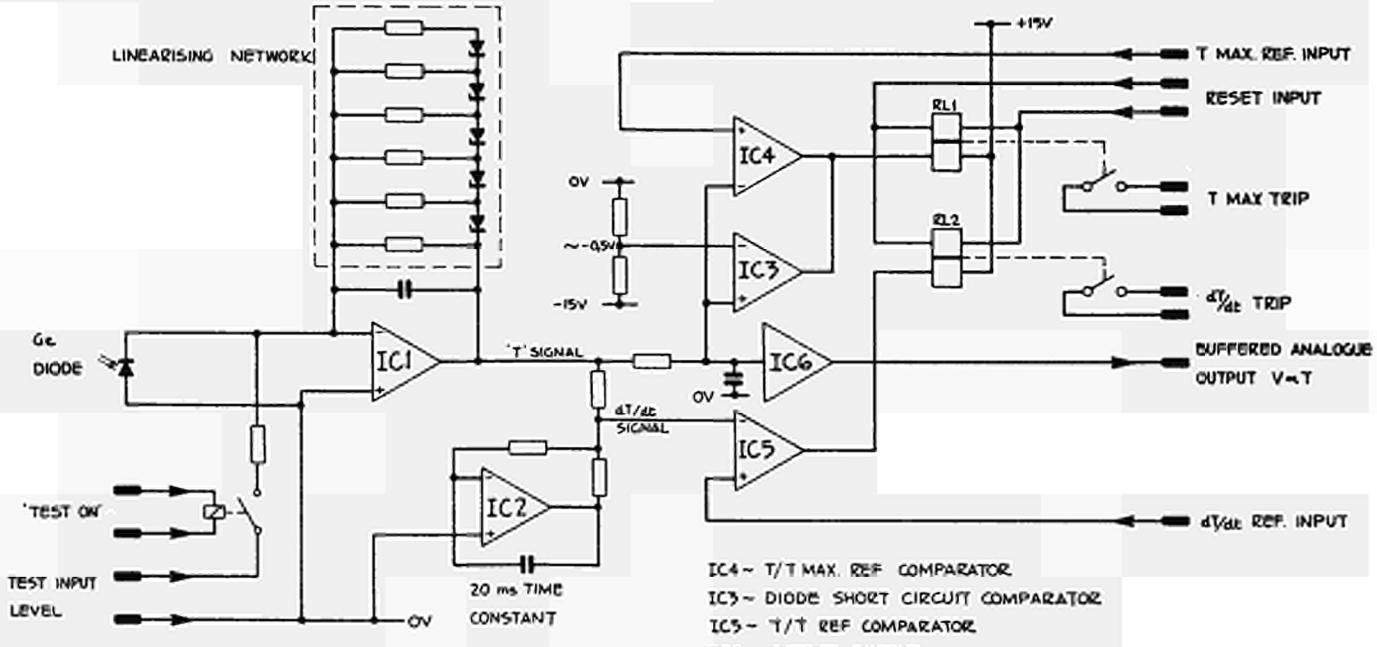

IC4 ~ T/T MAX. REF COMPARATOR
IC3 ~ DIODE SHORT CIRCUIT COMPARATOR
IC5 ~ Ṫ/Ṫ REF COMPARATOR
IC6 ~ OUTPUT BUFFER
RL1, 2 ~ SDS SEALED & GETTERED RELAYS

The trip amplifier provides outputs for a tile temperature trip (T_{max} trip) and a tile temperature derivative trip ($\dot{T}$ trip) with latched resettable trip relays. The diagnostic analogue measurement of tile temperatures is also available to the JET control system (CODAS). There are facilities for remote reset of trips via CODAS and checking of T_{max} and $\dot{T}$ trips by a CODAS-initiated ramp-generating circuit.
The UZL3 trip relays, being part of a safety system, are high reliability components with lifetimes of > 5.10^7 operations and sealed, gettered contacts.

Role of PPVS in the NBI safety system

PPVS trip inputs are part of the interlock chain of the JET Fast Beam Interlock System (FBIS) [3] and the trip inputs are used to gate a pulse train which is supplied to the sustaining power supplies of the JET NBI system. The disappearance of this pulse train leads to the immediate switch-off of the power supplies and termination of the pulse. The Fast Beam Interlock System receives trips from many sources including the JET Plasma Fault Protection System (PFPS) [4]. PFPS is a microprocessor-based system which interrogates plasma diagnostic signals for current (I_p); current derivative ($\dot{I}_p$); density ($\bar{n}_e$) and hard X-ray flux (Φ_{HX}). Using these signals it provides DISRUPTION and INSUFFICIENT DENSITY signals to the FBIS to terminate the beams and prevent shine through damage on the tiles. In this respect PPVS acts as a backup system to PFPS.

SYSTEM PERFORMANCE

In terms of overall performance, the major goals were to (a) obtain a reliable calibration of the temperature response of the diodes in the form $I_D = f(T_{FF})$ where I_D is the diode current and T_{FF} is the tile temperature, (b) linearize the output circuit to give an output voltage which was a linear function of T_{FF} over the widest possible range, and (c) establish uniformity of system response from channel to channel (so that replacement of a part of any one channel would not radically affect the safety level of that channel).

Calibration curve for the PPVS

The PPVS calibration was obtained in bench tests with a full-scale version of all components of the detection system (sapphire window/mirror/head optics/jumper fibre/bulkhead connector/main fibre/filter/Ge-diode) and with simulation of the tiles using a small area black body source capable of temperatures up to 1200°C. The calibration was then scaled to take account of the different solid angle seen by the PPVS detector on the Torus and the 'effective object area' (A_{OB}^{eff}) of the tile under view of the detection channel was taken as that circular area which at constant temperature equal to the maximum temperature in the field of view ($T_{FF,MAX}$) emits radiation equal to the radiation from the temperature profile from the beam footprint within the 0.2 m diameter circle seen by a PPVS diode.

To obtain A_{OB}^{eff} a beam transmission code 'ZAP' [5] was used to predict power density profiles on the tiles.
To extend the calibration curve outside the black body source range, transmission of power by individual PPVS elements was measured and calibration obtained from

$$I_D = f_\Omega \cdot t_W \cdot r_m \cdot t_L \cdot f_c \cdot t_{bhc} \cdot \exp(-\alpha \ell_{OF}) \cdot t_F \cdot \epsilon_c \cdot \sigma \cdot A_{ob}^{eff} \cdot \sum_{\Delta\lambda} R_{\Delta\lambda} \cdot f_{\Delta\lambda} (T_{FF,max}) \cdot T_{FF,max}^{n} \quad (1)$$

where
- σ = Stefan's constant
- $t_{W,L,F}$ = transmission through sapphire window/lens/filter
- r_m = reflection coeff. of mirror
- f_c = coupling efficiency of lens to fibre
- t_{bhc} = bulkhead coupler efficiency
- ℓ_{OF} = optical fibre length
- α = attenuation coefficient
- $R_{\Delta\lambda}$ = response curve of Ge diode (from manufacturer)
- $f_{\Delta\lambda}$ = spectrum function of black body radiation
- f_Ω = solid angle seen by PPVS optics
- ϵ_c = emissivity of Graphite tile

The fibre attenuation coefficient α was measured in bench tests using varying fibre lengths and found to be largely independent of the object temperature (i.e. $\alpha \neq f(\lambda)$). A constant α was used.

The calculated curve (1) was compared with bench measurements (figure 6) and found to agree within ~ 15% over the range 750°C to 1200°C. The steep temperature dependence of I_D ($I_D \sim (T_{FF}/1400)^8$ for 800°C < T_{FF} < 1200 C) implies that a fairly large error in I_D leads to only a small error in temperature measurement ($\Delta I_D \sim 25\%$) results in ΔT_{FF} ~ 50°C in this range.

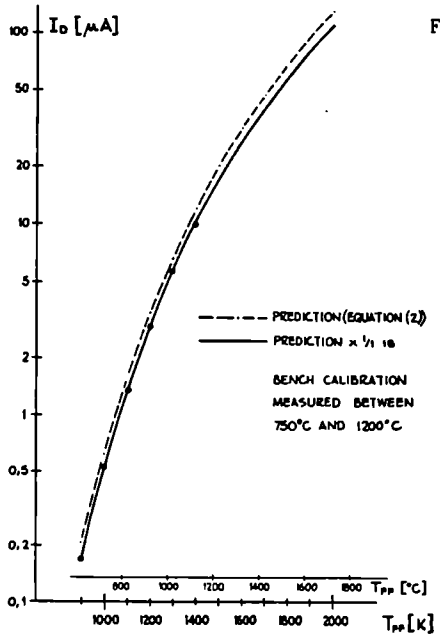

Figure 6 : Calibration curves for PPVS (predicted and measured)

Linearisation of response-sensitivity

The diode amplification electronics achieved a current input to the trip circuitry linear (to < ± 1%) with tempenature of the object under surveillance (T_{OB}) in the range 770°C < T_{OB} < 1700°C ((0.9μA < I_D < 10μA); (V_{trip} 0.9 → 10 V)).

Below 770°C the response is non-linear. The minimum sensitivity of the system is set by diode noise. Diode noise is only ~ 12 nA and so for a signal to noise ratio of 5:1 we have a minimum system sensitivity of ~ 60 nA. This corresponds to T_{OB} ~ 550°C giving a wide margin of safety for the T_{max} trip which is set at 1200°C.

Component (Number tested)	$I_D/\langle I_D\rangle$ variation	Corresponding ΔT_t at T_t = 1400°K
Head optics (8)	0.988 - 1.012	± 1.8°
Jumper fibres (8)	0.967 - 1.023	-6°, + 4°
Main fibres (8)	0.96 - 1.925	-7°, + 4°
Bulkhead connectors (16)	0.979 - 1.024	± 4°
Ge Diodes (10)	0.96 - 1.04	± 7°

Table 1 : Uniformity of System Response

Uniformity of System response

The similarity of nominally identical system elements was tested by inserting components individually into the bench test setup and measuring the diode current change obtained at fixed input radiation conditions. For each component an average diode current $\langle I_D\rangle$ was established and the variation in $I_D/\langle I_D\rangle$ found. The results are shown in table 1 indicating that system uniformity was very good.

TIME RESPONSE OF THE SYSTEM

Endurance times (τ_E) of the graphite tiles have been experimentally determined as a function of impinging power [6]. The T_{max} and $\dot{T}$ trips should have a response time < τ_E in order to save the tiles from thermal shock damage during a 'no plasma' fault situation with NBI. It is clear that response times will be determined by tile temperature at start of the fault. The minimum value of this temperature is that of the JET vacuum vessel (300°C) which gives us our worst case response times.

From the properties of the graphite tiles used in the 1986 experiments [7], taking a semi-infinite slab approximation for the tile with conduction across the face negligible, the surface temperature rise is given by

$$\Delta T_{surf} = 91 \cdot P_{NBI}(MW/m^2) \cdot \sqrt{\tau_p(s)}$$

which leads to a calculation of the response time for the T_{max} trip (τ_M) where $T(t=0) + \Delta T_{surf}$ exceeds 1200°C.

For the $\dot{T}$ trip to a first approximation the integration process in the electronics gives us

$$\Delta V/\Delta t\Big|_{\dot{T}\ comp} = (V(t) - V(t-20ms))/20\ ms,$$

where V(t) is the amplified voltage corresponding to the tile surface temperature at time t after the fault. This is plotted in figure 7 and gives a value for the reponse time (τ_D). The present trip level $\Delta V/\Delta t > 14$ V/s is set by the need to avoid tripping on shine through in a normal plasma pulse. The normal maximum allowable shine through is $\lesssim 5$ MW/m² and the corresponding maximum $\Delta V/\Delta t$ from this shine through would come from a case where the protection tiles were at their maximum allowable interpulse temperature (650°C) before the NBI pulse. This is shown in figure 7 where it is seen to determine the trip level ($\dot{T}_{ref}$). This restriction means that the trip level is only guaranteed to operate under all start conditions for $P_{NBI} > 12$ MW/m². The reaction times τ_M and τ_D are plotted against experimentally determined tile endurance times (τ_E) in figure 8. It can be seen that PPVS provides adequate double level protection (T_{max} and $\dot{T}$) for $P_{NBI} > 12$ MW/m² and single level protection below those values.

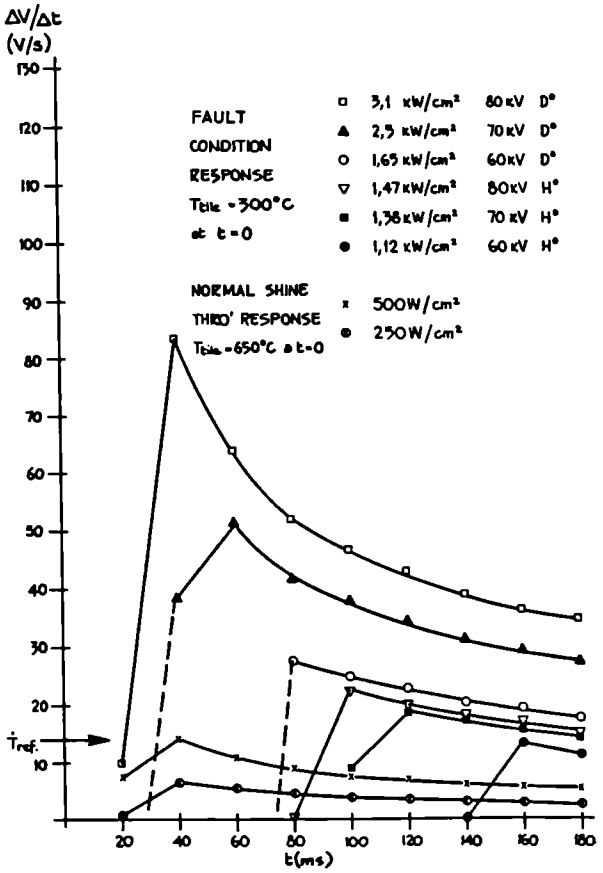

Figure 7 : Estimated response time of the PPVS time derivative trip.

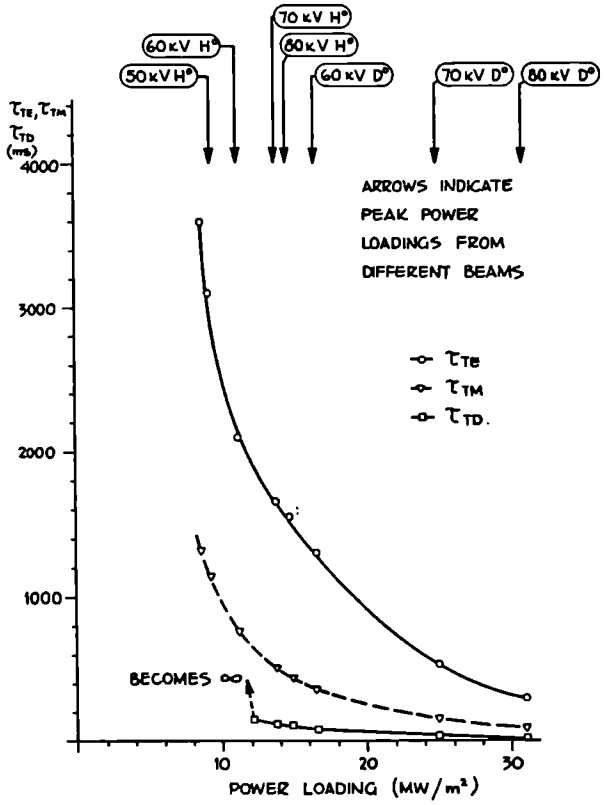

Figure 8 : Response times of the PPVS trips compared with measured tile endurance times.

CHECKING OF SYSTEM USING NO-PLASMA NBI PULSES

With the $\dot{T}$ trip overridden (in a fail safe manner using the JET NBI Safety System) short ($\leq$ 400 ms) NBI pulses have been fired into the JET vessel without plasma and the PPVS signals have been measured. In these cases the peak power on the tiles can be calculated from ZAP [5] predictions and NI Test Bed results [8].

The measured peak powers using the PPVS bench calibration results (equation (1)) are shown for H° beam shots together with the measurements from the Test Bed calorimeter [8] in figure 9. Reasonable agreement is obtained considering the assumptions.

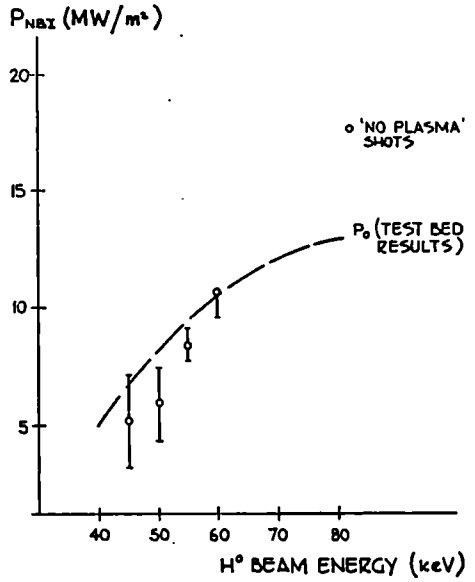

Figure 9 : PPVS unattenuated beam power measurements compared with predictions.

OPERATIONAL EXPERIENCE

The system has been operational on JET for 18 months and provided safety in over 500 NBI pulses. The long-term stability of the electronics and the optical system has proved good.
In early operation, carbonisation of the Tokamak led to some carbon deposits on the UHV window. The resulting signal deterioration (- 50%) did not radically affect the safety of the system. The window was cleaned after - 1 month and carbonisation (and clouding up) has not re-occurred.
In some Tokamak shots, plasma has been limited on Inner Wall tiles and occasionally the limiter area is directly in front of PPVS. Then thermal loading from plasma and also spectral light from Deuterium plasma lines (- 1.87 μm and 1.28 μm) and Carbon I lines (1.26 μm - 1.16 μm) have been seen. This light adds to the beam shine through signal and does not compromise the safety of the system.

Acknowledgements

The authors would like to acknowledge useful and stimulating discussions with Dr M J Mead.
Dr T T Jones contributed to the success of the integration of the PPVS into the JET CODAS computer control system and the help of Mr T Norman in planning and execution of installation and site testing was invaluable.

References

[1] G.Duesing et al., Fusion Technology 11 (1), 163-202 (1987).
[2] D.Stork et al., Proc. 14th SOFT, Avignon 1986, in 'Fusion Technology 1986', Vol 2., 1451-1460
[3] D.Cooper, D.Stork, M.J.Mead and D.Young, these proceedings.
[4] J.How et al., Proc. 14th SOFT, Avignon 1986, in 'Fusion Technology 1986', Vol 2, 1421-1426
[5] 'ZAP' Beamline code, R.Hemsworth and P.Brenan.
[6] A.Stäbler et al., JET-DN-C(85)19 (1985).
[7] M.Huguet et al, contrib paper 11th SOFE Austin Texas (1985), published in the proceedings.
[8] H.Falter et al, contrib paper 11th SOFE Austin Texas (1985), published in the proceedings.

A PRACTICAL EXPERIENCE OF USING SPECIAL REMOTE HANDLING TOOLS ON JET

S F Mills, J Schreibmaier, A Tesini, M Wykes,
JET Joint Undertaking, Abingdon, Oxon OX14 3EA. UK

Abstract

Over 50 cutting and 200 UHV welding operations were made during the installation of new water cooled belt limiters and ICRF Antennae into the JET Vacuum Vessel. This work was performed by the hands-on use of 45 special tools which have been specifically designed for use with the Mascot servomanipulator in preparation for the JET D-T phase when all maintenance will be performed remotely. This paper reports on the techniques used and the performance of the tools.

Introduction

The installation of the belt limiters [1] and ICRF Antennae [2] has greatly increased the complexity of JET in-vessel equipment. The belt limiter consists of 2 toroidal rings located above and below the equatorial plane of the vacuum vessel. Each of the 2 rings comprises a structure having finned water cooling pipes with graphite tiles installed between the fins. The ICRF antennae, 8 of which were installed, each incorporate a water cooled electrostatic screen located between the 2 rings of belt limiters.

The design of the necessary special tools [3] for this installation work was constrained by the restricted access inside the vacuum vessel and a need to be compatible with the handling capacity of the Mascot servomanipulator [4]

Installations into Ø91 mm Ports

The belt limiter cooling pipes and certain diagnostics were installed into Ø91 mm circular ports within the JET vacuum vessel. This necessitated the removal of 55 factory fitted blanks from the ports. Fig 1 shows a cross-section of such a port.

The Cutting Operation

The cutting technique used had to satisfy the following criteria:

a) cause minimal metallurgical changes in the cut area

b) produce a surface finish on the port that is suitable for rewelding without any further operation

c) cause minimal dimensional distortion of the joint element remaining on the machine after cutting

d) produce off-cut material which could easily be collected by a vacuum capture system

e) require no coolants or lubricants incompatible with the JET vacuum vessel clean conditions requirements.

The orbital lathe cutting principle was selected as being the most appropriate in meeting these functional requirements (Fig 2).

An AC electric motor having dynamic closed loop control drives a cutting tool bit at a constant presettable speed in the region of 0.15 to 0.20 (m/sec), while the optimum feed rate is in the range of 0.005 to 0.01 (mm/rev). With these parameters no lubricant is required, the off-cut material is in the chipped form and the power required to drive the tool is relatively low minimising the overall tool weight.

The feed is automatically achieved by means of a lead screw driven by an orbital drive through auxiliary gearing. The feed and orbit motions can be decoupled by a pneumatic clutch to allow fast axial positioning/withdrawing of the cutting head. The cutting tool is secured to the weldment by 3 water-hydraulically operated fingers. No reaction torque appears on the housing of the tool. A high speed steel tool bit was selected for its toughness and durability, especially for interrupted cutting. The tool bit can be adjusted by the Mascot once the tool is located onto the component.

Extracting the Blanks

A water hydraulic puller was used to extract the blanks from the ports (Fig 4). The tool was engaged in the groove in each blank (Fig 1) by means of 6 pawls. The pulling force was reacted on the port sleeve rim by means of a reaction sleeve. A pulling force of between 10 kN and 20 kN was normally adequate, but in some cases the maximum 95 kN was required. When this high extraction force was used there was severe galling of the port sleeve, and there was a tendency for the reaction sleeve to slip on the irregular curved profile of the remnant of the edge weld (Fig 3).

The design of component for all future installations (described in the following section) is not expected to demand such high extraction forces (2.5 kN is predicted) in which case the galling and slipping will be eliminated.

The Component Design

For the installations described here and for all future ones, a revised component sleeve design has been adopted. Because of the variations of the fabricated port sleeve dimensions and their poor circularity, a design of component sleeve was devised which could be matched to its corresponding port prior to installation. This ensures predictable installation forces and eliminates gaps between the port and component which are too large to weld without excessive filler material and heat input.

The procedure adopted was to calibrate each port sleeve, then expand the mouth of the component sleeve to give between 0.1 mm and 0.2 mm interference fit (Fig 5). When installed by a jacking system, the port sleeve is rounded by the component and large gaps are eliminated. The fit is also adequate to support the combined weight of the component and the welding tool. The sleeve also features an accurately machined location groove for the alignment of remote handling tools.

Installation and Welding

The components were installed to a depth of 4 mm (Fig 5) and the vacuum seal weld performed by the fillet welder shown in Fig 7. This tool is located in the component by means of a collet which engages in location ring. The whole chassis of the tool rotates relative to the collet, to produce a continuous weld. Rotation may be either continuous or pulsed. The weld head is mounted on

a motorised parallelogram mechanism which provides automated arc voltage control (AVC) along the axis of the electrode. Filler material is provided from a wire feed system delivering Ø0.8 mm Inconel 625 wire, via a conduit to the nozzle mounted on the weld head. Welding power and control was provided by an ESAB Protig sited in the Torus Hall and connected to the tool by a 40m long cable assembly.

The welding current for the seal weld was pulsed between 63A and 10A at 1 Hz in the ratio 60% to 40%. The rotation speed was one revolution in 180 seconds. The wire addition was pulse fed during peak current at a rate of 45 cm/min. Pure Argon shield gas was used.

Because the port rims had previously been manually edge welded they were irregularly radiused on the outside diameter, producing a feather edge after blank removal. Localised thinning of the port wall was also present principally due to the circular cutting of oval ports. Both these factors led to excessive heat buildup in the port rim and a tendency for the rim to be melted producing a scalloped edge (Fig 8).

These inconsistencies made it essential to visually monitor the weld in order to compensate by adjusting the welding parameters. This suggests that arc viewing will be essential to perform these welds remotely, and a system is currently being investigated at JET.

The use of filler material imposes a complication of the welding process and was the most common cause of irregularity. An autogenous weld procedure would offer the benefit of simplicity and produce a weld further from the port rim, but would only be successful if the joint gaps are small. This is to be established by further workshop tests.

During the shutdown described here, a total of 66 welds of this style were successfully performed on the JET vacuum vessel.

Assembly of the Ø50 mm Pipes of the Belt Limiters and ICRF Antennae

The JET belt limiters and antennae are water cooled, each circuit consisting of 2 limiter sectors and one antenna or bypass pipe. The interface pipes between the systems contain bellows to accommodate thermal expansion and to allow the pipe displacements required to align and abut the pipes prior to welding or to facilitate system installation.

The pipes comprising the remote handling interface welds were procured from a common melt to obviate the influences of cast to cast variations in chemical composition on weldability, particularly important with autogenous welds. All bellows in these pipe systems are single ply corrugated type with an axial rate of 100 to 120 N/mm.

Pipe Handling Tools

Tools to handle in-vessel coolant bellows pipe are required for 2 reasons: to retract the in-site pipe away from the insertion path of a system being installed (belt limiter sector, antenna screen or bypass pipe) to prevent damage to the weld face which would result from contact, and to extend and flex the bellows to attain the requisite standard of alignment and abutment of the pipes prior to welding. All tools of this type impart motion to the in-site bellows pipe through 2 diametrically disposed trunnions which are a common remote handling feature on all such pipes as shown in Fig 10. The bellows forces on the tools are reacted against adjacent rigid mechanical structure and the provision for this varies with the geometry of the work location.

Fig 11 shows a schematic of a tool designed both to compress and extend the limiter feedthrough bellows pipe.

Axial motion is imparted to the pipe trunnions through 2 lead screws turned by a chain and gear drive. This tool functioned satisfactorily in the compression mode but was deficient in extending the bellows pipes requiring an additional degree of freedom to allow rotation in the plane of the trunnions.

Fig 12 shows a tool dedicated to raising limiter bellows pipe to allow installation of an antenna screen. The tool head engages to the antenna structure on a double tongue and groove. The pivoted lifting fork engages with the pipe trunnions and is displaced through a spherical cone which rotates as the tool body is rotated 180 degrees. The tool body is disengageable from the tool head to clear the antenna screen, which when installed lies close behind the tool head. The tool is withdrawn by opening an access door in the antenna screen and re-engageing the tool body to the tool head by a bayonet attachment. This tool functioned well and the main problem foreseen for remote use is that of placement along a tortuous path with adverse viewing conditions.

Fig 13 shows a tool used for extending and flexing the limiter bellows pipe to align and abut it with the antenna pipe prior to welding. The principal design problems with this 5 degree of freedom tool were those of insertion along a tortuous path of very small access volume, and holding the tool in position to react the bellows forces. Since it was used in conjunction with the 50 mm orbital weld tool, the access depth was limited to 35 mm and to obtain the required rotation of the pivoted fork a series of "see-saw" links were used to transmit the motion from an outboard leadscrew.
Fig 14 shows the tool used for bellows retraction and extension during installation of bypass pipes between limiter sectors. The tool again works on the pivoted lifting fork principle, but the ample access space and the availability of a rigid tool fixation abutment greatly simplified design and operation. This tool worked well and is suitable for remote use.

Welding of Ø50 mm Water Pipes

The welding tool used was the Ø50 mm orbital TIG welder (Fig 15). It features a water cooled electrode holder which is housed in a "Syalon" ceramic arm which articulates on the orbiting ring gear. This articulation accommodates irregularities of pipe diameter and maintains a constant arc length. The ring gear has a side cut-out to allow it to be placed and rotated coaxially with the weld joint. Accurate location of the tool is achieved by means of a trapezoidal section ring which forms part of the weldment. The tool is hydraulically clamped to this ring. Welding power and shielding gas are transmitted to the orbiting weld head by means of a water cooled cable assembly.
Three equi-spaced tacks were made with the tool to secure the joint during the seal weld. They also enabled the tool to be removed in order to review the fit up. The seal weld program used a welding current pulsed between 68A and 10A at 1 Hz in the ratio 60% to 40%. The closed butt welds were made autogenously. The welding arc was established in a shield gas of pure Argon, then a mixture of Argon with 5% Hydrogen was introduced to the weld head. The addition of hydrogen achieved a full penetration weld without excessive current and pool size.

The restricted access to the joints and the welding tool design meant that there was no possibility to view the

welding arc. The welding process was principally monitored by the weld current and voltage. However, it was found that the sound of the arc, especially its initiation, was a useful indication of arc stability and hence weld quality. The provision of a microphone for remote handling is desirable.

Inspection of the completed weld was by visual means. The outer weld bead was directly viewed and the inner was viewed by means of a flexible fibrescope where feasible.

After visual examination of the weld quality all the 96 welds of this type passed a helium leak test (better than 10^{-9} mbar lit s^{-1}).

Conclusions

The principal difficulties anticipated for the remote performance of these tasks are the imitation of functions that currently require direct human senses. These include the viewing of welding arcs and inspection of welds, and the tactile requirements for the placement of tools and the judgement of joint misalignments. Mock-up trials of the complete remote system, scheduled for later this year, will establish the actual areas of deficiency.

Further workshop studies of the welding parameters are being performed to determine the extremes of joint mismatch which may be successfully welded, thereby reducing the required dexterity of the remote system. In general, an effort will be made to simplify the placement and operation of tools wherever possible.

References

1 The JET Belt Limiter: G Celentano et al (JET) - 14th SOFT, Avignon, France 1986.

2 Design and Manufacture of Water Cooled Electrostatic Screens for JET ICRF Antennae: C I Walker et al (JET) - 14th SOFT, Avignon, France 1986.

3 Remote Handling Tools for JET: M Wykes et al (JET) - 14th SOFT, Avignon, France 1986.

4 Design and Operation of Remote Maintenance Systems in JET: T Raimondi (JET) - Remote Systems and Robotics in Hostile Environments, Proceedings of International Topical Meeting, Pasco, Washington 1987.

NB: Figs 6 and 9 have been deleted from this text.

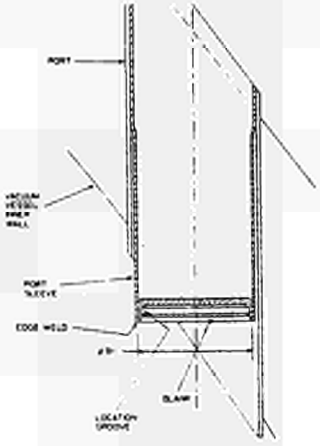

Fig 1 Ø91 mm Circular Port

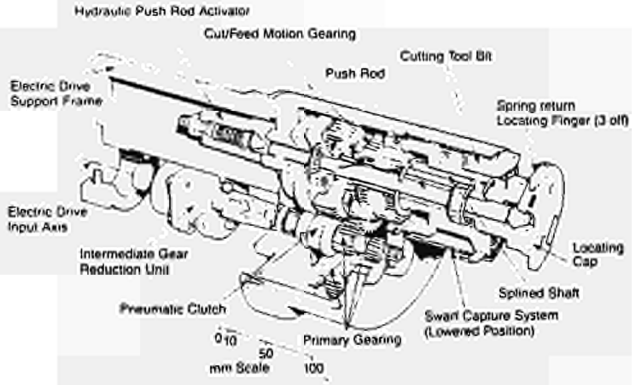

Fig 2 The Circular Port Cutting Tool

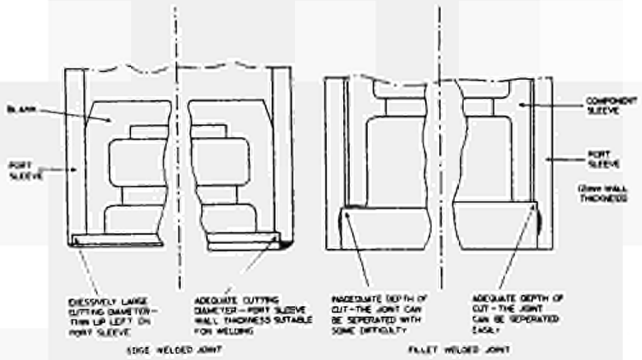

Fig 3 Details of Variations of Cutting Profile

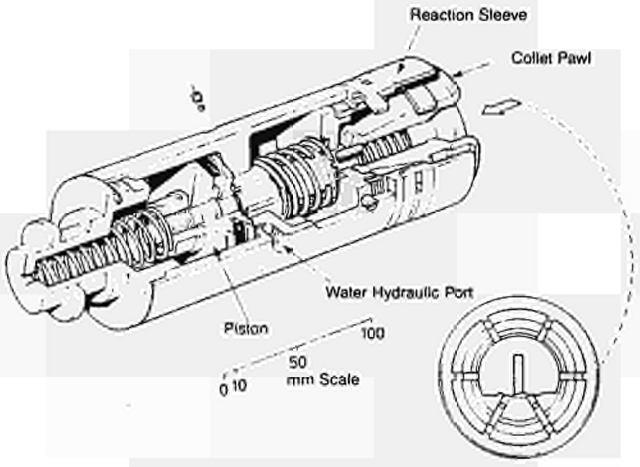

Fig 4 The Hydraulic Puller

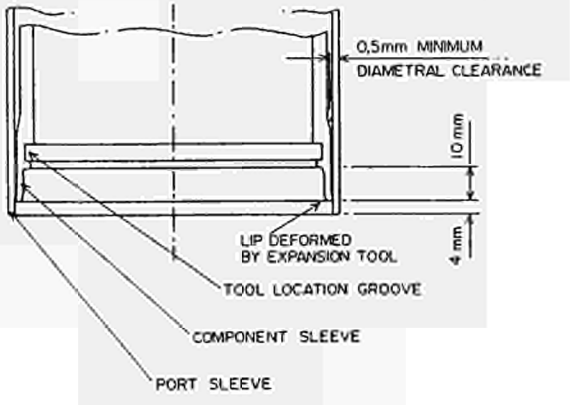

Fig 5 Component Installation

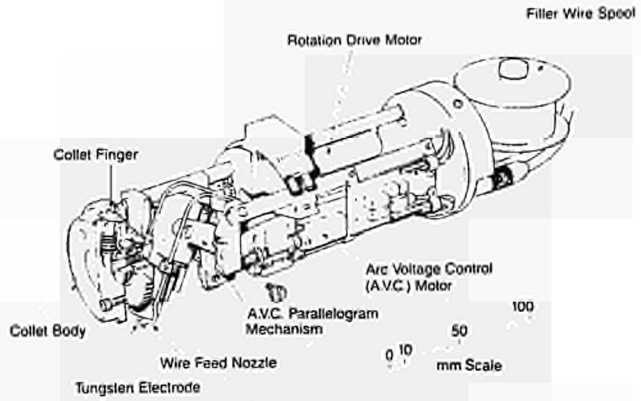

Fig 7 The Fillet Weld Tool

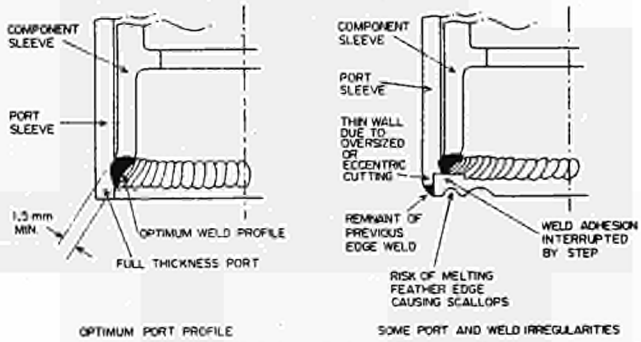

Fig 8 Welded Joint Geometries

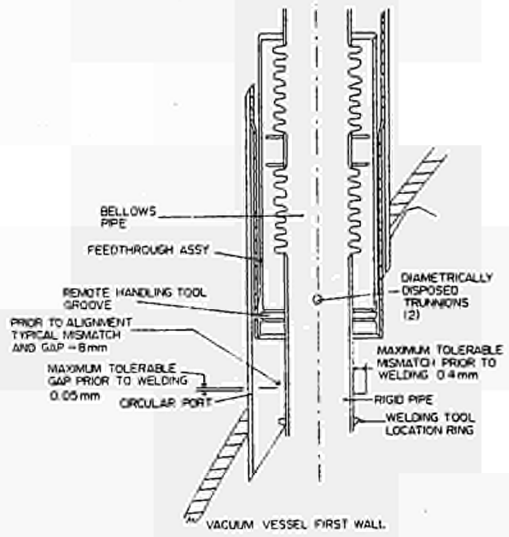

Fig 10 Typical Bellows Pipe Layout showing Remote Handling Tooling Features and Pipe Mismatches before and after Alignment

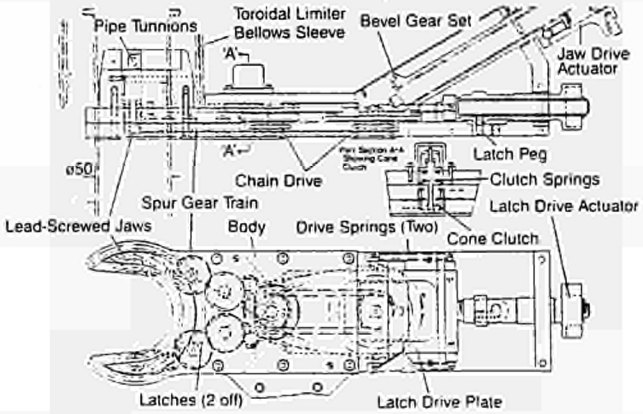

Fig 11 Handling Tool for Toroidal Limiter Bellows

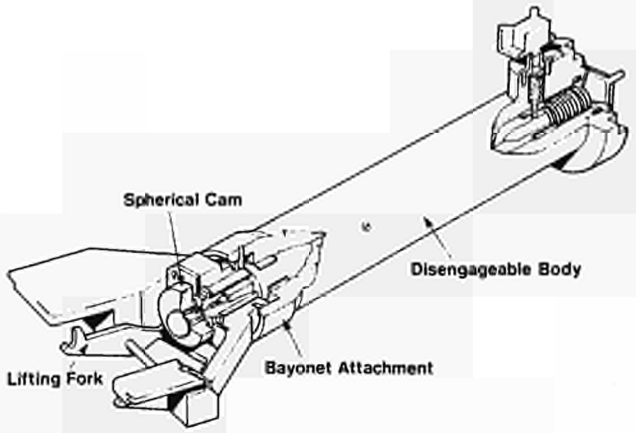

Fig 12 Bellows Pipe Retraction Tool

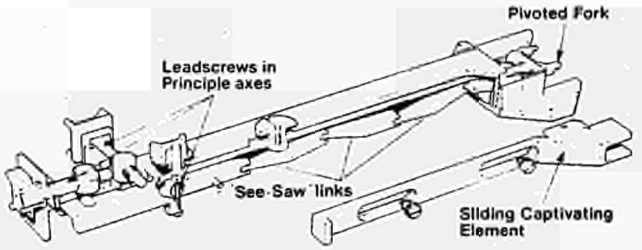

Fig 13 Bellows Pipe Extension Tool

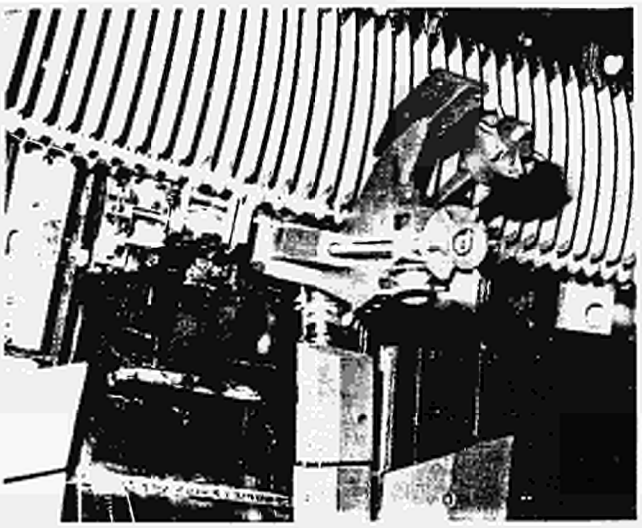

Fig 14 By-pass Pipe Bellows Handling Tool in Position on the First Wall

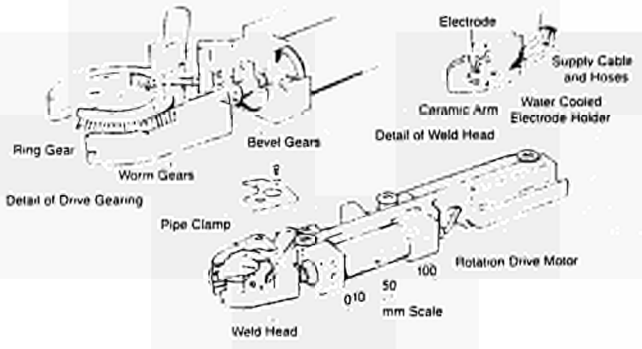

Fig 15 Ø50 mm Orbital Weld Tool

THE JET ACTIVE GAS HANDLING SYSTEM : CONCEPT AND STATUS

J L Hemmerich, A Dombra, C Gordon, J Gowman, E Groskopfs, R Haange,
M Huguet, A Konstantellos, E Kuessel, M Tschudin, K Walter
JET Joint Undertaking, Abingdon, Oxfordshire, England, OX14 3EA

Summary

The function of the JET Active Gas Handling System (AGHS), currently under design, is to gather mixtures of hydrogen isotopes (H, D, T) and impurities (tritiated water, hydrocarbons and others), to purify these mixtures and to resupply isotopically pure H_2, D_2 and T_2 for operation of the Torus and its subsystems (Neutral Beam Injectors, Multi-Pellet Injector). The design is based on a maximum total tritium inventory of 90 g T_2 with a daily throughput of ~ 30 g T_2.

The AGHS comprises four major subsystems:

(1) A cryogenic forevacuum system backing the JET turbomolecular high vacuum pumps. This system permits pumping of hydrogen isotopes and impurities by cryocondensation and helium by cryosorption as well as separation of helium, hydrogen isotopes and impurities. Hydrogen isotopes are transferred to intermediate storage for isotope separation. Helium and impurities are transferred to a tritium recovery loop.

(2) The impurity processing system extracts tritium from impurities and permits the release of detritiated impurities (CO_2, N_2, He etc) to atmosphere. Tritium, along with protium and deuterium recovered by this system, is subsequently transferred to intermediate storage for isotope separation.

(3) The isotope separation systems. Due to a relatively high throughput of protium (~ 3 m^3 per day, used as driver gas for pellet injection), a cryodistillation system was chosen to meet the overall operational requirements of JET [1]. This system will be backed up by a 4 column Gas Chromatography System capable of D/T separation in the absence of the pellet injector H_2 gas load.

(4) A mechanical vacuum system using dry scroll pumps (Normetex). This vacuum system is foreseen for roughing and for backing during standby periods. It contains water condensers to cope with potential accidents (eg coolant pipe rupture inside the Torus). This vacuum system is followed by an exhaust detritiation system with a catalytic recombiner and dryer beds to minimise tritium emission during Torus or AGHS maintenance.

Cryogenic Forevacuum System

At present, nearly all JET operational high vacuum systems are based on cryocondensation pumps (2 Neutral Injectors, 1 Pellet Injector). The Torus itself is pumped with 4 turbomolecular pumps [2]. With the installation of a cryocondensation pumped limiter (foreseen for 1989), all Torus systems will be cryopumped. This means that gas processing will start at the end of an operation day after defrosting of cryopumps. During Torus operation, the cryogenic forevacuum system will pump only helium by cryosorption (^{4}He from D-T fusion and ^{3}He added to plasma discharges from RF minority heating). A schematic of the cryogenic forevacuum system is shown in Fig 1. It includes 4 identical accumulation panels (ACP) in process cold boxes 1 and 2 for pumping hydrogen and impurities by cryocondensation, and helium by cryosorption. Helium accumulated during Torus operation is removed via a precooled cryotransfer pump (CTP) at 4 K and pumped into the impurity processing loop. A batch of Torus gas (DT with tritiated

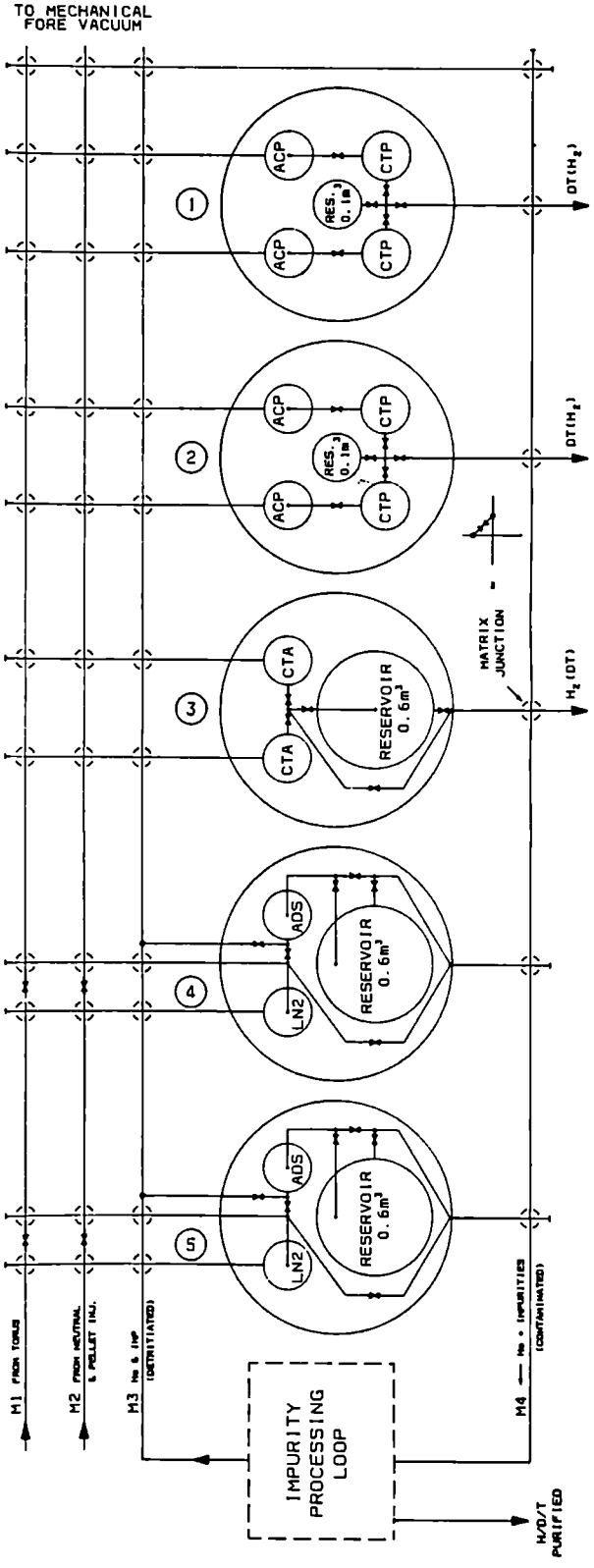

Fig 1 : Cryogenic Forevacuum System for cryogenic pumping, purification and compression of Torus exhaust gas mixtures

hydrocarbons) is then condensed on one panel and transferred to the cryotransfer pump. The cryotransfer pump is heated to ~ 25K to release the hydrogen isotopes and to transfer them to a gas reservoir, while impurities are retained in the cryotransfer pump. In order to avoid retention of hydrogen in the cryotransfer pump we intend to avoid the use of cryosorption for trapping of impurities. At present, experiments are carried out to establish the efficiency of "helipac" packing to cryocondense impurities above the liquid boiling at ~ 25 K. Subsequently, the cryotransfer pump is warmed to ~ 77 K to transfer impurities into the impurity processing loop.

Accumulation panels and cryotransfer pumps are designed to minimise the consumption of liquid helium used as refrigerant (Fig 2); liquid helium is supplied via vacuum insulated transfer lines to the cryocondensation/sorption areas, the evaporating helium precools incoming hydrogen mixtures in counterflow.

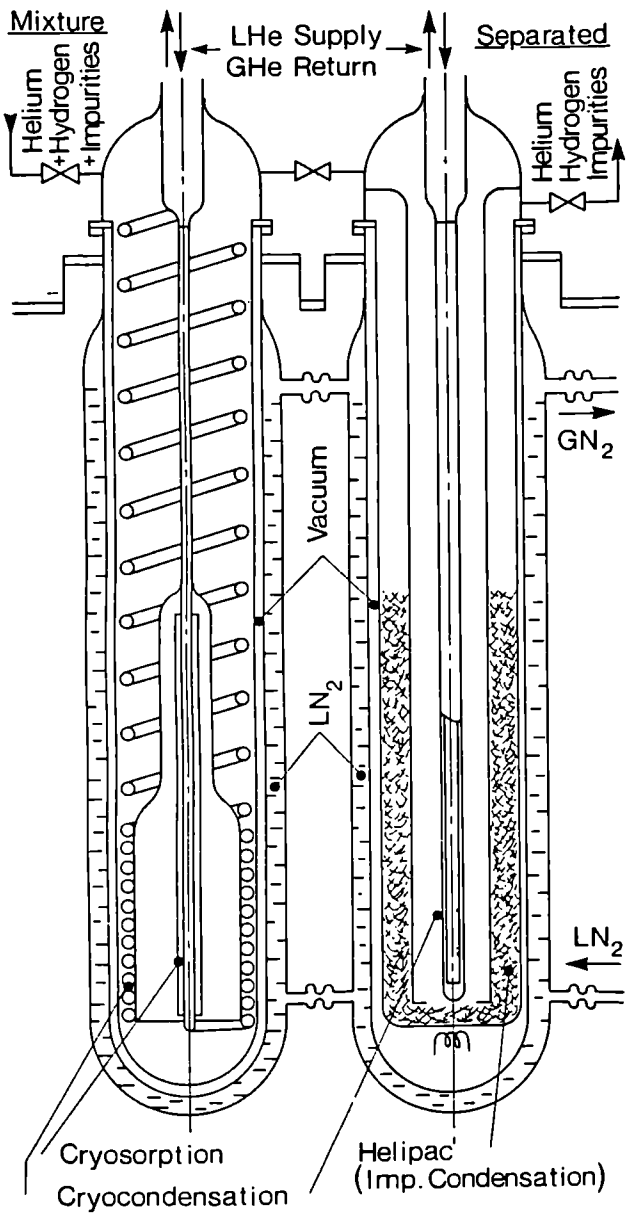

Fig 2 : Accumulation Panel and Cryo-transfer Pump

Typical LHe consumption rates with good quality transfer lines (loss rates < 0.1 W m^{-1}) are expected to be in the order of 4 ℓ LHe per hour for each element.

Cryotransfer accumulators (CTA) in the process cold box 3 (see Fig 1) are similarly designed to receive large gas batches (~ 3 STD m^3 H_2 with ~ 1% T_2) from the multi-pellet injector. Again, the use of helipac is intended to retain impurities.

The cryogenic forevacuum system contains also LN_2 cold traps and LN_2 cooled adsorbers in process cold boxes 4 and 5. These elements will be used primarily for Torus decontamination: graphite tiles are used extensively inside the Torus in areas of high power deposition (limiters, neutral beam shine-through protection, separatrix dump plates, general first wall protection against plasma disruptions). This use of carbon causes retention of hydrogen isotopes inside the Torus (later also tritium) in the form of co-deposited, dense and thermally stable carbon-hydrogen films containing ~ 40 at % hydrogen. This process, presently under quantitative investigation, makes it necessary to select a special method of tritium recovery : at TEXTOR [3] it was shown that a glow discharge in helium with 2% oxygen is well suited for efficient removal of hydrogen-carbon surface layers. This glow discharge will result in formation of HTO/DTO and CO/CO_2. In this case, the torus exhaust will be passed through LN_2 cold traps and LN_2 cooled adsorbers to retain all tritiated compounds, while pure helium is discharged by the mechanical vacuum system via the exhaust detritiation system (as a further safety backup). Tritium is subsequently recovered in the impurity processing system.

The LN_2 trap/adsorber system will also be used to separate air from hydrogen in the case of air leaks into the torus or injector vacuum. All batches of incoming gas have to be analysed for air (oxygen) prior to cryocompression to detect potentially explosive mixtures.

Impurity Processing System

A schematic of the impurity processing system is shown in Fig 3. Tritiated impurities from cryotransfer pumps (or LN_2 traps/absorbers as described earlier) are pumped into buffer tanks together with helium. At present, it is expected to process the equivalent of approximately 1 mole of tritiated methane per day. After analysis (not shown in Fig 3), a slightly larger than the stoichiometric amount of oxygen is added to permit full oxidation of all impurities (to $HTO/DTO/CO_2$). The mixture is recirculated via a recombiner and a cold trap, until the tritium (as indicated by ionisation chamber signal) is quantitatively frozen in the cold trap. The remaining gas ($He + CO_2 + N_2$ etc) is then discharged via the mechanical forevacuum system to the stack and replaced by pure helium. With the recombiner bypassed, the helium is recirculated through the gradually heated cold trap, releasing HTO/DTO, which is decomposed in a hot uranium bed ($2\,HTO + U \rightarrow UO_2 + 2\,HT$). The gas then flows through a cold uranium bed to remove HT/DT. Hydrogen isotopes gettered on cold uranium are subsequently (by heating the U-bed to 400°C) transferred to the isotope separation system.

The impurity processing system is designed in a modular way, each module contains one process element; this alleviates maintenance (replacement of U-beds) and permits the incorporation of advanced processing methods such as vapour phase electrolysis and palladium diffusion cell [4] and possibly other future developments at a later stage. Fig 4 shows a chemical process module with all process and manual maintenance

valves. These modules are fully double contained (vacuum pumped by Zr-Va-Fe regenerable getter cartridge [5]). One of the process lines is also used as a leak test manifold, permitting leak testing on all system connections after maintenance operations. When necessary, vacuum lids can be replaced by glove-box type lids for critical operations.

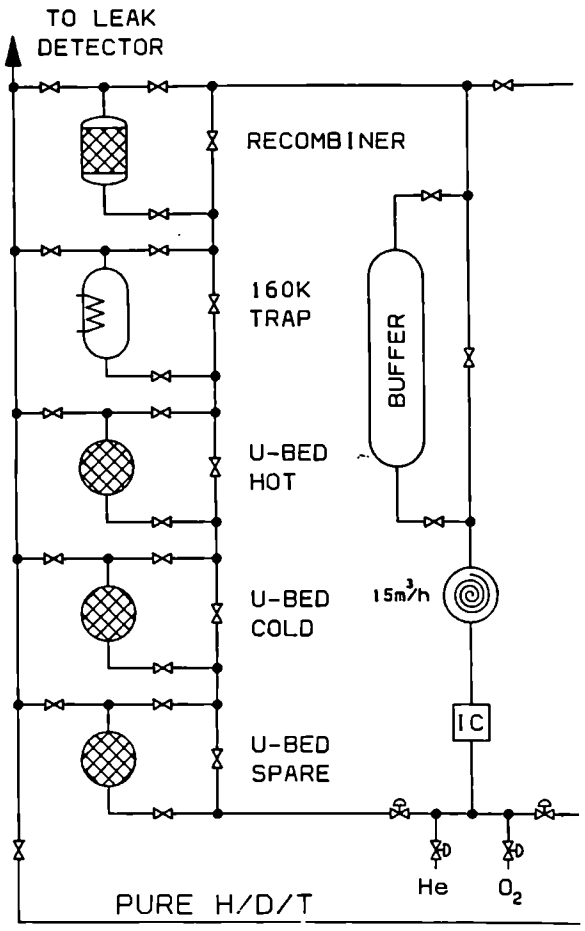

Fig 3 : Impurity Processing System Flow Schematic

Isotope Separation

For isotope separation under full operating conditions (including pellet injection), a cryodistillation system described separately [1] is under evaluation.

In addition (for operation without pellet injection and for rundown), 4 gas chromatography columns (25 weight % Pd on Al_2O_3) will be used. This system is presently under design in cooperation with D Leger and R Botter, CEA, France.

Both systems will be capable of processing each day approximately 400 ℓ (STP) of D-T mixtures with some protium; the cryodistillation system will handle an additional load of approximately 3000 ℓ (STP) of H_2 per day with either 1% T_2 (tritium pellets) or 2% D_2 (deuterium pellets) with traces of T_2 due to backstreaming from Torus after plasma discharges.

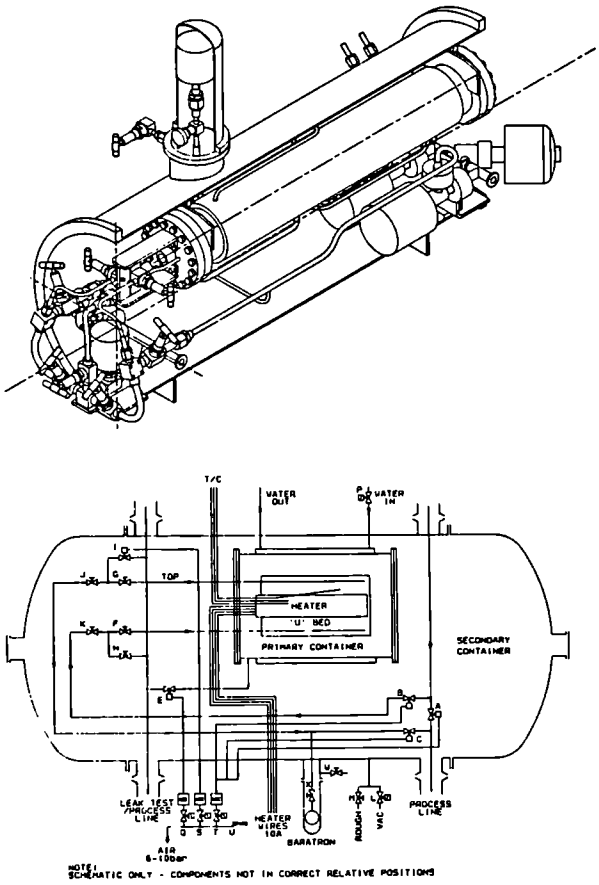

Fig 4 : Impurity Processing Module
Top : Assembly Drawing
Bottom : Internal Flow Schematic

Other Systems

Mechanical vacuum system

The mechanical forevacuum system consists of 4 scroll pumps (Normetex), 2 with a pumping speed of 600 $m^3\ h^{-1}$ and 2 with 150 $m^3\ h^{-1}$. Water condensers operated at - 4°C permit the retrieval of potentially tritium contaminated water in the case of accidents (coolant pipe rupture in Torus or neutral injector). Subsequently, further detritiation is performed by the exhaust detritiation system.

Exhaust detritiation system (EDS)

In addition to the cleanup of vacuum pump and plant exhaust streams, this system will be designed to support remote handling interventions on the Torus in case of failures such as breach of vacuum integrity, ie in cases where Torus decontamination by means of glow discharge cleaning is not possible. The EDS then maintains a positive air flow (up to 1600 $m^3\ h^{-1}$) into the opened Torus, thus preventing tritium contamination of the Torus Hall. The EDS will be designed for continuous operation similar to a system described by A Dombra [6].

Storage and transfer systems

Originally, it was intended to use $LaCo_5$ metal hydride storage and transfer systems. Equilibrium pressures of this hydride would have been ideally suited for storage and transfer (~ 5 kPa at 293 K, > 100 kPa at 378 K). An attempt to produce an industrial size batch (~ 100 kg) of this material, however, failed due to the low formation enthalpy of the intermetallic compound $LaCo_5$. The product contained large amounts of more stable phases ($LaCo_3$, $LaCo_{13}$) which made the sorption/desorption characteristics unsuitable for the intended purpose.

We are presently considering to use the gas reservoirs inside the cryogenic forevacuum cold boxes for intermediate storage of isotope mixtures. The transfer (with constant delivery pressure of ~ 1 bar) to the isotope separation system will be done via small (500 g each) palladium hydride compressors, as palladium hydriding characteristics are well established and suitable for transfer operations [7]. Palladium can also be used for safe T_2 product storage after isotope separation (~ 6 kg Pd required to store the maximum JET inventory of 90 g T_2). Other suitable and proven hydride storage systems will be used for H and D products. The main advantage of metal hydride storage lies in the fact that hydrogen isotopes can be safely stored in small volumes (equivalent to the density of liquid hydrogen) at sub-atmospheric pressure with minimal immediate release in case of container failure.

As an alternative to metal hydride transfer and storage systems, we have the option of using small cryotransfer pumps and storage tanks. An advantage of this latter method would be its inherent capability of direct inventory accounting for all isotopes.

Safety and Control Systems

All plant subsystems will be designed failsafe in case of failure of services, ie cryogenic supplies, compressed air supply or power. The intended use of hydride storage is a particularly attractive safety feature : when all services are interrupted, the plant subsystems will approach room temperature, in which case all hydrogen isotope pressures will settle at the equilibrium pressure of the chosen metal hydride (~ 10 kPa in case of palladium tritide).

Plant control systems will be based on individual PLC's for each major subsystem. The PLC's interface with a computer permitting remote plant operation by means of mimics and touchpanels. The computer will also supply information of plant status to the JET Control and Data Acquisition System and perform other supervisory functions, in particular keeping track of hydrogen isotope inventories in each individual subsystem.

Instrumentation

A variety of sensors and instrumentation systems are required for monitoring, control and safety purposes within the Active Gas Handling Plant.

Tritium monitoring will be based on in-line ionisation chambers with the following main features:

- all-metal/ceramic construction in an evacuated double containment
- operation at elevated temperatures together with inert internal surfaces (gold plating) to mimimise contamination and to achieve quick cleanup after exposure to high tritium concentrations.

General mass spectrometry will be performed with quadrupole mass spectrometers directly connected to process lines via leak valves and pumped with an Ion Getter pump throttled to ~ 1 $\ell\ s^{-1}$ pumping speed.

For Hydrogen/Helium isotope mixtures an Omegatron mass spectrometer with a resolution of ~ 2000 at mass 4 is considered [8]. Alternatives under evaluation are analytical gas chromatography, Raman spectroscopy and NMR methods.

General temperature measurements will be done with Platinum resistors and thermocouples; critical cryogenic temperatures will be measured with vapour pressure thermometers (^4He, H_2, D_2).

Pressures will be measured with single-sided absolute capacitance manometers; together with tanks of known volume and temperature, such pressure sensors will be used for inventory accounting.

Gas flow monitoring will be done with standard thermal mass flow meters.

Building

A dedicated building is presently under design to accommodate the above described active gas handling systems.

Time schedule

Subsystem tender action has started with the cryodistillation plant (longest lead item). Further systems will be procured as design proceeds.

The completion of the Active Gas Handling System is expected for end 1989, followed by a 6 month commissioning period prior to gradual introduction of tritium into the JET tokamak.

References

[1] R Sherman et al., paper 34-04. this conference.

[2] E Usselmann et al., Proc 13th SOFT, Varese, Italy, Vol 1, 150 (1984), Pergamon Press.

[3] J Winter, J Nucl Mat 145-147, 131 (1987).

[4] S Konishi et al., Fusion Tech 8, 2042 (1985)

[5] ST 707 Getter Systems: SAES Getters S.p.A, Via Gallarate 215, 20151 Milan, Italy.

[6] A H Dombra et al., Proc 14th SOFT, Avignon, France, Vol 2, 1511 (1986), Pergamon Press.

[7] R Lässer et al., Phys Rev B, 28, 748 (1983).

[8] T Winkel et al., J Vac Sci Technol., to be published.

THE JET MULTI-PELLET INJECTOR LAUNCHER - MACHINE INTERFACE

P Kupschus, W Bailey, M Gadeberg, L Hedley, P Twynam, T Szabo, D Evans
JET Joint Undertaking, Abingdon, Oxon, OX14 3EA, UK.

Abstract

Under a collaborative agreement between the Joint European Torus JET and the United States Department of Energy US DoE, JET and Oak Ridge National Laboratory (ORNL) jointly built a multi-pellet injector for fuelling and re-fuelling of the JET plasma. A three-barrel repetitive pneumatic pellet Launcher - built by ORNL - is attached to a JET pellet launcher-machine interface (in short: Pellet Interface) which is the subject of this paper. The present Launcher-Interface combination provides deuterium or hydrogen injection at moderate pellet speeds for the next two operational periods on JET. The Pellet Interface, however, takes into account the future requirements of JET. It was designed to allow the attachment of the high speed pellet launchers now under development at JET and complies with the requirements of remote handling and tritium operation. In addition the use of tritium pellets is being considered.

Introduction

Multi-pellet injection preferably at high pellet velocities for central fuelling and re-fuelling of the JET plasma was relatively late introduced into the programme, e.g. [1]. It was decided to keep the option of high-speed (>2 kms^{-1}) pellet injection open although its principle compatability to fuel the inner core of high temperature fusion-type plasmas [2] as well as the technical availability of sufficiently high pellet speeds have yet to be proven more clearly. For the latter part JET has in co-operation with European laboratories initiated a development programme to advance the pellet launcher technology to high pellet speeds towards 10 kms^{-1} [3,4]. On the other hand multi-pellet experiments were to be started on the basis of present gun technology as soon as possible. For that reason JET entered into an agreement on pellet injection collaboration with the US Department of Energy within the framework of the EURATOM-US DoE Bilateral Agreement on Fusion Research. The collaborative agreement calls for jointly performing experiments for two major operational periods at JET during 1987 to 1989 using a pellet injector formed by joining an Oak Ridge National Laboratory (ORNL) built launcher [5] - following closely the technology of the "RPI" employed successfully on TFTR at Princeton - to a JET launcher-machine interface (in short: Pellet Interface). The ORNL Launcher comprises three RPI type pneumatic guns capable of independently and repetitively launching respective pellets of sizes 2.7, 4 and 6 mm diameter/length, in numbers and with rates sufficient for JET, of deuterium or hydrogen, with speeds approaching 1.5 kms^{-1}; no provisions could be made to make this launcher compatible with the requirements for tritium operation and remote handling. The joint multi-pellet injector was brought into operation this summer about two years after negotiations had started between the partners.

The JET Pellet Interface which is the subject of this paper has thus the requirement to provide adequate matching of the ORNL Launcher to the JET machine as well as allowing - with a minimum of upgrading - any future launcher, with hopefully increased pellet speeds and suitable for the Active Phase, to be adapted. It is planned that a simple proto-type high-speed gun for first tests can be employed already in 1989 overlapping with the ORNL Launcher. It is thought at present that such a launcher will work by means of hot gas pneumatics employing the principles of two-stage gun adiabatic compression and/or arc heaters.

The main components of the Pellet Interface are: vacuum interface comprising also the structural elements for the mechanical support; liquid helium (LHe) supply and LHe intermediate storage for the launcher; primary fuel and propellant gas supply; specific pellet diagnostics and signal acquisition; control and data acquisition interface.

The Vacuum Interface

Requirements and problems

With regard to the propellant gas of a pneumatic gun as much as 30 bar.l per pellet shot and in the order of 100 bar.l per tokamak pulse (over roughly 10 seconds) may have to be pumped away before reaching the plasma; this leads to a daily pumping requirement in the range of several 1000 bar.l. Hydrogen is seen as the only candidate for high-speed propellant for reasons of highest sound velocity. The above numbers stem from extrapolation of two-stage gun scenarios and take the limits of pellet mass which can be delivered to the plasma into account; this is governed by particle confinement and pellet reheating balances. For high-speed pellets there is also the requirement of low foreland pressure of desirably not more than 10^{-2} mbar, i.e. the second pellet should not interact with the residual gas of the first pellet in case they pass through the same vacuum system. To keep a sudden burst of 30 bar.l to less than 1 mbar for example one needs already more than 30 m^3 of expansion volume and estimates on the time in which this gas load should be pumped away always end up in the several 10^5 ls^{-1} pumping speed range. Multi-stage scenarios pumping at high pressures suffer from the high conductance values of tubes connecting the differential stages while being sufficiently wide to enclose the trajectory scatter of the pellets which should not graze the tube walls. Guide tube techniques are surely not applicable for the final speeds aimed at; moreover, the use of fast valves, shutting off in milliseconds to bar-off hydrogen reaching subsequent stages or the plasma, pose severe maintenance problems for the Active Phase of JET.

The JET solution

Faced with the above requirements a solution for JET was almost at hand to compose an adequate system from already designed and proven components thus creating the minimum of manpower effort and time in designing, manufacturing and commissioning and in assuring the tritium and remote handling compatability needed for the Active Phase: The JET neutral injector boxes [6] - called NIBs in the JET jargon - are about 7m high, in the plan view wedge-shaped about 3.5m long boxes and their modification to become a pellet injector box - dubbed PIB - contains about 50 m^3; cf to schematics fig. 1 and 2 (letters in the following refer to these) and fig. 3 for an overall impression. The side-walls of the PIB are in the same way as those of the NIBs lined with open-structure (though liquid nitrogen shielded) liquid-helium (LHe) cryo-condensation pumps CP [7,8] with a total nominal pumping speed of 8.10^6 ls^{-1} for hydrogen and a final pressure (depending on the exact LHe temperature) of not more than 10^{-5} mbar. The time constant for the above system is according to the above figures around 6 msec. The above quoted 30 bar.l burst would raise the pressure to .6 mbar and its gas would be removed in about 2.10^{-2}s to less than 10^{-2} mbar. In reality the gun gas cannot be delivered to the box in a δ-function manner due to obstacles in the rear insert RI (e.g. μ-wave interferometer) and the above example presents a worst case estimate. Attempts with quick release of room temperature gas as well as large pressure

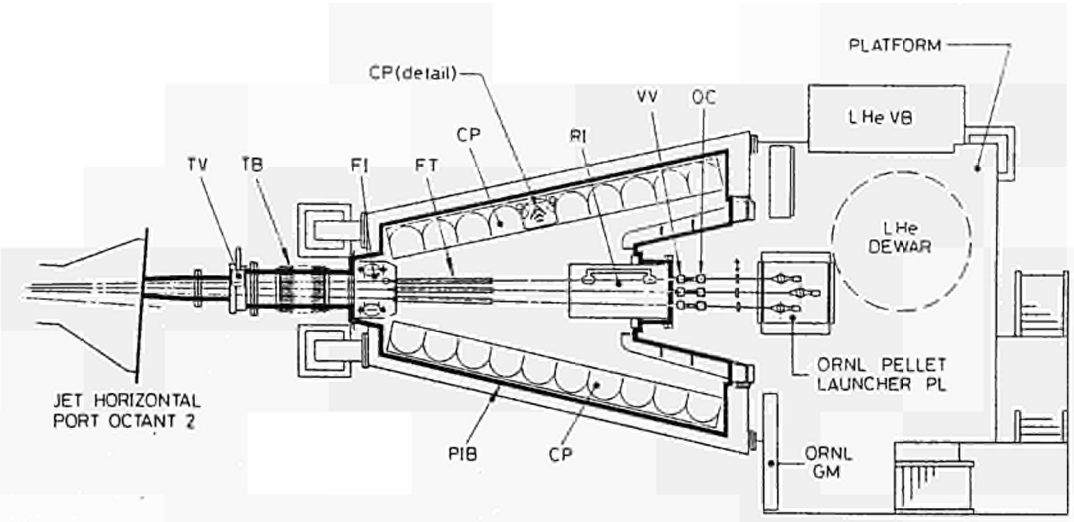

Fig. 1: Schematic of Multi-Pellet Injector - Plan View

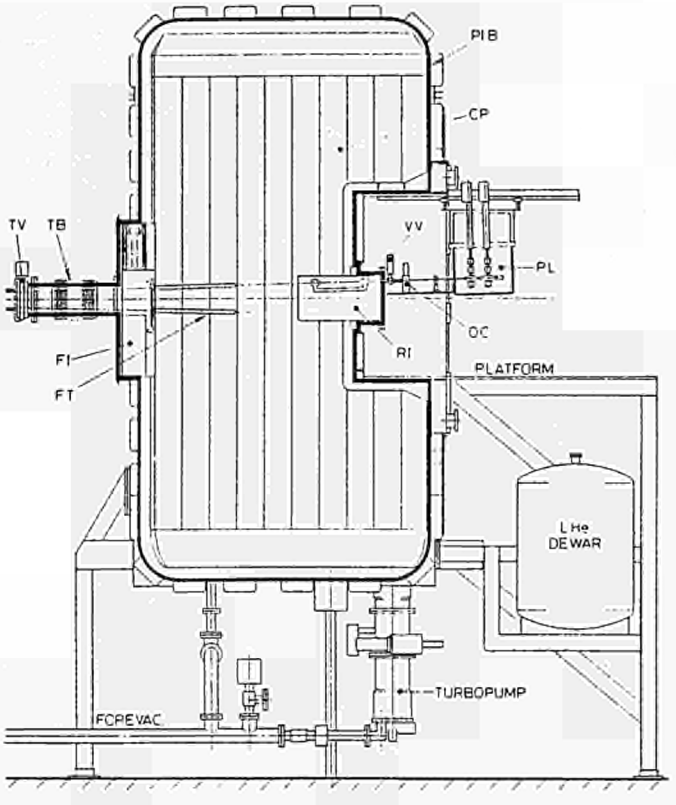

Fig. 2: Schematic of Multi-Pellet Injector - Side View

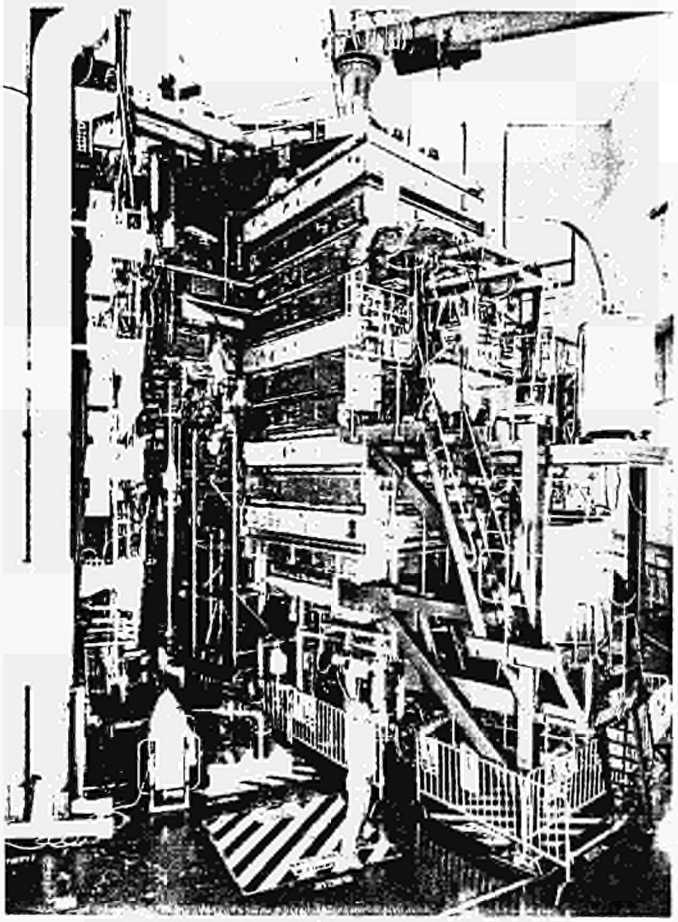

Fig. 3: Multi-Pellet Injector Overview

excursions as observed during re-generation processes (when the hydrogen is obviously released in large chunks from the upper part of the LHe panels while the LHe level is dropping) indicate that 30 bar.l bursts do not present a problem [8]. Due to the excellent accommodation of the LN$_2$ panels it is expected that the pumping characteristics due to gas from later "hot" guns will not change against the present performance.

The ORNL Launcher gives maximum bursts of typically a factor of 10 less than the above value but needs pumping for its excess deuterium extrudate which is also let into the PIB; this is of the order of 5 bar.l per extrusion per gun and tokamak pulse with an initial filling of about 30 bar.l per gun. The cryopump is in principle, according to estimates, capable of accommodating 5000 bar.l and a capacity of more than 3000 bar.l has experimentally been proven [8]. However, the NIB was originally conceived as a pure vacuum vessel with a required maximum capacity of far less than 1000 bar.l for regeneration typically once a week and not even the worst accident case mixture of air to that fixed amount of hydrogen will lead to deflagration maximum pressures in excess of 1 bar absolute (explosions are not possible due to the geometry of the vessel; however, the pressure increase in time is so rapid that bursting disc techniques are not capable of releasing the pressure sufficient to avoid damage of equipment and other subsequent hazards). So, the PIB at this moment is limited for safety reasons to operation with a maximum amount of

1000 bar.l aggregate hydrogen and deuterium requiring regeneration on a daily basis overnight. But measures are underway to modify and re-classify the PIB for higher pressures and at least 3 bar absolute - equivalent to an allowance of 3000 bar.l - seems likely to be the outcome.

The quoted pressure will cause a flow through the 400 mm diameter bellow section TB through the 250 mm diameter metal-sealed gate valve TV into the torus, which integrated over the pumping time to reach torus acceptable PIB vacuum for the quoted 30 bar.l burst as well as for the one for the ORNL Launcher, i.e. typically 3 bar.l, would certainly exceed a tolerable amount of gas to the torus. Flow restrainer tubes FT (ca 5 cm in diameter/1m long) with a nominal conductance of 60 ls^{-1} each and individually actuated flap valves to close unused gun lines limit this to a insignificant amount. In the ORNL case a 3 bar.l pellet shot (from the 6mm gun) can be estimated to not deliver more than about 2.10^{-2} mbar.l (leading in comparison to a tokamak filling particle pressure increase of ca 1.5 10^{-7} mbar); in reality this increase should be considerably less. However, for the 30 bar.l assumption - the flow restrainer tubes operating then into the viscous flow regime - investigations have still to show whether a further differential volume with a small cryopump close to the front bellow section TB will be necessary. To assess this, fast open Baratrons will be installed on the main PIB as well as on the front insert/bellow vacuum.

The PIB is conventionally pumped with a 3500 ls^{-1} turbopump connected via valves to the fore-vacuum line used by the NIBs as well; but during LHe operation the PIB can be completely valved off from the conventional pumping system. The PIB itself is an integral part of the support structure, fig.2, providing also a platform for Launcher maintenance and support for the Launcher LHe supply components.

LHe supply and intermediate storage

The cryopump within the PIB is supplied under the control of the JET cryoplant in the same way as the other two in the NIBs. However, more severe demands are put forward here for the regeneration every night, in general. The turn-around time here is still being optimised and it is hoped that the presently achieved 7 hours can be decreased by another 2 hours or so to leave more headroom for unforeseen circumstances; likely savings can be made during warm-up and over-lapping pumping and cool-down phases.

The Launcher is during operation supplied with LHe from a 1500 l dewar at the back of the PIB through a cryogenic valve box VB to allow other users to be provided with LHe as well, by means of co-axial (go and return) cryolines. The dewar supply pressure is regulated by a feed-back controlled heater (300 W) to suit the needs of the launcher (nominal 7 psi). The dewar is de-pressurised and refilled overnight - transfer needs 500 to 1000 l - from the cryoplant through a ca 80 m long co-axial line of the type used at CERN again through the valve box. The commissioning of this complex system was lengthy and troublesome although no principal design errors were detected. Many lessons had to be learned mostly on oscillations of LHe in the various volumes of the cryo transfer system mainly but not only when changing conditions and on cleanliness of the supplied cryofluids, in particular, in cool-down situations. Parameters and control cycles have now been established to have a satisfactory supply to the launcher and measures are under way to increase the rather low transfer rate of ca 100l/h to its desired level of more than a factor of two higher.

The primary fuel and propellant gas supply

Since the launcher takes the required gases from its gas manifold GM governed by the launcher controls the main purpose of the JET system is the reliable accounting of the hydrogen gas going into the PIB. The gases are let from the outdoor gas storage shed to a site near the LHe plant, into small intermediate storage volumes (2-5l) equipped with valves and gauges under the control of the PC (cf. controls). While intermediate storage volumes are cycled between a minimum and maximum value the PC adds the corresponding amounts into a register which is displayed to the operator.

At present foreseen are three fuel systems (D_2, H_2 and an arbitrary mixture with impurities) and one propellant system. Each system (and a spare) is available at the launcher manifold GM; it should, however, be kept in mind that GM permits at this moment only one fuel and one propellant (pressure) to be used for the entire Launcher. The hydrogen accounting is complemented by reading back from the launcher controls the number of extrusions and the number of pellet shots such that the operator has available the corresponding amounts and can also compare them to the decreasing pressure in the primary gas bottles (course check).

Pellet trajectory and pellet diagnostics

Pellets are passing from the Launcher's three barrels, each through an optical cube OC with windows, the absolute vacuum valves (both belonging to the ORNL Launcher), then through the rear diagnostic insert RI with μ-wave interferometers, through the flow restrainer tubes FT - allowing altogether for each gun a scatter of ± .4° around the ideal trajectory as seen from the muzzle - through the bellow connecting the PIB to the torus and entering the plasma nearly perpendicular to the torus axis in the tokamak midplane; this can best be envisaged by looking at fig. 1 and 2 (pellet flight pass from right to left). The rear insert and the front insert (this carrying the flow restrainer tubes FT and the flap valves) are both arranged to allow for 6 gun lines and are thought to be replaced according to the need of the final advanced launcher. The upper three of the gun lines are taken up by the ORNL launcher, the three lower ones are taken by the JET Diagnostic one-pellet injector for the time being and reserved for the high-speed prototype(s).

To monitor and assure the delivery of well-characterised pellets a number of diagnostics have been prepared.

The extrudate deuterium ice after having passed the chambering mechanism is monitored by a CCD camera and the image in the control room guides some parameter choices for the guns.

The optical cube OC for each respective barrel comprises a light barrier which - when interrupted by a pellet - provides a trigger to a repetitive 8ns-pulse flashlamp enabling still pictures of all the pellets to be stored on a CCD camera from which they are transferred to a magnetic tape or in the near future onto an optical disc. Pellet pictures of all three barrels are fed into one recording channel. Due to an optical mismatch on the triggering system we have not yet been able to reproduce the picture sequences obtained in the Launcher commissioning tests at Oak Ridge. For a later stage some provisions have been made to photograph the pellets after their passage through the μ-wave cavities rather than before.

In the rear diagnostic insert RI the pellets have to pass successively through two cavities (with respective 15 and 20 mm diameter holes and stub tubes for the pellets) of a μ-wave interferometer arm (rectangular waveguide WG12, pellet moving in H-direction) the other comparison arm being used for the mutual upper/lower gun line. These three interferometers are being fed through a power splitter by a crystal stabilised oscillator at 5GHz ± 10^{-6} and are zeroed out for minimum signal to three μ-wave diodes on the mixing coupler. A pellet offsets this balance due to the dielectric detuning of the cavity.

In the design of the interferometer attention has been paid to the long-term stability of its tuning - oscillator stability, temperature regulation of the copper waveguides - as well as to the minimising of the traverse dependence of the signal for pellets passing the 15 mm hole and so allowing to relatively assess the mass of the pellet. The second cavity is 416 mm further downstream and its traverse sensitivity is unsuitable for pellet mass determination but its signal is valuable for the speed assessment. The initial μ-wave measurements with the interferometer were done with PTFE pellets assumed to have the same detuning effect as deuterium pellets; the potential to measure the amount of deuterium with a certain accuracy has been deduced from these measurements as ±2, ±3 and ±4% for 6, 4 and 2.7 mm pellets, respectively. A fourth identical interferometer has been built for later calibration to absolute deuterium mass in the JET pellet teststand. The signals of unbroken deuterium pellets are noise-free, gaussian-like traces and should be suitable for later automatic evaluation.

In the front insert a target can be moved into either of the six gun lines behind the flap valves. The target consists of a titanium block with high-speed carbon piezo-sensors and the time correlation of their signals should give some indication of the impact location and therefore allow fine-tuning of the barrel direction which is until now preset by optical alignment but not yet checked while firing. We have seen promising signals from pretests with an conventional airgun and from a 6 mm deuterium pellet but the target is not yet commissioned due to the lack of a suitable trigger and the late delivery of fast transient recorders.

An existing periscope looking from the lower vertical port into the tokamak midplane has been modified to cover a field of view of the minor torus diameter times about 2 m toroidally which should well enclose all Dα/Hα radiation stemming directly from the ablating pellet. The corresponding CCD camera pictures will be dealt with in a second optical disc unit as in the case of the pellet photography; an optical beam splitter and an spatially integrating sphere on the periscope provides the Dα/Hα light as a function of time. This system is being commissioned and first traces have been seen.

The optical trigger, the μ-wave diode signal, the Dα/Hα traces and a trigger pulse - derived from an electronic unit, calculating the arrival of the pellet at the limiter some 7.3 m downstream of the muzzle, from two timing signals and issuing a trigger for other plasma diagnostics - are all being summed into one transient recorder channel in the Launcher data acquisition system.

Control and data acquisition interface

The multi-pellet injector has a dedicated computer (ND100, dubbed PL) in the chain of the individual subsystems in the JET control and data acquisition system CODAS. The Pellet Interface subsystems - vacuum services, LHe and gas supply to the launcher as well as the interlocking of the launcher to the PIB are controlled and monitored by a programmable controller (AB PC 5/15) which in turn communicates with PL for remote operation from the main control room. PL's second task is to collect the relevant pellet diagnostic data from the Launcher's computer to make them available for the JET pulse file. A plasma protection system PLPS under the guidance of PL provides pellet interlocks against conditions where the plasma would permit the pellet to reach the inner wall of the torus or would suffer avoidable disruptions.

Status

The major part of the Pellet Interface is commissioned and no major discrepancies with the intended design have been found. First bursts of pellets have been fired into the plasma. However, as can be expected with a complex interface as this and the time given to build it, a number of smaller points have still to be ironed out, the main ones being on the LHe supply logistics and economy, the upgrading of the maximum PIB pressure and the final commissioning of all pellet diagnostics.

Later Active Phase implications

The arrival of the high-speed gun will require the extension of the rear platform because of the likely use of longer barrels and rear and front insert may have to be redesigned if the number of gun lines for the advanced guns and the differential pumping capability have to be increased. The liquid helium valve box may have to get a number of additional outlets. However, the major part of the Pellet Interface already fulfills the Active Phase requirements when the gas handling is adequately dealt with: The formation of pellets of deuterium and likely tritium is thought to be of the cryocondensation type for reasons of minimum tritium inventory and the gas cycle has to be closed with the tritium recovery plant [9], the transfer of the PIB regeneration release may be done by a cryocompressor pump leaving the turbo-molecular pump for initial pump-down or for maintenance tasks. If the present assumption of an almost tritium-free hydrogen will materialise in the future then this will ease the maintenance of the propellant part of any future gun considerably and leave the tritium problem to be solved for the much less severe case of the (low pressure) pellet formation unit.

Acknowledgements

In designing and constructing the Pellet Interface the help of many JET groups, in particular from Neutral Injection and CODAS, as well as the lively individual interactions inside JET and with the US partners are very much appreciated and gratefully acknowledged.

References

[1] The JET Team, "The JET Technical and Scientific Performance and Future Plans", presented at 7th Topical Meeting on Technology of Fusion Energy, Reno, USA, June 1986.

[2] M. L. Watkins et.al., "Predictive Studies of Neutral Beam and Pellet Injection on JET", presented at 13th European Conference on Controlled Fusion and Plasma Heating, Schliersee FRG, April 14-18, 1986.

[3] P. Kupschus, "JET Pellet Injector Development", presented at the International Pellet Fuelling Workshop, La Jolla, USA, Oct 30-Nov 3, 1985.

[4] K. Sonnenberg et.al., "High Speed Pellet Development", this symposium.

[5] S. L. Milora et.al., "Design of a Repeating Pneumatic Pellet Injector for the Joint European Torus", this symposium.

[6] R. Haange et.al., "JET Neutral Injection Beamline System Manufacture and Assembly", in Proceedings of 11th Symposium on Fusion Engineering, Austin, USA, 1985, pp. 1259-1264.

[7] W. Obert et.al., "The JET Cryopump System and its Cryolines for Neutral Injection", in Proceedings of 13th Symposium on Fusion Technology (SOFT), Varese, Italy, 1984, pp. 311-318.

[8] W. Obert et.al., "Operation and Performance of the Large Scale JET Cryopump System", in Proceedings of 14th Symposium on Fusion Technology (SOFT), Avignon, France, 1986, pp. 479-486.

[9] J. Hemmerich, "The JET Tritium Recycling Systems Concept and Status", this symposium.

HIGH SPEED PELLET DEVELOPMENT

K Sonnenberg, P Kupschus, W Bailey: JET Joint Undertaking, Abingdon, Oxfordshire OX14 3EA;
J Helm, P Krehl: EMI; G Claudet, F Disdier, J Lafferranderie: CENG

Summary

Advanced pneumatic propulsion systems have been developed using two stage and arc heater guns. For pellet preparation a freezing cell for condensing the d_2-gas is incorporated into the gun barrel. Results on the optimization of condensation parameters to find the mechanical limits of deuterium ice and of accelerations tests using a 2-stage gun with plastic as well as d_2-pellets are discussed. It appears that two stage gun systems can provide a rather constant acceleration even in their low pressure regime suitable for pellet injection. The peak acceleration tolerable for d_2-pellets, however turned out to be less than 5.10^6 ms^{-2} and a serious erosion effect of the pellet makes the use of long gun barrel rather problematic.

At present it is concluded that only the sabot technique can overcome the stress and erosion effect limitations.

1. Introduction

Pellet injection far beyond the recycling zone aims at improved plasma properties such as an increased central density, a larger central particle confinement time and a reduced Z_{eff} (see e.g. [1,2]). Such improvements have been obtained at JET with pellet velocities of the order of 1 km/s; this is sufficient to deposit the main pellet mass beyond the q=1 surface for present plasma conditions. To inject pellets similarly deep into hotter plasmas with larger NB- and RF-powers, higher pellet velocities towards 10 km/s would be required.

For this reason JET has initiated a development program for high speed pellet injectors [3]. JET thereby concentrated on the development of pneumatic propulsion guns because alternative more advanced systems appear unlikely to be completed within the time frame of JET. Conventional pneumatic guns, consisting of a pressure reservoir at room temperature, from which the propellant gas is released via a fast valve, have the intrinsic problem that the driving pressure for the pellet decreases strongly when the gas velocity in the barrel exceeds the sound velocity (≈ 1300 m/s for H_2) [4]. To improve this situation the propellant gas has to be heated for higher sound velocity and the reservoir pressure must be increased during the acceleration process to keep the driving pressure as constant as possible.

2-stage gun systems in which the hydrogen propellant gas is heated by adiabatic compression in the first stage automatically provide also an increase of the reservoir pressure during acceleration. Employing 2-stage guns velocities of up to 10 km/s indeed have been achieved in the past [4]. These experiments however were performed with very high peak pressures (10^4 bar) and much stronger projectiles. In contrast d_2-ice can only withstand much lower pressures (probably ≤100 bar). In order to test whether a 2-stage gun is suitable for this particular problem a test stand has been set up at the Ernst Mach Institute (EMI) in Freiburg (Germany) which will be described in detail in section 2, together with some results for plastic pellets. Preliminary results employing deuterium pellets with the same set-up will be discussed in section 4. Recently another group has published some first results of d_2-pellet acceleration with a 2-stage gun [5].

An alternative method of heating the propellant gas and of tailoring the reservoir pressure is to use an electric arc the power of which can be controlled during the acceleration process. JET and the National Laboratory at Risø have set up such a test facility. Details of the status and results of this system will be described elsewhere [6]. Some earlier results for this method using a smaller device are published [7].

For the pellet preparation JET follows up the pipe gun system [e.g. 8], i.e. the pellet is produced by condensing deuterium gas into a freezing cell located at the end of the gun barrel. Results on the optimization of the condensation parameters will be discussed in section 3.

2. Two-Stage Gun at EMI, Freiburg

In order to obtain results as quickly as possible an extremely simple design for the 2-stage gun was chosen. In particular no effort was made to build the system for fast repetitive operation, which would of course be imperative for a final JET injector. During the initial phase of the experiment plastic (styrofoam) pellets were used with the same weight, same diameter and a similar strength as d_2-ice pellets.

The tests stand (see Figure 1) consists of a pressure reservoir, a driving cylinder and a gun barrel. The 3 components are separated by 2 rupture discs. By cutting the first disc with the punching tool the high pressure He-gas drives the piston into the cylinder thereby compressing and heating the H_2-propellant gas. When the pressure in the cylinder reaches the critical value the second bursting disc ruptures and the pellet starts being accelerated. The bursting pressure of this disc is chosen to be compatible with the strength of the pellet (≤100 bar). The pellet motion can be measured by time of flight sensors positioned along the barrel. This allows to calculate the velocity and with less accuracy the acceleration of the pellet as a function of time. The

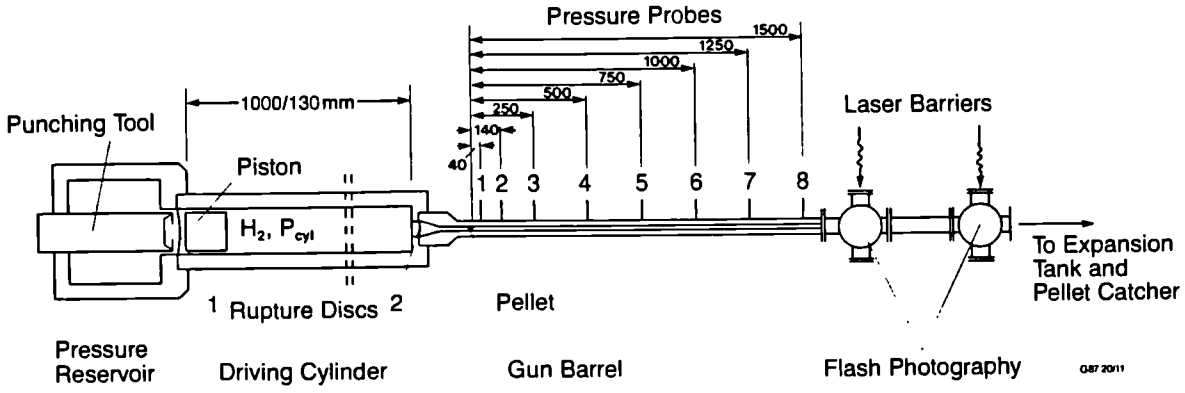

FIG. 1: Schematic Diagram of EMI 2-stage gun.

final pellet velocity is determined by two laser barriers outside the barrel which also trigger the flash photography of the pellet. Pressure probes are employed as time of flight sensors; they also provide approximate values of the static pressure of the propellant gas. The static pressure value shortly after the pellet has passed the sensor is a measure of the pressure causing the acceleration of the pellet. The time dependence of the pressure after the pellet has passed indicates how fast the compression wave generated by the piston can follow the pellet.

Given the mass (≈0.035g) and an upper limit for the strength of the pellet (≲100 bar) the geometry (length, diameter) of the driving cylinder and the gun barrel are then determining the optimal value for p_{res}, and the initial p_{cyl}. For the 2 lengths of cylinders studied so far (Fig. 1) numerical calculations employing a simple adiabatic heating model for the H_2-propellant gas suggest pressure values as listed in Table I. These values have been confirmed experimentally.

Table I

length of the driving cylinder	p_{res} (bar)	p_{cyl} (bar)
0.13 m	200-250	20-40
1.0 m	150-200	3-6

In figure 2a (L_{cyl} = 0.13m) and 2b (L_{cyl} = 1m) the measured pellet velocity and acceleration along the gun barrel are shown for typical shots. The acceleration generated by the short cylinder is falling quickly from its initial value of about $10^7 ms^{-2}$. In contrast for the longer cylinder, the acceleration goes through a maximum thus providing a higher average acceleration and final velocity (up to 4500 m/s). Qualitatively the same conclusion can be drawn from the pressure signals shown in Figure 3a, b. The static pressure values relevant for driving the pellet are encircled.

The reason for the much better performance of the long cylinder lies in a much higher gas temperature which is due to a higher compression ratio. The initial pressure in longer cylinder is much lower and consequently when the critical pressure (same in both cases) of the bursting disc is reached, the propellant gas is already more compressed and much hotter as a result of adiabatic heating.

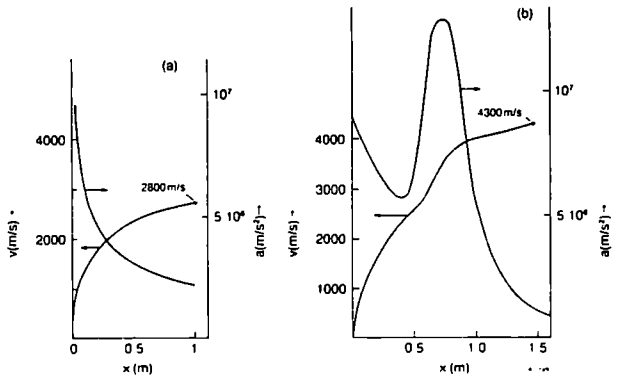

FIG. 2: Measured pellet velocities and acceleration along the gun barrel (a: 0.13 m cylinder; b: 1.0 m cylinder).

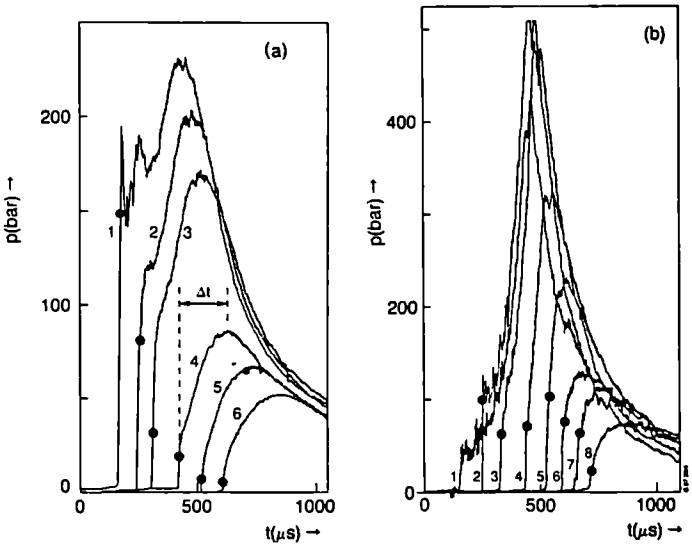

FIG. 3: Pressure as a function of time measured by the pressure probes along the gun barrel (a: short cylinder, b: long cylinder).

In the case of a constant reservoir pressure a higher gas temperature provides a higher driving pressure for a certain gas-, and pellet velocity or higher velocity for a certain driving pressure (see "gun equation" [4]). An additional effect is important for the 2-stage gun since the reservoir pressure is increasing during the pellet acceleration. This generates a compression wave which can travel faster into the gun barrel through a hotter and also faster streaming gas. This effect can be seen when comparing the timelag, Δt between the pressure peak and the pellet detected by the pressure sensor. It appears that the compression wave generated by the longer cylinder can catch up with the pellet resulting in a peaked acceleration as seen in Figure 3b.

JET is in the process of constructing a new 2-stage-gun test stand with several improvements. It will be equipped with even larger driving cylinders (length up to 3m; diameter 80 and 120mm respectively) and gun barrels (5m long). This will allow still higher gas temperatures and probably a more constant driving pressure during the acceleration. Efforts are made to develop the system towards a repetitive system, i.e. substituting the bursting disc by fast opening valves and take precautions to avoid damage on the piston upon impact onto the end face of the driving cylinder.

3. Pellet Preparation

Tests have been set up at CEN Grenoble to investigate the condition under which the deuterium gas must be condensed into the freezing cell of the pipe gun to achieve good mechanical properties of the d_2-ice. The main features of this test stand (for details see [8]) are schematically shown in Figure 4.

For studying the pressure limits which the d_2-ice can withstand, a fast electromagnetic valve has been developed and incorporated into a 300-bar reservoir. The unit can supply the H_2-propellant gas into the gun barrel at a rate to accelerate a 6 mm diameter, 8 mm long d_2-pellet with about $4.10^6 m/s^2$.

The formation of the pellet is controlled by:

- the temperature of the freezing cell, T_c
- the temperature gradient adjacent to the cell. The gradient is controlled by the temperature, T_g of cold sinks 20 mm apart from the freezing cell
- the condensation pressure, p
- the condensation time

The size of the pellet can be effected in the

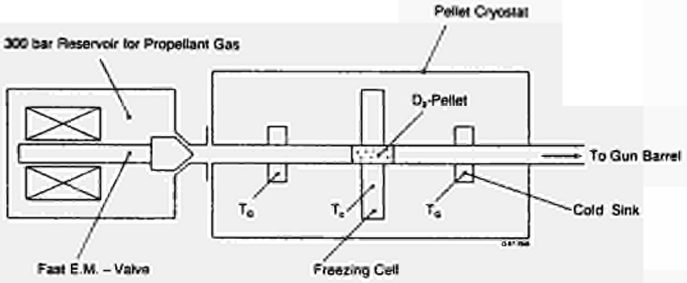

FIG. 4: Schematic diagram of pellet preparation and - test system at CEN Grenoble.

following way: The length increases with condensation time till equilibrium conditions are reached (typically after 10 min). For a range of parameter as listed in the second column of Table II the pellet can grow up to about twice the thickness of the freezing cell. For a fixed condensation time the pellet length increases with decreasing T_C, with decreasing temperature gradient and increasing condensation pressure. Qualitatively such a behaviour must be expected from the phase diagram of deuterium.

Table II

Parameter	Range	
	investigated	good ice quality
condensation time (min)	3-10	4
T_C (K)	6-15	10-12
T_g(K)	20-100	35-50
p (mbar)	8-185	10-20

Although an independent variation of all 4 parameters within the limits given in Table II (first column) have not been performed certain conditions have been unfolded which are less favourable for good quality pellets: A high condensation pressure generating a gas - liquid - solid phase transition results in concave shaped end faces which often break off during the acceleration. On the other hand pellets produced at a very low pressure (≤10 mbar) are also less strong. Very low cell temperatures (≤9K) particularly if associated with high temperature gradients ($T_g \geq 50$K) result in pellets which break up more easily. Broken pellets have been observed if condensation time is less than 3 min. Good quality pellets have been formed for conditions listed in column II of Table I.

It should be noted that it is important to accelerate the pellet with a low ice temperature. It seems that the pellet becomes too soft above ≈9K.

Another important aspect for efficient acceleration is a high pressure for breaking the ice off the freezing cell walls if rupture discs or fast opening valves behind the pellet can not be employed. This break away pressure seems to be determined by the shear strength of the ice and by the length of the pellet. For an ice temperature ≤9K and a pellet length of ≈ 8mm "breakaway" pressure values of ≈ 25 bar have been found.

A feature, probably characteristic for pellets produced by condensation, is shown in Figure 5. The pellets are fractured more or less parallel to the pellet axis. It has been observed (EMI-teststand) that this particular disintegration sometimes happens after the pellet has already left the gun barrel. It is not clear why the pellets break apart in this way but it may be due to the fact that the pellets often contain long pores and probably cracks which are aligned in the axial direction. Pressurising the pores by the driving gas could cause the disintegration of the pellet since the external pressure may be relieved faster.

FIG. 5: Fractured pellets.

4. Preliminary Results for D_2-Pellets at EMI:

A pellet forming cryostat has been combined with the 2-stage gun (long driving cylinder) at EMI. The following results have been observed:
Under conditions (p_{res}, p_{cyl} and a "100 bar" rupture disc) which provided the best results for plastic pellets, none of the d_2-pellets survived; probably due to two reasons: The earlier estimate that d_2-pellets can withstand accelerations of about 10^7 ms^{-2} could not be confirmed, instead an upper limit of 3-5.10^6 ms^{-2} has been found. These values, however, could only be obtained without employing bursting discs. It seems that shock waves generated by the disc rupture can destroy d_2-pellets under almost any pressure conditions.

D_2-pellets which reach velocities higher than ≈1500 m/s all show a more or less reduced diameter when photographed after leaving the gun barrel. Evaporation by heat conduction due to the contact with the warm (room temperature) gun barrel can be excluded. Pellets which move very slowly (≈ 50 m/s) through the gun barrel do not show any reduction in diameter although they are much longer in contact with the barrel. Another possibility is that hot driving gas bypasses the pellet, thereby vaporizing outer layers of the pellet. This would be consistent with the fact that a pressure increase (see Figure 6) is detected ahead of the pellet, which gets enhanced as the pellet moves down the barrel. Such an effect has never been

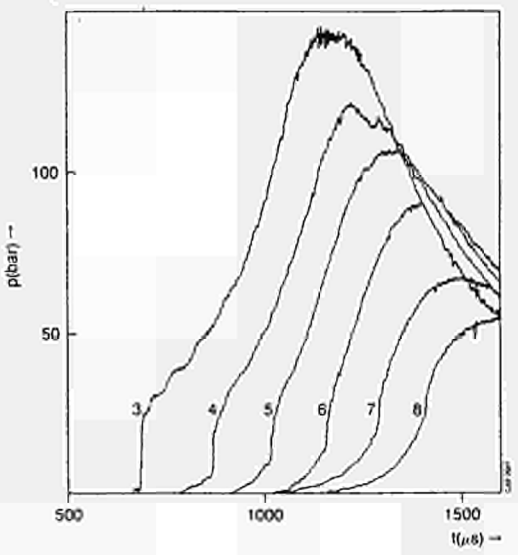

FIG. 6: Typical pressure signals measured during the acceleration of d_2-pellets.

observed for plastic pellets (compare Figure 3a, b). For this reason a d_2-pellet was fired together with a plastic pellet so that the ice pellet was riding on the front face of the plastic pellet. Even under these conditions which exclude any effect of a bypassing driver gas the same result has been observed. We believe that the vaporization is caused by friction between the pellet and the wall which is expected to increase with increasing pellet velocity.

The reduction in diameter has a serious consequence for the pellet acceleration since a pellet with a smaller diameter becomes less stable and may start tumbling in the barrel whereby the pellet would get destroyed.. It has been found that this effect is particularly harmful when the acceleration curve is peaked towards the end of the barrel, where the pellet is already unstable. Here pellets are found broken already at acceleration values as low as 2.10^6 ms^{-2}. The best results have been obtained, when the driving pressure peaks during an early state of the acceleration. A pellet fired under such conditions is shown in Figure 7. Using a reservoir pressure, p_{Res} = 90 bar and an initial H_2-pressure in the driving cylinder, p_{cyl} = 2.3 bar pellets have reached velocities of up to 2650 m/s. The maximum acceleration occurring after 0.25 - 0.5m is ≈ 5.10^6 ms^{-2}.

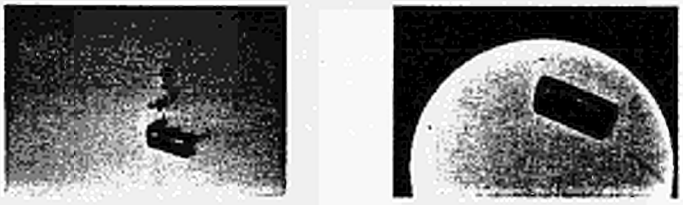

FIG. 7: D_2-Pellet flying with a velocity of about 2500m/s. Position 1 and 2 are about 100 mm and 300 mm respectively from the muzzle of the gun barrel. In position 2 the pellet is shown enlarged by a factor 1.8 as compared to position 1.

From the first experiments with d_2-pellets we must conclude that the objective to reach 5000 m/s cannot be achieved with the present set-up, mainly since

1) the tolerable peak acceleration value (<5.10^6) is less than half the estimated value,
2) the pellet is strongly eroded, probably due to friction effects.

The first problem could perhaps be solved by employing longer gun barrels together with larger sized driving cylinders. Because of the erosion effects, which make the pellet more unstable, it seems, however, unlikely that a much longer gun barrel can be used. A possible solution would be to employ a sabot technique for supporting the d_2-pellet. This would eliminate the erosion effect and would allow to use very long gun barrels. It is also very likely that higher acceleration can be applied since the d_2-ice would be very well supported. Furthermore shock waves generated by rupture discs will be less harmful.

The presently used cryostat is of course not very well suited to condense a d_2-pellet into a sabot, because the latter would reduce the heat exchange with the freezing cell. Nevertheless some preliminary tests have been performed using plastic (Vespel) sabots as shown in Figure 8c; 6 slots machined into the wall of the sabot provide a sufficient heat exchange with the freezing cell. Such a "cage" type sabot of course does not provide an optimal support for the d_2-pellet and it therefore cannot be expected to improve the peak acceleration substantially. It does, however, make the

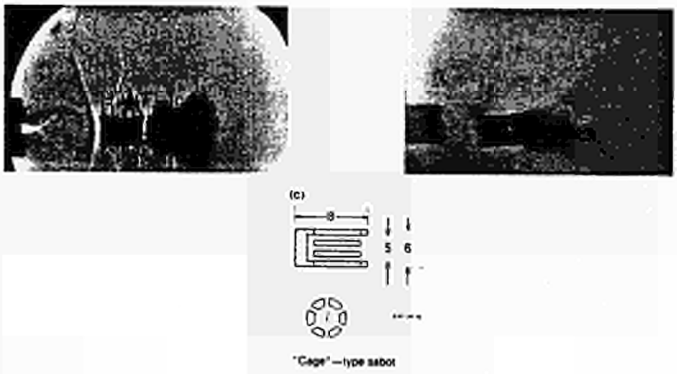

FIG. 8: After condensing a d_2-pellet into a plastic sabot (see c) positioned in the freezing cell, both were accelerated together.

pellet less susceptible to shock waves (bursting disc can be employed) and it prevents the pellet from tumbling. Fig. 8a,b show the plastic pellet and the d_2-pellet just outside the barrel (position 1) but already separated and ≈ 100 µs later in position 2. In the first position dense cold d_2-gas still comes off the d_2-pellet, whereas the shape of the solid d_2-pellet becomes clearly visible in Fig. 8b. Without changing the dimension of the driving cylinder and the gun barrel 3400 m/s have been reached with the "cage" type sabot. Higher values may be expected for larger 2-stage guns and employing closed sabots for a better support of the pellet.

References

[1] A. Gondhalekar, 11th Conference on Plasma Physics and Controlled Nuclear Fusion Research, Kyoto, Japan, 1986.
[2] A. Cheatham et.al., 14th European Conference on Controlled Fusion and Plasma Physics, Madrid, 1987.
[3] P. Kupschus, International Pellet Fuelling Workshop, La Jolla, 1985.
[4] A. E. Seigel, NATO Report, AGARD 91.
[5] A. Reggiori and F. Scaramussi, 14th SOFT, Avignon, France, 1986, p.1381.
[6] S. A. Andersen et.al., to be published.
[7] S. A. Andersen et.al., 14th SOFT, Avignon, France, 1986, p.1361.
[8] J. Lafferranderie et.al., 14th SOFT, Avignon, France, 1986, P.1367.

EXPERIENCE WITH GRAPHITE IN JET

M A Pick, G Celentano, E. Deksnis, K J Dietz, R Shaw, K Sonnenberg, M Walravens
JET Joint Undertaking, Abingdon, Oxfordshire OX13 3EA

Abstract

During the current operational period of JET more than 50% of the internal area of the machine is covered in graphite tiles. This includes the 15 m^2 of carbon tiles installed in the new toroidal limiter, the 40 poloidal belts of graphite tiles covering the U-joints and bellows as well as a two metre high ring (- 20 m^2) of carbon tiles on the inner wall of the Torus. A ring of tiles in the equatorial plane (3 tiles high) consists of carbon-carbon fibre tiles. Test bed results indicated that the fine grained graphite tiles cracked at ≈ 1 kW/cm^2 for 2s of irradiation whereas the carbon-carbon fibre tiles were able to sustain a flux, limited by the irradiation facility, of 3.5 kW for 3s without any damage. We report on the generally positive experience we have had with the installed graphite during the present and previous in-vessel configurations. This will include the physical integrity of the tiles under severe conditions such as high energy run-away electron beams, plasma disruptions and high heat fluxes. We report on the importance of the precise positioning of the inner wall and X-point tiles at the very high power fluxes of JET and the effect of deviations on both graphite and carbon-fibre tiles.

1. Introduction

The JET machine is successfully progressing along its prescribed path to reach near-reactor conditions. Plasma wall interactions form an integral part of the plasma confinement behaviour and the successful operation of JET is to a large part due to the generally favourable characteristics of the first wall of JET.

Early on it became clear that there are presently only two practical materials for the internal surfaces of the machine, carbon and beryllium [1]. Although beryllium may be utilised in JET in the future, till now only carbon has been used. During its relatively short lifetime JET has evolved into a machine whose inner surface is predominately covered in carbon. This carbon is in the form of high purity fine grain graphite tiles, carbon fibre reinforced graphite tiles and a carbonised inconel wall.

In order to summarise the experience with graphite in JET we will concentrate more on the few problems and their solutions than on the generally good behaviour under operation. The main reasons for the choice of graphite are:

- low Z, therefore low radiation losses.
- the ability to withstand high temperatures without melting.
- good resistance against thermal shock in particular due to the long mean free path of electrons in the material.
- the ability to use a simple method (glow discharge cleaning in mixtures of hydrogen and methane) to cover all surfaces with a layer of carbon.
- easy machinability.
- low toxicity.
- low price.

The main problems associated with the extensive use of graphite in tokamaks are related to its complicated interaction with hydrogen. This is caused in part by the porosity of the material as well as the chemical affinity of carbon to hydrogen. These properties can lead to problems with density control and particle balance and this is one area which is currently under in-depth investigation. Another potential problem, for future machines, is the fact that it is difficult to find a practical solution to cool graphite directly.

2. The Graphite Materials

The material of the fine grain graphite tiles installed in JET was, on the basis of tests [2,3], selected to be that supplied by two manufacturers:

EK 986 by Ringsdorff-Werke GmbH and
5890 PT by Le Carbone-Lorraine.

Tiles of these materials have been shown to operate well with a load of 5 MW/m^2 for 10 s [3]. Under these conditions the surface of the tile will tend to heat up to the 2000° operational temperature limit and just begin to erode material through sublimation. The tiles can take higher loads for shorter times; for example, at about 10MW/m^2 they begin to show evidence of thermal shock damage and fracture at times longer than 3 s.

The requirement to protect the inner wall of JET in the case of a failure of the neutral beam injection protection system in turn resulting in the exposure of the inboard wall to an unattenuated beam, led to the evaluation and testing of carbon fibre reinforced composite graphite (CFC) tiles [3]. It was shown that such tiles are capable of withstanding 35 MW/m^2 for times exceeding 3.5 s. The effect of such a thermal load on the selected CFC tiles is merely moderate surface erosion and no serious physical damage such as cracking. Two materials by the following suppliers were selected for installation:

DMS 678 by Dunlop and
A05G by Le Carbone Lorraine

Data on the materials selected for installation in JET as well as, for comparison, those for pyrolytic graphite and beryllium shown in Table I. Pyrolytic graphite and beryllium are considered as alternative materials for specific areas in JET exposed to high heat fluxes, i.e. pumped limiters, belt limiters etc. More detailed information is given in [4].

	Fine Grain Graphite		Carbon Fibre Composite		Pyrolitic Graphite	Beryllium
	Ringsdorff EK 986	Le Carbone Lorraine 5890 PT	Le Carbone Lorraine A05G	Dunlop DMS678		S65—B
Density kgm^{-3}	1850	1850	1770	1900	2200	1850
Thermal Conducitivity $Wm^{-1}K^{-1}$	90	∥ 92 ⊥ 75	200	∥ 250 ⊥ 70	∥ 300 ⊥ 1.5	120
Specific Heat	700	700	700	700	700	2700
Elastic Modulus GPa	11	∥ 16 ⊥ 14	17	30	29	220
Flexural Strength MPa	50	∥ 65 ⊥ 60	100	125	85	330 (Tensile)
Therm. Exp. Coeff. $\times 10^6$ K^{-1}	3.8	∥ 5.2 ⊥ 6.2	∥ 1.0 ⊥ 8.0	∥ 1.1 ⊥ 13.7	∥ 1.8 ⊥ 23	13
Porosity %	8	8	8	6	-	1

Table I: Data for various materials used in JET as well as those of possible future interest. Data is taken from suppliers' data sheets and given at ambient temperatures.

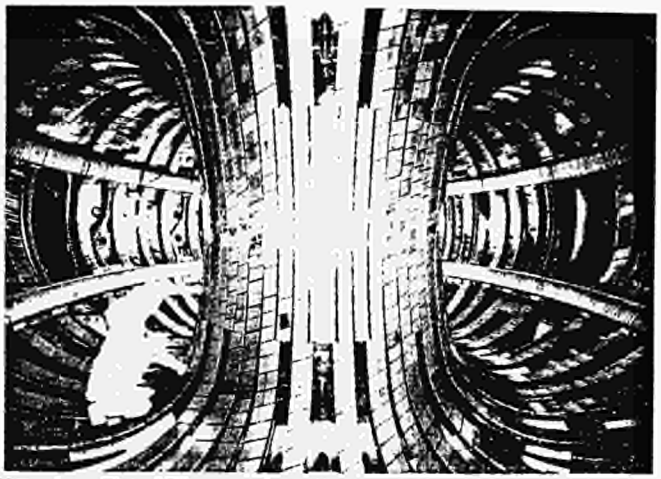

Fig. 1: The JET vessel with graphite tiles and belt limiter installed (mid 1987).

3. The Inner Wall of JET

3.1 The present configuration

Fig. 1 shows the interior of the JET machine in mid 1987 before the start-up of the present operational period. The present configuration of the first wall is a result of steady improvements based on experimental experience.

Over 50% of the internal surfaces are now covered with graphite. All octant- and bellows-joints are completely covered in graphite tiles. The inside wall is covered with graphite over an area extending one metre above and one metre below the mid-plane. The region of the mid-plane itself, three to four tiles high, is covered in carbon fibre reinforced graphite tiles. Carbon fibre reinforced graphite tiles have also been attached to those areas of the inner wall, not visible in this picture, which could be subjected to the neutral beam shine-through, as well as similar areas in the outer wall. The newly installed belt limiter, capable of withstanding 40 MW of power for 10 seconds, contains 1716 graphite tiles. These tiles are radiatively cooled by water cooled nickel fins located between them. Two of the new RF-antennae can be seen between the belt limiter rings. These antennae are also protected on both sides by a similar arrangement of radiatively cooled graphite tiles.

3.2 The inner wall after operational period

Figs. 2 and 3 show the inner wall of octants 3 to 6 after the 1986 operational period. During this period the total power in the plasma reached about 20 MW for up to 3 seconds with a plasma current of up to 5 MA. The inner wall was protected by graphite tiles throughout. It was also during this period that the inner wall was, contrary to its design, used as a limiter for numerous discharges. This was done due to the beneficial properties such discharges exhibited in terms of strongly decreased recycling coefficients, i.e. wall pumping [5,6]. Damage to the tiles was minimal but what did occur was concentrated at the mid-plane and the octant joint areas. Careful surveys of the inner wall of JET during previous shutdowns have established that the inner wall is not completely circular. These deviations are, in the first place, due to the design of the vessel. The vessel is comprised of forty sections, five sections are each connected with bellows to form an octant. The inner wall, therefore, is essentially a polygon. The results of a survey are shown in Fig. 4. In addition to those deviations which are inherent in the design of the vessel there are some slight deformations of the vessel, caused most probably by the support structure and the additional equipment attached to the torus, e.g. neutral beam, pumps and diagnostics. The cumultative result for the inner wall is that the areas in the region of all the octant joints protrude slightly into the vessel, in particular in the case of octant joint 3/4. All the octant joint tiles at the mid-plane suffered damage to some degree. The most severe, which occurred at octant joint 3/4 is shown in Fig. 5. The uniform power loading of the other octant joints indicates that the axis of the inner wall structure coincides with the axis of the magnetic field during operation.

Damage such as that observed on the inner wall tiles in Fig. 5 is caused primarily by runaway electrons which are generated during disruptions. At the end of a disruption these electrons typically impinge as a beam on the inner wall thereby damaging it as well as activating it and creating bursts of hard x-rays and neutrons. Runaway electrons can also be created during the initial plasma break down or during the steady state. These runaways tend to impinge on the mid-plane of the outer wall of tokamaks. The conditions which lead to such runaways, however, are now readily avoided in JET. There is only one example of damage, albeit slight, caused by runaways hitting the outer wall; that is described in [7]. The damage shown in Fig. 5, is caused, in part, by the non uniform heating of the inconel attachment rod within the tile [7]. Such a non-uniform heating of the rod will cause it to bend and thereby to exert forces on the tile.

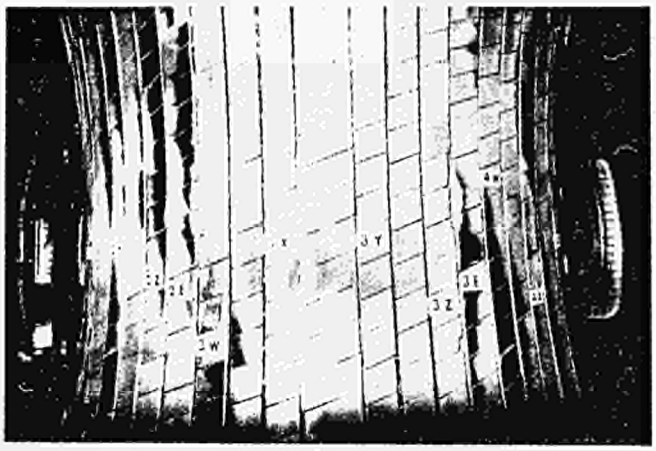

Fig. 2,3: The inner wall of JET, at octants 2 to 7, after the 1986 operational period. Damage to the tiles is concentrated at the mid-plane of the octant-joint areas, in particular the octant-joint 3/4.

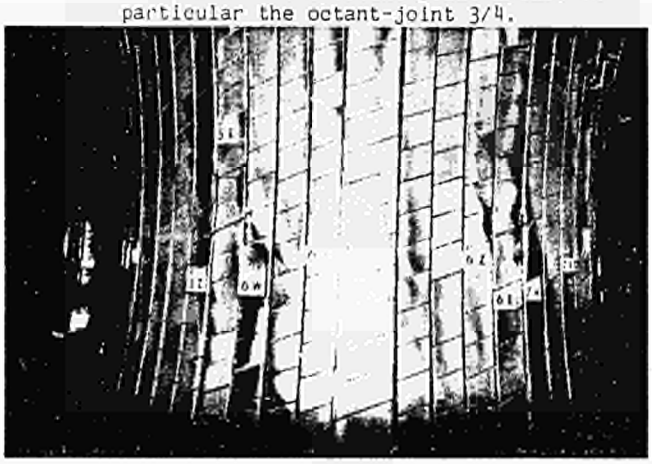

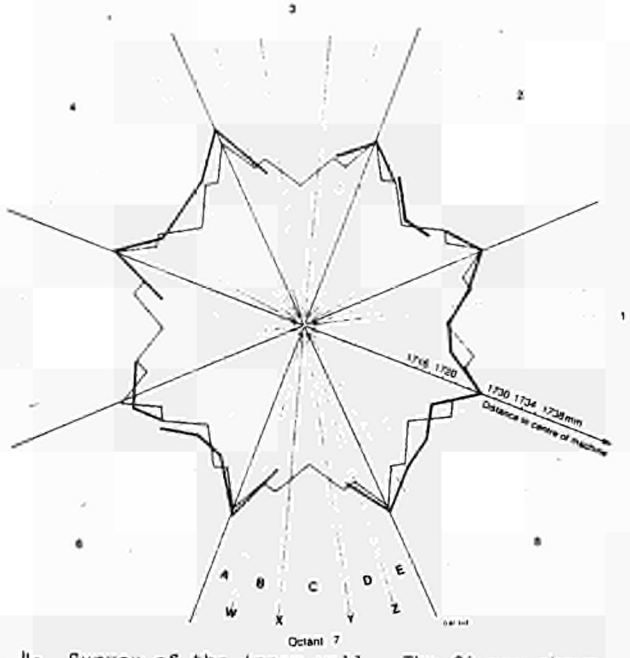

Fig. 4: Survey of the inner wall. The figure shows that the inner wall deviates from circularity by several millimeters. The thin line is the theoretical shape given by the design of the machine and the thick line represents the results of the survey.

Under extreme cirumstances this can result in fracturing of the tile in the region of the attachment rods. This region of the tile is inherently the weakest and is prone to fracturing under power loading even without the additional stress caused by the bending rods. In a new design of the tile attachment the diameter of the rods has been decreased from 10mm to 6mm in the central region between the attachment screws. The rods may, therefore, now bend slightly without causing undue forces on the tiles.

Fig. 5 Damage to the tiles at mid-plane of octant-joint 3/4. This is the most severe damage which occurred and is due to impinging high energy runaway electrons generated during disruptions.

3.3 Comparison of graphite- and CFC-tile damage

Figure 6 shows two tiles, one graphite and the other carbon fibre reinforced graphite, which were located at the same position at the mid-plane of the octant joint 3/4. The tile on the left is the fine grain graphite tile which was in the vessel during the 1986 operational period. During this time the total power in the plasma reached about 20 MW for up to 3 seconds with a plasma current of up to 5 MA. This tile suffered extensive damage caused by high energy runaway electrons, due to one or more disruptions, hitting this area which protrudes the furthest into the vessel. The tile exhibits large cracks, as the tiles shown in Fig. 5, and in addition it shows evidence of localised fine scale cracking characteristic of thermal shock.

The carbon fibre reinforced graphite tile, on the other hand, although it shows evidence of substantial erosion, is clearly intact and capable of still fulfilling its role as a protection of the vessel. This fibre reinforced tile was installed in JET during the previous main shutdown (1986-87). It was installed in the same position as the graphite tile shown next to it. Although it was only in the vessel for six weeks of operation it was, nevertheless, subjected to intense high energy runaway electron beams. During the six weeks of operation the total power in the vessel reached about 10 MW for up to 3 seconds with currents up to 3 MA. From the amount of material which has been eroded (about 2mm deep) we can deduce that this tile must have suffered a load of at least 2MJ over an area of 5 x 7 cm.

Fig. 6: Two tiles, one graphite (left) and one (CFC) carbon fibre reinforced graphite (right) which had been located at the same spot of the octant-joint 3/4. The graphite tile has fractured whereas the CFRC-tile, although eroded, is intact and still protects the vessel.

A noteworthy feature here is that the CFC tile has been found to contain substantial amounts of the excited isotope ^{7}Be. The presence of ^{7}Be can only be explained if the tile were hit by a substantial beam of electrons with an energy well above 30MeV. The threshold energy for the production of ^{7}Be from ^{12}C by the reaction $\{\gamma,x(x=\alpha n)\}$ is 26.3 MeV. The excited ^{7}Be falls to its ground state by the emission of 477.56 KeV γ-quants and a half life of $T_{1/2}$=53.4 days and it is these γ-quants which are recorded [8].

The preliminary experience with the installed CFC-tiles and the results of the previously conducted tests, together make a strong case for the installation of such tiles in all areas which are liable to be subjected to runaway electrons or power fluxes in excess of MW/m^2 for 10 seconds.

4. Conclusion

From a point of view of protecting the vessel it has been found that graphite and, in particular for areas where the power deposition can exceed 5 MW/m^2 for 10 s, carbon fibre reinforced graphite tiles can perform very well. As long as the power deposition is kept within the limits specified the major effect of the installed graphite is to dilute the plasma with carbon. A study of the cumultative erosion and redeposition of carbon on the graphite limiters during the 1986 campaign has been published [9]. It was estimated that during that campaign ~ 200 μm had been eroded from the limiter, or about 60 nm per discharge. Very high and localised loads such as can occur on the inner wall after disruptions do damage graphite tiles by causing the material to fracture at its weakest point. It is probably possible to raise the load limit on such graphite tiles by 20% by a very careful design of the tile fixing mechanism. At the moment it is the stress intensification (approximately a factor of 3) aggravated by the bending of the attachment rods, which occurs at the fixation holes, which determines the limit. This factor of intensification could be lowered somewhat in an integral design. The carbon fibre reinforced graphite tiles have proven to be particularly effective in their role as vessel protection. The combination of their more favourable properties (see Table I) results in merely enhanced erosion (sublimation) under extreme load conditions.

At present most of the damage to the inner wall tiles is due to, or has at least been aggravated by, the unequal loading. This is caused by the hitherto unappreciated slight variations in the radial distance of individual tiles from the centre of the machine. This variation, which is on the order of several millimeters, will have to be eliminated in order to distribute the power loading of the tiles more evenly thereby reducing the risk of tile damage. A very similar situation exists with regard to the X-point tiles at the top and bottom of the machine. The obvious next step, therefore, is to carefully reposition all tile fixations. From the fact that all the octant joints, with the exception of the 3/4 joint, have suffered what appears to be quite similar loadings, it is evident that the magnetic centre coincides with the structural centre of the JET machine to within 1-2 millimeters.

References

[1] P. H. Rebut et al., JET-R(85)03.

[2] A. Stabler et al., JET-DN-C(85)19.

[3] P. Massman et al., Proc. 14th SOFT, Avignon, 1986 (Pergamon Press, 1986), p.545.

[4] W. Delle et al., JÜL-Spez-401, May 1987.

[5] S. A. Cohen et al., 14th European Conf. on Controlled Fusion and Plasma Phys. (Madrid, Spain, June 1987) to be published in: Plasma Physics and Controlled Fusion.

[6] J. Ehrenberg et al., JET-P(87)23.

[7] M. Huguet et al., Proc. 11th Symp. Fusion Eng., Austin 1986 (IEE-publication, 1986), p.1238.

[8] G. Sadler et al., JET-IR(86)04, p.85.

[9] J. P. Coad et al., JET-P(87)23.